Transactions of the ASME®

Technical Editor, **LEWIS T. WHEELER**

Department of Mechanical Engineering,
University of Houston,
Houston, TX 77204-4792

APPLIED MECHANICS DIVISION

Chairman, **A. NEEDLEMAN**
Secretary, **S. KYRIAKIDES**
Associate Technical Editors,
J. R. BARBER (2000)
R. C. BENSON (2000)
M. M. CARROLL (2000)
W. J. DRUGAN (2000)
A. A. FERRI (2000)
J. W. JU (2001)
V. K. KINRA (2002)
D. KOURIS (2002)
S. KYRIAKIDES (2000)
A. K. MAL (2001)
B. MORAN (2002)
A. NEEDLEMAN (2001)
M. ORTIZ (2001)
N. C. PERKINS (2002)
M.-J. PINDERA (2000)
K. T. RAMESH (2000)
K. RAVI-CHANDRA (2002)
D. A. SIGINER (2000)

BOARD ON COMMUNICATIONS

Chairman and Vice-President
R. K. SHAH

OFFICERS OF THE ASME
President, **R. E. NICKELL**
Executive Director, **D. L. BELDEN**
Treasurer, **J. A. MASON**

PUBLISHING STAFF
Managing Director, Engineering
CHARLES W. BEARDSLEY
Director, Technical Publishing
PHILIP DI VIETRO
Managing Editor, Technical Publishing
CYNTHIA B. CLARK
Managing Editor, Transactions
CORNELIA MONAHAN
Production Coordinator
JUDITH SIERANT
Production Assistant
MARISOL ANDINO

Transactions of the ASME, Journal of Applied Mechanics (ISSN 0021-8936) is published quarterly (Mar., June, Sept., Dec.) for $250.00 per year by The American Society of Mechanical Engineers, Three Park Avenue, New York, NY 10016.
Periodicals postage paid at New York, NY and additional mailing office. POSTMASTER: Send address changes to Transactions of the ASME, Journal of Applied Mechanics, c/o THE AMERICAN SOCIETY OF MECHANICAL ENGINEERS, 22 Law Drive, Box 2300, Fairfield, NJ 07007-2300.
CHANGES OF ADDRESS must be received at Society headquarters seven weeks before they are to be effective. Please send old label and new address. **PRICES:** To members, $40.00; to nonmembers, $250.00; single issue, $100.00. Add $40.00 (airmail $60.00) for postage to countries outside the United States and Canada.
STATEMENT from By-Laws. The Society shall not be responsible for statements or opinions advanced in papers or . . . printed in its publications (B7.1, Para. 3).

COPYRIGHT © 1999 by The American Society of Mechanical Engineers. For authorization to photocopy material for internal or personal use under those circumstances not falling within the fair use provisions of the Copyright Act, contact the Copyright Clearance Center (CCC), 222 Rosewood Drive, Danvers, MA 01923, tel: 978-750-8400, www.copyright.com. Request for special permission or bulk copying should be addressed to Reprints/Permission Department.

INDEXED by Applied Mechanics Reviews and Engineering Information, Inc.
Canadian Goods & Services Tax Registration #126148048.

Journal of Applied Mechanics

Published Quarterly by The American Society of Mechanical Engineers

VOLUME 66 • NUMBER 3 • SEPTEMBER 1999

TECHNICAL PAPERS

585 **Penetration of Rigid Projectiles Through Quasi-Brittle Materials**
S. Mastilovic and D. Krajcinovic

593 **Reduction of the Sanders-Koiter Equations for Fully Anisotropic Circular Cylindrical Shells to Two Coupled Equations for a Stress and a Curvature Function**
T. J. McDevitt and J. G. Simmonds

598 **Elasticity Solution for a Radially Nonhomogeneous Hollow Circular Cylinder**
Xiangzhou Zhang and Norio Hasebe

607 **Conditions for Dual Compression in Perfectly Elastic Three-Dimensional Collisions**
J. A. Batlle

612 **Some Problems of a Rigid Elliptical Disk-Inclusion Bonded Inside a Transversely Isotropic Space: Part I**
M. Rahman

621 **Some Problems of a Rigid Elliptical Disk-Inclusion Bonded Inside a Transversely Isotropic Space, Part II: Solutions of the Integral Equations**
M. Rahman

631 **Finite Elastic Behavior of Flexible Fabric Composite Under Biaxial Loading**
S.-Y. Luo and A. Mitra

639 **The Full-Space Elastodynamic Green's Functions for Time-Harmonic Radial and Axial Ring Sources in a Homogeneous Isotropic Medium**
Y. Lu

646 **Prediction of Plastic Wrinkling Using the Energy Method**
J. Cao

653 **Dynamic Response of Complex Structural Intersections Using Hybrid Methods**
P. J. Halliday and K. Grosh

660 **A Stability Criterion for Parameter-Dependent Gyroscopic Systems**
R. O. Hryniv, P. Lancaster, and A. A. Renshaw

665 **Elastodynamic Green's Function for Laminated Anisotropic Circular Cylinders**
W. Zhuang, A. H. Shah, and S. B. Dong

675 **Half-Space Green's Functions for Transversely Isotropic Piezoelectric Solids**
M. L. Dunn and H. A. Wienecke

680 **Effective Elastic Stiffnesses of an Anisotropic Medium Permeated by Tilted Cracks**
C. Barret and S. Baste

687 **Approximate Analysis of a Shear Band in a Thermoviscoplastic Material**
H.-G. Kim and S. Im

695 **A Discrete Model of an Extensible String in Three-Dimensional Space**
K. Nishinari

702 **A Model for Mechanically Induced Densification of Glassy Polymers**
A. D. Drozdov

709 **Anisotropic Effective Moduli of Cracked Short-Fiber Reinforced Composites**
R. S. Feltman and M. H. Santare

714 **On Thermal Stress in a Bituminous Pavement: Analytic Solutions and Applications**
H.-H. Dai and G. Wu

(Contents continued on outside back cover)

This journal is printed on acid-free paper, which exceeds the ANSI Z39.48-1992 specification for permanence of paper and library materials. ♾™
♻ 85% recycled content, including 10% post-consumer fibers.

Downloaded 04 May 2010 to 171.66.16.52. Redistribution subject to ASME license or copyright; see http://www.asme.org/terms/Terms_Use.cfm

CONTENTS (CONTINUED)

720 **Heteroclinic Bifurcations in Rigid Bodies Containing Internally Moving Parts and a Viscous Damper**
G. L. Gray, D. C. Kammer, I. Dobson, and A. J. Miller

729 **Transmission of SH Waves Through an Elastic Layer Between Two Solids With Frictional Contact Interfaces**
Y.-S. Wang and G.-L. Yu

738 **A "Second Law" for Structures: An Insightful Approach to the Design of Plane Frames**
M. J. French

742 **Dynamic Analysis of Rotating Nonuniform Timoshenko Beams With an Elastically Restrained Root**
S. M. Lin

750 **Elastic-Plastic Stress Field in a Coated Continuous Fibrous Composite Subjected to Thermomechanical Loading**
L. You, S. Long, and L. Rohr

758 **Free Vibration of Axially Loaded Laminated Conical Shells**
L. Tong

764 **The Elasto-Electric Field for a Rigid Conical Punch on a Transversely Isotropic Piezoelectric Half-Space**
W.-Q. Chen, T. Shioya, and H.-J. Ding

772 **Experimental and Numerical Studies on Microscale Bending of Stainless Steel With Pulsed Laser**
G. Chen, X. Xu, C. C. Poon, and A. C. Tam

780 **Nonlinear Analysis of Particle Cavitation and Matrix Yielding Under Equitriaxial Stress**
S. Biwa

786 **Dynamic Analysis of Systems With Varying Constraints**
S. Djerassi

794 **Instability of Pipelines on Slopes**
A. C. Palmer, L. Tebboth, D. Miles, and C. R. Calladine

800 **Self-Excited Vibration in Flexible Rotating Disks Subjected to Various Transverse Interactive Forces: A General Approach**
J. Tian and S. G. Hutton

BRIEF NOTES

Thermoelastic Contact Problems for the Layer 806
J. L. Barber and L. G. Hector

On the Application of Potential Theory in Piezoelasticity 808
W.-Q. Chen

Application of the Cosserat Spectrum Theory to Stokes Flow 811
W. Liu and A. Plotkin

Nonlinear Thermal Vibrations on Elastic Shallow Spherical Shell Under Linear and Parabolic Temperature Distributions 814
U. K. Mandal and P. Biswas

815 Moment Value at the Center of Circular Plates Under Central Point Load
C. M. Wang and C. H. Ang

818 The Effect of Strain Rate on the Dynamic Expansion of Cylindrical Cavities
T. L. Warren

821 An Axisymmetric Interface Edge of Bonded Transversely Isotropic Piezoelectric Materials Under Torsion
Y.-H. Liu, J.-Q. Xu, and H.-J. Ding

DISCUSSION

824 **Hybrid Stochastic Finite Elements and Generalized Monte Carlo Simulation, by R. Ghanem—Discussion by M. Ostoja-Starzewski**

ANNOUNCEMENTS AND SPECIAL NOTES

645 Change of Address Form

686 CIMS 2000—Announcement

741 Periodicals on ASMENET

826 "As I Remember"

829 Worldwide Mechanics Meetings Conference List

832 Information for Authors

Downloaded 04 May 2010 to 171.66.16.52. Redistribution subject to ASME license or copyright; see http://www.asme.org/terms/Terms_Use.cfm

S. Mastilovic[1]

D. Krajcinovic
Fellow ASME

Mechanical and Aerospace Engineering,
Arizona State University,
Tempe, AZ 85287-6106

Penetration of Rigid Projectiles Through Quasi-Brittle Materials

The objective of this study is to formulate a simple, rational model for estimates of the penetration depth of rigid long rods through materials susceptible to microcracking. The proposed is based on the target resistance estimated using the particle dynamic simulations. All material parameters of the model can be identified and measured in laboratory. The accuracy of this simple model is found to be satisfactory.

1 Introduction

Deformation of solids penetrated by projectiles at large velocities is nonequilibrium, nonlinear, nonlocal, and irreversible thermodynamical process. In the neighborhood of the projectile tip the strains are large and locally discontinuous while the temperature cannot even be uniquely defined (Holian et al., 1995). The experimental data are, in general, limited to the velocity of the projectile, penetration depth, and observations of the crater after the event is terminated. The "virtual experiments" (Deitz, 1995) based on the shock physics (or hydro) codes are lately becoming a tool of choice in design of shields and projectiles. The objective of these codes, which require massive parallel systems of workstations, is to minimize the experimental aspects of engineering research and become the principal tool in the design of projectiles and shields. However, the same codes utilize phenomenological constitutive laws (such as those suggested by Pidsley (1984), Johnson and Cook (1985), Raftenberg (1992), and others) relating stresses, strains, strain rates, damage, and temperature. The functional dependence between kinetic and kinematic variables is often based on phenomenological observations. The relatively large correlation range of defects near the crater renders the partition of material near the projectile tip into finite elements difficult and potentially nonobjective.

The success of new and powerful codes depends on the constitutive laws and "material" parameters. The experimental validation of these relations requires that the stress field in the specimen be homogeneous. This requirement is very restrictive in consideration of rate effects. For example, application of Hopkinson bar and planar impact tests is limited to the strain rates below $10^4\ s^{-1}$ and $10^7\ s^{-1}$, respectively. The limitations are further increased when the imparted tractions have shear components. The kinetic data are typically deduced from the kinematic measurements by solving the wave propagation problem that a priori assumes a particular constitutive behavior. One cannot but agree with Nicholas and Bless (1985) who commented that "unique solutions cannot be guaranteed, because some other constitutive model (other than one used, authors' comment) may conceivable provide similar results in a particular wave propagation problem."

2 Resistance of "Brittle" Targets

Despite its shortcomings, various modifications of the Tate (1967) and Alekseevsky (1966) model were shown to be useful in estimates of penetration depth in metal targets. The reason for this success was that the deformation patterns of ductile targets exhibits universal trends (scaling similarity). Hence, the functional dependence of the target resistance of ductile metals on the strain and strain rate can often be deduced from the experience with similar targets, projectiles, and impact rates.

The deformation of targets made of materials predisposed to cracking (attributed to their inferior cohesive strength) shows much more variety. The response mode of brittle deformation of materials such as ceramics, rocks, concrete, etc., depends not only on the damage (crack density) but also on the sign of the normal stress (target confinement), frictional slip of two mating crack surfaces, microstructural disorder, etc. In general, the deformation pattern in these materials may include, in the order of their distance to the crater, transformed, process, and elastic zones (Fig. 1). The material of the transformed (comminuted) zone is crushed into a very fine granular phase. As the density of cracks (damage) approaches the maximum level deformation becomes similar to granular flow. The damage of the process zone is substantial as the cracks grow and self-organize into a multitude of shear bands. The stresses in the process zone are not sufficient to break stronger grain clusters. Thus, the damage ranges from zero (at interface with elastic zone) to maximum (at interface with transformed zone). The damage in the elastic zone is, by definition, close to zero.

The resistance of the material to the expansion of the cavity, and its capacity to absorb the imparted energy without breaking, depends on the relative widths of these three zones (Forrestal and Longcope, 1990; Mastilovic and Krajcinovic, 1999a, b). The widths of these zones depend on the rate of the void expansion and material disorder on the microscale (i.e., damage tolerance). The experimental data from which it would be possible to infer the width of three zones and their crack density are still not available. Some data are available in Shockey et al. (1990), Hauver et al. (1991), Curran et al. (1993), and references listed in these studies. In the absence of detailed micromechanical test data, this study will utilize the data of computer particle dynamic simulations performed by Mastilovic and Krajcinovic (1999a) performed on geometrically and structurally disordered two-dimensional, triangular, central-force particle lattices. A particle (lattice node) represents a grain (or aggregate) and the link connecting two particles the cementitious matrix bonding the grains together. Each particle of the lattice used in simulation is linked to its six closest neighbors by "chemical" links that are linear elastic in tension and non-linearly elastic in compression (Fig. 2(*a*)). The only exceptions are surface particles that are bonded to less than six neighbors. Introduction of the "mechanical" link, formed by two particles brought in contact by a compressive force (Fig. 2(*b*)), is necessary to simulate granular flow. The stiffness and strength (rupture strain ϵ_{cr} = const.) of a chemical link are determined from the corresponding parameters (elastic modulus of the rock and tensile strength of the cement) of limestone. The microstructural disorder is introduced by the normal distribution of link (force-

[1] Current address: Framatome Cogema Fuels, Las Vegas, NV 89134.

Contributed by the Applied Mechanics Division of THE AMERICAN SOCIETY OF MECHANICAL ENGINEERS for publication in the ASME JOURNAL OF APPLIED MECHANICS.

Discussion on the paper should be addressed to the Technical Editor, Professor Lewis T. Wheeler, Department of Mechanical Engineering, University of Houston, Houston, TX 77204-4792, and will be accepted until four months after final publication of the paper itself in the ASME JOURNAL OF APPLIED MECHANICS.

Manuscript received by the ASME Applied Mechanics Division, June 25, 1998; final revision, Apr. 2, 1999. Associate Technical Editor: M. Ortiz.

 Copyright © 1999 by ASME

Downloaded 04 May 2010 to 171.66.16.27. Redistribution subject to ASME license or copyright; see http://www.asme.org/terms/Terms_Use.cfm

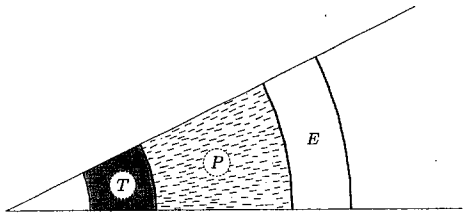


Fig. 1 Response regions during a high-velocity cavity expansion

free) lengths (i.e., grain radius) λ and uniformly distributed link stiffness k.

For a selected rate at which the void expands from zero to a given radius the force and elongation of each link is determined from Hamiltonian of the lattice. At a critical elongation a link ruptures and the released force is distributed to the extant links in the manner that minimizes the strain energy. The two-dimensional lattice corresponds to the plane-strain deformation of a three-dimensional body (Monette and Anderson, 1994). Hence, these particle dynamic simulations can be used to determine the forces with which a material predisposed to cracking resists the penetration of a sharp projectile that remains substantially undeformed during the penetration (Bishop et al., 1945).

Figure 3 shows the ruptured links of a two-dimensional central-force lattice for four different rates of void expansion $\dot{a} = 0.135$, 0.0135, 0.00135, and $0.000135C_L$, where C_L is the velocity of sound in the pristine material (Mastilovic and Krajcinovic, 1999a). The corresponding cracks are perpendicular to the ruptured links (represented by short lines). At very rapid cavity expansion[2] (Fig. 3(*a*)) the work of the compressive tractions applied to the perimeter of the expanding cavity is consumed primarily on the kinetic energy within the granular phase, i.e., on the rapid evacuation of particles away from the growing hole. The strain energy within the process and elastic zone is approximately twice as small as the kinetic energy while the contribution of the rupture energy (elastic release energy) is too small to be discerned in Fig. 4(*a*).

At void expansion at rate of $\dot{a} = 0.0135C_L$ the shear bands in the process zone become more prominent (Fig. 3(*b*)). Their pattern is reminiscent of the logarithmic slip-line field surrounding the expanding circular cavity in a ductile material (Kachanov, 1971). The crack (damage) growth for two slowest expansion rates (Figs. 3(*c*) and (*d*)) is characterized by the localization of microcracks into few large radial cleavage cracks. The distribution of energy, corresponding to the expansion rate of $\dot{a} = 0.00135C_L$, plotted in Fig. 4(*b*), shows that at slower void expansion rate the elastic strain energy (potential) dominates while the contribution of the rupture energy, still smallest of all three components, becomes at least visible. In other words, the target resistance is controlled by its mass at the largest rate of void expansion while the cohesive strength and stiffness of the material become important at slower rates.

The data in Fig. 4 also suggest that the localization of microcracks into microcrack take place close to the end of penetration as the penetration velocity (related to the velocity of the void expansion) slows down below a critical value. The material closest to the projectile is comminuted (Mescall zone). This conclusion is supported by experimental (Strassburger and Senf, 1996) and computed data (Shockey et al., 1993; Curran et al., 1993).

The radial tractions, imparted at the void perimeter, required for void expansion at a given rate, are plotted in Fig. 5 versus the nondimensional void expansion $\bar{r} = \Delta a/\lambda_c$ (where Δa is the change of void radius and λ_c average grain radius) for seven different expansion rates. The graphs in Fig. 5 were recorded until the elastic stress wave reached the lattice external perimeter. The change of radial tractions $\bar{\sigma}_r^o = \sigma_r\ (r = a)/K_o$ (where K_o is the bulk modulus of pristine lattice), imparted at the void perimeter and needed to maintain the void expansion at a desired constant rate $\dot{a}$, with $\bar{r}$ is characterized by a sharp, elastic peak followed by a decline to a level of stagnation. The rate of decline of externally applied radial tractions is inversely proportional to the void expansion rate. The only exception is the slowest expansion rate reminiscent of quasi-static, strain-controlled fracture processes.

Using the methods of statistical mechanics the raw simulation data are averaged over a smallest possible area to determine all components of the stress, strain, and effective stiffness tensors as a function of damage (density of ruptured links), location (radius), and time (Mastilovic and Krajcinovic, 1999a). The peak value of the radial traction needed to drive the void expansion at rate $\dot{a}$ is derived, by solving the problem of stress wave propagation generated by the expansion of a circular void at constant velocity $\dot{a} =$ const. within a two-dimensional elastic plate (Kromm, 1948), in the form

$$\sigma_r^F = \frac{1 - \upsilon_o}{(1 - 2\upsilon_o)(1 + \upsilon_o)} \frac{E_o \dot{a}}{C_L} \tag{1}$$

[2] The largest of expansion velocity exceeds the velocities of current projectiles. However, this velocity is substantially below the hydrodynamic limit at which projectile and target will melt.

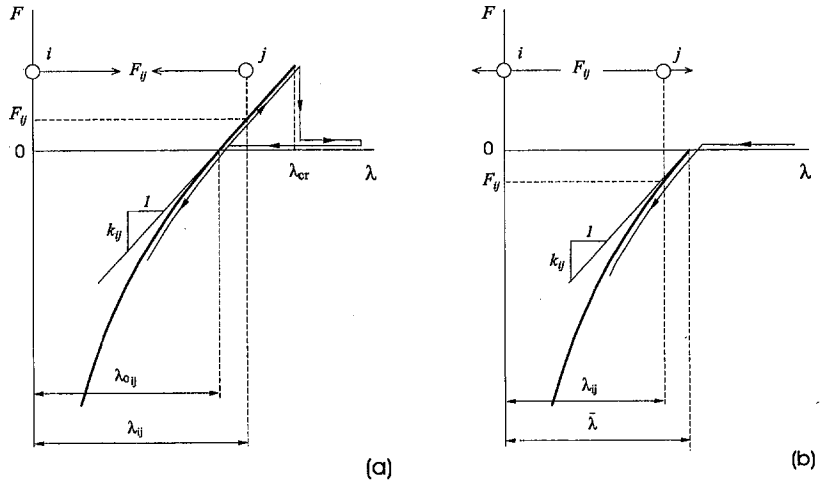


Fig. 2 Nonlinear elastic-brittle relation between link force and elongation. Interaction between particles that (*a*) are or were original the nearest neighbors and (*b*) were not originally the nearest neighbors

Downloaded 04 May 2010 to 171.66.16.27. Redistribution subject to ASME license or copyright; see http://www.asme.org/terms/Terms_Use.cfm

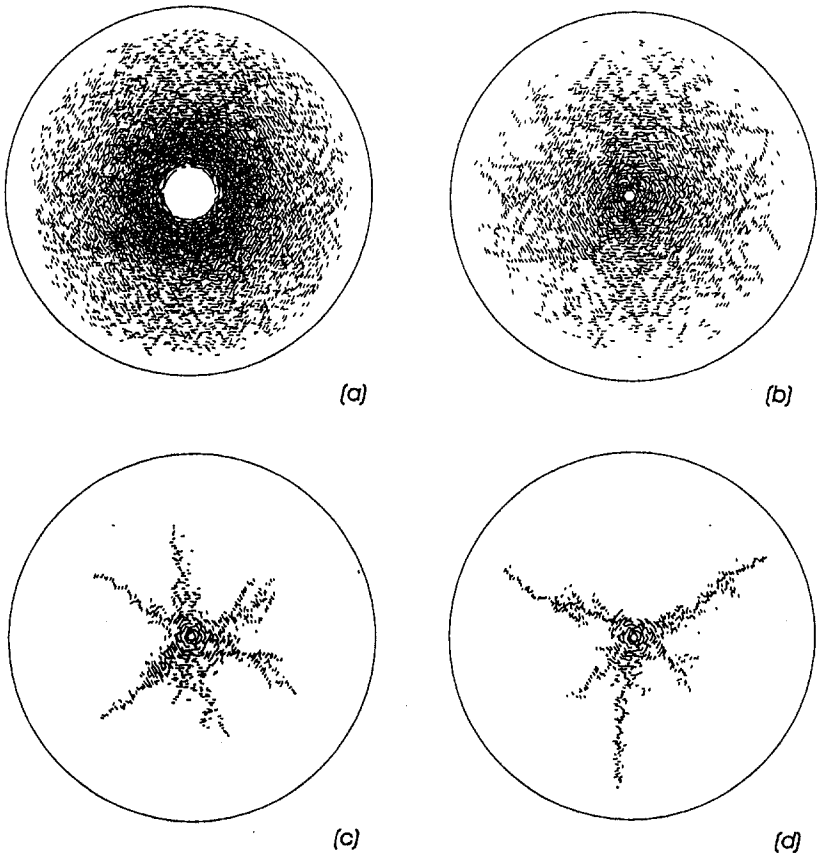


Fig. 3 Dependence of the damage evolution pattern on the cavity-expansion rate; (*a*) $\dot{a} = 0.135C_L$, $\dot{a} = 0.0135C_L$, $\dot{a} = 0.00135C_L$ and $\dot{a} = 0.000135C_L$

where E and υ are the elastic modulus and Poisson's ratio while the subscript "o" stands for pristine (damage-less) state. The radial traction at the void perimeter can finally be determined as a function of the void radius knowing the peak and stagnation tractions.

The stagnation values of the radial tractions at the cavity perimeter can also be derived from an analytical model based on the particle dynamic simulation and conservation principles (Mastilovic and Krajcinovic, 1998). Analytical solutions are shown in Fig. 5 by small hollow squares. A bilinear relation (solid line) or a quadratic parabola (dashed line) approximate the relation between the radial tractions σ_r^o (derived from simulations) and void expansion rate $\dot{a}$ with a similar accuracy (Fig. 6). The intercept with the ordinate (bold dot in Fig. 6) is the radial tractions σ_r^o at which the cavity perimeter starts to expand "quasi-statically" in an infinite medium. Following Forrestal and Longcope (1990) and Mastilovic and Krajcinovic (1999), these tractions are

$$\left(\frac{\sigma_r^o}{K_o}\right)_{st} = \left[\frac{3(1-2\upsilon_o)}{(1+\upsilon_o)(3-2\upsilon_o)}\frac{\sigma_f}{K_o}\right]^{1/2} \tag{2}$$

where the subscript "o" refers to pristine state and σ_f is the uniaxial tensile strength of the material estimated by uniaxial tensile simulations. Relation (2) of bilinear approximation is valid for $0 \le \dot{a} \le v_{nT}$, where v_{nT} is a material parameter. It is interesting to point out that the potential and kinetic energies are equal to each other at the transition velocity v_{nT} (Krajcinovic et al., 1998).

According to the simulations (Mastilovic and Krajcinovic,

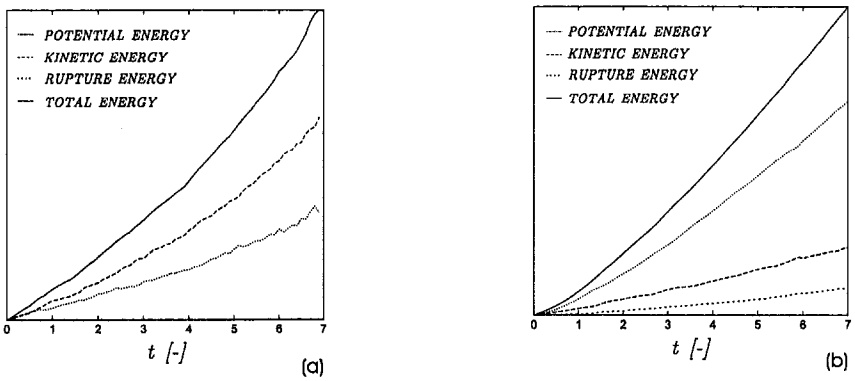


Fig. 4 Total, potential, and rupture energies during the high and low-velocity cavity expansion: (*a*) $\dot{a} = 0.135C_L$ and (*b*) $\dot{a} = 0.00135C_L$

Downloaded 04 May 2010 to 171.66.16.27. Redistribution subject to ASME license or copyright; see http://www.asme.org/terms/Terms_Use.cfm

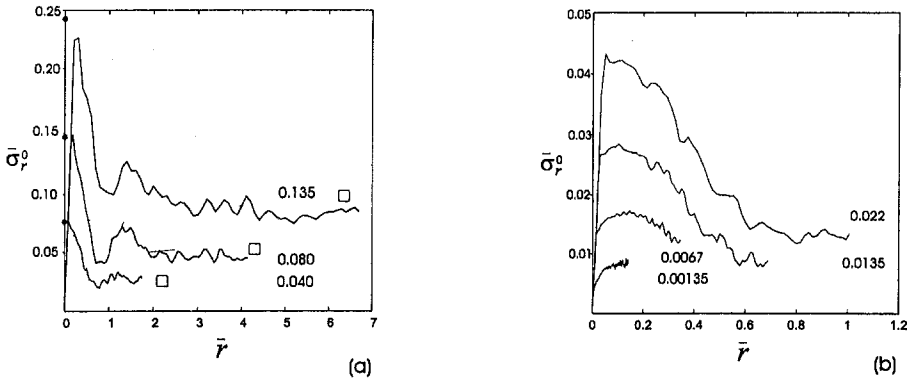


Fig. 5 Radial stress (traction) at the cavity perimeter versus change of the cavity radius seven velocities of cavity expansion: (*a*) $\dot{a}$ = (0.04 to 0.135)C_L, (*b*) $\dot{a}$ = (0.00135 to 0.022)C_L

1999a) the relation between the peak value of the radial tractions (1) and the saturated value is for all void expansion rates within the range (2.78, 3.12). Assuming that the ratio is equal to 3 the inclined part of the bilinear approximation (Fig. 6), that is valid at large penetration velocities, is defined by

$$\left(\frac{\sigma_r^o}{K_o}\right) = \left(\frac{\sigma_r^F}{3K_o}\right) = \frac{1-\upsilon_o}{1+\upsilon_o}\frac{\upsilon_n}{C_L} \quad \text{for } \dot{a} \geq \dot{a}_T = \upsilon_{nT}. \tag{3}$$

The relation (3) is, strictly speaking, a very good approximation of simulation data for the considered material characterized by reasonable large disorder.[3] The model based on expression (4) is deterministic since all material parameters are related to the corresponding parameters of the pristine material.

The transition velocity of void expansion $\upsilon_n = \upsilon_{nT}$, derived from (2) and (3), is

$$\frac{\upsilon_{nT}}{C_L} = \frac{1+\upsilon_o}{1-\upsilon_o}\left[\frac{3(1-2\upsilon_o)}{(1+\upsilon)(3-2\upsilon_o)}\bar{\sigma}_f\right]^{1/2}. \tag{4}$$

The quadratic parabola approximation, fitted from simulation data, is

$$(\sigma_r^o/K_o) = 0.0086 + 0.37(\dot{a}/C_L) + 1.25(\dot{a}/C_L)^2. \tag{5}$$

Functions (3) to (5) are fitted using the simulation data points for three different expansion rates $\{\dot{a}/C_L;\ \sigma_r^o/K_o\} = \{(0;\ 0086), (0.08;\ 0.046), (0.135;\ 0.081)\}$.

The simulation data plotted in Fig. 6 is equally well fitted by both bilinear and parabolic approximations. The largest difference between two curves corresponds to the transition from the localized to distributed damage pattern. The quadratic parabola provides for a simpler model and requires only two tests (static and one dynamic test), assuming that the curve has a zero slope at the intersection with the ordinate. Since this transition depends on the microstructural disorder, the deviations from the mean values may be largest as well. Hence, it seems prudent to consider both bilinear and quadratic approximations.

The proposed particle dynamics simulation model was validated on an array of benchmark problems for which the experimental data are available. This task was attended in Mastilovic and Krajcinovic (1999b) using benchmark test data such as stress wave features, rigid-anvil test, planar impact (spalling), etc. These tests were used to determine the size of lattice and averaging region, select the time-step, define initial conditions assuring homogeneous state of stress and size of the statistical sample. Admittedly, validation was done on rather small, two-dimensional lattices using a modest statistical sample. Despite these and possible other limitations the performed simulations clearly indicate that the constitutive relations related kinetic and kinematic variables can be inferred from the particle dynamic simulations using the rigorous, but seldom used, methods of statistical mechanics (Krajcinovic and Mastilovic, 1999).

3 Penetration of a Rigid Ogive Nosed Projectile Into a Brittle Target

An ogive nosed rigid projectile (Fig. 7(*a*)) consists of a long shank and a nose defined by a circular arc of radius s. The nose geometry is defined by

[3] A material is said to be "disordered" if the random fluctuations of its microtexture affects macroscale response (damage evolution).

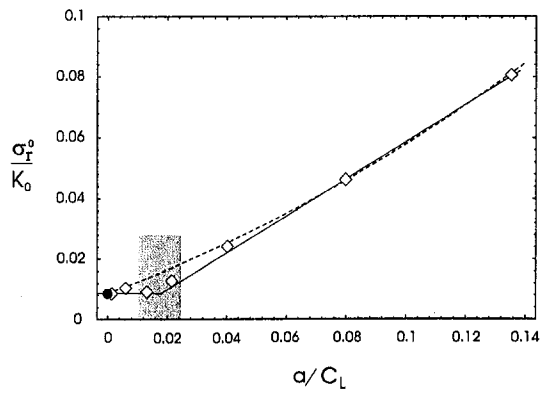


Fig. 6 Radial stress (tractions) at the cavity perimeter plotted versus velocity of cavity expansion

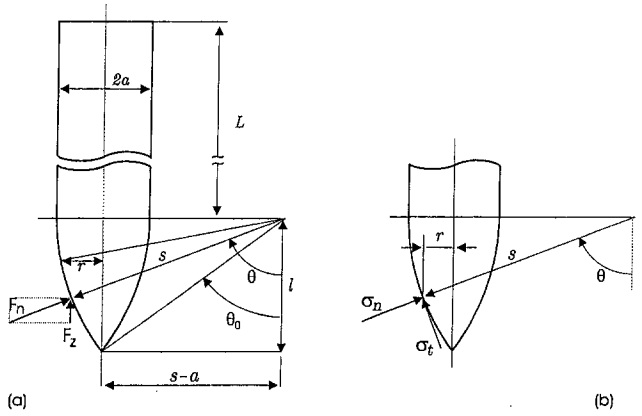


Fig. 7 (*a*) Geometry of the ogival nose projectile, (*b*) stress components at the ogival nose that resist penetration

Downloaded 04 May 2010 to 171.66.16.27. Redistribution subject to ASME license or copyright; see http://www.asme.org/terms/Terms_Use.cfm

$$\sin\theta_o = 1 - \frac{1}{2\psi} \quad \text{where} \quad \psi = \frac{s}{2a} \tag{6}$$

where a is the shank radius. The tractions that resist penetration are sketched in Fig. 7(b). The infinitesimal force normal to the ogive nose surface is

$$dF_n = (2\pi rsd\theta)d\sigma_n. \tag{7}$$

Following Forrestal et al. (1988), the relation between tangential and normal tractions applied to the nose are, in absence of test data, *assumed* to be related as

$$\sigma_t = \mu\sigma_n \tag{8}$$

where the parameter μ is often interpreted as a measure of "friction." The axial component of the resistance force is from (7) and (8) equal to

$$\begin{aligned} dF_z &= 2\pi rsd\theta(\cos\theta + \mu\sin\theta)\sigma_n \\ &= 2\pi s^2(\cos\theta + \mu\sin\theta)(\sin\theta - \sin\theta_o)\sigma_n d\theta. \end{aligned} \tag{9}$$

Hence,

$$F_z = 2\pi\left(\frac{s}{a}\right)^2 a^2 \int_{\theta_o}^{\pi/2} (\cos\theta + \mu\sin\theta) \times (\sin\theta - \sin\theta_o)\sigma_n d\theta. \tag{10}$$

Following Forrestal and Luk (1988) it is assumed that the normal traction $\sigma_n(v_z, \theta)$ on the ogive nose is actually equal to the tractions $\sigma_r^o(\dot{a})$ needed to expand the circular void at the rate $\dot{a}$, i.e., that

$$\sigma_n(\theta) = \sigma_r^o\,(r = a) \quad \text{and} \quad v_n = v_z\cos\theta = \dot{a}. \tag{11}$$

The assumptions in (11) are, strictly speaking, geometrically incorrect since the void is circular only in the planes perpendicular to the projectile axis. However, the error induced by these assumptions seems to be acceptable as argued in Bishop et al. (1945).

3(a) Bilinear Approximation of the Force-Void Expansion Rate. Consider first the case when the relation between the tractions void expansion rate is approximately bilinear. The normal tractions on the ogive nosed projectile are from (2), (3), (10), and (11)

$$\bar{\sigma}_n = \frac{\sigma_n}{K_o} = \begin{cases} (\bar{\sigma}_r^o)_{st} = \text{const.} = \left[\dfrac{3(1-2\upsilon_o)}{(1+\upsilon_o)(3-2\upsilon_o)}\,\bar{\sigma}_f\right]^{1/2} & \text{for } v_n \le v_{nT} \\ \dfrac{1-\upsilon_o}{1+\upsilon_o}\dfrac{v_n}{C_L} = \dfrac{1-\upsilon_o}{1+\upsilon_o}\dfrac{v_z}{C_L}\cos\theta & \text{for } v_n \ge v_{nT} \end{cases} \tag{12}$$

where v_z is fixed. The material parameter v_{nT}, defined by (4), is from (11(b))

$$v_{nT} = \frac{1+\upsilon_o}{1-\upsilon_o}(\bar{\sigma}_r^o)_{st}C_L = v_z\cos\theta_T = \dot{a}_T. \tag{13}$$

Therefore, if the penetration velocity is large, i.e., if $v_z > v_{nT}$, normal tractions σ_n imparted to the lower part of the ogive nose correspond to the case when the damage is distributed (Fig. 3(a)). The normal tractions σ_n on the upper part of the ogive nose, where $v_z < v_{nT}$, correspond to the damage localized into several macrocracks (Fig. 3(c, d)). Hence,

$$\bar{\sigma}_n = \begin{cases} (\bar{\sigma}_r^o)_{st} = \text{const.} & \text{for } \theta_T \le \theta \le \pi/2 \\ \dfrac{1-\upsilon_o}{1+\upsilon_o}\dfrac{v_z}{C_L}\cos\theta & \text{for } \theta_o \le \theta \le \theta_T \end{cases} \quad \text{iff } v_z > v_{zT} \tag{14}$$

where the angle

$$\theta_T = \arccos\left[\frac{1+\upsilon_o}{1-\upsilon_o}(\bar{\sigma}_r^o)_{st}\frac{C_L}{v_z}\right] \tag{15}$$

that separates two distinctly different tractions is derived from (13).

The angle θ_T (15) must satisfy two obvious conditions $-1 \le \cos\theta_T \le 1$ and $\theta_T \ge \theta_o$. At small penetration velocities, defined as $v_z \le v_{zT}$, these conditions are satisfied if

$$v_z \le \frac{1+\upsilon_o}{1-\upsilon_o}(\bar{\sigma}_r^o)_{st}\left(1 - \frac{1}{4\psi}\right)^{-1/2} C_L = v_{zT}, \quad \theta_T = \theta_o, \quad \text{and } \bar{\sigma}_n = (\bar{\sigma}_r^o)_{st}. \tag{16}$$

Equalities in (16) are satisfied when the target deformation is quasi-statical. The corresponding normal tractions are

$$\bar{\sigma}_n = (\bar{\sigma}_r^o)_{st} = \left[\frac{3(1-2\upsilon_o)}{(1+\upsilon_o)(3-2\upsilon_o)}\,\bar{\sigma}_f\right]^{1/2} = \text{const.} \quad \text{for } \theta_o \le \theta \le \pi/2. \tag{17}$$

The target resistance at small penetration velocities $v_z \le v_{zT}$ derived from (17) is

$$\begin{aligned} F_z &= 8\pi a^2\psi^2 K_o \int_{\theta_o}^{\pi/2} (\cos\theta + \mu\sin\theta)(\sin\theta - \sin\theta_o) \\ &\quad \times \bar{\sigma}_n(v_z, \theta)d\theta = 2\pi a^2\psi^2 K_o(\bar{\sigma}_r^o)_{st}[1 + \mu(\pi - 2\theta_o) \\ &\quad + 4\left(1 - \frac{a}{s}\right)(\sin\theta_o - \mu\cos\theta_o - 1) + \cos 2\theta_o \\ &\quad + \mu\sin 2\theta_o] = F_{II}. \end{aligned} \tag{18}$$

At large penetration velocities $v_z > v_{zT}$, the lower part of the nose $\theta_o \le \theta < \theta_T$ is in the regime defined by the inclined part of the graph in Fig. 6, while the upper part $\theta_T < \theta \le \pi/2$ of the nose is in regime of constant $\bar{\sigma}_r^o$ (14). The target resistance is

$$\begin{aligned} F_z &= 8\pi a^2\psi^2 K_o \int_{\theta_o}^{\theta_T} (\cos\theta + \mu\sin\theta)(\sin\theta - \sin\theta_o) \\ &\quad \times \frac{1-\upsilon_o}{1+\upsilon_o}\frac{v_z}{C_L}\cos\theta d\theta + (\bar{\sigma}_r^o)_{st}\int_{\theta_T}^{\pi/2} (\cos\theta + \mu\sin\theta) \\ &\quad \times (\sin\theta - \sin\theta_o)d\theta \end{aligned} \tag{19}$$

such that

$$F_z = 2\pi a^2\psi^2 K_o\left[\frac{1-\upsilon_o}{1+\upsilon_o}\frac{v_z}{C_L}I_1 + (\bar{\sigma}_r^o)_{st}I_2\right] = F_I \tag{20}$$

where

$$\begin{aligned} I_1 = -\Big\{ &2\left(1 - \frac{a}{s}\right)(\theta_T - \theta_o) + (\cos\theta_T - \cos\theta_o) + \frac{1}{3}(\cos 3\theta_T \\ &- \cos 3\theta_o) - \mu\left[\sin\theta_T - \sin\theta_o - \frac{1}{3}(\sin 3\theta_T - \sin 3\theta_o)\right] \\ &+ \left(1 - \frac{a}{s}\right)(\sin 2\theta_T - \sin 2\theta_o)\Big\} \end{aligned} \tag{21}$$

and

Downloaded 04 May 2010 to 171.66.16.27. Redistribution subject to ASME license or copyright; see http://www.asme.org/terms/Terms_Use.cfm

Table 1 Penetration depth of an ogive nosed rigid projectile through concrete

v_s (m/s)	D (m) biaxial $\mu = 0.1$	D (m) biaxial $\mu = 0.2$	D (m) parabolic $\mu = 0.1$	D (m) parabolic $\mu = 0.2$	D (m) tests
300	0.31	0.24	0.29	0.22	0.23
500	0.79	0.61	0.73	0.56	0.54
700	1.35	1.05	1.26	0.98	0.90
900	1.94	1.51	1.81	1.41	1.43
1100	2.53	1.99	2.34	1.84	2.06

$$I_2 = \left[1 - 4\left(1 - \frac{a}{s}\right)(1 + \mu \cos\theta_T - \sin\theta_T) + \mu(\pi - 2\theta_T) + \cos 2\theta_T + \mu \sin 2\theta_T \right]. \quad (22)$$

Maximum transition velocity $v_z = v_{cr}$, derived from $F_I = F_{II}$, is

$$\frac{v_{T\max}}{C_L} = \frac{1 + \upsilon_o}{1 - \upsilon_o} I_1^{-1}(\bar{\sigma}_r^o)_{st}\left[1 - I_2 + \mu(\pi - 2\theta_o) + 4\left(1 - \frac{a}{s}\right) \times (\sin\theta_o - \mu\cos\theta_o - 1) + \cos 2\theta_o + \mu \sin 2\theta_o \right]. \quad (23)$$

From the second Newton's law

$$m_p \frac{dv_z}{dt} = -F_z \quad (24)$$

where m_p is the projectile mass, the penetration depth D is

$$D = \int_o^D dz = -m_p \int_{v_s}^o \frac{v_z}{F_z} dz = m_p\left(\int_o^{v_{zT}} \frac{v_z}{F_{II}} dv_z + \int_{v_{zT}}^{v_s} \frac{v_z}{F_I} dv_z \right) = m_p\left(\frac{v_{zT}^2}{2F_{II}} + \int_{v_{zT}}^{v_s} \frac{v_z}{F_I} dv_z \right) \quad (25)$$

where v_s is the striking velocity.

3(b) Parabolic Approximation of the Force-Void Expansion Rate. A quadratic parabola (Fig. 6)

$$\bar{\sigma}_r^o = A_1 + A_2 \frac{\dot{a}}{C_L} + A_3\left(\frac{\dot{a}}{C_L}\right)^2 \quad (26)$$

is also used to approximate the relation between the radial tractions and rate of void expansion. Constants A_i in (26) are derived from the conditions

$$\frac{\dot{a}}{C_L} = 0, \quad \bar{\sigma}_r^o \equiv (\bar{\sigma}_r^o)_{st}$$

$$\frac{\dot{a}}{C_L} = 0, \quad \frac{d(\bar{\sigma}_r^o)}{d(\dot{a}/C_L)} = 0$$

$$\frac{\dot{a}}{C_L} = \left(\frac{\dot{a}}{C_L}\right)_{hv}, \quad \frac{d(\bar{\sigma}_r^o)}{d(\dot{a}/C_L)} = \frac{1 - \upsilon_o}{1 + \upsilon_o} \quad (27)$$

where $\dot{a}_{hv} = 0.1 C_L$ with subscript "hv" standing for high velocity.

After relatively obvious manipulations the radial tractions applied at the void edge are

$$\bar{\sigma}_n^o = (\bar{\sigma}_r^o)_{st} + \left[\frac{1}{2}\frac{1 - \upsilon_o}{1 + \upsilon_o}\left(\frac{\dot{a}}{C_L}\right)_{hv}\right]\left(\frac{\dot{a}}{\dot{a}_{hv}}\right)^2 = (\bar{\sigma}_r^o)_{st} + H v_n^2 \quad (28)$$

where $(\bar{\sigma}_r^o)_{st}$ is defined by (2) while the constant $H = (1/2)[(1 - \upsilon_o)/(1 + \upsilon_o)](1/C_L\dot{a}_{hv}^2)$. The target resistance force can be derived substituting (28) into (10) and performing rather simple but tedious integration.

The final form of the penetration depth is

$$D = \frac{m_p}{4\pi s^2 \beta K_o} \ln\left(1 + \frac{\beta}{\alpha} v_s^2\right) \quad (29)$$

where v_s is the striking velocity while the two constants α and β are

$$\alpha = \frac{1}{4}(\bar{\sigma}_r^o)_{st}\left[1 + \mu(\pi - 2\theta_o) + 2\frac{1 - 2\psi}{\psi}(1 + \mu\cos\theta_o - \sin\theta_o) + \cos 2\theta_o + \mu \sin 2\theta_o \right]$$

$$\beta = \frac{1}{16}\frac{1 - \upsilon_o}{1 + \theta_o}\frac{1}{C_L\dot{a}_{hv}}\left[\frac{17}{12} - \frac{1}{3\psi} + \frac{\mu}{2}(\pi - 2\theta_o) + (1 - 2\psi) \times (3 + \mu\cos\theta_o) + \cos 2\theta_o + \frac{1 - 2\psi}{3\psi}(\mu\cos 3\theta_o - 9\sin\theta_o - \sin 3\theta_o) + \frac{1}{4}(\cos\theta_o + \mu \sin 4\theta_o) \right]. \quad (30)$$

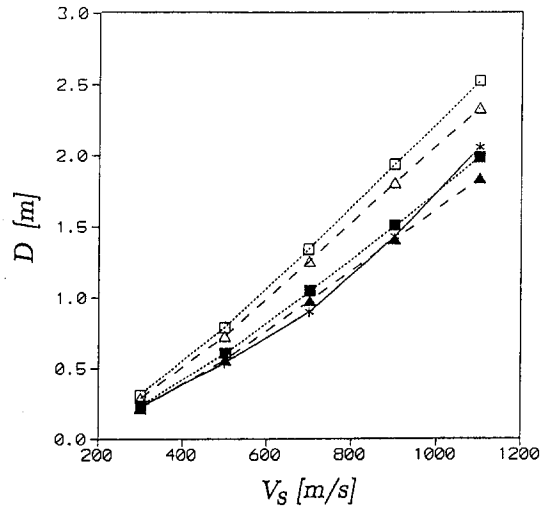


Fig. 8 Depth of penetration data for concrete (solid line) and model predictions (dotted lines—parabolic approximation and dashed lines—bilinear approximation). Asterix denotes the experimental data, full symbols correspond to $\mu = 0.2$ while empty symbols correspond to $\mu = 0.1$.

Downloaded 04 May 2010 to 171.66.16.27. Redistribution subject to ASME license or copyright; see http://www.asme.org/terms/Terms_Use.cfm

Table 2 Penetration depth of an ogive nosed rigid projectile through limestone

v_s (m/s)	D (m) biaxial $\mu = 0.1$	D (m) biaxial $\mu = 0.2$	D (m) parabolic $\mu = 0.1$	D (m) parabolic $\mu = 0.2$	D (m) tests
450	0.19	0.15	0.23	0.17	0.14
600	0.30	0.23	0.37	0.29	0.23
850	0.47	0.37	0.64	0.50	0.40
950	0.54	0.43	0.75	0.59	0.48
1130	0.66	0.53	0.94	0.74	0.63
1280	0.77	0.61	1.09	0.86	0.78
1400	0.86	0.68	1.21	0.95	0.90

4 Example

A concrete target is an appropriate example not only because the experimental data (i.e., penetration depth) are available but also since the inelastic deformation of concrete is almost always attributed to the damage in form of distributed microcracks. The particular concrete considered in Forrestal et al. (1996) and Forrestal and Tzou (1997) is defined by the following parameters:

$$K_o = 6.7 \text{ GPA}, \quad \nu_o = 0.22 \quad E_o = 11.3 \text{ GPA} \quad \sigma_f = 13 \text{ Pa}$$

$$\rho_o = 2260 \frac{\text{kg}}{\text{m}^3} \quad m_p = 1.6 \text{ kg}$$

$$C_L = \left[\frac{1-\nu_o}{(1+\nu_o)(1-2\nu_o)}\frac{E_o}{\rho_o}\right] = 2390 \frac{\text{m}}{\text{s}}.$$

The geometry of a projectile is defined by $a = 15.25$ mm, $\psi = 3.0$ and $s = 91.5$ mm. The penetration depths of an ogive nosed rigid long rod are computed from (25) and (29) for a range of striking velocity, arranged in Table 1 and plotted in Fig. 8. These results are compared with the available test data in Forrestal et al. (1996) and Forrestal and Tzou (1997). The computations were performed for two reasonable values of the fitting "frictional" parameter μ. All other parameters used in computations can be directly measured in laboratory and in situ. The deviations from test data range in the case of the bilinear model from 18 to 33 percent for $\mu = 0.1$ and -3.4 to 14 percent for $\mu = 0.2$. The model accuracy, for latter value of the "frictional" modulus, is most probably within the experimental scatter.

The same model, derived above, is used to predict the penetration depth of the ogive nosed projectile through the limestone. The material parameters of the limestone rock, compiled from Green (1992) and Frew et al. (1996), are

$$K_o = 22 \text{ GPa}, \quad \nu_o = 0.22,$$

$$E_o = 37 \text{ GPa}, \quad \sigma_f \cong 0.1\sigma_c \cong 5 \text{ MPa}$$

$$\rho_o = 2300 \text{ kg/m}^3 \quad C_L = 4285 \text{ m/s}.$$

The projectile is defined by

$$m_p = 0.117 \text{ kg} \quad a = 6.35 \text{ mm} \quad \psi = 3.0.$$

The test data cited in Table 2 are from Frew et al. (1996). The deviations from test data range in the case of the bilinear model from -4.6 to 26 percent for $\mu = 0.1$ and -24 to 6.6 percent for $\mu = 0.2$ (Fig. 9).

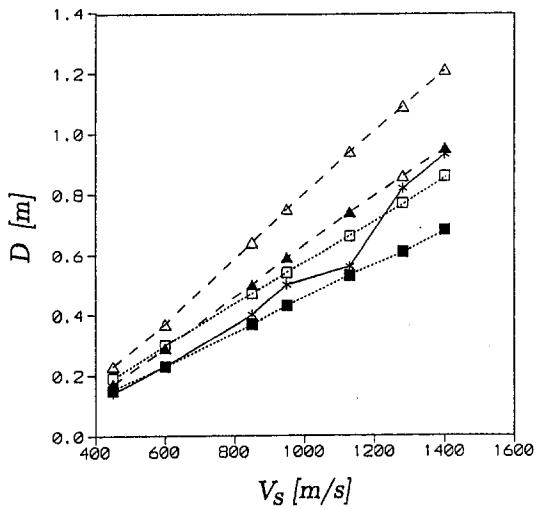


Fig. 9 Depth of penetration data for limestone (solid line) and model predictions (dotted lines—parabolic approximation and dashed lines—bilinear approximation). Asterix denotes the experimental data, full symbols correspond to $\mu = 0.2$ while empty symbols correspond to $\mu = 0.1$.

5 Summary and Conclusions

The simulations of the void expanding within a material of modest cohesive strength (Krajcinovic et al., 1998) clearly indicate that the pattern (and localization) of damage evolution strongly depends on the annealed disorder on the particle scale. This and another similar simulations (Krajcinovic, 1996; etc.) demonstrate the potential role of statistical mechanics in general, and particle dynamic simulations in particular, in application to penetration mechanics. All material parameters of the lattice, such as the properties of the lattice links, can be unambiguously identified and determined from the data of simple, static experiments. The determination of parameters related to the microstructural disorder requires the knowledge of the distribution of grain (aggregate) sizes and packing.

The model described in this study is intentionally reduced to its most simple form. For example, the deformation of the projectile and the first elastic peak (1) of the target resistance (Fig. 5) are neglected at this time. A simple relation between the elastic peak and stagnation levels of radial traction (2) is used to render the model deterministic. The only fitting parameter μ (8) is assumed to be constant. The links properties (Fig. 2) are defined by a minimum of parameters related to material parameters that can be easily measured in the laboratory.

In general, it may be that the deterministic relation (2) will introduce an unacceptable error. In this case the lattice parameters (microstructural disorder) must be deduced from the distribution of grain (aggregate) sizes and cement properties. The ratio between σ_r^F and σ_r^o (determined by simulations) may in this case differ from three (Mastilovic and Krajcinovic, 1999a, b). Hence, in this case the dynamic particle simulations become necessary.

In conclusion, the rigor of statistical mechanics and the already available computational power provide a strong motivation for further development of similar methods. New ingenious modifications of molecular dynamics and its coupling with computational models (see also Ortiz, 1995; Tadmor et al., 1996; Tadmor et al., 1996a; etc.) will eventually provide a very simple but powerful way of formulation of constitutive laws.

Downloaded 04 May 2010 to 171.66.16.27. Redistribution subject to ASME license or copyright; see http://www.asme.org/terms/Terms_Use.cfm

Acknowledgments

The authors gratefully acknowledge the financial support in form of the research grant from the U.S. Army Research Office, Engineering Science Division to the Arizona State University that made this work possible.

References

Alekseevskii, V. P., 1966, "Penetration of a Rod into Target at High Velocity," *Combus. Explos. Shock Waves,* Vol. 2, pp. 63–66.

Anderson, C. E., Walker, J. D., and Hauver, G. E., 1991, "Target Resistance for Long-Rod Penetration into Semi-infinite Targets," *Computational Impact Mechanics,* W. K. Kim, T. Belytshko, and T. Aizawa, eds., Elme Press.

Bishop, R. F., Hill, R., and Mott, N. F., 1945, "The Theory of Indentation and Hardness Tests," *The Proc. of the Phys Soc.,* Vol. 57, Part 3, pp. 147–159.

Curran, D. R., Seaman, L., Cooper, T., and Shockey, D. A., 1993, "Micromechanical Model for Comminution and Granular Flow of Brittle Material Under High Strain Rate Application to Penetration of Ceramic Targets," *Int. J. Impact Engng.,* Vol. 13, pp. 53–83.

Deitz, D., 1995, "Impact Codes for the Virtual Laboratory," *Mechanical Engn.,* Vol. 117, No. 5, pp. 66–70.

Forrestal, M. J., Frew, D. J., Hanchak, S. J., and Brar, N. S., 1996, "Penetration of Grout and Concrete Targets With Ogive-Nosed Steel Projectiles," *Int. J. Impact Engng.,* Vol. 18, pp. 465–476.

Forrestal, M. J., and Longcope, D. B., 1990, "Target Strength of Ceramic Materials for High-Velocity Penetration," *J. Appl. Phys.,* Vol. 67, pp. 3669–3672.

Forrestal, M. J., and Luk, V. K., 1988, "Dynamic Spherical Cavity-Expansion in a Compressible Elastic-Plastic Solid," ASME JOURNAL OF APPLIED MECHANICS, Vol. 55, pp. 755–760.

Forrestal, M. J., and Okajima, K., and Luk, V. K., 1988, "Penetration of 6061-T651 Aluminum Targets With Rigid Long Rods," ASME JOURNAL OF APPLIED MECHANICS, Vol. 55, pp. 755–760.

Forrestal, M. J., and Tzou, D. Y., 1997, "A Spherical Cavity-expansion Penetration Model for Concrete Targets," *Int. J. Solids Structures,* Vol. 34, pp. 4127–4146.

Frew, D. J., Forrestal, M. J., Hanchak, S. J., and Green, M. L., 1997, "Penetration into Limestone Targets with Ogive-nose Steele Projectiles," *Proc. 14th Army Symp. on Solid Mechanics,* K. R. Iyer and S.-c. Chou, eds., Battelle Press, Columbus, OH, pp. 121–128.

Green, M. L., 1992, *Laboratory Tests on Salem Limestone,* Geomech. Div., Struct. Lab., U.S. Army Waterways Exp. Station, Vicksburg, MS.

Hauver, G. E., Netherwood, P. H., Benck, R. F., Gooch, W. A., Perciballi, W. J., and Burkins, M. S., 1992, "Variation of Target Resistance During Long-rod Penetration into Ceramics," *13th Int. Symp. on Ballistics,* Stockholm, Sweden, preprint.

Hauver, G. E., Netherwood, P. H., Benck, R. F., and Melani, A., 1991, "Penetration of Shaped-Charge Jets into Glass and Crystalline Quartz," Tech. Rep. BRL-TR-3273, Aberdeen Proving Ground, MD.

Holian, B. L., Voter, A. F., and Ravelo, R., 1995, "Thermostated Molecular Dynamics: How to Avoid the tada Demon Hidden in Nose-Hoover Dynamics," *Phys. Rev.,* Vol. E52, pp. 2338–2347.

Johnson, G. R., and Cook, W. H., 1985, "Fracture Characteristic of Three Metals Subjected to Various Strains, Strain Rates, Temperatures and Pressures," *Eng. Fract. Mech.,* Vol. 21, pp. 31–48.

Kachanov, L. M., 1971, *Foundation of the Theory of Plasticity,* North-Holland, Amsterdam.

Krajcinovic, D., 1996, *Damage Mechanics* (North-Holland Series on Applied Mathematics and Mechanics, Vol. 41), Elsevier, Amsterdam.

Krajcinovic, D., and Mastilovic, S., 1999, "Statistical Models of Brittle Deformation: Part I—Introduction," *Int. J. of Plasticity,* Vol. 15, pp. 401–426.

Krajcinovic, D., Mastilovic, S., and Vujosevic, M., 1998, "Brittle to Quasi-brittle Transition," *Meccanica,* Vol. 33, pp. 363–379.

Kromm, A., 1948, "Zur Ausbreiting von Stosswellen in Kerislochscheiben," *Z. Angew. Math. Mech.,* Vol. 28, No. 10, pp. 297–303.

Kromm, A., 1948, "Zur Ausbreiting von Stosswellen in Kerislochscheiben," *Z. Angew. Math. Mech.,* Vol. 28, No. 4, pp. 104–114.

Mastilovic, S., and Krajcinovic, D., 1999a, "High Velocity Expansion of a Cavity Within a Brittle Material," *J. Mech. Phys. Solids,* Vol. 47, pp. 577–610.

Mastilovic, S., and Krajcinovic, D., 1999b, "Statistical Models of Brittle Deformation: Part II—Simulations," *Int. J. of Plasticity,* Vol. 15, pp. 427–456.

Nicholas, T., and Bless, S. J., 1985, "High Strain Rate Testing," *Mechanical Testing, Metals Handbook,* Vol. 8, Am. Soc. Metals, Metal Park, pp. 208–214.

Ortiz, M., 1996, "Computational Micromechanics," *Comput. Mechanics,* Vol. 18, pp. 321–339.

Pidsley, P. H., 1984, "A Numerical Study of Long Rod Impact onto a Large Target," *J. Mech. Phys. Solids,* Vol. 32, pp. 315–333.

Raftenberg, M. N., 1992, "Modeling RHA Plate Performation by a Shaped Charge Jet," Tech. Rep. BRL-TR-3363, Aberdeed Proving Ground, MD.

Shockey, D. A., Marchand, A. H., Skaggs, S. R., Cort, G. E., Burkett, M. W., and Parker, R., 1990, "Failure Phenomenology of Confined Ceramic Targets and Impacting Rods," *Int. J. Impact Engng.,* Vol. 9, pp. 263–275.

Strassburger, E., and Senf, H., 1995, "Experimental Investigation of Wave and Fracture Phenomena in Impacted Ceramics and Glasses," Report to U.S. Army Research Lab., Aberdeen, MD.

Tadmor, E. B., Ortiz, M., and Phillips, R., 1996, "Quasicontinuum Analysis of Defects in Solids," *Phil. Mag.,* Vol. A73, pp. 1529–1563.

Tadmor, E. B., Phillips, R., and Ortiz, M., 1996a, "Mixed Atomistic and Continuum Models of Deformation in Solids," *Langmuir,* Vol. 12, pp. 4529–4541.

Tate, A., 1967, "A Theory of the Deceleration of Long Rods After Impact," *J. Mech. Phys. Solids,* Vol. 15, pp. 387–399.

Tate, A., 1969, "Further Results in the Theory of Long Rod Penetration," *J. Mech. Phys. Solids,* Vol. 17, pp. 141E.B.

Downloaded 04 May 2010 to 171.66.16.27. Redistribution subject to ASME license or copyright; see http://www.asme.org/terms/Terms_Use.cfm

Reduction of the Sanders-Koiter Equations for Fully Anisotropic Circular Cylindrical Shells to Two Coupled Equations for a Stress and a Curvature Function

T. J. McDevitt
Department of Mathematics,
Millersville University,
Millersville, PA 17551

J. G. Simmonds
Department of Civil Engineering,
University of Virginia,
Charlottesville, VA 22903
Fellow ASME

With the aid of the static-geometric duality of Goldenveizer (1961), Cartesian tensor notation, and nondimensionalization, it is shown that the equations of linear shell theory of Sanders (1959) and Koiter (1959), when specialized to a circular cylindrical shell with stress-strain relations exhibiting full anisotropy (21 elastic-geometric constants), can be reduced, with no essential loss of accuracy, to two coupled fourth-order partial differential equations for a stress function F and a curvature function G. Auxiliary formulas for the midsurface displacement components are also given. For isotropic shells with uncoupled stress-strain relations, the equations reduce to a form given by Danielson and Simmonds (1969). The reduction is achieved by adding certain negligibly small terms to the given stress-strain relations. For orthotropic shells of mean radius R and thickness h with uncoupled stress-strain relations, it is shown that the very short decay length of $O(\sqrt{hR})$ and the very long decay length of $O(R\sqrt{R/h})$ (associated with separable solutions of the form $e^{-Rz}\sin n\theta$) depend, respectively, to within a relative error of $O(h/R)$, only on the products of different pairs of the eight possible elastic constants.

Introduction

Elastic tubes—circular cylindrical shells—are pervasive in nature, industry, the military, and everyday life. Think of arteries, piping, gun barrels, and straws. Thus any advance in their analyses should be welcome.

Thanks to their simple geometry and thanks to the existence of a relatively simple and sound set of equations for classical linear first-approximation shell theory due to Sanders (1959) and Koiter (1959), the reduction and analysis of the equations governing elastically *isotropic* circular cylindrical shells is well advanced. See, for example, reviews by Simmonds (1966) and Sanders (1983), and Chapter 11 of the book by Niordson (1985). In particular, the governing equations can be reduced to two coupled fourth-order equations for a stress function and the normal deflection or a curvature function.

For an orthotropic circular cylindrical shell described by four elastic constants (E_1, E_2, G, ν_1, ν_2 with $E_1\nu_1 = E_2\nu_2$), Cheng and He (1984) have reduced the governing equations of Flügge (1967) to a single eighth-order equation for the outward normal displacement w which they then factor into two fourth-order equations. They also list relatively complicated auxiliary formulas for the axial and circumferential displacements u and v. We show that simpler forms of their equations follow on specializing those developed below.

In what follows we reduce the linear Sanders-Koiter equations for a fully anisotropic circular cylindrical shell to two coupled fourth-order partial differential equations for a stress function F and a curvature function G. If one imagines the shell as composed of elastically anisotropic layers then, although each layer (being in an essentially plane state of stress) may be described by six elastic constants, if the layers have different thicknesses and different orientations, then the overall (suitably averaged) stress-strain relations will involve, in general, 21 elastic-geometric constants. Cartesian tensor notation and the static-geometric duality of Goldenveiser (1961)[1] prove to be indispensable in minimizing the algebra involved. We then specialize these equations to circular cylindrical shells with uncoupled orthotropic stress-strain relations (eight elastic constants) and show analytically how the very short and very long decay lengths associated with unsymmetric deformations depend, in each case, only on the product of a pair of these constants.

The Governing Equations

In a conventional set of polar cylindrical coordinates (r, θ, z) with associated unit base vectors $\{\mathbf{e}_r, \mathbf{e}_\theta, \mathbf{e}_z\}$, we denote the position of a point on the reference surface of our circular cylindrical shell by

$$C: \mathbf{r} = z\mathbf{e}_z + R\mathbf{e}_r(\theta) \equiv R[x_1\mathbf{e}_z + \mathbf{e}_r(x_2)], \tag{1}$$

where R is the constant midsurface radius. If we denote the metric and curvature tensors of C by $R^2a_{\alpha\beta}$ and $Rb_{\alpha\beta}$, respectively, then

$$a_{\alpha\beta} = \delta_{\alpha\beta} \quad \text{and} \quad b_{\alpha\beta} = \delta_{2\alpha}\delta_{2\beta}, \tag{2}$$

Contributed by the Applied Mechanics Division of THE AMERICAN SOCIETY OF MECHANICAL ENGINEERS for publication in the ASME JOURNAL OF APPLIED MECHANICS.
Discussion on the paper should be addressed to the Technical Editor, Professor Lewis T. Wheeler, Department of Mechanical Engineering, University of Houston, Houston, TX 77204-4792, and will be accepted until four months after final publication of the paper itself in the ASME JOURNAL OF APPLIED MECHANICS.
Manuscript received by the ASME Applied Mechanics Division, Dec. 23, 1998; final revision, Apr. 15, 1999. Associate Technical Editor: S. Kyriakides.

[1] This dates from 1940. See the footnote on page 95 of Goldenveizer (1961).

 Copyright © 1999 by ASME

Downloaded 04 May 2010 to 171.66.16.27. Redistribution subject to ASME license or copyright; see http://www.asme.org/terms/Terms_Use.cfm

where $\delta_{\alpha\beta}$ is the Kronecker delta.[2]

Let

$$\epsilon = h/R \tag{3}$$

be our fundamental small parameter and let

$$h^{-1}K_{\alpha\beta}, \quad EhN_{\alpha\beta}, \quad Eh^2M_{\alpha\beta} \tag{4}$$

denote, respectively, the symmetric bending strains and the (modified, symmetric) stress resultants and couples of the Sanders-Koiter theory, where E is some nominal Young's modulus; let $E_{\alpha\beta}$ denote the symmetric extensional strain. The equilibrium and compatibility conditions of the Sanders-Koiter theory, written in Cartesian tensor notation for a circular cylindrical shell free of surface loads, can then be given the form

$$(S_{\alpha\beta} + \epsilon e_{\alpha\beta}B_{\lambda\mu}M_{\lambda\mu}),_{\alpha} = 0 \tag{5}$$[3]

$$-\epsilon M_{\alpha\beta},_{\alpha\beta} + b_{\alpha\beta}N_{\alpha\beta} = 0 \tag{6}$$

$$(\hat{T}_{\alpha\beta} - \epsilon e_{\alpha\beta}B_{\lambda\mu}\hat{E}_{\lambda\mu}),_{\alpha} = 0 \tag{5*}$$

$$\epsilon\hat{E}_{\alpha\beta},_{\alpha\beta} + b_{\alpha\beta}\hat{K}_{\alpha\beta} = 0, \tag{6*}$$

where $e_{\alpha\beta}$ is the permutation symbol and a comma indicates partial differentiation. Here, to shorten the equations, we have set

$$S_{\alpha\beta} = N_{\alpha\beta} + \tfrac{1}{2}\epsilon(b_{\alpha\gamma}M_{\beta\gamma} + b_{\beta\gamma}M_{\alpha\gamma}) = S_{\beta\alpha}, \tag{7}$$

$$\hat{T}_{\alpha\beta} = \hat{K}_{\alpha\beta} - \tfrac{1}{2}\epsilon(b_{\alpha\gamma}\hat{E}_{\beta\gamma} + b_{\beta\gamma}\hat{E}_{\alpha\gamma}) = \hat{T}_{\beta\alpha}, \tag{7*}$$

and

$$2B_{\alpha\beta} = e_{\alpha\gamma}b_{\beta\gamma} + e_{\beta\gamma}b_{\alpha\gamma} = \delta_{1\alpha}\delta_{2\beta} + \delta_{1\beta}\delta_{2\alpha}. \tag{8}$$

Further, we have introduced the "hat" notation

$$\hat{A}_{\alpha\beta} \equiv e_{\alpha\lambda}e_{\beta\mu}A_{\lambda\mu} = \delta_{\alpha\beta}A_{\gamma\gamma} - A_{\beta\alpha}. \tag{9}$$

(Note for any two tensors $A_{\alpha\beta}$ and $B_{\alpha\beta}$ that $\hat{A}_{\alpha\beta}\hat{B}_{\beta\alpha} = B_{\alpha\beta}A_{\beta\alpha}$.) An equation with an asterisk (*) is the static-geometric dual of the corresponding equation without an asterisk. That is, (5)–(7) become (5*)–(7*) provided the variables below on the left are replaced by those on the right:

$$N_{\alpha\beta} : \hat{K}_{\alpha\beta}, \quad M_{\alpha\beta} : -\hat{E}_{\alpha\beta}, \quad S_{\alpha\beta} : \hat{T}_{\alpha\beta}. \tag{10}$$

The general solution of (5) has the form

$$S_{\alpha\beta} + \epsilon e_{\alpha\beta}B_{\lambda\mu}M_{\lambda\mu} = e_{\alpha\gamma}\chi_{\beta},_{\gamma}, \tag{11}$$

where χ_β is an arbitrary surface vector which we decompose further by setting

$$\chi_\beta = \epsilon P_\beta + e_{\beta\mu}F,_{\mu} + H,_{\beta}. \tag{12}$$

Here, F and H are arbitrary scalar functions and ϵP_β—the "particular" part of χ_β—is chosen to remove the antisymmetric term on the left of (11). That is,

$$\epsilon P_{\alpha},_{\alpha} + H,_{\alpha\alpha} = 2\epsilon B_{\lambda\mu}M_{\lambda\mu}. \tag{13}$$

Once we introduce appropriately modified stress-strain relations, we shall show that it is always possible to satisfy (13) with $H \equiv 0$. Thus, inserting (12) (with $H = 0$) into (11) and the symmetric part of the resulting expression—i.e., $S_{\alpha\beta}$—into (7), we obtain the representation

$$N_{\alpha\beta} + \tfrac{1}{2}\epsilon[b_{\alpha\gamma}M_{\beta\gamma} + b_{\beta\gamma}M_{\alpha\gamma} - (e_{\alpha\gamma}P_\beta + e_{\beta\gamma}P_\alpha),_{\gamma}] = e_{\alpha\lambda}e_{\beta\mu}F,_{\lambda\mu} \equiv N^{\#}_{\alpha\beta}. \tag{14}$$

We call F a *stress function.*

By the static-geometric duality (10), we may, without further calculation, write down the analogous expression involving $\hat{K}_{\alpha\beta}$, namely

$$\hat{K}_{\alpha\beta} - \tfrac{1}{2}\epsilon[b_{\alpha\gamma}\hat{E}_{\beta\gamma} + b_{\beta\gamma}\hat{E}_{\alpha\gamma} - (e_{\alpha\gamma}Q_\beta,_{\gamma} + e_{\beta\gamma}Q_\alpha,_{\gamma})] = e_{\alpha\lambda}e_{\beta\mu}G,_{\lambda\mu} \equiv \hat{K}^{\#}_{\alpha\beta}, \tag{14*}$$

where the new particular solution Q_α and the *curvature function* G are related to P_α and F by the static-geometric duality

$$F : G, \quad P_\alpha : -Q_\alpha. \tag{15}$$

The Stress-Strain Relations

Assume that the shell has a positive definite strain-energy density $Eh\Phi$, where

$$\Phi = \tfrac{1}{2}(E_{\alpha\beta\lambda\mu}\hat{E}_{\alpha\beta}\hat{E}_{\lambda\mu} + 2B_{\alpha\beta\lambda\mu}\hat{E}_{\alpha\beta}K_{\lambda\mu} + D_{\alpha\beta\lambda\mu}K_{\alpha\beta}K_{\lambda\mu}). \tag{16}$$

Here, $\{E_{\alpha\beta\lambda\mu}, B_{\alpha\beta\lambda\mu}, D_{\alpha\beta\lambda\mu}\}$ are a set of 6 + 9 + 6 independent elastic constants displaying the standard symmetries:

$$E_{\alpha\beta\lambda\mu} = E_{\beta\alpha\lambda\mu} = E_{\lambda\mu\alpha\beta}, \quad D_{\alpha\beta\lambda\mu} = D_{\beta\alpha\lambda\mu} = D_{\lambda\mu\alpha\beta},$$

$$B_{\alpha\beta\lambda\mu} = B_{\beta\alpha\lambda\mu} = B_{\alpha\beta\mu\lambda}. \tag{17}$$

The dimensionless stress resultants and couples are given by

$$\hat{N}_{\alpha\beta} = \Phi,_{\hat{E}_{\alpha\beta}} = E_{\alpha\beta\lambda\mu}\hat{E}_{\lambda\mu} + B_{\alpha\beta\lambda\mu}K_{\lambda\mu} \tag{18}$$

and

$$M_{\alpha\beta} = \Phi,_{K_{\alpha\beta}} = D_{\alpha\beta\lambda\mu}K_{\lambda\mu} + B_{\lambda\mu\alpha\beta}\hat{E}_{\lambda\mu}. \tag{19}$$

To exploit fully the static-geometric duality, we need to express $\hat{E}_{\alpha\beta}$ and $M_{\alpha\beta}$ in terms of $\hat{N}_{\alpha\beta}$ and $K_{\alpha\beta}$. Equations (18) comprise three linear, nonhomogeneous, nonsingular algebraic equations for $\hat{E}_{\alpha\beta}$ which, in practice, may always be solved. To carry out this inversion formally, define the inverse $A_{\alpha\beta\lambda\mu}$ such that

$$A_{\alpha\beta\lambda\mu}E_{\lambda\mu\kappa\rho} = \delta_{\alpha\kappa}\delta_{\beta\rho}. \tag{20}$$

Then, from (18),

$$-\hat{E}_{\alpha\beta} = -A_{\alpha\beta\lambda\mu}\hat{N}_{\lambda\mu} + C_{\alpha\beta\lambda\mu}K_{\lambda\mu}, \tag{21}$$

where, by the symmetries displayed in (17),

$$C_{\alpha\beta\lambda\mu} = A_{\alpha\beta\kappa\rho}B_{\kappa\rho\lambda\mu} = B_{\kappa\rho\lambda\mu}A_{\kappa\rho\alpha\beta}. \tag{22}$$

Substituting (21) into (19), noting (22), and relabeling dummy indices, we have

$$M_{\alpha\beta} = A^{*}_{\alpha\beta\lambda\mu}K_{\lambda\mu} + C^{*}_{\alpha\beta\lambda\mu}\hat{N}_{\lambda\mu} \tag{21*}$$

where $C^{*}_{\alpha\beta\lambda\mu} = C_{\lambda\mu\alpha\beta}$ and

$$A^{*}_{\alpha\beta\lambda\mu} = D_{\alpha\beta\lambda\mu} - B_{\kappa\rho\alpha\beta}C_{\kappa\rho\lambda\mu} \tag{23}$$

is the static-geometric dual of $-A_{\alpha\beta\lambda\mu}$. Here and in what follows we adopt the convention that the static-geometric dual of an elastic constant is denoted by an asterisk (*).

We note in passing that to make the field equations of shell theory reflect the static-geometric duality completely, one should introduce the (dimensionless) *mixed-energy density*

$$\Psi = \inf_{\hat{E}_{\alpha\beta}}\{\Phi(\hat{E}_{\alpha\beta}, K_{\alpha\beta}) - \hat{N}_{\alpha\beta}\hat{E}_{\alpha\beta}\} = \tfrac{1}{2}(M_{\alpha\beta}K_{\alpha\beta} - \hat{N}_{\alpha\beta}\hat{E}_{\alpha\beta})$$
$$= \tfrac{1}{2}(A^{*}_{\alpha\beta\lambda\mu}K_{\alpha\beta}K_{\lambda\mu} + C_{\alpha\beta\lambda\mu}\hat{N}_{\alpha\beta}K_{\lambda\mu} + C^{*}_{\alpha\beta\lambda\mu}K_{\alpha\beta}\hat{N}_{\lambda\mu} - \tfrac{1}{2}A_{\alpha\beta\lambda\mu}\hat{N}_{\alpha\beta}\hat{N}_{\lambda\mu}). \tag{24}$$

[2] In what follows we delay using these explicit forms of $a_{\alpha\beta}$ and $b_{\alpha\beta}$. Moreover, because the Gaussian curvature and any covariant derivative of $b_{\alpha\beta}$ are both zero on a circular cylinder, the equations to follow may be used with general surface coordinates merely by replacing all partial derivatives by covariant derivatives.

[3] For a general shell, this equation reads, in standard tensor notation, $(S^{\alpha\beta} + \epsilon e^{\alpha\beta}B_{\lambda\mu}M^{\lambda\mu})|_{\alpha} - b^{\beta}_{\alpha}|_{\gamma}M^{\alpha\gamma} = 0$, where a vertical bar denotes covariant differentiation. On a circular cylinder, $b^{\beta}_{\alpha}|_{\gamma} = 0$.

Downloaded 04 May 2010 to 171.66.16.27. Redistribution subject to ASME license or copyright; see http://www.asme.org/terms/Terms_Use.cfm

One then has $-\hat{E}_{\alpha\beta} = \Psi_{,\hat{N}_{\alpha\beta}}$ and $M_{\alpha\beta} = \Psi_{,K_{\alpha\beta}}$. Of course, the mixed-energy density is not positive definite.

Modification of the Stress-Strain Relations

We now introduce the *sole* hypothesis on which our reduction hinges, namely that *(14) and (14*) are such that*

$$N_{\alpha\beta} = N^{\#}_{\alpha\beta} + O(\epsilon\sqrt{M_{\alpha\beta}M_{\alpha\beta}}) \quad \text{and}$$
$$\hat{K}_{\alpha\beta} = \hat{K}^{\#}_{\alpha\beta} + O(\epsilon\sqrt{E_{\alpha\beta}E_{\alpha\beta}}). \tag{25}$$

But if this hypothesis is true—as we shall verify, a posteriori—then the stress-strain relations we obtain by replacing $\hat{N}_{\alpha\beta}$ by $\hat{N}^{\#}_{\alpha\beta}$ and $K_{\alpha\beta}$ by $K^{\#}_{\alpha\beta}$, that is, the stress-strain relations

$$-\hat{E}_{\alpha\beta} = -A_{\alpha\beta\lambda\mu}F_{,\lambda\mu} + C_{\alpha\beta\lambda\mu}G_{,\lambda\mu} \tag{26}$$

and

$$M_{\alpha\beta} = A^{*}_{\alpha\beta\lambda\mu}G_{,\lambda\mu} + C^{*}_{\alpha\beta\lambda\mu}F_{,\lambda\mu}, \tag{26*}$$

lead to equations whose solutions contain mean square errors of relative order ϵ, as shown by Simmonds (1971) and Koiter and Clément (1979). Note that this is true even if the modified stress-strain relations (26) and (26*) are not derivable from a strain-energy density—this was the point of Simmonds' analysis.

Determination of the Particular Function P

Inserting (26*) into (13) (with $H = 0$), we obtain

$$P_{\alpha,\alpha} = 2B_{\lambda\mu}(A^{*}_{\lambda\mu\kappa\rho}G_{,\kappa\rho} + C^{*}_{\lambda\mu\kappa\rho}F_{,\kappa\rho})$$
$$= 2B_{\lambda\mu}(A^{*}_{\lambda\mu\kappa\alpha}G + C^{*}_{\lambda\mu\kappa\alpha}F)_{,\kappa\alpha}, \tag{27}$$

which shows that we may take our particular function to be

$$P_{\alpha} = 2B_{\lambda\mu}(A^{*}_{\lambda\mu\kappa\alpha}G + C^{*}_{\lambda\mu\kappa\alpha}F)_{,\kappa}. \tag{28}$$

Substituting this relation and (26*) back into (14), we obtain an expression of the form

$$N_{\alpha\beta} = N^{\#}_{\alpha\beta} - \epsilon(H^{*}_{\alpha\beta\lambda\mu}\hat{N}^{\#}_{\lambda\mu} - I^{*}_{\alpha\beta\lambda\mu}K^{\#}_{\lambda\mu}), \tag{29}$$

where

$$H_{\alpha\beta\lambda\mu} = \tfrac{1}{2}(b_{\alpha\gamma}C_{\lambda\mu\beta\gamma} + b_{\beta\gamma}C_{\lambda\mu\alpha\gamma}) + B_{\kappa\gamma}(e_{\mu\alpha}C_{\lambda\beta\kappa\gamma} + e_{\mu\beta}C_{\lambda\alpha\kappa\gamma}) \tag{30}$$

and

$$I_{\alpha\beta\lambda\mu} = B_{\kappa\gamma}(e_{\alpha\mu}A_{\lambda\beta\kappa\gamma} + e_{\beta\mu}A_{\lambda\alpha\kappa\gamma}) - \tfrac{1}{2}(b_{\alpha\gamma}A_{\lambda\mu\beta\gamma} + b_{\beta\gamma}A_{\lambda\mu\alpha\gamma}). \tag{31}$$

Note that $I^{*}_{\alpha\beta\lambda\mu} = B_{\kappa\gamma}(e_{\alpha\mu}A^{*}_{\lambda\beta\kappa\gamma} + \ldots)$ is the dual of $-I_{\alpha\beta\lambda\mu}$. By the static-geometric duality, we know at once from (14*) that the relation dual to (29) has the form

$$\hat{K}_{\alpha\beta} = \hat{K}^{\#}_{\alpha\beta} - \epsilon(H_{\alpha\beta\lambda\mu}K^{\#}_{\lambda\mu} + I_{\alpha\beta\lambda\mu}\hat{N}^{\#}_{\alpha\beta}). \tag{29*}$$

Thus, the hypothesis (25) is fulfilled. Moreover, (29) and (29*), which are linear relations, could be solved for $\hat{N}^{\#}_{\alpha\beta}$ and $K^{\#}_{\alpha\beta}$ in terms of $\hat{N}_{\alpha\beta}$ and $K_{\alpha\beta}$ and substituted into the modified stress-strain relations (26) and (26*) to yield a (complicated) set of *initial* stress-strain relations of which (26) and (26*) would be *exact* consequences. In fact, it is obvious from (29) and (29*) that

$$N^{\#}_{\alpha\beta} = N_{\alpha\beta} + \epsilon(H^{*}_{\alpha\beta\lambda\mu}\hat{N}_{\lambda\mu} - I^{*}_{\alpha\beta\lambda\mu}K_{\lambda\mu}) + O(\epsilon^2) \tag{32}$$

and

$$\hat{K}^{\#}_{\alpha\beta} = \hat{K}_{\alpha\beta} + \epsilon(H_{\alpha\beta\lambda\mu}K_{\lambda\mu} + I_{\alpha\beta\lambda\mu}\hat{N}_{\alpha\beta}) + O(\epsilon^2). \tag{32*}$$

The Reduced Coupled Equations for F and G

Substituting (26*) and (29) into (6) and recalling that $\hat{N}^{\#}_{\alpha\beta} = F_{,\alpha\beta}$, $K^{\#}_{\alpha\beta} = G_{,\alpha\beta}$, and $b_{\alpha\beta}N_{\alpha\beta} = \hat{b}_{\alpha\beta}\hat{N}_{\alpha\beta}$, we obtain the first of our two reduced equations:

$$-\epsilon\mathcal{L}G + \mathcal{M}F = 0, \tag{33}$$

where

$$\mathcal{L}G = (A^{*}_{\alpha\beta\lambda\mu}G_{,\alpha\beta} - b_{\alpha\beta}I^{*}_{\alpha\beta\lambda\mu}G)_{,\lambda\mu} \tag{34}$$

and

$$\mathcal{M}F = [(\hat{b}_{\lambda\mu} - \epsilon b_{\alpha\beta}H^{*}_{\alpha\beta\lambda\mu})F - \epsilon C^{*}_{\alpha\beta\lambda\mu}F_{,\alpha\beta}]_{,\lambda\mu}. \tag{35}$$

By the static-geometric duality, we immediately have the second of our reduced equations:

$$-\epsilon\mathcal{L}^{*}F + \mathcal{M}^{*}G = 0. \tag{33*}$$

Because the differential operators $\mathcal{L}$, $\mathcal{M}$, $\mathcal{L}^{*}$, and $\mathcal{M}^{*}$ have constant coefficients (and hence commute), we may easily reduce the pair (33), (33*) to a single eight-order equation. For example eliminating either F or G we have

$$(-\epsilon^2\mathcal{L}\mathcal{L}^{*} + \mathcal{M}\mathcal{M}^{*})\{F, G\} = 0. \tag{36}$$

Equations for Displacements

Let Ru_{α} and Rw denote displacements in the midsurface and *outward* normal direction, respectively. Then from (26) and the Sanders-Koiter theory follows:

$$\delta_{\alpha\beta}(u_{\gamma,\gamma} + b_{\gamma\gamma}w) - \tfrac{1}{2}(u_{\alpha,\beta} + u_{\beta,\alpha}) - b_{\alpha\beta}w = (A_{\alpha\beta\lambda\mu}F - C_{\alpha\beta\lambda\mu}G)_{,\lambda\mu}. \tag{37}$$

We shall solve these equations in the next section when we introduce the surface coordinates x_1 and x_2 defined in (1).

The Governing Equations in the "Rectangular" Surface Coordinates x_1 and x_2

By $(2)_2$ and (8), the only nonzero components of $b_{\alpha\beta}$ and $B_{\alpha\beta}$ are $b_{22} = 1$ and $B_{12} = \frac{1}{2}$. Thus, from (30) and (31),

$$H_{22\lambda\mu} = C_{\lambda\mu22} + 2e_{\mu2}C_{\lambda212}, \quad I_{22\lambda\mu} = 2e_{2\mu}A_{\lambda212} - A_{\lambda\mu22}. \tag{38}$$

Thus, (33) and (33*) take the more explicit forms

$$-\epsilon[(C^{*}_{\alpha\beta\lambda\mu}F + A^{*}_{\alpha\beta\lambda\mu}G)_{,\alpha\beta} + (2e_{\mu2}C^{*}_{\lambda212} + C^{*}_{\lambda\mu22})F + (A^{*}_{\lambda\mu22} + 2e_{\mu2}A^{*}_{\lambda212})G]_{,\lambda\mu} + F_{,11} = 0 \tag{39}$$

and

$$-\epsilon[(C_{\alpha\beta\lambda\mu}G - A_{\alpha\beta\lambda\mu}F)_{,\alpha\beta} + (2e_{\mu2}C_{\lambda212} + C_{\lambda\mu22})G - (A_{\lambda\mu22}F + 2e_{\mu2}A_{\lambda212})F]_{,\lambda\mu} + G_{,11} = 0. \tag{39*}$$

The coupled Eqs. (39) and (39*) admit solutions of the form $F = F_0e^{-p_{\alpha}x_{\alpha}}$ and $G = G_0e^{-p_{\alpha}x_{\alpha}}$, where F_0, G_0, and the p_{α} are, in general, complex constants.

Turning to the determination of displacements, we first set $\alpha = \beta = 2$ in (37). Then, upon integrating with respect to x_1, we obtain

$$u_1 = \int (A_{22\lambda\mu}F - C_{22\lambda\mu}G)_{,\lambda\mu}dx_1. \tag{40}$$

Next, for $\alpha = 1$ and $\beta = 2$ and with a second (indefinite) integration with respect to x_1, we obtain, on inserting (40) into (37),

Downloaded 04 May 2010 to 171.66.16.27. Redistribution subject to ASME license or copyright; see http://www.asme.org/terms/Terms_Use.cfm

$$u_2 = 2\int (C_{12\lambda\mu}G - A_{12\lambda\mu}F),_{\lambda\mu}dx_1 + \int\left[\int (C_{22\lambda\mu}G - A_{22\lambda\mu}F),_{\lambda\mu}dx_1\right],_2 dx_1. \quad (41)$$

Finally, setting $\alpha = \beta = 1$ in (37) and inserting (41), we obtain

$$w = (A_{11\lambda\mu}F - C_{11\lambda\mu}G),_{\lambda\mu} + \left[2\int (A_{12\lambda\mu}F - C_{12\lambda\mu}G),_{\lambda\mu}dx_1\right],_2 + \left\{\int\left[\int (A_{22\lambda\mu}F - C_{22\lambda\mu}G),_{\lambda\mu}dx_1\right],_2 dx_1\right\},_2. \quad (42)$$

Note that the various "partial" indefinite integrals above contain arbitrary functions of integration, so that, for example, if the deformation is *inextensional* ($E_{\alpha\beta} = 0$), then (40)–(42) yield

$$u_1 = f(x_2), \quad u_2 = -x_1 f'(x_2) + g(x_2), \quad w = x_1 f''(x_2) - g'(x_2), \quad (43)$$

where f and g are arbitrary functions.

The Form of the Equations for Uncoupled Orthotropic Stress-Strain Relations

Here,

$$C_{\alpha\beta\lambda\mu} = D_{1211} = D_{1222} = A_{1211} = A_{1222} = 0 \quad (44)$$

which implies that (39) and (39*) reduce to

$$-\epsilon\mathcal{L}G + F,_{11} = 0 \quad \text{and} \quad -\epsilon\mathcal{L}^*F + G,_{11} = 0, \quad (45)$$

where

$$\mathcal{L}G = A^*_{1111}G,_{1111} + 4A^*_{1212}G,_{1122} + A^*_{2222}G,_{2222} + (2A^*_{1212} + A^*_{1122})G,_{11} + A^*_{2222}G,_{22}, \quad (46)$$

and $\mathcal{L}^*$ is the static-geometric dual of $\mathcal{L}$.

Decaying Unsymmetric Solutions

Let us look for solutions of the form

$$F = F_0 e^{-px_1}\sin(nx_2), \quad G = G_0 e^{-px_1}\sin(nx_2), \quad (47)$$

where F_0 and G_0 are constants and $n = 2, 3, \ldots$. (We exclude $n = 1$ which leads to nondecaying, beamlike solutions.) Then, (45) reduces to

$$-\epsilon[A^*_{1111}p^4 - 4A^*_{1212}p^2n^2 + A^*_{2222}n^4 + (2A^*_{1212} + A^*_{1122})p^2 - A^*_{2222}n^2]G_0 + p^2F_0 = 0 \quad (48)$$

and its dual.

Of the eight possible values of p, four correspond to growing solutions and four to decaying solutions, and, of the latter, two correspond to rapid decay (over a length of order $\sqrt{HR}$) while two correspond to slow decay (over a length of order $R\sqrt{R/H}$). To obtain an asymptotic formula for the two rapidly decaying roots, we set

$$p = r/\sqrt{\epsilon}. \quad (49)$$

Then, (48) and its dual yield

$$F_0 = A^*_{1111}r^2G_0 + O(\epsilon) \quad \text{and} \quad G_0 = -A_{1111}r^2F_0 + O(\epsilon). \quad (50)$$

Hence, the two rapidly decaying roots are

$$p_r = \frac{e^{\pm i\pi/4}}{\epsilon^{1/2}(A_{1111}A^*_{1111})^{1/4}} + O(\epsilon^{1/2}). \quad (51)$$

To obtain an asymptotic formula for the slowing decaying roots, we set

$$p = \sqrt{\epsilon}s. \quad (52)$$

Then (48) and its dual yield

$$s^2F_0 = A^*_{2222}(n^2 - 1)n^2G_0 + O(\epsilon) \quad \text{and} \quad s^2G_0 = -A_{2222}(n^2 - 1)n^2F_0 + O(\epsilon). \quad (53)$$

Hence the two slowly decaying roots are

$$p_s = [\epsilon(n^2 - 1)]^{1/2}n(A_{2222}A^*_{2222})^{1/4}e^{\pm i\pi/4} + O(\epsilon^{3/2}). \quad (54)$$

In an isotropic shell, $A_{1111}A^*_{1111} = A_{2222}A^*_{2222} = [12(1 - \nu^2)]^{-1}$. Thus, in an orthotropic shell, the rapid and slow decay rates may be either greater or less than for isotropy, depending on the values of A_{1111}, etc.

Using the values for boron/epoxy given in Table 2 of Cheng and He (1984), we find that

$$(A_{1111}A^*_{1111})^{1/4} = \left[\frac{E_1}{12E_2(1 - \nu_1\nu_2)}\right]^{1/4} = 0.9576$$

$$(A_{2222}A^*_{2222})^{1/4} = \left[\frac{E_2}{12E_1(1 - \nu_1\nu_2)}\right]^{1/4} = 0.3028. \quad (55)$$

Substituting these values into (51) and (54), setting $\sqrt{\epsilon} = 0.02632$, and, in the latter equation, $n = 2$, we find that

$$p_r = 28.06(1 \pm i) \quad \text{and} \quad p_s = 0.01952(1 \pm i), \quad (56)$$

which agree quite closely with the values listed in Table 4 by Cheng and He (1984).

Conclusions

The economy of tensor notation plus the remarkable properties of the static-geometric duality, especially when extended to material properties, helped immensely in reducing the governing linear equations of Sanders and Koiter for a fully anisotropic circular cylindrical shell to two coupled fourth-order partial differential equations. Another key factor was the slight modification of the given stress-strain relations, which is acceptable physically—after all, these are never known precisely—and can be justified using the arguments of Simmonds (1971) and Koiter and Clément (1979). Having two coupled fourth-order equations which are duals of one another allows us to conduct *analytical* parameter studies, as we have indicated for the special case of shells with uncoupled orthotropic stress-strain relations.

Some idea of the great efficiency of our scheme of reduction comes from a comparison with the analysis of Cheng and He (1984). For a specially orthotropic material with only *three* elastic constants—they make the special choice $2(1 + \sqrt{\nu_1\nu_2})G = \sqrt{E_1E_2}$—and after great algebraic labor to evaluate a 3×3 determinant involving the neglect of certain small terms, these authors obtain a single eighth-order equation for the normal deflection. By contrast, our dual fourth-order equations (33) and (33*), or, equivalently, (36), came with relatively little effort once the material-static-geometric duality was established. (In particular, there were no operator determinants to evaluate.) Furthermore, even though these equations contain 21 elastic constants in the general case, they are not so complicated as to preclude analytical solutions.

Acknowledgment

The work of JGS was supported by the National Aeronautics and Space Administration under Grant NAG-1-1854.

Downloaded 04 May 2010 to 171.66.16.27. Redistribution subject to ASME license or copyright; see http://www.asme.org/terms/Terms_Use.cfm

References

Cheng, S., and He, F. B., 1984, "Theory of Orthotropic and Composite Cylindrical Shells, Accurate and Simple Fourth-Order Governing Equations," ASME JOURNAL OF APPLIED MECHANICS, Vol. 51, pp. 736–744.

Danielson, D. A., and Simmonds, J. G., 1969, "Accurate Buckling Equations for Arbitrary and Cylindrical Elastic Shells," *Int. J. Engr. Sci.,* Vol. 7, pp. 459–468.

Flügge, W., 1967, *Stresses in Shells,* Springer-Verlag, Berlin.

Goldenveizer, A. L., 1961, *Theory of Thin Elastic Shells,* Pergamon, New York.

Koiter, W. T., 1959, "A Consistent First Approximation in the General Theory of Thin Elastic Shells," *The Theory of Thin Elastic Shells,* Proc. IUTAM Sympos. Delft, W. T. Koiter, ed., North-Holland, Amsterdam, pp. 12–33.

Koiter, W. T., and Clément, Ph., 1979, "On the So-Called Comparison Theorem in the Linear Theory of Elasticity," *Z.A.M.P.,* Vol. 30, pp. 534–536.

Niordson, F., 1985, *Shell Theory,* North-Holland, Amsterdam.

Sanders, J. L., Jr., 1959, "An Improved First-Approximation Theory for Thin Shells," NASA Report No. 24.

Sanders, J. L., Jr., 1983, "Analysis of Circular Cylindrical Shells," ASME JOURNAL OF APPLIED MECHANICS, Vol. 50, pp. 1165–1170.

Simmonds, J. G., 1966, "A Set of Simple Accurate Equations for Circular Cylindrical Elastic Shells," *Int. J. Solids Struct.,* Vol. 2, pp. 524–541.

Simmonds, J. G., 1970, "Simplification and Reduction of the Sanders-Koiter Linear Shell Equations for Various Midsurface Geometries," *Q. Appl. Math.,* Vol. 28, pp. 259–275.

Simmonds, J. G., 1971, "Extension of Koiter's L_2-Error Estimate to Approximate Shell Solutions With No Strain Energy Functional," *Z.A.M.P.,* Vol. 22, pp. 339–345.

Downloaded 04 May 2010 to 171.66.16.27. Redistribution subject to ASME license or copyright; see http://www.asme.org/terms/Terms_Use.cfm

Elasticity Solution for a Radially Nonhomogeneous Hollow Circular Cylinder

Xiangzhou Zhang
Department of Civil Engineering,
Shanghai Tiedao University,
Shanghai 200333,
P. R. China

Norio Hasebe
Department of Civil Engineering,
Nagoya Institute of Technology,
Nagoya 466-8555, Japan

An exact elasticity solution is developed for a radially nonhomogeneous hollow circular cylinder of exponential Young's modulus and constant Poisson's ratio. In the solution, the cylinder is first approximated by a piecewise homogeneous one, of the same overall dimension and composed of perfectly bonded constituent homogeneous hollow circular cylinders. For each of the constituent cylinders, the solution can be obtained from the theory of homogeneous elasticity in terms of several constants. In the limit case when the number of the constituent cylinders becomes unboundedly large and their thickness tends to infinitesimally small, the piecewise homogeneous hollow circular cylinder reverts to the original nonhomogeneous one, and the constants contained in the solutions for the constituent cylinders turn into continuous functions. These functions, governed by some systems of first-order ordinary differential equations with variable coefficients, stand for the exact elasticity solution of the nonhomogeneous cylinder. Rigorous and explicit solutions are worked out for the ordinary differential equation systems, and used to generate a number of numerical results. It is indicated in the discussion that the developed method can also be applied to hollow circular cylinders with arbitrary, continuous radial nonhomogeneity.

Introduction

The elasticity problem of a homogeneous hollow circular cylinder has sufficiently been treated in Muskhelishvili (1963), Timoshenko and Goodier (1970), Barber (1992), and in other monographs. This article investigates the same problem on the whole, except that the hollow cylinder concerned is of a radially nonhomogeneous material.

Nonhomogeneous materials can frequently be found in nature as well as in man-made structures. Porous substances, laminated composites, dissimilar media, and many others can be categorized as nonhomogeneous materials. However, typically nonhomogeneous materials seem to be those with elastic constants varying continuously in different spatial directions.

Continuous nonhomogeneity is a direct generalization of homogeneity in theory; besides, material nonhomogeneity becomes essential and must sufficiently be considered in a number of practical situations. For example, in seismic problems, the spatial variation of material constants cannot be neglected owing to the massive structure of the earth.

It appears that previous references on the elastic nonhomogeneity have been concentrated in the area of mixed boundary value, including crack problems. In earlier years, contact and similar problems were treated with use of integral transforms (Belik and Protsenko, 1967; Popov, 1973; Kassir and Chuaprasert, 1974; Bakirtas, 1980). Recently, using mainly the method of singular integral equation, there has been an intensive interest in crack problems (Delale and Erdogan, 1983; Erdogan, Kaya and Joseph, 1991a, 1991b; Gao and Kuang, 1992; Craster and Atkinson 1994; Choi, 1996). By successively extending the solution to a Fredholm integral equation of the first kind, Yong and Hanson (1994) solved some crack and contact problems for a nonhomogeneous medium. Of note, too, is Fabrikant's work (Fabrikant, 1985) on an external crack in a nonhomogeneous space, whose solution was obtained by the application of potential theory (Fabrikant, 1989). In all the referenced works, and in most of available solutions to elastic nonhomogeneity, it is assumed that the material is isotropic, the Poisson's ratio is constant, and the Young's modulus is either an exponential or a power function of a spatial variable (Delale and Erdogan, 1983; Fabrikant, 1989; Yong and Hanson, 1994; Choi, 1996).

Despite the considerable amount of existing references on mixed boundary value problems, exact solutions to basic problems in nonhomogeneous elasticity appear to be very few. In fact, such solutions can be used to best enunciate and substantiate the theory, and they hold ample potential for various applications. Consequently, it is worthwhile to develop exact solutions to basic problems for a complete and useful theory of nonhomogeneous elasticity.

This article develops an exact elasticity solution for a nonhomogeneous hollow circular cylinder, of constant Poisson's ratio and nonuniform Young's modulus in the form of an exponential function of the radial coordinate. To obtain the solution, the nonhomogeneous hollow circular cylinder is approximately substituted by a composite one, of the same overall geometry and consisting of a number of perfectly bonded constituent hollow circular cylinders, each of them is with uniform thickness and constant Young's modulus, identical in value to that of the original nonhomogeneous cylinder at a certain local point. This composite, piecewise homogeneous hollow circular cylinder approximates the original nonhomogeneous cylinder sufficiently accurately, when the thickness of the constituent hollow circular cylinders is sufficiently small. For each of the constituent cylinders, the solution can be obtained from the existing solution in the theory of homogeneous elasticity in terms of constant coefficients (Timoshenko and Goodier, 1970; Barber, 1992).

When the number of the constituent hollow circular cylinders becomes unboundedly large and their thickness tends to be infinitesimally small, the composite, piecewise homogeneous cylinder reverts to the original, nonhomogeneous cylinder at the end of the limit. Meanwhile, the groups of the discrete constant coefficients in the solutions for individual constituent cylinders turn into con-

Contributed by the Applied Mechanics Division of THE AMERICAN SOCIETY OF MECHANICAL ENGINEERS for publication in the ASME JOURNAL OF APPLIED MECHANICS.
Discussion on the paper should be addressed to the Technical Editor, Professor Lewis T. Wheeler, Department of Mechanical Engineering, University of Houston, Houston, TX 77204-4792, and will be accepted until four months after final publication of the paper itself in the ASME JOURNAL OF APPLIED MECHANICS.
Manuscript received by the ASME Applied Mechanics Division, Apr. 28, 1998; final revision, Feb. 25, 1999. Associate Technical Editor: J. R. Barber.

 Copyright © 1999 by ASME

Downloaded 04 May 2010 to 171.66.16.27. Redistribution subject to ASME license or copyright; see http://www.asme.org/terms/Terms_Use.cfm

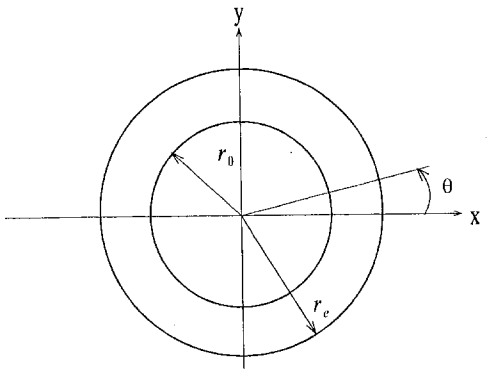


Fig. 1 The nonhomogeneous hollow circular cylinder

tinuous functions for the whole cylinder. These functions are determined rigorously and stand for the exact solution for the nonhomogeneous hollow circular cylinder.

Without resort to the theory and fundamental equations of nonhomogeneous elasticity, this article provides an exact solution to a basic problem in the theory of nonhomogeneous elasticity. Illustrative numerical results and discussion on the potential extention of the solution are also presented.

Problem and Basic Reduction

Consider the plane elasticity problem of a nonhomogeneous hollow circular cylinder shown in Fig. 1. It is assumed that the Poisson's ratio of the material, ν, is constant, while the Young's modulus E is a function of r such that $E(r) = Ae^{\beta r}$, where A and β are given constants. As indicated in the Introduction, such material properties have been used in the literature most popularly. Extension of the material properties to more general cases will be treated later in the discussion.

In the special case $\beta = 0$, the cylinder reduces to a homogeneous one. The plane elasticity solution to homogeneous hollow circular cylinders is well known. By using Michell's presentation, the solution can be summarized as follows (Barber, 1992; Timoshenko and Goodier, 1970):

$$\sigma_{rr} = \frac{1}{r}\frac{\partial \phi}{\partial r} + \frac{1}{r^2}\frac{\partial^2 \phi}{\partial \theta^2}, \quad \sigma_{\theta\theta} = \frac{\partial^2 \phi}{\partial r^2},$$

$$\sigma_{r\theta} = -\frac{\partial}{\partial r}\left(\frac{1}{r}\frac{\partial \phi}{\partial \theta}\right), \tag{1}$$

$$e_{rr} = \frac{\sigma_{rr}}{E'} - \frac{\nu'\sigma_{\theta\theta}}{E'}, \quad e_{\theta\theta} = \frac{\sigma_{\theta\theta}}{E'} - \frac{\nu'\sigma_{rr}}{E'}, \quad e_{r\theta} = \frac{\sigma_{r\theta}}{2\mu},$$

$$e_{rr} = \frac{\partial u_r}{\partial r}, \quad e_{\theta\theta} = \frac{1}{r}\frac{\partial u_\theta}{\partial \theta} + \frac{u_r}{r},$$

$$e_{r\theta} = \frac{1}{2}\left(\frac{1}{r}\frac{\partial u_r}{\partial \theta} + \frac{\partial u_\theta}{\partial r} - \frac{u_\theta}{r}\right), \tag{2}$$

$$\begin{aligned}\phi = {} & A_{01}r^2 + A_{02}r^2 \log r + A_{03} \log r + A_{04}\theta \\ & + (A_{11}r^3 + A_{12}r \log r + A_{14}r^{-1}) \cos\theta + A_{13}r\theta \sin\theta \\ & + (B_{11}r^3 + B_{12}r \log r + B_{14}r^{-1}) \sin\theta + B_{13}r\theta \cos\theta \\ & + \sum_{n=2}^{\infty} (A_{n1}r^{n+2} + A_{n2}r^{-n+2} + A_{n3}r^n + A_{n4}r^{-n}) \cos n\theta \\ & + \sum_{n=2}^{\infty} (B_{n1}r^{n+2} + B_{n2}r^{-n+2} + B_{n3}r^n + B_{n4}r^{-n}) \sin n\theta. \end{aligned} \tag{3}$$

In Eq. (2), $E' = E/(1 - \nu^2)$, $\nu' = \nu/(1 - \nu)$ for plane strain, and $E' = E$, $\nu' = \nu$ for generalized plane stress, μ is the shear modulus. Besides, in Eq. (3) we must have

$$\begin{aligned} A_{02} &= A_{12}(\kappa + 1) + A_{13}(\kappa - 1) \\ &= B_{12}(\kappa + 1) - B_{13}(\kappa - 1) = 0, \end{aligned} \tag{4}$$

where $\kappa = 3 - 4\nu$ for plane strain and $\kappa = (3 - \nu)/(1 + \nu)$ for generalized plane stress, to satisfy the requirement of single-valuedness of the displacements in the hollow cylinder.

Now let the nonhomogeneous hollow circular cylinder be sectioned into N constituent hollow circular cylinders of uniform thickness $h = (r_e - r_0)/N$, all of them are perfectly bonded at the interfaces. The resulted composite hollow circular cylinder, consisting of N constituent hollow circular cylinders, is completely equivalent to the original, nonhomogeneous one. Substitution of the Young's modulus of the jth constituent hollow circular cylinder, $Ae^{\beta r}$, $r_0 + (j - 1)h \leqq r \leqq r_0 + jh$, by a constant $E_j = Ae^{\beta[r_0 + (j-1)h]}$, $j = 1, 2, \ldots, N$, reduces the composite hollow circular cylinder into a piecewise homogeneous one, whose solution can be obtained from the homogeneous solution (3) and the conditions of continuity of displacements and stresses at the interfaces. These conditions of continuity take the following form:

$$\begin{aligned} r = r_j, \quad & u_r^{(j)} = u_r^{(j+1)}, \quad u_\theta^{(j)} = u_\theta^{(j+1)}, \\ & \sigma_{rr}^{(j)} = \sigma_{rr}^{(j+1)}, \quad \sigma_{r\theta}^{(j)} = \sigma_{r\theta}^{(j+1)} \end{aligned} \tag{5}$$

where $r_j = jh$, $j = 1, 2, \ldots, N - 1$ and the superscript (j) is used to denote that the affixed quantity belongs to the jth constituent cylinder.

To write Eq. (5) in terms of the coefficients of the stress function in Eq. (3), we note that the terms in the right-hand side of Eq. (3) can be divided into two groups, according to whether they are associated with symmetric or antisymmetric deformation to the x-axis. Consider the group that enforces the symmetric deformation. This group consists of the term $A_{13}r\theta \sin\theta$ and all the terms whose θ-dependent portion is $\cos n\theta$, $n = 0, 1, 2, \ldots$. The stresses and displacements induced by these terms can be determined by employing Eqs. (1), (2) and have been given explicitly in Barber (1992). After using Eq. (4) to eliminate the multivalued displacements induced by the three terms with coefficients A_{02}, A_{12}, and A_{13}, all the stresses and displacements can be expressed in the form of a function of r multiplied by $\cos n\theta$, $n = 0, 1, 2, \ldots$ or $\sin n\theta$, $n = 1, 2, \ldots$. Substituting the obtained stresses and displacements into Eq. (5) and equating the coefficients of the like terms of $\cos n\theta$ or $\sin n\theta$ in both sides of the equations yields

$$\begin{bmatrix} A_{01}^{(j+1)} \\ A_{03}^{(j+1)} \end{bmatrix} = \begin{bmatrix} D_{11}^{(j+1)} & D_{12}^{(j+1)} \\ D_{21}^{(j+1)} & D_{22}^{(j+1)} \end{bmatrix} \begin{bmatrix} A_{01}^{(j)} \\ A_{03}^{(j)} \end{bmatrix}, \tag{6}$$

$$\begin{bmatrix} A_{11}^{(j+1)} \\ A_{12}^{(j+1)} \\ A_{13}^{(j+1)} \\ A_{14}^{(j+1)} \end{bmatrix} = \begin{bmatrix} E_{11}^{(j+1)} & E_{12}^{(j+1)} & E_{13}^{(j+1)} & E_{14}^{(j+1)} \\ E_{21}^{(j+1)} & E_{22}^{(j+1)} & E_{23}^{(j+1)} & E_{24}^{(j+1)} \\ E_{31}^{(j+1)} & E_{32}^{(j+1)} & E_{33}^{(j+1)} & E_{34}^{(j+1)} \\ E_{41}^{(j+1)} & E_{42}^{(j+1)} & E_{43}^{(j+1)} & E_{44}^{(j+1)} \end{bmatrix} \begin{bmatrix} A_{11}^{(j)} \\ A_{12}^{(j)} \\ A_{13}^{(j)} \\ A_{14}^{(j)} \end{bmatrix}, \tag{7}$$

for $n = 2, 3, \ldots$

$$\begin{bmatrix} A_{n1}^{(j+1)} \\ A_{n2}^{(j+1)} \\ A_{n3}^{(j+1)} \\ A_{n4}^{(j+1)} \end{bmatrix} = \begin{bmatrix} F_{11}^{(j+1)} & F_{12}^{(j+1)} & F_{13}^{(j+1)} & F_{14}^{(j+1)} \\ F_{21}^{(j+1)} & F_{22}^{(j+1)} & F_{23}^{(j+1)} & F_{24}^{(j+1)} \\ F_{31}^{(j+1)} & F_{32}^{(j+1)} & F_{33}^{(j+1)} & F_{34}^{(j+1)} \\ F_{41}^{(j+1)} & F_{42}^{(j+1)} & F_{43}^{(j+1)} & F_{44}^{(j+1)} \end{bmatrix} \begin{bmatrix} A_{n1}^{(j)} \\ A_{n2}^{(j)} \\ A_{n3}^{(j)} \\ A_{n4}^{(j)} \end{bmatrix}, \tag{8}$$

where $j = 1, 2, \ldots, N - 1$. Explicit expressions for the entries of the matrices in Eqs. (6), (7), and (8) are given in the Appendix. When the deformation are antisymmetric to the x-axis, analogous equations for the coefficients can be obtained by a quite similar procedure; on account of this, only the symmetric case will be considered in the following.

Any boundary value problem in plane elasticity of the piecewise homogeneous hollow circular cylinder, can be solved with use of

Downloaded 04 May 2010 to 171.66.16.27. Redistribution subject to ASME license or copyright; see http://www.asme.org/terms/Terms_Use.cfm

Eqs. (1)–(8) by some elementary algebraic manipulations. In this sense, Eqs. (1)–(8) stand for the exact plane elasticity solution of the piecewise homogeneous cylinder. Obviously, this solution is also a good approximation to the original, nonhomogeneous hollow circular cylinder, providing the thickness h is sufficiently small.

Now suppose that the number N becomes unboundedly large and the thickness h approaches to zero following, for instance, the sequence $h = h_0, h_0/2, h_0/4, \ldots$, where h_0 is a small constant. For each term in the sequence, the corresponding solution of the piecewise homogeneous cylinder satisfies all the equations and conditions required by the theory of elasticity. Consequently, at the end of the process, that is, for $h \to 0$ and when the piecewise homogeneous cylinder reverts to the original nonhomogeneous hollow circular cylinder, the satisfaction still holds, and the corresponding solution becomes an exact one for the nonhomogeneous hollow circular cylinder. This is the basic reduction by which the solution of a nonhomogendous hollow circular cylinder is reduced to that of a piecewise homogeneous one, of which the thickness of the piece sections is infinitesimally small.

Exact Solutions

The solution for the piecewise homogeneous hollow circular cylinder is given in terms of the constant coefficients $A_{01}^{(j)}$, etc., in the stress functions. At the end of the limit process $h \to 0$, the aggregates of these discrete values, $A_{01}^{(j)}$, etc., turn into continuous functions, $A_{01}(r)$, etc., respectively. These continuous functions are the exact solution of the nonhomogeneous hollow circular cylinder.

First consider the coefficients $A_{01}^{(j)}$ and $A_{03}^{(j)}$. Using Eqs. (6) and (A1) in the Appendix, we obtain

$$A_{01}^{(j+1)} = (1 + \bar{D}_{11})A_{01}^{(j)} + \bar{D}_{12}\frac{A_{03}^{(j)}}{r_j^2}, \tag{9}$$

$$A_{03}^{(j+1)} = \bar{D}_{21}r_j^2 A_{01}^{(j)} + (1 + \bar{D}_{22})A_{03}^{(j)}, \tag{10}$$

where

$$\bar{D}_{11} = -\frac{\bar{D}_{21}}{2} = \frac{\kappa - 1}{\kappa + 1}\left(\frac{\mu_{j+1}}{\mu_j} - 1\right),$$

$$\frac{\bar{D}_{22}}{2} = -\bar{D}_{12} = \frac{1}{1 + \kappa}\left(\frac{\mu_{j+1}}{\mu_j} - 1\right). \tag{11}$$

Piecewise homogeneity of the material gives

$$\mu_j = \frac{Ae^{\beta r_j}}{2(1 + \nu)}, \quad \mu_{j+1} = \frac{Ae^{\beta(r_j + h)}}{2(1 + \nu)}. \tag{12}$$

When h is small, we have, approximately,

$$\frac{\mu_{j+1}}{\mu_j} = 1 + \beta h, \quad A_{01}^{(j+1)} = A_{01}^{(j)} + \frac{dA_{01}(r)}{dr}h,$$

$$A_{03}^{(j+1)} = A_{03}^{(j)} + \frac{dA_{03}(r)}{dr}h. \tag{13}$$

Substitution of Eq. (13) into Eqs. (9) and (10), we obtain

$$\frac{dA_{01}(r)}{dr} = d_{11}A_{01}(r) + d_{12}\frac{A_{03}(r)}{r^2}, \tag{14}$$

$$\frac{dA_{03}(r)}{dr} = d_{21}r^2 A_{01}(r) + d_{22}A_{03}(r), \tag{15}$$

where

$$d_{11} = -\frac{d_{21}}{2} = \frac{(\kappa - 1)\beta}{\kappa + 1}, \quad \frac{d_{22}}{2} = -d_{12} = \frac{\beta}{\kappa + 1}. \tag{16}$$

Equations (14) and (15) are simultaneous differential equations that approximately determine the two coefficients, $A_{01}^{(j)}$ and $A_{03}^{(j)}$, for the piecewise homogeneous cylinder. During the whole process $h \to 0$, Eqs. (14) and (15) remain unchanged and eventually become exact differential equations governing the two functions, $A_{01}(r)$ and $A_{03}(r)$, for the nonhomogeneous cylinder.

To find a solution for the system of differential Eqs. (14) and (15), we assume

$$A_{01}^{(1)}(r) = a_0 + a_1 r + a_2 r^2 + \ldots \tag{17}$$

$$A_{03}^{(1)}(r) = r^2(b_0 + b_1 r + b_2 r^2 + \ldots). \tag{18}$$

Substituting Eqs. (17) and (18) into (14) and (15), comparing and equating the coefficients of like terms in both sides of the resulted equations, it is obtained that

$$b_0 = 0, \quad a_j = \frac{\beta a_{j-1}}{j(j+1)}\left[j + 1 - \frac{4}{1 + \kappa}\right], \quad b_j = -\frac{2j}{j+2}a_j,$$
$$j = 1, 2, \ldots, \tag{19}$$

where a_0 is an arbitrary constant to be determined by boundary conditions in the problem.

For the second linearly independent solution to the system (14) and (15), suppose

$$A_{01}^{(2)}(r) = \frac{u_{-1}}{r} + u_0 + u_1 r + u_2 r^2 + \ldots + \lambda \log r(a_0 + a_1 r + a_2 r^2 + \ldots), \tag{20}$$

$$A_{03}^{(2)}(r) = r^2\left[\frac{v_{-2}}{r^2} + \frac{v_{-1}}{r} + v_0 + v_1 r + \ldots + \lambda \log r(b_0 + b_1 r + b_2 r^2 + \ldots)\right]. \tag{21}$$

Substituting Eqs. (20) and (21) into (14) and (15), comparing and equating the coefficients of like terms in both sides of the resulted equations, we obtain

$$u_{-1} = -d_{12}v_{-2}, \quad v_{-1} = d_{22}v_{-2}, \quad \lambda = \frac{d_{11}u_{-1} + d_{12}v_{-1}}{a_0},$$

$$u_0 = 0, \quad u_j = \frac{1}{j}\left\{\left[d_{11} - \frac{2(j-1)d_{12}}{j+1}\right]u_{j-1} - \lambda a_j - \frac{\lambda d_{12}}{j+1}(2a_{j-1} + b_{j-1})\right\},$$

$$v_k = -\frac{2(ku_k + \lambda a_k) + \lambda b_k}{k+2},$$
$$j = 1, 2, \ldots, \quad k = 0, 1, 2, \ldots, \tag{22}$$

with v_{-2} being an arbitrary constant to be determined by boundary conditions in the problem.

Next consider the coefficient group $A_{11}^{(j)}$, $A_{12}^{(j)}$, $A_{13}^{(j)}$, and $A_{14}^{(j)}$. By a similar analysis on Eq. (7), for the functions corresponding to the coefficients we find

$$A_{12}(r) = \Delta = \text{constant}, \quad A_{13}(r) = \frac{1 + \kappa}{1 - \kappa}\Delta, \tag{23}$$

$$\frac{dA_{11}(r)}{dr} = p_0 A_{11}(r) + \frac{p_1}{r^4}A_{14}(r) + \frac{p_2}{r^2}, \tag{24}$$

$$\frac{dA_{14}(r)}{dr} = p_0 r^4 A_{11}(r) + p_1 A_{14}(r) + p_2 r^2, \tag{25}$$

where

Downloaded 04 May 2010 to 171.66.16.27. Redistribution subject to ASME license or copyright; see http://www.asme.org/terms/Terms_Use.cfm

$$p_0 = \frac{\kappa\beta}{1+\kappa}, \quad p_1 = \frac{\beta}{1+\kappa}, \quad p_2 = \frac{\beta\Delta}{(\kappa+1)(\kappa-1)}, \tag{26}$$

and Δ is an arbitrary constant to be determined by boundary conditions in the problem.

After seeking out $A_{11}^{p}(r)$ and $A_{14}^{p}(r)$, the particular solution for Eqs. (24) and (25), these two equations can be solved by a procedure similar to that for solving Eqs. (14) and (15). The result is

$$A_{11}(r) = A_{11}^{A}(r) + A_{11}^{B}(r) + A_{11}^{P}(r), \tag{27}$$

$$A_{14}(r) = A_{14}^{A}(r) + A_{14}^{B}(r) + A_{14}^{P}(r), \tag{28}$$

where

$$A_{11}^{A}(r) = g_0 + g_1 r + g_2 r^2 + \ldots,$$

$$A_{14}^{A}(r) = r^4(k_0 + k_1 r + k_2 r^2 + \ldots),$$

$$g_1 = p_0 g_0, \quad k_0 = 0, \quad k_1 = p_0 g_0/5,$$

$$g_{j+1} = \frac{p_0 g_j + p_1 k_j}{j+1}, \quad k_{j+1} = \frac{p_0 g_j + p_1 k_j}{j+5}, \quad j = 1, 2, \ldots, \tag{29}$$

$$A_{11}^{B}(r) = A_{11}^{A}(r)\log r + \frac{\bar{g}_{-3}}{r^3} + \frac{\bar{g}_{-2}}{r^2} + \frac{\bar{g}_{-1}}{r} + \bar{g}_0 + \bar{g}_1 r + \ldots,$$

$$A_{14}^{B}(r) = A_{14}^{A}(r)\log r + \bar{k}_0 + \bar{k}_1 r + \bar{k}_2 r^2 + \ldots,$$

$$\bar{k}_0 = \frac{18 g_0}{p_1(p_0-p_1)(p_0-3p_1)(p_1-3p_0)}, \quad \bar{k}_1 = p_1\bar{k}_0,$$

$$\bar{g}_{-3} = -\frac{p_1\bar{k}_0}{3}, \quad \bar{k}_2 = -\bar{g}_{-2} = \frac{p_0\bar{g}_{-3} + p_1\bar{k}_1}{2},$$

$$\bar{k}_3 = -\frac{\bar{g}_{-1}}{3} = \frac{p_0\bar{g}_{-2} + p_1\bar{k}_2}{3},$$

$$\bar{k}_{j+1} = \frac{p_0\bar{g}_{j-4} + p_1\bar{k}_j - k_{j-3}}{j+1}, \quad j = 3, 4, \ldots,$$

$$\bar{g}_{j+1} = \frac{p_0\bar{g}_j + p_1\bar{k}_{j+4} - g_{j+1}}{j+1}, \quad j = 0, 1, 2, \ldots, \tag{30}$$

with g_0 and $\bar{g}_0$ being arbitrary constants to be determined by boundary conditions in the problem,

$$A_{11}^{P}(r) = \frac{q_{-3}}{r^3} + \frac{q_{-2}}{r^2}, \quad A_{14}^{P}(r) = s_0 + s_1 r + s_2 r^2,$$

$$q_{-3} = \frac{2p_2}{(p_1-p_0)(3p_1-p_0)}, \quad q_{-2} = \frac{p_2}{p_1-p_0},$$

$$s_0 = \frac{s_1}{p_1} = \frac{6p_2}{p_1(p_0-p_1)(3p_1-p_0)}, \quad s_2 = \frac{p_2}{p_0-p_1}. \tag{31}$$

Now turn to the coefficient group $A_{n1}^{(j)}$, $A_{n2}^{(j)}$, $A_{n3}^{(j)}$ and $A_{n4}^{(j)}$, $n = 2, 3, \ldots$. Applying an analysis similar to that used for other coefficient groups on Eq. (8), differential equations governing the corresponding functions for the coefficients are obtained as follows:

$$\frac{dA_{n1}(r)}{dr} = c_{11}A_{n1}(r) + c_{12}\frac{A_{n2}(r)}{r^{2n}} + c_{13}\frac{A_{n3}(r)}{r^2} + c_{14}\frac{A_{n4}(r)}{r^{2n+2}}, \tag{32}$$

$$\frac{dA_{n2}(r)}{dr} = c_{21}r^{2n}A_{n1}(r) + c_{22}A_{n2}(r) + c_{23}r^{2n-2}A_{n3}(r) + c_{24}\frac{A_{n4}(r)}{r^2}, \tag{33}$$

$$\frac{dA_{n3}(r)}{dr} = c_{31}r^2A_{n1}(r) + c_{32}\frac{A_{n2}(r)}{r^{2n-2}} + c_{33}A_{n3}(r) + c_{34}\frac{A_{n4}(r)}{r^{2n}}, \tag{34}$$

$$\frac{dA_{n4}(r)}{dr} = c_{41}r^{2n+2}A_{n1}(r) + c_{42}r^2A_{n2}(r) + c_{43}r^{2n}A_{n3}(r) + c_{44}A_{n4}(r), \tag{35}$$

where

$$c_{11} = c_{22} = \frac{\kappa\beta}{1+\kappa}, \quad c_{12} = c_{43} = -\frac{1-n}{1+\kappa}\beta, \quad c_{13} = c_{24} = 0,$$

$$c_{14} = -c_{23} = \frac{n\beta}{1+\kappa}, \quad c_{33} = c_{44} = \frac{\beta}{1+\kappa},$$

$$c_{21} = c_{34} = -\frac{n+1}{1+\kappa}\beta,$$

$$c_{31} = \frac{(n+1)(1-\kappa)}{n(1+\kappa)}\beta, \quad c_{32} = -c_{41} = -\frac{n^2-1+\kappa}{n(1+\kappa)}\beta,$$

$$c_{42} = \frac{(1-n)(\kappa-1)}{n(1+\kappa)}\beta. \tag{36}$$

Equations (32)–(35) form a system of ordinary differential equations of the first order with variable coefficients. As a first step to solve the system, we put

$$\bar{A}_{n1}(r) = A_{n1}(r), \quad \bar{A}_{n2}(r) = \frac{A_{n2}(r)}{r^{2n}},$$

$$\bar{A}_{n3}(r) = \frac{A_{n3}(r)}{r^2}, \quad \bar{A}_{n4}(r) = \frac{A_{n4}(r)}{r^{2n+2}}. \tag{37}$$

Substitution of Eq. (37) into Eqs. (32)–(35) yields

$$\frac{d\bar{A}_{n1}(r)}{dr} = c_{11}\bar{A}_{n1}(r) + c_{12}\bar{A}_{n2}(r) + c_{13}\bar{A}_{n3}(r) + c_{14}\bar{A}_{n4}(r), \tag{38}$$

$$\frac{d\bar{A}_{n2}(r)}{dr} = c_{21}\bar{A}_{n1}(r) + \left(c_{22} - \frac{2n}{r}\right)\bar{A}_{n2}(r) + c_{23}\bar{A}_{n3}(r) + c_{24}\bar{A}_{n4}(r), \tag{39}$$

$$\frac{d\bar{A}_{n3}(r)}{dr} = c_{31}\bar{A}_{n1}(r) + c_{32}\bar{A}_{n2}(r) + \left(c_{33} - \frac{2}{r}\right)\bar{A}_{n3}(r) + c_{34}\bar{A}_{n4}(r), \tag{40}$$

$$\frac{d\bar{A}_{n4}(r)}{dr} = c_{41}\bar{A}_{n1}(r) + c_{42}\bar{A}_{n2}(r) + c_{43}\bar{A}_{n3}(r) + \left(c_{44} - \frac{2n+2}{r}\right)\bar{A}_{n4}(r). \tag{41}$$

To find the first solution for the system (38)–(41), assume

$$\bar{A}_{n1}^{(1)}(r) = c_0 + c_1 r + c_2 r^2 + \ldots,$$

$$\bar{A}_{n2}^{(1)}(r) = d_0 + d_1 r + d_2 r^2 + \ldots,$$

Downloaded 04 May 2010 to 171.66.16.27. Redistribution subject to ASME license or copyright; see http://www.asme.org/terms/Terms_Use.cfm

$$\bar{A}_{n3}^{(1)}(r) = e_0 + e_1 r + e_2 r^2 + \ldots,$$
$$\bar{A}_{n4}^{(1)}(r) = f_0 + f_1 r + f_2 r^2 + \ldots. \quad (42)$$

Substituting Eq. (42) into (38), (39), (40), (41) and equating the coefficients for like terms in both sides of the resulted equations, we obtain

$$d_0 = e_0 = f_0 = 0,$$

$$c_j = \frac{1}{j}(c_{11}c_{j-1} + c_{12}d_{j-1} + c_{13}e_{j-1} + c_{14}f_{j-1}),$$

$$d_j = \frac{1}{2n+j}(c_{21}c_{j-1} + c_{22}d_{j-1} + c_{23}e_{j-1} + c_{24}f_{j-1}),$$

$$e_j = \frac{1}{2+j}(c_{31}c_{j-1} + c_{32}d_{j-1} + c_{33}e_{j-1} + c_{34}f_{j-1}),$$

$$f_j = \frac{1}{2n+2+j}(c_{41}c_{j-1} + c_{42}d_{j-1} + c_{43}e_{j-1} + c_{44}f_{j-1}),$$
$$j = 1, 2, \ldots, \quad (43)$$

where c_0 is an arbitrary constant to be determined by boundary conditions in the problem.

For the second linearly independent solution to the system (38), (39), (40), (41), we suppose

$$\bar{A}_{n1}^{(2)}(r) = \frac{w_{-1}}{r} + w_0 + w_1 r + \ldots + \lambda_1 \log r(c_0 + c_1 r + \ldots),$$

$$\bar{A}_{n2}^{(2)}(r) = \frac{x_{-1}}{r} + x_0 + x_1 r + \ldots + \lambda_1 \log r(d_0 + d_1 r + \ldots),$$

$$\bar{A}_{n3}^{(2)}(r) = \frac{y_{-2}}{r^2} + \frac{y_{-1}}{r} + y_0 + y_1 r + \ldots + \lambda_1 \log r(e_0 + e_1 r + \ldots),$$

$$\bar{A}_{n4}^{(2)}(r) = \frac{z_{-1}}{r} + z_0 + z_1 r + \ldots + \lambda_1 \log r(f_0 + f_1 r + \ldots). \quad (44)$$

Substitution of Eq. (44) into (38)–(41) and equalization of the coefficients for like terms in both sides of the resulted equations yields

$$w_{-1} = -c_{13}y_{-2}, \quad x_{-1} = \frac{c_{23}y_{-2}}{2n-1},$$

$$y_{-1} = c_{33}y_{-2}, \quad z_{-1} = \frac{c_{43}y_{-2}}{2n+1},$$

$$\lambda_1 = \frac{c_{11}w_{-1} + c_{12}x_{-1} + c_{13}y_{-1} + c_{14}z_{-1}}{c_0}, \quad w_0 = 0,$$

$$w_{j+1} = \frac{c_{11}w_j + c_{12}x_j + c_{13}y_j + c_{14}z_j - \lambda_1 c_{j+1}}{j+1},$$

$$x_j = \frac{c_{21}w_{j-1} + c_{22}x_{j-1} + c_{23}y_{j-1} + c_{24}z_{j-1} - \lambda_1 d_j}{2n+j},$$

$$y_j = \frac{c_{31}w_{j-1} + c_{32}x_{j-1} + c_{33}y_{j-1} + c_{34}z_{j-1} - \lambda_1 e_j}{2+j},$$

$$z_j = \frac{c_{41}w_{j-1} + c_{42}x_{j-1} + c_{43}y_{j-1} + c_{44}z_{j-1} - \lambda_1 f_j}{2n+2+j},$$
$$j = 0, 1, 2, \ldots, \quad (45)$$

with y_{-2} being an arbitrary constant to be determined by boundary conditions in the problem.

Employing a procedure of assumption, substitution, and equalization similar to that used for the first and second solutions, the third and fourth linearly independent solutions can be determined. The result is

$$\bar{A}_{n1}^{(3)}(r) = \sum_{-(2n-1)}^{\infty} \bar{w}_j r^j + \lambda_2 \log r\bar{A}_{n1}^{(2)}(r) + \lambda_3 \log^2 r\bar{A}_{n1}^{(1)}(r),$$

$$\bar{A}_{n2}^{(3)}(r) = \sum_{-2n}^{\infty} \bar{x}_j r^j + \lambda_2 \log r\bar{A}_{n2}^{(2)}(r) + \lambda_3 \log^2 r\bar{A}_{n2}^{(1)}(r),$$

$$\bar{A}_{n3}^{(3)}(r) = \sum_{-(2n-1)}^{\infty} \bar{y}_j r^j + \lambda_2 \log r\bar{A}_{n3}^{(2)}(r) + \lambda_3 \log^2 r\bar{A}_{n3}^{(1)}(r),$$

$$\bar{A}_{n4}^{(3)}(r) = \sum_{-(2n-1)}^{\infty} \bar{z}_j r^j + \lambda_2 \log r\bar{A}_{n4}^{(2)}(r) + \lambda_3 \log^2 r\bar{A}_{n4}^{(1)}(r), \quad (46)$$

where

$$\bar{w}_{-(2n-1)} = \frac{c_{12}\bar{x}_{-2n}}{1-2n}, \quad \bar{x}_{-(2n-1)} = c_{22}\bar{x}_{-2n},$$

$$\bar{y}_{-(2n-1)} = \frac{c_{32}\bar{x}_{-2n}}{3-2n}, \quad \bar{z}_{-(2n-1)} = \frac{c_{42}\bar{x}_{-2n}}{3},$$

$$\bar{w}_{-(2n-1-j)} = \frac{c_{11}\bar{w}_{-(2n-j)} + c_{12}\bar{x}_{-(2n-j)} + c_{13}\bar{y}_{-(2n-j)} + c_{14}\bar{z}_{-(2n-j)}}{1+j-2n},$$

$$\bar{x}_{-(2n-1-j)} = \frac{c_{21}\bar{w}_{-(2n-j)} + c_{22}\bar{x}_{-(2n-j)} + c_{23}\bar{y}_{-(2n-j)} + c_{24}\bar{z}_{-(2n-j)}}{j+1},$$

$$\bar{y}_{-(2n-1-j)} = \frac{c_{31}\bar{w}_{-(2n-j)} + c_{32}\bar{x}_{-(2n-j)} + c_{33}\bar{y}_{-(2n-j)} + c_{34}\bar{z}_{-(2n-j)}}{j+3-2n},$$

$$\bar{z}_{-(2n-1-j)} = \frac{c_{41}\bar{w}_{-(2n-j)} + c_{42}\bar{x}_{-(2n-j)} + c_{43}\bar{y}_{-(2n-j)} + c_{44}\bar{z}_{-(2n-j)}}{j+3},$$
$$j = 1, 2, \ldots, 2n-4,$$

$$\lambda_2 = \frac{c_{31}\bar{w}_{-3} + c_{32}\bar{x}_{-3} + c_{33}\bar{y}_{-3} + c_{34}\bar{z}_{-3}}{y_{-2}}, \quad \lambda_3 = -\frac{\lambda_1\lambda_2}{2},$$

$$\bar{w}_{-2} = -\frac{c_{11}\bar{w}_{-3} + c_{12}\bar{x}_{-3} + c_{13}\bar{y}_{-3} + c_{14}\bar{z}_{-3}}{2},$$

$$\bar{x}_{-2} = \frac{c_{21}\bar{w}_{-3} + c_{22}\bar{x}_{-3} + c_{23}\bar{y}_{-3} + c_{24}\bar{z}_{-3}}{2n-2},$$

$$\bar{y}_{-2} = \frac{y_t}{(1-2n)c_{14}c_{43} - (1+2n)c_{12}c_{23}},$$

$$\bar{z}_{-2} = \frac{c_{41}\bar{w}_{-3} + c_{42}\bar{x}_{-3} + c_{43}\bar{y}_{-3} + c_{44}\bar{z}_{-3}}{2n},$$

$$y_t = [(2n+1)c_{12}c_{21} + (2n-1)c_{14}c_{41} - (2n-1)(2n+1)c_{11}^2]\bar{w}_{-2} + [(2n+1)c_{12}c_{22} + (2n-1)c_{14}c_{42} - (2n-1)(2n+1)c_{11}c_{12}]\bar{x}_{-2} + [(2n-1)c_{14}c_{44} - (2n-1)(2n+1)c_{11}c_{14}]\bar{z}_{-2} + (2n-1)(2n+1)\lambda_2 w_{-1} - (2n+1)\lambda_2 c_{12}x_{-1} - (2n-1)\lambda_2 c_{14}z_{-1},$$

$$\bar{w}_{-1} = \lambda_2 w_{-1} - c_{11}\bar{w}_{-2} - c_{12}\bar{x}_{-2} - c_{13}\bar{y}_{-2} - c_{14}\bar{z}_{-2},$$

Downloaded 04 May 2010 to 171.66.16.27. Redistribution subject to ASME license or copyright; see http://www.asme.org/terms/Terms_Use.cfm

$$\bar{x}_{-1} = \frac{c_{21}\bar{w}_{-2} + c_{22}\bar{x}_{-2} + c_{23}\bar{y}_{-2} + c_{24}\bar{z}_{-2} - \lambda_2 x_{-1}}{2n-1},$$

$$\bar{y}_{-1} = c_{31}\bar{w}_{-2} + c_{32}\bar{x}_{-2} + c_{33}\bar{y}_{-2} + c_{34}\bar{z}_{-2} - \lambda_2 y_{-1},$$

$$\bar{z}_{-1} = \frac{c_{41}\bar{w}_{-2} + c_{42}\bar{x}_{-2} + c_{43}\bar{y}_{-2} + c_{44}\bar{z}_{-2} - \lambda_2 z_{-1}}{2n+1},$$

$$\bar{w}_0 = 0, \quad \bar{w}_{j+1} = \frac{c_{11}\bar{w}_j + c_{12}\bar{x}_j + c_{13}\bar{y}_j + c_{14}\bar{z}_j - \lambda_2 w_{j+1}}{j+1},$$

$$\bar{x}_j = \frac{c_{21}\bar{w}_{j-1} + c_{22}\bar{x}_{j-1} + c_{23}\bar{y}_{j-1} + c_{24}\bar{z}_{j-1} - \lambda_2 x_j}{2n+j},$$

$$\bar{y}_j = \frac{c_{31}\bar{w}_{j-1} + c_{32}\bar{x}_{j-1} + c_{33}\bar{y}_{j-1} + c_{34}\bar{z}_{j-1} - \lambda_2 y_j}{2+j},$$

$$\bar{z}_j = \frac{c_{41}\bar{w}_{j-1} + c_{42}\bar{x}_{j-1} + c_{43}\bar{y}_{j-1} + c_{44}\bar{z}_{j-1} - \lambda_2 z_j}{2n+2+j},$$

$$j = 0, 1, 2, \ldots, \quad (47)$$

$$\tilde{w}_{-(2n+1)} = -\frac{c_{14}\tilde{z}_{-(2n+2)}}{2n+1}, \quad \tilde{x}_{-(2n+1)} = -c_{24}\tilde{z}_{-(2n+2)},$$

$$\tilde{y}_{-(2n+1)} = \frac{c_{34}\tilde{z}_{-(2n+2)}}{1-2n}, \quad \tilde{z}_{-(2n+1)} = c_{44}\tilde{z}_{-(2n+2)},$$

$$\tilde{w}_{-2n} = -\frac{c_{11}\tilde{w}_{-(2n+1)} + c_{12}\tilde{x}_{-(2n+1)} + c_{13}\tilde{y}_{-(2n+1)} + c_{14}\tilde{z}_{-(2n+1)}}{2n},$$

$$\tilde{x}_{-2n} = 0,$$

$$\tilde{y}_{-2n} = \frac{c_{31}\tilde{w}_{-(2n+1)} + c_{32}\tilde{x}_{-(2n+1)} + c_{33}\tilde{y}_{-(2n+1)} + c_{34}\tilde{z}_{-(2n+1)}}{2-2n},$$

$$\tilde{z}_{-2n} = \frac{c_{41}\tilde{w}_{-(2n+1)} + c_{42}\tilde{x}_{-(2n+1)} + c_{43}\tilde{y}_{-(2n+1)} + c_{44}\tilde{z}_{-(2n+1)}}{2},$$

$$\lambda_4 = \frac{c_{21}\tilde{w}_{-(2n+1)} + c_{22}\tilde{x}_{-(2n+1)} + c_{23}\tilde{y}_{-(2n+1)} + c_{24}\tilde{z}_{-(2n+1)}}{\bar{x}_{-2n}},$$

$$\lambda_5 = -\frac{\lambda_2\lambda_4}{2}, \quad \lambda_7 = -\frac{\lambda_3\lambda_4}{3},$$

$$\tilde{w}_{-(2n-j)} = -\frac{c_{11}\tilde{w}_{-(2n-j+1)} + c_{12}\tilde{x}_{-(2n-j+1)} + c_{13}\tilde{y}_{-(2n-j+1)} + c_{14}\tilde{z}_{-(2n-j+1)} - \lambda_4\bar{w}_{-(2n-j)}}{2n-j},$$

$$\tilde{x}_{-(2n-j)} = \frac{c_{21}\tilde{w}_{-(2n-j+1)} + c_{22}\tilde{x}_{-(2n-j+1)} + c_{23}\tilde{y}_{-(2n-j+1)} + c_{24}\tilde{z}_{-(2n-j+1)} - \lambda_4\bar{x}_{-(2n-j)}}{j},$$

$$\tilde{y}_{-(2n-j)} = \frac{c_{31}\tilde{w}_{-(2n-j+1)} + c_{32}\tilde{x}_{-(2n-j+1)} + c_{33}\tilde{y}_{-(2n-j+1)} + c_{34}\tilde{z}_{-(2n-j+1)} - \lambda_4\bar{y}_{-(2n-j)}}{2-2n+j},$$

$$\tilde{z}_{-(2n-j)} = \frac{c_{41}\tilde{w}_{-(2n-j+1)} + c_{42}\tilde{x}_{-(2n-j+1)} + c_{43}\tilde{y}_{-(2n-j+1)} + c_{44}\tilde{z}_{-(2n-j+1)} - \lambda_4\bar{z}_{-(2n-j)}}{j+2},$$

where $\bar{x}_{-2n}$ is an arbitrary constant to be determined by boundary conditions in the problem.

$$\bar{A}^{(4)}_{n1}(r) = \sum_{-(2n+1)}^{\infty} \tilde{w}_j r^j + \lambda_4 \log r\bar{A}^{(3)}_{n1}(r) + (\lambda_5 \log r + \lambda_6)\log r\bar{A}^{(2)}_{n1}(r) + (\lambda_7 \log r + \lambda_8)\log^2 r\bar{A}^{(1)}_{n1}(r),$$

$$\bar{A}^{(4)}_{n2}(r) = \sum_{-(2n+1)}^{\infty} \tilde{x}_j r^j + \lambda_4 \log r\bar{A}^{(3)}_{n2}(r) + (\lambda_5 \log r + \lambda_6)\log r\bar{A}^{(2)}_{n2}(r) + (\lambda_7 \log r + \lambda_8)\log^2 r\bar{A}^{(1)}_{n2}(r),$$

$$\bar{A}^{(4)}_{n3}(r) = \sum_{-(2n+1)}^{\infty} \tilde{y}_j r^j + \lambda_4 \log r\bar{A}^{(3)}_{n3}(r) + (\lambda_5 \log r + \lambda_6)\log r\bar{A}^{(2)}_{n3}(r) + (\lambda_7 \log r + \lambda_8)\log^2 r\bar{A}^{(1)}_{n3}(r),$$

$$\bar{A}^{(4)}_{n4}(r) = \sum_{-(2n+2)}^{\infty} \tilde{z}_j r^j + \lambda_4 \log r\bar{A}^{(3)}_{n4}(r) + (\lambda_5 \log r + \lambda_6)\log r\bar{A}^{(2)}_{n4}(r) + (\lambda_7 \log r + \lambda_8)\log^2 r\bar{A}^{(1)}_{n4}(r), \quad (48)$$

where

$$j = 1, 2, \ldots, 2n-3,$$

$$\lambda_6 = \frac{c_{31}\tilde{w}_{-3} + c_{32}\tilde{x}_{-3} + c_{33}\tilde{y}_{-3} + c_{34}\tilde{z}_{-3} - \lambda_4\bar{y}_{-2}}{y_{-2}},$$

$$\lambda_8 = -\frac{\lambda_1\lambda_6}{2},$$

$$\tilde{w}_{-2} = -\frac{c_{11}\tilde{w}_{-3} + c_{12}\tilde{x}_{-3} + c_{13}\tilde{y}_{-3} + c_{14}\tilde{z}_{-3} - \lambda_4\bar{w}_{-2}}{2},$$

$$\tilde{x}_{-2} = \frac{c_{21}\tilde{w}_{-3} + c_{22}\tilde{x}_{-3} + c_{23}\tilde{y}_{-3} + c_{24}\tilde{z}_{-3} - \lambda_4\bar{x}_{-2}}{2n-2},$$

$$\tilde{y}_{-2} = \frac{y_{tt}}{(1-2n)c_{14}c_{43} - (1+2n)c_{12}c_{23}},$$

$$\tilde{z}_{-2} = \frac{c_{41}\tilde{w}_{-3} + c_{42}\tilde{x}_{-3} + c_{43}\tilde{y}_{-3} + c_{44}\tilde{z}_{-3} - \lambda_4\bar{z}_{-2}}{2n},$$

$$y_{tt} = (1-2n)(2n+1)c_{11}(c_{11}\tilde{w}_{-2} + c_{12}\tilde{x}_{-2} + c_{14}\tilde{z}_{-2} - \lambda_4\bar{w}_{-1} - \lambda_6 w_{-1}) + (2n+1)c_{12}(c_{21}\tilde{w}_{-2} + c_{22}\tilde{x}_{-2} + c_{24}\tilde{z}_{-2} - \lambda_4\bar{x}_{-1} - \lambda_6 x_{-1}) + (2n-1)c_{14}(c_{41}\tilde{w}_{-2} + c_{42}\tilde{x}_{-2} + c_{44}\tilde{z}_{-2} - \lambda_4\bar{z}_{-1} - \lambda_6 z_{-1})$$

Downloaded 04 May 2010 to 171.66.16.27. Redistribution subject to ASME license or copyright; see http://www.asme.org/terms/Terms_Use.cfm

$$+(1-2n)(1+2n)(\lambda_4\bar{w}_0+\lambda_6 w_0),$$

$$\tilde{w}_{-1}=\lambda_4\bar{w}_{-1}+\lambda_6 w_{-1}-c_{11}\tilde{w}_{-2}-c_{12}\tilde{x}_{-2}-c_{13}\tilde{y}_{-2}-c_{14}\tilde{z}_{-2},$$

$$\tilde{x}_{-1}=\frac{c_{21}\tilde{w}_{-2}+c_{22}\tilde{x}_{-2}+c_{23}\tilde{y}_{-2}+c_{24}\tilde{z}_{-2}-\lambda_4\bar{x}_{-1}-\lambda_6 x_{-1}}{2n-1},$$

$$\tilde{y}_{-1}=c_{31}\tilde{w}_{-2}+c_{32}\tilde{x}_{-2}+c_{33}\tilde{y}_{-2}+c_{34}\tilde{z}_{-2}-\lambda_4\bar{y}_{-1}-\lambda_6 y_{-1},$$

$$\tilde{z}_{-1}=\frac{c_{41}\tilde{w}_{-2}+c_{42}\tilde{x}_{-2}+c_{43}\tilde{y}_{-2}+c_{44}\tilde{z}_{-2}-\lambda_4\bar{z}_{-1}-\lambda_6 z_{-1}}{2n+1},$$

$$\tilde{w}_0=0,$$

$$\tilde{w}_{j+1}=\frac{c_{11}\tilde{w}_j+c_{12}\tilde{x}_j+c_{13}\tilde{y}_j+c_{14}\tilde{z}_j-\lambda_4\bar{w}_{j+1}-\lambda_6 w_{j+1}}{1+j},$$

$$\tilde{x}_j=\frac{c_{21}\tilde{w}_{j-1}+c_{22}\tilde{x}_{j-1}+c_{23}\tilde{y}_{j-1}+c_{24}\tilde{z}_{j-1}-\lambda_4\bar{x}_j-\lambda_6 x_j}{2n+j},$$

$$\tilde{y}_j=\frac{c_{31}\tilde{w}_{j-1}+c_{32}\tilde{x}_{j-1}+c_{33}\tilde{y}_{j-1}+c_{34}\tilde{z}_{j-1}-\lambda_4\bar{y}_j-\lambda_6 y_j}{2+j},$$

$$\tilde{z}_j=\frac{c_{41}\tilde{w}_{j-1}+c_{42}\tilde{x}_{j-1}+c_{43}\tilde{y}_{j-1}+c_{44}\tilde{z}_{j-1}-\lambda_4\bar{z}_j-\lambda_6 z_j}{2n+2+j},$$

$$j=0,\ 1,\ 2,\ \ldots, \quad (49)$$

with $\tilde{z}_{-(2n+2)}$ being an arbitrary constant to be determined by boundary conditions in the problem.

In general, solutions of systems of first-order ordinary differential equation are not expressible, explicitly or implicitly, in terms of elementary functions. Only a few very special first-order ordinary differential equations systems will have such solutions (Tenenbaum and Pollard, 1963). A semi-inverse method is used in this section to develop the required solutions. That is, we first select and assume basic forms for the solutions by means of test and try, then validate and complete the assumed solutions by substituting them into the differential equations whose solution is sought.

All the solutions developed in this section are exact ones. This conclusion follows the basic reduction detailed in the last section, and can be confirmed also by the satisfaction resulted from substituting these solutions directly into equations and conditions in the theory of nonhomogeneous elasticity. When the arbitrary constants contained in the solutions are determined by boundary conditions in the problem, the obtained solution will be a unique one. This is because the solution comes out as the limit of a series of solutions for piecewise homogeneous hollow circular cylinders, while each of them is unique by the theory of elasticity.

Numerical Results

Numerical results of stresses in the nonhomogeneous hollow circular cylinder worked out from the exact solutions are presented in graphic form in this section. For a nonhomogeneous hollow circular cylinder of $r_0=1$, $r_e=5$, $\kappa=3-4\nu$ (plane strain) and stressed by the normal traction $\sigma_0\cos m\theta$ on the inner boundary

$$r=r_0, \quad \sigma_{rr}=\sigma_0\cos m\theta, \quad \sigma_{r\theta}=0,$$

$$r=r_e, \quad \sigma_{rr}=\sigma_{r\theta}=0, \quad m=0,\ 4, \quad (50)$$

numerical values of σ_{rr} and $\sigma_{\theta\theta}$ for $m=0$ (uniform normal traction) with respect to various values of β calculated from Eqs. (17)–(22) are shown in Figs. 2–3, those values and $\sigma_{r\theta}$ for $m=4$ are calculated from Eqs. (42)–(49) and shown in Figs. 4–6. For a similar but thinner hollow circular cylinder of $r_e=2$, numerical values of $\sigma_{\theta\theta}(r_0)$ and $\sigma_{\theta\theta}(r_e)$ for internal normal traction (boundary condition (50), $m=0,\ 4,\ 8$) and for internal and external normal tractions

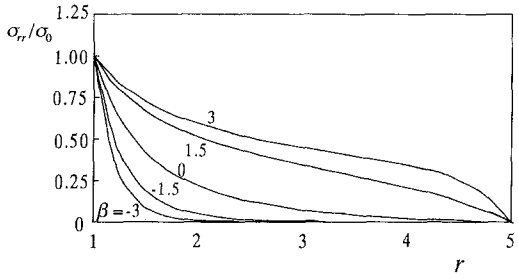


Fig. 2 Numerical values of σ_{rr}/σ_0 ($m=0$, $r_e=5$)

$$r=r_0,\ r_e, \quad \sigma_{rr}=\sigma_0\cos m\theta, \quad \sigma_{r\theta}=0, \quad m=0,\ 4,\ 8, \quad (51)$$

are depicted in Figs. 7 and 8, respectively.

For $\beta=0$, the cylinder reduces to a homogeneous one, the corresponding numerical values agree with those obtained from existing solutions (Barber, 1992; Timoshenko and Goodier, 1970; Muskhelishvili, 1963).

It is seen from all the figures that in general the magnitude of σ_{rr} in the nonhomogeneous cylinder is larger or less than that in the corresponding homogeneous cylinder, depending on β is larger or less than zero. Figure 2 shows all σ_{rr} decrease from σ_0 on the inner surface to zero on the outer surface with, however, different rapidity of convergence. For $\beta=0$, the homogeneous case, σ_{rr} decreases to zero sufficiently rapidly, the decrease is much more rapid for $\beta=-3$, while for $\beta=3$, it is very slow. Moreover, instead of decreasing to zero as it is in the homogeneous case, $|\sigma_{\theta\theta}/\sigma_0|$ increases from a small value on the inner surface to $|\sigma_{\theta\theta}/\sigma_0|=4.2433$ on the outer surface for $\beta=3$, as is depicted in Fig. 3. This result demonstrates that the stress distributions in nonhomo-

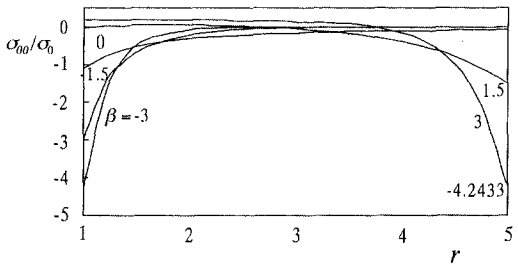


Fig. 3 Numerical values of $\sigma_{\theta\theta}/\sigma_0$ ($m=0$, $r_e=5$)

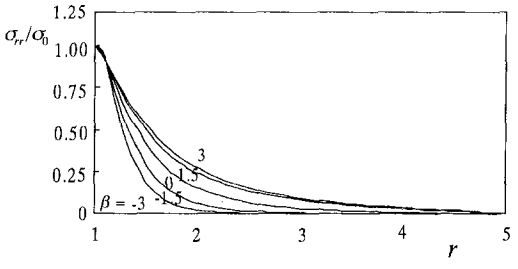


Fig. 4 Numerical values of σ_{rr}/σ_0 ($\theta=0$, $m=4$, $r_e=5$)

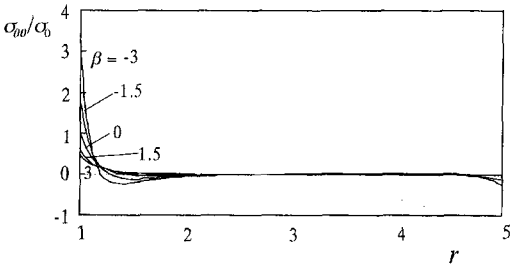


Fig. 5 Numerical values of $\sigma_{\theta\theta}/\sigma_0$ ($\theta=0$, $m=4$, $r_e=5$)

Downloaded 04 May 2010 to 171.66.16.27. Redistribution subject to ASME license or copyright; see http://www.asme.org/terms/Terms_Use.cfm

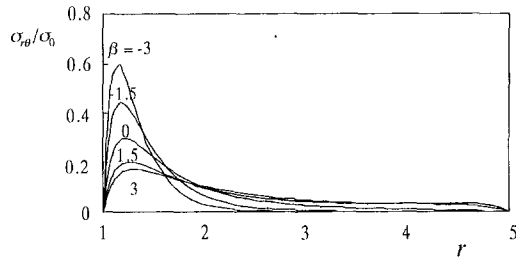


Fig. 6 Numerical values of $\sigma_{r\theta}/\sigma_0$ ($\theta = \pi/2m$, $m = 4$, $r_e = 5$)

geneous media can be quite different from the corresponding homogeneous ones.

The stress $\sigma_{\theta\theta}$ is important in engineering design. For $\beta < 0$, all numerical data in the figures show that the maximum value of $|\sigma_{\theta\theta}|$ always occurs at the inner surface and is higher than the corresponding homogeneous one. Besides, the difference between the two $|\sigma_{\theta\theta}|$'s increases monotonously and rapidly for increasing $|\beta|$.

For nonuniform external normal tractions, Figs. 4–6 demonstrate that stress behavior similar to that taking place in the case $m = 0$ still appears in the rough for $m = 4$. For example, $|\sigma_{\theta\theta}(r_0)|$ still increases monotonously with increasing $|\beta|$ for $\beta < 0$. However, the stress differs from that of a corresponding homogeneous cylinder in a lesser degree for larger m. For instance, the ratios of $\sigma_{\theta\theta}(r_0)$ for $\beta = -3$ to that for $\beta = 0$ are 3.9335, 2.9038, and 1.6061 for $m = 0$, 4, and 8, respectively. This fact is depicted Fig. 5, but the data for $m = 8$ are not shown in the figure.

When the cylinder is stressed by uniform normal traction applied on both of the surfaces, numerical values of $\sigma_{\theta\theta}(r_0)$ and $\sigma_{\theta\theta}(r_e)$ given in Fig. 8 shows that nonuniform stress distribution occurs within the nonhomogeneous cylinder when it is under the action of external traction of the type of static hydraulic pressure.

The stresses in the numerical examples will be independent of the material constants as well as the deformation state (plane strain or generalized plane stress) in case the cylinder is homogeneous. However, for nonhomogeneous cylinders they depend on the material constant β and the deformation state. The numerical values obtained in this section have been confirmed by the result of a parallel, approximate analysis, in which the nonhomogeneous hollow circular cylinder is taken to be consisting of a large number of

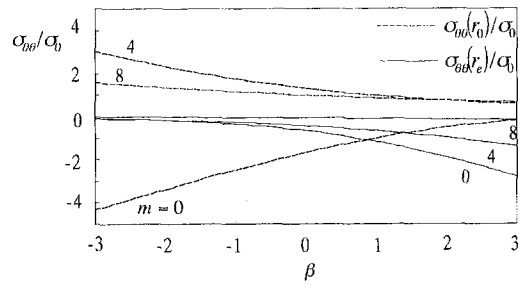


Fig. 7 Numerical values of $\sigma_{\theta\theta}/\sigma_0$ ($r_e = 2$, $\theta = 0$, unilateral normal traction)

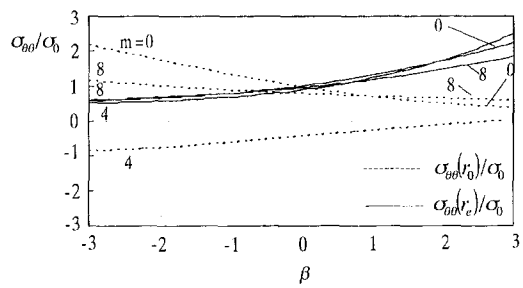


Fig. 8 Numerical values of $\sigma_{\theta\theta}/\sigma_0$ ($r_e = 2$, $\theta = 0$, bilateral normal traction)

piecewise homogeneous ones of small thickness. The series expressing the exact solutions are well convergent and easy to be handled numerically: Taking about 20 terms in the series is enough for obtaining accurate numerical results. An examination on the solutions discloses that when $\beta \neq 0$, the stresses are functions of the variable βr. This fact can be utilized to extend the applicability of the numerical results.

Discussion

The elasticity solutions for a nonhomogeneous hollow circular cylinder have been developed under the popularly employed assumption that Young's modulus of the material varying exponentially is in the radial direction, while the Poisson's ratio is a constant.

Consider the general case when the nonhomogeneous hollow circular cylinder is of Young's modulus $E(r)$ and Poisson's ratio $\nu(r)$, where $E(r)$ and $\nu(r)$ are arbitrary, continuous functions. Applying an analysis similar to that used previously for the nonhomogeneous cylinder of exponential Young's modulus and constant Poisson' ratio, in this general case it is found that the functions $A_{n1}(r)$, $A_{n2}(r)$, $A_{n3}(r)$ and $A_{n4}(r)$, $n = 2, 3, \ldots$, are still governed by Eqs. (32)–(35). However, the coefficients in the equations, $c_{11}, c_{12}, \ldots$, are generally not longer constants but functions of the variable r. As an example, we have

$$c_{11} = \frac{1}{1 + \kappa(r)}\left[\frac{\kappa(r)\mu'(r)}{\mu(r)} - \kappa'(r)\right] \tag{52}$$

where $\kappa(r) = 3 - 4\nu(r)$ for plane strain and $\kappa(r) = (3 - \nu(r))/(1 + \nu(r))$ for generalized plane stress. If the Young's modulus of the material varies exponentially, whereas the Poisson's ratio varies linearly with respect to r, c_{11} is a linear function of r. Similar remarks apply to $A_{01}(r)$, $A_{03}(r)$ and other functions in the solution.

To obtain an exact elasticity solution for the general case then again reduces to the solution of some systems of first-order ordinary differential equations of variable coefficients. For solving such differential equations systems, the method provided in this investigation for the case of all the coefficients c_{ij} being constant would be helpful.

The solutions for the nonhomogeneous hollow circular cylinder are obtained in this article by the method of matching a infinitely large number of homogeneous cylinder solutions. This method has the advantages of sufficiently utilizing the potential of existing homogeneous solutions, while fundamental equations in nonhomogeneous elasticity are virtually bypassed. Of course, the solution could also be sought by adopting the theory and fundamental equations of nonhomogeneous elasticity. In that case the stress function must be founded through solving a nonhomogeneous compatibility equation; which is a partial differential equation of order four with variable coefficients whose solution may be difficult to obtain. In this investigation, the solution is obtained by solving some systems of first-order ordinary differential equations, which appears a useful and possibly simpler alternative to the high-order partial differential equation.

References

Bakirtas, I., 1980, "The Problem of a Rigid Punch on a Nonhomogeneous Elastic Half Space," *Int. J. Eng. Sci.*, Vol. 18, pp. 597–610.

Barber, J. R., 1992, *Elasticity,* Kluwer, Dordrecht, The Netherlands.

Belik, G. I., and Protsenko, V. S., 1967, "The Contact Problem of a Half-Plane for Which the Modulus of Elasticity of the Material is Expressed by a Power Function of the Depth," *Prikladnaya Mekhanika,* Vol. 3, pp. 137–140.

Choi, H. J., 1996, "An Analysis of Cracking in a Layered Medium with a Functionally Graded Nonhomogeneous Interface," ASME JOURNAL OF APPLIED MECHANICS, Vol. 63, pp. 479–486.

Craster, R. V., and Atkinson, C., 1994, "Mixed Boundary Value Problems in Nonhomogeneous Elastic Materials," *Quar. J. Mechanics and Applied Mathematics,* Vol. 47, pp. 183–206.

Delale, F., and Erdogan, F., 1983, "The Crack Problem for a Nonhomogeneous Plane," ASME JOURNAL OF APPLIED MECHANICS, Vol. 50, pp. 609–614.

Erdogan, F., Kaya, A. C., and Joseph, P. F., 1991a, "The Crack Problem in Bonded

Downloaded 04 May 2010 to 171.66.16.27. Redistribution subject to ASME license or copyright; see http://www.asme.org/terms/Terms_Use.cfm

Nonhomogeneous Materials," ASME JOURNAL OF APPLIED MECHANICS, Vol. 58, pp. 410–418.

Erdogan, F., Kaya, A. C., and Joseph, P. F., 1991b, "The Mode III Crack Problem in Bonded Materials With a Nonhomogeneous Interfacial Zone," ASME JOURNAL OF APPLIED MECHANICS, Vol. 58, pp. 419–427.

Fabrikant, V. I., 1985, "External Crack in Non-Homogeneous Elasticity," *Engineering Fracture Mechanics,* Vol. 22, pp. 855–858.

Fabrikant, V. I., 1989, *Applications of Potential Theory in Mechanics,* Kluwer, Dordrecht, The Netherlands.

Gao, X., and Kuang, Z. B., 1992, "Mode I Fracture in Two Dissimilar Functional Nonhomogeneous Planes," *Engineering Fracture Mechanics,* Vol. 42, pp. 33–44.

Kassir, M. K., and Chuaprasert, M. F., 1974, "A Rigid Punch in Contact With a Nonhomogeneous Elastic Solid," ASME JOURNAL OF APPLIED MECHANICS, Vol. 42, pp. 1019–1024.

Muskhelishvili, N. I., 1963, *Some Basic Problems of the Mathematical Theory of Elasticity,* P. Noordhoff, Groningen-Holland.

Popov, G. I., 1973, "Axisymmetric Contact Problem for an Elastic Inhomogeneous Half Space in the Presence of Cohesion," *PMM,* Vol. 37, pp. 1052–1059.

Tenenbaum, M., and Pollard, H., 1963, *Ordinary Differential Equations,* Harper and Row, New York.

Timoshenko, S. P., and Goodier, J. N., 1970, *Theory of Elasticity,* 3rd Ed., McGraw-Hill, New York.

Yong, Z., and Hanson, M. T., 1994, "Three-Dimensional Crack and Contact Problems with a General Geometric Configuration," *J. Mech. Phys. Solids,* Vol. 42, pp. 215–239.

APPENDIX

$$D_{11}^{(j+1)} = \frac{2\mu_j + (\kappa_j - 1)\mu_{j+1}}{\mu_j(1 + \kappa_{j+1})}, \quad D_{12}^{(j+1)} = \frac{\mu_j - \mu_{j+1}}{\mu_j r_j^2(1 + \kappa_{j+1})},$$

$$D_{21}^{(j+1)} = \frac{2r_j^2[\mu_{j+1}(1 - \kappa_j) - \mu_j(1 - \kappa_{j+1})]}{\mu_j(1 + \kappa_{j+1})},$$

$$D_{22}^{(j+1)} = \frac{2(\mu_{j+1} - \mu_j) + \mu_j(1 + \kappa_{j+1})}{\mu_j(1 + \kappa_{j+1})}. \tag{A1}$$

$$E_{11}^{(j+1)} = \frac{\mu_j + \mu_{j+1}\kappa_j}{\mu_j(1 + \kappa_{j+1})}, \quad E_{12}^{(j+1)} = E_{13}^{(j+1)} = \frac{\mu_j - \mu_{j+1}}{2\mu_j(1 + \kappa_{j+1})r_j^2},$$

$$E_{14}^{(j+1)} = \frac{\mu_{j+1} - \mu_j}{\mu_j(1 + \kappa_{j+1})r_j^4}, \quad E_{21}^{(j+1)} = E_{23}^{(j+1)} = E_{24}^{(j+1)} = 0,$$

$$E_{22}^{(j+1)} = \frac{(1 + \kappa_j)(1 - \kappa_{j+1})}{(1 - \kappa_j)(1 + \kappa_{j+1})},$$

$$E_{31}^{(j+1)} = E_{32}^{(j+1)} = E_{34}^{(j+1)} = 0, \quad E_{33}^{(j+1)} = 1,$$

$$E_{41}^{(j+1)} = \frac{(\mu_{j+1}\kappa_j - \mu_j\kappa_{j+1})r_j^4}{\mu_j(1 + \kappa_{j+1})},$$

$$E_{42}^{(j+1)} = \frac{r_j^2}{\mu_j(1 + \kappa_{j+1})}\left[\frac{\mu_j - \mu_{j+1}}{2} - \frac{\kappa_{j+1} - \kappa_j}{1 - \kappa_j}\right],$$

$$E_{43}^{(j+1)} = \frac{(\mu_j - \mu_{j+1})r_j^2}{2\mu_j(1 + \kappa_{j+1})}, \quad E_{44}^{(j+1)} = \frac{\mu_{j+1} + \mu_j\kappa_{j+1}}{\mu_j(1 + \kappa_{j+1})}, \tag{A2}$$

$$F_{11}^{(j+1)} = \frac{\mu_j + \mu_{j+1}\kappa_j}{\mu_j(1 + \kappa_{j+1})},$$

$$F_{12}^{(j+1)} = \frac{1 - n}{r_j^{2n}}\frac{\mu_j - \mu_{j+1}}{\mu_j(1 + \kappa_{j+1})},$$

$$F_{13}^{(j+1)} = 0, \quad F_{14}^{(j+1)} = \frac{n(\mu_{j+1} - \mu_j)}{\mu_j(1 + \kappa_{j+1})r_j^{2n+2}},$$

$$F_{21}^{(j+1)} = \frac{(1 + n)r_j^{2n}}{1 + \kappa_{j+1}}\left(1 - \frac{\mu_{j+1}}{\mu_j}\right),$$

$$F_{22}^{(j+1)} = F_{11}^{(j+1)}, \quad F_{23}^{(j+1)} = \frac{nr_j^{2n-2}}{1 + \kappa_{j+1}}\left(1 - \frac{\mu_{j+1}}{\mu_j}\right), \quad F_{24}^{(j+1)} = 0,$$

$$F_{31}^{(j+1)} = \left(1 + \frac{1}{n}\right)\frac{r_j^2}{1 + \kappa_{j+1}}\left[\frac{\mu_{j+1}}{\mu_j}(1 - \kappa_j) + \kappa_{j+1} - 1\right],$$

$$F_{32}^{(j+1)} = \frac{r_j^{2-2n}}{n(1 + \kappa_{j+1})}\left[(1 - n^2)\left(\frac{\mu_{j+1}}{\mu_j} - 1\right) + \kappa_{j+1} - \frac{\kappa_j\mu_{j+1}}{\mu_j}\right],$$

$$F_{33}^{(j+1)} = \frac{\mu_{j+1} + \mu_j\kappa_{j+1}}{\mu_j(1 + \kappa_{j+1})}, \quad F_{34}^{(j+1)} = \frac{1 + n}{(1 + \kappa_{j+1})r_j^{2n}}\left(1 - \frac{\mu_{j+1}}{\mu_j}\right),$$

$$F_{41}^{(j+1)} = \frac{r_j^{2n+2}}{n(1 + \kappa_{j+1})}\left[(1 - n^2)\left(1 - \frac{\mu_{j+1}}{\mu_j}\right) - \kappa_{j+1} + \frac{\kappa_j\mu_{j+1}}{\mu_j}\right],$$

$$F_{42}^{(j+1)} = \frac{(1 - n)r_j^2}{n(1 + \kappa_{j+1})}\left[1 - \kappa_{j+1} + \frac{\mu_{j+1}}{\mu_j}(\kappa_j - 1)\right],$$

$$F_{43}^{(j+1)} = \frac{(n - 1)r_j^{2n}}{1 + \kappa_{j+1}}\left(\frac{\mu_{j+1}}{\mu_j} - 1\right), \quad F_{44}^{(j+1)} = F_{33}^{(j+1)}. \tag{A3}$$

Downloaded 04 May 2010 to 171.66.16.27. Redistribution subject to ASME license or copyright; see http://www.asme.org/terms/Terms_Use.cfm

Conditions for Dual Compression in Perfectly Elastic Three-Dimensional Collisions

J. A. Batlle
Department of Mechanical Engineering,
Polytechnical University of Catalunya,
Av. Diagonal, 647,
08028 Barcelona, Spain
Mem. ASME

The jamb (self-locking) process in single-point three-dimensional rough collisions in multibody systems may lead to a dual compression: a second compression phase develops after an initial compression-expansion one. In such a case the usual energetical restitution coefficient e_w is ill defined. This article presents a thorough analysis, by means of the incremental Routh's model, of the conditions leading to dual compression in the case of perfectly elastic collisions. For a given general collision configuration and for each value of the friction coefficient greater than the threshold value for jamb, there is always a domain of directions of the incident velocity leading to dual compression. An application example is presented.

1 Introduction

In single-point rough collisions the tangential force at the collision point may be responsible for an increase of the normal approaching velocity during a compression phase, or a decrease of a normal separating velocity reached after a previous compression-expansion phase (compression and expansion is normal to the contact surface). Such self-locking phenomenon, known also as jamb, cannot always last throughout the entire duration of contact. Eventually the end of sliding or the change in the sliding direction or the end of the collision stops it. The latter case may happen when jamb occurs during expansion. Though there has been an increasing interest in rigid-body collision theory, the jamb process in three-dimensional rough collisions has been paid little attention. Recently it has been addressed by Batlle (1998), under the Routh's incremental model for the general case of single-point rough collisions with infinite tangential stiffness at the collision point in multibody systems with frictionless constraints, that may have drivers that guarantee of continuity of a set of generalized velocities (Batlle, 1991, 1996). Three-dimensional jamb is far more complex than two-dimensional jamb. In two-dimensional collisions the sliding has a constant direction under jamb conditions and consequently jamb occurs from the beginning of the collision and lasts until the sliding stops. In contrast, three-dimensional jamb depends upon a variable sliding direction and, as a consequence, jamb may start after a first phase under a no-jamb condition ("access to jamb") and, if it is not stopped by the end of the collision, it may end before the sliding stops ("partial jamb" in contrast to "full jamb" that lasts until the sliding stops). When jamb starts during expansion, it may lead to a second compression phase. In such a case the usual energetical restitution coefficient e_w (the work done by the normal force is equal to $(1 - e_w^2)W_{comp}$, W_{comp} being the compression work) (Stronge, 1990, 1991) is ill-defined, as well as it is ill-defined the generalized Poisson's restitution coefficient.

This paper presents a thorough analysis, by means of the incremental Routh's model, of the conditions under which dual compression occurs in a perfectly elastic collision belonging to the general case just described. It is found that for any initial vector $\boldsymbol{\mu}^0 \equiv \mu\boldsymbol{\sigma}^0$ (μ being Coulomb's friction coefficient and $\boldsymbol{\sigma} \equiv \mathbf{v}_t/|\mathbf{v}_t|$ being the unit vector in the direction of sliding) belonging to an "access to (full or partial) jamb" domain, dual compression occurs for a certain range of the slope $v_n^0/|\mathbf{v}_t^0|$ of the initial velocity.

The conditions for dual compression are derived from modified $W_n(P_n)$ curves related to the work done by the normal force at the collision point. They are derived from a single W_n curve for each given $\boldsymbol{\mu}^0 \equiv \mu\boldsymbol{\sigma}^0$ in Section 3, and from a single W_n curve for each given μ and each access to jamb domain in Section 4. An application example presented in Section 5 is used throughout the article.

The simplifying assumption of infinite tangential stiffness at the collision point is clearly unphysical for isotropic materials, for which the values of both tangential and normal stiffness are of the same order. The tangential compliance may have a significant role on the impact behavior even if no energy dissipation is associated with the tangential deformation. However, in spite of this, it is interesting to explore the Routh's model potential concerning jamb and dual compression because it is a model widely used as a first approximation. The great simplicity of the Routh's model allows the obtaining of general properties, as those presented in this article, that give hints concerning the results to be obtained by means of more realistic models.

2 Dual Compression Analysis From $v_n(P_n)$ and $W_n(P_n)$ Curves

In the incremental Routh's model, the evolution equations of the normal separating velocity, under sliding (v_n^s) and nonsliding condition (v_n^{ns}), are

$$\frac{dv_n^s}{dP_n} = a - \mu\mathbf{h}^T\boldsymbol{\sigma}; \quad \frac{dv_n^{ns}}{dP_n} = a - \mathbf{h}^T[b]^{-1}\mathbf{h} = \text{const} > 0, \quad (1)$$

where P_n is the normal impulse, and "a" and $[b]$, which are definite positive, and $\mathbf{h}$ are elements that depend upon collision configuration only (Batlle, 1991, 1996). According to Eqs. (1), under a nonsliding condition, $v_n^{ns}(P_n)$ is a straight line whose slope depends upon configuration only. However, under a sliding condition the shape of $v_n^s(P_n)$ depends upon the evolution of $\boldsymbol{\sigma}(P_n)$; this evolution is associated with that of the sliding velocity $\mathbf{v}_t(P_n)$, which is determined by the autonomous flow

Contributed by the Applied Mechanics Division of THE AMERICAN SOCIETY OF MECHANICAL ENGINEERS for publication in the ASME JOURNAL OF APPLIED MECHANICS.
Discussion on the paper should be addressed to the Technical Editor, Professor Lewis T. Wheeler, Department of Mechanical Engineering, University of Houston, Houston, TX 77204-4792, and will be accepted until four months after final publication of the paper itself in the ASME JOURNAL OF APPLIED MECHANICS.
Manuscript received by the ASME Applied Mechanics Division, Oct. 8, 1998; final revision, Mar. 1, 1999. Associate Technical Editor: N. C. Perkins.

 Copyright © 1999 by ASME

Downloaded 04 May 2010 to 171.66.16.27. Redistribution subject to ASME license or copyright; see http://www.asme.org/terms/Terms_Use.cfm

$$\frac{d\mathbf{v}_t}{dP_n} = \mathbf{h} - \mu[b]\boldsymbol{\sigma}. \tag{2}$$

whose integration, from initial $\mathbf{v}_t^0$, leads to $\mathbf{v}_t[P_n, \mathbf{v}_t^0]$ and consequently to $\boldsymbol{\sigma}[P_n, \mathbf{v}_t^0]$. For a given initial sliding velocity $\mathbf{v}_t^0$, different values for initial normal velocity v_n^0 lead to curves $v_n(P_n)$ of the same shape but are displaced along the v_n axis, and with different end P_n^e value of the end normal impulse, as it is shown in Figs. 1–2. For perfectly elastic collisions the end of the collisions is associated with the first zero crossing of the work W_n done by the normal percussive force for increasing $P_n > 0$. The value of W_n can be calculated as

$$W_n(P_n) = \int_0^{P_n} v_n dP_n. \tag{3}$$

The points $v_n(P_n^{SJ})$ in Figs. 1–2 correspond to the start of jamb, while the points $v_n(P_n^{EJ})$ correspond to the end of jamb. For "full jamb," as in Figs. 1–2, there is a slope discontinuity in $v_n(P_n)$ curves at P_n^{EJ}. For "partial jamb" there is slope continuity with zero slope at P_n^{EJ}. Related points in $W_n(P_n)$ curves are inflection points. Those for P_n^{SJ} have zero curvature, while those for P_n^{EJ} have zero curvature in case of "partial jamb" and curvature discontinuity in case of "full jamb."

The curves $v_n(P_n)$ can be scaled for $|\mathbf{v}_t^0| = 1$. According to Eqs. (1) and (2), the dependence of the evolution equations of v_n^s and $\mathbf{v}_t$ upon v_n and $|\mathbf{v}_t|$ is limited to the unit vector $\boldsymbol{\sigma}$ in the sliding direction. They do not change, if v_n, $|\mathbf{v}_t|$ and P_n are scaled by the same arbitrary factor. The curves for a given value of $\mathbf{v}_t^0 = v_t^0\boldsymbol{\sigma}^0$ can be obtained from those calculated for $v_t^0 = 1$ and the same $\boldsymbol{\sigma}^0$, by multiplying v_n, $|\mathbf{v}_t|$ and P_n by v_t^0 and W_n by $(v_t^0)^2$. For $v_t^0 = 1$, the values of v_n^0 are equal to the slope of the initial velocity at the collision point.

Figures 1 and 2 show that in both cases there is a range $v_n^{**} \le v_n^0 < v_n^*$ of initial normal velocities leading to a second compression. In both cases v_n^{**} corresponds to v_n^0 leading to $v_n(P_n^{SJ}) = 0$, while v_n^* corresponds to v_n^0 leading to $v_n(P_n^{EJ}) = 0$ in Fig. 1 and to the double condition $v_n = 0$ and $W_n = 0$ at a certain $P_n^{SJ} < P_n < P_n^{EJ}$ in Fig. 2. In the last case, the collision with a $v_n(P_n)$ curve that would reach $v_n(P_n^{EJ}) = 0$ ends before reaching that point. For this reason the case in Fig. 2 will be referred as "truncated" while the case in Fig. 1 will be referred as "complete."

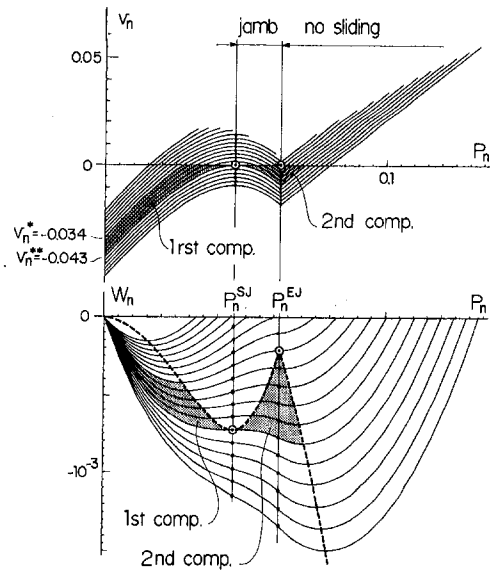


Fig. 1 "Complete" case of dual compression. Plots $v_n(P_n)$ and $W_n(P_n)$ for the application example with $\mu = 0{,}6$, $v_t^0 = 1$ and θ deg = ±80,80 deg. ($L = R\sqrt{15/32}$).

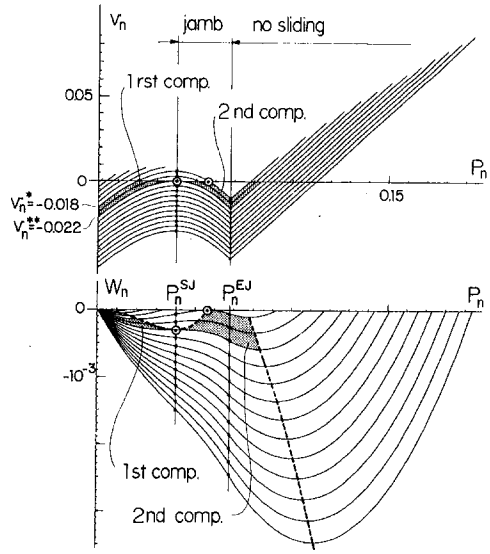


Fig. 2 "Truncated" case of dual compression. Plots $v_n(P_n)$ and $W_n(P_n)$ for the application example with $\mu = 0{,}6$, $v_t^0 = 1$ and θ deg = +70,23 deg. ($L = R\sqrt{15/32}$).

All collisions in which jamb does not start at the beginning of the collision but may start later if v_n^0 is great enough, lead to similar curves as those shown in Figs. 1–2 and, consequently, to a range $v_n^{**} \le v_n^0 < v_n$ for dual compression. The initial $\boldsymbol{\mu}^0$ vector for such collisions belongs to an access to jamb domain in the $\boldsymbol{\mu}$ plane.

3 Dual Compression Analysis From a Single W_n Curve for a Given Friction Coefficient and a Given Initial Sliding Direction

As it has been shown in Section 2, rough collisions studied under the Routh's model can be scaled to $v_t^0 = 1$, and by doing so, as far as initial conditions are concerned, only the initial sliding direction $\boldsymbol{\sigma}^0$ is relevant to investigate the initial normal velocity v_n^0 for dual compression. For a given $\boldsymbol{\sigma}^0$ such that $\boldsymbol{\mu}^0 \equiv \mu\boldsymbol{\sigma}^0$ belongs to an "access to jamb" domain, the set of W_n curves considered in Figs. 1–2 can be gathered into a single W_n curve: This curve corresponds to $v_n^0 = 0$ (regardless the lack of physical feasibility of the associated collision), and will be denoted as $W_n^{(0)}$.

$$W_n^{(0)}(P_n) \equiv W_n[P_n;\ v_n^0 = 0,\ \mathbf{v}_t = \boldsymbol{\sigma}^0] \tag{4}$$

For physically feasible collisions, for which $v_n^0 < 0$, W_n is given by

$$W_n(P_n) = W_n^{(0)}(P_n) - v_n^0 P_n, \tag{5}$$

its values are equal to the vertical distance (negative if they are downwards) from the right line passing through the origin with slope $-v_n^0$ to the $W_n^{(0)}$ curve, as shown in Fig. 3.

When jamb is possible, curve $W_n^{(0)}(P_n)$ has two points of inflection; I^{SJ} that corresponds to P_n^{SJ}, which has zero curvature, and I^{EJ} that corresponds to P_n^{EJ}, I^{EJ} has zero curvature in the case of access to partial jamb, and discontinuity of curvature in the case of access to full jamb.

Dual compression will occur for v_n^0 such that $W_n^{(0)}(P_n)$ has three points with slope $= -v_n^0$, as it is the case shown in Fig. 3: W_n is minimum at points A and A', and it is maximum at point B. The second compression takes place in the interval from B to A'.

The boundary values v_n^* and v_n^{**} of v_n for dual compression can be easily found from $W_n^{(0)}(P_n)$. The value $-v_n^{**}$ is equal to the slope of $W_n^{(0)}(P_n)$ at its first inflection point I^{SJ} in both complete or truncated cases, Figs. 4–5. The value $-v_n^*$ is equal to the slope of $W_n^{(0)}(P_n)$ at its second inflection point I^{EJ} in the complete case, Fig.

Downloaded 04 May 2010 to 171.66.16.27. Redistribution subject to ASME license or copyright; see http://www.asme.org/terms/Terms_Use.cfm

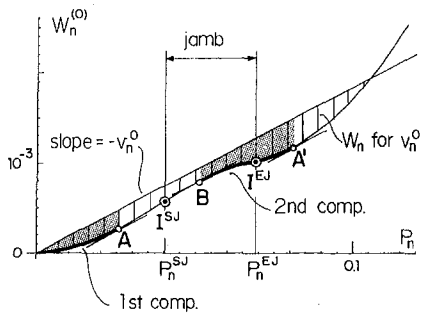


Fig. 3 Analysis of dual compression occurrence by means of the $W_n^{(0)}(P_n)$ plot for the application example with $\mu = 0{,}6$, and θ deg = ±80,80 deg. ($L = R\sqrt{15/32}$).

4, while it is equal to the slope of the tangent to $W_n^{(0)}(P_n)$ from the origin in the truncated case, as shown in Fig. 5.

4 Dual Compression Analysis From a Single W_n Curve

The analysis presented in Section 3 is specific for a given initial $\boldsymbol{\mu}^0 \equiv \mu\boldsymbol{\sigma}^0$. For a given value of μ each $\boldsymbol{\sigma}^0$ requires its own $W_n^{(0)}(P_n)$ curve. A more global insight may be derived from a single W_n curve associated with a given value of μ and a given access to jamb domain. Such a curve is calculated for $v_n^0 = 0$, $v_t^0 = 1$, $\boldsymbol{\sigma}^0 = \boldsymbol{\sigma}_{SJ}$ sliding direction at which jamb starts, and for positive and negative values of the normal impulse (regardless the lack of physical feasibility of the associated collision). This curve will be denoted $W_n'(P_n')$,

$$W_n'(P_n') = W_n[P_n';\ v_n^0 = 0,\ v_t^0 = 1,\ \boldsymbol{\sigma}^0 = \boldsymbol{\sigma}_{SJ}];\quad P_n' > 0. \tag{6}$$

From the geometry of jamb related domains (Batlle and Cardona, 1998) it is easily checked that μ for access to a partial jamb is smaller than μ for access to a full jamb, and that there is a single $\boldsymbol{\sigma}_{SJ}$ for access to a partial jamb, while there are one or two (symmetrical relative to $\boldsymbol{\sigma}_h \equiv \mathbf{h}/|\mathbf{h}|$)) vectors $\boldsymbol{\sigma}_{SJ}$ for access to a full jamb.

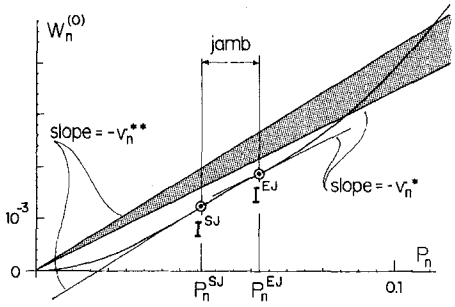


Fig. 4 Analysis of the "complete" case of dual compression illustrated in Fig. 1, by means of the $W_n^{(0)}(P_n)$ plot

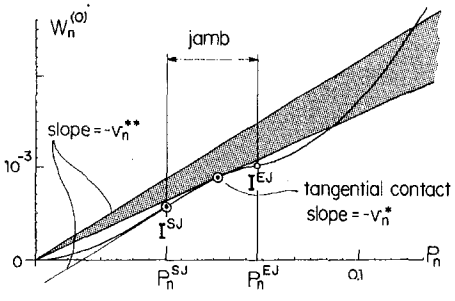


Fig. 5 Analysis of the "truncated" case of dual compression illustrated in Fig. 2, by means of the $W_n^{(0)}(P_n)$ plot

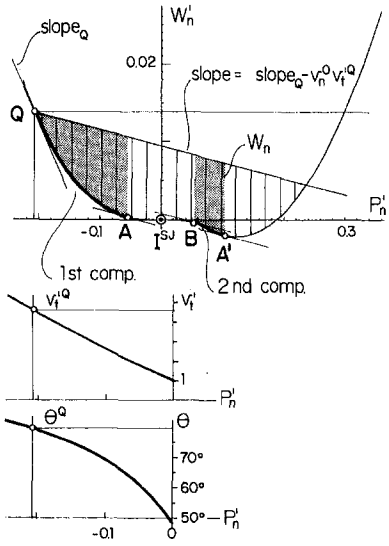


Fig. 6 Analysis of dual compression occurrence by means of the $W'(P_n')$ $v_t'(P_n')$ and $\theta(P_n')$ plots for the application example with $\mu = 0{,}6$. Initial conditions are $v_n^0 = 0$, $v_t^0 = 1$, $\boldsymbol{\sigma}^0 = \boldsymbol{\sigma}_{SJ}$ (θ deg = 48,2 deg). ($L = R\sqrt{15/32}$).

As it is shown in Fig. 6, the origin $P_n' = 0$ coincides with the first inflection point I^{SJ} of W_n', the one corresponding to the start of jamb. For each P_n' value, there is a corresponding $v_n(P_n')$ value—equal to the slope of W_n' at $P_n'-$, a $v_t'(P_n')$ value and a sliding direction $\boldsymbol{\sigma}(P_n')$ defined by angle θ. Let $v_n'^Q$ and $v_t'^Q\boldsymbol{\sigma}^Q$ be the normal and tangential velocities corresponding to point Q of W_n' at $P_n'^Q$. If $v_t^0 = 1$, $\boldsymbol{\sigma}^0 = \boldsymbol{\sigma}^Q$ and an arbitrary value of v_n^0 are taken as initial conditions, it is easily checked that for this collision, for which

$$P_n = (P_n' - P_n'^Q)/V_t'^Q, \tag{7}$$

the normal velocity v_n^{SJ} when jamb starts is

$$\begin{aligned} v_n^{SJ} \equiv v_n(P_n^{SJ}) &= v_n^0 - (v_n'^Q/v_t'^Q) \\ &= v_n^0 - (\text{slope of } W_n' \text{ at } Q)/v_t'^Q, \end{aligned} \tag{8}$$

and that the values $W_n(P_n)$ are equal to the vertical distances (negative if downwards) from the straight line through Q with slope $-v_n^{SJ}v_t'^Q$ to the W_n' curve for $P_n' = P_n v_t'^Q + P_n'^Q$ (Fig. 6). According to Eq. (8) the straight line slope = (slope of W_n' at Q) − $v_n^0 v_t'^Q$.

Dual compression will occur for v_n^0 values leading to v_n^{SJ} values such that W_n' has three points with slope equal to $-v_n^{SJ}v_t'^Q = -v_n^0 v_t'^Q - v_n'^Q$, as shown in Fig. 6: W_n is minimum at points A and A', and it is maximum at point B. The second compression takes place between B and A'.

Under the initial conditions considered, the lower boundary value v_n^{**Q} for dual compression corresponds to $v_n^{SJ} = 0$ and, consequently, to

$$v_n^{**Q} = v_n'^Q/v_t'^Q = (\text{slope of } W_n' \text{ at point } Q)/v_t'^Q. \tag{9}$$

For this boundary value the straight line through Q leading to the W_n values is horizontal.

The upper boundary value v_n^{*Q} for dual compression is easily found from the $W_n'(P_n')$ curve. The value v_n^{*Q} is equal to the scaled value, by a factor $(v_t'^Q)^{-1}$, of the difference between the slopes of W_n' at Q and at I^{EJ} in the "complete" case (Fig. 7), and of the difference between the slope of W_n' at Q and the slope of the tangent from Q to the W_n' curve in the "truncated" case (Fig. 8).

Downloaded 04 May 2010 to 171.66.16.27. Redistribution subject to ASME license or copyright; see http://www.asme.org/terms/Terms_Use.cfm

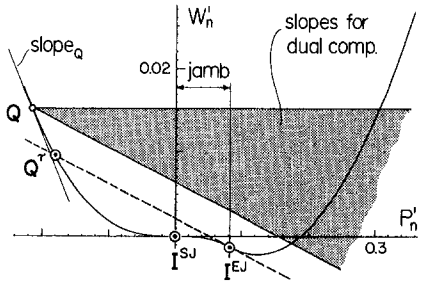


Fig. 7 Analysis of the "complete" case of dual compression illustrated in Fig. 1, by means of the $W'(P'_n)$ plot

$$v_n^{*Q} = \frac{\text{slope of } W'_n \text{ at } Q - \text{slope of } W' \text{ at } I^{EJ}}{v_t'^{Q}}; \quad \text{complete case,} \quad (10)$$

$$v_n^{*Q} = \frac{\text{slope of } W'_n \text{ at } Q - \text{slope of tangent from } Q \text{ to } W'_n}{v_t'^{Q}}; \quad \text{truncated case.} \quad (11)$$

There is a critical point Q^τ, given by the crossing of the tangent to W'_n at I^{EJ} and curve W'_n, which is the threshold between points Q corresponding to the complete or truncated cases, respectively.

The values v_n^{*Q} and v_n^{**Q} for different Q points can be plotted in polar form by means of the vectors $|v_n^{*Q}|\boldsymbol{\sigma}^Q$ and $|v_n^{**Q}|\boldsymbol{\sigma}^Q$ as in Fig. 9, in which the threshold initial normal velocity v_n^J for a jamb is also represented. These plots depend only on the value of μ and on the access to the jamb domain considered.

5 Application Example

The single-point collision of a rigid body with a rough fixed surface is considered. The rigid body is a solid homogeneous cylinder with a rigid massless attached rod. The geometrical parameters at the collision configuration and the generalized velocities used are shown in Fig. 10. The general expressions for "a", **h**, and $[b]$, in the absence of impulsional drivers, are (Batlle, 1991, 1996)

$$\begin{bmatrix} a & \mathbf{h}^T \\ \mathbf{h} & [b] \end{bmatrix} = [K]^T[M]^{-1}[K], \quad (12)$$

where $[M]$ is the inertia matrix and $[K]$ is the matrix of kinematical coefficients relating v_n and $\mathbf{v}_t$ to the generalized velocities.

$$\begin{Bmatrix} v_n \\ \mathbf{v}_t \end{Bmatrix} = [K]^T\{u\} \quad (13)$$

In this case the matrices $[M]$ and $[K]$ are

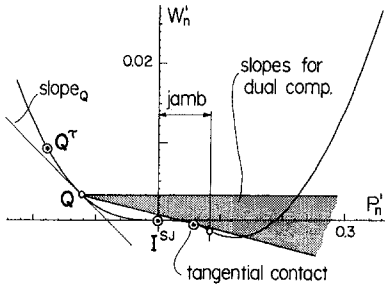


Fig. 8 Analysis of the "truncated" case of dual compression illustrated in Fig. 2, by means of the $W'(P'_n)$ plot

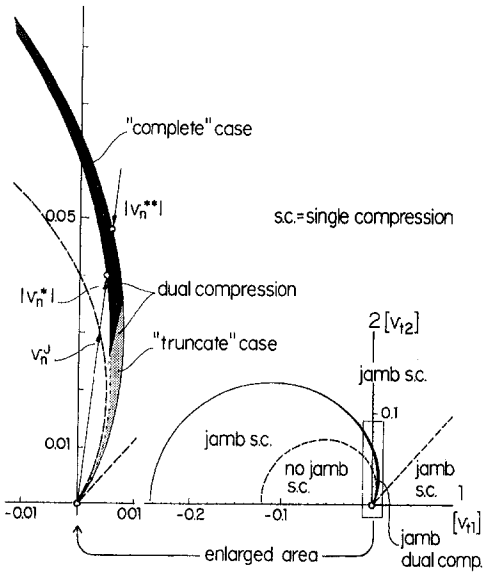


Fig. 9 Polar plot of range $|v_n^*| \le |v_n^0| < |v_n^{**}|$, for dual compression in the application example with μ = 0,6, as a function of the initial sliding direction. ($L = R\sqrt{15/32}$).

$$[M] = m\begin{bmatrix} 1 & 0 & 0 & & & \\ 0 & 1 & 0 & & & \\ 0 & 0 & 1 & & & \\ & & & \rho_T^2 & & \\ & & & & \rho_a^2 & \\ & & & & & \rho_T^2 \end{bmatrix}; \quad \rho_T^2 = \tfrac{1}{3}L^2 + \tfrac{1}{4}R^2 \quad \rho_a^2 = \tfrac{1}{2}R^2;$$

$$[K] = \begin{bmatrix} 1 & 0 & 0 \\ 0 & 1 & 0 \\ 0 & 0 & 1 \\ 0 & 0 & H \\ -S & -H & 0 \\ 0 & 0 & S \end{bmatrix}, \quad (14)$$

and, according to Eq. (12), they lead to

$$a = \frac{1}{m}\left[1 + \left(\frac{S}{\rho_a}\right)^2\right]; \quad \{h\} = \frac{1}{m}\begin{Bmatrix} 1 + \dfrac{SH}{\rho_a^2} \\ 0 \end{Bmatrix}$$

$$[b] = \frac{1}{m}\begin{bmatrix} 1 + \left(\dfrac{H}{\rho_a}\right)^2 & 0 \\ 0 & 1 + \dfrac{S^2 + H^2}{\rho_T^2} \end{bmatrix}. \quad (15)$$

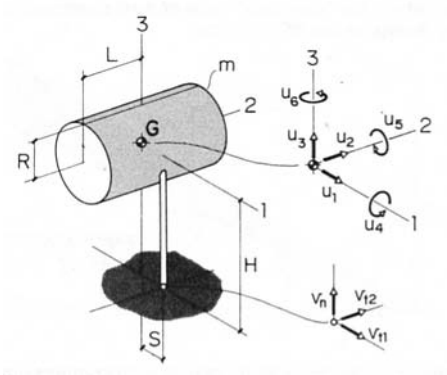


Fig. 10 Application example parameters and generalized velocities

Downloaded 04 May 2010 to 171.66.16.27. Redistribution subject to ASME license or copyright; see http://www.asme.org/terms/Terms_Use.cfm

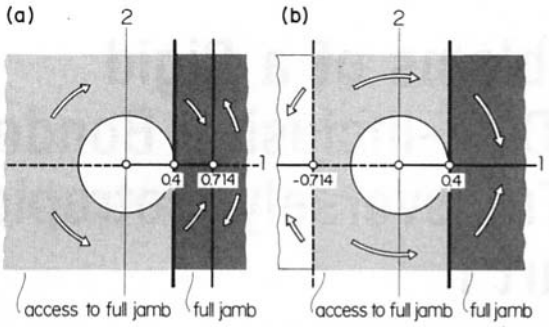


Fig. 11 Application example jamb related domains in the $\mu \equiv \mu\sigma$ plane; (*a*) for $L = R\sqrt{17/12}$; (*b*) for $L = R\sqrt{15/32}$

For values $S = (1/\sqrt{2})R$, $H = (5/\sqrt{2})R$; and $L = R\sqrt{17/12}$ or $L = R\sqrt{15/32}$, the expressions for a, $\mathbf{h}$, and $[b]$ reduce to

$$a = \frac{1}{m}2; \quad \{\mathbf{h}\} = \frac{1}{m}\begin{Bmatrix}5\\0\end{Bmatrix} \equiv \begin{Bmatrix}h\\0\end{Bmatrix};$$

$$[b] = \begin{bmatrix}26 & 0\\0 & 19\end{bmatrix} \quad \text{for} \quad \frac{L}{R} = \sqrt{\frac{17}{12}} \quad \text{and}$$

$$[b] = \begin{bmatrix}26 & 0\\0 & 33\end{bmatrix} \quad \text{for} \quad \frac{L}{R} = \sqrt{\frac{15}{32}}.$$

The boundary value of μ for the jamb is (Batlle, 1998)

$$\mu_J = \frac{a}{|\mathbf{h}|} = \frac{2}{5} = 0{,}4.$$

The geometry of the jamb related domains in the $\boldsymbol{\mu} \equiv \mu\boldsymbol{\sigma}$ plane is shown in Fig. 11 for both L/R values. In this example there is no domain of access to a partial jamb, and there are two symmetrical domains of access to a full jamb. For $\mu > \mu_J$ a full jamb starts for $\boldsymbol{\sigma} = \boldsymbol{\sigma}^{SJ}$, with an angle θ = arc cos (μ_J/μ), and leads to the centripetal asymptote. This asymptote has the direction $\boldsymbol{\sigma}_h$ for $L/R = \sqrt{15/32}$. For $L/R = \sqrt{17/12}$ it has the direction $\boldsymbol{\sigma}_h$ if $\mu \leq 5/7 \equiv \mu_a^*$ (Batlle, 1996), and it is inclined with an angle θ = arc cos (μ_a^*/μ) if $\mu > \mu_a^*$. In this example the hyperbola that determines the asymptotes or invariant lines in the $\boldsymbol{\mu}$ plane degenerates into two orthogonal straight lines.

Figures 1 to 9 have been calculated for $L/R = \sqrt{15/32}$ and μ = 0,6. The direction of sliding $\boldsymbol{\sigma}^\tau$ that is the threshold between the truncated and the complete cases has been numerically calculated as a function of μ, for $\mu > \mu_J$, and for both L/R values, and it has been used to divide the access to full jamb domain into the domains for complete and truncate cases by means of the $\mu\boldsymbol{\sigma}^\tau$ curve (Fig. 12).

Results of v_n^* and v_n^{**} for all values $\mu > \mu_J$ could be gathered in a single figure by means of two surfaces $v_n^*(\boldsymbol{\mu})$ and $v_n^{**}(\boldsymbol{\mu})$ over the access to (partial or full) jamb domains.

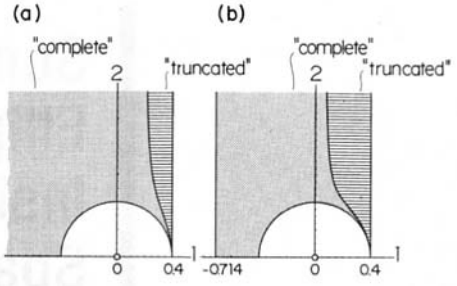


Fig. 12 Application example domains in the $\mu \equiv \mu\sigma$ plane for "complete" and "truncated" cases (*a*) for $L = R\sqrt{17/12}$; (*b*) for $L = R\sqrt{15/32}$

6 Conclusions

It has been shown that dual compression may happen in many single-point perfectly elastic three-dimensional rough collisions, with infinite tengential stiffness at the collision point, and in multibody systems with frictionless constraints that may have drivers that guarantee the continuity of a set of generalized velocities. Dual compression may happen when the initial vector $\boldsymbol{\mu}^0 \equiv \mu\boldsymbol{\sigma}^0$ ($\boldsymbol{\sigma}$ being the direction of sliding) belongs to an access to a (partial or full) jamb domain.

These domains may cover a substantial fraction of the $\boldsymbol{\mu}$ plane. For each $\boldsymbol{\mu}^0$ belonging to these domains, dual compression occurs for a certain range of slopes of the incident velocity, v_n/v_t.

For a given collision configuration and a value of μ greater than the threshold value for jamb, the initial conditions leading to a double compression can be derived from a set of three curves, $W_n'(P_n')$, $v_t'(P_n')$ and angle $\theta(P_n')$ of the sliding direction, associated with an access to the jamb domain. These curves are calculated from the initial conditions $v_n^0 = 0$, $v_t = 1$ and $\boldsymbol{\sigma}^0 = \boldsymbol{\sigma}_{SJ}$ = direction at which the jamb starts.

Acknowledgments

The author expresses his thanks to Gonçal Fortuny, for his collaboration in the numerical and graphical work implied in the application example, and to the referees, whose advise has been of great value in improving the final version of the paper.

This work has been conducted within the scope of the INTAS project 96-2138.

References

Batlle, J. A., and Condomines, A. B., 1991, "Rough Collisions in Multibody Systems," *Journal of Mechanism and Machine Theory,* Vol. 26, No. 6, pp. 565–577.

Batlle, J. A., 1996, "The Sliding Velocity Flow of Rough Collisions in Multibody Systems," ASME JOURNAL OF APPLIED MECHANICS, Vol. 63, pp. 804–809.

Batlle, J. A., and Cardona, S., 1998, "The Jamb (Self-locking) Process in Three-Dimensional Rough Collisions," ASME JOURNAL OF APPLIED MECHANICS, Vol. 65, pp. 417–423.

Stronge, W. J., 1990, "Rigid Body Collisions with Friction," *Proc. Royal Society London,* Vol. A431, pp. 169–181.

Stronge, W. J., 1991, "Friction in Collisions: Resolution of a Paradox," *J. Appl. Phys.,* Vol. 69, No. 2, pp. 610–612.

Downloaded 04 May 2010 to 171.66.16.27. Redistribution subject to ASME license or copyright; see http://www.asme.org/terms/Terms_Use.cfm

Some Problems of a Rigid Elliptical Disk-Inclusion Bonded Inside a Transversely Isotropic Space: Part I

M. Rahman
3019 W. 13 Mile Road, Apt. 214,
Royal Oak, MI 48073
e-mail: mrahman10@hotmail.com

The paper addresses the problem of contact of an elliptical inclusion in the form of a thin disk, bonded in the interior of a transversely isotropic space. The inclusion is assumed to be absolutely rigid and in perfect contact with the medium. Three different cases of loading are considered, namely, (a) the inclusion is loaded in its plane by a shearing force, whose line of action passes through the center of the disk; (b) the inclusion is rotated by a torque whose axis is perpendicular to the plane of the inclusion; (c) the medium is under uniform stress field at infinity in a plane parallel to the plane of the inclusion. In the first part of the article, the problems corresponding to all three cases are reduced, in a unified manner, to a system of coupled two-dimensional integral equations by using the theory of two-dimensional Fourier transforms. In the second part, closed-form solutions for these equations are obtained by using Dyson's theorem and Willis' generalization of Galin's theorem. Explicit expressions for the stress intensity factors near the edge of the inclusion are extracted from these solutions. Numerical results are plotted illustrating how these coefficients vary with transverse isotropy and the parametric angle of the ellipse. The results can be used to determine the critical failure load and angle of crack initiation for solids containing elliptical inclusions.

Introduction

Problems concerning stress concentrations in deformable solids containing different kinds of stress concentrators have long been the focus of investigations by researchers from many areas, such as mechanics, metallurgy, and materials science. Significance of such investigations is, of course, dictated by the applied nature of these problems. Practically all construction materials are inhomogeneous in their structure. In some cases, this is due to the technological imperfection of their production (porosity, different kinds of foreign inclusions) while in other cases, a secondary phase is introduced intentionally to render novel properties to the materials or to achieve a particular combination of properties, not characteristic to each of the constituents. However, whatever be the properties (physical, chemical, electrical, magnetic) of the composite material, from the strength point of view, a secondary phase is always regarded as a stress concentrator and hence it is an issue of significant theoretical and practical importance to assess the strength degradation of materials and determine the conditions preceding the crack initiation and crack propagation, such as the critical load and angle of crack initiation, near the edges of the inclusions. This is why over the past several decades, considerable amount of work has been done in the area of two and three-dimensional problems of stress concentrations near inclusions of various shapes. Since the literature on this subject is overwhelming, we will review only those works that are directly germane to the subject matter of our article, referring the readers interested in having excellent account of progress in this area to the works by Eshelby (1961), Galin (1976), Cherepanov (1979, 1983), Gladwell (1980), Podilchuk (1979), Panasiuk et al. (1982), Mura (1987), Pham-Thien and Kim (1994), and Ting (1994).

Historically, the works by Southwell and Gough (1926) and Goodier (1933) deserve special mention in the sense that they provided significant impetus to the subsequent research in this area. In the first of these works, Southwell and Gough derived the elastic field around a small spherical cavity in a statistically isotropic medium under uniform tension and applied the results to the fatigue fractures of shafts. In the second work, Goodier investigated the problem of determining stress concentration near a spherical inclusion and a cavity in an elastic solid under uniform tension. The disturbance caused by an ellipsoidal inclusion in an otherwise uniform stress field was studied by Eshelby (1961). The problem of an ellipsoidal inclusion undergoing translation and rotation, also known as Roben's problem, was investigated by Lure (1970). Kanwal and Sharma (1976), Phan-Thien (1993), Kim and Phan-Thien (1995), and Kim and Karrila (1991) investigated the problems of rigid spheroidal and ellipsoidal inclusions subjected to constant translation and rotation as well as the cases where the inclusions are in linear ambient and quadratic displacement fields, using the method of distributing point singularities, such as the Kelvin singularity, center of dilatation and center of rotation. Kim and Phan-Thien (1995) also extended the method to solve problems where the inclusions are *elastic*. In the special case where one of the principal axes of the ellipsoid vanishes, the solution of a flat elliptical disk-inclusion can be deduced from the above studies.

Collins (1962) solved the problem of a thin rigid circular disk in an infinite medium subjected to a constant displacement normal to its plane. Keer (1965) investigated the problem of a thin rigid circular disk in an infinite medium when it is given a constant displacement in its plane. He also studied the problem of a rigid sheet containing a circular hole. Kassir and Sih (1968) extended these results to the case of a thin rigid elliptical disk. They also considered the case of triaxial tension of a thin rigid elliptical disk. These authors then found the asymptotic representation of the elastic field near the border of the disk-inclusion and noted that the

Contributed by the Applied Mechanics Division of THE AMERICAN SOCIETY OF MECHANICAL ENGINEERS for publication in the ASME JOURNAL OF APPLIED MECHANICS.
Discussion on the paper should be addressed to the Technical Editor, Professor Lewis T. Wheeler, Department of Mechanical Engineering, University of Houston, Houston, TX 77204-4792, and will be accepted until four months after final publication of the paper itself in the ASME JOURNAL OF APPLIED MECHANICS.
Manuscript received by the ASME Applied Mechanics Division, May 5, 1998; final revision, Apr. 14, 1999. Associate Technical Editor: M.-J. Pindera.

 Copyright © 1999 by ASME

Downloaded 04 May 2010 to 171.66.16.27. Redistribution subject to ASME license or copyright; see http://www.asme.org/terms/Terms_Use.cfm

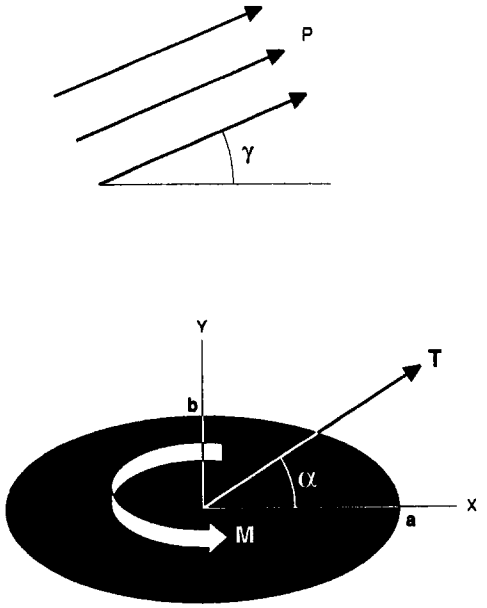


Fig. 1. A Rigid Elliptical Disk-Inclusion in a Transversely Isotropic Space Under Three Different Types of Loading

functional form of the stress distribution at the vicinity of the edge of the inclusion does not depend, as in the case of a flat elliptical crack (Kassir and Sih, 1966), on the geometry of the inclusion and the applied loads and displacements, the amplification of the local stress field being described by three parameters analogous to the three modes of stress intensity factors in the theory of cracks. The authors, as in their work (1966) and the paper by Green and Sneddon (1949), employed elliptical coordinates and elliptical harmonics for the Laplace equation to solve the problem. Alexandrov and Solov'ev (1966) investigated the problem of an absolutely flexible and inextensible elliptical disk bonded at the surface of an isotropic elastic half-space. They considered the cases where the disk is displaced in its own plane, the disk is rotated by a torque whose axis is perpendicular to the plane of the disk and the medium is under uniform stress field parallel to the plane of the disk at infinity. They reduced the problem to a set of two-dimensional integral equations, closed-form solutions of which were obtained by Galin's theorem. Extension of these results to a transversely isotropic half-space was recently given by Rahman (1999). It should, however, be emphasized that Galin's theorem is best suited for finding the solution of the problem for the interior of the disk only and it is generally not possible to find the field outside the disk using Galin's method. Hamstad and Bogy (1972) investigated the problem of a circular membrane bonded to a materially dissimilar half-space, which is loaded far from the membrane by a state of plane stress parallel to its boundary. Later, Alexandrov and Solov'ev (1993) also solved a problem similar to their earlier work (1966), using the same method (Galin's theorem) in which the elliptical disk-inclusion is embedded in the interior of an isotropic *full* space. To the best of the writer's knowledge, extension of these results to a transversely isotropic or a generally anisotropic medium is not available in the literature and this is the subject matter of the present article.

The article consists of two parts. In the first part, the problems corresponding to all three cases of loading are reduced, in a unified manner, to a set of coupled two-dimensional integral equations by applying two-dimensional Fourier transforms to the potential solutions for transversely isotropic materials. We next develop the method of solution of the integral equations, which is based on Dyson's theorem. This is an extremely powerful result in the theory of Newtonian potentials, which seems to have not yet received much attention of the elasticity community. It is shown that the well-known result by Galin widely known as Galin's theorem is only a particular case of Dyson's theorem. Furthermore, a brief description is given of Willis' generalization of Galin's theorem. Using Dyson's theorem in conjunction with Willis' generalization, the general structure of the solution of the integral equations is established. It is shown that Willis' generalization of Galin's theorem is also applicable to certain classes of coupled two-dimensional integral equations. The second part of the article is essentially devoted to the derivation of the solution of each of the problems. Complete elastic field (displacements and stresses) in the plane of the inclusion is determined. Closed-form expressions for the stress intensity factors for the inclusion are extracted from these solutions and numerical results are plotted illustrating how these factors are affected by transverse isotropy. Some of the analytical results derived have not been reported so far in the literature even in the area of isotropic elasticity. The results derived are important in the sense that they can be used, in conjunction with a failure criteria, to determine the critical load at which failure is expected to occur and the angle of crack initiation at the rim of the elliptical inclusion.

We begin by introducing the notation used in the article. We shall denote the operator of the two-dimensional Fourier transform by $\mathcal{F}_2$ and its inverse by $\mathcal{F}_2^*$ so that $\mathcal{F}_2$ is defined by

$$\mathcal{F}_2[f(\bar{x});\ \bar{\alpha}] \equiv \tilde{f}(\bar{\alpha}) = \frac{1}{2\pi}\int_{R^2} f(\bar{x}) e^{i(\bar{\alpha}\cdot\bar{x})} d\bar{x}$$

and $\mathcal{F}_2^*$ by

$$\mathcal{F}_2^*[\tilde{f}(\bar{\alpha});\ \bar{x}] \equiv f(\bar{x}) = \frac{1}{2\pi}\int_{R^2} \tilde{f}(\bar{\alpha}) e^{-i(\bar{\alpha}\cdot\bar{x})} d\bar{\alpha}$$

where $\bar{x} = (x, y) \in R^2$, $\bar{\alpha} = (\alpha_1, \alpha_2) \in R^2$ and $\bar{\alpha}\cdot\bar{x} = \alpha_1 x_1 + \alpha_2 x_2$ (Section 2.13 of Sneddon (1972).

We write the convolution theorem in the form

$$\mathcal{F}_2^*[\tilde{f}(\bar{\alpha})\tilde{g}(\bar{\alpha});\ \bar{x}] \equiv (f \circ g)(\bar{x}),$$

where $(f \circ g)(\bar{x})$ is defined by

$$(f \circ g)(\bar{x}) = \frac{1}{2\pi}\int_{R^2} f(\bar{x} - \bar{x}_0) g(\bar{x}_0) d\bar{x}_0.$$

1 Potential Solutions for Transversely Isotropic Bodies

In this section, we give a synopsis of the potential solutions for solids characterized by transverse isotropy as developed by Elliott (1948, 1949). However, the description here closely follows that given in Green and Zerna (1968). Consider a transversely isotropic body occupying the space ($|x| < \infty$, $|y| < \infty$, $|z| < \infty$). Further, assume that the axis of symmetry coincides with the z-axis. The equilibrium of the solid is described by the following equations:

$$\frac{\partial \sigma_{xx}}{\partial x} + \frac{\partial \sigma_{xy}}{\partial y} + \frac{\partial \sigma_{xz}}{\partial z} = 0,$$

$$\frac{\partial \sigma_{xy}}{\partial x} + \frac{\partial \sigma_{yy}}{\partial y} + \frac{\partial \sigma_{yz}}{\partial z} = 0,$$

$$\frac{\partial \sigma_{xz}}{\partial x} + \frac{\partial \sigma_{yz}}{\partial y} + \frac{\partial \sigma_{zz}}{\partial z} = 0. \tag{1}$$

For a transversely isotropic solid, the stress-strain relationships are given by the equations (Green and Zerna, (1968))

$$\sigma_{xx} = c_{11}\frac{\partial u}{\partial x} + c_{12}\frac{\partial v}{\partial y} + c_{13}\frac{\partial w}{\partial z},$$

$$\sigma_{yy} = c_{12}\frac{\partial u}{\partial x} + c_{11}\frac{\partial v}{\partial y} + c_{13}\frac{\partial w}{\partial z},$$

Downloaded 04 May 2010 to 171.66.16.27. Redistribution subject to ASME license or copyright; see http://www.asme.org/terms/Terms_Use.cfm

$$\sigma_{zz} = c_{13}\left(\frac{\partial u}{\partial x} + \frac{\partial v}{\partial y}\right) + c_{33}\frac{\partial w}{\partial z}, \quad \sigma_{yz} = c_{44}\left(\frac{\partial v}{\partial z} + \frac{\partial w}{\partial y}\right),$$

$$\sigma_{zx} = c_{44}\left(\frac{\partial u}{\partial z} + \frac{\partial w}{\partial x}\right), \quad \sigma_{xy} = \frac{1}{2}(c_{11} - c_{12})\left(\frac{\partial u}{\partial z} + \frac{\partial w}{\partial x}\right). \quad (2)$$

It is convenient to express the displacements and the stresses in terms of some potential functions so that the equilibrium and compatibility equations can be reduced to the well-investigated Laplace or biharmonic equations. For a transversely isotropic medium, Lekhnitskii (1963) showed that the equations of equilibrium and compatibility can be reduced to a biharmonic-type equation in terms of a Love-type stress function. However, because of the fact that the latter is a fourth-order partial differential equation, Lekhnitskii's approach leads to cumbersome manipulations. In what follows, we shall use Elliott's approach (1948, 1949) (see also Green and Zerna (1968)) who showed that the equations of equilibrium and the compatibility equations for a transversely isotropic solid can be reduced to some Laplace-type equations involving three potential functions, χ_α, ($\alpha = 1, 2, 3$):

$$\left(\nabla_1^2 + s_\alpha \frac{\partial^2}{\partial z^2}\right)\chi_\alpha = 0, \quad (3)$$

where

$$\nabla_1^2 = \frac{\partial^2}{\partial x^2} + \frac{\partial^2}{\partial y^2}, \quad s_3 = \frac{2c_{44}}{c_{11} - c_{12}}, \quad (4)$$

and s_1, s_2 are two distinct roots of the equation

$$c_{11}c_{44}s^2 + \{c_{13}(2c_{44} + c_{13}) - c_{11}c_{33}\}s + c_{33}c_{44} = 0. \quad (5)$$

In terms of χ_α, the components of the displacement vector and stress tensor are given by

$$u = \frac{\partial}{\partial x}(\chi_1 + \chi_2) + \frac{\partial \chi_3}{\partial y}, \quad v = \frac{\partial}{\partial y}(\chi_1 + \chi_2) - \frac{\partial \chi_3}{\partial x},$$

$$w = k_1\frac{\partial \chi_1}{\partial z} + k_2\frac{\partial \chi_2}{\partial z}, \quad \sigma_{zz} = \sum_{\alpha=1}^{2}(k_\alpha c_{33} - s_\alpha c_{13})\frac{\partial^2 \chi_\alpha}{\partial z^2},$$

$$\sigma_{yz} = c_{44}\left\{-\frac{\partial^2 \chi_3}{\partial x \partial z} + \sum_{\alpha=1}^{2}(1 + k_\alpha)\frac{\partial^2 \chi_\alpha}{\partial y \partial z}\right\},$$

$$\sigma_{zx} = c_{44}\left\{\frac{\partial^2 \chi_3}{\partial y \partial z} + \sum_{\alpha=1}^{2}(1 + k_\alpha)\frac{\partial^2 \chi_\alpha}{\partial x \partial z}\right\}, \quad (6)$$

where

$$k_\alpha = \frac{c_{11}s_\alpha - c_{44}}{c_{13} + c_{44}} = \frac{(c_{13} + c_{44})s_\alpha}{c_{33} - c_{44}s_\alpha}, \quad \alpha = 1, 2. \quad (7)$$

The remaining stress components are not listed above, because we shall not need them in the subsequent analysis. Using the argument that for real materials the strain energy density function should be always positive definite, Lekhnitskii (1963) showed that the roots of Eq. (5) may be either real (with the same sign) or complex conjugates, but they can never be purely imaginary. Furthermore, in order to insure that the displacements and the stresses be single-valued, it is necessary to adopt a convention, in the event s_1, s_2 are negative or complex conjugates, on which branch of the multivalued functions $\sqrt{s_1}$, $\sqrt{s_2}$ should be taken. In this article, we choose to take those branches which have positive real parts.

2 Formulation of the Problem

Consider an unbounded transversely isotropic medium in the interior of which there is an elliptical inclusion in the form of a thin rigid disk which is assumed to be perfectly rigid. Complete bonding is assumed to exist between the medium and the inclusion. We shall consider three different cases of loading of the inclusion (Fig. 1).

Case A: The inclusion is sheared by a force whose line of action makes an angle α with the semi-major axis of the ellipse.

Case B: The inclusion is rotated at an angle by a moment M whose axis is perpendicular to plane of the inclusion.

Case C: At infinity the solid is under uniform tensile stress p acting in a plane parallel to the plane of the inclusion. The direction of this stress makes an angle γ with the major axis of the ellipse, i.e., the x-axis.

Let, in the process of deformation, the inclusion be rotated in its plane at an angle φ and its center be displaced at a distance δ along a line whose direction makes an angle β with the major axis of the ellipse.

Then, the problem we address consists of determining the stress distribution at the interface between the inclusion and the medium as well as the relationships among the quantities T, M, p, α, γ and φ, δ, β.

We introduce the Cartesian coordinate system x, y, z such that the plane of inclusion is the plane $z = 0$ and the elliptical bonded contact region Ω between the inclusion and the medium is given by the relations: $z = 0$, $\forall(x, y) \in x^2/a^2 + y^2/b^2 - 1 \leq 0$ ($a > b$). We denote the compliment to the region Ω by $\tilde{\Omega}$ so that $\Omega \cup \tilde{\Omega}$ represents the entire $z = 0$ plane. Then, within the scope of linear elasticity, we can split the problem into three smaller ones corresponding to the above three cases of loading. The boundary conditions for these problems are as follows:

Problem 1:

$$w(x, y, 0) = 0, \quad (x, y) \in \Omega \cup \tilde{\Omega},$$

$$\sigma_{xz}(x, y, 0) = \sigma_{yz}(x, y, 0) = 0, \quad (x, y) \in \tilde{\Omega},$$

$$u(x, y, 0) = \delta \cos \beta, \quad v(x, y, 0) = \delta \sin \beta,$$

$$(x, y) \in \Omega. \quad (8)$$

The solution must satisfy the usual conditions at infinity, which state that the elastic field must decay as $R = \sqrt{x^2 + y^2 + z^2} \to \infty$. More specifically, the displacement field is $O(R^{-1})$ as $R \to \infty$ $\sqrt{x^2 + y^2 + z^2} \to \infty$.

Problem 2:

$$w(x, y, 0) = 0, \quad (x, y) \in \Omega \cup \tilde{\Omega},$$

$$\sigma_{xz}(x, y, 0) = \sigma_{yz}(x, y, 0) = 0, \quad (x, y) \in \tilde{\Omega},$$

$$u(x, y, 0) = -\varphi y, \quad v(x, y, 0) = \varphi x, \quad (x, y) \in \Omega. \quad (9)$$

Moreover, the solution of the problem must satisfy the conditions at infinity.

Problem 3:

$$w(x, y, 0) = 0, \quad (x, y) \in \Omega \cup \tilde{\Omega},$$

$$\sigma_{xz}(x, y, 0) = \sigma_{yz}(x, y, 0) = 0, \quad (x, y) \in \tilde{\Omega},$$

$$u(x, y, 0) = -\varphi y, \quad v(x, y, 0) = \varphi x, \quad (x, y) \in \Omega. \quad (10)$$

At infinity, we have

$$\sigma_{xx} = p \cos^2 \gamma, \quad \sigma_{yy} = p \sin^2 \gamma, \quad \sigma_{xy} = \frac{p}{2}\sin 2\gamma. \quad (11)$$

Downloaded 04 May 2010 to 171.66.16.27. Redistribution subject to ASME license or copyright; see http://www.asme.org/terms/Terms_Use.cfm

All other stress components vanish at infinity.

Within the scope of linear elasticity, the solution of Problem 3 can be obtained by superposing the solution of an unperturbed problem and a corrective solution. The unperturbed problem consists of finding the elastic field in the space without the inclusion under the conditions (11), while the corrective solution consists of determining the elastic field in the medium in the presence of the inclusion under the following boundary conditions:

$$w(x, y, 0) = 0, \quad (x, y) \in \Omega \cup \tilde{\Omega},$$

$$\sigma_{xz}(x, y, 0) = \sigma_{yz}(x, y, 0) = 0, \quad (x, y) \in \tilde{\Omega},$$

$$u(x, y, 0) = -\varphi y - u^0(x, y, 0),$$

$$v(x, y, 0) = \varphi x - v^0(x, y, 0), \quad (x, y) \in \Omega, \qquad (12)$$

where $u^0(x, y, z)$ and $v^0(x, y, z)$ are the solution of the unperturbed problem (see Rahman (1997)), namely,

$$u^0(x, y, z) = c_{44}^{-1} p(\Gamma_1 \cos^2 \gamma - \Gamma_2 \sin^2 \gamma)x + c_{44}^{-1} p\Gamma_3 y \sin 2\gamma,$$

$$v^0(x, y, z) = c_{44}^{-1} p\Gamma_3 x \sin 2\gamma + c_{44}^{-1} p(\Gamma_1 \cos^2 \gamma - \Gamma_2 \sin^2 \gamma)y, \qquad (13)$$

where

$$\Gamma_1 = \frac{c_{44}(c_{11}c_{33} - c_{13}^2)}{(c_{11} - c_{12})(c_{11}c_{33} + c_{12}c_{33} - 2c_{13}^2)},$$

$$\Gamma_2 = \frac{c_{44}(c_{12}c_{33} - c_{13}^2)}{(c_{11} - c_{12})(c_{11}c_{33} + c_{12}c_{33} - 2c_{13}^2)},$$

$$\Gamma_3 = \frac{\Gamma_1 + \Gamma_2}{2} = \frac{c_{44}}{2(c_{11} - c_{12})}. \qquad (14)$$

The solution of the perturbation problem defined by the Eqs. (12), (13), and (14) must satisfy the conditions at infinity.

3 Derivation of the Governing Integral Equations

Obviously, we can restrict our attention on one half-space, say $z \geq 0$, only.

A suitable solution of Eqs. (3) satisfying the conditions at infinity is given by

$$\chi_j(x, y, z) = \mathcal{F}_2^{-1}[A_j(\bar{\alpha})e^{-i\bar{\alpha}\cdot\bar{x} - m_j z}; \quad \bar{x}], \qquad (15)$$

where $m_j = \sqrt{(\alpha_1^2 + \alpha_2^2)/s_j}$, $i = \sqrt{-1}$ is the imaginary unit and A_j $(j = 1, 2, 3)$ are unknown functions to be determined using the boundary conditions of the problems.

With (15), we obtain the following expressions:

$$\tilde{u}(\alpha_1, \alpha_2, 0) = -i(\alpha_1 A_1 + \alpha_1 A_2 + \alpha_2 A_3),$$

$$\tilde{v}(\alpha_1, \alpha_2, 0) = -i(\alpha_2 A_1 + \alpha_2 A_2 - \alpha_1 A_3),$$

$$\tilde{w}(\alpha_1, \alpha_2, 0) = -k_1 m_1 A_1 - k_2 m_2 A_2,$$

$$\tilde{\sigma}_{xz}(\alpha_1, \alpha_2, 0) = ic_{44}[(1 + k_1)\alpha_1 m_1 A_1 + \alpha_2 m_3 A_3 + (1 + k_2)\alpha_1 m_2 A_2],$$

$$\tilde{\sigma}_{yz}(\alpha_1, \alpha_2, 0) = ic_{44}[(1 + k_1)\alpha_2 m_1 A_1 + (1 + k_2)\alpha_2 m_2 A_2 - \alpha_1 m_3 A_3],$$

$$\tilde{\sigma}_{zz}(\alpha_1, \alpha_2, 0) = (k_1 c_{33} - s_1 c_{13})m_1^2 A_1 + (k_2 c_{33} - s_2 c_{13})m_2^2 A_2. \qquad (16)$$

Now, since $w(x, y, 0) = 0$ on the entire plane $z = 0$ (for all three problems), from the third equation in (16), we get

$$A_2 = \frac{-k_1 m_1}{k_2 m_2} A_1. \qquad (17)$$

Putting (17) into the fourth and fifth equations in (16) and solving the resulting equations with respect to A_1 and A_3, we obtain

$$A_1 = \frac{\tilde{\sigma}_{xz}(\alpha_1, \alpha_2, 0)\alpha_1 + \tilde{\sigma}_{yz}(\alpha_1, \alpha_2, 0)\alpha_2}{m_1(k_2 - k_1)(\alpha_1^2 + \alpha_2^2)},$$

$$A_3 = \frac{\tilde{\sigma}_{xz}(\alpha_1, \alpha_2, 0)\alpha_2 - \tilde{\sigma}_{yz}(\alpha_1, \alpha_2, 0)\alpha_1}{k_2 m_3(\alpha_1^2 + \alpha_2^2)}. \qquad (18)$$

Putting (17) and (18) into the first, second, and sixth equations in (16), after simple manipulations, we obtain

$$\tilde{u}(\alpha_1, \alpha_2, 0) = \frac{-k_2\Lambda_2}{c_{44}} \tilde{\sigma}_{xz}(\alpha_1, \alpha_2, 0)\tilde{\Omega}_0(\alpha_1, \alpha_2) + \frac{k_2(\Lambda_1 + \Lambda_2)}{c_{44}} \tilde{\sigma}_{xz}(\alpha_1, \alpha_2, 0)\tilde{\Omega}_1(\alpha_1, \alpha_2) + \frac{k_2(\Lambda_1 + \Lambda_2)}{c_{44}} \tilde{\sigma}_{yz}(\alpha_1, \alpha_2, 0)\tilde{\Omega}_3(\alpha_1, \alpha_2),$$

$$\tilde{v}(\alpha_1, \alpha_2, 0) = \frac{-k_2\Lambda_2}{c_{44}} \tilde{\sigma}_{yz}(\alpha_1, \alpha_2, 0)\tilde{\Omega}_0(\alpha_1, \alpha_2) + \frac{k_2(\Lambda_1 + \Lambda_2)}{c_{44}} \tilde{\sigma}_{xz}(\alpha_1, \alpha_2, 0)\tilde{\Omega}_2(\alpha_1, \alpha_2) + \frac{k_2(\Lambda_1 + \Lambda_2)}{c_{44}} \tilde{\sigma}_{xz}(\alpha_1, \alpha_2, 0)\tilde{\Omega}_3(\alpha_1, \alpha_2),$$

$$\sigma_{zz}(\alpha_1, \alpha_2, 0) = -i \frac{\omega}{c_{44}} \tilde{\Omega}_0(\alpha_1, \alpha_2, 0)[\alpha_1 \tilde{\sigma}_{xz}(\alpha_1, \alpha_2, 0) + \alpha_2 \tilde{\sigma}_{yz}(\alpha_1, \alpha_2, 0)]. \qquad (19)$$

where the following notations are introduced:

$$\tilde{\Omega}_0 = \frac{1}{\sqrt{\alpha_1^2 + \alpha_2^2}}, \quad \tilde{\Omega}_1 = \frac{\alpha_1^2}{(\alpha_1^2 + \alpha_2^2)\sqrt{\alpha_1^2 + \alpha_2^2}}$$

$$\tilde{\Omega}_2 = \frac{\alpha_2^2}{(\alpha_1^2 + \alpha_2^2)\sqrt{\alpha_1^2 + \alpha_2^2}},$$

$$\tilde{\Omega}_3 = \frac{\alpha_1\alpha_2}{(\alpha_1^2 + \alpha_2^2)\sqrt{\alpha_1^2 + \alpha_2^2}}, \quad \Lambda_1 = \frac{k_1\sqrt{s_2} - k_2\sqrt{s_1}}{k_2(k_2 - k_1)};$$

$$\Lambda_2 = \frac{\sqrt{s_3}}{k_2},$$

$$\omega = \frac{k_1 k_2 c_{33}}{(k_2 - k_1)c_{44}}\left(\frac{1}{\sqrt{s_1}} - \frac{1}{\sqrt{s_2}}\right) + \frac{(k_1\sqrt{s_2} - k_2\sqrt{s_1})c_{13}}{k_2(k_2 - k_1)c_{44}}. \qquad (20)$$

Using the convolution theorem for Fourier transforms, we obtain

$$u(x, y, 0) = \frac{-k_2\Lambda_2}{2\pi c_{44}} \int_{-\infty}^{\infty}\int_{-\infty}^{\infty} \sigma_{xz}(x_0, y_0, 0)\Omega_0(x - x_0, y - y_0)dx_0dy_0 + \frac{k_2(\Lambda_1 + \Lambda_2)}{2\pi c_{44}} \int_{-\infty}^{\infty}\int_{-\infty}^{\infty} \sigma_{xz}(x_0, y_0, 0)\Omega_1(x - x_0, y - y_0)dx_0dy_0 - \frac{k_2(\Lambda_1 + \Lambda_2)}{2\pi c_{44}} \int_{-\infty}^{\infty}\int_{-\infty}^{\infty} \sigma_{yz}$$

Downloaded 04 May 2010 to 171.66.16.27. Redistribution subject to ASME license or copyright; see http://www.asme.org/terms/Terms_Use.cfm

$$\times (x_0, y_0, 0)\Omega_3(x - x_0, y - y_0)dx_0dy_0,$$

$$v(x, y, 0) = \frac{-k_2\Lambda_2}{2\pi c_{44}} \int_{-\infty}^{\infty}\int_{-\infty}^{\infty} \sigma_{yz}(x_0, y_0, 0)\Omega_0(x - x_0, y - y_0)dx_0dy_0 + \frac{k_2(\Lambda_1 + \Lambda_2)}{2\pi c_{44}} \int_{-\infty}^{\infty}\int_{-\infty}^{\infty} \sigma_{yz}(x_0, y_0, 0)\Omega_1 \times (x - x_0, y - y_0)dx_0dy_0 - \frac{k_2(\Lambda_1 + \Lambda_2)}{2\pi c_{44}} \int_{-\infty}^{\infty}\int_{-\infty}^{\infty} \sigma_{xz} \times (x_0, y_0, 0)\Omega_3(x - x_0, y - y_0)dx_0dy_0,$$

$$\sigma_{zz}(x, y, 0) = \frac{\omega}{2\pi}\frac{\partial}{\partial x} \int_{-\infty}^{\infty}\int_{-\infty}^{\infty} \sigma_{xz}(x_0, y_0, 0)\Omega_0(x - x_0, y - y_0)dx_0dy_0 + \frac{\omega}{2\pi}\frac{\partial}{\partial y} \int_{-\infty}^{\infty}\int_{-\infty}^{\infty} \sigma_{yz}(x_0, y_0, 0)\Omega_0 \times (x - x_0, y - y_0)dx_0dy_0, \quad (21)$$

where

$$\Omega_0(x, y) = \mathcal{F}_2^*[\tilde{\Omega}_0(\bar{\alpha}); \quad \bar{x}] \quad \Omega_1(x, y) = \mathcal{F}_2^*[\tilde{\Omega}_1(\bar{\alpha}); \quad \bar{x}],$$

$$\Omega_2(x, y) = \mathcal{F}_2^*[\tilde{\Omega}_2(\bar{\alpha}); \quad \bar{x}], \quad \Omega_3(x, y) = \mathcal{F}_2^*[\tilde{\Omega}_3(\bar{\alpha}); \quad \bar{x}].$$

It can be shown using tables of Fourier inverse transforms (Erdelyi et al., 1954) that

$$\Omega_0(x, y) = \frac{1}{R_0}, \quad \Omega_1(x, y) = \frac{y^2}{R_0^3},$$

$$\Omega_2(x, y) = \frac{x^2}{R_0^3}, \quad \Omega_3(x, y) = \frac{-xy}{R_0^3},$$

where $R_0 = \sqrt{x^2 + y^2}$.

Therefore, Eqs. (20) take the form

$$u(x, y, 0) = \frac{-k_2\Lambda_2}{2\pi c_{44}} \int_{-\infty}^{\infty}\int_{-\infty}^{\infty} \frac{\sigma_{xz}(x_0, y_0, 0)}{R} dx_0dy_0 + \frac{k_2(\Lambda_1 + \Lambda_2)}{2\pi c_{44}} \int_{-\infty}^{\infty}\int_{-\infty}^{\infty} \frac{(y - y_0)^2\sigma_{xz}(x_0, y_0, 0)}{R^3} dx_0dy_0 - \frac{k_2(\Lambda_1 + \Lambda_2)}{2\pi c_{44}} \int_{-\infty}^{\infty}\int_{-\infty}^{\infty} \frac{\sigma_{yz}(x, y, 0)(x - x_0)(y - y_0)}{R^3} \times dx_0dy_0,$$

$$v(x, y, 0) = \frac{-k_2\Lambda_2}{2\pi c_{44}} \int_{-\infty}^{\infty}\int_{-\infty}^{\infty} \frac{\sigma_{yz}(x_0, y_0, 0)}{R} dx_0dy_0 + \frac{k_2(\Lambda_1 + \Lambda_2)}{2\pi c_{44}} \int_{-\infty}^{\infty}\int_{-\infty}^{\infty} \frac{(x - x_0)^2\sigma_{yz}(x_0, y_0, 0)}{R^3} dx_0dy_0 - \frac{k_2(\Lambda_1 + \Lambda_2)}{2\pi c_{44}} \int_{-\infty}^{\infty}\int_{-\infty}^{\infty} \frac{\sigma_{xz}(x, y, 0)(x - x_0)(y - y_0)}{R^3} \times dx_0dy_0,$$

$$\sigma_{zz}(x, y, 0) = \frac{\omega}{2\pi}\frac{\partial}{\partial x} \int_{-\infty}^{\infty}\int_{-\infty}^{\infty} \frac{\sigma_{xz}(x_0, y_0, 0)}{R} dx_0dy_0 + \frac{\omega}{2\pi}\frac{\partial}{\partial y} \int_{-\infty}^{\infty}\int_{-\infty}^{\infty} \frac{\sigma_{yz}(x_0, y_0, 0)}{R} dx_0dy_0, \quad (22)$$

where

$$R = \sqrt{(x - x_0)^2 + (y - y_0)^2}.$$

Equations (22) can also be derived by using the Cerruti-type solution for a transversely isotropic half-space and the principle of superposition.

Now, using Eqs. (22) and the last two boundary conditions in (9), (10), and (11), we obtain the following integral equations to determine the unknown interfacial stresses:

$$\int\int_{\Omega} \left[\frac{1}{R} - \Gamma\frac{(y - y_0)^2}{R^3}\right]\sigma_{xz}(x_0, y_0)dx_0dy_0 + \Gamma\int\int_{\Omega} \frac{(x - x_0)(y - y_0)}{R^3}\sigma_{yz}(x_0, y_0) = \pi(a_0 + a_1x + a_2y),$$

$$\Gamma\int\int_{\Omega} \frac{(x - x_0)(y - y_0)}{R^3}\sigma_{xz}(x_0, y_0)dx_0dy_0 + \int\int_{\Omega} \left[\frac{1}{R} - \Gamma\frac{(x - x_0)^2}{R^3}\right]\sigma_{yz}(x_0, y_0)dx_0dy_0 = \pi(b_0 + b_1x + b_2y). \quad (23)$$

where

$$\Gamma = \frac{\Lambda_1 + \Lambda_2}{\Lambda_2}, \quad (24)$$

and the coefficients a_i, b_i $(i = 0, 1, 2)$ are given by the following equations:

Problem 1:

$$a_0 = \frac{-2c_{44}\delta\cos\beta}{k_2\Lambda_2}; \quad b_0 = \frac{-2c_{44}\delta\sin\beta}{k_2\Lambda_2};$$

$$a_1 = b_1 = a_2 = b_2 = 0. \quad (25)$$

Problem 2:

$$a_2 = \frac{2c_{44}\varphi}{k_2\Lambda_2}; \quad b_1 = \frac{-2c_{44}\varphi}{k_2\Lambda_2}; \quad a_0 = b_0 = a_1 = b_2 = 0. \quad (26)$$

Problem 3:

$$a_1 = \frac{-2p(\Gamma_1\cos^2\gamma - \Gamma_2\sin^2\gamma)}{k_2\Lambda_2},$$

$$a_2 = \frac{2c_{44}\varphi}{k_2\Lambda_2} - \frac{2p\Gamma_3\sin 2\gamma}{k_2\Lambda_2},$$

$$b_1 = \frac{-2c_{44}\varphi}{k_2\Lambda_2} - \frac{2p\Gamma_3\sin 2\gamma}{k_2\Lambda_2},$$

$$b_2 = \frac{-2p(\Gamma_1\sin^2\gamma - \Gamma_2\cos^2\gamma)}{k_2\Lambda_2},$$

$$a_0 = b_0 = 0. \quad (27)$$

For the case of an isotropic material, we have (Lekhnitskii, 1963)

Downloaded 04 May 2010 to 171.66.16.27. Redistribution subject to ASME license or copyright; see http://www.asme.org/terms/Terms_Use.cfm

$$c_{11} = c_{33} = \frac{2(1-\nu)\mu}{1-2\nu}, \quad c_{12} = c_{13} = \frac{2\nu\mu}{1-2\nu},$$

$$c_{44} = \mu, \tag{28}$$

where μ and ν are the shear modulus and Poisson's ratio. With (28), from Eqs. (5) and (14), we get

$$s_1 = s_2 = s_3 = 1, \quad \Gamma_1 = \frac{1}{2(1+\nu)},$$

$$\Gamma_2 = \Gamma_4 = \frac{\nu}{2(1+\nu)}, \quad \Gamma_3 = \frac{1}{4}. \tag{29}$$

If we now put the above values of s_1 and s_2 into equations for Λ_1 and ω (see Eqs. (20)), we see that they reduce to indeterminacies. In order to overcome this difficulty, we assume that $s_1 = 1 + i\epsilon$, $s_2 = 1 - i\epsilon$ and ϵ is a small positive quantity. Then, with this assumption, it can be shown that

$$k_{1,2} = 1 \pm 2i\epsilon(1-\nu), \quad \Lambda_1 = \frac{-(3-4\nu)}{4(1-\nu)}, \quad \Lambda_2 = 1,$$

$$\Gamma = \frac{1}{4(1-\nu)}, \quad \omega = \frac{1-2\nu}{2(1-\nu)}. \tag{30}$$

Thus, the problem corresponding to all three cases of loading is reduced to the solution of the system of coupled two-dimensional integral Eqs. (23). Solution of (23) will allow us to find $\sigma_{xz}(x, y, 0)$ and $\sigma_{yz}(x, y, 0)$ which, in conjunction with the expressions (21), will allow us to determine the elastic field inside and outside the inclusion.

4 Development of the Method of Solution

This section is devoted to the development of the method and structure of solution of the integral Eqs. (23). In particular, we will show that Dyson's theorem, in conjunction with Galin's and Willis' theorems, can be adapted to effect this in an elegant fashion.

Generalizing Ferrers' results (1877), Dyson (1891) showed that the matter distributed over an elliptical disk such that the surface density

$$\sigma(x, y) = \frac{\Gamma(\eta)\Gamma(\frac{1}{2})}{\pi ab\Gamma(\eta+\frac{1}{2})}\left(1 - \frac{x^2}{a^2} - \frac{y^2}{b^2}\right)^{\eta-(1/2)} f\left(\frac{x}{a}, \frac{y}{b}\right),$$

$$\eta \geq 0, \tag{31}$$

produces outside the disk a harmonic potential

$$V(x, y, z) = \int_\lambda^\infty \frac{d\psi}{\sqrt{\Delta}} \sum_{m=0}^\infty \frac{\Gamma(\eta) M^{\eta+m}\psi^m}{2^{2m}m!\Gamma(\eta+m+1)} D^m f\left(\frac{ax}{a^2+\psi}, \frac{by}{b^2+\psi}\right), \tag{32}$$

where $\Gamma(\ldots)$ is the Gamma function and

$$D = \frac{a^2+\psi}{a^2}\frac{d^2}{dx^2} + \frac{b^2+\psi}{b^2}\frac{d^2}{dy^2},$$

$$M = 1 - \frac{x^2}{a^2+\psi} - \frac{y^2}{b^2+\psi} - \frac{z^2}{\psi},$$

$$\Delta = (a^2+\psi)(b^2+\psi)\psi, \tag{33}$$

and λ is the largest positive root of the equation

$$1 - \frac{x^2}{a^2+\lambda} - \frac{y^2}{b^2+\lambda} = 0. \tag{34}$$

The potential in the interior of the disk can be found by letting $\lambda \to 0$ in Eq. (32).

It is helpful to note the following properties of the function $V(x, y, z)$:

$$\nabla^2 V = 0, \tag{35}$$

where ∇^2 is the Laplacian.

The function V and its derivatives $\partial^2 V/\partial x^2$, $\partial^2 V/\partial y^2$, $\partial^2 V/\partial x \partial y$ and $\partial^2 V/\partial z^2$ are all everywhere continuous. However, the normal derivative $\partial V/\partial z$ is discontinuous on the disk:

$$\left.\frac{\partial V}{\partial z}\right|_{z=\pm 0} = \pm 2\pi\sigma(x, y), \tag{36}$$

according as z vanishes through its negative or positive values.

In view of (35) and (36), the results (31) through (34) for $z = 0$ can be restated as

$$\int\int_\Omega \frac{\sigma(x_0, y_0)}{R} dx_0 dy_0 = V(x, y, 0). \tag{37}$$

In what follows, use will be made of this particular form of Dyson's results.

Consider the particular case where the function $\sigma(x, y)$ is given by

$$\sigma(x, y) = \left(1 - \frac{x^2}{a^2} - \frac{y^2}{b^2}\right)^{l-(1/2)} x^i y^j, \quad (l, i, j = 0, 1, 2, \ldots), \tag{38}$$

then using formulae (37), (31), and (32) we obtain

$$^{(l)}W_{ij}^{(\lambda)} \equiv \int\int_\Omega \frac{\left(1 - \frac{x_0^2}{a^2} - \frac{y_0^2}{b^2}\right)^{l-(1/2)} x_0^i y_0^j}{R} dx_0 dy_0$$

$$= \frac{\pi a^{i+1} b^{j+1}\Gamma\left(l+\frac{1}{2}\right)}{\sqrt{\pi}} \int_\lambda^\infty \frac{d\psi}{\sqrt{\Delta}} \sum_{m=0}^\infty \frac{M^{l+m}\psi^m}{2^{2m}m!(l+m)!}$$

$$\times D^m\left(\frac{ax}{a^2+\psi}\right)^i \left(\frac{by}{b^2+\psi}\right)^j, \quad l, i, j = 0, 1, 2, \ldots. \tag{39}$$

Note that the infinite sum in the integrand (39) conveniently terminates. Furthermore, it can be easily seen that in this case on the disk where $\lambda = 0$, $V(x, y, 0)$ reduces to a polynomial in x, y of order $2l + n$. This important result, now known as *Galin's theorem,* was first discovered by Galin (1947) via a different approach based on using ellipsoidal coordinates. It is in particular this result of Galin's that has got widespread applications in mixed boundary value problems of the elasticity theory. General explicit expressions for the internal and external potentials of the elliptical disk for this case have been recently given by Rahman (1999) in terms of the following integral:

$$I_{ij}^{(\lambda)} = \int_\lambda^\infty \frac{d\psi}{\sqrt{(a^2+\psi)^{2i+1}(b^2+\psi)^{2j+1}\psi}}, \quad (i, j = 0, 1, 2, \ldots). \tag{40}$$

Furthermore, integral (40) for all values of $i, j = 0, 1, 2, \ldots$ can be expressed in terms of the elliptic integrals of the first and second kinds (see the Appendix). However, in this paper, we will need expressions for $^{(l)}W_{ij}^{(\lambda)}$ for the cases where $l = 0$ and $i, j = 0, 1, 2$ only.

In these cases, from Eq. (39) we deduce the following expressions:

Downloaded 04 May 2010 to 171.66.16.27. Redistribution subject to ASME license or copyright; see http://www.asme.org/terms/Terms_Use.cfm

$$
{}^0W_{ij}^{(\lambda)} = \pi a^{2i+1} b^{2j+1} x^i y^j I_{ij}^{(\lambda)}, \quad (i, j = 0, 1),
$$

$$
{}^0W_{20}^{(\lambda)} = \frac{\pi a^3 b x^2}{2} (3a^2 I_{20}^{(\lambda)} - I_{10}^{(\lambda)}) + \frac{\pi a^3 b y^2}{2} (b^2 I_{11}^{(\lambda)} - I_{10}^{(\lambda)}) + \frac{\pi a^3 b}{2} (I_{00}^{(\lambda)} - a^2 I_{01}^{(\lambda)}),
$$

$$
{}^0W_{02}^{(\lambda)} = \frac{\pi a b^3 x^2}{2} (a^2 I_{11}^{(\lambda)} - I_{01}^{(\lambda)}) + \frac{\pi a b^3 y^2}{2} (3b^2 I_{02}^{(\lambda)} - I_{01}^{(\lambda)}) + \frac{\pi a b^3}{2} (I_{00}^{(\lambda)} - b^2 I_{01}^{(\lambda)}). \quad (41)
$$

An interesting generalization of Galin's theorem was presented by Willis (1966, 1967, 1968) who showed that if $P_N(x, y)$ is a polynomial in x, y of order N and $f(x, y)$ is an even and homogeneous function of x, y of degree -1, then the following result holds:

$$
\int\int_\Omega P_N(x_0, y_0) \left(1 - \frac{x_0^2}{a^2} - \frac{y_0^2}{b^2}\right)^{-1/2} f(x - x_0, y - y_0) dx_0 dy_0 = Q_N(x, y), \quad (42)
$$

where $Q_N(x, y)$ is a polynomial in x, y of order N. For the special case where $f(x, y) = 1/R_0$, with $R_0 = \sqrt{x^2 + y^2}$, Galin's result is obtained. Other particular cases of special interest are $f(x, y) = x^2/R_0^3$, y^2/R_0^3, xy/R_0^3. It follows that Willis' generalization will also hold for any linear combination of the equations of the type (42); speaking in other words, if the functions $f_m^{(j)}(x, y)(j = 1, \ldots p)$ are homogeneous of degree -1 and $\psi_n^{(j)}(x, y)$ are polynomials in x, y of order n ($a_m^{(j)}$ ($j = 1, \ldots p$) are some arbitrary constants),

$$
\begin{aligned}
&\sum_{m=1}^{p} \int\int_\Omega a_m^{(1)} \phi_m(x_0, y_0) f_m^{(1)}(x - x_0, y - y_0) dx_0 dy_0 = \psi_n^{(1)}(x, y),\\
&\sum_{m=1}^{p} \int\int_\Omega a_m^{(2)} \phi_m(x_0, y_0) f_m^{(2)}(x - x_0, y - y_0) dx_0 dy_0 = \psi_n^{(2)}(x, y),\\
&\vdots\\
&\sum_{m=1}^{p} \int\int_\Omega a_m^{(p)} \phi_m(x, y) f_m^{(p)}(x - x_0, y - y_0) dx_0 dy_0 = \psi_n^{(p)}(x, y),
\end{aligned} \quad (43)
$$

then treating $\phi_m(x, y)$ as the unknown functions, the structure of solution of the system (43) of coupled integral equations must be of the form:

$$
\phi_m(x, y) = l^{-1}(x, y) g_n(x, y), \qquad l(x, y) = \sqrt{1 - \frac{x^2}{a^2} - \frac{y^2}{b^2}}, \quad (44)
$$

where $g_n(x, y)$ is a polynomial in x, y of order n.

As a particular case of the system (43), consider the equations

$$
\int\int_\Omega \left[\frac{1}{R} - c \frac{(y - y_0)^2}{R^3}\right] \phi_1(x_0, y_0) dx_0 dy_0 + c \int\int_\Omega \frac{(x - x_0)(y - y_0)}{R^3} \phi_2(x_0, y_0) = \psi_1^{(1)}(x, y),
$$

$$
c \int\int_\Omega \frac{(x - x_0)(y - y_0)}{R^3} \phi_1(x_0, y_0) dx_0 dy_0 + \int\int_\Omega \left[\frac{1}{R} - c \frac{(x - x_0)^2}{R^3}\right] \phi_2(x_0, y_0) dx_0 dy_0 = \psi_1^{(2)}(x, y), \quad (45)
$$

where c is a constant. Note that Eqs. (45) with $c = \Gamma$ (see Eq. (24)) are exactly the same as the governing integral Eqs. (23). Hence, comparing integral Eqs. (23) with (45), we conclude that the solution of Eqs. (23) must be of the form

$$
\sigma_{xz}(x, y, 0) = l^{-1}(x, y)(c_0 + c_1 x + c_2 y), \qquad \sigma_{yz}(x, y, 0) = l^{-1}(x, y)(d_0 + d_1 x + d_2 y) \quad (46)
$$

where the coefficients c_i, d_i ($i = 0, 1, 2$) are to be determined.

We have thus established the structure of solution of the system of coupled integral Eqs. (23) by using Willis' generalization of Galin's theorem. The questions as to how to determine the coefficients c_i, d_i ($i = 0, 1, 2$) and thereby deduce the solution of each of the problems will be discussed in detail in Part II of the paper. Furthermore, we will see that the power of Dyson's theorem allows one to determine the elastic field in both inside and outside the inclusion in an easy and elementary fashion.

4 Closure

In the present paper, the problem of contact of a rigid elliptical inclusion in the form of a thin disk, bonded in the interior of a transversely isotropic space is considered. Three different types of loading have been considered, namely, (a) the inclusion is loaded in its plane by a shearing force, whose line of action passes through the center of the disk; (b) the inclusion is rotated by a torque whose axis is perpendicular to the plane of the inclusion; (c) the medium is under uniform stress field at infinity in a plane parallel to the plane of the inclusion. By using the theory of two-dimensional Fourier transforms, the problems corresponding to all three cases has been reduced, in a unified manner, to a system of coupled two-dimensional integral equations. The theorems of Dyson, Galin, and Willis have been employed to deduce the structure of solution of these equations. It is worth noting in this regard that the same method can be used to determine the structure of solution of certain classes of coupled integral equations of numerous mixed boundary value problems of the elasticity theory, e.g., the problem of tangential contact of elastic solids, the problem of a rigid sheet containing an elliptical hole where the sheet is given a displacement in the plane of the sheet. Some research in this direction is under the investigation of the writer and will be reported in a separate communication.

Acknowledgments

The writer wishes to express his gratitude to the Associate Editor Dr. M. J. Pindera for his insightful comments on an earlier version of the article. Helpful comments of three anonymous reviewers are also gratefully acknowledged.

References

Alexandrov, V. M., and Solov'ev, A. S., 1966, "Some Mixed Three-Dimensional Problems In the Theory of Elasticity," *Mechanics of Solids (Mekhanika Tverdogo Tela)*, Vol. 2, pp. 95–97.

Alexandrov, V. M., Smetanin, B. I., and Sobol, B. V., 1993, *Thin Stress Concentrators in Elastic Solids*, Nauka, Moscow (in Russian).

Cherepanov, G. P., 1979, *Mechanics of Brittle Fracture*, McGraw-Hill, New York.

Cherepanov, G. P., 1983, *Mechanics of Fracture of Composite Materials*, Nauka, Moscow (in Russian).

Collins, W. D., 1962, "Some Axially Symmetric Stress Distributions in Elastic Solids Containing Penny-Shaped Cracks. I. Cracks in an Infinite Solid and a Thick Plate," *Proceedings of the Royal Society of London*, Vol. A203, pp. 359–386.

Dyson, F. W., 1891, "The Potentials of Ellipsoids of Variable Densities," *Quarterly Journal of Pure and Applied Mathematics, Oxford Series*, Vol. XXV, pp. 259–288.

Elliott, H. A., 1948, "Three-Dimensional Stress Distribution in Hexagonal Aelo-

Downloaded 04 May 2010 to 171.66.16.27. Redistribution subject to ASME license or copyright; see http://www.asme.org/terms/Terms_Use.cfm

tropic Crystals," *Proceedings of the Cambridge Philosophical Society,* Vol. 44, pp. 522–533.

Elliott, H. A., 1949, "Axial Symmetric Stress Distributions in Hexagonal Aelotropic Crystals. The Problem of the Plane and Related Problems," *Proceedings of the Cambridge Philosophical Society,* Vol. 45, pp. 621–630.

Erdelyi, A., 1954, *Tables of Integral Transforms,* Vol. I, McGraw-Hill, New York.

Eshelby, J. D., 1961, "Elastic Inclusions and Inhomogeneities," *Progress in Solid Mechanics,* Vol. 2, I. N. Sneddon and R. Hill, eds., North-Holland, Amsterdam, pp. 89–140.

Ferrers, 1877, "On the Potentials of Ellipsoids, Ellipsoidal Shells, Elliptic Laminae and Elliptic Rings of Variable Densities," *Quarterly Journal of Pure and Applied Mathematics,* Vol. XIV, No. 1, pp. 1–22.

Galin, L. A., 1947, "On the Pressure of a Stamp of Elliptical Planform on an Elastic Half-Space," *Prikladnaya Matematikao I Mekhanina (PMM),* Vol. 11, No. 2 (in Russian).

Galin, L. A., ed., 1976, *Development of the Theory of Contact Problems in the USSR,* Nauka, Moscow (in Russian).

Gladwell, G. M. L., 1980, *Contact Problems in the Classical Theory of Elasticity,* Sijhoff & Noordhoff, Alphen aan den Rijn, The Netherlands.

Goodier, J. N., 1933, "Concentration of Stress Around Spherical and Cylindrical Inclusions and Flaws," ASME JOURNAL OF APPLIED MECHANICS, Vol. 55, pp. 17–39.

Green, A. E., and Sneddon, I. N., 1949, "The Distribution of Stress in the Neighbourhood of a Flat Elliptical Crack in an Elastic Solid," *Proceedings of the Cambridge Philosophical Society,* pp. 159–163.

Green, A. E., and Zerna, W., 1968, *Theoretical Elasticity,* Oxford University Press, Oxford, UK.

Hamstad, M., and Bogy, D. B., 1972, "Elastostatic Solution for a Circular Membrane Bonded to a Half-Space Under Plane Loading," *International Journal of Solids & Structures,* Vol. 6, No. 1, pp. 1–28.

Kanwal, R. P., and Sharma, D. L., 1976, "Singularity Methods for Elastostatics," *Journal of Elasticity,* Vol. 6, pp. 405–418.

Kassir, M. K., and Sih, G. C., 1968, "Some Three-Dimensional Inclusion Problems in Elasticity," *International Journal of Solids & Structures,* Vol. 4, pp. 225–241.

Kassir, M. K., and Sih, G. C., 1966, "Three-Dimensional Stress Distribution Around an Elliptical Crack Under Arbitrary Loadings," ASME JOURNAL OF APPLIED MECHANICS, Vol. 33, pp. 601–611.

Keer, L. M., 1965, "A Note on the Solution for Two Asymmetric Boundary Value Problems," *International Journal of Solids & Structures,* Vol. 1, pp. 257–264.

Kim, S., and Pham-Thien, N., 1995, "Faxen Relations and Some Rigid Inclusion Problems," *Journal of Elasticity,* Vol. 37, No. 2, pp. 93–111.

Lekhnitskii, S. G., 1963, *Theory of Elasticity of an Anisotropic Elastic Body,* Holden Day, San Francisco.

Lure, A. I., 1970, *Theory of Elasticity,* Nauka, Moscow (in Russian).

Mura, T., 1987, *Micromechanics of Defects in Solids,* Matinus Nijhoff, Dordrecht, The Netherlands.

Panasiuk, V. V., Stadnik, M. M., and Silovaniuk, V. P., 1986, *Stress Concentrations in Three-Dimensional Bodies with Thin Inclusions,* Naukova Dumka, Kiev (in Russian).

Pham-Thien, N., 1993, "Rigid Spherical Inclusion: The Multipole Expansion," *Journal of Elasticity,* Vol. 32, pp. 243–252.

Pham-Thien, N., and Kim, S., 1994, *Microstructures in Elastic Media: Principles and Computational Methods,* Oxford University Press, Oxford, UK.

Podilchuk, Yu. N., 1979, *Three-Dimensional Problems of the Theory of Elasticity,* Naukova Dumka, Kiev (in Russian).

Rahman, M., 1999, "Bonded Contact of a Flexible Elliptical Disk With a Transversely Isotropic Half-Space," *International Journal of Solids & Structures,* Vol. 36, No. 13, pp. 1965–1983.

Rahman, M., 1999, "A Note on the calculation of the potentials of inhomogeneous ellipsoids and elliptical disks," manuscript in preparation.

Sneddon, I. N., 1972, *The Use of Integral Transforms,* McGraw-Hill, New York.

Southwell, R. V., and Gough, H. J., 1926, "On the Concentration of Stress in the Neighbourhood of a Small Spherical Flaw and on the Propagation of Fatigue Fractures in Statistically Isotropic Materials," *Philosophical Magazine,* Vol. 1, No. 7, pp. 71–97.

Ting, T. C. T., 1996, *Anisotropic Elasticity,* Oxford University Press, Oxford, UK.

Willis, J. R., 1966, "Hertzian Contact of Anisotropic Bodies," *Journal of the Mechanics & Physics of Solids,* Vol. 14, pp. 163–176.

Willis, J. R., 1967, "Boussinesq Problems for an Anisotropic Half-space," *Journal of the Mechanics & Physics of Solids,* Vol. 15, pp. 331–339.

Willis, J. R., 1968, "The Stress Field Around an Elliptical Crack in an Anisotropic Elastic Medium," *International Journal of Engineering Science,* Vol. 6, pp. 253–263.

APPENDIX

Derivation of the Recurrence Relation for the Integral I_{ij}

The object of this Appendix is to develop a recurrence relationship for the integral

$$I_{ij}^{(\lambda)} = \int_{\lambda}^{\infty} \frac{d\psi}{\sqrt{(a^2+\psi)^{2i+1}(b^2+\psi)^{2j+1}\psi}}. \tag{A1}$$

Differentiating (A1) with respect to a, we obtain

$$\frac{\partial I_{ij}^{(\lambda)}}{\partial a} = -(2i+1)a \int_{\lambda}^{\infty} \frac{d\psi}{\sqrt{(a^2+\psi)^{2i+3}(b^2+\psi)^{2j+1}\psi}} - \frac{1}{\sqrt{(a^2+\lambda)^{2i+1}(b^2+\lambda)^{2j+1}\lambda}} \frac{\partial \lambda}{\partial a} = -(2i+1)aI_{i+1,j}^{(\lambda)} - \frac{1}{\sqrt{(a^2+\lambda)^{2i+1}(b^2+\lambda)^{2j+1}\lambda}} \frac{\partial \lambda}{\partial a}, \tag{A2}$$

where

$$I_{i+1,j}^{(\lambda)} = \frac{-1}{(2i+1)a} \frac{\partial I_{ij}^{(\lambda)}}{\partial a} + \frac{1}{(2i+1)a\sqrt{(a^2+\lambda)^{2i+1}(b^2+\lambda)^{2j+1}\lambda}} \frac{\partial \lambda}{\partial a}. \tag{A3}$$

Similarly differentiating (A1) with respect to b, we obtain

$$I_{i,j+1}^{(\lambda)} = \frac{-1}{(2j+1)b} \frac{\partial I_{ij}^{(\lambda)}}{\partial b} + \frac{1}{(2j+1)b\sqrt{(a^2+\lambda)^{2i+1}(b^2+\lambda)^{2j+1}\lambda}} \frac{\partial \lambda}{\partial b}. \tag{A4}$$

Knowing $I_{00}^{(\lambda)}$, it is possible to find closed-form expressions for any other $I_{ij}^{(\lambda)}$ for any $i, j \geq 0$. The integral $I_{00}^{(\lambda)}$ is evaluated in closed form by using the standard integral 3.152 (p. 294) from Gradshteyn and Ryzhik (1994),

$$I_{00}^{(\lambda)} = \frac{2}{a} F(\beta, e), \tag{A5}$$

where $F(\beta, e)$ is the incomplete elliptic integral of the first kind, $e = \sqrt{1 - (b^2/a^2)}$ is the eccentricity of the ellipse, and

$$\beta = \cot^{-1} \frac{\sqrt{\lambda}}{a}, \tag{A6}$$

where

$$\lambda = \frac{x^2 + y^2 - a^2 - b^2 + \sqrt{D}}{2} \tag{A7}$$

and

$$D = (x^2 + y^2 - a^2 - b^2)^2 + 4a^2b^2\left(\frac{x^2}{a^2} + \frac{y^2}{b^2} - 1\right). \tag{A8}$$

To use the relations (A3) and (A4), the following formulae for differentiation of the incomplete elliptic integrals of the first and second kinds, $F(\varphi, p)$ and $E(\varphi, p)$, are required (Gradshteyn and Ryzhik (1994)):

$$\frac{\partial E(\varphi, p)}{\partial p} = \frac{1}{p}[E(\varphi, p) - F(\varphi, p)],$$

$$\frac{\partial E(\varphi, p)}{\partial \varphi} = \sqrt{1 - p^2 \sin^2 \varphi},$$

$$\frac{\partial F(\varphi, p)}{\partial p} = \frac{1}{1-p^2}\left[\frac{1}{p}E(\varphi, p) - \frac{1-p^2}{p}F(\varphi, p) - \frac{p \sin 2\varphi}{2\sqrt{1 - p^2 \sin^2 \varphi}}\right],$$

$$\frac{\partial F(\varphi, p)}{\partial \varphi} = \frac{1}{\sqrt{1 - p^2 \sin^2 \varphi}}, \tag{A9}$$

so that in our case

Downloaded 04 May 2010 to 171.66.16.27. Redistribution subject to ASME license or copyright; see http://www.asme.org/terms/Terms_Use.cfm

$$\frac{\partial E(\beta, e)}{\partial a_i} = \frac{\partial E(\beta, e)}{\partial \beta}\bigg|_{e \text{ kept constant}} \frac{\partial \beta}{\partial a_i} + \frac{\partial E(\beta, e)}{\partial e}\bigg|_{\beta \text{ kept constant}} \frac{\partial e}{\partial a_i},$$

$$\frac{\partial F(\beta, e)}{\partial a_i} = \frac{\partial F(\beta, e)}{\partial a_i}\bigg|_{e \text{ kept constant}} \frac{\partial \beta}{\partial a_i} + \frac{\partial F(\beta, e)}{\partial e}\bigg|_{\beta \text{ kept constant}} \frac{\partial e}{\partial a_i} \tag{A10}$$

where $a_1 = a$, $a_2 = b$.

Thus, Eqs. (A3), (A4), and (A5) together with (A9) and (A10) establish a set of recurrence relations for the integral $I_{ij}^{(\lambda)}$.

For instance, the following expressions are obtained by means of these recurrence relations:

$$I_{10}^{(\lambda)} = \frac{2}{a^3 e^2}[F(\beta, e) - E(\beta, e)],$$

$$I_{01}^{(\lambda)} = \frac{2}{ab^2 e^2}[E(\beta, e) - k^2 F(\beta, e)] - \frac{2}{b^2}\sqrt{\frac{\lambda}{(a^2+\lambda)(b^2+\lambda)}},$$

$$I_{11}^{(\lambda)} = \frac{2}{a^3 b^2 e^4}\{(2 - e^2)E(\beta, e) - 2k^2 F(\beta, e)\} - \frac{2}{b^2(a^2 - b^2)}\sqrt{\frac{\lambda}{(a^2+\lambda)(b^2+\lambda)}},$$

$$I_{20}^{(\lambda)} = \frac{2}{3a^5 e^4}\{(2 + e^2)F(\beta, e) - 2(1 + e^2)E(\beta, e)\} + \frac{2}{3a^2(a^2 - b^2)}\sqrt{\frac{\lambda(b^2+\lambda)}{(a^2+\lambda)^3}},$$

$$I_{02}^{(\lambda)} = \frac{2}{3ab^4 e^4}\{2(-1 + 2e^2)E(\beta, e) + k^2(2 - 3e^2)F(\beta, e)\} - \frac{2[b^2(3a^2 - b^2) + \lambda(2a^2 - 3b^2)]}{3b^4(a^2 - b^2)}\sqrt{\frac{\lambda}{(a^2+\lambda)(b^2+\lambda)}}, \tag{A11}$$

where $k = \sqrt{1 - e^2} = b/a$. On the disk where $\lambda = 0$, expressions (11) simplify significantly; all the terms not containing elliptic integrals vanish and the incomplete elliptic integrals reduce to the corresponding complete elliptic integrals.

For a circular disk, we have

$$I_{10}|_{b\to a} = I_{01}|_{b\to a} = \frac{1}{a^3}\left(\sin^{-1}\frac{a}{r} - \frac{a}{r}\sqrt{1 - \frac{a^2}{r^2}}\right), \quad r \geq a$$

$$I_{11}|_{b\to a} = I_{20}|_{b\to a} = I_{02}|_{b\to a} = \frac{1}{4a^5}\left(-3\frac{a}{r}\sqrt{1 - \frac{a^2}{r^2}} - 2\left(\frac{a}{r}\right)^3\sqrt{1 - \frac{a^2}{r^2}} + 3\sin^{-1}\frac{a}{r}\right), \quad r \geq a,$$

$$I_{10}|_{b\to a} = I_{01}|_{b\to a} = \frac{\pi}{2a^3}, \quad I_{11}|_{b\to a} = I_{20}|_{b\to a} = I_{02}|_{b\to a} = \frac{3\pi}{8a^5}, \quad r \leq a. \tag{A12}$$

Expressions (A12) are obtained by letting $b \to a$ in formulae (A11).

Downloaded 04 May 2010 to 171.66.16.27. Redistribution subject to ASME license or copyright; see http://www.asme.org/terms/Terms_Use.cfm

Some Problems of a Rigid Elliptical Disk-Inclusion Bonded Inside a Transversely Isotropic Space, Part II: Solutions of the Integral Equations

M. Rahman
3019 W. 13 Mile Road, Apt. 214,
Royal Oak, MI 48073
e-mail: mrahman10@hotmail.com

This is a sequel to the first part of the two-part paper, which addresses the problem of contact of a rigid elliptical disk-inclusion bonded in the interior of a transversely isotropic space under three different types of loading, namely (a) the inclusion is loaded in its plane by a shearing force, whose line of action passes through the center of the inclusion; (b) the inclusion is rotated by a torque whose axis is perpendicular to the plane of the inclusion; (c) the medium is under uniform stress field at infinity in a plane parallel to the plane of the inclusion. In Part I, the problems corresponding to all three cases of loading have been reduced, in a unified manner, to a system of coupled two-dimensional integral equations. Next, based on Dyson's theorem and Willis' generalization of Galin's theorem, the general structure of solution of the coupled integral equations has been established. In this part, closed-form solutions to these equations are derived by using Dyson's theorem. Full elastic field in the plane of the inclusion is evaluated and it is shown that the stress field near the edge of the inclusion exhibits the familiar square root singularity in linear fracture mechanics. Explicit expressions for the stress intensity factors near the edge of the inclusion are extracted from these solutions. Numerical results are plotted illustrating how these coefficients vary with transverse isotropy and the parametric angle of the ellipse. The results can be used to determine the critical failure load and angle of initial crack propagation for solids containing elliptical inclusions.

1 Solution of the Problems

In the first part of the paper it has been shown that Willis' generalization of Galin's theorem can be extended to a certain class of coupled integral equations. Furthermore, based on this result, we have deduced the general structure of solution of the integral Eqs. (23) (Part I), which are given by Eqs. (46) (Part I), i.e.,

$$\sigma_{xz}(x, y, 0) = l^{-1}(x, y)(c_0 + c_1 x + c_2 y),$$
$$\sigma_{yz}(x, y, 0) = l^{-1}(x, y)(d_0 + d_1 x + d_2 y) \tag{1}$$

where the coefficients c_i, d_i $(i = 0, 1, 2)$ are to be determined.

In this part, we will derive explicit solutions for the integral Eqs. (23) and thereby give complete solutions to the three problems by using Dyson's results (1891). The prowess of Dyson's method lies in its capability to determine the field inside as well as outside the disk, while Galin's theorem (Galin, 1947) and its generalization by Willis (1966, 1967, 1968) do not in general allow one to determine the field outside the disk. The method of elliptical coordinates and ellipsoidal harmonics for the Laplace operator used in the works by Green and Sneddon (1949) and Kassir and Sih (1966, 1968), although mathematically the most natural and systematic way to solve problems involving ellipsoidal or elliptical inclusions or cavities, is extremely involved. In what follows, we will see that Dyson's results have certain unquestionable advantages in point of clearness and interpretativeness of the physical results, being given in Cartesian form.

It will be advantageous to introduce the following notations:

$$^{(m)}W_{ij}^{(\lambda)} = \int\int_{\Omega} \frac{x_0^i y_0^j l^{2m-1}(x_0, y_0)}{R}\, dx_0 dy_0,$$

$$^{(m)}A_{ij}^{(\lambda)} = \int\int_{\Omega} \frac{(x - x_0)^2 x_0^i y_0^j l^{2m-1}(x_0, y_0)}{R^3}\, dx_0 dy_0,$$

$$^{(m)}B_{ij}^{(\lambda)} = \int\int_{\Omega} \frac{(y - y_0)^2 x_0^i y_0^j l^{2m-1}(x_0, y_0)}{R^3}\, dx_0 dy_0,$$

$$^{(m)}C_{ij}^{(\lambda)} = \int\int_{\Omega} \frac{(x - x_0)(y - y_0) x_0^i y_0^j l^{2m-1}(x_0, y_0)}{R^3}\, dx_0 dy_0, \tag{2}$$

where $l(x, y) = \sqrt{1 - (x^2/a^2) - (y^2/b^2)}$. Furthermore, when both λ and m are zero, $^{(m)}W_{ij}^{(\lambda)}$, $^{(m)}A_{ij}^{(\lambda)}$, $^{(m)}B_{ij}^{(\lambda)}$, $^{(m)}C_{ij}^{(\lambda)}$ will be denoted simplify by the lower indices, i.e., W_{ij}, A_{ij}, B_{ij}, C_{ij}.

Integrals $^{(m)}A_{ij}^{(\lambda)}$, $^{(m)}B_{ij}^{(\lambda)}$, $^{(m)}C_{ij}^{(\lambda)}$ can be expressed through $^{(m)}W_{ij}^{(\lambda)}$ as

$$^{(m)}A_{ij}^{(\lambda)} = \frac{\partial\, ^{(m)}W_{i+1,j}^{(\lambda)}}{\partial x} - x\, \frac{\partial\, ^{(m)}W_{ij}^{(\lambda)}}{\partial x},$$

Contributed by the Applied Mechanics Division of THE AMERICAN SOCIETY OF MECHANICAL ENGINEERS for publication in the ASME JOURNAL OF APPLIED MECHANICS.
Discussion on the paper should be addressed to the Technical Editor, Professor Lewis T. Wheeler, Department of Mechanical Engineering, University of Houston, Houston, TX 77204-4792, and will be accepted until four months after final publication of the paper itself in the ASME JOURNAL OF APPLIED MECHANICS.
Manuscript received by the ASME Applied Mechanics Division, May 7, 1998; final revision, Apr. 14, 1999. Associate Technical Editor: M.-J. Pindera.

 Copyright © 1999 by ASME

Downloaded 04 May 2010 to 171.66.16.27. Redistribution subject to ASME license or copyright; see http://www.asme.org/terms/Terms_Use.cfm

$$ {}^{(m)}B_{ij}^{(\lambda)} = \frac{\partial\, {}^{(m)}W_{i,j+1}^{(\lambda)}}{\partial y} - y\,\frac{\partial\, {}^{(m)}W_{ij}^{(\lambda)}}{\partial y}, \quad i, j \geq 0, $$

$$ {}^{(m)}C_{ij}^{(\lambda)} = \left\{ \begin{array}{ll} \dfrac{\partial\, {}^{(m)}W_{i+1,j}^{(\lambda)}}{\partial y} - x\,\dfrac{\partial\, {}^{(m)}W_{ij}^{(\lambda)}}{\partial y}, & i \geq 0, \quad j \geq 1, \\ \dfrac{\partial\, {}^{(m)}W_{i,j+1}^{(\lambda)}}{\partial x} - y\,\dfrac{\partial\, {}^{(m)}W_{ij}^{(\lambda)}}{\partial x}, & i \geq 1, \quad j \geq 0 \end{array} \right\}, $$

$$ {}^{(m)}C_{00}^{(\lambda)} = 0. \tag{3} $$

Therefore, it suffices to evaluate ${}^{(m)}W_{ij}^{(\lambda)}$ only. Other quantities in (2) are then easily determined through Eqs. (3). Furthermore, in this article we will need expressions for ${}^{(0)}W_{ij}^{(\lambda)}$ for $i, j = 0, 1, 2$ only in which case they can be expressed as (see Eq. (41) in Part I)

$$ {}^{0}W_{ij}^{(\lambda)} = \pi a^{2i+1} b^{2j+1} x^i y^j I_{ij}^{(\lambda)}, \quad (i, j = 0, 1), $$

$$ {}^{0}W_{20}^{(\lambda)} = \frac{\pi a^3 b x^2}{2}\,(3a^2 I_{20}^{(\lambda)} - I_{10}^{(\lambda)}) + \frac{\pi a^3 b y^2}{2}\,(b^2 I_{11}^{(\lambda)} - I_{10}^{(\lambda)}) + \frac{\pi a^3 b}{2}\,(I_{00}^{(\lambda)} - a^2 I_{01}^{(\lambda)}), $$

$$ {}^{0}W_{02}^{(\lambda)} = \frac{\pi a b^3 x^2}{2}\,(a^2 I_{11}^{(\lambda)} - I_{01}^{(\lambda)}) + \frac{\pi a b^3 y^2}{2}\,(3b^2 I_{02}^{(\lambda)} - I_{01}^{(\lambda)}) + \frac{\pi a b^3}{2}\,(I_{00}^{(\lambda)} - b^2 I_{01}^{(\lambda)}). \tag{4} $$

For the definitions of $I_{ij}^{(\lambda)}$ the reader is referred to the Appendix of Part I. Putting (4) into (3), we express the integrals (2) in terms of the functions $I_{ij}^{(\lambda)}$:

$$ {}^{0}A_{10}^{(\lambda)} = \pi a^3 b x (3a^2 I_{20}^{(\lambda)} - 2I_{10}^{(\lambda)}) + \frac{\pi a^3 b}{2}\,[x^2(b^2 + \lambda) + y^2(a^2 + \lambda) + (a^2 + \lambda)(b^2 + \lambda)] \times \sqrt{\frac{\lambda}{(a^2 + \lambda)^5 (b^2 + \lambda)^3}}\,\frac{\partial \lambda}{\partial x}, $$

$$ {}^{0}A_{01}^{(\lambda)} = \pi a^3 b^3 y I_{11}^{(\lambda)} + \pi a b^3 x y \sqrt{\frac{\lambda}{(a^2 + \lambda)^3 (b^2 + \lambda)^3}}\,\frac{\partial \lambda}{\partial x}, $$

$$ {}^{0}B_{10}^{(\lambda)} = \pi a^3 b^3 x I_{11}^{(\lambda)} + \pi a^3 b x y \sqrt{\frac{\lambda}{(a^2 + \lambda)^3 (b^2 + \lambda)}}\,\frac{\partial \lambda}{\partial y}, $$

$$ {}^{0}B_{01}^{(\lambda)} = \pi a b^3 y (3b^2 I_{02}^{(\lambda)} - 2I_{01}^{(\lambda)}) + \frac{\pi a b^3}{2}\,[x^2(a^2 + \lambda) + y^2(b^2 + \lambda) + (a^2 + \lambda)(b^2 + \lambda)] \times \sqrt{\frac{\lambda}{(a^2 + \lambda)^3 (b^2 + \lambda)^5}}\,\frac{\partial \lambda}{\partial y}, $$

$$ {}^{0}C_{10}^{(\lambda)} = \pi a^3 b y (b^2 I_{11}^{(\lambda)} - I_{10}^{(\lambda)}) + \pi a^3 b x y \sqrt{\frac{\lambda}{(a^2 + \lambda)^3 (b^2 + \lambda)^3}}\,\frac{\partial \lambda}{\partial x}, $$

$$ {}^{0}C_{01}^{(\lambda)} = \pi a b^3 x (a^2 I_{11}^{(\lambda)} - I_{01}^{(\lambda)}) + \pi a b^3 x y \sqrt{\frac{\lambda}{(a^2 + \lambda)^3 (b^2 + \lambda)^3}}\,\frac{\partial \lambda}{\partial y}. \tag{5} $$

For the interior of the inclusion, i.e., for $\forall (x, y) \in \Omega$, $\lambda = 0$ and the quantities I_{ij}^{0} become independent of x, y; furthermore, they can be expressed in terms of the complete elliptic integrals of the first and second kinds for all $i, j \geq 0$ using the recurrence relations developed in the Appendix (Part I).

Putting (5) into Eqs. (23) of Part I and taking into view the fact that for the interior of the disk $\lambda = 0$, we obtain

$$ c_0(W_{00} - \Gamma B_{00}) + \Gamma d_0 C_{00} + c_1(W_{10} - \Gamma B_{10}) + \Gamma d_2 C_{01} + c_2(W_{01} - \Gamma B_{01}) + \Gamma d_1 C_{10} = \pi(a_0 + a_1 x + a_2 y), $$

$$ d_0(W_{00} - \Gamma A_{00}) + \Gamma c_0 C_{00} + d_1(W_{10} - \Gamma A_{10}) + \Gamma c_2 C_{01} + d_2(W_{01} - \Gamma A_{01}) + \Gamma c_1 C_{10} = \pi(b_0 + b_1 x + b_2 y). \tag{6} $$

The following closed-form expressions are derived by means of the Eqs. (4), (5) and ((A11) of Part I):

$$ W_{00} - \Gamma A_{00} = \pi b P_{00}, $$

$$ W_{10} - \Gamma A_{10} = \pi P_{10} b x, $$

$$ W_{01} - \Gamma A_{01} = \pi P_{01} b y, $$

$$ W_{00} - \Gamma B_{00} = \pi b Q_{00}, $$

$$ W_{10} - \Gamma B_{10} = \pi Q_{10} b x, $$

$$ W_{01} - \Gamma B_{01} = \pi Q_{01} b y, $$

$$ C_{00} = 0, \quad \Gamma C_{10} = \pi \Gamma R b y, \quad \Gamma C_{01} = \pi \Gamma S b x, \tag{7} $$

where

$$ P_{00} = \frac{2}{e^2}\,[(e^2 - \Gamma)K(e) + \Gamma E(e)], $$

$$ P_{10} = \frac{2}{e^4}\,[e^2 K(e) + \Gamma(e^2 + 2)K(e) - (e^2 - 2\Gamma)E(e)], $$

$$ P_{01} = \frac{2}{e^4}\,[(e^2 - 1)(e^2 - 2\Gamma)K(e) + (e^2 + \Gamma e^2 - 2\Gamma)E(e)], $$

$$ Q_{00} = \frac{2}{e^2}\,[(e^2 - \Gamma e^2 + \Gamma)K(e) - \Gamma E(e)], $$

$$ Q_{10} = \frac{2}{e^4}\,[(e^2 - 2\Gamma e^2 + 2\Gamma)K(e) - (e^2 - \Gamma e^2 + 2\Gamma)E(e)], $$

$$ Q_{01} = \frac{2}{e^4}\,[(e^2 - 1)(e^2 + 2\Gamma - \Gamma e^2)K(e) + (e^2 - 2\Gamma e^2 + 2\Gamma)E(e)], $$

$$ R = \frac{-2}{e^4}\,[(2 - e^2)K(e) - 2E(e)], \tag{8} $$

$$ S = \frac{-2(1 - e^2)}{e^4}\,[(2 - e^2)K(e) - 2E(e)], $$

where e is the eccentricity of the ellipse and $K(e)$, $E(e)$ are the complete elliptic integrals of the first and second kinds, respectively.

It can be shown that for a circular domain (i.e., $e = 0$), expressions (8) reduce to the following formulae:

$$ P_{00} = Q_{00} = \frac{\pi}{2}\,(2 - \Gamma), \quad P_{10} = Q_{01} = \frac{\pi}{8}\,(4 - \Gamma), $$

$$ P_{01} = Q_{10} = \frac{\pi}{8}\,(4 - 3\Gamma), \quad R = S = \frac{-\pi}{8}. \tag{9} $$

Downloaded 04 May 2010 to 171.66.16.27. Redistribution subject to ASME license or copyright; see http://www.asme.org/terms/Terms_Use.cfm

Taking account of (7) and (8) and equating like powers of x, y in both sides of equations (6), we obtain a system of linear algebraic equation whose solution is

$$c_0 = \frac{a_0}{bQ_{00}}, \quad c_1 = \frac{a_1P_{01} - b_2\Gamma S}{b(P_{01}Q_{10} - \Gamma^2RS)},$$

$$c_2 = \frac{a_2P_{10} - b_1\Gamma R}{b(P_{10}Q_{01} - \Gamma^2RS)},$$

$$d_0 = \frac{b_0}{bP_{00}}, \quad d_1 = \frac{b_1Q_{01} - a_2\Gamma S}{b(P_{10}Q_{01} - \Gamma^2RS)},$$

$$d_2 = \frac{b_2Q_{10} - a_1\Gamma R}{b(P_{01}Q_{10} - \Gamma^2RS)}. \tag{10}$$

We now proceed to the detailed consideration of each problem.

Problem 1: For this case, the coefficients a_i, b_i are given by Eqs. (25) of Part I. Then, using Eqs. (1) and (10), we obtain the following expressions for the interfacial stresses:

$$\sigma_{xz}(x, y, 0) = \frac{-2c_{44}\delta \cos\beta}{k_2\Lambda_2 bQ_{00}l(x, y)},$$

$$\sigma_{yz}(x, y, 0) = \frac{-2c_{44}\delta \sin\beta}{k_2\Lambda_2 bP_{00}l(x, y)}. \tag{11}$$

Therefore, the components of the resultant shearing force along the x and y-axes are

$$T_x = 2\iint_\Omega \sigma_{xz}(x, y, 0)dxdy = \frac{-8\pi c_{44}\delta a \cos\beta}{k_2\Lambda_2 Q_{00}},$$

$$T_y = 2\iint_\Omega \sigma_{yz}(x, y, 0)dxdy = \frac{-8\pi c_{44}\delta a \sin\beta}{k_2\Lambda_2 P_{00}}, \tag{12}$$

and the magnitude of the resultant shearing force is

$$T = \sqrt{T_x^2 + T_y^2} = \frac{8\pi c_{44}\delta a}{k_2\Lambda_2}\left(\frac{\cos^2\beta}{Q_{00}^2} + \frac{\sin^2\beta}{P_{00}^2}\right)^{1/2}. \tag{13}$$

The slope of the line of action of the force T with respect to the x-axis is

$$\tan\alpha = \frac{T_y}{T_x} = \frac{Q_{00}}{P_{00}}\tan\beta. \tag{14}$$

On the other hand, solving Eq. (13) for δ and substituting into Eqs. (11), we obtain the formulae

$$\sigma_{xz}(x, y, 0) = \frac{-T\cos\alpha}{4ab\pi}\left(1 - \frac{x^2}{a^2} - \frac{y^2}{b^2}\right)^{-1/2},$$

$$\sigma_{yz}(x, y, 0) = \frac{-T\sin\alpha}{4ab\pi}\left(1 - \frac{x^2}{a^2} - \frac{y^2}{b^2}\right)^{-1/2}, \tag{15}$$

determining the interfacial stresses through the shearing force T.

We next proceed to determine the normal stresses: Putting (11) into the third equation in (22) of Part I, we obtain

$$\sigma_{zz}(x, y, 0) = \frac{-2\omega c_{44}\delta}{k_2\Lambda_2 b}\left(\frac{\cos\beta}{Q_{00}}\frac{\partial}{\partial x} + \frac{\sin\beta}{P_{00}}\frac{\partial}{\partial y}\right){}^{(0)}W_{00}^{(\lambda)}(x, y), \quad -\infty < x, y < \infty. \tag{16}$$

Hence, expressing ${}^0W_{00}^{(\lambda)}(x, y)$ via $I_{00}^{(\lambda)}(x, y)$ by Eq. (4) and using the expression (A11) of Part I in (16), we see that within the entire elliptical region, normal stresses are zero while outside the inclusion, the normal stresses are given by the equation:

$$\sigma_{zz}(x, y, 0) = \frac{4\omega\delta a c_{44}}{k_2\Lambda_2\sqrt{\lambda(a^2 + \lambda)(b^2 + \lambda)\lambda D}}\left[x\frac{b^2 + \lambda}{Q_{00}}\cos\beta + y\frac{a^2 + \lambda}{P_{00}}\sin\beta\right], \quad (x, y) \in \bar{\Omega}. \tag{17}$$

The definitions of the quantities λ and D are given by Eqs. (A7) and (A8) of Part I.

The solution corresponding to a rigid elliptical disk-inclusion in an *isotropic* space can be deduced from the Eqs. (11) and using Eqs. (28), (29), and (30) of Part I,

$$\sigma_{xz}(x, y, 0) = \frac{-2\mu\delta\cos\beta}{b\bar{Q}_{00}l(x, y)}, \quad \sigma_{yz}(x, y, 0) = \frac{-2\mu\delta\sin\beta}{b\bar{P}_{00}l(x, y)},$$

$$\sigma_{zz}(x, y, 0) = \frac{2\mu\delta a(1 - 2\nu)}{(1 - \nu)\sqrt{\lambda(a^2 + \lambda)(b^2 + \lambda)\lambda D}} \times\left[x\frac{b^2 + \lambda}{\bar{Q}_{00}}\cos\beta + y\frac{a^2 + \lambda}{\bar{P}_{00}}\sin\beta\right], \quad (x, y) \in \bar{\Omega}, \tag{18}$$

where $\bar{P}_{00}$, $\bar{Q}_{00}$ are given by P_{00}, Q_{00} with Γ replaced by $1/(4(1 - \nu))$.

The first two equations in (18) are consistent with Alexandrov and Solov'ev (1993) (they did not calculate the normal stresses).

On the other hand, the solution of the problem corresponding to the case of a rigid circular disk in a transversely isotropic space can be obtained by letting $e \to 0$ in Eqs. (11) and using (9) with the results

$$\sigma_{xz}(x, y, 0) = \frac{-4c_{44}\delta\cos\beta}{\pi k_2\Lambda_2(2 - \Gamma)\sqrt{a^2 - r^2}},$$

$$\sigma_{yz}(x, y, 0) = \frac{-4c_{44}\delta\sin\beta}{\pi k_2\Lambda_2(2 - \Gamma)\sqrt{a^2 - r^2}},$$

where it follows that the solution corresponding to the case of an isotropic medium is

$$\sigma_{xz}(x, y, 0) = \frac{-16(1 - \nu)\mu\delta\cos\beta}{\pi(7 - 8\nu)\sqrt{a^2 - r^2}},$$

$$\sigma_{yz}(x, y, 0) = \frac{-16(1 - \nu)\mu\delta\sin\beta}{\pi(7 - 8\nu)\sqrt{a^2 - r^2}}. \tag{19}$$

For $\beta = 0$, Eqs. (20) reduce to the form

$$\sigma_{xz}(x, y, 0) = \frac{-16(1 - \nu)\mu\delta}{\pi(7 - 8\nu)\sqrt{a^2 - r^2}}, \quad \sigma_{yz}(x, y, 0) = 0. \tag{20}$$

Solution (20) is consistent with the results obtained by Keer (1965).

The solution for σ_{zz} corresponding to a rigid circular disk-inclusion in an isotropic solid can be deduced from Eq. (20) by letting $b \to a$ and using the relationships (9) and Eqs. (28) to (30) of Part I with the result

$$\sigma_{zz}(x, y, 0) = \frac{8(1 - 2\nu)\mu\delta a\cos(\beta - \theta)}{\pi(7 - 8\nu)r\sqrt{r^2 - a^2}}, \quad r > a, \tag{21}$$

which for $\beta = 0$ conforms with the solution given by Kassir and Sih (1968), but not with Keer (1965). Keer's solution is in error for reasons explained by Kassir and Sih (1968).

We now determine the displacement field outside the inclusion. Putting (11) into the first two equations in (22) of Part I, we obtain

Downloaded 04 May 2010 to 171.66.16.27. Redistribution subject to ASME license or copyright; see http://www.asme.org/terms/Terms_Use.cfm

$$u(x, y, 0) = \frac{\delta \cos\beta}{\pi b Q_{00}} \left[W_{00} - \Gamma B_{00} + \frac{\Gamma Q_{00} \tan\beta}{P_{00}} C_{00} \right],$$

$$v(x, y, 0) = \frac{\delta \sin\beta}{\pi b P_{00}} \left[W_{00} - \Gamma A_{00} + \frac{\Gamma P_{00} \cot\beta}{Q_{00}} C_{00} \right]. \quad (22)$$

Omitting details, we give here the final results:

$$u(x, y, 0) = \frac{2\delta \cos\beta}{Q_{00}} \left[F(\beta, e) - \frac{\Gamma}{e^2} \{E(\beta, e) - k^2 F(\beta, e)\} + \Gamma a \sqrt{\frac{\lambda}{(a^2+\lambda)(b^2+\lambda)}} + \frac{\Gamma Q_{00} axy \tan\beta}{P_{00}} \sqrt{\frac{\lambda}{(a^2+\lambda)(b^2+\lambda)D}} \right],$$

$$v(x, y, 0) = \frac{2\delta \sin\beta}{P_{00}} \left[F(\beta, e) - \frac{\Gamma}{e^2} \{E(\beta, e) - F(\beta, e)\} + \frac{\Gamma P_{00} axy \cot\beta}{Q_{00}} \sqrt{\frac{\lambda}{(a^2+\lambda)(b^2+\lambda)D}} \right]. \quad (23)$$

The above expressions are also valid for the interior of the inclusion, provided λ is assumed to be equal to zero.

The displacement field corresponding to a rigid circular disk-inclusion can be obtained by letting $e \to 0$ in (23) and using the relations (9) with the result

$$u(x, y, 0) = \frac{2\delta \cos\beta}{\pi(2-\Gamma)} \left[(2-\Gamma) \sin^{-1}\frac{a}{r} + \Gamma\left(\frac{a}{r}\right)^2 \sqrt{1-\left(\frac{a}{r}\right)^2} + \frac{\Gamma}{2}\left(\frac{a}{r}\right) \tan\beta \sin 2\theta \sqrt{1-\left(\frac{a}{r}\right)^2} \right],$$

$$v(x, y, 0) = \frac{2\delta \sin\beta}{\pi(2-\Gamma)} \left[(2-\Gamma) \sin^{-1}\frac{a}{r} + \frac{1}{2}\Gamma\left(\frac{a}{r}\right) \cot\beta \sin 2\theta \sqrt{1-\left(\frac{a}{r}\right)^2} \right]. \quad (24)$$

For an isotropic solid, the above equations reduce to

$$u(x, y, 0) = \frac{2\delta \cos\beta}{\pi} \left[\sin^{-1}\frac{a}{r} + \frac{1}{7-8\nu}\left(\frac{a}{r}\right)^2 \sqrt{1-\left(\frac{a}{r}\right)^2} + \frac{1}{2(7-8\nu)}\left(\frac{a}{r}\right) \tan\beta \sin 2\theta \sqrt{1-\left(\frac{a}{r}\right)^2} \right],$$

$$v(x, y, 0) = \frac{2\delta \sin\beta}{\pi} \left[\sin^{-1}\frac{a}{r} + \frac{1}{2(7-8\nu)}\left(\frac{a}{r}\right) \cot\beta \sin 2\theta \sqrt{1-\left(\frac{a}{r}\right)^2} \right]. \quad (25)$$

Problem 2: In this case, the constants a_i, b_i are given by Eqs. (26) of Part I. Upon substituting into Eqs. (1) and (10), we obtain the following equations for the interfacial stresses:

$$\sigma_{xz}(x, y, 0) = \frac{2c_{44}\varphi(P_{10}+\Gamma R)y}{bk_2\Lambda_2(P_{10}Q_{01}-\Gamma^2 RS)l(x, y)},$$

$$\sigma_{yz}(x, y, 0) = \frac{-2c_{44}\varphi(Q_{01}+\Gamma S)x}{bk_2\Lambda_2(P_{10}Q_{01}-\Gamma^2 RS)l(x, y)}. \quad (26)$$

The moment M and the angle of rotation φ are related by the equation

$$M = 2\int\int_{\Omega} [y\sigma_{xz}(x, y, 0) - x\sigma_{yz}(x, y, 0)]dxdy$$

$$= \frac{8c_{44}a\varphi\pi}{3k_2\Lambda_2(P_{10}Q_{01}-\Gamma^2 RS)} [(P_{10}+\Gamma S)b^2 + (Q_{01}+\Gamma R)a^2] \quad (27)$$

Formulae (27) can be rewritten, eliminating φ from Eq. (26), in terms of the moment M:

$$\sigma_{xz}(x, y, 0) = \frac{3M(P_{10}+\Gamma R)y}{4\pi ab[(P_{10}+\Gamma S)b^2 + (Q_{01}+\Gamma R)a^2]l(x, y)},$$

$$\sigma_{yz}(x, y, 0) = \frac{-3M(Q_{01}+\Gamma S)x}{4\pi ab[(P_{10}+\Gamma S)b^2 + (Q_{01}+\Gamma R)a^2]l(x, y)}. \quad (28)$$

The solution corresponding to the case of a rigid circular disk-inclusion can be obtained by letting $e \to 0$ in Eqs. (27) and (28) and using the results (9), namely,

$$M = \frac{32c_{44}\varphi a^3}{3k_2\Lambda_2},$$

$$\sigma_{\theta z}(r, 0) = \frac{4c_{44}\varphi r}{\pi k_2\Lambda_2\sqrt{a^2-r^2}} = \frac{3Mr}{8\pi a^3\sqrt{a^2-r^2}}. \quad (29)$$

For an isotropic body, formulae (29) take the form:

$$M = \frac{32\mu\varphi a^3}{3},$$

$$\sigma_{\theta z}(r, 0) = \frac{4\mu\varphi r}{\pi k\sqrt{a^2-r^2}} = \frac{3Mr}{8\pi a^3\sqrt{a^2-r^2}}. \quad (30)$$

which are in accord with the well-known results (Galin, 1976).

Putting (26) into the third equation of in (22) of Part I, we obtain

$$\sigma_{zz}(x, y, 0) = \frac{3M\omega}{8\pi^2 ab[(P_{10}+\Gamma S)b^2 + (Q_{01}+\Gamma R)a^2]} \times \left((P_{10}+\Gamma R)\frac{\partial^0 W_{01}^{(\lambda)}}{\partial x} + (Q_{01}+\Gamma S)\frac{\partial^0 W_{10}^{(\lambda)}}{\partial y} \right). \quad (31)$$

Using Eqs. (4) and (A22) of Part I, we see that within the elliptical region, the normal stresses are zero and outside the inclusion they assume the form

$$\sigma_{zz}(x, y, 0) = \frac{3M\omega xy}{4\pi\sqrt{\lambda(a^2+\lambda)(b^2+\lambda)D}} \times \frac{Q_{01}+\Gamma S - k^2(P_{10}+\Gamma R)}{Q_{01}+\Gamma R + k^2(P_{10}+\Gamma S)}. \quad (32)$$

The solution corresponding to a rigid circular disk-inclusion can be obtained from Eq. (32) by letting $b \to a$ and using the relationships (9), namely,

$$\sigma_{zz}(x, y, 0) = 0, \quad r \geq a.$$

Thus the normal stresses are zero everywhere in the plane of the rigid circular inclusion as expected.

We now turn to determine the displacement field outside the inclusion. Putting (26) into the first two equations of (22), we obtain the following formulae for the displacement field outside the inclusion:

Downloaded 04 May 2010 to 171.66.16.27. Redistribution subject to ASME license or copyright; see http://www.asme.org/terms/Terms_Use.cfm

$$u(x, y, 0) = \frac{k_2\Lambda_2}{2\pi c_{44}} (\zeta_1\Gamma^0 A_{10}^{(\lambda)} - \zeta_2^0 W_{01}^{(\lambda)} - \zeta_1\Gamma^0 C_{01}^{(\lambda)}),$$

$$v(x, y, 0) = \frac{k_2\Lambda_2}{2\pi c_{44}} (\zeta_2\Gamma^0 A_{10}^{(\lambda)} - \zeta_2^0 W_{10}^{(\lambda)} - \zeta_1\Gamma^0 C_{01}^{(\lambda)}), \quad (33)$$

where the following notations are introduced:

$$\Gamma = \frac{\Lambda_1 + \Lambda_2}{\Lambda_2},$$

$$\zeta_1 = \frac{3M(P_{10} + \Gamma R)}{4\pi ab[(P_{10} + \Gamma S)b^2 + (Q_{01} + \Gamma R)a^2]},$$

$$\zeta_2 = \frac{-3M(Q_{01} + \Gamma S)}{4\pi ab[(P_{10} + \Gamma S)b^2 + (Q_{01} + \Gamma R)a^2]}. \quad (34)$$

Closed-form expressions for all the ${}^{(m)}W_{ij}^{(\lambda)}$, ${}^{(m)}A_{ij}^{(\lambda)}$, ${}^{(m)}B_{ij}^{(\lambda)}$, ${}^{(m)}C_{ij}^{(\lambda)}$ entering in Eqs. (33) are given by Eqs. (4) and (5).

The corresponding solution for a circular disk-inclusion can be deduced from Eqs. (33) and (34) by letting $b \to a$ and using the relations (A12) of Part I and Eqs. (9). This task is left for the reader as an exercise.

Problem 3: For this case, the coefficients a_i, b_i are given by Eqs. (27) of Part I. Substituting into Eqs. (1) and (10), we obtain the following formulae for determining the interfacial stresses:

$$\sigma_{xz}(x, y, 0) = -\frac{2px}{bk_2\Lambda_2(P_{01}Q_{10} - \Gamma^2 RS)} \times [P_{01}(\Gamma_1 \cos^2\gamma - \Gamma_2 \sin^2\gamma) - \Gamma S(\Gamma_1 \sin^2\gamma - \Gamma_2 \cos^2\gamma)]l^{-1}(x, y) + \frac{2y}{bk_2\Lambda_2(P_{10}Q_{01} - \Gamma^2 RS)} [c_{44}\varphi(P_{10} + \Gamma R) - p\Gamma_3(P_{10} - \Gamma R) \sin 2\gamma]l^{-1}(x, y),$$

$$\sigma_{yz}(x, y, 0) = \frac{-2x}{k_2\Lambda_2 b(P_{10}Q_{01} - \Gamma^2 RS)} [c_{44}\varphi(Q_{01} + \Gamma S) + p\Gamma_3 \times (Q_{01} - \Gamma S) \sin 2\gamma]l^{-1}(x, y) - \frac{2py}{bk_2\Lambda_2(P_{01}Q_{10} - \Gamma^2 RS)} \times [Q_{10}(\Gamma_1 \sin^2\gamma - \Gamma_2 \cos^2\gamma) - \Gamma R(\Gamma_1 \cos^2\gamma - \Gamma_2 \sin^2\gamma)]l^{-1}(x, y). \quad (35)$$

The angle of rotation φ of the disk can be found from the traction-free condition of the surface, i.e., $T_x = T_y = 0$, $M = 0$. Equation $M = 0$ yields the required relationship between the quantities p, α, and φ, namely,

$$\varphi = \frac{-\Gamma_3 \sin 2\gamma}{(P_{01} - \Gamma S)a^2 + (Q_{10} - \Gamma R)b^2} \{(P_{01} - S)a^2 - (Q_{10} - R)b^2\}. \quad (36)$$

Equations (35) and (36) complete the solution of Problem 3.

As a particular case, we consider the case where the elastic half-space is loaded at infinity by two mutually perpendicular systems of uniformly distributed forces of intensity p in a plane parallel to the plane of the inclusion. The line of action of one of the systems is inclined at an angle γ with the major semi-axis of the inclusion, then using formulae (35) and (36), we find that

$$\sigma_{xz}(x, y, 0) = \frac{2px(\Gamma_1 - \Gamma_2)(\Gamma S - P_{01})}{bk_2\Lambda_2(P_{01}Q_{10} - \Gamma^2 RS)} \left(1 - \frac{x^2}{a^2} - \frac{y^2}{b^2}\right)^{-1/2},$$

$$\sigma_{yz}(x, y, 0) = \frac{2py(\Gamma_1 - \Gamma_2)(\Gamma R - Q_{10})}{bk_2\Lambda_2(P_{01}Q_{10} - \Gamma^2 RS)} \left(1 - \frac{x^2}{a^2} - \frac{y^2}{b^2}\right)^{-1/2}. \quad (37)$$

Putting Eqs. (37) into the third equation in (22) of Part I, we calculate the normal stresses in the plane of the inclusion; we find that

$$\sigma_{zz}(x, y, 0) = \frac{p\omega(\Gamma_1 - \Gamma_2)}{\pi bk_2\Lambda_2(P_{01}Q_{10} - \Gamma^2 RS)} \left[(\Gamma S - P_{01}) \frac{\partial^0 W_{10}^{(\lambda)}}{\partial x} + (\Gamma R - Q_{01}) \frac{\partial^0 W_{01}^{(\lambda)}}{\partial y}\right]. \quad (38)$$

Using expressions (4) and ((A11) of Part I), we see that on the disk, the normal stresses are constant, being given by

$$\sigma_{zz}(x, y, 0) = \frac{2p\omega(\Gamma_1 - \Gamma_2)}{e^2k_2\Lambda_2(P_{01}Q_{10} - \Gamma^2 RS)} [(\Gamma S - P_{01})\{K(e) - E(e)\} + (\Gamma R - Q_{10})\{E(e) - k^2K(e)\}]. \quad (39)$$

Outside the inclusion, i.e., for $(x, y) \in \tilde{\Omega}$, we have

$$\sigma_{zz}(x, y, 0) = \frac{2p\omega(\Gamma_1 - \Gamma_2)}{e^2k_2\Lambda_2(P_{01}Q_{10} - \Gamma^2 RS)} [(\Gamma S - P_{01})\{F(\beta, e) - E(\beta, e)\} + (\Gamma R - Q_{10})\{E(\beta, e) - k^2F(\beta, e)\}] - \frac{2p(\Gamma_1 - \Gamma_2)\omega}{k_2\Lambda_2(P_{01}Q_{10} - \Gamma^2 RS)} \left[\frac{a\sqrt{\lambda}}{\sqrt{(a^2 + \lambda)(b^2 + \lambda)}} \times (\Gamma S - Q_{10}) + \frac{a^3x^2}{\sqrt{(a^2 + \lambda)^3\lambda D}} \sqrt{b^2 + \lambda} (\Gamma S - P_{01}) + \frac{ab^2y^2}{\sqrt{(b^2 + \lambda)^3\lambda D}} \sqrt{a^2 + \lambda} (\Gamma S - Q_{10})\right]. \quad (40)$$

The solution corresponding to the case of a rigid circular disk-inclusion can be obtained by letting $e \to 0$ in Eqs. (37), (39), and (40) and using the relations (9); the result is

$$\sigma_{xz}(x, y, 0) = \frac{-4px(\Gamma_1 - \Gamma_2)}{\pi k_2\Lambda_2(1 - \Gamma)\sqrt{a^2 - r^2}},$$

$$\sigma_{yz}(x, y, 0) = \frac{-4py(\Gamma_1 - \Gamma_2)}{\pi k_2\Lambda_2(1 - \Gamma)\sqrt{a^2 - r^2}},$$

$$\sigma_{zz}(x, y, 0) = \begin{cases} \dfrac{-2p(\Gamma_1 - \Gamma_2)\omega}{k_2\Lambda_2(1 - \Gamma)}, & 0 \le r \le a, \\ \dfrac{4p(\Gamma_1 - \Gamma_2)\omega}{\pi k_2\Lambda_2(1 - \Gamma)} \left[\left(\dfrac{a}{r}\right)^2 \sqrt{\dfrac{r^2}{a^2} - 1} + \dfrac{\left(\dfrac{a}{r}\right)^2}{\sqrt{\dfrac{r^2}{a^2} - 1}} - \sin^{-1}\dfrac{a}{r}\right], & r > a \end{cases} \quad (41)$$

so that the axisymmetric interfacial stress distribution is given by the formula

$$\sigma_{rz}(r) = \sqrt{\sigma_{xz}^2 + \sigma_{yz}^2} = \frac{4pr(\Gamma_1 - \Gamma_2)}{\pi k_2\Lambda_2(1 - \Gamma)\sqrt{a^2 - r^2}}, \quad 0 \le r < a,$$

Downloaded 04 May 2010 to 171.66.16.27. Redistribution subject to ASME license or copyright; see http://www.asme.org/terms/Terms_Use.cfm

$$\sigma_{zz}(x, y, 0) = \begin{cases} \dfrac{-2p(\Gamma_1 - \Gamma_2)\omega}{k_2\Lambda_2(1-\Gamma)}, & 0 \le r \le a, \\ \dfrac{4p(\Gamma_1 - \Gamma_2)\omega}{\pi k_2\Lambda_2(1-\Gamma)}\left[\left(\dfrac{a}{r}\right)^2 \sqrt{\dfrac{r^2}{a^2}-1} + \dfrac{\left(\dfrac{a}{r}\right)^2}{\sqrt{\dfrac{r^2}{a^2}-1}} - \sin^{-1}\dfrac{a}{r}\right], & r > a \end{cases} \quad (42)$$

For an isotropic body, formulae (42), with the use of the Eqs. (28), (29), and (30) of Part I, take the following form:

$$\sigma_{rz}(r, 0) = \frac{(1-\nu)^2}{(1+\nu)(3-4\nu)} \frac{8pr}{\pi\sqrt{a^2 - r^2}}, \quad 0 \le r \le a,$$

$$\sigma_{zz}(r, 0) = \begin{cases} \dfrac{-(1-2\nu)(1-\nu)p}{(1+\nu)(3-4\nu)}, & 0 \le r \le a, \\ \dfrac{2(1-2\nu)(1-\nu)p}{\pi(1+\nu)(3-4\nu)}\left[\left(\dfrac{a}{r}\right)^2 \sqrt{\dfrac{r^2}{a^2}-1} + \dfrac{\left(\dfrac{a}{r}\right)^2}{\sqrt{\left(\dfrac{r}{a}\right)^2-1}} - \sin^{-1}\dfrac{a}{r}\right], & r > a \end{cases} \quad (43)$$

Expression for $\sigma_{rz}(r, 0)$ in Eqs. (43) is in agreement with the result obtained by Alexandrov et al. (1993) (Alexandrov et al. did not calculate the normal stresses).

Finally, let us evaluate the displacement field outside the inclusion. Putting (37) into the first equations in (22) of Part I, we have

$$u(x, y, 0) = \frac{-k_2\Lambda_2}{2\pi c_{44}}(\eta_1^0 W_{10}^{(\lambda)} - \eta_2\Gamma^0 B_{10}^{(\lambda)} + \eta_2\Gamma^0 C_{10}^{(\lambda)}),$$

$$v(x, y, 0) = \frac{-k_2\Lambda_2}{2\pi c_{44}}, \quad (\eta_2^0 W_{01}^{(\lambda)} - \eta_1\Gamma^0 A_{01}^{(\lambda)} + \eta_1\Gamma^0 C_{10}^{(\lambda)}) \quad (44)$$

where the following notations are introduced:

$$\eta_1 = \frac{2(\Gamma_1 - \Gamma_2)(\Gamma S - P_{01})}{bk_2\Lambda_2(P_{01}Q_{10} - \Gamma^2 RS)},$$

$$\eta_2 = \frac{2(\Gamma_1 - \Gamma_2)(\Gamma R - Q_{10})}{bk_2\Lambda_2(P_{01}Q_{10} - \Gamma^2 RS)}. \quad (45)$$

The particular forms of ${}^{(m)}W_{ij}^{(\lambda)}$, ${}^{(m)}A_{ij}^{(\lambda)}$, ${}^{(m)}B_{ij}^{(\lambda)}$, ${}^{(m)}C_{ij}^{(\lambda)}$ appearing in expressions (44) are given by Eqs. (5).

The solution corresponding to a rigid circular disk-inclusion can be obtained by letting $b \to a$ in (44) and using the relations (9); the result is

$$u(x, y, 0) = \frac{2c_{33}px}{\pi(c_{11}c_{33} + c_{12}c_{33} - 2c_{13}^2)}\left(\sin^{-1}\frac{a}{r} - \frac{a}{r}\sqrt{1 - \frac{a^2}{r^2}}\right),$$

$$v(x, y, 0) = \frac{2c_{33}py}{\pi(c_{11}c_{33} + c_{12}c_{33} - 2c_{13}^2)} \times \left(\sin^{-1}\frac{a}{r} - \frac{a}{r}\sqrt{1 - \frac{a^2}{r^2}}\right) \quad (46)$$

so that the axisymmetric displacement field is given by

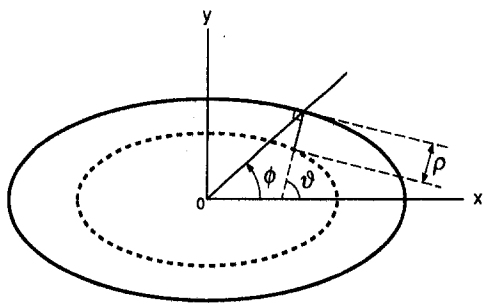


Fig. 1 Derivation of the asymptotic behavior of the stress field near the vicinity of the inclusion

$$u_r(r, 0) = u(x, y, 0)n_x + v(x, y, 0)n_y = \frac{2c_{33}pr}{\pi(c_{11}c_{33} + c_{12}c_{33} - 2c_{13}^2)}\left(\sin^{-1}\frac{a}{r} - \frac{a}{r}\sqrt{1 - \frac{a^2}{r^2}}\right),$$

$$u_\theta(r, 0) = 0, \quad u_z(r, 0) = 0. \quad (47)$$

Furthermore, the solution corresponding to the case of a rigid circular disk-inclusion in an isotropic medium can be obtained by using the relations ((28), Part I) with the result

$$u_r(r, 0) = u(x, y, 0)n_x + v(x, y, 0)n_y = \frac{(1-\nu)pr}{(1+\nu)\pi\mu}\left(\sin^{-1}\frac{a}{r} - \frac{a}{r}\sqrt{1 - \frac{a^2}{r^2}}\right),$$

$$u_\theta(r, 0) = 0, \quad u_z(r, 0) = 0. \quad (48)$$

2 The Singular Stress Field

From the viewpoint of fracture mechanics, it is of great interest to find the behavior of the stress field in the immediate vicinity of the edge of the inclusion. To this end, we construct a closed curve by displacing the contour of the ellipse by a very small amount ρ along the inward normal for $\sigma_{xz}(x, y, 0)$, $\sigma_{yz}(x, y, 0)$ (Fig. 1) and outward normal for $\sigma_{zz}(x, y, 0)$. From elementary geometry, it follows that the slope of the normal is

$$\tan\vartheta = \frac{a}{b}\tan\phi, \quad (49)$$

where ϑ is the angle between the normal and the x-axis and ϕ is the parametric angle of the ellipse (see Fig. 1). Then, the equation of the new curve is given by the relations:

$$x = a\cos\phi \mp \rho\cos\vartheta, \quad y = b\sin\phi \mp \rho\sin\vartheta, \quad (50)$$

where the minus sign corresponds to σ_{xz} and σ_{yz}, while the plus sign to σ_{zz}.

Now, putting (50) into Eqs. (11), (17), (28), (32), (37), and (40) and expanding the resulting expressions in ρ, we obtain for smaller ρ, the following expressions.

Problem 1:

$$\sigma_{xz}(x, y, 0) = \frac{-2c_{44}\delta\cos\beta}{k_2\Lambda_2 Q_{00}\sqrt{2\rho}\sqrt{b}(1 - e^2\cos^2\phi)^{1/4}} + O(\sqrt{\rho}),$$

$$\sigma_{yz}(x, y, 0) = \frac{-2c_{44}\delta\sin\beta}{k_2\Lambda_2 P_{00}\sqrt{2\rho}\sqrt{b}(1 - e^2\cos^2\phi)^{1/4}} + O(\sqrt{\rho}),$$

$$\sigma_{zz}(x, y, 0) = \frac{2\omega\delta c_{44}}{k_2\Lambda_2\sqrt{\rho}\sqrt{b}(1 - e^2\cos^2\phi)^{3/4}}\left(\frac{\sin\phi\sin\beta}{P_{00}} + k\frac{\cos\phi\cos\beta}{Q_{00}}\right) + O(\sqrt{\rho}) \quad (51)$$

Downloaded 04 May 2010 to 171.66.16.27. Redistribution subject to ASME license or copyright; see http://www.asme.org/terms/Terms_Use.cfm

Problem 2:

$$\sigma_{xz}(x, y, 0) = \frac{3M(P_{10} + \Gamma R)k^3 \sin\phi}{4\pi b^{5/2}[(P_{10} + \Gamma S)k^2 + (Q_{01} + \Gamma R)]\sqrt{2\rho}\,(1 - e^2\cos^2\phi)^{1/4}} + O(\sqrt{\rho}),$$

$$\sigma_{yz}(x, y, 0) = \frac{-3M(Q_{01} + \Gamma S)k^2 \cos\phi}{4\pi b^{5/2}[(P_{10} + \Gamma S)k^2 + (Q_{01} + \Gamma R)]\sqrt{2\rho}\,(1 - e^2\cos^2\phi)^{1/4}} + O(\sqrt{\rho}),$$

$$\sigma_{zz}(x, y, 0) = \frac{3M\omega k^2 \sin 2\phi}{8\pi b^2\sqrt{\rho}\,\sqrt{b}\,(1 - e^2\cos^2\phi)^{3/4}} \frac{Q_{01} + \Gamma S - k^2(P_{10} + \Gamma R)}{Q_{01} + \Gamma R + k^2(P_{10} + \Gamma S)} + O(\sqrt{\rho}). \quad (52)$$

Problem 3:

$$\sigma_{xz}(x, y, 0) = \frac{2p(\Gamma_1 - \Gamma_2)\sqrt{b}\,(\Gamma S - P_{01})\cos\phi}{kk_2\Lambda_2(P_{01}Q_{10} - \Gamma^2 RS)\sqrt{2\rho}\,(1 - e^2\cos^2\phi)^{1/4}} + O(\sqrt{\rho}),$$

$$\sigma_{yz}(x, y, 0) = \frac{2p(\Gamma_1 - \Gamma_2)\sqrt{b}(\Gamma R - Q_{10})\sin\phi}{kk_2\Lambda_2(P_{01}Q_{10} - \Gamma^2 RS)\sqrt{2\rho}(1 - e^2\cos^2\phi)^{1/4}} + O(\sqrt{\rho}),$$

$$\sigma_{zz}(x, y, 0) = \frac{-2p\omega(\Gamma_1 - \Gamma_2)\sqrt{b}}{\sqrt{\rho}k_2\Lambda_2(P_{01}Q_{10} - \Gamma^2 RS)(1 - e^2\cos^2\phi)^{3/4}}[\cos^2\phi(\Gamma S - P_{01}) + \sin^2\phi(\Gamma R - Q_{10})] + O(\sqrt{\rho}). \quad (53)$$

From Eqs. (51) to (53), we see that the material surrounding the elliptical disk-inclusion experiences both normal and edge-sliding kinematic movements. According to the Griffith-Irwin theory of fracture, these modes of fracture can be best described by their corresponding stress intensity factors, which may be extracted from the equations (51), (52), and (53).

Problem 1:

$$K_I = \frac{2\omega\delta c_{44}}{k_2\Lambda_2\sqrt{b}(1 - e^2\cos^2\phi)^{3/4}}\left(\frac{\sin\phi\sin\beta}{P_{00}} + k\frac{\cos\phi\cos\beta}{Q_{00}}\right),$$

$$K_{III} = \frac{2c_{44}\delta}{k_2\Lambda_2\sqrt{2}\,\sqrt{b}\,(1 - e^2\cos^2\phi)^{1/4}}\sqrt{\frac{\cos^2\beta}{Q_{00}^2} + \frac{\sin^2\beta}{P_{00}^2}}. \quad (54)$$

Problem 2:

$$K_I = \frac{3M\omega k^2 \sin 2\phi}{8\pi b^2\sqrt{b}(1 - e^2\cos^2\phi)^{3/4}} \frac{Q_{01} + \Gamma S - k^2(P_{10} + \Gamma R)}{Q_{01} + \Gamma R + k^2(P_{10} + \Gamma S)},$$

$$K_{III} = \frac{3Mk^2}{4\pi b^{5/2}[(P_{10} + \Gamma S)k^2 + (Q_{01} + \Gamma R)]\sqrt{2}\,(1 - e^2\cos^2\phi)^{1/4}} \times \sqrt{k^2(P_{10} + \Gamma R)^2\sin^2\phi + (Q_{01} + \Gamma S)^2\cos^2\phi}. \quad (55)$$

Problem 3:

$$K_I = \frac{-2p\omega(\Gamma_1 - \Gamma_2)\sqrt{b}}{k_2\Lambda_2(P_{01}Q_{10} - \Gamma^2 RS)(1 - e^2\cos^2\phi)^{3/4}}[\cos^2\phi(\Gamma S - P_{01}) + \sin^2\phi(\Gamma R - Q_{10})],$$

$$K_{II} = \frac{2p(\Gamma_1 - \Gamma_2)\sqrt{b}}{kk_2\Lambda_2(P_{01}Q_{10} - \Gamma^2 RS)\sqrt{2}\,(1 - e^2\cos^2\phi)^{1/4}} \times \sqrt{(\Gamma S - P_{01})^2\cos^2\phi + (\Gamma R - Q_{10})^2\sin^2\phi}. \quad (56)$$

It should be mentioned here that Kassir and Sih's (1968) result on K_I corresponding to Problem 1 is in error, their expression being in conflict with Eq. (21).

Table 1 Elastic constants for some transversely isotropic materials

	c_{11}	c_{12}	c_{13}	c_{33}	c_{44}
cadmium	12.1	4.81	4.42	5.13	1.85
beta-quartz	11.66	1.67	3.28	11.04	3.606
zinc	16.1	3.42	5.01	6.10	3.83
barium titanate	16.8	7.82	7.10	18.9	5.46
magnesium	5.97	2.62	2.17	6.17	1.64

Note: Above constants have units of 10^{11} dyne/cm^2.

3 Numerical Results

Because of the closed-form nature of the solutions, only some representative numerical results will be presented. The stress intensity factors for all three problems have been calculated for some transversely isotropic materials, namely, cadmium, zinc, beta quartz, barium titanate, and magnesium. The values of the elastic moduli c_{ij} of these materials are given in Table 1 (they are taken from Huntington's article (Seitz and Turnbull, 1958). All numerical results have been carried out for $e = 0.5$. Further, for Problem 1, numerical results have been carried out for the case where the shearing force T acts in the direction of the x-axis, i.e., $\beta = 0$. The stress intensity factors are normalized as follows:

For **Problem 1:**

$$\bar{K}_I^{(1)} = \frac{K_I\sqrt{b}}{\delta(c_{44})_{\text{zinc}}}, \quad \bar{K}_{III}^{(1)} = \frac{K_{III}\sqrt{b}}{\delta(c_{44})_{\text{zinc}}},$$

where $(c_{44})_{\text{zinc}}$ is the c_{44} of zinc.

For **Problem 2:**

$$\bar{K}_I^{(2)} = \frac{K_I b^2\sqrt{b}}{M}, \quad \bar{K}_{III}^{(2)} = \frac{K_{III}b^2\sqrt{b}}{M}.$$

For **Problem 3:**

$$\bar{K}_I^{(3)} = \frac{K_I}{p\sqrt{b}}, \quad \bar{K}_{II}^{(3)} = \frac{K_{II}}{p\sqrt{b}}.$$

Numerical results for these normalized stress intensity factors are plotted versus the parametric angle of the ellipse for cadmium, zinc, beta quartz, barium titanate, and magnesium. These results are shown in Figs. 2 to 6. Although numerical results are plotted for the range 0 to 90 degrees of the parametric angle of the ellipse, the results for the complete range, i.e., 0 to 360 degrees can be easily found by using the symmetric and antisymmetric properties of the solutions. It should be mentioned here that compressive model I stress intensity factors are observed for some of these materials. Such is the case with beta quartz and magnesium (for Problem 1), with all of the above-mentioned materials for Problem 2, and with zinc for Problem 3. This phenomenon is evidently indicative of the fact that the material particles at the edge of the inclusion interpenetrate into each other, thus rendering these results physically meaningless. It is likely that the phenomenon has connection with the violation of *factual compatibility* in the sense

Downloaded 04 May 2010 to 171.66.16.27. Redistribution subject to ASME license or copyright; see http://www.asme.org/terms/Terms_Use.cfm

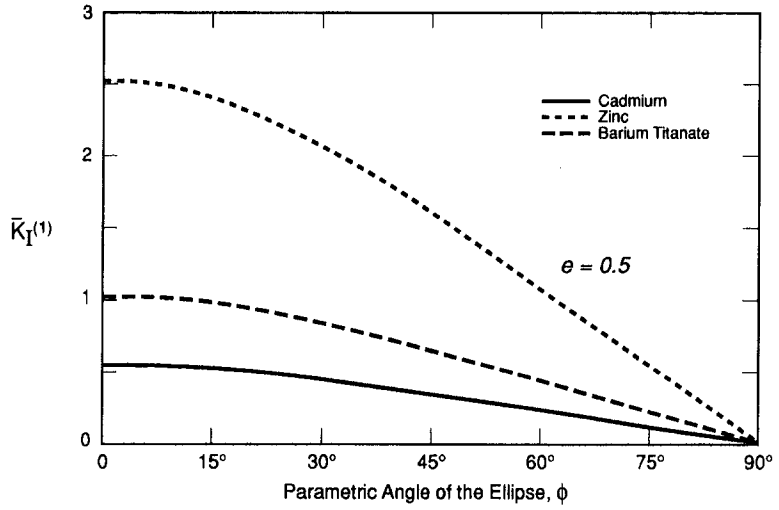


Fig. 2 Variations of the normalized mode I stress intensity factor with the parametric angle of the ellipse (problem 1)

of Savin and Rvachev. Factual compatibility is defined by Savin and Rvachev (1963a, b) as the deformation field in which the surface bounding any single connected part of the solid does not change its orientation in the process of deformation, i.e., the exterior of the part remains as exterior and interior as interior, which insures preclusion of interpenetration of material particles in the process of deformation. These authors also showed that although in the process of solving an elasticity problem correctly one takes into consideration the equilibrium equations, equations of compatibility, and the boundary conditions, nonetheless there are numerous problems whose solutions otherwise satisfying all these equations guarantee factual compatibility not everywhere in the medium. In the context of mixed boundary value problems, this phenomenon is discussed in greater detail in a recent article by Rahman (1999). Savin and Rvachev showed that for factual compatibility to be guaranteed in a region, the Jacobian of deformation should be positive, i.e.,

$$I(x_1, x_2, x_3) = \det\left[\delta_{ij} + \frac{\partial u_i}{\partial x_i}\right] > 0, \quad (\delta_{ij} \text{ is the Kronecker's delta}). \quad (57)$$

It is of significant interest to determine, using Eq. (57), the extent of the medium corresponding to the three problems considered in the article, where factual compatibility is violated. Knowing the extent of this region, one might proceed in different ways to derive a physically meaningful solution. First, one might model this region as a contact zone as is usually done in the area of interface crack problems. In the context of mixed boundary value problems, Savin and Rvachev showed that the pathological trend of violation of factual compatibility is essentially associated with the violation of factual compatibility in Boussinesq or Cerruti solutions, which enter into the integral equations of the mixed boundary value problems as kernels. It therefore seems reasonable to anticipate that physically meaningful solutions of our three problems should be based on starting with a modified Cerruti solution that is approximately equal to the Cerruti solution at a distance far from the plane $z = 0$ and that at the same time does not induce any violation of factual compatibility. In the context of the Boussinesq problem, Savin and Rvachev (1963a, b) (see also Rahman (1999)) showed how this could be achieved by using an interpolation scheme. However, the price of such a modification is extremely costly, because the modified Boussinesq or Cerruti

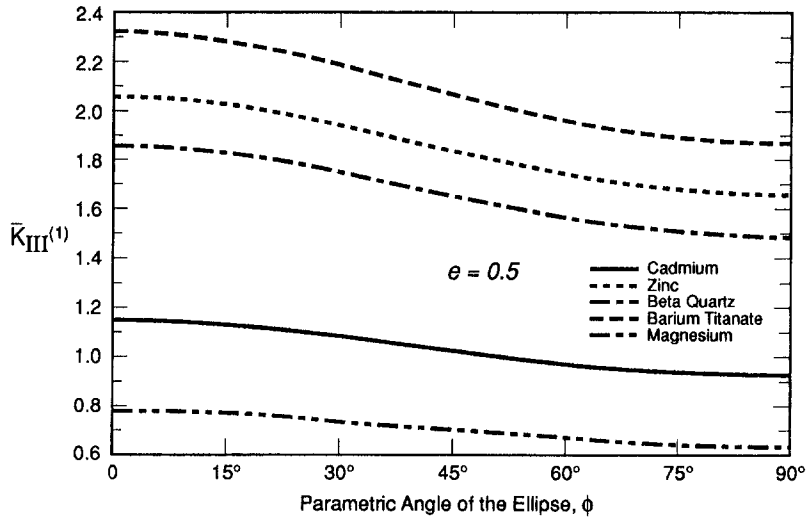


Fig. 3 Variations of the normalized mode III stress intensity factor with the parametric angle of the ellipse (problem 1)

Downloaded 04 May 2010 to 171.66.16.27. Redistribution subject to ASME license or copyright; see http://www.asme.org/terms/Terms_Use.cfm

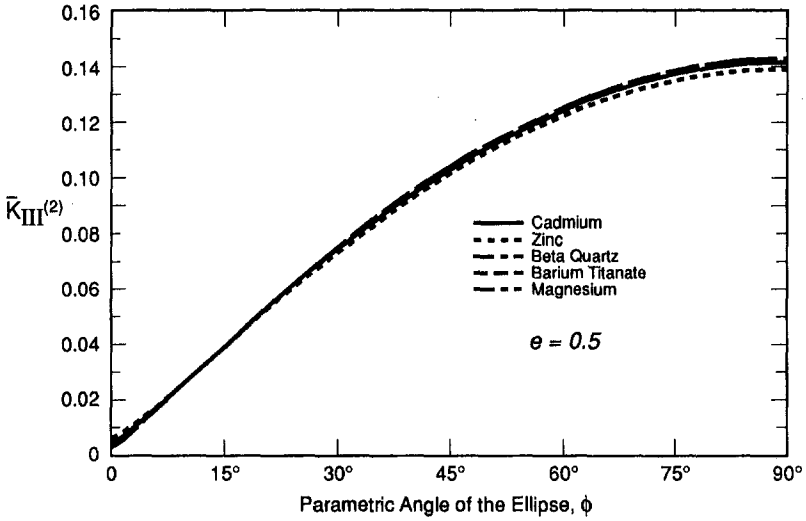


Fig. 4 Variations of the normalized mode III stress intensity factor with the parametric angle of the ellipse (problem 2)

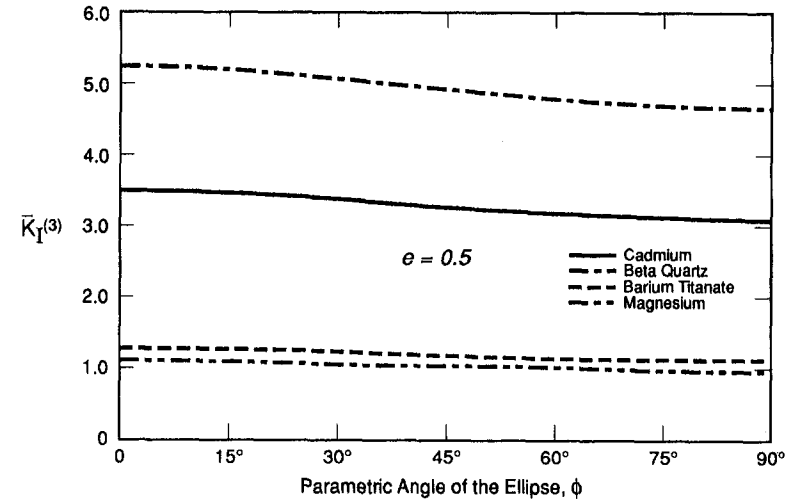


Fig. 5 Variations of the normalized mode I stress intensity factor with the parametric angle of the ellipse (problem 3)

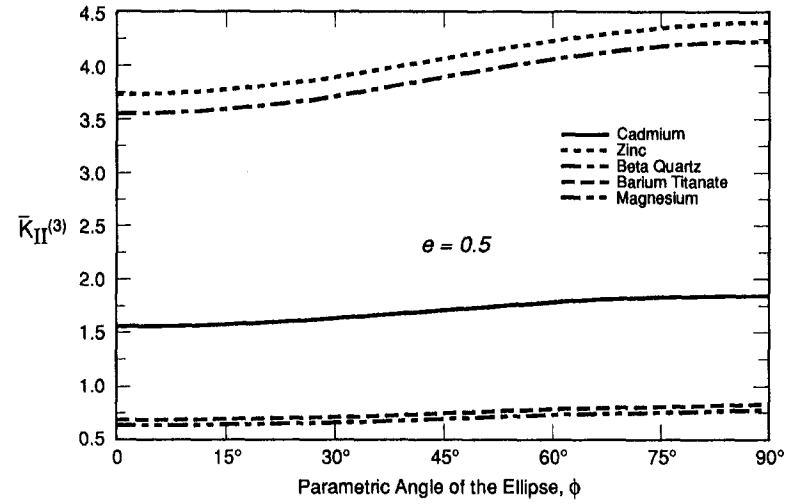


Fig. 6 Variations of the normalized mode II stress intensity factor with the parametric angle of the ellipse (problem 3)

Downloaded 04 May 2010 to 171.66.16.27. Redistribution subject to ASME license or copyright; see http://www.asme.org/terms/Terms_Use.cfm

solution ceases to be linear and hence we are deprived of using the superposition principle, the "blood" of linearized elasticity. In the context of our problems, the consequence of such a modification would be that we will no longer be able to formulate them in the form of integral equations. The problems will thus turn to be fully nonlinear and as such can be solved in an incremental fashion only. The writer hopes to cast some thoughts on this issue in a future communication.

Finally, having solutions for the stress intensity factors it is possible to postulate a failure criteria in terms of all three modes of stress intensity factors by means of which one can determine the critical failure load and the angle of initial crack propagation at the edge of the inclusion by using different failure models, e.g., that proposed by Andreikiv (1982). Alternatively, it may be possible to find a relationship involving the semi-axes of the elliptical inclusion or a combinations of them and the moduli of the transversely isotropic medium, violation of which will cause initiation and propagation of fractures near the edge of the inclusion. In isotropic elasticity, some solutions of this kind had been obtained by Sack (1946). It is of significant interest to see how Sack-type solutions extend over elliptical inclusions in transversely isotropic materials.

4 Concluding Remarks

In the present paper we have examined the elastostatic problem of an absolutely rigid elliptical inclusion in the form of a thin disk bonded in the interior of a transversely isotropic space. Three different loading schemes have been considered, namely, (a) the medium is under uniform stress field at infinity; (b) the inclusion is loaded by a shearing force in its plane; (c) the disk is rotated at an angle by a moment whose axis is perpendicular to its plane. The problems corresponding to all three cases, have been reduced, in a unified manner, to a system of integral equations. Closed-form solutions for these equations have been obtained by using Dyson's theorem. To the best of the writer's knowledge, these solutions are new. The method developed in the article can be employed to solve a number of new problems of a more complicated nature, such as, the problems of a system of elliptical disk-inclusions in a full-space/half-space and in a layer. Research in this direction will be reported elsewhere.

Acknowledgments

The author is indebted to the Associate Editor Professor M. J. Pindera for his insightful comments on an earlier version of the article. He also wishes to gratefully acknowledge the kind remarks from three anonymous reviewers.

References

Alexandrov, V. M., Smetanin, B. I., and Sobol, B. V., 1993, *Thin Stress Concentrators in Elastic Solids,* Nauka, Moscow (in Russian).

Andreikiv, A. E., 1982, *Spatial Crack Problems,* Naukova Dumka, Kiev (in Russian).

Dyson, F. W., 1891, "The Potentials of Ellipsoids of Variable Densities," *Quarterly Journal of Pure and Applied Mathematics, Oxford Series,* Vol. XXV, pp. 259–288.

Huntington, H. B., 1958, "The Elastic Constants of Crystals," *Solid State Physics,* ed. by F. Seitz and D. Turnbull, eds., Academic Press, San Diego, CA, pp. 213–351.

Kassir, M. K., and Sih, G. C., 1968, "Some Three-Dimensional Inclusion Problems in Elasticity," *International Journal of Solids & Structures,* Vol. 4, pp. 225–241.

Keer, L. M., 1965, "A Note on the Solution for Two Asymmetric Boundary Value Problems," *International Journal of Solids & Structures,* Vol. 1, pp. 257–264.

Rahman, M., 1999, "The Savin-Rvachev Observation on Violation of Factual Compatibility in Linear Elastostatics and Some of its Implications," *International Journal of Engineering Science,* Vol. 37, pp. 1277–1288.

Sack, R. A., 1946, "Extension of Griffith's Theory of Rapture to Three Dimensions," *Proceedings of the Physical Society,* Vol. 58, pp. 729–736.

Savin, G. N., and Rvachev, V. L., 1963a, "On the Violation of Compatibility of Deformation in Some Problems of the Theory of Elasticity," *Doklady of the Ukrainian SSR,* No. 3, pp. 354–357 (in Russian).

Savin, G. N., and Rvachev, V. L., 1963b, "On Formal and Factual Compatibility of Deformations," *Doklady of the Ukrainian SSR,* No. 1, pp. 35–39 (in Russian).

Downloaded 04 May 2010 to 171.66.16.27. Redistribution subject to ASME license or copyright; see http://www.asme.org/terms/Terms_Use.cfm

S.-Y. Luo
Associate Professor,
Department of Mechanical Engineering,
University of Nevada, Reno,
Reno, NV 89557
Mem. ASME

A. Mitra
Engineering Instructor,
Division of Arts and Science,
Western Nevada Community College,
Carson City, NV 89703
Mem. ASME

Finite Elastic Behavior of Flexible Fabric Composite Under Biaxial Loading

A new modeling technique has been introduced to predict the large deformation of flexible composites reinforced by plain-weave fabrics under biaxial loading. The only input required for calculations are the mechanical properties of the constituents and the fabric geometry. The constitutive equations are derived based on a strain energy approach, where fiber and matrix are accounted separately and the curved yarns are assumed to be in sinusoidal shape. Both material and geometrical nonlinearities are considered in the formulation. Good agreement has been found between predictions and experiments under various biaxial loading.

1 Introduction

Fabric-reinforced flexible composites, such as rubber-coated fabrics, can undergo relatively large deformation (about 30 percent for the material system in this work). They have very good formability while retaining high strength. There are many applications; for instance, air-bag material, surgical replacements, inflatable structures, etc.

Constitutive models for fabric composites with rigid matrix have been proposed by many researchers (Chou, 1992). Usually, the classical lamination theory is used in their analyses. However, under large deformation, high nonlinear mechanical behaviors have been observed from experiments on fabric-reinforced flexible composites. Especially under biaxial loading, the patterns of the nonlinear stress-strain curves are significantly different from those of unidirectional composite laminates. In some cases, despite the tensile loads applied in both x and y-directions, the strain in one of the directions could be negative at first, and then increase to a positive range (Stubbs, 1988; Luo and Mitra, 1995). This phenomenon can neither be observed in conventional composites nor explained by the Poisson's ratio effect. It is interesting to note that similar nonlinear patterns can be found in the biaxial test results of many soft biological tissues (for instance, Humphrey and Yin, 1988). The geometrical displacement of the reinforcements within the composite could be the major cause of such nonlinearity. The behavior of the fabric-reinforced flexible composites is also different from that of pure fabric. Because the fabric geometric displacement is restricted by the matrix (even with a very soft one), the composite becomes much harder (at the initial part of deformation) than pure fabric (Kawabata, 1988).

Many factors contribute to the fabric geometrical rearrangement, including the initial position of the yarns, biaxial load conditions, mechanical interaction between the yarns, and the properties of yarn and matrix. A change in any one of these factors may produce a significant change in the nonlinear pattern of the stress-strain relation. Because of the large nonlinear deformation, and especially because of the existence of large fabric-structure rearrangement, the theory of superposition is no longer applicable. In other words, the deformation of the composite under biaxial loading cannot be obtained by combining the results of that under the loads individually based upon the Hooke's Law.

To analyze the finite nonlinear deformations of rubber-coated fabrics, space truss models are often used (Clark, 1980; Testa and Yu, 1987; Stubbs, 1988). Usually in these models, the curved yarns and the pure matrix region are replaced by equivalent straight bars. It is therefore very critical to determine the parameters representing these equivalent truss structures; for example, the equivalent fiber orientation and the equivalent bar property representing the role of matrix. The determination of these parameters is difficult because the predictions are very sensitive to the parameters defined. Thus, biaxial experimental data for each particular fabric composite, used to determine the parameters through a regression analysis, are essential for truss models. Finite elastic deformation of flexible composites reinforced with both unidirectional and wavy fibers has been studied based on finite elasticity (Luo and Chou, 1988, 1990). However, the theories based on finite elasticity are difficult to apply to the study of fabric-reinforced flexible composites because nonhomogeneous deformation exists in the composite due to the complicated textile structure.

In the present work, a theoretical model has been proposed for the plain-weave fabric-reinforced flexible composites under biaxial large deformations. The constitutive equations are derived through a strain energy approach and energy variation theorem. Because of the nonhomogeneous deformation within the composite, the strain energies stored in fiber and in matrix are separately taken into account. Only the material properties of fiber and matrix, as well as the geometry of the fabric, are required as the input for the constitutive equations. The curved yarns in the composites are assumed to be in sinusoidal shape. These parameters with real physical meaning can be determined from the constituents directly, and no composite biaxial pretest is necessary. Both fiber material nonlinearity and geometrical nonlinearity caused by fabric rearrangement are considered in the theory. Comparisons have been made between theoretical predictions and experimental results obtained from biaxial tests of cruciform specimen. Good correlation has been found. This research approach may have the broad implications to study a class of materials where soft matrix is reinforced by curved fibers, such as textile composites and biotissues. In addition, this analysis may be extended to study the failure of fabric flexible composite under large deformation.

2 Bi-axial Deformation of an Unit-Cell

The composite used in this work is assumed to be a thin lamina consisting of a layer of woven fabric in a soft elastic matrix, which can sustain large deformation. Also, it is assumed that the yarns in

Contributed by the Applied Mechanics Division of THE AMERICAN SOCIETY OF MECHANICAL ENGINEERS for publication in the ASME JOURNAL OF APPLIED MECHANICS.
Discussion on the paper should be addressed to the Technical Editor, Professor Lewis T. Wheeler, Department of Mechanical Engineering, University of Houston, Houston, TX 77204-4792, and will be accepted until four months after final publication of the paper itself in the ASME JOURNAL OF APPLIED MECHANICS.
Manuscript received by the ASME Applied Mechanics Division, Sept. 30, 1998; final revision, Feb. 23, 1999. Associate Technical Editor: I. M. Daniel.

 Copyright © 1999 by ASME

Downloaded 04 May 2010 to 171.66.16.27. Redistribution subject to ASME license or copyright; see http://www.asme.org/terms/Terms_Use.cfm

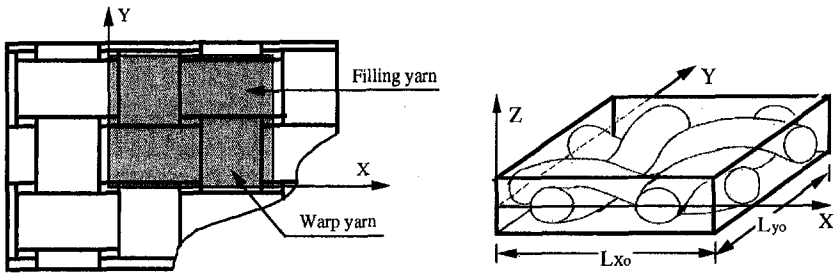


Fig. 1 (*a*) Plain weave fabric and (*b*) the unit cell

the fabric are elastic. Plain-weave fabric is the simplest form of orthogonal woven fabric, and is often used in coated-fabric structures. Therefore, it is chosen as the reinforcement material for this research. To understand the mechanical behavior of a fabric composite's structure, a unit-cell must first be identified. A unit-cell is the smallest representative element with a fabric structure similar to that of the whole. If a reliable constitutive equation for a unit-cell is established, the force-deformation relation of the whole fabric composite's structure can be determined (Ko et al., 1987).

2.1 Undeformed Unit-Cell. As shown in Fig. 1(*a*), a plain-weave fabric consists of two sets of interlaced yarns, "warp" and "filling." The warp yarn runs the length of the fabric and the filling yarn runs the width. The shaded area of Fig. 1(*a*) shows a selected unit-cell, which is sketched in Fig. 1(*b*) as a three-dimensional unit-cell of a plain-weave fabric composite. It contains two curved warp yarns and two curved filling yarns in a matrix, interlaced over and under one another.

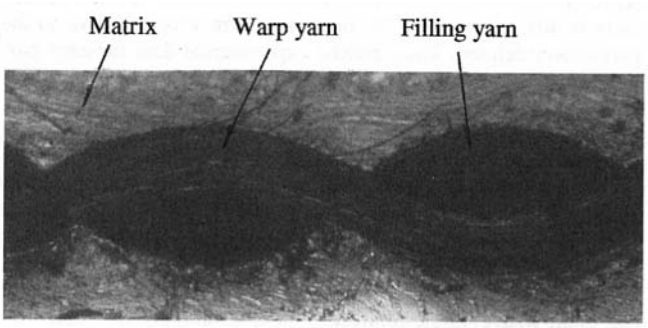


Fig. 2 Photograph of the cross section of a fabric composite

After examining the cross sections of fabric composite like the one shown in Fig. 2, the shape of a typical yarn in the longitudinal direction may be described as a sinusoidal curve. Referring to Fig. 1(*b*), let the coordinates x and y represent the filling and warp yarns' directions, and let z be the direction along the thickness of the plate. Hence, the position of the central line of a yarn (Fig. 3) is mathematically represented as

$$z = \pm a \sin\left(\frac{2\pi\xi}{L}\right) \tag{1}$$

where a and L represent the amplitude and wavelength of the sinusoidal curve along ξ (x or y) direction. The total length (S) of the yarn per unit wavelength (L) can be expressed as (Luo and Chou, 1990)

$$S = \int_0^L \sqrt{1 + \left(\frac{2\pi a}{L}\right)^2 \cos^2\left(\frac{2\pi\xi}{L}\right)}\, d\xi. \tag{2}$$

For mathematical simplicity, in this work, the right-hand integration is carried out numerically and a polynomial curve fitting is applied to the numerical results, which yields a quadratic relationship between (S/L) and $(a/L)^2$ as follows:

$$\frac{S}{L} = 1 + 9.6\left(\frac{a}{L}\right)^2 - 49.2\left[\left(\frac{a}{L}\right)^2\right]^2. \tag{3}$$

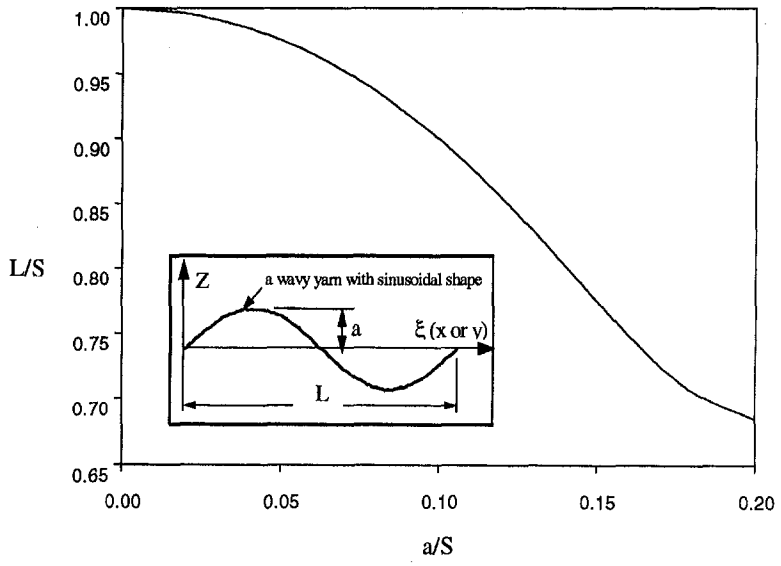


Fig. 3 Normalized relationship between wavelength (*L*) and amplitude (*a*) for a wavy yarn without stretch (i.e., *S* = constant)

Downloaded 04 May 2010 to 171.66.16.27. Redistribution subject to ASME license or copyright; see http://www.asme.org/terms/Terms_Use.cfm

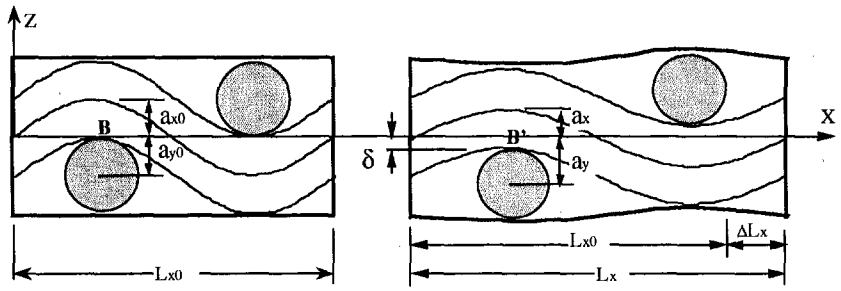


Fig. 4 Change in amplitude due to a rigid body displacement, δ along the *x*-axis; (*a*) undeformed element and (*b*) deformed element

The above equation is obtained in the range of $0.0 \leq a/L \leq 0.25$ with a correlation coefficient of 0.9997. It can be noted that when $a/L = 0$ (in absence of undulation), the total length of the yarn equals the wavelength, while for $a/L = 0.25$, the total length of the yarn is about 1.4 times the wavelength. Figure 3 is a plot of Eq. (3), which shows the normalized relationship between the wave length (L) and amplitude (a) for a yarn with constant length (S). Strong dependence between a and L can be observed.

2.2 Deformation of a Unit-Cell. Consider a rectangular unit-cell subjected to a biaxial deformation. The overall in-plane deformations of the unit-cell written in Lagrangian strains (Luo and Chou, 1990) are

$$E_{11} = \tfrac{1}{2}(g_{11}^2 + g_{21}^2 - 1)$$

$$E_{22} = \tfrac{1}{2}(g_{12}^2 + g_{22}^2 - 1)$$

$$E_{12} = E_{21} = \tfrac{1}{2}(g_{11}g_{12} + g_{21}g_{22}) \tag{4}$$

where g_{ij} are the deformation gradients. Because of no in-plane shear deformation, they are expressed as

$$g_{11} = \frac{L_x}{L_{x0}}$$

$$g_{22} = \frac{L_y}{L_{y0}}$$

$$g_{12} = g_{21} = 0 \tag{5}$$

where $L_{\xi 0}$ and L_ξ are the dimensions of the unit-cell before and after deformation. Referring to Fig. 1(*b*), $L_{\xi 0}$ and L_ξ ($\xi = x$ or y) also represent the original and current wavelengths of a yarn, respectively.

2.3 Yarn Deformation. During large deformation, the yarn in the composite moves in accordance with the overall composite deformation by means of the fabric geometric rearrangement and yarn axial extension. The geometric rearrangement is mainly achieved through the yarns' vertical movements to keep the yarns less axially stretched. Although the axial strain of a yarn is much smaller than the deformation range of the matrix, it affects the composite behavior significantly. Because fiber is much stiffer than matrix, it absorbs much of the energy stored in a deformed composite.

To determine the axial strain of a yarn, it is assumed that the yarns retain sinusoidal shape after deformation. With Eq. (3), the current total length (S_ξ) of a deformed yarn can be defined by its current amplitude (a_ξ) and wavelength (L_ξ). Thus, the axial extension of the yarn is $S_\xi - S_{\xi 0}$, and the average axial engineering strain of the yarn is expressed as

$$\epsilon_{f-\xi} = \frac{S_\xi - S_{\xi 0}}{S_{\xi 0}} = \frac{L_\xi}{S_{\xi 0}}\left[1 + 9.6\left(\frac{a_\xi}{L_\xi}\right)^2 - 49.2\left(\frac{a_\xi}{L_\xi}\right)^4\right] - 1. \tag{6}$$

The subindex ξ represents x and y-yarn.

Unlike a unidirectional fiber laminate, for fabric composites, there is a strong mechanical interaction between x and y-yarns during fabric rearrangement. This is illustrated in Fig. 4, showing the x-z cross-sectional plane of a unit-cell before and after deformation, where an x-yarn runs through the element and the cross sections of two y-yarns are presented by the shadowed areas. At the contact points of the x and y-yarns (i.e., point B of Fig. 4(*a*)), the vertical displacements of the two yarns always remain complementary. When B moves down to B′ with a vertical displacement δ, the amplitude of the x-yarn (a_x) decreases while that of the y-yarn increases. For a unit-cell with given deformed lengths, L_x and L_y, this displacement will increase the stretching level of y-yarns and release the tension in x-yarns. To achieve a stable position, the contact points must move optimally to minimize the energy stored in the unit-cell. Thus, the axial strains of the yarns ($\epsilon_{f\text{-}x}$ and $\epsilon_{f\text{-}y}$) are not only functions of the in-plane deformation of the unit-cell, but also coupled through the complementary change in undulation of the x and y-yarns. This coupling effect between warp and filling yarns makes the bi-axial behaviors of the flexible fabric composites significantly different from unidirectional fiber laminates, and has a strong influence on the nonlinear patterns of the biaxial stress-strain curves.

The change in amplitude of a yarn is due to two different factors: (1) vertical displacement at the contact points as discussed above, and (2) yarn strain in the z (thickness) direction. They are demonstrated in Fig. 4 and Fig. 5, where Fig. 4(*a*) and 5(*a*) are identical. For an element with a deformation ΔL_x, without considering the z-strain, the vertical rigid-body displacements occur along the element with the maximum value δ at the contact points (Fig. 4(*b*)). The magnitudes of the amplitude change for both x and y yarns are equal, δ, but a_x decreases while a_y increases. In Fig. 5(*b*), the element also has a deformation ΔL_x, while the contact point remains at its original vertical position. In this case, the change of the amplitude is due to the z-direction strain caused by in-plane deformations through Poisson's ratio. Near the contact point, the warp and filling yarns may be considered as a 0 deg/90 deg crossover bar structure. Since the yarn is much stiffer in the axial direction, it is assumed that the yarns carry all the applied forces parallel to them in the crossover areas. Thus, the strain of the longitudinal yarn is also the strain of the crossover structure in this direction. Let a unit-cell, with two filling yarns and two warp yarns, be subjected to the bi-axial stress resultants of N_{xx} and N_{yy}. At the crossover areas, the yarn strains in the z-direction due to the Poisson's ratio effect can be estimated as

$$\epsilon_z = -\mu_f \frac{\sigma_{f-x}}{E_f} - \mu_f \frac{\sigma_{f-y}}{E_f} = -\mu_f \frac{N_{xx}L_{y0} + N_{yy}L_{x0}}{2A_fE_f} \tag{7}$$

where, E_f is the yarn initial modulus, μ_f is the fiber Poisson's ratio, and A_f is the yarn cross-sectional area. Notice that same material properties are assumed for both x and y-yarns. If the mechanical properties of the yarns are not identical, Eq. (7) needs to be modified accordingly. By accommodating both aspects demon-

Downloaded 04 May 2010 to 171.66.16.27. Redistribution subject to ASME license or copyright; see http://www.asme.org/terms/Terms_Use.cfm

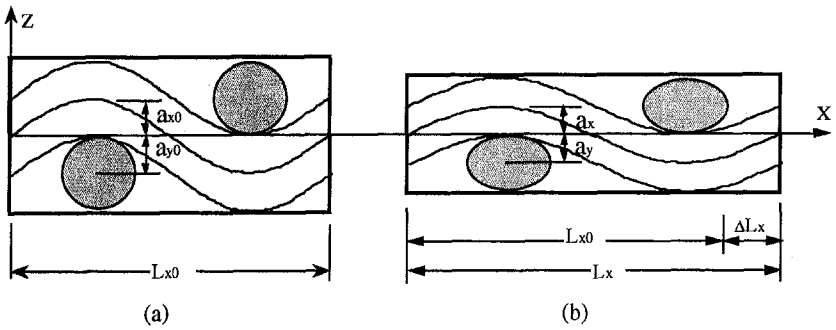


Fig. 5 Change in amplitude due to thickness strain along the *z*-axis; (*a*) undeformed element and (*b*) deformed element

strated in Figs. 4 and 5, the current amplitudes of the deformed yarns are written as

$$a_x = a_{x0}(1 + \epsilon_z) - \delta$$
$$a_y = a_{y0}(1 + \epsilon_z) + \delta. \tag{8}$$

It should be noted that the change in amplitude may be ignored for rigid matrix fabric composite, because the coupling effect between x and y-yarns is insignificant. However, for fabric-reinforced flexible composites under large deformation, both of these factors are no longer negligible. Otherwise, the important linkages between x and y-yarns remain unaccounted. This may be the major reason why the composite lamination theory can not be applied to fabric flexible composites under large biaxial deformation.

2.4 Bending Deformation. Referring to Fig. 4(*b*), the out-of-plane deformation causes the bending of the unit-cell and the yarns, the midplane lateral deflection (w) of the unit-cell may be described by a double sine function:

$$w = -\delta \operatorname{Sin} \frac{2\pi x}{L_{x0}} \operatorname{Sin} \frac{2\pi y}{L_{y0}}. \tag{9}$$

3 Strain Energy in a Deformed Unit-Cell

Due to the nonhomogeneous deformation within the unit-cell, the strain energy stored in fiber and matrix are calculated separately in terms of the overall deformation of the unit-cell (i.e., L_x, L_y, and δ). Let the total strain energy stored in a unit-cell be U, and

$$U = U_f + U_m + U_b \tag{10}$$

where U_f is the energy due to the axial strain of yarns, U_m is the in-plane strain energy stored in the matrix, and U_b is the bending energy due to the lateral deflection.

3.1 Axial Strain Energy in Yarns. Within a unit-cell, there are two x-yarns and two y-yarns with length S_{x0} and S_{y0}, respectively. The total strain energy due to the axial strain of all yarns is written as

$$U_f = 2A_f[S_{x0}(\tfrac{1}{2}E_f\epsilon_{f-x}^2 + \tfrac{1}{4}E_{f3}\epsilon_{f-x}^4 + \tfrac{1}{6}E_{f5}\epsilon_{f-x}^6) + S_{y0}(\tfrac{1}{2}E_f\epsilon_{f-y}^2 + \tfrac{1}{4}E_{f3}\epsilon_{f-y}^4 + \tfrac{1}{6}E_{f5}\epsilon_{f-y}^6)]. \tag{11}$$

This function is based on a one-dimensional nonlinear stress-strain ($\sigma_f - \epsilon_f$) relationship of a yarn:

$$\sigma_f = \frac{\partial U_f}{\partial \epsilon_f} = (E_f\epsilon_f + E_{f3}\epsilon_f^3 + E_{f5}\epsilon_f^5) \tag{12}$$

where E_f is the initial yarn modulus, E_{f3} and E_{f5} are the constants representing the nonlinear behavior of the yarn. They are obtained from the curve fitting to the experimental results (Luo and Mitra, 1995). If the yarn is linear, the nonlinear terms E_{f3} and E_{f5} in the above equation can be dropped. Also, if the properties of x and y-yarns are not identical, different values of the constants should be specified for x and y-yarns.

3.2 Strain Energy in Matrix. With no in-plane shear deformation, the energy stored due to the in-plane deformation of the matrix can be expressed in terms of Lagrangian strains as follows:

$$U_m = \frac{E_m V}{2(1 - \mu_m^2)}(E_{11}^2 + E_{22}^2 + 2\mu_m E_{11}E_{22}) \tag{13}$$

where E_m is the matrix modulus, μ_m is the matrix Poisson's ratio, and V ($=L_{x0}L_{y0}t_0$) is the total volume of a unit-cell. Notice that due to the existence of the transverse direction yarns, the actual effective modulus, Poison's ratio, and the volume of the matrix may vary. However, the matrix is much softer and less important than the yarns for flexible composites in terms of storing energy. Thus, the assumptions used in Eq. (13) for the matrix material simplify the requirements for input information, but has minimal impact on the predictions. Parametric study (Luo and Taban, 1999) has also shown that only negligible difference has been found in the predicted results by varying these parameters for the material system used in this work.

3.3 Bending Energy. Even under in-plane loading, bending deformation takes place due to fabric rearrangements. Referring to Eq. (9), the bending energy is associated with the vertical displacement δ, and the following form is assumed:

$$U_b = \tfrac{1}{2}K\delta^2, \tag{14}$$

where K is the effective stiffness coefficient relating the bending energy and the vertical displacement. The K may be determined experimentally through a unidirectional tensile test (Luo and Taban, 1999). For preliminary design purpose, where the actual composite specimen is not available, the following provides an analytical estimation.

The energies of yarn bending and matrix bending are treated separately. Because the maximum strain of yarn due to bending is much smaller than that due to yarn axial extension, only the initial modulus (E_f) is used in estimating the yarn bending energy. For simplicity, one-half of a yarn is assumed as a straight beam with length $S_0/2$ and simply supported. It is subjected to a central load at the contact point with a deflection δ. Using the simple beam theory of deflection and the principle of conservation of energy, we have

$$\text{Energy in a half of a yarn} = \frac{1}{2}\left\{\frac{48E_fI_f\delta}{(S_{g0}/2)^3}\right\}\delta = 192\,\frac{E_fI_f}{(S_{g0})^3}\,\delta^2 \tag{15}$$

where $I_f = (A_f^2/4\pi^2)$ is the moment of inertia of a yarn, and a circular cross section is assumed.

The matrix bending energy is determined as a plate of the size

Downloaded 04 May 2010 to 171.66.16.27. Redistribution subject to ASME license or copyright; see http://www.asme.org/terms/Terms_Use.cfm

of the unit-cell subjected to the deformation of Eq. (9) (Timoshenko and Woinowsky, 1959)

$$U_{mb} = \frac{D}{2}\int_0^{L_{x0}}\int_0^{L_{y0}}\left\{\left(\frac{\partial^2 w}{\partial x^2}+\frac{\partial^2 w}{\partial y^2}\right)^2 - 2(1-\mu_m)\left[\frac{\partial^2 w}{\partial x^2}\frac{\partial^2 w}{\partial y^2}-\left(\frac{\partial^2 w}{\partial y \partial x}\right)^2\right]\right\}dxdy \quad (16)$$

where $D = (E_m t_o^3/12(1-\mu_m^2))$ and t_0 is the thickness of the unit-cell. From Eqs. (9), (15), (16), and considering four yarns in a unit-cell, the total bending energy is

$$U_b = 2D\pi^4\delta^2\left(\frac{1}{L_{x0}^2}+\frac{1}{L_{y0}^2}\right)^2 L_{x0}L_{y0} + 768\left[\frac{1}{(S_{x0})^3}+\frac{1}{(S_{y0})^3}\right]E_f I_f \delta^2. \quad (17)$$

Referring to Eq. (14), the estimated K is

$$K = 4D\pi^4\left(\frac{1}{L_{x0}^2}+\frac{1}{L_{y0}^2}\right)^2 L_{x0}L_{y0} + 1536\left[\frac{1}{(S_{x0})^3}+\frac{1}{(S_{y0})^3}\right]E_f I_f. \quad (18)$$

4 Constitutive Equation

Following Rivlin (1970), the constitutive relations associated with a strain energy function are written as

$$\Pi_{11} = \frac{1}{V}\frac{\partial U}{\partial g_{11}}$$

$$\Pi_{22} = \frac{1}{V}\frac{\partial U}{\partial g_{22}} \quad (19)$$

where Π_{ij} are the Lagrangian stress components (force per unit undeformed area). Because no external force is applied at the contact points along the z-direction, with the energy variation method, a third equation can be found,

$$0 = \frac{\partial U}{\partial \delta}. \quad (20)$$

The total strain energy (U) stored in a unit-cell is obtained by substituting Eqs. (11), (14), and (17) into Eq. (10). Notice that, with the expressions of Eqs. (4)–(6), U is in terms of the overall deformations L_x, L_y, and δ. With Eq. (5) and applying the chain rule, the following constitutive equations are obtained from Eqs. (19) and (20),

$$\Pi_{11} = \frac{1}{V}\left\{B_x\frac{\partial S_x}{\partial g_{11}} + W_{11}g_{11}\right\}$$

$$\Pi_{22} = \frac{1}{V}\left\{B_y\frac{\partial S_y}{\partial g_{22}} + W_{22}g_{22}\right\}$$

$$0 = B_x\frac{\partial S_x}{\partial \delta} + B_y\frac{\partial S_y}{\partial \delta} + 1536E_f I_f\left[\frac{1}{(S_{x0})^3}+\frac{1}{(S_{y0})^3}\right]\delta + 4D\pi^4\left(\frac{1}{L_{x0}^2}+\frac{1}{L_{y0}^2}\right)^2 L_{x0}L_{y0}\delta \quad (21)$$

where

$$B_\xi = 2A_f(E_f\epsilon_{f-\xi} + E_{f3}\epsilon_{f-\xi}^3 + E_{f5}\epsilon_{f-\xi}^5)$$

$$W_{11} = \frac{E_m V}{[1-(\mu_m)^2]}\{E_{11} + \mu_m E_{22}\}$$

$$W_{22} = \frac{E_m V}{[1-(\mu_m)^2]}\{E_{22} + \mu_m E_{11}\}$$

$$\frac{\partial S_x}{\partial g_{11}} = L_{x0}\left[1 - 9.6\left(\frac{a_x}{L_x}\right)^2 + 147.6\left(\frac{a_x}{L_x}\right)^4\right]$$

$$\frac{\partial S_y}{\partial g_{22}} = L_{y0}\left[1 - 9.6\left(\frac{a_y}{L_y}\right)^2 + 147.6\left(\frac{a_y}{L_y}\right)^4\right]$$

$$\frac{\partial S_x}{\partial \delta} = 196.8\left(\frac{a_x}{L_x}\right)^3 - 19.2\left(\frac{a_x}{L_x}\right)$$

$$\frac{\partial S_y}{\partial \delta} = -196.8\left(\frac{a_y}{L_y}\right)^3 + 19.2\left(\frac{a_y}{L_y}\right). \quad (22)$$

Equation (21) is the constitutive equation for the flexible composite reinforced by plain weave fabric under biaxial loading. It contains three nonlinear equations and five variables: L_x, L_y, δ, Π_{11}, and Π_{22}. Thus, once any two of these variables are specified, the remaining three unknowns can be solved numerically. In this work, a standard IMSL library routine is used for solving the nonlinear equations with the input of biaxial loads (i.e., Π_{11} and Π_{22}). If the biaxial deformations (i.e., L_x and L_y) are specified as the inputs, a typical spread sheet program may be used for predictions.

5 Comparative Study

In order to benchmark the theory developed, a comparative study has been conducted with experimental data. The material system examined is silicon elastomer matrix reinforced by plain-weave nylon fabric. The inputs in the theoretical predictions are the fabric geometry, material properties of matrix and fiber. These properties are obtained from the measurements of yarn and matrix. The biaxial test results used in the comparisons are obtained from cruciform specimens under various biaxial ratios of loading. The details regarding the experiments can be found in Luo and Mitra (1995) and Mitra (1995).

5.1 Material Properties. The stress-strain curve of the matrix (silicon elastomer) exhibits linear trend up to 30 percent of deformation, and $E_m = 1.69$ Mpa is measured. The experimental force-strain curve for a single yarn detached from the fabric is nonlinear and can be described by

$$F = A_f\sigma_f = 0.248\epsilon_f + 5.56\epsilon_f^3 - 40.9\epsilon_f^5 \text{ KN} \quad (23)$$

where A_f is the total fiber cross-sectional area of a yarn. Referring to Eq. (12), the following values are used in the constitutive equations: $E_f = 1.22$ Gpa, $E_{f3} = 27.3$ Gpa, and $E_{f5} = -201$ Gpa with $A_f = 0.2035$ mm^2. Notice that: (1) the yarn cross-sectional area may differ from the fiber cross-sectional area of a yarn. Since A_f and E_{fi} are always used together as a group of $A_f E_{fi}$ in the calculation, the definition difference will not affect the prediction as long as Eq. (23) is used. (2) Under compression, yarn property may differ from that in tension and local buckling may occur. In our calculation program, matrix property is assumed for yarn compression modulus for the possible situation where negative yarn strain occurs. (3) The yarn property of Eq. (23) is obtained from tensile tests of yarns detached from fabrics. The property may differ from the yarn detached from the composite where the fibers in the yarn are bonded by the matrix, the possible impact is commented in the discussion part. Typical Poisson's ratios of $\mu_f = 0.41$ and $\mu_m = 0.5$ are used for nylon and rubber, respectively. The undulations of the yarns are determined experimentally, and are described by the sinusoidal curve with the parameters $L_{x0} = 2.254$ mm, $L_{y0} = 2.304$ mm, $a_{x0} = 0.287$ mm, and $a_{y0} = 0.258$ mm.

5.2 Results and Discussion. Comparisons between theoretical predictions and experimental results, for specimen under var-

Downloaded 04 May 2010 to 171.66.16.27. Redistribution subject to ASME license or copyright; see http://www.asme.org/terms/Terms_Use.cfm

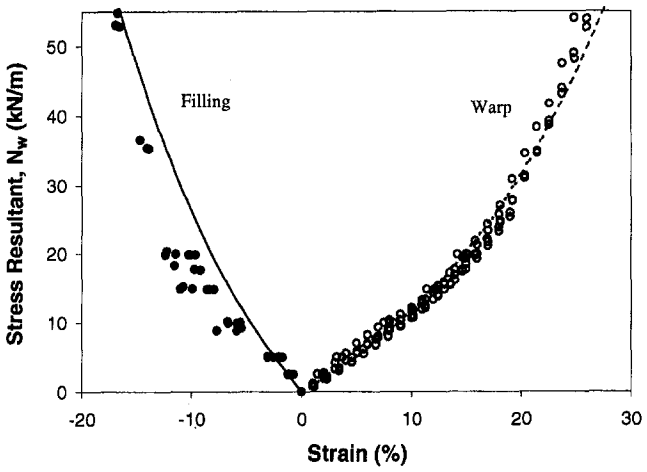


Fig. 6 Theoretical versus experimental results for specimens under uniaxial loading (N_f:N_w = 0:1)

ious biaxial loading ratios, are presented in graphical form (Figs. 6, 8, 9, and 10). For each case, stress resultant (kN/m) versus engineering strain (percent) is plotted for both filling and warp directions. The stress resultants applied in the warp and filling directions are represented as N_w and N_f, respectively. The experimental data are shown as legends, where the hollow and solid legends represent the warp and filling directions, respectively. Theoretical predictions are shown as lines, where the hatched lines represent the warp direction and the solid lines represent the filling.

Figure 6 is the comparisons for the specimen under uniaxial loading (N_f:N_w = 0:1), which is an extreme condition of biaxial deformation. The thickness of the specimens is 1.67 mm. In the loading direction (i.e., warp), theoretical predictions mostly agree with the experimental results. At the initial stage, the curved yarns tend to be straight with less axial stretching. This fabric rearrangement makes the composite "soft." When the fabric rearrangement becomes stable, the yarns carry most of the load and hence the composite becomes "stiff." This phenomenon is reflected by the energy distribution plotted in Fig. 7(*a*). The *x*-axis indicates the strain of warp yarn direction. The *y*-axis indicates the normalized energy in percentage, where the energies due to bending, yarn axial extension, and matrix in-plane deformation are normalized

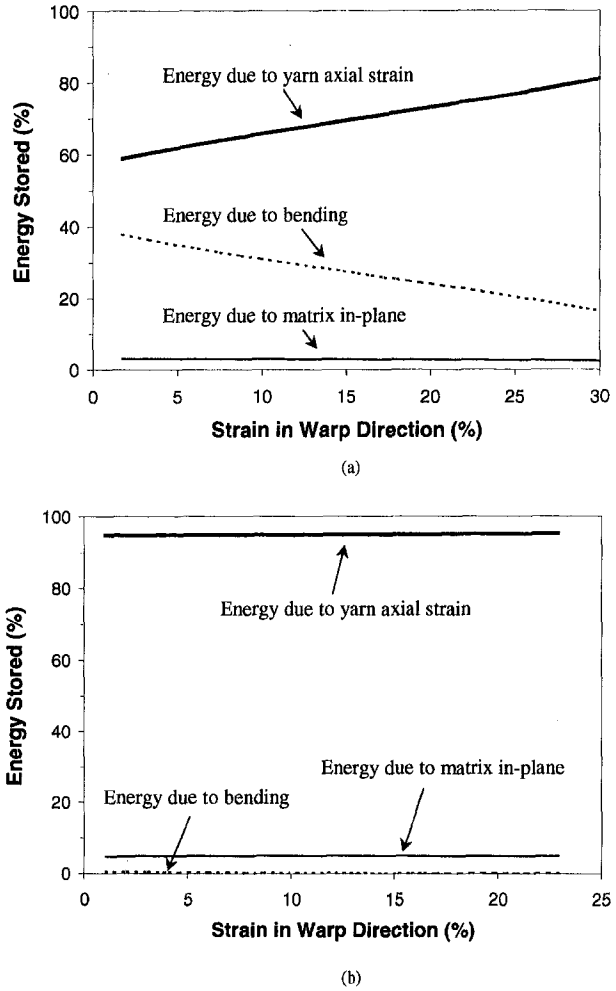


Fig. 7 Energy distribution in a deformed specimen under (*a*) uniaxial loading and (*b*) equibiaxial loading

by the total energy stored in the unit-cell. It can be observed that the bending energy is relatively high at the beginning, which indicates large fabric rearrangement. When the deformation in-

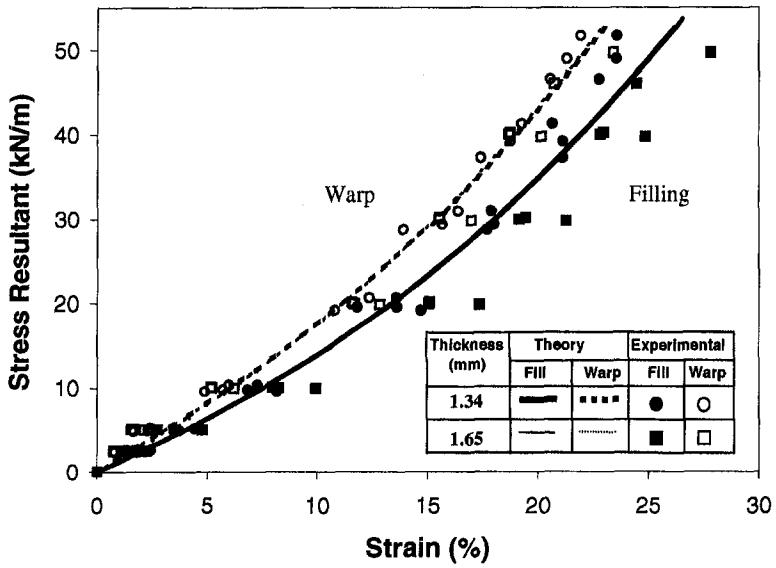


Fig. 8 Theoretical versus experimental results for specimens under equibiaxial loading (N_f:N_w = 1:1)

Downloaded 04 May 2010 to 171.66.16.27. Redistribution subject to ASME license or copyright; see http://www.asme.org/terms/Terms_Use.cfm

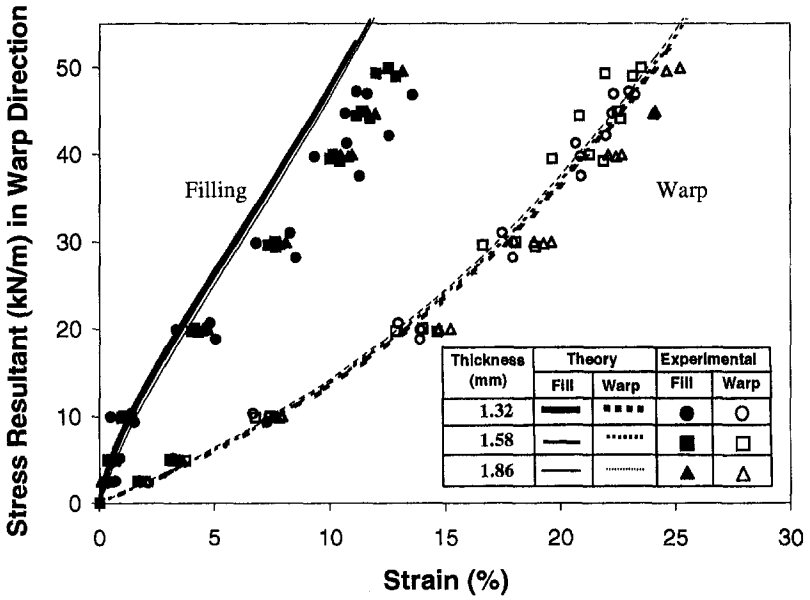


Fig. 9 Theoretical versus experimental results for specimens under biaxial loading (N_f:N_w = 1:2.5)

creases and fabric structure tends to be stable, the percentage of bending energy decreases while fiber energy increases. The energy stored in matrix due to in-plane strain is relatively small.

Figure 8 shows the comparison for the specimen under equibiaxial loading (N_f:N_w = 1:1), which is the other extreme condition of biaxial deformation. Two groups of specimens with different thickness (1.34 mm and 1.65 mm) are used. Notice that: (1) if the yarns in both directions were identical, identical stress-strain curves in both directions would be expected, with the δ in the Eq. (8) being zero. The difference observed in Fig. 8 is mainly caused by the slight difference in undulation of filling and warp yarns (the ratio of amplitude/wavelength). (2) thickness has very small effect for this equibiaxial loading case, which is observed from both predictions and experiments (Fig. 8) with the consideration of experimental uncertainties. This can be explained by the energy distribution plotted in Fig. 7(*b*), it shows that the bending energy and matrix energy are very small because only minimal fabric rearrangement occurs in this case. The additional energy stored in the thicker specimen is only due to the extra matrix layers at the top and bottom of the specimen, which is very small comparing to the total energy.

Similarly, comparisons for cases of N_f:N_w = 1:2.5 and N_f:N_w = 1:5 are shown in Figs. 9 and 10, respectively. In Fig. 9, there are three groups of specimen with thickness of 1.32 mm, 1.58 mm, and 1.86 mm. In Fig. 10, the specimen thickness is 1.29 mm. The y-axis is the magnitude of stress resultant applied in the warp direction (N_w). It is interesting to observe that, despite the positive loads applied, the strain in the filling direction decreases first (to a negative value) and then increases to a positive range. This phenomenon usually cannot be observed for conventional composites, which indicates that there is a strong mechanical interaction between the filling and warp yarns. At the initial stage, because the load in warp is larger than that in filling, the amplitude of the warp yarn decreases while the amplitude of filling yarn increases. To

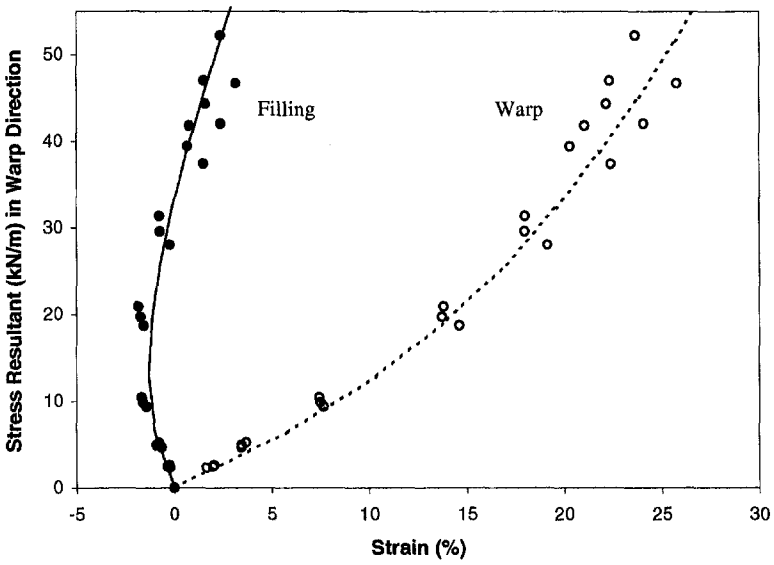


Fig. 10 Theoretical versus experimental results for specimens under biaxial loading (N_f:N_w = 1:5)

Downloaded 04 May 2010 to 171.66.16.27. Redistribution subject to ASME license or copyright; see http://www.asme.org/terms/Terms_Use.cfm

keep the filling yarns less stretched, its wavelength must be reduced and that forces the composite to shrink in the filling direction with the magnitude larger than the possible Poisson's effect of fiber and matrix. When the fabric rearrangement becomes stable, the deformations in both directions are positive due to the tensile loads.

In all the above cases, considering the finite deformation range and the experimental uncertainties, very good agreements between the predictions and experimental results are found. Notice that the following approximations of input have been used in the predictions: (1) The Effective stiffness coefficient K is estimated by Eq. (8), which is higher than experimentally measured value (Luo and Taban, 1999). (2) There is a slight difference in stiffness between actual warp and filling yarns (Luo and Mitra, 1995) and the average values are used in this work. (3) The yarn in the composite which fibers are impregnated with matrix may be stiffer than the pure yarn tested. Numerical simulations show that the modification of these factors will lead in a direction favorable to the results of this work. However, the modifications require more input information, but only give small improvement in prediction. Thus, it is not introduced in the course of this work. Besides, the compression property of yarn is not investigated, because in most of the cases of this work the yarns are in tension.

6 Conclusion

A new modeling technique is used to establish the constitutive model predicting the nonlinear, large deformation of flexible composites reinforced by plain-weave fabrics under biaxial loading. Due to fabric geometrical rearrangement during deformation, the patterns of the stress-strain curve of these composites differ from those of conventional composites. The constitutive equations derived are based on an energy approach, which counts the strain energies in fiber and in matrix separately. This model includes the geometric nonlinearity caused by the fabric rearrangement and the mechanical interaction between yarns, and the fiber material nonlinearity.

To apply the constitutive equations, no information from composite pretesting is required. Only the actual properties of the constituents are needed as inputs. Comparisons have been made between theoretical predictions and experiments for composites under various biaxial stress ratios. Good correlation has been found considering the large deformation range. This model may provide a basis for studying a class of composite materials where soft matrix is reinforced by wavy fibers, such as soft tissue. Also, the theoretical model used in this work may be extended to study the failure of fabric composites. These possibilities are under investigation.

Acknowledgments

The authors wish to acknowledge the support of the National Science Foundation and TREC grant (a Nevada EPSCoR project).

References

Chou, T. W., 1992, *Microstructural Design of Fiber Composites,* Cambridge University Press, New York.

Clark, S. K., 1980, "The Role of Textiles in Pneumatic Tires," *Mechanics of Flexible Fiber Assembles,* J. W. S. Hearle, J. J. Thwaites, and J. Amirbayat, eds., Sijthoff and Noordhoff, The Netherlands.

Humphrey, J. D., and Yin, F. C. P., 1987, "On Constitutive Relations and Finite Deformations of Passive Cardiac Tissue: I. A Pseudostrain-Energy Function," ASME *Journal of Biomechanical Engineering,* Vol. 109, pp. 298–304.

Kawabata, S., 1988, "Nonlinear Mechanics of Woven and Knitted Materials," *Textile Structural Composites,* edited by T. W. Chou and F. K. Ko, eds., Elsevier, Amsterdam.

Ko, F. K., Pastore, C. M., Lei, C., and Whyte, D. W., 1987, "A Fabric Geometry Model for 3-D Braid Reinforced FP/Al-Li Composites," 1987 International SAMPE Metals Conference, NJ.

Luo, S. Y., and Chou, T. W., 1988, "Finite Deformation and Nonlinear Elastic Behavior of Flexible Composites," ASME JOURNAL OF APPLIED MECHANICS, Vol. 55, pp. 149–155.

Luo, S. Y., and Chou, T. W., 1990, "Finite Deformation of Composites," *Proceedings of the Royal Society of London,* Vol. A429, pp. 569–586.

Luo, S. Y., and Taban, F., 1999, "Characterization of Flexible Fabric Composites Through a Uni-axial Test," under review.

Luo, S. Y., and Mitra, A., 1995, "An Experimental Study of Biaxial Behavior of Flexible Fabric Composite," *Innovative Processing and Characterization of Composite Material,* R. F. Gibson, T. W. Chou, and P. K. Raju, eds., ASME, New York, pp. 317–328.

Mitra, A., 1995, "Mechanical Behavior of Flexible Fabric Composite," Ph.D. dissertation, University of Nevada, Reno, NV.

Rivlin, R. S., 1970, *Centro Internazionale Matematico Estivo* (Ciclo, II and R. S. Rivlin eds., Edizioni Cremonese, Roma.

Stubbs, N., 1988, "Elastic and Inelastic Response of Coated Fabrics to Arbitrary Loading Paths," *Textile Structural Composites,* T. W. Chou and F. K. Ko, eds. Elsevier, Amsterdam.

Testa, B., and Yu, L. M., 1987, "Stress-Strain Relation for Coated Fabrics," *Journal of Engineering Mechanics,* Vol. 113, No. 11, pp. 1631–1646.

Timoshenko, S. P., and Woinowsky-Krieger, S., 1959, *Theory of Plates and Shells,* McGraw-Hill, New York.

Downloaded 04 May 2010 to 171.66.16.27. Redistribution subject to ASME license or copyright; see http://www.asme.org/terms/Terms_Use.cfm

The Full-Space Elastodynamic Green's Functions for Time-Harmonic Radial and Axial Ring Sources in a Homogeneous Isotropic Medium

Y. Lu
Southwestern Research Institute,
P.O. Drawer 28510,
San Antonio, TX 78228-0510
Mem. ASME

The elastodynamic Green's functions for time-harmonic radial and axial ring sources in a homogeneous, isotropic, linear elastic full-space medium are derived using the Fourier-Hankel transform. The Green's functions are found to have the same logarithmic singularities as the Legendre functions of positive and negative half-degree of the second kind. As the frequency approaches zero, the Green's functions approach the corresponding elastostatic Green's functions. The far-field displacement and stress components are also derived.

Introduction

In a previous paper (Lu, 1998), the elastodynamic Green's function in a homogeneous, isotropic, linear elastic full-space medium for a time-harmonic torsional ring source was derived using the Fourier-Hankel transform. The Green's function was found to have the same singularity as the Legendre function of half-degree of the second kind. As mentioned in the paper, torsional-guided elastic wave modes have indeed been generated in steel rods and tubes. The torsional wave modes are useful for detecting longitudinal flaws in cylindrical materials.

Most guided wave modes that are used in ultrasonic pipe or tube inspection, however, are longitudinal modes, because the longitudinal wave modes can be easily generated and detected (Ditri and Rose, 1992; Cawley and Alleyne, 1996; Kwun and Bartels, 1996). The longitudinal wave modes are useful for detecting transverse flaws and corrosion defects. While for a torsional mode the only nonvanishing displacement is the circumferential displacement, for a longitudinal mode there are two nonvanishing displacement components—axial and radial—which are coupled. This means that the equations of motion for a longitudinal wave mode must consist of two coupled equations.

Here we extend our previous work to the Green's functions for time-harmonic radial and axial ring sources. The medium is again homogeneous, isotropic, and linear elastic. The Green's functions are again derived using the Fourier-Hankel transform. The Green's functions are found to be functions of two basic integrals, which play the same pivotal role as the exponential function for the Green's functions for a point source, and the Hankel's function for the Green's functions for a line source (Achenbach, Gautesen, and McMaken, 1982). We show that the Green's functions have the same logarithmic singularities as the Legendre functions of positive and negative half-degree of the second kind. As the frequency approaches zero, the Green's functions approach the corresponding elastostatic Green's functions. The far-field displacement and stress components are also derived.

Contributed by the Applied Mechanics Division of THE AMERICAN SOCIETY OF MECHANICAL ENGINEERS for publication in the ASME JOURNAL OF APPLIED MECHANICS.
Discussion on the paper should be addressed to the Technical Editor, Professor Lewis T. Wheeler, Department of Mechanical Engineering, University of Houston, Houston, TX 77204-4792, and will be accepted until four months after final publication of the paper itself in the ASME JOURNAL OF APPLIED MECHANICS.
Manuscript received by the ASME Applied Mechanics Division, Oct. 10, 1998; final revision, Apr. 9, 1999. Associate Technical Editor: A. A. Mal.

Two Basic Integrals and Their Singularities

In the previous paper (Lu, 1998), an integral was evaluated:

$$I_1(r, z; r', z'; k) = \frac{1}{2}\int_0^\infty \frac{e^{-\sqrt{\xi^2-k^2}|z-z'|}}{\sqrt{\xi^2-k^2}} J_1(\xi r')J_1(\xi r)\xi d\xi$$

$$= \frac{e^{ik\sqrt{|z-z'|^2+r^2+r'^2}}}{2\pi\sqrt{rr'}} Q_{1/2}\left(\frac{|z-z'|^2+r^2+r'^2}{2rr'}\right)$$

$$+ \frac{e^{ik\sqrt{|z-z'|^2+r^2+r'^2}}}{2\sqrt{|z-z'|^2+r^2+r'^2}}$$

$$\times \sum_{n=0}^{\infty} \frac{1}{n!(n+1)!}\left(\frac{krr'}{2i\sqrt{|z-z'|^2+r^2+r'^2}}\right)^{2n+1}$$

$$\times \sum_{m=0}^{2n} \frac{(2n+1+m)!}{m!(2n+1-m)!}\left(\frac{i}{2k\sqrt{|z-z'|^2+r^2+r'^2}}\right)^m \quad (1)$$

where $I_1(r, z; r', z'; k)$ is the solution for the equation

$$\left(\nabla^2 - \frac{1}{r^2} + k^2\right) I_1(r, z; r', z'; k) = -\frac{\delta(r'-r)\delta(z'-z)}{r} \quad (2)$$

$$\nabla^2 = \frac{1}{r}\frac{\partial}{\partial r}\left(r\frac{\partial}{\partial r}\right) + \frac{\partial^2}{\partial z^2} \quad (3)$$

and has the same logarithmic singularity as the Legendre function of half-degree of the second kind at $r = r'$, $z = z'$. Using exactly the same manner, we can prove

$$I_2(r, z; r', z'; k) = \frac{1}{2}\int_0^\infty \frac{e^{-\sqrt{\xi^2-k^2}|z-z'|}}{\sqrt{\xi^2-k^2}} J_0(\xi r')J_0(\xi r)\xi d\xi$$

$$= \frac{e^{ik\sqrt{|z-z'|^2+r^2+r'^2}}}{2\pi\sqrt{rr'}} Q_{-1/2}\left(\frac{|z-z'|^2+r^2+r'^2}{2rr'}\right)$$

$$+ \frac{e^{ik\sqrt{|z-z'|^2+r^2+r'^2}}}{2\sqrt{|z-z'|^2+r^2+r'^2}}$$

 Copyright © 1999 by ASME

Downloaded 04 May 2010 to 171.66.16.27. Redistribution subject to ASME license or copyright; see http://www.asme.org/terms/Terms_Use.cfm

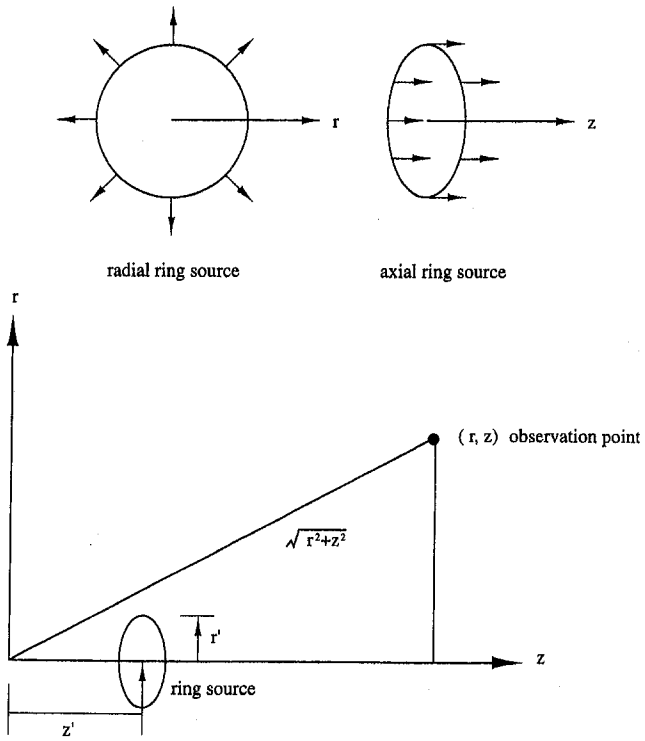


Fig. 1 A homogeneous, isotropic, linear elastic full-space medium with either a radial or an axial ring source

$$\times \sum_{n=1}^{\infty} \frac{1}{n!n!}\left(\frac{krr'}{2i\sqrt{|z-z'|^2+r^2+r'^2}}\right)^{2n}$$

$$\times \sum_{m=0}^{2n-1} \frac{(2n+m)!}{m!(2n-m)!}\left(\frac{i}{2k\sqrt{|z-z'|^2+r^2+r'^2}}\right)^{m} \quad (4)$$

where $I_2(r, z; r', z'; k)$ is the solution for the equation

$$(\nabla^2 + k^2)I_2(r, z; r', z'; k) = -\frac{\delta(r'-r)\delta(z'-z)}{r}. \quad (5)$$

Since (Abramowitz and Stegun, 1964)

$$Q_{-1/2}(z) = \sqrt{\frac{2}{1+z}}\,K\left(\sqrt{\frac{2}{1+z}}\right), \quad z \geq 1 \quad (6)$$

where $K(z)$ is the complete elliptic integral of the first kind and has the logarithmic singularity at $z = 1$ (Cayley, 1961), it follows that $I_2(r, z; r', z'; k)$ has the same logarithmic singularity at $r = r'$, $z = z'$.

The solutions for Eqs. (2) and (5) in the forms of semi-infinite integrals as in Eqs. (1) and (4) appeared before in many monographs (Stakgold, 1968; Felsen and Marcuvitz, 1973; Dudley, 1994).

The Green's Functions

Consider a homogeneous, isotropic, linear elastic full-space medium with a time-harmonic radial ring source (Fig. 1), varying as $e^{-j\omega t}$, where $\omega = 2\pi f$ is the circular frequency and f is the frequency. We use the cylindrical coordinate system (r, θ, z), and the ring source is located at $r = r'$, $z = z'$. Since the problem is axisymmetric, the only nonvanishing displacement components are $U_{rr}(r, z)$ and $U_{zr}(r, z)$, where the first subscript denotes the direction of the displacement, and the second one the direction of the ring source. The equations of motion for $U_{rr}(r, z)$ and $U_{zr}(r, z)$ are (Malvern, 1969)

$$(\lambda+2\mu)\frac{\partial}{\partial r}\left[\frac{1}{r}\frac{\partial}{\partial r}(rU_{rr})\right] + \mu\frac{\partial^2 U_{rr}}{\partial z^2} + (\lambda+\mu)\frac{\partial^2 U_{zr}}{\partial r \partial z} + \rho\omega^2 U_{rr} = -\frac{\delta(r'-r)\delta(z'-z)}{r} \quad (7a)$$

$$(\lambda+\mu)\frac{\partial}{\partial z}\left[\frac{1}{r}\frac{\partial}{\partial r}(rU_{rr})\right] + (\lambda+2\mu)\frac{\partial^2 U_{zr}}{\partial z^2} + \frac{\mu}{r}\frac{\partial}{\partial r}\left(r\frac{\partial U_{zr}}{\partial r}\right) + \rho\omega^2 U_{zr} = 0 \quad (7b)$$

where λ and μ are Lamé's elastic constants, and ρ is the density. The term

$$\frac{\delta(r'-r)\delta(z'-z)}{r}$$

represents the radial ring source.

We apply the Fourier transform to the axial coordinate, z, and the Hankel transform to the radial coordinate, r. The Fourier transform is defined as

$$U(r, z; r', z') = \frac{1}{2\pi}\int_{-\infty}^{\infty} U^*(r, \eta; r', z')e^{i\eta z}d\eta \quad (8a)$$

$$U^*(r, \eta; r', z') = \int_{-\infty}^{\infty} U(r, z; r', z')e^{-i\eta z}dz \quad (8b)$$

while the Hankel transform is defined as

$$U^*_{rr}(r, \eta; r', z') = \int_0^{\infty} \bar{U}^*_{rr}(\xi, \eta; r', z')J_1(\xi r)\xi d\xi \quad (9a)$$

$$\bar{U}^*_{rr}(\xi, \eta; r', z') = \int_0^{\infty} U^*_{rr}(r, \eta; r', z')J_1(\xi r)r dr \quad (9b)$$

$$U^*_{zr}(r, \eta; r', z') = \int_0^{\infty} \bar{U}^*_{zr}(\xi, \eta; r', z')J_0(\xi r)\xi d\xi \quad (9c)$$

$$\bar{U}^*_{zr}(\xi, \eta; r', z') = \int_0^{\infty} U^*_{zr}(r, \eta; r', z')J_0(\xi r)r dr \quad (9d)$$

where η and ξ are transform parameters, and $J_0(Z)$ and $J_1(Z)$ are the Bessel functions of the first kind.

Applying Eq. (8*b*) to Eqs. (7*a*) and (7*b*), we obtain

$$(\lambda+2\mu)\frac{\partial}{\partial r}\left[\frac{1}{r}\frac{\partial}{\partial r}(rU^*_{rr})\right] - \mu\eta^2 U^*_{rr} + i\eta(\lambda+\mu)\frac{\partial U^*_{zr}}{\partial r} + \rho\omega^2 U^*_{rr} = -\frac{\delta(r'-r)}{r}e^{-i\eta z'} \quad (10a)$$

$$i\eta(\lambda+\mu)\frac{1}{r}\frac{\partial}{\partial r}(rU^*_{rr}) - (\lambda+2\mu)\eta^2 U^*_{zr} + \frac{\mu}{r}\frac{\partial}{\partial r}\left(r\frac{\partial U^*_{zr}}{\partial r}\right) + \rho\omega^2 U^*_{zr} = 0. \quad (10b)$$

Applying Eqs. (9*b*) and (9*d*) to Eqs. (10*a*) and (10*b*), respectively, then yields

Downloaded 04 May 2010 to 171.66.16.27. Redistribution subject to ASME license or copyright; see http://www.asme.org/terms/Terms_Use.cfm

$$[\rho\omega^2 - (\lambda + 2\mu)\xi^2 - \mu\eta^2]\bar{U}^*_{rr} - i(\lambda + \mu)\xi\eta\bar{U}^*_{zr} = -J_1(\xi r')e^{-i\eta z'} \quad (11a)$$

$$i(\lambda + \mu)\xi\eta\bar{U}^*_{rr} + [\rho\omega^2 - \mu\xi^2 - (\lambda + 2\mu)\eta^2]\bar{U}^*_{zr} = 0. \quad (11b)$$

Using the Cramer's rule $\bar{U}^*_{rr}$ and $\bar{U}^*_{zr}$ can be obtained as

$$\bar{U}^*_{rr}(\xi, \eta; r', z') = -\frac{\omega^2 - c_L^2\eta^2 - c_T^2\xi^2}{\rho c_L^2 c_T^2[\eta^2 - (k_L^2 - \xi^2)][\eta^2 - (k_T^2 - \xi^2)]} J_1(\xi r')e^{-i\eta z'} \quad (12a)$$

$$\bar{U}^*_{zr}(\xi, \eta; r', z') = \frac{i(c_L^2 - c_T^2)\xi\eta}{\rho c_L^2 c_T^2[\eta^2 - (k_L^2 - \xi^2)][\eta^2 - (k_T^2 - \xi^2)]} J_1(\xi r')e^{-i\eta z'} \quad (12b)$$

where $c_L = \sqrt{(\lambda + 2\mu)/\rho}$ is the longitudinal velocity, $c_T = \sqrt{\mu/\rho}$ is the shear velocity, $k_L = \omega/c_L$ is the longitudinal wave number, and $k_T = \omega/c_T$ is the shear wave number.

Now we apply Eq. (8*a*) to Eqs. (12*a*) and (12*b*):

$$\bar{U}_{rr}(\xi, z; r', z') = -\frac{J_1(\xi r')}{2\pi\rho c_L^2 c_T^2}\int_{-\infty}^{\infty} \frac{(\omega^2 - c_L^2\eta^2 - c_T^2\xi^2)e^{i\eta(z-z')}}{[\eta^2 - (k_L^2 - \xi^2)][\eta^2 - (k_T^2 - \xi^2)]}\, d\eta \quad (13a)$$

$$\bar{U}_{zr}(\xi, z; r', z') = \frac{i(c_L^2 - c_T^2)}{2\pi\rho c_L^2 c_T^2} J_1(\xi r')\xi \times \int_{-\infty}^{\infty} \frac{\eta e^{i\eta(z-z')}}{[\eta^2 - (k_L^2 - \xi^2)][\eta^2 - (k_T^2 - \xi^2)]}\, d\eta. \quad (13b)$$

On the complex η-plane, the denominator in Eqs. (13*a*) and (13*b*) has four simple poles:

$$\eta = \pm\sqrt{k_T^2 - \xi^2}; \quad \eta = \pm\sqrt{k_L^2 - \xi^2}. \quad (14)$$

To satisfy the radiation condition, we choose

$$\eta_1 = \sqrt{k_T^2 - \xi^2}, \quad z > z' \quad (15a)$$

$$\eta_2 = -\sqrt{k_T^2 - \xi^2}, \quad z < z' \quad (15b)$$

$$\eta_3 = \sqrt{k_L^2 - \xi^2}, \quad z > z' \quad (15c)$$

$$\eta_4 = -\sqrt{k_L^2 - \xi^2}, \quad z < z' \quad (15d)$$

with

$$\mathrm{Im}(\sqrt{k_T^2 - \xi^2}) > 0, \quad \mathrm{Im}(\sqrt{k_L^2 - \xi^2}) > 0. \quad (16)$$

Using the Residual Theorem (Churchill, 1960), Eqs. (13*a*) and (13*b*) can be evaluated:

$$\bar{U}_{rr}(\xi, z; r', z') = -i\frac{J_1(\xi r')}{\rho c_L^2 c_T^2}\left\{\frac{\omega^2 - c_L^2(k_T^2 - \xi^2) - c_T^2\xi^2}{2(k_T^2 - k_L^2)\sqrt{k_T^2 - \xi^2}} e^{i\sqrt{k_T^2 - \xi^2}|z-z'|} + \frac{\omega^2 - c_L^2(k_L^2 - \xi^2) - c_T^2\xi^2}{2(k_L^2 - k_T^2)\sqrt{k_L^2 - \xi^2}} e^{i\sqrt{k_L^2 - \xi^2}|z-z'|}\right\} \quad (17a)$$

$$\bar{U}_{zr}(\xi, z; r', z') = -\frac{c_L^2 - c_T^2}{\rho c_L^2 c_T^2} \times J_1(\xi r')\xi\left\{\frac{e^{i\sqrt{k_T^2 - \xi^2}|z-z'|}}{2(k_T^2 - k_L^2)} + \frac{e^{i\sqrt{k_L^2 - \xi^2}|z-z'|}}{2(k_L^2 - k_T^2)}\right\}, \quad (17b)$$

but

$$\omega^2 - c_L^2(k_T^2 - \xi^2) - c_T^2\xi^2 = -(c_L^2 - c_T^2)(k_T^2 - \xi^2) \quad (18a)$$

$$\omega^2 - c_L^2(k_L^2 - \xi^2) - c_T^2\xi^2 = (c_L^2 - c_T^2)\xi^2 \quad (18b)$$

$$\frac{c_L^2 - c_T^2}{k_T^2 - k_L^2} = \frac{c_T^2}{k_L^2}. \quad (18c)$$

We have, after using the radiation condition Eq. (16),

$$\bar{U}_{rr}(\xi, z; r', z') = \frac{1}{2\rho\omega^2}\left\{-\sqrt{\xi^2 - k_T^2}e^{-\sqrt{\xi^2 - k_T^2}|z-z'|} + \frac{\xi^2}{\sqrt{\xi^2 - k_L^2}} e^{-\sqrt{\xi^2 - k_L^2}|z-z'|}\right\} J_1(\xi r') \quad (19a)$$

$$\bar{U}_{zr}(\xi, z; r', z') = -\frac{1}{2\rho\omega^2}\{e^{-\sqrt{\xi^2 - k_T^2}|z-z'|} - e^{-\sqrt{\xi^2 - k_L^2}|z-z'|}\} J_1(\xi r')\xi. \quad (19b)$$

Using the Eqs. (9*b*) and (9*d*), we then obtain

$$U_{rr}(r, z; r', z') = \frac{1}{2\rho\omega^2}\left\{-\int_0^{\infty} \sqrt{\xi^2 - k_T^2}e^{-\sqrt{\xi^2 - k_T^2}|z-z'|} J_1(\xi r')J_1(\xi r)\xi d\xi + \int_0^{\infty} \frac{e^{-\sqrt{\xi^2 - k_L^2}|z-z'|}}{\sqrt{\xi^2 - k_L^2}} J_1(\xi r')J_1(\xi r)\xi^3 d\xi\right\} \quad (20a)$$

$$U_{zr}(r, z; r', z') = \frac{-1}{2\rho\omega^2}\left\{\int_0^{\infty} e^{-\sqrt{\xi^2 - k_T^2}|z-z'|} J_1(\xi r')J_0(\xi r)\xi^2 d\xi - \int_0^{\infty} e^{-\sqrt{\xi^2 - k_L^2}|z-z'|} J_1(\xi r')J_0(\xi r)\xi^2 d\xi\right\}. \quad (20b)$$

We now show that the integrals appearing in Eqs. (20*a*) and (20*b*) can be obtained as derivatives of the integral in Eq. (1). Taking the derivatives of $I_1(r, z; r', z'; k)$ under the integral sign, we have

$$\frac{\partial^2}{\partial z^2} I_1(r, z; r', z'; k) = \frac{1}{2}\int_0^{\infty} \sqrt{\xi^2 - k^2}e^{-\sqrt{\xi^2 - k^2}|z-z'|} J_1(\xi r')J_1(\xi r)\xi d\xi \quad (21a)$$

$$\frac{\partial}{\partial r}\left\{\frac{1}{r}\frac{\partial}{\partial r}[rI_1(r, z; r', z'; k)]\right\} = -\frac{1}{2}\int_0^{\infty} \frac{e^{-\sqrt{\xi^2 - k^2}|z-z'|}}{\sqrt{\xi^2 - k^2}} J_1(\xi r')J_1(\xi r)\xi^3 d\xi \quad (21b)$$

$$\frac{1}{r}\frac{\partial}{\partial r}\left[r\frac{\partial I_1(r, z; r', z'; k)}{\partial z}\right] = -\frac{1}{2}\int_0^{\infty} e^{-\sqrt{\xi^2 - k^2}|z-z'|} J_1(\xi r')J_0(\xi r)\xi^2 d\xi. \quad (21c)$$

Substituting Eqs. (21*a*), (21*b*), and (21*c*) into Eqs. (20*a*) and (20*b*), we then obtain

Downloaded 04 May 2010 to 171.66.16.27. Redistribution subject to ASME license or copyright; see http://www.asme.org/terms/Terms_Use.cfm

$$U_{rr}(r, z; r', z') = \frac{1}{\rho\omega^2}\left\{-\frac{\partial^2 I_1(r, z; r', z'; k_T)}{\partial z^2} - \frac{\partial}{\partial r}\left(\frac{1}{r}\frac{\partial}{\partial r}[rI_1(r, z; r', z'; k_L)]\right)\right\} \quad (22a)$$

$$U_{zr}(r, z; r', z') = \frac{1}{\rho\omega^2}\frac{1}{r}\frac{\partial}{\partial r}\left\{r\frac{\partial}{\partial z}[I_1(r, z; r', z'; k_T) - I_1(r, z; r', z'; k_L)]\right\}. \quad (22b)$$

Since $I_1(r, z; r', z'; k)$ satisfies Eq. (2), and $\omega^2 = k_T^2 c_T^2 = k_T^2\mu/\rho$, we finally obtain

$$U_{rr}(r, z; r', z') = \frac{1}{\mu}\{I_1(r, z; r', z'; k_T) + \frac{1}{k_T^2}\left[\frac{\partial}{\partial r}\left(\frac{1}{r}\frac{\partial}{\partial r}\{r[I_1(r, z; r', z'; k_T) - I_1(r, z; r', z'; k_L)]\}\right)\right]\} \quad (23a)$$

$$U_{zr}(r, z; r', z') = \frac{1}{\mu k_T^2}\frac{1}{r}\frac{\partial}{\partial r}\left\{r\frac{\partial}{\partial r}[I_1(r, z; r', z'; k_T) - I_1(r, z; r', z'; k_L)]\right\}. \quad (23b)$$

If in Eqs. (7*a*) and (7*b*) we have an axial ring source (Fig. 1) instead of a radial ring source, the equations of motion become

$$(\lambda + 2\mu)\frac{\partial}{\partial r}\left[\frac{1}{r}\frac{\partial}{\partial r}(rU_{rz})\right] + \mu\frac{\partial^2 U_{rz}}{\partial z^2} + (\lambda + \mu)\frac{\partial^2 U_{zz}}{\partial r\partial z} + \rho\omega^2 U_{rz} = 0 \quad (7c)$$

$$(\lambda + \mu)\frac{\partial}{\partial r}\left[\frac{1}{r}\frac{\partial}{\partial r}(rU_{rz})\right] + (\lambda + 2\mu)\frac{\partial^2 U_{zz}}{\partial z^2} + \frac{\mu}{r}\frac{\partial}{\partial r}\left(r\frac{\partial U_{zz}}{\partial r}\right) + \rho\omega^2 U_{zz} = -\frac{\delta(r' - r)\delta(z' - z)}{r}. \quad (7d)$$

Repeating exactly the same steps as we have followed for solving U_{rr} and U_{zr}, we obtain

$$U_{rz}(r, z; r', z') = \frac{1}{\mu k_T^2}\frac{\partial^2}{\partial r\partial z}\{I_2(r, z; r', z'; k_T) - I_2(r, z; r', z'; k_L)\} \quad (23c)$$

$$U_{zz}(r, z; r', z') = \frac{1}{\mu}\left\{I_2(r, z; r', z'; k_T) + \frac{1}{k_T^2}\frac{\partial^2}{\partial z^2}[I_2(r, z; r', z'; k_T) - I_2(r, z; r', z'; k_L)]\right\}. \quad (23d)$$

Since at $r = r'$, $z = z'$, I_1 has the same singularity as $Q_{1/2}$ and I_2 as $Q_{-1/2}$, it follows that $U_{rr}(r, z; r', z')$ has the same logarithmic singularity as $Q_{1/2}(r, z; r', z')$ and $U_{zz}(r, z; r', z')$ as $Q_{-1/2}(r, z; r', z')$; $U_{zr}(r, z; r', z')$ and $U_{rz}(r, z; r', z')$ are regular at $r = r'$, $z = z'$. Equations (23*a*), (23*b*), (23*c*), and (23*d*) are desired expressions for the Green's functions.

The Green's Functions as the Frequency Approaches Zero

One of the necessary conditions for the elastodynamic Green's functions is that they must approach the corresponding elastostatic Green's functions are $\omega \to 0$. To verify this, we first write the series representations of $Q_{1/2}(Z)$ and $Q_{-1/2}(Z)$:

$$Q_{1/2}(Z) = \pi\sum_{n=0}^{\infty}\frac{(4n + 1)!}{n!(n + 1)!(2n)!2^{2n}2^{2n+1}}\left(\frac{1}{2Z}\right)^{2n+3/2} \quad (24a)$$

$$Q_{-1/2}(Z) = \pi\sum_{n=0}^{\infty}\frac{(4n)!}{n!n!(2n)!2^{2n}2^{2n}}\left(\frac{1}{2Z}\right)^{2n+1/2}. \quad (24b)$$

We next expand the functions $I_1(r, z; r', z'; k)$ and $I_2(r, z; r', z'; k)$ in the power of k up to k^2:

$$I_1(r, z; r', z'; k) = \frac{1}{2\pi\sqrt{rr'}}Q_{1/2}\left(\frac{|z - z'|^2 + r^2 + r'^2}{2rr'}\right) + \frac{k^2}{4\pi}\frac{(|z - z'|^2 + r^2 + r'^2)}{\sqrt{rr'}}Q_{1/2}\left(\frac{|z - z'|^2 + r^2 + r'^2}{2rr'}\right) - \frac{k^2}{2}\sqrt{rr'}\sum_{n=1}^{\infty}\frac{(4n)!}{n!(n + 1)!(2n - 1)!2^{2n+1}2^{2n}} \times\left(\frac{|z - z'|^2 + r^2 + r'^2}{rr'}\right)^{-(4n+1)/2} + O(k^3) \quad (25a)$$

$$I_2(r, z; r', z'; k) = \frac{1}{2\pi\sqrt{rr'}}Q_{-1/2}\left(\frac{|z - z'|^2 + r^2 + r'^2}{2rr'}\right) - \frac{k^2}{4\pi}\frac{(|z - z'|^2 + r^2 + r'^2)}{\sqrt{rr'}} \times Q_{-1/2}\left(\frac{|z - z'|^2 + r^2 + r'^2}{2rr'}\right) + k^2\sqrt{rr'} \times\sum_{n=1}^{\infty}\frac{2n(4n - 2)!}{n!n!(2n - 1)!2^{2n}2^{2n}} \times\left(\frac{|z - z'|^2 + r^2 + r'^2}{2rr'}\right)^{-(4n-1)/2} + O(k^3). \quad (25b)$$

Then

$$\frac{\partial}{\partial z}[I_1(r, z; r', z'; k_T) - I_1(r, z; r', z'; k_L)] = -\frac{(k_T^2 - k_L^2)}{4\pi}\frac{(z - z')}{\sqrt{rr'}}Q_{1/2}\left(\frac{|z - z'|^2 + r^2 + r'^2}{2rr'}\right) + O(k_T^3, k_L^3) \quad (26a)$$

$$\frac{\partial}{\partial z}[I_2(r, z; r', z'; k_T) - I_2(r, z; r', z'; k_L)] = -\frac{(k_T^2 - k_L^2)}{4\pi}\frac{(z - z')}{\sqrt{rr'}}Q_{-1/2}\left(\frac{|z - z'|^2 + r^2 + r'^2}{2rr'}\right) + O(k_T^3, k_L^3). \quad (26b)$$

Now, utilizing Eqs. (2) and (5) and substituting Eqs. (26*a*) and (26*b*) into Eqs. (23*a*) through (23*d*), we obtain

$$\lim_{\omega\to 0} U_{rr}(r, z; r', z') = \frac{1}{8\pi\mu\sqrt{rr'}}\left\{\frac{3 - 4\nu}{1 - \nu}Q_{1/2}\left(\frac{|z - z'|^2 + r^2 + r'^2}{2rr'}\right) + \frac{1}{(1 - \nu)}\frac{(z - z')^2}{rr'}Q'_{1/2}\left(\frac{|z - z'|^2 + r^2 + r'^2}{2rr'}\right)\right\} \quad (27a)$$

Downloaded 04 May 2010 to 171.66.16.27. Redistribution subject to ASME license or copyright; see http://www.asme.org/terms/Terms_Use.cfm

$$\lim_{\omega\to 0} U_{zr}(r, z; r', z')$$

$$= -\frac{1}{8\pi\mu(1-\nu)}\frac{(z-z')}{r\sqrt{rr'}}\left[\frac{1}{2}Q_{1/2}\left(\frac{|z-z'|^2+r^2+r'^2}{2rr'}\right)\right.$$

$$+\left(\frac{r}{r'}-\frac{|z-z'|^2+r^2+r'^2}{2rr'}\right)$$

$$\left.\times Q'_{1/2}\left(\frac{|z-z'|^2+r^2+r'^2}{2rr'}\right)\right] \quad (27b)$$

$$\lim_{\omega\to 0} U_{rz}(r, z; r', z')$$

$$= \frac{1}{8\pi\mu(1-\nu)}\frac{(z-z')}{r\sqrt{rr'}}\left[\frac{1}{2}Q_{-1/2}\left(\frac{|z-z'|^2+r^2+r'^2}{2rr'}\right)\right.$$

$$-\left(\frac{r}{r'}-\frac{|z-z'|^2+r^2+r'^2}{2rr'}\right)$$

$$\left.\times Q'_{-1/2}\left(\frac{|z-z'|^2+r^2+r'^2}{2rr'}\right)\right] \quad (27c)$$

$$\lim_{\omega\to 0} U_{zz}(r, z; r', z')$$

$$= \frac{1}{8\pi\mu\sqrt{rr'}}\left[\frac{3-4\nu}{1-\nu}Q_{-1/2}\left(\frac{|z-z'|^2+r^2+r'^2}{2rr'}\right)\right.$$

$$\left.-\frac{1}{(1-\nu)}\frac{(z-z')^2}{rr'}Q'_{-1/2}\left(\frac{|z-z'|^2+r^2+r'^2}{2rr'}\right)\right]. \quad (27d)$$

In Eqs. (27*a*) through (27*d*), the prime sign on $Q_{1/2}$ and $Q_{-1/2}$ denotes the derivative with respect to the argument, and ν is the Poisson's ratio. Equations (27*a*) through (27*d*) agree with the elastostatic Green's functions (Cruse, Snow, Wilson, 1977) except the factor 2π, which is the difference between our ring sources and theirs. It is easy to see that the Green's function for a torsional ring source (Lu, 1998) reduces to $U_{\theta\theta}$ (Hartmann, 1989) as $k_T \to 0$.

The Far-Field Expressions

Let us now study the far-field expressions of the Green's functions. As $r, z \to \infty$,

$$\frac{|z-z'|^2+r^2+r'^2}{2rr'} \to \infty \quad (28)$$

$$\frac{krr'}{2i\sqrt{|z-z'|^2+r^2+r'^2}} \sim O(1) \quad (29a)$$

$$\frac{i}{2k\sqrt{|z-z'|^2+r^2+r'^2}} \sim o(1). \quad (29b)$$

Using Eqs. (24), (25), (28), and (29), we can obtain

$$Q_{1/2}\left(\frac{|z-z'|^2+r^2+r'^2}{2rr'}\right) \sim \frac{\pi}{2}\left(\frac{rr'}{|z-z'|^2+r^2+r'^2}\right)^{3/2} \quad (30a)$$

$$Q_{-1/2}\left(\frac{|z-z'|^2+r^2+r'^2}{2rr'}\right) \sim \pi\left(\frac{rr'}{|z-z'|^2+r^2+r'^2}\right)^{1/2} \quad (30b)$$

$$I_1(r, z; r', z'; k) \sim \frac{e^{ik\sqrt{|z-z'|^2+r^2+r'^2}}}{2\sqrt{|z-z'|^2+r^2+r'^2}}$$

$$\times \sum_{n=0}^{\infty}\frac{1}{n!(n+1)!}\left(\frac{krr'}{2i\sqrt{|z-z'|^2+r^2+r'^2}}\right)^{2n+1}$$

$$= -i\frac{e^{ik\sqrt{|z-z'|^2+r^2+r'^2}}}{2\sqrt{|z-z'|^2+r^2+r'^2}}$$

$$\times J_1\left(\frac{krr'}{\sqrt{|z-z'|^2+r^2+r'^2}}\right) \quad (31a)$$

$$I_2(r, z; r', z'; k) \sim \frac{e^{ik\sqrt{|z-z'|^2+r^2+r'^2}}}{2\sqrt{|z-z'|^2+r^2+r'^2}}$$

$$+\frac{e^{ik\sqrt{|z-z'|^2+r^2+r'^2}}}{2\sqrt{|z-z'|^2+r^2+r'^2}}$$

$$\times \sum_{n=1}^{\infty}\frac{1}{n!n!}\left(\frac{krr'}{2i\sqrt{|z-z'|^2+r^2+r'^2}}\right)^{2n}$$

$$= \frac{e^{ik\sqrt{|z-z'|^2+r^2+r'^2}}}{2\sqrt{|z-z'|^2+r^2+r'^2}}$$

$$\times J_0\left(\frac{krr'}{\sqrt{|z-z'|^2+r^2+r'^2}}\right) \quad (31b)$$

Since as $r, z \to \infty$,

$$\sqrt{|z-z'|^2+r^2+r'^2} \sim \sqrt{r^2+z^2} - z'\hat{z} \quad (32a)$$

$$\frac{1}{\sqrt{|z-z'|^2+r^2+r'^2}} \sim \frac{1}{\sqrt{r^2+z^2}} \quad (32b)$$

where

$$\hat{r} = \frac{r}{\sqrt{r^2+z^2}}, \quad \hat{z} = \frac{z}{\sqrt{r^2+z^2}} \quad (33)$$

we have

$$I_1(r, z; r', z'; k) \sim \frac{e^{ik\sqrt{r^2+z^2}}}{2\sqrt{r^2+z^2}}J_1(kr'\hat{r})e^{-ik(z'\hat{z}+\pi/2)} \quad (34a)$$

$$I_2(r, z; r', z'; k) \sim \frac{e^{ik\sqrt{r^2+z^2}}}{2\sqrt{r^2+z^2}}J_0(kr'\hat{r})e^{-ikz'\hat{z}}. \quad (34b)$$

Equations (34*a*) and (34*b*) are the far-field expressions for $I_1(r, z; r', z'; k)$ and $I_2(r, z; r', z'; k)$.

Substituting Eqs. (34*a*) and (34*b*) into Eqs. (23*a*) through (23*d*), we obtain the far-field displacement components for the Green's functions

$$U_{\alpha r}(r, z; r', z') = A^L_{\alpha r}\frac{e^{ik_L\sqrt{r^2+z^2}}}{2\sqrt{r^2+z^2}}J_1(k_Lr'\hat{r})e^{-i(k_Lz'\hat{z}+\pi/2)}$$

$$+A^T_{\alpha r}\frac{e^{ik_T\sqrt{r^2+z^2}}}{2\sqrt{r^2+z^2}}J_1(k_Tr'\hat{r})e^{-i(k_Tz'\hat{z}+\pi/2)},$$

$$\alpha, \beta, \gamma = r, z \quad (35a)$$

$$U_{\alpha z}(r, z; r', z') = A^L_{\alpha z}\frac{e^{ik_L\sqrt{r^2+z^2}}}{2\sqrt{r^2+z^2}}J_0(k_Lr'\hat{r})e^{-ik_Lz'\hat{z}}$$

$$+A^T_{\alpha z}\frac{e^{ik_T\sqrt{r^2+z^2}}}{2\sqrt{r^2+z^2}}J_0(k_Tr'\hat{r})e^{-ik_Tz'\hat{z}} \quad (35b)$$

where

Downloaded 04 May 2010 to 171.66.16.27. Redistribution subject to ASME license or copyright; see http://www.asme.org/terms/Terms_Use.cfm

$$A^L_{\alpha\beta} = \frac{\hat{x}_\alpha \hat{x}_\beta}{\lambda + 2\mu}, \quad \hat{x}_r = \hat{r}, \quad \hat{x}_z = \hat{z} \tag{36a}$$

$$A^T_{\alpha\beta} = \frac{\delta_{\alpha\beta} - \hat{x}_\alpha \hat{x}_\beta}{\mu} \tag{36b}$$

while the far-field Green's function for a torsional ring source (Lu, 1998) can be written as

$$U_{\theta\theta}(r, z; r', z') = \frac{e^{ik_T\sqrt{r^2+z^2}}}{2\mu\sqrt{r^2+z^2}} J_1(k_T r' \hat{r}) e^{-i(k_T z'\hat{z} + \pi/2)}. \tag{35c}$$

The far-field stress components are

$$\sigma_{\alpha\beta r}(r, z; r', z') = ik_L B^L_{\alpha\beta r} \frac{e^{ik_L\sqrt{r^2+z^2}}}{2\sqrt{r^2+z^2}} J_1(k_L r' \hat{r}) e^{-i(k_L z'\hat{z} + \pi/2)} + ik_T B^T_{\alpha\beta r} \frac{e^{ik_T\sqrt{r^2+z^2}}}{2\sqrt{r^2+z^2}} J_1(k_T r' \hat{r}) e^{-i(k_T z'\hat{z} + \pi/2)} \tag{37a}$$

$$\sigma_{\alpha\beta z}(r, z; r', z') = ik_L B^L_{\alpha\beta z} \frac{e^{ik_L\sqrt{r^2+z^2}}}{2\sqrt{r^2+z^2}} J_0(k_L r' \hat{r}) e^{-ik_L z'\hat{z}} + ik_T B^T_{\alpha\beta z} \frac{e^{ik_T\sqrt{r^2+z^2}}}{2\sqrt{r^2+z^2}} J_0(k_T r' \hat{r}) e^{-ik_T z'\hat{z}} \tag{37b}$$

where

$$B^L_{\alpha\beta\gamma} = \left[\left(1 - \frac{2}{\kappa^2}\right)\delta_{\alpha\beta} + \frac{2}{\kappa^2}\hat{x}_\alpha \hat{x}_\beta\right]\hat{x}_\gamma \tag{38a}$$

$$B^T_{\alpha\beta\gamma} = (\delta_{\alpha\gamma}\hat{x}_\beta + \delta_{\beta\gamma}\hat{x}_\alpha - 2\hat{x}_\alpha\hat{x}_\beta\hat{x}_\gamma) \tag{38b}$$

$$\sigma_{\alpha\theta\theta}(r, z; r', z') = ik_T \hat{x}_\alpha \frac{e^{ik_T\sqrt{r^2+z^2}}}{2\sqrt{r^2+z^2}} J_1(k_T r' \hat{r}) e^{-i(k_T z'\hat{z} + \pi/2)} \tag{39}$$

$$\kappa^2 = \frac{2(1-\nu)}{1-2\nu}. \tag{40}$$

Equations (35) through (39) show that the Green's functions in the far-field decay at the rate proportional to the inverse of the distance between the observation location and the source location, the same rate as the Green's function for a point source. They are modulated in the radial direction by the Bessel functions $J_0(Z)$ and $J_1(Z)$.

A close examination of the Green's functions derived here and those for a point source and a line source allows us to draw important conclusions about their near and far-field behavior. In the near field, a point source produces a singularity of the order of $(1/r)$ (Achenbach, Gautesen, and McMaken, 1982), while a line source produces a logarithmic singularity. In the far field, a localized source produces a decaying rate proportional to the inverse of the distance between the observation location and the source location, while a line source extending into infinity produces a decaying rate proportional to the inverse of the square of the distance between the observation location and the nearest point on the source.

The Convergence of the Green's Functions

Using Eq. (1), we can write

$$\left| I_1(r, z; r', z'; k) - \frac{e^{ik\sqrt{|z-z'|^2+r^2+r'^2}}}{2\pi\sqrt{rr'}} Q_{1/2}\left(\frac{|z-z'|^2 + r^2 + r'^2}{2rr'}\right)\right|$$

$$= \left|\frac{e^{ik\sqrt{|z-z'|^2+r^2+r'^2}}}{2\sqrt{|z-z'|^2+r^2+r'^2}} \times \sum_{n=0}^{\infty} \frac{1}{n!(n+1)!}\left(\frac{krr'}{2i\sqrt{|z-z'|^2+r^2+r'^2}}\right)^{2n+1} \times \sum_{m=0}^{2n} \frac{(2n+1+m)!}{m!(2n+1-m)!}\left(\frac{i}{2k\sqrt{|z-z'|^2+r^2+r'^2}}\right)^m\right|$$

$$\leq \frac{1}{2\sqrt{|z-z'|^2+r^2+r'^2}} \times \sum_{n=0}^{\infty} \frac{(-1)^n}{n!(n+1)!}\left(\frac{krr'}{2\sqrt{|z-z'|^2+r^2+r'^2}}\right)^{2n+1} \times \sum_{m=0}^{2n} \frac{1}{m!}\left(\frac{1}{2k\sqrt{|z-z'|^2+r^2+r'^2}}\right)^m$$

$$\leq \frac{\exp\left(\frac{1}{2k\sqrt{|z-z'|^2+r^2+r'^2}}\right)}{2\sqrt{|z-z'|^2+r^2+r'^2}} \times J_1\left(\frac{krr'}{\sqrt{|z-z'|^2+r^2+r'^2}}\right). \tag{41a}$$

Similarly, we can write

$$\left| I_2(r, z; r', z'; k) - \frac{e^{ik\sqrt{|z-z'|^2+r^2+r'^2}}}{2\pi\sqrt{rr'}} Q_{-1/2}\left(\frac{|z-z'|^2 + r^2 + r'^2}{2rr'}\right)\right|$$

$$\leq \frac{\exp\left(\frac{1}{2k\sqrt{|z-z'|^2+r^2+r'^2}}\right)}{2\sqrt{|z-z'|^2+r^2+r'^2}} \times J_0\left(\frac{krr'}{\sqrt{|z-z'|^2+r^2+r'^2}}\right). \tag{41b}$$

Equations (41a) and (41b) show that $I_1(r, z; r', z'; k)$ and $I_2(r, z; r', z'; k)$ converge at least at the same rate as $J_0(Z)$ and $J_1(Z)$. Since our Green's functions are expressed in terms of I_1 and I_2, it follows that the Green's functions converge at least at the same rate as $J_0(Z)$ and $J_1(Z)$.

Conclusion

In this paper, we started with the Green's functions for two scalar wave equations with time-harmonic circular ring sources, which were termed two basic integrals here. We then built the elastodynamic Green's functions for time-harmonic radial and axial ring sources upon the two basic integrals. By expanding the two integrals into power series of the wave number k, we showed that the elastodynamic Green's functions approach the corresponding elastostatic Green's functions as the frequency approaches zero. Finally, by studying the far-field behavior of the two integrals, we obtained the far-field expressions for the displacement and stress components of the elastodynamic Green's functions.

Acknowledgment

This work is supported by the Advisory Committee for Research, Southwest Research Institute. The author wishes to thank anonymous reviewers for their helpful suggestions.

Downloaded 04 May 2010 to 171.66.16.27. Redistribution subject to ASME license or copyright; see http://www.asme.org/terms/Terms_Use.cfm

References

Abramowitz, M., and Stegun, I. A., eds., 1964, *Handbook of Mathematical Functions,* National Bureau of Standards, Washington, DC.

Achenbach, J. D., Gautesen, A. K., and McMaken, H., 1982, *Ray Methods for Waves in Elastic Solids: With Applications to Scattering by Cracks,* Pitman Advanced Publishing Program, Boston.

Carley, A., 1961, *An Elementary Treatise on Elliptic Functions,* Dover, New York.

Cawley, P., and Alleyne, D., 1996, "The Use of Lamb Waves for the Long-Range Inspection of Large Structures," *Ultrasonics,* Vol. 34, pp. 287–290.

Churchill, R. V., 1960, *Introduction to Complex Variables and Applications,* 2nd ed., McGraw-Hill, New York.

Cruse, T. A., Snow, D. W., and Wilson, R. B., 1977, "Numerical Solutions in Axisymmetric Elasticity," *Computers and Structures,* Vol. 7, pp. 445–451.

Ditri, J. J., and Rose, J. L., 1992, "Excitation of Guided Elastic Wave Modes in Hollow Cylinders by Applied Surface Tractions," *J. Appl. Phys.,* Vol. 72, No. 7, pp. 2589–2597.

Dudley, D. G., 1994, *Mathematical Foundations for Electromagnetic Theory,* IEEE Press, New York.

Felsen, L. B., and Marcuvitz, N., 1973, *Radiation and Scattering of Waves,* Prentice-Hall, Englewood Cliffs, NJ.

Hartmann, F., 1989, *Introduction to Boundary Elements, Theory and Applications,* Springer-Verlag, Berlin.

Kwun, H., and Bartels, K. A., 1996, "Experimental Observation of Elastic-Wave Dispersion in Bounded Solids of Various Configurations," *J. Acoust. Soc. Am.,* Vol. 99, No. 2, pp. 962–968.

Lu, Y., 1998, "The Elastodynamic Green's Function for a Torsional Ring Source," ASME JOURNAL OF APPLIED MECHANICS, Vol. 65, pp. 566–568.

Malvern, L. E., 1969, *Introduction to the Mechanics of a Continuous Medium,* Prentice-Hall, Englewood Cliffs, NJ.

Stakgold, I., 1968, *Boundary Value Problems of Mathematical Physics, Vol. II,* Macmillan, New York.

Downloaded 04 May 2010 to 171.66.16.27. Redistribution subject to ASME license or copyright; see http://www.asme.org/terms/Terms_Use.cfm

Prediction of Plastic Wrinkling Using the Energy Method

J. Cao
Department of Mechanical Engineering,
Northwestern University,
2145 Sheridan Road,
Evanston, IL 60208-3111
e-mail: jcao@nwu.edu
Assoc. Mem. ASME

The prediction and prevention of wrinkling during a sheet metal forming process have been challenging issues on the design of part shape, die geometry, and processing parameters. In an effort to provide a reliable and efficient tool to assess the onset of wrinkling, analytical models for flange wrinkling and straight side-wall wrinkling are presented here. Using a combination of energy conservation and plastic bending theory, the critical buckling wavelength and stress are calculated as functions of the boundary conditions (displacement constraint and binder pressure). Comparisons between the numerical and experimental results are given for both cases and excellent agreement is obtained.

Introduction

With ever-increasing global competition, industries are under tremendous pressure to deliver better products at cheaper manufacturing costs. With developments in computational methods and high-speed computers, numerical simulation has become a realistic tool for assisting in the design of products and their manufacturing processes. One element critical to successful implementation is the ability to predict failures with numerical simulation. In sheet metal forming, this includes the prediction of wrinkling, tearing, and springback. Wrinkling and tearing are phenomena associated with structural and material instability while springback is the result of bending/unbending of the sheet metal. Wrinkles can limit the ability to stretch sheet metal during processing and adversely affect final part appearance, assembly and functionality. Severe wrinkles may damage or even destroy dies. In this paper, focus will be given to the prediction of plastic wrinkling.

In a typical drawing process, a restraining force is applied to the blank through a friction force between the tooling and the blank and/or through a bending/unbending force imposed by drawbeads (Fig. 1). Such a restraining force determines how the material flows and consequently the stress states in the sheet. When in-plane compressive stress exists in the sheet, wrinkling could initiate in the frustum region where the blank is free of normal constraint or in the flange area where a pressure is imposed onto the sheet by the binder.

Research efforts on the understanding and prediction of wrinkling behavior have spanned the last 50 years with increasing activities in the last 15 years. Experimental work includes the Yoshida buckling test proposed by Yoshida et al. (1981) to study the material resistance to wrinkling by stretching a square sheet along one of its diagonals; drawing of elastic-plastic circular plates using a spherical punch (Zhang and Yu, 1991; etc.); and deep drawing of a conical cup and square cup (Senior, 1956; Jalkh et al., 1993; Bakkenstuen, 1994; etc.). Through study of these various cases, Thomson (1989) concluded that a wrinkling limit diagram based on the final strain state in the sheet metal does not exist. Instead, wrinkling depends on the current local stress state in the sheet as concluded in the analysis of Hutchinson and Neale (1985).

Analytical investigation on plastic wrinkling initiated from the study on columns (Shanley, 1947), followed by the study on plates and shells including the onset of buckling and post-buckling study (Tvergaard, 1977; Needleman and Tvergaard, 1982; etc.). Many other important papers have published in this area, which covered the prediction of elastic buckling and problems not exactly related to the sheet metal forming. These papers are not cited here but can be found in the review articles, such as Sewell (1972) and Tomita (1994). Hill's general theory of bifurcation and uniqueness (Hill, 1958) built a foundation for much of the subsequent research on buckling. Hutchinson (1974) detailed the bifurcation theory for structures where the material is in the plastic range. An application of the theory to predict flange wrinkling was given in Triantafyllidis and Needleman (1980) by modeling the binder as an elastic foundation. Their results were found to compare favorably with some previous empirical models where there was no binder constraint. However, no comparison was made in the cases where the stiffness of the elastic foundation is nonzero. The correlation between the elastic stiffness and the binder pressure obtained from test data was not presented, thus hampering the implementation of this method for directing the design of practical forming processes. Bifurcation theory was utilized to study the wrinkling of annular plates with inward radial drawing without normal constraint in Tomita et al. (1988).

Alternatively, Yu and Johnson (1982) used an energy criterion to determine the critical conditions for flange wrinkling and also quantitatively investigated the effects of a binder on the critical stress and wave number. Again, the concept of elastic stiffness for modeling the binder constraint was used but not linked to the binder pressure. A similar method was presented in Yossifon and Tirosh (1984) to predict critical fluid pressure to prevent plastic buckling during a hydroforming process.

Numerical solutions using the finite element method have become a prime tool to predict wrinkling behavior in forming parts with complex geometry. In the forward mode, where process parameters and tooling geometry, and initial blank shape are given, shell elements coupled with dynamic analysis using explicit integration are commonly used in the simulation. In these cases, wrinkling could be naturally developed since the accumulated computation error serves the purpose of the imperfections which initiate the wrinkling. However, the frequency of the wrinkles and when they initiate depends heavily on model input parameters, for example, the mesh density. In the inverse mode where the final geometry is given and numerical simulation is used to generate the initial blank shape, membrane elements are the most widely chosen elements due to their reasonable accuracy and computational efficiency. However, lack of bending stiffness in the membrane elements prevents the prediction of wrinkling in these simulations.

In an effort to provide the design community with a reliable and efficient tool for predicting wrinkling in complicated forming problems, a wrinkling criterion (referred as *C-B* wrinkling criterion in this paper) for flange wrinkling based on energy conserva-

Contributed by the Applied Mechanics Division of THE AMERICAN SOCIETY OF MECHANICAL ENGINEERS for publication in the ASME JOURNAL OF APPLIED MECHANICS.
Discussion on the paper should be addressed to the Technical Editor, Professor Lewis T. Wheeler, Department of Mechanical Engineering, University of Houston, Houston, TX 77204-4792, and will be accepted until four months after final publication of the paper itself in the ASME JOURNAL OF APPLIED MECHANICS.
Manuscript received by the ASME Applied Mechanics Division, Nov. 11, 1998; final revision, Feb. 11, 1999. Associate Technical Editor: W. K. Liu.

 Copyright © 1999 by ASME

Downloaded 04 May 2010 to 171.66.16.27. Redistribution subject to ASME license or copyright; see http://www.asme.org/terms/Terms_Use.cfm

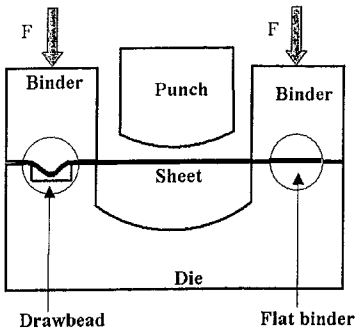


Fig. 1 Diagram of a stamping process where flat binder and/or drawbead provides the restraining force to the sheet during the forming process

tion principles was proposed in Cao and Boyce (1997). Unlike the other criteria, the critical buckling stress and the resulting buckling wavelength are specifically defined as functions of binder pressure. The methodology of combining this wrinkling criterion with membrane elements to assist the tooling and process design was presented in Cao et al. (1997), where excellent agreement between the numerical results and the experimental results was obtained.

In this paper, the *C-B* wrinkling criterion is reviewed briefly followed by the analytical determination of this wrinkling criterion for a sheet under tri-axial loading, that is, flange wrinkling. The energy method is then modified to obtain the analytical solution for the straight side-wall wrinkling. The critical buckling stress is expressed as a function of the current stress-state, material properties, sheet thickness, and geometrical dimensions. A stress predictor based on the effective compressive width is proposed. Finally, comparisons between the models and the results of several experiments are given for the purpose of verification and demonstration.

Review of the *C-B* Wrinkling Criterion for Flange Wrinkling

In a typical drawing process (Fig. 1), sheet material under the blank holder is drawn into the deformation zone by the punch movement, thus a compressive stress develops in the plane of the sheet under the blank holder. The level of this compressive stress depends on the tooling/blank geometry and the restraining force applied via friction force and/or drawbead bending/unbending force. When the binder force is insufficient to suppress the out-of-plane displacement caused by the compressive stress, wrinkling will occur. Although the distribution of the compressive stress under the binder is not uniform, the initiation of wrinkling is most likely a local phenomenon, as indicated in Hutchinson and Neale (1974), dependent on material properties, stress state, and sheet thickness of the material points in the region under compression. Therefore, at each material point in the region being examined for wrinkling in a drawing operation, the problem can be simplified to the analysis of wrinkling in a rectangular plate (Fig. 2). The plate is subjected to in-plane compressive stress in one direction, in-plane tensile stress in the other direction, and normal constraint denoted by a uniform binder pressure p.

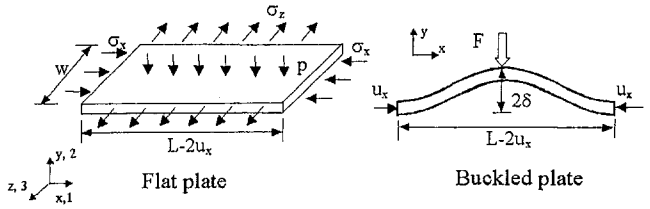


Fig. 2 Schematics of the simplified model in *C-B* wrinkling criterion

In the above simplified model, it is found that at a certain edge compression, the strain energy in a perfectly flat plate, E_0, is larger than that in a buckled plate, E_w, if both plates are free of normal constraint. This difference between the two energies under any given edge displacement u_x is equivalent to the external work, W_n, produced by the normal force F in suppressing the buckling. Therefore, the wrinkling problem can be formulated in terms of the following energy conservation principle

$$W_n = E_0 - E_w = \int_0^{2\delta} F du_y \tag{1}$$

where u_y is the buckled deflection, δ is the maximum buckled height of one wavelength at an edge displacement of u_x, and n represents the buckling mode. Usually, mode 1 is a half sinusoid wave, and mode 2 is a full sinusoid wave as shown in Fig. 2, therefore, $L/2$ denotes the buckling wavelength here. Assuming $F = F_{\max} - F_{\max}(u_y/\delta - 1)^2$, the critical pressure, which is the minimum binder pressure required to suppress the buckling of the nth mode at a given normalized edge displacement u_x/L, can be expressed as

$$p_n = \frac{F_{\max}}{Lw} = \frac{3(E_0 - E_{wn})}{4\delta_n Lw}. \tag{2}$$

Figure 3 provides an illustration of the relationship between the calculated p_1 and p_2 as functions of edge compression u_x/L from Eq. (2). Notice that there exists a transition pressure p_{12} where the favored buckling mode switches from mode 1 to mode 2. Specifically, in the case of applied binder pressure $p < p_{12}$, we have $u_1 < u_2$, meaning that the critical buckling stress for mode 1 is lower than that for mode 2, and thus the plate would favor mode 1 buckling. On the other hand, in the case of $p^* > p_{12}$, we have $u_2^* < u_1^*$, and hence the buckling would occur in mode 2. This criterion thus quantitatively determines the critical buckling stress, which is defined as the associated stress at the critical or transit edge displacement u_{xcr}/L, and also the buckling mode at the presence of a given binder pressure. By performing the above analysis for plates of buckling wavelength $L_1, L_2, \ldots, L_\infty$, continuous curves of critical buckling stress versus binder pressure and wavelength versus binder pressure can be obtained to characterize the wrinkling behavior of a plate under normal constraint. Such reference curves clearly define the condition of the onset of wrinkling as a function of normal pressure and can be easily incorporated to examine the flange wrinkling problem in a general forming case. All the above formulae and more details about this criterion were presented in Cao and Boyce (1997).

Analytical Model for Flange Wrinkling

In the work presented in Cao and Boyce (1997), the strain energy and the buckling amplitude were recorded from the finite

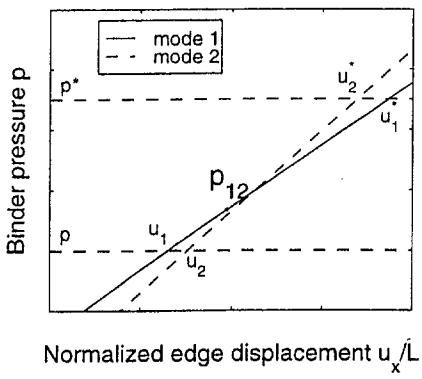


Fig. 3 Pressures as functions of edge displacement for modes 1 and 2 to illustrate the concept of the *C-B* wrinkling criterion

Downloaded 04 May 2010 to 171.66.16.27. Redistribution subject to ASME license or copyright; see http://www.asme.org/terms/Terms_Use.cfm

element method simulations of a plate under compression, which is referred as Cao and Boyce's numerical approach in this paper. With the aim of fully utilizing the potential of this criterion, an analytical solution is developed here to calculate the strain energy and the buckling amplitude at any given edge displacement, and ultimately to obtain the critical wrinkling condition.

For a perfectly flat plate and a buckled plate in Fig. 2, the loading is taken to be applied through a monotonically and proportionally increasing edge displacement u_x. Tensile stress σ_z is applied proportionally with respect to the compression in the x-direction, σ_x, i.e., $\sigma_z/\sigma_x = \alpha$, where the stress ratio α is assumed to be a constant. Note that the normal stresses are coincident with the principle stresses by ignoring the shear stresses, i.e., $\sigma_3/\sigma_1 = \sigma_z/\sigma_x = \alpha$ (Fig. 2); thus, principle stresses and strains are used to describe the stress states in the following. For simplicity, by assuming proportional loading paths, the deformation theory of plasticity without unloading is utilized in the analysis. The plates under the transverse tension have elongation in the 3-direction, which is a constant due to the boundary constraint in this direction. Assume that the buckled plate and the flat plate have the same amount of strain increment in the 3-direction, $\Delta\epsilon_3$, due to the tension.

The material is modeled as planar isotropic with normal anisotropy characterized by the parameter R. This parameter is defined as the ratio of the width plastic strain in the plane of the sheet to the plastic strain through the thickness in a simple tension test. Here, Hill's 1948 quadratic yield criterion for normal anisotropic materials is used (Hill, 1948). The Swift's equation is taken to describe the strain-hardening behavior of the material $\bar{\sigma} = K(\epsilon_0 + \bar{\epsilon})^n$, where K is the material strength coefficient, n is the strain hardening exponent, ϵ_0 is the prestrain, and $\bar{\sigma}$, $\bar{\epsilon}$ are effective stress and strain, respectively.

Following the above assumptions, the calculation for the strain energy per unit width of the flat plate, E_0, under edge compression and transverse tension is trivial. It can be obtained as

$$E_0 = \frac{1}{w}\int\int \bar{\sigma} d\bar{\epsilon} dV = \frac{KLt}{n+1}(\epsilon_0 + c_1\epsilon_{1_0})^{n+1} \tag{3}$$

where

$$c_1 = -\sqrt{\frac{1+R}{1+2R}}\left(1 + \frac{R(1+\alpha)^2 + (\alpha + \alpha R - R)^2}{(1+R-\alpha R)^2}\right)$$

$$\epsilon_{1_0} = \ln(1 - 2u_x/L). \tag{4}$$

The strain energy per unit width of a buckled plate (Fig. 2), E_w, can be obtained in the following manner. At a given edge displacement u_x/L, the deformed shape of the buckled plate, i.e., the mode shape, is assumed to be of a sinusoid wave $y = \delta(1 + \cos(mx))$, in which m is the frequency of the corresponding mode as $m = 2\pi/(L - 2u_x)$. Based on the assumptions of material incompressibility and no thickness variation,[1] the deflection amplitude of the mode shape can be obtained through the Taylor expansion as

$$\delta = \frac{1}{\sqrt{2\pi}}\sqrt{\left(\frac{L}{1+\Delta\epsilon_3}\right)^2 - (L - 2u_x)^2}. \tag{5}$$

Let r_i and r_o denote the radii of the curvatures of the inside and outside surfaces of the bent plate, respectively. r_i and r_o can be obtained from the curvature of the buckled plate as

$$r_i = -\frac{(1+y'^2)^{3/2}}{y''} = \frac{(1+\delta^2 m^2\sin^2(mx))^{3/2}}{\delta m^2\cos(mx)} \tag{6}$$

$$r_o = r_i + t. \tag{7}$$

[1] The discussion on the assumption of no thickness variation is given in the section of "Comparisons and Discussions" in Cao and Wang (1999).

Based on the observation of the strain and stress output from a finite element method analysis using continuum elements with reduced integration, the shear stresses and strains are ignored compared to the in-plane normal stresses and strains for the buckled plate. These simplifications make the buckling of the plate a pure bending problem. In the case without transverse tension, the displacement u_z is considered as uniform so that the corresponding strain ϵ_z is constant, which is relatively insignificant and taken to be zero. In the case under tension, the buckled plate and the flat plate are assumed to have the same amount of strain increment $\Delta\epsilon_3$. As usually $\Delta\epsilon_3 \ll \epsilon_\theta$, the effective strain of the buckled plate can be simplified as

$$\bar{\epsilon}_w = c_2\left|\ln\left(\frac{r}{r_u}\right)\right| + c_3 \tag{8}$$

with

$$c_2 = \frac{1+R}{\sqrt{1+2R}}, \quad c_3 = \frac{R}{\sqrt{1+2R}}\Delta\epsilon_3 \tag{9}$$

where r is the radius of the curvature, and r_u is the radius of the curvature of the unstretched surface, which is coincident with the middle surface of the bent plate.

Using the deformation theory, the strain energy of the buckled plate per unit width under edge compression and transverse tension, E_w, can be expressed as

$$E_w = \int\int\left(\int_0^{\bar{\epsilon}_w}\bar{\sigma}_w d\bar{\epsilon}_w\right) drds = \frac{K}{n+1}\int\int\left(c_2\left|\ln\left(\frac{r}{r_u}\right)\right| + c_3\right)^{n+1} drds \tag{10}$$

and can be approximated through the Taylor expansions as

$$E_w = \frac{2Kt}{(n+1)}\left(\frac{c_2 t}{2} + (\epsilon_0 + c_3)\left(\frac{1}{m^2\delta} + \frac{t}{2}\right)\right)^{n+1} \times \left(\frac{1}{m^2\delta} + \frac{t}{2}\right)^{-n}\tan^{-1}(m\delta). \tag{11}$$

Having calculated the strain energy of the flat plate E_0 (Eq. (3)) the strain energy of the buckled plate E_w (Eq. (11)), and maximum buckled height δ (Eq. (5)) analytically, we can obtain the critical binder pressure as a function of u_x/L from Eq. (2) as

$$p = \frac{3Kt}{4(n+1)\delta}\left\{\left(\epsilon_0 + c_1\ln\left(1 - \frac{2u_x}{L}\right)\right)^{n+1} - \frac{2}{L}\left(\frac{c_2 t}{2} + (\epsilon_0 + c_3)\left(\frac{1}{m^2\delta} + \frac{t}{2}\right)\right)^{n+1} \times \left(\frac{1}{m^2\delta} + \frac{t}{2}\right)^{-n}\tan^{-1}(m\delta)\right\}. \tag{12}$$

The specific $u_{x_{cr}}/L$ corresponding to the transition pressure for certain wavelengths L_1 and L_2 can be obtained from

$$p_1(L_1, u_{x_{cr}}/L) - p_2(L_2, u_{x_{cr}}/L) = 0. \tag{13}$$

Thus, we can quantitatively determine the critical buckling stress at the transit edge displacement $u_{x_{cr}}/L$ as

$$\sigma_{cr} = K\sqrt{\frac{1+R}{1+\alpha^2+R(1-\alpha)^2}}\left(\epsilon_0 + c_1\ln\left(1 - \frac{2u_{x_{cr}}}{L}\right)\right)^n. \tag{14}$$

Downloaded 04 May 2010 to 171.66.16.27. Redistribution subject to ASME license or copyright; see http://www.asme.org/terms/Terms_Use.cfm

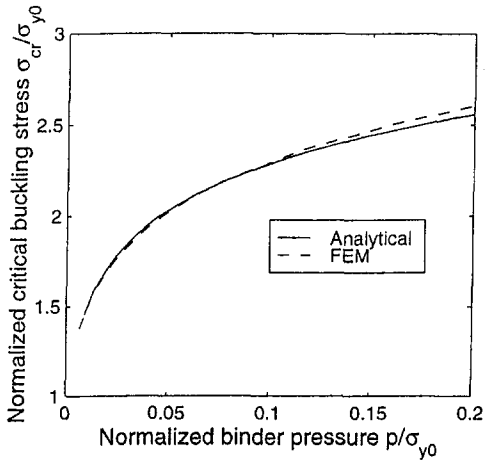


Fig. 4 Comparison of the critical buckling stress for flange wrinkling between the analytical solution and the numerical solution in Cao and Boyce (1997)

Results and Comparison of Flange Wrinkling

The analytical results obtained from the present analysis will be compared to the numerical results in Cao and Boyce (1997). The comparisons between the numerical and the experimental results were presented in Cao and Boyce (1997) and Cao et al. (1997), and will be briefly reviewed below.

Figures 4 and 5 show the comparisons between the analytical and the numerical results, where the parameters are taken as $\alpha = 0$, $t = 0.76$ mm, $K = 717$ MPa, $n = 0.23$, $\epsilon_0 = 0.005$, and $R = 1.31$. Excellent agreement between the predictions of the critical buckling stress is obtained (Fig. 4). In general, the wavelength prediction agrees very well when the wavelength is longer than $6t$. For the modes where the wavelength is less than $6t$, the analytical results underestimate the wavelength compared to the numerical data. This discrepancy is due mainly to some of the assumptions made in the analytical model, which are not very suitable to the sharp bending of a plate. When the plate is bent at a small radius of the curvature, the sinusoid wave form is not accurate enough to describe the mode shape, and this affects the prediction of strain and stress distributions in the buckled plate. Additionally, the pure bending theory also meets challenges at these extreme cases due to the present of the shear deformation. On the other hand, the short wavelength modes tend to develop under a relatively high binder pressure, where another failure mode, tearing, is most likely to occur before the initiation of wrinkling.

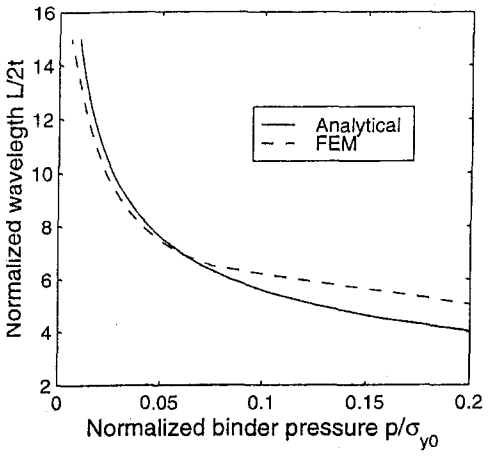


Fig. 5 Comparison of the critical buckling wavelength for flange wrinkling between the analytical solution and the numerical solution in Cao and Boyce (1997)

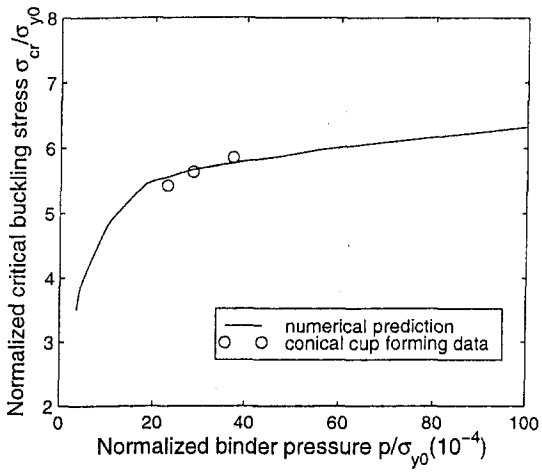


Fig. 6(*a*)

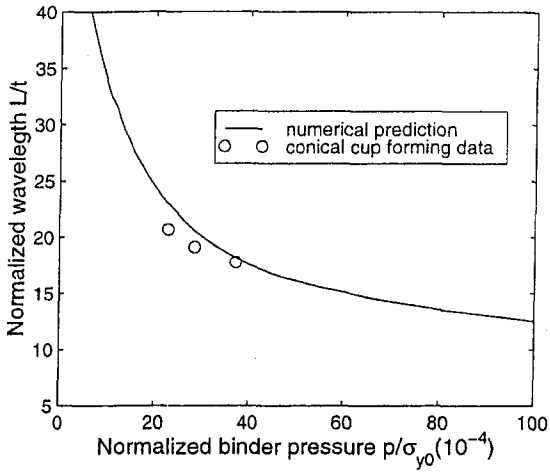


Fig. 6(*b*)

Fig. 6 Comparison of critical buckling stress and wavelength between numerical predictions using proposed wrinkling criterion and experimental results for a conical cup forming (Cao and Boyce 1997)

From the analytical model, the critical wrinkling stress depends on the applied binder pressure, stress states and material parameters through the following parameter groups:

$$\sigma_{cr} = f(p, \alpha, n, K, R, \epsilon_0). \tag{15}$$

It is found that ϵ_0 has essentially no influence on the critical wrinkling conditions. With increasing σ_3 in tension, the critical stress under the same binder pressure decreases, that is, buckling occurs earlier. The case of $\sigma_3 = 0$ represents the stress state at the outer edge of the flange, while the case of $\sigma_3 > 0$ reflects the stress state at the inner edge near the die radius. Our analysis shows that wrinkling is most likely initiated from the inner edge. However, the resulting wavelengths are almost the same in the entire flange area, which is verified by experimental observations. The strain-hardening exponent n strongly affects the wrinkling resistance. As n increases, the normalized critical stress and the buckling wavelength decrease. An increase in K strongly increases the wrinkling stress limit and the resulting wavelength. The effect of the anisotropy parameter R is relatively insignificant.

The comparison between experiments and numerical simulations using the wrinkling criterion of forming an aluminum conical cup and a square pan were presented in Cao and Boyce (1997) and Cao et al. (1997), respectively. Results are shown here in Figs. 6 and 7 with more details available in the references. Notice that in

Downloaded 04 May 2010 to 171.66.16.27. Redistribution subject to ASME license or copyright; see http://www.asme.org/terms/Terms_Use.cfm

Fig. 7, which shows results obtained from a General Electric's internal membrane code combined with our wrinkling criterion, a buckling index above 1 indicates the onset of wrinkling. Excellent results were obtained in both cases demonstrating the effectiveness of the criterion.

Analytical Model for Straight Side-Wall Wrinkling

Side-wall wrinkling differs significantly from the flange wrinkling in its lack of normal constraint from the binder. The *C-B* wrinkling criterion presented above simplified the flange wrinkling problem into the stability of an infinite plate under in-plane compression and normal constraint. Such an assumption does not hold in the case of side-wall wrinkling which depends strongly on the boundary conditions and the geometric constraint provided by both the punch radius and the die radius. In the following derivation of our analytical model for the straight side-wall wrinkling, geometry constraint is incorporated.

Consider a rectangular thin plate under plane stress condition (Fig. 8) with length a, width b, and thickness t. The plate is compressed along the sides $x = 0$ and $x = a$, and is stretched along the sides $y = 0$ and $y = b$. The elastic buckling of this thin plate was studied in Timoshenko (1961). The present equilibrium state of the system is stable if any admissible displacement makes the increment of the internal energy of the system larger than the incremental work done by the external load. In our case, the increment of the internal energy of the system is the bending energy of the buckled plate, ΔU, and the incremental work done by the external load is the work done by the in-plane membrane forces, ΔT.

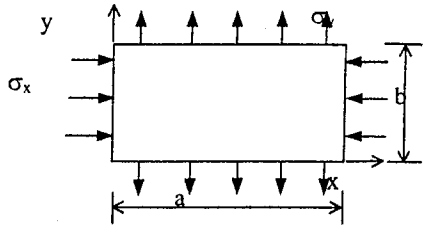


Fig. 8 A simplified plate model used in the side-wall wrinkling criterion

$$\Delta U = \frac{D}{2}\int_0^b \int_0^a \left(\frac{\partial^2 w}{\partial x^2} + \frac{\partial^2 w}{\partial y^2}\right)^2 - 2(1-\nu)\left(\frac{\partial^2 w}{\partial x^2}\frac{\partial^2 w}{\partial y^2} - \left(\frac{\partial^2 w}{\partial x \partial y}\right)^2\right) dxdy \quad (16)$$

where $w(x, y)$ is the assumed normal deflection field, the bending rigidity $D = Et^3/12(1 - \nu^2)$, E is Young's modulus, and ν is the Poisson's ratio. And

$$\Delta T = -\frac{t}{2}\int_0^b \int_0^a \left(\sigma_x\left(\frac{\partial w}{\partial x}\right)^2 + \sigma_y\left(\frac{\partial w}{\partial y}\right)^2\right) dxdy. \quad (17)$$

Here, the extension of the above method to plastic analysis is implemented by using equivalent D^p instead of the bending rigidity D, where ν is replaced by its incompressible equivalent $\nu = \frac{1}{2}$ for plastic range, and E by the so-called Karman modulus E_0 defined as

$$E_0 = \frac{4EE_t}{(E^{1/2} + E_t^{1/2})^2} \quad (18)$$

in which the tangential modulus E_t is defined as $d\bar{\sigma}/d\bar{\epsilon}$, $\bar{\sigma}$, and $\bar{\epsilon}$ are the equivalent stress and strain, respectively. Hence, we have plastic bending rigidity as $D^p = E_0 t^3/9$. The general expression for the plastic bending energy can be obtained as

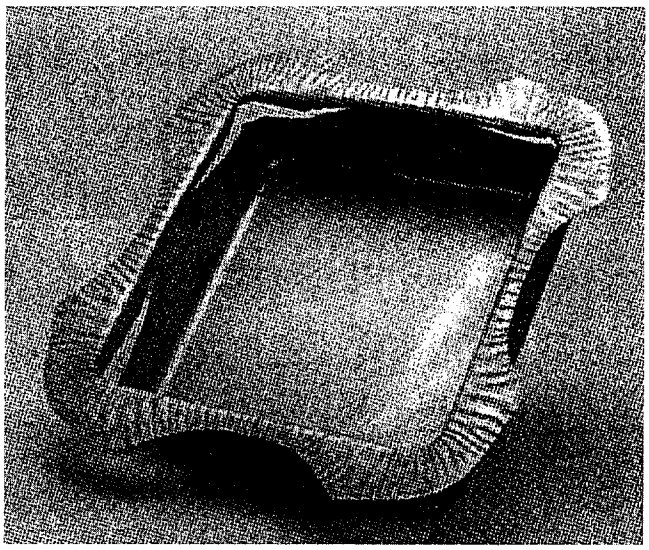


Fig. 7(*a*)

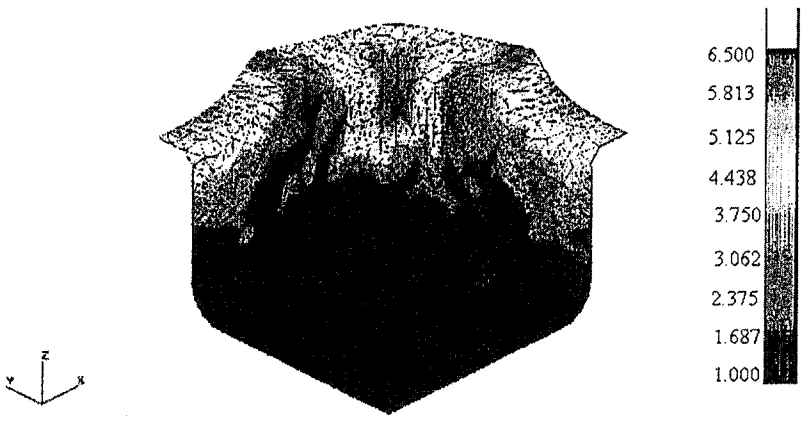


Fig. 7(*b*)

Fig. 7 Comparison of flange wrinkling between the prediction given in numerical simulation with the calculated buckling criterion and experiments at GE (Cao et al., 1997)

Downloaded 04 May 2010 to 171.66.16.27. Redistribution subject to ASME license or copyright; see http://www.asme.org/terms/Terms_Use.cfm

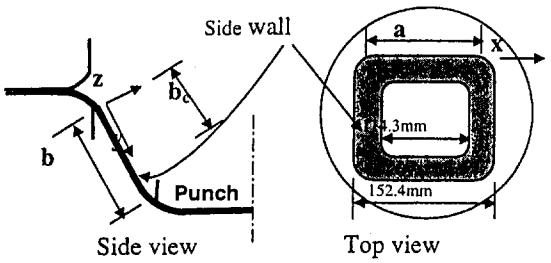


Fig. 9 The geometry and the notations of the square cup studied in the side-wall wrinkling case

$$\Delta U = \frac{D^p}{2}\int_0^b\int_0^a\left(\left(\frac{\partial^2 w}{\partial x^2}+\frac{\partial^2 w}{\partial y^2}\right)^2 - \left(\frac{\partial^2 w}{\partial x^2}\frac{\partial^2 w}{\partial y^2}-\left(\frac{\partial^2 w}{\partial x\partial y}\right)^2\right)\right)dxdy. \quad (19)$$

For thin plates, the boundary condition strongly affects the critical buckling condition. Therefore, the deflection form should be appropriately assumed to reflect the restriction in the region being examined for wrinkling. By equating the energy $\Delta U = \Delta T$, the critical buckling stress can be calculated analytically as a function of stress state, material properties, and geometry parameters.

Side Wall Buckling Stress

In an attempt to verify the predictive capability of this criterion, forming of an aluminum square cup (Fig. 9) was studied. The stress field is assumed to be uniform in the prebuckling plate model. However, in reality, the stress distribution will not be uniform and even the hoop stress along the x-direction (Fig. 9) is not completely compressive in the side wall of the cup during forming. To compensate for this discrepancy, an effective compressive length b_c, instead of the total length of the side wall b, is proposed for determining the critical buckling stress since wrinkling can be initiated only under the presence of compressive stress.

Considering the geometry constraint, the sidewall in the square cup forming can be simplified as a plate clamped at four sides assuring the condition of zero slopes at the boundaries. Thus, the deflection form is assumed as

$$w = \frac{w_0}{4}\left(1-\cos\left(\frac{m\pi x}{a}\right)\right)\left(1-\cos\left(\frac{n\pi y}{b_c}\right)\right) \quad (20)$$

where b_c is the actual length under compression. Following the energy method and let $\Delta U = \Delta T$, the buckling stress σ_{comp} can be obtained as

$$\sigma_{\text{comp}} = -\sigma_x = \frac{\pi^2 D^p}{t}\left(1-\left(\frac{an}{mb_c}\right)^2\alpha\right)^{-1} \times\left(\left(\frac{m}{a}\right)^2+\left(\frac{a}{m}\right)^2\left(\frac{n}{b_c}\right)^4+\frac{2}{3}\left(\frac{n}{b_c}\right)^2\right) \quad (21)$$

where $\alpha = |\sigma_y/\sigma_x|$ is the ratio of radial tensile stress to hoop compression stress. The critical buckling stress, σ_{cr}, is the lowest value among all the values of σ_{comp} obtained from the above equation when wave numbers m and n vary. Since m and n need to satisfy the boundary conditions, it easily can be seen that n should be taken as 2 in Eq. (21) to obtain the critical buckling stress, which indicates that there is a full wave in the draw-in direction (y-direction).

Results and Comparison of Side-Wall Wrinkling Prediction

The geometry of the square cup is shown in Fig. 9, where the radii of punch, binder, and die profiles are 6.35 mm. The cross dimension of the punch is 114.3 mm with the corner radii of 31.75 mm, and the cross dimension of the die is 152.4 mm with the corner radii of 50.8 mm. The circular blank of AL2008-T4 has an initial diameter of 230.0 mm and a thickness of 1.0 mm. Given the advantages of using the stress-based wrinkling criterion incorporated into the finite element analysis presented in the flange wrinkling section, a similar approach is given here for predicting the side-wall wrinkling. The commercial finite element code ABAQUS/Standard with an implicit integration solver is employed. Material is characterized as an elastic-plastic material following a hardening law $\bar{\sigma} = K\bar{\epsilon}^n$, where $K = 515$ MPa and $n = 0.26$, with an initial yield stress $\sigma_{yo} = 125$ MPa. Hill's 1948 yield criterion is used to describe normal anisotropic behavior of the material with $R = 0.71$. Due to the symmetry condition, one-eighth of the entire square cup is modeled. The friction coefficient between the punch and the sheet is taken to be 0.30, and 0.17 for that between the binder/die and the sheet (Jalkh et al., 1993). The stress predictor in Eq. (21) is used to predict the onset of wrinkling based on the values of stress ratio α and the effective compression width b_c obtained from the simulation. If the current compressive stress at one material point exceeds the calculated σ_{cr}, the buckling will initiate.

Figure 10 shows the predicted cup failure heights due to buckling in the side wall at various binder forces along with experimental results. The analytical predictions from the present approach are in excellent agreement with experimental results in Bakkenstuen (1994). In a deep drawing process, the blank holder force plays an important role in the formability of the blank. Figure 10 demonstrates an increase in the critical buckling height as binder force increases. Experimental results show that another type of failure, tearing, was most likely to occur before the initiation of the wrinkling when the binder force was beyond 115 KN.

As noticed in the case of flange wrinkling, tension in the plane of the sheet would reduce the critical buckling stress. The same effect exists in the side-wall wrinkling. From Eqs. (18) and (21), it can be shown that an increase in tension results in a reduction of E_o and, consequently, of D^p and therefore of the critical buckling stress σ_{comp}. This effect is not easily observed from Fig. 10. Figure 10 might be wrongly interrupted that the increase in tension as a result of the increasing blank holder force would increase the wrinkling limit as evidenced by an increase in the cup forming height. In fact, from the finite element method analysis, it is noticed that by increasing the restraining force, the effective width b_c is decreased for the square pan forming (Fig. 11). This decrease dramatically increases the buckling stress. Therefore, the decreased compressive width, not the increased tensile stress, accounts for the improvement of buckling resistance. From this point

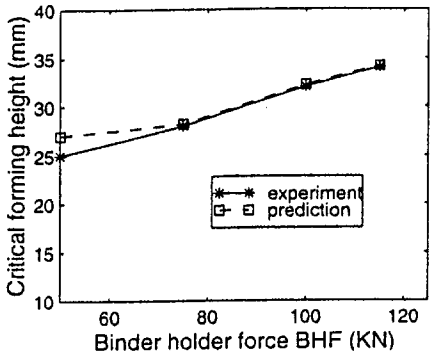


Fig. 10 Comparison between the calculated forming heights with experimental results obtained from the square cup forming

Downloaded 04 May 2010 to 171.66.16.27. Redistribution subject to ASME license or copyright; see http://www.asme.org/terms/Terms_Use.cfm

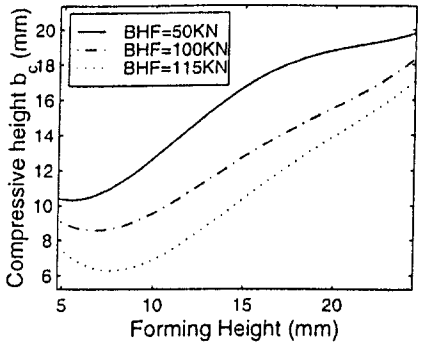


Fig. 11 Effect of the effective buckling width b on the critical buckling stress

of view, the effective width in compression is more essential than the total forming width in governing the onset of wrinkling.

Note that the present approach is not applied to the analysis of cup forming where the length of the straight side is small compared with the corner radius. In that case, the effect of the transition between the corner section and the straight wall is significant so that the assumed boundary condition will be inappropriate.

Conclusions

Analytical models for predicting the onset of flange wrinkling and straight side-wall wrinkling using an energy method have been presented. Both models employ stress-based criteria, which provide the critical buckling stress and the resulting buckling wavelength as functions of current stress states in the material.

For flange wrinkling, the model was developed based on the wrinkling criterion proposed in Cao and Boyce (1997) using an energy conservation law. The minimum binder pressure to suppress the wrinkling is calculated from the difference between strain energies in a perfectly flat plate and a buckled plate. Here, the strain energies are obtained analytically using the plate bending theory and the assumption of material imcompressibility. The analytical solution agrees well with the numerical results presented in Cao and Boyce (1997) (Figs. 4 and 5), especially in terms of the prediction of the critical buckling stress. The numerical results were validated by the experiments of a conical cup and a square cup forming (Figs. 6 and 7).

For the straight side-wall wrinkling, the geometry constraint is incorporated into the energy method by selecting an effective plate width b_c in a simplified plate model. This effective plate width is the length of the side-wall under compression. As discovered from our analytical model, a shorter effective width would result in a higher critical buckling stress and an increase in the in-plane tensile stress will reduce the buckling stress. By examining the forming of a square cup (Fig. 9, which has the different geometry from Fig. 7, has side-wall wrinkling as opposed to the flange wrinkling in Fig. 7), it is found that the reduced compressive width in the side-wall has a more significant effect than the increased tension in the side-wall due to an increase in binder force. Therefore, the failure height of the cup due to buckling increases as the binder force increases. Hence, the effective compressive width employed to obtain the critical conditions in the buckling criterion is a very important concept. The numerical prediction of the cup forming height due to the constraint of side-wall wrinkling has an excellent agreement with the experimental results (Fig. 10).

The stress-based wrinkling criterion can have a significant impact on the design of sheet metal forming processes. For example, in the case where rapid assessment of failure is necessary at an early design stage, the criterion can be incorporated into the finite element method simulation using membrane elements to achieve the previously impossible task. Additionally, since the criterion can predict the wavelength of wrinkles, if any, it can be utilized to provide a guideline on how fine the mesh should be to capture the right post-buckling behavior. The criterion and the approach have been adopted in the internal forming code at General Electric. The study on the prediction of wrinkling would be more complete if the analytical solution for the curved side-wall wrinkling existed, which has been under our investigation.

Acknowledgments

This work is supported by the National Science Foundation through a GOALI award (DMI-9713744) and matching funds from General Electric.

References

Bakkenstuen, R. S., 1994, "Closed Loop Control of Forming Stability During Aluminum Stamping," M.S. thesis, MIT, Cambridge, MA.

Cao, J., and Boyce, M., 1997, "Wrinkling Behavior of Rectangular Plates Under Lateral Constraint," *International Journal of Solids & Structure,* Vol. 34, No. 2, pp. 153–176.

Cao, J.,'Karafillis, A., and Ostrowski, M., 1997, "Prediction of Flange Wrinkles in Deep Drawing," *Advanced Methods in Material Processing Defects,* M. Predeleanu and P. Gilormini, eds., pp. 301–310.

Cao, J., and Wang, X., 1998, "An Analytical Model for Plate Wrinkling Under Tri-axial Loading and its Application," *International Journal of Mechanical Science,* to appear.

Hill, R., 1958, "A Theory of the Yielding and Plastic Flow of Anisotropic Metals," *Proc. R. Soc. Lond.,* Vol. A193, p. 281.

Hutchinson, J. W., 1974, "Plastic Buckling," *Advances in Applied Mechanics,* Vol. 14, pp. 67–144.

Hutchinson, J. W., and Neale, K. W., 1985, "Wrinkling of Curved Thin Sheet Metal," *Plastic Instability,* Presses Ponts et Chaussées, Paris, pp. 71–78.

Jalkh, P., Cao, J., Hardt, D., and Boyce, M. C., 1993, "Optimal Forming of Al 2008-T4 Conical Cups Using Force Trajectory Control," *Journal of Materials & Manufacturing,* Vol. 102, Section 5, pp. 416–427.

Needleman, A., and Tvergaard, V., 1982, "Aspects of Plastic Post-buckling Behavior," *Mechanics of Solids,* H. G. Hopkins and M. J. Sewell, eds. Pergamon Press, Oxford, pp. 453–498.

Senior, B. W., 1956, "Flange Wrinkling in Deep-Drawing Operations," *Journal of Mechanics and Physics of Solids,* Vol. 4, pp. 235–246.

Sewell, M. J., 1972, "A Survey of Plastic Buckling," *Stability,* H. Leipholz, ed., University of Waterloo Press, Waterloo, pp. 85–197.

Shanley, F. R., 1947, "Inelastic Column Theory," *J. Aero. Sci.,* Vol. 14, pp. 261–268.

Thomson, P. F., 1989, *Determining the Buckling Limit Diagram, Forming Limit Diagrams: Concepts, Methods and Applications,* edited by R. H. Wagnor, et al., eds. The Minerals, Metals & Materials Society, Warrendale, PA, pp. 61–70.

Timoshenko, S., and Gere, J. M., 1961, *Theory of Elastic Stability,* McGraw-Hill, New York.

Tomita, Y., 1994, "Simulations of Plastic Instabilities in Solid Mechanics," ASME *Applied Mechanics Reviews,* Vol. 47, pp. 171–205.

Tomita, Y., Shindo, A., and Fatnassi, A., 1988, "Bounding Approach to the Bifurcation Point of Annular Plates With Nonassociated Flow Law Subjected to Uniform Tension at Their Outer Edges," *International Journal of Plasticity,* Vol. 4, pp. 251–263.

Triantafyllidis, N., and Needleman, A., 1980, "An Analysis of Wrinkling in the Swift Cup Test," *Journal of Engineering Materials and Technology,* Vol. 102, pp. 241–248.

Tvergaard, V., 1977, "Buckling Behavior of Plate and Shell Structures," *Procs. 14th Int. Congr. Theoretical and Appl. Mech.* W. T. Koiter, ed., North-Holland, Amsterdam.

Yossifon, S., and Tirosh, J., 1984, "On Suppression of Plastic Buckling in Hydroforming Process," *International Journal of Mechanical Science,* Vol. 26, pp. 389–402.

Yoshida, K., Hayashi, J., Hirata, M., et al., 1981, "Yoshida Buckling Test," *IDDRG,* Kyoto, Japan.

Yu, T. X., and Johnson, W., 1982, "The Buckling of Annular Plates in Relation to the Deep-Drawing Process," *International Journal of Mechanical Science,* Vol. 24, pp. 175–188.

Yu, T. X., and Zhang, L. C., 1996, *Plastic Bending: Theory and Applications,* World Scientific, River Edge, NJ.

Zhang, L. C., and Yu, T. X., 1991, "An Experimental Investigation on Stamping of Elastic-Plastic Circular Plates," *Journal of Material Processing Technologies,* Vol. 28, pp. 321–334.

Downloaded 04 May 2010 to 171.66.16.27. Redistribution subject to ASME license or copyright; see http://www.asme.org/terms/Terms_Use.cfm

P. J. Halliday

K. Grosh
Mem. ASME

Department of Mechanical Engineering
and Applied Mechanics,
University of Michigan,
3124 G. G. Brown Building,
Ann Arbor, MI 48109-2125

Dynamic Response of Complex Structural Intersections Using Hybrid Methods

A novel application of Lagrange multipliers to couple domains modeled independently with linear elastodynamic and reduced-order theories is presented herein. This method is developed from a variational formulation of the continuous problem and is easily implemented within a finite element code. Applications include, but are not limited to, modeling of inhomogeneities such as joints, cracks, holes, and welds within a frame-like structure. Results from this method compare well with a full elastodynamic discretization and existing methods for modeling such problems.

1 Introduction

Within many common structures there are regions in which reduced-order models such as beam, rod, plate, and shell theories are appropriate based on the physical parameters of the system. Use of these theories will decrease the number of degrees-of-freedom required to accurately model a problem compared to a three-dimensional elastodynamic discretization, thereby reducing the memory and time requirements to perform computations. However, one deficiency in reduced-order models is their inability to represent the complex fields present around geometric and material inhomogeneities such as connections, holes and stiffeners. Regions such as these require an elastodynamic discretization to accurately capture the true variations.

The purpose of this work is to develop from first principles a method which consistently couples regions of inhomogeneity where elastodynamic theory is needed to less complex domains where reduced-order theory can be used. This method relates the through-the-thickness displacements of an arbitrary elastodynamic representation to the reduced-order Timoshenko beam kinematics on the interface between domains via Lagrange multiplier formalism similar to the interface traction link described by Zienkiewicz and Taylor (1989). The transition formulation is developed in the context of a variational framework and is merged seamlessly with either exact or approximate solutions for the response in the domain corresponding to the reduced theory. This paper is concerned with time-harmonic linear wave propagation in inhomogeneous structures. The method developed in this work can be extended to both nonlinear vibration and transient analysis.

Previous efforts to develop a transition methodology for connecting beam elements to elasticity elements have used several different methods. Transitions from a three-degree-of-freedom beam node (axial and transverse displacement as well as rotation) to a single elasticity element through the thickness have been developed by Bathe (1996), Kim and Hong (1995), and Surana (1979, 1980), but one obvious drawback to this approach is that there is no possibility for variation in displacements or stresses through-the-thickness without incorporating a nonuniform transition from a single element through-the-thickness to a more refined discretization. A three-dimensional analog of this method was presented by Gmur and Kauten (1993) which is subject to the same limitations. A Lagrange multiplier method which couples a beam to one node of an elasticity domain has been used by Giles and Norwood (1994), but this method does not allow for elasticity degrees of freedom through-the-thickness. Finally, a superelement condensation of an elasticity region in which the Timoshenko beam rigid director kinematic hypothesis is strongly enforced on the boundary displacements of the elasticity region has been developed by Gopalakrishnan and Doyle (1995). While this approach gives good results, it is not based on a statement of a modified boundary value problem but rather on a constraint applied to the discrete problem.

This paper describes a new Lagrange multiplier based transition formulation which weakly constrains displacements on and balances stresses over interfaces between beam and elasticity domains. The approach used in this paper is related to the concept of nonconforming finite elements for plates described by Mang and Gallagher (1977) and Jones' work on nonuniform elasticity representations (Jones, 1964). Numerical experiments are performed comparing the present method to other approximations of the joint dynamics.

2 Problem Formulation

The model problem for the transition element formulation consists of a beam-like structure made up of two regions, one of which is uniform and appropriately modeled using a reduced-order rod and beam theory, and another which is nonuniform and requires an elasticity discretization. A schematic of the elastodynamic configuration is shown in Fig. 1, with Ω^S denoting the structural domain where beam and rod theories are applicable, and Ω^E representing the elasticity domain where full linear elastodynamic theory is needed. The interface between Ω^S and Ω^E is denoted by Γ^I. The boundary of Ω^S is the union of the nonoverlapping sets Γ^S and Γ^I. Similarly, the boundary of Ω^E is $\Gamma^E \cup \Gamma^I$. A superscript S will be used to denote a structural response variable while a superscript E will imply elasticity herein.

2.1 Structural Domain. In the structural domain, Ω^S, Timoshenko beam theory is used to model the transverse deflection of the midsurface, denoted by w^S, and the rotation due to bending, θ^S, of the beam. Longitudinal motion, decoupled from transverse motion in the linear theory, is denoted by u^S and modeled by first-order rod theory. The governing equations of motion, for time-harmonic motion of the assumed form $e^{-i\omega t}$, are

$$EAu^S_{,xx} + \rho A\omega^2 u^S = f^D(x) \tag{1a}$$

$$GA\kappa[w^S_{,xx} - \theta^S_{,x}] + \rho A\omega^2 w^S = q^D(x) \tag{1b}$$

$$EI\theta^S_{,xx} + GA\kappa[w^S_{,x} - \theta^S] + \rho I\omega^2\theta^S = 0 \tag{1c}$$

Contributed by the Applied Mechanics Division of THE AMERICAN SOCIETY OF MECHANICAL ENGINEERS for publication in the ASME JOURNAL OF APPLIED MECHANICS.
Discussion on the paper should be addressed to the Technical Editor, Professor Lewis T. Wheeler, Department of Mechanical Engineering, University of Houston, Houston, TX 77204-4792, and will be accepted until four months after final publication of the paper itself in the ASME JOURNAL OF APPLIED MECHANICS.
Manuscript received by the ASME Applied Mechanics Division, Jan. 27, 1999; final revision, Mar. 30, 1999. Associate Technical Editor: M. Ortiz.

 Copyright © 1999 by ASME

Downloaded 04 May 2010 to 171.66.16.27. Redistribution subject to ASME license or copyright; see http://www.asme.org/terms/Terms_Use.cfm

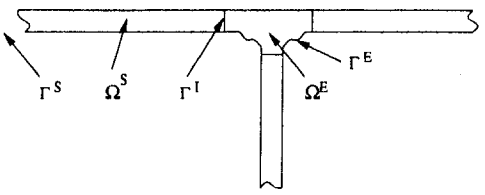


Fig. 1 Schematic of computational domains

where $f^D(x)$ and $q^D(x)$ are distributed loads. The force and moment resultants acting on a cross section of the beam are

$$f^S(x) = EAu^S_{,x} \tag{2a}$$

$$q^S(x) = GA\kappa[w^S_{,x} - \theta^S] = -EI\theta^S_{,xx} - \rho I\omega^2\theta^S \tag{2b}$$

$$M^S(x) = EI\theta^S_{,x}. \tag{2c}$$

A finite element formulation could be used to approximate the beam solution. However, to isolate errors associated with the transition element from other discretization issues, an exact Timoshenko beam solution is used for the beam elements. Several groups have developed methods for incorporating analytic solutions for straight Timoshenko beams and rods into a numerical model (Pestel and Leckie, 1963; Wang and Kinsman, 1970; Lunden and Akesson, 1983; Chen, 1987; Doyle and Farris, 1990; Gopalakrishnan et al., 1992). These elements represent the exact dynamic stiffness of the domain modeled by beam theory.

Evaluating a finite beam of length, L, with no distributed loads results in a solution of the form

$$u^S(x) = C_1 e^{-ik_R x} + C_4 e^{+ik_R(L-x)} \tag{3a}$$

$$w^S(x) = P_1 C_2 e^{-ik_1 x} + P_2 C_3 e^{-ik_2 x} - P_1 C_5 e^{+ik_1(L-x)} - P_2 C_6 e^{+ik_2(L-x)} \tag{3b}$$

$$\theta^S(x) = C_2 e^{-ik_1 x} + C_3 e^{-ik_2 x} + C_5 e^{+ik_1(L-x)} + C_6 e^{+ik_2(L-x)} \tag{3c}$$

where $k_R = \omega\sqrt{\rho/E}$ satisfies the dispersion relationship for the rod, k_1 and k_2 are the wave numbers of mode 1 and 2 satisfying the dispersion relationship for the Timoshenko beam (Graff, 1991; Gopalakrishnan et al., 1992), C_i are frequency-dependent amplitude coefficients which are dependent on the boundary conditions at the ends of the beam, and P_1 and P_2 are amplitude ratios relating displacement to rotation such that

$$w^S_j = i\left[\frac{EIk_j^2 + GA\kappa - \rho I\omega^2}{GA\kappa k_j}\right]\theta^S_j = P_j\theta^S_j, \quad j = 1, 2 \tag{4}$$

for the two allowed modes (Doyle and Farris, 1990; Gopalakrishnan et al., 1992; Graff, 1991). Using this solution form, a relationship can be written between the unknown coefficients and the degrees-of-freedom at the ends of the beam. By then substituting the solution, Eq. (3), into Eq. (2), a relationship can be found of the form

$$\mathbf{f}^S = \mathbf{K}^S\mathbf{d}^S \tag{5}$$

such that the nodal forcing vector $\mathbf{f}^S = \{f^S(0)\ q^S(0)\ M^S(0)\ f^S(L)\ q^S(L)\ M^S(L)\}^T$ is given by the multiplication of the exact dynamic stiffness matrix, $\mathbf{K}^S \in C^{6\times 6}$, and the displacement vector, $\mathbf{d}^S = \{u^S(0)\ w^S(0)\ \theta^S(0)\ u^S(L)\ w^S(L)\ \theta^S(L)\}^T$. This is the classical dynamic stiffness matrix for a Timoshenko beam (Pestel and Leckie, 1963).

It is important to note that in the absence of damping, the exact stiffness matrix is singular at the clamped-clamped natural frequencies of each element. However, this is easily remedied by introducing a complex Young's modulus, $E' = E(1 + i\epsilon)$.

2.2 Elasticity Domain. In order to accurately model regions of inhomogeneity, a finite element discretization of linear elasticity theory is used. In these regions, Ω^E, the strong form of the problem is to find the displacement vector $\mathbf{u}$ which satisfies

$$-\rho\omega^2 u_i - C_{ijkl}u_{(k,l)} = f_i \tag{6a}$$

$$u_i = g_i \text{ on } \Gamma_{g_i} \tag{6b}$$

$$\sigma_{ij}n_j = h_i \text{ on } \Gamma_{h_i} \tag{6c}$$

where essential boundary conditions are specified in the ith direction on Γ_{g_i}, natural boundary conditions are enforced on Γ_{h_i}, and n_i are the components of the outward pointing normal. Also, the notation $u_{(i,j)}$ represents the symmetric part of the gradient operator such that $u_{(i,j)} \equiv \frac{1}{2}(u_{i,j} + u_{j,i})$. The associated weak form of the problem—which is the basis for the finite element approximation—is to find $\mathbf{u}$ (a vector whose components are u_i) such that for all admissible variations (or weighting functions), $\delta\mathbf{u}$, the variational equations

$$a(\delta\mathbf{u}^E, \mathbf{u}^E)_{\Omega^E} = (\delta\mathbf{u}^E, \mathbf{f}^E)_{\Omega^E} + (\delta u^E, h_i)_{\Gamma_{h_i}} \tag{7}$$

are satisfied, where

$$a(\delta\mathbf{u}^E, \mathbf{u}^E)_{\Omega^E} \equiv \int_{\Omega^E} [\delta u_{(i,j)}C_{ijkl}u_{(i,j)} - \rho\omega^2\delta u_i u_i]d\Omega \tag{8a}$$

$$(\delta\mathbf{u}, \mathbf{v})_\Omega \equiv \int \delta u_i v_i d\Omega. \tag{8b}$$

Finite element interpolation functions are introduced into the variational equations at this point and standard arguments lead to a matrix equation of the form

$$\mathbf{K}^E\mathbf{d}^E = \mathbf{f}^E \tag{9}$$

where $\mathbf{K}^E$ is the dynamic stiffness matrix, $\mathbf{d}^E$ is the nodal displacement vector, and $\mathbf{f}^E$ is the nodal forcing vector. For the purposes of this paper, bilinear quadrilateral elements are used (Hughes, 1987).

3 Coupling the Two Domains

A method for coupling the structural and elasticity domains based on a Lagrange multiplier technique to weakly enforce the Timoshenko beam kinematic hypothesis on the elasticity displacements over Γ^I is developed in this section. This transition from one domain to another can be accomplished on an element-by-element basis or through a superelement which replaces the elasticity region through condensation.

3.1 Lagrange Multiplier Transition Formulation. A typical interface between the elasticity and structural domains is shown in Fig. 2. The variational formulation and resulting finite element implementation are presented.

3.1.1 Variational Formulation and Euler-Lagrange Equations. To couple the elasticity displacements through-the-thickness of the beam to the rigid director kinematic hypothesis of Timoshenko beam theory, constraints between the elasticity and beam displacements on the beam-elasticity interface, Γ^I, are enforced using Lagrange multipliers. These equations

$$u^S|_{\Gamma^I} - \frac{1}{A}\int_{\Gamma^I} u^E_1 d\Gamma^I = 0 \tag{10a}$$

$$w^S|_{\Gamma^I} - \frac{1}{A}\int_{\Gamma^I} u^E_2 d\Gamma^I = 0 \tag{10b}$$

Downloaded 04 May 2010 to 171.66.16.27. Redistribution subject to ASME license or copyright; see http://www.asme.org/terms/Terms_Use.cfm

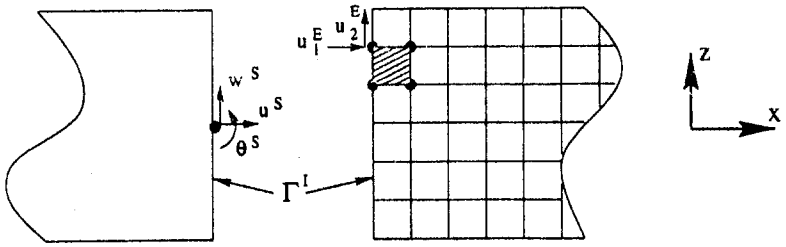


Fig. 2 Discretization near a typical interface

$$\theta^S|_{\Gamma^I} - \frac{1}{I}\int_{\Gamma^I} u_1^E z d\Gamma^I = 0 \qquad (10c)$$

are multiplied by Lagrange multipliers and added to the potential energy functional to couple elasticity and beam equations. The Lagrange multipliers will be seen to be stress resultants on Γ^I. In the absence of distributed loads in Ω^S, the combined beam-elasticity functional with the added constraints is

$$\Pi = \lambda_u \int_{\Gamma^I} (u^S - u^E) d\Gamma^I + \lambda_v \int_{\Gamma^I} (w^S - w^E) d\Gamma^I + \lambda_\theta \int_{\Gamma^I} (z^2\theta^S - zu^E) d\Gamma^I + \int_{\Omega^S} \tfrac{1}{2}\{EA(u^S_{,x})^2 + EI(\theta^S_{,x})^2 + GA\kappa[w^S_{,x} - \theta^S]^2 - \rho\omega^2[A(u^S)^2 + A(w^S)^2 + I(\theta^S)^2]\} d\Omega^S + \int_{\Gamma^S} \{f^S u^S + q^S w^S + M^S\theta^S\} d\Gamma^S + \tfrac{1}{2} a(\mathbf{u}^E, \mathbf{u}^E)_{\Omega^E} + (\mathbf{u}^E, \mathbf{f}^E)_{\Omega^E} + (\mathbf{u}^E, \mathbf{h})_{\Gamma^E}. \qquad (11)$$

The first line of Eq. (11) represents the Lagrange multiplier contribution to the augmented potential function. The second and third lines are the standard functionals for the Timoshenko beam and elastodynamic regions.

Taking the first variation of Eq. (11) and setting the result to zero yields the variational equation which forms the basis of the finite element discretization.

$$0 = \delta u^S \lambda_u A + \delta w^S \lambda_w A + \delta\theta^S \lambda_\theta I + \int_{\Gamma^I} \delta u_1^E(\lambda_\theta z - \lambda u) d\Gamma^I - \int_{\Gamma^I} \delta u_2^E \lambda_w d\Gamma^I + \delta\lambda_u[Au^S - \int_{\Gamma^I} u_1^E d\Gamma^I] + \delta\lambda_w[Aw^S - \int_{\Gamma^I} u_2^E d\Gamma^I + \delta\lambda_\theta[I\theta^S - \int_{\Gamma^I} zu_1^E d\Gamma^I] + \int_{\Omega^S} \{\delta u^S_{,x} EAu^S_{,x} + \delta\theta^S_{,x} EI\theta^S_{,x} + [\delta w^S_{,x} - \delta\theta^S]GA\kappa[w^S_{,x} - \theta^S] - \rho\omega^2[\delta u^S Au^S + \delta w^S Aw^S + \delta\theta^S I\theta^S]\} d\Omega^S + \int_{\Gamma^S} \{f^S\delta u^S + q^S\delta w^S + M^S\delta\theta^S\} d\Gamma^S + a(\delta\mathbf{u}^E, \mathbf{u}^E)_{\Omega^E} + (\delta\mathbf{u}^E, \mathbf{f}^E)_{\Omega^E} + (\delta\mathbf{u}^E, \mathbf{h})_{\Gamma^E} \qquad (12)$$

The Euler-Lagrange equations can now be extracted from Eq. (12) by using the divergence theorem or integration by parts and are as follows:

$$\delta u^S: EAu^S_{,xx} + \rho\omega^2 A = 0 \qquad (13a)$$

$$EAu^S_{,x} = f^S \text{ or } u^S = c_u^S \text{ on } \Gamma^S$$

$$EAu^S_{,x} = -\lambda_u A \text{ on } \Gamma^I$$

$$\delta w^S: GA\kappa(w^S_{,x} - \theta^S)_{,x} + \rho\omega^2 Aw^S = 0 \qquad (13b)$$

$$GA\kappa(w^S_{,x} - \theta^S) = q^S \text{ or } w^S = c_w^S \text{ on } \Gamma^S$$

$$GA\kappa(w^S_{,x} - \theta^S) = -\lambda_w A \text{ on } \Gamma^I$$

$$\delta\theta^S: GA\kappa(w^S_{,x} - \theta^S) + EI\theta_{,xx} = 0 \qquad (13c)$$

$$EI\theta_{,x} = M^S \text{ or } \theta^S = c_\theta^S \text{ on } \Gamma^S$$

$$EI\theta_{,x} = -\lambda_\theta I \text{ on } \Gamma^I$$

$$\delta u_i^E: C_{ijkl}u^E_{(k,l)_j} + \rho\omega^2 u_i^E = f_i^E \qquad (13d)$$

$$C_{ijkl}u_{(k,l)}n_j = h_i^E \text{ or } u_i^E = g_i \text{ on } \Gamma^E$$

$$C_{1jkl}u_{(k,l)}n_j = \lambda_u - \lambda_\theta z \text{ and } C_{2jkl}u_{(k,l)}n_j = \lambda_w \text{ on } \Gamma^I$$

$$\delta\lambda_u: Au^S - \int_\Gamma u_1^E d\Gamma = 0 \text{ on } \Gamma^I \qquad (13e)$$

$$\delta\lambda_w: Aw^S - \int_\Gamma u_2^E d\Gamma = 0 \text{ on } \Gamma^I \qquad (13f)$$

$$\delta\lambda_\theta: I\theta^S - \int_\Gamma zu_1^E d\Gamma = 0 \text{ on } \Gamma^I. \qquad (13g)$$

The Timoshenko beam and rod equations (Eq. (1)) are recovered in Eq. (13*a–c*) and the elastodynamic equations (Eq. (6)) in Eq. (13*d*) along with the associated admissible boundary conditions. Further, Eq. (13*e–g*) are new field equations associated with variations of the Lagrange multipliers which return the original constraint equations (Eq. (10)). It is through these new field equations and boundary terms that the structural and elasticity domains are coupled. To satisfy the Euler-Lagrange equations, it is clear that the Lagrange multipliers are the resultant stresses on the interface, Γ^I (see the last line in each of Eq. (13*a–d*)).

3.1.2 Finite Element Equations. This Lagrange multiplier-based transition is straightforward to implement within a finite element code. As was seen in Eq. (13) the governing equations in the elasticity and structural domains are unchanged except in the boundary terms on Γ^I. Therefore, the dynamic stiffness matrices for the elasticity and structural domains remain unchanged from a standard finite element formulation. The coupling of the two domains is achieved through the Lagrange multipliers and may be implemented in the finite element code as a separate element.

It can be seen from Eq. (13) that tractions on Γ^I for both Ω^S and Ω^E are functions of the Lagrange multipliers. The field equations associated with the Lagrange multipliers are functions of the structural and elasticity displacements on the interface. By incor-

Downloaded 04 May 2010 to 171.66.16.27. Redistribution subject to ASME license or copyright; see http://www.asme.org/terms/Terms_Use.cfm

porating the three Lagrange multipliers for an interface into the system as unknown degrees-of-freedom, a transition matrix can be written to account for the boundary terms and Lagrange multiplier field equations. Implementation of this transition can be done on an element-by-element basis through the thickness of the beam. Thus, to completely model the interface between the structural and elasticity domains, one such element must be included for each elasticity element through-the-thickness of the beam.

The assembled dynamic stiffness matrix for the coupled problem will be symmetric with zeroes on the block diagonal element corresponding to the Lagrange multiplier degrees-of-freedom, $\mathbf{d}^{\lambda}$, and has the following form:

$$\begin{bmatrix} \mathbf{K}^E & 0 & \mathbf{T}_{\lambda}^E \\ 0 & \mathbf{K}^S & \mathbf{T}_{\lambda}^S \\ (\mathbf{T}_{\lambda}^E)^T & (\mathbf{T}_{\lambda}^S)^T & 0 \end{bmatrix} \begin{Bmatrix} \mathbf{d}^E \\ \mathbf{d}^S \\ \mathbf{d}^{\lambda} \end{Bmatrix} = \begin{Bmatrix} \mathbf{0} \\ \mathbf{f}^S \\ \mathbf{0} \end{Bmatrix} \tag{14}$$

Here $\mathbf{K}^S$ and $\mathbf{K}^E$ are the dynamic stiffness matrices described in Eq. (5) and Eq. (9), respectively. The transition blocks $\mathbf{T}_{\lambda}^S$ and $\mathbf{T}_{\lambda}^E$ arise from the contributions to the variational equation by the constraint equations. Note that only three additional degrees-of-freedom per interface are engendered by the transition formulation. However, all of the elasticity degrees-of-freedom on an interface are coupled through the Lagrange multipliers.

The interpolation of displacements in the transition element is the same as that used in the elasticity domain. Results presented in this paper were found using a bilinear interpolation as was previously mentioned. The extension to time-domain computations is straightforward; there is no change in the transition element formulation.

3.1.3 Dynamic Joint Stiffness With Lagrange Multipliers. The Lagrange multiplier transition formulation can be used to develop a dynamic stiffness matrix for an inhomogeneity of any geometry. This matrix may be written in terms of only the structural degrees-of-freedom, $\mathbf{d}^S$, on its interfaces by condensing out the elasticity and Lagrange multiplier degrees-of-freedom. In this way, it is possible to examine the effects of geometric and material variations on a structure's response. Further, for inhomogeneities which occur multiple times in a structure, such a stiffness matrix can be calculated once and used repeatedly to model all of the similar regions.

Development of a superelement for modeling an inhomogeneity begins with the partitioning of the assembled dynamic stiffness matrix into submatrices relating elasticity, Lagrange multiplier, and structural degrees-of-freedom. Thus, a matrix equation in the form of Eq. (14) results. Through manipulation of the submatrices, it is found that the global equation can be written

$$\mathbf{f}^S = [\mathbf{K}^S + \mathbf{K}^{\Delta}]\mathbf{d}^S \tag{15}$$

where

$$\mathbf{K}^{\Delta} \equiv \mathbf{T}_{\lambda}^S[(\mathbf{T}_{\lambda}^E)^T(\mathbf{K}^E)^{-1}\mathbf{T}_{\lambda}^E]^{-1}(\mathbf{T}_{\lambda}^S)^T \tag{16}$$

such that the problem is cast only in terms of the structural degrees-of-freedom and forcing. The resulting dynamic stiffness matrix for an inhomogeneity is $\mathbf{K}^{\Delta} \in C^{3n\times 3n}$ where n is the number of structural-elasticity interfaces. Forcing on the interior of the elasticity domain may also be included.

3.2 Displacement-Based Superelement. An alternative formulation developed by Gopalakrishnan and Doyle (Gopalakrishnan and Doyle, 1995) couples the elasticity and structural formulations by placing constraints directly on the finite element elasticity displacements. In this method, the elasticity degrees-of-freedom are subdivided into those on an interface and those on the interior of the domain. The dynamic stiffness matrix representing Ω^E is partitioned to interior degrees of freedom, $\mathbf{d}_i^E$, and those on the beam-elasticity interface, $\mathbf{d}_{\Gamma I}^E$, such that the matrix equation can be written as

$$\begin{bmatrix} \mathbf{K}_{\Gamma\Gamma} & \mathbf{K}_{\Gamma i} \\ \mathbf{K}_{\Gamma i}^T & \mathbf{K}_{ii} \end{bmatrix} \begin{Bmatrix} \mathbf{d}_{\Gamma I}^E \\ \mathbf{d}_i^E \end{Bmatrix} = \begin{Bmatrix} \mathbf{f}_{\Gamma I}^E \\ 0 \end{Bmatrix}. \tag{17}$$

It is assumed that there is no forcing in the elasticity domain. By condensing out the interior degrees-of-freedom, this equation can be rewritten as

$$\mathbf{f}_{\Gamma I}^E = [\mathbf{K}_{\Gamma\Gamma} - \mathbf{K}_{\Gamma i}\mathbf{K}_{ii}^{-1}\mathbf{K}_{\Gamma i}^T]\mathbf{d}_{\Gamma I}^E. \tag{18}$$

In order to couple the displacement representation in the elasticity domain to a beam model, Eq. (10) is enforced pointwise on Γ in the Gopalakrishnan and Doyle method. A transition matrix $\mathbf{Q}$ is defined such that Eq. (10) are strongly enforced on the discrete displacements

$$\mathbf{d}_{\Gamma I}^E = \mathbf{Q}\mathbf{d}_{\Gamma I}^S \tag{19}$$

where the elasticity displacements conform exactly to the reduced-order kinematic hypothesis. The elasticity forces are converted into beam resultants by assuming that they transform according to the same rules (i.e., $\mathbf{Q}^T\mathbf{f}_{\Gamma I}^E = \mathbf{f}_{\Gamma I}^S$), such that

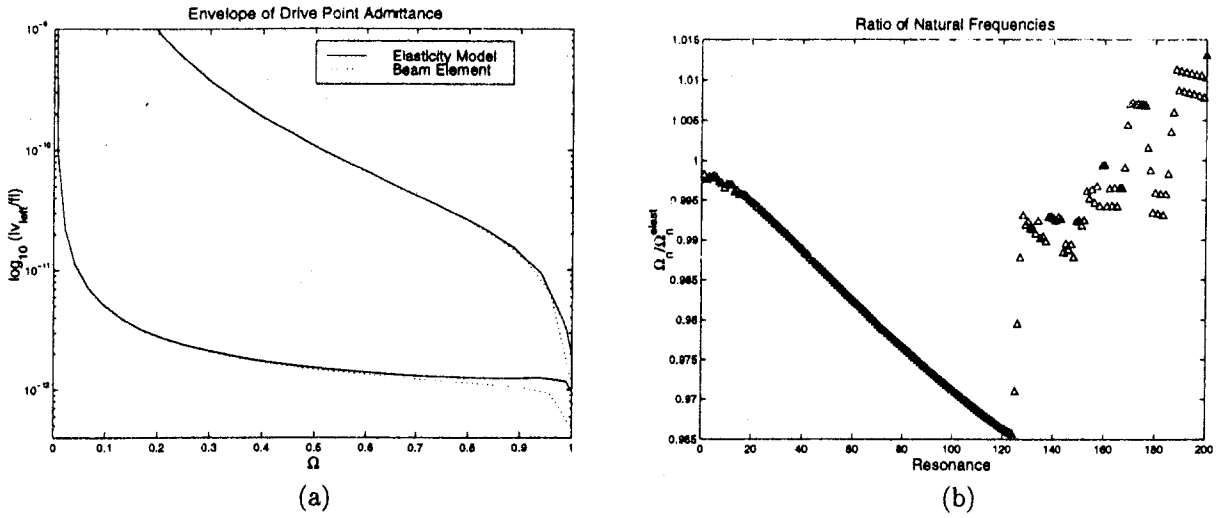


Fig. 3 (*a*) Upper and lower envelope of the drive point admittance of Timoshenko beam and elasticity models versus frequency normalized to ω_c, the cut in frequency of the second propagating mode. (*b*) Natural frequency ratio of Timoshenko beam and elastodynamic finite element models. Note that mode 124 corresponds to $\Omega = 1$.

Downloaded 04 May 2010 to 171.66.16.27. Redistribution subject to ASME license or copyright; see http://www.asme.org/terms/Terms_Use.cfm

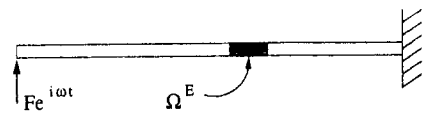


Fig. 4 Cantilevered beam with elasticity inclusion

$$\mathbf{f}^{S}_{\Gamma' I} = \mathbf{Q}^{T}[\mathbf{K}_{\Gamma\Gamma} - \mathbf{K}_{\Gamma i}\mathbf{K}_{ii}^{-1}\mathbf{K}_{\Gamma i}^{T}]\mathbf{Q}\mathbf{d}^{S}_{\Gamma' I} = \mathbf{K}^{SE}\mathbf{d}^{S}_{\Gamma' I}. \quad (20)$$

Here $\mathbf{K}^{SE}$ is a symmetric $3n \times 3n$ dynamic stiffness matrix for an elasticity domain with n interfaces.

4 Results

To test the transition formulations presented herein, a set of numerical experiments was conducted. In all cases, finite element discretizations of the complete domains provide the baseline for evaluating the accuracy of various methods. These experiments included analysis of a cantilevered beam and a cantilevered T-beam.

For all of the test cases run, the material properties were: $E' = 2.1 \times 10^{11}(1 + .001i)$ Pa, $\rho = 7800$ kg/m^3, and $\nu = 0.29$. All beam sections had a thickness of 0.01 m and the value of κ was set to 0.833 for the Timoshenko models. The finite element discretization for all cases was performed using square elements with ten elements through the thickness of the beam, thus a typical element was 0.001 m on a side. This was found to be a converged discretization for the frequency range studied.

4.1 Comparison of Timoshenko Theory to Numerical Experiment. The first test case compares the response predicted by a Timoshenko beam model of a one-meter cantilevered beam driven transversely at the free end to a linear elastic finite element model of the same problem. Results for Timoshenko beam theory are compared to an elasticity solution to provide insight into the range of validity for Timoshenko beam theory. Next, the same physical problem was modeled, this time including a region modeled by elasticity elements coupled to the beam theory through the Lagrange multiplier technique to provide an example of how combining two domains would affect a simple problem.

In Fig. 3(*a*), a the envelope of the drive point admittance is shown. The plots are made by finding the maximum and minimum values of the admittance versus forcing frequency and creating a spline by connecting these points. The envelopes of the admittance for the test case predicted by elastodynamic and beam theory are virtually identical until $\Omega = 0.65$, where $\Omega \equiv \omega/\omega_c$ and $\omega_c \equiv \sqrt{GA\kappa/\rho I}$. In Fig. 3(*b*), the ratio of Timoshenko beam to elasticity natural frequency for each mode shape is plotted versus mode number. It is seen that the Timoshenko beam model is less stiff than the elastodynamic beam model until the 124th mode which occurs at the cut in of the second propagating mode (when $\Omega = 1$). At very low frequencies, the natural frequency ratio asymptotes to 0.998 rather than 1.0 due to the differences in modeling the built in end of the beam in the elasticity and Timoshenko models. The error in the natural frequencies of the reduced-order model increases almost linearly until there is approximately a 3.5 percent error immediately before the second mode cuts in. Further, there are five more resonances predicted by the Timoshenko model than by the elastodynamic discretization before the cut in frequency as beam theory predicts lower natural frequencies.

From these results, it can be inferred that the Timoshenko beam model will predict displacements with a good degree of accuracy in a global sense. However, at any specific frequency the predicted displacements will not necessarily agree with finite element method results due to the possibility of being slightly offset from a natural frequency. Also, for frequencies in excess of ω_c the Timoshenko model will not perform well. This is expected since the reduced-order beam hypothesis does not admit the kinematics of higher modes (but does provide a parameter, κ, for fitting some of the response characteristics of the second mode).

As an initial test of the transition element, the same cantilevered beam was modeled with an inclusion of elasticity elements. The included elasticity domain comprised one tenth of the total beam length and was coupled using the Lagrange multiplier technique (Fig. 4). Within the elasticity domain, there were ten elements through-the-thickness as in the elastodynamic discretization of the full model.

The purpose of this test was to ensure that no spurious reflections are caused by the transition formulation. As can be seen in Fig. 5(*a*), the envelope of the drive point admittance is still correctly predicted with the elasticity domain inclusion. The inclusion of the elasticity domain, with the associated Lagrange multiplier transition elements, results in natural frequencies which are closer to the full elastodynamic formulation as shown in Fig. 5(*b*). Modeling more of the beam with elasticity theory gives a result which is even closer to the full elastodynamic discretization.

The use of the Lagrange multiplier transition elements does not introduce any unexpected behavior into the system. Instead, the results tend towards the elasticity model as is desired.

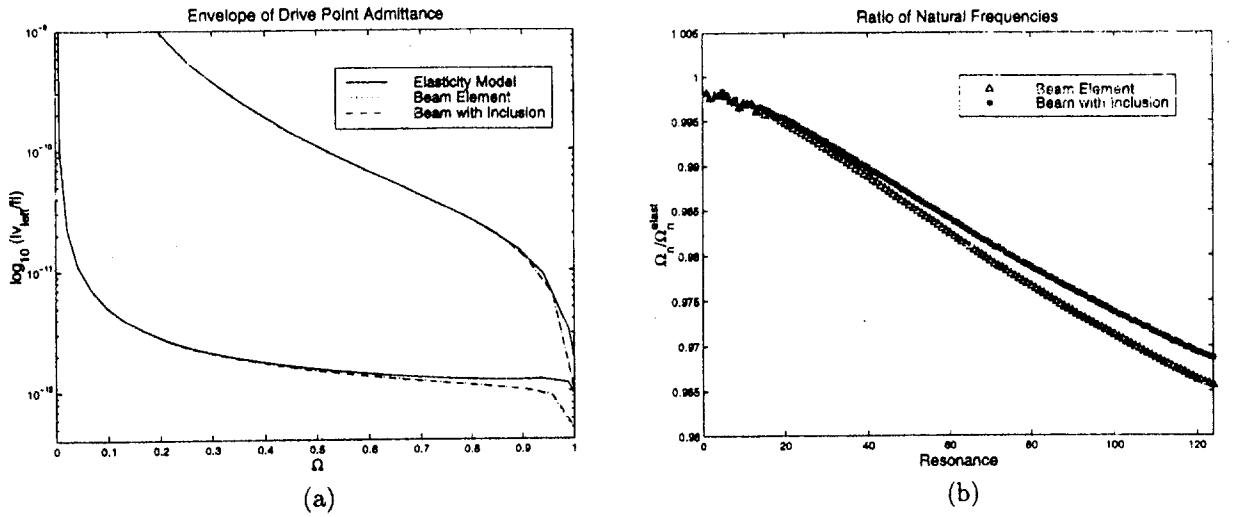


Fig. 5 (*a*) Envelope of the drive point admittance of cantilevered beam with elasticity inclusion modeled using Lagrange multiplier technique as well as a rigid connection and elastodynamics. (*b*) Natural frequency ratios. Note that the first 15 ratios are affected by the precision to which the natural frequencies are determined.

Downloaded 04 May 2010 to 171.66.16.27. Redistribution subject to ASME license or copyright; see http://www.asme.org/terms/Terms_Use.cfm

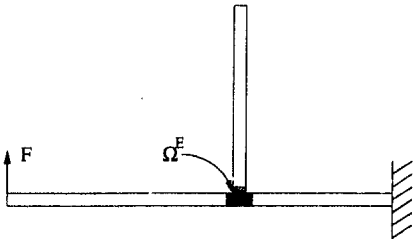


Fig. 6 Cantilevered T-beam with elasticity model of joint

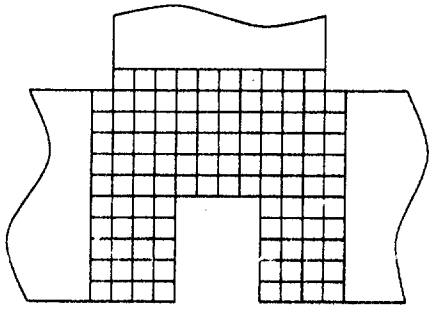


Fig. 8 Discretization of the notched joint

4.2 Analysis of T-Beam. To test the effectiveness of the transition methodologies, a cantilevered T-beam was modeled as in Fig. 6. The horizontal bar (as pictured) is of the same dimensions as the cantilevered beam modeled previously. The vertical bar, which is half the length of the horizontal with the same cross-sectional properties, is joined at a position 35 percent of the total length from the cantilevered end.

Four different techniques were used to model the intersection of the T-beam. In the first, the entire structure was discretized using elastodynamic finite elements as described previously. A second model was created using only three exact beam elements. This method enforced continuity of displacements and rotation at the intersection, thereby implying a rigid connection. The final two models shared a geometry, but one used the Lagrange multiplier transition elements developed in this work and the other the displacement based superlement of Gopalakrishnan and Doyle (1995). These models were created by combining exact beam elements with an elasticity discretization of the intersection (see Fig. 6). The junction elasticity domain, Ω^E, was modeled using elements the same size as in the full discretization and extended only one row of elements into the beam-like region. Thus, the junction-beam model consisted of 130 elasticity elements and three beam elements plus the coupling transition elements as opposed to 14,900 elements for the full elastodynamic solution. In general, modeling the joint one beam thickness into the beam-like region with elasticity elements will ensure that the beam elements start sufficiently far from the discontinuity to accurately capture the displacement field. However, in the problem modeled here, it was found from experimentation that accuracy was not lost in using the smaller model described above.

The results of forcing the T-beam transversely at the free end are shown in Fig. 7. The different models predict the solution envelope relatively well as is evidenced by Fig. 7(*a*). Note that the admittance plot is a qualitative measure of the accuracy of the various approximations due to its sensitivity to slight inaccuracies in estimating natural frequencies for a given method. However, Fig. 7(*b*) provides a better, more quantitative means of comparison. After the 60th resonance, the rigid connection becomes overly stiff compared to the elasticity discretization. This implies that there is some flexibility in the joint which is not being captured by a rigid connection and the assumption that an angle between beams will be preserved is not valid. Predictions from Lagrange multiplier transition and strict enforcement of the rigid director kinematics are very close to each other until mode 110. After this point, the two methods diverge, but neither develops an error in excess of five percent before the cut in frequency is reached.

4.3 Notched Joint. A similar T-beam was modeled as in Fig. 6, but with a rectangular notch cut into the underside of the joint shown in Fig. 8. This test highlights the importance of modeling such small defects even at low frequencies. The results of modeling the notched joint with the Lagrange multiplier transition method were compared to an elastodynamic discretization of the entire structure as well as to the joint model without the notch from the previous section.

The simulation was run for frequencies in the range $0 \leq \Omega \leq 0.1$. Over these frequencies there was a one-to-one correspondence in the number and location of natural frequencies between the full elasticity and Lagrange multiplier model. Errors in the natural frequencies were less than 1.0 percent in this range. This demonstrates the ability of the Lagrange multiplier transition method to accurately replicate the response.

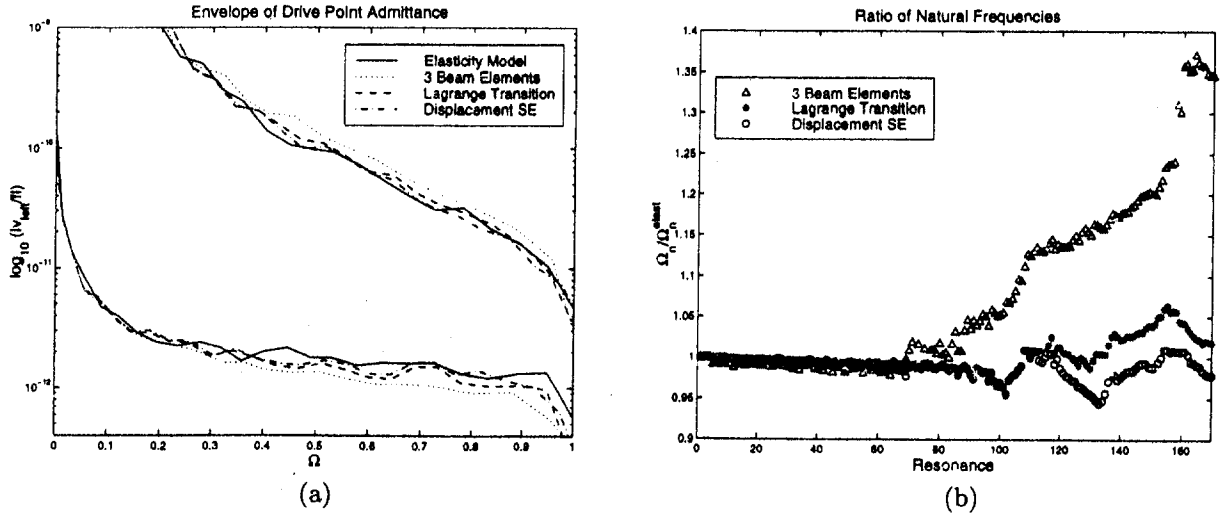


Fig. 7 (*a*) Envelope of the drive point admittance for a cantilevered T-beam with transverse harmonic forcing at the free end. Models are elastodynamic, rigid joint, Lagrange multiplier transition, and displacement-based superelement. (*b*) Natural frequency ratio of various methods to elastodynamic results. Note that mode 165 corresponds to $\Omega = 1$.

Downloaded 04 May 2010 to 171.66.16.27. Redistribution subject to ASME license or copyright; see http://www.asme.org/terms/Terms_Use.cfm

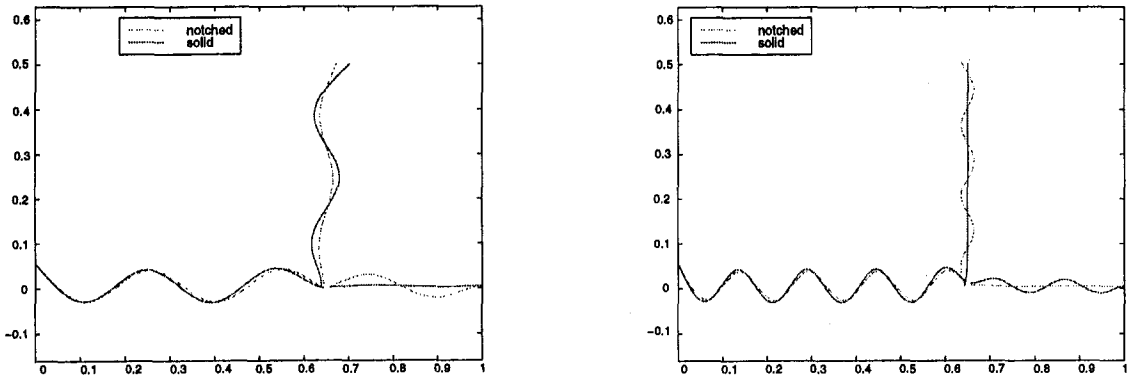


Fig. 9 (*a*) Mode 11 of the T-beam with and without a notched joint. (*b*) Mode 22 of the T-beam.

By examining the results from the notched and unnotched models, large discrepancies become apparent even at low frequencies. In Fig. 9, the results for two frequencies which show significant differences between the response of the notched and solid joint are illustrated. In the 11th deformed mode, the model with a solid joint has most of its deformation to the left of and above the joint while the section between the joint and the wall is hardly moving. Meanwhile, the notched model exhibits displacement in all three sections. The differences in the 22nd mode are even more striking. It can be seen that the solid joint model has significant displacements to the left and right of the joint but not above it while the notched model has significant displacements to the left and top of the joint.

5 Conclusions

This work provides a new means of coupling reduced-order models with elastodynamics. A Lagrange multiplier technique was used to couple the beam degrees-of-freedom to elastodynamic degrees-of-freedom through-the-thickness, thus allowing for an arbitrary discretization in the elasticity domain. It has been shown that this Lagrange multiplier technique is an effective, accurate, and variationally consistent method for accomplishing the transition. This method provides a degree of accuracy as good or better than previous methods and is simple to implement. Further, the importance of modeling small inhomogeneities is highlighted by the rather striking effect on the mode shapes of a T-beam when a notch is included in the joint.

The Lagrange multiplier technique presented here compares favorably with the approach of Gopalakrishnan and Doyle (Gopalakrishnan and Doyle, 1995). It is easier to implement on an element by element basis, but is not as straightforward to use in a superelement formulation. However, the Lagrange multiplier method does have the advantage of being derived from first principles and all assumptions are explicitly related to the original governing differential equations. Hence, this paper represents a contribution by developing the constraints based on the continuous problem rather than the discrete approximation as has been done in the past.

While the specific application presented in this paper was for time harmonic oscillations, a time-dependent case may be handled using the same formulation. Also, the application to a nonlinear analysis will use the same approach. Logical extensions of this formulation include three-dimensional space frames—including bending, longitudinal vibration, and torsion. Also of interest would be the development of a plate to elasticity transition formulation.

Acknowledgment

This work has been supported in part by grants from the Office of Naval Research; Dr. Rhosdy Barsoum, Program Monitor; and The University of Michigan Horace H. Rackham School of Graduate Studies.

References

Bathe, K. J., 1996, *Finite Element Procedures,* Prentice-Hall, Englewood Cliffs, NJ.

Chen, Y. H., 1987, "General Dynamic-Stiffness Matrix of a Timoshenko Beam for Transverse Vibrations," *Earthquake Engineering and Structural Dynamics,* Vol. 15, pp. 391–402.

Doyle, J. F., and Farris, T. N., 1990, "A Spectrally Formulated Element for Wave Propagation in 3-D Frame Structures," *The International Journal of Analytical and Experimental Modal Analysis,* Vol. 5, No. 4, pp. 223–237.

Giles, G. L., and Norwood, K., 1994, "Coupling Equivalent Plate and Finite Element Formulations in Multiple Method Structural Analyses," *Journal of Aircraft,* Vol. 31, No. 5, pp. 1189–1196.

Gmur, T. C., and Kauten, R. H., 1993, "Three-Dimensional Solid-to-Beam Transition Elements for Structural Dynamics Analysis," *International Journal for Numerical Methods in Engineering,* Vol. 36, pp. 1429–1444.

Gopalakrishnan, S., and Doyle, J. F., 1995, "Spectral Super-Elements for Wave Propagation in Structures With Local Non-uniformities," *Computer Methods in Applied Mechanics and Engineering,* Vol. 121, pp. 77–90.

Gopalakrishnan, S., Martin, M., and Doyle, J. F., 1992, "A Matrix Methodology for Spectral Analysis of Wave Propagation in Multiple Connected Timoshenko Beams," *Journal of Sound and Vibration,* Vol. 158, No. 1, pp. 11–24.

Graff, K. F., 1991, *Wave Motion in Elastic Solids,* Dover, New York.

Hughes, T. J. R., 1987, *The Finite Element Method,* Prentice-Hall, Englewood Cliffs, NJ.

Jones, R. E., 1964, "A Generalization of the Direct-Stiffness Method of Structural Analysis," *American Institute of Aeronautics and Astronautics,* Vol. 2, No. 5, pp. 821–826.

Kim, H. S., and Hong, S. M., 1995, "Formulation of Transition Elements for the Analysis of Coupled Wall Structures," *Computers and Structures,* Vol. 57, pp. 333–344.

Lunden, R., and Akesson, B., 1983, "Damped Second-Order Rayleigh-Timoshenko Beam Vibration in Space—an Exact Complex Dynamic Member Stiffness Matrix," *International Journal for Numerical Methods in Engineering,* Vol. 19, pp. 431–449.

Mang, H. A., and Gallagher, R. H., 1977, "A Critical Assessment of the Simplified Hybrid Displacement Method," *International Journal for Numerical Methods in Engineering,* Vol. 11, pp. 145–167.

Pestel, E. C., and Leckie, F. A., 1963, *Matrix Methods in Elastomechanics,* McGraw-Hill, New York.

Surana, K. S., 1979, "Isoparametric Elements for Cross-Sectional Properties and Stress Analysis of Beams," *International Journal for Numerical Methods in Engineering,* Vol. 14, pp. 475–497.

Surana, K. S., 1980, "Shape Functions for the Isoparametric Transition Elements for Cross-Sectional Properties and Stress Analysis of Beams," *International Journal for Numerical Methods in Engineering,* Vol. 15, pp. 1403–1407.

Wang, T. M., and Kinsman, T. A., 1970, "Vibrations of Frame Structures According to the Timoshenko Theory," *Journal of Sound and Vibration,* Vol. 14, pp. 215–227.

Zienkiewicz, O. C., and Taylor, R. L., 1989, *The Finite Element Method,* McGraw-Hill, New York.

Downloaded 04 May 2010 to 171.66.16.27. Redistribution subject to ASME license or copyright; see http://www.asme.org/terms/Terms_Use.cfm

R. O. Hryniv[1]

P. Lancaster

Department of Mathematics and Statistics,
The University of Calgary
2500 University Drive, N.W.,
Calgary, Alberta T2N 1N4,
Canada

A. A. Renshaw
Department of Mechanical Engineering,
Columbia University,
M/C 4703,
New York, NY 10027

A Stability Criterion for Parameter-Dependent Gyroscopic Systems

A stability criterion for parameter-dependent gyroscopic systems is established and three examples are used to illustrate its application to typical engineering problems. In a number of practical situations, the criterion can be used to predict system stability with little actual computation and without solving any eigenvalue problem or approximating the eigenvalue locus. Thus, the criterion provides designers with a quick and accurate tool for assessing the stability consequences of potential design changes.

1 Introduction

In a recent series of papers, Renshaw and Mote (1996), Lancaster and Kliem (1998), and Renshaw (1998) proposed and tested a stability criterion for gyroscopic systems that depend on an independent system parameter, herein denoted α. That criterion predicts whether the eigenvalue locus, $\lambda(\alpha)$, associated with a particular vanishing eigenvalue at $\alpha = \alpha_0$ has a positive real part in the neighborhood of α_0 based solely on properties of the eigensolutions associated with $\lambda(\alpha_0) = 0$. In the series of three papers, the criterion was presented only for the case of the onset of divergence instability and was proved only for two-degree-of-freedom systems. Renshaw and Mote (1996) originally proposed the criterion as a conjecture and verified it for several continuous, gyroscopic systems. Lancaster and Kliem (1998) presented three, two-degree-of-freedom counter-examples that proved the original criterion false. Renshaw (1998) reformulated the criterion to account for these counter examples and established its validity only for systems with two degrees-of-freedom.

The purpose of this paper is to present a generalized stability criterion that predicts the onset of both divergence and flutter instability and to give a proof of the criterion. Consequently, this work constitutes a substantial generalization and validation of the fairly restrictive results presented in the authors' previous papers. The focus of this work is engineering applications, and several examples are included to illustrate the practical value of the criterion. These examples, together with those given in Renshaw and Mote (1996) (to which the criterion still applies), demonstrate the utility and ease of use of the criterion. In a number of practical situations, the criterion can be used to predict system stability with little actual computation and without solving any eigenvalue problem or approximating the eigenvalue locus. Those readers interested in a more theoretical treatment of this and more general problems are referred to Hryniv and Lancaster (1998).

2 Mathematical Preliminaries

A gyroscopic system with infinitely (finitely) many degrees-of-freedom is described by the equation

$$M\frac{d^2u(t)}{dt^2} + G\frac{du(t)}{dt} + Ku(t) = 0, \tag{1}$$

where $u(t)$ is a function with values in some Hilbert (Euclidean) space H; t is time; and M, G, and K are operators (matrices) in H satisfying the symmetry conditions

$$M^* = M > 0, \quad G^* = -G, \quad K^* = K. \tag{2}$$

Associated with (1) is the operator-valued function of a complex variable λ

$$L(\lambda) = \lambda^2 M + \lambda G + K. \tag{3}$$

A complex number λ_0 for which the nullspace of the operator $L(\lambda_0)$ (written $N(L(\lambda_0))$) is nontrivial is called an *eigenvalue* of $L(\lambda)$ and any nonzero vector x_0 satisfying the relation $L(\lambda_0)x_0 = 0$ is a corresponding *eigenvector*. The set of all eigenvalues of $L(\lambda)$ constitutes its (point) *spectrum* $\sigma(L)$.

The operator L'_λ is defined to be the derivative of L with respect to λ:

$$L'_\lambda \equiv \frac{\partial L}{\partial \lambda} = 2\lambda M + G. \tag{4}$$

We say that x_1 is a *generalized eigenvector* associated with the eigenvalue λ_0 if there exists an eigenvector x_0 such that

$$L'_\lambda(\lambda_0)x_0 + L(\lambda_0)x_1 = 0 \tag{5}$$

(Gohberg et al., 1982). Eigenvalues λ_0 that admit a generalized eigenvector are termed *degenerate*. Eigenvalues λ_0 that are nondegenerate are also said to be *semisimple* (or *simple* if dim $N(L(\lambda_0)) = 1$).

Suppose that λ_0 is a purely imaginary degenerate eigenvalue (this admits $\lambda_0 = 0$) so that (5) holds and let $y_0 \in N(L(\lambda_0))$. The symmetries (2) imply that $L(\lambda_0)$ is self-adjoint and thus the inner product of (5) with y_0 gives

$$\begin{aligned} 0 &= (L'_\lambda(\lambda_0)x_0 + L(\lambda_0)x_1, y_0) \\ &= (L'_\lambda(\lambda_0)x_0, y_0) + (x_1, L(\lambda_0)y_0). \end{aligned} \tag{6}$$

Then $L(\lambda_0)y_0 = 0$ implies that

$$(L'_\lambda(\lambda_0)x_0, y_0) = 0. \tag{7}$$

Therefore, a purely imaginary eigenvalue λ_0 is semisimple if for every nonzero $x_0 \in N(L(\lambda_0))$ there exists a $y_0 \in N(L(\lambda_0))$ such that $(L'_\lambda(\lambda_0)x_0, y_0) \neq 0$.

[1] Post Doctoral Fellow of the Pacific Institute for Mathematical Sciences.

Contributed by the Applied Mechanics Division of THE AMERICAN SOCIETY OF MECHANICAL ENGINEERS for publication in the ASME JOURNAL OF APPLIED MECHANICS.

Discussion on the paper should be addressed to the Technical Editor, Professor Lewis T. Wheeler, Department of Mechanical Engineering, University of Houston, Houston, TX 77204-4792, and will be accepted until four months after final publication of the paper itself in the ASME JOURNAL OF APPLIED MECHANICS.

Manuscript received by the ASME Applied Mechanics Division, Aug. 27, 1998; final revision, Jan. 15, 1999. Associate Technical Editor: N. C. Perkins.

 Copyright © 1999 by ASME

Downloaded 04 May 2010 to 171.66.16.27. Redistribution subject to ASME license or copyright; see http://www.asme.org/terms/Terms_Use.cfm

3 System Stability

The system (1) is called *stable* if all of its solutions are bounded for $t \in \Re_+ = [0, \infty)$. It is straightforward to check that for every eigenpair $\{\lambda_0, x_0\}$ the function $u_0 = x_0 e^{\lambda_0 t}$ is a solution of (1). This solution is bounded if $\mathrm{Re}[\lambda_0] \leq 0$ and is unbounded if $\mathrm{Re}[\lambda_0] > 0$.

Due to the symmetries (2), if λ_0 is an eigenvalue of $L(\lambda)$, so is $-\bar{\lambda}_0$, where the overbar indicates complex conjugation. Consequently $\sigma(L)$ is symmetric with respect to the imaginary axis, and (1) can only be stable when the spectrum of $L(\lambda)$ lies on the imaginary axis.

It is well known, however, that this condition does not guarantee stability. In particular, if λ_0, x_0, and x_1 satisfy (5), then the function $u_1(t) = e^{\lambda_0 t}(tx_0 + x_1)$ is a solution of (1). Hence, each degenerate purely imaginary eigenvalue λ_0 causes instability of (1).

Equation (1) is stable if all the eigenvalues of the operator function $L(\lambda)$ are purely imaginary and semisimple provided a suitable completeness property of the system of eigenvectors and generalized eigenvectors is fulfilled (Miloslavskii, 1983). Such completeness always holds in the finite dimensional case (Gohberg et al., 1982) and for most problems of practical interest. We suppose that this is the case for Eq. (1). Consequently, to study the stability of (1) we can consider each eigenvalue of $L(\lambda)$ separately.

4 Stability Criterion for Parametric-Dependent Systems

Suppose that coefficients M, G, and K in (1) depend analytically on some physical parameter α. This implies that $M(\alpha)$, $G(\alpha)$, and $K(\alpha)$ have Taylor expansions at every point $\alpha = \alpha_0$ of interest. Then the spectrum of the corresponding operator-valued function $L(\lambda, \alpha)$ and, as a result, the stability of (1) depend on α as well. Since the point spectrum of $L(\lambda, \alpha)$ is continuous in α, we can consider each eigenvalue as a continuous function of α. We say that a purely imaginary eigenvalue $\lambda_0 = \lambda(\alpha_0)$ is *α-stable* if all eigenvalues $\lambda(\alpha)$ such that $\lambda(\alpha_0) = \lambda_0$ are purely imaginary and semisimple in some punctured real neighborhood of α_0; otherwise it is *α-unstable.*

Renshaw and Mote (1996) conjectured that, if a zero (and therefore purely imaginary) eigenvalue at α_0 is semisimple, then it is α-stable, and if a zero eigenvalue at α_0 is degenerate, then it is α-unstable. Lancaster and Kliem (1998) showed by example that both statements are false, in general. Thus, a semisimple eigenvalue at α_0 may be α-unstable, and a degenerate eigenvalue at α_0 may be α-stable. Here we show that, at the expense of an additional condition, the Renshaw-Mote dichotomy can be recovered and generalized to include *all* purely imaginary eigenvalues.

Given the additional condition, the result implies that, if a purely imaginary eigenvalue λ_0 and its eigenfunctions at $\alpha = \alpha_0$ are known, we can predict the α-stability of this eigenvalue without explicitly calculating the eigenvalue locus $\lambda(\alpha)$.

To begin with, all purely imaginary, simple eigenvalues $\lambda_0(\alpha_0)$ are α-stable due to symmetry and continuity in α. Consequently, the stability question concerns purely imaginary, nonsimple eigenvalues.

Define α_0 to be a critical value of α if there is a purely imaginary eigenvalue $\lambda(\alpha_0)$ that is nonsimple. Then $\lambda(\alpha_0)$ is said to be a critical eigenvalue. Define the operator L'_α to be the derivative of L with respect to α evaluated at $\alpha = \alpha_0$ and $\lambda = \lambda_0$, i.e.,

$$L'_\alpha \equiv \frac{\partial L(\lambda_0, \alpha_0)}{\partial \alpha}. \tag{8}$$

The following criterion determines whether critical eigenvalues $\lambda(\alpha_0)$ are α-stable or α-unstable.

Stability Criterion. Suppose that $\alpha = \alpha_0$ is a critical value with the corresponding nonsimple purely imaginary eigenvalue $\lambda_0 = \lambda(\alpha_0)$. Suppose also that, for all nonzero eigenvectors $x_0 \in N(L(\lambda_0, \alpha_0))$, the inequality $(L'_\alpha x_0, x_0) \neq 0$ holds. Then the eigenvalue λ_0 is α-stable when λ_0 is semisimple and α-unstable when λ_0 is degenerate.

In other words, with this hypothesis a stable system (i.e., one with only simple and semisimple eigenvalues) remains stable in some neighborhood of α_0, while an unstable one (i.e., one with degenerate eigenvalues) is unstable in at least one of a left or right open neighborhood of α_0.

The algorithm for applying the criterion is the following:

1 Find the nullspace $N \equiv N(L(\lambda_0, \alpha_0))$; put $n = \dim N(\leq \infty)$.

2 Choose an orthonormal basis $e_1, \ldots, e_n$ of N.

3 Form the Gram matrix $A = (a_{ij}) \equiv (L'_\alpha e_i, e_j)$. The criterion applies if A is either positive or negative definite.

4 Study the solvability of Eq. (5). If the matrix $B = (b_{ij}) \equiv (L'_\lambda e_i, e_j)$ is nonsingular, then (5) has no solutions, and the eigenvalue λ_0 is semisimple and is α-stable. Otherwise λ_0 is degenerate and is α-unstable.

Observe that steps (2) and (3) are unnecessary if $L'_\alpha > 0$ or $L'_\alpha < 0$, conditions that apply in many physical problems (Renshaw, 1998). The criterion can also be applied without explicitly finding N provided the appropriate inner products can still be evaluated. For instance, in Example 2 below, the criterion is applied simply by knowing that the eigenfunctions are separable in θ. In fact, as shown by the examples below, it is in the special case when L'_α is definite and the inner products $(L'_\alpha e_i, e_j)$ can be evaluated without explicitly knowing the e_i that the criterion is most useful. This is true for a number of important engineering systems.

5 Proof

Under the definiteness assumption $(L'_\alpha x_0, x_0) \neq 0$, each eigenvalue locus $\lambda(\alpha)$ with $\lambda(\alpha_0) = \lambda_0$ defines an invertible function, and the inverse function $\alpha(\lambda)$ is analytic at $\lambda = \lambda_0$. Moreover, the eigenvector $x(\lambda)$ satisfying

$$L(\lambda, \alpha)x(\lambda) = 0 \tag{9}$$

for $\alpha = \alpha(\lambda)$ is an analytic function of λ at $\lambda = \lambda_0$ as well (Hryniv and Lancaster, 1998). In particular,

$$\alpha_0(\lambda) = \alpha_0 + c_1(\lambda - \lambda_0) + c_2(\lambda - \lambda_0)^2 + \ldots, \tag{10}$$

with $i^k c_k$ real. The value of c_1 can be found by differentiating (9) with respect to λ, evaluating at $\alpha = \alpha_0$ and $\lambda = \lambda_0$, and taking inner products with $x_0 \equiv x_0(\lambda_0)$:

$$(\alpha'_0(\lambda_0)L'_\alpha(\lambda_0, \alpha_0)x_0 + L'_\lambda(\lambda_0, \alpha_0)x_0 + L(\lambda_0, \alpha_0)x'_0, x_0) = 0, \tag{11}$$

i.e.,

$$c_1 = \alpha'_0(\lambda_0) = -(L'_\lambda(\lambda_0, \alpha_0)x_0, x_0)/(L'_\alpha(\lambda_0, \alpha_0)x_0, x_0) \tag{12}$$

provided the denominator is nonzero. If for $\alpha = \alpha_0$ there is a generalized eigenvector corresponding to λ_0 and x_0, then $c_1 = 0$ due to (7). Conversely, if $c_1 = 0$, then the vector $x_1 = x'_0$ is a generalized eigenvector satisfying (5).

Let c_q, $q \geq 1$, be the first nonzero coefficient in (10). Inverting this series, we get a Puiseux expansion (having q different branches according to the choice of the qth root of 1)

$$\lambda_0(\alpha) - \lambda_0 = ((c_q^{-1}(\alpha - \alpha_0))^{1/q} + \ldots. \tag{13}$$

From (13) we conclude that if $q > 1$, i.e., if λ_0 is a degenerate eigenvalue of $L(\lambda, \alpha_0)$, then for α in at least one of a left or right open neighborhood of α_0, the eigenvalue $\lambda_0(\alpha)$ (more exactly, at least one of its branches in (13)) goes off the imaginary axis. Conversely, in case $q = 1$, the semisimple eigenvalue $\lambda_0(\alpha_0)$ remains purely imaginary for all real α close to α_0.

Downloaded 04 May 2010 to 171.66.16.27. Redistribution subject to ASME license or copyright; see http://www.asme.org/terms/Terms_Use.cfm

6 Examples

Presented below are three examples illustrating possible uses of the stability criterion for engineering analysis and design. These examples together with those of Renshaw and Mote (1996) demonstrate the computational advantages and insight afforded by the criterion.

Example 1: Two-Degree-of-Freedom Systems. Consider the two-dimensional system

$$L(\lambda) = \lambda^2 M + \lambda\alpha G_1 + K_0 + \alpha^2 K_1, \tag{14}$$

$$M = \begin{bmatrix} 1 & 0 \\ 0 & 1 \end{bmatrix}, \quad G_1 = \begin{bmatrix} 0 & -2 \\ 2 & 0 \end{bmatrix},$$

$$K_0 = \begin{bmatrix} k_1 & 0 \\ 0 & k_2 \end{bmatrix}, \quad K_1 = \begin{bmatrix} \Gamma_1 & 0 \\ 0 & \Gamma_2 \end{bmatrix}, \tag{15}$$

where $\Gamma_1 < 0$ and $\Gamma_2 < 0$. When $\Gamma_1 = \Gamma_2 = -1$, (14) and (15) can be used to model shaft whirl, the motion of a discrete point particle of unit mass attached to a flexible massless shaft with principal lateral stiffnesses k_1 and k_2 (both positive numbers) that rotates at angular speed α (Huseyin and Plaut, 1974–1975; Done and Simpson, 1977). This system exhibits divergence instability at certain speeds when $k_1 \neq k_2$, no divergence instability when $k_1 = k_2$, and does not exhibit flutter instability. Equations (14) and (15) can also be used to model an elastic pipe conveying fluid at speed α when $\Gamma_1 \neq \Gamma_2$ (Plaut, 1976). Unlike the shaft whirl problem, this system can exhibit both divergence and flutter instabilities.

For this system, the stability criterion predicts the same *potential* divergence and flutter stability boundaries given by direct analysis of the system's characteristic equation. However, unlike the characteristic equation analysis, the criterion is able to differentiate when, in fact, instability arises.

Characteristic Equation Analysis. The characteristic equation associated with (14) is

$$\lambda^4 + (k_1 + k_2 + \alpha^2(4 + \Gamma_1 + \Gamma_2))\lambda^2 + (k_1 + \Gamma_1\alpha^2)(k_2 + \Gamma_2\alpha^2) = 0, \tag{16}$$

which is quadratic in both λ^2 and α^2. The onset of divergence instability requires $\lambda = 0$ which implies

$$(k_1 + \Gamma_1\alpha^2)(k_2 + \Gamma_2\alpha^2) = 0. \tag{17}$$

Hence the two critical speeds are $\alpha_1 = (-k_1/\Gamma_1)^{1/2}$ and $\alpha_2 = (-k_2/\Gamma_2)^{1/2}$. The onset of flutter instability requires repeated roots, or

$$4(k_1 + \alpha^2\Gamma_1)(k_2 + \alpha^2\Gamma_2) = [k_1 + k_2 + \alpha^2(4 + \Gamma_1 + \Gamma_2)]^2. \tag{18}$$

This condition is quadratic in α^2 and can be solved to identify those α at which flutter may occur. For shaft whirl, $\Gamma_1 = \Gamma_2 = -1$, and (18) reduces to

$$\alpha^2 = \frac{-(k_1 - k_2)^2}{8(k_1 + k_2)} \leq 0, \tag{19}$$

which has no physically relevant solutions. Consequently, flutter does not occur. For other cases, flutter can occur. For example, when $\Gamma_1 = -1$ and $\Gamma_2 = -9$,

$$\alpha^2 = \frac{(k_1 - k_2)^2}{8(k_2 - 3k_1)}, \tag{20}$$

which does have physically relevant solutions for $k_2 > 3k_1$. However, both the divergence and flutter instability analyses require additional calculations to determine if, in fact, instability occurs.

The Stability Criterion. Now consider system stability using the stability criterion. For the onset of divergence instability, the critical speeds associated with $\lambda = 0$ are $\alpha_1 = (-k_1/\Gamma_1)^{1/2}$ and $\alpha_2 = (-k_2/\Gamma_2)^{1/2}$. When $\alpha_1 = \alpha_2$, the eigenvectors span $\Re^2$ and

$$(L'_\lambda x_0, y_0) = \alpha(G_1 x_0, y_0) = \alpha \bar{y}_0^T G_1 x_0 \neq 0 \tag{21}$$

whenever x_0 and y_0 are linearly independent. Therefore the eigenvalue $\lambda = 0$ is semisimple. Since

$$(L'_\alpha x_0, x_0) = 2\alpha(K_1 x_0, x_0) \neq 0, \tag{22}$$

the eigenvalue must be α-stable and no divergence instability occurs. When $\alpha_1 \neq \alpha_2$, the eigenvectors span a one-dimensional subspace of $\Re^2$, so

$$(L'_\lambda x_0, x_0) = \alpha(G_1 x_0, x_0) = \alpha \bar{x}_0^T G_1 x_0 = 0, \tag{23}$$

and therefore the eigenvalue is degenerate. Since (22) remains valid, both critical speeds α_1 and α_2 correspond to the onset of divergence, which occurs for $\alpha_1 < \alpha < \alpha_2$.

At the onset of flutter $\lambda = i\omega \neq 0$, two eigenvectors of the eigenvalue problem

$$\begin{bmatrix} \lambda^2 + k_1 + \alpha^2\Gamma_1 & -2\alpha\lambda \\ 2\alpha\lambda & \lambda^2 + k_2 + \alpha^2\Gamma_2 \end{bmatrix} x = 0, \tag{24}$$

are

$$x_0 = [2\alpha\lambda(\lambda^2 + k_1 + \alpha^2\Gamma_1)]^T,$$
$$y_0 = [(\lambda^2 + k_2 + \alpha^2\Gamma_2) - 2\alpha\lambda]^T. \tag{25}$$

Since $\lambda \neq 0$, these two solutions are not linearly independent and the critical eigenvectors only span a one-dimensional subspace of C^2. The condition

$$(L'_\lambda x_0, y_0) = (2\lambda M x_0 + \alpha G_1 x_0, y_0) = \bar{y}_0^T \begin{bmatrix} 2\lambda & -2\alpha \\ 2\alpha & 2\lambda \end{bmatrix} x_0 = 0 \tag{26}$$

is required for the onset of flutter instability. Equation (26) reduces to

$$3\lambda^4 + (k_1 + k_2 + \alpha^2(4 + \Gamma_1 + \Gamma_2))\lambda^2 - (k_1 + \alpha^2\Gamma_1)(k_2 + \alpha^2\Gamma_2) = 0. \tag{27}$$

After subtracting (16), this equation is equivalent to (18). Hence, the stability criterion predicts the same potential flutter boundary as the characteristic equation.

Condition (18) is only necessary for flutter. The additional condition

$$(L'_\alpha x_0, x_0) = (\lambda G_1 x_0 + 2\alpha K_1 x_0, x_0) = \bar{x}_0^T \begin{bmatrix} 2\alpha\Gamma_1 & -2\lambda \\ 2\lambda & 2\alpha\Gamma_2 \end{bmatrix} x_0 \neq 0 \tag{28}$$

is required to *guarantee* that flutter occurs.

Consider two specific cases.

When $k_1 = 1$, $k_2 = 5$, $\Gamma_1 = -1$, and $\Gamma_2 = -7$, there are repeated, imaginary roots $\lambda = \sqrt{3 - 4/\sqrt{3}}\, i \sim 0.831i$ when $\alpha = (4/3)^{1/4} \sim 1.07$. The only eigenvector is proportional to $x_0 = [2\alpha\lambda\ (\alpha^2 - 2)]^T$, for which $(L'_\lambda x_0, x_0) = 0$ and $(L'_\alpha x_0, x_0) \neq 0$. Consequently, flutter instability occurs.

When Γ_2 is changed to -9, the characteristic equation is $\lambda^4 = 0$ at $\alpha = 1$, whose solution is $\lambda = 0$, repeated four times. The only eigenvector is proportional to $x_0 = [1\ 0]^T$, for which $(L'_\lambda x_0, x_0) = 0$ and $(L'_\alpha x_0, x_0) \neq 0$. Consequently, the eigenvalues are α-unstable at $\alpha = 1$. In fact, divergence instability occurs in some neighborhood $1 - \epsilon < \alpha < 1$, $\epsilon > 0$, while flutter instability occurs in a neighborhood $1 < \alpha < 1 + \epsilon$.

Downloaded 04 May 2010 to 171.66.16.27. Redistribution subject to ASME license or copyright; see http://www.asme.org/terms/Terms_Use.cfm

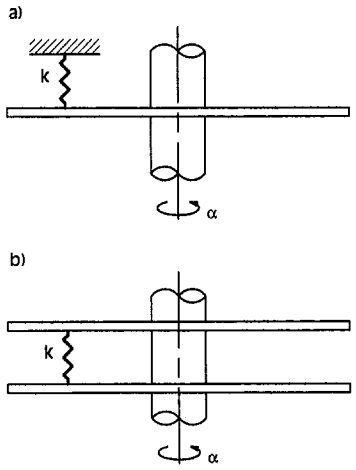


Fig. 1 Alternative spring-loaded rotating disk systems analyzed in Example 2

Example 2: Coupled, Rotating Disk Stacks. In Examples 2 and 3, we consider the divergence instability of different rotating disk systems. Models of this sort are relevant to the design of industrial circular saws and computer disk drives. Renshaw and Mote (1996) presented several rotating disk examples whose key results we briefly summarize.

The eigenvalue problem for an axisymmetric disk rotating at speed α is (Iwan and Moeller, 1976)

$$\lambda^2 Ix + \lambda\alpha G_1 x + K_0 x + \alpha^2 K_1 x = 0, \tag{29}$$

$$G_1 = 2\frac{\partial}{\partial\theta},$$

$$K_0 = \nabla^4, \quad K_1 = \frac{\partial^2}{\partial\theta^2} - \frac{1}{r}\frac{\partial}{\partial r}\left(r\sigma_r\frac{\partial}{\partial r}\right) - \frac{1}{r^2}\sigma_\theta\frac{\partial^2}{\partial\theta^2}, \tag{30}$$

where $x(r, \theta)$ is the transverse deflection of the disk, I is the identity operator, ∇^4 is the biharmonic operator, and $\alpha^2\sigma_r$ and $\alpha^2\sigma_\theta$ are the radial and hoop stresses, respectively. It is well known that this system possesses critical speeds α_0 at which nontrivial critical eigenfunctions with $\lambda = 0$ exist of the form

$$x_0(r, \theta) = (c_1 \sin(n\pi\theta) + c_2 \cos(n\pi\theta))u(r), \tag{31}$$

where n is an integer greater than one (Renshaw and Mote, 1992) and c_1 and c_2 are arbitrary constants. No divergence instability occurs at these critical speeds since $(L'_\lambda x_0, y_0) = \alpha_0(G_1 x_0, y_0) \neq 0$ for every x_0 and some y_0 and $(L'_\alpha x_0, x_0) = 2\alpha_0(K_1 x_0, x_0) \neq 0$ for every x_0.

However, for a rotating disk loaded by a stationary transverse spring of stiffness k located at $r = r_0$ and $\theta = 0$, such as illustrated in Fig. 1(a), the operator K_0 is

$$K_0 = \nabla^4 + k\delta(r - r_0)\delta(\theta)/r, \tag{32}$$

and the critical eigenfunctions are only

$$x_0(r, \theta) = c_1 \sin(n\pi\theta)u(r), \tag{33}$$

due to the presence of the spring. In this case divergence instability occurs since $\alpha_0(G_1 x_0, x_0) = 0$ for every x_0.

In Renshaw and Mote (1996), the divergence instability caused by a stationary transverse spring was eliminated by considering design changes to the central clamp of the disk. Here we consider the design modification shown in Fig. 1(b) in which a stack of two rotating disks on a single spindle are coupled by a stationary spring located between the two disks. This model is representative of a computer hard disk drive comprised of multiple disks and read/write heads (Shen and Ku, 1997). Denoting the deflections of the lower and upper disks by x and y, respectively, the eigenvalue problem for the coupled disk system is

$$\lambda^2 Ix + \lambda\alpha G_1 x + K_0 x + \alpha^2 K_1 x + k(x - y)\delta(r - r_0)\delta(\theta)/r = 0,$$

$$\lambda^2 Iy + \lambda\alpha G_1 y + K_0 y + \alpha^2 K_1 y - k(x - y)\delta(r - r_0)\delta(\theta)/r = 0. \tag{34}$$

For this coupled problem, the critical eigenfunctions have the form

$$x_0 = y_0 = (c_1 \sin(n\pi\theta) + c_2 \cos(n\pi\theta))u(r). \tag{35}$$

For (35), $\alpha_0(G_1 x_0 + G_1 y_0, z_0) \neq 0$ for some critical z_0. Therefore, divergence instability does not occur.

Note that these conclusions are drawn without knowing $u(r)$. This is one of the important advantages of this criterion.

Example 3: Absence of Aeroelastic Divergence Instability in Rotating Disks. According to the criterion, the stability of vanishing eigenvalues is independent of the mass operator, M, of the system. Therefore the stability of vanishing eigenvalues for systems that differ only in M must be identical.

One such pair of systems is a disk rotating in a vacuum and a disk rotating in and coupled to an incompressible inviscid fluid. The disk rotating in a vacuum has, of course, no divergence instabilities. If it can be shown that the fluid coupling only affects the mass operator, then the aerodynamically coupled disk can possess no divergence instabilities as well.

Let $x(r, \theta)e^{\lambda t}$ be the transverse deflection of the disk and $p(r, \theta, z)e^{\lambda t}$ be the fluid pressure. The disk lies in the $z = 0$ plane. The equation of motion of the disk reduces to

$$\lambda^2 Ix + \lambda\alpha G_1 x + K_0 x + \alpha^2 K_1 x = p|_{z=0}, \tag{36}$$

where the operators are given by (30). The fluid motion is described by a velocity potential ϕ that satisfies $\nabla^2\phi = 0$ throughout the volume occupied by the fluid. The fluid pressure is given by $p = \lambda\phi$ and the fluid problem is driven by the inhomogeneous coupling boundary condition $\partial\phi/\partial z|_{z=0} = \lambda x$. All other boundary conditions are homogeneous. The fluid problem can be solved in terms of x by use of an inverse or Green's function operator (Renshaw and Mote, 1994). As a result, the pressure loading on the disk can be written in the form

$$p|_{z=0} = -\lambda^2 Rx \tag{37}$$

where R is a positive self-adjoint operator (Sneddon, 1966). The stability of the coupled fluid/disk system is therefore determined by the eigenvalue problem

$$\lambda^2(I + R)x + \lambda\alpha G_1 x + K_0 x + \alpha^2 K_1 x = 0. \tag{38}$$

Physically, R represents the added mass of the fluid. Because it is the only change in the system afforded by the fluid coupling, the aerodynamically coupled disk exhibits no divergence instabilities, only flutter instabilities. Similar reasoning also applies to aerodynamically coupled stacks of disks (Tseng and Wickert, 1998).

8 Conclusion

A stability criterion for parameter dependent gyroscopic systems is presented together with its proof. Three examples are used to illustrate its application to typical engineering problems. In a number of practical situations, the criterion can be used to predict system stability with little actual computation and without solving any eigenvalue problem or approximating the eigenvalue locus. Thus, the criterion provides designers with a quick and accurate tool for assessing the stability consequences of potential design changes.

Downloaded 04 May 2010 to 171.66.16.27. Redistribution subject to ASME license or copyright; see http://www.asme.org/terms/Terms_Use.cfm

Acknowledgment

The authors are grateful to the reviewers for thoughtful comments which have helped to improve the exposition of this paper.

References

Done, G. T. S., and Simpson, A., 1977, "Dynamic Instability of Certain Conservative and Non-Conservative Systems," *Journal of Mechanical Engineering Science,* Vol. 19, No. 6, pp. 251–263.

Gohberg, I., Lancaster, P., and Rodman, L., 1982, *Matrix Polynomials,* Academic Press, New York.

Hryniv, R., and Lancaster, P., 1998, "On the Perturbation of Analytic Matrix Functions," *Integral Equations and Operator Theory,* to appear.

Huseyin, K., and Plaut, R. H., 1974–1975, "Transverse Vibrations and Stability of Systems with Gyroscopic Forces," *Journal of Structural Mechanics,* Vol. 3, No. 2, pp. 163–177.

Iwan, W. D., and Moeller, T. L., 1976, "The Stability of a Spinning Elastic Disk with a Transverse Load System," ASME JOURNAL OF APPLIED MECHANICS, Vol. 43, pp. 485–490.

Lancaster, P., and Kliem, W., 1998, "Comments on Stability Properties of Conservative Gyroscopic Systems," ASME Journal of Applied Mechanics, accepted for publication.

Miloslavskii, A. I., 1983, "Foundations of the Spectral Approach in Nonconservative Problems of the Theory of Elastic Stability," *Functional Analysis and Its Applications,* Vol. 17, pp. 233–235.

Plaut, R. H., 1976, "Alternative Formulations for Discrete Gyroscopic Eigenvalue Problems," *AIAA Journal,* Vol. 14, pp. 431–435.

Renshaw, A. A., and Mote, Jr., C. D., 1992, "Absence of One Nodal Diameter Critical Speed Modes in an Axisymmetric Rotating Disk," ASME JOURNAL OF APPLIED MECHANICS, Vol. 59, pp. 687–688.

Renshaw, A. A., D'Angelo, III, C., and Mote, Jr., C. D., 1994, "Aerodynamically Excited Vibration of a Rotating Disk," *Journal of Sound and Vibration,* Vol. 177, pp. 577–590.

Renshaw, A. A., and Mote, Jr., C. D., 1996, "Local Stability of Gyroscopic Systems Near Vanishing Eigenvalues," ASME JOURNAL OF APPLIED MECHANICS, Vol. 63, pp. 116–120.

Renshaw, A. A., 1998, "Stability of Gyroscopic Systems Near Vanishing Eigenvalues," ASME JOURNAL OF APPLIED MECHANICS, accepted for publication.

Shen, I. Y., and Ku, C.-P. R., 1997, "A Nonclassical Vibration Analysis of a Multiple Rotating Disk and Spindle Assembly," ASME JOURNAL OF APPLIED MECHANICS, Vol. 64, pp. 165–174.

Sneddon, I. N., 1966, *Mixed Boundary Value Problems in Potential Theory,* Elsevier, New York.

Tseng, J. G., and Wickert, J. A., 1998, "Split Vibration Modes in Acoustically-Coupled Disk Stacks," *Journal of Vibration and Acoustics,* Vol. 120, pp. 234–239.

Downloaded 04 May 2010 to 171.66.16.27. Redistribution subject to ASME license or copyright; see http://www.asme.org/terms/Terms_Use.cfm

Elastodynamic Green's Function for Laminated Anisotropic Circular Cylinders

W. Zhuang
Graduate Student

A. H. Shah
Professor

Civil and Geological Engineering Department,
University of Manitoba,
Winnipeg, Manitoba R3T 2N2, Canada

S. B. Dong
Professor Emeritus
University of California,
Los Angeles, CA 90095-1593
Mem. ASME

The construction of a steady-state Green's function for a laminated anisotropic circular cylinder is presented herein. The cylinder's profile through its depth consists of any number of perfectly bonded, uniform thickness concentric cylindrical layers, with each able of having its own distinct elastic cylindrically anisotropic properties. Green's function is predicated on the superposition of numerically generated modal solutions from a system of equations based on a semi-analytical finite element formulation. Two methods are proposed for its construction, both relying on the same set of eigendata. One is by means of an integral transform. The other may be viewed as the forced vibration of a cylinder with cylindrically monotropic properties under symmetry/antisymmetry conditions on the cross section containing the source load. The second method, being more restrictive with respect to material properties, was intended primarily as a cross-check of the integral transform version of Green's function. Numerical implementation details are discussed in terms of two example thickness profiles to show the essential keys for the convergence and accuracy of Green's function.

Introduction

The circular cylinder is a universal geometry and such structural components fabricated from laminated composite materials are expanding rapidly into many technological realms. Their manifold advantages are of sufficient common knowledge, so that there is no need in dwelling further on them. With increasing usage of such structures must come some means for monitoring their structural integrity in operating environments. One feature of a monitoring program will naturally include techniques for detecting and characterizing flaws such as cracks and delaminations during an operating life cycle.

In this paper, attention is devoted to the development of a steady-state elastodynamic Green's function for a composite circular cylinder. The cylinder may be composed of perfectly bonded concentric layers, each with a distinct thickness and cylindrically anisotropic mechanical properties. Establishing a Green's function supports an ultimate goal of quantitative nondestructive evaluation (QNDE) for locating and estimating the size and extent of cracks, delaminations, and other flaws in such structures. In view of the complexities in addressing an arbitrary laminate profile for the composite cylinder, the construction of Green's function will be pursued numerically herein by superposing finite element modal solutions. These solutions are obtained by extracting eigendata from an algebraic eigensystem based on a semi-analytical finite element (SAFE) formulation. It is envisioned that Green's function will be used in a boundary element method for studying realistic cracks and other flaws that may occur from fabrication and other field service conditions. Attention herein, however, is restricted to Green's function as many issues concerning convergence and accuracy of the proposed modal representation require careful examination.

There exist a substantial body of literature related to the dispersive wave propagation characteristics in cylinders. A review by Soldatos (1994) contains many references to the general problem of dynamics of cylinders and cylindrical shells. There are several papers based on a SAFE formulation of the governing equations and the eigensolution that are directly pertinent to the present study, i.e., Nelson, Dong, and Kalra (1971), Huang and Dong (1984), and Rattanawangcharoen, Shah, and Datta (1992, 1994a). They are similar in terms of the one-dimensional finite element modeling of the thickness profile and the Rayleigh-Ritz formulation for determination of all spectral data (i.e., the dispersion relations). Other references of related studies to this general problem can be found in these papers.

Studies of wave reflection at a free end of the cylinder and wave propagation through a region of a cylinder containing material disturbances have also appeared in the literature. In Rattanwangcharoen (1993) and Rattanwangcharoen, Shah, and Datta (1994b), the wave reflection analysis is carried out by a superposition of all admissible traveling waves and end modes to mathematically satisfy a traction-free end condition. Recently, hybrid methods have been proposed to study the scattering of waves in a flawed region. Such methods rely on combining two-dimensional finite element modeling of the inner field (i.e., the flawed region) with spectral data for the outer field under properly enforced interface conditions. Zhu and Shah (1997) studied transient wave scattering in composite plates with this method, and Rattanawangchareon, Zhuang, Shah, and Datta (1997) and Zhuang, Shah, and Datta (1997) applied it to cylinders containing surface cracks and V-shaped weldments.

Use of Green's function in conjunction with the boundary element method represents a different QNDE strategy for detecting flaws. This approach is attractive because of the relative ease in forming the boundary element in the presence of crack-tip stress singularities. It has been applied by Zhu, Shah, and Datta (1995), Zhu (1996), and Zhu, Shah, and Datta (1996) for plane strain waves in laminated composite plates.

Two methodologies are given for constructing a steady-state elastodynamic Green's function for a laminated circular cylinder, one based on integral transform and the other on forced vibration. The forced vibration method, given for a cylindrically monotropic cylinder and is thus more restrictive constitutively, was intended to verify the integral transform version of Green's function. While many similarities with Green's function for composite plates can be observed, there is major difference in that a double series is

Contributed by the Applied Mechanics Division of The American Society of Mechanical Engineers for publication in the ASME Journal of Applied Mechanics.
Discussion on the paper should be addressed to the Technical Editor, Professor Lewis T. Wheeler, Department of Mechanical Engineering, University of Houston, Houston, TX 77204-4792, and will be accepted until four months after final publication of the paper itself in the ASME Journal of Applied Mechanics.
Manuscript received by the ASME Applied Mechanics Division, Apr. 21, 1998; final revision, Jan. 15, 1999. Associate Technical Editor: V. K. Kinra.

 Copyright © 1999 by ASME

Downloaded 04 May 2010 to 171.66.16.27. Redistribution subject to ASME license or copyright; see http://www.asme.org/terms/Terms_Use.cfm

needed for cylinders as opposed with a single series for plates. Thus, its precision in relation to the attendant computational effort must be explored. The first parts of the paper deal with the formulation of the finite element governing equations, the general solution procedure for steady-state loads, and the algebraic eigenproblem of any given circumferential mode. Then, the methodologies for generating Green's function are given along with a discussion of the numerical implementation details.

Preliminaries

Adopt a system of cylindrical coordinates (r, θ, z) with the origin fixed at the center of a generic cross section of the cylinder, as shown in Fig. 1, and let t denote time. The mechanical variables of the problem are the displacement $\mathbf{u}$, stress $\boldsymbol{\sigma}$ and strain $\boldsymbol{\epsilon}$ with components

$$\mathbf{u}(r, \theta, z, t) = [u, v, w]^T \tag{1}$$

$$\boldsymbol{\sigma}(r, \theta, z, t) = [\sigma_{rr}, \sigma_{\theta\theta}, \sigma_{zz}, \sigma_{\theta z}, \sigma_{rz}, \sigma_{r\theta}]^T \tag{2}$$

$$\boldsymbol{\epsilon}(r, \theta, z, t) = [\epsilon_{rr}, \epsilon_{\theta\theta}, \epsilon_{zz}, \gamma_{\theta z}, \gamma_{rz}, \gamma_{r\theta}]^T. \tag{3}$$

In anticipation of a separation of variables solution strategy, the differential operators that relate the components of $\boldsymbol{\epsilon}$ to $\mathbf{u}$ are written in split form as

$$\boldsymbol{\epsilon} = (L_r + L_\theta + L_z)\mathbf{u} \tag{4}$$

where (L_r, L_θ, L_z) are 6×3 matrices whose components are

$$L_r = \begin{bmatrix} \frac{\partial}{\partial r} & \cdots & \cdots \\ \frac{1}{r} & \cdots & \cdots \\ \cdots & \cdots & \cdots \\ \cdots & \cdots & \cdots \\ \cdots & \cdots & \frac{\partial}{\partial r} \\ \cdots & \frac{\partial}{\partial r} - \frac{1}{r} & \cdots \end{bmatrix}; \quad L_\theta = \begin{bmatrix} \cdots & \cdots & \cdots \\ \cdots & \frac{1}{r}\frac{\partial}{\partial \theta} & \cdots \\ \cdots & \cdots & \cdots \\ \cdots & \cdots & \frac{1}{r}\frac{\partial}{\partial \theta} \\ \cdots & \cdots & \cdots \\ \frac{1}{r}\frac{\partial}{\partial \theta} & \cdots & \cdots \end{bmatrix};$$

$$L_z = \begin{bmatrix} \cdots & \cdots & \cdots \\ \cdots & \cdots & \cdots \\ \cdots & \cdots & \frac{\partial}{\partial z} \\ \cdots & \frac{\partial}{\partial z} & \cdots \\ \frac{\partial}{\partial z} & \cdots & \cdots \\ \cdots & \cdots & \cdots \end{bmatrix}. \tag{5}$$

The constitutive relation for any layer in the laminated cylinder is

$$\boldsymbol{\sigma} = \mathbf{D}\boldsymbol{\epsilon} \tag{6}$$

where $\mathbf{D}$ is a (6×6) matrix of cylindrically anisotropic elastic moduli with the anisotropy axis coinciding with the z-axis. In the case of a solid cylinder, the properties as $r \to 0$ must exhibit a transition from anisotropy to transverse isotropy in order for a physically meaningful axisymmetric structure, i.e., $D_{11} = D_{22}$, $D_{13} = D_{23}$, $D_{44} = D_{55}$. No such restrictions are necessary if the cylinder is hollow.

Governing Equations Based on Semianalytical Finite Elements

A semi-analytical finite element method is used to formulate the governing equations. By this method, the axial, circumferential, and time dependencies of $\mathbf{u}$ are left undetermined at the outset,

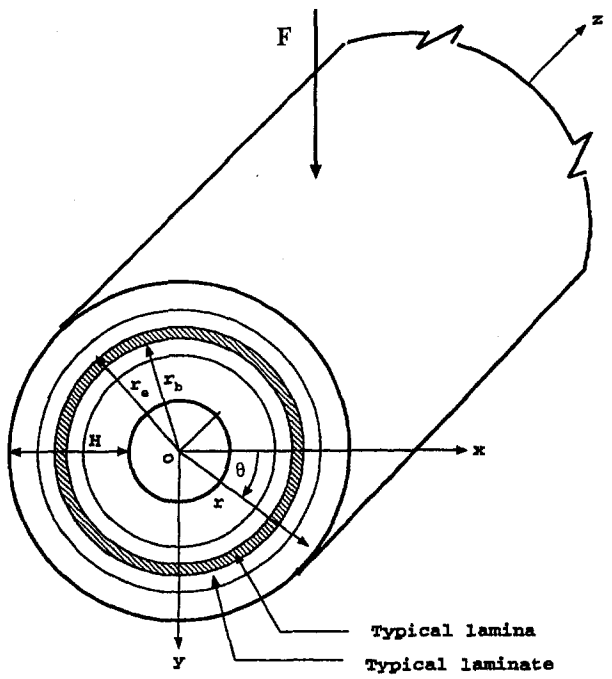


Fig. 1 Geometry of a laminated cylinder

leaving the radial dependence to be treated by finite element modeling. The thickness profile is therefore discretized radially into cylindrical laminas, and within each lamina, quadratic interpolations over three equally spaced nodal surfaces characterize their kinematic behavior. Each lamina is a separate entity enjoying distinct mechanical properties and thickness, so that a system of such elements can represent a laminated, anisotropic cylinder with an arbitrary number of bonded layers.

Isoparametric finite element methodology is employed; the interpolation functions $\mathbf{n}$'s in the parent element in terms of local variable $\zeta(-1 \le \zeta \le +1)$ are given by

$$\mathbf{n}(\zeta) = [\eta_b(\zeta), \eta_m(\zeta), \eta_e(\zeta)]$$
$$= [\tfrac{1}{2}\zeta(\zeta - 1), (1 - \zeta^2), \tfrac{1}{2}\zeta(\zeta + 1)] \tag{7}$$

where subscripts b, m, e denote the inner, middle, and outer nodal surfaces. Accordingly, interpolations of r and any field variable, say x, over the isoparametric element appear as

$$r = \eta_b(\zeta)r_b + \eta_m(\zeta)r_m + \eta_e(\zeta)r_e;$$
$$x = \eta_b(\zeta)x_b + \eta_m(\zeta)x_m + \eta_e(\zeta)x_e. \tag{8}$$

Casting $\mathbf{u}$ as an assembled interpolation field over the complete thickness profile of the cylinder gives

$$\begin{bmatrix} u(r, \theta, z, t) \\ v(r, \theta, z, t) \\ w(r, \theta, z, t) \end{bmatrix} = \begin{bmatrix} N(r\{\zeta\}) & \cdot & \cdot \\ \cdot & N(r\{\zeta\}) & \cdot \\ \cdot & \cdot & N(r\{\zeta\}) \end{bmatrix} \begin{bmatrix} U(\theta, z, t) \\ V(\theta, z, t) \\ W(\theta, z, t) \end{bmatrix} \tag{9}$$

or

$$\mathbf{u}(r, \theta, z, t) = \mathbf{N}(r)\mathbf{U}(\theta, z, t) \tag{9a}$$

with $\mathbf{N}(r)$ as the assembled $\mathbf{n}(\zeta)$'s interpolations from all elements and $\mathbf{U}(\theta, z, t)$ as its corresponding system array of nodal degrees-of-freedom. Substituting Eq. (9) into Eq. (4) gives the strains as

$$\boldsymbol{\epsilon} = \mathbf{B}_1\mathbf{U} + \mathbf{B}_2\mathbf{U}_{,\theta} + \mathbf{B}_3\mathbf{U}_{,z} \tag{10}$$

Downloaded 04 May 2010 to 171.66.16.27. Redistribution subject to ASME license or copyright; see http://www.asme.org/terms/Terms_Use.cfm

where the components of strain-transformation matrices $\mathbf{B}_i$ ($i = 1, 2, 3$) are given by

$$\mathbf{B}_1 = \begin{bmatrix} N_{,r} & \cdots & \cdots \\ N/r & \cdots & \cdots \\ \cdots & \cdots & \cdots \\ \cdots & \cdots & \cdots \\ \cdots & \cdots & N_{,r} \\ \cdots & N_{,r} - N/r & \cdots \end{bmatrix}; \quad \mathbf{B}_2 = \begin{bmatrix} \cdots & \cdots & \cdots \\ \cdots & N/r & \cdots \\ \cdots & \cdots & \cdots \\ \cdots & \cdots & N/r \\ \cdots & \cdots & \cdots \\ N/r & \cdots & \cdots \end{bmatrix};$$

$$\mathbf{B}_3 = \begin{bmatrix} \cdots & \cdots & \cdots \\ \cdots & \cdots & \cdots \\ \cdots & \cdots & N \\ \cdots & N & \cdots \\ N & \cdots & \cdots \\ \cdots & \cdots & \cdots \end{bmatrix} \tag{11}$$

and a comma denotes partial differentiation with respect to the variable that follows.

The governing displacement equations of motion are obtained by Hamilton's principle,

$$\delta \int_{t_1}^{t_2} (T - V)dt = 0, \tag{12}$$

with T and V as the kinetic and total potential energies given by

$$T = \frac{1}{2}\int_{\text{vol}} \rho \dot{\mathbf{u}}^T \dot{\mathbf{u}} d\text{vol}; \quad V = \frac{1}{2}\int_{\text{vol}} \boldsymbol{\epsilon}^T \mathbf{D} \boldsymbol{\epsilon} d\text{vol} + V_e \tag{13}$$

where ρ represents the mass density and V_e is the potential energy of external forces given by

$$V_e = -\mathbf{U}^T \mathbf{P} \tag{14}$$

where $\mathbf{P}$ represents the consistent load vector, whose specific form involves the product of applied surface traction and their corresponding displacement interpolations. Substituting $\dot{\mathbf{u}}$ from differentiating Eq. (9) into T and $\boldsymbol{\epsilon}$ of Eq. (10) into V transforms the integrand of Eq. (12) completely in terms of the kinematic variables of the problem. Its variation leads to a discrete system of governing equations of motion for the cylinder.

$$\mathbf{K}_1\mathbf{U} + \mathbf{K}_2\mathbf{U}_{,\theta} + \mathbf{K}_3\mathbf{U}_{,z} - \mathbf{K}_4\mathbf{U}_{,\theta\theta} - \mathbf{K}_5\mathbf{U}_{,\theta z} - \mathbf{K}_6\mathbf{U}_{,zz} + \mathbf{M}\ddot{\mathbf{U}} = \mathbf{F} \tag{15}$$

where the system stiffness matrices, $\mathbf{K}_i$'s, mass $\mathbf{M}$ and consistent load vector $\mathbf{F}$ are defined by

$$\mathbf{K}_1 = 2\pi \int \mathbf{B}_1^T \mathbf{D} \mathbf{B}_1 r dr; \quad \mathbf{K}_2 = 2\pi \int (\mathbf{B}_1^T \mathbf{D} \mathbf{B}_2 - \mathbf{B}_2^T \mathbf{D} \mathbf{B}_1) r dr$$

$$\mathbf{K}_4 = 2\pi \int \mathbf{B}_2^T \mathbf{D} \mathbf{B}_2 r dr; \quad \mathbf{K}_3 = 2\pi \int (\mathbf{B}_1^T \mathbf{D} \mathbf{B}_3 - \mathbf{B}_3^T \mathbf{D} \mathbf{B}_1) r dr$$

$$\mathbf{K}_6 = 2\pi \int \mathbf{B}_3^T \mathbf{D} \mathbf{B}_3 r dr; \quad \mathbf{K}_5 = 2\pi \int (\mathbf{B}_2^T \mathbf{D} \mathbf{B}_3 + \mathbf{B}_3^T \mathbf{D} \mathbf{B}_2) r dr \tag{16}$$

$$\mathbf{M} = 2\pi \int \rho \mathbf{N}^T \mathbf{N} r dr \tag{17}$$

$$\mathbf{F} = 2\pi \int \mathbf{N}^T \mathbf{P} r dr. \tag{18}$$

Observe the algebraic structures of the stiffness matrices $\mathbf{K}_i$'s as given by formula (16). Note that $\mathbf{K}_1$, $\mathbf{K}_4$, $\mathbf{K}_5$, and $\mathbf{K}_6$ are symmetric while $\mathbf{K}_2$ and $\mathbf{K}_3$ are antisymmetric.

Solution Procedure for Steady-State Loading

In addressing governing Eq. (15), consider time harmonic applied loads $\mathbf{F}$ of frequency ω. The steady-state response $\mathbf{U}$ must be periodic with the same frequency ω. Let the θ-dependence of the loads and response be expressed by Fourier series. Hence, $\mathbf{F}$ and $\mathbf{U}$ can be written as

$$\mathbf{F}(\theta, z, t) = e^{i\omega t}\mathbf{F}(\theta, z) = e^{i\omega t} \sum_{n=-\infty}^{n=+\infty} e^{in\theta} \bar{\mathbf{F}}_n(z)$$

$$\mathbf{U}(\theta, z, t) = e^{i\omega t}\mathbf{U}(\theta, z) = e^{i\omega t} \sum_{n=-\infty}^{n=+\infty} e^{in\theta} \bar{\mathbf{U}}_n(z). \tag{19}$$

Substituting Eq. (19) into Eq. (15) yields a system of ordinary differential equations in z for the Fourier coefficient functions $\bar{\mathbf{U}}_n$'s, the nth term of which has the form

$$(\mathbf{K}_1 + in\mathbf{K}_2 + n^2\mathbf{K}_4 - \omega^2\mathbf{M})\bar{\mathbf{U}}_n + (\mathbf{K}_3 - in\mathbf{K}_5)\bar{\mathbf{U}}_{n,z} - \mathbf{K}_6\bar{\mathbf{U}}_{n,zz} = \bar{\mathbf{F}}_n. \tag{20}$$

The z-dependence is treated by means of a Fourier integral transform. The transform pairs are defined in terms of the transform parameter k_n as

$$f(k_n) = \int_{-\infty}^{\infty} \bar{f}(z) e^{-ik_n z} dz; \quad \bar{f}(z) = \frac{1}{2\pi}\int_{-\infty}^{\infty} f(k_n) e^{ik_n z} dk_n. \tag{21}$$

Application of the Fourier transform to Eq. (20) gives

$$(\mathbf{K}_1 + in\mathbf{K}_2 + n^2\mathbf{K}_4 - \omega^2\mathbf{M})\mathbf{U}_n + ik_n(\mathbf{K}_3 - in\mathbf{K}_5)\mathbf{U}_n + k_n^2\mathbf{K}_6\mathbf{U}_n = \mathbf{F}_n. \tag{22}$$

Equation (22) is the governing equation for the nth circumferential harmonic in the transformed domain. In the solution to Eq. (22), the first step involves the consideration of the homogeneous equation, which has the form of a three-parameter algebraic eigensystem, in which either ω, n, or k_n can be called upon to be the eigenvalue parameter. Herein, k_n is adopted as the eigenvalue parameter and specific values are assigned to ω and n. The quadratic eigenproblem (22) for k_n can be recast into first-order form as

$$[\mathbf{A}(n, \omega) - k_n\mathbf{B}(n)]\mathbf{Q}_n = \mathbf{P}_n \tag{23}$$

where

$$\mathbf{A}(n, \omega) = \begin{bmatrix} \mathbf{0} & (\mathbf{K}_1 + in\mathbf{K}_2 + n^2\mathbf{K}_4 - \omega^2\mathbf{M}) \\ (\mathbf{K}_1 + in\mathbf{K}_2 + n^2\mathbf{K}_4 - \omega^2\mathbf{M}) & i(\mathbf{K}_3 - in\mathbf{K}_5) \end{bmatrix};$$

$$\mathbf{B}(n) = \begin{bmatrix} (\mathbf{K}_1 + in\mathbf{K}_2 + n^2\mathbf{K}_4 - \omega^2\mathbf{M}) & \mathbf{0} \\ \mathbf{0} & -\mathbf{K}_6 \end{bmatrix} \tag{24}$$

$$\mathbf{Q}_n = \begin{bmatrix} \mathbf{U}_n \\ k_n\mathbf{U}_n \end{bmatrix}; \quad \mathbf{P}_n = \begin{bmatrix} \mathbf{0} \\ \mathbf{F}_n \end{bmatrix}. \tag{25}$$

By extracting the eigendata from homogeneous form of Eq. (23), the response to the nth circumferential mode in the Fourier series representation of the applied loads can be constructed by modal summation. The eigendata herein serve as the basis for constructing a Green's function, the details of which are given in a subsequent section.

Downloaded 04 May 2010 to 171.66.16.27. Redistribution subject to ASME license or copyright; see http://www.asme.org/terms/Terms_Use.cfm

The Circumferential Mode Eigenproblem and Modal Summation

If the dimension of displacement vector $\mathbf{U}_n$ is M, then $\mathbf{Q}_n$ that emerges from the transformation of Eq. (22) to Eq. (23) is twice as long or $2M$. Nontrivial homogeneous solutions of Eq. (23) are found by requiring the determinant of the coefficient matrix of $\mathbf{Q}_n$ to vanish. The polynomial equation in k_n from expansion of the determinant yields $2M$ roots. This equation serves as the *dispersion relation* in our finite element model of the cylinder. The $2M$ roots of k_n (denoted as k_{nm}'s) represent axial wave numbers for all modes of the assigned frequency ω and circumferential wave number n, and they may be real, purely imaginary, or complex. For a k_{nm} real, the eigenvalue is associated with a propagating wave. For a k_{nm} purely imaginary or complex, the eigenvalue portrays a standing vibration in a semi-infinitely long cylinder in which the amplitude exhibits either monotonic or sinusoidal exponential decay away from a cross-section at the origin. Half of the $2M$ eigendata relate to traveling or decaying modes from the origin along the positive z-direction and the other half are their counterparts from the origin in the opposite direction.

Associated with each eigenvalue k_{nm} are right-handed and left-handed eigenvectors, $\boldsymbol{\phi}^R_{nm}$ and $\boldsymbol{\phi}^L_{nm}$. These eigenvectors represent the nodal displacement distributions over the finite element model of the thickness profile, and they satisfy the equations

$$[\mathbf{A}(n,\omega) - k_{nm}\mathbf{B}(n)]\boldsymbol{\phi}^R_{nm} = \mathbf{0};$$
$$[\mathbf{A}^T(n,\omega) - k_{nm}\mathbf{B}^T(n)]\boldsymbol{\phi}^L_{nm} = \mathbf{0}. \quad (26)$$

The dual sets of left and right-handed eigenvectors also satisfy bi-orthogonality relations

$$\boldsymbol{\Phi}^{L^T}_{nm}\mathbf{B}\boldsymbol{\Phi}^R_{np} = \text{diag}\,(B_{nm}); \quad \boldsymbol{\Phi}^{L^T}_{nm}\mathbf{A}\boldsymbol{\Phi}^R_{np} = \text{diag}\,(k_{nm}B_{nm}) \quad (27)$$

where diag ( ) denotes a diagonal matrix. Since $\mathbf{Q}_n$ is a vector of length $2M$ in which the upper half is $\mathbf{U}_n$ and the lower half is the product of $\mathbf{U}_n$ with k_n as defined by Eq. (25), an eigenvector can then be partitioned into upper and lower halves as follows:

$$\boldsymbol{\phi}^R_{nm} = \begin{bmatrix} \boldsymbol{\phi}^R_{nmu} \\ \boldsymbol{\phi}^R_{nml} \end{bmatrix} = \begin{bmatrix} \boldsymbol{\phi}^R_{nmu} \\ k_{nm}\boldsymbol{\phi}^R_{nmu} \end{bmatrix};$$
$$\boldsymbol{\phi}^L_{nm} = \begin{bmatrix} \boldsymbol{\phi}^L_{nmu} \\ \boldsymbol{\phi}^L_{nml} \end{bmatrix} = \begin{bmatrix} \boldsymbol{\phi}^L_{nmu} \\ k_{nm}\boldsymbol{\phi}^L_{nmu} \end{bmatrix}. \quad (28)$$

Then, bi-orthogonality relations Eq. (27) expressed explicitly in terms of the upper half eigenvectors become

$$\boldsymbol{\phi}^{L^T}_{npu}(\mathbf{K}_1 + in\mathbf{K}_2 + n^2\mathbf{K}_4 - \omega^2\mathbf{M})\boldsymbol{\phi}^R_{nmu} - k_{np}k_{nm}\boldsymbol{\phi}^{L^T}_{npu}\mathbf{K}_6\boldsymbol{\phi}^R_{nmu} = \delta_{pm}B_{nm}$$
$$(k_{nm} + k_{np})\boldsymbol{\phi}^{L^T}_{npu}(\mathbf{K}_1 + in\mathbf{K}_2 + n^2\mathbf{K}_4 - \omega^2\mathbf{M})\boldsymbol{\phi}^R_{nmu} + ik_{np}K_{nm}\boldsymbol{\phi}^{L^T}_{npu}(\mathbf{K}_3 - in\mathbf{K}_5)\boldsymbol{\phi}^R_{nmu} = \delta_{pm}k_{nm}B_{nm}. \quad (29)$$

With the knowledge of the eigendata, the solution vector $\mathbf{Q}_n$ in Eq. (23) can be represented by a summation of the right eigenvectors as

$$\mathbf{Q}_n = \sum_{m=1}^{2M} Q_{nm}\boldsymbol{\phi}^R_{nm}. \quad (30)$$

The coefficients Q_{nm} are found by substituting Eq. (30) into Eq. (23) and using bi-orthogonality relations (27) to give

$$Q_{nm} = \frac{\boldsymbol{\phi}^{L^T}_{mn}\mathbf{P}_n}{(k_{nm} - k_n)B_{nm}} \quad (31)$$

so that the explicit form of $\mathbf{Q}_n$ is

$$\mathbf{Q}_n = \sum_{m=1}^{2M} \frac{\boldsymbol{\phi}^{L^T}_{mn}\mathbf{P}_n}{(k_{nm} - k_n)B_{nm}}\boldsymbol{\phi}^R_{nm}. \quad (32)$$

In view of Eqs. (25), (28), and (32), the solution vector $\mathbf{U}_n$ that occupies the upper half of $\mathbf{Q}_n$ takes the form

$$\mathbf{U}_n = \sum_{m=1}^{2M} \frac{k_{nm}\boldsymbol{\phi}^{L^T}_{mnu}\mathbf{F}_n}{(k_{nm} - k_n)B_{nm}}\boldsymbol{\phi}^R_{nmu}$$
$$= \sum_{m=1}^{2M} \frac{\boldsymbol{\phi}^{L^T}_{mnu}\mathbf{F}_n}{(1 - K_n/k_{nm})B_{nm}}\boldsymbol{\phi}^R_{nmu}. \quad (33)$$

The inverse Fourier transform of Eq. (33) yields the nth circumferential harmonic $\bar{\mathbf{U}}_n(z)$ as

$$\bar{\mathbf{U}}_n(z) = \frac{1}{2\pi}\sum_{m=1}^{2M}\int_{-\infty}^{\infty} \frac{\boldsymbol{\phi}^{L^T}_{mnu}\mathbf{F}_n}{(1 - k_n/k_{nm})B_{nm}}\boldsymbol{\phi}^R_{nmu}e^{ik_nz}dk_n. \quad (34)$$

In many problems, $\mathbf{F}_n$, $\boldsymbol{\phi}^L_{mnu}$, $\boldsymbol{\phi}^R_{nmu}$, and B_{nm} will be independent of wave number k_n, so that application of the Cauchy residue theorem yields the modal response $\bar{\mathbf{U}}_n(z)$ in a straightforward way. Moreover, the eigendata are equally divided into two groups according to traveling and decaying motions from the origin along the $\pm z$-directions. Thus, the modal response $\bar{\mathbf{U}}_n(z)$ can be expressed as two summations, each over a range of M for these two oppositely directed motions.

$$\bar{\mathbf{U}}_n(z) = -i\sum_{m=1}^{M} \frac{k_{nm}\boldsymbol{\phi}^{L^T}_{mnu}\mathbf{F}_n}{B_{nm}}\boldsymbol{\phi}^R_{nmu}e^{ik_{nm}z} - i\sum_{m=M+1}^{2M} \frac{k_{nm}\boldsymbol{\phi}^{L^T}_{mnu}\mathbf{F}_n}{B_{nm}}\boldsymbol{\phi}^R_{nmu}e^{-ik_{nm}z} \quad (35)$$

Green's Function-Integral Transform

For construction of Green's function, let the source point steady-state unit concentrated force be in the cross-sectional plane $z = 0$ of the cylinder at some radial distance r_0 from its axis. Moreover, let r_0 coincide with a finite element nodal surface. The spatial representation of this force by $\mathbf{F}(\theta, z)$ in Eq. (19) takes the form

$$\mathbf{F}(\theta, z) = \delta(\theta)\delta(z)\mathbf{F}_0 \quad (36)$$

with $\delta(\,)$ as the Dirac Delta function and $\mathbf{F}_0$ as the radial distribution vector. For a concentrated load, $\mathbf{F}_0$ contains zero entries everywhere except at the nodal surface $r = r_0$, where the (r, θ, z) components are $(\alpha_{Fr}, \alpha_{F\theta}, \alpha_{Fz})$, i.e.,

$$\mathbf{F}^T_0 = \langle \mathbf{F}^T_{0r}; \mathbf{F}^T_{0\theta}; \mathbf{F}^T_{0z} \rangle$$
$$= \langle 0, 0, \ldots, \alpha_{Fr}, \ldots, 0; 0, 0, \ldots, \alpha_{F\theta}, \ldots, 0; 0, 0, \ldots, \alpha_{Fz}, \ldots, 0 \rangle. \quad (37)$$

Since the load's magnitude is unity, $(\alpha_{Fr}, \alpha_{F\theta}, \alpha_{Fz})$ are also the direction cosines of the unit vector $\mathbf{e}_F$ defining the direction of the load, i.e.,

$$\mathbf{e}_F = \alpha_{Fr}\mathbf{e}_r + \alpha_{F\theta}\mathbf{e}_\theta + \alpha_{Fz}\mathbf{e}_z \quad (38)$$

with $(\mathbf{e}_r, \mathbf{e}_\theta, \mathbf{e}_z)$ as the base vectors of the cylindrical coordinate system.

Our solution methodology relies on the expansion of $\delta(\theta)$ in a Fourier series. It is well known that the Fourier series representation of a δ-function is nonconvergent. Therefore, it is necessary to replace it with a narrow spatial pulse of a uniform intensity q_0 over a circumferential distance $2r_0\theta_0$ where the equivalence with $\delta(\theta)$ requires that

Downloaded 04 May 2010 to 171.66.16.27. Redistribution subject to ASME license or copyright; see http://www.asme.org/terms/Terms_Use.cfm

$$\int_{-\theta_0}^{+\theta_0} q_0 r_0 d\theta = 1 \quad \text{or} \quad q_0 = \frac{1}{2r_0\theta_0}. \tag{39}$$

The representation of $\mathbf{F}(\theta, z)$ with the Fourier series expansion in the circumferential direction takes the form

$$\mathbf{F}(\theta, z) = \sum_{n=-\infty}^{n=+\infty} e^{in\theta} \frac{1}{2\pi r_0} \frac{\sin(n\theta_0)}{n\theta_0} \mathbf{F}_0 \delta(z)$$

$$= \sum_{n=-\infty}^{n=+\infty} e^{in\theta} \bar{\mathbf{F}}_n(z) \tag{40}$$

where

$$\bar{\mathbf{F}}_n(z) = \frac{1}{2\pi r_0} \frac{\sin(n\theta_0)}{n\theta_0} \mathbf{F}_0 \delta(z) \tag{41}$$

and the Fourier transform of $\bar{\mathbf{F}}_n(z)$ is

$$\mathbf{F}_n = \frac{1}{2\pi r_0} \frac{\sin(n\theta_0)}{n\theta_0} \mathbf{F}_0. \tag{42}$$

Substitution of Eq. (42) into Eq. (34) gives

$$\bar{\mathbf{U}}_n(z) = \frac{1}{4\pi^2 r_0} \sum_{m=1}^{2M} \int_{-\infty}^{\infty} \frac{\boldsymbol{\phi}_{mnu}^{L^T} \mathbf{F}_0}{(1 - k_n/k_{nm}) B_{nm}} \frac{\sin(n\theta_0)}{n\theta_0} \times \boldsymbol{\phi}_{nmu}^{R} e^{ik_n z} dk_n. \tag{43}$$

Apply the Cauchy residue theorem to Eq. (43) and consider motions only in the $+z$-direction yield the nth circumferential mode of the displacement Green's function as

$$\bar{\mathbf{U}}_n(z) = -\frac{i}{2\pi r_0} \sum_{m=1}^{M} \frac{k_{nm} \boldsymbol{\phi}_{mnu}^{L^T} \mathbf{F}_0}{B_{nm}} \frac{\sin(n\theta_0)}{n\theta_0} \boldsymbol{\phi}_{nmu}^{R} e^{ik_{nm} z}. \tag{44}$$

Thus, the steady-state unit concentrated force point source is converted into the summation of a series of circular ring-like sources, and the displacement Green's function is represented by the summation of their individual circumferential modal responses.

Green's Function-Modal Summation

The nth harmonic of Green's function may also be represented by another summation of right-handed eigenvectors $\boldsymbol{\phi}_{nmu}^{R}$'s. In this approach, imagine the infinitely long cylinder to be partitioned into two halves with a series of source circular ring-like loads acting on both sides of the interface cross section. Each source load term, which is of amplitude $\sin n\theta_0 / 4\pi r_0 n\theta_0$, may be decomposed into symmetric and antisymmetric components, $(\alpha_{Fr}/2, \alpha_{F\theta}/2)$ and $\alpha_{Fz}/2$, respectively, along with symmetry and antisymmetry interface conditions. The sum of these two problems yields the nth harmonic Green's function. Decomposition into two semi-infinitely long cylinders requires the cross-sectional plane to be a structural symmetry plane so that cylindrically monotropy material symmetry or better is necessary. By this alternate approach, it is possible to verify the nth mode of Green's function representation of Eq. (44) for a cylindrically monotropic cylinder. This modal summation method was used by Zhu, Shah, and Datta (1995), and Zhu (1996) in his formulation of the steady-state Green's function for plane strain vibrations.

Considering motions only in the $+z$-direction, the displacement vector $\bar{\mathbf{U}}_n(z)$ can be approximated by the modal sum

$$\bar{\mathbf{U}}_n(z) = \sum_{m=1}^{M} A_{nm} \boldsymbol{\phi}_{nmu}^{R} e^{ik_{nm} z} \tag{45}$$

where A_{nm}'s are complex amplitude coefficients to be determined. For discussion purposes, let $\boldsymbol{\phi}_{nmu}^{R}$ be arranged as

$$\boldsymbol{\phi}_{nmu}^{R} = \langle u_{1m}, \ldots, u_{(2N+1)m}; v_{1m}, \ldots, v_{(2N+1)m}; w_{1m}, \ldots, w_{(2N+1)m} \rangle \tag{46}$$

where $\mathbf{N}$ is the number of sublayers in the finite element model. The corresponding stress modal sum can be obtained by substituting Eq. (45) into the strain-transformation Eq. (10) and using constitutive relation (6). Then, consistent load vectors for the $(\sigma_{rz}, \sigma_{\theta z}, \sigma_{zz})$ components that represent the forcing functions can be computed using Eq. (18). The resulting consistent load vector has the form

$$\bar{\mathbf{F}}_n(z) = \sum_{m=1}^{M} A_{nm} \mathbf{F}_{nm}^{R} e^{ik_{nm} z} \tag{47}$$

where

$$\mathbf{F}_{nm}^{R} = \langle f_{r1m}, \ldots, f_{r(2N+1)m}; f_{\theta 1m}, \ldots, f_{\theta(2N+1)m}; f_{z1m}, \ldots, f_{z(2N+1)m} \rangle \tag{48}$$

with f_{rim}, $f_{\theta im}$, and f_{zim} as nodal forces in (r, θ, z)-directions, respectively, at the ith node of the finite element model. Their explicit form may be found in Rattanawangchareon (1993).

Evaluation of Eqs. (45) and (47) at $z = 0$ gives

$$\bar{\mathbf{U}}_n(0) = \boldsymbol{\Phi}_n \mathbf{A}_n = [\boldsymbol{\phi}_{n1u}^{R}, \boldsymbol{\phi}_{n2u}^{R}, \ldots, \boldsymbol{\phi}_{nMu}^{R}] \mathbf{A}_n$$

$$\bar{\mathbf{F}}_n(0) = \mathbf{F}_n \mathbf{A}_n = [\mathbf{F}_{n1}^{R}, \mathbf{F}_{n2}^{R}, \ldots, \mathbf{F}_{nM}^{R}] \mathbf{A}_n \tag{49}$$

where the modal columns of $\boldsymbol{\Phi}_n$ and $\mathbf{F}_n$ are indicated as shown and $\mathbf{A}_n$ is a column vector of the undetermined amplitudes.

$$\mathbf{A}_n^T = \langle A_{n1}, A_{n2}, \ldots, A_{nM} \rangle \tag{50}$$

For discussion of the analysis details in what follows, it is convenient to recast the modal columns of $\boldsymbol{\Phi}_n$ and $\mathbf{F}_n$ of Eq. (49) in partitioned form according to their r, θ, z components as

$$\boldsymbol{\Phi}_n = \begin{bmatrix} \Phi_r \\ \cdots \\ \Phi_\theta \\ \cdots \\ \Phi_z \end{bmatrix}; \quad \mathbf{F}_n = \begin{bmatrix} F_r \\ \cdots \\ F_\theta \\ \cdots \\ F_z \end{bmatrix}. \tag{51}$$

Selective force/displacement components of $\bar{\mathbf{U}}_n(0)$ and $\bar{\mathbf{F}}_n(0)$ in Eq. (49) must be equated to the prescribed data of the symmetric and antisymmetric problems. Write all displacements and consistent loads at $z = 0$ as

$$\bar{\mathbf{U}}_n(0) = \begin{bmatrix} \bar{\mathbf{U}}_{nr}^{*} \\ \cdots \\ \bar{\mathbf{U}}_{n\theta}^{*} \\ \cdots \\ \bar{\mathbf{U}}_{nz}^{*} \end{bmatrix}; \quad \bar{\mathbf{F}}_n(0) = \begin{bmatrix} \bar{\mathbf{F}}_{nr}^{*} \\ \cdots \\ \bar{\mathbf{F}}_{n\theta}^{*} \\ \cdots \\ \bar{\mathbf{F}}_{nz}^{*} \end{bmatrix} \tag{52}$$

where the superscript * denotes a prescribed or unknown value. Obviously, if a displacement/force quantity is prescribed, then its corresponding force/displacement quantity is unknown.

First, consider the symmetric components $(\alpha_{Fr}/2, \alpha_{F\theta}/2)$ of the nth circumferential harmonic. Symmetric interface conditions require that $\bar{\mathbf{U}}_n(0)$ and $\bar{\mathbf{F}}_n(0)$ have the form

$$\bar{\mathbf{U}}_n(0) = \begin{bmatrix} \bar{\mathbf{U}}_{nr}^{*} \\ \cdots \\ \bar{\mathbf{U}}_{n\theta}^{*} \\ \cdots \\ 0 \end{bmatrix}; \quad \bar{\mathbf{F}}_n(0) = \begin{bmatrix} \bar{\mathbf{F}}_{nr}^{*} \\ \cdots \\ \bar{\mathbf{F}}_{n\theta}^{*} \\ \cdots \\ \bar{\mathbf{F}}_{nz}^{*} \end{bmatrix} \tag{53}$$

where $\bar{\mathbf{U}}_{nr}^{*}$, $\bar{\mathbf{U}}_{n\theta}^{*}$, $\bar{\mathbf{F}}_{nz}^{*}$ are unknown and

Downloaded 04 May 2010 to 171.66.16.27. Redistribution subject to ASME license or copyright; see http://www.asme.org/terms/Terms_Use.cfm

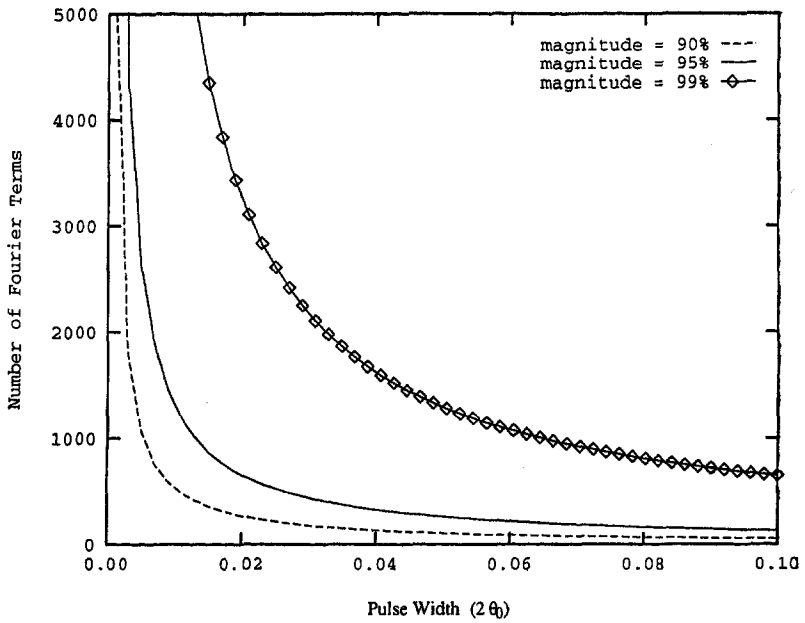


Fig. 2 Relation between pulse width and total number of terms

$$\bar{\mathbf{F}}^T_{nr}(0) = \frac{1}{2\pi r_0}\frac{\sin(n\theta_0)}{n\theta_0}\langle 0, 0, \ldots, \alpha_{Fr}/2, \ldots, 0\rangle$$

$$\bar{\mathbf{F}}^T_{n\theta}(0) = \frac{1}{2\pi r_0}\frac{\sin(n\theta_0)}{n\theta_0}\langle 0, 0, \ldots, \alpha_{F\theta}/2, \ldots, 0\rangle. \quad (54)$$

These force components occupy entries in these arrays that correspond to the r_0 node of the finite element model. Let $\mathbf{A}'_n$ denote the unknown amplitudes for this part. Imposing these conditions at $z = 0$ involve selecting the appropriate parts of the partitioned matrices in Eq. (51) and repacking them into the following two sets of equations where the right-hand sides are either completely known or unknown, i.e.,

$$\mathbf{R}\mathbf{A}'_n = \begin{bmatrix} F_r \\ \cdots \\ F_\theta \\ \cdots \\ \Phi_z \end{bmatrix}\mathbf{A}'_n = \begin{bmatrix} \bar{\mathbf{F}}^*_{nr} \\ \cdots \\ \bar{\mathbf{F}}^*_{n\theta} \\ \cdots \\ 0 \end{bmatrix};$$

$$\mathbf{S}\mathbf{A}'_n = \begin{bmatrix} \Phi_r \\ \cdots \\ \Phi_\theta \\ \cdots \\ F_z \end{bmatrix}\mathbf{A}'_n = \begin{bmatrix} \bar{\mathbf{U}}^*_{nr} \\ \cdots \\ \bar{\mathbf{U}}^*_{n\theta} \\ \cdots \\ \bar{\mathbf{F}}^*_{nz} \end{bmatrix}. \quad (55)$$

Applying the principle of virtual work by letting the unknown displacements and forces execute excursions over their corresponding known values yields

$$\mathbf{A}'_n = [\mathbf{S}^H\mathbf{R}]^{-1}\mathbf{S}^H\begin{bmatrix} \bar{\mathbf{F}}^*_{nr} \\ \cdots \\ \bar{\mathbf{F}}^*_{n\theta} \\ \cdots \\ 0 \end{bmatrix} \quad (56)$$

where the superscript H denotes complex conjugate transpose.

For the antisymmetric force component, the boundary conditions are

$$\bar{\mathbf{U}}_n(0) = \begin{bmatrix} 0 \\ \cdots \\ 0 \\ \cdots \\ \mathbf{U}^*_{nz} \end{bmatrix}; \quad \bar{\mathbf{F}}_n(0) = \begin{bmatrix} \bar{\mathbf{F}}^*_{nr} \\ \cdots \\ \bar{\mathbf{F}}^*_{n\theta} \\ \cdots \\ \bar{\mathbf{F}}^*_{nz} \end{bmatrix} \quad (57)$$

where $\bar{\mathbf{U}}^*_{nz}$, $\bar{\mathbf{F}}^*_{nr}$, and $\bar{\mathbf{F}}^*_{n\theta}$ are unknown and

$$\bar{\mathbf{F}}^T_{nz}(0) = \frac{1}{2\pi r_0}\frac{\sin(n\theta_0)}{n\theta_0}\langle 0, 0, \ldots, \alpha_{Fz}/2, \ldots, 0\rangle. \quad (58)$$

Let $\mathbf{A}''_n$ be the unknown amplitudes for this case. The two solution sets of equations for $\mathbf{A}''_n$ are

$$\mathbf{S}\mathbf{A}''_n = \begin{bmatrix} \Phi_r \\ \cdots \\ \Phi_\theta \\ \cdots \\ F_z \end{bmatrix}\mathbf{A}''_n = \begin{bmatrix} 0 \\ \cdots \\ 0 \\ \cdots \\ \bar{\mathbf{F}}^*_{nz} \end{bmatrix};$$

$$\mathbf{R}\mathbf{A}''_n = \begin{bmatrix} F_r \\ \cdots \\ F_\theta \\ \cdots \\ \Phi_z \end{bmatrix}\mathbf{A}''_n = \begin{bmatrix} \mathbf{F}^*_{nr} \\ \cdots \\ \mathbf{F}^*_{n\theta} \\ \cdots \\ \bar{\mathbf{U}}^*_{nz} \end{bmatrix} \quad (59)$$

and its solution is

$$\mathbf{A}''_n = [\mathbf{R}^H\mathbf{S}]^{-1}\mathbf{R}^H\begin{bmatrix} 0 \\ \cdots \\ 0 \\ \cdots \\ \bar{\mathbf{F}}^*_{nz} \end{bmatrix}. \quad (60)$$

For both formulations of Green's function, the accuracy of the representation of the source point unit load is dependent on the width of the circumferential pulse, the number of terms for the $\delta(\theta)$ series and the number of eigenvectors in the representation of each θ-mode. These issues will be discussed in the next section.

Numerical Implementation

The precision of Green's function is tied to the number of terms used in the double summation of its series representation. Two issues are involved in its numerical implementation. One concerns the approximation of replacing $\delta(\theta)$ of the source load by a narrow circumferential pulse of half-angle width θ_0 (in radians). The other involves an understanding between an acceptable precision in the displacements and stresses of the series representation versus the number of terms required. Computer programs were written for developing data to indicate the numerical evaluation effort corre-

Downloaded 04 May 2010 to 171.66.16.27. Redistribution subject to ASME license or copyright; see http://www.asme.org/terms/Terms_Use.cfm

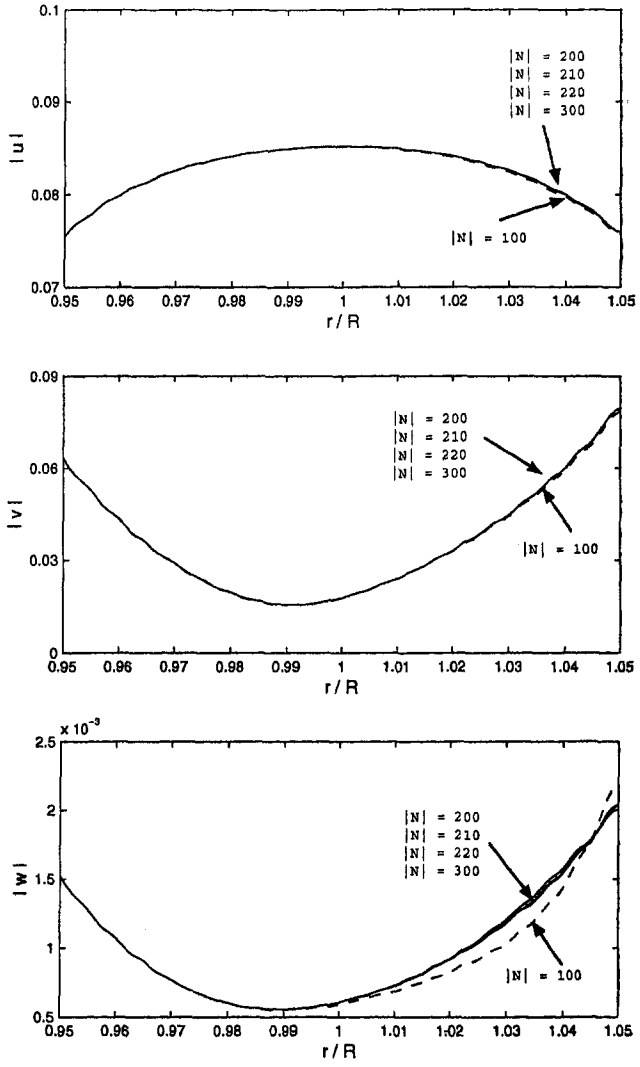


Fig. 3(*a*) Displacement components of Green's function for isotropic cylinder, *R*/*H* = 10 and Ω = 15

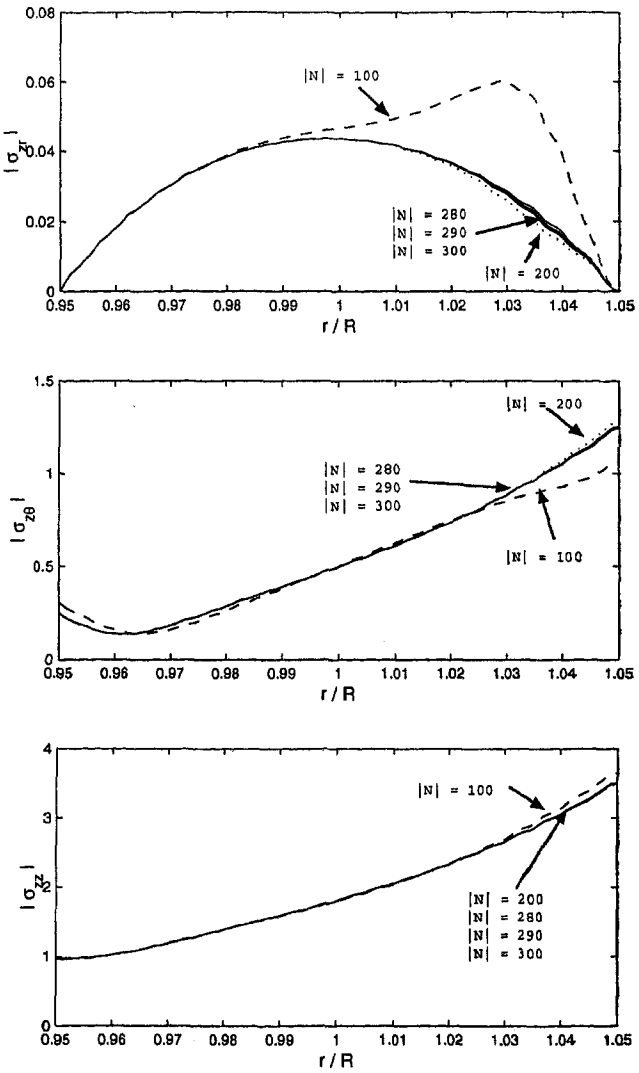


Fig. 3(*b*) Stress components of Green's function for isotropic cylinder, *R*/*H* = 10 and Ω = 15

sponding to various levels of accuracy. Both versions of Green's function were coded, i.e., the integral transform and mode superposition methods.

Setting $\mathbf{F}_0 = 1$ in the Fourier series of the circumferential pulse in Eq. (40) and integrating over its width yield the pulse's magnitude, which for the infinite sum is unity. Hence, the finite sum over $\pm N$, denoted by $\tilde{\mathbf{F}}_N$, represents a fraction of the total.

$$\tilde{\mathbf{F}}_N = \sum_{n=-N}^{n=+N} \int_{-\theta_0}^{+\theta_0} e^{in\theta} \frac{1}{2\pi r_0} \frac{\sin(n\theta_0)}{n\theta_0} r_0 d\theta \tag{61}$$

Thus, $\tilde{\mathbf{F}}_N$ measures the fidelity of the narrow pulse width approximation for a sum of $2N + 1$ terms. The relationship between the total number of terms and its circumferential width is illustrated in Fig. 2, where the parametric lines partition regions between pulse magnitudes of 90, 95, and 99 percent. That decreasing pulse width is accompanied by increasing number of Fourier terms abides with common intuition. For example, about 2700 terms are needed for 90 percent for half range $\theta_0 = 0.001$ rad. Although this appears to be an inordinately large number of terms, a comparable precision in the displacements and stresses requires substantially fewer terms as seen in the subsequent discussion.

Two material systems were used in of our study of the precision characteristics of the series representation of the displacements and stresses. They are (1) isotropic cylinder and (2) composite two-layer [+30°/−30°] angle-ply cylinder. For the isotropic cylinder, Poisson's ratio $\nu = \frac{1}{3}$ and the normalized frequency is defined by

$$\Omega = \frac{\omega R}{\sqrt{\mu/\rho}} . \tag{62}$$

The elastic properties of the composite material comprising the two-layer [+30°/−30°] angle-ply cylinder are

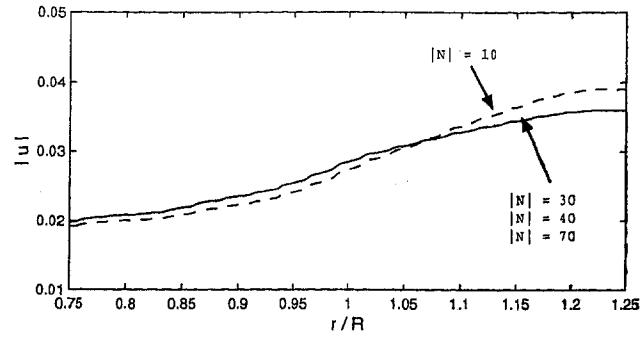
$$E_L = 13.9274 \times 10^{10}\ \text{N/m}^2, \quad E_T = 1.5169 \times 10^{10}\ \text{N/m}^2,$$

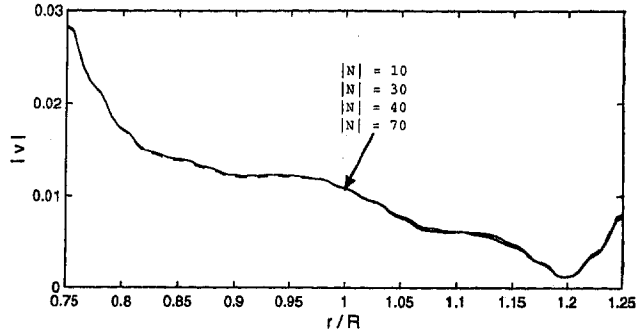
$$G_{LT} = G_{TT} = 0.5861 \times 10^{10}\ \text{N/m}^2, \quad \nu_{LT} = \nu_{TT} = 0.21 \tag{63}$$

where L and T denote directions along and transverse to the fiber direction. The corresponding elastic properties D_{ij} of this material at ±30 deg orientations with the coordinate directions are

$$D_{\pm 30\ \text{deg}} = \begin{bmatrix} 1.5986 & 0.3608 & 0.3924 & \mp 0.0273 & \cdot & \cdot \\ 0.3608 & 2.3730 & 2.7589 & \mp 1.3492 & \cdot & \cdot \\ 0.3924 & 2.7589 & 8.6233 & \mp 4.0630 & \cdot & \cdot \\ \mp 0.0273 & \mp 1.3492 & \mp 4.0630 & 2.9368 & \cdot & \cdot \\ \cdot & \cdot & \cdot & \cdot & 0.5861 & \cdot \\ \cdot & \cdot & \cdot & \cdot & \cdot & 0.5861 \end{bmatrix} \times 10^{10}\ \text{N/m}^2 \tag{64}$$

Downloaded 04 May 2010 to 171.66.16.27. Redistribution subject to ASME license or copyright; see http://www.asme.org/terms/Terms_Use.cfm





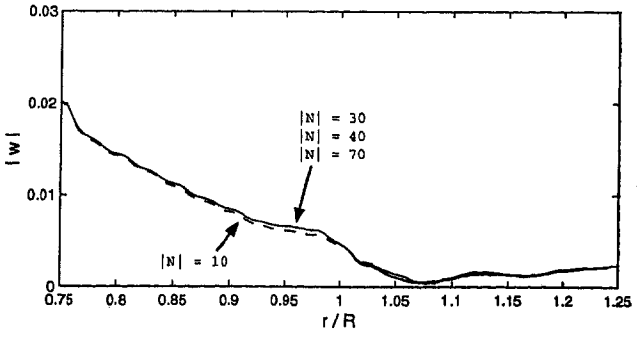
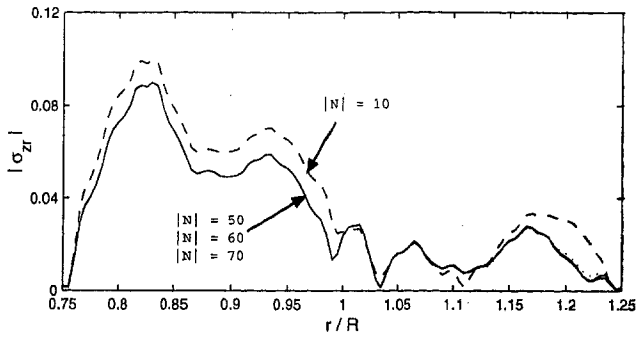
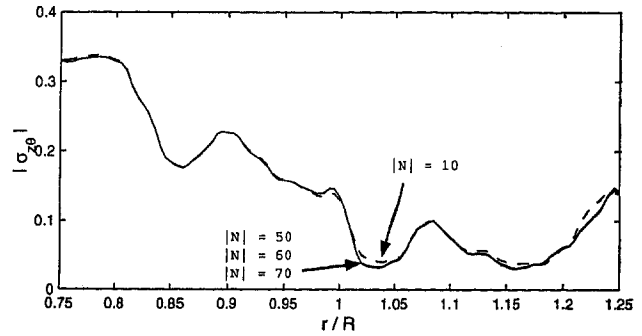


Fig. 4(*a*) Displacement components of Green's function for [+30°/−30°] laminated composite cylinder, $R/H = 2$ and $\Omega = 3$





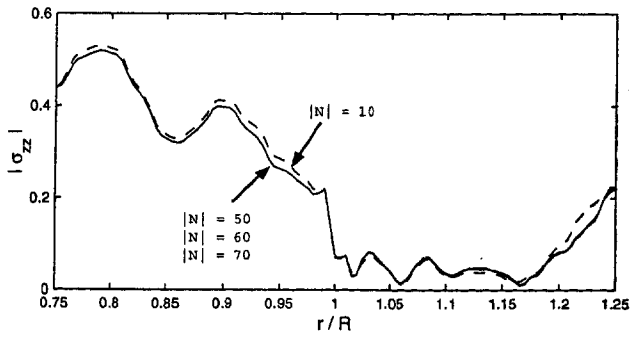


Fig. 4(*b*) Stress components of Green's function for [+30°/−30°] laminated composite cylinder, $R/H = 2$ and $\Omega = 3$

and the normalized frequency for the composite cylinder in this case is

$$\Omega = \frac{\omega R}{\sqrt{E_T/\rho}} \,. \tag{65}$$

In both cases, the total thickness H was taken to be unity, and the radius/thickness ratio R/H was varied.

As the series representation entails a double summation, each summation involves its own set of issues for precision. Consider first the sum of the modal components associated with a given ring-like circumferential mode of the source load in Green's function. Its accuracy is primarily dependent upon a viable discretized thickness profile. In application of Green's function to the boundary element method, accurate near-field displacements and stresses are essential and all modes of a given discretization should be summed. In precision studies of this sum, a radial source ring-like load at the outer surface $r = r_{out}$ of the cylinder at cross-sectional plane $z = 0$ was considered. Different circumferential mode numbers n were investigated to assess the influence of this parameter. For an isotropic cylinder with $R/H = 10$ and normalized frequency $\Omega = 15$, displacements and stresses for thickness profiles of 21, 31, 41, 51 nodal surfaces and $n = 0, 5, 40, 100$ were calculated. For all these different circumferential mode numbers, it was found that at least 41 nodal surfaces were needed to yield good near-field precision for displacements (u, v, w) and stresses (σ_{zr}, $\sigma_{z\theta}$, σ_{zz}) at $z = H/4$ from the cross section containing the ring-like load. It is noted that for comparable precision between the near-field displacements and stresses, the discretized model for displacements (u, v, w) can be cruder than that for stresses. However, the accuracy level of the stresses dictates using the finer of these two discretizations. For the two-layer angle-ply profile, two cases were considered, viz., (1) $R/H = 2$ with $\Omega = 3$ with circumferential modes $n = 0, 5, 40$ and (2) $R/H = 10$ with $\Omega = 15$ with $n = 0, 5, 100$. In both cases, finite element models with 21, 41, 61, and 81 nodal surfaces were used. Accurate near-field displacements and stresses at $z = H/4$ necessitated a model with at least 61 nodal surfaces. The larger size of this model vis-a-vis the isotropic cylinder model must be due to greater detail of the two-layer thickness profile. For brevity sake, none of these results are presented here. It is also noted that both the integral transform and mode superposition methods led to the same results, a reassurance of the validity of our computer codes.

The second summation in Green's function occurs in the circumferential direction. Consider a source load with the half range width of $\theta_0 = 0.001$ at (r_{out}, 0, 0) acting on the aforementioned isotropic and two-layer composite cylinders. Plots revealing the precision of the displacements (u, v, w) and stresses (σ_{zr}, $\sigma_{z\theta}$, σ_{zz}) in Green's function for the homogeneous, isotropic cylinder using a 41 nodal surface model are shown in Figs. 3(a) and 3(b), respectively. These data are

Downloaded 04 May 2010 to 171.66.16.27. Redistribution subject to ASME license or copyright; see http://www.asme.org/terms/Terms_Use.cfm

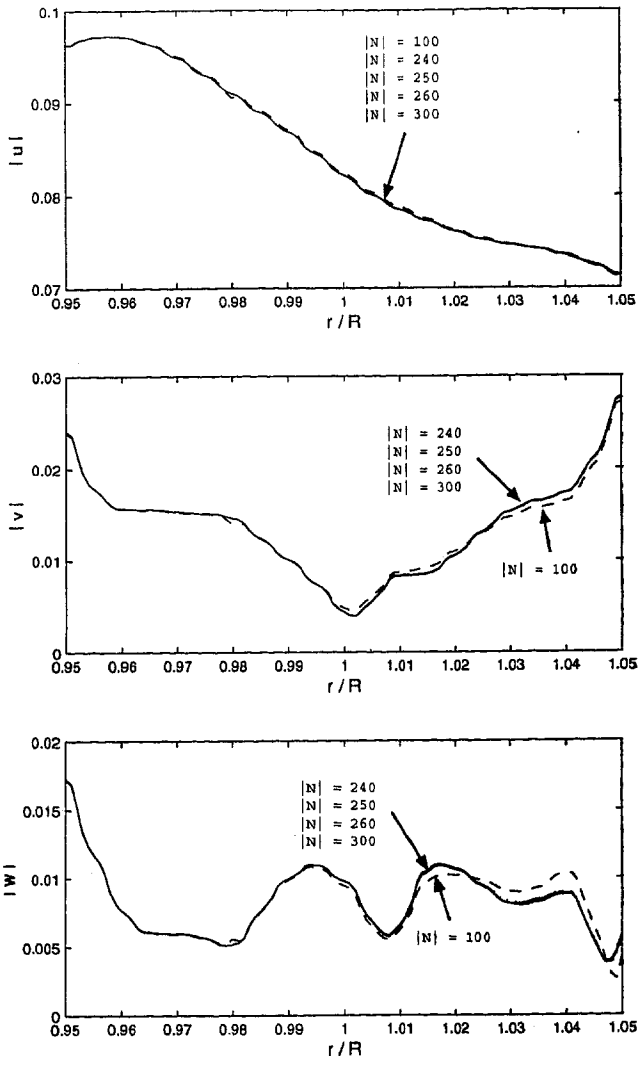


Fig. 5(*a*) Displacement components of Green's function for [+30°/−30°] laminated composite cylinder, $R/H = 10$ and $\Omega = 15$

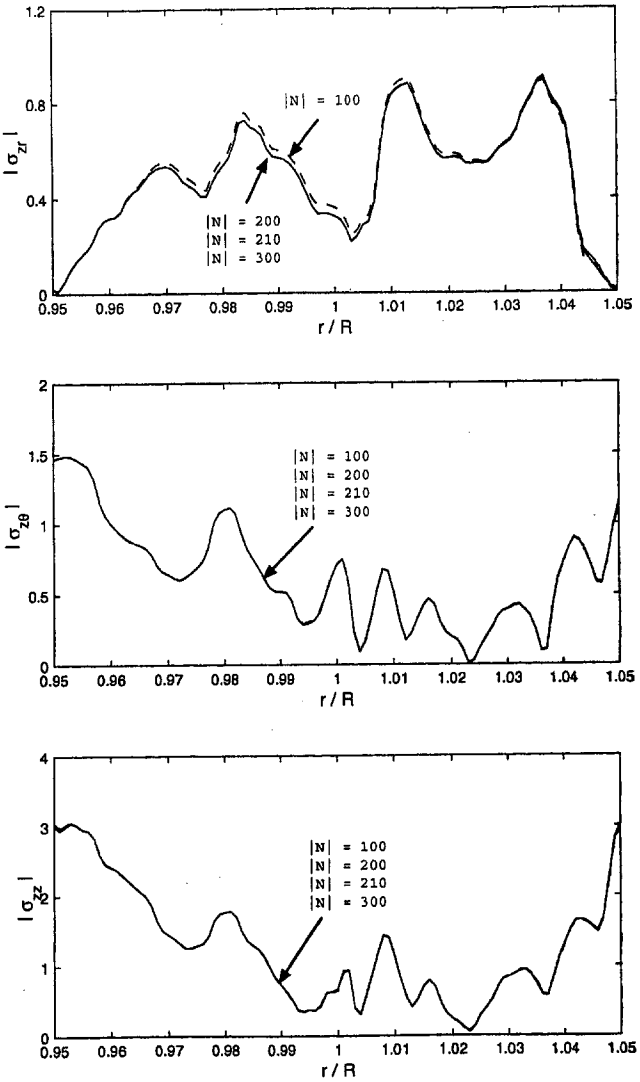


Fig. 5(*b*) Stress components of Green's function for [+30°/−30°] laminated composite cylinder, $R/H = 10$ and $\Omega = 15$

radial distributions in the near field at $z = H/4$, $\theta = \pi/4$. Convergence of the displacements is essentially achieved with circumferential mode summation index $N = \pm 200$. Summations with $|N| > 200$ offer a diminishing return as the differences with that of $N = \pm 200$ are imperceptible. Figure 3(*b*) shows the convergence of stresses (σ_{zr}, $\sigma_{z\theta}$, σ_{zz}), which required $|N| \geq 280$ or a minimum of 160 more terms beyond that for displacements. The slower convergence of the stresses is manifestation of differentiation with respect to θ in their expressions. Similar comparisons of radial distributions of the near-field displacements and stresses at $z = H/4$, $\theta = \pi/4$ for the two-layer composite cylinders modeled by 61 nodal surfaces are shown in Figs. 4(*a*), 4(*b*) and Figs. 5(*a*), 5(*b*) for $R/H = 2$ and $R/H = 10$, respectively. In the case $R/H = 2$, a summation index of $N = \pm 30$ was sufficient for the convergence of the displacements, while for stresses, $N = \pm 50$ was needed. For $R/H = 10$ case, a summation index of $N = \pm 240$ was needed for the convergence of the displacements, but $N = \pm 200$ was needed for the stresses. That the smaller radius/thickness ratio cylinder, i.e., $R/H = 2$, requires a substantially fewer number of circumferential modes for convergence than $R/H = 10$ is probably due to the larger relative distance from the source point to the observation point. That fewer terms are needed for stress convergence in the case of $R/H = 10$ is likely to be an anomaly of the position of this particular observation point. In general, it is expected that more terms must be used for stress convergence than for displacement convergence. The studies herein offer some insight into the extent of the additional number of terms.

Conclusions

Green's function in a laminated cylinder was constructed by two methods, both of which rely on modal summation of two series, one of the axial modes and the other of the circumferential modes. The circumferential modes were needed because of the Fourier series representation of a narrow spatial pulse load in circumferential direction instead of a δ-function load. The convergence and precision of Green's function were studied in two example thickness profiles, one for a homogeneous, isotropic cylinder and the other for a two-layer angle-ply cylinder. Two geometric configurations, i.e., R/H radius/thickness ratios, were considered in order to understand the differences between them. The numerical results show that the precision of Green's function depends on the number of nodal surfaces in finite element model of the radial discretization and on the number of circumferential modes used in the summation of a given width of a narrow loading pulse, that was in lieu of the δ-function representation of the source load. It is seen that different numbers of nodal surfaces and circumferential modes are required according to the material properties and geometry (the radius-thickness ratio of the cylinder) for accepted precision. In general, the cylinder's geometry affects convergence and precision more than the material properties. With the need of differentiation to express the stress components, the stress data of Green's function converge slower than the displacement data.

Downloaded 04 May 2010 to 171.66.16.27. Redistribution subject to ASME license or copyright; see http://www.asme.org/terms/Terms_Use.cfm

References

Huang, K. H., and Dong, S. B., 1984, "Propagating Waves and Edge Vibrations in Anisotropic Composite Cylinders," ASME *Journal of Sound and Vibration,* Vol. 96, No. 3, pp. 363–379.

Nelson, R. B., Dong, S. B., and Kalra, R. D., 1971, "Vibration and waves in Laminated Orthotropic Circular Cylinders," ASME *Journal of Sound and Vibration,* Vol. 18, No. 3, pp. 429–444.

Rattanawangcharoen, N., 1993, "Propagation and Scattering of Elastic Waves in Laminated Circular Cylinders," Ph.D. Dissertation, University of Manitoba, Winnipeg, Manitoba, Canada.

Rattanawangcharoen, N., Shah, A. H., and Datta, S. K., 1992, "Wave Propagation in Laminated Composite Cylinders," *Int. J. Solids Structures,* Vol. 29, pp. 767–781.

Rattanawangcharoen, N., Shah, A. H., and Datta, S. K., 1994a, "Non-axisymmetric Guided Waves in a Composite Cylinder with Transversely Isotropic Core," *Geophys. J. Int.,* Vol. 118, pp. 317–324.

Rattanawangcharoen, N., Shah, A. H., and Datta, S. K., 1994b, "Reflection of Waves at the Free Edge of a Laminated Circular Cylinder," ASME JOURNAL OF APPLIED MECHANICS, Vol. 61, pp. 323–329.

Rattanawangcharoen, N., Zhuang, W., Shah, A. H., and Datta, S. K., 1997, "Axisymmetric Guided Waves in Jointed Laminated Cylinders," *J. of the Engineering Mechanics Div. (ASCE),* Vol. 123, No. 10, pp. 1020–1026.

Soldatos, K. P., 1994, "Review of Three-Dimensional Dynamic Analyses of Circular Cylinders and Cylindrical Shells," ASME *Appl. Mech. Rev.,* Vol. 47, pp. 501–516.

Zhu, J., Shah, A. H., and Datta, S. K., 1995, "Modal Representation of Two-Dimensional Elastodynamic Green's Functions," *J. Engng. Mech. Div. ASCE,* Vol. 121, No. 1, pp. 26–36.

Zhu, J., 1996, "Numerical Modelling for Elastic Waves in Laminated Composite Plates," Ph.D. Dissertation, University of Manitoba, Winnipeg, Manitoba, Canada.

Zhu, J., Shah, A. H., and Datta, S. K., 1996, "The Evaluations of Cauchy Principal Value Integrals and Weakly Singular Integrals in BEM and Their Applications," *Int. J. Numer. Methods Engng.,* Vol. 39, pp. 1017–1028.

Zhu, J., and Shah, A. H., 1997, "A Hybrid Method for Transient Wave Scattering by Flaws in Composite Plates," *Int. J. Solids Structures,* Vol. 34, No. 14, pp. 1719–1734.

Zhuang, W., Shah, A. H., and Datta, S. K., 1997, "Axisymmetric Guided Wave Scattering by Cracks in Welded Steel Pipes," ASME *J. Pressure Vessel Tech.,* Vol. 19, pp. 401–406.

Downloaded 04 May 2010 to 171.66.16.27. Redistribution subject to ASME license or copyright; see http://www.asme.org/terms/Terms_Use.cfm

Half-Space Green's Functions for Transversely Isotropic Piezoelectric Solids

M. L. Dunn
Assoc. Mem. ASME

H. A. Wienecke

Department of Mechanical Engineering,
University of Colorado,
Boulder, CO 80309

We obtain explicit closed-form solutions for the half-space Green's functions for a transversely isotropic piezoelectric solid. The boundary of the half-space is taken to be a plane normal to the unique material axis. The Green's functions are obtained using a formulation where general solutions in transversely isotropic piezoelectricity are expressed in terms of two potential functions; one satisfying a weighted triharmonic equation and the other satisfying a weighted harmonic equation. By assuming a series solution for the potentials we derive explicit expressions for the Green's functions.

1 Introduction

Green's functions are prevalent in many aspects of theoretical and computational mechanics and physics of solids. Many studies have been directed toward obtaining full-space Green's functions for elastic solids in isotropic and anisotropic media (Lord Kelvin, 1882; Freedholm, 1900; Lifshitz and Rozentsveig, 1947; Kroner, 1953; Synge, 1957; Willis, 1965; Mura and Kinoshita, 1971; Pan and Chou, 1976; Wang, 1995). Comprehensive reviews of the subject can be found in the review of Bacon, Barnett, and Scattergood (1978) and texts of Mura (1987) and Nemat-Nasser and Hori (1993).

Half-space Green's functions arise in problems where a free surface exists such as indentation analyses, and the analysis of surface and near-surface cracks. They are also the key to problems involving the interaction of inclusions and defects with a free surface and similar problems in bimaterial and film-substrate systems. Half-space Green's functions in elastic media have also been studied by many. The fundamental work here is the Mindlin (1936) solution for an isotropic half-space. The only other explicit solution is that of Pan and Chou (1979) for transversely isotropic solids. Solutions for more complex material symmetries require numerical evaluation. Such analyses are usually based on Fourier or related transform methods (Walker, 1993).

In piezoelectricity, the electric and elastic responses are anisotropic and coupled. Transverse isotropy is perhaps the most technologically important material symmetry in piezoelectricity since poled ceramics exhibit such symmetry. The first work in the area of piezoelectric Green's functions was that of Deeg (1980) who used Radon transforms to obtain a contour integral representation for the piezoelectric Green's functions. More recent studies regarding Green's functions in piezoelectric solids have been carried out by Wang (1992), Benveniste (1992), and Chen (1993) who all used Fourier transform formalism to obtain representations of the Green's functions in the transformed domain. Chen and Lin (1993) presented a numerical algorithm to compute the derivatives of the piezoelectric Green's functions. Dunn (1994) obtained expressions for the Green's functions for transversely isotropic piezoelectric solids through use of the Radon transform with the inversion accomplished by contour integration in the complex plane. Dunn and Wienecke (1996) obtained explicit closed-form expressions for the transversely isotropic piezoelectric Green's functions using a formulation where the electroelastic fields are derived from two potential functions. In the context of two-dimensional plane piezoelectricity, Lee and Jiang (1994) obtained Green's functions using Fourier transforms, and Sosa and Castro (1994) obtained solutions for point loads on the surface of a piezoelectric half-plane. Point forces on the surface of a piezoelectric half-space were recently analyzed by Ding et al. (1996). No work, however, has been directed towad half-space piezoelectric Green's functions where the source and observation point may lie anywhere in the half-space, including the limiting case of the surface. The latter problem is the focus of this work.

2 Basic Equations and General Solutions

A three-dimensional Cartesian coordinate system is employed and both indicial (x_i) and Latin (x, y, z) notations are utilized. For stationary behavior in the absence of free electric charge or body forces, the field equations of transversely isotropic linear piezoelectricity consist of

$$\sigma_{ij,j} = 0, \quad D_{i,i} = 0 \tag{1a}$$

$$\epsilon_{ij} = \tfrac{1}{2}(u_{i,j} + u_{j,i}), \quad E_i = -\phi_{,i} \tag{1b}$$

$$\sigma_{11} = C_{11}\epsilon_{11} + (C_{11} - 2C_{66})\epsilon_{22} + C_{13}\epsilon_{33} - e_{31}E_3$$

$$D_1 = 2e_{15}\epsilon_{13} + \kappa_{11}E_1$$

$$\sigma_{22} = (C_{11} - 2C_{66})\epsilon_{11} + C_{11}\epsilon_{22} + C_{13}\epsilon_{33} - e_{31}E_3$$

$$D_2 = 2e_{15}\epsilon_{23} + \kappa_{11}E_2$$

$$\sigma_{33} = C_{13}(\epsilon_{11} + \epsilon_{22}) + C_{33}\epsilon_{33} - e_{33}E_3$$

$$D_3 = e_{31}(\epsilon_{11} + \epsilon_{22}) + e_{33}\epsilon_{33} + \kappa_{33}E_3$$

$$\sigma_{23} = 2C_{44}\epsilon_{23} - e_{15}E_2$$

$$\sigma_{13} = 2C_{44}\epsilon_{13} - e_{15}E_1$$

$$\sigma_{12} = 2C_{66}\epsilon_{12}. \tag{1c}$$

Here we have taken the x_3 (z)-axis to be normal to the plane of isotropy and thus only ten material constants are required for the constitutive description: five elastic, three piezoelectric, and two dielectric. In these equations, σ_{ij}, ϵ_{ij}, and u_i are the elastic stress, strain, and displacement, respectively; D_i, E_i, and ϕ are the electric displacement, field, and potential, respectively; C_{ij}, e_{ij}, and κ_{ij} are the elastic (measured in a constant electric field), the piezoelectric, and the dielectric moduli (measured at a constant

Contributed by the Applied Mechanics Division of THE AMERICAN SOCIETY OF MECHANICAL ENGINEERS for publication in the ASME JOURNAL OF APPLIED MECHANICS.
Discussion on the paper should be addressed to the Technical Editor, Professor Lewis T. Wheeler, Department of Mechanical Engineering, University of Houston, Houston, TX 77204-4792, and will be accepted until four months after final publication of the paper itself in the ASME JOURNAL OF APPLIED MECHANICS.
Manuscript received by the ASME Applied Mechanics Division, Oct. 9, 1996; final revision, Feb. 14, 1999. Associate Technical Editor: J. L. Bassani.

 Copyright © 1999 by ASME

Downloaded 04 May 2010 to 171.66.16.27. Redistribution subject to ASME license or copyright; see http://www.asme.org/terms/Terms_Use.cfm

strain), respectively. Here we have adopted the well-known Voigt two-index notation. The symmetry conditions satisfied by the electroelastic moduli are given by Nye (1957), and C_{ij} and κ_{ij} are positive definite.

Substituting Eqs. (1*b*) into Eqs. (1*c*), and the result into Eqs. (1*a*) gives four linear homogeneous second-order partial differential equations in the three independent variables x, y, z and the four independent variables u, v, w, and ϕ (u, v, and w are u_1, u_2, and u_3, respectively). We have recently shown that a general solution to this problem can be reduced to finding two potential functions g and ψ that satisfy the following z-weighted triharmonic and harmonic equations Dunn and Wienecke (1996):

$$\left(\frac{\partial^2}{\partial x^2}+\frac{\partial^2}{\partial y^2}+\frac{1}{\nu_1^2}\frac{\partial^2}{\partial z^2}\right)\left(\frac{\partial^2}{\partial x^2}+\frac{\partial^2}{\partial y^2}+\frac{1}{\nu_2^2}\frac{\partial^2}{\partial z^2}\right)\times\left(\frac{\partial^2}{\partial x^2}+\frac{\partial^2}{\partial y^2}+\frac{1}{\nu_3^2}\frac{\partial^2}{\partial z^2}\right)g=0$$

$$\left(\frac{\partial^2}{\partial x^2}+\frac{\partial^2}{\partial y^2}+\frac{1}{\nu_0^2}\frac{\partial^2}{\partial z^2}\right)\psi=0 \tag{2}$$

where $\nu_0=\sqrt{C_{66}/C_{44}}$ and $-1/\nu_1^2$, $-1/\nu_2^2$, and $-1/\nu_3^2$ are the roots of the cubic equation:

$$s^3+\frac{a}{d}s^2+\frac{b}{d}s+\frac{c}{d}=0 \tag{3}$$

where

$$\begin{aligned}a&=C_{11}(\kappa_{11}C_{33}+2e_{15}e_{33})-\kappa_{11}C_{13}(C_{13}+2C_{44})\\&\quad+C_{44}(\kappa_{33}C_{11}+e_{31}^2)-2e_{15}C_{13}(e_{31}+e_{15})\\b&=C_{33}[\kappa_{11}C_{44}+\kappa_{33}C_{11}+e_{31}(e_{31}+e_{15})]\\&\quad-C_{13}\kappa_{33}(C_{13}+2C_{44})+(e_{31}+e_{15})(C_{33}e_{15}-2C_{13}e_{33})\\&\quad+e_{33}(C_{11}e_{33}-2C_{44}e_{31})\\c&=C_{44}(\kappa_{33}C_{33}+e_{33}^2)\\d&=C_{11}(\kappa_{11}C_{44}+e_{15}^2).\end{aligned} \tag{4}$$

Once g and ψ are found, u, v, w, and ϕ are computed from

$$\begin{aligned}u&=\left[(C_{13}e_{15}-C_{44}e_{31})\frac{\partial^2}{\partial x\partial z}\left(\frac{\partial^2}{\partial x^2}+\frac{\partial^2}{\partial y^2}\right)+[(C_{44}+C_{13})e_{33}-C_{33}(e_{15}+e_{31})]\frac{\partial^4}{\partial x\partial z^3}\right]g-\frac{\partial\psi}{\partial y}\\v&=\left[(C_{13}e_{15}-C_{44}e_{31})\frac{\partial^2}{\partial y\partial z}\left(\frac{\partial^2}{\partial x^2}+\frac{\partial^2}{\partial y^2}\right)+[(C_{44}+C_{13})e_{33}-C_{33}(e_{15}+e_{31})]\frac{\partial^4}{\partial y\partial z^3}\right]g+\frac{\partial\psi}{\partial x}\\w&=\left[-C_{11}e_{15}\left(\frac{\partial^2}{\partial x^2}+\frac{\partial^2}{\partial y^2}\right)\left(\frac{\partial^2}{\partial x^2}+\frac{\partial^2}{\partial y^2}\right)-C_{44}e_{33}\frac{\partial^4}{\partial z^4}+[C_{13}(e_{15}+e_{31})+C_{44}e_{31}-C_{11}e_{33}]\frac{\partial^2}{\partial z^2}\left(\frac{\partial^2}{\partial x^2}+\frac{\partial^2}{\partial y^2}\right)\right]g\\\phi&=\left[C_{44}C_{11}\left(\frac{\partial^2}{\partial x^2}+\frac{\partial^2}{\partial y^2}\right)\left(\frac{\partial^2}{\partial x^2}+\frac{\partial^2}{\partial y^2}\right)+C_{44}C_{33}\frac{\partial^4}{\partial z^4}+(C_{11}C_{33}-2C_{44}C_{13}-C_{13}^2)\frac{\partial^2}{\partial z^2}\left(\frac{\partial^2}{\partial x^2}+\frac{\partial^2}{\partial y^2}\right)\right]g.\end{aligned} \tag{5}$$

The formalism described here is strictly valid only for the case when the roots of Eq. (3) are distinct. In the case of repeated roots, additional general solutions can be easily generated. The reader is referred to Haojiang et al. (1996) and Dunn and Wienecke (1996, 1997) for a detailed discussion of the degenerate cases.

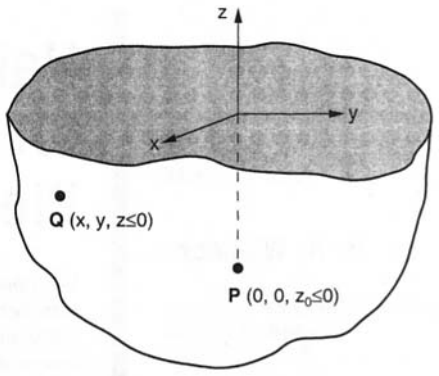


Fig. 1 Coordinate system for the piezoelectric half-space, and the location of the source (*P*) and observation (*Q*) points

3 Half-Space Green's Functions

We consider a transversely isotropic piezoelectric solid with its unique material axis aligned with the z-axis. It occupies the lower half space $z \le 0$ as shown in Fig. 1. With no loss of generality, we assume that the point force (F_x, F_y, F_z) and point charge (Q) are applied at the point $(0, 0, z_0 \le 0)$. The half-space Green's function $G_{MJ} + H_{MJ}$ is then defined as

$$\begin{bmatrix}u\\v\\w\\\phi\end{bmatrix}=\left[\begin{bmatrix}G_{11}&G_{12}&G_{13}&G_{14}\\G_{21}&G_{22}&G_{23}&G_{24}\\G_{31}&G_{32}&G_{33}&G_{34}\\G_{41}&G_{42}&G_{43}&G_{44}\end{bmatrix}+\begin{bmatrix}H_{11}&H_{12}&H_{13}&H_{14}\\H_{21}&H_{22}&H_{23}&H_{24}\\H_{31}&H_{32}&H_{33}&H_{34}\\H_{41}&H_{42}&H_{43}&H_{44}\end{bmatrix}\right]\begin{bmatrix}F_x\\F_y\\F_z\\-Q\end{bmatrix}. \tag{6}$$

Here G_{MJ} ($M, J = 1$–4) are the infinite body Green's functions that we derived previously (Dunn and Wienecke, 1996). In a slightly rearranged form they can be expressed as

$$G_{11}=D_0\frac{x^2+z_0^2+z_0R_0}{R_0R_0^{*2}}-\sum_{i=1}^{3}D_i\lambda_i^{uv}\frac{y^2+z_i^2+z_iR_i}{R_iR_i^{*2}}$$

$$G_{12}=G_{21}=D_0\frac{xy}{R_0R_0^{*2}}+\sum_{i=1}^{3}D_i\lambda_i^{uv}\frac{xy}{R_iR_i^{*2}}$$

$$G_{13}=G_{31}=\sum_{i=1}^{3}B_i\lambda_i^{uv}\frac{x}{R_iR_i^{*}}=\sum_{i=1}^{3}D_i\lambda_i^{w}\frac{x}{R_iR_i^{*}}$$

$$G_{14}=G_{41}=-\sum_{i=1}^{3}A_i\lambda_i^{uv}\frac{x}{R_iR_i^{*}}=\sum_{i=1}^{3}D_i\lambda_i^{\phi}\frac{x}{R_iR_i^{*}}$$

$$G_{22}=D_0\frac{y^2+z_0^2+z_0R_0}{R_0R_0^{*2}}-\sum_{i=1}^{3}D_i\lambda_i^{uv}\frac{x^2+z_i^2+z_iR_i}{R_iR_i^{*2}}$$

$$G_{23}=G_{32}=\sum_{i=1}^{3}B_i\lambda_i^{uv}\frac{y}{R_iR_i^{*}}=\sum_{i=1}^{3}D_i\lambda_i^{w}\frac{y}{R_iR_i^{*}}$$

Downloaded 04 May 2010 to 171.66.16.27. Redistribution subject to ASME license or copyright; see http://www.asme.org/terms/Terms_Use.cfm

$$G_{24} = G_{42} = -\sum_{i=1}^{3} A_i \lambda_i^{uv} \frac{y}{R_i R_i^*} = \sum_{i=1}^{3} D_i \lambda_i^{\phi} \frac{y}{R_i R_i^*}$$

$$G_{33} = \sum_{i=1}^{3} B_i \lambda_i^{w} \frac{1}{R_i}$$

$$G_{34} = G_{43} = -\sum_{i=1}^{3} A_i \lambda_i^{w} \frac{1}{R_i} = \sum_{i=1}^{3} B_i \lambda_i^{\phi} \frac{1}{R_i}$$

$$G_{44} = -\sum_{i=1}^{3} A_i \lambda_i^{\phi} \frac{1}{R_i}. \tag{7}$$

The position-dependent terms in Eqs. (7) are

$$R_i = \sqrt{x^2 + y^2 + z_i^2}$$

$$R_i^* = R_i + z_i$$

$$z_i = \nu_i (z - z_0).$$

The constants A_i, B_i, and D_i are functions only of the ten material constants describing a transversely isotropic piezoelectric material and are given by

$$A_1 = \frac{1}{4\pi\gamma_e} \frac{(\nu_1^2 - 1)(\nu_2^2 - 1)(\nu_3^2 - 1)}{\nu_1(\nu_1^2 - \nu_2^2)(\nu_1^2 - \nu_3^2)}$$

$$B_1 = \frac{1}{2\pi\gamma_a} (\nu_1^2 - 1)[n_2^e \lambda_3^{uv}(\nu_3^2 - 1) - n_3^e \lambda_2^{uv}(\nu_2^2 - 1)]$$

$$D_0 = \frac{1}{4\pi C_{44} \nu_0}$$

$$D_1 = \frac{1}{4\pi\gamma_t} \frac{(\lambda_2^{\phi}\lambda_3^{w} - \lambda_3^{\phi}\lambda_2^{w})}{C_{44}}.$$

The constants A_2 (B_2, D_2) and A_3 (B_3, D_3) are obtained from A_1 (B_1, D_1) by cyclically permuting the indices 1, 2, and 3. The remaining material constants are

$$\gamma_a = (\nu_1^2 - 1)\lambda_1^{uv}(n_2^a n_3^e - n_3^a n_2^e) + (\nu_2^2 - 1)\lambda_2^{uv}(n_3^a n_1^e - n_1^a n_3^e) + (\nu_3^2 - 1)\lambda_3^{uv}(n_1^a n_2^e - n_2^a n_1^e)$$

$$\gamma_e = (\kappa_{11} - \kappa_{33})[C_{11}(C_{44} - C_{33}) + C_{44}(C_{33} + 2C_{13}) + C_{13}^2] + C_{11}(e_{33} - e_{15})^2 + C_{33}(e_{31} + e_{15})^2 - C_{44}(e_{33} + e_{31})^2 + 2C_{13}[e_{15}(e_{15} + e_{31} - e_{33}) - e_{33}e_{31}]$$

$$\gamma_t = \nu_1\lambda_1^{uv}(\lambda_3^{\phi}\lambda_2^{w} - \lambda_2^{\phi}\lambda_3^{w}) + \nu_2\lambda_2^{uv}(\lambda_1^{\phi}\lambda_3^{w} - \lambda_3^{\phi}\lambda_1^{w}) + \nu_3\lambda_3^{uv}(\lambda_2^{\phi}\lambda_1^{w} - \lambda_1^{\phi}\lambda_2^{w})$$

$$n_i^a = 2[\lambda_i^{uv}(C_{13} + C_{44}\nu_i^2) + \nu_i\lambda_i^{w}(C_{44} - C_{33}) + \nu_i\lambda_i^{\phi}(e_{15} - e_{33})]$$

$$n_i^e = 2[-\lambda_i^{uv}(e_{15}\nu_i^2 + e_{31}) + \nu_i\lambda_i^{w}(e_{33} - e_{15}) + \nu_i\lambda_i^{\phi}(\kappa_{11} - \kappa_{33})]$$

$$\lambda_i^{uv} = [(C_{13} + C_{44})e_{33} - C_{33}(e_{31} + e_{15})]\nu_i^3 + (C_{44}e_{31} - C_{13}e_{15})\nu_i$$

$$\lambda_i^{w} = -C_{44}e_{33}\nu_i^4 - [e_{31}(C_{13} + C_{44}) - e_{33}C_{11} + e_{15}C_{13}]\nu_i^2 - e_{15}C_{11}$$

$$\lambda_i^{\phi} = C_{44}C_{33}\nu_i^4 + [C_{13}(C_{13} + 2C_{44}) - C_{11}C_{33}]\nu_i^2 + C_{44}C_{11}.$$

The problem at hand thus consists of finding H_{MJ} so that the singularity as $z \to z_0$ is preserved, and the prescribed boundary conditions on the surface $z = 0$ are satisfied. We consider the case of a free surface where the traction and normal component of the electric displacement vanish. Other boundary conditions can be readily handled in a similar manner.

The approach is to obtain the complete Green's functions by solving two problems: (i) an applied point charge and point force in the z-direction (axisymmetric loading), and (ii) an applied point force in the x-direction (transverse loading). The solution for an applied force in the y-direction then immediately follows due to symmetry. To determine the Green's functions we seek suitable potential functions using the series solution formalism described by Dunn and Wienecke (1996). This leads to

For Axisymmetric Loading:

$$g = \sum_{i=1}^{3} A_i[3(3R_i^2 - 5z_i^2)z_i \ln R_i^* - (4R_i^2 - 15z_i^2)R_i - 6z_i^3] + \sum_{i=1}^{3}\sum_{j=1}^{3} A_{ij}\Big[3(3R_{ij}^2 - 5z_{ij}^2)z_{ij} \ln R_{ij}^* - (4R_{ij} - 15z_{ij}^2)R_{ij} - 6z_{ij}^3\Big] \tag{8}$$

$$\psi = 0.$$

For Transverse Loading:

$$g = \sum_{i=1}^{3} D_i\left[3(R_i^2 - 5z_i^2)x \ln R_i^* + \frac{(13R_i^2 - 15z_i^2)xz_i}{R_i^*} + 4xz_i^2\right] + \sum_{i=1}^{3}\sum_{j=1}^{3} D_{ij}\left[3(R_{ij}^2 - 5z_{ij}^2)x \ln R_{ij}^* + \frac{(13R_{ij}^2 - 15z_{ij}^2)xz_{ij}}{R_{ij}^*} + 4xz_{ij}^2\right] \tag{9}$$

$$\psi = -\frac{D_0 y}{R_0^*} - \frac{D_0 y}{R_{00}^*}.$$

In Eq. (8) we introduce the unknown constants A_{ij} ($i, j = 1$–3). These will have different values depending on whether the applied charge or applied force is considered. In the following we will reserve A_{ij} for the case of an applied charge, and use B_{ij} for the case of an applied force. These constants, along with D_{ij} in Eq. (9), are to be determined from boundary conditions. We have also introduced the following position-dependent terms:

$$z_{ij} = -(\nu_i z + \nu_j z_0)$$

$$R_{ij} = \sqrt{x^2 + y^2 + z_{ij}^2}$$

$$R_{ij}^* = R_{ij} + z_{ij}.$$

The infinite-body Green's functions G_{MJ} are obtained from the single summation terms in the potential functions. The double summation terms lead to H_{MJ}. Using the prescriptions of Eqs. (5) we arrive at

$$H_{11} = D_0 \frac{(x^2 + z_{00}^2 + z_{00}R_{00})}{R_{00}R_{00}^{*2}} + \sum_{i=1}^{3}\sum_{j=1}^{3} D_{ij}\lambda_i^{uv} \frac{(y^2 + z_{ij}^2 + z_{ij}R_{ij})}{R_{ij}R_{ij}^{*2}}$$

Downloaded 04 May 2010 to 171.66.16.27. Redistribution subject to ASME license or copyright; see http://www.asme.org/terms/Terms_Use.cfm

$$H_{12} = H_{21} = D_0 \frac{xy}{R_{00}R_{00}^{*2}} - \sum_{i=1}^{3}\sum_{j=1}^{3} D_{ij}\lambda_i^{uv} \frac{xy}{R_{ij}R_{ij}^{*2}}$$

$$H_{13} = -\sum_{i=1}^{3}\sum_{j=1}^{3} B_{ij}\lambda_i^{uv} \frac{x}{R_{ij}R_{ij}^{*}}$$

$$H_{14} = \sum_{i=1}^{3}\sum_{j=1}^{3} A_{ij}\lambda_i^{uv} \frac{x}{R_{ij}R_{ij}^{*}}$$

$$H_{22} = D_0 \frac{(y^2 + z_{00}^2 + z_{00}R_{00})}{R_{00}R_{00}^{*2}} + \sum_{i=1}^{3}\sum_{j=1}^{3} D_{ij}\lambda_i^{uv} \frac{(x^2 + z_{ij}^2 + z_{ij}R_{ij})}{R_{ij}R_{ij}^{*2}}$$

$$H_{23} = -\sum_{i=1}^{3}\sum_{j=1}^{3} B_{ij}\lambda_i^{uv} \frac{y}{R_{ij}R_{ij}^{*}}$$

$$H_{24} = \sum_{i=1}^{3}\sum_{j=1}^{3} A_{ij}\lambda_i^{uv} \frac{y}{R_{ij}R_{ij}^{*}}$$

$$H_{31} = \sum_{i=1}^{3}\sum_{j=1}^{3} D_{ij}\lambda_i^{w} \frac{x}{R_{ij}R_{ij}^{*}}$$

$$H_{32} = \sum_{i=1}^{3}\sum_{j=1}^{3} D_{ij}\lambda_i^{w} \frac{y}{R_{ij}R_{ij}^{*}}$$

$$H_{33} = \sum_{i=1}^{3}\sum_{j=1}^{3} B_{ij}\lambda_i^{w} \frac{1}{R_{ij}}$$

$$H_{34} = -\sum_{i=1}^{3}\sum_{j=1}^{3} A_{ij}\lambda_i^{w} \frac{1}{R_{ij}}$$

$$H_{41} = \sum_{i=1}^{3}\sum_{j=1}^{3} D_{ij}\lambda_i^{\phi} \frac{x}{R_{ij}R_{ij}^{*}}$$

$$H_{42} = \sum_{i=1}^{3}\sum_{j=1}^{3} D_{ij}\lambda_i^{\phi} \frac{y}{R_{ij}R_{ij}^{*}}$$

$$H_{43} = \sum_{i=1}^{3}\sum_{j=1}^{3} B_{ij}\lambda_i^{\phi} \frac{1}{R_{ij}}$$

$$H_{44} = -\sum_{i=1}^{3}\sum_{j=1}^{3} A_{ij}\lambda_i^{\phi} \frac{1}{R_{ij}}. \tag{11}$$

From Eq. (3) it follows that the real part of v_j is greater than zero. This implies that H_{MJ} is bounded in the lower half space. It is clear that H_{MJ} goes to zero as the distance between the source and observation points goes to infinity. Thus H_{MJ} represents a valid general solution and all that remains is to apply the boundary conditions to solve for the A_{ij}, B_{ij}, and D_{ij}. To solve for the 27 constants A_{ij}, B_{ij}, and D_{ij}, we first differentiate $G_{MJ} + H_{MJ}$ with respect to position to determine the displacement and potential gradients. We then compute the stress and electric displacement using the constitutive equations.

We then set $D_z = \sigma_{xz} = \sigma_{yz} = \sigma_{zz} = 0$ on $z = 0$ to enforce the free surface boundary conditions on the plane $z = 0$. Since the coefficients of all position-dependent terms in each of these equations must vanish identically, we obtain 27 linear equations for the 27 unknowns. The solution is

$$A_{11} = \frac{p_4}{p_1} A_1$$

$$A_{12} = 2\frac{(h_{12}h_{33} - h_{32}h_{13})h_{22}}{p_1} A_2$$

$$A_{13} = 2\frac{(h_{12}h_{33} - h_{32}h_{13})h_{23}}{p_1} A_3$$

$$A_{21} = 2\frac{(h_{31}h_{13} - h_{11}h_{33})h_{21}}{p_1} A_1$$

$$A_{22} = \frac{p_2}{p_1} A_2$$

$$A_{23} = 2\frac{(h_{31}h_{13} - h_{11}h_{33})h_{23}}{p_1} A_3$$

$$A_{31} = 2\frac{(h_{32}h_{11} - h_{12}h_{31})h_{21}}{p_1} A_1$$

$$A_{32} = 2\frac{(h_{32}h_{11} - h_{12}h_{31})h_{22}}{p_1} A_2$$

$$A_{33} = \frac{p_3}{p_1} A_3. \tag{12}$$

Equations for B_{ij} (D_{ij}) are obtained from these equations simply by replacing A_{ij} with B_{ij} (D_{ij}) and A_i with B_i (D_i). The material constants h_{ij} and p_i are given by

$$h_{1j} = e_{33}\nu_j\lambda_j^{w} - e_{31}\lambda_j^{uv} - \kappa_{33}\nu_j\lambda_j^{\phi}$$

$$h_{2j} = C_{44}\lambda_j^{w} + C_{44}\nu_j\lambda_j^{uv} + e_{15}\lambda_j^{\phi} \qquad \text{no sum on } j$$

$$h_{3j} = C_{33}\nu_j\lambda_j^{w} - C_{13}\lambda_j^{uv} + e_{33}\nu_j\lambda_j^{\phi} \tag{13}$$

$$p_1 = |h_{ij}|$$

$$p_2 = h_{31}h_{22}h_{13} + h_{12}h_{31}h_{23} - h_{11}h_{22}h_{33} - h_{21}h_{12}h_{33} - h_{32}h_{11}h_{23} + h_{21}h_{32}h_{13}$$

$$p_3 = -h_{31}h_{22}h_{13} + h_{11}h_{22}h_{33} + h_{32}h_{11}h_{23} + h_{21}h_{32}h_{13} - h_{12}h_{31}h_{23} - h_{21}h_{12}h_{33}$$

$$p_4 = -h_{21}h_{32}h_{13} - h_{32}h_{11}h_{23} + h_{12}h_{31}h_{23} + h_{11}h_{22}h_{33} - h_{31}h_{22}h_{13} + h_{21}h_{12}h_{33}. \tag{14}$$

The H_{MJ} given above, when added to the infinite-body G_{MJ} constitute explicit closed-form solutions for the half-space Green's functions in transversely isotropic piezoelectricity.

To validate our solution, we have directly verified that it satisfies the divergence equations and boundary conditions. We also verified that in the absence of piezoelectric coupling, our solution recovers the transversely isotropic elastic half-space Green's functions (Pan and Chou, 1979; Yu et al., 1995), and the corresponding electrostatic half-space Green's function for a transversely isotropic dielectric. It is also easily shown that for z finite, as $z_0 \to \infty$, the influence of the free surface diminishes and $H_{MJ} \to 0$. Thus the infinite-body Green's functions G_{MJ} are recovered.

Finally, we comment on the degeneracies of our solution. We

Downloaded 04 May 2010 to 171.66.16.27. Redistribution subject to ASME license or copyright; see http://www.asme.org/terms/Terms_Use.cfm

have previously shown that three degeneracies exist for the infinite-body Greens functions: (i) $\nu_j = 1$ for some $j > 0$, (ii) $\nu_j = \nu_k$ for some $j \neq k$, and (iii) $\lambda_j^{\mu\nu} = \lambda_j^{w} = \lambda_j^{\phi} = 0$ for some j. The first occurs when the material is uncoupled and either mechanically or electrically isotropic. The second occurs when the material is uncoupled and mechanically isotropic. The third occurs when the material is uncoupled. All three can also occur under more general circumstances. For the half-space Green's functions presented here, the only additional degenerate case occurs when $|h_{ij}| = 0$. We emphasize that these degeneracies present no real obstacle to the practical application of the solution. Even for a degenerate set of the ten electroelastic moduli, we can obtain a valid numerical solution by slightly perturbing one of the material constants to lift the degeneracy.

4 Conclusion

We derived closed-form expressions for the half-space Green's functions for a transversely isotropic piezoelectric medium where the surface of the half-space is a plane normal to the unique material axis. The simplicity of our expressions renders them immediately useful for the analysis of many problems in the mechanics and physics of piezoelectric solids.

Acknowledgments

The support of the National Science Foundation (grant CMS-9409840) is gratefully acknowledged. We also thank Dr. Ernian Pan of the Department of Civil, Architectural, and Environmental Engineering, University of Colorado for his help in validating our solution.

References

Bacon, D. J., Barnett, D. M., and Scattergood, R. O., 1978, "Anisotropic Continuum Theory of Lattice Defects," *Progress in Materials Science Series,* Vol. 23, pp. 51–262.

Benveniste, Y., 1992, "The Determination of the Elastic and Electric Fields in a Piezoelectric Inhomogeneity," *Journal of Applied Physics,* Vol. 72, pp. 1086–1095.

Chen, T., 1993, "Green's Functions and the Non-Uniform Transformation Problem in a Piezoelectric Medium," *Mechanics Research Communications,* Vol. 20, pp. 271–278.

Chen, T., and Lin, F. Z., 1993, "Numerical Evaluation of Derivatives of the Anisotropic Piezoelectric Green's Functions," *Mechanics Research Communications,* Vol. 20, pp. 501–506.

Deeg, W. F., 1980, "The Analysis of Dislocation, Crack, and Inclusion Problems in Piezoelectric Solids," Ph.D. dissertation, Stanford University, Stanford, CA.

Ding, H. J., Chenbuo, and Liangjian, 1996, "General Solutions for Coupled Equations for Piezoelectric Media," *Int. J. Solids Structures,* Vol. 33, pp. 2283–2298.

Dunn, M. L., 1994, "Electroelastic Green's Functions for Transversely Isotropic Piezoelectric Media and Their Application to the Solution of Inclusion and Inhomogeneity Problems," *International Journal of Engineering Science,* Vol. 32, pp. 119–131.

Dunn, M. L., and Wienecke, H. A., 1996, "Green's Functions for Transversely Isotropic Piezoelectric Solids," *Int. J. Solids Structures,* Vol. 33, pp. 4571–4581.

Dunn, M. L., and Wienecke, H. A., 1996b, "Inclusions and Inhomogeneities in Transversely Isotropic Piezoelectric Solids," *Int. J. Solids Structures,* Vol. 34, pp. 3571–3582.

Eshelby, J. D., 1957, "The Determination of the Elastic Field of an Ellipsoidal Inclusion, and Related Problems," *Proceedings of the Royal Society of London,* Vol. A241, pp. 376–396.

Freedholm, I., 1900, "Sur Les Equations de L'Equilibre D'um Corps Solide Elastique," *Acta Mathematica,* Vol. 23, pp. 1–42.

Hu, H. C., 1953, "On the Three-Dimensional Problems of the Theory of Elasticity of a Transversely Isotropic Body," *Sci. Sinica,* Vol. 2, pp. 145–151.

Lee, J. S., and Jiang, L. Z., 1994, "A Boundary Integral Formulation and 2D Fundamental Solution for Piezoelectric Media," *Mechanics Research Communications,* Vol. 21, pp. 47–54.

Mindlin, R. D., 1936, "Force at a Point in the Interior of a Semi-Infinite Solid," *Physics,* Vol. 7, pp. 195–202.

Mura, T., 1987, *Micromechanics of Defects in Solids,* 2nd Ed., Martinus Nijhoff. Dordrecht, The Netherlands.

Nye, J. F., 1957, *Physical Properties of Crystals,* Oxford University Press, London, UK.

Pan, Y. C., and Chou, T. W., 1976, "Point Force Solution for an Infinite Transversely Isotropic Solid," ASME JOURNAL OF APPLIED MECHANICS, Vol. 43, pp. 608–612.

Pan, Y. C., and Chou, T. W., 1979, "Green's Function Solutions for Semi-Infinite Transversely Isotropic Materials," *International Journal of Engineering Science,* Vol. 17, pp. 545–551.

Sosa, H. A., and Castro, M. A., 1994, "On Concentrated Loads at the Boundary of a Piezoelectric Half Plane," *J. Mech. Phys. Solids,* Vol. 42, pp. 1105–1122.

Synge, J. L., 1957, *The Hypercircle in Mathematical Physics,* Cambridge University Press, London, UK.

Thompson, W., Sir, (Lord Kelvin), 1882, "Note on the Integration of the Equations of Equilibrium of an Elastic Solid," *Mathematical and Physical Systems,* Cambridge University Press, London, pp. 97–98.

Walker, K. P., 1993, "Fourier Integral Representation of the Green Function for an Anisotropic Half-Space," *Proceedings of the Royal Society of London,* Vol. A443, pp. 367–389.

Wang, B., 1992, "Three-Dimensional Analysis of an Ellipsoidal Inclusion in a Piezoelectric Material," *Int. J. Solids Structures,* Vol. 29, pp. 293–308.

Wang, Z., and Zheng, B., 1995, "The General Solution of Three-Dimensional Problems in Piezoelectric Media," *Int. J. Solids Structures,* Vol. 32, pp. 105–115.

Yu, H. Y., Sanday, S. C., Rath, B. B., and Chang, C. I., 1995, "Elastic Fields Due to Defects in Transversely Isotropic Bimaterials," *Proceedings of the Royal Society of London,* Vol. A449, pp. 1–30.

Downloaded 04 May 2010 to 171.66.16.27. Redistribution subject to ASME license or copyright; see http://www.asme.org/terms/Terms_Use.cfm

Effective Elastic Stiffnesses of an Anisotropic Medium Permeated by Tilted Cracks

C. Barret

S. Baste

Laboratoire de Mecanique Physique,
C. N. R. S. UMR 5469,
Universite Bordeaux 1,
351, Cours de la Liberation,
33405 Talence Cedex, France

This paper is concerned with the relationship between the effective stiffness tensor and the intensity of damage in individual modes for an anisotropic material with tilted cracks. The predictions are compared favorably with the experimentally measured load-induced changes of the 13 stiffnesses of a two-dimensional C/C–SiC ceramic matrix composite subjected to an off-axis solicitation. By taking into account the thickness of the cracks, it is possible to understand the change of the elastic anisotropy of the material and of its inelastic strain.

1 Introduction

In composite materials, failure mechanisms favor the generation of microcracks oriented normally to the tensile stress (Evans and Zok, 1994). An off-axis tensile loading creates microcracks whose orientation does not coincide with the fiber axes (Aubard et al., 1994; Lynch and Evans, 1996) and induces a fully anisotropic elastic degradation. To emphasize the induced anisotropy and the loss of elastic symmetry caused by off-principal solicitations, the measurement of the changes of all the stiffness tensor components has been done for a two-dimensional C–C–SiC composite material (Baste and Aristégui, 1998), subjected to a tensile solicitation at 30 deg from one of the fiber directions. The load-induced changes of the 13 stiffnesses, associated with a monoclinic symmetry, have been recovered from ultrasonic velocity data.

A way to analyze the change observed is concerned with the prediction of the stiffness reduction in a body containing cracks. This point of view, which may be termed micromechanics, has been the focus of considerable research since the pioneer work of Eshelby (1957), see Willis (1964), Bhargava and Radhakrishna (1964), Hill (1965), Budiansky and O'Connel (1976), Hoenig (1979), Hori and Nemat-Nasser (1983), McLaughlin (1977), Laws and Dvorak (1987), Hashin (1988), and Deng and Nemat-Nasser (1992). By using a homogenization method that provides the relationship between the effective stiffness tensor and the intensity of damage in the individual modes, it is possible to relate the micro-and-macro level damage measurement. This approach provides coherent and comprehensive physical explanations for the observed experimental phenomenology.

This paper treats the anisotropy induced by tilted cracks in a two-dimensional woven ceramic matrix composite. The tensile solicitation along a non principal direction creates a matrix microcracking normal to the loading direction. The extension of the cracks is limited by the waviness of the bundles and experimental observation of inelastic strains implies that crack-opening displacement is not negligible. Therefore, it is necessary to consider three-dimensional defined cracks and to calculate the P-tensor for three-dimensional defined tilted cracks in order to evaluate the effective stiffness tensor of the damaged material by using a similar approach to Laws et al. (1983). As the classical formula of the P-tensor components is given in the crack's frame, we have to consider a more general symmetry for the solid. Indeed, the material is no longer orthotropic but monoclinic when tilted cracks are created. Therefore, the prediction of the effective stiffness tensor requires the evaluation of 13 $Pijkl$ in order to study the damage process. Then, we pay particular attention to the influence of the crack's thickness on the damage. Finally, a comparison between experimental data and the predictions of the stiffness tensor changes and of the inelastic strain variation is done.

2 Experimental Results

In a previous paper (Baste and Aristégui, 1998), damage in a ceramic-matrix composite consisting of carbon fibers embedded in a chemical vapor infiltration (CVI)-processed C–SiC matrix (two-dimensional C/C–SiC composite), subjected to an off-axis loading was studied by means of an ultrasonic method. Because of its bi-directional structure, the material possesses three perpendicular planes of symmetry and it satisfies the hypothesis of an orthorhombic symmetry. Moreover, the two fiber directions being mutually orthogonal and symmetrically equivalent, the composite presents a tetragonal symmetry with six independent stiffnesses. Table 1 shows the stiffnesses in the material principal coordinate system $R^f = (\mathbf{x}_1, \mathbf{x}_2^f, \mathbf{x}_3^f)$ associated with the fibers. The observation coordinate system $R = (\mathbf{x}_1, \mathbf{x}_2, \mathbf{x}_3)$ associated with the sample is chosen in such a way that axis $\mathbf{x}_1$ corresponds to the normal to the plate. The plane $(\mathbf{x}_2, \mathbf{x}_3)$ is the cloths' plane. As the sample is cut out according to a 30-deg angle from fiber axes (Fig. 1), its elasticity is described by 13 stiffnesses in the coordinate system $R = (\mathbf{x}_1, \mathbf{x}_2, \mathbf{x}_3)$, given in Table 2. Those stiffnesses, in Tables 1 and 2, are actually the components of the same tensor in two different bases.

In order to study accurately the damage evolution in composites, an experimental device that couples an ultrasonic immersion tank to a tensile machine and an extensometer has been developed (Baste and Aristégui, 1998). As it gives access to the complete stiffness tensor, it is possible to know which stiffness coefficients are affected during the damage process (Fig. 2). It also allows to know accurately which part of the global strain is either elastic or inelastic (Fig. 3). Damage-induced changes of the 13 stiffnesses (C_{IJ}) identified in the geometric coordinate system of the sample are plotted in Fig. 2 as a function of the applied tensile stress. The loss of stiffness along the tensile axis $\mathbf{x}_3$ is very important and occurs from the first stress levels. The variations of the experimental stiffnesses C_{33}, C_{44}, and C_{55} lead us to consider that the matrix microcracking oriented normally to the tensile loading is the main damage mode (Laws et al., 1983) and induces a fully anisotropic degradation. In particular, the coupling stiffnesses C_{34}, C_{24}, C_{14}, and C_{56}, which are naturally about zero at 0 MPa, become non-negligible at 40 MPa. After 60 MPa, they decrease

Contributed by the Applied Mechanics Division of THE AMERICAN SOCIETY OF MECHANICAL ENGINEERS for publication in the ASME JOURNAL OF APPLIED MECHANICS.

Discussion on the paper should be addressed to the Technical Editor, Professor Lewis T. Wheeler, Department of Mechanical Engineering, University of Houston, Houston, TX 77204-4792, and will be accepted until four months after final publication of the paper itself in the ASME JOURNAL OF APPLIED MECHANICS.

Manuscript received by the ASME Applied Mechanics Division, May 7, 1998; final revision, Jan. 10, 1999. Associate Technical Editor: J. W. Ju.

 Copyright © 1999 by ASME

Downloaded 04 May 2010 to 171.66.16.27. Redistribution subject to ASME license or copyright; see http://www.asme.org/terms/Terms_Use.cfm

Table 1 Stiffnesses (in GPa) of the two-dimensional C/C–SiC in the material principal coordinate system associated to the fibers axes. The numbers in the parentheses indicate the confidence interval (in GPa) associated with each elasticity constant

C_{11}	C_{12}	C_{13}	C_{22}	C_{23}	C_{33}	C_{44}	C_{55}	C_{66}
17.2	5.6	5.2	98.0	0.0	98.0	33.0	8.9	9.2
(0.1)	(0.4)	(0.4)	(8.0)	(6.8)	(9.0)	(4.3)	(0.1)	(0.2)

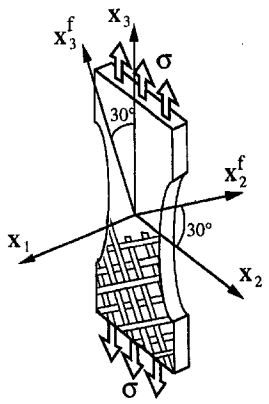


Fig. 1 The 30-deg off-axis solicitation sample, cut out according to a 30-deg angle from fiber axes, and loading in this direction. $R = (x_1, x_2, x_3)$ is the observation coordinate system associated with the sample, i.e., the stress principal frame, and $R^f = (x_1, x_2^f, x_3^f)$ the material principal coordinate system associated with the fibers

and recover their initial value of about zero. It coincides with the increase of inelastic strain (Fig. 3). The fibrous reinforcement stops and deviates the matrix microcracking in mode II. Sliding occurs in the fiber-matrix interphase and leads to other cracking modes consisting in slit cracks whose orientations coincide with the directions of the fibers (Fig. 4). The experimental changes of the stiffnesses C_{11}, C_{22}, C_{66}, C_{55}, and C_{12} point out the generation of these cracking modes.

The under load strain partition (Baste and Morvan, 1996) in the direction $\mathbf{x}_3$ with respect to the applied stress is plotted in Fig. 3. The part of inelastic strain increases with the stress. As it is the macroscopic result of the crack-opening displacement (He et al., 1994), the inelastic strain is associated with an increase in the thickness of the matrix microcracks.

3 Analytical Prediction of the Stiffness Tensor

Our purpose is to describe the damage on the two-dimensional C/C–SiC studied in the previous part by establishing the relationship between the effective stiffness tensor and the intensity of damage. The matrix microcracking oriented normally to the tensile stress requires particular attention to fully understand the experimental changes observed during the load. The material microstructure and the increase of inelastic strain lead us to consider three-dimensional defined tilted cracks for the evaluation of effective stiffness changes due to this cracking mode.

3.1 Governing Equations. Consider an ellipsoidal inclusion,

$$\frac{x_1^2}{a^2} + \frac{x_2^2}{c^2} + \frac{x_3^2}{b^2} \le 1, \tag{1}$$

with stiffness C_r and compliance S_r, which is embedded in an infinite homogeneous solid whose stiffness and compliance tensors are, respectively, C and S. The material is loaded by uniform stress, $\bar{\sigma}$, or subjected to uniform strain, $\bar{\varepsilon}$, at infinity. Let the stress and strain fields in the inclusion be σ_r and ε_r, respectively, so that

$$\sigma_r = C_r\varepsilon_r, \quad \varepsilon_r = S_r\sigma_r. \tag{2}$$

It is well known that the elastic field in the ellipsoidal inclusion is uniform (Eshelby, 1957) and can be evaluated as

$$\varepsilon_r = [I + P(C_r - C)]^{-1}\bar{\varepsilon}, \ \sigma_r = [I + Q(S_r - S)]^{-1}\bar{\sigma}. \tag{3}$$

The solution of this problem requires the determination of the tensor Q defined by

$$Q = C - CPC \tag{4}$$

and the determination of the tensor P whose components are given by Faivre (1971),

$$P_{ijkl} = \frac{abc}{4\pi}\int_\Omega \frac{D_{ijkl}(\omega_n)}{(a^2\omega_1^2 + c^2\omega_2^2 + b^2\omega_3^2)^{3/2}}\, d\Omega, \tag{5}$$

where Ω is the surface of the unit sphere centred at the origin of $(\omega_1, \omega_2, \omega_3)$ space. The fourth-order tensor D is defined by

$$D_{ijkl} = \omega_l\omega_j g_{ik} \quad \text{with} \quad g_{ik} = [C_{ijkl}\omega_j\omega_l]^{-1}_{(ik)}. \tag{6}$$

Turning now to the basic equations for composites, we note that in order for the concept of overall moduli to be meaningful, it is necessary to consider macroscopically uniform loading (Hill, 1965). In such a case, the applied stress is equal to the average stress, $\bar{\sigma}$, and the phase average stresses and strains are related to the overall averages through

$$\overline{\varepsilon_r} = A_r\bar{\varepsilon}, \quad \overline{\sigma_r} = B_r\bar{\sigma}. \tag{7}$$

Let c_r denote the volume concentration of the rth phase. Since

$$\sum c_r = 1, \quad \bar{\sigma} = \sum c_r\overline{\sigma_r}, \quad \bar{\varepsilon} = \sum c_r\overline{\varepsilon_r}, \tag{8}$$

it follows (Hill, 1963) that the overall stiffness C and compliance S are given by

$$C = \sum c_r C_r A_r, \quad S = \sum c_r S_r B_r. \tag{9}$$

From (3) and (7), we obtain

$$A_r = [I + P(C_r - C)]^{-1}, \quad B_r = [I + Q(S_r - S)]^{-1}. \tag{10}$$

We emphasize that the P and Q tensors appearing in (10) depend upon the shape of the considered inclusion and the stiffness of the effective medium C. That leads to the self-consistent scheme. In the following parts of the paper, we replace C with C_0, the stiffness tensor of the uncracked material, in (3), (4), (6), and (10). This method, similar to the Mori-Tanaka method (Mori and Tanaka, 1973), requires less calculations and gives a good approximation of the effective stiffness tensor for reasonable volume concentration of cracks.

3.2 Tilted Cracks. In the two-dimensional C/C–SiC, the damage starts with the creation of cracks oriented normally to the

Table 2 Stiffnesses (in GPa) of the two-dimensional C/C–SiC sample in the observation coordinate system associated with the sample. The numbers in the parentheses indicate the confidence interval (in GPa) associated with each elasticity constant

C_{11}	C_{12}	C_{13}	C_{14}	C_{22}	C_{23}	C_{24}	C_{33}	C_{34}	C_{44}	C_{55}	C_{56}	C_{66}
18.0	6.5	4.4	−0.3	95.8	8.4	−0.3	74.0	−0.2	40.0	9.0	0.2	9.5
(0.1)	(0.2)	(0.3)	(0.2)	(2.6)	(2.2)	(8.8)	(2.8)	(9.7)	(0.1)	(0.1)	(0.1)	(0.1)

Downloaded 04 May 2010 to 171.66.16.27. Redistribution subject to ASME license or copyright; see http://www.asme.org/terms/Terms_Use.cfm

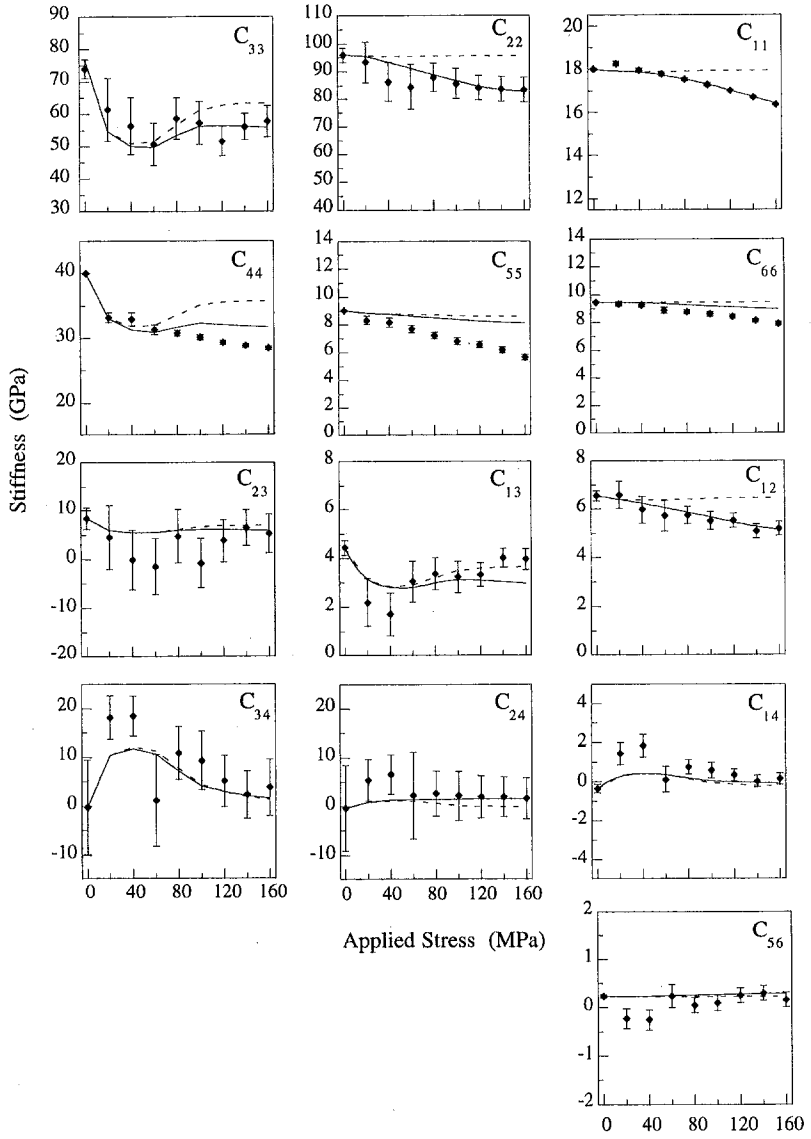


Fig. 2 Variation of the stiffness tensor as a function of a tensile stress applied within direction 3. ◆ experimental values with their 90 percent confidence interval, —— prediction of the stiffness changes, ----- predictions of the tilted crack's influence

stress direction (Fig. 5). As the governing equations lie to the effective stiffness tensor in the axes of the ellipsoidal crack (1), we have to consider the components of C in the principal coordinate system $R = (\mathbf{x}_1, \mathbf{x}_2, \mathbf{x}_3)$ of the ellipsoid.

The two-dimensional C/C–SiC is orthotropic in the material principal coordinate system $R^f = (\mathbf{x}_1, \mathbf{x}_2^f, \mathbf{x}_3^f)$:

$$C_{IJ}(R^f) = \begin{bmatrix} C_{11} & C_{12} & C_{13} & 0 & 0 & 0 \\ & C_{22} & C_{23} & 0 & 0 & 0 \\ & & C_{33} & 0 & 0 & 0 \\ & \text{Sym} & & C_{44} & 0 & 0 \\ & & & & C_{55} & 0 \\ & & & & & C_{66} \end{bmatrix}. \quad (11)$$

The stiffness tensor becomes in the coordinate system $R = (\mathbf{x}_1, \mathbf{x}_2, \mathbf{x}_3)$, by using the fourth-rank tensor rotation law (Auld, 1973),

$$(C_{IJ}^R) = (M_{IJ}^{Rf \to R})(C_{IJ}^{Rf})(M_{IJ}^{Rf \to R})^t, \quad (12)$$

where M is the transformation matrix:

$$(C_{IJ}^R) = \begin{bmatrix} C_{11} & C_{12} & C_{13} & C_{14} & 0 & 0 \\ & C_{22} & C_{23} & C_{24} & 0 & 0 \\ & & C_{33} & C_{34} & 0 & 0 \\ & \text{Sym} & & C_{44} & 0 & 0 \\ & & & & C_{55} & C_{56} \\ & & & & & C_{66} \end{bmatrix}. \quad (13)$$

As the cracks principal axes coincide with the coordinate system R, the material remains monoclinic during the damage process.

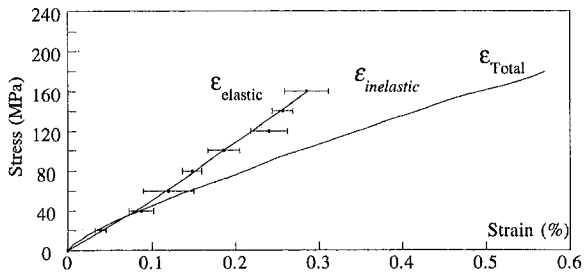


Fig. 3 Variation of the total strain, of the elastic strain and of the inelastic strain as a function of applied tensile stress

Downloaded 04 May 2010 to 171.66.16.27. Redistribution subject to ASME license or copyright; see http://www.asme.org/terms/Terms_Use.cfm

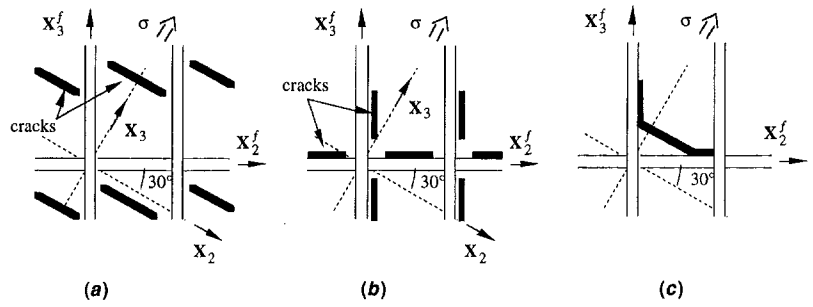


Fig. 4 Damage modes taking place during the 30-deg off-axis solicitation: (*a*) matrix transverse microcracking normal to the loading direction, (*b*) microcracking deviation at the fiber-matrix interphase, (*c*) "zigzag" shape of the resulting microcracking

The 3 × 3 matrix g and the fourth-order tensor D, (6), are calculated with the stiffness tensor given in (13) and D has the same form as C^R. It follows from (5) that the P tensor has the same nonzero components as D and C^R.

The effective medium is considered as a two-phase medium (Laws et al., 1983). Let phase 1 be the uncracked fiber-reinforced composite material. Phase 2 is a set of ellipsoids consisting of voids. The overall stiffness tensor for the two-phase medium follows from (9)

$$C = c_1 C_1 A_1 + c_2 C_2 A_2. \tag{14}$$

Also from (7) and (8) we have

$$c_1 A_1 + c_2 A_2 = I. \tag{15}$$

It is convenient to use (15) to eliminate the concentration factors for the uncracked medium ($r = 1$) from (14), to give

$$C = C_1 + c_2 (C_2 - C_1) A_2. \tag{16}$$

As we consider phase 2 to consist of ellipsoidal voids, $C_2 \to 0$. From (16) we have

$$C = C_1 - c_2 C_1 A_2 = C_1 [I - c_2 A_2] = C_1 [I + c_2 A_2]^{-1}, \tag{17}$$

where we obtain A_2 from (10) and (4)

$$A_2 = [I - PC_1]^{-1} = Q_2^{-1} C_1. \tag{18}$$

By introducing (18) in (17), the effective stiffness tensor is given by

$$C = C_1 [I + c_2 Q_2^{-1} C_1]^{-1}. \tag{19}$$

Equation (19) is the equation used to evaluate the effective stiffness tensor for an anisotropic medium permeated by ellipsoidal cracks. It requires the determination of the tensor Q and P by a numerical evaluation of (5).

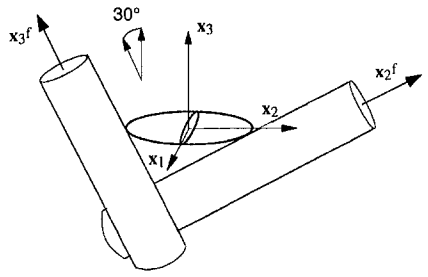


Fig. 5 Principal coordinate system of the matrix microcracks

4 Influence of the Thickness of the Crack

The experimental inelastic strain (Fig. 3) leads us to consider that a crack-opening displacement occurs during the load for the tilted cracks. To fully understand the relationship between the macroscopic changes and the microscopic phenomena, it is necessary to study the influence of the crack-opening displacement on the effective stiffness tensor. The variations of the stiffness tensor are directly related to c_2 (19). Nevertheless the crack shape also affects the stiffnesses C_{IJ}. Figure 6 represents the variations of Q_{IJ}^{-1} rather than C to insist on the influence of the thickness crack aspect ratio, $\delta = b/c$, and to avoid the effect of c_2. By considering the C_{IJ} of the two-dimensional C/C–SiC defined in Table 2, we have calculated the Q^{-1} tensor for a crack (1) with an ellipticity crack aspect ratio, $\gamma = a/c$, equal to 0.1. Indeed in such a material, the waviness of the bundles limits the extension of the cracks. The results (Fig. 6) are given with respect to δ. We have plotted only the most affected components Q_{33}^{-1}, Q_{44}^{-1}, Q_{34}^{-1}, Q_{55}^{-1}, Q_{14}^{-1}, and Q_{24}^{-1}.

The weaker δ is, the more important its influence on the variations of the considered components of the tensor Q^{-1} is. Whereas the three most affected components, Q_{33}^{-1}, Q_{44}^{-1}, and Q_{34}^{-1} reach a similar rate for the weakest crack thickness aspect ratios, their variations are strongly different for higher crack thickness aspect ratios. Indeed, the value of Q_{34}^{-1} remains near zero up to $\delta = 0.001$ and then increases rapidly while Q_{33}^{-1} and Q_{44}^{-1} grow more regularly. Those variations throw light on the experimental results. At the beginning of load, the inelastic strain is about zero (Fig. 3) and the change of the coupling stiffnesses C_{34}, C_{24}, and C_{14} is nonnegligible (Fig. 2). Then, after 60 MPa, as the part of inelastic strain increases, the crack-opening displacement starts and these stiffnesses decrease.

5 Comparison Between Experimental Stiffness Changes and Predictions

5.1 Stiffness Changes due to the Tilted Cracks. The evaluation of the stiffness changes for a material containing tilted cracks is performed by using (19). It requires the determination of the volume concentration of the cracks during the load. It is given by

$$c_c = \frac{4\pi}{3} \cdot \frac{a}{2x_1} \cdot \frac{c}{2x_2} \cdot \frac{b}{2x_3} = \frac{\pi}{6} \cdot \frac{2a}{2x_1} \cdot \frac{2c}{2x_2} \cdot \beta \cdot \delta, \tag{20}$$

where β is the crack density parameter in the direction 3, δ is the thickness crack aspect ratio, $2x_i$ is the distance between two cracks in the direction i and a, c, and b are the semi-axes of the ellipsoid (1). As the waviness of the material limits the crack length in the plane (1, 2), $2a$, $2x_1$, $2c$ and $2x_2$ are constant and respectively equal to 150 μm, 200 μm, 1500 μm, and 2000 μm (Camus et al., 1996). Therefore, we have to identify the evolution laws of β and δ in order to evaluate the effective stiffness tensor C, by resolving

Downloaded 04 May 2010 to 171.66.16.27. Redistribution subject to ASME license or copyright; see http://www.asme.org/terms/Terms_Use.cfm

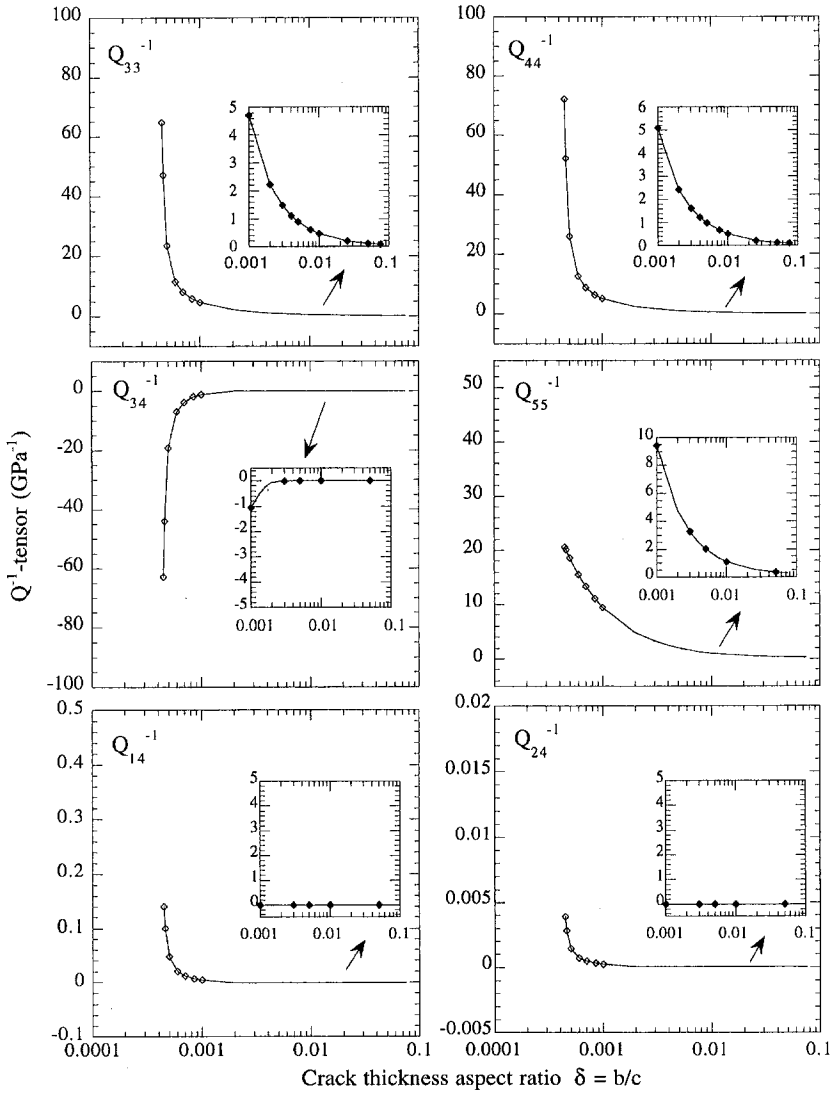


Fig. 6 The most influenced inclusion compliances Q_{ij}^{-1} as a function of the crack thickness aspect ratio $\delta = b/c$

the inverse problem. Indeed, the experimental data, the stiffness changes and the inelastic strain, are used to compare the predictions obtained for different values of β and δ and allow the determination of the optimum variations of these two parameters. The variations of the experimental stiffnesses C_{33}, C_{44}, and C_{34} lead us to consider that the matrix microcracking starts with a weak thickness crack aspect ratio and a rapid increase of the density of cracks. Then after 60 MPa as the coupling stiffnesses C_{34}, C_{24}, and C_{14} decrease more quickly than the others (Fig. 2), the crack-opening displacement starts and the evolution of β is less important (Fig. 7).

Moreover, the comparison between the experimental inelastic strain (Baste and Morvan, 1996) and its prediction (Fig. 8) given by

$$\varepsilon^{\text{inelastic}} = \beta \cdot \delta \tag{21}$$

(see Morvan and Baste (1998)) allows us to validate the choice of β and δ. There is a good agreement between experimental values of the inelastic strain and the predictions plotted in straight lines except for the first levels of stress. Indeed, until 60 MPa, inelastic strain is not predicted. Its value, about zero, implies a thickness crack aspect ratio weaker than the considered for the evaluation of C. As the numerical evaluation of the P and Q^{-1} tensors requires a nonzero thickness, we have calculated the first levels with a δ

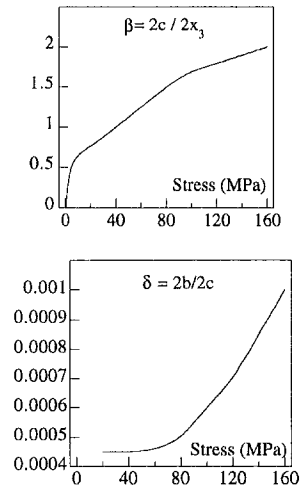


Fig. 7 Variation of the crack density parameter and of the thickness crack aspect ratio for the matrix microcracking normal to the loading direction as a function of applied stress

Downloaded 04 May 2010 to 171.66.16.27. Redistribution subject to ASME license or copyright; see http://www.asme.org/terms/Terms_Use.cfm

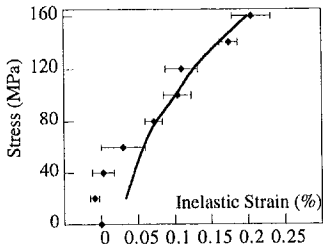


Fig. 8 Variation of the inelastic strain as a function of applied tensile stress. The marks represent the experimental data and the straight lines, the predictions

equal to 4.5 10^{-4} to avoid numerical problem. It is probably less important but this choice allows numerical calculations and gives quite good results for C.

The effective stiffnesses are plotted in dotted line in Fig. 2. The loss of stiffness observed for C_{33} and C_{44} and the rapid increase of C_{34} at the beginning of the load is predicted. Moreover, the crack-opening displacement taken into account after 60 MPa allows to recover the variation of the coupling stiffnesses C_{34}, C_{24}, and C_{14} at the end of the damage process. It points out the influence of the thickness of the tilted cracks on the damage-induced anisotropy. Indeed, whereas cracks with weak thickness have a high anisotropic effect, the crack-opening displacement induces a less important anisotropy. The coupling stiffnesses C_{34}, C_{24}, and C_{14} recover their initial value at the end of the load. As C_{11}, C_{12}, C_{22}, C_{55}, and C_{66} remain not predicted, it is necessary to take into account the other crack systems in order to predict the effective stiffness tensor variations accurately.

5.2 Evaluation of the Total Effective Stiffness Tensor. There are three other crack systems whose orientations coincide with the material axes (Baste and Aristégui, 1998): two fiber-matrix debonding, noted "l" and "t," representative of the mode II deflection of the matrix cracks along the axes $\mathbf{x}_3^f$ and $\mathbf{x}_2^f$, respectively, and a "i" damage mode which may be regarded mainly as interply delamination. They consist in slit cracks and their influence on the effective stiffness tensor is evaluated by using the infinite elliptic cylinder method with a thickness near from zero (Laws, 1977):

$$\Lambda(C_0) = \lim_{\delta \to 0} \delta Q^{-1}(C_0), \tag{22}$$

where C_0 is the stiffness tensor of the uncracked material. The evaluation of the total effective stiffness tensor requires the determination of the evolution law of the crack density parameters $\tilde{\beta}_i$, $\tilde{\beta}_l$, and $\tilde{\beta}_t$ (Fig. 9) which measure the distance between regularly spaced cracks of the same crack system (Laws et al., 1983). It is done by calculating the compliance tensor of the material containing tilted cracks in the material axes:

$$(S_{IJ}^{Rf}) = (M_{IJ}^{R \to Rf})^t (C_{IJ}^{-1\,R})(M_{IJ}^{R \to Rf}), \tag{23}$$

and by considering $S_{\exp}^{Rf}$ the experimental compliance tensor in this coordinate system with

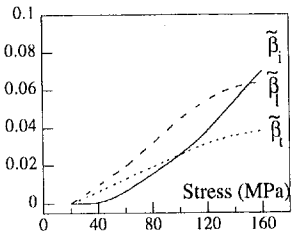


Fig. 9 Variation of the crack density parameters as a function of 30-deg off-axis tensile stress for the crack systems extended along the fibers

$$\tilde{\beta}_i = \frac{S_{\exp}^{Rf}(1,1) - S^{Rf}(1,1)}{\Lambda_i^{Rf}(1,1)}, \quad \tilde{\beta}_l = \frac{S_{\exp}^{Rf}(2,2) - S^{Rf}(2,2)}{\Lambda_l^{Rf}(2,2)} \quad \text{and}$$

$$\tilde{\beta}_t = \frac{S_{\exp}^{Rf}(3,3) - S^{Rf}(3,3)}{\Lambda_t^{Rf}(3,3)}. \tag{24}$$

Then, the three tensors Λ_i, Λ_l, and Λ_t are calculated in the coordinate system of the sample, cut out according to a 30-deg angle from fiber axes, using the fourth-rank tensor rotation law:

$$(\Lambda_{IJ}^R) = (M_{IJ}^{Rf \to R})^t (\Lambda_{IJ}^{Rf})(M_{IJ}^{Rf \to R}). \tag{25}$$

Finally, the prediction of the total damage-induced changes is calculated with

$$C_{\text{tot}} = C\left[I + \left(\frac{\pi}{4} \tilde{\beta}_l \Lambda_l^R + \frac{\pi}{4} \tilde{\beta}_t \Lambda_t^R + \frac{\pi}{4} \tilde{\beta}_i \Lambda_i^R \right) C \right]^{-1}, \tag{26}$$

where C is the effective stiffness tensor of the material containing tilted cracks (19). The variations of the total effective stiffness tensor are plotted in a straight line in Fig. 2. A good agreement is observed between experimental values and predictions except for C_{44}, C_{55}, and C_{66}. As the method used to evaluate the effective stiffness tensor is based on the Mori-Tanaka method, it does not take into account the effect of interaction between the cracks. It will be interesting to develop a self-consistent method to obtain more realistic evaluation of the damage-induced changes.

6 Conclusion

The model developed in this paper relates the micro-and-macro level damage measurement. The load-induced changes of the stiffness tensor can be described by a single parameter, the density of cracks. This parameter is considered as an internal variable of a constitutive law that describes the fully anisotropy induced by a crack system which does not coincide with the material axes. Moreover, taking into account the thickness of the cracks, i.e., the crack-opening displacement, allows us to understand and to predict the experimental results. The stiffness tensor changes during the damage process and the inelastic strain are favorably predicted when the microscopic damage level is identified and introduced in the homogenization method. Indeed, whereas a slit tilted crack leads to a high anisotropic level, a nonzero thickness tilted crack has a far less important influence on the damage-induced anisotropy.

Therefore, the response of a damaged elastic material to any stress is totally predicted when the evolution of the crack density parameter and of the thickness crack aspect ratio is identified according to the crack orientation and the stress history.

Acknowledgment

C. Barret is grateful to the Région Aquitaine for its partial financial support.

References

Aubard, X., Lamon, J., and Allix, O., 1994, "Model of the non-linear mechanical behavior of 2D SiC–SiC CVI-composites," *J. Am. Ceram. Soc.*, Vol. 77, No. 8, pp. 2118–2126.

Auld, B. A., 1973, *Acoustic Fields and Waves in Solids*, Vol. 1, Wiley-Interscience, New York.

Baste, S., and Aristégui, C., 1998, "Induced anisotropy and crack systems orientations of a ceramic matrix composite under off-principal axis loading," *Mech. of Mater.*, Vol. 29, pp. 19–41.

Baste, S., and Morvan, J. M., 1996, "Under Load Strain Partition of a Ceramic Matrix Composite Using an Ultrasonic Method," *Experimental Mechanics*, Vol. 36, pp. 148–154.

Bhargava, R. D., and Radhakrishna, H. C., 1964, "Elliptic Inclusion in Orthotropic Medium," *Journal of The Physical Society of Japan*, Vol. 19, pp. 396–405.

Budiansky, B., and O'Connel, R., 1976, "Elastic Moduli of a Cracked Solid," *Int. J. Solids Structures*, Vol. 12, pp. 81–97.

Camus, G., Guillaumat, L., and Baste, S., 1996, "Development of Damage in a 2D

Downloaded 04 May 2010 to 171.66.16.27. Redistribution subject to ASME license or copyright; see http://www.asme.org/terms/Terms_Use.cfm

Woven C/SiC Composite under Mechanical Loading. Part I: Mechanical Characterization," *C. Sci. and Tech.,* Vol. 56, pp. 1363–1372.

Deng, H., and Nemat-Nasser, S., 1992, "Microcrack arrays in isotropic solids," *Mechanics of Materials,* Vol. 13, pp. 15–36.

Eshelby, J. D., 1957, "The determination of the elastic field of an ellipsoidal inclusion, and related problems," *Proc. Roy. Soc.,* Vol. A241, pp. 376–396.

Evans, A. G., and Zok, F. W., 1994, "The physics and mechanics of fiber-reinforced brittle matrix composites," *J. Materials Science,* Vol. 29, pp. 3857–3896.

Faivre, G., 1971, "Hétérogénéités ellipsoïdales dans un milieu élastique anisotrope," *Journal de Physique,* Vol. 32, pp. 325–331.

Hashin, Z., 1988, "The differential scheme and its applications to cracked materials," *J. Mech. Phys. Solids,* Vol. 36, pp. 719–734.

He, M. Y., Wu, B.-X., Evans, A. G., and Hutchinson, J. W., 1994, "Inelastic strains due to matrix cracking in unidirectional fiber-reinforced composites," *Mech. Mater.,* Vol. 18, pp. 213–229.

Hill, R., 1963, "Elastic properties of reinforced solids: Some theoretical principles," *J. Mech. Phys. Solids,* Vol. 11, p. 357.

Hill, R., 1965, "A self consistent mechanics of composite materials," *J. Mech. Phys. Solids,* Vol. 13, pp. 213–222.

Hoenig, A., 1979, "Elastic moduli of a non-randomly cracked body," *Int. J. Solids Structures,* Vol. 15, pp. 137–154.

Horii, H., and Nemat-Nasser, S., 1983, "Overall moduli of solids with microcracks: load-induced anisotropy," *J. Mech. Phys. Solids,* Vol. 31, pp. 155–171.

Laws, N., 1977, "A note on interaction energies associated with cracks in anisotropic solids," *Phil. Mag.,* Vol. 36, pp. 367–372.

Laws, N., Dvorak, G. J., and Hejazi, M., 1983, "Stiffness changes in unidirectional composites caused by crack systems," *Mech. Mater.,* Vol. 2, pp. 123–137.

Laws, N., and Dvorak, G. J., 1987, "The effect of fiber breaks and aligned penny-shaped cracks on the stiffness and energy release rates in unidirectional composites," *Int. J. Solids Struct.,* Vol. 23, pp. 1269–1283.

Lynch, C. S., and Evans, A. G., 1996, "Effects of Off-Axis Loading on the Tensile Behavior of a Ceramic-Matrix Composite," *J. Am. Ceram. Soc.,* Vol. 79, pp. 3113–3123.

McLaughlin, R., 1977, "A study of the differential scheme for composite materials," *Int. J. Enggng. Sci.,* Vol. 15, pp. 237–244.

Mori, T., and Tanaka, K., 1973, "Average stress in matrix and average energy of materials with misfitting inclusions," *Acta Metallurgica,* Vol. 21, pp. 571–574.

Morvan, J. M., and Baste, S., 1998, "Effect of the opening/closure of microcracks on the non linear behavior of a 2D C-SiC composite under cyclic loading," *Int. J. Damage Mechanics,* Vol. 7, pp. 381–402.

Willis, J. R., 1964, "Anisotropic elastic inclusion problems," *Quart. J. Mech. and Applied Math.,* Vol. 17, pp. 157–174.

Downloaded 04 May 2010 to 171.66.16.27. Redistribution subject to ASME license or copyright; see http://www.asme.org/terms/Terms_Use.cfm

Approximate Analysis of a Shear Band in a Thermoviscoplastic Material

H.-G. Kim
Graduate Student

S. Im[1]
Professor,
Mem. ASME

Department of Mechanical Engineering,
Korea Advanced Institute of Science and Technology,
Science Town,
Taejon 305-701 Korea

Shear localization is systematically examined with the aid of an approximate model for the three stages of deformation in the formation and development of a shear band, which comprise: the growth of inhomogeneous deformation, the stress collapse, and the post-collapse state. A basic model of one-dimensional simple shear deformation for a thermoviscoplastic material is employed with a linear thermal softening in the absence of strain hardening. The evolution of plastic strain rate at the center of the shear band is explicitly obtained, and an approximate scaling law for the critical strain, at which the stress collapse begins, is proposed in terms of material parameters and boundary velocity. All state variables including stress, plastic strain rate, and temperature after the stress collapse are evaluated, and the overshoot of the plastic strain rate during stress collapse is explained in terms of a nondimensional parameter and elastic unloading. Finally, numerical experiments confirm the analytical results.

1 Introduction

The major mechanism of (adiabatic) shear localization in ductile metals is caused by thermal softening effects due to the lack of sufficient time for heat to diffuse away when the thermal softening becomes significant. In many experimental observations (Hartley et al., 1987; Marchand and Duffy, 1988; Duffy and Chi, 1992), it has been shown that plastic deformations consist of three stages which start with a stage of growing inhomogeneous deformations, followed by an abrupt stress drop wherein shear localization develops into a very narrow band, and finally a post-localization state or fully developed state.

There have been a number of theoretical studies using various stability analyses for finding a condition of localization in terms of material parameters, internal variables and boundary conditions. Among these researches, stability of governing equations linearized with respect to perturbations has been examined as a useful tool for understanding the formation of the shear band (Clifton, 1980; Bai, 1982; Burn and Trucano, 1982; Fressengeas and Molinari, 1987; Shawki and Clifton, 1989). However, notable is the fact that the growth rates obtained by the linear stability analyses are only valid for a short time after the onset of instability, which occurs earlier than the abrupt stress drop or the stress collapse (Wright and Walter, 1987; Leroy and Chapuis, 1991). Cherukuri and Shawki (1995) predicted the critical time associated with this severe localization using an inflection point in the total kinetic energy evolution obtained by numerical calculations. Molinari and Clifton (1987) have presented the critical conditions with the concept of L_∞-localization for several flow rules as a function of the defects, material parameters, and boundary conditions with neglect of heat conduction, inertia, and elasticity. Through numerical analyses, Wright and Walter (1987) identified thermal softening and strain rate hardening as key parameters for the timing of the severe localization. Moreover, Wright (1990) suggested a scaling law for the shear band susceptibility through various levels of approximations.

After stress collapse, the heat flow may balance a heat generation to lead to a quasi-steady state, and the plastic strain rate may reach a fully developed profile. The existence and uniqueness of a steady solution for velocity boundary conditions have been shown by Wright (1987) and Leroy and Molinari (1992). Wright (1987) proposed a quadrature for several viscoplastic materials, but the specification of the plastic strain rate and the temperature at the center is required for obtaining the complete solutions. A simple expression for the width of the shear band at the post-state after stress collapse has been obtained with characteristic quantities of the stress, the strain rate, and the temperature by Dodd and Bai (1985). An explicit expression for the band width at the post-state was given as a function of the material parameters and the boundary velocity by Wright and Ockendon (1992). Analyses of one-dimensional shear band models by Olmstead et al. (1994) and Glimm et al. (1996) have been carried out under the assumption that the narrow zone of localization could be treated as a line of discontinuity. Recently, Dilellio and Olmstead (1997) determined the evolution of the bandwidth by taking the shear band to be a boundary layer with nonzero thickness.

We are concerned with a systematic approximate analysis regarding the formation and evolution of the shear band based upon a linear thermal softening model. First, we obtain an approximation to the evolution of the plastic strain rate at the center and to the critical strain for the onset of severe localization in terms of the material parameters, the boundary velocity, and the initial perturbations after reducing the governing equations to a simple system of ordinary differential equation, which yields results similar to those given by Molinari and Clifton (1987) and Wright (1990). Secondly, we determine the structure of the shear band at the post-state through a slightly different procedure from that of Wright and Ockendon (1992). An approximate distribution of the plastic strain rate and the temperature is obtained, and furthermore, the evolution of the stress and temperature at the center of the shear band after the critical time is explicitly presented by the solution of an integral equation for the temperature. Finally, the strong transition stage of stress collapse is studied to explain the effect of the elastic unloading by introducing a nondimensional parameter in an approximate manner.

2 Development of Shear Band and Critical Strain

In this section, we analyze the development of a shear band in a thermoviscoplastic material from the onset of initial perturba-

[1] To whom all correspondence should be addressed. e-mail: sim@kaist.ac.kr.

Contributed by the Applied Mechanics Division of THE AMERICAN SOCIETY OF MECHANICAL ENGINEERS for publication in the ASME JOURNAL OF APPLIED MECHANICS.

Discussion on the paper should be addressed to the Technical Editor, Professor Lewis T. Wheeler, Department of Mechanical Engineering, University of Houston, Houston, TX 77204-4792, and will be accepted until four months after final publication of the paper itself in the ASME JOURNAL OF APPLIED MECHANICS.

Manuscript received by the ASME Applied Mechanics Division, July 17, 1998; final revision, Mar. 31, 1999. Associate Technical Editor: W. J. Drugan.

 Copyright © 1999 by ASME

Downloaded 04 May 2010 to 171.66.16.27. Redistribution subject to ASME license or copyright; see http://www.asme.org/terms/Terms_Use.cfm

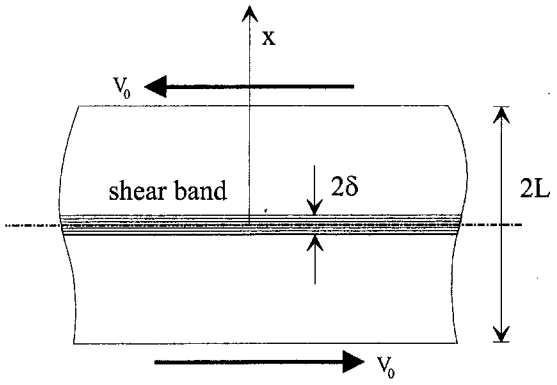


Fig. 1 Schematic of simple shearing, where 2δ is the band width

tions to a critical time, which is defined to be the time at which the maximum change of plastic strain rate occurs together with a rapid stress drop. Initial perturbations grow slowly with competition between softening and hardening, and the stress changes slowly as if there were no perturbations at all. Since strong nonlinearity exists in this stage, the exact solutions may not be easily obtained by analytical methods. We make some approximations to determine the evolution of the strain rate at the center before the critical time. Negligible contributions from heat conduction and the elastic properties (Batra, 1987; Molinari and Clifton, 1987; Glimm et al., 1996; Dilellio and Olmstead, 1997) make possible simplification of the governing equations. These approximations via the adiabatic energy equation and rigid-plastic material model give an ordinary differential equation with respect to the strain rate at the center. We analyze the case of no inertia and no strain hardening as a basic model for finding a susceptibility to the critical strain for the case of a constant velocity prescribed on the boundary as shown in Fig. 1.

The governing equations neglecting inertia are written as

$$\frac{\partial \tau}{\partial x} = 0 \text{ and } k\frac{\partial^2 \theta}{\partial x^2} + \kappa \tau \dot{\gamma}^p = \rho c \frac{\partial \theta}{\partial t} \qquad (1a,b)$$

where τ is the shear stress, θ is the temperature, $\dot{\gamma}^p$ is the plastic strain rate, and κ is the factor for converting plastic work into thermal energy. We identify the plastic strain rate $\dot{\gamma}^p$ with the strain rate $\dot{\gamma}$ under the assumption of rigid-plastic response before the critical time. We find from Eq. (1*a*) that the shear stress is only a function of time not of space. For simplicity, we shall restrict our attention to the flow rule with linear thermal softening and no strain hardening:

$$\tau = \tau_0 \left(\frac{f}{\dot{\gamma}_0}\right)^m (1 - \alpha\theta) \quad \text{or}$$

$$\theta(x, t) = \frac{1}{\alpha} - \frac{\dot{\gamma}_0^m}{\alpha \tau_0} \tau(t) f(x, t)^{-m} \qquad (2)$$

where α, τ_0, $\dot{\gamma}_0$, and m are material constants, and $f(x, t)$ is the strain rate.

In accordance with the flow rule (2) with small rate sensitivity m, which is common for most metals, the heat diffusion becomes a small fraction in the energy Eq. (1*b*) before the stress collapse, as mentioned before, because the strain rates at the center and at the boundary regions are not substantially different in this stage. Hence we neglect heat diffusion in the energy equation during this stage. It should be noted that heat diffusion in the energy equation might not be negligible for large rate sensitivity m and small nominal strain rate V_0/L due to a large temperature variation in position and sufficient time available for heat diffusion, respectively.

Applying the flow rule (2) to the energy Eq. (1*b*) at the center, neglecting heat diffusion, we obtain the following differential equation:

$$m\frac{\dot{f}}{f} - \frac{\dot{\tau}}{\tau} = \frac{\kappa \alpha \tau_0}{\rho c \dot{\gamma}_0^m} f^{1+m} \qquad (3)$$

where superscript dot means differentiation with respect to time. The stress evolution from a small initial perturbation is almost the same as the results obtained without initial perturbations (Wright and Walter, 1987). Thus, the stress term in Eq. (3) may be approximated from the homogeneous solution without initial perturbation:

$$\frac{\dot{\tau}}{\tau} = (-)\frac{\kappa \alpha \tau_0}{\rho c \dot{\gamma}_0^m} \left(\frac{V_0}{L}\right)^{1+m}. \qquad (4)$$

Approximation $f^{1+m} \approx (V_0/L)^m f$ in Eq. (3) for small rate sensitivity and substitution of Eq. (4) into (3) lead to

$$\dot{f} = \chi f\left(f - \frac{V_0}{L}\right) \text{ with } \chi = \frac{\kappa \alpha \tau_0}{\rho c m \dot{\gamma}_0^m}\left(\frac{V_0}{L}\right)^m. \qquad (5a,b)$$

This has the solution

$$f(\bar{\gamma}) = \frac{V_0}{L}\left(\frac{f_I}{f_I - (f_I - V_0/L)e^{\chi\bar{\gamma}}}\right) \qquad (6)$$

where $\bar{\gamma}$ is the nominal strain with reference to the configuration at the time of imposing a perturbation, i.e., $\bar{\gamma} = V_0(t - t_0)/L$ with t_0 being the imposing time, and f_I is the initial strain rate including the effect due to the initial perturbation. Note that the errors in Eq. (6) are unacceptably large after the critical strain is reached, because heat diffusion becomes a significant factor at this time in the energy equation. The critical nominal strain $\bar{\gamma}_c$ at which infinite strain rate is obtained at the center is now written as

$$\bar{\gamma}_c = \frac{1}{\chi} \ln\left[\frac{f_I}{f_I - V_0/L}\right]. \qquad (7)$$

We define the initial perturbation at the center with a parameter ε as

$$f_I = (1 + \varepsilon)\frac{V_0}{L}. \qquad (8)$$

Consequently, the evolution of the strain rate at the center and the critical strain are then recast in terms of the initial perturbation parameter ε:

$$f(\bar{\gamma}) = \frac{V_0}{L}\left(\frac{1+\varepsilon}{1 + \varepsilon - \varepsilon e^{\chi\bar{\gamma}}}\right) \text{ and } \bar{\gamma}_c = \frac{1}{\chi}\ln\left(1 + \frac{1}{\varepsilon}\right). \qquad (9a,b)$$

The above equation shows the inverse relationship between the critical nominal strain $\bar{\gamma}_c$ and the nondimensional parameter χ, and the logarithmic relation for the initial perturbation parameter ε and $\bar{\gamma}_c$. This nondimensional parameter χ defined in Eq. (5*b*) plays a key role at the time of severe strain localization. The point of critical nominal strain is reached earlier for a small rate sensitivity m, a large nominal strain rate V_0/L, a large coefficient of the thermal softening α, a large reference shear stress τ_0, and a low density ρ. The stabilizing and delaying effects of strain rate sensitivity have been also explained by Molinari and Clifton (1987) and Pan et al. (1983). The time of a sudden stress drop or stress collapse accompanying the onset of severe localization is known to be dependent on the size of the initial perturbations (Wright, 1990; Leroy and Chapuis, 1991), and its experimental verification has been performed by Duffy and Chi (1992). The logarithmic dependence on the initial perturbations has also been addressed by Molinari and Clifton (1987) and Wright (1990). Although the result presented by Molinari and Clifton (1987) for the velocity boundary condition is not a logarithmic function of the initial perturbations, it gives a relation similar to Eq. (9*b*) for small initial

Downloaded 04 May 2010 to 171.66.16.27. Redistribution subject to ASME license or copyright; see http://www.asme.org/terms/Terms_Use.cfm

perturbation. Moreover, we present the evolution of the strain rate in the explicit form Eq. (9*a*) after solving the simple Eq. (5*a*). According to the preceding adiabatic assumption, the nondimensionalized parameter χ does not include the effect of the thermal conductivity k. The indifference of the thermal conductivity to the critical strain was shown by Batra (1987) through numerical experiments. However, this may not be valid for the cases of small strain rate due to the increasing heat diffusion in the energy equation. Actually, the heat diffusion has the effect of delaying the critical time because the heat is spread to the outer region from the band and the softening is reduced. Therefore, the occurrence of the critical strain may be retarded for smaller nominal strain rates compared with the prediction by Eq. (9*b*). The verification of these relations for the critical strain will be presented with numerical experiments in Section 5.

There may be many kinds of initial perturbations which evolve into a severe localization, and we consider the possibility of an initial temperature perturbation. We examine how the initial temperature perturbation leads to the critical state. Since the stress remains nearly identical with the stress for an unperturbed response without thermal softening until it suddenly falls down at the critical strain, the flow rule can be initially approximated as

$$\tau = \tau_0 \left(\frac{V_0}{L\dot{\gamma}_0} \right)^m. \tag{10}$$

Denoting by θ_ε a perturbed temperature at the center, we can approximately obtain the relation between θ_ε and ε from Eqs. (2) and (10) as

$$1 + \varepsilon = \left(\frac{1}{1 - \alpha\theta_\varepsilon} \right)^{1/m} \approx 1 + \frac{\alpha\theta_\varepsilon}{m}. \tag{11}$$

The above approximation is valid when α is small, which is reasonable for most metals. Applying the above results to Eq. (9*b*), we may write the critical strain in terms of the temperature perturbation parameter θ_ε as

$$\bar{\gamma}_c \approx \frac{1}{\chi} \ln \left(1 + \frac{m}{\alpha\theta_\varepsilon} \right). \tag{12}$$

As a consequence, the logarithmic dependence of the critical strain $\bar{\gamma}_c$ upon the initial temperature perturbations is also explained from the above result.

3 Fully Developed State

The deformations after the stress collapse have a tendency to stabilize to a quasi-steady state under the velocity boundary condition (Wright, 1987; Leroy and Molinari, 1992), and approximate analyses may enlighten the structure of the shear band at this state. In the quasi-steady state, the rates of stress and temperature are small, and the inertia term may then be ignored in the equation of motion. The governing equations for the fully developed state are then written as

$$\frac{\partial \tau}{\partial x} = 0 \quad \text{and} \quad k\frac{\partial^2 \theta}{\partial x^2} + \kappa\tau\dot{\gamma}^p = 0. \tag{13a,b}$$

Contrary to the state before a critical time, the heat diffusion in the energy equation becomes significant for the fully developed state in that there is enough time for the heat generated inside the band to transfer to the region outside the band. The elastic constants do not affect the post behavior if these constants have sufficiently large values (Leroy and Molinari, 1992). We assume this, and we identify the plastic strain rate $\dot{\gamma}^p$ with the total strain rate $\dot{\gamma}$.

Our attention is focused only on the velocity boundary condition on both sides as shown in Fig. 1. Since the strain rate outside the band is almost zero at the post-state, integration of the strain rate inside the band may have the boundary velocity

$$\int_0^\delta \dot{\gamma} dx = V_0 \tag{14}$$

where δ is the half bandwidth. The procedures in our approaches for finding the quasi-steady solutions at the post-state are similar to those of Chen et al. (1989) and Leroy and Molinari (1992). Substituting the flow rule (2) into the energy Eq. (13*b*), we obtain the following equation:

$$\frac{mk}{\rho c}\left(\frac{f''}{f} - (1+m)\left(\frac{f'}{f} \right)^2 \right) + \frac{\kappa\alpha\tau_0}{\rho c \dot{\gamma}_0^m} f^{1+m} = 0. \tag{15}$$

At this point, we take 1 for $1 + m$ on account of weak strain rate sensitivity in metals. Making this approximation, we can obtain the corresponding solution, and a correction is made to this solution by substituting it into Eq. (15) at $x = 0$. Then we reach the following expression:

$$f = \frac{2f_{\max}}{1 + \cosh\sqrt{2B_p f_{\max}}x} \quad \text{with} \quad B_p = \frac{\kappa\alpha\tau_0}{mk\dot{\gamma}_0^m} f_{\max}^m. \tag{16a,b}$$

The velocity distribution $V(x)$ thus reduces to

$$V(x) = \sqrt{\frac{2f_{\max}}{B_p}} \tanh \sqrt{\frac{B_p f_{\max}}{2}}\, x. \tag{17}$$

Following Wright (1987), we define the bandwidth as

$$f(0) = Gf(\delta) \tag{18}$$

where G is a large positive constant, say $10 \sim 100$. Applying Eq. (18) to (16*a*), we find a relation between the band width and the maximum strain rate:

$$\delta = \frac{C}{\sqrt{2B_p f_{\max}}} \tag{19}$$

where $C = \cosh^{-1}(2G - 1)$. Now that we have the bandwidth, the velocity boundary condition (14) reduces to

$$\int_0^\delta f(x)dx = \sqrt{\frac{2f_{\max}}{B_p}} \sqrt{\frac{G-1}{G}} \approx \sqrt{\frac{2f_{\max}}{B_p}}. \tag{20}$$

Combining the results of Eqs. (19) and (20), we obtain the following:

$$\delta = \frac{C}{\sqrt{2B_p f_{\max}}} = \frac{C}{B_p V_0} = \frac{CV_0}{2f_{\max}} \quad \text{and}$$

$$f_{\max} = \frac{1}{2}B_p V_0^2 = \frac{C^2}{2B_p\delta^2} = \frac{CV_0}{2\delta} \tag{21a,b}$$

$$\text{with } B_p = \left(\frac{\kappa\alpha\tau_0}{mk\dot{\gamma}_0^m} \right)^{1/(1-m)} \left(\frac{V_0^2}{2} \right)^{m/(1-m)}. \tag{21c}$$

From these results, the characteristics of the shear band may be related to the material parameters and the boundary velocity. Note that the post behavior is not affected by the nature of the initial perturbations (Merzer, 1982; Wright and Walter, 1987; Wright, 1990). The bandwidth approximately has a linear relationship with $1/V_0$ and $1/\sqrt{f_{\max}}$, and the maximum plastic strain rate with V_0^2 and $1/\delta^2$ if the material parameters are fixed. Consequently, $f_{\max}\,\delta$ is proportional to the boundary velocity V_0 regardless of the material parameters. Such an inverse relation between the band width and the maximum strain rate was also reported by Wright and Ockendon (1992), Cherukuri and Shawki (1995) and Dilellio and Olmstead (1997). As the strain rate hardening exponent m becomes smaller, the bandwidth becomes narrower and the maximum strain rate higher, respectively. It is noted that the bandwidth and the maximum strain rate can be evaluated for the type of flow

Downloaded 04 May 2010 to 171.66.16.27. Redistribution subject to ASME license or copyright; see http://www.asme.org/terms/Terms_Use.cfm

rules presented here without resort to information concerning the stress and the temperature.

Substitution of the plastic strain rate (16*a*) into the energy Eq. (13*b*) leads to the temperature distribution

$$\theta(x) = \theta_{\max} - \frac{2\kappa\tau}{kB_p} \ln\left(\cosh\sqrt{\frac{B_p f_{\max}}{2}}x\right) = \theta_{\max} - \frac{2\kappa\tau}{kB_p} \ln\left(\cosh\frac{C}{2\delta}x\right) \tag{22}$$

where $\theta_{\max}$ is the temperature at the center. This distribution of temperature is not valid for $x \gg \delta$, because the plastic strain rate in Eq. (16*a*) is too small in that region. Our aim here is to obtain the maximum temperature $\theta_{\max}$ and the stress τ for finding the complete structure of the shear band at the post-state. From the flow rule (2), the temperature and the stress have the following relation at the center:

$$\tau = \tau_0\left(\frac{f_{\max}}{\dot\gamma_0}\right)^m (1 - \alpha\theta_{\max}). \tag{23}$$

The trivial solution is $\theta_{\max} = 1/\alpha$ and $\tau = 0$ for the post-state when $t \to \infty$. The stress after the stress collapse slowly decreases, and then the stress in general has a finite value some time after the critical time. The temperature distribution inside the band may be approximately obtained by assuming heat generation along the center line due to high concentration of the dissipation energy in a narrow band, because its thickness is very small compared with the boundary region adjacent to the shear band (Glimm et al., 1996). In order to construct the complete solution for the temperature distribution, we track the evolution of the stress and the temperature at the center after the critical time. Assuming that the shear band is a line source of constant heat generation $\kappa\tau V_0$, which is from the integration of the heat source $\kappa\tau\dot\gamma$ inside the band, we have the following:

$$\theta^*_{\max}(t^*) = \theta_c + \frac{\kappa V_0}{\sqrt{\rho c k \pi}} \int_0^{t^*} \frac{\tau(t_c + \zeta)}{\sqrt{t^* - \zeta}} d\zeta \tag{24}$$

where $t^* = t - t_c$ and $\theta_c = \theta^*_{\max}(0)$ is the center temperature at the critical time t_c. The expression (24) is the solution at $x = 0$ to the two-dimensional heat conduction problem wherein the heat flux of $\kappa\tau V_0$ per unit length is imposed at the left edge ($x = 0$) of a semi-infinite plate (Carslaw and Jaeger, 1959). The plastic strain rate at the center inside the band changes rapidly, just after the critical time, to the value at the post-state as shown in the numerical calculations (see Fig. 8). Therefore, we take the maximum plastic strain rate in Eq. (23) to be given by Eq. (21*b*) at the post-state. As a result, the evolution Eq. (24) for the maximum temperature can be written as

$$\theta^*_{\max}(t^*) = \theta_c + \frac{\kappa\tau_0 V_0}{\sqrt{\rho c k \pi}}\left(\frac{B_p V_0^2}{2\dot\gamma_0}\right)^m \int_0^{t^*} \frac{1 - \alpha\theta^*_{\max}(\zeta)}{\sqrt{t^* - \zeta}} d\zeta \tag{25}$$

which is a Volterra integral equation. The solution to this integral equation can be obtained by taking the Laplace-transform and applying the transform formula of the convolution integral. The solution is

$$\theta^*_{\max}(t^*) = \frac{1}{\alpha}[1 - (1 - \alpha\theta_c)e^{\alpha^2 Z^2 \pi t^*} \operatorname{erfc}(\alpha Z\sqrt{\pi t^*})] \text{ with}$$

$$Z = \frac{\kappa\tau_0 V_0}{\sqrt{\rho c k \pi}}\left(\frac{B_p V_0^2}{2\dot\gamma_0}\right)^m \tag{26a,b}$$

where $\operatorname{erfc}(\cdot)$ is the complementary error function. If the temperature θ_c at the critical time is given, the evolution of the temperature at the center and the stress can be evaluated from Eqs. (26) and (23). The assumptions made in the approximate treatment concerning the temperature at the center after the critical time will be verified numerically in the next section.

4 Stress Collapse

As previously mentioned, inhomogeneous deformations, growing slowly in the first stage, are abruptly localized at a critical time, which accompanies the shooting up of the plastic strain rate inside the band and the rapid falling down of stress. During this unloading process, the plastic strain rate outside the band becomes almost zero, and the elastic energy is abruptly released due to the strong stress drop. The deformations inside and outside the band undergo a softening process and an elastic unloading process, respectively. The aim of this part is to describe the deformation behavior during stress collapse.

On the basis of the aforementioned observation, the stresses inside and outside the band during stress collapse, neglecting inertia, are given by the following relations:

$$\dot\tau = \mu(\dot\gamma - \dot\gamma^p) \text{ for } |x| < \delta \quad \text{and} \quad \dot\tau = \mu\dot\gamma \text{ for } |x| > \delta. \tag{27a,b}$$

From the velocity boundary conditions on both ends, the compatibility condition is written as

$$\int_0^\delta \dot\gamma dx + \int_\delta^L \dot\gamma dx = V_0. \tag{28}$$

Substituting Eq. (27*b*) into (28) and taking into account Eq. (27*a*), we obtain

$$\int_0^\delta \dot\gamma^p dx = V_0 - L\frac{\dot\tau}{\mu}. \tag{29}$$

The last term on the right side of Eq. (29) represents the rate of elastic unloading energy released over the entire domain when both sides are multiplied by the stress, and this energy contributes to the shooting up of the plastic strain rate inside the band. Accordingly, the plastic strain rate inside the band may overshoot above the value at the post state when the rate of elastic unloading energy release is high. On the contrary, a low rate of elastic unloading energy release may lead to a weak overshooting of the plastic strain rate and a smooth transition to the post-state from the critical point. Here we define a nondimensional parameter ξ to characterize the stability of the stress collapse.

$$\xi = (-)\frac{\tau L\dot\tau/\mu}{\int_0^\delta \tau\dot\gamma^p dx} \approx (-)\frac{\kappa\tau L\dot\tau/\mu}{\int_0^\delta \rho c\dot\theta dx}. \tag{30}$$

The approximation in the above equation is valid in the early stages of the stress collapse due to the lack of sufficient time for heat diffusion in the energy equation. Since the critical time, corresponding to the most rapid change of plastic strain rate inside the band, takes place in this stage, the approximation in Eq. (30) may be valid for explaining the behavior at the critical time. Note that at the critical time the plastic strain rate abruptly increases and the stress suddenly drops, so that the deformation path undergoes a drastic change. Furthermore, if the nondimensional parameter ξ is greater than one, the stress collapse becomes unstable in that the boundary input power becomes negative and the plastic strain rate goes up to an extremely large value while the stress undergoes an abrupt drop. Note that this is closely related to a low viscosity of metals: that is, metals behave like an invicid material due to their very small rate sensitivity "*m*." Kim and Im (1999) introduced the so-called *energy-balance number* in terms of the material parameters and the boundary velocity to predict this instability behavior

Downloaded 04 May 2010 to 171.66.16.27. Redistribution subject to ASME license or copyright; see http://www.asme.org/terms/Terms_Use.cfm

of the stress collapse. This number is directly related to the nondimensional parameter ξ which indicates the ratio of the portion converted into heat of the unloading elastic energy released relative to the heat absorption capacity of the material inside the band. From another viewpoint, we define the elastic boundary velocity to be $V_0^e = L\,\dot{\tau}/\mu$, and we introduce the following nondimensional parameter:

$$\eta = (\ -\ )\frac{V_0^e}{V_0}. \tag{31}$$

For $\eta \ll 1$ the nondimensional parameter ξ is also small when the denominator of (30) remains unchanged, while for $\eta \gg 1$ the instability of the stress collapse, occuring when $\xi > 1$, may be encountered during the stress collapse. In this section, we examine the deformation behavior of the stress collapse depending upon the nondimensional parameter η.

From the energy Eq. (1*b*) and the flow rule (2), we can approximate the governing differential equation for a small rate sensitivity:

$$m\frac{\dot{f}}{f} - \frac{\dot{\tau}}{\tau} = \frac{mk}{\rho c}\left(\frac{f''}{f} - \left(\frac{f'}{f}\right)^2\right) + \frac{\kappa\alpha\tau_0}{\rho c\dot{\gamma}_0^m}\left(\frac{V_0}{L}\right)^m f. \tag{32}$$

In the above equation, we make the approximations $1 + m \approx 1$ and $f^{1+m} \approx (V_0/L)^m f$, which is a good approximation before the post-state. Note that heat diffusion becomes a leading term in the energy equation only at the last stage of the stress collapse. To find an approximate solution to Eq. (32), we assume the solution form to be

$$f(x,\ t) = \frac{2f_{\max}(t)}{1 + \cosh\sqrt{2B_c(t)f_{\max}(t)}x} \tag{33}$$

where $f_{\max}(t)$ is the plastic strain rate at the center, and

$$B_c(t) = (1 - w(t))\bar{B} \quad \text{with} \quad \bar{B} = \frac{\kappa\alpha\tau_0}{mk\dot{\gamma}_0^m}\left(\frac{V_0}{L}\right)^m. \tag{34a,b}$$

In the above equations, the definition of $\bar{B}$ is similar to Eq. (16*b*), and $w(t)$ is an unknown function that decreases monotonically from a value a little less than one to a smaller value. Decreasing $w(t)$ indicates that the plastic deformation undergoes an abrupt localization leading to the narrowing process of the shear band. Ultimately, Eq. (33) represents an approximate solution for the fully developed state when $w(t)$ approaches zero. This solution form may produce errors for the distribution of the plastic strain during the stress collapse, but the evolution characteristic of the plastic strain rate at the center may be traced by introducing appropriate $w(t)$. In our analysis, we do not try to determine $w(t)$ during stress collapse, because the main concern is to describe the typical deformation behaviors, not to find the solution. Using this approximation (33), Eq. (29) can be written as

$$\sqrt{\frac{2f_{\max}}{B_c}} = V_0 - V_0^e \tag{35}$$

where the integration of $\dot{\gamma}^p$ in Eq. (29) has been given by Eq. (20). Applying Eqs. (33) and (35) to the energy Eq. (32), the differential equation at the center becomes

$$\dot{f}_{\max} = \frac{k}{\rho c}(\bar{B} - B_c)f_{\max}^2 - \frac{\mu}{mL\tau}\sqrt{\frac{2}{B_c}}f_{\max}^{3/2} + \frac{\mu V_0}{mL\tau}f_{\max}. \tag{36}$$

The bandwidth with the same definition as given in Eq. (18) is expressed as

$$\delta = \frac{C}{\sqrt{2B_c f_{\max}}} \tag{37}$$

where C is defined in Eq. (19). The bandwidth may be abruptly narrowed by rapid increase of the parameter $B_c = B_c(t)$ and the plastic strain rate $f_{\max}$ at the center.

If the stress drop rate is not severe and the shear modulus is large, which corresponds to $\eta \ll 1$, the elastic boundary velocity V_0^e in Eq. (35) may be negligible compared with the boundary velocity. Considering that the stress drop tends to get smooth as the shear modulus increases, we may ignore the elastic energy released during the stress drop for a large shear modulus. For this case, the governing differential Eq. (36) reduces to

$$\dot{f}_{\max} = \left(\frac{k\bar{B}}{\rho c} - \frac{2k}{\rho c V_0^2}\ f_{\max}\right)f_{\max}^2. \tag{38}$$

The solution to the differential Eq. (38) has the feature that $f_{\max}$ monotonically approaches the maximum plastic strain rate at the post-state without any overshooting phenomenon. When the rate of elastic unloading energy release is small, the plastic strain rate may not overshoot above the value at the post-state. As a consequence, the bandwidth (37) during stress collapse may not be smaller for such cases than the value at the post-state because $B_c < B_p$ and $f_{\max} < (f_{\max})_p$, where B_p is given in Eq. (21*c*) and $(f_{\max})_p$ is the maximum plastic strain rate at the post-state.

When the unloading rate of the elastic energy is large, corresponding to $\eta \gg 1$, the elastic velocity at the boundary becomes a dominant term in Eq. (35). For this case, the magnitude of the boundary velocity V_0 in Eq. (35) may be much smaller than the elastic velocity V_0^e at the boundary. For this case, the governing differential Eq. (36) becomes

$$\dot{f}_{\max} = f_{\max}\left(\frac{kw(t)\bar{B}}{\rho c}\ f_{\max} + \frac{\mu V_0^e}{mL\tau}\right) \tag{39}$$

where $w(t)$ has been introduced in Eq. (34*a*). The maximum plastic strain rate from Eq. (39), which is Bernoulli's equation, may become infinite in a short time during the stress collapse, and the plastic strain rate at the center may generally overshoot up to a very large value beyond the value at the post state. Another important result from this response is that the bandwidth (37) may decrease below the value of the post state. That is, the bandwidth undergoes narrowing and then widening processes during the stress collapse when a large amount of elastic unloading energy is released during the stress collapse. The widening of the shear bandwidth is affected by the balance of heat generation and heat diffusion. The band narrowing mechanism was also mentioned by Dilellio and Olmstead (1997), who treated the shear band as a thin boundary layer.

The aforementioned behaviors describe a basic feature of the stress collapse, but the propagation of an unloading wave originating from the center has not been considered. If the inertia term is included in the governing equations, the deformation behavior during the stress collapse may change due to unloading wave propagation: it will result in a stabilizing effect and lead to reduction of the strain rate.

5 Numerical Examples

In this section, a numerical solution via the finite element method is obtained for the one-dimensional simple shear problem in a thermoviscoplastic material to confirm the analytical results presented in the previous sections. Half of the model height L is $3.47 \times 10^{-3}\ m$, and the reference material parameters are listed in Table 1 (Walter, 1992).

The dimensionless variables denoted by a superposed $\wedge$ are introduced in order to exclude dimensional effects in the numerical calculation. The dimensionless quantities are defined by

$$\hat{\rho} = \rho L^2\dot{\bar{\gamma}}^2/\tau_0, \quad \hat{k} = k/\rho c L^2\dot{\bar{\gamma}}, \quad \hat{\mu} = \mu/\tau_0, \quad \dot{\bar{\gamma}}_0 = \dot{\gamma}_0/\dot{\bar{\gamma}},$$

$$\hat{\alpha} = \alpha\tau_0/\rho c, \quad \hat{x} = x/L, \quad \hat{t} = t\dot{\bar{\gamma}}, \quad \hat{V} = V/L\dot{\bar{\gamma}},$$

Downloaded 04 May 2010 to 171.66.16.27. Redistribution subject to ASME license or copyright; see http://www.asme.org/terms/Terms_Use.cfm

Table 1 Reference material properties

Property	Symbol	Reference value
Density	ρ	7860.0 kg/m^3
Specific heat	c	473.0 J/kg K
Thermal conductivity	k	49.2 W/m K
Dissipation factor	κ	1.0
Reference shear stress	τ_0	6.02×10^8 N/m^2
Strain rate hardening exponent	m	0.0251
Reference strain rate	$\dot{\gamma}_0$	1.0×10^{-4} s^{-1}
Softening coefficient	α	6.43×10^{-4} K^{-1}

$$\hat{\tau} = \tau/\tau_0, \quad \hat{\theta} = \theta\rho c/\tau_0, \quad \hat{\dot{\gamma}}^p = \dot{\gamma}^p/\bar{\dot{\gamma}} \tag{40}$$

where $\bar{\dot{\gamma}}$ is the nominal strain rate V_0/L with V_0 being a velocity prescribed at the boundary. All of the numerical calculations are carried out with these nondimensional variables, but all results are presented with dimensional variables.

The boundary is prescribed to be thermally insulated and initial perturbations are taken in the following form:

$$\hat{\theta}(\hat{x}, 0) = \hat{\theta}_\varepsilon(1 - \hat{x}^2)^9 e^{-5\hat{x}^2}. \tag{41}$$

This form of initial perturbation was used by Wright and Walter (1987). To obtain a highly refined mesh near the center region wherein localization occurs, we construct the finite element mesh according to the following equation:

$$x_i = \left(\frac{i-1}{N}\right)^r L, \; 1 \le i \le N+1 \tag{42}$$

where N is the total number of elements and r is the refinement index. In our calculation, N is 50, and r is 5.0, which is found to be sufficient to capture half the shear band thickness at the post-state.

The full simulation up to the post state requires a robust computational algorithm, because numerical calculation becomes unstable during the stress collapse. We use an implicit finite element method and an iterative Euler backward method (Lush et al., 1989) for integrating the state variables. Since usual iterative Euler backward methods without a proper initial guess become easily unstable at the critical time, the initial guess for an iterative Euler backward method is calculated from the forward gradient method (Peirce et al., 1984).

5.1 The Critical Strain. The scaling laws for the critical strain presented here are examined via numerical analyses. The inertia term is ignored in the calculations. The evolution of the strain rate under the nominal strain rate $V_0/L = 1500$ s^{-1} and the initial perturbation parameter $\varepsilon = 0.2$, which corresponds to $\alpha\theta_\varepsilon = 5.02 \times 10^{-3}$, is plotted in Fig. 2. We see that the evolution of the strain rate from the analytical expression (9*a*) shows a trend similar to the numerical result. The strain rate increases slowly before the critical strain, but rapidly shoots up as the nominal strain $\bar{\gamma}$ approaches the critical strain $\bar{\gamma}_c$. The inverse relation (9*b*) between the critical strain $\bar{\gamma}_c$ and the nondimensional scaling parameter χ defined in Equation (5*b*) is shown in Fig. 3. For variations in the density ρ, the specific heat c, the strain rate hardening exponent m, the softening coefficient α and the reference shear stress τ_0, the proposed relation between the critical strain and the nondimensional parameter χ shows excellent agreement with the numerical results. In addition, the critical strain versus the nominal strain rate is plotted in Fig. 4. The trends of the analytical and numerical results are in good agreement except for low nominal strain rates, wherein heat diffusion is not negligible in the energy equation. Next, we examine the logarithmic relation (9*b*) between the critical strain $\bar{\gamma}_c$ and the perturbation parameter ε. Figure 5 shows how well the relation between the critical strain $\bar{\gamma}_c$ and $\ln(1 + 1/\varepsilon)$ matches the numerical results. As shown in this figure, the parameter $\ln(1 + 1/\varepsilon)$ is a good indicator for the critical strain. As previously mentioned, our numerical computation shows

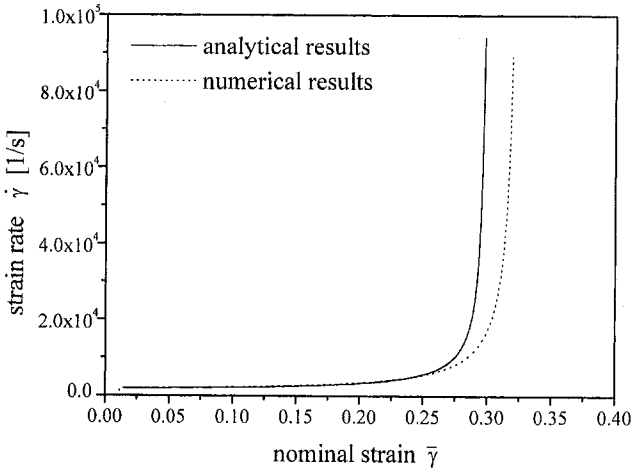


Fig. 2 Evolution of strain rate from analytical and numerical analyses. Nominal strain rate is 1500 s^{-1} and the initial perturbation parameter ε is 0.2.

that the thermal conductivity k has a negligible effect on the change of the critical strain if this value is not too large, and this provides the justification for the assumption of negligible heat diffusion in the energy equation before the critical strain.

5.2 Post Behavior. All numerical calculations for the analysis of the post-state are made for the nominal strain rate of $\bar{\dot{\gamma}} = 1500$ s^{-1}. The distribution of the plastic strain rate when the nominal strain $\bar{\gamma}$ reaches 0.59, which is a fully developed state, is shown in Fig. 6. In this figure, the maximum plastic strain rate and the bandwidth, where G in Eq. (18) has been taken to be 10.0, are about 8.2×10^6 s^{-1} and 1.2×10^{-6} m, respectively. The distribution of the plastic strain rate (16*a*) almost coincides with the numerical results. Consequently, the maximum plastic strain rate (21*a*) and the bandwidth (21*b*) will predict very well the structure of the shear band at the post-state. Another concern is focused on the distribution of the temperature near the band at the post-state, which is shown in Fig. 6. The distribution of the temperature obtained from the numerical solution coincides well with the results from the approximate analytical solution (22) near the band.

The evolutions of the center temperature and the stress from the numerical results and from the analytical results of Eq. (26*a*) are shown in Fig. 7. The initial temperature in calculating Eq. (26*a*) is taken from the results near the critical strain in the numerical

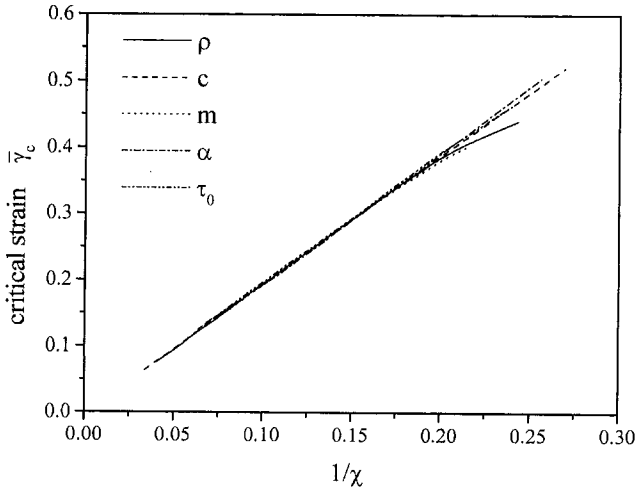


Fig. 3 Critical strain as a function of χ with variation of material parameters. Nominal strain rate is 1500 s^{-1} and the initial perturbation parameter ε is 0.2.

Downloaded 04 May 2010 to 171.66.16.27. Redistribution subject to ASME license or copyright; see http://www.asme.org/terms/Terms_Use.cfm

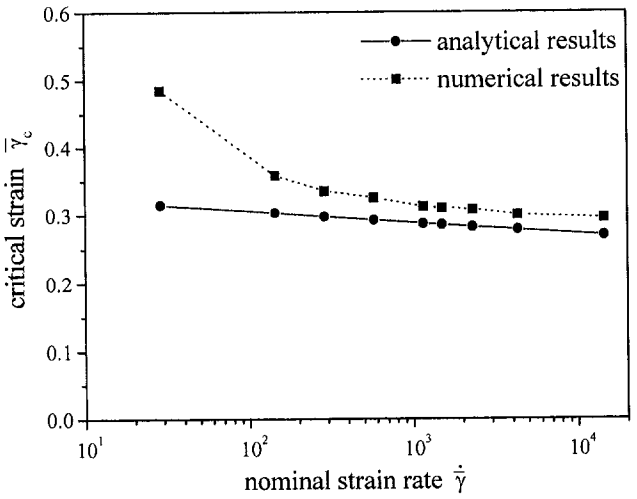


Fig. 4 Critical strain as a function of nominal strain rate (the initial perturbation parameter ε is 0.2)

calculation. From these figures, we verify the analytic expression for the evolution of the temperature and the stress at the center, and this agreement justifies our prediction based upon Eq. (26*a*).

5.3 Stress Collapse. In Section 4, we explain the effect of the elastic unloading energy release on the deformation behavior at the critical strain. Figure 8 shows the evolution of the plastic strain

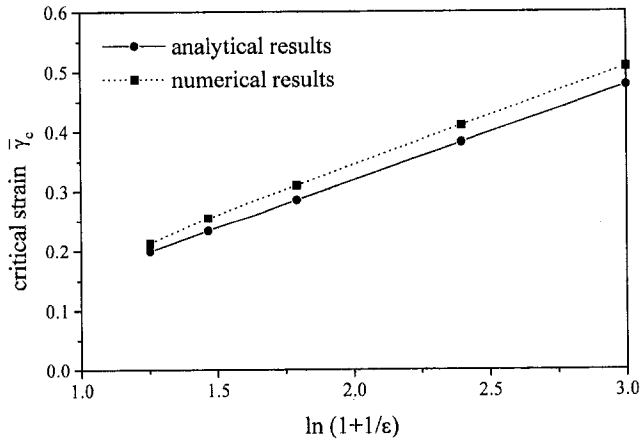


Fig. 5 Critical strain as a function of the initial perturbation parameter ε

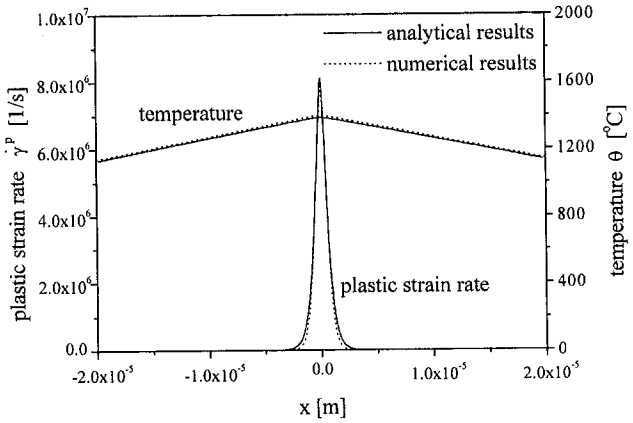


Fig. 6 Distribution of plastic strain rate and temperature at the post-localization state for nominal strain $\bar{\gamma}$ = 0.59 and nominal strain rate $\dot{\bar{\gamma}}$ = 1500 s^{-1}

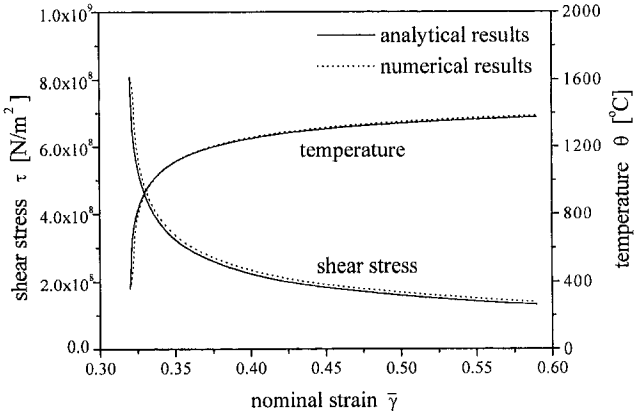


Fig. 7 Evolution of temperature at the center and stress after the critical strain is attained. Nominal strain rate $\dot{\bar{\gamma}}$ is 1500 s^{-1}.

rate for two shear moduli $\mu = 3.82 \times 10^{11}$ N/m^2 and $\mu = 8 \times 10^{11}$ N/m^2. The plastic strain rate overshoots the value at the post-state for a small shear modulus, but there is no overshoot for a large shear modulus. The overshoot of the plastic strain rate is due to the concentration into the shear band of the elastic energy released throughout the domain. This overshoot accompanies the drastic stress drop or stress collapse.

We now examine the evolution of the bandwidth during the stress collapse. As shown in Fig. 9, the bandwidth undergoes narrowing below the width at the post-state if the shear modulus is small. This narrowing mechanism originates from the lack of sufficient time for diffusion of heat generated from the overshoot of the plastic strain rate. As the shear modulus decreases, the plastic strain rate becomes very large, and the bandwidth decreases to an extremely small value.

6 Conclusions

The formation and development of a shear band has been systematically examined through some approximate analyses based upon the model of one-dimensional simple shear with a linear thermal softening. The three stages analyzed in this paper include the slow growth stage of inhomogeneous deformation, the stage of stress collapse, and the fully developed stage of post-localization. Approximate analytical relations characterizing the deformation behavior for the three stages have been obtained, and subsequently confirmed via comparison to numerical solutions.

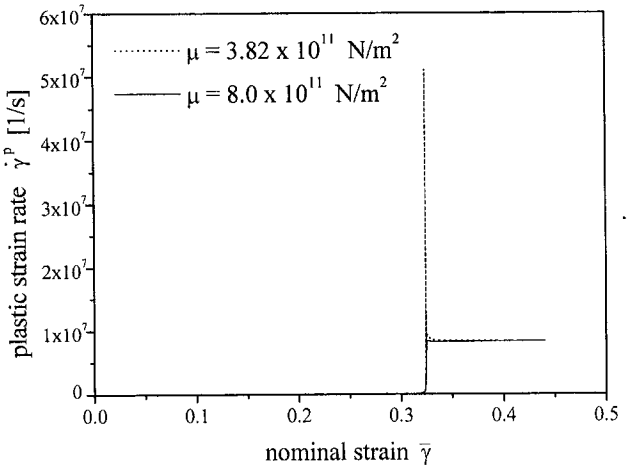


Fig. 8 Evolution of plastic strain rate in the first element for two shear moduli (nominal strain rate $\dot{\bar{\gamma}}$ is 1500 s^{-1}). No overshooting occurs for 8.0 × 10^{11} N/m^2.

Downloaded 04 May 2010 to 171.66.16.27. Redistribution subject to ASME license or copyright; see http://www.asme.org/terms/Terms_Use.cfm

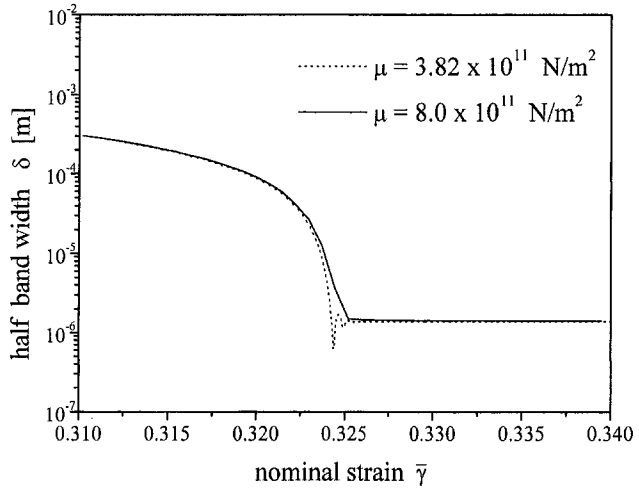


Fig. 9 Evolution of bandwidth for two shear moduli. Nominal strain rate $\dot{\bar{\gamma}}$ is 1500 s^{-1}.

We first derived some relations concerning the critical strain by solving a simple ordinary differential equation under the assumption that the heat diffusion before the critical time is negligible and the stress evolution coincides with the homogeneous solution. The nondimensional parameter χ for the critical strain proposed in this paper shows excellent agreement with the numerical results, and a useful prediction for the critical strain could be made. In addition, the logarithmic relation for the initial perturbations is explained by introducing scaling parameters.

The post-localization behavior is expressed in terms of the material parameters and the boundary velocity. In particular, the evolution of the center temperature and the stress after the critical strain can be explicitly obtained on the basis of a line heat source at the center. We have seen that the analytical results for the post-localization behavior are shown to be in a very good agreement with the numerical results.

Finally, we have explained that the elastic unloading and the heat absorption capacity of a material have significant effects on the behaviors of the stress drop and the plastic strain rate during stress collapse. If the rate of the unloading elastic energy released is greater than the heat absorption capacity of a material inside the shear band, the instability of the stress collapse may occur and the maximum plastic strain rate at the band center may go to an extremely large value. However, the inertia term leads to a stabilizing effect during the stress collapse.

Acknowledgments

This study has been supported by KOSEF (The Korea Science and Engineering Foundation) under Grant 961-1004-034-2. This support is gratefully acknowledged.

References

Bai, Y. L., 1982, "Thermo-plastic instability in simple shear," *J. Mech. Phys. Solids,* Vol. 30, pp. 195–207.

Batra, R. C., 1987, "Effect of material parameters on the initiation and growth of adiabatic shear bands," *Int. J. Solids and Struct.,* Vol. 23, pp. 1435–1446.

Burn, T. J., and Truncano, T. G., 1982, "Instability in simple shear deformations of strain-softening materials," *Mech. Mater.,* Vol. 1, pp. 313–324.

Carslaw, H. S., and Jaeger, J. C., 1959, *Conduction of Heat in Solids,* Oxford University Press, Oxford, UK.

Chen, H. T., Douglas, A. S., and Malek-Madani, R., 1989, "An asymptotic stability condition for inhomogeneous simple shear," *Quarterly Appl. Math.,* Vol. 47, pp. 247–262.

Cherukuri, H. P., and Shawki, T. G., 1995, "An energy-based localization theory I. Basic framework," *Int. J. Plasticity,* Vol. 11, pp. 15–40.

Clifton, R. J., 1980, "Adiabatic shear banding," *Materials Response to Ultra-High Loading Rates,* National Material Advisory Board (NRC) NMAB-356, pp. 129–142.

Dilellio, J. A., and Olmstead, W. E., 1997, "Temporal evolution of shear band thickness," *J. Mech. Phys. Solids,* Vol. 45, pp. 345–359.

Dodd, B., and Bai, Y., 1985, "Width of adiabatic shear bands," *Mater. Sci. Tech.,* Vol. 1, pp. 38–40.

Duffy, J., and Chi, Y. C., 1992, "On the measurement of local strain and temperature during the formation of adiabatic shear bands," *Mater. Sci. Eng.,* Vol. A157, pp. 195–210.

Fressengeas, C., and Molinari, A., 1987, "Instability and localization of plastic flow in shear at high strain rates," *J. Mech. Phys. Solids,* Vol. 35, pp. 185–211.

Glimm, J. G., Plohr, B. J., and Sharp, D. H., 1996, "Tracking of shear band I. The one-dimensional case," *Mech. Mater.,* Vol. 24, pp. 31–41.

Hartley, K. A., Duffy, J., and Hawley, R. H., 1987, "Measurement of the temperature profile during shear band formation in steels deforming at high strain rate," *J. Mech. Phys. Solids,* Vol. 35, pp. 283–301.

Kim, H.-G., and Im, S., 1999, "Stress collapse for an adiabatic shear band in a thermoviscoplastic material," manuscript in preparation.

Leroy, Y. M., and Chapuis, O., 1991, "Localization in strain-rate-dependent solids," *Comp. Methods Appl. Mech. Engrg.,* Vol. 90, pp. 969–986.

Leroy, Y. M., and Molinari, A., 1992, "Stability steady states in shear zones," *J. Mech. Phys. Solids,* Vol. 40, pp. 181–212.

Lush, A. M., Weber, G., and Anand, L., 1989, "An implicit time-integration procedure for a set of internal variable constitutive equations for isotropic elastoplasticity," *Int. J. Plasticity,* Vol. 5, pp. 521–549.

Marchand, A., and Duffy, J., 1988, "An experimental study of the formation process of adiabatic shear bands in a structural steel," *J. Mech. Phys. Solids,* Vol. 36, pp. 251–283.

Merzer, A. M., 1982, "Modelling of adiabatic shear band development from small imperfections," *J. Mech. Phys. Solids,* Vol. 30, pp. 323–338.

Molinari, A., and Clifton, R. J., 1987, "Analytical Characterization of Shear Localization in Thermoviscoplastic Materials," ASME JOURNAL OF APPLIED MECHANICS, VOL. 54, PP. 806–812.

Olmstead, W. E., Nemat-Nasser, J., and Ni, L., 1994, "Shear bands as surfaces of discontinuity," *J. Mech. Phys. Solids,* Vol. 42, pp. 697–709.

Pan, J., Saje, M., and Needleman, A., 1983, "Localization of deformation in rate sensitive porous plastic solids," *Int. J. Fracture,* Vol. 21, pp. 262–278.

Peirce, D., Shih, C. F., and Needleman, A., 1984, "A tangent modulus method for rate dependent solids," *Cmptut. & Struct.,* Vol. 18, pp. 875–887.

Shawki, T. G., and Clifton, R. J., 1989, "Shear band formation in thermal viscoplastic materials," *Mech. Mater.,* Vol. 8, pp. 13–43.

Walter, J. W., 1992, "Numerical experiments on adiabatic shear band formation in one dimension," *Int. J. Plasticity,* Vol. 8, pp. 657–693.

Wright, T. W., 1987, "Steady shearing in a viscoplastic solid," *J. Mech. Phys. Solids,* Vol. 35, pp. 269–282.

Wright, T. W., and Walter, J. W., 1987, "On stress collapse in adiabatic shear bands," *J. Mech. Phys. Solids,* Vol. 35, pp. 701–720.

Wright, T. W., 1990, "Approximate analysis for the formation of adiabatic shear bands," *J. Mech. Phys. Solids,* Vol. 38, pp. 515–530.

Wright, T. W., and Ockendon, H., 1992, "A model for fully formed shear bands," *J. Mech. Phys. Solids,* Vol. 40, pp. 1217–1226.

Downloaded 04 May 2010 to 171.66.16.27. Redistribution subject to ASME license or copyright; see http://www.asme.org/terms/Terms_Use.cfm

A Discrete Model of an Extensible String in Three-Dimensional Space

K. Nishinari[1]
Department of Mechanical Engineering,
Faculty of Engineering,
Yamagata University,
Yonezawa, Yamagata 992, Japan

In this paper, a discrete model of an extensible string in three-dimensional space is presented. The model contains the bending and twisting of a string, and becomes the special Cosserat string in the continuous limit. We also present a new method of analyzing a string in space by the soliton theory, which can reduce the basic equations to a simpler tractable form. Some exact solutions are obtained by the soliton theory. The discrete basic equations are also shown to be suitable for numerical simulations of string dynamics.

1 Introduction

Research on the dynamics of one-dimensional objects, such as elastic strings, is important for both engineering and science. In engineering systems, elastic strings are used as cables and belts in many mechanical devices and studied in detail (Gerbert, 1981; Jiang, 1995). The dynamics of a tether in satellite systems has recently been studied extensively (Misra and Modi, 1992). In many branches of science there are various objects that can be considered as one-dimensional media, such as polymers (Doi and Edwards, 1986), and a vortex filament in fluid dynamics (Fukumoto, 1997). There may be common issues among these one-dimensional objects and results of one field will be helpful to other branches.

In analyzing the behavior of strings it is effective to treat the string as a discrete system, such as a combination of beads and springs. We can treat various one-dimensional objects generally by discrete modeling and it is also suitable for computer simulations. In an earlier paper by the present author (Nishinari, 1998), a model of an extensible string in a plane was proposed and loop solitons were studied in detail by both the discrete soliton theory and numerical simulations. In this paper we propose a discrete model of an extensible string in three-dimensional space by extending the previous results, which contains the bending and twisting of a string. Moreover, it is shown that the new model produces the special Cosserat string (Antman, 1995) in the continuous limit.

We also point out that the soliton theory will be quite effective when we study one-dimensional media. The reason is that the Frenet-Serret formula can be considered as the Lax pair in the soliton theory (Nakayama et al., 1992). Goldstein and Petrich (1991) have shown that the dynamics of a curve in a plane is governed geometrically by the modified Korteveg-de Vries (mKdV) equation in a particular case. Doliwa and Santini (1994) extended the theory to a discrete version and they apply their theory to the dynamics of a discrete curve. A mathematical curve, however, is different from a physical string, which has finite cross section. Thus in the previous papers (Nishinari, 1997, 1998) we have proposed a way of applying these soliton approaches to analyze dynamics of physically continuous and discrete strings in a plane. We use this method in this paper and consider dynamics of a string in three-dimensional space. The merit of using soliton theory is that it provides a systematic way to obtaining exact solutions. Some exact solutions are presented by using the complex mKdV (CmKdV) equation, which is integrable by the soliton theory (Nakayama et al., 1992). It is noted that our method is also suitable for computer calculations. There are many numerical methods to simulate elastic strings, such as the finite element method (Grigolyuk and Shalashilin, 1991). Adding to these methods we obtain a new scheme by using the discrete modeling of a string and the discrete soliton theory.

This paper is organized as follows. Basic equations for a continuous string and analysis by the soliton approach are given in Section 2. We discretize the results of Section 2 in Section 3 by proposing a discrete modeling of a string. A way of obtaining exact solutions by using the soliton theory are presented in the Section 4. Results of numerical simulations are given in Section 5 and concluding discussions are given in Section 6.

2 An Extensible Continuous String and the Soliton Theory

2.1 Dynamics of a String in Space. Let us consider an extensible string in the three-dimensional space. The axis of the string is parametrized by σ, which represents the unstretched length of the string. It forms a space curve with position $\mathbf{r} = \mathbf{r}(\sigma, t)$. The unit tangent vector $\mathbf{t}$ for the axial curve is given by the relation

$$\frac{\partial \mathbf{r}}{\partial \sigma} = \sqrt{g}\mathbf{t}, \tag{1}$$

where g is a metric which represents the stretch of the axis defined by

$$g = \frac{\partial \mathbf{r}}{\partial \sigma} \cdot \frac{\partial \mathbf{r}}{\partial \sigma}. \tag{2}$$

Using g, the arclength s of the string is given by

$$s = \int_0^\sigma \sqrt{g(\sigma', t)}\, d\sigma'. \tag{3}$$

At each point of the curve, one can define a local orthonormal basis $\mathbf{t}$, $\mathbf{n}$, and $\mathbf{b}$ by

$$\frac{\partial}{\partial s}\begin{pmatrix}\mathbf{t}\\ \mathbf{n}\\ \mathbf{b}\end{pmatrix} = \begin{pmatrix}0 & \kappa & -\eta\\ -\kappa & 0 & \tau\\ \eta & -\tau & 0\end{pmatrix}\begin{pmatrix}\mathbf{t}\\ \mathbf{n}\\ \mathbf{b}\end{pmatrix}, \tag{4}$$

where η and κ are called components of curvature and τ the twist.

The conservation of linear and angular momentum leads to

---

[1] Presently at the Department of Applied Mathematics and Informatics, Ryukoku University, Seta, Ohtsu 520-2194, Japan. e-mail: knishi@rins.ryukoku.ac.jp.

Contributed by the Applied Mechanics Division of THE AMERICAN SOCIETY OF MECHANICAL ENGINEERS for publication in the ASME JOURNAL OF APPLIED MECHANICS.
Discussion on the paper should be addressed to the Technical Editor, Professor Lewis T. Wheeler, Department of Mechanical Engineering, University of Houston, Houston, TX 77204-4792, and will be accepted until four months after final publication of the paper itself in the ASME JOURNAL OF APPLIED MECHANICS.
Manuscript received by the ASME Applied Mechanics Division, May 18, 1998; final revision, Jan. 27, 1999. Associate Technical Editor: R. C. Benson.

 Copyright © 1999 by ASME

Downloaded 04 May 2010 to 171.66.16.27. Redistribution subject to ASME license or copyright; see http://www.asme.org/terms/Terms_Use.cfm

equations for the force and the moment which take the form (Coleman and Dill, 1992)

$$\rho Z \frac{d^2\mathbf{r}}{dt^2} = \frac{\partial \mathbf{S}}{\partial \sigma} \tag{5}$$

$$\rho I\left(\mathbf{n} \times \frac{d^2\mathbf{n}}{dt^2} + \mathbf{b} \times \frac{d^2\mathbf{b}}{dt^2}\right) = \frac{\partial \mathbf{M}}{\partial \sigma} + \frac{\partial \mathbf{r}}{\partial \sigma} \times \mathbf{S}, \tag{6}$$

where $\mathbf{S}$ and $\mathbf{M}$ are the resultant stress and moment, ρ the line density, Z the area of a cross section, and I the geometrical moment of inertia of the string. Here we assume the string is uniform and the cross section is circular and the distortion of the cross section does not occurs in both extension and flexure. The assumption of circular cross sections is needed in order to avoid warping (Antman, 1995). The total derivative with respect to time is written as

$$\frac{d}{dt} = \frac{\partial}{\partial t} + \frac{ds}{dt}\frac{\partial}{\partial s} = \frac{\partial}{\partial t} + \left(\int \frac{d}{dt} \ln \sqrt{g} ds\right)\frac{\partial}{\partial s}. \tag{7}$$

It is noted that $\partial/\partial\sigma = \sqrt{g}\partial/\partial s$ and the derivative with respect to t does not commute with the derivative with respect to s but with σ because of the stretching effect. In (5) and (6) the stress and moment are represented by

$$\mathbf{S} = F\mathbf{t} + Q_1\mathbf{n} + Q_2\mathbf{b}, \tag{8}$$

$$\mathbf{M} = M_1\mathbf{t} + M_2\mathbf{n} + M_3\mathbf{b}, \tag{9}$$

where F and M_i are given by linear constitutive equations:

$$F = EZ(\sqrt{g} - 1), \tag{10}$$

$$M_1 = GJ\tau\sqrt{g}, \tag{11}$$

$$M_2 = EI\eta\sqrt{g}, \tag{12}$$

$$M_3 = EI\kappa\sqrt{g}, \tag{13}$$

where E is the modulus of elasticity and G is the shear modulus and $J = 2I$ because of neglect of the warping. The resultant shears Q_1 and Q_2 are not determined by constitutive equations and are considered as reactive parameters in the equations of balance of momentum (Coleman and Dill, 1992; Nishinari, 1997).

2.2 Analysis of a Curve by the Soliton Theory. Next, following the procedure given in the previous paper (Nishinari, 1998), we present a way of analyzing the string in three-dimensional space by the soliton theory. Let the curve dynamics be of the form

$$\frac{d\mathbf{r}}{dt} = U\mathbf{t} + W\mathbf{n} + V\mathbf{b} \tag{14}$$

and

$$\frac{d}{dt}\begin{pmatrix}\mathbf{t}\\ \mathbf{n}\\ \mathbf{b}\end{pmatrix} = \begin{pmatrix}0 & A & B\\ -A & 0 & C\\ -B & -C & 0\end{pmatrix}\begin{pmatrix}\mathbf{t}\\ \mathbf{n}\\ \mathbf{b}\end{pmatrix} \tag{15}$$

without loss of generality, where U, W, and V are components of a velocity of the string and A, B, and C represent dynamics of a basis which are determined below. Differentiating (2) with respect to time and using (14) we obtain

$$\frac{d}{dt}g = 2g\left(\frac{\partial U}{\partial s} - \kappa W + \eta V\right). \tag{16}$$

From (3) and (16) we have the commutation

$$\frac{\partial}{\partial s}\frac{d}{dt} - \frac{d}{dt}\frac{\partial}{\partial s} = \left(\frac{\partial U}{\partial s} - \kappa W + \eta V\right)\frac{\partial}{\partial s}. \tag{17}$$

Differentiating (14) with respect to s and using (4), (15), and (17) we obtain the expressions for A and B as

$$A = \frac{\partial W}{\partial s} + \kappa U - \tau V, \tag{18}$$

$$B = \frac{\partial V}{\partial s} + \tau W - \eta U. \tag{19}$$

Using (17), compatibility condition for (4) and (15), gives dynamics of curvatures

$$\frac{d\kappa}{dt} = \frac{\partial A}{\partial s} - \eta C - \tau B - \left(\frac{\partial U}{\partial s} - \kappa W + \eta V\right)\kappa, \tag{20}$$

$$\frac{d\eta}{dt} = -\frac{\partial B}{\partial s} + \kappa C - \tau A + \left(\frac{\partial U}{\partial s} - \kappa W + \eta V\right)\eta, \tag{21}$$

$$\frac{d\tau}{dt} = \frac{\partial C}{\partial s} + \kappa B + \eta A - \left(\frac{\partial U}{\partial s} - \kappa W + \eta V\right)\tau. \tag{22}$$

It is noted that (20)–(22) contain soliton equations as special cases by selecting U, W, and V as special functions of curvatures (Doliwa and Santini, 1994).

Finally, differentiating (14) with respect to time gives

$$\frac{d^2\mathbf{r}}{dt^2} = \left(\frac{dU}{dt} - WA - VB\right)\mathbf{t} + \left(\frac{dW}{dt} + UA - VC\right)\mathbf{n} + \left(\frac{dV}{dt} + WC + UB\right)\mathbf{b}. \tag{23}$$

Substituting (8)–(13) into (5) and (6), the compatibility conditions for (23) and (5) are

$$\rho Z\left(\frac{dU}{dt} - WA - VB\right) = EZ\frac{\partial\sqrt{g}}{\partial\sigma} - \kappa\sqrt{g}Q_1 + \eta\sqrt{g}Q_2, \tag{24}$$

$$\rho Z\left(\frac{dW}{dt} + UA - VC\right) = \frac{\partial Q_1}{\partial\sigma} + EZ\kappa\sqrt{g}(\sqrt{g} - 1) - \eta\sqrt{g}Q_2, \tag{25}$$

$$\rho Z\left(\frac{dV}{dt} + WC + UB\right) = \frac{\partial Q_2}{\partial\sigma} - EZ\eta\sqrt{g}(\sqrt{g} - 1) + \eta\sqrt{g}\,Q_1 \tag{26}$$

by comparing the coefficients of $\mathbf{t}$, $\mathbf{n}$, and $\mathbf{b}$, respectively. Similarly substitute (15) into the left-side hand of (6) and compare the coefficients of $\mathbf{t}$, $\mathbf{n}$, and $\mathbf{b}$ to obtain

$$2\rho I\frac{dC}{dt} = GJ\frac{\partial\tau\sqrt{g}}{\partial\sigma}, \tag{27}$$

$$\rho I\left(-\frac{dB}{dt} + AC\right) = EI\frac{\partial\eta\sqrt{g}}{\partial\sigma} - \sqrt{g}Q_2 + \alpha g\kappa\tau, \tag{28}$$

$$\rho I\left(\frac{dA}{dt} + BC\right) = EI\frac{\partial\kappa\sqrt{g}}{\partial\sigma} + \sqrt{g}Q_1 - \alpha g\eta\tau, \tag{29}$$

where $\alpha = GJ - EI$. As mentioned above, the resultant shears Q_1 and Q_2 are considered to be determined by the equations of balance of momentum (28) and (29). Therefore we neglect the inertia terms in (28) and (29) because of consideration of the string, which has quite a small geometrical moment of inertia, and obtain

$$Q_1 = -EI\frac{\partial\kappa\sqrt{g}}{\partial s} + \alpha\sqrt{g}\eta\tau, \tag{30}$$

Downloaded 04 May 2010 to 171.66.16.27. Redistribution subject to ASME license or copyright; see http://www.asme.org/terms/Terms_Use.cfm

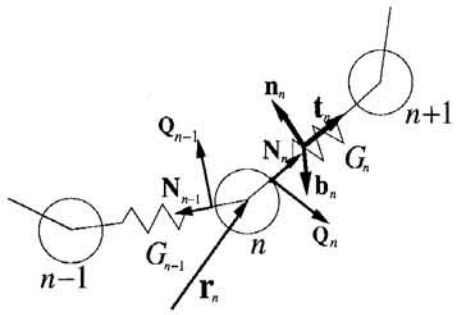


Fig. 1(*b*) Mechanism for generation of the bending moment between beads. The magnitude of the moment is proportional to the angle between successive two tangent vectors of the string.

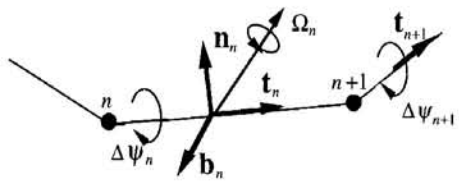


Fig. 1(*c*) Twisting of the string, which is generated by the difference of the successive two angles of the rotation around the tangent vector

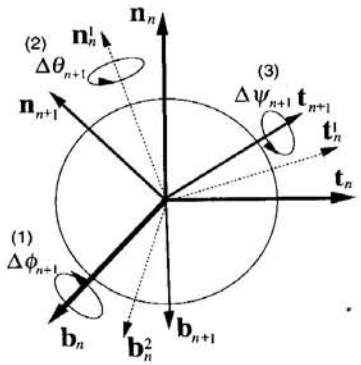


Fig. 1(*d*) Definition of relative Euler angles $\Delta\psi_n$, $\Delta\theta_n$, and $\Delta\phi_n$

$$Q_2 = EI\,\frac{\partial\eta\sqrt{g}}{\partial s} + \alpha\sqrt{g}\kappa\tau. \tag{31}$$

When we consider dynamics of the twist, we must take into effect the inertia, i.e., an finite area of cross section. Thus we employ (22) and (27) for dynamics of τ. The variable C plays the role of an auxiliary variable in this theory. Therefore, eight equations (16), (20), (21), (22), (24), (25), (26), and (27) for unknown variables G, κ, η, τ, U, W, V, and C are considered new basic equations for the extensible string. Variables A, B, Q_1, and Q_2 are given as the function of these eight variables in (18), (19), (30), and (31), respectively.

3 A Discrete Model for an Extensible String

3.1 A Discrete Model and the Continuous Limit. In this section we propose a discrete model of an extensible string discussed in the previous section. The equation for balance of the force is given by

$$m\,\frac{d^2\mathbf{r}_n}{dt^2} = \mathbf{N}_n - \mathbf{N}_{n-1} - \mathbf{Q}_n + \mathbf{Q}_{n-1} \equiv \mathbf{F}_n, \tag{32}$$

where m is mass of a bead; $\mathbf{r}_n$ is a position vector in the space; and $\mathbf{N}_n$ and $\mathbf{Q}_n$ are resultant axial force and shear force of a spring, respectively (Fig. 1(*a*)). The linear constitutive equations for $\mathbf{N}_n$ and $\mathbf{Q}_n$ are given by

$$\mathbf{N}_n = k\,\frac{|\mathbf{r}_{n+1} - \mathbf{r}_n| - l}{l}\,\mathbf{t}_n \equiv k\,\frac{G_n - l}{l}\,\mathbf{t}_n, \tag{33}$$

$$\mathbf{Q}_n = \frac{\mathbf{M}_{n+1}^l - \mathbf{M}_n^r + \mathbf{R}_n}{G_n}, \tag{34}$$

where

$$\mathbf{M}_n^r = \frac{K}{l}\,\frac{\alpha_n}{\sin\alpha_n}\,(-\mathbf{t}_{n-1} + \cos\alpha_n\mathbf{t}_n), \tag{35}$$

$$\mathbf{M}_n^l = \frac{K}{l}\,\frac{\alpha_n}{\sin\alpha_n}\,(\mathbf{t}_n - \cos\alpha_n\mathbf{t}_{n-1}), \tag{36}$$

$$\mathbf{R}_n = \mathbf{\Omega}_n \times \mathbf{t}_n, \tag{37}$$

$$\mathbf{\Omega}_n = \frac{h}{l}\,(\Delta\psi_{n+1}\mathbf{t}_{n+1} - \Delta\psi_n\mathbf{t}_n). \tag{38}$$

$\mathbf{M}_n^r$ and $\mathbf{M}_n^l$ are the bending moment applied to a bead from the right and left side, respectively (Fig. 1(*b*)). $\mathbf{\Omega}_n$ is a twist vector of the axis spring (Fig. 1(*c*)) and $\mathbf{R}_n$ is the shear force which comes from twisting. In these equations k is a spring constant for the axis, K is a spring constant for bending, and l is an unstretched length of an axis spring. α_n is defined in (40) and $\Delta\phi_n$ is one of the relative Euler's angles, and they relate local orthonormal bases as

$$E_n\begin{pmatrix}\mathbf{t}_n\\ \mathbf{n}_n\\ \mathbf{b}_n\end{pmatrix} = \begin{pmatrix}P1_{n+1} & P2_{n+1} & P3_{n+1}\\ P4_{n+1} & P5_{n+1} & P6_{n+1}\\ P7_{n+1} & P8_{n+1} & P9_{n+1}\end{pmatrix}\begin{pmatrix}\mathbf{t}_n\\ \mathbf{n}_n\\ \mathbf{b}_n\end{pmatrix}, \tag{39}$$

where E_n is a shift operator defined by $E_n f(n) = f(n+1)$. Pi_n $(n = 1, \ldots, 9)$ are expressed by relative Euler's angles $\Delta\psi_n$, $\Delta\theta_n$, and $\Delta\phi_n$ as follows (Fig. 1(*d*)):

$$P1_n = \cos\Delta\phi_n\cos\Delta\theta_n \equiv \cos\alpha_n,$$

$$P2_n = \cos\Delta\theta_n\sin\Delta\phi_n,$$

$$P3_n = -\sin\Delta\theta_n,$$

$$P4_n = -\cos\Delta\psi_n\sin\Delta\phi_n + \cos\Delta\phi_n\sin\Delta\psi_n\sin\Delta\theta_n,$$

$$P5_n = \cos\Delta\phi_n\cos\Delta\psi_n + \sin\Delta\phi_n\sin\Delta\psi_n\sin\Delta\theta_n,$$

$$P6_n = \cos\Delta\theta_n\sin\Delta\psi_n,$$

$$P7_n = \sin\Delta\phi_n\sin\Delta\psi_n + \cos\Delta\phi_n\cos\Delta\psi_n\sin\Delta\theta_n,$$

$$P8_n = -\cos\Delta\phi_n\sin\Delta\psi_n + \cos\Delta\psi_n\sin\Delta\phi_n\sin\Delta\theta_n,$$

$$P9_n = \cos\Delta\psi_n\cos\Delta\theta_n. \tag{40}$$

The Eq. (39) is considered as a discrete version of (4). In fact, we divide (39) by G_n and also taking $G_n \to 0$ with the formula $G_n/l \to \sqrt{g}$ in the limit (Nishinari, 1998), we obtain by neglecting nonlinear terms of relative Euler's angles,

Downloaded 04 May 2010 to 171.66.16.27. Redistribution subject to ASME license or copyright; see http://www.asme.org/terms/Terms_Use.cfm

$$\frac{\partial}{\partial s}\begin{pmatrix}\mathbf{t}\\ \mathbf{n}\\ \mathbf{b}\end{pmatrix} = \lim_{G_n\to 0}\begin{pmatrix} 0 & \frac{\Delta\phi_n}{G_n} & -\frac{\Delta\theta_n}{G_n}\\ -\frac{\Delta\phi_n}{G_n} & 0 & \frac{\Delta\psi_n}{G_n}\\ \frac{\Delta\theta_n}{G_n} & -\frac{\Delta\psi_n}{G_n} & 0\end{pmatrix}\begin{pmatrix}\mathbf{t}\\ \mathbf{n}\\ \mathbf{b}\end{pmatrix}, \quad (41)$$

where we put $(\mathbf{t}_{n+1} - \mathbf{t}_n)/G_n \to \partial\mathbf{t}/\partial s$. Thus from (4) we obtain the relations

$$\kappa = \lim_{G_n\to 0}\frac{\Delta\phi_n}{G_n},$$

$$\eta = \lim_{G_n\to 0}\frac{\Delta\theta_n}{G_n},$$

$$\tau = \lim_{G_n\to 0}\frac{\Delta\psi_n}{G_n}.$$

Next we consider the limit of (33). Following the same procedure above, we obtain from $G_n/l \to \sqrt{g}$

$$\mathbf{N} = k(\sqrt{g} - 1)\mathbf{t}. \quad (42)$$

This coincides with (10) if $k = EZ$. In the case of (34), first we have in the limit

$$\lim_{G_n\to 0}\frac{\mathbf{M}^l_{n+1} - \mathbf{M}^r_n}{G_n} = \lim_{G_n\to 0} K\left(\frac{\Delta\phi_n - \Delta\phi_{n-1} + \Delta\psi_{n-1}\Delta\theta_{n-1}}{lG_n}\mathbf{n}_n + \frac{-\Delta\theta_n + \Delta\theta_{n-1} + \Delta\psi_{n-1}\Delta\phi_{n-1}}{lG_n}\mathbf{b}_n\right), \quad (43)$$

$$\lim_{G_n\to 0}\frac{\mathbf{R}_n}{G_n} = \lim_{G_n\to 0}\frac{h}{lG_n}\Delta\psi_{n+1}(-\Delta\theta_n\mathbf{n}_n - \Delta\phi_n\mathbf{b}_n). \quad (44)$$

From (43) and (44) we obtain the continuous limit of the shear force $\mathbf{Q}$ as

$$\mathbf{Q} = \left(K\frac{\partial\kappa\sqrt{g}}{\partial s} + (K-h)\sqrt{g}\tau\eta\right)\mathbf{n} + \left(-K\frac{\partial\eta\sqrt{g}}{\partial s} + (K-h)\sqrt{g}\tau\kappa\right)\mathbf{b} \quad (45)$$

$$= -Q_1\mathbf{n} - Q_2\mathbf{b}.$$

Thus these also coincide with (30) and (31) if $K = EI$ and $h = GJ$. Putting $m = \rho l$ and dividing (32) by l and using

$$\lim_{l\to 0}\frac{\mathbf{N}_n - \mathbf{N}_{n-1} - \mathbf{Q}_n + \mathbf{Q}_{n-1}}{l} = \frac{\partial\mathbf{N}}{\partial\sigma} - \frac{\partial\mathbf{Q}}{\partial\sigma}, \quad (46)$$

it is apparent that (32) becomes (5) in the continuous limit.

Next, we consider dynamics of twisting of the discrete string. Since this discrete model naturally contains the representation of (30) and (31), then we only consider the $\mathbf{t}_n$ component of equations for the moment as discussed in the previous section. Such a discrete equation is given by (Fig. 1(*c*))

$$\rho I\left(\mathbf{n}_n\times\frac{d^2\mathbf{n}_n}{dt^2} + \mathbf{b}_n\times\frac{d^2\mathbf{b}_n}{dt^2}\right)_{\mathbf{t}_n} = \left(\frac{\mathbf{\Omega}_n}{l}\right)_{\mathbf{t}_n}, \quad (47)$$

where picking up the $\mathbf{t}_n$ component is represented by $(\ldots)_{\mathbf{t}_n}$. Since

$$\lim_{l\to 0}\left(\frac{\mathbf{\Omega}_n}{l}\right)_{\mathbf{t}_n} = h\frac{\partial\tau\sqrt{g}}{\partial\sigma}, \quad (48)$$

(47) coincides with the $\mathbf{t}_n$ component of (6) in the limit.

3.2 The Discrete Soliton Theory. Let us introduce the discrete soliton theory in order to analyze the discrete model of a string. Following Section 2.2, we put velocity of a bead and dynamics for the orthonormal basis as

$$\frac{d\mathbf{r}_n}{dt} = U_n\mathbf{t}_n + W_n\mathbf{n}_n + V_n\mathbf{b}_n, \quad (49)$$

$$\frac{d}{dt}\begin{pmatrix}\mathbf{t}_n\\ \mathbf{n}_n\\ \mathbf{b}_n\end{pmatrix} = \begin{pmatrix} 0 & A_n & B_n\\ -A_n & 0 & C_n\\ -B_n & -C_n & 0\end{pmatrix}\begin{pmatrix}\mathbf{t}_n\\ \mathbf{n}_n\\ \mathbf{b}_n\end{pmatrix}. \quad (50)$$

Differentiating

$$\mathbf{r}_{n+1} = \mathbf{r}_n + G_n\mathbf{t}_n \quad (51)$$

with respect to t and using (49), (39), and (50), we obtain

$$\frac{dG_n}{dt} = -U_n + P1_{n+1}U_{n+1} + P4_{n+1}W_{n+1} + P7_{n+1}V_{n+1}, \quad (52)$$

$$A_n = \frac{1}{G_n}(-W_n + P2_{n+1}U_{n+1} + P5_{n+1}W_{n+1} + P8_{n+1}V_{n+1}), \quad (53)$$

$$B_n = \frac{1}{G_n}(-V_n + P3_{n+1}U_{n+1} + P6_{n+1}W_{n+1} + P9_{n+1}V_{n+1}). \quad (54)$$

From the compatibility condition of (39) and (50),

$$\frac{d}{dt}\begin{pmatrix}P1_{n+1} & P2_{n+1} & P3_{n+1}\\ P4_{n+1} & P5_{n+1} & P6_{n+1}\\ P7_{n+1} & P8_{n+1} & P9_{n+1}\end{pmatrix}\begin{pmatrix}\mathbf{t}_n\\ \mathbf{n}_n\\ \mathbf{b}_n\end{pmatrix} = E_n\begin{pmatrix} 0 & A_n & B_n\\ -A_n & 0 & C_n\\ -B_n & -C_n & 0\end{pmatrix}\begin{pmatrix}\mathbf{t}_n\\ \mathbf{n}_n\\ \mathbf{b}_n\end{pmatrix},$$

we obtain time evolution equations for relative Euler's angles:

$$\frac{d\Delta\phi_n}{dt} = -A_{n-1} + A_n\frac{\cos\Delta\psi_n}{\cos\Delta\theta_n} - B_n\frac{\sin\Delta\psi_n}{\cos\Delta\theta_n} + B_{n-1}\sin\Delta\phi_n\tan\Delta\theta_n - C_{n-1}\tan\Delta\theta_n\cos\Delta\phi_n, \quad (55)$$

$$\frac{d\Delta\theta_n}{dt} = B_{n-1}\cos\Delta\phi_n - B_n\cos\Delta\psi_n + C_{n-1}\sin\Delta\phi_n - A_n\sin\Delta\psi_n, \quad (56)$$

$$\frac{d\Delta\psi_n}{dt} = C_n - C_{n-1}\frac{\cos\Delta\phi_n}{\cos\Delta\theta_n} + B_{n-1}\frac{\sin\Delta\phi_n}{\cos\Delta\theta_n} - B_n\sin\Delta\psi_n\tan\Delta\theta_n + A_n\tan\Delta\theta_n\cos\Delta\psi_n. \quad (57)$$

These equations also contain discrete soliton equations as special cases as in the continuous case discussed in the previous section, and these are a discrete version of (20)–(22).

Substituting (38) and (50) into the moment Eq. (47) we obtain

$$\frac{dC_n}{dt} = \frac{h}{2\rho Il^2}(\Delta\psi_{n+1}\cos\Delta\phi_{n+1}\cos\Delta\theta_{n+1} - \Delta\psi_n). \quad (58)$$

Next, differentiating the velocity (49) with respect to time gives

$$\frac{d^2\mathbf{r}_n}{dt^2} = \left(\frac{dU_n}{dt} - A_nW_n - B_nV_n\right)\mathbf{t}_n + \left(\frac{dW_n}{dt} + A_nU_n - C_nV_n\right)\mathbf{n}_n + \left(\frac{dV_n}{dt} + B_nU_n + C_nW_n\right)\mathbf{b}_n. \quad (59)$$

Comparing coefficients of (59) and (32), we obtain

Downloaded 04 May 2010 to 171.66.16.27. Redistribution subject to ASME license or copyright; see http://www.asme.org/terms/Terms_Use.cfm

$$\frac{dU_n}{dt} = A_n W_n + B_n V_n + \frac{(\mathbf{F}_n)_{\mathbf{t}_n}}{m}, \tag{60}$$

$$\frac{dW_n}{dt} = -A_n U_n + C_n V_n + \frac{(\mathbf{F}_n)_{\mathbf{n}_n}}{m}, \tag{61}$$

$$\frac{dV_n}{dt} = -B_n U_n - C_n W_n + \frac{(\mathbf{F}_n)_{\mathbf{b}_n}}{m}. \tag{62}$$

Therefore eight equations (52), (55), (56), (57), (58), (60), (61), and (62) for G_n, $\Delta\phi$, $\Delta\theta$, $\Delta\psi$, C_n, U_n, W_n, and V_n are basic equations for the discrete string. These are a discrete version of the continuous equations given in the previous section.

4 Analyses by the Soliton Theory

As we pointed out in previous sections, our new basic equations of both continuous and discrete-type contain soliton equations as special cases. In this section we focus upon the continuous equations discussed in Section 2 and consider the case that Eqs. (20)–(22) become the complex modified KdV (CmKdV) equation, which can be solved exactly by the soliton theory.

It is well known that the soliton theory matches well with the mathematical theory of curves, but a mathematical curve is different from a physical string. Thus soliton solutions do not always satisfy elastic equations. Such problems are studied in previous papers in the case of the two-dimensional space (Nishinari, 1997, 1998). Let us investigate the correspondence of the soliton theory and the elastic theory in the three-dimensional space by using the CmKdV equation. In the two-dimensional space it is shown that the modified KdV (mKdV) equation is the fundamental equation that describes dynamics of a curve (Goldstein and Petrich, 1991; Matsutani, 1995). Then it is natural to consider the CmKdV equation in the three-dimensional case because it is a complex generalization of the mKdV equation. We restrict ourselves to the equation in this paper, although we have many integrable equations by choosing U, W, and V as special forms (Doliwa and Santini, 1994). We assume the metric g of the string to be constant g_0 in this section. This simplifies the procedure of calculating soliton equations and solutions (Krylov and Rosenau, 1996; Nishinari, 1997).

The CmKdV equation is

$$\psi_t + 3|\psi|^2\psi_s + 2\psi_{sss} = 0. \tag{63}$$

We put

$$\psi = (\kappa - i\eta)\exp\left(i\int \tau ds\right) \tag{64}$$

then the real and imaginary part of the CmKdV equation are

$$\kappa_t + \eta\int \tau_t ds + 3(\kappa^2+\eta^2)(\kappa_s + \eta\tau) + 2(\kappa_{sss} + 3\eta_{ss}\tau + 3\eta_s\tau_s + \eta\tau_{ss} - 3\kappa_s\tau^2 - 3\kappa\tau\tau_s - \eta\tau^3) = 0, \tag{65}$$

$$-\eta_t + \kappa\int \tau_t ds + 3(\kappa^2+\eta^2)(-\eta_s + \kappa\tau) + 2(-\eta_{sss} + 3\kappa_{ss}\tau + 3\kappa_s\tau_s + \kappa\tau_{ss} + 3\eta_s\tau^2 + 3\eta\tau\tau_s - \kappa\tau^3) = 0, \tag{66}$$

respectively.

It is found that if we put

$$U = -\kappa^2 - \eta^2 \tag{67}$$

$$W = -2(\kappa_s + \tau\eta) \tag{68}$$

$$V = 2(\eta_s - \tau\kappa) \tag{69}$$

then we obtain

$$U_s - \kappa W + \eta V = 0. \tag{70}$$

Thus from (16) the metric g becomes constant. From (18) and (19) we have

$$A = -2\left(\kappa_{ss} + (\tau\eta)_s + \tau\eta_s - \tau^2\kappa + \frac{\kappa}{2}(\kappa^2+\eta^2)\right), \tag{71}$$

$$B = -2\left(-\eta_{ss} + (\tau\kappa)_s + \tau\kappa_s + \tau^2\eta - \frac{\eta}{2}(\kappa^2+\eta^2)\right). \tag{72}$$

Substituting (71) and (72) into (22) we obtain, by integrating with respect to s,

$$C = \int \tau_t ds + 2(\eta\kappa_s - \kappa\eta_s + \tau(\kappa^2+\eta^2)). \tag{73}$$

Substituting (73) into (20) and (21) we obtain (65) and (66), respectively. Therefore, selecting velocities as (67)–(69) leads to the dynamics of the string described by the CmKdV equation.

In the following we seek solutions of the traveling wave type that satisfy $\partial_t = v\partial_s$. Moreover, we consider the case that τ is constant. This is a usual assumption when we consider soliton solutions (Tsuru, 1987). Then from (4) and (15) we have $A = v\kappa$, $B = -v\eta$ and $C = v\tau$, or

$$v\kappa = -2\left(\kappa_{ss} + 2\tau\eta_s - \tau^2\kappa + \frac{\kappa}{2}(\kappa^2+\eta^2)\right), \tag{74}$$

$$-v\eta = -2\left(-\eta_{ss} + 2\tau\kappa_s + \tau^2\eta - \frac{\eta}{2}(\kappa^2+\eta^2)\right). \tag{75}$$

Equations (20) and (21) are automatically satisfied by those A, B, and C.

First, in the case $\tau = 0$, it is easily seen that (74) and (75) lead to the equation

$$v\kappa + 2\kappa_{ss} + 2\kappa^3 = 0 \tag{76}$$

by assuming that $\eta = \kappa$. This is considered as a symmetry equation for the mKdV equation (Nishinari, 1997). In fact, when $\eta = \kappa$ and $\tau = 0$ we have $\psi = (1-i)\kappa$ and the CmKdV equation becomes

$$\kappa_t + 2\kappa_{sss} + 6\kappa^2\kappa_s = 0. \tag{77}$$

This is the mKdV equation and the reduction $\partial_t = v\partial_s$ becomes the symmetry Eq. (76). We have investigated in detail on this case in our previous papers, since dynamics described by (76) is a loop soliton on a plane.

The next example of a solution of the CmKdV equation is obtained by putting τ to be a nonzero constant. Then it is easily checked that Eqs. (74) and (75) can be solved by

$$\kappa = \kappa_f \cos l(s+vt), \tag{78}$$

$$\eta = \kappa_f \sin l(s+vt), \tag{79}$$

where $l = \tau - \sqrt{\kappa_f^2/2 + v/2}$ and κ_f is a constant. This solution corresponds to a trivial solution of the CmKdV equation $\psi = \kappa_f \exp(is\sqrt{\kappa_f^2/2 + v/2} + i(2\kappa_f^2 - v)t)$. Although the solution is trivial, it represents a helix in three-dimensional space. The next step is to investigate whether this solution is compatible with the equation of motion or not. From equations of the conservation of linear momentum we obtain

$$0 = EIg(\kappa\kappa_s + \eta\eta_s) \tag{80}$$

$$\rho Z v^2\kappa = EZ\sqrt{g}(\sqrt{g}-1)\kappa - EIg\kappa_{ss} + \alpha g(\eta\tau)_s - EIg\eta\eta_s - \alpha g\eta\kappa\tau \tag{81}$$

Downloaded 04 May 2010 to 171.66.16.27. Redistribution subject to ASME license or copyright; see http://www.asme.org/terms/Terms_Use.cfm

$$-\rho Z v^2 \eta = -EZ\sqrt{g}(\sqrt{g}-1)\eta + EIg\eta_{ss} + \alpha g(\kappa\tau)_s - EIg\eta\kappa_s + \alpha g\eta^2\tau. \quad (82)$$

Thus in order that (78) and (79) be a solution of these equations we can see that the following condition must be satisfied:

$$v = \pm\sqrt{\frac{E}{\rho}\sqrt{g}(\sqrt{g}-1)}, \quad (83)$$

$$EIl + \alpha\tau = 0. \quad (84)$$

In other words, the solution (78) and (79) are compatible with elastic equations under the above conditions.

Relations between curvatures and the Euler angles ϕ, θ, and ψ, which correspond to that of discussed in Section 3, are given by (Antman, 1995)

$$\tau = \psi_s - \phi_s \sin\theta, \quad (85)$$

$$\eta = \theta_s \cos\psi + \phi_s \cos\theta \sin\psi, \quad (86)$$

$$\kappa = -\theta_s \sin\psi + \phi_s \cos\theta \cos\psi. \quad (87)$$

Comparing these representations and the helix solution obtained above, we get the solution of the Euler angles as $\theta = \theta_0$, $\phi = p(s + vt)$ and $\psi = l(s + vt)$, where $\tan\theta_0 = -\sqrt{(\kappa_f^2 + v)/2}/\kappa_f$ and $p = \pm\sqrt{3\kappa_f^2/2 + v/2}$. Then using the relation (Antman, 1995; Tsuru, 1987)

$$\mathbf{t} = \cos\phi\cos\theta\mathbf{e}_x + \sin\phi\cos\theta\mathbf{e}_y - \sin\theta\mathbf{e}_z, \quad (88)$$

where $\mathbf{e}_x$, etc., are the basis of fixed xyz frame, we can calculate the position of the string by integrating (1)

$$x = \frac{\cos\theta_0}{p}\sin p(s + vt), \quad (89)$$

$$y = \frac{\cos\theta_0}{p}(1 - \cos p(s + vt)), \quad (90)$$

$$z = -\sin\theta_0(s - 3\kappa_f^2 t), \quad (91)$$

where we assume $\mathbf{r} = 0$ when $t = 0$ and $s = 0$. It is noted that a helical solution is already obtained in papers (Krylov and Rosenau, 1996; Krylov et al., 1998) but they neglect shearing force Q_1 and Q_2 and bending moments. Our solution is an extended one including an effect of the bending.

5 Numerical Simulations

In this section we demonstrate that the proposed discrete model in Section 3 is suitable for computer simulation of dynamics of a string. First let us put basic equations again in order in the following:

$$\frac{dG_n}{dt} = -U_n + P1_{n+1}U_{n+1} + P4_{n+1}W_{n+1} + P7_{n+1}V_{n+1} \quad (92)$$

$$\frac{d\Delta\phi_n}{dt} = -A_{n-1} + A_n\frac{\cos\Delta\psi_n}{\cos\Delta\theta_n} - B_n\frac{\sin\Delta\psi_n}{\cos\Delta\theta_n} + B_{n-1}\sin\Delta\phi_n\tan\Delta\theta_n - C_{n-1}\tan\Delta\theta_n\cos\Delta\phi_n \quad (93)$$

$$\frac{d\Delta\theta_n}{dt} = B_{n-1}\cos\Delta\phi_n - B_n\cos\Delta\psi_n + C_{n-1}\sin\Delta\phi_n - A_n\sin\Delta\psi_n \quad (94)$$

$$\frac{d\Delta\psi_n}{dt} = C_n - C_{n-1}\frac{\cos\Delta\phi_n}{\cos\Delta\theta_n} + B_{n-1}\frac{\sin\Delta\phi_n}{\cos\Delta\theta_n} - B_n\sin\Delta\psi_n\tan\Delta\theta_n + A_n\tan\Delta\theta_n\cos\Delta\psi_n \quad (95)$$

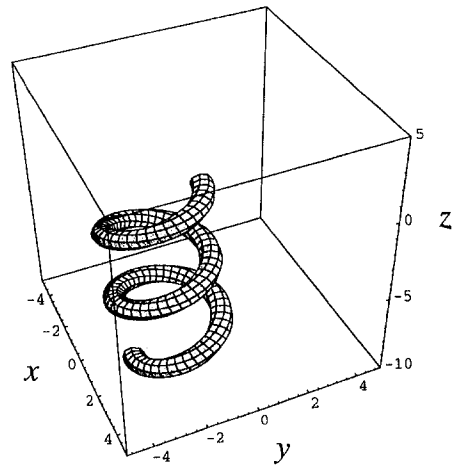


Fig. 2(*a*)

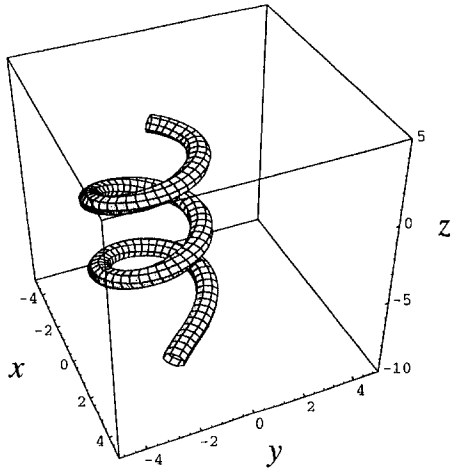


Fig. 2(*b*)

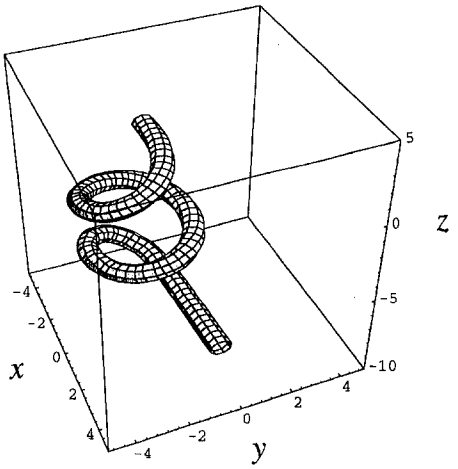


Fig. 2(*c*)

Fig. 2 Simulations of the moving helix with the free boundary condition. Initial condition is given by Fig. 2(*a*), and time evolutions of it are given by (*b*) and (*c*) in the case of $l = 0$ and $l = 0.3$, respectively. We see that the string are swelling out in the case of (*c*). Parameters are set as $E = 1.0$, $G = 0.2$, $\kappa_f = -0.5$, $\rho = 0.5$, and $\sqrt{g} = 1.02$.

$$\frac{dC_n}{dt} = \frac{h}{2\rho Il^2}(\Delta\psi_{n+1}\cos\Delta\phi_{n+1}\cos\Delta\theta_{n+1} - \Delta\psi_n) \quad (96)$$

$$\frac{dU_n}{dt} = A_n W_n + B_n V_n + \frac{(\mathbf{F}_n)_{t_n}}{m} \quad (97)$$

Downloaded 04 May 2010 to 171.66.16.27. Redistribution subject to ASME license or copyright; see http://www.asme.org/terms/Terms_Use.cfm

$$\frac{dW_n}{dt} = -A_n U_n + C_n V_n + \frac{(\mathbf{F}_n)_{\mathbf{n}_n}}{m} \tag{98}$$

$$\frac{dV_n}{dt} = -B_n U_n - C_n W_n + \frac{(\mathbf{F}_n)_{\mathbf{b}_n}}{m}. \tag{99}$$

We can integrate these eight equations with respect to time by some explicit methods, such as the Runge-Kutta method and we did not use matrix calculations. This is an advantageous point to the famous finite element method and the Lagrange multiplier approach which needs a large matrix and memories and devices to calculate dynamics of a string (Pereira and Ambrósio, 1995). Moreover, as shown in Section 3, these equations converge to the Cosserat string in the $l \to 0$ limit. Thus we can simulate dynamics of an elastic string in a desired accuracy by choosing small l.

Let us calculate helical dynamics of the string by using this scheme. The helical solution in the previous section is for infinite length of a string. Thus we investigate an effect of the free end by numerical calculations. Boundary conditions are that one end is driven along the exact trajectory (89)–(91) and the other end is set free. We change the parameter I in order to see an effect of the bending. Time integration is done by both the Cash-Karp Runge-Kutta method of the fifth order and Bulirsch-Store method with desired accuracy (Press et al., 1992). The number of beads is 100 and we set $l = 0.3$. Time evolution of a helix is given in Fig. 2. We see that in all the calculations the free end deviates from the trajectory of the helix due to lack of terminal forces. When the case $I = 0$, the string moves exactly as the helical solution in regardless of the free end (Fig. 2(*b*)). This shows the accuracy of our calculations. If we increase the magnitude of I, then the helix will swell out because of the existence of the bending moment and the free end will expand outward faster than the case $I = 0$ (Fig. 2(*c*)). We also see from meshes on the string in Fig. 2 that the twist of the helix will vanish from the free end in the course of time.

6 Concluding Discussions

In this paper we have proposed a discrete model for an extensible string in three-dimensional space, which coincides with the continuous theory in the limit. We have also obtained a set of reduced equations by using the soliton theory and the discrete version of them are easy to treat numerically with various boundary conditions. We expect that this approach can be applied to analyze any one-dimensional media-like string.

In Section 3.2 discrete equations are obtained by the discrete soliton theory. In this paper, however, we only use the continuous theory in Section 4 and did not use the discrete theory to obtain discrete exact solutions as was done in the previous paper with the two-dimensional case (Nishinari, 1998). It is noted that such problems for a "mathematical curve" in three-dimensional space are discussed by Doliwa and Santini (1994). In Section 4 we consider the CmKdV equation and its solutions as examples of dynamics of a string. We can obtain many other soliton equations, such as the nonlinear Schrödinger equation, the derivative nonlinear Schrödinger equation, the sine-Gordon equation, and the Lund-Regge equation (Sasa and Satsuma, 1991; Fukumoto, 1997). Full investigation of these equations and its discrete versions will be one of the exciting problems of the future. Moreover, the assumption of constant metric will be eliminated by changing a coordinate s to σ (Nakayama and Wadati, 1993). Recently a nontrivial soliton solution for nonconstant metric was obtained in the case where the unperturbed string had the shape of a helix (Krylov and Rosenau, 1996). In their solution, the stretch propagates as a soliton. Their method is using complex representation of the basic equations and assuming the shape of the solution a priori. Thus underlying soliton equations are not clear for the solution. The quest for these solitons in a string and the correspondence between these solutions and soliton equations are open problems.

Acknowledgment

The author is grateful to Prof. Kazumi Watanabe for fruitful discussions and helpful comments. He also would like to express his sincere gratitude to Prof. Junkichi Satsuma, Dr. Yasuhiro Ohta, and Dr. Shigeki Matsutani for stimulating discussions and valuable comments. This work is partially supported by the Sasagawa Scientific Research Grant from The Japan Science Society and Grant-in-Aid from the Ministry of Education, Science and Culture (No. 09750078).

References

Antman, S. S., 1995, *Nonlinear Problems of Elasticity,* Springer-Verlag, New York.

Coleman, B. D., and Dill, E. H., 1992, "Flexure Waves in Elastic Rods," *Journal of the Acoustical Society of America,* Vol. 91, pp. 2663–2673.

Doi, M., and Edwards, S. F., 1986, *The Theory of Polymer Dynamics* Oxford University Press, New York.

Doliwa, A., and Santini, P. M., 1994, "An Elementary Geometric Characterization of the Integrable Motions of a Curve," *Physics Letters A,* Vol. 185, pp. 373–384.

Fukumoto, Y., 1997, "Stationary Configurations of a Vortex Filament in Background Flows," *Proceedings of the Royal Society of London,* Vol. A453, pp. 1205–1232.

Gerbert, B. G., 1981, "Some Notes on V-Belt Drives," ASME JOURNAL OF APPLIED MECHANICS, Vol. 103, pp. 8–18.

Goldstein, R. E., and Petrich, D. M., 1991, "The Korteweg-de Vries Hierarchy as Dynamics of Closed Curves in the Plane," *Physical Review Letters,* Vol. 67, pp. 3203–3206.

Grigolyuk, E. I., and Shalashilin, V. I., 1991, *Problems of Nonlinear Deformation,* Kluwer, Boston.

Jiang, W., 1995, "A General Formulation of the Theory of Wire Ropes," ASME JOURNAL OF APPLIED MECHANICS, Vol. 62, pp. 747–755.

Krylov, V., and Rosenau, P., 1996, "Solitary Waves in an Elastic String," *Physics Letters A,* Vol. 217, pp. 31–42.

Krylov, V., Parnes, R., and Slepyan, L., 1998, "Nonlinear Waves in an Inextensible Flexible Helix," *Wave Motion,* Vol. 27, pp. 117–136.

Matsutani, S., 1995, "Geometrical Construction of the Hirota Bilinear Form of the Modified Korteweg-de Vries Equation on a Thin Elastic Rod: Bosonic Classical Theory," *Internal Journal of Modern Physics A,* Vol. 10, No. 22, pp. 3109–3123.

Misra, A. K., and Modi, V. J., 1992, "Three-Dimensional Dynamics and Control of Tether-Connected N-Body Systems," *Acta Astronautica,* Vol. 26, No. 2, pp. 77–84.

Nakayama, K., Segur, H., and Wadati, M., 1992, "Integrability and the Motion of Curves," *Physical Review Letters,* Vol. 69, pp. 2603–2606.

Nakayama, K., and Wadati, M., 1993, "Motion of Curves in the Plane," *Journal of the Physical Society of Japan,* Vol. 62, No. 2, pp. 473–479.

Nishinari, K., 1997, "Nonlinear Dynamics of Solitary Waves in an Extensible Rod," *Proceedings of the Royal Society of London,* Vol. A453, pp. 817–833.

Nishinari, K., 1998, "Discrete Modeling of a String and Analysis of a Loop Soliton," ASME JOURNAL OF APPLIED MECHANICS, Vol. 65, pp. 737–747.

Pereira, M. F. O. S., and Ambrósio, J. A. C., eds., 1995, *Computational Dynamics in Multibody Systems,* Kluwer, Boston.

Press, W. H., Teukolsky, S. A., Vetterling, W. T., and Flannery, B. P., 1992, *Numerical Recipes in C,* 2nd Ed., Cambridge University Press, New York.

Sasa, N., and Satsuma, J., 1991, "New-Type of Soliton Solutions for a Higher-Order Nonlinear Schrödinger Equation," *Journal of the Physical Society of Japan,* Vol. 60, No. 2, pp. 409–417.

Tsuru, H., 1987, "Equilibrium Shapes and Vibrations of Thin Elastic Rod," *Journal of the Physical Society of Japan,* Vol. 56, No. 7, pp. 2309–2324.

Downloaded 04 May 2010 to 171.66.16.27. Redistribution subject to ASME license or copyright; see http://www.asme.org/terms/Terms_Use.cfm

A Model for Mechanically Induced Densification of Glassy Polymers

A. D. Drozdov
Institute for Industrial Mathematics,
Four Hanachtom Street,
Beersheba 84311, Israel

Constitutive equations are derived for the isothermal viscoelastic response of glassy polymers at small strains. An amorphous polymer is modeled as a composite material consisting of a temporary network of long chains, immobile voids, and free volume gas diffusing through the network. The model is applied to analyze stress-induced densification of polymers in tensile and compressive relaxation tests. It is demonstrated that the stress-strain relations adequately predict a decrease in the specific volume observed in uniaxial experiments on polycarbonate.

1 Introduction

This paper is concerned with the viscoelastic behavior of glassy polymers at isothermal loading. Our purpose is to describe densification of polymers observed in tensile and compressive relaxation tests in the subyield region. Densification of glassy polymers in tensile relaxation tests (an increase in the specific volume at the instant when external loads are applied followed by a slow decrease in the volume strain with time) has been observed in polypropylene (Benham and McCammond, 1971), styrene-butadiene random copolymers (Merriman and Caruthers, 1981), polyethylene (Delin et al., 1994), polycarbonate (Colucci et al., 1997), and poly(methyl methacrylate) (Lu et al., 1997). Time-dependent densification in compressive tests has been revealed by Colucci et al. (1997) on two grades of polycarbonate. A review of dilatometric experiments on glassy polymers is found in Naqui and Robinson (1993).

To derive constitutive relations, we model a polymer as a composite material consisting of (i) a network of long chains connected to temporary junctions, (ii) microvoids freezed in the bulk medium, and (iii) clusters of free volume diffusing through the network.

A concept of transient networks has been developed by Green and Tobolsky (1946), Yamamoto (1956), Lodge (1968) and Tanaka and Edwards (1992) for rubbery polymers. A polymer is modeled as a network of long chains connected to temporary junctions. A chain is treated as an incompressible strip which does not resist bending. Mechanical energy of a chain is neglected, and the effect of macro-strains on its free energy is accounted for through the configurational entropy. These hypotheses are acceptable at elevated temperature, when the average distance between junctions is rather large and the contribution of entropy of long chains into the free energy exceeds that of the mechanical energy of long chains and crosslinks.

At the glass transition temperature Θ_g, the average distance between junctions substantially decreases, because of the growth in the number of entanglements. This causes a decrease in the configurational entropy of long chains and an increase in the mechanical energy of physical crosslinks and entanglements. For a glassy polymer, the configurational entropy of long chains is neglected compared to the mechanical energy of crosslinks. Temporary crosslinks are modeled as elastic springs, which break and reform due to thermal motion (Drozdov, 1998).

Two types of free volume (the interstitial free volume and the hole free volume) were introduced by Vrentas and Duda (1977a, 1977b) to describe molecular transport in polymers in the framework of the free volume theory (Turnbull and Cohen, 1961; Cohen and Grest, 1979). Immobile holes model free volume clusters with large potential energies that cannot freely move being thermally activated, whereas interstitial free volume represents "genuine" free volume elements that do not require activation energy for redistribution.

Holes filled with a gas represent flaws (defects) in a bulk material. The gas is thought of as a mixture of air, monomer units, and molecules of plasticizer. Voids are randomly distributed in a polymer and are immobile with respect to the bulk medium. Based on experimental data obtained using positron annihilation lifetime spectroscopy and fluorescent probe studies, we assume that the average radius of a void is so small that the surface tension of gas exceeds macro-stresses in the bulk medium. The average hole radius is about 0.35 nm for polycarbonate (Kluin et al., 1993) and 0.4 nm for polystyrene (Victor and Torkelson, 1988). Since the average distance between two neighboring voids substantially exceeds the characteristic size of a void (the average radius of a cooperatively rearranging region at the glass transition temperature Θ_g varies from 1.5 nm (Rizos and Ngai, 1999) to 7.0 nm (Arndt et al., 1997)), voids are treated as mutually independent, and diffusion of free volume clusters is analyzed in the vicinity of an individual hole. The latter means that phenomena connected with the size of a macroscopic specimen are not taken into account. This assertion is in agreement with observations (McKenna, 1989) which demonstrate that macroscopic diffusion of free volume in and out of the boundaries of samples cannot describe vitrification of amorphous polymers.

Interstitial free volume is modeled as a gas diffusing through a temporary network. Since its volume fraction is small (the total amount of free volume in an amorphous polymer at the glass transition temperature is estimated as 2.5 percent (Robertson, 1979)), a polymer is treated as a dilute solution of free volume in the network. The equilibrium concentration of the solution is determined by macro-pressure in the network. When external loads are applied to a specimen, the absolute value of the pressure grows causing an increase in the equilibrium concentration of free volume. The solution becomes subsaturated, which results in mass flux from voids to the network. The mass flux leads to a decrease in the volume of voids, which is observed as a stress-induced densification of the bulk material.

In tensile tests on compressible specimens, an initial positive jump in the specific volume caused by loads decreases with time because of stress relaxation and shrinkage of voids driven by diffusion of gas. In

Contributed by the Applied Mechanics Division of THE AMERICAN SOCIETY OF MECHANICAL ENGINEERS for publication in the ASME JOURNAL OF APPLIED MECHANICS.
Discussion on the paper should be addressed to the Technical Editor, Professor Lewis T. Wheeler, Department of Mechanical Engineering, University of Houston, Houston, TX 77204-4792, and will be accepted until four months after final publication of the paper itself in the ASME JOURNAL OF APPLIED MECHANICS.
Manuscript received by the ASME Applied Mechanics Division, June 23, 1998; final revision, Mar. 31, 1999. Associate Technical Editor: I. M. Daniel.

 Copyright © 1999 by ASME

Downloaded 04 May 2010 to 171.66.16.27. Redistribution subject to ASME license or copyright; see http://www.asme.org/terms/Terms_Use.cfm

compressive tests, loads engender an initial negative jump in the specific volume. Because of stress relaxation, the stresses decrease, which results in some growth of the specific volume with time. On the other hand, the growth of pressure induces an increase in the equilibrium concentration of free volume in the network and mass flux from voids. When shrinkage of voids driven by diffusive flow dominates volume recovery caused by stress relaxation, the specific volume of a polymer decreases in time.

This qualitative description of densification in glassy polymers is confirmed by experimental data (Colucci et al., 1997) which show that the rate of decrease in the specific volume at tension essentially exceeds that at compression. The objective of this study is to provide a quantitative analysis of this phenomenon. The exposition is organized as follows. In Section 2 we introduce rates of loss and reformation for a transient network. Strain energy density of an amorphous polymer is determined in Section 3 by averaging potential energies of temporary links. Constitutive relations for a network are derived in Section 4. Diffusion of free volume is analyzed in Section 5 using the Plesset-Zwick method (Plesset and Zwick, 1952). Results of numerical simulation are compared with experimental data in uniaxial tests in Section 6. Some concluding remarks are formulated in Section 7.

2 Reformation of a Temporary Network

A temporary network consists of long chains connected by M kinds of links (which model physical and chemical crosslinks and entanglements) with different rates of reformations. Breakage and creation of temporary links are described by the functions $\Xi_m(t, \tau)$ which equal the numbers of links (of the mth kind) per unit volume that have arisen before time τ and exist at time t. The number of permanent links (whose lifetime exceeds the duration of test) per unit volume is denoted by Ξ_0. The concentrations with respect to the initial volume and to the current volume are not distinguished at small strains.

The kinetics of reformation is determined by the relative rates of creation (the ratios of the rates of creation to the initial numbers of links)

$$\gamma_m(\tau) = \frac{1}{\Xi_m^\circ}\frac{\partial \Xi_m}{\partial \tau}(t, \tau)\Big|_{t=\tau}, \quad \Xi_m^\circ = \Xi_m(0, 0), \tag{1}$$

and the relative rates of breakage (the ratios of the numbers of links lost per unit time to the numbers of existing links)

$$\Gamma_{m0}(t) = -\frac{1}{\Xi_m(t, 0)}\frac{\partial \Xi_m}{\partial t}(t, 0),$$

$$\Gamma_m(t, \tau) = -\left[\frac{\partial \Xi_m}{\partial \tau}(t, \tau)\right]^{-1}\frac{\partial^2 \Xi_m}{\partial t \partial \tau}(t, \tau). \tag{2}$$

For nonaging media, the total numbers of links remain unchanged, and the rates of breakage and reformation are time-independent,

$$\Xi_m(t, t) = \Xi_m^\circ, \quad \gamma_m(t) = \Gamma_{m0}(t) = \Gamma_m(t, \tau) = \Gamma_m^\circ. \tag{3}$$

The solutions of Eqs. (2) with the initial conditions (1) and coefficients (3) read

$$\Xi_m(t, 0) = \Xi^\circ \eta_m \exp(-\Gamma_m^\circ t),$$

$$\frac{\partial \Xi_m}{\partial \tau}(t, \tau) = \Xi^\circ \eta_m \Gamma_m^\circ \exp[-\Gamma_m^\circ (t - \tau)], \tag{4}$$

where

$$\Xi^\circ = \Xi_0 + \sum_{m=1}^{M} \Xi_m^\circ, \quad \eta_m = \frac{\Xi_m^\circ}{\Xi^\circ}.$$

3 Strain Energy Density of a Transient Network

Consider a link which arises at time τ and connects junctions A and B. At the instant τ, the link has a small length δ, and it is directed along the unit vector $\bar{l}$. At time t, the junctions occupy points with the radius vectors $\bar{r}_A(t) = \bar{r}_A(\tau) + \bar{u}(t, \tau, \bar{r}_A(\tau))$ and $\bar{r}_B(t) = \bar{r}_B(\tau) + \bar{u}(t, \tau, \bar{r}_B(\tau))$, where $\bar{u}(t, \tau, \bar{r})$ is the displacement vector at point $\bar{r}$ for transition from the actual configuration of the network at time τ to its actual configuration at time t. The end-to-end vectors for the link at times τ and t are calculated as

$$d\bar{r}(\tau) = \delta\bar{l},$$

$$d\bar{r}(t) = \delta\bar{l} + [\bar{u}(t, \tau, \bar{r}_A(\tau) + \delta\bar{l}) - \bar{u}(t, \tau, \bar{r}_A(\tau))].$$

Neglecting terms beyond the first order compared to δ, we find that

$$d\bar{r}(t) = d\bar{r}(\tau) \cdot [\hat{I} + \bar{\nabla}(\tau)\bar{u}(t, \tau)], \tag{5}$$

where $\bar{\nabla}(t)$ is the gradient operator in the actual configuration at time t, $\hat{I}$ is the unit tensor, the dot stands for inner product, and the argument $\bar{r}_A$ is omitted. The length of a link ds is given by $ds^2 = d\bar{r} \cdot d\bar{r}$. Substitution of Eq. (5) into this equality results in

$$ds^2(t) = ds^2(\tau) + 2\delta^2 \bar{l} \cdot \hat{\mathscr{E}}(t, \tau) \cdot \bar{l},$$

$$\hat{\mathscr{E}}(t, \tau) = \tfrac{1}{2}[\bar{\nabla}(\tau)\bar{u}(t, \tau) + (\bar{\nabla}(\tau)\bar{u}(t, \tau))^\top],$$

where $\top$ denotes transpose and terms beyond the second order compared to δ are omitted. Since the natural (stress-free) configuration of a temporary link created at instant τ coincides with the actual configuration of the network, the nominal strain for a link is given by

$$\epsilon_*(t, \tau) = \frac{ds^2(t) - ds^2(\tau)}{2ds^2(\tau)} = \bar{l} \cdot \hat{\mathscr{E}}(t, \tau) \cdot \bar{l}. \tag{6}$$

The potential energy of a link (treated as a linear elastic spring) reads

$$w = \tfrac{1}{2}\mu\epsilon_*^2, \tag{7}$$

where μ is the rigidity (the same for all kinds of links).

Denote by $\bar{e}_k$ the eigenvectors and by $\mathscr{E}_k$ the eigenvalues of the symmetrical tensor $\hat{\mathscr{E}}$,

$$\hat{\mathscr{E}} = \mathscr{E}_1\bar{e}_1\bar{e}_1 + \mathscr{E}_2\bar{e}_2\bar{e}_2 + \mathscr{E}_3\bar{e}_3\bar{e}_3. \tag{8}$$

The position of the unit vector $\bar{l}$ with respect to the vectors $\bar{e}_k$ is determined by the spherical angles φ and ϑ,

$$\bar{l} = \cos\vartheta\bar{e}_1 + \sin\vartheta(\cos\varphi\bar{e}_2 + \sin\vartheta\bar{e}_3). \tag{9}$$

For isotropic networks with the spatially uniform distribution of end-to-end vectors, the probability density for the vector $\bar{l}$ reads

$$f(\vartheta, \varphi) = \frac{1}{4\pi}\sin\vartheta. \tag{10}$$

The average mechanical energy of a link $\langle w\rangle$ is given by

$$\langle w\rangle = \int_0^\pi d\vartheta \int_0^{2\pi} wf d\varphi. \tag{11}$$

Substitution of expressions (6) to (10) into Eq. (11) results in

$$\langle w\rangle = \frac{\mu}{8\pi}\int_0^\pi \sin\vartheta d\vartheta \int_0^{2\pi} [\mathscr{E}_1\cos^2\vartheta + \sin^2\vartheta(\mathscr{E}_2\cos^2\varphi + \mathscr{E}_3\sin^2\varphi)]^2 d\varphi = \frac{\mu}{30}\left(\frac{5}{3}\mathscr{E}^2 + 2\hat{\mathscr{E}}_d{:}\hat{\mathscr{E}}_d\right), \tag{12}$$

where $\mathscr{E}$ is the first invariant and $\hat{\mathscr{E}}_d$ is the deviatoric part of the strain tensor $\hat{\mathscr{E}}$.

The strain energy density of a polymer $W(t)$ equals the sum of

Downloaded 04 May 2010 to 171.66.16.27. Redistribution subject to ASME license or copyright; see http://www.asme.org/terms/Terms_Use.cfm

the mechanical energies of individual links $W_1(t)$ and the energy of their interaction $W_2(t)$. The specific energy (per unit volume) of initial links of the mth kind is calculated as $w_m(t, 0) = \Xi_m(t, 0)\langle w(t, 0)\rangle$, and the specific energy (per unit volume) of links of the mth kind created within the interval $[\tau, \tau + d\tau]$ is given by

$$dw_m(t, \tau) = \frac{\partial \Xi_m}{\partial \tau}(t, \tau)\langle w(t, \tau)\rangle d\tau.$$

Summing these expressions for links of various kinds, we find the specific mechanical energy of temporary links

$$W_1(t) = \Xi_0\langle w(t, 0)\rangle + \sum_{m=1}^{M}\left[\Xi_m(t, 0)\langle w(t, 0)\rangle + \int_0^t \frac{\partial \Xi_m}{\partial \tau}(t, \tau)\langle w(t, \tau)\rangle d\tau\right].$$

The specific energy of interaction between crosslinks depends on the first invariant $\mathcal{E}_0(t)$ of the strain tensor $\hat{\mathcal{E}}_0(t)$ for transition from the initial configuration of the network to its actual configuration (Tanaka and Edwards, 1992). For the linear response, this energy reads $W_2(t) = \frac{1}{2}K_0[\mathcal{E}_0(t)]^2$, where K_0 is the bulk modulus for the network. Summing the potential energy of links existing at time t and the energy of their interaction, using Eqs. (4), and taking into account that $\hat{\mathcal{E}}(t,\tau) = \hat{\mathcal{E}}_0(t) - \hat{\mathcal{E}}_0(\tau)$, we arrive at the strain energy density (per unit volume) of a glassy polymer

$$W(t) = G\{[1 - \sum_{m=1}^{M}\eta_m(1 - \exp(-\Gamma_m^\circ t))] \times [\tfrac{5}{6}(\mathcal{E}_0(t))^2 + \hat{\mathcal{E}}_{0d}(t):\hat{\mathcal{E}}_{0d}(t)] + \sum_{m=1}^{M}\eta_m\Gamma_m^\circ\int_0^t \exp(-\Gamma_m^\circ(t-\tau))[\tfrac{5}{6}(\mathcal{E}_0(t) - \mathcal{E}_0(\tau))^2 + (\hat{\mathcal{E}}_{0d}(t) - \hat{\mathcal{E}}_{0d}(\tau)):(\hat{\mathcal{E}}_{0d}(t) - \hat{\mathcal{E}}_{0d}(\tau))]d\tau\} + \tfrac{1}{2}K_0[\mathcal{E}_0(t)]^2, \quad (13)$$

where $G = \mu\Xi^\circ/15$ is the shear modulus for the network, and $\hat{\mathcal{E}}_{0d}(t)$ is the deviatoric part of the strain tensor $\hat{\mathcal{E}}_0(t)$.

4 Constitutive Relations

Equation (13) determines the specific mechanical energy $W(t)$ in terms of the strain tensor for the network $\hat{\mathcal{E}}_0(t)$, but not in terms of the strain tensor for the medium $\hat{\epsilon}(t)$. Assuming mass transfer across the boundaries of voids not to change their shapes, we find that the deviatoric parts $\hat{e}(t)$ and $\hat{\mathcal{E}}_{0d}(t)$ of the strain tensors $\hat{\epsilon}(t)$ and $\hat{\mathcal{E}}_0(t)$ coincide,

$$\hat{e}(t) = \hat{\mathcal{E}}_{0d}(t). \quad (14)$$

Referring to conventional theories of mixtures (Green and Naghdi, 1995), we suppose that the volume strain $\epsilon(t)$ for transition from the initial configuration of the bulk medium to its actual configuration equals the sum of the volume strain for the network $\mathcal{E}_0(t)$ and the volume strain for voids $\omega(t)$,

$$\epsilon(t) = \mathcal{E}_0(t) + \omega(t). \quad (15)$$

Since the volume fraction of voids in a polymeric network Λ is small, the function $\omega(t)$ is calculated as

$$\omega(t) = \Lambda\frac{V(t) - V_0}{V_0}, \quad (16)$$

where V_0 and $V(t)$ are the average volumes of a void at the initial and current times.

The first invariant σ and the deviatoric part $\hat{s}$ of the Cauchy stress tensor $\hat{\sigma}$ are determined by the formulas

$$\sigma(t) = 3\frac{\partial W(t)}{\partial \epsilon(t)}, \quad \hat{s}(t) = \frac{\partial W(t)}{\partial \hat{e}(t)}. \quad (17)$$

Substituting expression (13) into Eqs. (17) and using Eqs. (14) and (15), we arrive at the constitutive equations

$$\sigma(t) = 3K[\epsilon(t) - \omega(t)] - 5G\sum_{m=1}^{M}\eta_m\Gamma_m^\circ\int_0^t \exp(-\Gamma_m^\circ(t-\tau)) \times [\epsilon(\tau) - \omega(\tau)]d\tau,$$

$$\hat{s}(t) = 2G[\hat{e}(t) - \sum_{m=1}^{M}\eta_m\Gamma_m^\circ\int_0^t \exp(-\Gamma_m^\circ(t-\tau))\hat{e}(\tau)d\tau], \quad (18)$$

where $K = K_0 + 5G/3$ is the bulk modulus for a polymer.

5 Diffusion of Free Volume in a Network

We assume that voids are mutually independent and analyze diffusion of gas (interstitial free volume) in the vicinity of a hole (a spherical opening with the current radius R) in an infinite space. The mass concentration of interstitial free volume χ at time t at point with a polar radius r satisfies the diffusion equation

$$\frac{\partial \chi}{\partial t} = \frac{D}{r^2}\frac{\partial}{\partial r}\left(r^2\frac{\partial \chi}{\partial r}\right) \quad (19)$$

with the initial and boundary conditions

$$\chi(0, r) = \tilde{\chi}_0, \quad \chi(t, \infty) = \tilde{\chi}_0, \quad \chi(t, R(t)) = \tilde{\chi}(t). \quad (20)$$

Here D is a constant diffusivity, and $\tilde{\chi}_0$ and $\tilde{\chi}(t)$ are the equilibrium concentrations of gas at the initial and current instants. The quantity $\tilde{\chi}$ depends on the macro-pressure P only,

$$\tilde{\chi}(t) = \tilde{\chi}_0 + \Psi_0(P(t)), \quad (21)$$

where Ψ_0 is a material function, which is positive for any value of P (either positive or negative). The macro-pressure P is used in Eq. (21), because pressure at any point of a viscoelastic space surrounding a spherical cavity coincides with the pressure at infinity.

Hypothesis (21) means that any volume deformation of a bulk medium activates a polymeric network and causes an increase in the equilibrium concentration of free volume. This contradicts some simplified constitutive models based on the free-volume theory, which presume that hydrostatic tension decreases relaxation times, whereas hydrostatic compression leads to their growth (see Drozdov (1998) for references). Assumption (21) is confirmed fairly well by observations for poly(vinyl chloride) which demonstrate that (i) relaxation times decrease with the growth of longitudinal load both in tensile and compressive tests (Dean et al., 1995) and (ii) retardation times for densified specimens exceed those for nondensified samples (Bree et al., 1974). To explain these results, we refer to Struik (1997), who states that subyield strains in the vicinity of a hole (arised at macro-tension, as well as at macro-compression) cause fracture of the van der Waals bonds and activate the micro-cavitation mechanism in the same way as it is described by conventional concepts of toughening (Evans et al., 1986). The necessity to account for micro-voiding mechanisms in the subyield region is revealed by experimental data obtained using positron annihilation lifetime spectroscopy on stretched polycarbonate specimens (Ruan et al., 1992). Observations show that the relative increase of the hole volume exceeds that for the bulk volume by ten times, which means that a large amount of free

Downloaded 04 May 2010 to 171.66.16.27. Redistribution subject to ASME license or copyright; see http://www.asme.org/terms/Terms_Use.cfm

volume is produced even at moderate strains of two to three percent.

To determine the radius $R(t)$, we treat deformation of gas in the opening as adiabatic, which implies that the mass density ρ depends on the gas pressure p only: $\rho = \Phi(p)$, where Φ is a given function. The quantity p is determined by the Laplace law $p = 2\Sigma R^{-1}$, where Σ is a constant surface tension. According to Fick's law, the rate of changes in mass of gas in a spherical void $\mathcal{M}(t) = \frac{4}{3}\pi\rho(t)R^3(t)$ equals the mass flux per unit time across the boundary of the void,

$$\frac{d\mathcal{M}}{dt}(t) = 4\pi DR^2(t)\frac{\partial\chi}{\partial r}(t, R(t)),$$

which results in the formula

$$\frac{\partial\chi}{\partial r}(t, R(t)) = \frac{1}{3DR^2(t)}\frac{d}{dt}\left[R^3(t)\Phi\left(\frac{2\Sigma}{R(t)}\right)\right]. \quad (22)$$

Introducing the variable $\xi = \frac{1}{3}[r^3 - R^3(t)]$, we present Eq. (19) as

$$\frac{\partial\chi}{\partial t} = D\frac{\partial}{\partial\xi}\left(r^4\frac{\partial\chi}{\partial\xi}\right). \quad (23)$$

We set

$$\chi(t, \xi) - \tilde{\chi}_0 = \frac{\partial\theta}{\partial\xi}(t, \xi), \quad (24)$$

where $\theta(t, r)$ is a new unknown function that satisfies the initial condition

$$\theta(0, \xi) = 0, \quad (25)$$

substitute expression (24) into Eq. (23) and integrate the result with respect to ξ,

$$\frac{\partial\theta}{\partial t} = Dr^4\frac{\partial^2\theta}{\partial\xi^2} + \psi(t), \quad (26)$$

where $\psi(t)$ is a function of time. Since $\theta(t, \xi)$ is determined by Eq. (24) up to an arbitrary function of time t, we set $\psi(t) = 0$ in Eq. (26). Introducing the variable

$$\tau = \int_0^t R^4(s)ds, \quad (27)$$

we present Eq. (26) as

$$\frac{\partial\theta}{\partial\tau} = D\left[1 + \frac{3\xi}{R^3(t)}\right]^{4/3}\frac{\partial\theta}{\partial\xi^2}. \quad (28)$$

Bearing in mind that

$$\frac{\partial\chi}{\partial r}(t, R(t)) = R^2(t)\frac{\partial^2\theta}{\partial\xi^2}(t, 0),$$

we write boundary conditions (20) and (22) as follows:

$$\frac{\partial^2\theta}{\partial\xi^2}(t, 0) = q(t), \quad \frac{\partial\theta}{\partial\xi}(t, \infty) = 0, \quad (29)$$

where

$$q(t) = \frac{1}{3DR^4(t)}\frac{d}{dt}\left[R^3(t)\Phi\left(\frac{2\Sigma}{R(t)}\right)\right]. \quad (30)$$

The Plesset-Zwick method is based on the hypothesis that the unknown function θ substantially changes only in the region $0 \le \xi \ll R^3(t)$. This allows the second term in the brackets in Eq. (28) to be neglected, which results in

$$\frac{\partial\theta}{\partial\tau} = D\frac{\partial\theta}{\partial\xi^2}. \quad (31)$$

Equation (31) with initial condition (25) and boundary conditions (29) is solved by the Laplace transform method. Omitting technical details (Plesset and Zwick, 1952), we find that ($q_*(\tau) = q(t(\tau))$)

$$\frac{\partial\theta}{\partial\xi}(\tau, \xi) = -\sqrt{\frac{D}{\pi}}\int_0^\tau \frac{q_*(s)}{\sqrt{\tau - s}}\exp\left[-\frac{\xi^2}{4D(\tau - s)}\right]ds. \quad (32)$$

Combining Eqs. (24) and (32), setting $\xi = 0$ in the resulting equality and using Eq. (20), we arrive at the formula

$$\tilde{\chi}_*(\tau) - \tilde{\chi}_0 = -\sqrt{\frac{D}{\pi}}\int_0^\tau \frac{q_*(s)}{\sqrt{\tau - s}}ds,$$

where $\tilde{\chi}_*(\tau) = \tilde{\chi}(t(\tau))$. The solution of the Abel equation reads

$$q_*(\tau) = -\frac{1}{\sqrt{\pi D}}\frac{d}{d\tau}\int_0^\tau \frac{\tilde{\chi}_*(s) - \tilde{\chi}_0}{\sqrt{\tau - s}}ds. \quad (33)$$

We substitute Eqs. (21) and (30) into Eq. (33), integrate the resulting equality from 0 to τ, take into account that $P = -\sigma/3$, and find that

$$R_*^3(\tau)\Phi\left(\frac{2\Sigma}{R_*(\tau)}\right) = R_0^3\Phi\left(\frac{2\Sigma}{R_0}\right) - 3\sqrt{\frac{D}{\pi}}\int_0^\tau \frac{\Psi(\sigma_*(s))ds}{\sqrt{\tau - s}}, \quad (34)$$

where $R_*(\tau) = R(t(\tau))$, $\sigma_*(\tau) = \sigma(t(\tau))$, $\Psi(\sigma) = \Psi_0(-\sigma/3)$, and R_0 is the initial radius of a void. For a perfect gas with $\Phi(p) = \rho_0(p/p_0)^{1/\kappa}$, where ρ_0 is the initial mass density, p_0 is the initial pressure in a void, and κ is the ratio of the specific heat at a fixed pressure to that at a fixed volume, Eq. (34) reads

$$R_*(\tau) = R_0\left[1 - \frac{3}{\rho_0 R_0^3}\sqrt{\frac{D}{\pi}}\int_0^\tau \frac{\Psi(\sigma_*(s))ds}{\sqrt{\tau - s}}\right]^{\kappa/(3\kappa-1)}.$$

We set $s = \tau(s_1)$, return to the absolute time t using Eq. (27), and obtain

$$R(t) = R_0\left\{1 - \frac{3}{\rho_0 R_0^3}\sqrt{\frac{D}{\pi}}\int_0^t \Psi(\sigma(s_1))R^4(s_1)\times\left[\int_{s_1}^t R^4(s)ds\right]^{-1/2}ds_1\right\}^{\kappa/(3\kappa-1)}.$$

Integrating by parts and introducing the dimensionless variable

$$T(t) = \int_0^t\left[\frac{R(s)}{R_0}\right]^4 ds,$$

we arrive at the nonlinear integro-differential equation

$$\frac{dT}{dt}(t) = \left\{1 - \frac{6R_0}{\rho_0}\sqrt{\frac{D}{\pi}}\left[\Psi(\sigma(0))\sqrt{T(t)} + \int_0^t \frac{d\Psi}{d\sigma}(\sigma(s))\frac{d\sigma}{ds}(s)\sqrt{T(t) - T(s)}ds\right]\right\}^{4\kappa/(3\kappa-1)} \quad (35)$$

with the initial condition $T(0) = 0$. For the function $\Psi(\sigma) = A|\sigma|$, where A is an adjustable parameter, Eq. (35) reads

Downloaded 04 May 2010 to 171.66.16.27. Redistribution subject to ASME license or copyright; see http://www.asme.org/terms/Terms_Use.cfm

Table 1 Adjustable parameters Γ_m s^{-1} and η_m for polycarbonate CP PC at room temperature

	η_m					
Γ_m	$\epsilon_1 = 0.01$	$\epsilon_1 = 0.02$	$\epsilon_1 = 0.03$	$\epsilon_1 = -0.015$	$\epsilon_1 = -0.02$	$\epsilon_1 = -0.025$
0.0001	0.0526	0.0538	0.0391	0.0195	0.0496	0.0366
0.0010	0.0396	0.0306	0.0414	0.0537	0.0428	0.0586
0.0100	0.0243	0.0405	0.0356	0.0443	0.0496	0.0520
0.1000	0.0212	0.0249	0.0407	0.0287	0.0310	0.0296
1.0000	0.0221	0.0076	0.0254	0.0021	0.0224	0.0160

$$\frac{dT}{dt}(t) = \left\{1 - L\left[|\sigma(0)|\sqrt{T(t)} + \int_0^t \operatorname{sign}\sigma(s)\frac{d\sigma}{ds}(s)\sqrt{T(t) - T(s)}ds\right]\right\}^{4\kappa/(3\kappa-1)}, \quad (36)$$

where $L = 6AR_0\sqrt{D}/(\sqrt{\pi}\,\rho_0)$. It follows from Eq. (23) and (36) that

$$\epsilon(t) = \Lambda\left\langle\left\{1 - L\left[|\sigma(0)|\sqrt{T(t)} + \int_0^t \operatorname{sign}\sigma(s) \times \frac{d\sigma}{ds}(s)\sqrt{T(t) - T(s)}ds\right]\right\}^{3\kappa/(3\kappa-1)} - 1\right\rangle. \quad (37)$$

We assume the heat capacity for the hole free volume to coincide with that for air: $\kappa = 1.4$. In this case, constitutive Eqs. (18), (36), and (37) contain only two additional parameters, L and Λ, compared to conventional stress-strain relations in linear viscoelasticity. To determine these parameters, we analyze uniaxial extension of a specimen.

6 Uniaxial Extension of a Bar

We introduce Cartesian coordinates with unit vectors $\bar{e}_i$ and present the strain tensor $\hat{\epsilon}$ in the form

$$\hat{\epsilon}(t) = \epsilon_1(t)\bar{e}_1\bar{e}_1 + \epsilon_2(t)(\bar{e}_2\bar{e}_2 + \bar{e}_3\bar{e}_3), \quad (38)$$

where ϵ_1 is the longitudinal strain, and ϵ_2 is the lateral strain. Substituting expression (38) into Eqs. (18) and using the boundary condition in stresses on the lateral surface of the bar, we find the longitudinal stress

$$\sigma_1(t) = 2G\{[1 + \nu(t)]\epsilon_1(t) - \sum_{m=1}^{M}\eta_m\Gamma_m^\circ\int_0^t \exp[-\Gamma_m^\circ(t-\tau)] \times [1 + \nu(\tau)]\epsilon_1(\tau)d\tau\}, \quad (39)$$

where $\nu = -\epsilon_2/\epsilon_1$ is Poisson's ratio. Since σ_1 is the only nonzero component of the stress tensor, we write $\sigma_1(t) = \sigma(t)$.

To determine adjustable parameters of the model, we use observations in relaxation tests for polycarbonate at room temperature. For a detailed description of the experimental procedure, see Colucci et al. (1997).

Given M and Γ_m°, we determine the parameters η_m which ensure the best fit of the longitudinal stress $\sigma_1(t)$ by using the least squares method. Poisson's ratio $\nu(t)$ in Eq. (39) is calculated using

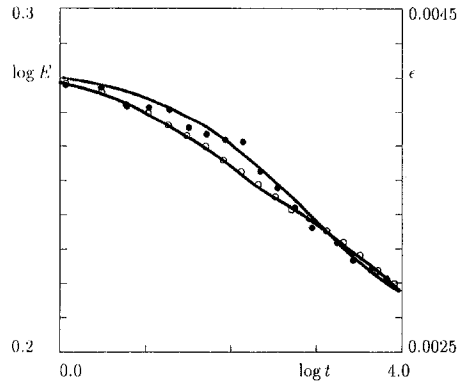


Fig. 2 The Young modulus E GPa (unfilled circles) and the volume strain ϵ (filled circles) versus time t s for uniaxial extension of polycarbonate CP PC at room temperature. Circles: experimental data obtained by Colucci et al. (1997) at $\epsilon_1 = 0.02$. Solid lines: predictions of the model with $K = 3.0712$ GPa, $G = 0.6857$ GPa, $L = 0.6529$ GPa$^{-1} \cdot$ s$^{-1/2}$, log $\Lambda = -3.0$, and the adjustable parameters η_m and Γ_m listed in Table 1.

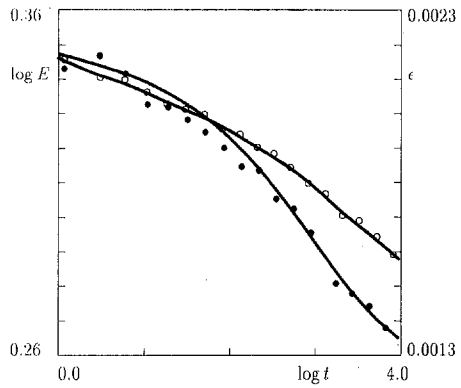


Fig. 1 The Young modulus E GPa (unfilled circles) and the volume strain ϵ (filled circles) versus time t s for uniaxial extension of polycarbonate CP PC at room temperature. Circles: experimental data obtained by Colucci et al. (1997) at $\epsilon_1 = 0.01$. Solid lines: predictions of the model with $K = 3.3898$ GPa, $G = 0.8124$ GPa, $L = 1.1077$ GPa$^{-1} \cdot$ s$^{-1/2}$, log $\Lambda = -3.14$, and the adjustable parameters η_m and Γ_m listed in Table 1.

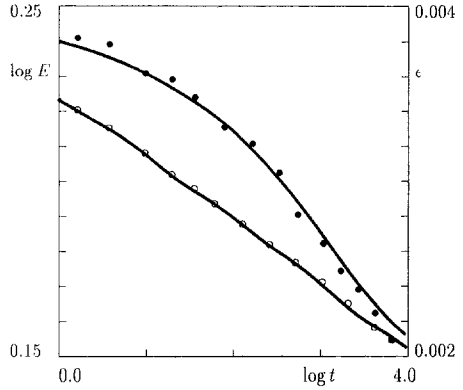


Fig. 3 The Young modulus E GPa (unfilled circles) and the volume strain ϵ (filled circles) versus time t s for uniaxial extension of polycarbonate CP PC at room temperature. Circles: experimental data obtained by Colucci et al. (1997) at $\epsilon_1 = 0.03$. Solid lines: predictions of the model with $K = 4.3760$ GPa, $G = 0.5950$ GPa, $L = 0.3904$ GPa$^{-1} \cdot$ s$^{-1/2}$, log $\Lambda = -2.85$, and the adjustable parameters η_m and Γ_m listed in Table 1.

Downloaded 04 May 2010 to 171.66.16.27. Redistribution subject to ASME license or copyright; see http://www.asme.org/terms/Terms_Use.cfm

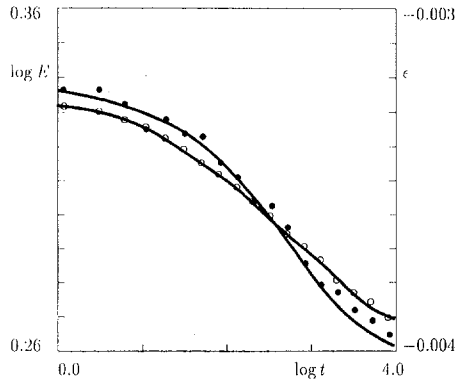


Fig. 4 The Young modulus E GPa (unfilled circles) and the volume strain ϵ (filled circles) versus time t s for uniaxial compression of polycarbonate CP PC at room temperature. Circles: experimental data obtained by Colucci et al. (1997) at $\epsilon_1 = -0.015$. Solid lines: predictions of the model with $K = 3.3644$ GPa, $G = 0.9290$ GPa, $L = 0.7741$ GPa$^{-1} \cdot$ s$^{-1/2}$, log $\Lambda = -2.95$, and the adjustable parameters η_m and Γ_m listed in Table 1.

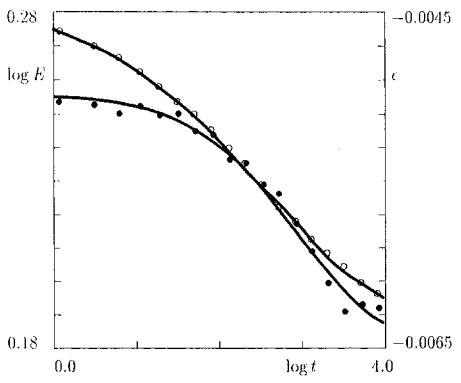


Fig. 6 The Young modulus E GPa (unfilled circles) and the volume strain ϵ (filled circles) versus time t s for uniaxial compression of polycarbonate CP PC at room temperature. Circles: experimental data obtained by Colucci et al. (1997) at $\epsilon_1 = -0.025$. Solid lines: predictions of the model with $K = 3.1986$ GPa, $G = 0.6817$ GPa, $L = 0.5237$ GPa$^{-1} \cdot$ s$^{-1/2}$, log $\Lambda = -2.67$, and the adjustable parameters η_m and Γ_m listed in Table 1.

data for the volume strain $\epsilon(t)$. It follows from Eqs. (18) that the function $F(t) = \epsilon(t) - \omega(t)$ is determined as

$$F(t) = \frac{1}{3K}\left[\sigma_1(t) + 5G \sum_{m=1}^{M} \eta_m F_m(t)\right]. \tag{40}$$

Here the bulk modulus K is expressed in terms of the shear modulus G and the initial Poisson ratio $\nu(0)$ by the conventional formula, and the functions

$$F_m(t) = \Gamma_m^\circ \int_0^t \exp[-\Gamma_m^\circ(t - \tau)]F(\tau)d\tau$$

obey the ordinary differential equations

$$\frac{dF_m}{dt}(t) = \Gamma_m^\circ[F(t) - F_m(t)], \quad F_m(0) = 0. \tag{41}$$

The adjustable parameters L and Λ are determined from the condition of the best fit of the curves $\omega = \omega(t)$. The function $\omega(t)$ is found by the integration of Eqs. (36) and (37), where the parameter L is chosen to ensure that the slope of the graph log ω(log t) coincides with that calculated from Eqs. (40) and (41). Afterward, the graph log ω(log t) is shifted along the ordinate axis, and the parameter Λ is obtained from the condition of the best approximation of the experimental curve.

To verify the model, we calculate the volume strain $\epsilon(t)$ from Eqs. (36) and (37) with the adjustable parameters found according to this algorithm and compare results of numerical simulation with observations. Figures 1 to 6 demonstrate fair agreement between predictions of the model and experimental data in tensile and compressive tests at various longitudinal strains. Adjustable parameters in the constitutive equations demonstrate physically plausible trends with an increase in the longitudinal strain ϵ_1: (i) the moduli K and G decreases with $|\epsilon_1|$, which is typical of fitting observations in the region of weakly nonlinear response by linear stress-strain relations; (ii) the parameter L also decreases with $|\epsilon_1|$, since the parameter A becomes smaller (at large values of P, the function $\Psi_0(P)$ in Eq. (21) approaches its limiting value); (iii) the shape of the relaxation spectrum (determined by the coefficients η_m) changes, and the mean rate of reformation increases.

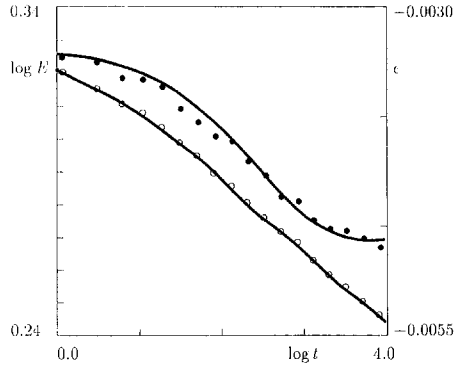


Fig. 5 The Young modulus E GPa (unfilled circles) and the volume strain ϵ (filled circles) versus time t s for uniaxial compression of polycarbonate CP PC at room temperature. Circles: experimental data obtained by Colucci et al. (1997) at $\epsilon_1 = -0.02$. Solid lines: predictions of the model with $K = 3.3991$ GPa, $G = 0.7641$ GPa, $L = 1.0550$ GPa$^{-1} \cdot$ s$^{-1/2}$, log $\Lambda = -2.855$, and the adjustable parameters η_m and Γ_m listed in Table 1.

7 Concluding Remarks

Constitutive relations are derived for amorphous glassy polymers at isothermal loading with small strains. A polymer is modeled as a composite material consisting of a temporary network of long chains, voids, and interstitial free volume dissolved in the network. Nonlinear integro-differential Eqs. (36) and (37) are developed for dilatation driven by mass transfer. Stress-strain relations (18), (36), and (37) contain two additional adjustable parameters compared to conventional models in linear viscoelasticity. These parameters are found by fitting experimental data for polycarbonate. Fair agreement is demonstrated between observations and results of numerical simulation.

Acknowledgment

The research was supported by the Israeli Ministry of Science through grants 9641-1-96 and 1202-1-98.

References

Arndt, M., Stannarius, R., Groothues, H., Hempel, E., and Kremer, F., 1997, "Length Scale of Cooperativity in the Dynamic Glass Transition," *Physical Review Letters,* Vol. 79, pp. 2077–2080.

Benham, P. B., and McCammond, D., 1971, "Studies of Creep and Contraction Ratio in Thermoplastics," *Plastics and Polymer,* Vol. 4, pp. 130–136.

Bree, H. W., Heijboer, J., Struik, L. C. E., and Tak, A. G. M., 1974, "The Effect of Densification on the Mechanical Properties of Amorphous Glassy Polymers," *Journal of Polymer Science: Polymer Physics Edition,* Vol. 12, pp. 1857–1864.

Cohen, M. H., and Grest, G. S., 1979, "Liquid-Glass Transition: A Free-Volume Approach," *Physical Review B,* Vol. 20, pp. 1077–1098.

Downloaded 04 May 2010 to 171.66.16.27. Redistribution subject to ASME license or copyright; see http://www.asme.org/terms/Terms_Use.cfm

Colucci, D. M., O'Connell, P. A., and McKenna, G. B., 1997, "Stress Relaxation Experiments in Polycarbonate: A Comparison of Volume Changes for Two Commercial Grades," *Polymer Engineering and Science,* Vol. 37, pp. 1469–1474.

Dean, G. D., Tomlins, P. E., and Read, B. E., 1995, "A Model for Nonlinear Creep and Physical Aging in Poly(vinyl chloride)," *Polymer Engineering and Science,* Vol. 35, pp. 1282–1289.

Delin, M., Rychwalski, R. W., Kubat, J., Kubat, M. J., Bertilsson, H., and Klason, C., 1994, "Volume Changes During Flow of Solid Polymers," *Journal of Non-Crystalline Solids,* Vol. 172–174, pp. 779–785.

Drozdov, A. D., 1998, *Mechanics of Viscoelastic Solids,* Wiley, Chichester, UK.

Evans, A. G., Ahmad, Z. B., Gilbert, D. G., and Beaumont, P. W. R., 1986, "Mechanisms of Toughening in Rubber Toughened Polymers," *Acta Metallurgica,* Vol. 34, pp. 79–87.

Green, A. E., and Naghdi, P. M., 1995, "A Unified Procedure for Construction of Theories of Deformable Media. 3. Mixtures of Interacting Continua," *Proceeding of the Royal Society of London,* Vol. A448, pp. 379–388.

Green, M. S., and Tobolsky, A. V., 1946, "A New Approach to the Theory of Relaxing Polymeric Media," *Journal of Chemical Physics,* Vol. 14, pp. 80–92.

Kluin, J.-E., Yu, Z., Vleeshouwers, S., McGervey, J. D., Jamieson, A. M., Simha, R., and Sommer, K., 1993, "Ortho-Positronium Lifetime Studies of Free Volume in Polycarbonates of Different Structures: Influence of Hole Size Distribution," *Macromolecules,* Vol. 26, pp. 1853–1861.

Lodge, A. S., 1968, "Constitutive Equations from Molecular Network Theories for Polymer Solutions," *Rheologica Acta,* Vol. 7, pp. 379–392.

Lu, H., Zhang, X., and Knauss, W. G., 1997, "Uniaxial, Shear, and Poisson Relaxation and Their Conversion to Bulk Relaxation: Studies on Poly(methyl methacrylate)," *Polymer Engineering and Science,* Vol. 37, pp. 1053–1064.

McKenna, G. B., 1989, "Glass Formation and Glassy Behavior," *Comprehensive Polymer Science,* Vol. 2, C. Booth and C. Price, eds., pp. 311–362.

Merriman, H. G., and Caruthers, J. M., 1981, "Nonlinear Stress Relaxation of a Styrene-Butadiene Random Copolymer," *Journal of Polymer Science: Polymer Physics Edition,* Vol. 19, pp. 1055–1071.

Naqui, S. I., and Robinson, I. M., 1993, "Tensile Dilatometric Studies of Deformation in Polymeric Materials and Their Composites," *Journal of Materials Science,* Vol. 28, pp. 1421–1429.

Plesset, M. S., and Zwick, S. A., 1952, "A Non-Steady Heat Diffusion Problem with Spherical Symmetry," *Journal of Applied Physics,* Vol. 23, pp. 95–98.

Rizos, A. K., and Ngai, K. L., 1999, "Experimental Determination of the Cooperativity Length Scale of a Glass-Forming Liquid Near the Glass Transition Temperature," *Physical Review E,* Vol. 59, pp. 612–617.

Robertson, R. E., 1979, "Effect of Free Volume Fluctuations on Polymer Relaxation in the Glassy State. 2. Calculated Results," *Journal of Polymer Science: Polymer Physics Edition,* Vol. 17, pp. 597–613.

Ruan, M. Y., Moaddel, H., Jamieson, A. M., Simha, R., and McGervey, J. D., 1992, "Positron Annihilation Lifetime Studies of Free Volume Changes in Polycarbonate Under Static Tensile Deformation," *Macromolecules,* Vol. 25, pp. 2407–2411.

Struik, L. C. E., 1997, "On the Rejuvenation of Physically Aged Polymers by Mechanical Deformation," *Polymer,* Vol. 38, pp. 4053–4057.

Tanaka, F., and Edwards, S. F., 1992, "Viscoelastic Properties of Physically Cross-Linked Networks. Transient Network Theory," *Macromolecules,* Vol. 25, pp. 1516–1523.

Turnbull, D., and Cohen, M. H., 1961, "Free-Volume Model of the Amorphous Phase: Glass Transition," *The Journal of Chemical Physics,* Vol. 34, pp. 120–125.

Victor, J. G., and Torkelson, J. M., 1988, "Photochromic and Fluorescent Probe Studies in Glassy Polymer Matrices. 3. Effects of Physical Aging and Molar Weight on the Size Distribution of Local Free Volume in Polystyrene," *Macromolecules,* Vol. 21, pp. 3490–3497.

Vrentas, J. S., and Duda, J. L., 1977a, "Diffusion in Polymer-Solvent Systems. I. Reexamination of the Free-Volume Theory," *Journal of Polymer Science: Polymer Physics Edition,* Vol. 15, pp. 403–416.

Vrentas, J. S., and Duda, J. L., 1977b, "Diffusion in Polymer-Solvent Systems. 2. A Predictive Theory for the Dependence of Diffusion Coefficients on Temperature, Concentration, and Molecular Weight," *Journal of Polymer Science: Polymer Physics Edition,* Vol. 15, pp. 417–439.

Yamamoto, M., 1956, "The Visco-Elastic Properties of Network Structure. I. General Formalism," *Journal of Physical Society of Japan,* Vol. 11, pp. 413–421.

Downloaded 04 May 2010 to 171.66.16.27. Redistribution subject to ASME license or copyright; see http://www.asme.org/terms/Terms_Use.cfm

Anisotropic Effective Moduli of Cracked Short-Fiber Reinforced Composites

R. S. Feltman

M. H. Santare
Mem. ASME

Department of Mechanical Engineering,
University of Delaware,
Newark, DE 19716

A model is presented to analyze the effect of fiber fracture on the anisotropic elastic properties of short-fiber reinforced composite materials. The effective moduli of the material are modeled using a self-consistent scheme which includes the calculated energy dissipated through the opening of a crack in an arbitrarily oriented elliptical inclusion. The model is an extension of previous works which have modeled isotropic properties of short-fiber reinforced composites with fiber breakage and anisotropic properties of monolithic materials with microcracks. Two-dimensional planar composite systems are considered. The model allows for the calculation of moduli under varying degrees of fiber alignment and damage orientation. In the results, both aligned fiber systems and randomly oriented fiber systems with damage-induced anisotropy are examined.

Introduction

Microcracking in brittle materials and fiber breakage in fiber-reinforced composite materials are common modes of damage in these materials. At subcritical loading levels, the cracks can cause a significant degradation in the elastic properties of the material. As the loading progresses, the number of cracks increases and eventually these cracks coalesce into macrocracks, leading to catastrophic failure. It is thus important to understand the behavior of composite and monolithic brittle materials under the effects of microcracking.

Models to address the effect of cracking on the effective moduli of monolithic materials have been developed by a number of researchers. Budianski and O'Connell (1976) developed a self-consistent scheme for randomly oriented cracks surrounded by an infinitely extended effective medium. Gottesman et al. (1980) developed a self-consistent material model containing a perfectly aligned array of cracks. Horii and Nemat-Nasser (1983) modeled a material with random crack orientations, introducing anisotropy through friction along the crack surfaces. The self-consistent schemes used in Budianski and O'Connell (1976), Gottesman et al. (1980), and Horii and Nemat-Nasser (1983) overestimate the effect of large crack concentrations on the effective material moduli. Aboudi and Benveniste (1987) developed a generalized self-consistent scheme for a material with randomly oriented cracking using a model of a crack inside a circular inclusion surrounded by an effective medium. Santare, Crocombe, and Anlas (1995) extended Aboudi and Benveniste's analysis to consider anisotropic effective moduli by using a model of an arbitrarily oriented crack inside an elliptical inclusion as the basis for a generalized self-consistent scheme. Work has also been done to predict the effect of damage on fiber-reinforced composite material systems. Taya and Mura (1981) studied the effect of fiber end cracks on the strength and stiffness of the composite. Wang et al. (1987) modeled the change in properties of a randomly oriented short-fiber reinforced composite using a self-consistent approach based on a solution by Hoenig (1979) for a circular crack in an infinite medium. Hoenig used a flattened ellipsoidal void to represent the crack in his model. This representation does not accurately model the stress field in the vicinity of a sharp crack. Anlas, Santare, and Hall (1995) modeled a two-dimensional composite system with fiber breakage using a self-consistent scheme. The crack model in Anlas, Santare, and Hall (1995) was based on a dislocation solution and therefore was representative of a sharp crack.

In the present work the models developed by Santare et al. (1995) and Anlas et al. (1995) are extended to allow for the consideration of broken fibers in an anisotropic effective medium. Both the fiber and cracked fiber orientation distributions may be arbitrarily specified, although the cracks are always assumed to be oriented perpendicular to the axis of the fibers. This model can then be used to calculate the effective moduli of nominally aligned composite systems with a specified degree of fiber misalignment or of randomly oriented systems with specified cracking orientations.

Formulation of Model

In the present analysis, the composite is modeled as a two-dimensional planar system with an arbitrarily specified orientation distribution of cracked fibers. The undamaged mechanical properties may be either planar isotropic (for the case of randomly oriented composite systems) or orthotropic (for the case of nominally aligned systems). The composite is considered to be a statistically homogeneous medium containing cracked fibers. The cracked fibers are modeled as elliptical inclusions with cracks coinciding with the minor axis of each ellipse. A self-consistent formulation is used to calculate the effective moduli. In obtaining the equations for the effective moduli, the strain energy of the cracked effective medium is equated to the strain energy of the undamaged material plus the energy dissipated due to cracks opening. The energy dissipated from the crack opening is calculated from the solution of a completely cracked inclusion surrounded by an infinitely extended orthotropic medium possessing the unknown effective properties. This energy balance therefore represents a set of nonlinear equations in which the effective moduli are the unknown quantities. The energy balance equation, per Aboudi and Benveniste (1987), can be written as

$$\frac{1}{2} S^*_{ijkl}\sigma^0_{ij}\sigma^0_{kl} = \frac{1}{2} S^{(0)}_{ijkl}\sigma^0_{ij}\sigma^0_{kl} + \frac{1}{2V}\sum_{k=1}^{M}\int_{C_k}[u_i]t^0_i dC_k. \quad (1)$$

In Eq. (1), S^*_{ijkl} is the compliance of the cracked effective medium, $S^{(0)}_{ijkl}$ is the compliance of the undamaged effective composite medium, σ^0_{ij} is the remotely applied stress, $[u_i]$ is the displacement

Contributed by the Applied Mechanics Division of THE AMERICAN SOCIETY OF MECHANICAL ENGINEERS for publication in the ASME JOURNAL OF APPLIED MECHANICS.
Discussion on the paper should be addressed to the Technical Editor, Professor Lewis T. Wheeler, Department of Mechanical Engineering, University of Houston, Houston, TX 77204-4792, and will be accepted until four months after final publication of the paper itself in the ASME JOURNAL OF APPLIED MECHANICS.
Manuscript received by the ASME Applied Mechanics Division, Nov. 19, 1996; final revision, Mar. 5, 1999. Associate Technical Editor: J. L. Bassani.

 Copyright © 1999 by ASME

Downloaded 04 May 2010 to 171.66.16.27. Redistribution subject to ASME license or copyright; see http://www.asme.org/terms/Terms_Use.cfm

jump (crack-opening displacement) across the crack surfaces, and t_i^0 is the traction that would exist inside the inclusion at the crack surface locations in the absence of a crack. M is the number of cracks in a representative volume V. For an orthotropic material four independent homogeneous load cases are required to characterize the in-plane properties. These can be chosen as remote uniaxial tension in each of the two principle material directions, remote shear, and remote biaxial tension, per Santare et al. (1985). The equations for determining the four independent orthotropic moduli can thus be written as

$$\frac{1}{2E_1^*}p_1^2A = \frac{1}{2E_1}p_1^2A + \frac{1}{2}\sum_{k=1}^{M}\int_{C_k}[u_i]^{p_1}t_i^{p_1}dC_k \tag{2}$$

$$\frac{1}{2E_2^*}p_2^2A = \frac{1}{2E_2}p_2^2A + \frac{1}{2}\sum_{k=1}^{M}\int_{C_k}[u_i]^{p_2}t_i^{p_2}dC_k \tag{3}$$

$$\frac{1}{2\mu^*}q^2A = \frac{1}{2\mu}q^2A + \frac{1}{2}\sum_{k=1}^{M}\int_{C_k}[u_i]^{q}t_i^{q}dC_k \tag{4}$$

$$\frac{1}{2K^*}h^2A = \frac{1}{2K}h^2A + \frac{1}{2}\sum_{k=1}^{M}\int_{C_k}[u_i]^{h}t_i^{h}dC_k. \tag{5}$$

In the Eqs. (2)–(5), p_1 and p_2 are the homogeneous remote tensions in the x_1 and x_2 material directions, q is a remote shear related to the x_1x_2 system, and h is remote biaxial tension. A is the two-dimensional area corresponding to V in Eq. (1). E_1^*, E_2^*, E_1, and E_2 are the tensile moduli in the x_1 and x_2 directions for the damaged and undamaged effective mediums. μ^* and μ are the shear moduli and K^* and K are effective biaxial moduli for the damaged and undamaged effective mediums defined in Taya and Mura (1981) as

$$K^* = \frac{E_1^*E_2^*}{E_1^* + E_2^*(1 - 2\nu_1^*)} \tag{6}$$

and

$$K = \frac{E_1E_2}{E_1 + E_2(1 - 2\nu_1)}, \tag{7}$$

where ν_1^* and ν_1 are effective Poissons ratios for the damaged and undamaged mediums.

Determination of Crack-Opening Displacements

The crack-opening displacements are calculated by solving the problem of a cracked elliptical inclusion of known mechanical properties surrounded by an infinite orthotropic effective medium. In solving the crack problem for a monolithic material, the crack is embedded in a fictitious inclusion of undamaged material surrounded by an infinite effective medium as shown in Fig. 1. This approach leads to a generalized self-consistent material model. In the model for the cracked-fiber reinforced composite, the inclusion is fully cracked as shown in Fig. 2 and the mechanical properties of the fiber reinforcement are used. This formulation is thus a self-consistent model for the composite with cracked fibers.

The crack problem is solved by first obtaining the elastic field for a dislocation in an isotropic inclusion surrounded by an infinite anisotropic medium. This is used as the Green's function for the crack problem. The appropriate dislocation solution has been derived by Santare (1995). The crack-opening displacements can be expressed in terms of normal and tangential dislocation density functions $b_n(t)$ and $b_t(t)$ by the relationships

$$b_n(t) = \frac{d}{dt}[u_n]$$

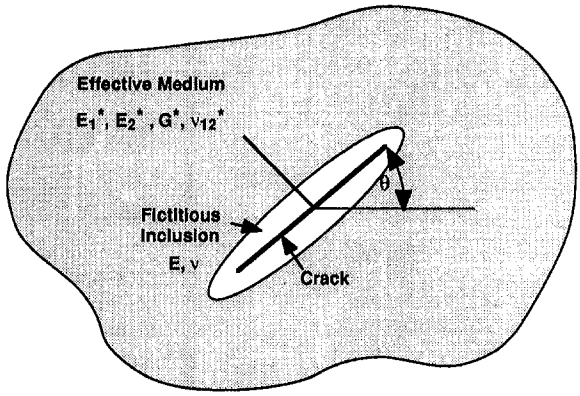


Fig. 1 Generalized self-consistent model for cracked monolithic material

$$b_t(t) = \frac{d}{dt}[u_t]. \tag{8}$$

The dislocation density functions are obtained from the solution of a pair of singular integral equations relating the tractions along the crack face due to the dislocations to the tractions that would exist along the crack face location in the absence of a crack. These equations are given in Santare et al. (1995) and Anlas et al. (1995) as

$$\int_{C_k} K_n(x, t)b_n(t)dt = F_n(x) \tag{9}$$

and

$$\int_{C_k} K_t(x, t)b_t(t)dt = F_t(x). \tag{10}$$

In Eqs. (9) and (10), the kernels $K_n(t)$ and $K_t(t)$ are the normal and tangential tractions at point x due to a dislocation of magnitude 1 at point t inside an elliptical inclusion. The terms $F_n(x)$ and $F_t(x)$ on the right-hand sides of Eqs. (9) and (10) are the tractions inside the inclusion that would exist in absence of a crack. The elastic field solution for an uncracked isotropic inclusion in an anisotropic medium is obtained via the method outlined by Milne-Thompson (1960) as shown in Santare et al. (1995). For a given set of material properties and a designated far-field load, Eqs. (9) and (10) can be solved for the unknown dislocation density functions. This solution must be found through the use of approximate numerical methods, due to the complexity of the kernels. In addition, as shown on Fig. 2, the cracks terminate at the interface of two materials. To solve this type of problem, we must follow the

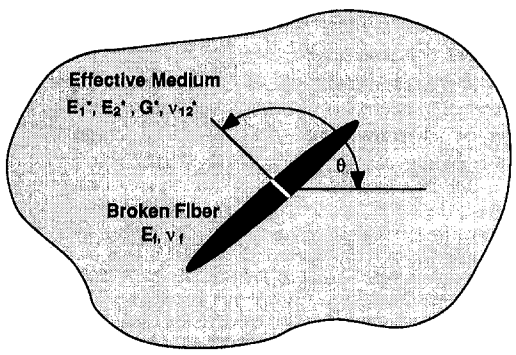


Fig. 2 Self-consistent model for composite material with broken fibers

Downloaded 04 May 2010 to 171.66.16.27. Redistribution subject to ASME license or copyright; see http://www.asme.org/terms/Terms_Use.cfm

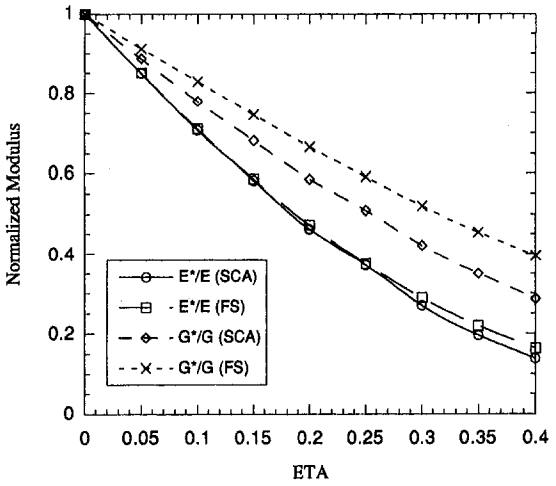


Fig. 3 Modulus change versus crack density parameter for monolithic material with randomly oriented cracks

technique of Erdogan and Gupta (1975), as outlined in Anlas et al. (1995). The crack-opening displacements are then obtained by integration of the dislocation density functions as in Eq. (8).

Calculation of Effective Moduli

In the previous section a procedure is outlined for determining the opening displacement of a crack inside an elliptical inclusion. The dependence of the stress field and crack-opening displacements on the inclusion orientation is implicit in the formulation. In an actual material system there will be a distribution of inclusions at various orientations. Even in nominally aligned systems the fiber reinforcements will exhibit some degree of misalignment. For a statically homogeneous material, the summations in Eqs. (2)–(5) can be rewritten as orientation averaging integrals in the following way:

$$\frac{E_1}{E_1^*} = 1 + \frac{E_1 M}{2\pi A}\int_{-\pi}^{\pi}\Phi(\theta)\int_{C_k}[\bar{u}_i]^{p_1}\bar{t}_i^{p_1}dC_k \qquad (11)$$

$$\frac{E_2}{E_2^*} = 1 + \frac{E_2 M}{2\pi A}\int_{-\pi}^{\pi}\Phi(\theta)\int_{C_k}[\bar{u}_i]^{p_2}\bar{t}_i^{p_2}dC_k \qquad (12)$$

$$\frac{\mu}{\mu^*} = 1 + \frac{\mu M}{2\pi A}\int_{-\pi}^{\pi}\Phi(\theta)\int_{C_k}[\bar{u}_i]^{q}\bar{t}_i^{q}dC_k \qquad (13)$$

$$\frac{K}{K^*} = 1 + \frac{K\mu M}{2\pi A}\int_{-\pi}^{\pi}\Phi(\theta)\int_{C_k}[\bar{u}_i]^{h}\bar{t}_i^{h}dC_k. \qquad (14)$$

In Eqs. (11)–(14), $\Phi(\theta)$ is the orientation distribution function of the microcracks. In cracked-fiber reinforced composite systems, the fiber breaks occur at right angles to the fiber longitudinal axes. Thus the orientation distribution function of the broken fibers is equal to the orientation distribution function of the cracks rotated by the angle $\pi/2$. The quantities $[\bar{u}_i]$ and $\bar{t}_i$ are the crack-opening displacements and uncracked inclusion tractions normalized with respect to the external load. The quantity M/A is the number of cracks per unit area of sample. For fiber-reinforced systems this quantity can be expressed as

$$\frac{M}{A} = \frac{d_f v_f}{\pi ab} \qquad (15)$$

where v_f is the total volume fraction of the fibers, d_f is the fraction fibers which are broken, and the quantity πab is the planar area of the (fiber) inclusion. For cracked monolithic material systems, M/A can be expressed in terms of a crack density parameter η, such that

$$\frac{M}{A} = \frac{\eta}{c^2} \qquad (16)$$

where c is one the half crack length and η is defined as in Aboudi and Benveniste (1987) and Santare et al. (1995) as

$$\eta = \frac{c^2}{\pi ab}. \qquad (17)$$

When integrating Eqs. (11)–(14), an additional condition which does not allow negative mode I crack-opening displacements is imposed. This constraint is implemented in the numerical calculation by the statement

$$[\bar{u}_n] = 0 \quad \text{for} \quad \bar{t}_n < 0. \qquad (18)$$

Results and Discussion

Numerical examples of this work for cracked monolithic material are shown in Figs. 3 and 4 for comparison to the work performed by Santare, Crocombe, and Anlas (1995). The curves labeled FS in Figs. 3 and 4 refer to the present work while the curves labeled SCA refer to the work presented in Santare et al. (1995). The present model differs from the model used in Santare et al. (1995) in that crack face overlap is elimated by the condition imposed in Eq. (18). Figure 3 illustrates the effect of the crack density parameter as defined by Eq. (17) on the moduli of a monolithic material with a randomly oriented array of cracks. In this case the material remains isotropic regardless of the extent of cracking. It is observed from comparison to the results given by Santare et al. (1995) that the tensile modulus for an isotropic material is only slightly affected by the deletion of crack energy due to compressive forces while the shear modulus is affected to a much greater degree. Figure 4 illustrates the effect of an aligned array of cracks oriented at ± 1 deg from the x_1-axis. In this case the material becomes increasingly anisotropic as the crack density increases. The deletion of crack energy due to compressive forces has no effect in the case where the cracks are aligned with a principle material direction. In both cases the effect of sliding friction on the crack surfaces during compressive loadings was not addressed.

Figures 5–8 illustrate numerical examples for planar random and aligned short-fiber reinforced composite systems with broken fibers. The material properties used represent an Al_2O_3-Al com-

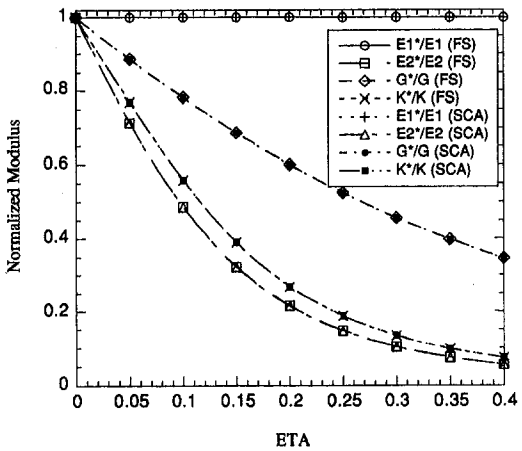


Fig. 4 Modulus change versus crack density parameter for monolithic material with aligned cracks

Downloaded 04 May 2010 to 171.66.16.27. Redistribution subject to ASME license or copyright; see http://www.asme.org/terms/Terms_Use.cfm

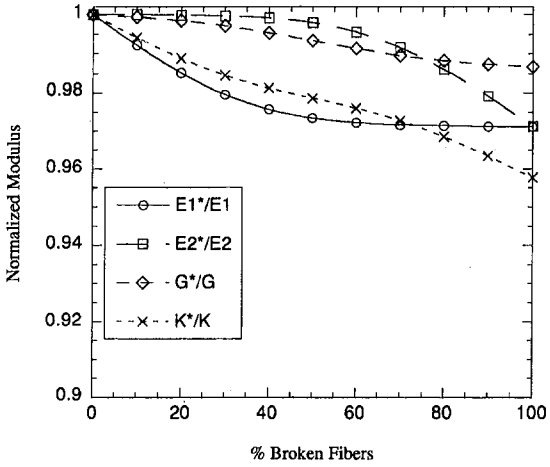


Fig. 5 Modulus change versus percentage of broken fibers for a 15 percent fiber volume fraction Al_2O_3-Al composite with randomly oriented fibers and progressive crack orientation distribution

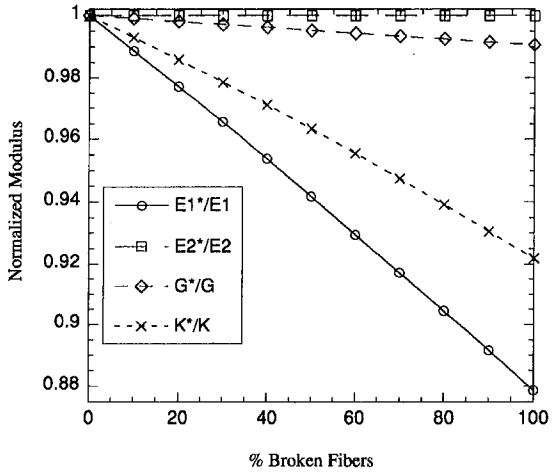


Fig. 8 Modulus change versus percentage of broken fibers for a 25 percent fiber volume fraction Al_2O_3-Al composite with aligned fibers and crack orientation distribution

posite system with the fiber Young's modulus and Poisson's ratio given as 300 Gpa and 0.3 respectively and the matrix Young's modulus and Poisson's ratio given as 69 Gpa and 0.33 respectively. A fiber aspect ratio of 10 was assumed and fiber volume fractions of 0.15 and 0.25 were analyzed. Although the present work is based on the previous work of Anlas, Santare, and Hall (1995), a direct comparison of numerical results is not useful due to the different calculation schemes used to integrate the crack energy as a function of orientation over the crack orientation angle θ. The model given in Anlas et al. (1995) used an analytical integration approach and was limited to isotropic effective material properties. Thus it could only be used for random crack orientation distributions. The present model uses a more generally applicable numerical integration approach, and is formulated so that the effective material properties can be anisotropic. Thus arbitrary crack orientations can be considered. It was also found that in Anlas et al. (1995) simplifying assumptions about the dependence of the crack-opening displacements on the crack orientation angle were made to expedite the analytical integration which affected the numerical results. No such assumptions were necessary in the present work due to the more robust integration method used. Figures 5 and 6 illustrate the normalized effective tensile moduli, shear modulus, and the biaxial modulus K^*, as defined by Eq. (6), for composite systems with fiber volume fraction of 0.15 and 0.25. The crack orientation distribution is assumed to be uniform over the angles $\pi/2 \pm \theta_0$, with θ_0 given by

$$\theta_0 = \frac{\pi}{2} \times \frac{(\text{percentage broken fibers})}{100}. \tag{19}$$

The numerical results in Figs. 5 and 6 show that a composite system which is initially isotropic becomes increasingly anisotropic until 50 percent fiber breakage is realized. The anisotropy then decreases at greater percentages of fiber breakage, until the system is again isotropic at 100 percent fiber breakage. Equation (19) represents a simple model used to demonstrate the effects of the crack orientation distribution on the effective moduli of an initially planar isotropic system. The degree of anisotropy induced into planar random composite systems in general is dependent on the relationship between the crack orientation distribution and the percentage of broken fibers.

Figures 7 and 8 illustrate the effect of fiber breakage on aligned fiber systems with fiber volume fractions of 0.15 and 0.25. The crack orientation distribution is given by $\theta_0 = 5$ deg with the nominal orientation of the cracks being parallel to the x_2-axis. In this case, the reduction in effective modulus is nearly linear since the crack orientation distribution remains constant. As expected for this case, the tensile modulus in the x_1-direction with all fibers broken is reduced to a greater degree than in the randomly oriented (isotropic) case. The shear modulus is affected to a smaller degree than in the isotropic case. In the cases in which the cracks are

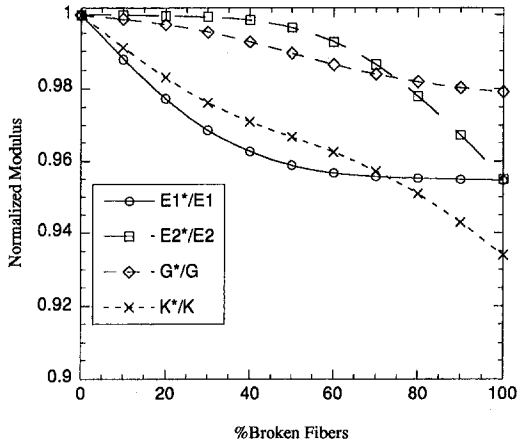


Fig. 6 Modulus change versus percentage of broken fibers for a 25 percent fiber volume fraction Al_2O_3-Al composite with randomly oriented fibers and progressive crack orientation distribution

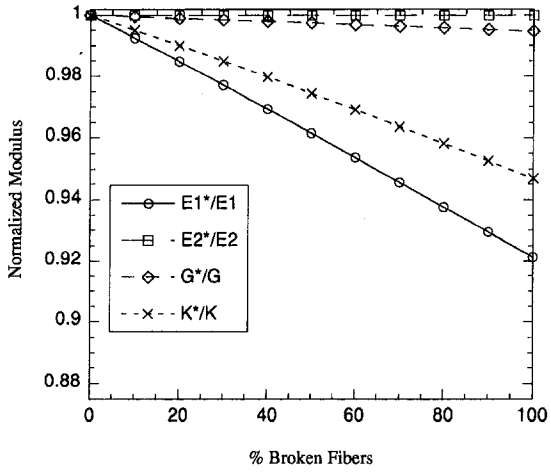


Fig. 7 Modulus change versus percentage of broken fibers for a 15 percent fiber volume fraction Al_2O_3-Al composite with aligned fibers and crack orientation distribution

Downloaded 04 May 2010 to 171.66.16.27. Redistribution subject to ASME license or copyright; see http://www.asme.org/terms/Terms_Use.cfm

aligned with a principle material direction, the primary effect of shear on the cracks is a mode II (sliding) displacement. The greatest mode I displacement during a remote shear loading occurs when the cracks are oriented at 45 deg with respect to the principle material axes. Thus in the randomly oriented cases, the cracks oriented in the vicinity of 45 deg from the material axes are the major contributors to the reduction in shear stress. It is observed that for the case of an aligned system of cracks in a monolithic material (Fig. 4), the reduction in the effective moduli is much more pronounced than in the aligned fiber-reinforced systems. Given the short crack length present in the moderate to high aspect ratio fibers considered, these examples would correspond to very low values of the crack density parameter η. Examination of the linear portion of Fig. 4 ($\eta < 0.05$) in fact shows similar trends to the results in Figs. 7 and 8. Fiber/matrix debonding, which can contribute significantly to shear modulus degradation in fiber reinforced composites, is not addressed in the present model.

It should be noted that multiple fiber fractures are likely to occur in damaged fiber-reinforced composite systems. The present model conciders each broken fiber as an elliptical inclusion with a single crack coincident with the minor axis and does not allow for multiple cracks in a single fiber to be modeled. It should also be noted that the numerical results of the present model should be viewed cautiously for fiber volume fractions above 0.25–0.3, especially when low aspect ratio reinforcements are considered. A generalized self-consistent model, consisting of both fiber and matrix phases surrounded by an effective composite medium, is suggested for consideration of higher fiber volume fraction composite systems.

Acknowledgments

The authors wish to thank the Army Research Laboratory and Dr. Ian Hall of the Materials Science department at the University of Delaware for providing the funding necessary to complete this work. Thanks are also due to Dr. Gunay Anlas for his helpful insights in developing the methods used to perform our research.

References

Aboudi, J., and Benveniste, Y., 1987, "The Effective Modulus of Cracked Bodies in Plane Deformation," *Engng. Fracture Mech.,* Vol. 26, No. 2, pp. 171–184.

Anlas, G., Santare, M. H., and Hall, I. W., 1995, "Modelling the Effect of Fiber Breakage on the Elastic Properties of Short Fiber Composites," *Composites Science and Technology,* Vol. 54, pp. 113–122.

Budianski, B., and O'Connell, R. J., 1976, "Elastic Moduli of a Cracked Solid," *Int. J., Solids Structures,* Vol. 12, pp. 81–97.

Erdogan, F., and Gupta, G. D., 1975, "The Inclusion Problem With a Crack Crossing the Boundary," *International Journal of Fracture,* Vol. 11, pp. 13–27.

Gottesman, T., Hashin, Z., and Brull, M. A., 1980, "Effective Elastic Moduli of Cracked Fiber Composites," *Advances in Composite Materials,* A. R. Bunsell, ed., pp. 749–758.

Hoenig, A., 1979, "Elastic Moduli of Non-randomly Cracked Bodies," *Int. J. Solids Struct.,* Vol. 15, pp. 137–154.

Horii, H., and Nemat-Nasser, S., 1983, "Overall Elastic Moduli of Solids With Microcracks: Load-Induced Anisotropy," *J. Mech. Phys. Solids,* Vol. 31, pp. 155–171.

Milne-Thompson, L. M., 1960, *Plane Elastic Systems,* Springer, Berlin.

Santare, M. H., 1995, "Dislocation in an Isotropic Elliptical Inclusion Surrounded by a Anisotropic Matrix," ASME JOURNAL OF APPLIED MECHANICS, Vol. 62, pp. 537–539.

Santare, M. H., Crocombe, A. D., and Anlas, G., 1995, "Anisotropic Effective Moduli of Materials With Microcracks," *Engng. Fracture Mech.,* Vol. 52, No. 5, pp. 833–842.

Taya, M., and Mura, T., 1981, "On the Stiffness and Strength of Aligned Short Fiber Reinforced Composites Containing Fiber End Cracks Under Uniaxial Applied Stress," ASME JOURNAL OF APPLIED MECHANICS, Vol. 48, pp. 361–367.

Wang, S. S., Chim, E. S., and Suemasu, H., 1987, "Mechanics of Fatigue Damage and Degradation in Random Short Fiber Composites, Part II: Analysis of Anisotropic Property Degradation," ASME JOURNAL OF APPLIED MECHANICS, Vol. 53, pp. 347–353.

Downloaded 04 May 2010 to 171.66.16.27. Redistribution subject to ASME license or copyright; see http://www.asme.org/terms/Terms_Use.cfm

H.-H. Dai
Department of Mathematics,
City University of Hong Kong,
Tat Chee Avenue,
Kowloon, Hong Kong

G. Wu
Department of Mathematics,
Foshan University,
Guangdong 528000, P. R. China

On Thermal Stress in a Bituminous Pavement: Analytic Solutions and Applications

In this paper, the analytic solution for simulating the thermal stress field in a bituminous pavement is put forward based on a two-dimensional thermoviscoelastic layered system. The numerical analysis is made for the thermal stress field under the typical weather conditions in the north of China. Some new results are obtained. A discussion on the optimum thickness design for the bituminous pavement is given in the final section.

1 Introduction

The semi-rigid pavement (also called bituminous pavement) i.e., the structure in which a bituminous surfacing is paved over a semi-rigid road base, has been the main development direction for a highway. Thermal cracking is an important factor that leads to the early-stage damages of bituminous pavement.

Since the 1960s, many works have been published on the theoretical studies for a thermal stress field in a bituminous pavement based on the one-dimensional linear viscoelastic system (see Hills and Brien, 1966; Monismith and Secor, 1965; Hajek and Hass, 1972; Shahin and McCullough, 1974; Thompson, 1989; Wang, 1991; Sa, 1993; etc.). There are two main disadvantages in their works: (1) suppose that temperature is uniformly distributed along the thickness of bituminous pavement; (2) the effect of the temperature contraction between the semi-rigid road base and the bituminous pavement is neglected. But both of the two aspects are very important for analyzing the thermal stress and predicting the thermal cracking in a bituminous pavement. Lytton et al. (1993) developed a new thermal cracking model, called TCMODEL, under the Strategic Highway Research Program of American (see SHRP A Report, PA357). Based on the analysis of the thermal stress in a bituminous pavement structure, they made further studies and considered the temperature gradients in the various pavement layers. Also, many researchers studied it based on the thermal elastic theory or experiment methods (see Halim, 1986; Majidaeh, Abdulshafi, Ilves, and McLaughlin, 1987; Wu, 1992; Wu, 1993; Sa, 1993; etc.).

This paper aims to solve the existing problems mentioned above in analyzing the thermal stress in a bituminous pavement structure. For this end, the authors first build an analytic model for simulating the thermal stress field based on a two-dimensional thermoviscoelastic layered system. In this model, the temperature gradient nonuniformly distributed along the thickness of each layer and the frictional drag between the semi-rigid road base and the bituminous surfacing are both considered. Next, the authors simulate and analyze the thermal stress field in a bituminous pavement under the typical weather conditions in the north of China by applying the analytic method, and some new results are discovered. Finally, the authors discuss and suggest an idea on the optimum thickness design of bituminous pavement.

Contributed by the Applied Mechanics Division of THE AMERICAN SOCIETY OF MECHANICAL ENGINEERS for publication in the ASME JOURNAL OF APPLIED MECHANICS.
Discussion on the paper should be addressed to the Technical Editor, Professor Lewis T. Wheeler, Department of Mechanical Engineering, University of Houston, Houston, TX 77204-4792, and will be accepted until four months after final publication of the paper itself in the ASME JOURNAL OF APPLIED MECHANICS.
Manuscript received by the ASME Applied Mechanics Division, Jan. 24, 1997; final revision, Mar. 20, 1999. Associate Technical Editor: I. M. Daniel.

2 Mathematical Model and Its Analytic Solution

Let $\Delta T(x, y)$ be the thermal difference at the point (x, y) in an elastic body, i.e.,

$$\Delta T(x, y) = T(x, y, t_1) - T(x, y, t_2), \tag{2.1}$$

where $T(x, y, t)$ is the temperature field at the moment t. The analytic method for simulating such a temperature field was put forward in Wu (1992 and 1997) based on the two-dimensional layered system. Because of the temperature difference ΔT, a normal strain will be induced at every infinitesimal element in the neighborhood of point (x, y). If the deformation is free under the assumption of a homogeneous isotropic material we have

$$\epsilon_x = \epsilon_y = \epsilon_z = \alpha \Delta T, \quad \gamma_{xy} = \gamma_{zy} = \gamma_{zx} = 0, \tag{2.2}$$

where $\epsilon_x, \epsilon_y, \ldots, \gamma_{zx}$ are the strain components at the point (x, y). However, because the body is actually subject to various constraints it cannot deform freely. As a result, the thermal stress will be induced, and this again results in additional strains due to the body elasticity.

Take a cross section of a semi-rigid pavement structure for consideration (see Fig. 1). As assumed, this cross section is in the state of plain strain, i.e.,

$$\epsilon_z = 0, \quad \gamma_{yz} = \gamma_{xz} = 0. \tag{2.3}$$

As shown in Fig. 1, the forward direction of the y-axis points to the pavement body. The pavement structure consists of n layers. The first layer is bituminous surfacing, the other layers are semi-rigid base and earth base. E_i, α_i, ΔT_i, and g_i are Young's modulus, the thermal expansion coefficient, thermal difference function, and the thickness of the ith layer ($g_n = \infty$), respectively. Let $\sigma_{xi}, \sigma_{yi}, \tau_{xyi}, \sigma_{zi}$ be the stress components in the ith layer, and $h_k = \sum_{i1}^{k} g_i, (k \le n - 1)$. Because the difference of Poisson's ratios in different pavement material layers is very small, it is usually assumed that they have the same value. Then we have

$$\sigma_{yi} = \frac{E_i(1-\mu)}{(1+\mu)(1-2\mu)}\left(\epsilon_x + \frac{\mu}{1-\mu}\epsilon_y\right) - \frac{E_i\alpha_i\Delta T_i}{1-2\mu}$$

$$\sigma_{xi} = \frac{E_i(1-\mu)}{(1+\mu)(1-2\mu)}\left(\epsilon_y + \frac{\mu}{1-\mu}\epsilon_x\right) - \frac{E_i\alpha_i\Delta T_i}{1-2\mu}$$

$$\tau_{xyi} = \frac{E_i}{2(1+\mu)}\gamma_{xy}$$

$$\sigma_{zi} = \mu(\sigma_{xi} + \sigma_{yi}) - E_i\alpha_i\Delta T_i. \tag{2.4}$$

According to the equilibrium equations and the geometry equations, one can easily obtain the governing equations

 Copyright © 1999 by ASME

Downloaded 04 May 2010 to 171.66.16.27. Redistribution subject to ASME license or copyright; see http://www.asme.org/terms/Terms_Use.cfm

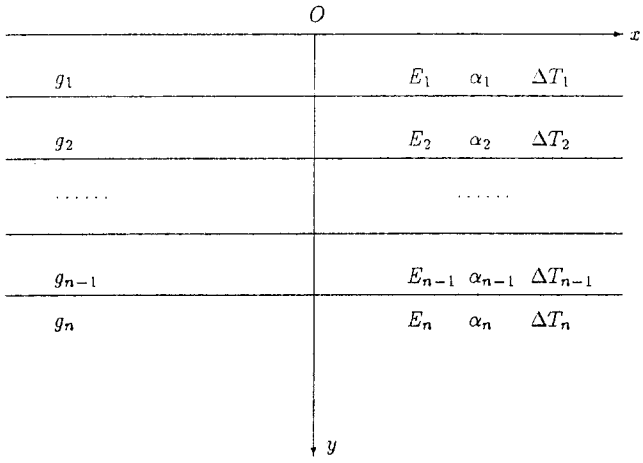


Fig. 1 A cross section of the semi-rigid pavement

$$\frac{\partial^2 u}{\partial x^2} + (1-\nu)\frac{\partial^2 v}{\partial x \partial y} + \nu\frac{\partial^2 u}{\partial z^2} - \frac{1+\mu}{1-\mu}\frac{\partial(\alpha\Delta T)}{\partial x} = 0,$$

$$\nu\frac{\partial^2 w}{\partial x^2} + (1-\nu)\frac{\partial^2 u}{\partial x \partial y} + \frac{\partial^2 v}{\partial y^2} - \frac{1+\mu}{1-\mu}\frac{\partial(\alpha\Delta T)}{\partial y} = 0, \quad (2.5)$$

where u, v are the displacement components in x, y-direction, respectively, and ν is a constant, related only to Poisson's ratios μ. On the surface of the bituminous pavement, the boundary conditions are given in the following forms:

$$\frac{\partial v}{\partial y} + \frac{\mu}{1-\mu}\frac{\partial u}{\partial x} = \frac{1+\mu}{1-\mu}\alpha\Delta T,$$

$$\frac{\partial v}{\partial x} + \frac{\partial u}{\partial y} = 0. \quad (2.6)$$

Finally, we assume that the considered pavement structure be fixed at infinity, i.e.,

$$u(x, y) \to 0, \quad v(x, y) \to 0, \quad (|x| \to \infty, |y| \to \infty). \quad (2.7)$$

Integrating Eq. (2.5) to (2.7), we form the mathematical model for simulating the thermal stress field based on the elastic theory at the moment t. As the first step in building the analytic method of thermal stress based on the two-dimensional viscoelasticity theory, we first need to give the analytic solution for the mathematical model.

Introduce a potential function $\psi(x, y)$ and let

$$u' = \frac{\partial \psi}{\partial x}, \quad v' = \frac{\partial \psi}{\partial y}. \quad (2.8)$$

It is easy to prove that u', v' are a special solution of (2.5) if $\psi(x, y)$ satisfies

$$\nabla^2 \psi = 2G(x, y) \equiv \frac{1+\mu}{1-\mu}\alpha\Delta T(x, y). \quad (2.9)$$

Let u'', v'' be the general solutions of the homogeneous equation corresponding to Eq. (2.6), then

$$u = u' + u'', \quad v = v' + v'' \quad (2.10)$$

are the general solutions of Eqs. (2.5)

To determine u', v', u'', v'', we introduce the following notations and definitions:

$$z = x + iy, \quad \bar{z} = x - iy,$$

$$f' = u' + iv', \quad f'' = u'' + iv'', \quad f = u + iv = f' + f'',$$

$$\frac{\partial}{\partial z} = \frac{1}{2}\left(\frac{\partial}{\partial x} - i\frac{\partial}{\partial y}\right), \quad \frac{\partial}{\partial \bar{z}} = \frac{1}{2}\left(\frac{\partial}{\partial x} + i\frac{\partial}{\partial y}\right). \quad (2.11)$$

Then Eq. (2.11) can be rewritten as follows:

$$\frac{\partial f'}{\partial z} = G(z). \quad (2.12)$$

According to Vekua (1962) and Rodin (1987) we have

$$f'(z) \equiv \bar{T}G(z) = -\frac{1}{\pi}\iint_E \frac{G(\xi, \eta)}{\bar{w} - \bar{z}}\, d\xi d\eta, \quad (2.13)$$

where E is the lower half-plane ($y > 0$).

To determine the general solution f'', we can easily derive the complex equation

$$(1-\nu)\frac{\partial^2 f''}{\partial z^2} + (1+\nu)\frac{\partial^2 \overline{f''}}{\partial \bar{z}\partial z} = 0. \quad (2.14)$$

Making use of the generalized analytic function theory, we can obtain

$$f''(z) = \frac{\nu - 1}{4\nu} z\overline{\varphi(z)} + \frac{\nu + 1}{4\nu}\Phi(z) + \overline{\Psi(z)}, \quad (2.15)$$

where $\varphi(z)$, $\Psi(z)$ are analytical functions on variable z in domain E, and

$$\Phi(z) = \int_0^z \varphi(s)ds. \quad (2.16)$$

Then, the general solution $f(z)$ of Eq. (2.5) is obtained:

$$f(z) = \bar{T}G(z) + \frac{\nu - 1}{4\nu} z\overline{\varphi(z)} + \frac{\nu + 1}{4\nu}\Phi(z) + \overline{\Psi(z)}. \quad (2.17)$$

To determine the two analytic functions, we can rewrite the boundary condition (2.6) as follows by putting (2.17) into (2.6):

$$\varphi(\tau) + \overline{\varphi(\tau)} - \tau\overline{\varphi'(\tau)} + 4(1-2\mu)\overline{\Psi'(\tau)} = F(\tau),$$

$$\tau \in (-\infty, +\infty) \quad (2.18)$$

where $\varphi(\tau)$, $\varphi'(\tau)$, and $\Psi'(\tau)$ are the boundary values of analytic function $\varphi(z)$, $\varphi'(z)$, and $\Psi'(z)$ on $y = 0$, and

$$F(\tau) = -4\mu G + 4(1-2\mu)\bar{\Pi}G \quad (2.19)$$

$$\bar{\Pi}G \equiv \frac{\partial \bar{T}G}{\partial \bar{z}} = -\frac{1}{\pi}\iint_E \frac{G(\xi, \eta)}{(\bar{w} - \bar{z})^2}\, d\xi d\eta. \quad (2.20)$$

According to (2.9), without loss of generalization, we can assume

$$|\Delta T(z)| \le Be^{-M|z|}, \quad |z| \to \infty. \quad (2.21)$$

From this, it is easy to conclude that

$$F(z) = O(z^{-(2/p)}), \quad (p > 2), \quad z \to \infty. \quad (2.22)$$

This property of $F(z)$ can satisfy all conditions necessary for us (see Wong, 1989).

By applying the techniques of complex integral equation to boundary Eq. (2.18), we obtain the following analytic expressions:

$$\varphi(z) = -\frac{1}{2\pi i}\int_{-\infty}^{+\infty} \frac{F(\tau)}{\tau - z}\, d\tau, \quad (2.23)$$

Downloaded 04 May 2010 to 171.66.16.27. Redistribution subject to ASME license or copyright; see http://www.asme.org/terms/Terms_Use.cfm

$$\Psi'(z) = \frac{1}{4(1-2\mu)}\left[-\frac{1}{2\pi i}\int_{-\infty}^{+\infty}\frac{F(\tau)-\overline{F(\tau)}}{\tau - z}\,d\tau - \frac{z}{2\pi i}\int_{-\infty}^{+\infty}\frac{F(\tau)}{(\tau - z)^2}\,d\tau\right] \quad (2.24)$$

We can see from (2.17) that the strain components are analytically obtained, i.e.,

$$\epsilon_x = G + \mathrm{Re}(\bar{\Pi}G) + \frac{1}{2}\mathrm{Re}(\varphi(z)) + \frac{\nu-1}{4\nu}\mathrm{Re}(z\overline{\varphi'(z)}) + \mathrm{Re}(\overline{\Psi'(z)}),$$

$$\epsilon_x = G - \mathrm{Re}(\bar{\Pi}G) + \frac{1}{2}\mathrm{Re}(\varphi(z)) - \frac{\nu-1}{4\nu}\mathrm{Re}(z\overline{\varphi'(z)}) - \mathrm{Re}(\overline{\Psi'(z)}),$$

$$\gamma_{xy} = -2\,\mathrm{Re}(i\bar{\Pi}G) - \frac{1}{2}\mathrm{Re}(\varphi(z)) - \frac{\nu-1}{4\nu}\mathrm{Re}(z\overline{\varphi'(z)}) - 2\,\mathrm{Re}(\overline{\Psi'(z)}). \quad (2.25)$$

Again from (2.4), the analytical expressions for the stress components are given. For the purpose of convenience, we drop the suffixes and simply write

$$\sigma = E \cdot H(x, y, \Delta T, \alpha) \quad (2.26)$$

where $H(x, y, \Delta T, \alpha)$ is used to represent the terms on the right side of (2.4), excluding the modulus E_i. Because we are mainly concerned about the thermal stress along the road direction, we regard σ as σ_z unless it is specified otherwise.

Now we have to consider the viscoelastic property of bituminous pavement materials. Thermal cracking in bituminous pavement occurs mainly during winter. In winter, as the temperature goes down, the viscous effect of the bituminous mixture decreases and the elastic effect increases, the elastic modulus gradually increases and the pavement becomes hard and hard. Then the maximum strain occurring in the bituminous pavement is far less than 0.1 percent. According to Monismith et al. (1965), we may use the linear viscoelasticity theory to analyze the thermal relaxation stresses in the bituminous pavement. So Maxwell's relaxation model is suitable for simulating the thermal stress relaxation process, that is

$$\sigma = \sigma_0 e^{-(E/\eta)\theta}, \quad (2.27)$$

where σ_0 is the constant stress before the relaxation, η is the viscosity coefficient of the bituminous mixture, E is the elastic modulus, and θ is the relaxation time. The bending stress relaxation tests (see Sa, 1993) indicate that typical stress relaxation law for the bituminous mixtures can be approximately expressed by exponential functions. Let $E_r = E_r(\theta, T)$ be the relaxation elastic modulus (in practice, it can be replaced by the stress relaxation modulus $S_r = S_r(\theta, T)$). By using the analysis techniques of infinitesimal element and Boltzman's superposition principle, we finally obtain the analytic solution for the thermal stress concerned:

$$\sigma(x, y, \tau) = \int_{-\infty}^{\tau} E_r(\tau - t, T) \cdot H(x, y, T', \alpha)dt. \quad (2.28)$$

This formula evidently indicates the relation between the thermal stress and its influence factors, such as temperature distribution, temperature speed, relaxation modulus, relaxation time, thermal expansion coefficient, pavement thickness, and Poisson ratio, etc. For the layers of elastic materials we have

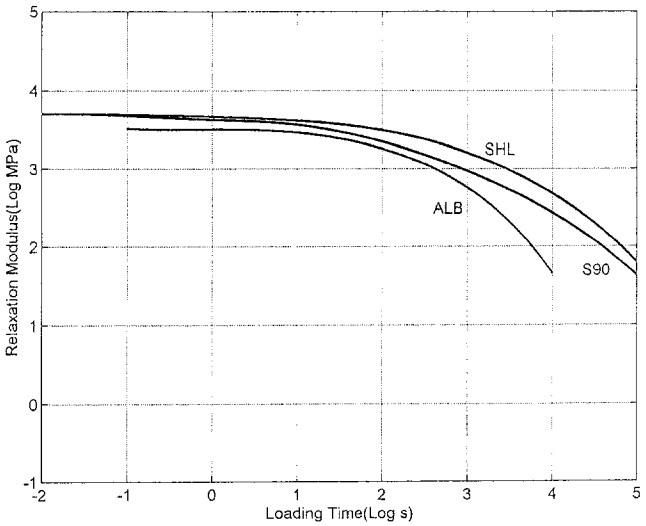


Fig. 2 Curves of the stress relaxation modulus

$$\sigma(x, y, \tau) = E_i \int_{-\infty}^{\tau} H(x, y, T', \alpha)dt. \quad (2.29)$$

3 Analysis and Applications

3.1 Computation Parameters. Examples for simulating and analyzing the thermal stress field in a bituminous pavement are given in this section. To illustrate the applications, we consider the typical weather conditions in Changchun, Jilin, China on Nov. 10, 1993 and Jan. 10, 1994. On these specified days, the maximum temperatures were 5°C and −15°C respectively, the minimum temperatures were −5°C and −25°C, respectively, the total radiation for both were 10 (MJ/m^2) and the average wind speeds were 1.0 (m/s).

The bituminous pavement structure analyzed later consisted of four layers, they were 15 cm bituminous surfacing + a 20 cm top semi-rigid base of cement stable macadam + a 25 cm bottom semi-rigid base of the mixtures with lime and coal ash + an earth base of neutral clay.

Three types of bituminous mixtures were selected for comparing the effect between the material properties and thermal stresses. They were S90, SHL, and ALB. Here, the mixture S90, SHL, and ALB are, respectively, mixed with ShanJiaShi asphalt, Shell asphalt, and Albania asphalt, according to the method AH-90, AH-90, and AH-70 in the Chinese Flexible Pavement Design Standards. Their stress relaxation modulus are presented in Fig. 2 (see also Wang, 1991).

In Fig. 2, the datum temperature is −10°C, the modulus curves under other temperature conditions can be obtained according to the shift factors (see Wang, 1991; Sa, 1993). Finally, the thermal expansion coefficients for the three types of bituminous mixtures are shown in Table 1.

In this section, unless otherwise specified, the thermal expansion coefficients of the top semi-rigid base, the bottom semi-rigid base and the earth base are 1.0×10^{-5} (1/°C), 1.5×10^{-5} (1/°C), and 50.0×10^{-5} (1/°C), respectively. The elastic modulus of the top

Table 1 Thermal expansion coefficients (10^{-4}/°C)

Asphalt mixtures	20 ~ 10°C	10 ~ 0°C	0 ~ −10°C	−10 ~ −20°C	−20 ~ −30°C
S90	0.34	0.31	0.27	0.25	0.24
SHL	0.33	0.35	0.26	0.24	0.23
ALB	0.40	0.32	0.28	0.26	0.23

Downloaded 04 May 2010 to 171.66.16.27. Redistribution subject to ASME license or copyright; see http://www.asme.org/terms/Terms_Use.cfm

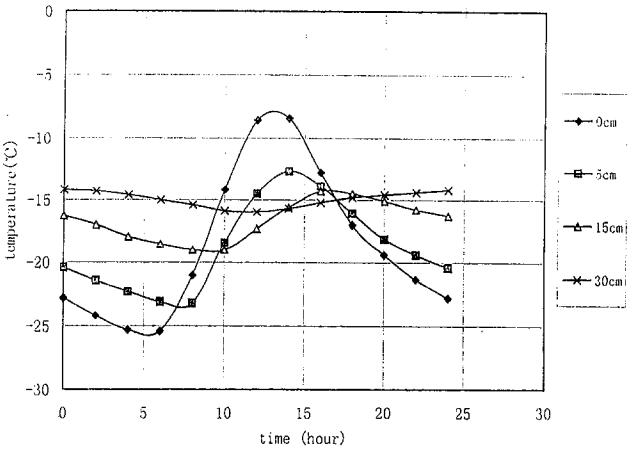


Fig. 3 Curves of the temperature distribution. The numbers in the right column express the depth y.

semi-rigid base, the bottom semi-rigid base, and the earth base are 2000 (MPa), 1000 (MPa), and 32 (MPa) respectively. Poisson's ratio is 0.25.

3.2 Numerical Result and Analysis. To reveal the internal relation between the temperature field and the thermal stress, we first compute the pavement temperature field on Jan. 10, 1994 by the analytic method put forward in Wu (1997) (see Fig. 3).

Suppose that the pavement is paved by S90. We calculate the corresponding thermal stress distributions according to the parameters presented in Section 2 (see Fig. 4).

The following characters are observed from Fig. 4:

1 The maximum value and the largest variation amplitude of the thermal stress are reached on the surface of the bituminous pavement.
2 Approximately, contraction stress ($\sigma > 0$) occurs during the night and the expansion stress ($\sigma < 0$) occurs during the daytime. The thermal stress changes its stress state (contraction or expansion), almost coinciding with the time of sunset or sunrise;
3 As the depth increases, the variation amplitude of the thermal stress gradually decreases. At the depth of 15 cm, the amplitude is about one third of that of the surface. Also, as the depth increases, the phase of the thermal stress curve changes, at the depth of 5 cm, the phase difference is about one hour, and at the depth 15 cm, it is about 4 ~ 5 hours. At the middle of the semi-rigid base, the stress state is almost opposite to that of the surface.
4 The thermal stress reaches its maximum at about 5 a.m. and reaches its minimum at about 1 p.m., the stress amplitude is about 1 (MPa). Because of the counteraction between expansion and contraction, the actual maximum contraction stress is only about 0.6 (MPa).

From Fig. 4 we see that the pavement is in a high level of contraction stress at about 5 a.m. The period during which the thermal stress is above 0.5 (MPa) covers about four hours, and the period during which the thermal stress is above 0.55 (MPa) covers about two and one-half hours. Such conditions are very harmful to the pavement. According to the tests on the tensile strength of bituminous mixtures (Wang, 1991), under the action of the same load, the longer the loading time, the less the tensile strength. The maximum value of the thermal stress in a day may not exceed the instant damage strength, but if the pavement is in a high level of contraction stress for a long time, it will also crack once the stress exceeds the corresponding tensile strength. It means that the time factor is an important factor for predicting thermal cracking of bituminous pavements. Based on these analysis results, we developed a new cracking criterion for bituminous pavement. It can be stated as follows:

Compute the thermal stress curves as time t and temperature T vary in a day.

Let θ be the loading time of the thermal stress. If the thermal stress $\sigma(\theta, T)$ is not less than the tensile strength $R(\theta, T)$, that is

$$\sigma(\theta, T) \geq R(\theta, T), \tag{3.1}$$

then the bituminous pavement will crack transversely.

Geometrically, this criterion is explained as follows. In the three-dimensional coordinate system (θ, T, σ), if the surface $\sigma(\theta, T)$ intersects the surface $R(\theta, T)$, then the pavements will crack. Obviously, if one of the following two conditions is satisfied,

$$\sigma(\theta_0, T) \geq R(\theta_0, T) \tag{3.2}$$

and

$$\sigma(\theta, T_0) \geq R(\theta, T_0), \tag{3.3}$$

the pavement will also crack.

Cracking prediction methods of bituminous pavements have been studied by many researchers (see Hills and Brien, 1966; Hajek and Hass, 1972; Shahin and McCullough, 1974; etc.). Comparing our criterion to their work, the most important fact is that we consider the effect of the loading time of thermal stress in predicting the cracking of bituminous pavement—so it not only explains the cracking phenomenon in the northern cold areas, but also explains the cracking phenomenon in areas where the climate is far less cold. It can be used to make the selection of appropriate bituminous pavement materials to reduce the cracking of the pavements in the pavement design.

To estimate the effect between the relaxation properties of materials and the thermal stress fields, we make a calculation and analysis on the thermal stress field for the three types of material presented in Fig. 2. The numerical results indicate that, under the same temperature conditions, the pavement paved by the mixture ALB has the minimum thermal stress and the pavement paved by the mixture SHL has the maximum thermal stress. Moreover, as the pavement temperature rises, the relaxation ability of the pavement gradually increases and the corresponding thermal stress gradually decreases. Thus, the pavement paved by the mixture ALB has the best crack-resistance ability. This is already verified by the usage results of bituminous pavements in the northern area of China (see Wang, 1991; Sa, 1993).

To analyze the effect between temperature speed and the ther-

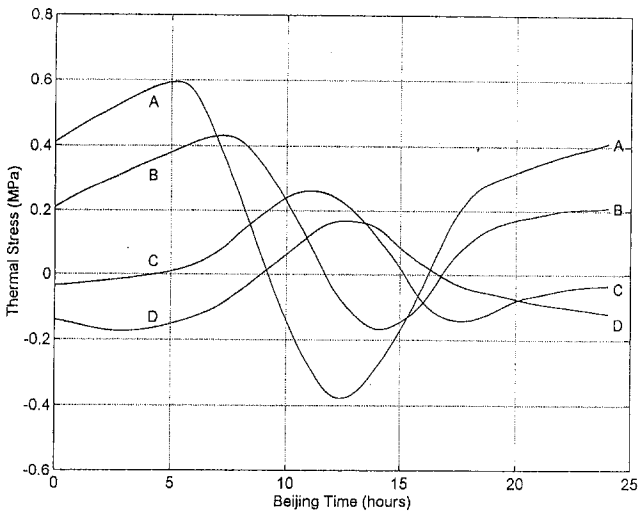


Fig. 4 Curves of the thermal stress distribution. Curve A: on the surface $y = 0$; Curve B: at the depth $y = 5$ cm; Curve C: at the depth $y = 15$ cm; Curve D: at the depth $y = 30$ cm.

Downloaded 04 May 2010 to 171.66.16.27. Redistribution subject to ASME license or copyright; see http://www.asme.org/terms/Terms_Use.cfm

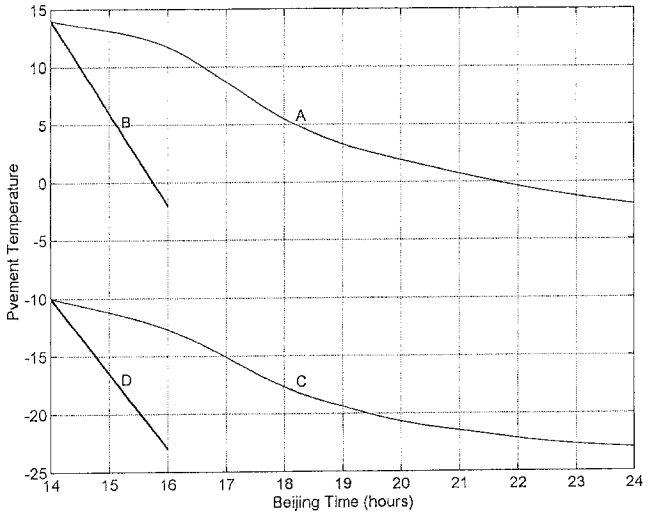


Fig. 5 Curves of the pavement temperature (°C) at the point (0, 0). Curve A and B are for Nov. 10, 1993 and Curve C and D are for Jan. 10, 1994.

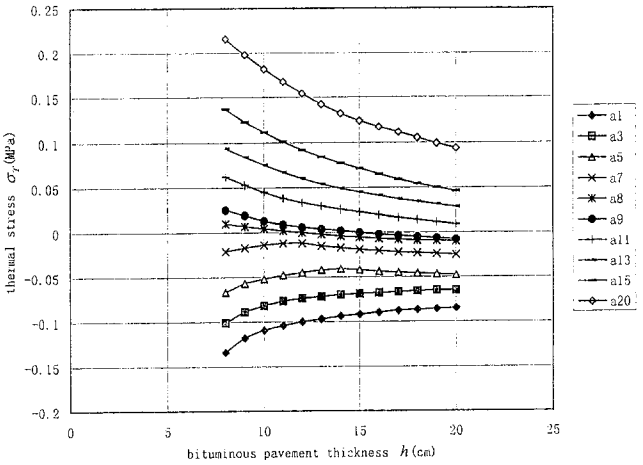


Fig. 7 Distribution curves of the thermal stress varied as the thickness of the bituminous pavement ($\alpha_1 = 2.5 \times 10^{-5}$/°C)

mal stress we consider two different temperature processes which have the same temperature amplitude, see Fig. 5 for Nov. 10, 1993 and Jan. 10, 1994. Curve A and C simulates the natural temperature condition. Curve B and D simulates the temperature condition for the indoor test. The numerical results corresponding to Fig. 5 are plotted in Fig. 6.

From the two figures, we can see that, under the same temperature variation amplitude, the larger the temperature speed, the larger the thermal stress is. The results indicate that temperature speed has a great influence on the thermal stresses and thermal cracking. The fact that thermal cracking of bituminous pavements generally appears in the early winter also verifies our analysis.

Our numerical analysis also indicates that the temperature gradient distributed not uniformly along the pavement thickness has also a great influence on the thermal stress distribution along the thickness, and this is related to the design of the pavement thickness. We can see this effect in the following section.

4 Thickness Design for Bituminous Pavements

How to design the thickness of the bituminous pavement is an important task in a semi-rigid pavement design. To determine the optimum thickness, we not only need to consider the problems of the cracks and ruts in the bituminous pavement, but also need to consider the problems of the economic cost for building the pavement structure. Generally speaking, increasing the thickness of the bituminous surfacing is a good way to reduce the thermal cracking. Based on this point, it was thought that the thickness should not be less than 18 cm during the eighties. However, recent studies (Wang, 1991; Sa, 1993) indicate that the rut deepens as the thickness of the bituminous surfacing increases. So far, how to deal with the contradiction and how to determine the optimum thickness are unsolved problems.

In this section we advance a method for designing the optimum thickness based on the point where thermal contraction property of the pavement materials has a great effect on the thermal stress distributions. Here we shall show an example.

Suppose the pavement is paved by mixture S90, the maximum temperature difference on the surface is -10°C, the difference distribution along the pavement thickness can be determined by the method presented in Wu (1992) and Wu (1997). Let σ_B and σ_T be the thermal stresses on the bottom of the bituminous surfacing and on the top of the top semi-rigid base, respectively. When $\alpha_1 = 2.5 \times 10^{-5}$/°C, the distribution curves of the thermal stresses varied as the thickness of bituminous surfacing and varied as the thermal contraction coefficients are plotted in Fig. 7 and Fig. 8, respectively. When $\alpha_1 = 3.5 \times 10^{-5}$/°C, the corresponding curves are plotted in Figs. 9 and 10, respectively.

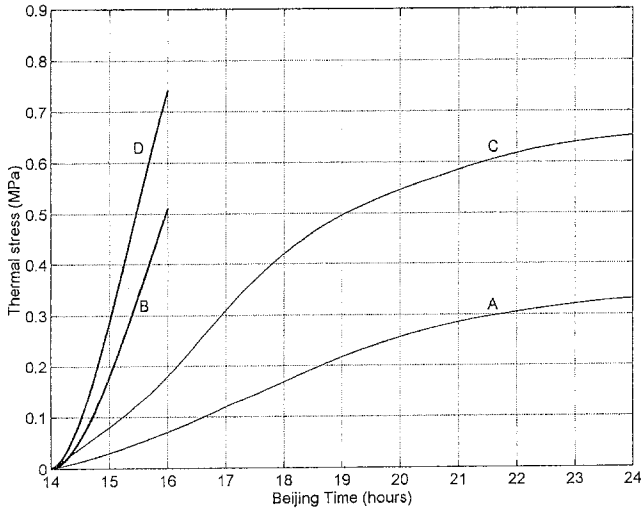


Fig. 6 Curves of the thermal stress at the point (0, 0) corresponding to the temperature distribution curves in Fig. 5

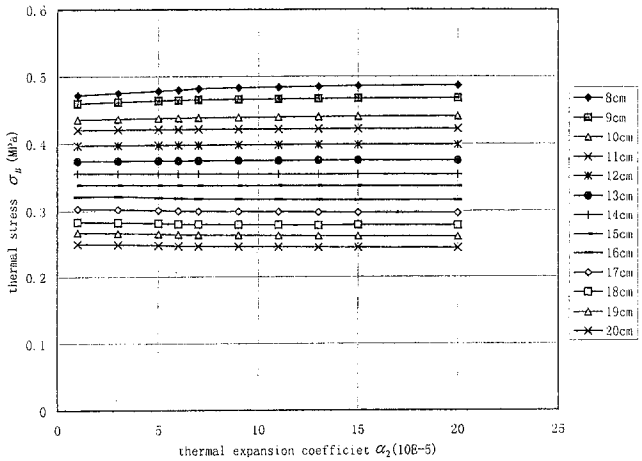


Fig. 8 Distribution curves of the thermal stress varied as the thermal expansion coefficients of the top semi-rigid base ($\alpha_1 = 2.5 \times 10^{-5}$/°C)

Downloaded 04 May 2010 to 171.66.16.27. Redistribution subject to ASME license or copyright; see http://www.asme.org/terms/Terms_Use.cfm

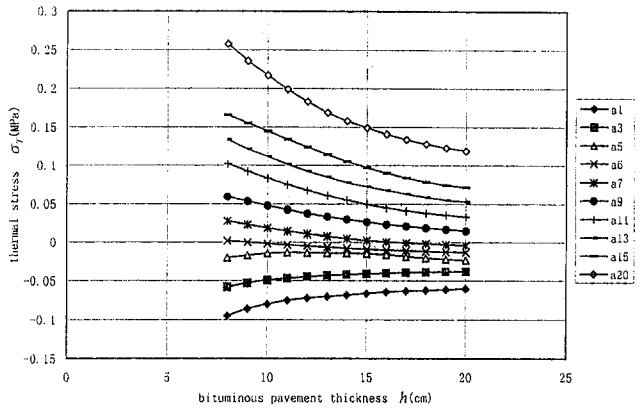


Fig. 9 Distribution curves of the thermal stress varied as the thickness of the bituminous pavement ($\alpha_1 = 3.5 \times 10^{-5}$/°C)

In the right-hand columns of Figs. 7 and 9, a1 expresses the thermal expansion coefficient $\alpha_2 = i(\times 10^{-5}$/°C) of the top semi-rigid base. In the right-hand column of Figs. 8 and 10, the number i cm expresses the distance from the surface. From Figs. 7 to 10, we observed the following features:

1 σ_T increases as α_2 increases (see Figs. 7 and 9). When $h \leq 13$ cm, σ_B increases as α_2 increases; when $h \geq 14$ cm, σ_B decreases as α_2 increases (see Figs. 8 and Figs. 10). This fact indicates that there is a critical thickness between 13 cm and 14 cm in which the thermal contraction property of the semi-rigid base has a minimum on the thermal stress field.
2 From Fig. 7 in which $\alpha_1 = 2.5 \times 10^{-5}$/°C, σ_T has the minimum absolute value when $\alpha_2 = 6.0 \times 10^{-5}$/°C, and from Fig. 9 in which $\alpha_1 = 3.5 \times 10^{-5}$/°C, σ_B has a minimum absolute value when $\alpha_2 = 8.0 \times 10^{-5}$/°C.

According to the above analysis, we suggest that the optimum design be $h = 13 \sim 14$ cm, $\alpha_2 = 6.0 \sim 8.0(\times 10^{-5}$/°C) for the problem concerned. This example indicates that it is possible for us to determine the optimum thickness of bituminous pavement and the best semi-rigid base materials based on the theoretical analysis.

Under the major project 85-65J of the Communications Ministry of China, a research group made a road test for the purpose of testing the crack resistance of different semi-rigid bases in Changzhi City, Shanxi, China in September of 1987 (see Wang, 1991). The same bituminous mixture is paved over five different semi-

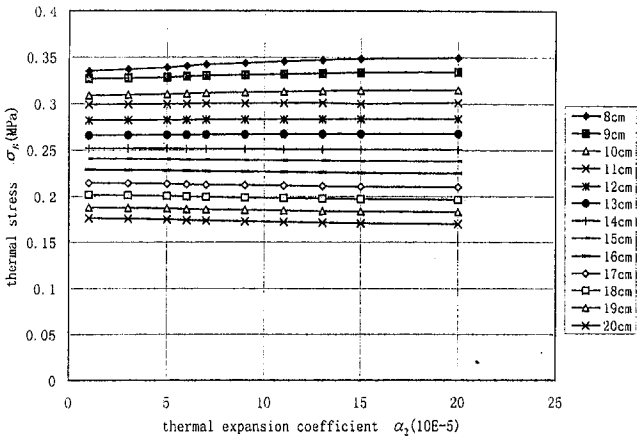


Fig. 10 Distribution curves of the thermal stress varied as the thickness of the bituminous pavement ($\alpha_1 = 3.5 \times 10^{-5}$/°C)

Table 2 The test results

Type of bases	Aggregate content	Type of cracks	Crack ratio (%)
Lime, earth, and gravel	0%	reticulated	14.9
	25%	reticulated	7.2
	50%	transverse	1.2
	75%	transverse	1.5
Lime, earth, and macadam	50%	transverse	0.8
Lime, coal ash, macadam	50%	transverse	0
Lime, coal ash, and gravel	50%	transverse	0
Cement gravel	60%	transverse	1.8

rigid bases, the thickness of bituminous surfacing is about 3 ~ 5 cm. In April of 1988, the group investigated the pavement cracks. The test results are listed in Table 2.

We can see from Table 2 that there were no cracks on the bituminous surfacing over the third and the fourth type of semi-rigid base. According to Wang (1991), among the five types of semi-rigid base materials, the mixture of lime, coal ash, and macadam or gravel with an aggregate content of 50 percent has the minimum thermal contraction coefficient with an average value of about 8.5×10^{-5}/°C. This is relatively close to the optimum value $6.0 \sim 8.0 \times 10^{-5}$/°C. These test results confirmed our theoretical results.

Acknowledgment

This work was funded by a strategic research grant from the City University of Hong Kong.

References

Hajek, J. J., and Hass, R. C. G., 1972, "Predicting low temperature cracking frequency of asphalt concrete pavement," *Transportation Research Record,* Vol. 407, pp. 39–52.

Halim, A., 1986, "Experimental and field investigation of the influence of relative rigidity on the problem of reflection cracking," *Transportation Research Record,* Vol. 1060, pp. 88–98.

Hills, J. F., and Brien, D., 1966, "The fracture of bituminous and asphalt mixes by temperature induced stresses," *Proceedings, Association of Asphalt Paving Technologists,* Vol. 35, pp. 292–309.

Lytton, et al., 1993, "Development and validation of Performance prediction models and specifications for asphalt binders and paving mixes," SHRP A Report (1993), PA357, pp. 516–526.

Majidadeh, K., Abdulshafi, A., Ilves, G. J., and McLaughlin, A., 1987, "A mechanistic model for thermally induced reflection cracking of Portland cement concrete pavement with reinforced asphalt pavement," *Transportation Research Record,* Vol. 1117, pp. 83–93.

Monismith, C. L., Secor, G. A., and Secor, K. E., 1965, "Temperature induced stresses and deformations in asphalt pavement, Proceedings," *Association of Asphalt Paving Technologists,* Vol. 34, pp. 248–285.

Rodin, Y. L., 1987, *Generalized Analytical Functions on Riemann Surfaces,* Springer Verlag, New York.

Sa, Q., 1993, *The Structure Design of Bituminous Pavements Over a Semi-Rigid Base for Advanced Highways,* The Building Industry Press of China, Bejing, P.R. China.

Shahin, M. Y., and McCullough, B. F., 1974, "Damage model for predicting temperature cracking in flexible pavement," *Transportation Research Record,* Vol. 521, pp. 30–46.

Thompson, M. R., 1989, "Breaking, cracking and seating concrete pavement," Transportation Research Board, Report No. TRB/NCHPR.SYN-144.

Vekua, I. N., 1962, *Generalized Analytic Functions,* Pergamon Press, London.

Wang, Z. R., 1991, *Semi-Rigid Pavements,* The People's Traffic Publishing House, Bejing, P.R. China.

Wong, R., 1989, *Asymptotic Approximations of Integrals,* Academic Press, New York.

Wu, G., 1997, "The analytic theory of the temperature fields of the bituminous pavement over a semi-rigid road base," *Appl. Math. Mech.,* Vol. 18, pp. 169–176.

Wu, G., 1992, "Analysis of the pavement temperature field of a layered system," *Chinese Journal of Highway and Transportation,* Vol. 5, pp. 14–24.

Wu, G., 1993, "Analysis of the thermal stress field in a bituminous pavement of a layered system," *Chinese Journal of Highway and Transport,* Vol. 6, pp. 1–9.

Wu, G., and Lin, T., 1998, "The analysis of development mechanism of thermal crack of the semi-rigid road-base," *Chinese Journal of Highway and Transport,* Vol. 1, pp. 21–28.

Downloaded 04 May 2010 to 171.66.16.27. Redistribution subject to ASME license or copyright; see http://www.asme.org/terms/Terms_Use.cfm

G. L. Gray
Assistant Professor,
Department of Engineering Science
and Mechanics,
The Pennsylvania State University,
227 Hammond Building,
University Park, PA 16802-1401
e-mail: gray@engr.psu.edu
Mem. ASME

D. C. Kammer
Associate Professor,
Department of Engineering Physics,
University of Wisconsin-Madison,
1500 Engineering Drive,
Madison, WI 53706-1687
e-mail: kammer@coefac.engr.wisc.edu
Mem. ASME

I. Dobson
Associate Professor,
Department of Electrical and
Computer Engineering,
University of Wisconsin-Madison,
1415 Engineering Drive,
Madison, WI 53706-1691
e-mail: dobson@engr.wisc.edu

A. J. Miller
Graduate Student,
Department of Engineering Science
and Mechanics,
The Pennsylvania State University,
227 Hammond Building,
University Park, PA 16802-1401
e-mail: ajm138@psu.edu

Heteroclinic Bifurcations in Rigid Bodies Containing Internally Moving Parts and a Viscous Damper

Melnikov's method is used to analytically study chaotic dynamics in an attitude transition maneuver of a torque-free rigid body in going from minor axis to major axis spin under the influence of viscous damping and nonautonomous perturbations. The equations of motion are presented, their phase space is discussed, and then they are transformed into a form suitable for the application of Melnikov's method. Melnikov's method yields an analytical criterion for homoclinic chaos in the form of an inequality that gives a necessary condition for chaotic dynamics in terms of the system parameters. The criterion is evaluated for its physical significance and for its application to the design of spacecraft. In addition, the Melnikov criterion is compared with numerical simulations of the system. The dependence of the onset of chaos on quantities such as body shape and magnitude of damping are investigated. In particular, it is found that for certain ranges of viscous damping values, the rate of kinetic energy dissipation goes down when damping is increased. This has a profound effect on the criterion for chaos.

Introduction

The determination and control of attitude evolution are important problems in modern spacecraft dynamics. The equations of motion describing the attitude dynamics of complex nonrigid spacecraft can be derived, but their analytical solution is elusive. Solutions to these highly nonlinear equations can be obtained using numerical simulation, but many interesting features of the dynamics can be lost in the numerical data. Fortunately, a great deal of physical insight into the behavior of these complex systems can be obtained by using a simpler "rigid body with perturbations" approximation for the spacecraft. This paper deals with the dynamics of the attitude transition from minor axis to major axis spin of a viscously damped, rigid body that is being perturbed by small oscillating masses. In particular, chaotic dynamics occurring during spin-axis transition will be investigated. We obtain an analytical test for chaos in terms of system parameters.

A single-body spacecraft is directionally unstable in the presence of energy dissipation when perturbed from spinning about its minor axis (Hughes, 1986). In the absence of active stabilization, the body will eventually reorient itself and spin about the major axis. Oscillating subbodies can produce chaos in a region of the phase space traversed by the spacecraft during this attitude maneuver. It is often important to be able to accurately predict the timing of this attitude maneuver and the presence of chaotic dynamics could render useless any attempt at this prediction. Therefore we suggest the spacecraft be designed such that chaos is avoided. It should be noted that the type of chaos considered herein is transient in nature and is distinct from chaos in a strange attractor (Guckenheimer and Holmes, 1983), though numerical investigations show that it can, in many cases, be difficult to tell the difference between strange attractor-type chaos and the type of chaos exhibited by these spacecraft models (Campbell, 1997).

Some aspects of related attitude maneuvers have been studied for dual-spin spacecraft. These spacecraft are reoriented by spin-up of rotors relative to the main spacecraft body. Attitude resonances in this maneuver, occurring during the spin-up or spin-down, have been investigated using perturbation techniques and numerical simulation (see, for example, Adams, 1980; Barba and Aubrun, 1976; Cochran and Holloway, 1980; Gebman and Mingori, 1976; Hall and Rand, 1994; Or, 1991; Or, 1998b). In addition, Or (1998a) has studied chaotic dynamics in dual-spin spacecraft using Melnikov's method, though Or does little in the way of interpreting these results.

In the case of single-body satellites, the direction and control of the final major axis orientation have been studied (Barba et al., 1973; Chinnery and Hall, 1995; Cronin, 1978; Kaplan and Cenker, 1973; Levi, 1989; Rahn and Barba, 1991), as have the dynamics

Contributed by the Applied Mechanics Division of THE AMERICAN SOCIETY OF MECHANICAL ENGINEERS for publication in the ASME JOURNAL OF APPLIED MECHANICS.
Discussion on the paper should be addressed to the Technical Editor, Professor Lewis T. Wheeler, Department of Mechanical Engineering, University of Houston, Houston, TX 77204-4792, and will be accepted until four months after final publication of the paper itself in the ASME JOURNAL OF APPLIED MECHANICS.
Manuscript received by the ASME Applied Mechanics Division, Oct. 15, 1997; final revision, Feb. 14, 1999. Associate Technical Editor: N. C. Perkins.

 Copyright © 1999 by ASME

Downloaded 04 May 2010 to 171.66.16.27. Redistribution subject to ASME license or copyright; see http://www.asme.org/terms/Terms_Use.cfm

and evolution of the maneuver itself, as found in Tsiotras and Longuski (1991) and Longuski and Tsiotras (1993a, b), in which they study the attitude evolution of near-symmetric rigid bodies under a variety of torque conditions. So far, little work has investigated the fundamental nature and causes of the observed and predicted dynamics. The work herein is another step in the process of obtaining that understanding.

The non-Hamiltonian perturbations of the rigid-body dynamics dealt with in this paper are due to time-periodic enforced motions of subbodies and viscous damping within a single rigid-body satellite. While the occurrence of chaos in this class of systems is not surprising (Lichtenberg and Lieberman, 1992), our application of Melnikov's method to detect the onset of chaos in this class of systems is new. As with earlier work (Gray et al., 1992, 1996), we have overcome considerable difficulties in model formulation and in the application of Melnikov's method to obtain a criterion for chaos which can be used in spacecraft design. Some of the closely related work is limited to chaos in spacecraft attitude dynamics when the perturbations are Hamiltonian (Dovbysh, 1989; Holmes and Marsden, 1983; Koiller, 1984). Some work has been done for non-Hamiltonian perturbations to spacecraft dynamics, but it has dealt almost exclusively with the stability of equilibria (Baillieul and Levi, 1987; Krishnaprasad, 1985; Krishnaprasad and Marsden, 1987; Rubanovskii, 1988). In other recent work, Tong and Tabarrok (1997) use Melnikov's method to investigate the the attitude motion of self-excited rigid bodies subject to small perturbation torques in a viscous medium. In contrast, the non-Hamiltonian perturbations studied in the current work are explicit functions of time, resulting in equations of motion with time-dependent coefficients, and in which the damping is implemented via internal viscosity. This class of perturbations is of considerable practical importance in spacecraft design. For example, the enforced time-dependent motion can include reciprocating masses, unbalanced rotors with constant angular velocities, and rotors with time-dependent spin rates.

Melnikov's method has been recently applied by Gray et al. (1992, 1996, 1998) to a problem which is similar to the one considered in this paper. The damping was assumed to be small and was implemented through a quantitative energy sink such that additional degrees-of-freedom would not be added to the system. A criterion was derived in terms of the system's physical parameters for the existence of chaos. This investigation considers a more realistic case consisting of larger damping that is implemented using an actual damping mechanism onboard the rigid body. Considering a physical damping mechanism greatly complicates the analysis. The current work, therefore, extends and complements our earlier investigations and serves as a paradigm for the study of a large class of problems that are "close" to the free rigid body.

Rigid-Body Model

The model used in this study is a torque-free, viscously damped rigid body that is perturbed by time-dependent subbody motion. Viscous damping is implemented by a rotor immersed in a viscous fluid within the rigid body. The subbodies and the angular momentum of the rotor relative to the platform are assumed to have a small, $\mathcal{O}(\epsilon)$ effect on the rigid carrier body and are therefore not included in the dynamics of the unperturbed system. The specific rigid body model is shown in Fig. 1.

The model is described as follows: The system's mass center c does not move relative to the carrier body since the two subbodies oscillate symmetrically with respect to c along the x-axis. The position of the subbodies relative to the carrier is a known periodic function of time and is denoted by $\eta(t)$. The $\eta = 0$ position is located a distance l from the mass center c. We let x, y, z denote a body-fixed orthogonal coordinate system aligned with the principal axes of the carrier body and centered at c. The principal moments of inertia of the carrier and the rotor with respect to c are designated I_1, I_2, I_3. The moments of inertia are distinct and we assume $I_1 < I_2 < I_3$. The mass center of the rotor lies on the y-axis and its spin axis is aligned with the y-axis. The rotor is immersed in a cavity containing a viscous fluid with a coefficient of viscous damping γ. The rotor spins relative to the carrier body with angular velocity ω_r and its moment of inertia about the y-axis is I_r.

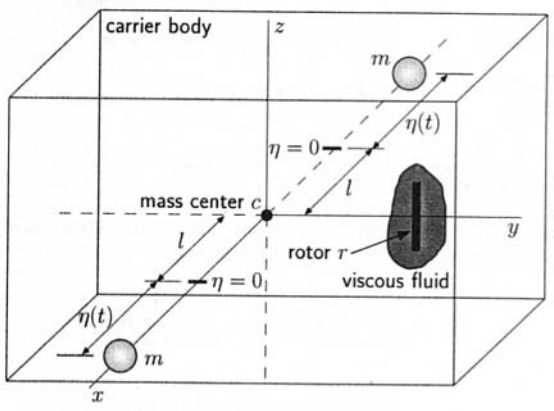


Fig. 1 The model rigid-body configuration

In order to apply Melnikov's method, it is assumed that the subbodies of mass m are "small" in comparison to the main body. In addition, the angular momentum of the rotor with respect to the carrier body is assumed to be "small." What we mean by "small" will be defined later with respect to a perturbation parameter ϵ. Therefore, both the subbodies and the rotor angular momentum are assumed to have an $\mathcal{O}(\epsilon)$ perturbing effect on the rigid carrier body.

Equations of Motion

Using standard methods such as Lagrange's equations or Newton-Euler techniques, and defining the following principal body angular momentum components h_1, h_2, h_3,

$$h_1 = A\omega_1 \quad h_2 = B\omega_2 + I_r\omega_r \quad h_3 = C\omega_3,$$

the equations of motion can be written as

$$\dot{h}_1 = \frac{1}{B+\Delta}\left(I_r\omega_r h_3 - \frac{C-B}{C+\Delta}h_2h_3\right) \tag{1}$$

$$\dot{h}_2 = \left(\frac{1}{A} - \frac{1}{C+\Delta}\right)h_1h_3 \tag{2}$$

$$\dot{h}_3 = \left(\frac{1}{B+\Delta} - \frac{1}{A}\right)h_1h_2 - \frac{I_r}{B+\Delta}\omega_r h_1 \tag{3}$$

$$\dot{\omega}_r = \frac{1}{I_r - B - \Delta}\left[\left(\frac{1}{A} - \frac{1}{C+\Delta}\right)h_1h_3 + \frac{\gamma}{I_r}(B+\Delta)\omega_r - \dot{\Delta}\left(\frac{h_2 - I_r\omega_r}{B+\Delta}\right)\right] \tag{4}$$

where $A \triangleq I_1$, $B \triangleq I_2 + 2ml^2$, $C \triangleq I_3 + 2ml^2$, $\Delta = \Delta(t) \triangleq 2m\eta(t)[2l + \eta(t)]$, and $(\dot{})$ denotes differentiation with respect to time. Note that Δ is the term that embodies the assumed to be known, time-dependent subbody motion (i.e., known frequency and amplitude).

It is now convenient to nondimensionalize the equations of motion and explicitly introduce the perturbation parameter ϵ. This makes clearer which terms are small, and therefore higher order, and which terms are to be retained. Defining the following nondimensional quantities

Downloaded 04 May 2010 to 171.66.16.27. Redistribution subject to ASME license or copyright; see http://www.asme.org/terms/Terms_Use.cfm

$$\epsilon \triangleq ml^2/B \qquad \tau \triangleq Ht/B \quad \tilde{h}_i \triangleq h_i/H \quad \tilde{h}_i' \triangleq \left(\frac{B}{H^2}\right)\dot{h}_i$$

$$\tilde{\Delta} \triangleq \frac{\Delta}{\epsilon B} \qquad \tilde{\gamma} \triangleq \gamma/H \quad r_1 \triangleq C/B \quad r_2 \triangleq A/B$$

$$\tilde{\omega}_r \triangleq \left(\frac{B}{H\sqrt{\epsilon}}\right)\omega_r \quad \tilde{I}_r \triangleq \frac{I_r}{B\sqrt{\epsilon}} \quad \tilde{h}_r \triangleq \tilde{I}_r\tilde{\omega}_r \quad \tilde{\omega}_r' \triangleq \left(\frac{B^2}{H^2\sqrt{\epsilon}}\right)\dot{\omega}_r,$$

where H is the magnitude of the angular momentum vector, the equations of motion, Eqs. (1)–(4), become

$$\tilde{h}_1' = \frac{1}{1+\epsilon\tilde{\Delta}}\left(\epsilon\tilde{h}_r\tilde{h}_3 - \frac{r_1-1}{r_1+\epsilon\tilde{\Delta}}\tilde{h}_2\tilde{h}_3\right) \tag{5}$$

$$\tilde{h}_2' = \left(\frac{1}{r_2} - \frac{1}{r_1+\epsilon\tilde{\Delta}}\right)\tilde{h}_1\tilde{h}_3 \tag{6}$$

$$\tilde{h}_3' = \left(\frac{1}{1+\epsilon\tilde{\Delta}} - \frac{1}{r_2}\right)\tilde{h}_1\tilde{h}_2 - \frac{\epsilon}{1+\epsilon\tilde{\Delta}}\tilde{h}_r\tilde{h}_1 \tag{7}$$

$$\tilde{\omega}_r' = \frac{-\left[\left(\frac{1}{r_2} - \frac{1}{r_1+\epsilon\tilde{\Delta}}\right)\tilde{h}_1\tilde{h}_3 + \tilde{\gamma}(1+\epsilon\tilde{\Delta})\frac{\tilde{\omega}_r}{\tilde{I}_r} - \epsilon\tilde{\Delta}'\left(\frac{\tilde{h}_2-\epsilon\tilde{h}_r}{1+\epsilon\tilde{\Delta}}\right)\right]}{\sqrt{\epsilon}-\epsilon\tilde{I}_r+\epsilon^{3/2}\tilde{\Delta}}. \tag{8}$$

Equations (5)–(8) are the full equations of motion with no simplifying assumptions. As will be seen, these equations must be transformed into a form consisting of an unperturbed part[1] plus perturbation terms in order to apply Melnikov's method. This is done by expanding the equations in powers of ϵ and keeping terms through $\mathcal{O}(\epsilon)$. The expanded equations can be written as

$$\tilde{h}_1' = \frac{1-r_1}{r_1}\tilde{h}_2\tilde{h}_3 + \epsilon\left[\tilde{h}_r\tilde{h}_3 + \tilde{\Delta}\left(\frac{r_1^2-1}{r_1^2}\right)\tilde{h}_2\tilde{h}_3\right] + O(\epsilon^2) \tag{9}$$

$$\tilde{h}_2' = \left(\frac{r_1-r_2}{r_1r_2}\right)\tilde{h}_1\tilde{h}_3 + \epsilon\frac{\tilde{\Delta}}{r_1^2}\tilde{h}_1\tilde{h}_3 + O(\epsilon^2) \tag{10}$$

$$\tilde{h}_3' = \left(\frac{r_2-1}{r_2}\right)\tilde{h}_1\tilde{h}_2 - \epsilon(\tilde{\Delta}\tilde{h}_1\tilde{h}_2 + \tilde{h}_r\tilde{h}_1) + O(\epsilon^2) \tag{11}$$

$$\sqrt{\epsilon}\,\tilde{\omega}_r' = -\left(\frac{r_1-r_2}{r_1r_2}\right)\tilde{h}_1\tilde{h}_3 - \tilde{\gamma}\frac{\tilde{\omega}_r}{\tilde{I}_r} - \sqrt{\epsilon}\left[\left(\frac{r_1-r_2}{r_1r_2}\right)\tilde{I}_r\tilde{h}_1\tilde{h}_3 + \tilde{\gamma}\tilde{\omega}_r\right] - \epsilon\left[\left(\frac{r_2-r_1}{r_1r_2}+\frac{1}{r_1^2}\right)\tilde{\Delta}\tilde{h}_1\tilde{h}_3 - \tilde{h}_2\tilde{\Delta}' - \left(\frac{r_2-r_1}{r_1r_2}\right)\tilde{I}_r^2\tilde{h}_1\tilde{h}_3 + \tilde{\gamma}\tilde{I}_r\tilde{\omega}_r\right] + O(\epsilon^{3/2}). \tag{12}$$

The assumed order of various physical quantities gives the form of the equations of motion given above—different assumptions would change the form. In particular, our choice of assumed orders leads to equations of motion for which the unperturbed solution can be obtained. It should be noted that making the assumptions that I_r and ω_r are $\mathcal{O}(\sqrt{\epsilon})$ quantities in no way invalidates our results; it merely reduces the size that we must assign to ϵ when saying that our results are valid "for sufficiently small ϵ."

The Unperturbed Phase Space

In order to apply Melnikov's method to the system of Eqs. (9)–(12), there must be a heteroclinic cycle (Guckenhiemer and Holmes, 1983) in the unperturbed phase space, and the unperturbed system must be integrable. It can be shown that the attitude dynamics of a torque-free rigid body, when measured in body angular momentum components, occur on the surface of the angular momentum sphere (see Fig. 2). This sphere is also the reduced phase space corresponding to Euler's equations of motion for a torque-free rigid body. In terms of the nondimensional quantities defined herein, these equations are given by

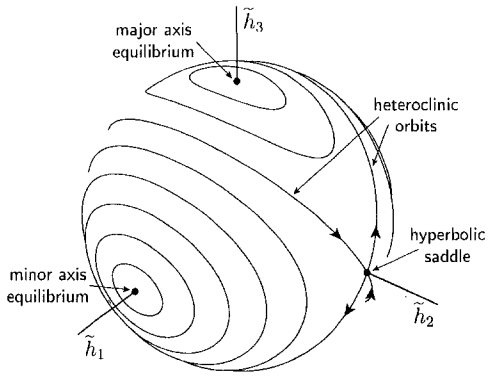


Fig. 2 The momentum sphere illustrating the heteroclinic orbits and the hyperbolic saddle points. The curves are orbits of constant energy.

$$\tilde{h}_1' = \left(\frac{1-r_1}{r_1}\right)\tilde{h}_2\tilde{h}_3 \tag{13}$$

$$\tilde{h}_2' = \left(\frac{r_1-r_2}{r_1r_2}\right)\tilde{h}_1\tilde{h}_3 \tag{14}$$

$$\tilde{h}_3' = \left(\frac{r_2-1}{r_2}\right)\tilde{h}_1\tilde{h}_2. \tag{15}$$

Equations (13)–(15) are just the first three equations of motion for the system considered here, Eqs. (5)–(7), with $\epsilon = 0$, i.e., they are the unperturbed equations of motion. Euler's equations are integrable in terms of Jacobi elliptic functions for nearly all admissible values of angular momentum and kinetic energy, but for a given angular momentum, there is a value of kinetic energy such that they are integrable in terms of hyperbolic functions. These integral curves will play a very important role in the following development.

The phase space for Euler's equations is $\mathbb{R}^3$, but the motion is confined to the surface of the momentum sphere. This phase space possesses six fixed points or equilibria corresponding to positive and negative spin about each of the three principal moment of inertia axes of the rigid body. Two of the equilibria correspond to spin about the major principal axes and two correspond to spin about the minor principal axes. Topologically, all four of these equilibria are centers, in that the linearization of Euler's equations at these points has two complex eigenvalues with zero real parts (ignoring the unimportant dimension orthogonal to the surface of the momentum sphere). The other two equilibria correspond to spin about the intermediate principal axes and are hyperbolic fixed points or saddles (the linearization has two real eigenvalues, one positive and one negative). The phase space also has four heteroclinic orbits linking the hyperbolic fixed points, thus giving heteroclinic cycles, as shown in Fig. 2. These heteroclinic orbits are the integral curves that can be written in terms of hyperbolic functions that were described above. During the transition of an energy dissipating rigid body from spin near the minimum moment of inertia axis to spin about the maximum moment of inertia axis, the trajectory must cross the heteroclinic orbits in the phase space. More precisely, the trajectory of the damped system must cross a heteroclinic orbit of the undamped system (the heteroclinic orbits break up in the presence of damping). We study the chaotic motion in the perturbed system that may occur near these heteroclinic orbits.

[1] Found by setting $\epsilon = 0$. The unperturbed equations are just the equations for a torque-free rigid body.

Downloaded 04 May 2010 to 171.66.16.27. Redistribution subject to ASME license or copyright; see http://www.asme.org/terms/Terms_Use.cfm

Melnikov's Method and Equation Transformation

Melnikov's method (Melnikov, 1963) is applied to detect chaos in the system of Eqs. (9)–(12). For a detailed exposition of Melnikov theory, see Holmes (1980), Holmes (1981), Guckenheimer and Holmes (1983) or Wiggins (1990). Briefly, Melnikov's method is a perturbation technique for proving the existence of transverse heteroclinic[2] orbits to hyperbolic periodic orbits in a class of time-periodic vector fields. Although it is a perturbation technique, Melnikov's method gives *global* information about the system's dynamics. The existence of transverse heteroclinic orbits implies the existence of horseshoes and chaos via the Smale-Birkhoff theorem. In phase space, the chaos appears near the unperturbed heteroclinic orbit. The essential idea is to use the globally computable solutions to the unperturbed *integrable* system in studying the perturbed solution.

The form of Melnikov's method we are using considers systems of the form

$$\dot{x} = f(x) + \epsilon g(x, t; \mu), \tag{16}$$

where $x \in \mathbb{R}^2$, f is a vector field possessing two hyperbolic fixed points, p_1 and p_2, connected to one another by a heteroclinic orbit, $q_0(t)$ (i.e., $\lim_{t\to\infty} q_0(t) = p_1$ and $\lim_{t\to-\infty} q_0(t) = p_2$), g is a small perturbation of period T in t, and $\mu \in \mathbb{R}^k$ is a vector of parameters. If the Melnikov function is denoted $\mathcal{M}(t_0)$, it can be written as the integral

$$\mathcal{M}(t_0) = \int_{-\infty}^{\infty} \left\{ [f(q_0(t)) \wedge g(q_0(t), t + t_0)] \times \exp\left[-\int_0^t \text{trace}(Df)(q_0(s))ds \right] \right\} dt, \tag{17}$$

where the symbol $\wedge$ is the wedge operator, defined by $a \wedge b = a_1 b_2 - a_2 b_1$, and $Df = [\partial f_i/\partial x_j]$ is the Jacobian matrix of the first partial derivatives of f. We note that this is not the same Melnikov integral seen in most expositions of the theory as our unperturbed vector field in transformed coordinates is not Hamiltonian.

The unperturbed phase space (the momentum sphere) has the structure necessary (heteroclinic orbits connecting hyperbolic saddles) to apply Melnikov's method. The initial tasks are:

1. solving for the heteroclinic orbit $q_0(t)$ of the unperturbed system (i.e., finding the hyperbolic solutions along the heteroclinic orbits on the surface of the momentum sphere),
2. writing the perturbed equations of motion, Eqs. (9)–(12), in the form of Eq. (16) such that only terms through $\mathcal{O}(\epsilon)$ are kept, and
3. obtaining two independent equations of motion (in convenient coordinates) describing the dynamics on the surface of the momentum sphere.

Unperturbed Heteroclinic Orbits $q_0(t)$. For a torque-free rigid body with equations of motion given by Eqs. (13)–(15), there are two integrals of the motion: momentum and energy. In nondimensional coordinates, these integrals are given by

$$\tilde{h}_1^2 + \tilde{h}_2^2 + \tilde{h}_3^2 = 1 \quad \text{(momentum)} \tag{18}$$

$$\frac{\tilde{h}_1^2}{r_2} + \tilde{h}_2^2 + \frac{\tilde{h}_3^2}{r_1} = \tilde{T} \quad \text{(energy)} \tag{19}$$

where $\tilde{T} \triangleq 2BT/H^2$ is the nondimensional total energy and T is the total energy. Any trajectory on the momentum sphere is determined by the intersection of the momentum sphere S defined by Eq. (18) and the energy ellipsoid $\mathcal{E}$ defined by Eq. (19). Recall that when viewed in body coordinates, the angular momentum vector appears to move such that its tip always remains on a particular intersection of S and $\mathcal{E}$. The radius of S, which is $\tilde{H} = 1$, must lie between the smallest and largest semiaxes of the ellipsoid. Since $A < B < C$, or nondimensionally $0 < r_2 < 1 < r_1$,[3] the condition on the radius of S is given by $r_2\tilde{T} < 1 < r_1\tilde{T}$. Since the heteroclinic orbits are formed when the S and $\mathcal{E}$ surfaces are tangent at the points $(0, \pm 1, 0)$, the energy level for the heteroclinic orbits must be given by $T = H^2/(2B)$, or $\tilde{T} = 1$ nondimensionally. The energy integral then becomes

$$\frac{\tilde{h}_1^2}{r_2} + \tilde{h}_2^2 + \frac{\tilde{h}_3^2}{r_1} = 1. \tag{20}$$

Using Eqs. (13)–(15), (18), and (20), it can be shown that the solutions for the $\tilde{h}_i$ along the heteroclinic orbits are given by (also see Hughes, 1986)

$$\tilde{h}_{1u} = s_1 \left[\frac{r_2(1 - r_1)}{r_2 - r_1} \right]^{1/2} \text{sech} \left\{ \left[\frac{(r_2 - 1)(1 - r_1)}{r_1 r_2} \right]^{1/2} \tau \right\} \tag{21}$$

$$\tilde{h}_{2u} = s_2 \tanh \left\{ \left[\frac{(r_2 - 1)(1 - r_1)}{r_1 r_2} \right]^{1/2} \tau \right\} \tag{22}$$

$$\tilde{h}_{3u} = s_3 \left[\frac{r_1(r_2 - 1)}{r_2 - r_1} \right]^{1/2} \text{sech} \left\{ \left[\frac{(r_2 - 1)(1 - r_1)}{r_1 r_2} \right]^{1/2} \tau \right\}, \tag{23}$$

where the subscript u signifies an unperturbed quantity, $\tau = 0$ has been chosen to eliminate constants of integration, and s_1, s_2, s_3 are each ± 1 and are chosen such that their product $s_1 s_2 s_3 = +1$.

In addition to the unperturbed solutions for the $\tilde{h}_i$, the equation for the rotor must be incorporated. This is done using a technique similar to that used by Holmes (1983) and by Volosov (1962). We were able to integrate Eqs. (9)–(11) to obtain Eqs. (21)–(23) since they decouple from the rotor equation, Eq. (12), when $\epsilon = 0$. Due to this uncoupling, the unperturbed solution for the rotor is readily obtained by using the solutions given in Eqs. (21)–(23). For $\epsilon = 0$, Eq. (12) becomes

$$\left(\frac{r_1 - r_2}{r_1 r_2} \right) \tilde{h}_{1u} \tilde{h}_{3u} + \tilde{\gamma} \frac{\tilde{\omega}_{ru}}{\tilde{I}_r} = 0,$$

and it can be readily seen that

$$\tilde{h}_{ru} = \tilde{I}_r \tilde{\omega}_{ru} = \frac{\tilde{I}_r^2}{\tilde{\gamma}} \left(\frac{r_2 - r_1}{r_1 r_2} \right) \tilde{h}_{1u} \tilde{h}_{3u}. \tag{24}$$

Equation (24) can now be substituted into the perturbations in Eqs. (9)–(11) to obtain the equations to which Melnikov's method is applied. This process of "eliminating" the degree-of-freedom associated with the rotor was facilitated by the assumptions made on the sizes of all the variables and parameters in the system. We are saying that the rotor is a higher-order perturbation to the system dynamics and that Eq. (24) gives the rotor the motion that would occur if the carrier body were *forced* to move as a free rigid body.

Transforming the $\mathcal{O}(\epsilon)$ Equations of Motion. We now transform to spherical coordinates so that the surface of the momentum sphere is mapped to a plane. This is done since Eqs. (9)–(11) are not independent, that is, the *three* equations are describing motion in $\mathbb{R}^2$. Transforming to spherical coordinates will give two independent equations, though the unperturbed part will no longer be Hamiltonian. It is convenient to choose the coordinate transformation so that one of the new coordinates is zero along an unperturbed trajectory. This can easily be done since the heteroclinic orbits are great circles on the momentum sphere.

Consider the heteroclinic orbit that lies in the region $\tilde{h}_1 > 0$ and $\tilde{h}_3 > 0$. The angle ν between the $\tilde{h}_1$–$\tilde{h}_2$ plane and this heteroclinic orbit can be shown to be

[2] The method applies equally well to systems with homoclinic orbits.

[3] The complete condition on r_1 and r_2 is $0 < r_2 < 1 < r_1 < 1 + r_2$.

Downloaded 04 May 2010 to 171.66.16.27. Redistribution subject to ASME license or copyright; see http://www.asme.org/terms/Terms_Use.cfm

$$\nu = \arctan\left[\frac{r_1(r_2-1)}{r_2(1-r_1)}\right]^{1/2}. \tag{25}$$

Starting with a set of coordinates ξ_1, ξ_2, ξ_3 aligned with the $\tilde{h}_1$, $\tilde{h}_2$, $\tilde{h}_3$ system, rotate the ξ coordinate system through the angle $-\nu$ about the $\tilde{h}_2$-axis so that the positive ξ_1-axis pierces the heteroclinic orbit in the region $\tilde{h}_1 > 0$, $\tilde{h}_3 > 0$. We can then transform from the ξ coordinates to the dimensionless spherical coordinates ϕ and θ to obtain the following equations relating the $\tilde{h}_i$, and ν, θ, and ϕ:

$$\tilde{h}_1 = \cos\nu\cos\theta\cos\phi - \sin\nu\sin\phi, \tag{26}$$

$$\tilde{h}_2 = \sin\theta\cos\phi, \tag{27}$$

$$\tilde{h}_3 = \sin\nu\cos\theta\cos\phi + \cos\nu\sin\phi. \tag{28}$$

The θ coordinate is measured in the ξ_1–ξ_2 plane as a positive rotation about the ξ_3-axis and the ϕ coordinate is measured in the "new" ξ_1–ξ_3 plane as a positive rotation about the "new" ξ_1-axis. Also note that there is no radial dependence since the angular momentum sphere has a constant radius. The derivatives with respect to τ are also needed and they are given by

$$\tilde{h}_1' = \phi'(-\cos\nu\sin\phi\cos\theta - \sin\nu\cos\phi) - \theta'\cos\nu\sin\theta\cos\phi, \tag{29}$$

$$\tilde{h}_2' = \theta'\cos\theta\cos\phi - \phi'\sin\theta\sin\phi, \tag{30}$$

$$\tilde{h}_3' = \phi'(\cos\nu\cos\phi - \sin\nu\cos\theta\sin\phi) - \theta'\sin\nu\sin\theta\cos\phi. \tag{31}$$

Equations (26)–(31) are now substituted into Eqs. (9)–(11) and *any* two of the resulting three equations are then solved for θ' and ϕ'. This gives the final two first-order differential equations to which Melnikov's method is applied:

$$\begin{aligned}\theta' = {} & \{(r_1-r_2)\cos\theta\cos\nu\cos 2\phi\sec\phi\sin\nu \\ & + (2r_1r_2 - r_1 - r_2)\sin\phi\}/(r_1r_2) \\ & + \epsilon\{4r_2\tilde{\gamma}\tilde{\Delta}[\cos\theta\cos 2\phi\sec\phi\sin 2\nu + 2\cos^2\nu\sin\phi \\ & - 2\cos^2\theta\sin^2\nu\sin\phi - 2r_1^2\sin^2\theta\sin\phi] \\ & + \tilde{I}_r^2 r_1(r_1-r_2)\sin\theta\tan\phi[\sin 2\nu(-1+\cos 2\theta \\ & + 3\cos 2\phi + \cos 2\theta\cos 2\phi) \\ & + 4\cos\theta\cos 2\nu\sin 2\phi]\}/(8\tilde{\gamma}r_1^2r_2)\end{aligned} \tag{32}$$

$$\begin{aligned}\phi' = {} & \{(r_1-r_2)\cos\nu\sin\nu\sin\theta\sin\phi\}/(r_1r_2) \\ & + \epsilon\{r_2\tilde{\gamma}\tilde{\Delta}\sin\theta[\sin\nu(\cos\theta\cos\phi\sin\nu + \cos\nu\sin\phi) \\ & - r_1^2\cos\theta\cos\phi] + \tfrac{1}{8}r_1(r_1-r_2)\tilde{I}_r^2\cos\theta[\sin 2\nu(-1 \\ & + \cos 2\theta + 3\cos 2\phi + \cos 2\theta\cos 2\phi) \\ & + 4\cos\theta\cos 2\nu\sin 2\phi]\}/(\tilde{\gamma}r_1^2r_2).\end{aligned} \tag{33}$$

These equations are in the form of Eq. (16), or $\phi' = f_1 + \epsilon g_1$ and $\theta' = f_2 + \epsilon g_2$.

Finally, the unperturbed solutions given by Eqs. (21)–(23) must be transformed to this same set of spherical coordinates. This transformation gives

$$\sin\theta_u = \tanh\left\{\left[\frac{(r_2-1)(1-r_1)}{r_1r_2}\right]^{1/2}\tau\right\} \tag{34}$$

$$\cos\theta_u = \operatorname{sech}\left\{\left[\frac{(r_2-1)(1-r_1)}{r_1r_2}\right]^{1/2}\tau\right\} \tag{35}$$

$$\phi_u = 0 \tag{36}$$

along the selected unperturbed heteroclinic orbit.

The Melnikov Function

We begin by prescribing the time-dependent, periodic form of η, by letting $\tilde{\eta} \triangleq \eta/l$, $\tilde{\Omega} \triangleq \Omega B/H$, and $\eta \triangleq \eta_0\cos(\Omega t)$. This definition corresponds to a simple harmonic oscillation of the masses. It follows that the nondimensional form of Δ is

$$\tilde{\Delta} = \tilde{\eta}^2 + 4\tilde{\eta}\cos(\tilde{\Omega}\tau) + \tilde{\eta}^2\cos(2\tilde{\Omega}\tau). \tag{37}$$

Substituting the unperturbed solutions $q_0(\tau)$, specified by Eqs. (34)–(36), into $f(q_0(\tau))$ and $g(q_0(\tau), \tau + \tau_0)$ of Eqs. (32) and (33), carrying out the wedge product, substituting the result into the Melnikov integral given by Eq. (17), noting that the term in the exponential

$$\operatorname{trace}(Df) = \frac{\sin\theta\sin\phi}{r_1r_2}(r_1-r_2)\sin\nu\cos\nu\tan\phi, \tag{38}$$

is zero when evaluated along the unperturbed heteroclinic trajectory (i.e., $\operatorname{trace}(Df)(q_0(s)) = 0$ when $\phi_u = 0$), and finally eliminating terms that are zero due to having an odd integrand, we obtain

$$\begin{aligned}\mathcal{M}(\tau_0) = {} & \frac{C_1^2\tilde{I}_r^2}{\tilde{\gamma}}\int_{-\infty}^{\infty}\operatorname{sech}^4(C_1\tau)d\tau \\ & - 4\tilde{\eta}C_2\sin(\tilde{\Omega}\tau_0)\int_{-\infty}^{\infty}\sin(\tilde{\Omega}\tau)\tanh(C_1\tau)\operatorname{sech}^2(C_1\tau)d\tau \\ & - \tilde{\eta}^2C_2\sin(2\tilde{\Omega}\tau_0)\int_{-\infty}^{\infty}\sin(2\tilde{\Omega}\tau)\tanh(C_1\tau)\operatorname{sech}^2(C_1\tau)d\tau\end{aligned} \tag{39}$$

where

$$C_1 \triangleq \left[\frac{(r_1-1)(1-r_2)}{r_1r_2}\right]^{1/2} \tag{40}$$

$$C_2 \triangleq \left(\frac{r_1-1}{r_1}\right)^2\left(\frac{r_2-r_1-1}{r_1-r_2}\right)\left[\frac{r_1(1-r_2)}{r_2(r_1-1)}\right]^{1/2}. \tag{41}$$

Interestingly, even though the divergence of the transformed unperturbed vector field (given by Eqs. (32) and (33) with $\epsilon = 0$) is *not* equal to zero as it would be for a Hamiltonian system, it *is* zero when it is evaluated along the heteroclinic trajectory. This will be true for Melnikov's method applied to all systems perturbed off of Euler's equations, Eqs. (13)–(15), and then transformed using spherical coordinates (as we have done in Gray et al., 1992, 1996, 1998). That is, one can apply Melnikov's method to the system transformed using spherical coordinates as if the unperturbed system were Hamiltonian.

The evaluation of these integrals can be accomplished via residue theory. Upon carrying out the integration, the following Melnikov function is obtained:

$$\mathcal{M}(\tau_0) = \frac{4\tilde{I}_r^2C_1^4}{3\tilde{\gamma}} - 2\pi\tilde{\Omega}^2\tilde{\eta}C_2\left[\frac{\sin(\tilde{\Omega}\tau_0)}{\sinh[\pi\tilde{\Omega}/(2C_1)]} + \tilde{\eta}\frac{\sin(2\tilde{\Omega}\tau_0)}{\sinh(\pi\tilde{\Omega}/C_1)}\right]. \tag{42}$$

Melnikov theory states that the condition for transverse heteroclinic orbits and therefore chaos is that $\mathcal{M}(\tau_0)$ change sign for some τ_0 (Guckenheimer and Holmes, 1983). Inspection of the Melnikov function reveals that there are two harmonic terms, one

Downloaded 04 May 2010 to 171.66.16.27. Redistribution subject to ASME license or copyright; see http://www.asme.org/terms/Terms_Use.cfm

with twice the frequency of the other. Therefore, the maximum amplitude of the factor containing the harmonic terms is some function F_{max} of *both* of the harmonic amplitudes. It can be shown that F_{max} is given by

$$F_{max} = \frac{1}{4}\left[3A + \sqrt{A^2 + 32B^2}\right] \times \left[\frac{1}{2} + \frac{A}{32B^2}\left(\sqrt{A^2 + 32B^2} - A\right)\right]^{1/2} \quad (43)$$

where $A = \text{csch}\,[\pi\tilde{\Omega}/(2C_1)]$ and $B = \tilde{\eta}\ \text{csch}\ (\pi\tilde{\Omega}/C_1)$. The analytical criterion for chaos becomes

$$2\pi\tilde{\Omega}^2\tilde{\eta}|C_2 F_{max}| > \frac{4\tilde{I}_r^2 C_1^4}{3\tilde{\gamma}}. \quad (44)$$

Close inspection of Eq. (44) reveals that since $C_1 = C_1(r_1, r_2)$, $C_2 = C_2(r_1, r_2)$, and $F_{max} = F_{max}(r_1, r_2, \tilde{\eta}, \tilde{\Omega})$, Eq. (44) is a function of the six system parameters, r_1, r_2, $\tilde{I}_r$, $\tilde{\eta}$, $\tilde{\Omega}$, and $\tilde{\gamma}$. If Eq. (44) is satisfied, then the system modeled by Eqs. (5)–(8) exhibits chaotic dynamics near the heteroclinic orbits for sufficiently small ϵ.

Numerical Simulations

A complete numerical investigation of this system is far beyond the scope of this paper and will be presented in future work. On the other hand, we include some of numerical simulations to attempt to demonstrate the range of validity of Melnikov's method on a system such as the one considered herein. A representative example of the result of some of our numerical simulations is shown in Fig. 3. This figure shows how variations in the nondimensional forcing frequency $\tilde{\Omega}$ (vertical axis in each part) versus the nondimensional damping coefficient forcing amplitude $\tilde{\gamma}$ (horizontal axis in each part) affect the rigid-body motion. In addition, the nondimensional forcing amplitude is given by $\tilde{\eta} = 0.100$ in the top figure, $\tilde{\eta} = 0.575$ in the middle figure, and $\tilde{\eta} = 1.25$ (Yes, the masses do pass through one another.) in the bottom figure. The other system parameters have been fixed at $r_1 = 1.5$, $r_2 = 0.6$, and $\tilde{I}_r = 1.0$. In each part of this figure, the solid black dots indicate trajectories which are chaotic, the open circles indicate limit cycle trajectories (of various periods), and the "pluses" indicate trajectories which damp to major axis spin. Superimposed on the this figure is a black line indicating the boundary between regions of phase space predicted to be chaotic according to Melnikov's method and those that are not. Points to the right of the Melnikov curve are those predicted to be chaotic according to Eq. (44) for this set of system parameters.

To generate this figure, many phase space trajectories were generated and visually examined. This visual examination clearly showed three different classes of trajectories: those that simply decayed to major axis spin (Fig. 4), those that settled into some type of limit cycle (Fig. 5), and those that were chaotic (Fig. 6). It is, of course, impractical to follow this procedure for the approximately 60,000 different parameters sets we have investigated. Consequently, we have devised a "physically intuitive" scheme for automatically selecting between the three types of motion for each trajectory. We utilize the ordinary differential equation solver, lsode (Hindmarsh, 1983), integrate for 2^{16} nondimensional time intervals, and include three statistical measures in the code. These three statistical measures are as follows:

Measure I. When a rigid body reorients itself from minor axis to major axis spin, the angular momentum component in the $\tilde{h}_1$ and

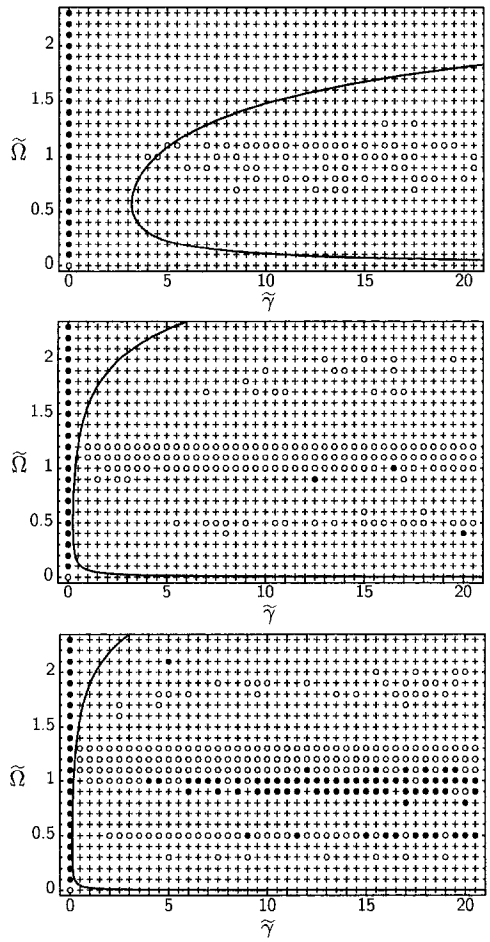


Fig. 3 Three frames in a parameter space evolution showing nondimensional frequency $\tilde{\Omega}$ versus nondimensional viscous damping. From top to bottom, the three plots show $\tilde{\eta} = 0.100$, $\tilde{\eta} = 0.575$, $\tilde{\eta} = 1.25$. See text for further details.

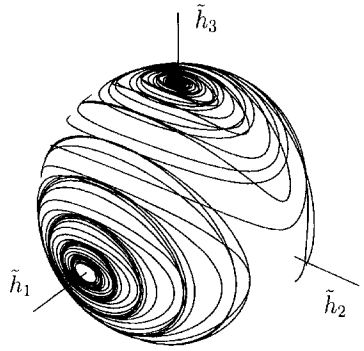


Fig. 4 Major axis spin trajectory where $\tilde{\gamma} = 5.0$, $\tilde{\Omega} = 0.10$, $\tilde{\eta} = 0.9$, $r_1 = 1.5$, $r_2 = 0.6$, and $\tilde{I}_r = 1.0$

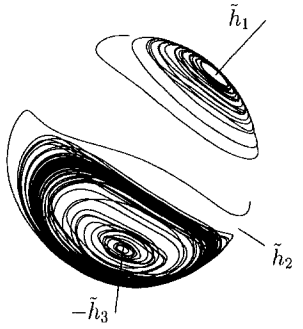


Fig. 5 Periodic trajectory where $\tilde{\gamma} = 5.0$, $\tilde{\Omega} = 1.1$, $\tilde{\eta} = 0.9$, $r_1 = 1.5$, $r_2 = 0.6$, and $\tilde{I}_r = 1.0$

Downloaded 04 May 2010 to 171.66.16.27. Redistribution subject to ASME license or copyright; see http://www.asme.org/terms/Terms_Use.cfm

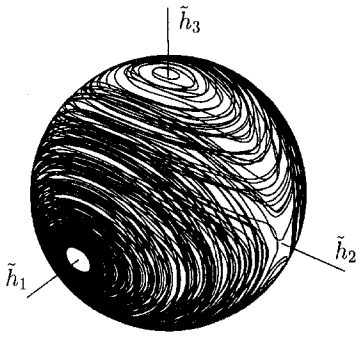


Fig. 6 Chaotic trajectory where $\tilde{\gamma} = 25.0$, $\tilde{\Omega} = 1.0$, $\tilde{\eta} = 0.9$, $r_1 = 1.5$, $r_2 = 0.6$, and $\tilde{I}_r = 1.0$

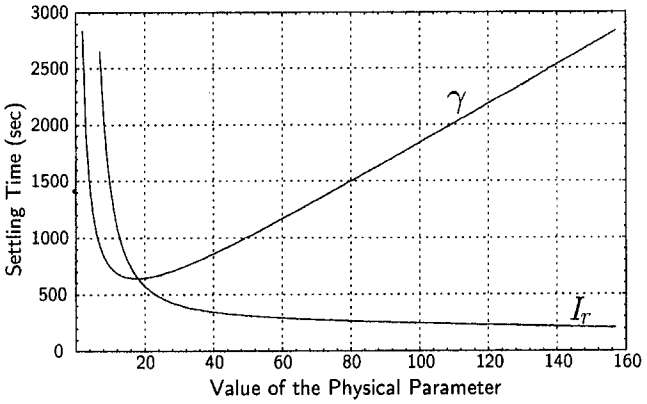


Fig. 7 Time required for the kinetic energy to decay through 95 percent of the difference between the initial kinetic energy and the minimum kinetic energy state. For the γ curve, $I_r = 18.0$ and for the I_r curve, $\gamma = 20.0$.

$\tilde{h}_2$-direction should be very nearly zero and in the $\tilde{h}_3$-direction should be close to one. However, chaotic trajectories often spin about the major axis for a sizable period of time before they depart to another portion of the momentum sphere. Therefore, we need to know if the angular momentum components $\tilde{h}_1$ and $\tilde{h}_2$ have a small variance for a substantial period of time near the end of the integration time period. The exact condition we used is that the variances $\sigma^2(\tilde{h}_1)$ and $\sigma^2(\tilde{h}_2)$ are both less than 0.001 for the last two percent of the integration time.

Measure II. When the satellite's trajectory degenerates into a limit cycle on the surface of the momentum sphere, the path is not a circle in $\mathbb{R}^2$, but a curve in $\mathbb{R}^3$. In this case periodic orbits are bounded by the unperturbed heteroclinic orbits and follow the curvature of the momentum sphere. Consequently a limit cycle ends up being periodic in all three of its angular momentum components. We consider a trajectory to be periodic if the variance $\sigma^2(\tilde{h}_3)$ is less than 0.175. The variance of $\tilde{h}_3$ is much less than the variance in the other two directions since limit cycles are centered about the major axis spin fixed point and are bounded by the unperturbed heteroclinic orbits. We have found that the value 0.175 is the smallest value of $\sigma^2(\tilde{h}_3)$ for which the computer is able to correctly identify each visually identified periodic orbit.

Measure III. If a trajectory failed either of the previous two variance conditions we deemed it to be chaotic. Several visually identified chaotic trajectories are used to verify that the algorithm is able to differentiate between the different trajectory types.

Investigation and Discussion of Results

Analytical Results: The Melnikov Criterion. We begin by qualitatively studying Eq. (44) to see what can be learned about chaos in this system. It can be seen that no immediate conclusions can be drawn about the dependence on the parameters $\tilde{\eta}$, $\tilde{\Omega}$, r_1, and r_2 since Eq. (44) is such a complicated function of each of these parameters. On the other hand, we can immediately see that as the rotor inertia $\tilde{I}_r$ is increased, it becomes more difficult to achieve chaos. In addition, as the damping $\tilde{\gamma}$ is increased, it becomes increasingly *easier* to have chaos. This damping result is counter to what one might expect in a mechanical system—that increased damping *suppresses* chaos, not enhances it.

Further investigation reveals that the $\tilde{I}_r$ and $\tilde{\gamma}$ results are consistent with the dynamics. To see this, we define the *settling time* as the time required for the kinetic energy to decay through 95 percent of the difference between the initial kinetic energy and the minimum kinetic energy state. Figure 7 shows the settling time of the kinetic energy for the damped, *unperturbed* rigid body when γ and I_r (the dimensional quantities) are independently varied.[4] It is immediately clear that as the rotor inertia is increased, kinetic energy is dissipated more quickly. This is consistent with the above observation that as $\tilde{I}_r$ is increased, chaos is more easily achieved and with the idea that increased energy dissipation tends to suppress chaos. It is the relative angular velocity, $\tilde{\omega}_r$, between the carrier body and the rotor that produces the damping. It seems, therefore, that as the rotor inertia $\tilde{I}_r$ is increased it is more difficult to get the rotor spinning and therefore the relative angular velocity between the rotor and the carrier body is increased, leading to an increased energy dissipation rate.

Similarly, as the viscous damping coefficient is initially increased from a small value, the energy dissipation rate increases, as expected. However, as the viscous damping coefficient is increased further, the coupling between the carrier body and the rotor becomes stronger, thus restricting the relative movement between the two bodies and thus $\tilde{\omega}_r$. For large values of $\tilde{\gamma}$, the increased coupling predominates and damping is diminished, and for small values of $\tilde{\gamma}$, damping is decreased because there is little viscosity. It is expected that there should be an optimal value for $\tilde{\gamma}$ such that the rate of damping or kinetic energy dissipation is maximized. This effect is easily seen in Fig. 7 as well as in Fig. 8, which illustrates the system's kinetic energy time histories for various values of damping. Since we have assumed that $\tilde{\gamma} = \mathcal{O}(1)$, our Melnikov result is exhibiting behavior consistent with the right half of the damping curve in Fig. 7—increasing $\tilde{\gamma}$ decreases energy dissipation and therefore makes chaos easier to attain.

Since the parameter space for studying the boundaries between chaotic and nonchaotic motion is six-dimensional, we investigate three-dimensional subspaces by fixing three of the parameters and

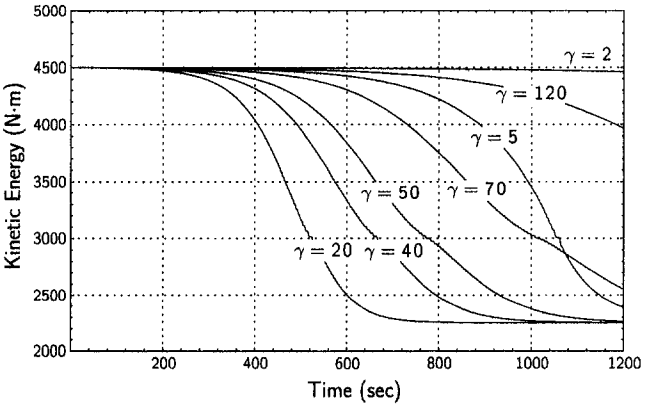


Fig. 8 Rigid-body kinetic energy as a function of time for different values of damping γ

[4] Figures 7 and 8 integrate the unperturbed dimensional equations of motion (Eqs. (1)–(4) with $\Delta = 0$) for $A = 1000$ kg · m^2, $B = 1500$ kg · m^2, and $C = 2000$ kg · m^2.

Downloaded 04 May 2010 to 171.66.16.27. Redistribution subject to ASME license or copyright; see http://www.asme.org/terms/Terms_Use.cfm

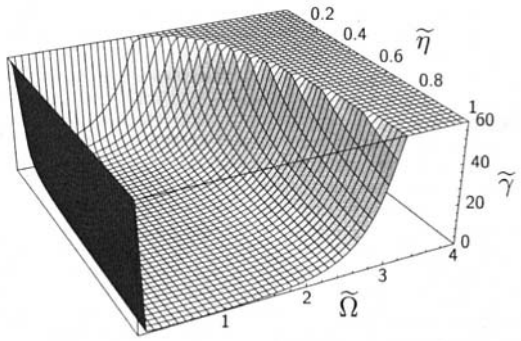


Fig. 9 Surface separating chaotic from nonchaotic motion in $\tilde{\gamma}$, $\tilde{\eta}$, $\tilde{\Omega}$ space. $r_1 = 1.5$, $r_2 = 0.6$, and $\tilde{I}_r = 1.0$.

then plotting the other three. The surface shown in Fig. 9 shows the boundary between chaotic and nonchaotic motion in $\tilde{\gamma}$, $\tilde{\eta}$, $\tilde{\Omega}$ space. In this figure, and all figures that follow, points in parameter space *above* the surface are chaotic. We also note that the drastic change in slope that occurs for small values of $\tilde{\Omega}$ in Figs. 9, 11, and 12 is a result of practical limits on plotting resolution. In reality, the surface does rise sharply for small $\tilde{\Omega}$, but does so smoothly (see detailed cross section in Fig. 10). In any case, we note that the Melnikov result is not valid for very small $\tilde{\Omega}$, since we have assumed that $\tilde{\Omega} = \mathcal{O}(1)$. Figure 9 shows, as expected, that for $\tilde{\eta} = 0$, chaotic motion is impossible for all values of $\tilde{\Omega}$ and $\tilde{\gamma}$—without a time-dependent perturbation, chaos cannot occur. We also see the inverse dependence of the chaos criterion on $\tilde{\gamma}$—chaos occurs for larger values of $\tilde{\gamma}$ instead of smaller.

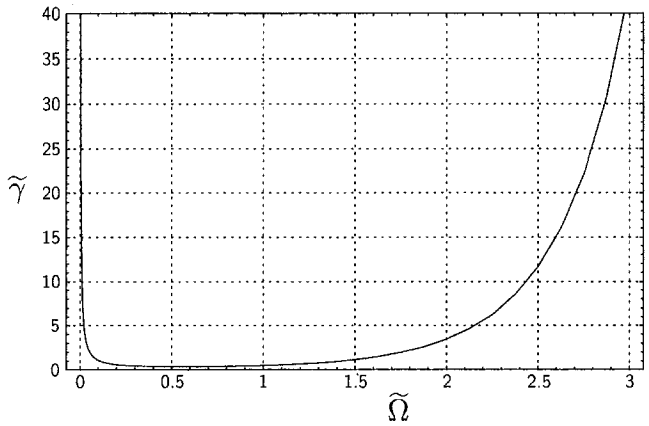


Fig. 10 Cross section of Fig. 9. Line separating chaotic from nonchaotic motion in $\tilde{\gamma}$, $\tilde{\Omega}$ space. $r_1 = 1.5$, $r_2 = 0.6$, $\tilde{I}_r = 1.0$, and $\tilde{\eta} = 0.9$.

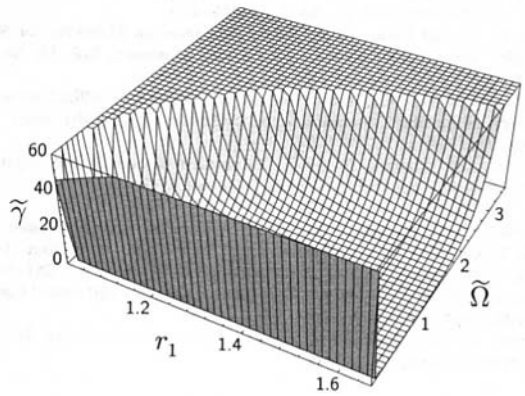


Fig. 11 Surface separating chaotic from nonchaotic motion in $\tilde{\gamma}$, r_1, $\tilde{\Omega}$ space. $\tilde{\eta} = 0.75$, $r_2 = 0.667$, and $\tilde{I}_r = 1.0$.

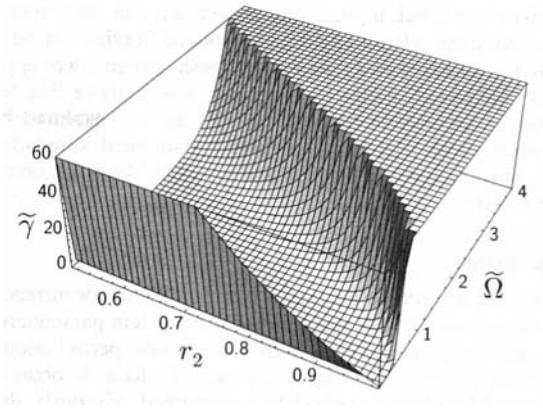


Fig. 12 Surface separating chaotic from nonchaotic motion in $\tilde{\gamma}$, r_2, $\tilde{\Omega}$ space. $\tilde{\eta} = 0.75$, $r_1 = 1.5$, and $\tilde{I}_r = 1.0$.

Figure 11 shows the dependence of the criterion for chaos on the shape of the rigid body. We see that for values of $r_1 \to 1$, which corresponds to a nearly symmetric prolate body, no chaotic motion occurs. Analogous to the previous figure, as the forcing frequency $\tilde{\Omega} \to 0$, no chaotic motion occurs since a zero forcing frequency implies no perturbation. As in Fig. 11, Fig. 12 shows the chaotic dependence on the shape of the rigid body, but this time for r_2 instead of r_1. We see that for $r_2 \to 1$, chaotic motion is impossible to obtain for any value of $\tilde{\gamma}$ or $\tilde{\Omega}$. This shape corresponds to a nearly symmetric oblate carrier body. Figures 13 and 14 show many of the same trends that the previous three figures did, but they also show the chaotic dependence on $\tilde{\eta}$. As $\tilde{\eta} \to 0$ there can be no chaotic motion since that implies a zero perturbation. In addition, we see that as we increase $\tilde{\eta}$, chaotic motion is assured for all values of the system parameters—a large enough perturbation can overcome all other factors.

Comparison Numerical and Melnikov Results. The summary of numerical simulations shown in Fig. 3 demonstrate that

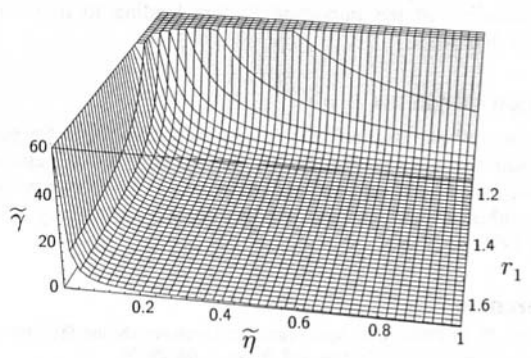


Fig. 13 Surface separating chaotic from nonchaotic motion in $\tilde{\gamma}$, r_1, $\tilde{\eta}$ space. $\tilde{\Omega} = 1.0$, $r_2 = 0.667$, and $\tilde{I}_r = 1.0$.

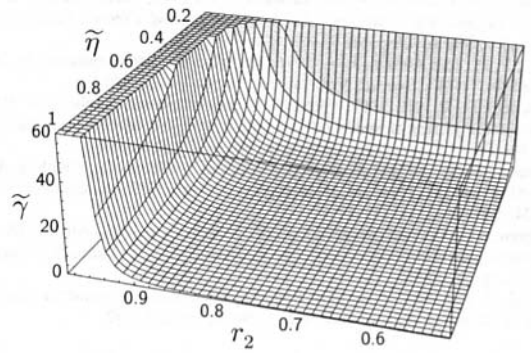


Fig. 14 Surface separating chaotic from nonchaotic motion in $\tilde{\gamma}$, r_2, $\tilde{\eta}$ space. $\tilde{\Omega} = 1.0$, $r_1 = 1.5$, and $\tilde{I}_r = 1.0$.

Downloaded 04 May 2010 to 171.66.16.27. Redistribution subject to ASME license or copyright; see http://www.asme.org/terms/Terms_Use.cfm

Melnikov's method, though very conservative in some regions of parameter space, clearly gives a good bound in others. In addition, within the accuracy of the parameter mesh chosen, there appear to be no "nonlinear" points in parameter space (those that lead to chaotic or limit cycle trajectories) that are not captured by the Melnikov curve. Extensive additional numerical simulation for many other ranges of the parameter values does not contradict these results.

Conclusion

We have derived an analytical criterion for the occurrence of a chaotic region of phase space in terms of system parameters for a viscously damped rigid body with time-periodic perturbations. The analytical criterion for the occurrence of chaos is obtained by applying Melnikov's method to a perturbed, viscously damped rigid-body model. It is obvious from the modern theory of nonlinear dynamics that chaos can occur via the breakup of heteroclinic orbits in this class of systems. The contribution of this paper is the formulation of physically reasonable spacecraft models, using rigid-body approximations, to which Melnikov's method can be applied and the performance of the difficult calculations required to obtain an uncomplicated criterion for chaos that can easily be used for spacecraft design. We have also explained a result that was, at first, "counterintuitive" to us—increased viscous damping *enhances* the onset of chaotic dynamics. This is an important consideration when placing viscous dampers on spacecraft.

In addition, subspaces of the full-parameter space are studied analytically and numerically to obtain a qualitative and quantitative understanding of the interactions of the various parameters leading to nonlinear motion. The complete Melnikov result is easily used to obtain the quantitative information needed when a spacecraft and its subsystems are being designed. Numerical simulations indicate that the Melnikov result, though conservative, gives investigators an excellent gauge on the region of parameter space in which to look for nonlinear motion. Future work will extend this approach to better understand the onset of chaos in other classes of spacecraft and to attempt to obtain a fundamental understanding of the important factors leading to unpredictable chaotic dynamics.

Acknowledgments

We would like to thank the reviewers of this paper for pointing out some technical issues, which, though they did not change the results, led us to a much deeper understanding of our work. The third author gratefully acknowledges funding in part by NSF PYI grant ECS-9157192.

References

Adams, G. J., 1980, "Dual-Spin Spacecraft Dynamics During Platform Spinup," *Journal of Guidance and Control,* Vol. 3, No. 1, pp. 29–36.

Baillieul, J., and Levi, M., 1987, "Rotational Elastic Dynamics," *Physica,* Vol. 27D, pp. 43–62.

Barba, P. M., Furumoto, N., and Leliakov, I. P., 1973, "Techniques for Flat-Spin Recovery of Spinning Satellites," *AIAA Guidance and Control Conference,* Key Biscayne, Florida, AIAA paper 73-859.

Barba, P. M., and Aubrun, J. N., 1976, "Satellite Attitude Acquisition by Momentum Transfer," *AIAA Journal,* Vol. 14, No. 10, pp. 1382–1386.

Campbell, D. R., III, 1997, "Analytical and Numerical Analysis of Nonlinear Phenomena for a Class of Spacecraft Attitude Acquisition Maneuvers," Ph.D. dissertation, The Pennsylvania State University, University Park, PA.

Chinnery, A. E., and Hall, C. D., 1995, "Motion of a Rigid Body with an Attached Spring-Mass Damper," *Journal of Guidance, Control, and Dynamics,* Vol. 18, No. 6, pp. 1404–1409.

Cochran, J. E., and Holloway, H. E., 1980, "Resonances in the Attitude Motions of Asymmetric Dual-Spin Spacecraft," *The Journal of the Astronautical Sciences,* Vol. 28, No. 3, pp. 231–254.

Cronin, D. L., 1978, "Flat Spin Recovery of a Rigid Asymmetric Spacecraft," *Journal of Guidance and Control,* Vol. 1, No. 4, pp. 281–282.

Dovbysh, S. A., 1989, "Some New Dynamical Effects in the Perturbed Euler-Poinsot Problem Due to Splitting of Separatrices," *Journal of Applied Mathematics and Mechanics,* Vol. 53, No. 2, pp. 165–173.

Gebman, J. R., and Mingori, D. L., 1976, "Perturbation Solution for the Flat Spin Recovery of a Dual-Spin Spacecraft," *AIAA Journal,* Vol. 14, No. 7, pp. 859–867.

Gray, G. L., Dobson, I., and Kammer, D. C., 1996, "Chaos in a Spacecraft Attitude Maneuver Due to Time-Periodic Perturbations," ASME JOURNAL OF APPLIED MECHANICS, Vol. 63, pp. 501–508.

Gray, G. L., Kammer, D. C., and Dobson, I., 1992, "Chaos in an Attitude Maneuver of a Damped Satellite Due to Time-Periodic Perturbations," *AAS/AIAA Spaceflight Mechanics Conference,* Colorado Springs, CO, Paper AAS 92-171.

Gray, G. L., Mazzoleni, A. P., and Campbell, D. R., III, 1998, "Analytical Criterion for Chaotic Dynamics in Flexible Satellites with Nonlinear Controller Damping," *Journal of Guidance, Control, and Dynamics,* Vol. 21, No. 4, pp. 558–565.

Guckenheimer, J., and Holmes, P., 1983, *Nonlinear Oscillations, Dynamical Systems, and Bifurcations of Vector Fields,* Springer-Verlag, New York.

Hall, C. D., and Rand, R. H., 1994, "Spinup Dynamics of Axial Dual-Spin Spacecraft," *Journal of Guidance, Control, and Dynamics,* Vol. 17, No. 1, pp. 30–37.

Hindmarsh, A. C., 1983, "ODEPACK, A Systematized Collection of ODE Solvers," *Scientific Computing,* R. S. Stepleman et al., eds., North-Holland, Amsterdam, pp. 55–64. (Also see http://gams.nist.gov/ to obtain the source code.)

Holmes, P. J., 1980, "Averaging and Chaotic Motions in Forced Oscillations," *SIAM Journal of Applied Mathematics,* Vol. 38, No. 1, pp. 65–80.

Holmes, P. J., 1981, "Errata and Addenda: Averaging and Chaotic Motions in Forced Oscillations," *SIAM Journal of Applied Mathematics,* Vol. 40, No. 1, pp. 167–168.

Holmes, P., 1983, "Bifurcation and Chaos in a Simple Feedback Control System," *Proceedings of the 22nd IEEE Conference on Decision and Control,* San Antonio, TX, IEEE, Piscataway, NJ, pp. 365–370.

Holmes, P. J., and Marsden, J. E., 1983, "Horseshoes and Arnold Diffusion for Hamiltonian Systems on Lie Groups," *Indiana University Mathematics Journal,* Vol. 32, No. 2, pp. 273–309.

Hughes, P. C., 1986, *Spacecraft Attitude Dynamics,* John Wiley and Sons, New York.

Kaplan, M. H., and Cenker, R. J., 1973, "Control of Spin Ambiguity During Reorientation of an Energy Dissipating Body," *Journal of Spacecraft and Rockets,* Vol. 10, No. 12, pp. 757–760.

Koiller, J., 1984, "A Mechanical System with a 'Wild' Horseshoe," *Journal of Mathematical Physics,* Vol. 25, No. 5, pp. 1599–1604.

Krishnaprasad, P. S., 1985, "Lie-Poisson Structures, Dual-Spin Spacecraft and Asymptotic Stability," *Nonlinear Analysis, Theory, Methods & Applications,* Vol. 9, No. 10, pp. 1011–1035.

Krishnaprasad, P. S., and Marsden, J. E., 1987, "Hamiltonian Structures and Stability for Rigid Bodies with Flexible Attachments," *Archive for Rational Mechanics and Analysis,* Vol. 98, No. 1, pp. 71–93.

Levi, M., 1989, "Morse Theory for a Model Space Structure," *Proceedings of the AMS-IMS-SIAM Joint Summer Research Conference in the Mathematical Sciences on Control Theory and Multibody Systems,* Bowdoin College, Brunswick, ME, J. E. Marsden, P. S. Krishnaprasad, and J. C. Simo, eds., in the series *Contemporary Mathematics,* Vol. 97, American Mathematical Society, Providence, RI, pp. 209–216.

Lichtenberg, A. J., and Lieberman, M. A., 1992, *Regular and Chaotic Dynamics,* 2nd Ed., Springer-Verlag, New York.

Longuski, J. M., and Tsiotras, P., 1993a, "Analytic Solution for a Spinning Rigid Body Subject to Time-Varying Body-Fixed Torque, Part I: Constant Axial Torque," ASME JOURNAL OF APPLIED MECHANICS, Vol. 60, No. 4, pp. 970–975.

Longuski, J. M., and Tsiotras, P., 1993b, "Analytic Solution for a Spinning Rigid Body Subject to Time-Varying Body-Fixed Torque, Part II: Time-Varying Body-Fixed Torque," ASME JOURNAL OF APPLIED MECHANICS, Vol. 60, pp. 976–981.

Melnikov, V. K., 1963, "On the Stability of the Center for Time-Periodic Perturbations," *Transactions of the Moscow Mathematical Society,* Vol. 12, pp. 1–56.

Or, A. C., 1991, "Resonances in the Despin Dynamics of Dual-Spin Spacecraft," *Journal of Guidance, Control, and Dynamics,* Vol. 14, No. 2, pp. 321–329.

Or, A. C., 1998a, "Chaotic Motions of a Dual-Spin Body," ASME JOURNAL OF APPLIED MECHANICS, Vol. 65, pp. 150–156.

Or, A. C., 1998b, "Dynamics of an Asymmetric Gyrostat," *Journal of Guidance, Control, and Dynamics,* Vol. 21, No. 3, pp. 416–420.

Rahn, C. D., and Barba, P. M., 1991, "Reorientation Maneuver for Spinning Spacecraft," *Journal of Guidance, Control, and Dynamics,* Vol. 14, No. 4, pp. 724–728.

Rubanovskii, V. N., 1988, "On the Relative Equilibria of a Satellite-Gyrostat, Their Branchings and Stability," *Journal of Applied Mathematics and Mechanics,* Vol. 52, No. 6, pp. 710–714.

Tong, X., and Tabarrok, B., 1997, "Bifurcation of Self-Excited Rigid Bodies Subjected to Small Perturbation Torques," *Journal of Guidance, Control, and Dynamics,* Vol. 20, No. 1, pp. 123–128.

Tsiotras, P., and Longuski, J. M., 1991, "A Complex Analytic Solution for the Attitude Motion of a Near-Symmetric Rigid Body Under Body-Fixed Torques," *Celestial Mechanics and Dynamical Astronomy,* Vol. 51, No. 3, pp. 281–301.

Volosov, V. M., 1962, "Averaging in Systems of Ordinary Differential Equations," *Russian Mathematical Surveys,* Vol. 17, pp. 1–126.

Wiggins, S., 1990, *Introduction to Applied Nonlinear Dynamical Systems and Chaos,* Springer-Verlag, New York.

Downloaded 04 May 2010 to 171.66.16.27. Redistribution subject to ASME license or copyright; see http://www.asme.org/terms/Terms_Use.cfm

Transmission of SH Waves Through an Elastic Layer Between Two Solids With Frictional Contact Interfaces

Y.-S. Wang
Professor,
Institute of Engineering Mechanics,
e-mail: yswang@center.njtu.edu.cn

G.-L. Yu
Associate Professor,
Department of Civil Engineering,

Northern Jiaotong University,
Beijing 100044, P. R. China

The propagation of SH waves in a three-layered medium containing an interlayer between two semi-infinite solids with frictional contact interfaces is studied. The incident wave, which propagates through the layer from one half-space to another with subcritical angle, is assumed to be strong enough so that friction may be broken, and the local slip may take place at the interfaces. The mixed boundary conditions involving inequalities and unknown intervals lead to a set of recurrence relations. Special examples are given for the case of identical materials to illustrate the mathematical procedure to obtain final results. The interface tractions and relative slip velocities are presented. The interaction between the two interfaces is discussed. It is shown that the slip of the interface near the incident wave may restrain the slip of the interface far from the incident wave, while that the latter may facilitate the former. We also find the instability of the system for similar values of the two interface friction coefficients. Finally, the energy transmitted through the interlayer and dissipated by the friction of the two interfaces are examined.

Introduction

Wave propagation in layered media is a subject of interest in many fields such as geophysics, earthquake engineering, laminated composite materials, etc. The interfaces between layers were generally assumed to be perfectly bonded in most previous studies. Such an interface can transmit both tensile and compressive tractions without discontinuity in displacements. The associated boundary conditions contain only equalities and thus the interface is called the "bilateral interface." An opposite case is the contact interface which cannot transmit tensile traction and allows for the separation and/or frictional slip. Such an interface with boundary conditions involving inequalities and unknown intervals is described as the "unilateral interface." It is noted that some works concerning frictional interfaces are based on the linear models (the bilateral interfaces), where the interface stress is proportional to the slip velocity (see, for instance, Sezawa and Kanai (1940) and Schoenberg (1980), among others). Wave propagation in layered media with unilateral interfaces has received less attention up to now because the nonlinearity increases the level of mathematical difficulty.

Several authors have attacked the interaction of elastic waves with a contact interface between two elastic half-spaces in presence of the local separation and/or frictional slip. Comninou and Dundurs developed an exact approach based on the Fourier analysis and the singular integral equation technique, and made an extensive investigation. Their works include the reflection and refraction of both harmonic and inharmonic elastic waves at a smoothly or frictionally contact interface (Chez, Dundurs, and Comninou, 1978, 1983; Comninou, Barber, and Dundurs, 1982; Comninou and Dundurs, 1977a, b, 1978a, 1979a, b, 1980; Comninou, Dundurs, and Chez, 1979; Dundurs and Comninou, 1979) and the propagation of interface waves (Comninou and Dundurs, 1977c, 1978b). Miller (1977, 1978) and Miller and Tran (1979, 1981) considered the similar problems using an approximate method—the equivalent linearization method. Their analysis excluded the possibility of separation but involved the effects of various friction models (Miller, 1978). Mendelsohn and Doong (1989) presented a boundary element analysis on transient dynamic elastic frictional contact with examples of SH motion. Another interesting problem—the re-polarization of elastic waves at a frictional interface was studied by the present authors (Wang, Yu, and Gai, 1998a; Wang and Yu, 1999; and Yu, Wang, and Gai, 1998).

When one of the half-spaces is replaced by a layer of finite thickness, the mathematical procedure of the problem will become very difficult due to the involved characteristic length. No one has been found to attack such problems except Miller (1979) who examined the propagation of Love-type surface waves in an elastic layer bonded by Coulomb friction to an elastic half-space and obtained the asymptotic results when the attenuation in the system is very small. The authors of the present paper recently studied the propagation of both harmonic and inharmonic SH waves in a layered half-space with a frictional contact interface by employing the exact method similar to that of Comninou and Dundurs' (Yu, Wang, and Gai, 1997; and Wang, Yu, and Gai, 1997, 1998b). In this paper we will consider the propagation of SH waves in a three-layered medium containing an interlayer between two semi-infinite solids with frictional contact interfaces. The analysis is presented for different layer and half-space materials, but only numerical results for the identical material case are given. Our interest is the interaction between the two frictional interfaces. The solution of the problem should be of interest to scientists working with laboratory and field seismic data in regions where an SH-wave causes the slip of an interlayer. One can also expect its potential applicability to wave propagation in mechanical systems with bolted or press-fit connections (e.g., Zharii, 1995, 1996).

Problem Formulation

Consider the problem shown in Fig. 1. An elastic interlayer with thickness H is bonded by friction to two elastic half-spaces which are loaded by remote pressure p_0 and antiplane shearing traction τ_0. The two half-spaces have the same shear modulus and the

Contributed by the Applied Mechanics Division of THE AMERICAN SOCIETY OF MECHANICAL ENGINEERS for publication in the ASME JOURNAL OF APPLIED MECHANICS.
Discussion on the paper should be addressed to the Technical Editor, Professor Lewis T. Wheeler, Department of Mechanical Engineering, University of Houston, Houston, TX 77204-4792, and will be accepted until four months after final publication of the paper itself in the ASME JOURNAL OF APPLIED MECHANICS.
Manuscript received by the ASME Applied Mechanics Division, Jan. 13, 1998; final revision, Nov. 28, 1998. Associate Technical Editor: R. C. Benson.

 Copyright © 1999 by ASME

Downloaded 04 May 2010 to 171.66.16.27. Redistribution subject to ASME license or copyright; see http://www.asme.org/terms/Terms_Use.cfm

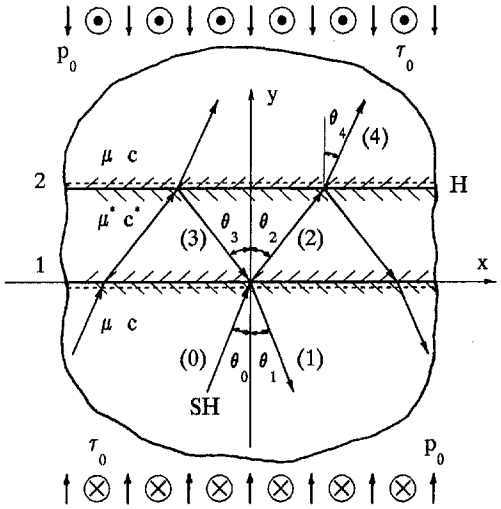


Fig. 1 Propagation of SH waves through an interlayer with frictional contact interfaces

transverse wave speed denoted, respectively, by μ and c. The quantities with asterisks in affix position refer to those of the interlayer. The Coulomb friction model is adopted along the two interfaces, 1 and 2, with static and kinetic friction coefficients as f_{sj} and f_{kj} ($j = 1, 2$). Generally $f_{kj} \leq f_{sj}$. A harmonic SH wave propagates through the interlayer from the lower half-space at the angle θ_0. The indices (0), (1), (2), (3), and (4) which may appear as superscripts are used to distinguish between various waves. Denote the shearing tractions and relative slip velocities at the interfaces by S_j and V_j, respectively. If the incident wave is strong enough to break friction, the boundary conditions can be written as

$$|S_j| = f_{kj} p_0, \quad \text{sgn}\,(S_j) = \text{sgn}\,(V_j) \tag{1}$$

in the slip zones, and

$$V_j = 0, \quad |S_j| < f_{sj} p_0 \tag{2}$$

in the stick zones. It is noted that the above conditions involve inequalities with the unknown regions where they hold. Therefore the problem is indeed nonlinear.

The displacements associated with different waves are taken as the real part of the typical form

$$w^{(n)} = C_n \exp(i\zeta_n), \quad n = 0, 1, 2, 3, 4 \tag{3}$$

where

$$\begin{aligned} \zeta_n &= k[x \sin\theta_n + (-1)^n y \cos\theta_n - ct], \quad n = 0, 1 \\ &= k^*[x \sin\theta_n + (-1)^n y \cos\theta_n - c^* t], \quad n = 2, 3 \\ &= k[x \sin\theta_n + (y - H)\cos\theta_n - ct], \quad n = 4 \end{aligned} \tag{4}$$

with $k = \omega/c$ and $k^* = \omega/c^*$ being wave numbers. C_0 is generally complex but taken to be real and positive in the following analysis. $C_n (n = 1, 2, 3, 4)$ are unknown complex functions of ζ_n. The incident wave $w^{(0)}$ is simply a sinusoidal or cosinoidal harmonic wave. The reflected and transmitted waves, however, become distorted in relation to the incident wave and contain higher frequency modes because of the nonlinearity in the boundary conditions.

The Snell's law yields

$$kc = k^* c^*,$$

$$c^* \sin\theta_0 = c^* \sin\theta_1 = c \sin\theta_2 = c \sin\theta_3 = c^* \sin\theta_4.$$

Then we have $\theta_0 = \theta_1 = \theta_4$ and $\theta_2 = \theta_3$. When $(c^*/c) \sin\theta_0 > 1$, the incident wave is totally reflected. We exclude this case because only a small amount of energy can be transmitted through the interlayer.

The linearity of the governing equations allows us to construct the solution by adding the corrective solution $[\bar{w}^{(n)}, \bar{\tau}_{yz}^{(n)}]$ to the results for the bilateral interfaces (the welded interfaces) $\{w^{(n)}, \tau_{yz}^{(n)}\}$. Then the interface tractions and the relative slip velocities may be expressed as

$$\begin{aligned} S_1(\eta) &= \tau_0 + [\tau_{yz}^{(0)} + \tau_{yz}^{(1)} + \bar{\tau}_{yz}^{(1)}]_{y=0} \\ &= \tau_0 + [\tau_{yz}^{(2)} + \tau_{yz}^{(3)} + \bar{\tau}_{yz}^{(2)} + \bar{\tau}_{yz}^{(3)}]_{y=0}, \end{aligned} \tag{5}$$

$$\begin{aligned} S_2(\eta) &= \tau_0 + [\tau_{yz}^{(4)} + \bar{\tau}_{yz}^{(4)}]_{y=H} \\ &= \tau_0 + [\tau_{yz}^{(2)} + \tau_{yz}^{(3)} + \bar{\tau}_{yz}^{(2)} + \bar{\tau}_{yz}^{(3)}]_{y=H}. \end{aligned} \tag{6}$$

$$V_1(\eta) = [\dot{\bar{w}}^{(2)} + \dot{\bar{w}}^{(3)} - \dot{\bar{w}}^{(1)}]_{y=0}, \tag{7}$$

$$V_2(\eta) = [\dot{\bar{w}}^{(4)} - \dot{\bar{w}}^{(2)} - \dot{\bar{w}}^{(3)}]_{y=H}, \tag{8}$$

where $\eta = \zeta_n|_{y=0}$. The shearing tractions along the bilateral interfaces can be obtained by the method described in Ewing et al. (1957). The results are

$$\begin{aligned} [\tau_{yz}]_{y=0} &= [\tau_{yz}^{(0)} + \tau_{yz}^{(1)}]_{y=0} = [\tau_{yz}^{(2)} + \tau_{yz}^{(3)}]_{y=0} \\ &= \text{Re}[iA_{10} \exp(i\eta)] = -A_{1s} \sin\eta - A_{1c} \cos\eta \end{aligned} \tag{9}$$

$$\begin{aligned} [\tau_{yz}]_{y=H} &= [\tau_{yz}^{(4)}]_{y=H} = [\tau_{yz}^{(2)} + \tau_{yz}^{(3)}]_{y=H} = \text{Re}\,[iA_{20} \exp(i\eta)] \\ &= -A_{2s} \sin\eta - A_{2c} \cos\eta \end{aligned} \tag{10}$$

where

$$\{A_{10}, A_{20}\} = \frac{2\mu k C_0 \cos\theta_0}{(1 + \Delta^2)\sin\gamma + 2i\Delta\cos\gamma} \times \{\sin\gamma + i\Delta\cos\gamma, i\Delta\} \tag{11}$$

$$\{A_{1s}, A_{2s}\} = \frac{2\mu k C_0 \cos\theta_0}{(1 + \Delta^2)^2 \sin^2\gamma + 4\Delta^2\cos^2\gamma} \times \{(1 + \Delta^2)\sin^2\gamma + 2\Delta^2\cos^2\gamma, 2\Delta^2\cos\gamma\} \tag{12}$$

$$\{A_{1c}, A_{2c}\} = \frac{2\mu k C_0 \cos\theta_0}{(1 + \Delta^2)^2 \sin^2\gamma + 4\Delta^2\cos^2\gamma} \times \{\Delta(1 - \Delta^2)\sin\gamma\cos\gamma, \Delta(1 + \Delta^2)\sin\gamma\}. \tag{13}$$

For the case of identical materials, we have

$$[\tau_{yz}]_{y=0} = -A_0 \sin\eta, \quad [\tau_{yz}]_{y=H} = -A_0 \sin(\eta + \gamma) \tag{14}$$

with $A_0 = \mu k C_0 \cos\theta_0$ and $\gamma = k^* H \cos\theta_2$. The physical meaning of the parameter γ is the phase difference of the wave motion between two interfaces. It can be also interpreted as the number of waves with width of $(k^* \cos\theta_2)^{-1}$ included in the thickness of the interlayer.

Corrective Solution

The displacement components in the corrective solution may be written as Fourier series containing all higher frequencies:

$$\bar{w}^{(n)} = \text{Re} \sum_{m=1}^{\infty} F_m^{(n)} \exp(im\zeta_n), \quad n = 1, 2, 3, 4 \tag{15}$$

where $F_m^{(n)} = D_m^{(n)} + iE_m^{(n)}$ with $D^{(n)}$ and $E^{(n)}$ being real. Note that the sum from $m = -1$ to $-\infty$ does not appear because the waves are assumed to propagate to the right. To account for the global sliding of the solids induced by the applied shearing traction τ_0, we should add the term $U_1 t$ to $\bar{w}^{(2)}$ or $\bar{w}^{(3)}$, and $(U_1 + U_2)t$ to $\bar{w}^{(4)}$, where U_1 is the averaged speed of the global sliding of the

Downloaded 04 May 2010 to 171.66.16.27. Redistribution subject to ASME license or copyright; see http://www.asme.org/terms/Terms_Use.cfm

interlayer with respect to the lower half-space, and U_2 is that of the upper half-space with respect to the interlayer.

The requirement that the shearing tractions be continuous across the interfaces leads to

$$F_m^{(1)} = \Delta^{-1}(F_m^{(3)} - F_m^{(2)}),$$
$$F_m^{(4)} = \Delta^{-1}[\exp(im\gamma)F_m^{(2)} - \exp(-im\gamma)F_m^{(3)}], \quad (16)$$

where $\Delta = \mu c^* \cos\theta_0/(\mu^* c \cos\theta_2)$. Substituting (15) and (16) into (5)–(8) and taking the real parts, we have

$$V_1(\eta) = U_1 + kc \sum_{m=1}^{\infty} m\{[(1+\Delta^{-1})E_m^{(2)} + (1-\Delta^{-1})E_m^{(3)}] \times \cos m\eta + [(1+\Delta^{-1})D_m^{(2)} + (1-\Delta^{-1})D_m^{(3)}] \sin m\eta\}, \quad (17)$$

$$V_2(\eta) = U_2 - kc \sum_{m=1}^{\infty} m\{[(1-\Delta^{-1})(E_m^{(2)} \cos m\gamma + D_m^{(2)} \sin m\gamma) + (1+\Delta^{-1})(E_m^{(3)} \cos m\gamma - D_m^{(3)} \sin m\gamma)] \cos m\eta + [(1-\Delta^{-1})(-E_m^{(2)} \sin m\gamma + D_m^{(2)} \cos m\gamma) + (1+\Delta^{-1})(E_m^{(3)} \sin m\gamma + D_m^{(3)} \cos m\gamma)] \sin m\eta\}, \quad (18)$$

$$S_1(\eta) = \tau_0 + [\tau_{yz}]_{y=0} - \frac{\mu k \cos\theta_0}{\Delta} \sum_{m=1}^{\infty} m\{(E_m^{(2)} - E_m^{(3)}) \cos m\eta + (D_m^{(2)} - D_m^{(3)}) \sin m\eta\}, \quad (19)$$

$$S_2(\eta) = \tau_0 + [\tau_{yz}]_{y=H} - \frac{\mu k \cos\theta_0}{\Delta} \times \sum_{m=1}^{\infty} m\{[E_m^{(2)} \cos m(\eta+\gamma) + D_m^{(2)} \sin m(\eta+\gamma)] - [E_m^{(3)} \cos m(\eta-\gamma) + D_m^{(3)} \sin m(\eta-\gamma)]\}. \quad (20)$$

Equations (17) and (18) are indeed Fourier series of which the coefficients U_1, U_2, $E_m^{(2)}$, $E_m^{(3)}$, $D_m^{(2)}$, $D_m^{(3)}$ can be represented by $V_1(\eta)$ and $V_2(\eta)$. Substituting the results into (19) and (20), we obtain

$$S_1(\eta) = \tau_0 + [\tau_{yz}]_{y=0} + \frac{\mu k \cos\theta_0}{\pi} \int_{-\pi}^{\pi} [\phi_1(\xi)P_1(\eta,\xi) + \phi_2(\xi)P_2(\eta,\xi)]d\xi, \quad (21)$$

$$S_2(\eta) = \tau_0 + [\tau_{yz}]_{y=H} + \frac{\mu k \cos\theta_0}{\pi} \int_{-\pi}^{\pi} [\phi_1(\xi)P_2(\eta,\xi) + \phi_2(\xi)P_1(\eta,\xi)]d\xi, \quad (22)$$

where we have denoted $\phi_j(\eta) = -(kc)^{-1}V_j(\eta)$ and

$$P_1(\eta,\xi) = \sum_{m=1}^{\infty} \frac{1}{\Lambda_m}\{[(1+\Delta)^3 + (1-\Delta)^3] \cos m(\eta-\xi) - (1-\Delta)(1+\Delta)^2 \cos m(\eta-\xi+2\gamma) - (1+\Delta)(1-\Delta)^2 \cos m(\eta-\xi-2\gamma)\}, \quad (23)$$

$$P_2(\eta,\xi) = 2\sum_{m=1}^{\infty} \frac{\Delta}{\Lambda_m}\{(1+\Delta)^2 \cos m(\eta-\xi+\gamma) - (1-\Delta)^2 \cos m(\eta-\xi-\gamma)\}, \quad (24)$$

with

$$\Lambda_m = [(1+\Delta)^4 + (1-\Delta)^4] - 2(1-\Delta^2)^2 \cos 2m\gamma.$$

Expand Λ_m^{-1} in a Fourier series in terms of $(2m\gamma)$:

$$\Lambda_m^{-1} = \frac{1}{(1+\Delta)^4 - (1-\Delta)^4} \times \sum_{n=0}^{\infty} \epsilon_n \left(\frac{1-\Delta}{1+\Delta}\right)^{2n} \cos 2nm\gamma, \quad (25)$$

where $\epsilon_0 = 1$ and $\epsilon_n = 2 (n \geq 2)$. Then (23) and (24) may be rewritten as

$$P_1(\eta,\xi) = \frac{1}{1+\Delta} \sum_{m=1}^{\infty} \left[\cos m(\eta-\xi) - \sum_{n=1}^{\infty} \frac{\Delta(1-\Delta)^{2n-1}}{(1+\Delta)^{2n}} \cos m(\eta-\xi+2n\gamma)\right], \quad (26)$$

$$P_2(\eta,\xi) = \frac{2\Delta}{(1+\Delta)^2} \sum_{m=1}^{\infty} \left[\cos m(\eta-\xi+\gamma) + \sum_{n=1}^{\infty} \left(\frac{1-\Delta}{1+\Delta}\right)^{2n} \cos m(\eta-\xi+(2n+1)\gamma)\right], \quad (27)$$

which when substituted into (21) and (22) yield

$$S_1(\eta) = \tau_0 + [\tau_{yz}]_{y=0} + \frac{\mu \cos\theta_0}{c}\left\{\frac{3+\Delta^2}{4(1+\Delta)} U_1 + \frac{U_2}{2}\right\} + \frac{\mu k \cos\theta_0}{1+\Delta}\left[\phi_1(\eta) - \sum_{n=1}^{\infty} \frac{\Delta(1-\Delta)^{2n-1}}{(1+\Delta)^{2n}} \phi_1(\eta+2n\gamma)\right] + \frac{2\Delta\mu k \cos\theta_0}{(1+\Delta)^2}\left[\phi_2(\eta+\gamma) + \sum_{n=1}^{\infty}\left(\frac{1-\Delta}{1+\Delta}\right)^{2n} \times \phi_2(\eta+(2n+1)\gamma)\right], \quad (28)$$

$$S_2(\eta) = \tau_0 + [\tau_{yz}]_{y=H} + \frac{\mu \cos\theta_0}{c}\left\{\frac{3+\Delta^2}{4(1+\Delta)} U_2 + \frac{U_1}{2}\right\} + \frac{\mu k \cos\theta_0}{1+\Delta}\left[\phi_2(\eta) - \sum_{n=1}^{\infty} \frac{\Delta(1-\Delta)^{2n-1}}{(1+\Delta)^{2n}} \phi_2(\eta+2n\gamma)\right] + \frac{2\Delta\mu k \cos\theta_0}{(1+\Delta)^2}\left[\phi_1(\eta+\gamma) + \sum_{n=1}^{\infty}\left(\frac{1-\Delta}{1+\Delta}\right)^{2n} \times \phi_1(\eta+(2n+1)\gamma)\right], \quad (29)$$

where we have used the relation

$$\sum_{m=1}^{\infty} \cos mx = -\frac{1}{2} + \pi \sum_{m=-\infty}^{\infty} \delta(x - 2\pi m). \quad (30)$$

Downloaded 04 May 2010 to 171.66.16.27. Redistribution subject to ASME license or copyright; see http://www.asme.org/terms/Terms_Use.cfm

One may find the physical meaning involved in (28) and (29). For instance, the appearance of $\phi_2(\eta + (2n + 1)\gamma)$ $(n \geq 0)$ in (28) is due to the effects of the disturbance along interface 2 after the nth reflection at interface 1, and $\phi_1(\eta + 2n\gamma)$ $(n \geq 1)$ is the contribution of the disturbance along interface 1 after the nth reflection at interface 2.

When γ may be expressed as the product of a rational number and π, i.e., $\gamma = \pi m/m'$ with (m, m') being irreducible integers, the infinite series in (28) and (29) can be replaced by finite series with m' terms, otherwise we have to truncate the infinite series to $n = N$. The truncation error of the series

$$\sum_{n=1}^{\infty} \frac{\Delta(1-\Delta)^{2n-1}}{(1+\Delta)^{2n}} \phi_j(\eta)$$

is

$$\frac{A_j|1-\Delta|^{2N+1}}{4(1+\Delta)^{2N}},$$

where A_j is the upper bound of $|\phi_j(\eta)|$. The expected accuracy may be reached by choosing a proper value of N.

Substituting (28) and (29) into the boundary condition in the slip zones given by (1), we have a set of recurrence relations which, together with $\phi_j(\eta) = 0$ in the stick zones, can yield $\phi_j(\eta)$ in the slip zones. The leading edges of the unknown slip zones are determined by $S_j(\eta) = f_{sj}p_0$ and the trailing edges by $S_j(\eta) = f_{kj}p_0$ with consideration of the inequality in (2). Special examples for identical materials will be discussed in detail in the next section.

Examples for Identical Materials

In order to illustrate the procedure in solving the obtained recurrence equations and to give more explicit exploration of the interaction between the two frictional interfaces, we consider the special case of identical materials and ignore the effects of the applied shearing traction τ_0 and the "kinematic locking." Then we have $\Delta = 1$, $\tau_0 = 0$, $U_1 = U_2 = 0$ and $f_{sj} = f_{kj}$ $(j = 1, 2)$. In this case the following relations must be true:

$$\phi_j(\eta \pm \pi) = -\phi_j(\eta). \tag{31}$$

Equations (28) and (29) then reduce to

$$S_1(\eta) = -A_0 \sin \eta + \tfrac{1}{2}\mu k \cos\theta_0[\phi_1(\eta) + \phi_2(\eta + \gamma)], \tag{32}$$

$$S_2(\eta) = -A_0 \sin(\eta + \gamma) + \tfrac{1}{2}\mu k \cos\theta_0[\phi_1(\eta + \gamma) + \phi_2(\eta)]. \tag{33}$$

If the interfaces do not slip, the above two equations give the results for the bilateral interfaces, which reach the peak values at $\eta = (l + \frac{1}{2})\pi$ $(l = 0, \pm1, \pm2, \ldots)$ on interface 1 and at $\eta + \gamma = (l + \frac{1}{2})\pi$ $(l = 0, \pm1, \pm2, \ldots)$ on interface 2. Increase the strength of the incident wave and/or decrease the friction. Local slip may take place near these points. Denote $(\alpha_{1i}, \beta_{1i})$ $(i = 1, 2)$ as the slip zones near $\eta = (-1)^i\pi/2$ on interface 1, and $(\alpha_{2i}, \beta_{2i})$ $(i = 1, 2)$ as those near $\eta + \gamma = (-1)^i\pi/2$ on interface 2 (as illustrated in Fig. 3). Then we have

$$(\alpha_{j2}, \beta_{j2}) = (\alpha_{j1}, \beta_{j1}) + \pi, \quad j = 1, 2. \tag{34}$$

Take $A_0 > 0$ so that the shearing traction in $(\alpha_{j1}, \beta_{j1})$ is positive and that in $(\alpha_{j2}, \beta_{j2})$ is negative. The boundary conditions in the slip zones (Eq. (1)) yields

$$\bar{\phi}_1(\eta) + \bar{\phi}_2(\eta + \gamma) = \sin\eta - (-1)^i f_{k1}p_0/A_0, \quad \eta \in (\alpha_{1i} + 2l\pi, \beta_{1i} + 2l\pi), \tag{35}$$

$$\bar{\phi}_1(\eta + \gamma) + \bar{\phi}_2(\eta) = \sin(\eta + \gamma) - (-1)^i f_{k2}p_0/A_0, \quad \eta \in (\alpha_{2i} + 2l\pi, \beta_{2i} + 2l\pi), \tag{36}$$

where $\bar{\phi}_j(\eta) = (2A_0)^{-1}\mu k \cos\theta_0\phi_j(\eta)$. Knowing that $\bar{\phi}_j(\eta) = 0$ in the stick zones, we can obtain $\bar{\phi}_j(\eta)$ in the slip zones by recurrence relations (35) and (36). However, the slip zones are still unknown, which makes the problem more difficult to solve. Here we will make use of an iterative method similar to that we suggested in the previous papers (Yu, Wang, and Gai, 1997; Wang, Yu, and Gai, 1998b). It is noted that the solution of the problem depends on the parameters γ and $f_{kj}p_0/A_0$, where the relative value of f_{k1} and f_{k2} plays an important role in determining the local slip of the two interfaces. Therefore, two cases, $f_{k1} < f_{k2}$ and $f_{k1} > f_{k2}$, will be discussed separately. The special case of $f_{k1} = f_{k2}$ will also be considered.

(1) $f_{k1} < f_{k2}$

When $f_{k1}p_0/A_0 > 1$, there are no slip zones on both interfaces. Decrease $f_{k1}p_0/A_0$ to a value smaller than 1. Interface 1 then slips locally. If f_{k2} is so big that interface 2 cannot slip, we have $\bar{\phi}_2(\eta) \equiv 0$. Equation (35) yields

$$\bar{\phi}_1(\eta) = \sin\eta - (-1)^i f_{k1}p_0/A_0, \quad \eta \in (\alpha_{1i} + 2l\pi, -\beta_{1i} + 2l\pi). \tag{37}$$

The traction $S_1(\eta)$ is

$$S_1(\eta)/A_0 = -\sin(\eta) + \bar{\phi}_1(\eta). \tag{38}$$

The slip zone $(\alpha_{11}, \beta_{11})$ is given by

$$\beta_{11} = -\alpha_{11} - \pi = -\arcsin(f_{k1}p_0/A_0), \tag{39}$$

and $(\alpha_{12} + 2l\pi, \beta_{12} + 2l\pi)$ may be obtained by using relation (34). $S_2(\eta)$ can be calculated from (33) as

$$\begin{aligned} S_2(\eta)/A_0 &= -\sin(\eta + \gamma) + \bar{\phi}_1(\eta + \gamma) \\ &= -\sin(\eta + \gamma), \quad \eta + \gamma \notin (\alpha_{11} + 2l\pi, \beta_{11} + 2l\pi) \cup (\alpha_{12} + 2l\pi, \beta_{12} + 2l\pi) \\ &= (-1)^{i+1} f_{k1}p_0/A_0, \quad \eta + \gamma \in (\alpha_{1i} + 2l\pi, \beta_{1i} + 2l\pi), \end{aligned} \tag{40}$$

which is proved to be lower than $f_{k2}p_0$. Therefore, no local slip can take place on interface 2. Now we have arrived at the solution for $f_{k1} < f_{k2}$, which satisfy all boundary conditions (1) and (2). The solution is universal for arbitrary values of γ and independent of f_{k2} $(> f_{k1})$. The interface shearing tractions and the relative slip velocities in this case are shown schematically in Fig. 2 where $V_1^*(\eta) = V_1(\eta)/(C_0kc)$. The dashed lines present the results for the bilateral interfaces. It is seen that the slip of interface 1 reduces the stress on interface 2 to the level of $f_{k1}p_0$ which is lower than $f_{k2}p_0$. The above solution holds until $f_{k1} \to f_{k2} - 0$. The results for the limiting case of $f_{k1} = f_{k2}$ cannot be yielded by the solution. This limiting situation is included in the case of $k_1 > f_{k2}$ which will be discussed next.

(2) $f_{k1} > f_{k2}$

Suppose $f_{k2}p_0/A_0 < 1$ and f_{k1} is big enough so that interface 2 slips locally, while interface 1 does not. Then we have $\bar{\phi}_1(\eta) \equiv 0$, and (36) gives

$$\bar{\phi}_2(\eta) = \sin(\eta + \gamma) - (-1)^i f_{k2}p_0/A_0, \quad \eta \in (\alpha_{2i} + 2l\pi, \beta_{2i} + 2l\pi). \tag{41}$$

It follows from (33) that

$$S_2(\eta)/A_0 = -\sin(\eta + \gamma) + \bar{\phi}_2(\eta). \tag{42}$$

The interval $(\alpha_{21}, \beta_{21})$ is given by

$$\beta_{21} = -\alpha_{21} - \pi - 2\gamma = -\gamma - \arcsin(f_{k2}p_0/A_0), \tag{43}$$

Downloaded 04 May 2010 to 171.66.16.27. Redistribution subject to ASME license or copyright; see http://www.asme.org/terms/Terms_Use.cfm

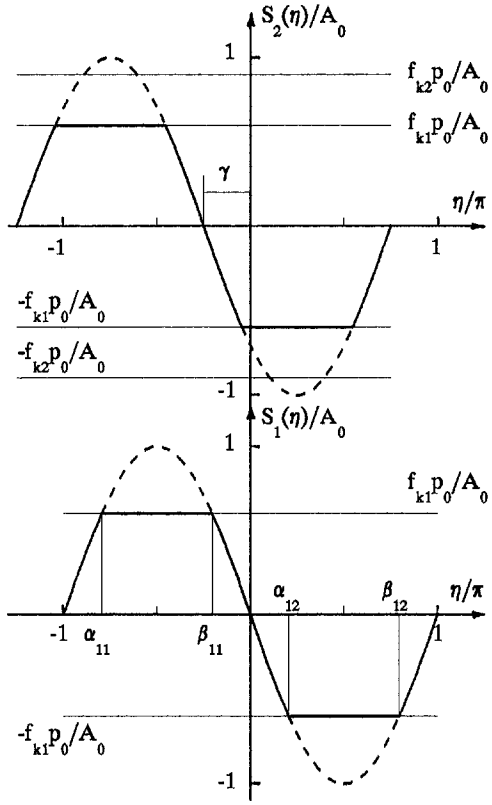


Fig. 2(*a*)

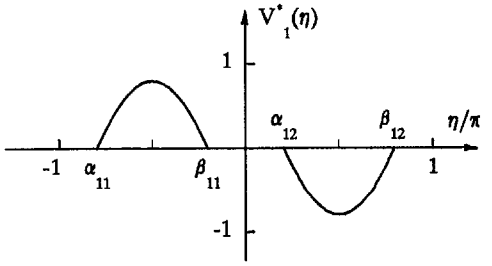


Fig. 2(*b*)

Fig. 2 Sketch map for distribution of interface shearing tractions (*a*) and relative slip velocities (*b*) for $f_{k1} < f_{k2}$. The dashed lines show the results for bilateral interfaces. The values of γ and $f_{k2}(>f_{k1})$ may be arbitrary.

and $(\alpha_{22} + 2l\pi, \beta_{22} + 2l\pi)$ is determined by (34). $S_1(\eta)$ can be obtained from (32) as

$$
\begin{aligned}
S_1(\eta)/A_0 &= -\sin\eta + \bar{\phi}_2(\eta + \gamma) \\
&= -\sin\eta, \quad \eta + \gamma \notin (\alpha_{21} + 2l\pi, \beta_{21} + 2l\pi) \\
&\quad \cup (\alpha_{22} + 2l\pi, \beta_{22} + 2l\pi) \\
&= 2\sin\gamma\cos(\eta + \gamma) - (-1)^i f_{k2}p_0/A_0, \\
&\qquad \eta + \gamma \in (\alpha_{2i} + 2l\pi, \beta_{2i} + 2l\pi). \quad (44)
\end{aligned}
$$

when

$$
f_{k1}p_0/A_0 \geq \max_{\eta' \in (\alpha_{21}, \beta_{21})} \{1, |2\sin\gamma\cos\eta' + f_{k2}p_0/A_0|\}, \quad (45)
$$

interface 1 does not slip and the above results satisfy all boundary conditions. If (45) is violated, local slip may take place on interface 1 and (41)–(44) do not yield corrective solution any more. The solution in this case should be derived by using recurrence relations (35) and (36). The results vary with different values of γ. Because $S_1(\eta)$ given by (44) is a periodic function in γ with π as the period and $S_1(-\eta, \gamma) = -S_1(\eta, \gamma + \pi/2)$, only the case of $0 < \gamma \leq \pi/2$ need to be considered. Other cases may be analyzed similarly.

We first consider a simple case, $\gamma = \pi/2$. Suppose that interface 2 slips, while that interface 1 does not. It is seen that $|S_1(\eta)/A_0|$ given by (44) reaches the peak value of $(2 - f_{k2}p_0/A_0)$ at $\eta = (2l \pm \frac{1}{2})\pi$. Consequently when $f_{k2}p_0/A_0 < f_{k1}p_0/A_0 < 2 - f_{k2}p_0/A_0$, local slip will take place at these points on interface 1. We anticipate that the regions where $S_1(\eta)$ exceeds $f_{k1}p_0$ are possible slip zones and denote the one near $\eta = -\pi/2$ by $(\alpha_{11}, \beta_{11})$. Then it follows from $S_1(\alpha_{11}) = S_1(\beta_{11}) = f_{k1}p_0$ that

$$
\beta_{11} = -\alpha_{11} - \pi = -\arcsin\frac{(f_{k1} + f_{k2})p_0/A_0}{2}. \quad (46)
$$

Equation (35) holds in $(\alpha_{11}, \beta_{11})$, i.e.,

$$
\bar{\phi}_1(\eta) + \bar{\phi}_2(\eta + \pi/2) = \sin\eta + f_{k1}p_0/A_0, \quad \eta \in (\alpha_{11}, \beta_{11}). \quad (47)
$$

Note that $\eta + \pi/2 \in (\alpha_{11} + \pi/2, \beta_{11} + \pi/2) \subseteq (\alpha_{22}, \beta_{22})$ with $(\alpha_{22}, \beta_{22})$ determined by (34) and (46). Therefore, for $\eta \in (\alpha_{11}, \beta_{11})$, $\bar{\phi}_2(\eta + \pi/2)$ should satisfy (36) which reduces to

$$
\bar{\phi}_1(\eta + \pi) + \bar{\phi}_2(\eta + \pi/2) = -\sin\eta - f_{k2}p_0/A_0, \quad \eta \in (\alpha_{11}, \beta_{11}). \quad (48)
$$

Combination of (47) and (48) with account of (31) yields

$$
\bar{\phi}_1(\eta) = \sin\eta + \frac{(f_{k1} + f_{k2})p_0}{2A_0}, \quad \bar{\phi}_2(\eta + \pi/2) = \frac{(f_{k1} - f_{k2})p_0}{2A_0}, \quad \eta \in (\alpha_{11}, \beta_{11}). \quad (49)
$$

It can be easily verified that $\bar{\phi}_1(\alpha_{11}) = \bar{\phi}_1(\beta_{11}) = 0$. For $\eta + \pi/2 \in (\alpha_{22}, \beta_{22})\backslash(\alpha_{11} + \pi/2, \beta_{11} + \pi/2)$ (where "\" represents the difference set), $\bar{\phi}_1(\eta)$ vanishes and $\bar{\phi}_2(\eta + \pi/2)$ is given by (41) with $i = 2$. With $\bar{\phi}_j(\eta)$ in hand, we can calculate $S_j(\eta)$ using (32) and (33). The results are proved to satisfy all boundary conditions (1) and (2), that is to say, the estimated slip zones given by (43) and (46) are really existing ones. Now we have obtained the solution for $\gamma = \pi/2$. Figure 3 demonstrates the distribution of the interface shearing tractions and slip velocities for $f_{k1}p_0/A_0 = 1$ and $f_{k2}p_0/A_0 = 0.6$. The dashed lines show the results for bilateral interfaces, and the dotted lines are for the case of $f_{k1}p_0/A_0 > 1.4$ with interface 1 perfectly bonded. It is seen that the slip of interface 2 increases the shearing stress on interface 1 and therefore makes the slipping easier, while that the slip of interface 1 decreases the slip velocity of interface 2 until the local slip disappears.

The solution for the limiting case, $f_{k1} = f_{k2}$, can be derived from the above results. In this situation, $(\alpha_{11} + \pi/2, \beta_{11} + \pi/2) = (\alpha_{22}, \beta_{22})$ and $\bar{\phi}_2(\eta) \equiv 0$. Consequently, there are no slip zones on interface 2 although the maximum shearing traction is $f_{k2}p_0$.

For the case of $\gamma < \pi/2$, the solution is more complex. Here we suggest an iterative method as follows:

(i) Suppose that the regions where $S_1(\eta)$ given by (44) exceeds $f_{k1}p_0$ are possible slip zones which are determined by $S_1(\eta) = \pm f_{k1}p_0$.

(ii) Solve (35) and (36) for $\bar{\phi}_j(\eta)$ based on the estimated slip zones, and then calculate $S_j(\eta)$ by (32) and (33).

(iii) Check whether the boundary conditions (1) and (2) are all satisfied. If not, make a new guess for the slip zones on the assumption similar to step (i).

(iv) Repeat steps (ii) and (iii) until all boundary conditions are satisfied.

Downloaded 04 May 2010 to 171.66.16.27. Redistribution subject to ASME license or copyright; see http://www.asme.org/terms/Terms_Use.cfm

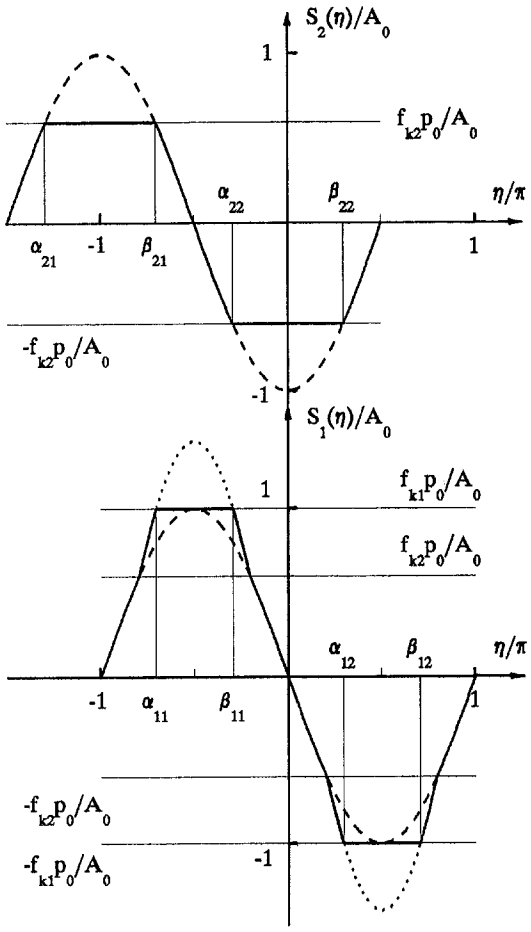


Fig. 3(*a*)

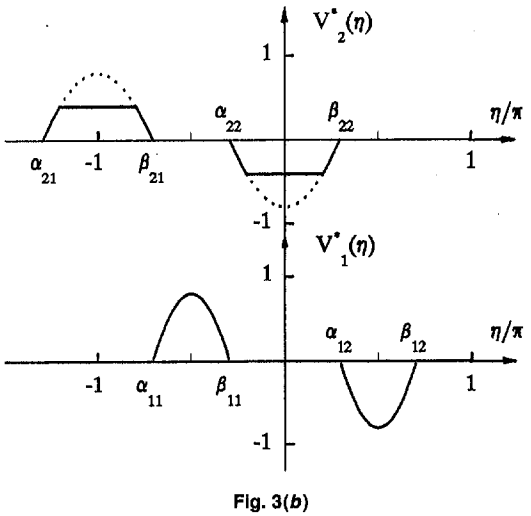


Fig. 3(*b*)

Fig. 3 Distribution of interface shearing tractions (*a*) and relative slip velocities (*b*) for $f_{k1} > f_{k2}$ with $\gamma = \pi/2$ and $f_{k2}p_0/A_0 = 0.6$. The dashed lines show the results for bilateral interfaces. The dotted lines give the results when interface 1 is perfectly bonded.

The above iterative procedure is proved to be quite efficient. Indeed one may find that the closed-form solution can be obtained after one or two iterations. As an example we present the results for $\gamma = \pi/4$. It is found, in this special case, that the local slip takes place on both interfaces when $f_{k2}p_0/A_0 < 1$ and $f_{k1}p_0/A_0 < \max\{1, \sqrt{2} - f_{k2}p_0/A_0\}$. In particular, when

$$\sin[\arccos(f_{k2}p_0/A_0)] < f_{k1}p_0/A_0 < \min\{1, \sqrt{2} - f_{k2}p_0/A_0\}$$

with $f_{k2}p_0/A_0 < \sqrt{2}/2$, there are additional slip zones near $\eta = (2l \pm \frac{1}{2} + \frac{1}{4})\pi$ besides the main slip zones near $\eta = (2l \pm \frac{1}{2})\pi$.

The interface shearing tractions and relative slip velocities for $\gamma = \pi/4$ are illustrated in Fig. 4 for $f_{k2}p_0/A_0 = \frac{1}{2}$. The dashed lines are for $f_{k1}p_0/A_0 = \sqrt{3}/2$; the solid lines for $f_{k1}p_0/A_0 = \sqrt{2}/2$; the dot-dashed lines for $f_{k1}p_0/A_0 = \frac{1}{2}$, the dotted lines for the case where no slip takes place on interface 1; and the thin dashed lines for the bilateral interfaces. It is observed that the slip of interface 2 increases the stress near $\eta = l\pi$ on interface 1, and therefore make interface 1 slip more easily. The slip of interface 1, on the other hand, reduces the slip velocities of interface 2, and even

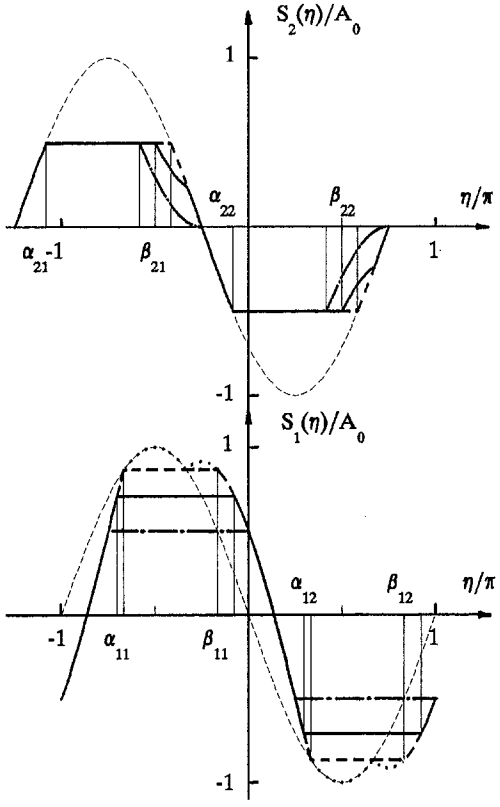


Fig. 4(*a*)

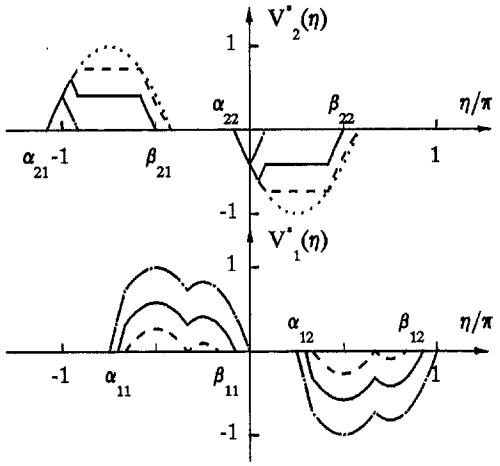


Fig. 4(*b*)

Fig. 4 Distribution of interface shearing tractions (*a*) and relative slip velocities (*b*) for $f_{k1} > f_{k2}$ with $\gamma = \pi/4$ and $f_{k2}p_0/A_0 = \frac{1}{2}$. The thin dashed lines show the results for bilateral interfaces. The dotted lines give the results when interface 1 is perfectly bonded. The thick dashed lines are for the case of $f_{k1}p_0/A_0 = \sqrt{3}/2$. The solid lines for the case of $f_{k1}p_0/A_0 = \sqrt{2}/2$. The dot-dashed lines for the case of $f_{k1}p_0/A_0 = \frac{1}{2}$.

Downloaded 04 May 2010 to 171.66.16.27. Redistribution subject to ASME license or copyright; see http://www.asme.org/terms/Terms_Use.cfm

make the slip zones smaller when $f_{k1}p_0/A_0$ is relatively lower. It is noted that there are two couples of slip zones in one representative period on interface 1 when $\sqrt{3}/2 < f_{k1}p_0/A_0 < 1$.

The solution for the limiting case of $f_{k1} \to f_{k2} + 0$ or $f_{k1} = f_{k2}$ can be obtained. The result is shown in Fig. 4 by the dot-dashed lines where only small slip zones exist on interface 2. It is noted that the solution for the physical limiting case of equal interface friction, $f_{k1} = f_{k2}$, is always found as the limit from above of the solution for $f_{k1} < f_{k2}$ (i.e., as $f_{k1} \to f_{k2} + 0$) and is generally different from that for $f_{k1} \to f_{k2} - 0$.

Finally we examine a special case, $\gamma = m\pi$ ($m = 1, 2, \ldots$). Because the maximum value of $|S_1(\eta)|$ given by (44) is $f_{k2}p_0$ which is lower than $f_{k1}p_0$, interface 1 does not slip. Therefore Eqs. (41)–(44) gives the corrective solution which holds until $f_{k2} \to f_{k1} - 0$. For the case of $f_{k1} = f_{k2} = f_k$, Eqs. (35) and (36), with consideration of (31) and (34), may be rewritten as

$$\bar{\phi}_1(\eta) + (-1)^m\bar{\phi}_2(\eta) = \sin\eta + f_k p_0/A_0, \quad \eta \in (\alpha_{11} + 2l\pi, \beta_{11} + 2l\pi), \quad (50)$$

$$(-1)^m\bar{\phi}_1(\eta) + \bar{\phi}_2(\eta) = (-1)^m \sin\eta + (-1)^m f_k p_0/A_0, \quad \eta \in (\alpha_{21} + (2l - m)\pi, \beta_{21} + (2l - m)\pi), \quad (51)$$

which are of the same form and cannot yield unique solution. However, we argue that

$$\bar{\phi}_1(\eta) = (-1)^m\bar{\phi}_2(\eta), \ (\alpha_{11}, \beta_{11}) = (\alpha_{21}, \beta_{21}) - m\pi \quad (52)$$

for the steady-state motion considered here because the stresses on the two interfaces are either exactly the same or different only in the sign. Substituting (52) into (50) or (51) and then into (32) and (33), we arrive at the final results for $\gamma = m\pi$.

It is noted that the case of $f_{k1} \geq f_{k2}$ is quite different from the case of $f_{k1} < f_{k2}$ in that the solution depends strongly on both γ and f_{k2}, and the solution exhibits a continuous limit as f_{k1} approaches f_{k2} from above, as implied by Fig. 4 for a particular value of γ. The limit always exists and for some exceptional values of γ is the same as the solution for $f_{k1} \to f_{k2} - 0$ in Fig. 2, but for most values of γ the solution for $f_{k1} \to f_{k2} + 0$ or $f_{k1} = f_{k2}$ is totally different, involving a different frictional state of stick/slip, than the solution for $f_{k1} < f_{k2}$. The fact that the limits for $f_{k2} \to f_{k1} \pm 0$ are different implies that the system is unstable when the two friction coefficients are slightly different, and therefore a small error in measuring the friction coefficients in practical cases may cause a large difference in the results.

It is perhaps helpful for us to understand the solution further by examining in detail the state of the two interfaces in $f_{k1}p_0/A_0$, $f_{k2}p_0/A_0$ plane for a given value of γ. When $f_{k1}p_0/A_0$, $f_{k2}p_0/A_0 \geq 1$, both two interfaces are perfectly bonded. This case is denoted as Case I. The previous analysis states that interface 1 slips while interface 2 sticks when $f_{k1}p_0/A_0 < f_{k2}p_0/A_0 \leq 1$ or $f_{k1}p_0/A_0 < 1 \leq f_{k2}p_0/A_0$ (Case II). For $f_{k2}p_0/A_0 \leq f_{k1}p_0/A_0 < 1$, either only interface 2 slips (Case III) or both interfaces slip (Case IV). The result depends on not only the relative value of the two friction coefficients but also the value of the parameter γ. These four cases and the regions they occupy in the $f_{k1}p_0/A_0$, $f_{k2}p_0/A_0$ plane are shown in Fig. 5. The dashed line is the boundary between Case III and IV for $\gamma = \pi/2$ and the dot-dashed line for $\gamma = \pi/4$. The shade area indicates the case that two couples of slip zones exist in one representative period on interface 1.

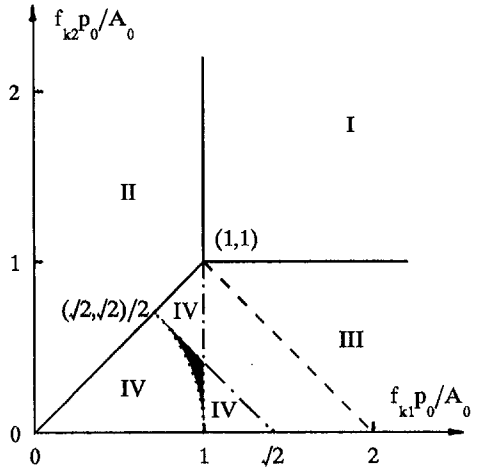


Fig. 5 Classification of four situations in $f_{k1}p_0/A_0$, $f_{k2}p_0/A_0$ plane. Case I—both interfaces are perfectly bonded; Case II—interface 1 slips locally with interface 2 perfectly bonded; Case III—opposite to Case II; Case IV—both interfaces slip locally. The dashed line is for $\gamma = \pi/2$; the dot-dashed line for $\gamma = \pi/4$. The shade area bounded by $f_{k1}p_0/A_0 = 1$, $f_{k1}p_0/A_0 - f_{k2}p_0/A_0 = \sqrt{2}$ and $(f_{k1}p_0/A_0)^2 + (f_{k2}p_0/A_0)^2 = 1$ shows the case that interface 1 involves two couples of slip zones.

Energy Transmission and Dissipation

It may be interesting to seismologists or geophysicists to discuss the energy transmitted through the interlayer and dissipated by friction. We examine the power averaged over a wavelength or a period of the incident wave, which is inputted to, extracted from, and dissipated at the block of material containing the whole interlayer and two interfaces as indicated in Fig. 1 by dashed lines. The power input of the applied antiplane shearing traction is

$$P_\tau = \tau_0(U_1 + U_2), \quad (53)$$

whereas the input of the incident wave is

$$P_0 = -\frac{1}{2\pi}\int_{-\pi}^{\pi}[\tau_{yz}^{(0)}\dot{w}^{(0)}]_{y=0}d\eta = \frac{1}{2}A_0C_0kc. \quad (54)$$

The power extracted from the block by the reflected wave (1) is

$$P_1 = \frac{1}{2\pi}\int_{-\pi}^{\pi}[(\tau_{yz}^{(1)} + \bar{\tau}_{yz}^{(1)})(\dot{w}^{(1)} + \dot{\bar{w}}^{(1)})]_{y=0}d\eta, \quad (55)$$

and that of the transmitted wave (4) is

$$P_4 = -\frac{1}{2\pi}\int_{-\pi}^{\pi}[(\tau_{yz}^{(4)} + \bar{\tau}_{yz}^{(4)})(\dot{w}^{(4)} + \dot{\bar{w}}^{(4)})]_{y=H}d\eta. \quad (56)$$

The power dissipated by friction at the two interfaces is

$$P_{d1} = \frac{1}{2\pi}\int_{-\pi}^{\pi}S_1(\eta)V_1(\eta)d\eta,$$

$$P_{d2} = \frac{1}{2\pi}\int_{-\pi}^{\pi}S_2(\eta)V_2(\eta)d\eta. \quad (57)$$

It follows from the energy conservation that

$$P_0 + P_\tau = P_1 + P_4 + P_{d1} + P_{d2} \quad (58)$$

which can be used as a check on the numerical computations.

For the identical material case with $\tau_0 = 0$, a straightforward calculation yields

$$\dot{w}^{(1)} = 0, \quad \dot{\bar{w}}^{(1)} = -[V_1(\eta) + V_2(\eta + \gamma)]/2,$$

$$\dot{w}^{(4)} = C_0kc\sin(\eta + \gamma), \quad \dot{\bar{w}}^{(4)} = [V_1(\eta + \gamma) + V_2(\eta)]/2,$$

$$[\tau_{yz}^{(1)} + \bar{\tau}_{yz}^{(1)}]_{y=0} = S_1(\eta) + A_0\sin\eta = -\frac{\mu\cos\theta_0}{2c}[V_1(\eta) + V_2(\eta + \gamma)],$$

Downloaded 04 May 2010 to 171.66.16.27. Redistribution subject to ASME license or copyright; see http://www.asme.org/terms/Terms_Use.cfm

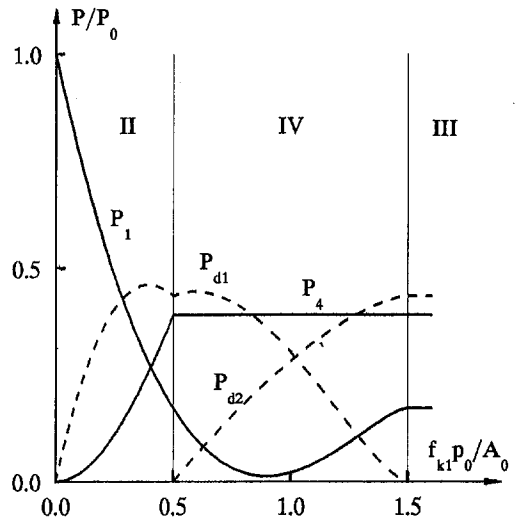


Fig. 6 Reflected, transmitted, and dissipated energy versus $f_{k1}p_0/A_0$ for $f_{k2}p_0/A_0 = \frac{1}{2}$ and $\gamma = \pi/2$

$$[\tau_{yz}^{(4)} + \bar{\tau}_{yz}^{(4)}]_{y=H} = S_2(\eta) = -A_0 \sin(\eta + \gamma) - \frac{\mu \cos\theta_0}{2c}[V_1(\eta + \gamma) + V_2(\eta)].$$

Then we have

$$\frac{P_1}{P_0} = \frac{1}{4\pi}\int_{-\pi}^{\pi}[V_1^*(\eta) + V_2^*(\eta + \gamma)]^2 d\eta,$$

$$\frac{P_4}{P_0} = \frac{1}{4\pi}\int_{-\pi}^{\pi}[V_1^*(\eta + \gamma) + V_2^*(\eta)]^2 d\eta, \tag{59}$$

$$\frac{P_{d1}}{P_0} = \frac{2f_{k1}p_0}{\pi A_0}\int_{\alpha_{11}}^{\beta_{11}} V_1^*(\eta) d\eta,$$

$$\frac{P_{d1}}{P_0} = \frac{2f_{k2}p_0}{\pi A_0}\int_{\alpha_{21}}^{\beta_{21}} V_2^*(\eta) d\eta, \tag{60}$$

where V_j^* is the relative slip velocity normalized with C_0kc.

As an example, we here present the numerical results for $\gamma = \pi/2$. Figure 6 illustrates the curves of the power ratios $\{P_1/P_0, P_4/P_0, P_{d1}/P_0, P_{d2}/P_0\}$ versus $f_{k1}p_0/A_0$ for $f_{k2}p_0/A_0 = 0.5$. Three cases, $0 \le f_{k1}p_0/A_0 < \frac{1}{2}$, $\frac{1}{2} \le f_{k1}p_0/A_0 < \frac{3}{2}$ and $f_{k1} \ge \frac{3}{2}$ correspond, respectively, to Case II, IV, and III as shown in Fig. 5. We examine the increasing process of $f_{k1}p_0/A_0$. At the starting point of $f_{k1}p_0/A_0 = 0$, no wave motion can be transmitted through interface 1. Concequently we have $P_{d1} = P_4 = 0$ and $P_1 = P_0$. As $f_{k1}p_0/A_0$ increases, P_1 decreases rapidly and continues decreasing after $f_{k1}p_0/A_0$ passing beyond 0.5 until it reaches a minimum value near $f_{k1}p_0/A_0 = 0.9$. After then it increases to a certain value at $f_{k1}p_0/A_0 = 1.5$. P_4 increases in Case II and then remains a constant once $f_{k1}p_0/A_0$ is larger than 0.5. P_{d1} increases first and then decreases. After $f_{k1}p_0/A_0$ surpasses 0.5, it increases slightly again and then decreases to zero at $f_{k1}p_0/A_0 = 1.5$. $P_{d2} = 0$ in Case II and increases from zero at $f_{k1}p_0/A_0 = 0.5$ to a certain value at $f_{k1}p_0/A_0 = 1.5$. All power ratios are unchanged when $f_{k1}p_0/A_0 > 1.5$ because interface 1 does not slip any more.

We also demonstrate the variation of the power ratios with $f_{k2}p_0/A_0$ for $f_{k1}p_0/A_0 = 1.5$ in Fig. 7. For $0 < f_{k2}p_0/A_0 \le 0.5$, both interfaces slip locally (Case IV). While for $f_{k2}p_0/A_0 \ge 1$, both interfaces are perfectly bonded (Case I). When $f_{k2}p_0/A_0$ is between 0.5 and 1.0, only interface 2 slips locally, which corresponds to Case III. At $f_{k2}p_0/A_0 = 0$, no wave can be transmitted through interface 2 and thus $P_4 = P_{d2} = 0$. We note that this case is exactly the same as what we studied for a layer frictionally bonded with a half space (Yu, Wang, and Gai, 1997). With increase of $f_{k2}p_0/A_0$, P_1 decreases to zero at $f_{k2}p_0/A_0 = 1$ and P_{d1} to zero at $f_{k2}p_0/A_0 = 0.5$. P_4 increases and finally is equal to P_0 at $f_{k2}p_0/A_0 = 1$, which is due to the fact that no wave is reflected when both interfaces are perfectly bonded. P_{d2} first increases and then decreases to zero at $f_{k2}p_0/A_0 = 1$. It is noted that Case II and III are the same as that of two half-spaces with identical materials which was considered by Chez, Dundurs, and Comninou (1983).

Discussion

The propagation of SH waves through an elastic interlayer frictionally bonded to two semi-infinite solids of the same material constants is studied in this paper with consideration of the local slip of the interfaces caused by the incident wave strong enough. By the Fourier analysis, the problem is cast to a set of recurrence equations with unknown boundaries between the slip and stick zones. An iterative method is suggested to obtain the final results and the special case of identical material is discussed in detail. The interaction between the two interfaces is examined. It is found that the state of the system depends strongly upon the relative value of the two friction coefficients, f_{k1} and f_{k2}, as well as γ, a parameter involving the thickness of the interlayer and the frequency of the incident wave:

1 When f_{k1} is strictly less than f_{k2} the solution is given by (37)–(40) in closed forms and is independent of f_{k2}. The solution is found to be universal for arbitrary values of parameter γ. The local slip, in this case, cannot take place on interface 2 because the slip of interface 1 reduces the stress on interface 2 to a level lower than the friction $f_{k2}p_0$;

2 When f_{k1} is strictly greater than f_{k2}, the solution is derived by an iterative method. The solution depends continuously on f_{k2} and approaches the $f_{k1} = f_{k2}$ limiting solution. The results are also quite different for various values of parameter γ. Both interfaces may slip locally in this case. The slip of interface 2 generally increases the stress on interface 1, while that the slip of interface 1 decreases the slip velocity on interface 2.

3 When $f_{k1} = f_{k2}$ the solution is yielded from that for $f_{k1} > f_{k2}$ as f_{k1} approaches f_{k2} from above. The solution is usually different in distribution of stress and slip velocity as well as the state of stick and slip than the solution for f_{k1} very close to but less than f_{k2}. In this case interface 2 does not slip or only slips in small intervals

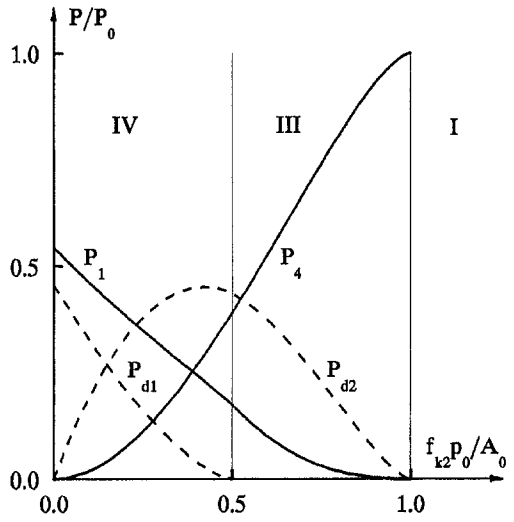


Fig. 7 Reflected, transmitted, and dissipated energy versus $f_{k2}p_0/A_0$ for $f_{k1}p_0/A_0 = \frac{3}{2}$ and $\gamma = \pi/2$

Downloaded 04 May 2010 to 171.66.16.27. Redistribution subject to ASME license or copyright; see http://www.asme.org/terms/Terms_Use.cfm

except for the case of $\gamma = m\pi$, where we argue that there are equal slip zones on both interfaces.

From the results obtained in this paper, we could conclude that the slip of the interface near the incident wave may restrain the slip of the interface far from the incident wave, while that the latter may facilitate the former. The states of the system are generally different for the limiting cases of $f_{k1} \to f_{k2} \pm 0$, which means the instability for a system with slightly different friction coefficients of the interfaces. This is crucial to the use of the solution of the problem.

Finally we mention that the present method is expected to be applied to in-plane wave motion and multilayered media. As one may note, the key step in the mathematical procedure is the expansion of the integral kernels $P_j(\eta, \xi)$ in Fourier series in γ. For the case of in-plane motion or multilayered media, the associated integral kernels should be expanded in multiple Fourier series. The resulting equations are definitely complicated and their solution is quite difficult.

Acknowledgments

Support by the China National Science Foundation under Grant No. 19472026 is gratefully acknowledged. The authors are grateful to the reviewers for their helpful comments.

References

Chez, E. L., Dundurs, J., and Comninou, M., 1978, "Reflection and refraction of SH waves in presence of slip and friction," *Bulletin of the Seismological Society of America,* Vol. 68, pp. 999–1011.

Chez, E. L., Dundurs, J., and Comninou, M., 1983, "Energy relations for SH waves interacting with a frictional contact interface," *International Journal of Solids and Structures,* Vol. 19, pp. 579–586.

Comninou, M., Barber, J. R., and Dundurs, J., 1982, "Disturbance at a Frictional Interface Caused by a Plane Elastic Pulse," ASME JOURNAL OF APPLIED MECHANICS, Vol. 49, pp. 361–365.

Comninou, M., and Dundurs, J., 1977a, "Reflection from a rigid boundary involving separation," *Journal of Engineering Mechanics, Division Proceedings of ASCE,* Vol. 103, pp. 285–294.

Comninou, M., and Dundurs, J., 1977b, "Reflexion and refraction of elastic waves in presence of separation," *Proceedings of the Royal Society of London,* Vol. A356, pp. 509–528.

Comninou, M., and Dundurs, J., 1977c, "Elastic Interface Waves Involving Separation," ASME JOURNAL OF APPLIED MECHANICS, Vol. 44, pp. 222–226.

Comninou, M., and Dundurs, J., 1978a, "Singular Reflexion and Refraction of Elastic Waves due to Separation," ASME JOURNAL OF APPLIED MECHANICS, Vol. 45, pp. 548–552.

Comninou, M., and Dundurs, J., 1978b, "Elastic Interface Waves and Sliding Between Two Solids," ASME JOURNAL OF APPLIED MECHANICS, Vol. 45, pp. 325–330.

Comninou, M., and Dundurs, J., 1979a, "Interaction of elastic waves with a unilateral interface," *Proceedings of the Royal Society of London,* Vol. A368, pp. 141–154.

Comninou, M., and Dundurs, J., 1979b, "Interface separation in the transonic range caused by a plane stress pulse," *Journal of Sound and Vibration,* Vol. 62, pp. 317–325.

Comninou, M., and Dundurs, J., 1980, "Interface slip caused by an SH pulse," *International Journal of Solids and Structures,* Vol. 16, pp. 283–289.

Comninou, M., Dundurs, J., and Chez, E. L., 1979, "Total reflection of SH waves in presence of slip and friction," *Journal of the Acoustic Society of America,* Vol. 66, pp. 789–793.

Dundurs, J., and Comninou, M., 1979, "Interface separation caused by an plane elastic wave of arbitrary form," *Wave Motion,* Vol. 1, pp. 17–23.

Ewing, W. M., Jardetzky, W. S., and Press, F., 1957, *Elastic Waves in Layered Media,* McGraw-Hill, New York.

Mendelsohn, D. A., and Doong, J.-M., 1989, "Transient dynamic elastic frictional contact: a general 2D boundary element formulation with examples of SH motion," *Wave Motion,* Vol. 11, pp. 1–21.

Miller, R. K., 1977, "An Approximate Method of Analysis of the Transmission of Elastic Waves Through a Friction Boundary," ASME JOURNAL OF APPLIED MECHANICS, Vol. 44, pp. 652–656.

Miller, R. K., 1978, "The effects of boundary friction on the propagation of elastic waves," *Bulletin of the Seismology Society of America,* Vol. 68, pp. 987–998.

Miller, R. K., 1979, "An estimate of the properties of Love-type surface waves in a frictionally bonded layer," *Bulletin of the Seismology Society of America,* Vol. 69, pp. 305–317.

Miller, R. K., and Tran, H. T., 1979, "Reflection, Refraction, and Absorption of Elastic Waves at a Frictional Interface: SH Motion," ASME JOURNAL OF APPLIED MECHANICS, Vol. 46, pp. 625–630.

Miller, R. K., and Tran, H. T., 1981, "Reflection, Refraction, and Absorption of Elastic Waves at a Frictional Interface: P and SV Motion," ASME JOURNAL OF APPLIED MECHANICS, Vol. 48, pp. 155–160.

Schoenberg, M., 1980, "Elastic wave behavior across linear slip interfaces," *Journal of the Acoustic Society of America,* Vol. 68, pp. 1516–1521.

Sezawa, K., and Kanai, K., 1940, "A fault surface or a block absorbs seismic wave energy," *Bulletin of Earthquake Research Institute, Tokyo University,* Vol. 18, pp. 465–482.

Wang, Y.-S., and Yu, G.-L., 1999, "Re-polarization of elastic waves at a frictional contact interface. Part II, Incidence of an P or SV wave," *International Journal of Solids and Structures,* Vols. 36, pp. 4563–4586.

Wang, Y.-S., Yu, G.-L., and Gai, B.-Z., 1997, "Slip with friction between an elastic layer and a substrate caused by an SH pulse," *Mechanics Research Communications,* Vol. 24, pp. 85–91.

Wang, Y.-S., Yu, G.-L., and Gai, B.-Z., 1998a, "Re-polarization of elastic waves at a frictional contact interface. Part I, Incidence of an SH wave," *International Journal of Solids and Structures,* Vol. 35, pp. 2002–2021.

Wang, Y.-S., Yu, G.-L., and Gai, B.-Z., 1998b, "Propagation of SH waves in a layered half-space with a frictional contact interface," *Bulletin of the Seismological Society of America,* Vol. 88, pp. 1300–1310.

Yu, G.-L., Wang, Y.-S., and Gai, B.-Z., 1997, "Slip With Friction Between an Elastic Layer and a Substrate Caused by SH Waves," ASME JOURNAL OF APPLIED MECHANICS, Vol. 64, pp. 1019–1021.

Yu, G.-L., Wang, Y.-S., and Gai, B.-Z., 1998, "In-plane motion induced by an SH pulse at a frictional contact interface," *Mechanics Research Communications,* Vol. 25, pp. 203–210.

Zharii, O. Y., 1995, "Adhesive Contact Between the Surface Wave and a Rigid Strip," ASME JOURNAL OF APPLIED MECHANICS, Vol. 62, pp. 368–371.

Zharii, O. Y., 1996, "Frictional Contact Between the Surface Wave and a Rigid Strip," ASME JOURNAL OF APPLIED MECHANICS, Vol. 63, pp. 15–20.

Downloaded 04 May 2010 to 171.66.16.27. Redistribution subject to ASME license or copyright; see http://www.asme.org/terms/Terms_Use.cfm

A "Second Law" for Structures: An Insightful Approach to the Design of Plane Frames

M. J. French
Department of Engineering,
Lancaster University,
Lancaster, LA1 4YR, UK
e-mail: m.french@lancaster.ac.uk

This paper introduces a new aid to the design of economical plane structures, based on the twin concepts of structural task, *which is an invariant for a given load system and given constraints on where material may be placed, and (absolute)* pertinacity, *which is the product of force and member length. An optimum (Michell) structure has task equal to pertinacity for every element of every member. The ratio u of task to pertinacity is unity everywhere in an optimum structure, and constitutes a utility factor: u may be negative for a member, that is, it is possible for a member to increase the task to be borne by the rest of the structure. A parallel is drawn with First and Second Law analysis in thermodynamics.*

1 Introduction

This paper introduces a new approach to the design of some components having an important structural role. It quantifies the structural function as the structural task, T, which is in units with the dimensions of work, e.g., 4 MJ. The task depends solely upon the load system to be sustained and any restrictions upon the space that the structure may occupy. Any element of the structure performs a certain amount of the task, T_r, and the sum of the T_r over the whole structure is T. The essence of the finding is that T is unique.

The concept of pertinacity p is also used. In this paper, the pertinacity of a member of a frame (from the Latin, "holding through") is the product of the force in it by its length, although a more general version is referred to below. Unfortunately, it is necessary to consider both the absolute value of pertinacities (taken as positive whether the force is tensile or compressive) and the signed or algebraic form p_s, which is negative when the force is compressive.

If there is a given allowable stress f in the material, the same in tension as compression, then the necessary volume of material in a structure is equal to the total absolute pertinacity divided by f. An optimum structure, using the least possible material, is thus one which has the minimum absolute pertinacity. If the allowable stresses in tension and compression differ, or if different materials are used, then there will be complications, usually of a trivial nature, which will not be treated here.

The absolute pertinacity of a member is equal to or greater than its task. This can be expressed by

$$T_r = up_r, \quad \text{where } 1 \geq u \geq -1. \tag{1}$$

A negative value of u indicates that a member is *adding* to the structural task, rather than helping to perform it.

In an optimum structure or structure of least weight, u is everywhere equal to one and

$$T = \sum p_r \tag{2}$$

where the summation is taken over the whole structure.

Contributed by the Applied Mechanics of THE AMERICAN SOCIETY OF MECHANICAL ENGINEERS for publication in the ASME JOURNAL OF APPLIED MECHANICS.

Discussion on the paper should be addressed to the Technical Editor, Professor Lewis T. Wheeler, Department of Mechanical Engineering, University of Houston, Houston, TX 77204-4792, and will be accepted until four months after final publication of the paper itself in the ASME JOURNAL OF APPLIED MECHANICS.

Manuscript received by the ASME Applied Mechanics Division, Feb. 11, 1998; final revision, Feb. 14, 1999. Associate Technical Editor: W. K. Liu.

As the pertinacity is a measure of the material content of the member, it is desirable to keep u as high as possible. In this paper, an expression for u is given and its use is explained.

There is an interesting parallel between the pertinacity and task relationships and First and Second Law analyses in thermodynamics. Pertinacity corresponds to gross energy, like internal energy, and task to available energy. The first is an overall measure, while the second measures only the contribution to the function. Improvement of a cycle occurs when irreversibilities are reduced, and improvement of a structure when u's are increased. The *utility factor* u may be regarded as a kind of efficiency. The mean u for a structure, averaged with respect to p, is equal to the task divided by the total pertinacity.

2 Michell Structures

To apply this approach to structures and before u can be evaluated, it is necessary to know the form of the optimum solution for a structure to bear the system of loads concerned. Fortunately the solutions have been determined for many useful cases, many of which may be found in Cox (1965) and Hemp (1973). Such structures are known as Michell structures, and they were extensively studied in the sixties. The approach suggested in this paper is possible because of the pioneering work of Michell and its extension by subsequent workers in the field.

Figure 1(a) shows an example of an optimum structure. It carries a loading system consisting of two downward forces F, F at $A(r, 0)$ and $B(-r, 0)$ and is supported at the origin O, so the system of loads is completed by an upward force of $2F$ at O. To complete the description of the example it is necessary to add any restrictions on the space which may be occupied by the structure, e.g., none of it may be in the region where y is positive. In this case, however, we make no such restrictions.

In this case the optimum structure consists of the four straight members AC, AF, BD, and BE, the arches CD and EF of radius $r/\sqrt{2}$, and two 90-deg fans of infinitely thin, infinitely many spokes of length $r/\sqrt{2}$ radiating from O. The straight members and the arches carry a load, positive or negative, of $F/\sqrt{2}$. The total radial load carried by each fan is $\pi F/2\sqrt{2}$ and so each has a pertinacity of $\pi Fr/4$. Multiplying the length of each member by the force in it and adding yields the total absolute pertinacity, which is $(\pi + 2)Fr$.

If the loads F were not concentrated but distributed uniformly along AB, then the member AC would have to be replaced by an infinite number of infinitely thin members parallel to AC, the arch CD by an infinite number of infinitely thin arches, etc. (see Fig. 1(b)). Consider the upper fan. It may be replaced by a membrane,

 Copyright © 1999 by ASME

Downloaded 04 May 2010 to 171.66.16.27. Redistribution subject to ASME license or copyright; see http://www.asme.org/terms/Terms_Use.cfm

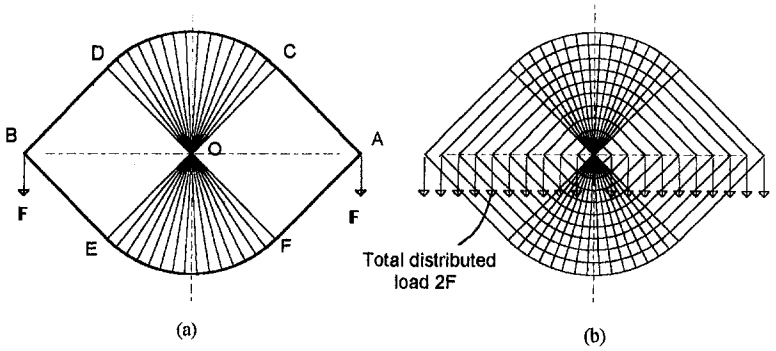


Fig. 1 Michell structures

in compression radially and in tension circumferentially. The members in the triangular region ACO may be replaced by a membrane which is in tension parallel to AC. All the areas can be characterized by two mutually orthogonal principal axes of stress, and it is the directions of these axes that we need to know in order to proceed (in the triangular areas, one principal stress is zero). The total absolute pertinacity is $(\pi + 2)rF/2$, half the previous value, reflecting the fact that dimensionally, the average distance of the load from the origin being half, the task must be half also (for this ideal structure, the task is the total absolute pertinacity).

Structures like those in Fig. 1 are called Michell structures, after the pioneer worker in the field (Michell, 1904). They are characterized by orthogonal sets of curves lying along principal axes of stress (or strain, in the derivation), forming Hencky nets. In Fig. 1 these curves are arcs of circles and straight lines, but other forms are possible, e.g., involutes, equiangular spirals or cycloids. Such fields are familiar in slip-field theory.

It should be noted in passing that the structures in Fig. 1 are not really structures at all, but mechanisms in equilibrium under the loads upon them. In Fig. 1(a), for example, one square can deform into a parallelogram if at the same time the other deforms the opposite way, say, if the axes CF and OF both lengthen by the same amount. In a practical structure this state of affairs would not be acceptable. However, practical structures which approach the efficiency (the average u) of Michell structures do not usually have this peculiarity, which is therefore of no practical importance. Also, although the Michell structures have an infinite number of members, practical approximations to them have relatively few members: for example, an approximation to Fig. 1(a) with ten members uses only 12 percent more material.

3 The Reduction in Task Effected by a Given Member in a General Plane Frame

If we know the Michell structure corresponding to a given system of loads, then we can find u, which is the ratio of the task done by an element of a member to its pertinacity. It is simply given by

$$u = \cos 2\theta \tag{3}$$

where θ is the angle between the member or element and the appropriate principal axis of stress. "Appropriate" means having the same sign of stress. Thus in the fan CDO in Fig. 1(a) the appropriate axis for a tension member or element is the circumferential. Equation (3) will not be derived formally here, but may be seen from the following argument. The force and length factors of the pertinacity of an element dl carrying a load P may be resolved separately in the appropriate or ideal direction to give an element of pertinacity

$$Pdl \cos^2 \theta \tag{4}$$

which is task. Unfortunately, the pertinacity must also be resolved in the inappropriate direction, to give a negative element of task

$$-Pdl \sin^2 \theta. \tag{5}$$

Combining expressions (4) and (5) gives the net task, which is

$$Pdl \cos 2\theta = u \times (\text{pertinacity}). \tag{6}$$

With this result the value of a particular member in a particular location can be calculated, although it is often more convenient to use one of the two integrals derived in the next section. Before proceeding, however, it is convenient to look at another aspect of pertinacity, the result established by Maxwell.

Maxwell's Lemma. Maxwell established the result that in frameworks, the total *algebraic* pertinacity is a function of the loading system only, from which it can be calculated (1869, 1975). A more general form of the lemma may be found in French (1994). In the structures in Fig. 1, the algebraic pertinacity is zero. The sum of the tensile (positive) pertinacities must therefore be equal to the absolute sum of the compressive (negative) pertinacities.

Two Useful Results for Fans. Consider a straight member MR carrying a tensile load P, and within that member an element dl (see Fig. 2). Let the Hencky net be a fan, center O, and let N be the foot of the perpendicular from O on to MR. Let S be a general point in MR, such that NOS is the angle θ. Then if the tensile principal stress axis is circumferential, then θ is the correct angle to use in Eq. (6). Integrating Eq. (6) over the length of MR between $\theta = \alpha$ and $\theta = \beta$ gives

$$\int udl = \{2(\beta - \alpha) - (\tan \beta - \tan \alpha)\}h \tag{7}$$

where h is the distance ON.

Dividing through by the length over which the integration has been taken gives

$$\text{mean } u,\ u_m = 2(\beta - \alpha)/(\tan \beta - \tan \alpha) - 1. \tag{8}$$

Another useful result comes from Eq. (7). If it is multiplied by P, the right-hand side is the task T_r. The second term on the right-hand side is the pertinacity p. In the first term on the

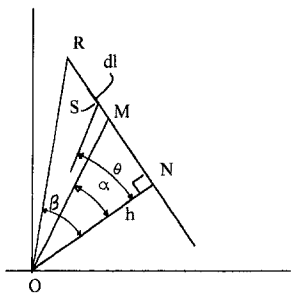


Fig. 2 Average value of u in MR

Downloaded 04 May 2010 to 171.66.16.27. Redistribution subject to ASME license or copyright; see http://www.asme.org/terms/Terms_Use.cfm

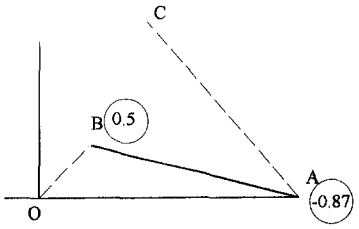


Fig. 3 Evaluating a member, example 1

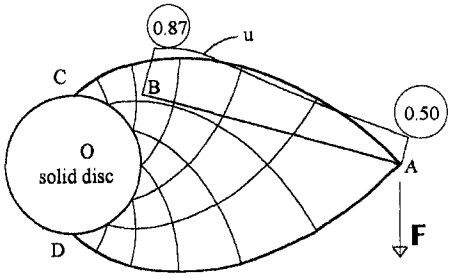


Fig. 4 Second example

right-hand side, the product Ph is the moment M of P about O, so that we can write

$$T_r = 2M(\beta - \alpha) - p. \tag{9}$$

These two results, Eqs. (8) and (9), are simple and convenient, and useful in making decisions about structural layout. They apply only to fans, but as these are commonly the case encountered they are very useful.

An interesting implication of Maxwell's lemma is that if the total tensile pertinacity can be reduced, there must be an equal decrease in the total absolute compressive pertinacity, since the difference between the two must remain unchanged. If we can reduce the amount of tensile material, we will save the same amount of compressive material. In the particular (but common) case in which the difference is zero, as in Fig. 1, summing over all members

$$T = 2 \sum M(\beta - \alpha) - \sum p, \tag{10}$$

Eqs. (7) to (10) are only applicable to fans, but the differential form of (9), that is

$$dT = 2Md\alpha - dp, \tag{11}$$

is general, where M is the moment of P about the center of curvature of the appropriate line of principal stress through the element.

Demonstration. These results depend ultimately on the summation of tasks having a unique value T for any plane frame R subject to a given loading system A, that is

$$T = \sum T_r \tag{12}$$

must be independent of R. Proof of this depends upon showing that T is equal to the value for the Michell structure. But Eq. (6) was derived so as to ensure this equality, so the result is proved. An alternative demonstration is given elsewhere (French, 1999).

4 An Example

Consider the load system of Fig. 1 in the application in Fig. 3, with the additional specification that structure is excluded from the region $y < 0$. Assume also that there is a member AB already provided for some other purpose, which carries no load when the loads F, F are acting. We ask the question, will it help to incorporate AB into the structure to carry F, F, since it is available and not doing anything?

To answer this question, we must look at the task of AB when helping to support F, F. In this case the entire field is a fan, center O (this is the result of the exclusion of structure from the region $y < 0$), and the mean value of u, u_m, can be found from Eq. (8). For the example in the figure, and assuming the appropriate direction is circumferential, i.e., P is a tension, u_m is -0.502. It follows that, far from saving material, if AB is in tension it adds to the structural task to be performed by the remainder of the structure. On the other hand, if AB is arranged to be in compression, it will contribute, since then u_m will be positive. This suggests that the other member radiating from A, necessary to triangulate A, should be in the direction AC not AO (see figure), so that AB is in compression. Nevertheless, the low absolute value of u_m for AB and the poor value of u_m for a member like AC make it doubtful whether it is worth trying to incorporate AB at all. Note that if structure were not excluded from the negative-y region, u_m for AB in tension would rise to the positive value of 0.5.

5 A Second Example

This second example has a net of equiangular spirals, to illustrate a more general case in which the center of curvature is not a fixed point. Figure 4 shows a Michell structure, in which the loading system is a force F at r_o, resisted by reactions on a circle of radius r_b, center O. The equiangular spirals make an angle of $\pi/4$ with the radial direction (so the two sets are orthogonal). The spirals AC and AD represent finite members, but those in the interior are infinitely thin and infinitely many, but with a finite total area. The directions of the principal axes in this case are along the spirals, at 45 deg to the radial, so that

$$\theta = \pi/4 + \alpha \text{ or } \pi/4 - \alpha, \tag{13}$$

according to the sign of the force in the element, yielding

$$u = \pm \sin 2\alpha. \tag{14}$$

The mean value of u is given by

$$u_m = \pm 2 \ln (\cos \alpha / \cos \beta)/(\tan \beta - \tan \alpha) \tag{15}$$

which gives $u_m = 0.766$ for P tensile.

6 Uses of the Approach

The two examples just given show one use of the approach, the assessment of the likely advantage from incorporating an existing component in a structure. The result in the first example, that it would be a positive disadvantage, is somewhat counterintuitive.

It is recommended that in such cases it is usually sufficient to examine the local values of u at the ends of members (examples are given in a forthcoming paper) to give all the insight which is necessary. These values have been inserted in circles at the ends of AB in Fig. 3 and 4, in each case for P tensile. In Fig. 4, u has also been plotted along AB to show the typical form of variation.

Once the appropriate nets have been sketched, it is a matter of minutes to check the u's at the ends and this will often show how the layout can be improved.

7 Conclusion

The idea of structural task has been introduced, and with it a new approach to structural design which has some parallels with Second Law analysis in thermodynamics. The treatment is confined to plane frames but that is sufficient to cover many practical cases. There is much room for further work, including a rigorous establishment of the existence of a unique value of structural task and possibly the extension to continua and to three dimensions. As it is, this approach has some practical use, particularly in the

Downloaded 04 May 2010 to 171.66.16.27. Redistribution subject to ASME license or copyright; see http://www.asme.org/terms/Terms_Use.cfm

problem of layout, for which the rapid and simple procedure of evaluating the utility factor u at the ends of members is recommended.

8 Note on Michell Structures

Most of the major results in the theory of these structures were developed using strain fields and virtual work (e.g., Hemp, 1973). Professor Hemp has pointed out that in these terms, u is the ratio of the strain in the field in the direction of the member to the principal strain. However, all these results can be derived by statics alone, without recourse to strain fields.

References

Cox, H. L., 1965, *The Design of Structures of Least Weight,* Pergamon Press, Oxford, UK.

French, M. J., 1994, "On the Minimum Volume of Material in Temperature-Compensating Devices," *Proc. Instn. Mech. Engrs.*, Vol. 208, pp. 139–141.

French, M. J., 1999, *Proc. Instn. Mech. Engrs. ca Dec.,* to be published.

Hemp, W. S., 1973, *Optimum Structures,* Clarendon Press, Oxford, UK.

Maxwell, J. C., 1975, *Scientific Papers II,* Cambridge University Press, Cambridge, UK.

Michell, A. G. M., 1904, "The Limit of Economy of Material in Frame Structures," *Phil. Mag.*, Vol. 8, No. 4.

Owen, J. B. B., 1965, *The Analysis and Design of Light Structures,* Arnold, London.

Downloaded 04 May 2010 to 171.66.16.27. Redistribution subject to ASME license or copyright; see http://www.asme.org/terms/Terms_Use.cfm

Dynamic Analysis of Rotating Nonuniform Timoshenko Beams With an Elastically Restrained Root

S. M. Lin
Associate Professor,
Mechanical Engineering Department,
Kung Shan Institute of Technology,
Tainan, Taiwan 710-03, R.O.C.

A systematic solution procedure for studying the dynamic response of a rotating nonuniform Timoshenko beam with an elastically restrained root is presented. The partial differential equations are transformed into the ordinary differential equations by taking the Laplace transform. The two coupled governing differential equations are uncoupled into two complete fourth-order differential equations with variable coefficients in the flexural displacement and in the angle of rotation due to bending, respectively. The general solution and the generalized Green function of the uncoupled system are derived. They are expressed in terms of the four corresponding linearly independent homogenous solutions, respectively. The shifting relations of the four homogenous solutions of the uncoupled governing differential equation with constant coefficients are revealed. The generalized Green function of an nth order ordinary differential equation can be obtained by using the proposed method. Finally, the influence of the elastic root restraints, the setting angle, and the excitation frequency on the steady response of a beam is investigated.

1 Introduction

Rotating beams, which have importance in many practical applications such as turbine blades, helicopter rotor blades, airplane propellers, and robot manipulators, has been investigated for a long time. An interesting review of the subject can be found in the papers by Leissa (1981), Ramamurti and Balasubramanian (1984), Rao (1987), and Lee and Lin (1994). Much attention has been focused on the eigenvalue problems such as the free vibration problems and the stability problems. But little research has been done on the forced vibration problem because of its complexity. And no closed-form solution of the dynamic system has been presented.

Carlson and Wong (1978) obtained an exact solution for the static bending of a rotating uniform Bernoulli-Euler beam. Rao and Carnegie (1970) and Hodges (1979) studied the steady response of a rotating cantilever nonuniform Bernoulli-Euler beam by using the Rayleigh-Ritz method. Ko (1989) studied the flexural behavior of rotating sandwich tapered beams with linearly distributed loads by using the finite difference technique. Hernried (1991) determined the lead-lag and flapping dynamic deflections of rotating twisted Bernoulli-Euler beams by using the mode superposition approach. Argento et al. (1994) examined the flapping dynamic response of a rotating uniform cantilever Rayleigh beam subjected to moving loads using the Galerkin method. No research has been devoted to the forced vibration problems of a rotating nonuniform Timoshenko beam with setting angle and an elastically restrained root.

This paper is the generalization of that given by Lee and Lin (1994). Lee and Lin studied the free vibration problem of a rotating Timoshenko beam. In this paper, the governing differential equations for the bending vibrations of a rotating nonuniform Timoshenko beam with setting angle, hub radius, tip mass, and rotating at a constant angular velocity, subjected to any transverse external forces and the end force and moment excitation at the free end, are derived by using Hamilton's principle. The effect of Coriolis force is not considered. Taking the Laplace transform, the partial differential equations become the ordinary differential equations. The two coupled transformed governing differential equations are uncoupled into two complete fourth-order ordinary differential equations with variable coefficients in the flexural displacement and in the angle of rotation due to bending, respectively. The explicit relations between the flexural displacement and the angle of rotation due to bending are established. The generalized Green function of the transformed fourth-order ordinary differential equation with a forcing function composed of the delta function and its derivatives is derived. The function is the generalization of the classical Green function of a differential equation with a forcing function composed of the delta function only (Lin, 1997). The general solution of the transformed system is derived. The general solution and the Green function are expressed in terms of the four corresponding linearly independent homogeneous solutions, respectively. If the coefficients of the uncoupled governing differential equation are constant, alternative generalized Green's function was obtained by Lin (1998). Equating the two Green functions derived by using the two different methods, the relations of the four homogenous solutions of the equation are investigated. A generalized Green's function of an nth order ordinary differential equation can be obtained by using the proposed method. Finally, the influence of the elastic root restraints, the setting angle, and the excitation frequency on the steady response of a rotating beam is investigated.

2 Nonuniform Timoshenko Beams

Consider the dynamic response of a doubly symmetric nonuniform Timoshenko beam with tip mass and elastically restrained, mounted with setting angle θ on a hub with radius R, rotating with constant angular velocity Ω, subjected to any transverse external force $P(x, t)$ and end moment $F_1(t)$ and force $F_2(t)$, as shown in Fig. 1. The displacement fields of the beam are

Contributed by the Applied Mechanics Division of THE AMERICAN SOCIETY OF MECHANICAL ENGINEERS for publication in the ASME JOURNAL OF APPLIED MECHANICS.
Discussion on the paper should be addressed to the Technical Editor, Professor Lewis T. Wheeler, Department of Mechanical Engineering, University of Houston, Houston, TX 77204-4792, and will be accepted until four months after final publication of the paper itself in the ASME JOURNAL OF APPLIED MECHANICS.
Manuscript received by the ASME Applied Mechanics Division, Sept. 12, 1997; final revision, Jan. 19, 1999. Associate Technical Editor: A. A. Ferri.

 Copyright © 1999 by ASME

Downloaded 04 May 2010 to 171.66.16.27. Redistribution subject to ASME license or copyright; see http://www.asme.org/terms/Terms_Use.cfm

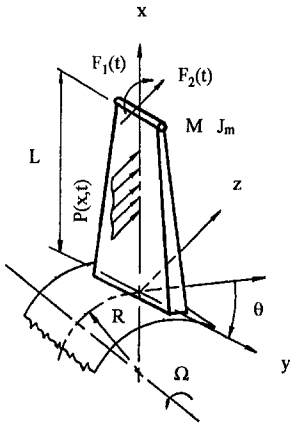


Fig. 1 Geometry and coordinate system of a rotating nonuniform Timoshenko beam with time-dependent elastic boundary conditions, subjected to transverse force

$$U(x, t) = U_0 - z\Psi(x, t), \quad V = 0, \quad W = W(x, t), \tag{1}$$

where U, V, and W denote the displacements of the beam in the x, y, and z-directions, respectively. Ψ is the angle of rotation due to bending, U_0 is the axial neutral displacement due to axial force. The velocity vector of a point (x, y, z) in the beam is given by

$$\mathbf{V} = \left[\frac{\partial U}{\partial t} + \Omega \sin\theta(z + W) - y\Omega\cos\theta\right] i + [(x + R + U)\Omega\cos\theta]j + \left[\frac{\partial W}{\partial t} - (x + R + U)\Omega\sin\theta\right]k. \tag{2}$$

The total potential energy Π and the kinetic energy T of the beam are

$$\Pi = \int_0^L \int_A (\tfrac{1}{2}\sigma_{xx}\epsilon_{xx} + \sigma_{xz}\epsilon_{xz})dAdx + \tfrac{1}{2}K_\theta\Psi^2(0, t) + \tfrac{1}{2}K_T W^2(0, t) - \int_0^L P(x, t)W(x, t)dx - F_1(t)\Psi(L, t) - F_2(t)W(L, t), \tag{3}$$

and

$$T = \frac{1}{2}\int_0^L \int_A \mathbf{V}\cdot\mathbf{V}\rho dAdx + \frac{1}{2}J_m\left(\Omega - \frac{\partial\Psi(L, t)}{\partial t}\right)^2 + \frac{1}{2}M\mathbf{V}(L, t)\cdot\mathbf{V}(L, t), \tag{4}$$

respectively, where σ_{ij} and ϵ_{ij} are stresses and strains, respectively. t is time and L is the length of the beam. $A(x)$ denotes the cross-sectional area. J_m and M are the rotatory inertia of the attached mass and the concentrated mass attached at the free end of the beam, respectively. $\rho(x)$ is the mass per unit volume of the beam. K_T and K_θ are the translational spring constant and the rotational spring constant at the root of the beam, respectively.

It is assumed that the beam is inextensional and the Coriolis forces effect is neglected. Application of Hamilton's principle yields the following governing differential equations:

$$-\frac{\partial}{\partial x}\left[N(x)\frac{\partial W}{\partial x} + \kappa(x)G(x)A(x)\left(\frac{\partial W}{\partial x} - \Psi\right)\right] + \rho(x)A(x) \times \left(\frac{\partial^2 W}{\partial t^2} - W\Omega^2\sin^2\theta\right) = P(x, t), \tag{5}$$

$$\frac{\partial}{\partial x}\left[E(x)I(x)\frac{\partial\Psi}{\partial x}\right] + \kappa(x)G(x)A(x)\left(\frac{\partial W}{\partial x} - \Psi\right) - J(x)\left(\frac{\partial^2\Psi}{\partial t^2} - \Psi\Omega^2\right) = 0, \tag{6}$$

and the associated time-dependent boundary conditions

at $x = 0$:

$$K_T W - N\frac{\partial W}{\partial x} - \kappa GA\left(\frac{\partial W}{\partial x} - \Psi\right) = 0, \tag{7}$$

$$K_\theta\Psi - EI\frac{\partial\Psi}{\partial x} = 0, \tag{8}$$

at $x = L$:

$$EI\frac{\partial\Psi}{\partial x} + J_m\frac{\partial^2\Psi}{\partial t^2} = F_1(t), \tag{9}$$

$$-M\left(\alpha^2\sin^2\theta W - \frac{\partial^2 W}{\partial t^2}\right) + N\frac{\partial W}{\partial x} + \kappa GA\left(\frac{\partial W}{\partial x} - \Psi\right) = F_2(t), \tag{10}$$

where the centrifugal force is $N(x) = \Omega^2[\int_x^L \rho(\chi)A(\chi)(R + \chi)d\chi + M(L + R)]$, $G(x)$ is the shear modulus, $E(x)$ is the Young modulus, and κ is the shear correction factor. $I(x)$ and $J(x)$ denote the area moment of inertia and the mass moment of inertia per unit length, respectively. The associated initial conditions of the motion are

$$W(x, 0) = W_0(x), \quad \Psi(x, 0) = \Psi_0(x), \quad \frac{\partial W(x, 0)}{\partial t} = \dot{W}_0(x), \quad \frac{\partial\Psi(x, 0)}{\partial t} = \dot{\Psi}_0(x), \tag{11}$$

where $W_0(x)$, $\Psi_0(x)$, $\dot{W}_0(x)$, and $\dot{\Psi}_0(x)$ are four prescribed initial functions.

In terms of the following dimensionless quantities,

$$b(\xi) = \frac{E(x)I(x)}{E(0)I(0)}, \quad f_1(\tau) = \frac{F_1(t)L}{E(0)I(0)}, \quad f_2(\tau) = \frac{F_2(t)L^2}{E(0)I(0)}, \quad m(\xi) = \frac{\rho(x)A(x)}{\rho(0)A(0)},$$

$$n(\xi) = \alpha^2\int_\xi^1 m(\chi)(r + \chi)d\chi + \delta_2\alpha^2(1 + r),$$

$$p(\xi, \tau) = \frac{P(x, t)L^3}{E(0)I(0)}, \quad g(\xi) = \frac{J(x)}{J(0)}, \quad q(\xi) = \frac{\kappa(x)G(x)A(x)}{\kappa(0)G(0)A(0)},$$

$$r = \frac{R}{L}, \quad w(\xi, \tau) = \frac{W(x, t)}{L}, \quad \alpha^2 = \frac{\rho(0)A(0)\Omega^2L^4}{E(0)I(0)},$$

$$\beta_T = \frac{K_T L^3}{E(0)I(0)}, \quad \beta_\theta = \frac{K_\theta L}{E(0)I(0)}, \quad \tau = \frac{t}{L^2}\sqrt{\frac{E(0)I(0)}{\rho(0)A(0)}},$$

$$\xi = \frac{x}{L}, \quad \eta = \frac{J(0)}{\rho(0)A(0)L^2}, \quad \mu = \frac{E(0)I(0)}{\kappa(0)G(0)A(0)L^2},$$

$$\delta_1 = \frac{J_m}{\rho(0)A(0)L^3}, \quad \delta_2 = \frac{M}{\rho(0)A(0)L}, \quad \gamma_{11} = \frac{\beta_T}{1 + \beta_T},$$

$$\gamma_{12} = \frac{1}{1 + \beta_T}, \quad \gamma_{21} = \frac{\beta_\theta}{1 + \beta_\theta}, \quad \gamma_{22} = \frac{1}{1 + \beta_\theta}, \tag{12}$$

the two coupled dimensionless governing differential equations of the system are

Downloaded 04 May 2010 to 171.66.16.27. Redistribution subject to ASME license or copyright; see http://www.asme.org/terms/Terms_Use.cfm

$$-\frac{\partial}{\partial\xi}\left[n(\xi)\frac{\partial w}{\partial\xi}+\frac{q(\xi)}{\mu}\left(\frac{\partial w}{\partial\xi}-\Psi\right)\right]+m(\xi)\left(\frac{\partial^2 w}{\partial\tau^2}-w\alpha^2\sin^2\theta\right)=p(\xi,\tau), \quad (13)$$

$$\frac{\partial}{\partial\xi}\left[b(\xi)\frac{\partial\Psi}{\partial\xi}\right]+\frac{q(\xi)}{\mu}\left(\frac{\partial w}{\partial\xi}-\Psi\right)-\eta g(\xi)\left(\frac{\partial^2\Psi}{\partial\tau^2}-\Psi\alpha^2\right)=0, \quad (14)$$

the associated time-dependent boundary conditions are

at $\xi = 0$:

$$\gamma_{11}w-\gamma_{12}n\frac{\partial w}{\partial\xi}-\gamma_{12}\frac{1}{\mu}\left(\frac{\partial w}{\partial\xi}-\Psi\right)=0, \quad (15)$$

$$\gamma_{21}\Psi-\gamma_{22}\frac{\partial\Psi}{\partial\xi}=0, \quad (16)$$

at $\xi = 1$:

$$b\frac{\partial\Psi}{\partial\xi}+\delta_1\frac{\partial^2\Psi}{\partial\tau^2}=f_1(\tau), \quad (17)$$

$$-\delta_2\left(\alpha^2\sin^2\theta w-\frac{\partial^2 w}{\partial\tau^2}\right)+n\frac{\partial w}{\partial\xi}+\frac{q}{\mu}\left(\frac{\partial w}{\partial\xi}-\Psi\right)=f_2(\tau), \quad (18)$$

and the associated dimensionless initial conditions of the motion are

$$w(\xi,0)=w_0(\xi), \quad \Psi(\xi,0)=\Psi_0(\xi),$$
$$\frac{\partial w(\xi,0)}{\partial\tau}=\dot{w}_0(\xi), \quad \frac{\partial\Psi(\xi,0)}{\partial\tau}=\dot{\Psi}_0(\xi). \quad (19)$$

Taking the Laplace transform with respect to the dimensionless time variable τ, the following coupled ordinary differential equations and boundary conditions are obtained:

$$-\frac{d}{d\xi}\left[n\frac{d\bar{w}}{d\xi}+\frac{q(\xi)}{\mu}\left(\frac{d\bar{w}}{d\xi}-\bar{\Psi}\right)\right]+m(\xi)(s^2-\alpha^2\sin^2\theta)\bar{w}=\bar{p}_1(\xi,s), \quad (20)$$

$$\frac{d}{d\xi}\left[b(\xi)\frac{d\bar{\Psi}}{d\xi}\right]+\frac{q(\xi)}{\mu}\left(\frac{d\bar{w}}{d\xi}-\bar{\Psi}\right)-\eta g(\xi)(s^2-\alpha^2)\bar{\Psi}=\bar{p}_2(\xi,s), \quad (21)$$

at $\xi = 0$:

$$\gamma_{11}\bar{w}-\gamma_{12}n\frac{d\bar{w}}{d\xi}-\gamma_{12}\frac{1}{\mu}\left(\frac{d\bar{w}}{d\xi}-\bar{\Psi}\right)=0, \quad (22)$$

$$\gamma_{21}\bar{\Psi}-\gamma_{22}\frac{d\bar{\Psi}}{d\xi}=0, \quad (23)$$

at $\xi = 1$:

$$b\frac{d\bar{\Psi}}{d\xi}+\delta_1 s^2\bar{\Psi}=\bar{f}_1(s), \quad (24)$$

$$-\delta_2(\alpha^2\sin^2\theta-s^2)\bar{w}+n\frac{d\bar{w}}{d\xi}+\frac{q}{\mu}\left(\frac{d\bar{w}}{d\xi}-\bar{\Psi}\right)=\bar{f}_2(s), \quad (25)$$

where

$$\bar{w}(\xi,s)=\int_0^\infty w(\xi,\tau)e^{-s\tau}d\tau, \quad \bar{\Psi}(\xi,s)=\int_0^\infty\Psi(\xi,\tau)e^{-s\tau}d\tau,$$

$$\bar{p}_1(\xi,s)=\int_0^\infty p(\xi,\tau)e^{-s\tau}d\tau+m(\xi)[sw_0(\xi)+\dot{w}_0(\xi)],$$

$$\bar{p}_2(\xi,s)=-\eta g(\xi)[s\Psi_0(\xi)+\dot{\Psi}_0(\xi)],$$

$$\bar{f}_1(s)=\int_0^\infty f_1(\tau)e^{-s\tau}d\tau+\delta_1[s\Psi_0(1)+\dot{\Psi}_0(1)],$$

$$\bar{f}_2(s)=\int_0^\infty f_2(\tau)e^{-s\tau}d\tau+\delta_2[sw_0(1)+\dot{w}_0(1)]. \quad (26)$$

2.1 Governing Differential Equation and Associated Boundary Conditions in Terms of the Angle of Rotation due to Bending. Equation (21) can be written as

$$\frac{d\bar{w}}{d\xi}=\frac{\mu}{q(\xi)}\left\{-\frac{d}{d\xi}\left[b(\xi)\frac{d\bar{\Psi}}{d\xi}\right]+\left[\frac{q(\xi)}{\mu}+\eta g(\xi)(s^2-\alpha^2)\right]\bar{\Psi}+\bar{p}_2(\xi,s)\right\}. \quad (27)$$

Upon substituting Eq. (27) into Eq. (20), the dimensionless flexural displacement can be explicitly expressed in terms of the angle of rotation due to bending,

$$\bar{w}(\alpha^2\sin^2\theta-s^2)=\frac{1}{m}\left\{\frac{d}{d\xi}\left\{\left(1+\frac{\mu n}{q}\right)\frac{d}{d\xi}\left(b\frac{d\bar{\Psi}}{d\xi}\right)+\left[\eta g(\alpha^2-s^2)\left(1+\frac{\mu n}{q}\right)-n\right]\bar{\Psi}\right\}-\bar{p}_1-\frac{d}{d\xi}\left[\left(1+\frac{\mu n}{q}\right)\bar{p}_2\right]\right\}. \quad (28)$$

Substituting Eq. (28) back into Eq. (21), one obtains the governing characteristic differential equation of motion, which is a fourth-order ordinary differential equation with variable coefficients, in terms of the angle of rotation due to bending,

$$q\frac{d}{d\xi}\left\{\frac{1}{m}\frac{d}{d\xi}\left\{\left(1+\frac{\mu n}{q}\right)\frac{d}{d\xi}\left(b\frac{d\bar{\Psi}}{d\xi}\right)+\left[\eta g(\alpha^2-s^2)\left(1+\frac{\mu n}{q}\right)-n\right]\bar{\Psi}\right\}\right\}+(\alpha^2\sin^2\theta-s^2)\left\{\mu\frac{d}{d\xi}\left(b\frac{d\bar{\Psi}}{d\xi}\right)+[\mu\eta g(\alpha^2-s^2)-q]\bar{\Psi}\right\}=\mu(\alpha^2\sin^2\theta-s^2)\bar{p}_2+q\frac{d}{d\xi}\left\{\frac{1}{m}\left[\bar{p}_1+\frac{d}{d\xi}\left[\left(1+\frac{\mu n}{q}\right)\bar{p}_2\right]\right]\right\}$$
$$\xi\in(0,1). \quad (29)$$

Substituting Eqs. (27) and (28) into Eqs. (22) and (25), the four boundary conditions in terms of $\bar{\Psi}$ are obtained as follows:

$$\bar{c}_{14}\frac{d^3\bar{\Psi}}{d\xi^3}+\bar{c}_{13}\frac{d^2\bar{\Psi}}{d\xi^2}+\bar{c}_{12}\frac{d\bar{\Psi}}{d\xi}+\bar{c}_{11}\bar{\Psi}|_{\xi=0}=\bar{e}_1(0), \quad (30)$$

$$\bar{c}_{24}\frac{d^3\bar{\Psi}}{d\xi^3}+\bar{c}_{23}\frac{d^2\bar{\Psi}}{d\xi^2}+\bar{c}_{22}\frac{d\bar{\Psi}}{d\xi}+\bar{c}_{21}\bar{\Psi}|_{\xi=0}=\bar{e}_2(0), \quad (31)$$

Downloaded 04 May 2010 to 171.66.16.27. Redistribution subject to ASME license or copyright; see http://www.asme.org/terms/Terms_Use.cfm

$$\bar{c}_{34}\frac{d^3\bar{\Psi}}{d\xi^3}+\bar{c}_{33}\frac{d^2\bar{\Psi}}{d\xi^2}+\bar{c}_{32}\frac{d\bar{\Psi}}{d\xi}+\bar{c}_{31}\bar{\Psi}|_{\xi=1}=\bar{e}_3(1), \quad (32)$$

$$\bar{c}_{44}\frac{d^3\bar{\Psi}}{d\xi^3}+\bar{c}_{43}\frac{d^2\bar{\Psi}}{d\xi^2}+\bar{c}_{42}\frac{d\bar{\Psi}}{d\xi}+\bar{c}_{41}\bar{\Psi}|_{\xi=1}=\bar{e}_4(1), \quad (33)$$

where

$$\bar{c}_{14}=\gamma_{11}a_2b|_{\xi=0}, \quad \bar{c}_{13}=\gamma_{11}(2a_2b'+a_2'b)+\gamma_{12}a_1a_2b|_{\xi=0},$$
$$\bar{c}_{12}=\gamma_{11}(a_2b''+a_2'b'+a_3a_2-n)+\gamma_{12}a_1a_2b'|_{\xi=0},$$
$$\bar{c}_{11}=\gamma_{11}(a_3a_2-n)'+\gamma_{12}a_1(a_3a_2-n)|_{\xi=0},$$
$$\bar{e}_1=\gamma_{11}[\bar{p}_1+(a_2\bar{p}_2)']+\gamma_{12}a_1a_2\bar{p}_2|_{\xi=0};$$
$$\bar{c}_{24}=\bar{c}_{23}=\bar{e}_2=0, \quad \bar{c}_{22}=-\gamma_{22}, \quad \bar{c}_{21}=\gamma_{21};$$
$$\bar{c}_{34}=\bar{c}_{33}=0, \quad \bar{c}_{32}=b(1), \quad \bar{c}_{31}=-\delta_1 s^2, \quad \bar{e}_3=\bar{f}_1(s);$$
$$\bar{c}_{44}=\delta_2a_2b|_{\xi=1}, \quad \bar{c}_{43}=\delta_2(a_2'b+2a_2b')+a_2bm|_{\xi=1},$$
$$\bar{c}_{42}=\delta_2(a_2b''+a_2'b'+a_3a_2-n)+ma_2b'|_{\xi=1},$$
$$\bar{c}_{41}=\delta_2(a_3a_2-n)'+m(a_3a_2-n)|_{\xi=1},$$
$$\bar{e}_4=\delta_2[\bar{p}_1+(a_2\bar{p}_2)']+m(a_2\bar{p}_2-\bar{f}_2)|_{\xi=1}; \quad (34)$$

in which $a_1=m(\alpha^2\sin^2\theta-s^2)$, $a_2=1+\mu n/q$, $a_3=\eta g(\alpha^2-s^2)$.

2.2 Governing Differential Equation and Associated Boundary Conditions in Terms of the Dimensionless Flexural Displacement. Equation (20) can be written as

$$\frac{d\bar{\Psi}}{d\xi}=\frac{1}{q}\left\{\frac{d}{d\xi}\left[(q+\mu n)\frac{d\bar{w}}{d\xi}\right]+\mu m(\alpha^2\sin^2\theta-s^2)\bar{w}-\frac{dq}{d\xi}\bar{\Psi}+\mu\bar{p}_1\right\}. \quad (35)$$

Upon substituting Eq. (35) into Eq. (21) and multiplying it by a factor μq^2, the angle of rotation due to bending is explicitly expressed in terms of the dimensionless flexural displacement

$$\bar{\Psi}=\frac{1}{\mu\zeta-q^3}\left\{\mu\left(2b\frac{dq}{d\xi}-q\frac{db}{d\xi}\right)\left[\frac{d}{d\xi}\left[(q+\mu n)\frac{d\bar{w}}{d\xi}\right]+\mu m(\alpha^2\sin^2\theta-s^2)\bar{w}\right]-\mu bq\frac{d}{d\xi}\left[\frac{d}{d\xi}\left[(q+\mu n)\frac{d\bar{w}}{d\xi}\right]+\mu m(\alpha^2\sin^2\theta-s^2)\bar{w}\right]-q^3\frac{d\bar{w}}{d\xi}+\mu^2\left(2b\frac{dq}{d\xi}-q\frac{db}{d\xi}\right)\bar{p}_1-\mu bq\frac{d\bar{p}_1}{d\xi}+\mu^2q^2\bar{p}_2\right\}, \quad (36)$$

where $\zeta=2b(dq/d\xi)^2-qd(bdq/d\xi/d\xi+\eta g(\alpha^2-s^2)q^2$.

Substituting Eq. (36) into Eq. (20), the governing characteristic differential equation can be expressed in terms of the dimensionless flexural displacement

$$\frac{d}{d\xi}\left\{n\frac{d\bar{w}}{d\xi}-\frac{q}{\mu\zeta-q^3}\left[\left(2b\frac{dq}{d\xi}-q\frac{db}{d\xi}\right)\left[\frac{d}{d\xi}\left[(q+\mu n)\frac{d\bar{w}}{d\xi}\right]+\mu m(\alpha^2\sin^2\theta-s^2)\bar{w}\right]-bq\frac{d}{d\xi}\left[\frac{d}{d\xi}\left[(q+\mu n)\frac{d\bar{w}}{d\xi}\right]+\mu m(\alpha^2\sin^2\theta-s^2)\bar{w}\right]+\frac{q}{\mu\zeta-q^3}\left[2b\left(\frac{dq}{d\xi}\right)^2-q\frac{d}{d\xi}\left(b\frac{dq}{d\xi}\right)+\eta g(\alpha^2-s^2)q^2\right]\frac{d\bar{w}}{d\xi}\right\}+m(\alpha^2\sin^2\theta-s^2)\bar{w}=\bar{p}_1-\frac{d}{d\xi}\left\{\frac{q}{\mu\zeta-q^3}\left[\mu\left(2b\frac{dq}{d\xi}-q\frac{db}{d\xi}\right)\bar{p}_1-\mu bq\frac{d\bar{p}_1}{d\xi}+q^2\bar{p}_2\right]\right\}. \quad (37)$$

Substituting Eqs. (35) and (36) into Eqs. (22)–(25), the four boundary conditions in terms of $\bar{w}$ are obtained as follows:

$$\tilde{c}_{14}\frac{d^3\bar{w}}{d\xi^3}+\tilde{c}_{13}\frac{d^2\bar{w}}{d\xi^2}+\tilde{c}_{12}\frac{d\bar{w}}{d\xi}+\tilde{c}_{11}\bar{w}|_{\xi=0}=\tilde{e}_1(0), \quad (38)$$

$$\tilde{c}_{24}\frac{d^3\bar{w}}{d\xi^3}+\tilde{c}_{23}\frac{d^2\bar{w}}{d\xi^2}+\tilde{c}_{22}\frac{d\bar{w}}{d\xi}+\tilde{c}_{21}\bar{w}|_{\xi=0}=\tilde{e}_2(0), \quad (39)$$

$$\tilde{c}_{34}\frac{d^3\bar{w}}{d\xi^3}+\tilde{c}_{33}\frac{d^2\bar{w}}{d\xi^2}+\tilde{c}_{32}\frac{d\bar{w}}{d\xi}+\tilde{c}_{31}\bar{w}|_{\xi=1}=\tilde{e}_3(1), \quad (40)$$

$$\tilde{c}_{44}\frac{d^3\bar{w}}{d\xi^3}+\tilde{c}_{43}\frac{d^2\bar{w}}{d\xi^2}+\tilde{c}_{42}\frac{d\bar{w}}{d\xi}+\tilde{c}_{41}\bar{w}|_{\xi=1}=\tilde{e}_4(1), \quad (41)$$

where the associated coefficients are listed in the Appendix.

3 Nonuniform Bernoulli-Euler Beams

For Bernoulli-Euler beams, both shear deformation and rotatory inertia are not considered. By letting $\mu=\eta g=0$ in Eqs. (29) and (37), the governing differential equation in terms of $\bar{\Psi}$ and $\bar{w}$, respectively, are obtained:

$$\frac{d}{d\xi}\left\{\frac{1}{m}\frac{d}{d\xi}\left[\frac{d}{d\xi}\left(b\frac{d\bar{\Psi}}{d\xi}\right)-n\bar{\Psi}\right]-q(\alpha^2\sin^2\theta-s^2)\bar{\Psi}\right\}-(\alpha^2\sin^2\theta-s^2)\bar{\Psi}=\frac{d}{d\xi}\left[\frac{1}{m}\left(\bar{p}_1+\frac{d\bar{p}_2}{d\xi}\right)\right], \quad \xi\in(0,1) \quad (42)$$

and

$$\frac{d^2}{d\xi^2}\left(b\frac{d^2\bar{w}}{d\xi^2}\right)-\frac{d}{d\xi}\left(n\frac{d\bar{w}}{d\xi}\right)-m(\alpha^2\sin^2\theta-s^2)\bar{w}=-\left(\bar{p}_1+\frac{d\bar{p}_2}{d\xi}\right), \quad (43)$$

respectively. By letting $\mu=\eta g=0$ in Eqs. (30)–(33) and (38)–(41), the associated boundary conditions in terms of $\bar{\Psi}$ and $\bar{w}$, respectively, are obtained.

4 Solution Method

In the previous sections the uncoupled governing differential equations and the associated boundary conditions for the Timoshenko and Bernoulli-Euler beams were derived in the form of a fourth-order differential equation and four nonhomogeneous third-order differential equations.

Upon expanding the governing differential equation and the associated boundary conditions for the Timoshenko and Bernoulli-Euler beams, they will take the following forms:

$$c_4(\xi)\frac{d^4V}{d\xi^4}+c_3(\xi)\frac{d^3V}{d\xi^3}+c_2(\xi)\frac{d^2V}{d\xi^2}+c_1(\xi)\frac{dV}{d\xi}+c_0(\xi)V=\sum_{i=0}^{3}\frac{d^ie_i(\xi)}{d\xi^i}, \quad \xi\in(0,1) \quad (44)$$

at $\xi=0$:

$$a_{14}V'''+a_{13}V''+a_{12}V'+a_{11}V=e_1^*, \quad (45)$$

$$a_{24}V'''+a_{23}V''+a_{22}V'+a_{21}V=e_2^*, \quad (46)$$

Downloaded 04 May 2010 to 171.66.16.27. Redistribution subject to ASME license or copyright; see http://www.asme.org/terms/Terms_Use.cfm

at $\xi = 1$:

$$a_{34}V''' + a_{33}V'' + a_{32}V' + a_{31}V = e_3^*, \tag{47}$$

$$a_{44}V''' + a_{43}V'' + a_{42}V' + a_{41}V = e_4^*, \tag{48}$$

where the leading coefficient c_4 does not vanish anywhere on the closure domain.

The general solution $V(\xi)$ which may be the transformed flexural displacement $\bar{w}$ or the transformed angle of rotation due to bending $\bar{\Psi}$, can be written as

$$V(\xi) = V_p(\xi) + \sum_{i=1}^{4} D_i V_i(\xi), \tag{49}$$

where $V_p(\xi)$ is the particular solution. $\{D_i\}$ are the constants to be determined. $\{V_i(\xi)\}$ are the four linearly independent homogeneous solutions of Eq. (44), which satisfy the following normalized condition:

$$\begin{bmatrix} V_1(0) & V_2(0) & V_3(0) & V_4(0) \\ V_1'(0) & V_2'(0) & V_3'(0) & V_4'(0) \\ V_1''(0) & V_2''(0) & V_3''(0) & V_4''(0) \\ V_1'''(0) & V_2'''(0) & V_3'''(0) & V_4'''(0) \end{bmatrix} = \begin{bmatrix} 1 & 0 & 0 & 0 \\ 0 & 1 & 0 & 0 \\ 0 & 0 & 1 & 0 \\ 0 & 0 & 0 & 1 \end{bmatrix}, \tag{50}$$

and can be obtained by using the method given by Lee and Lin (1994). The particular solution $V_p(\xi)$ of Eq. (44) can be written as

$$V_p(\xi) = \sum_{i=0}^{3} \int_0^1 e_i(\zeta) E_i(\xi, \zeta) d\zeta, \tag{51a}$$

where $\{E_i(\xi, \zeta)\}$ are the Green functions of the following equations, respectively,

$$c_4(\xi)\frac{d^4E_i}{d\xi^4} + c_3(\xi)\frac{d^3E_i}{d\xi^3} + c_2(\xi)\frac{d^2E_i}{d\xi^2} + c_1(\xi)\frac{dE_i}{d\xi} + c_0(\xi)E_i = \frac{d^i\delta(\xi - \zeta)}{d\xi^i}, \quad i = 0, 1, 2, 3, \tag{51b}$$

in which δ is the Dirac delta function.

Let the Green functions $\{E_i(\xi, \zeta)\}$ be

$$E_i(\xi, \zeta) = G_i(\xi, \zeta)H(\xi - \zeta), \quad i = 0, 1, 2, 3 \tag{52a}$$

where

$$G_i(\xi, \zeta) = \sum_{j=1}^{4} b_{ij}(\zeta) V_j(\xi), \tag{52b}$$

and $H(\xi - \zeta)$ is the Heaviside function. Substituting Eqs. (52) into Eq. (51b), the following equation is obtained:

$$c_4(\xi)\frac{d^4E_i}{d\xi^4} + c_3(\xi)\frac{d^3E_i}{d\xi^3} + c_2(\xi)\frac{d^2E_i}{d\xi^2} + c_1(\xi)\frac{dE_i}{d\xi} + c_0(\xi)E_i = \alpha_0\delta(\xi - \zeta) + \alpha_1\frac{d\delta(\xi - \zeta)}{d\xi} + \alpha_2\frac{d^2\delta(\xi - \zeta)}{d\xi^2} + \alpha_3\frac{d^3\delta(\xi - \zeta)}{d\xi^3}, \tag{53a}$$

where

$$\alpha_0 = c_4(\zeta)G'''(\zeta, \zeta) + [c_3(\zeta) - c_4'(\zeta)]G''(\zeta, \zeta) + [c_4''(\zeta) - c_3'(\zeta) + c_2(\zeta)]G'(\zeta, \zeta) + [-c_4'''(\zeta) + c_3''(\zeta) - c_2'(\zeta) + c_1(\zeta)]G(\zeta, \zeta),$$

$$\alpha_1 = c_4(\zeta)G''(\zeta, \zeta) + [c_3(\zeta) - 2c_4'(\zeta)]G'(\zeta, \zeta) + [3c_4''(\zeta) - 2c_3'(\zeta) + c_2(\zeta)]G(\zeta, \zeta),$$

$$\alpha_2 = c_4(\zeta)G'(\zeta, \zeta) + [c_3(\zeta) - 3c_4'(\zeta)]G(\zeta, \zeta),$$

$$\alpha_3 = c_4(\zeta)G(\zeta, \zeta). \tag{53b}$$

Letting $\alpha_0 = 1$, and $\alpha_1 = \alpha_2 = \alpha_3 = 0$, the fundamental solution E_0 is obtained. Its coefficients are

$$\begin{bmatrix} b_{01}(\zeta) \\ b_{02}(\zeta) \\ b_{03}(\zeta) \\ b_{04}(\zeta) \end{bmatrix} = [T]\begin{bmatrix} 0 \\ 0 \\ 0 \\ 1/c_4(\zeta) \end{bmatrix}, \tag{54a}$$

where

$$[T] = \begin{bmatrix} V_1(\zeta) & V_2(\zeta) & V_3(\zeta) & V_4(\zeta) \\ V_1'(\zeta) & V_2'(\zeta) & V_3'(\zeta) & V_4'(\zeta) \\ V_1''(\zeta) & V_2''(\zeta) & V_3''(\zeta) & V_4''(\zeta) \\ V_1'''(\zeta) & V_2'''(\zeta) & V_3'''(\zeta) & V_4'''(\zeta) \end{bmatrix}^{-1}. \tag{54b}$$

Letting $\alpha_1 = 1$, and $\alpha_0 = \alpha_2 = \alpha_3 = 0$, the fundamental solution E_1 is obtained. Its coefficients are

$$\begin{bmatrix} b_{11}(\zeta) \\ b_{12}(\zeta) \\ b_{13}(\zeta) \\ b_{14}(\zeta) \end{bmatrix} = [T]\begin{bmatrix} 0 \\ 0 \\ 1/c_4(\zeta) \\ [c_4'(\zeta) - c_3(\zeta)]/c_4^2(\zeta) \end{bmatrix}. \tag{55}$$

Letting $\alpha_2 = 1$, and $\alpha_0 = \alpha_1 = \alpha_3 = 0$, the fundamental solution E_2 is obtained. Its coefficients are

$$\begin{bmatrix} b_{21}(\zeta) \\ b_{22}(\zeta) \\ b_{23}(\zeta) \\ b_{24}(\zeta) \end{bmatrix} = [T]\begin{bmatrix} 0 \\ \dfrac{1}{c_4(\zeta)} \\ \dfrac{2c_4'(\zeta) - c_3(\zeta)}{c_4^2(\zeta)} \\ \dfrac{1}{c_4^2(\zeta)}\left\{\dfrac{2(c_4'(\zeta))^2 - 3c_4'(\zeta)c_3(\zeta) + c_3^2(\zeta)}{c_4(\zeta)} - c_4''(\zeta) + c_3'(\zeta) - c_2(\zeta)\right\} \end{bmatrix}. \tag{56}$$

Letting $\alpha_3 = 1$, and $\alpha_0 = \alpha_1 = \alpha_2 = 0$, the fundamental solution E_3 is obtained. Its coefficients are

$$\begin{bmatrix} b_{31}(\zeta) \\ b_{32}(\zeta) \\ b_{33}(\zeta) \\ b_{34}(\zeta) \end{bmatrix} = [T]\begin{bmatrix} 1 \\ \dfrac{1}{c_4(\zeta)} \\ q_1 \\ q_2 \\ q_3 \end{bmatrix}, \tag{57a}$$

Downloaded 04 May 2010 to 171.66.16.27. Redistribution subject to ASME license or copyright; see http://www.asme.org/terms/Terms_Use.cfm

Table 1 Verification of the shifting relation of the homogeneous solutions (64). ($\bar{w} = V_j(\xi - 0.2)$, $\hat{w}_j = \sum_{i=1}^{4} T_{ij}(0.2)V_i(\xi)$.)

	ξ					
	0.0	0.2	0.4	0.6	0.8	1.0
$\bar{w}_1(\xi)$	1.00007	1.00000	1.00007	1.00107	1.00547	1.01744
$\hat{w}_1(\xi)$	1.00007	1.00000	1.00007	1.00107	1.00547	1.01744
$\bar{w}_2(\xi)$	−0.20000	0.00000	0.20000	0.40009	0.60065	0.80277
$\hat{w}_2(\xi)$	−0.20000	0.00000	0.20000	0.40009	0.60065	0.80277
$\bar{w}_3(\xi)$	0.02007	0.00000	0.02007	0.08108	0.18553	0.33781
$\hat{w}_3(\xi)$	0.02007	0.00000	0.02007	0.08108	0.18553	0.33781
$\bar{w}_4(\xi)$	−0.00134	0.00000	0.00134	0.01075	0.03666	0.08815
$\hat{w}_4(\xi)$	−0.00134	0.00000	0.00134	0.01075	0.03666	0.08815

where

$$q_1 = \frac{3c_4'(\zeta) - c_3(\zeta)}{c_4^2(\zeta)},$$

$$q_2 = \frac{1}{c_4^2(\zeta)}\left\{\frac{6(c_4'(\zeta))^2 - 5c_4'(\zeta)c_3(\zeta) + c_3^2(\zeta)}{c_4(\zeta)} - 3c_4''(\zeta) + 2c_3'(\zeta) - c_2(\zeta)\right\}$$

$$q_3 = \frac{-1}{c_4(\zeta)}\left\{[c_3(\zeta) - c_4'(\zeta)]q_1 + [c_4''(\zeta) - c_3'(\zeta) - c_2(\zeta)]q_2 - [c_4'''(\zeta) - c_3''(\zeta) + c_2'(\zeta) - c_1(\zeta)]\frac{1}{c_4(\zeta)}\right\}. \quad (57b)$$

Substituting Eqs. (51)–(57) into Eq. (49), the general solution of the general system is obtained as follows:

$$V(\xi) = \sum_{i=1}^{4}\left\{D_i + \sum_{j=0}^{3}\int_0^{\xi} b_{ji}(\zeta)f_j(\zeta)d\zeta\right\}V_i(\xi). \quad (58)$$

After substituting the general solution (58) into the boundary conditions (45)–(48), the constants D_1, D_2, D_3, and D_4 are obtained:

$$\begin{bmatrix} D_1 \\ D_2 \\ D_3 \\ D_4 \end{bmatrix} = \begin{bmatrix} a_{11} & a_{12} & a_{13} & a_{14} \\ a_{21} & a_{22} & a_{23} & a_{24} \\ \bar{a}_{31} & \bar{a}_{32} & \bar{a}_{33} & \bar{a}_{34} \\ \bar{a}_{41} & \bar{a}_{42} & \bar{a}_{43} & \bar{a}_{44} \end{bmatrix}^{-1}\begin{bmatrix} e_1^* \\ e_2^* \\ \bar{e}_3^* \\ \bar{e}_4^* \end{bmatrix}, \quad (59a)$$

where

$$\bar{a}_{3i} = \sum_{j=1}^{4} a_{3j}V_i^{(j-1)}(1), \quad \bar{a}_{4i} = \sum_{j=1}^{4} a_{4j}V_i^{(j-1)}(1),$$

$$\bar{e}_3^* = e_3^* - \sum_{j=1}^{4} a_{3j}V_p^{(j-1)}(1),$$

$$\bar{e}_4^* = e_4^* - \sum_{j=1}^{4} a_{4j}V_p^{(j-1)}(1). \quad (59b)$$

After taking the inverse Laplace transform, the dynamic response of the system will be given as

$$v(\xi, \tau) = \frac{1}{2\pi i}\int_{c-i\infty}^{c+i\infty} V(\xi, s)e^{s\tau}ds, \quad (60)$$

where $v(\xi, \tau)$ may be the flexural displacement $w(\xi, \tau)$ or the angle of rotation due to bending $\Psi(\xi, \tau)$.

If the excitation forces and moment are sinusoidal in time, i.e., $p(\xi, \tau) = p^*(\xi)\sin\omega\tau$, $f_1(\tau) = f_1^*\sin\omega\tau$ and $f_2(\tau) = f_2^*\sin\omega\tau$, respectively, where ω is the force excitation frequency, then it is not necessary to use the Laplace transform and the inverse Laplace transform. One can assume that $w(\xi, \tau) = w^*(\xi)\sin\omega\tau$ and $\Psi(\xi, \tau) = \Psi^*(\xi)\sin\omega\tau$. Then the variable $V(\xi)$ may represent the amplitudes $w^*(\xi)$ or $\Psi^*(\xi)$. Replacing the Laplace transform parameter s^2 by $-\omega^2$ where ω is the excitation frequency, the amplitudes $w^*(\xi)$ and $\Psi^*(\xi)$ can be obtained readily. Moreover, for the free vibration problems, the frequency equation of the beams can be obtained by first replacing the Laplace transform parameter s^2 by $-\omega^2$, where ω is the angular natural frequency, then letting the determinant of the square matrix term $[a_{ij}]$ of Eq. (59*a*) equal to zero.

It should be noted that if the geometric and the material properties of the beam can be expressed in polynomial forms, then the exact solutions of the system can be obtained by utilizing the proposed method and the method (Lee and Lin, 1994) to determine the homogeneous solutions. Moreover, the generalized Green function of an nth order differential equation can be derived by using the proposed method. The results can be applied to any boundary value or initial value problem in the mathematical form.

Table 2 The amplitudes of the steady response of Timoshenko beam subjected to harmonic excitations. ($r = 0.1$; $\theta = 45$ deg, $\eta = 0.01$, $\mu = 0.0312$, $b = g = (1 - 0.1\xi)^3$, $m = q = (1 - 0.1\xi)$, $\delta_1 = \delta_2 = 0$, $p_1 = \delta(\xi - 0.5)\sin\omega\tau$.)

α		ξ	0.1	0.2	0.4	0.6	0.8	1.0
1	$w(\xi)$	*	0.01857	0.05316	0.15956	0.29355	0.43668	0.58056
		**	0.01857	0.05316	0.15956	0.29355	0.43668	0.58056
	$\Psi(\xi)$	*	0.17549	0.32478	0.54178	0.65329	0.69997	0.70832
		**	0.17549	0.32478	0.54178	0.65329	0.69997	0.70832
5	$w(\xi)$	*	0.00488	0.01163	0.02872	0.04511	0.05884	0.07274
		**	0.00488	0.01163	0.02872	0.04511	0.05884	0.07274
	$\Psi(\xi)$	*	0.03042	0.05206	0.07392	0.07246	0.07061	0.07055
		**	0.03042	0.05206	0.07392	0.07246	0.07061	0.07055

* in terms of the flexural displacement
** in terms of the angle of rotation due to bending

Downloaded 04 May 2010 to 171.66.16.27. Redistribution subject to ASME license or copyright; see http://www.asme.org/terms/Terms_Use.cfm

5 Verification and Examples

To verify the previous analysis and investigate the properties of the four homogeneous solutions of Eq. (44) and the influence of the setting angle and the spring constants and the rotating speed on the dynamic response several results are presented and discussed.

Example 1: If the coefficients of the governing differential Eq. (44) are constant, the general solution can be obtained by taking the proper limiting procedure. In addition, the alternative method given by Lin (1998) can also be taken to solve the limiting problem. The relation of the two sets of the Green functions derived by two different methods is examined as follows:

The set of the Green functions of Eq. (52) with constant coefficients are

$$E_0 = \frac{1}{c_4} V_4(\xi - \zeta) H(\xi - \zeta),$$

$$E_1 = \left[\frac{1}{c_4} V_3(\xi - \zeta) - \frac{c_3}{c_4^2} V_4(\xi - \zeta)\right] H(\xi - \zeta),$$

$$E_2 = \left[\frac{1}{c_4} V_2(\xi - \zeta) - \frac{c_3}{c_4^2} V_3(\xi - \zeta) + \frac{c_3^2 - c_2 c_4}{c_4^3} V_4(\xi - \zeta)\right] H(\xi - \zeta),$$

$$E_3 = \left[\frac{1}{c_4} V_1(\xi - \zeta) - \frac{c_3}{c_4^2} V_2(\xi - \zeta) + \frac{c_3^2 - c_2 c_4}{c_4^3} V_3(\xi - \zeta) - \frac{c_3^3 + c_1 c_4^2}{c_4^4} V_4(\xi - \zeta)\right] H(\xi - \zeta). \quad (61)$$

Equating Eqs. (52) with (61), the following shifting relation is obtained:

$$V_j(\xi - \zeta) = \sum_{i=1}^{4} T_{ij}(\zeta) V_i(\xi), \quad j = 1, 2, 3, 4 \qquad (62)$$

where T_{ij} are the element of matrix (54*b*).

Example 2: Consider the Laplace transformed dimensionless equation of a nonrotating uniform beam employing either Timoshenko or Bernoulli-Euler theory. Letting $n = \bar{p}_2 = 0$ and $\bar{p}_1 = \delta(\xi - \xi_0)$, the governing differential Eq. (43) in the flexural displacement can be written as follows:

$$\frac{d^4V}{d\xi^4} - \lambda \frac{d^2V}{d\xi^2} - \delta^4 V = k_1 \delta(\xi - \xi_0) + k_2 \frac{d^2\delta(\xi - \xi_0)}{d\xi^2}. \quad (63)$$

The four linearly independent normalized homogeneous solutions of Eq. (63) are

$$V_1(\xi) = \frac{1}{\lambda_1^2 + \lambda_2^2}[\lambda_2^2 \cosh \lambda_1 \xi + \lambda_1^2 \cos \lambda_2 \xi],$$

$$V_2(\xi) = \frac{1}{\lambda_1^2 + \lambda_2^2}\left[\frac{\lambda_2^2}{\lambda_1} \sinh \lambda_1 \xi + \frac{\lambda_1^2}{\lambda_2} \sin \lambda_2 \xi\right],$$

$$V_3(\xi) = \frac{1}{\lambda_1^2 + \lambda_2^2}[\cosh \lambda_1 \xi - \cos \lambda_2 \xi],$$

$$V_4(\xi) = \frac{1}{\lambda_1^2 + \lambda_2^2}\left[\frac{1}{\lambda_1} \sinh \lambda_1 \xi - \frac{1}{\lambda_2} \sin \lambda_2 \xi\right], \quad (64a)$$

where

$$\lambda_1 = \sqrt{\frac{\lambda + \sqrt{\lambda^2 + 4\delta^4}}{2}}, \quad \lambda_2 = \sqrt{\frac{-\lambda + \sqrt{\lambda^2 + 4\delta^4}}{2}}. \quad (64b)$$

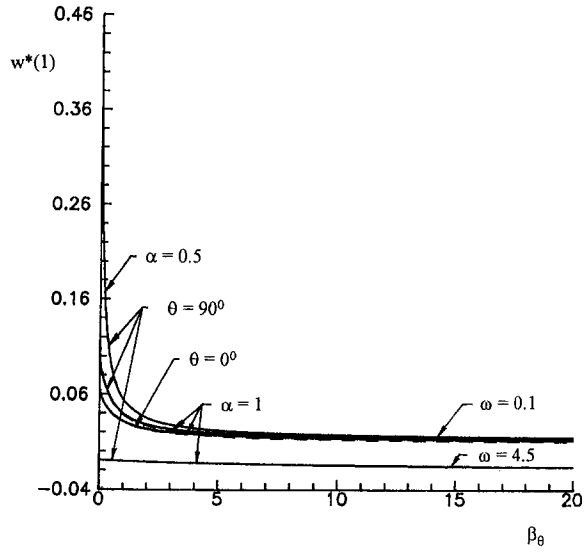


Fig. 2(*a*) The influence of the dimensionless rotational spring constant on the steady response of beams subjected to a harmonic transverse force excitation. [$b = g = (1 - 0.1\xi)^3$, $m = q = (1 - 0.1\xi)$, $f_1 = f_2 = \delta_1 = \delta_2 = 0$, $r = 1$, $\beta_T \to \infty$, $p_1 = 0.1\delta(\xi - 0.5) \sin \omega\tau$; —: $\eta = 0.01$, $\mu = 0.0312$; – – –: $\eta = \mu = 0$].

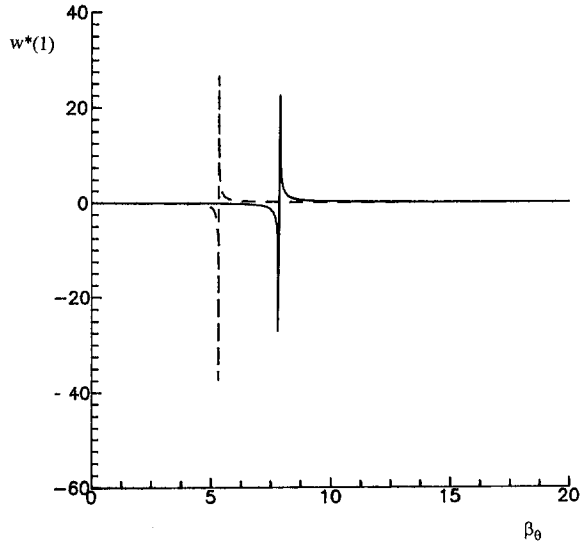


Fig. 2(*b*) The influence of the dimensionless rotational spring constant on the steady response of a Timoshenko beam subjected to a harmonic transverse force excitation. [$b = g = (1 - 0.1\xi)^3$, $m = q = (1 - 0.1\xi)$, $f_1 = f_2 = \delta_1 = \delta_2 = 0$, $r = 1$, $\beta_T \to \infty$, $p_1 = 0.1\delta(\xi - 0.5) \sin 3\tau$; $\eta = 0.01$, $\mu = 0.0312$; —: $\theta = 90$ deg; – – –: $\theta = 0$ deg]

The general solution is obtained as follows:

$$V(\xi) = \sum_{i=1}^{4} D_i V_i(\xi) + \frac{1}{\lambda_1^2 + \lambda_2^2}\left[\frac{k_1 + \lambda_1^2 k_2}{\lambda_1} \sinh \lambda_1(\xi - \xi_0) - \frac{k_1 - \lambda_2^2 k_2}{\lambda_2} \sin \lambda_2(\xi - \xi_0)\right] H(\xi - \xi_0). \quad (65)$$

It should be noted that the general solution is the same as that given by (Lueschen et al., 1996). The shifting relations of the four homogeneous functions (64) are verified and listed in Table 1.

Example 3: Consider the vibration of a rotating Timoshenko beam with constant width and linear varied depth, subjected to a harmonic transverse concentrated force at the middle of beam. The

Downloaded 04 May 2010 to 171.66.16.27. Redistribution subject to ASME license or copyright; see http://www.asme.org/terms/Terms_Use.cfm

dimensionless material properties and applied transverse force are given as

$$b(\xi) = g(\xi) = (1 + \lambda\xi)^3, \quad m(\xi) = q(\xi) = 1 + \lambda\xi,$$
$$p(\xi, \tau) = \gamma_0 \sin(\omega\tau)\delta(\xi - 0.5). \tag{66}$$

The steady-state solutions can be assumed to take the form

$$w(\xi, \tau) = w^*(\xi) \sin(\omega\tau),$$
$$\Psi(\xi, \tau) = \Psi^*(\xi) \sin(\omega\tau). \tag{67}$$

It is shown in Table 2 that the amplitudes $w^*(\xi)$ and $\Psi^*(\xi)$ of the cantilever Timoshenko beams determined by employing the general solutions in the angle of rotation due to bending are the same as those determined by employing the general solutions in the dimensionless flexural displacement.

Figure 2(*a*) shows the influence of the rotational spring constant β_θ on the steady response of beams with infinite translational spring constant, subjected to a harmonic transverse force. First, let the excitation frequency be 0.1 which is smaller than the first natural frequency of the beam with no restraint against the rotation at the root, i.e., $\beta_\theta = 0$. When $\beta_\theta = 0$, the response is large. Moreover, the smaller the rotating speed, the larger the response. It is because the centrifugal force increases the stiffness of the beam. When β_θ increases from zero, the steady response decreases rapidly. When β_θ increases greater than a critical value of almost 5, the response approaches a constant. The greater the setting angle, the greater the response. There is no difference between the response of the Timoshenko beam and that of the Bernoulli-Euler beam. Second, let the excitation frequency be 4.5 which is between the first natural frequency of the beam with infinite restraint against the rotation and the second natural frequency of the beam with no restraint against the rotation. When $\beta_\theta = 0$, the corresponding response is not as large as that of the first case. Finally, let the first natural frequency of beam with no restraint against the rotation be smaller than the excitation frequency. It is shown in Fig. 2(*b*) that when the rotational spring constant increases, the first natural frequency increases and will be greater than the excitation frequency. If the frequency approaches the excitation frequency, the response increases rapidly and becomes infinite as the natural frequency coincide with the excitation frequency.

6 Conclusion

A systematic solution procedure for studying the dynamic response of a rotating nonuniform Timoshenko beam with an elastically restrained root is proposed. The general solutions and the generalized Green functions of the uncoupled systems are obtained. The shifting relation of the four homogeneous solutions of fourth-order ordinary differential governing equation with constant coefficients is revealed. If the geometric and the material properties of the beam can be expressed in polynomial forms, then the exact steady solutions of the system can be obtained. The generalized Green function of an nth order differential equation can be derived by using the proposed method. For a rotating beam hinged at the root the influence of the excitation frequency smaller than the first natural frequency on the response is significantly greater than that of the excitation frequency larger than the first natural frequency.

References

Argento, A., Morano, H. L., and Scott, R. A., 1994, "Accelerating Load on a Rotating Rayleigh Beam," ASME *Journal of Vibration and Acoustics,* Vol. 116, pp. 397–403.

Carlson, R. M., and Wong, J. T., 1978, "An Exact Solution for the Static Bending of Uniform Rotating Beams," *Journal of the American Helicopter Society,* Vol. 23, No. 4, pp. 36–38.

Hernried, A. G., 1991, "Forced Vibration response of a Twisted Nonuniform Rotating Blade," *Computers & Structures,* Vol. 41, No. 2, pp. 207–212.

Hodges, D. H., 1979, "Vibration and Response of Nonuniform Rotating Beans with Discontinuities," *Journal of the American Helicopter Society,* Vol. 24, pp. 43–50.

Huang, W. H., 1981, "Free and Forced Vibrations of Closely Turbomachinery Blades," *AIAA Journal,* Vol. 19, No. 7, pp. 918–924.

Ko, C. L., 1989, "Flexural Behavior of a Rotating Sandwich Tapered Beam," *AIAA Journal,* Vol. 27, No. 3, pp. 359–369.

Lee, S. Y., and Lin, S. M., 1994, "Bending Vibrations of Rotating Nonuniform Timoshenko Beam With an Elastically Restrained Root," ASME JOURNAL OF APPLIED MECHANICS, Vol. 61, pp. 949–955.

Leissa, A., 1981, "Vibrational Aspects of Rotating Turbomachinery Blades," ASME *Applied Mechanics Reviews,* Vol. 34, pp. 629–635.

Lin, S. M., 1997, "Exact Solutions for the Analysis of a Non-Conservative Beam System with Nonhomogeneous Elastic Boundary Conditions," *Journal of Sound and Vibration,* Vol. 206, No. 3, pp. 425–434.

Lin, S. M., 1998, "Exact Solutions for Extensible Circular Curved Timoshenko Beams with Nonhomogeneous Elastic Boundary Conditions," *Acta Mechanica,* Vol. 130, pp. 67–79.

Lueschen, G. G. G., and Bergman, L. A., 1996, "Green's Functions for Uniform Timoshenko Beams," *Journal of Sound and Vibration,* Vol. 194, No. 1, pp. 93–102.

Ramamurti, V., and Balasubramanian, P., 1984, "Analysis of Turbomachine Blades: A Review," *The Shock and Vibration Digest,* Vol. 16, pp. 13–28.

Rao, J. S., 1987, "Turbomachine Blade Vibration," *The Shock and Vibration Digest,* Vol. 19, No. 5, pp. 3–10.

Rao, J. S., and Carnegie, W., 1970, "Non-Linear Vibration of Rotating Cantilever Beams," *The Aeronautical Journal of the Royal Aeronautical Society,* Vol. 74, pp. 161–165.

APPENDIX

The coefficients of Eqs. (38)–(41) are as follows:

$$\tilde{c}_{14} = \gamma_{12}B_4|_{\xi=0}, \quad \tilde{c}_{13} = \gamma_{12}B_3|_{\xi=0},$$

$$\tilde{c}_{12} = \gamma_{12}[B_2 - \zeta - n(\mu\zeta - q^3)]|_{\xi=0},$$

$$\tilde{c}_{11} = \gamma_{11}(\mu\zeta - q^3) + \gamma_{12}B_1|_{\xi=0}, \quad \tilde{e}_1 = -\gamma_{12}B_0|_{\xi=0};$$

$$\tilde{c}_{24} = \mu(\gamma_{21} + \gamma_{22}q')B_4|_{\xi=0},$$

$$\tilde{c}_{23} = \mu(\gamma_{21} + \gamma_{22}q')B_3 - \gamma_{22}(1 + \mu n)(\mu\zeta - q^3)|_{\xi=0},$$

$$\tilde{c}_{22} = (\gamma_{21} + \gamma_{22}q')(\mu B_2 - q^3) - \gamma_{22}(q' + \mu n')(\mu\zeta - q^3)|_{\xi=0},$$

$$\tilde{c}_{21} = (\gamma_{21} + \gamma_{22}q')\mu B_1 - \gamma_{22}\mu(\alpha^2 \sin^2\theta - s^2)(\mu\zeta - q^3)|_{\xi=0}$$

$$\tilde{e}_2 = \mu\gamma_{22}\bar{p}_1(\mu\zeta - q^3) - \mu(\gamma_{21} + \gamma_{22}q')B_0|_{\xi=0};$$

$$\tilde{c}_{34} = -\mu(bq' - \delta_1 qs^2)B_4|_{\xi=1},$$

$$\tilde{c}_{33} = -\mu(bq' - \delta_1 qs^2)B_3 + b(q + \mu n)(\mu\zeta - q^3)|_{\xi=1},$$

$$\tilde{c}_{32} = -(bq' - \delta_1 qs^2)(\mu B_2 - q^3) + b(q' + \mu n')(\mu\zeta - q^3)|_{\xi=1},$$

$$\tilde{c}_{31} = -\mu(bq' - \delta_1 qs^2)B_1 + \mu bm(\alpha^2 \sin^2\theta - s^2)(\mu\zeta - q^3)|_{\xi=1},$$

$$\tilde{e}_3 = (q\bar{f}_1 - \mu b\bar{p}_1)(\mu\zeta - q^3) + \mu(bq' - \delta_1 qs^2)B_0;$$

$$\tilde{c}_{44} = -qB_4|_{\xi=1}, \quad \tilde{c}_{43} = -qB_3|_{\xi=1},$$

$$\tilde{c}_{42} = n(\mu\zeta - q^3) + q\zeta - qB_2|_{\xi=1},$$

$$\tilde{c}_{41} = qB_1 - \mu\delta_2(\alpha^2 \sin^2\theta - s^2)(\mu\zeta - q^3)|_{\xi=1},$$

$$\tilde{e}_4 = \bar{f}_2(\mu\zeta - q^3) + qB_0|_{\xi=1},$$

where

$$B_0(\xi) = \mu(2bq' - qb')\bar{p}_1 - \mu bq\bar{p}_1' + q^2\bar{p}_2,$$

$$B_1(\xi) = \mu(\alpha^2 \sin^2\theta - s^2)(2bmq' - b'mq - bm'q),$$

$$B_2(\xi) = (2bq' - b'q)(q' + \mu n') - bq(q'' + \mu n'') - \mu bmq(\alpha^2 \sin^2\theta - s^2),$$

$$B_3(\xi) = \mu(2bnq' - 2bqn' - b'qn) - b'q^2,$$

$$B_4(\xi) = -bq(q + \mu n).$$

Downloaded 04 May 2010 to 171.66.16.27. Redistribution subject to ASME license or copyright; see http://www.asme.org/terms/Terms_Use.cfm

L. You
College of Mechanical Engineering,
Chongqing University,
400044, Chongqing, China

S. Long
College of Mechanical Engineering,
Chongqing University,
400044 Chongqing, China and
Swiss Federal Laboratories for
Materials Testing and Research,
Thun CH-3602,
Switzerland

L. Rohr
Swiss Federal Laboratories for
Materials Testing and Research,
Thun CH-3602, Switzerland

Elastic-Plastic Stress Field in a Coated Continuous Fibrous Composite Subjected to Thermomechanical Loading

A micromechanics investigation was performed in the present work to analyze the stress field in a coated continuous fibrous composite subjected to thermal and mechanical loading based on a four-concentric-cylinders model. A temperature-independent stress-plastic strain relationship for the metallic matrix and coating layer with linear strain-hardening behaviour were introduced. Tresca's yield criterion and the associated flow law were employed to derive the governing equation of the coating and matrix. The closed-form solution of the governing equation was obtained. Some numerical examples were given. The numerical results indicate that the plasticity of the coating greatly decreases the circumferential and axial stresses in the coating itself, but has very limited influence on the stresses in other constituents of the composite. The plasticity of the matrix imposes no significant influence on all the stresses in the composite.

Introduction

Large temperature changes superimposed with external stress loading often occur in the fabrication processing and service exposure of composite structures. Modeling of a coated fiber composite subjected to thermomechanical loading is an important issue due to the demand of their processing and the potential commercial applications.

Using a geometrical model consisting of four concentric cylinders, the elastic stress field in a coated continuous fiber composite under thermomechanical loading was analyzed by Mikata and Taya (1985a). An elastic solution has been derived by Avery and Herakovich for a composite consisting of an orthotropic fiber embedded in an isotropic matrix subjected to a uniform thermal loading (Avery and Herakovich, 1986). Then, Mikata et al. employed both two and four-concentric-cylinder elastic models to calculate the thermal residual stresses during the fabrication of a Ni-coated fiber composite (Mikata et al., 1987). More recently, Warwick and Clyne used a multi layer coaxial-cylindrical model to predict the principal stresses in a SiC monofilament reinforced Ti alloy subjected to a temperature change and/or an applied stress (Warwick and Clyne, 1991).

In the previous studies, the coating and matrix were treated elastically with temperature-independent properties. In fact, subjected to temperature changes superimposed with mechanical loading, the mismatches of the thermal expansion coefficients and Young's modulus between the components of composites can induce plastic deformation into the plastically deformable components of the composites, and the stress distributions in the composites will be altered accordingly. In the present work, to take the influences of plastic deformation on the stress distribution into consideration, a coated fibrous composite is theoretically analyzed based upon a linear strain-hardening stress-plastic strain relationship. The basic equation describing the plastic status of the coating and matrix is developed according to Tresca's yield criterion and the associated flow law, and the closed-form solution is obtained. As an application example of the established analytical method, the obtained formulae are used to numerically analyze the stress fields in a fibrous composite subjected to a temperature change superimposed with externally applied radial and/or axial stresses.

Contributed by the Applied Mechanics Division of THE AMERICAN SOCIETY OF MECHANICAL ENGINEERS for publication in the ASME JOURNAL OF APPLIED MECHANICS.

Discussion on the paper should be addressed to the Technical Editor, Professor Lewis T. Wheeler, Department of Mechanical Engineering, University of Houston, Houston, TX 77204-4792, and will be accepted until four months after final publication of the paper itself in the ASME JOURNAL OF APPLIED MECHANICS.

Manuscript received by the ASME Applied Mechanics Division, Apr. 1, 1998; final revision, Feb. 15, 1999. Associate Technical Editor: I. M. Daniel.

Mathematical Modeling

To facilitate the mathematical formulation of the stress distribution in continuous fibrous composites with elastic-plastic coating layer between fiber and matrix, a geometrical model consisting of four concentric circular cylinders with perfect interfacial binding, as shown in Fig. 1, is employed.

In the model, the four concentric circular cylinders are, respectively, the central fiber, outward coating, matrix, and surrounding composite. The fiber radius and the outer radii of the coating, matrix, and surrounding body are denoted by r_4, r_3, r_2, and r_1, respectively; and the interface radius between the elastic and plastic regions in the matrix by r_ξ. The coating and matrix are treated as isotropic, linear strain-hardening elastic-plastic solids with temperature-independent properties. Since the coating is very thin, it is assumed to be either fully elastic or fully plastic for simplicity. The fiber is assumed to be transversely isotropic. The surrounding body is considered to possess the composite properties that can be predicted by the Rule of Mixture. Also, it is assumed that the composite is subjected to an axisymmetric temperature change and externally applied radial and/or axial stresses due to the following reasons:

1 The fibers in a continuous fibrous composite is oriented in the direction of maximum stress transmission so that full advantage is taken of the dominant strength characteristics. The matrix is to carry the secondary stress applied in the transverse direction. The capacity of the fibers against transverse loading is very small and the matrix is very weak compared to the fiber reinforcement. Therefore, this unidirectional fibrous composite as we are studying is designed for the applications where the axial mechanical loading is predominant. In case the transverse loading is considerable or predominant, two-dimensional and three-dimensional reinforcements are applied to achieve reinforcement in those directions. Therefore, the axial loading is always predominant in the continuous fibrous composite.

2 Since the axial mechanical loading is dominant, our main

 Copyright © 1999 by ASME

Downloaded 04 May 2010 to 171.66.16.27. Redistribution subject to ASME license or copyright; see http://www.asme.org/terms/Terms_Use.cfm

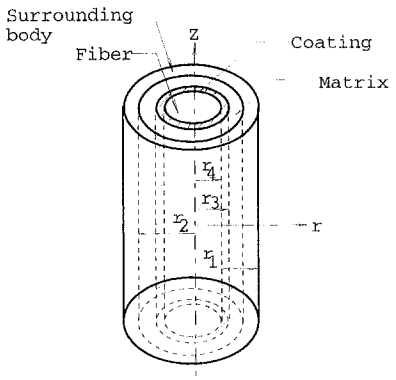


Fig. 1 The four-phase concentric cylinder model for unidirectional fibrous composites

aim is to study the stress field in the fibrous composite subject to this mechanical loading and axisymmetric thermal loading. These loads mainly cause different volume change, i.e., different dimension change in the axial and radial directions for all the components of the composite. The above concentric cylinder model is suitable for describing this deformation. Other mechanical loading which will be incorporated into this research must produce the same deformation behaviours as those caused by the axisymmetric thermal loading and axial mechanical loading. The deformation from axisymmetric radial mechanical loading has the same behaviors. Therefore this loading may be taken into account in the research. Whereas, transverse mechanical loading will cause quite different deformation behaviors. As mentioned above, the transverse loading is mainly carried by the matrix. Therefore, all the concentric cylinder models are not suitable for this situation. The geometrical model, physical model, and mathematical analysis for the transverse mechanical loading will be quite different from those used for the axisymmetric thermomechanical loading.

3 In addition, the micromechanics of the fibrous composite is very complicated. Therefore, some simplifications have to be made. A lot of examples can be listed for this. As we know, a single fiber pull-out is an impossibility in realistic fracture situations of the composite. However, it has been used to study the fiber pull-out mechanism (Kumar and Reddy, 1996). Strictly speaking, the liquid infiltration process for fabrication of continuous fibrous composites is a three-dimensional problem. However, it is treated as a one-dimensional problem in the existing researches (Long et al., 1994, 1995). The stresses acting a concentric cylinder model of the composite under thermal-mechanical loading are very difficult or impossible to determine accurately. Even the composite is only subjected to uniform temperature change, the stresses acting the cylinder model is not axisymmetric due to the change in the diameter of fibers and the nonuniform distribution of the fibers in the composite. However, in order to avoid the difficulty of the mathematical treatment, the axisymmetric models of the composite under thermal loading are very popular (Avery and Heravokich, 1986). This axisymmetric treatment can be also found in other researches of composite mechanics such as the research on the creep of composites (McMeeking, 1993). The method simplifying a specified problem was widely applied in the other fields of scientific research as well. For example, without considering acceleration and deceleration rotations, rotating disks with constant angular velocity were studied (You and Zhang, 1999; You et al., 1997). Compared to the axisymmetric thermal loading, the thermomechanical loading will bring in more complicated mathematical treatment. Therefore, the simplification on the mechanical loading has to be made to obtain the solution of the problem studied.

4 This simplification has been made and the axisymmetric thermalmechanical loading has been widely applied by many researchers (Mikata and Taya, 1985a; Warwick and Clyne, 1991; Sutcu, 1992; Zhang et al., 1994). This loading model is very useful in exploring the general nature of the stress field of the fibrous composite under thermal-mechanical loading. Moreover, only uniaxial mechanical loading or axisymmetric biaxial mechanical loading has been adopted in the previous research on a coated short-fiber composite (Mikata and Taya, 1985b). We think that the treatment of axisymmetric thermomechanical loading is reasonable. Therefore, this paper will adopt this axisymmetric thermal-mechanical loading, i.e., axisymmetric temperature change and externally applied radial and/or axial stresses.

Subjected to the axisymmetric thermomechanical loading, the stresses and deformations in every component of the composite are axisymmetric, i.e., the circumferential displacement is zero, the stresses and strains are independent of θ, and there is no shear-extension coupling.

With the above assumptions, the displacements within the model composite are

$$u = u(r)$$

$$v = 0$$

$$w = w(z) \tag{1}$$

where u, v, w are radial, circumferential, and axial displacements, respectively.

The displacements can be related to strains as follows:

$$\varepsilon_r = \frac{du}{dr}$$

$$\varepsilon_\theta = \frac{u}{r}$$

$$\varepsilon_z = \frac{dw}{dz}. \tag{2}$$

The deformation compatibility equation can be derived from Eq. (2) which has the form of

$$r\frac{d\varepsilon_\theta}{dr} + \varepsilon_\theta - \varepsilon_r = 0. \tag{3}$$

The equilibrium equation for the current axisymmetric problem can be expressed as

$$\frac{d\sigma_r}{dr} + \frac{1}{r}(\sigma_r - \sigma_\theta) = 0$$

$$\frac{d\sigma_z}{dz} = 0. \tag{4}$$

Using both the subscripts and superscripts f for the fiber, c for the coating, and m for the matrix and b for the surrounding body, the elastic stress-strain relationship for all the four constituent materials can be written as

$$\sigma_{ri} = c_{11}^{(i)}\varepsilon_{ri} + c_{12}^{(i)}\varepsilon_{\theta i} + c_{13}^{(i)}\varepsilon_{zi} - \beta_{1i}\Delta T$$

$$\sigma_{\theta i} = c_{12}^{(i)}\varepsilon_{ri} + c_{11}^{(i)}\varepsilon_{\theta i} + c_{13}^{(i)}\varepsilon_{zi} - \beta_{1i}\Delta T$$

$$\sigma_{zi} = c_{13}^{(i)}\varepsilon_{ri} + c_{13}^{(i)}\varepsilon_{\theta i} + c_{33}^{(i)}\varepsilon_{zi} - \beta_{3i}\Delta T \tag{5}$$

and

$$\beta_{1i} = (c_{11}^{(i)} + c_{12}^{(i)})\alpha_{Ti} + c_{13}^{(i)}\alpha_{Li}$$

$$\beta_{3i} = 2c_{13}^{(i)}\alpha_{Ti} + c_{33}^{(i)}\alpha_{Li} \tag{6}$$

where $i = f$, c, m and b; $c_{11}^{(i)}$, $c_{12}^{(i)}$, $c_{13}^{(i)}$, and $c_{33}^{(i)}$ are the elastic constants of the component materials, and α_{Ti} and α_{Li} are their thermal expansion coefficients in the transverse and axial direc-

Downloaded 04 May 2010 to 171.66.16.27. Redistribution subject to ASME license or copyright; see http://www.asme.org/terms/Terms_Use.cfm

tions, respectively; and ΔT is the uniform temperature change applied.

For the isotropic materials, the elastic constants are

$$c_{11}^{(i)} = c_{33}^{(i)} = \frac{E_i(1-\mu_i^2)}{(1-2\mu_i)(1+\mu_i)^2}$$

$$c_{12}^{(i)} = c_{13}^{(i)} = \frac{E_i\mu_i(1+\mu_i)}{(1-2\mu_i)(1+\mu_i)^2} \tag{7}$$

where E_i and μ_i $(i = c, m)$ are, respectively, Young's modulus and Poisson's ratio of the coating and matrix.

Subjected to a uniform temperature change, the elastic stresses and displacements of the above four constituents can be obtained as follows from Eqs. (2), (4), and (5):

$$\sigma_{ri} = (c_{11}^{(i)} + c_{12}^{(i)})A_i + (c_{12}^{(i)} - c_{11}^{(i)})B_i r^{-2} + c_{13}^{(i)}D_i - \beta_{1i}\Delta T$$

$$\sigma_{\theta i} = (c_{11}^{(i)} + c_{12}^{(i)})A_i + (c_{11}^{(i)} - c_{12}^{(i)})B_i r^{-2} + c_{13}^{(i)}D_i - \beta_{1i}\Delta T$$

$$\sigma_{zi} = 2c_{13}^{(i)}A_i + c_{33}^{(i)}D_i - \beta_{3i}\Delta T$$

$$u_i = A_i r + B_i r^{-1}$$

$$w_i = D_i z + F_i \tag{8}$$

where A_i, B_i, D_i, and F_i $(i = f, c, m, b)$ are integration constants.

To apply Tresca's yield criterion, it is essential to be aware of the order of the three component stresses $\sigma_{\theta i}$, σ_{ri}, and σ_{zi} in magnitude that is unknown and varies with the nature of the applied thermal and mechanical loading. Therefore, it is unlikely to be able to derive a single basic equation and to find its closed-form solution applicable to all the possible stress states corresponding to different loading conditions. However, for a prescribed stress state, the basic equation is derivable and its correspondent closed-form solution is achievable. In the following, such a basic equation and its closed-form solution for a prescribed stress state is to be derived as an example to demonstrate the method of seeking the solution for the other different stress states.

Assuming that $\sigma_{\theta i} > \sigma_{ri} > \sigma_{zi}$, i.e., the circumference stress $\sigma_{\theta i}$ is the largest and the axial stress σ_{zi} is the smallest in the coating or matrix of the composite, Tresca's yield criterion can be written as follows for the linear strain-hardening component materials:

$$\sigma_{ei} = \sigma_{\theta i} - \sigma_{zi} = \sigma_{0i}(1 + \eta_i\varepsilon_{ei}^p) \tag{9}$$

where σ_{ei} and ε_{ei}^p $(i = c, m)$ are, respectively, the equivalent stress and plastic strain of the coating and matrix; σ_{0i} and η_i $(i = c, m)$ are, respectively, their initial yield stress and hardening parameter that are treated as temperature-independent in the present study.

According to the flow law associated with Tresca's yield criterion, the incompressibility of plastic strains, and the equivalence of plastic work, one obtains the following relationships among the equivalent plastic strain and plastic strains:

$$\varepsilon_{ei}^p = \varepsilon_{\theta i}^p$$

$$\varepsilon_{zi}^p = -\varepsilon_{\theta i}^p$$

$$\varepsilon_{ri}^p = 0 \tag{10}$$

where the superscript p represents plastic strains.

With Eqs. (9) and (10), the relationships between the strains and stresses can be written as

$$\varepsilon_{\theta i}^p = \frac{1}{\eta_i}\left[\frac{1}{\sigma_{0i}}(\sigma_{\theta i} - \sigma_{zi}) - 1\right]$$

$$\varepsilon_{zi}^p = -\frac{1}{\eta_i}\left[\frac{1}{\sigma_{0i}}(\sigma_{\theta i} - \sigma_{zi}) - 1\right]$$

$$\varepsilon_{ri}^p = 0. \tag{11}$$

The summation of the elastic, plastic, and thermal strains leads to the following expressions of the total strains:

$$\varepsilon_{\theta i} = \varepsilon_{\theta i}^e + \varepsilon_{\theta i}^p + \varepsilon_{\theta i}^T = \frac{1}{E_i}[\sigma_{\theta i} - \mu_i(\sigma_{ri} + \sigma_{zi})] + \frac{1}{\eta_i}\left[\frac{1}{\sigma_{0i}}(\sigma_{\theta i} - \sigma_{zi}) - 1\right] + \alpha_i\Delta T$$

$$\varepsilon_{zi} = \varepsilon_{zi}^e + \varepsilon_{zi}^p + \varepsilon_{zi}^T = \frac{1}{E_i}[\sigma_{zi} - \mu_i(\sigma_{\theta i} + \sigma_{ri})] - \frac{1}{\eta_i}\left[\frac{1}{\sigma_{0i}}(\sigma_{\theta i} - \sigma_{zi}) - 1\right] + \alpha_i\Delta T$$

$$\varepsilon_{ri} = \varepsilon_{ri}^e + \varepsilon_{ri}^p + \varepsilon_{ri}^T = \frac{1}{E_i}[\sigma_{ri} - \mu_i(\sigma_{\theta i} + \sigma_{zi})] + \alpha_i\Delta T \tag{12}$$

where the superscripts e and T, respectively, denote elastic and thermal strains, α_i $(i = c, m)$ is the thermal expansion coefficient of the coating and matrix, and $\alpha_i = \alpha_{Ti} = \alpha_{Li}$ due to the assumed isotropic nature.

The expression for σ_{zi} can be obtained by integrating the second one of Eq. (4). With the known σ_{zi}, the radial stress equilibrium expression in Eq. (4), and the compatibility Eq. (3), the basic equation can be written as

$$r^2\frac{d^2\sigma_{ri}}{dr^2} + 3r\frac{d\sigma_{ri}}{dr} + \frac{E_i}{E_i + \eta_i\sigma_{0i}}\sigma_{ri} = \frac{E_i\sigma_{0i}}{E_i + \eta_i\sigma_{0i}}\left(1 + \frac{D_{pi}}{\sigma_{0i}}\right). \tag{13}$$

The integration of Eq. (13) gives the closed-form solution of σ_{ri}. Then making use of Eqs. (4), (12), and (2), and using the subscript and superscript p for plastic regions, one obtains the following stresses and displacements in the coating and matrix:

$$\sigma_{ri}^p = D_{pi} + A_{pi}r^{\lambda_{i1}} + B_{pi}r^{\lambda_{i2}} + \sigma_{0i}$$

$$\sigma_{\theta i}^p = D_{pi} + A_{pi}(1 + \lambda_{i1})r^{\lambda_{i1}} + B_{pi}(1 + \lambda_{i2})r^{\lambda_{i2}} + \sigma_{0i}$$

$$\sigma_{zi}^p = D_{pi}$$

$$u_i^p = \frac{1-2\mu_i}{E_i}D_{pi}r + \frac{E_i + (1-\mu_i)\eta_i\sigma_{0i} + (E_i + \eta_i\sigma_{0i})\lambda_{i1}}{E_i\eta_i\sigma_{0i}}A_{pi}r^{\lambda_{i1}+1} + \frac{E_i + (1-\mu_i)\eta_i\sigma_{0i} + (E_i + \eta_i\sigma_{0i})\lambda_{i2}}{E_i\eta_i\sigma_{0i}}B_{pi}r^{\lambda_{i2}+1} + \frac{1-\mu_i}{E_i}\sigma_{0i}r + \alpha_i\Delta Tr$$

$$w_i^p = \frac{1-2\mu_i}{E_i}D_{pi}z - \frac{E_i + 2\mu_i\eta_i\sigma_{0i} + (E_i + \mu_i\eta_i\sigma_{0i})\lambda_{i1}}{E_i\eta_i\sigma_{0i}}A_{pi}zr^{\lambda_{i1}} - \frac{E_i + 2\mu_i\eta_i\sigma_{0i} + (E_i + \mu_i\eta_i\sigma_{0i})\lambda_{i2}}{E_i\eta_i\sigma_{0i}}B_{pi}zr^{\lambda_{i2}} - \frac{2\mu_i}{E_i}\sigma_{0i}z + \alpha_i\Delta Tz + F_{pi} \tag{14}$$

where A_{pi}, B_{pi}, D_{pi}, and F_{pi} $(i = c, m)$ are integration constants.

The same method is applied for the other stress states and the formulae similar to Eq. (14) are obtained accordingly. For sim-

Downloaded 04 May 2010 to 171.66.16.27. Redistribution subject to ASME license or copyright; see http://www.asme.org/terms/Terms_Use.cfm

Table 1 Material properties of Ni-coated graphite fiber/ Aluminum 6061 composite

	Matrix	Fiber	Coating
Material	Al 6061	Graphite T300	Ni
E_T (GPa)	68.6	22.0	207
E_L (GPa)	68.6	226	207
μ_{12}	0.345	0.42	0.31
μ_{13}	0.345	0.30	0.31
G_L (GPa)	25.5	4.83	79.0
α_T (1/°C)	23.5×10^{-6}	27.0×10^{-6}	13.3×10^{-6}
α_L (1/°C)	23.5×10^{-6}	-1.50×10^{-6}	13.3×10^{-6}

plicity, these formulae for all the possible stress states are summarised in their unified form as follows:

$$\sigma_{ri}^p = G_{i0}D_{pi} + A_{pi}r^{\lambda_{i1}} + B_{pi}r^{\lambda_{i2}} + G_{i1}\ln r + G_{i2}$$

$$\sigma_{\theta i}^p = G_{i0}D_{pi} + A_{pi}(1+\lambda_{i1})r^{\lambda_{i1}} + B_{pi}(1+\lambda_{i2})r^{\lambda_{i2}} + G_{i1}\ln r + G_{i3}$$

$$\sigma_{zi}^p = D_{pi}$$

$$u_i^p = G_{i4}D_{pi}r + G_{i5}A_{pi}r^{\lambda_{i1}+1} + G_{i6}B_{pi}r^{\lambda_{i2}+1} + G_{i7}r\ln r + G_{i8}r$$

$$w_i^p = G_{i9}D_{pi}z + G_{i10}A_{pi}zr^{\lambda_{i1}} + G_{i11}B_{pi}zr^{\lambda_{i2}} + G_{i12}z\ln r + G_{i13}z + F_{pi} \quad (15)$$

where λ_{i1}, λ_{i2} $(i = c, m)$ and G_{ij} $(i = c, m; j = 0, 1, 2, \ldots 13)$ are given in the Appendix for the different stress states.

The boundary conditions for the fibrous composite under combined thermal and mechanical loading are

$$\begin{aligned} \sigma_{rb} &= \sigma_{0r} && \text{at } r = r_1 \\ w_f = w_c^p = w_m^p = w_m^e &= w_b = 0 && \text{at } z = 0 \\ u_f &\text{ is a bounded value} && \text{at } r = 0 \end{aligned} \quad (16)$$

in which σ_{0r} is the applied radial stress, and the superscript e indicates that the quantities are in the elastic region of the matrix determined by Eq. (8).

The continuity conditions for the displacements and stresses in the composite are

$$\begin{aligned} u_f = u_c^p,\ w_f = w_c^p,\ \sigma_{rf} = \sigma_{rc}^p &&& \text{at } r = r_4 \\ u_c^p = u_m^p,\ w_c^p = w_m^p,\ \sigma_{rc}^p = \sigma_{rm}^p &&& \text{at } r = r_3 \\ u_m^p = u_m^e,\ w_m^p = w_m^e,\ \sigma_{rm}^p = \sigma_{rm}^e,\ \sigma_{\theta m}^p = \sigma_{\theta m}^e &&& \text{at } r = r_\xi \\ u_m^e = u_b,\ w_m^e = w_b,\ \sigma_{rm}^e = \sigma_{rb} &&& \text{at } r = r_2. \end{aligned} \quad (17)$$

The equilibrium condition for axial force is

$$\int_0^{r_4}\sigma_{zf}rdr + \int_{r_4}^{r_3}\sigma_{zc}^p rdr + \int_{r_3}^{r_\xi}\sigma_{zm}^p rdr + \int_{r_\xi}^{r_2}\sigma_{zm}^e rdr + \int_{r_2}^{r_1}\sigma_{zb}rdr = \int_0^{r_1}\sigma_{0z}rdr \quad (18)$$

in which σ_{0z} is the applied axial stress.

All the unknown integration constants in Eqs. (8) and (15) may be determined by substituting these equations into Eq. (16) to (18) and solving the algebraic linear equations.

Numerical Results

To facilitate the comparison of the stress distribution in the same composite with and without the consideration of the plasticity of the component materials, the above analytical method is used to determine the stress distributions in a composite consisting of Ni-coated graphite fibers and Aluminum 6061 alloy as specified in Mikata and Taya (1985a). The material properties of the fiber, coating, and matrix of the composite are cited in Table 1.

For Ni coating, the linear strain-hardening stress-plastic strain relationship is

$$\sigma_{ec} = 317(1 + 320\varepsilon_{ec}^p). \quad (19)$$

For Al 6061 matrix, the relationship is

$$\sigma_{em} = 310(1 + 300\varepsilon_{em}^p). \quad (20)$$

The values of the initial yield stresses and hardening parameters in Eqs. (19) and (20) may be inaccurate, and are used here only for parametric and illustrative purposes.

The relative geometrical parameters of the composite are: $r_4/r_2 = 0.6$, $r_3/r_2 = 0.65$. The corresponding volume fraction of the fiber, coating, and matrix are, respectively, 0.36, 0.06, and 0.58.

To demonstrate the effect of plasticity on the stress distributions, two cases for each loading condition are respectively considered: one takes both coating and matrix as fully elastic, the other takes the coating to be fully plastic and the matrix as elastic-plastic. The loading conditions for the numerical calculations are:

1 a 300°C temperature increase superimposed on an applied radial stress 0.183 GPa,
2 a 300°C temperature increase superimposed on an applied axial stress 0.9 GPa, and
3 a 300°C temperature increase superimposed on an applied radial stress 0.35 GPa and an applied axial stress 0.3 GPa.

The stress distributions in the composite subjected to the above three kinds of loading combinations are plotted in Fig. 2 to Fig. 4,

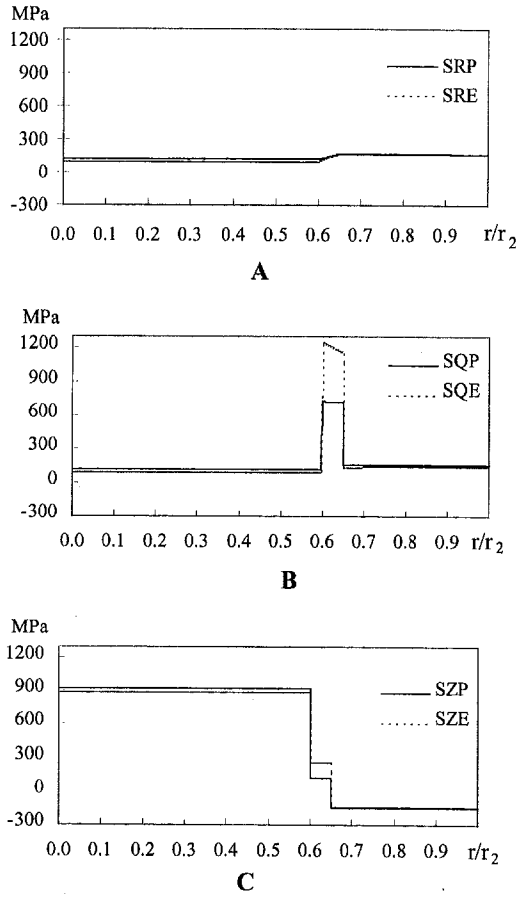


Fig. 2 The distributions of radial A, circumferential B, and axial C stresses in the composite subjected to a 300°C temperature increase and a 0.183 GPa radial stress

Downloaded 04 May 2010 to 171.66.16.27. Redistribution subject to ASME license or copyright; see http://www.asme.org/terms/Terms_Use.cfm

respectively. In all the figures of the present study, SRP, SQP, and SZP, respectively, represent the radial, circumferential, and axial elastic-plastic stresses calculated with the elastic-plastic method developed in the present study. SRE, SQE, and SZE respectively denote the elastic radial, circumferential, and axial stresses calculated with the elastic method (Mikata and Taya, 1985a).

The numerical results in the figures indicate that subjected to any one of the specified loading combinations, the radial stress in the composite remains at a relatively low level and the introduction of the plasticity into the coating and matrix affects little this stress component. However, the circumferential and axial stresses in the coating are found to be affected significantly according to the nature of loading combinations.

Due to the low Young's modulus and high thermal expansion coefficient of the matrix as compared with those of the coating, the elastic circumferential and axial stresses in the matrix are much lower than those in the coating for the above loading cases. The introduction of the plasticity into the coating and matrix changes little the stresses in the matrix, but alter the stresses in the coating significantly. In the transverse direction, the Young's modulus of the coating is much bigger than that of the fiber, but its thermal expansion coefficient is only half of that of the fiber. Consequently, a much higher circumferential stress in the coating than that in the fiber is generated as shown by the figures.

In the axial direction, the coating and the fiber possess the Young's moduli of almost the same value, but the coating has very high thermal expansion coefficient as compared with the negative thermal expansion coefficient of the fiber. This axial mismatch in thermal expansion coefficient causes a great difference between the axial stresses of the coating and the fiber. The high circumferential and axial stresses in the coating and fiber may result in the initiation of radial and axial cracking in these components or the debonding at the interface between the coating and the fiber. After the introduction of the plasticity into the coating and matrix, the circumferential and axial stresses in the coating are greatly decreased, leaving the circumferential and axial stresses in the fiber almost unchanged.

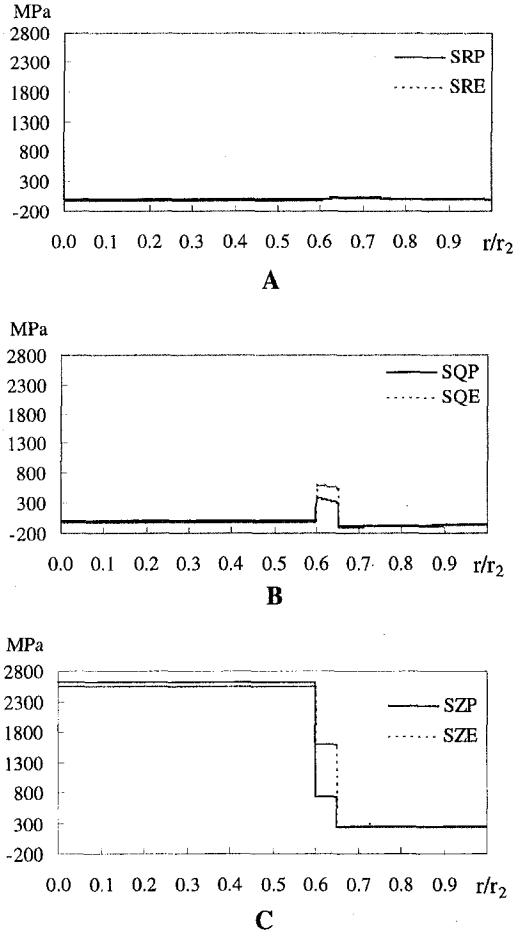


Fig. 3 The distributions of radial A, circumferential B, and axial C stresses in the composite subjected to a 300°C temperature increase and a 0.9 GPa axial stress

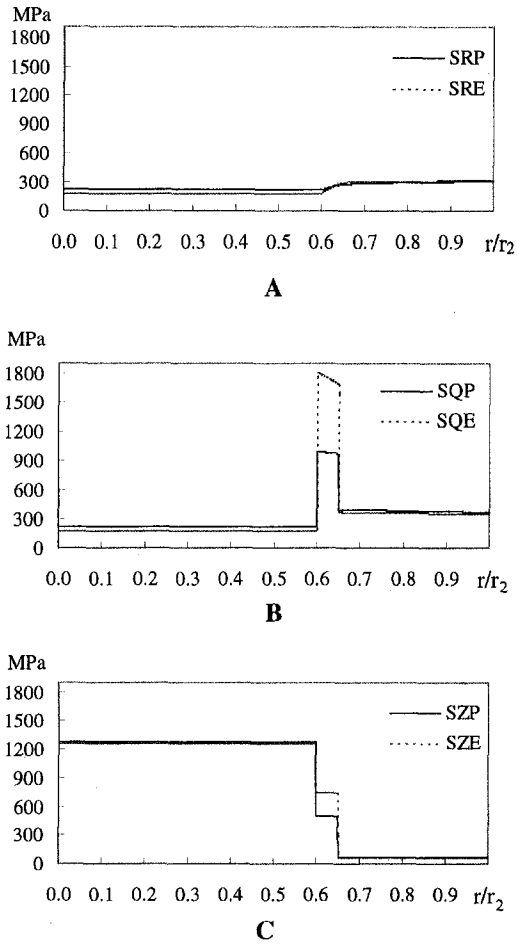


Fig. 4 The distributions of radial A, circumferential B, and axial C stresses in the composite subjected to a 300°C temperature increase, a 0.35 GPa radial stress and a 0.3 GPa axial stress

To identify the contribution of matrix plasticity, the stress distributions in the composite, consisting of an elastic-plastic matrix and elastic fiber, coating and surrounding composite body, is calculated under a loading combination of a 100°C temperature increase and a 0.32 GPa radial stress. The numerical stress distributions are given in Fig. 5. In comparison, the stress distributions in the full elastic composites subjected to the same loading are given.

As Fig. 5 shows, the effect of the plasticity of the matrix on all the stresses in the composite is very limited. Since the deformation of the coating and the fiber in the radial and circumferential directions are strongly restricted by the matrix, the plasticity of the matrix has almost no influence on the stresses in these two directions. In contrary, due to the weak restraint of the matrix in the axial direction, the plasticity of the matrix causes small changes of the axial stress in both the coating and fiber.

The most unchanged stress state in coating indicates that the introduction of plasticity into matrix provide little capability to accommodate the great stress difference between the fiber and coating, and suggests the importance of the coating plasticity. To elucidate the effect of the coating plasticity, the stress distribution in a composite consisting of elastic components, but a plastic coating is numerically presented in Fig. 6 in

Downloaded 04 May 2010 to 171.66.16.27. Redistribution subject to ASME license or copyright; see http://www.asme.org/terms/Terms_Use.cfm

comparison with the fully elastic composite. The loading combination applied is a 600°C temperature increase and a 0.2 GPa radial stress.

As indicated by Fig. 6, the plasticity of the coating significantly decreases the circumferential and axial stresses in the coating itself. However, since the coating is very thin, the plasticity of the coating imposes little influence on the stresses in the fiber and matrix. Compared with the almost unchanged stress distribution in the matrix by the introduction of matrix plasticity, the obtained results do suggest that, as far as interfacial stresses are concerned, it may be reasonable to consider only the plasticity of the coating in the determination of the stress fields in order to facilitate the mathematical processing without losing the required accuracy from the viewpoint of composite engineering.

The results of the above numerical analyses on Ni coated T300 carbon fiber/Al system make it clear that the plasticity of the coating can significantly change the circumferential and axial stress distribution in the coating itself, resulting in significant reduction of the circumferential stress difference between the component materials. Therefore, the employment of a plastic coating cannot only reduce the stresses in the coating itself, but also be able to smooth out the circumferential stress difference caused by the mismatch of material properties between the coating and other constituents, decreasing the risk of cracking initiation in the interfacial region.

Finally, it must be mentioned that as the mathematical formulation indicates, the stress fields in the composite are codetermined by the material properties of the components, such as the thermal expansion coefficient, Young's modulus, etc., and the nature of the applied loading. The changes in the material properties of the component materials can considerably alter the stress fields in the composite (You and Long, 1998). In the reality of fibrous composites, besides various coating available, fibers of different ceramics, graphite, glass, polymers, and metal alloys and matrices of various metallic alloys, intermetallics, ceramics, glasses, carbon, and polymers can be found in the composites oriented to different applications. Therefore, the properties of the component materials available can change widely, as well as the stress fields in the composites even subjected to the same thermal and mechanical loading combination. Therefore, the results obtained in the present numerical examples are valid only for the composites consisting of the components with similar material properties.

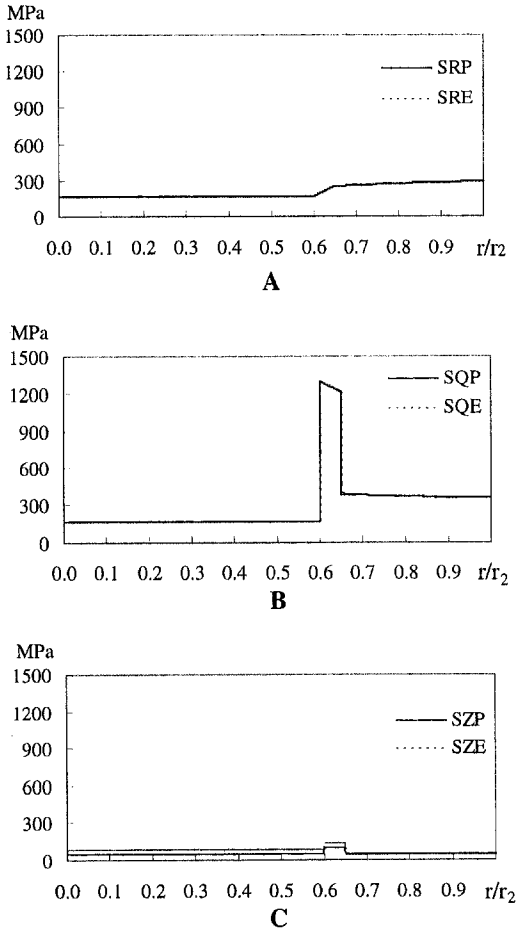


Fig. 5 The distributions of radial A, circumferential B, and axial C stresses in the composite with and without a plastic matrix, subjected to a 100°C temperature increase and a 0.32 GPa radial stress

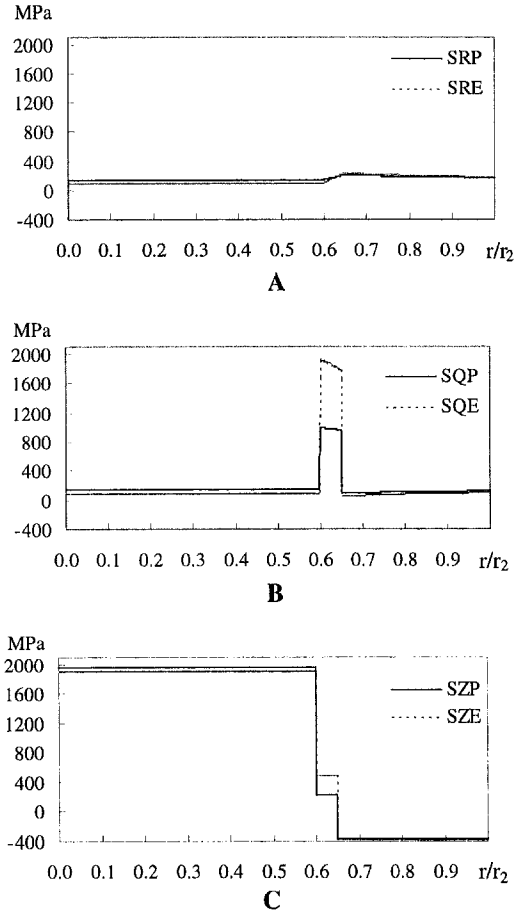


Fig. 6 The distributions of radial A, circumferential B, and axial C stresses in the composite with and without a plastic coating, subjected to a 600°C temperature increase and a 0.2 GPa radial stress

Conclusion

The stress distribution in a coated continuous fibrous composite subjected to a temperature change and externally applied stresses is mathematically formulated based upon a four-concentric-cylinders model consisting of elastic fiber, plastic coating, and elastic-plastic matrix with linear strain-hardening behavior and surrounding elastic composite body. Their basic equation is derived from Tresca's criterion, equilibrium, and compatibility conditions and the closed-form solutions are obtained.

With the obtained closed-form solutions, numerical calculations of the stress distributions in a composite consisting of Ni-coated carbon fiber and Al alloy matrix subjected to thermal and mechanical loading are performed in comparison with the established full elastic model. It is found that the plasticity of the coating greatly decreases the circumferential and axial stresses in the coating itself and alleviates the circumferential

Downloaded 04 May 2010 to 171.66.16.27. Redistribution subject to ASME license or copyright; see http://www.asme.org/terms/Terms_Use.cfm

stress difference induced by the mismatches of physical and mechanical properties between the coating and other constituents. However, the introduction of the coating plasticity has very limited influence on its radial stress and the stresses in the matrix.

References

Avery, W. B., and Herakovich, C. T., 1986, "Effect of Fiber Anisotropy on Thermal Stresses in Fibrous Composites," ASME JOURNAL OF APPLIED MECHANICS, Vol. 53, pp. 751–756.

Kumar, R. K., and Reddy, J. N., 1996, "Stress Distributions During Fiber Pull-out," ASME JOURNAL OF APPLIED MECHANICS, Vol. 63, pp. 301–306.

Long, S., You, L., and Flower, H. M., 1997, "Axial Effect of Fiber-Matrix Chemistry on Interfacial Structure, Fracture Behaviour and Tensile Strength of Cast CFMMS's," International Conference on Interfacial Phenomena of Composite Materials, Sept., Hungary.

Long, S., Zhang, Z., and Flower, H. M., 1994, "Hydrodynamic Analysis of Liquid Infiltration of Unidirectional Fibre Arrays by Squeeze Casting," *Acta Metall. Mater.*, Vol. 42, No. 4, pp. 1389–1397.

Long, S., Zhang, Z., and Flower, H. M., 1995, "Characterization of Liquid Metal Infiltration of a Chopped Fibre Preform Aided by External Pressure—II. Modelling of Liquid Metal Infiltration Process," *Acta Metall. Mater.*, Vol. 43, No. 9, pp. 3499–3509.

McMeeking, R. M., 1993, "Power Law Creep of a Composite Material Containing Discontinuous Rigid Aligned Fibers," *International Journal of Solids and Structures*, Vol. 30, No. 13, pp. 1807–1823.

Mikata, Y., Takahashi, S., Su, S., and Uchida, Y., 1987, "Development of Functionalized Materials Using Organometallic Compounds—IV. Thermal Residual Stresses During the Fabrication of a Ni-Coated Continuous Carbon Fiber Aluminum Composite," *Bull. Chem. Soc. Jpn.*, Vol. 60, pp. 2593–2598.

Mikata, Y., and Taya, M., 1985a, "Stress Field in a Coated Continuous Fiber Composite Subjected to Thermomechanical Loading," *J. Comp. Mater.*, Vol. 19, pp. 554–578.

Mikata, Y., and Taya, M., 1985b, "Stress Field in and Around a Coated Short Fiber in an Infinite Matrix Subjected to Uniaxial and Biaxial Loadings," ASME JOURNAL OF APPLIED MECHANICS, Vol. 52, pp. 19–24.

Sutcu, M., 1992, "A Recursive Concentric Cylinder Model for Composites Containing Coated Fibers," *International Journal of Solids and Structures*, Vol. 29, No. 2, pp. 197–213.

Warwick, C. M., and Clyne, T. W., 1991, "Development of Composite Coaxial Cylinder Stress Analysis Model and Its Application to SiC Monofilament Systems," *J. Mater. Sci.*, Vol. 26, pp. 3817–3827.

You, L., and Long, S., 1998, "Effects of Material Properties of Interfacial Layer on Stresses in Fibrous Composites Subjected to Thermal Loading," *Composites*, Part A, Vol. 29A, pp. 1185–1192.

You, L., Long, S., and Zhang, J., 1997, "Perturbation Solution of Rotating Solid Disks With Nonlinear Strain-Hardening," *Mechanics Research Communications*, Vol. 24, No. 6, pp. 649–658.

You, L., and Zhang, J., 1999, "Elastic-Plastic Stresses in a Rotating Solid Disk," *International Journal of Mechanical Sciences*, Vol. 41, pp. 269–282.

Zhang, H., Anderson, P. M., and Daehn, G. S., 1994, "Analysis of Thermally Induced Stress and Strain in Continuous Fiber-Reinforced Composites," *Metallurgical and Materials Transactions A*, Vol. 25A, pp. 415–425.

APPENDIX

The expressions for λ_{i1}, λ_{i2} $(i = c, m)$ and G_{ij} $(i = c, m; j = 0, 1, 2, \ldots 13)$.

(1) For $\sigma_{\theta i} \geq \sigma_{ri} \geq \sigma_{zi}$ and $\sigma_{zi} \geq \sigma_{ri} \geq \sigma_{\theta i}$

$$\lambda_{i1,i2} = -1 \pm \sqrt{\frac{\eta_i \sigma_{0i}}{E_i + \eta_i \sigma_{0i}}}$$

$$G_{i0} = 1$$

$$G_{i1} = 0$$

$$G_{i2} = \sigma_{0i} \quad \text{for } \sigma_{\theta i} \geq \sigma_{ri} \geq \sigma_{zi}$$
$$G_{i2} = -\sigma_{0i} \quad \text{for } \sigma_{zi} \geq \sigma_{ri} \geq \sigma_{\theta i}$$

$$G_{i3} = G_{i2}$$

$$G_{i4} = \frac{1 - 2\mu_i}{E_i}$$

$$G_{i5} = \frac{1}{E_i \eta_i \sigma_{0i}} [E_i + (1 - \mu_i)\eta_i \sigma_{0i} + (E_i + \eta_i \sigma_{0i})\lambda_{i1}]$$

$$G_{i6} = \frac{1}{E_i \eta_i \sigma_{0i}} [E_i + (1 - \mu_i)\eta_i \sigma_{0i} + (E_i + \eta_i \sigma_{0i})\lambda_{i2}]$$

$$G_{i7} = 0$$

$$G_{i8} = \frac{1 - \mu_i}{E_i} \sigma_{0i} + \alpha_i \Delta T \quad \text{for } \sigma_{\theta i} \geq \sigma_{ri} \geq \sigma_{zi}$$
$$G_{i8} = -\frac{1 - \mu_i}{E_i} \sigma_{0i} + \alpha_i \Delta T \quad \text{for } \sigma_{zi} \geq \sigma_{ri} \geq \sigma_{\theta i}$$

$$G_{i9} = G_{i4}$$

$$G_{i10} = -\frac{1}{E_i \eta_i \sigma_{0i}} [E_i + 2\mu_i \eta_i \sigma_{0i} + (E_i + \mu_i \eta_i \sigma_{0i})\lambda_{i1}]$$

$$G_{i11} = -\frac{1}{E_i \eta_i \sigma_{0i}} [E_i + 2\mu_i \eta_i \sigma_{0i} + (E_i + \mu_i \eta_i \sigma_{0i})\lambda_{i2}]$$

$$G_{i12} = 0$$

$$G_{i13} = -\frac{2\mu_i \sigma_{0i}}{E_i} + \alpha_i \Delta T \quad \text{for } \sigma_{\theta i} \geq \sigma_{ri} \geq \sigma_{zi}$$
$$G_{i13} = \frac{2\mu_i \sigma_{0i}}{E_i} + \alpha_i \Delta T \quad \text{for } \sigma_{zi} \geq \sigma_{ri} \geq \sigma_{\theta i}$$

(2) For $\sigma_{\theta i} \geq \sigma_{zi} \geq \sigma_{ri}$ and $\sigma_{ri} \geq \sigma_{zi} \geq \sigma_{\theta i}$

$$\lambda_{i1} = -2$$

$$\lambda_{i2} = 0$$

$$G_{i0} = 0$$

$$G_{i1} = \frac{E_i \sigma_{0i}}{E_i + \eta_i \sigma_{0i}} \quad \text{for } \sigma_{\theta i} \geq \sigma_{zi} \geq \sigma_{ri}$$
$$G_{i1} = -\frac{E_i \sigma_{0i}}{E_i + \eta_i \sigma_{0i}} \quad \text{for } \sigma_{ri} \geq \sigma_{zi} \geq \sigma_{\theta i}$$

$$G_{i2} = 0$$

$$G_{i3} = G_{i1}$$

$$G_{i4} = -\frac{\mu_i}{E_i}$$

$$G_{i5} = -\frac{(1 + \mu_i)\eta_i \sigma_{0i} + 2E_i}{E_i \eta_i \sigma_{0i}}$$

$$G_{i6} = \frac{1 - \mu_i}{E_i}$$

$$G_{i7} = \frac{(1 - \mu_i)\sigma_{0i}}{E_i + \eta_i \sigma_{0i}} \quad \text{for } \sigma_{\theta i} \geq \sigma_{zi} \geq \sigma_{ri}$$
$$G_{i7} = -\frac{(1 - \mu_i)\sigma_{0i}}{E_i + \eta_i \sigma_{0i}} \quad \text{for } \sigma_{ri} \geq \sigma_{zi} \geq \sigma_{\theta i}$$

$$G_{i8} = \alpha_i \Delta T$$

$$G_{i9} = \frac{1}{E_i}$$

$$G_{i10} = 0$$

$$G_{i11} = -\frac{2\mu_i}{E_i}$$

Downloaded 04 May 2010 to 171.66.16.27. Redistribution subject to ASME license or copyright; see http://www.asme.org/terms/Terms_Use.cfm

$$G_{i12} = -\frac{2\mu_i\sigma_{0i}}{E_i + \eta_i\sigma_{0i}} \quad \text{for } \sigma_{\theta i} \geq \sigma_{zi} \geq \sigma_{ri}$$

$$G_{i12} = \frac{2\mu_i\sigma_{0i}}{E_i + \eta_i\sigma_{0i}} \quad \text{for } \sigma_{ri} \geq \sigma_{zi} \geq \sigma_{\theta i}$$

$$G_{i13} = -\frac{\mu_i\sigma_{0i}}{E_i + \eta_i\sigma_{0i}} + \alpha_i\Delta T \quad \text{for } \sigma_{\theta i} \geq \sigma_{zi} \geq \sigma_{ri}$$

$$G_{i13} = \frac{\mu_i\sigma_{0i}}{E_i + \eta_i\sigma_{0i}} + \alpha_i\Delta T \quad \text{for } \sigma_{ri} \geq \sigma_{zi} \geq \sigma_{\theta i}$$

(3) For $\sigma_{zi} \geq \sigma_{\theta i} \geq \sigma_{ri}$ and $\sigma_{ri} \geq \sigma_{\theta i} \geq \sigma_{zi}$

$$\lambda_{i1,i2} = -1 \pm \sqrt{\frac{E_i + \eta_i\sigma_{0i}}{\eta_i\sigma_{0i}}}$$

$$G_{i0} = 1$$

$$G_{i1} = 0$$

$$G_{i2} = -\sigma_{0i} \quad \text{for } \sigma_{zi} \geq \sigma_{\theta i} \geq \sigma_{ri}$$
$$G_{i2} = \sigma_{0i} \quad \text{for } \sigma_{ri} \geq \sigma_{\theta i} \geq \sigma_{zi}$$

$$G_{i3} = G_{i2}$$

$$G_{i4} = \frac{1 - 2\mu_i}{E_i}$$

$$G_{i5} = \frac{1 - \mu_i + \lambda_{i1}}{E_i}$$

$$G_{i6} = \frac{1 - \mu_i + \lambda_{i2}}{E_i}$$

$$G_{i7} = 0$$

$$G_{i8} = -\frac{(1 - \mu_i)\sigma_{0i}}{E_i} + \alpha_i\Delta T$$

$$G_{i9} = \frac{1 - 2\mu_i}{E_i}$$

$$G_{i10} = -\left[\frac{\mu_i}{E_i}(2 + \lambda_{i1}) + \frac{1}{\eta_i\sigma_{0i}}\right]$$

$$G_{i11} = -\left[\frac{\mu_i}{E_i}(2 + \lambda_{i2}) + \frac{1}{\eta_i\sigma_{0i}}\right]$$

$$G_{i12} = 0$$

$$G_{i13} = \frac{2\mu_i\sigma_{0i}}{E_i} + \alpha_i\Delta T \quad \text{for } \sigma_{zi} \geq \sigma_{\theta i} \geq \sigma_{ri}$$

$$G_{i13} = -\frac{2\mu_i\sigma_{0i}}{E_i} + \alpha_i\Delta T \quad \text{for } \sigma_{ri} \geq \sigma_{\theta i} \geq \sigma_{zi}$$

Downloaded 04 May 2010 to 171.66.16.27. Redistribution subject to ASME license or copyright; see http://www.asme.org/terms/Terms_Use.cfm

Free Vibration of Axially Loaded Laminated Conical Shells

L. Tong
Department of Aeronautical Engineering,
University of Sydney,
New South Wales 2006
Australia

Analytical solutions for the three displacements are obtained, in the form of power series, directly from the three governing equations for free vibration of laminated conical shells under axial load. Numerical results are presented for free vibration of axially loaded laminated conical shells with different geometric parameters and under two types of boundary conditions. It is found that an axial tension increases the frequencies while an axial compression decreases the frequencies. For the shells studied, the effect of axial load on the lowest frequency of the shell is found to be not sensitive to change in semivertex angle when the applied axial load is kept as a constant fraction of the critical buckling load. However, the axial load effect becomes very sensitive to variation in semivertex angle when a constant axial load is applied.

1 Introduction

Due to their high stiffness and strength-to-weight ratios, composite materials have been widely used in aerospace structures, particularly in thin-walled plate and shell-type structures, which have received the continuous attention of researchers and engineers in the past decades. As a special geometrical configuration, the conical shell finds many applications in many industry sectors. For example, a conical shell can be used as a transition structural component between two cylindrical shells of different diameters. Laminated conical shells can be manufactured, for example, using the filament winding technique and have been used in rocket shell structures or in pipeline structures. To achieve an efficient design of laminated conical shells in a shell structure, it is imperative to understand various fundamental behaviors of laminated conical shells. In this paper, the effect of axial load on the free-vibration characteristics will be addressed. The free-vibration problem of isotropic conical shells has been studied by many researchers using different methods, for example, the Rayleigh-Ritz technique (Saunders et al., 1960; Garnet and Kempner, 1964; Siu and Bert, 1970), the numerical integration method (Goldberg et al., 1960; Kalnins, 1964), and the transfer-matrix approach (Irie et al., 1982, 1984).

For free vibration of orthotropic conical shells there have been a few studies (Yang, 1974; Wilkins et al., 1970). For free vibration of laminated conical shells, Tong (1993) obtained a simple and exact solution using the Donnell-type classical shell theory. However, there have been no reports available on the investigation of the axial load effect on free vibration of laminated conical shells. Thus this study focuses on understanding the effect of axial load on frequencies and vibration modes of laminated conical shells and its sensitivity to the semivertex angle of the shell.

The equivalent axial membrane force for the axial load is incorporated into the three governing equilibrium equations. Simple solutions in the form of series are obtained for the three displacements directly from the governing equilibrium equations. Numerical results are presented for free vibration of antisymmetrically crossplied conical shells to show the effect of the axial load on the frequencies in terms of reducing the frequencies when in compression and increasing the frequencies when in tension. The sensitivity of this effect to the semivertex angle is also discussed.

Contributed by the Applied Mechanics Division of THE AMERICAN SOCIETY OF MECHANICAL ENGINEERS for publication in the ASME JOURNAL OF APPLIED MECHANICS.
Discussion on the paper should be addressed to the Technical Editor, Professor Lewis T. Wheeler, Department of Mechanical Engineering, University of Houston, Houston, TX 77204-4792, and will be accepted until four months after final publication of the paper itself in the ASME JOURNAL OF APPLIED MECHANICS.
Manuscript received by the ASME Applied Mechanics Division, July 28, 1998; final revision, Dec. 14, 1998. Associate Technical Editor: W. K. Liu.

2 Governing Equations

Consider a truncated circular conical shell as shown in Fig. 1. The radii at its small and large end are denoted by R_1 and R_2, respectively. The semivertex angle is denoted by α, and the slant length is represented by L. The x-ϕ coordinate system is also shown in Fig. 1, where x is measured along the shell's slant length direction starting at the middle length and ϕ is the circumferential coordinate. Using this coordinate system, we can define the shell's radius at any point along its length as

$$R(x) = R_0 + x \sin \alpha, \tag{1}$$

where R_0 is the average radius of the shell as shown in Fig. 1, i.e., $R_0 = (R_1 + R_2)/2$.

For free vibration of laminated conical shells under axial load, let us denote the displacements of the shell's middle surface along the directions of x, ϕ and the through-thickness direction normal to the middle surface (outward positive) by U, V, and W, respectively. Using the Donnell-type classical shell theory, three equilibrium equations of the shell under axial load P can be written in terms of the three displacements as

$$L_{11}U + L_{12}V + L_{13}W = -\rho h\omega^2 U$$

$$L_{21}U + L_{22}V + L_{23}W = -\rho h\omega^2 V$$

$$L_{31}U + L_{32}V + L_{33}W + L_N W = \rho h\omega^2 W \tag{2}$$

where ρ, ω, and h denote the mass density, frequency, and thickness of the shells, respectively. L_{ij} $(i, j = 1, 2, 3)$ and L_N are the partial differential operators given by

$$L_{11} = A_{11}\frac{\partial^2}{\partial x^2} + \frac{A_{11}\sin\alpha}{R(x)}\frac{\partial}{\partial x} - \frac{A_{22}\sin^2\alpha}{R^2(x)} + \frac{A_{33}}{R^2(x)}\frac{\partial^2}{\partial\phi^2}$$

$$L_{12} = \frac{(A_{12}+A_{33})}{R(x)}\frac{\partial^2}{\partial x\partial\phi} - \frac{(A_{22}+A_{33})\sin\alpha}{R^2(x)}\frac{\partial}{\partial\phi}$$

$$L_{21} = \frac{(A_{12}+A_{33})}{R(x)}\frac{\partial^2}{\partial x\partial\phi} + \frac{(A_{22}+A_{33})\sin\alpha}{R^2(x)}\frac{\partial}{\partial\phi}$$

$$L_{22} = A_{33}\left[\frac{\partial^2}{\partial x^2} + \frac{\sin\alpha}{R(x)}\frac{\partial}{\partial x} - \frac{\sin^2\alpha}{R^2(x)}\right] + \frac{A_{22}}{R^2(x)}\frac{\partial^2}{\partial\phi^2}$$

$$L_{13} = -\frac{A_{12}\cos\alpha}{R(x)}\frac{\partial}{\partial x} + \frac{A_{22}\sin\alpha\cos\alpha}{R^2(x)} - B_{11}\frac{\partial^3}{\partial x^3}$$

$$-\frac{(B_{12}+2B_{33})}{R^2(x)}\frac{\partial^3}{\partial x\partial\phi^2} - \frac{B_{11}\sin\alpha}{R(x)}\frac{\partial^2}{\partial x^2}$$

 Copyright © 1999 by ASME

Downloaded 04 May 2010 to 171.66.16.27. Redistribution subject to ASME license or copyright; see http://www.asme.org/terms/Terms_Use.cfm

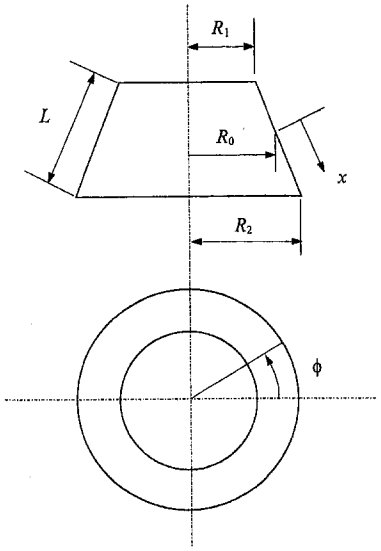


Fig. 1 Geometry and notations of a conical shell

$$+\frac{(B_{12}+B_{22}+2B_{33})\sin\alpha}{R^3(x)}\frac{\partial^2}{\partial\phi^2}+\frac{B_{22}\sin^2\alpha}{R^2(x)}\frac{\partial}{\partial x}$$

$$L_{23}=-\frac{A_{22}\cos\alpha}{R^2(x)}\frac{\partial}{\partial\phi}-\frac{(B_{12}+2B_{33})}{R(x)}\frac{\partial^3}{\partial x\partial\phi^2}-\frac{B_{22}}{R^3(x)}\frac{\partial^3}{\partial\phi^3}$$
$$-\frac{B_{22}\sin\alpha}{R^2(x)}\frac{\partial^2}{\partial x\partial\phi}$$

$$L_{31}=-\frac{A_{12}\cos\alpha}{R(x)}\frac{\partial}{\partial x}-\frac{A_{22}\sin\alpha\cos\alpha}{R^2(x)}-B_{11}\frac{\partial^3}{\partial x^3}$$
$$-\frac{(B_{12}+2B_{33})}{R^2(x)}\frac{\partial^3}{\partial x\partial\phi^2}-\frac{2B_{11}\sin\alpha}{R(x)}\frac{\partial^2}{\partial x^2}$$
$$+\frac{B_{22}\sin^2\alpha}{R^2(x)}\frac{\partial}{\partial x}-\frac{B_{22}\sin\alpha}{R^3(x)}\frac{\partial^2}{\partial\phi^2}-\frac{B_{22}\sin^3\alpha}{R^3(x)}$$

$$L_{32}=-\frac{A_{22}\cos\alpha}{R^2(x)}\frac{\partial}{\partial\phi}-\frac{(B_{12}+2B_{33})}{R(x)}\frac{\partial^3}{\partial x\partial\phi^2}-\frac{B_{22}}{R^3(x)}\frac{\partial^3}{\partial\phi^3}$$
$$+\frac{B_{22}\sin\alpha}{R^2(x)}\frac{\partial^2}{\partial x\partial\phi}-\frac{B_{22}\sin^2\alpha}{R^3(x)}\frac{\partial}{\partial\phi}$$

$$L_{33}=\frac{A_{22}\cos^2\alpha}{R^2(x)}+\frac{2B_{12}\cos\alpha}{R(x)}\frac{\partial^2}{\partial x^2}+\frac{2B_{22}\cos\alpha}{R^3(x)}\frac{\partial^2}{\partial\phi^2}$$
$$+\frac{B_{22}\cos\alpha\sin^2\alpha}{R^3(x)}+D_{11}\frac{\partial^4}{\partial x^4}+\frac{2(D_{12}+2D_{33})}{R^2(x)}$$
$$\times\frac{\partial^4}{\partial x^2\partial\phi^2}+\frac{D_{22}}{R^4(x)}\frac{\partial^4}{\partial\phi^4}+\frac{2D_{11}\sin\alpha}{R(x)}\frac{\partial^3}{\partial x^3}$$
$$-\frac{2(D_{12}+2D_{33})\sin\alpha}{R^3(x)}\frac{\partial^3}{\partial x\partial\phi^2}-\frac{D_{22}\sin^2\alpha}{R^2(x)}\frac{\partial^2}{\partial x^2}$$
$$+\frac{2(D_{12}+D_{22}+2D_{33})\sin^2\alpha}{R^4(x)}\frac{\partial^2}{\partial\phi^2}+\frac{D_{22}\sin^3\alpha}{R^3(x)}\frac{\partial}{\partial x}$$

$$L_N=\frac{P}{2\pi R(x)\cos\alpha}\frac{\partial^2}{\partial x^2} \tag{3}$$

in which A_{ij}, B_{ij} and D_{ij} $(i, j = 1, 2, 3)$ are the components of the stretching stiffness matrix, the membrane-bending coupling matrix, and the bending stiffness matrix of the laminated shells (Tong, 1993). For simplicity, it is assumed that there exist no twisting-coupling terms in the three matrices, namely, $A_{13} = A_{23} = 0$, $B_{13} = B_{23} = 0$, and $D_{13} = D_{23} = 0$.

There exist four boundary conditions along any boundary edge of the shell for the three displacements. In this study, the associated boundary conditions at both ends $x = \pm 0.5L$ of the truncated shell can be expressed, in general, as

$$N_x = 0 \quad \text{or} \quad U = 0$$

$$N_{x\phi} = 0 \quad \text{or} \quad V = 0$$

$$Q_x = 0 \quad \text{or} \quad W = 0$$

$$M_x = 0 \quad \text{or} \quad \frac{\partial W}{\partial x} = 0 \tag{4}$$

where N_x, $N_{x\phi}$, Q_x, and M_x are the membrane stress resultants, transverse shear force, and bending moment, respectively.

Equations (2) and (3) are complex partial differential equations with variable coefficients, and they can be solved using a power series solution procedure. In the following section, general solutions for these three complex governing equations will be described.

3 Solution Procedure

The solution procedure developed in the previous studies (Tong and Wang, 1992; Tong, 1993) was used to study free vibration and buckling of the composite laminated shells separately. In this study, effect of axial load on free vibration of laminated conical shells is included by combining the two solutions. Similar to the previously developed solution forms, let us assume that the solutions for Eqs. (2) take the following form:

$$U = \sum_{m=0}^{\infty} a_m x^m \cos n\phi,$$

$$V = \sum_{m=0}^{\infty} b_m x^m \sin n\phi,$$

$$W = \sum_{m=0}^{\infty} c_m x^m \cos n\phi \tag{5}$$

where n is an integer representing the circumferential wave number of the shell, a_m, b_m, and c_m are constants to be determined later, and m is an integer and represents the number of terms in the power series. In numerical calculation, finite terms will be used instead of infinite number of terms.

Multiplying the first two equations in Eq. (2) with $R^3(x)$ and the third one with $R^4(x)$ yields three modified equations. The coefficients of the modified differential operators in the modified equations are polynomial functions of x only. Substituting Eqs. (5) into these modified equations and matching the terms of the same order in x, the following three recurrence equations for the unknown coefficients in Eqs. (5) can be derived as

$$a_{m+2} = G_{1,1}a_{m+1} + G_{1,2}a_m + G_{1,3}a_{m-1} + G_{1,4}a_{m-2} + G_{1,5}a_{m-3}$$
$$+ G_{1,6}b_{m+1} + G_{1,7}b_m + G_{1,8}b_{m-1} + G_{1,9}c_{m+3}$$
$$+ G_{1,10}c_{m+2} + G_{1,11}c_{m+1} + G_{1,12}c_m + G_{1,13}c_{m-1}$$

$$b_{m+2} = G_{2,1}a_{m+1} + G_{2,2}a_m + G_{2,3}a_{m-1} + G_{2,4}b_{m+1} + G_{2,5}b_m$$
$$+ G_{2,6}b_{m-1} + G_{2,7}b_{m-2} + G_{2,8}b_{m-3} + G_{2,9}c_{m+2}$$
$$+ G_{2,10}c_{m+1} + G_{2,11}c_m + G_{2,12}c_{m-1}$$

Downloaded 04 May 2010 to 171.66.16.27. Redistribution subject to ASME license or copyright; see http://www.asme.org/terms/Terms_Use.cfm

$$c_{m+4} = G_{3,1}a_{m+3} + G_{3,2}a_{m+2} + G_{3,3}a_{m+1} + G_{3,4}a_m + G_{3,5}a_{m-1} + G_{3,6}a_{m-2} + G_{3,7}b_{m+2} + G_{3,8}b_{m+1} + G_{3,9}b_m + G_{3,10}b_{m-1} + G_{3,11}b_{m-2} + G_{3,12}c_{m+3} + G_{3,13}c_{m+2} + G_{3,14}c_{m+1} + G_{3,15}c_m + G_{3,16}c_{m-1} + G_{3,17}c_{m-2} + G_{3,18}c_{m-3} + G_{3,19}c_{m-4} \quad (m = 0, 1, 2, \ldots) \quad (6)$$

where the coefficients $G_{i,j}$ ($(i, j) = (1, 13)$, $(2, 12)$, and $(3, 19)$) can be determined from m and n as well as the geometrical and material parameters. By neglecting the high-order terms in the coefficients $G_{i,j}$ and using the sign alternating property of the series, the convergence condition for the series solutions in Eqs. (5) becomes $R_1 \geq 0$ (Tong, 1993). This indicates that the solution convergence is guaranteed for all truncated shells. By using a very small radius at its small end of the shell, a complete cone can be approximately treated as a truncated one. The above recurrence relations allow us to define the unknown coefficients a_m, b_m ($m = 2, 3, 4, \ldots$) and c_m ($m = 4, 5, 6, \ldots$) in terms of a_k, b_k, and c_l ($k = 0, 1$; $l = 0, 1, 2, 3$), which are the eight unknown constants to be determined by imposing eight boundary conditions at both ends of the shell. The free-vibration frequencies and the related vibration modes can then be determined by setting the determinant of the coefficient matrix, which is obtained via imposing the eight boundary conditions at both ends, to zero.

The solution procedure has been applied separately to buckling and free vibration of laminated conical shells. For the case of buckling of laminated conical shells in axial compression, it was validated numerically (Tong and Wang, 1992) and experimentally (Tong, 1998). For the case of free vibration of laminated conical shells, validity of the solution procedure was demonstrated only numerically due to lack of experimental results in the public literature (Tong, 1993).

4 Results and Discussion

Numerical results are presented for the shells with the following two types of boundary conditions, namely, CC4: $U = W = W_{,x} = V = 0$ and SS4: $N_x = W = M_x = V = 0$, at both ends of the shells. In all calculations, 30 terms in all series were used, and the circumferential wave number was varied from 0 to 12. As the present solution is a combination of the previously validated two solutions (Tong and Wang, 1992; Tong, 1993), only the results for the free vibration of laminated shells under axial load are presented in this section.

Before presenting any results, let us introduce the following notations:

$$\omega_p = \sqrt{\rho h/A_{11}}\,\omega R_2, \quad r = P/P_{cl} \quad (7)$$

where ω denotes the frequency of the shell and ω_p is the frequency parameter, h represents the total wall thickness of the shell, P denotes the actual axial load, and P_{cl} is the modified classical critical buckling load given by

$$P_{cl} = \frac{2\pi E_x h^2 \cos^2\alpha}{\sqrt{3(1 - \nu_{x\phi}^2)}} \quad (8)$$

which originates from the formula proposed by Seide (1956).

To investigate the effect of the membrane-bending coupling terms B_{ij}, let us assume that the shell's lay-up sequence is antisymmetric crossply. In this case, the nonzero terms of A_{ij}, B_{ij} and D_{ij} ($i, j = 1, 2, 3$) are given by

$$A_{11} = A_{22} = \tfrac{1}{2}(Q_{11} + Q_{22})h \quad A_{12} = Q_{12}h, \quad A_{66} = Q_{66}h$$

$$B_{11} = -B_{22} = \pm\frac{1}{4\bar{N}}(Q_{11} - Q_{22})h^2$$

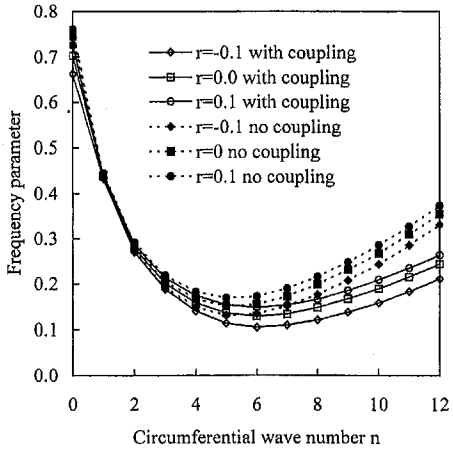


Fig. 2 Frequency parameter versus circumferential wave number n for antisymmetrically crossplied conical shell with α = 30 deg, R_0/t = 100, L/R_0 = 4/3 and C4 boundary conditions

$$D_{11} = D_{22} = \tfrac{1}{24}(Q_{11} + Q_{22})h^3 \quad D_{12} = \tfrac{1}{12}Q_{12}h^3, \quad D_{66} = \tfrac{1}{12}Q_{66}h^3$$

where Q_{ij} are material constants (Tong, 1993), $\bar{N}$ is the total number of layers. The laminated shell attains its maximum membrane-bending coupling when $\bar{N}$ is set to 2. The membrane-bending coupling becomes zero or can be approximated as zero when $\bar{N}$ is set to a big number ($\bar{N}$ was set to 200,000 to approximate no coupling case in this study). It was assumed that all shells are laminated using AS4/3501-6 carbon/epoxy plies. The material properties are: E_x = 142 GPa, E_ϕ = 10.3 GPa, $G_{x\phi}$ = 7.2 GPa, and $\nu_{x\phi}$ = 0.27. For all calculations, the ratio of the average radius to the total wall thickness of the shell, R_0/t, was kept as 100. To study the effect of the axial load on the vibration frequencies and modes, three values of the axial load ratio defined in Eq. (7) were considered, i.e., $r = -0.1$, 0.0, and 0.1. Obviously, the shell is under axial compression when $r = -0.1$ and is under axial tension when $r = 0.1$.

Figures 2–4 show the graphs of the frequency parameter versus the circumferential wave number for laminated shells with both ends clamped (C4) and a semivertex angle of 30, 45, and 60 degrees, respectively. The ratio of the slant length L to the average radius was kept as 4/3. These figures clearly show that the membrane-bending coupling decreases the frequency parameter and this decreasing effect seems to be more significant for the frequencies with large circumferential wave numbers and for those shells with a large semivertex angle. In addition, the membrane-bending coupling also changes the circumferential wave number of the lowest frequency. The axial load doesn't seem to change the ranking sequence of various vibration modes although it changes the values of the frequencies. It can be seen that a compressive load decreases the frequencies indicating a softening effect while a tensile load increases the frequencies showing a stiffening effect.

Figures 5–8 depict the variation of the lowest frequency parameter versus semivertex angle for shells clamped (C4) or simply supported (S4) at both ends and with a ratio of L/R_0 = 2 and 4/3, respectively. It is clearly shown that for a constant axial load ratio r the lowest frequency parameter decreases with an increasing semivertex angle for both long and short shells with both types of boundary conditions and with or without membrane-bending coupling. For long shells, the effect of the membrane-bending coupling on the lowest frequency parameter becomes smaller with an increasing semivertex angle as shown in Figs. 5 and 7. In addition, a comparison between the circumferential wave numbers corresponding to the lowest frequency parameters was conducted. For the two cases studied, it was found that corresponding to the lowest frequency the vibration modes of the shells with membrane-

Downloaded 04 May 2010 to 171.66.16.27. Redistribution subject to ASME license or copyright; see http://www.asme.org/terms/Terms_Use.cfm

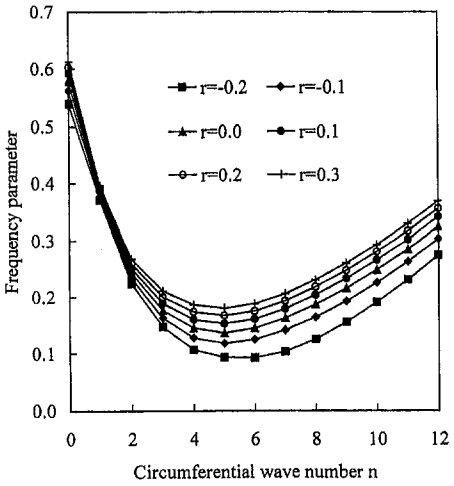


Fig. 3(*a*) Frequency parameter versus circumferential wave number *n* for antisymmetrically crossplied conical shells with α = 45 deg, R_0/t = 100, L/R_0 = 4/3 and C4 boundary conditions and with zero membrane-bending coupling

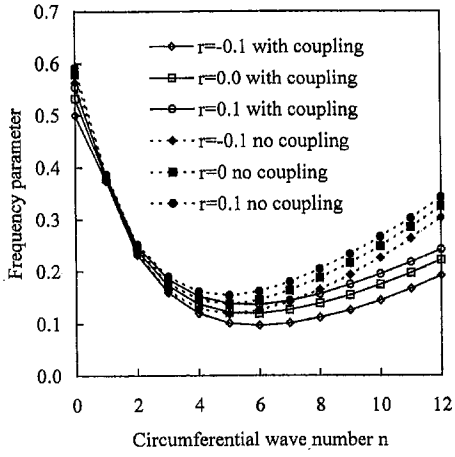


Fig. 3(*b*) Frequency parameter versus circumferential wave number *n* for antisymmetrically crossplied conical shells with α = 45 deg, R_0/t = 100, L/R_0 = 4/3 and C4 boundary conditions

bending coupling are either the same as or have one extra half-sine wave compared to those without membrane-bending coupling.

It is evident that the lowest frequency of a shell decreases when it is subjected to an axial compression and increases when is under

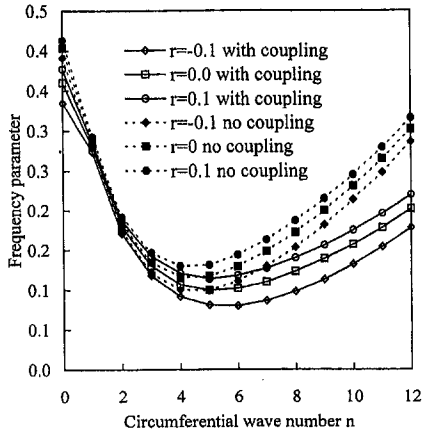


Fig. 4 Frequency parameter versus circumferential wave number *n* for antisymmetrically crossplied shells with α = 60 deg, R_0/t = 100, L/R_0 = 4/3 and C4 boundary conditions

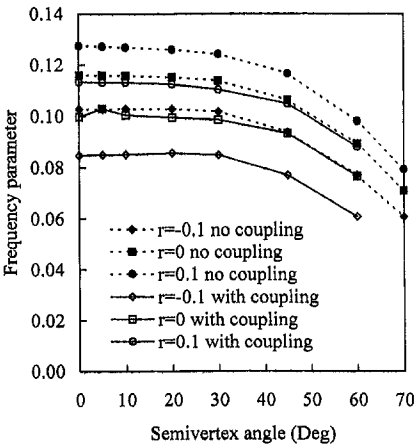


Fig. 5 Lowest frequency parameter versus semivertex angle α for antisymmetrically crossplied conical shell with C4 boundary conditions, L/R_0 = 2 and R_0/t = 100

an axial tension. A comparison of the circumferential wave numbers related to the lowest frequencies shows that an axial compression can cause an increase in the circumferential wave number n and an axial tension can yield a decrease in the circumferential wave number n. For the present two cases, it is found that the vibration mode of a shell under axial load can be changed only one-half wave more or less than those without axial load.

To understand the sensitivity of the axial load effect to the semivertex angle, the following formula was introduced to define the relative difference between the lowest frequency parameters of the loaded and unloaded shells

$$RD = \frac{\omega_p(\alpha, r)/\omega_p(\alpha, r = 0)}{\omega_p(\alpha = 0, r)/\omega_p(\alpha = 0, r = 0)} - 1 \qquad (9)$$

For the present two cases, i.e., $r = -0.1$ and $r = 0.1$, the relative differences were then calculated using the above equation. A comparison of the relative difference reveals that the effect of the axial load on the lowest frequency parameter is not sensitive to the variation of the semivertex angle up to 60 degrees for all shells with both types of boundary conditions. It is found that the relative difference is within one percent when the semivertex angle is less than 60 degrees and is less five

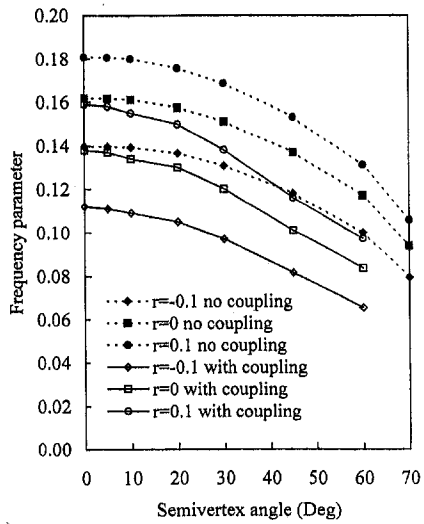


Fig. 6 Lowest frequency parameter versus semivertex angle α for antisymmetrically crossplied conical shell with C4 boundary conditions, L/R_0 = 4/3 and R_0/t = 100

Downloaded 04 May 2010 to 171.66.16.27. Redistribution subject to ASME license or copyright; see http://www.asme.org/terms/Terms_Use.cfm

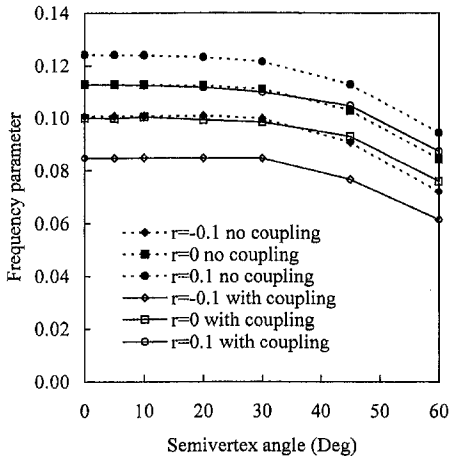


Fig. 7 Lowest frequency parameter versus semivertex angle α for antisymmetrically crossplied conical shell with S4 boundary conditions, $L/R_0 = 2$ and $R_0/t = 100$

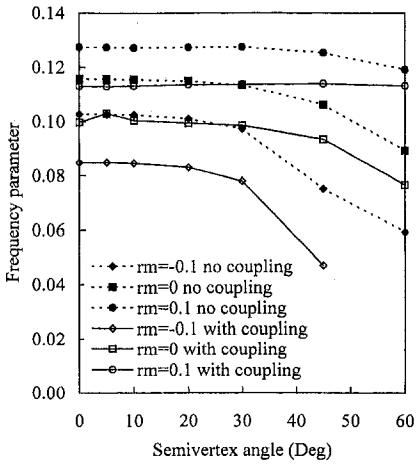


Fig. 9 Lowest frequency parameter versus semivertex angle α for antisymmetrically crossplied conical shell with C4 boundary conditions, $L/R_0 = 2$ and $R_0/t = 100$ and applied constant axial load

percent when the semivertex angle ranges from 60 to 70 degrees. This insensitivity may be attributed to the constant axial load ratio r defined by Eq. (8). As the critical buckling loads for laminated conical shells can be approximated as being proportional to the square of the cosine value of the semivertex angle (Tong, 1994), a constant axial load ratio r means a constant fraction, either positive or negative, of the critical buckling load of the shell. Thus it can be said that the effect of axial load on the lowest frequency is not sensitive to change in the semivertex angle when the applied axial load is a constant fraction of the critical buckling load of the shell. Numerical results also show that the number of circumferential half sine waves tends to decrease with an increasing semivertex angle, namely, from $n = 6$ to $n = 4$ for short shells and from $n = 6$ to $n = 5$ for long shells.

Figure 9 depicts the plots of the lowest frequency parameters versus the semivertex angle for shells clamped (C4) at both ends and with a ratio of $L/R_0 = 2$. In the calculation related to this figure, the axial load was kept as a constant when the semivertex angle was varied. The axial load was defined as

$$P = r_m \frac{2\pi E_x h^2}{\sqrt{3(1 - \nu_{x\phi}^2)}} \tag{10}$$

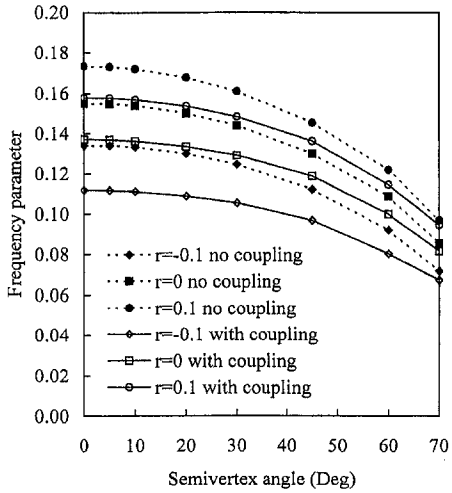


Fig. 8 Lowest frequency parameter versus semivertex angle α for antisymmetrically crossplied conical shell with S4 boundary conditions and $L/R_0 = 4/3$ and $R_0/t = 100$

which is independent of the semivertex angle. When the shells are under an axial tension, the relative differences calculated using Eq. (9) are less than two percent when α is less than 30 degrees, However, when α is greater than 30 degrees, the relative differences become quite significant. For the shells without membrane-bending coupling, the relative differences are 7 percent and 21 percent when $\alpha = 45$ deg and $\alpha = 60$ deg, and for the shells with the membrane-bending coupling, the relative differences becomes 8 percent and 31 percent when $\alpha = 45$ deg and $\alpha = 60$ deg. When the shells are subjected to an axial compression, the calculated relative differences are less than two percent when the semivertex angle is less than 20 degrees. For these shells without membrane-bending coupling, the relative differences are 4 percent, 20 percent, and 25 percent, when $\alpha = 30$ deg, 45 deg, and 60 deg, respectively. For the shells with the stretch-bending coupling, the relative differences become 7 percent and 41 percent for $\alpha = 30$ percent and 45 percent. This observed sensitivity to the semivertex angle could be attributed to the constant applied axial load defined in Eq. (10) that results in an axial load ratio dependent on the semivertex angle α.

5 Conclusions

Based on the present numerical results, the following points can be drawn: (a) the frequencies of the shells decrease with an increasing axial compression and increase with an increasing axial tension; (b) the effect of axial load on the lowest frequencies is not sensitive to variation in the semivertex angle when the applied axial load is kept as a constant fraction of the critical buckling load of the shell; (c) application of the axial load re-ranks the low-order frequencies of the shells in terms of changing the circumferential wave number and has a negligible effect on the high-order frequencies; and (d) shells with membrane-bending coupling have lower frequencies than those without the coupling.

References

Garnet, H., and Kempner, J., 1964, "Axisymmetric Free Vibrations of Conical Shells," ASME JOURNAL OF APPLIED MECHANICS, Vol. 31, pp. 458–466.

Goldberg, J. E., Bogdanoff, J. L., and Marcus, L., 1960, "On the Calculation of the Axisymmetric Modes and Frequencies of Conical Shells," *Journal of Acoustical Society of America,* Vol. 32, p. 738.

Irie, T., Yamada, G., and Kaneko, Y., 1982, "Free Vibration of a Conical Shell With Variable Thickness," *Journal of Sound and Vibration,* Vol. 82, pp. 83–94.

Irie, T., Yamada, G., and Kaneko, Y., 1984, "Natural Frequencies of Truncated Conical Shells," *Journal of Sound and Vibration,* Vol. 92, pp. 447–453.

Kalnins, A., 1964, "Free Vibration of Rotationally Symmetric Shells," *Journal of Acoustical Society of America,* Vol. 36, pp. 1355–1365.

Saunders, H., Wisniewski, E. J., and Pasley, P. R., 1960, "Vibration of Conical Shells," *Journal of Acoustical Society of America,* Vol. 32, pp. 765–772.

Downloaded 04 May 2010 to 171.66.16.27. Redistribution subject to ASME license or copyright; see http://www.asme.org/terms/Terms_Use.cfm

Seide, P., 1956, "Axisymmetrical Buckling of Circular Cones Under Axial Compression," ASME JOURNAL OF APPLIED MECHANICS, Vol. 23, p. 626.

Siu, C. C., and Bert, C. W., 1970, "Free Vibration Analysis of Sandwich Conical Shells With Free Edges," *Journal of Acoustical Society of America,* Vol. 47, p. 943.

Tong, L., 1993, "Free Vibration of Composite Laminated Conical Shells," *International Journal of Mechanical Science,* Vol. 35, pp. 47–61.

Tong, L., 1994, "Buckling Load of Composite Conical Shells Under Axial Compression," ASME JOURNAL OF APPLIED MECHANICS, Vol. 61, pp. 718–719.

Tong, L., 1998, "Buckling of Filament Wound Composite Conical Shells Under Axial Compression," *Proceedings of the 39th AIAA/ASME/ASCE/AHS/ASC Structures, Structural Dynamics, and Materials Conference,* Apr. 20–23, Long Beach, CA, AIAA paper no. 98-1769, pp. 585–594.

Tong, L., and Wang, T. K., 1992, "Simple Solutions for Buckling of Laminated Conical Shells," *International Journal of Mechanical Science,* Vol. 34, pp. 93–111.

Wilkins, Jr., D. J., Bert, C. W., and Egle, D. M., 1970, "Free Vibration of Orthotropic Sandwich Conical Shells With Various Boundary Conditions," *Journal of Sound and Vibration,* Vol. 13, p. 211.

Yang, C. C., 1974, "On Vibration of Orthotropic Conical Shells," *Journal of Sound and Vibration,* Vol. 34, p. 552.

Downloaded 04 May 2010 to 171.66.16.27. Redistribution subject to ASME license or copyright; see http://www.asme.org/terms/Terms_Use.cfm

W.-Q. Chen
Department of Civil Engineering,
Zhejiang University,
Hangzhou 310027,
P. R. China
e-mail: chen_wq@usa.net

T. Shioya
Department of Aeronautics
and Astronautics,
The University of Tokyo,
Tokyo 113-8656, Japan

H.-J. Ding
Department of Civil Engineering,
Zhejiang University,
Hangzhou 310027,
P. R. China

The Elasto-Electric Field for a Rigid Conical Punch on a Transversely Isotropic Piezoelectric Half-Space

This paper exactly analyzes the problem of a rigid conical punch indenting a transversely isotropic piezoelectric half-space. The potential theory method is employed and generalized to include the piezoelectric effect. By using the previous results of pure elasticity, exact solution is derived. It is found that all the elastoelectric variables are expressed in terms of elementary functions. Numerical results are finally performed.

1 Introduction

The indentation of an elastic half-space by rigid punches has been of particular interest and constituted one basic problem in contact mechanics (Gladwell, 1980). Love (1939) firstly investigated the indentation of an isotropic half-space by a rigid cone. Subsequent famous works on this topic include Harding and Sneddon (1945), Sneddon (1948), and Elliot (1949). An excellent description of these works was recently given by Hanson (1992a), who considered the conical indentation including sliding friction for transverse isotropy. Directly integrating the point force Green's functions for a transversely isotropic half-space, Hanson (1992a) obtained expressions of the elastic field in terms of elementary functions by utilizing Fabrikant's results (Fabrikant, 1989). A little later, Hanson (1993a) also presented corresponding solutions for the isotropic case that were derived from the previous solutions for transverse isotropy (Hanson, 1992a) through a limiting procedure. Hanson has also presented exact solutions for spherical Hertzian contact (Hanson, 1992b; Hanson and Johnson, 1993b) and the inclined circular punch (Hanson, 1994). His method is very effective, however, the contact stress in the contact region should be predetermined. It should be noted that in Fabrikant's analysis (Fabrikant, 1988) of a circular punch frictionless indentation, which was based on the new results in potential theory developed by himself, the distribution of the normal stress in the contact region was obtained as part of the complete solution.

Due to the particular coupling effect between mechanical deformation and electric field, piezoelectric materials (PZMs) have been widely used in various areas of science and technology (Rao and Sunar, 1994). A lot of theoretical investigations on piezoelectric materials and structures have appeared (see Pak (1990), Ding et al. (1997a, 1997b), Ashida and Tauchert (1998), and Chen (1999) for examples).

The method of sharp indentation (microhardness indentation measurement) has been effectively used to evaluate toughness levels in brittle ceramics (Hertzberg, 1989). Also, abrasive wear of ceramic surfaces by sharp asperities or wear debris can be modeled as sharp indentation (Hanson, 1992a). It is therefore of practical importance to understand the mechanics of sharp indentation and the resulting stress field. Though great efforts have been made to analyze the sharp indentation of isotropic and transversely isotropic elastic materials as mentioned above, there is entirely no work for PZMs. The only relative study was recently conducted by Fan et al. (1996), who considered the two-dimensional contact problem of a piezoelectric half-plane by the means of Stroh's formalism.

The purpose of this paper is to develop a closed-form solution for the problem of a rigid conical and electrically conductive punch indenting a transversely isotropic piezoelectric half-space. The general solution recently proposed by Ding et al. (1997b) allows us to employ the potential theory method, which is generalized in the paper by the introduction of a new potential that corresponds to the electric field in PZM. Since the two derived integral equations have the same form as that for pure elasticity, the results of Fabrikant (1989) can be applied. Some results presented in Hanson (1992a) are also used to obtain the exact expressions for the elastoelectric field.

2 Governing Equations and the General Solution

In Cartesian coordinates (with the z-axis being normal to the plane of isotropy), the linear constitutive relations of a transversely isotropic piezoelectric medium can be expressed as (Tiersten, 1969)

$$\sigma_x = c_{11}\frac{\partial u}{\partial x} + (c_{11} - 2c_{66})\frac{\partial v}{\partial y} + c_{13}\frac{\partial w}{\partial z} + e_{31}\frac{\partial \Phi}{\partial z},$$

$$\tau_{xz} = c_{44}\left(\frac{\partial u}{\partial z} + \frac{\partial w}{\partial x}\right) + e_{15}\frac{\partial \Phi}{\partial x},$$

$$\sigma_y = (c_{11} - 2c_{66})\frac{\partial u}{\partial x} + c_{11}\frac{\partial v}{\partial y} + c_{13}\frac{\partial w}{\partial z} + e_{31}\frac{\partial \Phi}{\partial z},$$

$$\tau_{yz} = c_{44}\left(\frac{\partial v}{\partial z} + \frac{\partial w}{\partial y}\right) + e_{15}\frac{\partial \Phi}{\partial y},$$

$$\sigma_z = c_{13}\frac{\partial u}{\partial x} + c_{13}\frac{\partial v}{\partial y} + c_{33}\frac{\partial w}{\partial z} + e_{33}\frac{\partial \Phi}{\partial z},$$

$$\tau_{xy} = c_{66}\left(\frac{\partial u}{\partial y} + \frac{\partial v}{\partial x}\right),$$

$$D_x = e_{15}\left(\frac{\partial u}{\partial z} + \frac{\partial w}{\partial x}\right) - \epsilon_{11}\frac{\partial \Phi}{\partial x},$$

Contributed by the Applied Mechanics Division of THE AMERICAN SOCIETY OF MECHANICAL ENGINEERS for publication in the ASME JOURNAL OF APPLIED MECHANICS.
Discussion on the paper should be addressed to the Technical Editor, Professor Lewis T. Wheeler, Department of Mechanical Engineering, University of Houston, Houston, TX 77204-4792, and will be accepted until four months after final publication of the paper itself in the ASME JOURNAL OF APPLIED MECHANICS.
Manuscript received by the ASME Applied Mechanics Division, Aug. 14, 1998; final revision, Jan. 11, 1999. Associate Technical Editor: J. R. Barber.

 Copyright © 1999 by ASME

Downloaded 04 May 2010 to 171.66.16.27. Redistribution subject to ASME license or copyright; see http://www.asme.org/terms/Terms_Use.cfm

$$D_y = e_{15}\left(\frac{\partial v}{\partial z} + \frac{\partial w}{\partial y}\right) - \epsilon_{11}\frac{\partial \Phi}{\partial y},$$

$$D_z = e_{31}\frac{\partial u}{\partial x} + e_{31}\frac{\partial v}{\partial y} + e_{33}\frac{\partial w}{\partial z} - \epsilon_{33}\frac{\partial \Phi}{\partial z}, \quad (1)$$

where Φ and D_i are the electric potential and electric displacement vector, respectively; the displacements are denoted as u, v, and w in the x, y, and z-directions, respectively; σ_i and τ_{ij} are the normal and shear stresses, respectively. c_{ij}, ϵ_{ij}, and e_{ij} are the elastic, dielectric, and piezoelectric constants, respectively. The governing equations also can be found in Tiersten (1969). By introducing the tangential complex displacement $U = u + iv$, these equations can be rewritten in a complex manner as follows:

$$\frac{1}{2}(c_{11} + c_{66})\Delta U + c_{44}\frac{\partial^2 U}{\partial z^2} + \frac{1}{2}(c_{11} - c_{66})\Lambda^2 \bar{U} + (c_{13} + c_{44})\Lambda\frac{\partial w}{\partial z} + (e_{15} + e_{31})\Lambda\frac{\partial \Phi}{\partial z} = 0,$$

$$\frac{1}{2}(c_{13} + c_{44})\frac{\partial}{\partial z}(\bar{\Lambda}U + \Lambda\bar{U}) + c_{44}\Delta w + c_{33}\frac{\partial^2 w}{\partial z^2} + e_{15}\Delta\Phi + e_{33}\frac{\partial^2 \Phi}{\partial z^2} = 0,$$

$$\frac{1}{2}(e_{15} + e_{31})\frac{\partial}{\partial z}(\bar{\Lambda}U + \Lambda\bar{U}) + e_{15}\Delta w + e_{33}\frac{\partial^2 w}{\partial z^2} - \epsilon_{11}\Delta\Phi - \epsilon_{33}\frac{\partial^2 \Phi}{\partial z^2} = 0, \quad (2)$$

where $\Delta = \partial^2/\partial x^2 + \partial^2/\partial y^2$, $\Lambda = \partial/\partial x + i\partial/\partial y$, and the overbar indicates the complex conjugate value. Ding et al. (1997b) recently presented a simple form general solution to the governing equations of a transversely isotropic piezoelectric body. The solution can be rewritten in the following form:

$$U = \Lambda\left(\sum_{i=1}^{3} F_i + iF_4\right), \quad w = \sum_{i=1}^{3}\alpha_{i1}\frac{\partial F_i}{\partial z_i},$$

$$\Phi = \sum_{i=1}^{3}\alpha_{i2}\frac{\partial F_i}{\partial z_i}, \quad (3)$$

where

$$\alpha_{i1} = \frac{c_{11}\epsilon_{11} - m_3 s_i^2 + c_{44}\epsilon_{33}s_i^4}{(m_1 - m_2 s_i^2)s_i},$$

$$\alpha_{i2} = \frac{c_{11}e_{15} - m_4 s_i^2 + c_{44}e_{33}s_i^4}{(m_1 - m_2 s_i^2)s_i},$$

$$m_1 = \epsilon_{11}(c_{13} + c_{44}) + e_{15}(e_{15} + e_{31}),$$

$$m_2 = \epsilon_{33}(c_{13} + c_{44}) + e_{33}(e_{15} + e_{31}),$$

$$m_3 = c_{11}\epsilon_{33} + c_{44}\epsilon_{11} + (e_{15} + e_{31})^2,$$

$$m_4 = c_{11}e_{33} + c_{44}e_{15} - (c_{13} + c_{44})(e_{15} + e_{31}) \quad (4)$$

and $z_i = s_i z$, $s_4^2 = c_{66}/c_{44}$, and s_i^2 $(i = 1, 2, 3)$ are the roots of the following algebraic equation:

$$n_0 s^6 - n_1 s^4 + n_2 s^2 - n_3 = 0, \quad (5)$$

where

$$n_0 = c_{44}(e_{33}^2 + c_{33}\epsilon_{33}),$$

$$n_1 = c_{33}m_3 + \epsilon_{33}[c_{44}^2 - (c_{13} + c_{44})^2] + e_{33}(2m_4 - c_{11}e_{33}),$$

$$n_2 = c_{44}m_3 + \epsilon_{11}[c_{11}c_{33} - (c_{13} + c_{44})^2] + e_{15}(2m_4 - c_{44}e_{15}),$$

$$n_3 = c_{11}(e_{15}^2 + c_{44}\epsilon_{11}).$$

It is noted here that the general solution as shown in Eq. (3) is only valid for distinct s_i^2, while different forms should be adopted for other cases (Ding et al., 1997b).

In addition, function $F_i(z)$ satisfies the following quasi-harmonic equation:

$$\left(\Delta + \frac{\partial^2}{\partial z_i^2}\right)F_i = 0, \quad (i = 1, 2, 3, 4). \quad (6)$$

From Eqs. (1) and (3), the expressions for stresses and electric displacements are derived:

$$\sigma_1 = 2\sum_{i=1}^{3}[(c_{66} - c_{11}) + c_{13}s_i\alpha_{i1} + e_{31}s_i\alpha_{i2}]\frac{\partial^2}{\partial z_i^2}F_i$$

$$= 2\sum_{i=1}^{3}[(c_{11} - c_{66}) - c_{13}s_i\alpha_{i1} - e_{31}s_i\alpha_{i2}]\Delta F_i,$$

$$\sigma_2 = 2c_{66}\Lambda^2(F_1 + F_2 + F_3 + iF_4),$$

$$\sigma_z = \sum_{i=1}^{3}\gamma_{1i}\frac{\partial^2}{\partial z_i^2}F_i = -\sum_{i=1}^{3}\gamma_{1i}\Delta F_i,$$

$$\tau_z = \Lambda\left(\sum_{i=1}^{3}[c_{44}(s_i + \alpha_{i1}) + e_{15}\alpha_{i2}]\frac{\partial}{\partial z_i}F_i + is_4c_{44}\frac{\partial}{\partial z_4}F_4\right),$$

$$D = \Lambda\left\{\sum_{i=1}^{3}[e_{15}(s_i + \alpha_{i1}) - \epsilon_{11}\alpha_{i2}]\frac{\partial}{\partial z_i}F_i + is_4e_{15}\frac{\partial}{\partial z_4}F_4\right\},$$

$$D_z = \sum_{i=1}^{3}\gamma_{2i}\frac{\partial^2}{\partial z_i^2}F_i = -\sum_{i=1}^{3}\gamma_{2i}\Delta F_i, \quad (7)$$

where

$$\sigma_1 = \sigma_x + \sigma_y, \quad \sigma_2 = \sigma_x - \sigma_y + 2i\tau_{xy},$$

$$\tau_z = \tau_{xz} + i\tau_{yz}, \; D = D_x + iD_y,$$

$$\gamma_{1i} = -c_{13} + c_{33}s_i\alpha_{i1} + e_{33}s_i\alpha_{i2},$$

$$\gamma_{2i} = -e_{31} + e_{33}s_i\alpha_{i1} - \epsilon_{33}s_i\alpha_{i2}. \quad (8)$$

3 The Potential Theory Method

At first, let's consider the general mixed boundary value problem of a transversely isotropic piezoelectric half-space $z \geq 0$, with the following boundary conditions on the surface $z = 0$:

$$w = \omega(x, y), \quad \Phi = \varphi(x, y), \quad \text{for} \quad (x, y) \in S;$$

$$\sigma_z = D_z = 0, \quad \text{for} \quad (x, y) \notin S;$$

$$\tau_z = 0, \quad \text{for} \quad -\infty < (x, y) < \infty, \quad (9)$$

where S represents the contact area. In general, the displacement and electric potential are prescribed in the contact region (Fan et al., 1996), as denoted by ω and φ, respectively, in Eq. (9). Now assume

$$F_i(z) = c_i G(z_i) + d_i H(z_i), \quad (i = 1, 2, 3); \quad F_4(z) = 0, \quad (10)$$

Downloaded 04 May 2010 to 171.66.16.27. Redistribution subject to ASME license or copyright; see http://www.asme.org/terms/Terms_Use.cfm

where c_i and d_i are undetermined constants. To satisfy the third condition in Eq. (9), noticing the identity $\gamma_{1i}s_i = c_{44}(s_i + \alpha_{i1}) + e_{15}\alpha_{i2}$, one may set

$$\sum_{i=1}^{3} c_i\gamma_{1i}s_i = 0, \quad \sum_{i=1}^{3} d_i\gamma_{1i}s_i = 0. \tag{11}$$

The two functions G and H are given as

$$G(\rho, \phi, z) = \int\int_S \ln [R(M, N) + z]\sigma_0(N)dS,$$

$$H(\rho, \phi, z) = \int\int_S \ln [R(M, N) + z]D_0(N)dS, \tag{12}$$

where $\sigma_0(N)$ and $D_0(N)$ stand for values of σ_z and D_z at the point $N(r, \psi, 0)$, respectively, $R(M, N)$ is the distance between the points $M(\rho, \phi, z)$ and $N(r, \psi, 0)$, and the integration is taken over the contact region S. Hereafter, the cylindrical coordinates (ρ, ϕ, z) are alternatively used for the sake of convenience. In contrast to pure elasticity (Fabrikant, 1989), a new potential H has been introduced above to take consideration of the effect of the electric field in PZM. Making use of the property of the potential of a simple layer, it is known that the second condition in Eq. (9) is identically satisfied, while inside the contact region S one has

$$\left.\frac{\partial^2 G}{\partial z^2}\right|_{z=0} = -2\pi\sigma_0, \quad \left.\frac{\partial^2 H}{\partial z^2}\right|_{z=0} = -2\pi D_0. \tag{13}$$

The following relations then can be obtained from Eqs. (7), (10), and (13):

$$\sum_{i=1}^{3} c_i\gamma_{1i} = -\frac{1}{2\pi}, \quad \sum_{i=1}^{3} d_i\gamma_{1i} = 0,$$

$$\sum_{i=1}^{3} c_i\gamma_{2i} = 0, \quad \sum_{i=1}^{3} d_i\gamma_{2i} = -\frac{1}{2\pi}. \tag{14}$$

Solving Eqs. (11) and (14) gives

$$\begin{Bmatrix} c_1 \\ c_2 \\ c_3 \end{Bmatrix} = -\frac{1}{2\pi}\begin{bmatrix} \gamma_{11}s_1 & \gamma_{12}s_2 & \gamma_{13}s_3 \\ \gamma_{11} & \gamma_{12} & \gamma_{13} \\ \gamma_{21} & \gamma_{22} & \gamma_{23} \end{bmatrix}^{-1}\begin{Bmatrix} 0 \\ 1 \\ 0 \end{Bmatrix},$$

$$\begin{Bmatrix} d_1 \\ d_2 \\ d_3 \end{Bmatrix} = -\frac{1}{2\pi}\begin{bmatrix} \gamma_{11}s_1 & \gamma_{12}s_2 & \gamma_{13}s_3 \\ \gamma_{11} & \gamma_{12} & \gamma_{13} \\ \gamma_{21} & \gamma_{22} & \gamma_{23} \end{bmatrix}^{-1}\begin{Bmatrix} 0 \\ 0 \\ 1 \end{Bmatrix}. \tag{15}$$

The expressions for displacements and electric potential can be derived from Eqs. (3), (10), and (12). It is then shown that the first condition in Eq. (9) gives rise to the following integral equations:

$$\omega(N_0) = g_1\int\int_S \frac{\sigma_0(N)}{R(N_0, N)}\,dS + g_2\int\int_S \frac{D_0(N)}{R(N_0, N)}\,dS,$$

$$\varphi(N_0) = g_3\int\int_S \frac{\sigma_0(N)}{R(N_0, N)}\,dS + g_4\int\int_S \frac{D_0(N)}{R(N_0, N)}\,dS, \tag{16}$$

where both the points N_0, $N \in S$, and

$$g_1 = \sum_{i=1}^{3} c_i\alpha_{i1}, \quad g_2 = \sum_{i=1}^{3} d_i\alpha_{i1},$$

$$g_3 = \sum_{i=1}^{3} c_i\alpha_{i2}, \quad g_4 = \sum_{i=1}^{3} d_i\alpha_{i2}. \tag{17}$$

From Eq. (16) it is obtained that

$$g_4\omega(N_0) - g_2\varphi(N_0) = A\int\int_S \frac{\sigma_0(N)}{R(N_0, N)}\,dS, \tag{18}$$

$$g_1\varphi(N_0) - g_3\omega(N_0) = A\int\int_S \frac{D_0(N)}{R(N_0, N)}\,dS, \tag{19}$$

where $A = g_1g_4 - g_2g_3$. Thus, for an arbitrarily shaped punch, two integral equations that have the same structure as that for pure elasticity have been set up. In general, Eqs. (18) and (19) can be solved using numerical methods. For the case that the contact area is circular, Eqs. (18) and (19) can be written in the following forms:

$$g_4\omega(\rho_0, \phi_0) - g_2\varphi(\rho_0, \phi_0) = A\int_0^{2\pi}\int_0^a \frac{\sigma_0(r, \psi)}{[\rho_0^2 + r^2 - 2\rho_0 r\cos(\phi_0 - \psi)]^{1/2}}\,rdrd\psi, \tag{20}$$

$$g_1\varphi(\rho_0, \phi_0) - g_3\omega(\rho_0, \phi_0) = A\int_0^{2\pi}\int_0^a \frac{D_0(r, \psi)}{[\rho_0^2 + r^2 - 2\rho_0 r\cos(\phi_0 - \psi)]^{1/2}}\,rdrd\psi, \tag{21}$$

where a is the radius of the contact region. By using the results of Fabrikant (1989), closed-form expressions for G and H can be obtained from Eqs. (20), (21), and (12) as follows:

$$G(\rho, \phi, z) = \frac{1}{\pi^2 A}\int_0^{2\pi}\int_0^a K(\rho, \phi, z; \rho_0, \phi_0) \times [g_4\omega(\rho_0, \phi_0) - g_2\varphi(\rho_0, \phi_0)]\rho_0 d\rho_0 d\phi_0,$$

$$H(\rho, \phi, z) = \frac{1}{\pi^2 A}\int_0^{2\pi}\int_0^a K(\rho, \phi, z; \rho_0, \phi_0) \times [g_1\varphi(\rho_0, \phi_0) - g_3\omega(\rho_0, \phi_0)]\rho_0 d\rho_0 d\phi_0, \tag{22}$$

where function K reads

$$K(\rho, \phi, z; \rho_0, \phi_0) = -\frac{1}{R_0}\tan^{-1}\left(\frac{h}{R_0}\right) + \frac{1}{(a^2 - \rho_0^2)^{1/2}}\left\{\ln\left[\frac{a + (a^2 - l_1^2)^{1/2}}{l_1}\right] + \frac{1}{(\zeta - 1)^{1/2}}\tan^{-1}\left[\frac{(a^2 - l_1^2)^{1/2}}{a(\zeta - 1)^{1/2}}\right] + \frac{1}{(\bar{\zeta} - 1)^{1/2}}\tan^{-1}\left[\frac{(a^2 - l_1^2)^{1/2}}{a(\bar{\zeta} - 1)^{1/2}}\right]\right\}, \tag{23}$$

with

$$\zeta = e^{i(\phi - \phi_0)}\rho/\rho_0,$$

$$R_0 = [\rho^2 + \rho_0^2 - 2\rho\rho_0\cos(\phi - \phi_0) + z^2]^{1/2},$$

$$l_1 = \tfrac{1}{2}\{[(\rho + a)^2 + z^2]^{1/2} - [(\rho - a)^2 + z^2]^{1/2}\},$$

$$h = (a^2 - l_1^2)^{1/2}(a^2 - \rho_0^2)^{1/2}/a. \tag{24}$$

All the Green's functions related to elastoelectric field of displacements, stresses, electric displacements and electric potential can be

Downloaded 04 May 2010 to 171.66.16.27. Redistribution subject to ASME license or copyright; see http://www.asme.org/terms/Terms_Use.cfm

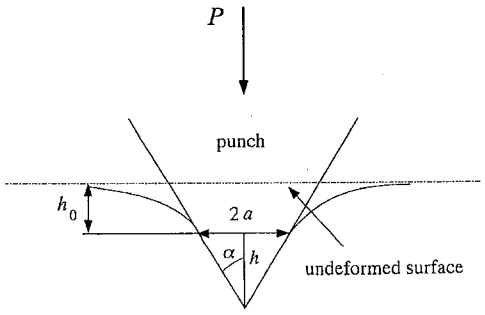


Fig. 1 Geometry of the conical indentation

obtained in elementary functions from Eq. (23) by differentiation; these can be found in Fabrikant (1988) and are not repeated here.

4 The Complete Solution for a Conical Indentation

The indentation of a transversely isotropic piezoelectric half-space by a rigid circular cone is now considered. It is assumed the cone is applied centrally by a concentrated force P that yields settlement h_0 at the edge of the contact region and $h + h_0$ at the center. The geometry of the problem is shown in Fig. 1. This gives the expression for the normal displacement in the contact region as $\omega(\rho, \phi) = h_0 + h(1 - \rho/a)$ for $\rho \le a$. It is further assumed that the cone is electrically conductive and is maintained at a constant electric potential Φ_0 (For practical convenience, it can be grounded so that $\Phi_0 = 0$), i.e., $\varphi(\rho, \phi) = \Phi_0$ for $\rho \le a$. It can be seen from Eq. (22) that the complete solution can be divided into two parts: The first part corresponds to ω and the second to φ. In what follows, they will be dealt separately with the first one labeled by superscript I and the second by II.

The solution of the first part can be obtained by comparing with the solution for pure elasticity (Hanson, 1992a)

$$\sigma_0^{\mathrm{I}}(\rho, \phi) = \frac{g_4 h}{2\pi A a} \cosh^{-1}\left(\frac{a}{\rho}\right),$$

$$D_0^{\mathrm{I}}(\rho, \phi) = -\frac{g_3 h}{2\pi A a} \cosh^{-1}\left(\frac{a}{\rho}\right), \tag{25}$$

with $h_0 = (\pi/2 - 1)h$. Substitution of Eq. (25) into Eq. (12) gives the expressions of G and H of the first part as follows:

$$G^{\mathrm{I}}(\rho, \phi, z) = \frac{g_4 h}{2\pi a A}\,\Omega(\rho, \phi, z),$$

$$H^{\mathrm{I}}(\rho, \phi, z) = -\frac{g_3 h}{2\pi a A}\,\Omega(\rho, \phi, z), \tag{26}$$

where function $\Omega(\rho, \phi, z)$ has been calculated by Hanson (1992a),

$$\Omega(\rho, \phi, z) = 2\pi\Bigg\{ az \sin^{-1}\left(\frac{a}{l_2}\right) + \frac{1}{4}(2a^2 + \rho^2 - 2z^2) \times \ln\left[l_2 + (l_2^2 - \rho^2)^{1/2}\right] - \frac{3z(\rho^2 + z^2)^{1/2}}{4} + \frac{3l_2(\rho^2 - 2l_1^2)(a^2 - l_1^2)^{1/2}}{4\rho l_1} - \frac{\rho^2 - 2z^2}{4} \times \ln\left[\rho + (\rho^2 + z^2)^{1/2}\right]\Bigg\} \tag{27}$$

where $l_2 = \frac{1}{2}\{[(\rho + a)^2 + z^2]^{1/2} + [(\rho - a)^2 + z^2]^{1/2}\}$. The solution of the second part can be easily obtained by utilizing Fabrikant's results for a centrally loaded circular flat punch (Fabrikant, 1988). In fact, it can be shown

$$\sigma_0^{\mathrm{II}}(\rho, \phi) = -\frac{g_2 \Phi_0}{\pi^2 A (a^2 - \rho^2)^{1/2}},$$

$$D_0^{\mathrm{II}}(\rho, \phi) = \frac{g_1 \Phi_0}{\pi^2 A (a^2 - \rho^2)^{1/2}}, \tag{28}$$

and

$$G^{\mathrm{II}}(\rho, \phi, z) = -\frac{2g_2\Phi_0}{\pi A}\left\{ z \sin^{-1}\left(\frac{a}{l_2}\right) - (a^2 - l_1^2)^{1/2} + a \ln\left[l_2 + (l_2^2 - \rho^2)^{1/2}\right]\right\},$$

$$H^{\mathrm{II}}(\rho, \phi, z) = \frac{2g_1\Phi_0}{\pi A}\left\{ z \sin^{-1}\left(\frac{a}{l_2}\right) - (a^2 - l_1^2)^{1/2} + a \ln\left[l_2 + (l_2^2 - \rho^2)^{1/2}\right]\right\}. \tag{29}$$

Substitution of Eqs. (26) and (29) into Eq. (10) and these in turn into Eqs. (3) and (7) gives rise to the expressions for all elasto-electric field variables. They are expressed in terms of elementary functions as follows:

$$U^{\mathrm{I}} = \frac{he^{i\phi}}{Aa}\sum_{i=1}^{3} k_{1i} \times \left\{ \frac{(\rho l_{2i} - 2a l_{1i})(l_{2i}^2 - \rho^2)^{1/2}}{2\rho^2} + \frac{\rho}{2}\ln\left[l_{2i} + (l_{2i}^2 - \rho^2)^{1/2}\right] - \frac{z_i(\rho^2 + z_i^2)^{1/2}}{2\rho} - \frac{\rho}{2}\ln\left[z_i + (z_i^2 + \rho^2)^{1/2}\right] + \frac{a^2}{2\rho}\right\},$$

$$w^{\mathrm{I}} = \frac{h}{Aa}\sum_{i=1}^{3} \alpha_{i1} k_{1i}\Big\{ a \sin^{-1}\left(\frac{a}{l_{2i}}\right) + (l_{2i}^2 - a^2)^{1/2} - (\rho^2 + z_i^2)^{1/2} - z_i \ln\left[l_{2i} + (l_{2i}^2 - \rho^2)^{1/2}\right] + z_i \ln\left[z_i + (\rho^2 + z_i^2)^{1/2}\right]\Big\},$$

$$\Phi^{\mathrm{I}} = \frac{h}{Aa}\sum_{i=1}^{3} \alpha_{i2} k_{1i} \times \left\{ a \sin^{-1}\left(\frac{a}{l_{2i}}\right) + (l_{2i}^2 - a^2)^{1/2} - (\rho^2 + z_i^2)^{1/2} - z_i \ln\left[l_{2i} + (l_{2i}^2 - \rho^2)^{1/2}\right] + z_i \ln\left[z_i + (\rho^2 + z_i^2)^{1/2}\right]\right\},$$

$$\sigma_1^{\mathrm{I}} = -\frac{2h}{Aa}\sum_{i=1}^{3} k_{1i}[(c_{66} - c_{11}) + c_{13}s_i\alpha_{i1} + e_{31}s_i\alpha_{i2}] \times \{\ln\left[l_{2i} + (l_{2i}^2 - \rho^2)^{1/2}\right] - \ln\left[z_i + (z_i^2 + \rho^2)^{1/2}\right]\},$$

$$\sigma_2^{\mathrm{I}} = \frac{2hc_{66}e^{i2\phi}}{Aa}\sum_{i=1}^{3} k_{1i} \times \left[\frac{(2a^2 - l_{2i}^2)(a^2 - l_{1i}^2)^{1/2}}{a\rho^2} + \frac{z_i(\rho^2 + z_i^2)^{1/2} - a^2}{\rho^2}\right],$$

Downloaded 04 May 2010 to 171.66.16.27. Redistribution subject to ASME license or copyright; see http://www.asme.org/terms/Terms_Use.cfm

$$\sigma_z^{\mathrm{I}} = -\frac{h}{Aa}\sum_{i=1}^{3}\gamma_{1i}k_{1i} \times \{\ln[l_{2i} + (l_{2i}^2 - \rho^2)^{1/2}] - \ln[z_i + (z_i^2 + \rho^2)^{1/2}]\},$$

$$\tau_z^{\mathrm{I}} = \frac{he^{i\phi}}{Aa}\sum_{i=1}^{3}[c_{44}(s_i + \alpha_{i1}) + e_{15}\alpha_{i1}] \times k_{1i}\frac{(l_{2i}^2 - a^2)^{1/2} - (\rho^2 + z_i^2)^{1/2}}{\rho},$$

$$D^{\mathrm{I}} = \frac{he^{i\phi}}{Aa}\sum_{i=1}^{3}[e_{15}(s_i + \alpha_{i1}) - \epsilon_{11}\alpha_{i2}] \times k_{1i}\frac{(l_{2i}^2 - a^2)^{1/2} - (\rho^2 + z_i^2)^{1/2}}{\rho},$$

$$D_z^{\mathrm{I}} = -\frac{h}{Aa}\sum_{i=1}^{3}\gamma_{2i}k_{1i} \times \{\ln[l_{2i} + (l_{2i}^2 - \rho^2)^{1/2}] - \ln[z_i + (z_i^2 + \rho^2)^{1/2}]\}, \quad (30)$$

for the first part, and

$$U^{\mathrm{II}} = \frac{2\Phi_0 ae^{i\phi}}{\pi A\rho}\sum_{i=1}^{3}k_{2i}\left[1 - \frac{(a^2 - l_{1i}^2)^{1/2}}{a}\right],$$

$$w^{\mathrm{II}} = \frac{2\Phi_0}{\pi A}\sum_{i=1}^{3}\alpha_{i1}k_{2i}\sin^{-1}\left(\frac{a}{l_{2i}}\right),$$

$$\Phi^{\mathrm{II}} = \frac{2\Phi_0}{\pi A}\sum_{i=1}^{3}\alpha_{i2}k_{2i}\sin^{-1}\left(\frac{a}{l_{2i}}\right),$$

$$\sigma_1^{\mathrm{II}} = -\frac{4\Phi_0}{\pi A} \times \sum_{i=1}^{3}k_{2i}[(c_{66} - c_{11}) + c_{13}s_i\alpha_{i1} + e_{31}s_i\alpha_{i2}]\frac{(a^2 - l_{1i}^2)^{1/2}}{l_{2i}^2 - l_{1i}^2},$$

$$\sigma_2^{\mathrm{II}} = \frac{4\Phi_0 c_{66}e^{2i\phi}}{\pi A} \times \sum_{i=1}^{3}k_{2i}\left\{\frac{(a^2 - l_{1i}^2)^{1/2}}{l_{2i}^2 - l_{1i}^2} - \frac{2a}{\rho^2}\left[1 - \frac{(a^2 - l_{1i}^2)^{1/2}}{a}\right]\right\},$$

$$\sigma_z^{\mathrm{II}} = -\frac{2\Phi_0}{\pi A}\sum_{i=1}^{3}\gamma_{1i}k_{2i}\frac{(a^2 - l_{1i}^2)^{1/2}}{l_{2i}^2 - l_{1i}^2},$$

$$\tau_z^{\mathrm{II}} = -\frac{2\Phi_0 e^{i\phi}}{\pi A}\sum_{i=1}^{3}[c_{44}(s_i + \alpha_{i1}) + e_{15}\alpha_{i1}]k_{2i}\frac{l_{1i}(l_{2i}^2 - a^2)^{1/2}}{l_{2i}(l_{2i}^2 - l_{1i}^2)},$$

$$D^{\mathrm{II}} = -\frac{2\Phi_0 e^{i\phi}}{\pi A}\sum_{i=1}^{3}[e_{15}(s_i + \alpha_{i1}) - \epsilon_{11}\alpha_{i2}]k_{2i}\frac{l_{1i}(l_{2i}^2 - a^2)^{1/2}}{l_{2i}(l_{2i}^2 - l_{1i}^2)},$$

$$D_z^{\mathrm{II}} = -\frac{2\Phi_0}{\pi A}\sum_{i=1}^{3}\gamma_{2i}k_{2i}\frac{(a^2 - l_{1i}^2)^{1/2}}{l_{2i}^2 - l_{1i}^2}, \quad (31)$$

for the second part. In Eqs. (30) and (31), $k_{1i} = c_i g_4 - d_i g_3$ and $k_{2i} = d_i g_1 - c_i g_2$, and the notations $l_{1;2i} = \frac{1}{2}\{[(\rho + a)^2 + z_i^2]^{1/2} \mp [(\rho - a)^2 + z_i^2]^{1/2}\}$ have been employed.

5 Contact Parameters and the Intensity Factors

Integrating $\sigma_0^{\mathrm{I}} + \sigma_0^{\mathrm{II}}$ over the contact area gives

$$P = P^{\mathrm{I}} + P^{\mathrm{II}} = -\frac{g_4 ha}{2A} + \frac{2g_2\Phi_0 a}{\pi A}. \quad (32)$$

Since $h = a\cot\alpha$ (see Fig. 1), it can be seen from Eq. (32) that a, the main contact parameter, can be determined in terms of the applied concentrated force P, the maintained electric potential Φ_0, the half-angle of the cone α and consequently the material constants involved. Since the resulting equation about a is a quadratic one (the positive root gives the value of a), it seems a little complicated. It is therefore noted that integrating $D_0^{\mathrm{I}} + D_0^{\mathrm{II}}$ over the contact area gives the "equivalent concentrated electric charge" as follows:

$$Q = Q^{\mathrm{I}} + Q^{\mathrm{II}} = -\frac{g_3 ha}{2A} + \frac{2g_1\Phi_0 a}{\pi A}. \quad (33)$$

Then the following simple relations can be established from Eqs. (32) and (33),

$$ah = -2(g_1 P - g_2 Q) = -2AP^{\mathrm{I}}/g_4 = -2AQ^{\mathrm{I}}/g_3, \quad (34)$$

and

$$a\Phi_0 = -\frac{\pi}{2}(g_3 P - g_4 Q) = \pi AP^{\mathrm{II}}/(2g_2) = \pi AQ^{\mathrm{II}}/(2g_1). \quad (35)$$

Equation (34) is very similar to that for pure elasticity (Hanson, 1992a). The following contact parameters then can be obtained:

$$a = \sqrt{-2(g_1 P - g_2 Q)\tan\alpha} = \sqrt{-2AP^{\mathrm{I}}\tan\alpha/g_4} = \sqrt{-2AQ^{\mathrm{I}}\tan\alpha/g_3}, \quad (36)$$

or

$$a = -\frac{\pi}{2\Phi_0}(g_3 P - g_4 Q) = \frac{\pi}{2g_2\Phi_0}AP^{\mathrm{II}} = \frac{\pi}{2g_1\Phi_0}AQ^{\mathrm{II}}, \quad (37)$$

and $h = a\cot\alpha$, $h_0 = h(\pi/2 - 1)$.

If the depth of indentation $d_P = h + h_0$ is known, the radius of the contact a and the total applied force P can be determined as follows:

$$a = \frac{2}{\pi}d_P\tan\alpha, \quad P = (2g_2\Phi_0 - g_4 d_p)\frac{2}{\pi^2 A}d_p\tan\alpha. \quad (38)$$

It is interesting to consider the singular behaviors of the normal stress σ_z and electric displacement D_z at the surface $z = 0$. Allowing for the following property:

$$l_{1i} \to \min(a, \rho), \quad \text{and} \quad l_{2i} \to \max(a, \rho), \quad \text{when} \quad z = 0, \quad (39)$$

it can be found that σ_z and D_z exhibit logarithmic singularity at the center and square-root singularity at the edge of the contact region, respectively. In fact, by defining the intensity factors,

$$k_\sigma^{\mathrm{I}} = \lim_{\rho\to 0}\{\sigma_z/\ln\rho\}, \qquad k_D^{\mathrm{I}} = \lim_{\rho\to 0}\{D_z/\ln\rho\},$$
$$k_\sigma^{\mathrm{II}} = \lim_{\rho\to a}\{(a - \rho)^{1/2}\sigma_z\}, \quad k_D^{\mathrm{II}} = \lim_{\rho\to a}\{(a - \rho)^{1/2}D_z\}, \quad \text{for } z = 0, \quad (40)$$

the following expressions can be derived from Eqs. (30) and (31):

Downloaded 04 May 2010 to 171.66.16.27. Redistribution subject to ASME license or copyright; see http://www.asme.org/terms/Terms_Use.cfm

Table 1 The nondimensional contact parameter $a\sqrt{c_{44}/P}$ for different cases

Materials	α	$\beta = \Phi_0 e_{33}/\sqrt{c_{44}P}$				
		0	-0.1	0.1	-0.5	0.5
PZT-4	$\pi/6$	0.3307 (0.3465)	0.3467	0.3155	0.4177	0.2619
	$\pi/4$	0.4353 (0.4560)	0.4631	0.4091	0.5907	0.3208
	$\pi/3$	0.5729 (0.6001)	0.6215	0.5280	0.8525	0.3850
PZT-5	$\pi/6$	0.3257 (0.3411)	0.3409	0.3111	0.4086	0.2596
	$\pi/4$	0.4286 (0.4489)	0.4552	0.4036	0.5766	0.3186
	$\pi/3$	0.5641 (0.5908)	0.6105	0.5211	0.8302	0.3833
PZT-7A	$\pi/6$	0.3067 (0.3262)	0.3197	0.2942	0.3770	0.2495
	$\pi/4$	0.4036 (0.4293)	0.4263	0.3821	0.5289	0.3080
	$\pi/3$	0.5312 (0.5650)	0.5708	0.4943	0.7559	0.3733
$BaTiO_3$	$\pi/6$	0.3618 (0.3659)	0.3776	0.3467	0.4470	0.2929
	$\pi/4$	0.4762 (0.4816)	0.5036	0.4502	0.6280	0.3610
	$\pi/3$	0.6227 (0.6338)	0.6746	0.5821	0.8992	0.4368

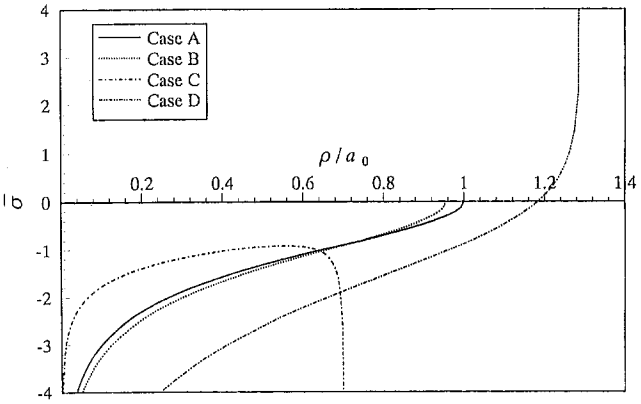


Fig. 3 Distribution of the nondimensional stress $\bar{\sigma} = \pi a_0^2 \sigma_z / P$ in the contact region

$$k_\sigma^{\mathrm{I}} = \frac{h}{Aa}\sum_{i=1}^{3}\gamma_{1i}k_{1i}, \quad k_D^{\mathrm{I}} = \frac{h}{Aa}\sum_{i=1}^{3}\gamma_{2i}k_{1i},$$

$$k_\sigma^{\mathrm{II}} = -\frac{2\Phi_0}{\pi A}\left(\frac{1}{2a}\right)^{1/2}\sum_{i=1}^{3}\gamma_{1i}k_{2i},$$

$$k_D^{\mathrm{II}} = -\frac{2\Phi_0}{\pi A}\left(\frac{1}{2a}\right)^{1/2}\sum_{i=1}^{3}\gamma_{2i}k_{2i}. \tag{41}$$

Noticing Eqs. (14), (32), and (33), these intensity factors can be written in more concise forms,

$$k_\sigma^{\mathrm{I}} = -\frac{hg_4}{2\pi Aa} = \frac{P^{\mathrm{I}}}{\pi a^2}, \quad k_D^{\mathrm{I}} = \frac{hg_3}{2\pi Aa} = -\frac{Q^{\mathrm{I}}}{\pi a^2},$$

$$k_\sigma^{\mathrm{II}} = -\frac{g_2\Phi_0}{\pi^2 A}\left(\frac{1}{2a}\right)^{1/2} = -\frac{P^{\mathrm{II}}}{\pi}\left(\frac{1}{2a}\right)^{3/2},$$

$$k_D^{\mathrm{II}} = \frac{g_1\Phi_0}{\pi^2 A}\left(\frac{1}{2a}\right)^{1/2} = \frac{Q^{\mathrm{II}}}{\pi}\left(\frac{1}{2a}\right)^{3/2}. \tag{42}$$

6 Numerical Examples

The first example is to show the effects of various parameters involved on the main contact parameter, a, i.e., the radius of the contact region. Values of the nondimensional parameter $a\sqrt{c_{44}/P}$ are listed in Table 1 for several different cases ($P \neq 0$). The material constants of the four piezoelectric materials as shown in Table 1 can be found in Dunn and Taya (1994), for example. Data in parentheses are for elastic materials (the piezoelectric effect in the corresponding piezoelectric materials is ignored).

It can be seen from Table 1 that for all four materials, the piezoelectric effect leads to the shrink of the contact region for a grounded punch. Moreover, for piezoelectric materials, if the punch is simultaneously maintained at a positive (negative) electric potential, the contact radius will become smaller (larger). In other words, the positive electric potential acts like a concentrated force that uplifts the punch and vice versa. In this respect, to make the punch be pressed against the half-space, the punch should be given a negative electric potential, provided that no mechanical force is applied.

The second example is to display distributions of normal stress σ_z in the contact region and normal displacement w at the surface. Calculation is performed for PZT-4 for four cases. Case A is purely elastic that the piezoelectric effect in PZT-4 is neglected. Case B, C, D are piezoelectric with the nondimensional electric potential parameter $\beta = \Phi_0 e_{33}/\sqrt{c_{44}P}$ be 0, 0.5 and -0.5, respectively. As in the first example, it is assumed that the applied force P does not equal to zero.

Curves of the nondimensional surface displacement $\bar{w} = c_{44}a_0 w/P$ versus the nondimensional radial coordinate ρ/a_0 for the above four cases are shown in Fig. 2. Here to make comparison, the same base length a_0, i.e., the contact radius for case A is used in the nondimensionalization. The corresponding value of the nondimensional parameter $a_0\sqrt{c_{44}/P}$ is 0.4560 as given in Table

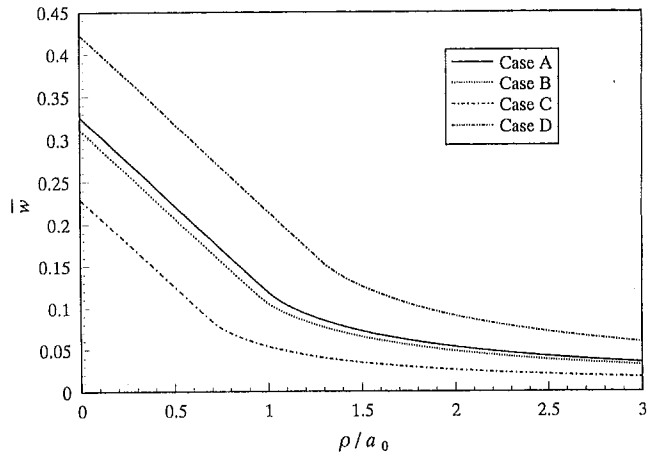


Fig. 2 Distribution of the nondimensional displacement $\bar{w} = c_{44}wa_0/P$ at the surface

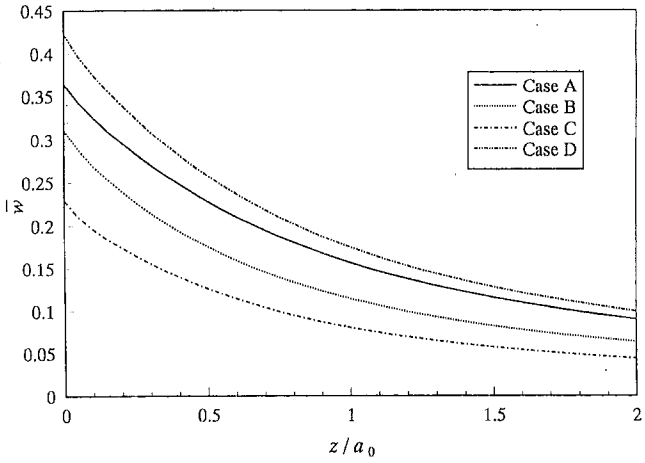


Fig. 4 Distribution of the nondimensional displacement $\bar{w} = c_{44}wa_0/P$ along the symmetric axis ($\rho = 0$)

Downloaded 04 May 2010 to 171.66.16.27. Redistribution subject to ASME license or copyright; see http://www.asme.org/terms/Terms_Use.cfm

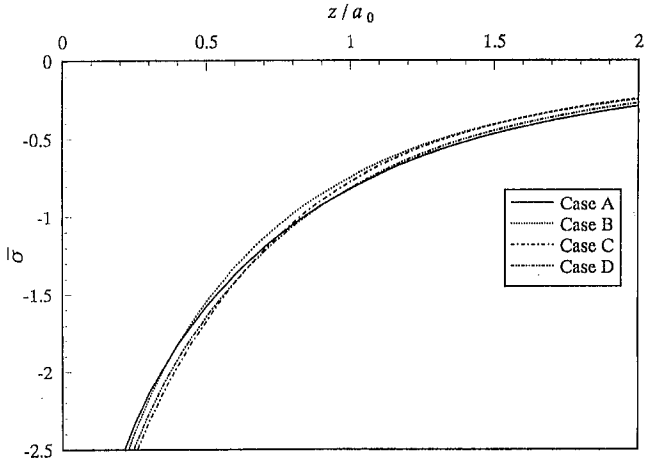


Fig. 5 Distribution of the nondimensional stress $\bar{\sigma} = \pi a_0^2 \sigma_z / P$ along the symmetric axis ($\rho = 0$)

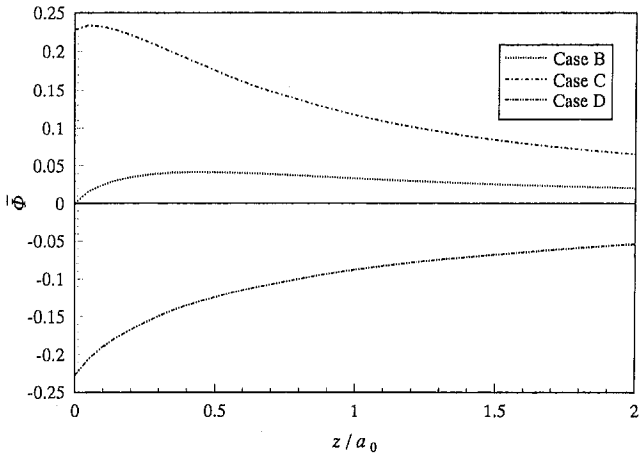


Fig. 7 Distribution of the nondimensional electric potential $\bar{\Phi} = e_{33} a_0 \Phi / P$ along the symmetric axis ($\rho = 0$)

1. It is seen from Fig. 2 that the parameter β has an obvious effect on both the contact radius and the value of the surface displacement. Figure 3 displays the distribution of the nondimensional stress $\bar{\sigma} = \pi a_0^2 \sigma_z / P$ in the contact region (outside the contact region, σ_z vanishes as one can see from Eq. (9)). The size of the contact region and the singularities are clearly shown in Fig. 3. In particular, as discussed in the last section, for all four cases, there is a logarithmic singularity at the center of the contact region due to the conical punch. For cases C and D, there is a square-root singularity at the contact edge due to the constant electric potential applied on the punch.

As the last example, distributions of the nondimensional normal displacement $\bar{w} = c_{44} a_0 w / P$ and stress $\bar{\sigma} = \pi a_0^2 \sigma_z / P$ for all four cases and the nondimensional normal electric displacement $\bar{D} = c_{44} a_0^2 D_z / (e_{33} P)$ and electric potential $\bar{\Phi} = e_{33} a_0 \Phi / P$ for cases B, C, and D along the symmetric axis ($\rho = 0$) are given in Fig. 4, 5, 6, and 7, respectively. It can be seen that the electric field in PZM has an effect on $\bar{w}$ greater than on $\bar{\sigma}$. The parameter β has a very important effect on both the distributions of $\bar{D}$ and $\bar{\Phi}$.

Though all numerical calculations are carried out for $P \neq 0$, it is not difficult to consider the case of $P = 0$, for which, however, other nondimensional variables should be introduced.

7 Conclusion

The indentation of a transversely isotropic piezoelectric half-space by a rigid cone has been exactly analyzed by the potential theory method, which was generalized in the paper by introducing a new potential to take account of the piezoelectric effect. Exact expressions for the elastoelectric field are derived in terms of elementary functions. It is found that there exist two kinds of singularity: the first due to the settlement of the cone exhibits logarithmic singularity at the center of the contact region while the second due to the constant electric potential exhibits square-root singularity at the edge of the contact region. Simple form expressions for the corresponding intensity factors are derived.

It is of importance to point out that all the results presented in the paper degenerate identically to those for pure elasticity for transversely isotropy (Hanson, 1992a) when the piezoelectric effect is omitted. Exact solution for a sliding conical punch with shear traction in the form of Coulomb friction in the contact region can be obtained by integrating the shear point force Green's functions for a transversely isotropic piezoelectric half-space that can be found in Ding et al. (1997b). The derivation is very similar to that presented in Hanson (1992a) and is not presented here for the sake of simplicity.

As noted by Hanson (1992a) for elasticity, sharp indentation involves contained plastic deformation under the indenter apex. For piezoelectric materials, more complicated procedure will take place due to the coupling effect between mechanical deformation and electric field. It is far beyond of the scope of this paper. However, the solution presented above can be regarded as a starting point for succeeded analysis.

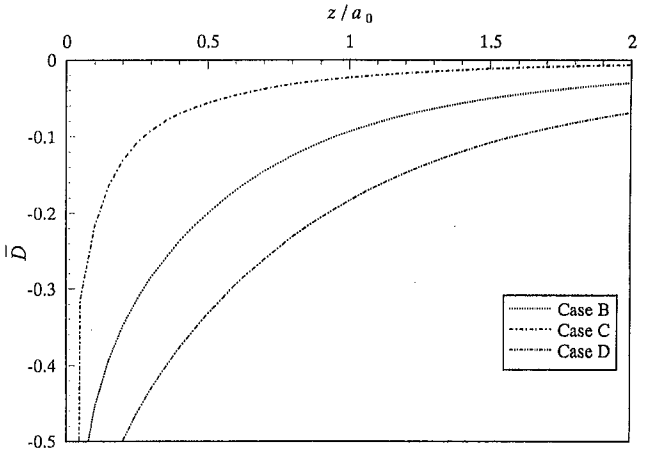


Fig. 6 Distribution of the nondimensional electric displacement $\bar{D} = c_{44} a_0^2 D_z / (e_{33} P)$ along the symmetric axis ($\rho = 0$)

Acknowledgments

Financial support from the Japanese Ministry of Education, Science, Sports and Culture is acknowledged. The work of CWQ and DHJ was also supported by the Natural Science Foundation of China (No. 19872060).

References

Ashida, F., and Tauchert, T. R., 1998, "Transient response of a piezothermoelastic circular disk under axisymmetric heating," *Acta Mechanica,* Vol. 128, pp. 1–14.

Chen, W. Q., 1999, "Problems of radially polarized piezoelastic bodies," *International Journal of Solids and Structures,* Vol. 36, pp. 4317–4332.

Ding, H. J., Wang, G. Q., and Chen, W. Q., 1997a, "Green's functions for a two-phase infinite piezoelectric plane," *Proceedings of the Royal Society of London,* Vol. A453, pp. 2241–2257.

Ding, H. J., Chen, B., and Liang, J., 1997b, "On the Green's functions for two-phase transversely isotropic piezoelectric media," *International Journal of Solids and Structures,* Vol. 34, pp. 3041–3057.

Dunn, M. L., and Taya, M., 1994, "Electroelastic Field Concentrations in and Around Inhomogeneities in Piezoelectric Solids," ASME JOURNAL OF APPLIED MECHANICS, Vol. 61, pp. 474–475.

Downloaded 04 May 2010 to 171.66.16.27. Redistribution subject to ASME license or copyright; see http://www.asme.org/terms/Terms_Use.cfm

Elliot, H. A., 1949, "Axial symmetric stress distributions in aeolotropic hexagonal crystals, the problem of the plane and related problem," *Proceedings of Cambridge Philosophical Society,* Vol. 45, pp. 621–630.

Fabrikant, V. I., 1988, "Elastic Field Around a Circular Punch," ASME JOURNAL OF APPLIED MECHANICS, Vol. 55, pp. 604–610.

Fabrikant, V. I., 1989, *Applications of Potential Theory in Mechanics: A selection of New Results,* Kluwer Academic Publishers, The Netherlands.

Fan, H., Sze, K. Y., and Yang, W., 1996, "Two dimensional contact on a piezoelectric half-space," *International Journal of Solids and Structures,* Vol. 33, pp. 1305–1315.

Gladwell, G. M. L., 1980, *Contact Problems in the Classical Theory of Elasticity,* Sijthoff and Noordhoff, Alphen ann den Rijn, The Netherlands.

Hanson, M. T., 1992a, "The Elastic Field for Conical Indentation Including Sliding Friction for Transverse Isotropy," ASME JOURNAL OF APPLIED MECHANICS, Vol. 59, pp. S123–S130.

Hanson, M. T., 1992b, "The Elastic Field for Spherical Hertzian Contact Including Sliding Friction for Transverse Isotropy," ASME *Journal of Tribology,* Vol. 114, pp. 604–610.

Hanson, M. T., 1993a, "The Elastic Field for a Sliding Conical Punch on an Isotropic Half-Space," ASME JOURNAL OF APPLIED MECHANICS, Vol. 60, pp. 557–559.

Hanson, M. T., and Johnson, T., 1993, "The Elastic Field for Spherical Hertzian Contact of Isotropic Bodies Revisited, Some Alternative Expressions," ASME *Journal of Tribology,* Vol. 115, pp. 327–332.

Hanson, M. T., 1994, "The elastic field for an upright or tilted sliding circular flat punch on a transversely isotropic half space," *International Journal of Solids and Structures,* Vol. 31, pp. 567–586.

Harding, J. W., and Sneddon, I. N., 1945, "The elastic stresses produced by the indentation of the plane surface of a semi-infinite elastic solid by a rigid cone," *Proceedings of the Cambridge Philosophical Society,* Vol. 41, pp. 16–26.

Hertzberg, R. W., 1989, *Deformation and Fracture Mechanics of Engineering Materials,* John Wiley and Sons, New York.

Love, A. E. H., 1939, "Boussinesq's problem for a rigid cone," *Quarterly Journal of Mathematics,* Vol. 10, pp. 167–175.

Pak, Y. E., 1990, "Crack Extension Force in a Piezoelectric Material," ASME JOURNAL OF APPLIED MECHANICS, Vol. 57, pp. 647–653.

Rao, S. S., and Sunar, M., 1994, "Piezoelectricity and its use in disturbance sensing and control of flexible structures: a survey," ASME *Applied Mechanics Reviews,* Vol. 47, pp. 113–123.

Sneddon, I. N., 1948, "Boussinesq's problem for a rigid cone," *Proceedings of the Cambridge Philosophical Society,* Vol. 44, pp. 492–507.

Tiersten, H. F., 1969, *Linear Piezoelectric Plate Vibrations,* Plenum Press, New York.

Downloaded 04 May 2010 to 171.66.16.27. Redistribution subject to ASME license or copyright; see http://www.asme.org/terms/Terms_Use.cfm

G. Chen
Mem. ASME

X. Xu[1]
Assoc. Mem.

School of Mechanical Engineering,
Purdue University,
West Lafayette, IN 47907

C. C. Poon

A. C. Tam

IBM Almaden Research Center,
650 Harry Road,
San Jose, CA 95190

Experimental and Numerical Studies on Microscale Bending of Stainless Steel With Pulsed Laser

Laser forming or laser bending is a newly developed, flexible technique which modifies the curvature of sheet metal by thermal residual stresses instead of external forces. The process is influenced by many parameters such as laser parameters, material properties, and target dimensions. In this work, a pulsed Nd:YLF laser was used as the energy source. The laser beam was focused into a line shape irradiating on the stainless steel specimen to induce bending. The bending angle was measured at various processing conditions. A finite element analysis was performed with the use of a two-dimensional plane strain model to calculate the thermoelastoplastic deformation process. Experimental measurements and computational results were in good agreement. Numerical sensitivity studies were performed to evaluate the effects of the unavailable material property data at high temperature. It was found that both optical reflectivity and thermal expansion coefficient influenced the bending angle significantly, while other extrapolated material properties at high temperature yielded acceptable results.

1 Introduction

Laser forming is a newly developed, flexible technique which modifies the surface curvature of sheet metal by thermal residual stresses instead of external forces (Namba, 1986; Scully, 1987; Geiger, 1994). In the laser-forming processes reported in literature, continuous wave (CW) CO_2 or YAG lasers with powers on the order of kilowatts or higher are used to form complex shapes, or straighten automobile body shells and ship bodies distorted by preceding welding operations. Laser forming also has potential applications in the microelectronic industry, where modification of curvatures with high precision is needed. Compared with conventional metal forming processes, laser forming is contact free, which eliminates the need of component-specific hard tooling, and is much more precise in microscale bending applications.

Three laser-bending mechanisms, the temperature gradient mechanism, the buckling mechanism, and the upsetting mechanism have been discussed in literature (Vollertsen, 1994a; Arnet and Vollertsen, 1995). For the temperature gradient mechanism, a sharp temperature gradient develops due to rapid heating of the surface. Compressive plastic strains are generated when thermal expansion is hindered, causing bending towards the direction of the incoming laser beam after cooling (Chen et al., 1998). For most of the applications involving pulsed lasers, the temperature gradient mechanism is responsible for bending. The thermal mechanical response of the material during pulsed laser bending is similar to that in the laser welding process, which has been studied extensively (Radaj, 1992; Bae and Na, 1996).

Results of laser bending are influenced by many parameters. Among these, laser parameters, materials properties, and target geometry are expected to have strong effects on the process mechanics and the obtained bending angle. To date, few systematic investigations on these parameters have been reported. While analytical modeling (Vollertsen, 1994b) is limited to a specific set of parameters, it is not applicable to other cases where the target material and processing parameters are different from those the analytical modeling was constructed for. Further, analytical modeling is not capable of accounting for temperature-dependent thermal-mechanical properties. In order to compute the laser-bending process, the finite element method (Vollertsen et al., 1993; Alberti et al., 1994) has been applied.

In this work, a pulsed, diode-pumped Nd:YLF laser is used as the energy source. The laser beam with a Gaussian distribution is focused into a line shape irradiating on the stainless steel specimen to induce bending, as shown in Fig. 1. In an actual pulsed laser-bending operation, the Gaussian laser beam is scanned in the x-direction, thus, the temperature and stress/strain development in the target are three-dimensional. However, such three-dimensional bending is rather difficult to compute. In the present study, experiments are performed using the line-shape laser beam so that a much simpler, two-dimensional analysis can be carried out. A finite element code, ABAQUS (HKS, Inc., Pawtucket, RI) is used for both heat transfer and thermal stress analyses with a two-dimensional plane-strain assumption. The numerical analysis helps to validate the theoretical description of the laser bending process, and also determines the key parameters that influence bending. Numerical sensitivity studies are also performed to analyze the influence of the initial residual stress, strain hardening, hardening rule, and the extrapolated thermal-physical property data at high temperature on bending.

2 Experimental Setup

Figure 1(*a*) illustrates the experimental setup for pulsed-laser bending as well as for measuring the bending angle. The laser used is a pulsed Nd:YLF laser with about 10 nsec of full width at half maximum (FWHM) and a wavelength at 1047 nm. The pulsed laser beam is expanded by a beam expander and focused onto the target using a cylindrical focusing lens. As shown in Fig. 1(*b*), after the cylindrical lens, the collimated circular laser beam condenses in the y-direction only, and keeps the dimension in the x-direction unchanged. Thus, a line-shape (actually a slender ellipse) laser beam is obtained on the specimen which covers the

[1] To whom all correspondence should be addressed.

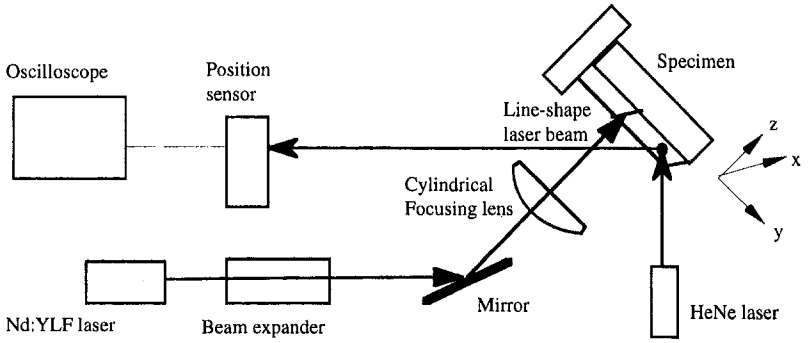
Contributed by the Applied Mechanics Division of THE AMERICAN SOCIETY OF MECHANICAL ENGINEERS for publication in the ASME JOURNAL OF APPLIED MECHANICS.

Discussion on the paper should be addressed to the Technical Editor, Professor Lewis T. Wheeler, Department of Mechanical Engineering, University of Houston, Houston, TX 77204-4792, and will be accepted until four months after final publication of the paper itself in the ASME JOURNAL OF APPLIED MECHANICS.

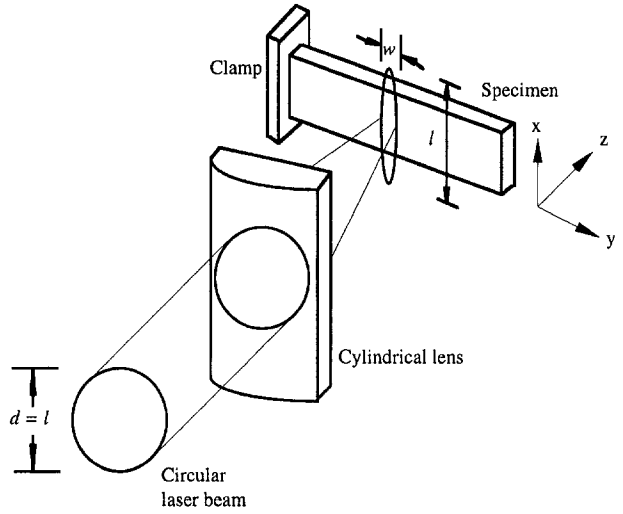
Manuscript received by the ASME Applied Mechanics Division, Aug. 14, 1998; final revision, Jan. 16, 1999. Associate Technical Editor: V. K. Kinra.

 Copyright © 1999 by ASME

Downloaded 04 May 2010 to 171.66.16.27. Redistribution subject to ASME license or copyright; see http://www.asme.org/terms/Terms_Use.cfm



(a)



(b)

Fig. 1 Experimental set-up

whole width of the specimen in the x-direction. The measured length of the laser beam in the x-direction is about 1.55 mm and the specimen width is about 0.8 mm. Placing the specimen at the center of the laser beam, the laser intensity at the specimen edge is about 60 percent of the maximum intensity at the beam center. With one end of the target clamped, bending is mainly achieved in the z-direction.

A HeNe laser beam is focused at the free end of the specimen to measure the bending angle in the z-direction, which is defined as the rotated angle of the surface between the laser irradiated area and the free end due to laser irradiation. The reflected HeNe laser beam is received by a position sensitive detector with a position sensitivity of 1 μm. When the distance between the sensor and the specimen is long enough, a small movement at the free end of the specimen produces a measurable displacement of the HeNe laser beam at the position sensor. The position change of the HeNe laser beam at the sensor can be converted to the bending angle of the specimen using straightforward geometrical calculations. The accuracy of the bending angle measurement is about ± 2.4 μrad. The whole apparatus is set on a vibration-isolation table to avoid environmental disruption.

The specimens used are full-hard 301 stainless steels. The laser and specimen parameters are shown in Table 1. Some specimens were heat treated by stress relief annealing at 752 F for half an hour to remove initial residual stresses. The laser beam width can be adjusted by moving the target in the z-direction. The bending angle is measured as a function of the beam width at the maximum pulse energy of 118.5 μJ as well as a function of pulse energy at a constant beam width of 29.2 μm. Experimental data will be presented in Section 4 and compared with the numerical results.

3 Computational Model

The pulsed laser-bending process is simulated using the finite element analysis. In what follows, a qualitative description of laser bending is first given, then modeling of the thermal and thermal-mechanical responses of the target is described.

Table 1 Laser and specimen parameters used in experiments

laser pulse energy Q_p (μJ)	40 ~ 118.5
laser pulse width t_p (nsec)	10
laser beam width w (μm)	29.2 ~ 87.3
laser beam length l (mm)	1.55
specimen length (mm)	10.0
specimen width (mm)	0.8
specimen thickness (μm)	100

Downloaded 04 May 2010 to 171.66.16.27. Redistribution subject to ASME license or copyright; see http://www.asme.org/terms/Terms_Use.cfm

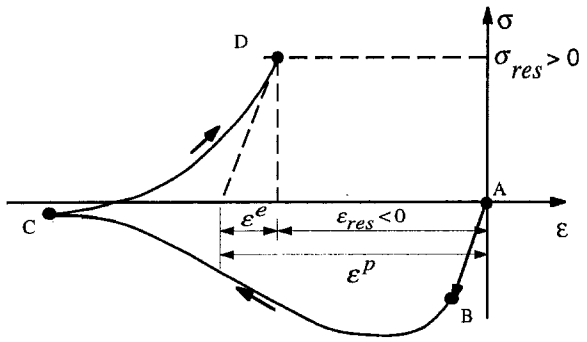


Fig. 2 Stress-strain relation at the center of laser heated area during pulsed laser bending

3.1 Theoretical Description of Pulsed Laser Bending. When the laser pulse irradiates the specimen surface, the temperature of the irradiated area increases rapidly within several nanoseconds, with the highest temperature achieved at the center of the laser heated area. Because of the short laser pulses used in this work (~10 nsec), a sharp temperature gradient is established in the thickness direction (z-direction) within several micrometers below the surface. The thermal-mechanical response of the target near the centerline of the irradiated area is depicted qualitatively in Fig. 2, which is explained as follows. During heating, compressive stresses arise because of the thermal expansion of the heated zone and the bulk constraint of the materials surrounding the heated area. From point A to point B, the material is being heated in the linear elastic region. From point B to point C (when the temperature is the maximum), plastic deformation occurs as the yield strength decreases and the thermal expansion coefficient increases with the increasing temperature. Due to the temperature-dependencies of the yield strength, thermal expansion coefficient and Young's modulus, the compressive strains increase but stresses decrease with the increasing temperature. During the heating period, the thermal expansion of the materials causes the target to bend away from the laser beam.

During the cooling period as indicated from point C to point D in Fig. 2, heat flows into the adjacent zones and the stresses change from compression to tension due to thermal shrinkage. The compressive strains generated during heating are not completely canceled out due to the following reasons: first, the thermal expansions of the adjacent zones help to lower the tensile stresses developed in the heated zone during cooling. On the other hand, when the yield strength increases with the decreasing temperature, less tensile strains are generated when the material in the heated zone yields in tensile stress. Therefore, the compressive strains remain in the heated zone after the target completely cools down. The surface layer of the target is compressed more than those underneath it, and a bending angle towards the laser beam (which is defined as positive in this paper) develops.

The above description indicates that the bending process is caused by the plastic deformation induced by thermal stresses and temperature-dependent materials properties; the bending process is strongly dependent on the transient temperature field. On the other hand, heat dissipation due to the plastic deformation is small compared with heat provided by the laser pulse. Therefore, an uncoupled thermomechanical analysis can be used to study the bending process, in which a transient temperature field is obtained first in the thermal analysis, and is then used as a thermal loading in the subsequent stress analysis to obtain the transient stress, strain, and displacement distributions.

To simulate the pulsed laser bending process, a two-dimensional thermal and plane-strain model is used. During the experiments, the laser beam intensity in the x-direction is not exactly uniform, with a variation of about 40 percent from the center of the laser beam to the edge of the specimen. An averaged laser intensity in the x-direction is used in the simulation. The nonlinear finite element solver, ABAQUS, is employed to solve both the thermal and the mechanics parts of the problem. The computational domain is 600 μm by 100 μm as shown in Fig. 3. The domain length in the y-direction is a small portion of the total length of the specimen, with the left edge fixed and the right edge free. These treatments should be very close to the real situation since the computational domain is large enough compared to the size of the residual stress region, and the free edge of the target only undergoes a rigid rotation. To verify that the computational domain is indeed large enough, the domain size is increased to 1200 μm long. In doing so, displacements at 300 μm from the center are found to be zero and the stresses at that location are three orders of magnitude less than the stresses at the laser irradiated area, while the bending angle does not change from that calculated from a 600-μm long domain. In the experiments, the irradiated area is always kept more than 1 mm away from the clamp, which is far enough to eliminate the effect of the clamp on bending since the laser beam width used in the experiment and the heat and stress affected zone obtained are much less than 1 mm. The experiment also shows that, the bending angle does not change with the location of the laser irradiated area, as long as the laser irradiated area is more than 1 mm away from the clamp. The experiment also shows the measured bending angle does not depend on the location where the reflective measurement is taken.

Eight-node quadratic two-dimensional solid elements are applied in the analyses. The mesh is about 1.9 nm near the specimen surface and the centerline because of the large temperature gradient there, and is stretched away from the surface and the centerline. The peak temperature achieved is lower than the melting temperature so that no phase change needs to be considered. The time-step is controlled according to the criterion that the temperature change between any two adjacent time-steps is less than 5 K. The analysis is proceeded up to the time of 1 sec when the temperatures inside the specimen are expected to cool down approximately to the room temperature of 300 K. Mesh tests are performed by increasing the mesh density until the calculated temperature field does not change. 121 and 41 nodes are discretized in the y and z-directions respectively, which correspond to a total of 1200 elements.

Temperature-dependent thermomechanical properties shown in Fig. 4 (Maykuth, 1980) are used in the simulation. The thermal expansion coefficient for the full-hard steel is unknown to the authors, and the data for extra-hard specimen are used. The data for the Young's modulus and yield strength are in a certain range, and the averaged values for Young's modulus and the lower bound of the yield strength in Fig. 4 are used in the calculation. Influences of the uncertainties of these data will be investigated using the numerical sensitivity studies (see Section 4.3).

3.2 Thermal Analysis. The heat transfer analysis is based on solving the two-dimensional heat conduction equation in the cross section of the y-z plane as shown in Fig. 3. The initial condition is that the whole specimen is at the room temperature. Since the left and right boundaries as well as the bottom surface are far away from the laser beam, the boundary conditions at these

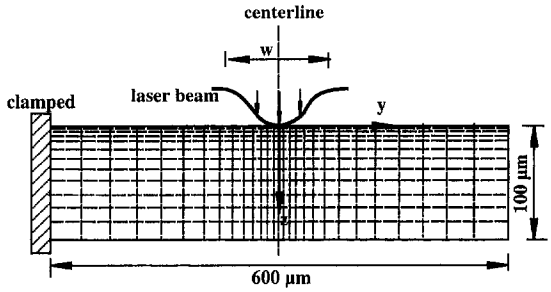


Fig. 3 Computational domain and mesh

Downloaded 04 May 2010 to 171.66.16.27. Redistribution subject to ASME license or copyright; see http://www.asme.org/terms/Terms_Use.cfm

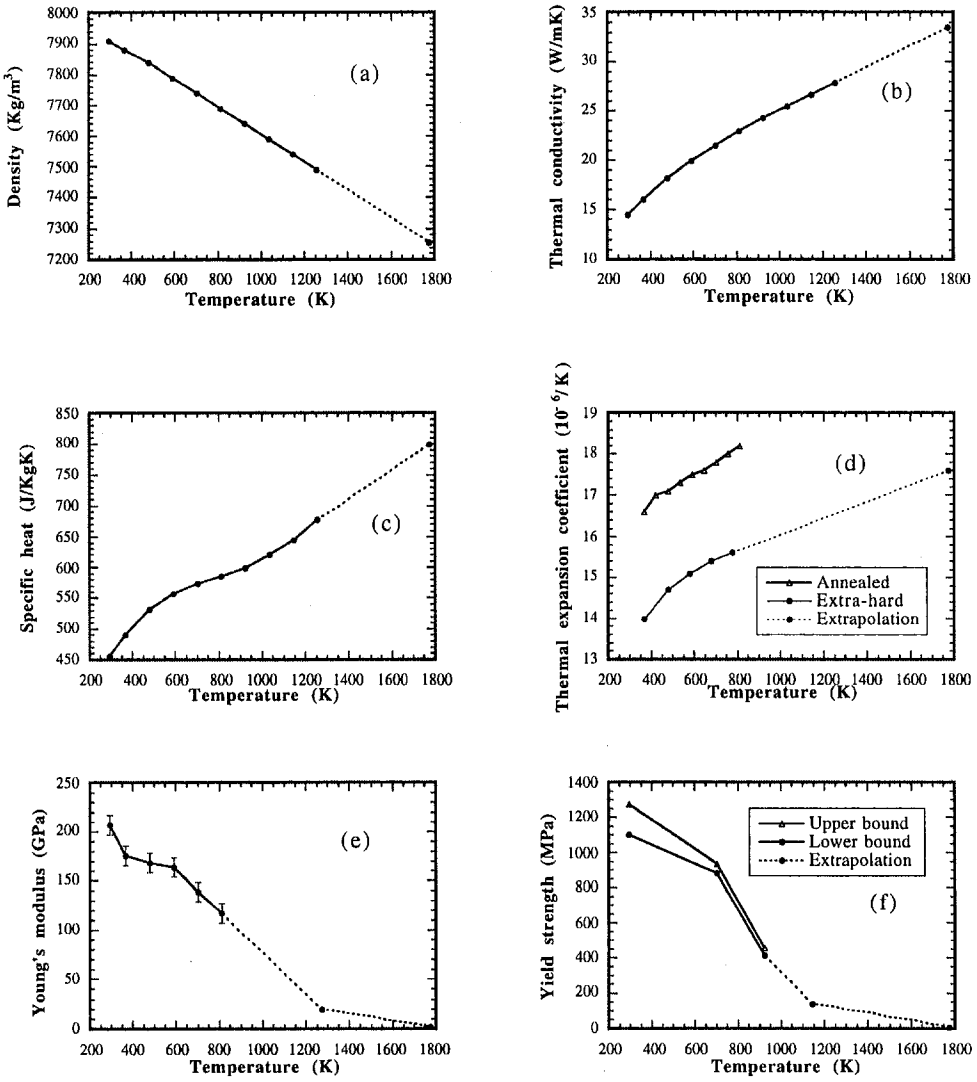


Fig. 4 Thermal and mechanical properties of full-hard 301 stainless steel

locations are prescribed as the room temperature. The boundary condition of the top surface irradiated by the laser beam needs some special considerations. Instead of prescribing the heat flux on the top surface, the laser flux is handled as the volumetric heat source absorbed by the target. Assuming the laser intensity is uniform in the x-direction, the laser flux on the target surface $I_s(y, t)$ is considered as Gaussian distribution in the y-direction only, which can be expressed as

$$I_s(y, t) = I_0(t) \exp\left(-\frac{8y^2}{w^2}\right) \tag{1}$$

where $I_0(t)$ is the time-dependent laser intensity at the center point $y = 0$, and w is the beam width. The temporal profile of the laser intensity is treated as increasing linearly from zero to the maximum at 10 nsec, then decreasing linearly to zero at the end of the pulse at 20 nsec. $I_0(t)$ can be expressed through the total pulse energy Q_p and pulse width t_p (FWHM, 10 nsec) as

$$I_0(t) = \begin{cases} \sqrt{\frac{8}{\pi}} \frac{Q_p t}{l w t_p^2} & 0 \le t < t_p \\ \sqrt{\frac{8}{\pi}} \frac{Q_p (2t_p - t)}{l w t_p^2} & t_p \le t < 2t_p \end{cases} \tag{2}$$

where l is the laser beam length. The local radiation intensity $I(y, z, t)$ within the target is calculated considering exponential attenuation and surface reflection as

$$I(y, z, t) = (1 - R_f) I_s(y, t) e^{-\alpha z} \tag{3}$$

where α is the absorption coefficient given by

$$\alpha = \frac{4\pi\kappa}{\lambda}. \tag{4}$$

The refractive index of iron at the Nd:YLF laser wavelength, $\lambda = 1.047$ μm is $\hat{n} = n + i\kappa = 3.275 + i4.5$ (Lynch and Hunter, 1985). The temperature-dependence of the complex refractive index is unknown to the authors, and is neglected in the calculation. R_f is reflectivity calculated from the complex refractive index, $R_f = 0.66$. Absorptivity of iron at the Nd:YLF laser wavelength (1.047 μm) is therefore much larger than that at the wavelength of a CO_2 laser (10.6 μm). Because the optical properties of stainless steel 301 are unavailable, the absorption coefficient and reflectivity calculated from the refractive index of iron are employed. Specular reflectivity of the stainless steel 301 specimen is measured to be 0.60, smaller than the calculated value. The influence of the uncertainty of reflectivity on the computational results will be discussed later (Section 4.3). The final form of the volumetric heat source term, $Q_{ab}(y, z, t)$ can be expresses as

$$Q_{ab}(y, z, t) = -\frac{dI(y, z, t)}{dz} = (1 - R_f)\alpha I_s(y, t) e^{-\alpha z}. \tag{5}$$

Since the laser energy is treated as volumetric absorption, the boundary condition at the top surface is considered adiabatic.

Downloaded 04 May 2010 to 171.66.16.27. Redistribution subject to ASME license or copyright; see http://www.asme.org/terms/Terms_Use.cfm

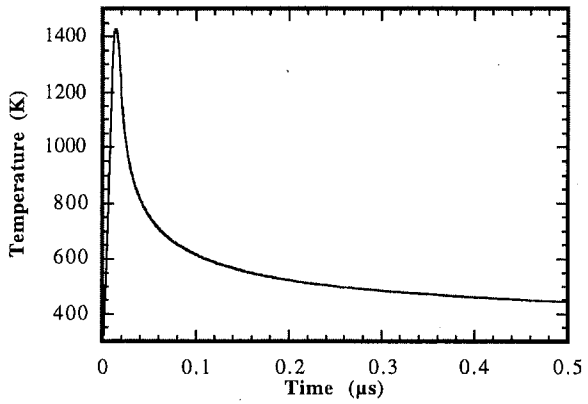


Fig. 5 Temperature history at the center point on the irradiated surface

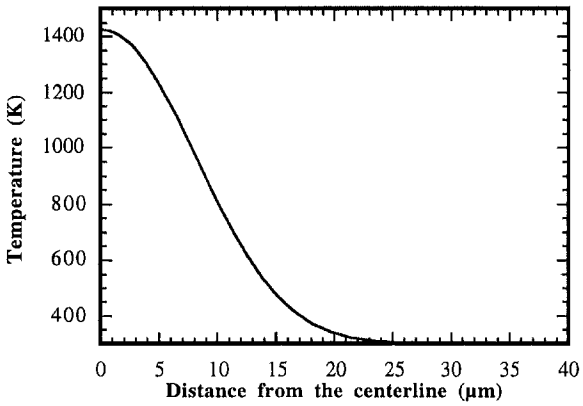


Fig. 6 Surface temperature distribution at t = 13 ns

Convection and radiation losses to the surrounding are neglected since these quantities are several orders of magnitude smaller compared with the incident laser intensity and the conduction heat flux.

3.3 Stress Analysis. Using the transient temperature field obtained from the thermal analysis, the transient stress, strain, and displacement distributions can be analyzed numerically. Quasi-static states in the stress analysis are adopted. The mesh used in the stress analysis is the same as that for the thermal analysis. Eight-node biquadratic plane-strain elements are employed.

The material is assumed to be linearly elastic-perfectly plastic; the strain-hardening effect is considered later in numerical sensitivity studies. The commonly used von Mises yield criterion is employed. Whenever possible, the material properties are considered temperature-dependent. The strain rate is high in the pulsed laser bending process, however, the yield strength is considered temperature-dependent only; the strain-rate enhancement effect is neglected because of unavailability of these data. To simplify the problem, it is also assumed that the local strain is due to the thermal stress only, other possible strains such as the one arising from phase transformation are not accounted for. Creep is neglected due to rapid heating and cooling. Temperature-dependent Poisson's ratio is unknown to the authors, therefore, a constant value of 0.3 (Maykuth, 1980) is used.

The boundary conditions are simple for this problem. As shown in Fig. 3, the left edge is completely constrained, and all other boundaries are stress free. Initially, the specimen is assumed to be stress and strain free, and the effects of the initial stress and strain are discussed later. After the numerical computation, the bending angle is calculated as the ratio of the z displacement at the upper tip node on the right edge to the half-length of the computational domain. The simulation shows that the calculated bending angle is almost constant when different nodes on the right edge are used.

4 Results and Discussions

Results of the numerical simulation for a benchmark case are presented first to illustrate the transient temperature, stress, strain, and displacement development. The calculated bending angles are compared with experimental data. Numerical sensitivity studies are then performed to evaluate the influence of the extrapolated material property data on bending.

4.1 Numerical Results and Comparison With Experimental Data. The numerical simulation was carried out first using a laser beam width of 29.2 μm and a pulse energy of 118.5 μJ. The surface temperature at the center of the laser irradiated area is shown in Fig. 5. The temperature reaches its peak value within the laser pulse duration at t = 13.7 ns. With the prescribed laser pulse energy, the maximum temperature obtained is below the melting temperature of steel. The temperature decreases rapidly at first due to heat conduction to the neighbor zone, then the rate of decrease slows down when the temperatures of the neighbor zone increase. The temperature decreases to 0.1 K over the room temperature of 300 K at about t = 2.4 ms. The temperature distributions along the surface and the centerline at t = 13.7 ns are shown in Figs. 6 and 7, respectively. The heat diffusion depth is less than 1 μm at this moment, therefore, the temperature gradient in the thickness direction is large, on the order of 1×10^9 K/m. The transient temperature development in the specimen is critical for the subsequent bending analysis. However, the temperature is not readily verified by experiments, since no general temperature measurement techniques are available to measure the temperature with a micrometer spatial resolution and a nanosecond time resolution.

Stress and plastic strain distributions along the irradiated surface at different times are shown in Figs. 8 and 9, respectively. The stress is compressive in the heated zone during the heating period (t = 5.17 ns and t = 13.7 ns). Plastic deformation has initiated at t = 5.17 ns which corresponds to a temperature of 700 K at the center point on the surface and the compressive plastic strain continues to increase till 13.7 ns when the maximum temperature is achieved. The plastically deformed zone on the irradiated surface is about 13 μm from the center point, which is close to the half of laser beam width. Notice that, at t = 13.7 ns, the compressive stress in the center area is close to zero, much lower than that at t = 5.17 ns. This is because the yield strength decreases as the temperature increases and is almost zero near the melting temperature (see Fig. 4). The same reason explains why, at t = 13.7 ns, the compressive stress at the center area is lower than that of its neighboring areas as shown in Fig. 8. During the cooling period, the stress changes direction from compressive to tensile, and yields again in the center area. Part of the compressive strain generated in the heating period is canceled out in the cooling period. The residual strain is compressive as seen in Fig. 9.

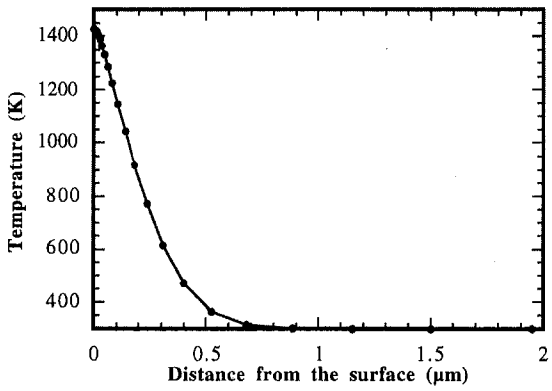


Fig. 7 Temperature distribution along the centerline at t = 13 ns

Downloaded 04 May 2010 to 171.66.16.27. Redistribution subject to ASME license or copyright; see http://www.asme.org/terms/Terms_Use.cfm

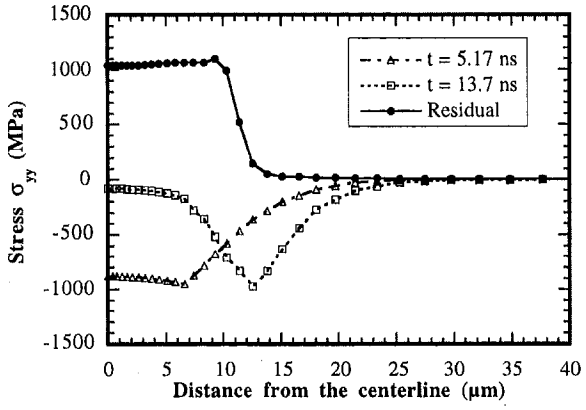


Fig. 8 Stress distributions along the surface at different times

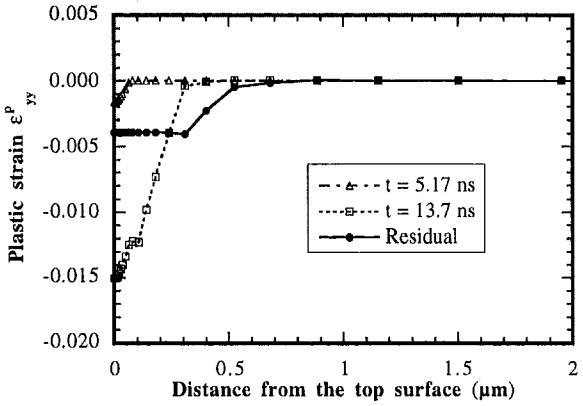


Fig. 11 Plastic strain distributions along the centerline at different times

Stress and plastic strain distributions along the centerline are shown in Figs. 10 and 11, respectively. The stress distributions are similar to Fig. 8. During heating, the stresses vary from compression in the region of about 0.7 μm from the surface, to tension in the region below 0.7 μm. The residual stress near the surface is tensile, but the region below 0.7 μm has a compressive residual stress in order to keep force equilibrium. The plastic strain distributions shown in Fig. 11 are similar to Fig. 9, except that the plastically deformed depth increases with time when heat flows into the sublayer during the cooling process. The final plastically deformed depth is 0.7 μm. Consistent with Fig. 9, the residual plastic strain is always compressive, which explains the formation of the bending angle towards the laser beam. If a longer laser pulse is used which induces a thicker heat affected and plastically deformed layer, a larger bending angle will result.

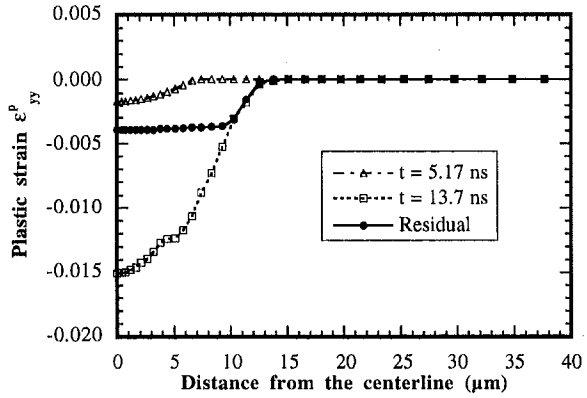


Fig. 9 Plastic strain distributions along the surface at different times

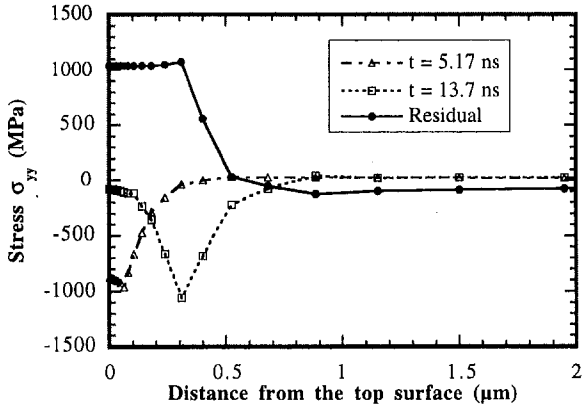


Fig. 10 Stress distributions along the centerline at different times

The beam deflection history is shown in Fig. 12. It agrees with the theoretical prediction—bending is in the direction away from the laser beam during heating and towards the laser beam during cooling. Note that the bending angle resumes to zero from negative at $t = 0.5$ ms, which corresponds to a temperature of 302 K at the center point of the surface, long after the laser pulse stops. The reason is that the laser pulse width is so short that the heat diffusion depth and correspondingly the plastically deformed depth are as thin as 0.7 μm, as seen in Figs. 6 and 11. The thicker, cooler neighboring material provides a strong constraint on the plastic zone. The target does not bend to the laser beam until the thermal strain is less than the summation of the plastic and elastic strains.

The calculated bending angles are compared to experimental values. Figure 13 shows the bending angle as a function of the laser beam width at a constant laser pulse energy of 118.5 μJ. The bending angle decreases with increasing laser beam width because the decreased laser intensity leads to the decrease of the temperature rise. It is seen that the calculated values agree with the experimental results within the experimental uncertainty. Figure 14 shows the bending angle as a function of the laser pulse energy at a constant laser beam width of 29.2 μm. Both the simulation and the experiment show that the bending angle increases almost linearly with the pulse energy. Again the calculated values agree with the experimental results within the experimental uncertainty. These agreements validate the computational model.

In the current model with the plane strain assumption, the strain in the x-direction is ruled out and bending is only allowed around the x-axis, although the distortion in the x-direction, thus bending around the y-axis is also possible because of the thermal expansion. Generally speaking, bending around the y-axis is small compared to that around the x-axis so that the two-dimensional

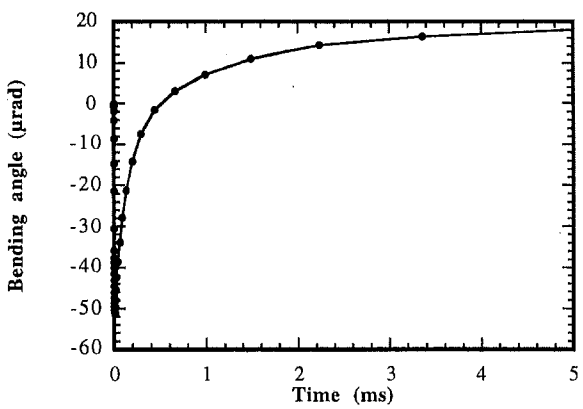


Fig. 12 Bending angle history

Downloaded 04 May 2010 to 171.66.16.27. Redistribution subject to ASME license or copyright; see http://www.asme.org/terms/Terms_Use.cfm

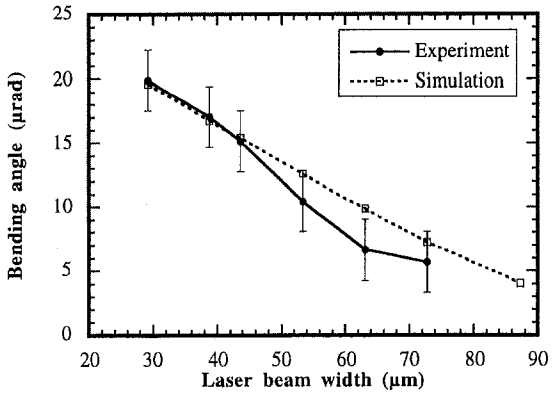


Fig. 13 Bending angle as a function of laser beam width at pulse energy of 118.5 μJ

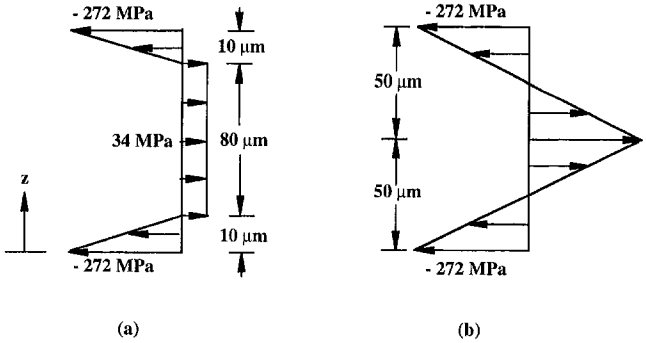


Fig. 15 Assumed distributions of σ_{yy} as a function of z

plane-strain assumption is a reasonable approximation to the essentially three-dimensional problem. If alternatively, the benchmark case is simulated with the generalized plane-strain assumption, i.e., the specimen is assumed to be bounded by two faces in the yz-plane that may move as rigid bodies with respect to each other, the calculated bending angle will decrease by about 20 percent. The computer code used is capable of performing the three-dimensional simulation. However, the three-dimensional simulation of this problem is currently not feasible due to both time and hardware (very fast workstation and huge memory) needed for performing such simulations.

4.2 Effect of Initial Residual Stresses. The bending angles obtained for un-annealed specimens are compared with those of annealed specimens. It is seen from Fig. 14 that the bending angles of the unannealed specimens are about 20 ~ 30 percent larger. The differences are caused by the initial residual stresses present in the un-annealed specimens due to cold rolling and grinding in specimen manufacturing and preparation. Using the X-ray diffraction technique, the residual stresses at the surface of the unannealed specimens are measured to be −272 MPa.

In order to numerically evaluate the influence of initial residual stresses on the bending angle, stress distributions have to be assumed since the X-ray measurement only provides stresses at the surface. Two types of stress distributions of σ_{yy} which satisfy self-equilibrium are assumed as a function of z, as shown in Fig. 15(a) and (b). The initial stresses σ_{zz} and σ_{yz} are assumed to be zero since in the bending problem, the stress σ_{yy} dominates the process. Thus the above assumed stress distributions are simplifications to the complicated residual stresses present in the specimens. Boundary pressures with the same distributions in Fig. 15(a) or (b) are applied to the right side of the computational domain in Fig. 3 to keep the boundary conditions satisfied. The displacements caused by the initial stresses and boundary conditions are negligible.

With the initial residual stresses shown in Fig. 15(a) and (b), the calculated bending angles at the laser pulse energy of 118.5 μJ and the laser beam width of 29.2 μm are increased to 25.46 μrad and 25.58 μrad, respectively, about 30 percent larger than that calculated with the initial stress-free condition, which agrees with the measurement. The bending angle is almost not affected by the difference in stress distributions since the plastically deformed depth is as thin as 0.7 μm, as shown in Fig. 11. Increasing the surface stress to −1000 MPa will increase the bending angle to 61.67 μrad, while changing the sign of the surface stress to tension will decrease the bending angle.

The effect of initial residual stresses is also evaluated by simulating bending caused by a second laser pulse irradiating on the same position as the first one. Because of the high tensile residual stresses on the surface caused by the first pulse (see Fig. 8 and 10), the calculated additional bending angle due to the second pulse is only 0.2 percent of that for the first one. This result agrees with the experimental observation that the bending angle from the second pulse is smaller than the experimental resolution.

4.3 Sensitivity Studies of Unknown Materials Properties. Materials properties at high temperatures are not known and are extrapolated in the calculation. The dashed lines in Fig. 4 are the extrapolated values. Density, thermal conductivity, and specific heat are linearly extrapolated at temperatures above 1255 K. Since the peak temperature achieved is 1427 K, the uncertainties in extrapolations of these properties from 1255 K to 1427 K would not significantly influence the computation results. For example, if the value of 710 J/kgK for specific heat is used instead of the linearly extrapolated value of 800 J/kgK at 1773 K, thermal diffusivity is increased and the calculated peak temperature should decrease. Calculations show that the peak temperature only decreases from 1427 K to 1421 K. Using the same mechanical property data, the calculated bending angles using the two temperature fields differ by 0.5 percent. Therefore, linear extrapolations of thermal property data have little influence on the computational results.

Optical reflectivity of the specimen surface near the normal direction was measured to be 0.6 at the wavelength of 1047 nm. The measured reflectivity only includes the specular component, diffusely reflected light is not captured by the measurement apparatus. Therefore, the actual surface reflectivity could be a little higher than 0.6. If the measured value, 0.6, instead of the value of 0.66 calculated from the refractive index of iron, is used, the peak temperature will increase to 1584 K and the corresponding bending angle will have a 23 percent increase, from 19.60 μrad to 24.16 μrad.

The thermal expansion coefficient above 811 K in Fig. 4(d) is the extra-hard specimen data linearly extrapolated to 17.6 × 10^{-6}/K at 1773 K. The bending angle changes about 0.25 percent

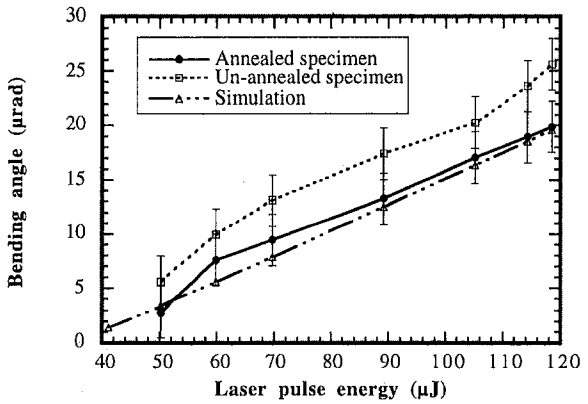


Fig. 14 Bending angle as a function of laser pulse energy at a laser beam width of 29.2 μm

Downloaded 04 May 2010 to 171.66.16.27. Redistribution subject to ASME license or copyright; see http://www.asme.org/terms/Terms_Use.cfm

if the extrapolated value is increased or decreased by 1.0×10^{-6}/K. However, if the data for the annealed steel (Fig. 4(*d*)), which are about 15–18 percent larger than those for the extra-hard steel, are used, there will be an 18 percent increase in the bending angle.

As shown in Fig. 4(*e*), the Young's modulus at temperatures above 811 K is not available and is set to be 20 GPa at 1273 K and 2.0 GPa at 1773 K. Linear interpolations are used between 811 K and 1273 K and between 1273 K and 1773 K. Changing values to 50 GPa (or 2.0 GPa) at 1273 K and 10 GPa (or 0.2 GPa) at 1773 K does not change the bending angle because these values mainly affect the magnitude of elastic strain in the region whose temperatures are greater than 811 K. When the temperatures cool down, the elastic strains resume so that the residual strain and stress are not affected. On the other hand, between the room temperature and 811 K, the Young's modulus data have an uncertainty range of ± 10 GPa as indicated in Fig. 4(*e*). If the entire curve of the Young's modulus is increased (or decreased) by 10 GPa, there will be about four percent increase (or decrease) in the bending angle. The reason that the higher Young's modulus yields larger bending angle is as follows: (1) The higher the Young's modulus at that neighboring region that is at lower temperatures, the greater the compressive stress resulting from more restriction of thermal expansion, i.e., the greater the compressive strain. (2) During the cooling process, the stress in the plastically compressed zone changes from compression to tension. A larger Young's modulus corresponds to a smaller tensile elastic strain at the same stress level. These two effects increase the residual compressive strain which causes more bending.

The yield strength for temperatures above 922 K is not available, and values of 140 MPa at 1143 K and 10 MPa at 1773 K are assumed (Fig. 4(*f*)). The literature data also have lower and upper bounds of the yield strength at temperatures below 922 K, and the lower bound values are used in the calculation. Linear interpolations are used between 922 K and 1143 K and between 1143 K and 1773 K. If instead, 210 MPa and 70 MPa are used at these two temperatures, there is only 0.2 percent decrease in the bending angle. If the upper bound of yield strength in Fig. 4(*f*) is used, which corresponds to 1276 MPa at room temperature instead of 1103 MPa used in the previous calculations, then there is about five percent increase in the bending angle. This is because with higher yield strength at lower temperatures, less compressive strain is offset when the heated zone yields in tension during the cooling process.

The strain-hardening parameter is not available in literature, and a linearly elastic-perfectly plastic material model is applied in the above calculations. If a constant (although it is temperature-dependent) strain hardening parameter of 0.03 (the ratio of the slope of strain hardening to the Young's modulus) with the isotropic hardening rule is used, the bending angle is increased by about six percent since isotropic hardening has the similar effect as higher yield strengths at lower temperatures. To the contrary, if the kinematic hardening rule is used with the same strain-hardening parameter, the bending angle will decrease by about six percent.

The temperature-dependent data of the Poisson's ratio is not available, and a constant value of 0.30 at the room temperature is used in the above calculations. Poisson's ratio is not expected to be important in this work because in the bending process, the stress in the y-direction is much larger than those in other directions, and an approximately uniaxial stress state presents near the surface. In fact, if the Poisson's ratio is assumed to vary linearly from 0.30 at 293 K to 0.45 at 1773 K, the calculated bending angle only increases six percent.

In summary, the numerical sensitivity studies show that both optical reflectivity and thermal expansion coefficient significantly influence the bending angle, while the possible errors resulting from extrapolating other material properties at high temperatures are within the experimental uncertainty. Therefore, the numerical results are acceptable although the extrapolated material properties used in the calculations are somewhat arbitrary. If the numerical uncertainties caused by uncertain material properties need to be reduced, experiments with better accuracy are needed.

5 Conclusions

Pulsed laser bending of stainless steel was studied in this work. Experimental studies were conducted to find out the relations between the obtained bending angle and the processing parameters, including the laser beam width and the pulse energy. The pulsed laser-bending process with a single, line-shape laser pulse was analyzed with a finite element, two-dimensional plane-strain model. It was found that the bending angle decreased with the increasing laser beam width at constant laser energy, and increased almost linearly with the laser pulse energy. The calculated bending angle compared well with experimental data within the experimental uncertainty range. It was demonstrated by the numerical simulation that pulsed laser bending could be interpreted as the thermally induced plastic compression in the heated zone near the target surface. Initial compressive residual stresses on the specimen surface are beneficial to increasing the bending angle. Sensitivity studies of the materials properties showed that both optical reflectivity and thermal expansion coefficient significantly influenced the bending angle, while the extrapolated material properties at high temperatures yielded acceptable results.

Acknowledgment

Supports to this work by the Purdue Research Foundation and by the National Science Foundation (DMI-9813758) are gratefully acknowledged. G. C. and X. X. would also like to thank Prof. Klod Kokini of the School of Mechanical Engineering, Purdue University for many valuable discussions.

References

Alberti, I., Franiti, L., and Micari, F., 1994, "Numerical Simulation of the Laser Bending Processing by a Coupled Thermal Mechanical Analysis," *Laser Assisted Net Shape Engineering, Proc. of the LANE'94,* Vol. 1, pp. 327–336.

Arnet, H., and Vollertsen, F., 1995, "Extending Laser Bending for the Generation of Convex Shapes," *Proc. Instn. Mech. Engrs.,* Vol. 209, pp. 433–442.

Bae, K.-Y., and Na, S.-J., 1996, "An Analysis of Thermal Stress and Distortion in Bead-on-Plate Welding using laminated Isotropic Plate Theory," *Journal of Materials Processing Technology,* Vol. 57, pp. 337–344.

Chen, G., Xu, X., Poon, C. C., and Tam, A. C., 1998, "Laser-Assisted Microscale Deformation of Stainless Steels and Ceramics," *Optical Engineering,* Vol. 37, pp. 2837–2842.

Geiger, M., 1994, "Synergy of Laser Material Processing and Metal Forming," *Annals of the CIRP,* Vol. 43, pp. 563–570.

Lynch, D. W., and Hunter, W. R., 1985, "Comments on the Optical Constants of Metals and an Introduction to the Data for Several Metals," *Handbook of the Optical Constants of Solids,* E. D. Palik, ed., Academic Press, Orlando, FL, pp. 385–396.

Maykuth, D. J., 1980, *Structural Alloys Handbook,* Vol. 2, Metals and Ceramics Information Center, Battelle Columbus Laboratory, Columbus, OH, pp. 1–61.

Namba, Y., 1986, "Laser Forming in Space," *Int. Conf. On Lasers '85,* C. P. Wang, ed., pp. 403–407.

Radaj, D., 1992, *Heat Effects of Welding—Temperature Field, Residual Stress, Distortion,* Springer-Verlag, Berlin.

Scully, K., 1987, "Laser Line Heating," *Journal of Ship Production,* Vol. 3, pp. 237–246.

Vollertsen, F., Geiger, M., and Li, W. M., 1993, "FDM- and FEM-Simulation of Laser Forming: A Comparative Study," *Advanced Technology of Plasticity,* Z. R. Wang and Y. He, eds., International Academic Publishers, Beijing, China, pp. 1793–1798.

Vollertsen, F., 1994a, "Mechanisms and Models for Laser Forming," *Laser Assisted Net Shape Engineering, Proc. of the LANE'94,* Vol. 1, pp. 345–360.

Vollertsen, F., 1994b, "Model for the Temperature Gradient Mechanism of Laser Bending," *Laser Assisted Net Shape Engineering, Proc. of the LANE'94,* Vol. 1, pp. 371–378.

Downloaded 04 May 2010 to 171.66.16.27. Redistribution subject to ASME license or copyright; see http://www.asme.org/terms/Terms_Use.cfm

Nonlinear Analysis of Particle Cavitation and Matrix Yielding Under Equitriaxial Stress

S. Biwa
Department of Micro System Engineering,
Nagoya University,
Nagoya 464-8603, Japan

Cavitation of a rubber particle is a possible microscopic mechanism for toughness improvement of polymer materials, as it reduces the stress triaxiality and promotes shear yielding in the matrix. This phenomenon is presently studied theoretically by examining the radial deformation of a particle-matrix composite sphere. The rubber particle is modeled as a nonlinear elastic sphere and the surrounding matrix as a concentric elastoplastic shell. Two possible modes of deformation are identified: One represents the pure expansion of the particle and the other corresponds to particle cavitation. The analysis accounts for finite bulk stiffness of the particle and possibility of plastic yielding in the matrix. Based on the analytical expressions for the finite deformation and the stress fields derived, numerical solutions are demonstrated to illustrate the effect of cavitation to suppress the increase of triaxial stress and enhance the plastic yielding in the matrix.

Introduction

It is well known that polymers can be toughened by incorporation of fine elastomeric particles, typically with increase of fracture toughness and impact resistance by an order of magnitude. Microscopy studies have revealed that under excessive stress conditions, internal rubber phases undergo voiding or cavitation. Cavitation of rubber particles has been found in a broad range of material systems such as HIPS and ABS blends (Beahan et al., 1976), epoxy-CTBN rubber system (Yee and Pearson, 1986), rubber-modified PVC (Breuer et al., 1977), and nylon-rubber blends (Bucknall et al., 1989), to name but a few. Among other toughening mechanisms proposed, particle cavitation has been recognized to play a crucial role for the toughness improvement by suppressing the growth of triaxial stress and promoting shear yielding in the matrix.

Cavities also tend to be created in "bulk" rubbers when subjected to high triaxial stress fields, as observed by, e.g., Gent and Lindley (1958). A theoretical formulation was given by Ball (1982) for cavitation in the context of bifurcation of equilibrium solutions in nonlinear elasticity. The cavitation phenomenon was viewed in mathematical terms as the occurrence of a cavity-opening deformation mode at a critical point on the solution path representing pure volume expansion. The theoretical approach has had many followers, and an outline of the recent progress as well as relevant references can be found in a review provided by Horgan and Polignone (1995).

The objective of the present study is to apply this type of analysis to cavitation in an elastomeric particle embedded in an elastoplastic matrix, and to show how the stress state and the development of plastic deformation in the matrix is influenced by the occurrence of cavitation. Namely, cavitation is examined for a nonlinear elastic sphere contained in an elastoplastic matrix subjected to prescribed radial displacement. A similar problem of cavitation in a concentric composite sphere has been analyzed by Horgan and Pence (1989). They employed incompressible neo-Hookean elastic models both for the inner sphere and the outer shell, so that the whole composite sphere also deformed in an isochoric manner. The present study incorporates a finite bulk stiffness of the particle as well as the possibility of plastic deformation in the matrix. To the present purpose, these two features seem rather essential for the following reasons. First, an inelastic framework is indispensable when applied to rubber-toughened polymer materials, albeit within a simple problem setting. Further, although rubbery solids are reasonably approximated as incompressible materials in ordinary situations, bulk moduli of rubbers are only comparable to, or even smaller than, those of polymeric matrix materials. Therefore, when a rubber particle is contained in a polymer matrix, the nonzero feature of its bulk compliance should be taken into account.

In what follows, the constitutive model and the radial deformation fields are described for a spherical particle characterized by a neo-Hookean model with slight compressibility and a concentric elastoplastic spherical shell. The equilibrium solutions for the two phases are connected by appropriate boundary conditions for the particle-matrix interface. Numerical analysis is carried out for the stress and strain fields in the composite sphere system for the cases with and without the occurrence of cavitation. Based on the numerical results, effects of particle cavitation on the stress state and the growth of plastic strains in the matrix are illustrated in detail.

Formulation of the Problem

Deformation and Equilibrium. Consider a particle-matrix system consisting of a rubbery elastic particle of radius A and a concentric spherical elastoplastic matrix shell with outer radius B (Fig. 1(a)). This composite sphere system is subjected to uniform radial displacement on the outermost surface. The resulting deformation is radially symmetric, and described by the radial coordinate r in the deformed state as a function of its undeformed counterpart R. In the initial state, the particle occupies the region $0 \le R < A$ and the rest $A \le R \le B$ corresponds to the matrix. The radial deformation $r(R)$ implies the deformation gradient of the form

$$\mathbf{F} = r'\hat{\mathbf{i}}_r \otimes \hat{\mathbf{i}}_r + \frac{r}{R}(\hat{\mathbf{i}}_\theta \otimes \hat{\mathbf{i}}_\theta + \hat{\mathbf{i}}_\phi \otimes \hat{\mathbf{i}}_\phi), \tag{1}$$

where $\hat{\mathbf{i}}_r$, $\hat{\mathbf{i}}_\theta$, and $\hat{\mathbf{i}}_\phi$ constitute an orthonormal basis and $r' \equiv dr/dR$. The positive nature of the Jacobian $J = r'(r/R)^2$ requires $r' > 0$. For the radial deformation at hand, the only nontrivial condition for static equilibrium is

Contributed by the Applied Mechanics Division of THE AMERICAN SOCIETY OF MECHANICAL ENGINEERS for publication in the ASME JOURNAL OF APPLIED MECHANICS.
Discussion on the paper should be addressed to the Technical Editor, Professor Lewis T. Wheeler, Department of Mechanical Engineering, University of Houston, Houston, TX 77204-4792, and will be accepted until four months after final publication of the paper itself in the ASME JOURNAL OF APPLIED MECHANICS.
Manuscript received by the ASME Applied Mechanics Division, Oct. 15, 1998; final revision, Mar. 8, 1999. Associate Technical Editor: A. Needleman.

 Copyright © 1999 by ASME

Downloaded 04 May 2010 to 171.66.16.27. Redistribution subject to ASME license or copyright; see http://www.asme.org/terms/Terms_Use.cfm

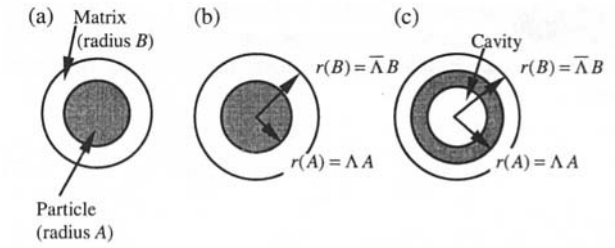


Fig. 1 Composite sphere model and two expansion modes. (*a*) Undeformed particle-matrix system, (*b*) noncavitating solution, and (*c*) cavitating solution.

$$\frac{d\tau_r}{dR} + \frac{2r'}{r}(\tau_r - \tau_\theta) = 0 \tag{2}$$

for the radial and the circumferential Cauchy stress components, τ_r and τ_θ, respectively, when the material coordinate R is chosen as a primary variable.

The prescribed radial deformation applied to the outer surface of the matrix is expressed by

$$r(B) = \bar{\Lambda} B, \tag{3}$$

where $\bar{\Lambda} > 1$ is the expansion ratio applied to the composite sphere. At the particle-matrix boundary, the continuity of the radial traction and the radial displacement are required. Furthermore, a nonvanishing value of $r_c = r(0)$ is allowed to account for the formation of a spherical cavity at the center of the particle, which is assumed to be traction-free. This situation is formulated as the condition

$$r(0) = 0 \quad \text{or} \quad \tau_r(0) = 0, \tag{4}$$

which is common to most cavitation analyses, cf. Horgan and Polignone (1995).

Constitutive Law for the Particle. The stress-stretch relation of homogeneous, isotropic and hyperelastic solid for the radial deformation is given by

$$\tau_r = \frac{1}{J}\frac{\partial W}{\partial \lambda_1}\lambda_1, \quad \tau_\theta = \frac{1}{J}\frac{\partial W}{\partial \lambda_2}\lambda_2,$$

$$\lambda_1 = r', \quad \lambda_2 = \lambda_3 = \frac{r}{R}, \tag{5}$$

where the function $W = W(\lambda_1, \lambda_2, \lambda_3)$ represents the strain energy stored per unit undeformed volume. Among various constitutive models of rubber elasticity, Stringfellow and Abeyaratne (1989) have given support to the use of the simple neo-Hookean model in the context of cavitation analysis via comparison with experimental findings. For the reason mentioned in Introduction, presently the particle is modelled to be a compressible neo-Hookean solid for which the strain energy function has been proposed as (Levinson and Burgess, 1971)

$$W = \frac{\mu}{2}\{\lambda_1^2 + \lambda_2^2 + \lambda_3^2 - 3 - 2(J-1) + \beta(J-1)^2\}, \tag{6}$$

where the material constant μ denotes the shear modulus for infinitesimal deformation, and β represents the resistance against volume expansion. When $\beta \to \infty$, the kinematical constraint $J = 1$ is equivalently imposed and the above model reduces to that for incompressible neo-Hookean solids. This model is a fair representation of rubbery materials when β takes on a high value, namely, for slightly compressible solids. Alternative parameter defined by $\epsilon = 1/\beta$ is also used in the following discussion to represent the compressibility of the material. For this material, the bulk modulus K_p and Poisson's ratio ν_p at undeformed state read

$$K_p = \frac{\mu}{3}(3\beta - 1), \quad \nu_p = \frac{\beta - 1}{2\beta}. \tag{7}$$

Constitutive Law for the Matrix. The matrix material is assumed to be an elastoplastic solid which constitutive equation is given by a finite-strain generalization of the classical Prandtl-Ruess model obeying the J_2-flow theory (see Durban and Baruch, 1977, for details). In the present spherically symmetric setting, the Mises stress τ_e controlling the onset of plastic yielding reduces to $\tau_e = |\tau_\theta - \tau_r| = m(\tau_\theta - \tau_r)$, where $m = \text{sgn}(\tau_\theta - \tau_r)$. The strain-hardening characteristics of the matrix can be specified as $\epsilon_e^P = \epsilon_e^P(\tau_e)$ giving the Odqvist parameter of accumulated distortion (equivalent plastic strain) ϵ_e^P as a monotonic function of its energy-conjugate τ_e. Although it is noted in passing that much progress has been made concerning more elaborate constitutive modeling of inelastic response of polymers (cf., van der Giessen, 1997) meriting incorporation in the future study, this classical model is chosen here to take advantage of the existing analytical results as introduced later.

Description of Equilibrium Solutions

Equilibrium Solution for the Particle. In this chapter, equilibrium solutions will be described for the hyperelastic particle and the elastoplastic matrix, respectively, and later combined together accounting for appropriate continuity conditions for the interface traction and displacement.

One immediately finds that the following form is a solution satisfying the equilibrium (2) as well as the condition $(4)_1$ and represents pure expansion of the sphere (Fig. 1(*b*));

$$r(R) = \Lambda R. \tag{8}$$

In the above expression $\Lambda > 1$ is the expansion ratio of the particle. For this solution the stress and the stretch are uniform in the particle. For the material given by (6), the radial Cauchy traction on the surface of the particle, $T = \tau_r(A)$, becomes

$$T = \mu\{\Lambda^{-1} - 1 + \beta(\Lambda^3 - 1)\}, \tag{9}$$

which expresses the response of the particle under pure dilatation.

On the other hand, the cavity-opening mode with $r(0) > 0$ (Fig. 1(*c*)), which satisfies $(4)_2$ and the surface radial displacement $r(A) = \Lambda A$, is examined below. To this end, transformation of variable is carried out employing the local circumferential stretch r/R as an independent variable and the local radial stretch r' as dependent;

$$t = r(R)/R, \quad s(t) = r'(R). \tag{10}$$

After some lengthy manipulation upon substituting the particular constitutive law (5) and (6) into (2) and using (10), the equation for equilibrium reduces to

$$(1 + \beta t^2)\frac{ds(t)}{dt} = -2(1 + \beta s t^3). \tag{11}$$

This differential equation admits a total differential form by an integration factor, and yields the following solution:

$$s(t) = \{C_0 - \psi(t)\}/\sqrt{1 + \beta t^4}, \tag{12}$$

$$\psi'(t) = 2/\sqrt{1 + \beta t^4}, \tag{13}$$

where C_0 is an integration constant. It suffices here to consider the case where $\epsilon = 1/\beta$ is sufficiently small as the model in (6) is more justifiable for slight compressibility. Then to the first order in ϵ the solution is written by

$$s(t) = \frac{\Delta\Lambda^2}{t^2}\left\{1 + \frac{\epsilon}{2}(\Lambda^{-4} - t^{-4})\right\} - \frac{2\epsilon}{t^2}(\Lambda^{-1} - t^{-1}), \tag{14}$$

where $\Delta = s(\Lambda)$ is the radial stretch at $R = A$.

Downloaded 04 May 2010 to 171.66.16.27. Redistribution subject to ASME license or copyright; see http://www.asme.org/terms/Terms_Use.cfm

From (5), (6), and (10), the radial stress is evaluated in terms of t and $s(t)$, and the condition in $(4)_2$ is enforced to establish the relation between Δ and Λ as

$$\Delta = \Lambda^{-2}\{1 + \epsilon(1 + 2\Lambda^{-1} - \Lambda^{-4}/2)\}. \tag{15}$$

As a consequence, the radial stress at $R = A$ is written by

$$T = \tau_r(A)$$
$$= \mu\{2\Lambda^{-1} + \Lambda^{-4}/2 + \epsilon\Lambda^{-4}(1 + 2\Lambda^{-1} - \Lambda^{-4}/2)\}, \tag{16}$$

which gives the overall response of the cavitated particle for radial deformation. The deformation field can be readily determined from (10) using t as a parameter. It can be shown (cf., Biwa, 1995) but is presently assumed a priori that the relation between the original variable R and the introduced one t is monotonic and $dR/dt < 0$, which further implies $s(t) < t$ from (10). Therefore, $\Delta < \Lambda$ and from (15), this type of solution is subjected to the following restriction:

$$F(\Lambda) \equiv \Lambda^3 - 1 - \epsilon(1 + 2\Lambda^{-1} - \Lambda^{-4}/2) > 0. \tag{17}$$

Equilibrium Solution for the Matrix. The analytical solution for the radial deformation of an elastoplastic thick spherical shell has been obtained by Durban and Baruch (1977). Due to the limited space, only the outcome of their theory is summarized here for later use. Further, for the present purpose the monotonic loading situation with $m = \text{sgn}(\tau_\theta - \tau_r) = 1$ for $A \le R \le B$ throughout the deformation process will suffice so that the following description assumes $\tau_e = \tau_\theta - \tau_r$.

In the theoretical derivation, it is convenient to employ the local Mises stress τ_e as a primary variable, on the assumption that a monotonic relation exists between τ_e and R. Then, through somewhat lengthy manipulation, the equilibrium deformation and stress fields can be obtained as described below. Prior to explicitly showing the required results, it turns out convenient to normalize stress variables as $\tilde{\tau} = \tau_e/\tau_Y$, where τ_Y is any reference stress, later taken as a particular value. Young's modulus E and Poisson's ratio ν of the matrix are used to characterize the elastic property of the matrix. With the above normalization, $\epsilon_Y \equiv \tau_Y/E$ is also used.

The deformation field is given by

$$R = B \exp\left[-\tfrac{1}{2}\int_{\tilde{\tau}_B}^{\tilde{\tau}} \tilde{e}(\tilde{\tau})\xi(\tilde{\tau})d\tilde{\tau}\right], \tag{18}$$

$$r = \bar{\Lambda}B \exp\left[-\tfrac{1}{2}\int_{\tilde{\tau}_B}^{\tilde{\tau}} \xi(\tilde{\tau})d\tilde{\tau}\right] \tag{19}$$

with the normalized local Mises stress $\tilde{\tau}$ as a parameter, where

$$\tilde{e}(\tilde{\tau}) = \exp\left\{\frac{(1+\nu)\tau_e}{E} + \frac{3}{2}\epsilon_e^P(\tau_e)\right\}, \quad \tau_e = \tau_Y\tilde{\tau}, \tag{20}$$

$$\xi(\tilde{\tau}) = \frac{2(1-\nu)\epsilon_Y + d\epsilon_e^P/d\tilde{\tau}}{\tilde{e}(\tilde{\tau}) - 1 + 2(1-2\nu)\epsilon_Y\tilde{\tau}}, \tag{21}$$

and $\tilde{\tau}_B$ is the value of $\tilde{\tau}$ evaluated at $R = B$. The distribution of the stress is governed by

$$\frac{\tau_r}{\tau_Y} = \frac{\bar{T}}{\tau_Y} - \int_{\tilde{\tau}_B}^{\tilde{\tau}} \tilde{\tau}\xi(\tilde{\tau})d\tilde{\tau}, \quad \frac{\tau_\theta}{\tau_Y} = \tilde{\tau} + \frac{\tau_r}{\tau_Y}, \tag{22}$$

where $\bar{T} = \tau_r(B)$ is the radial stress at $R = B$. The relation between $\bar{T}$ and $\bar{\Lambda}$ is established as

$$\ln\bar{\Lambda} = (1-2\nu)\epsilon_Y\frac{\bar{T}}{\tau_Y} + (1-\nu)\epsilon_Y\tilde{\tau}_B + \frac{1}{2}\epsilon_e^P(\tau_Y\tilde{\tau}_B) \tag{23}$$

using $\tilde{\tau}_B$.

Let $\tilde{\tau}_A$ be the value of $\tilde{\tau}$ at $R = A$, and let $\Lambda = r(A)/A$ in the same notation as in the previous section. From (18) and (19), the boundary values $\tilde{\tau}_A$ and $\tilde{\tau}_B$ must satisfy the following two conditions:

$$\ln\left(\frac{B}{A}\right) = \frac{1}{2}\int_{\tilde{\tau}_B}^{\tilde{\tau}_A} \tilde{e}(\tilde{\tau})\xi(\tilde{\tau})d\tilde{\tau}, \tag{24}$$

$$\ln\left(\frac{\bar{\Lambda}B}{\Lambda A}\right) = \frac{1}{2}\int_{\tilde{\tau}_B}^{\tilde{\tau}_A} \xi(\tilde{\tau})d\tilde{\tau}. \tag{25}$$

If the radial stress at $R = A$ is denoted by T, $(22)_1$ implies

$$\frac{\bar{T}}{\tau_Y} - \frac{T}{\tau_Y} = \int_{\tilde{\tau}_B}^{\tilde{\tau}_A} \tilde{\tau}\xi(\tilde{\tau})d\tilde{\tau}, \tag{26}$$

which gives $T < \bar{T}$ as the integral in the right-hand side is positive.

Solution for the Particle-Matrix System. For a prescribed value of $\bar{\Lambda}$ in the boundary condition (3), the four conditions (23)–(26), supplemented by the particle response Eq. (9) or (16), and the interface continuity conditions for $r(R)$ and $\tau_r(R)$ at $R = A$, constitute a system of equations to determine five parameters $\tilde{\tau}_A$, $\tilde{\tau}_B$, Λ, T, and $\bar{T}$. The interface conditions have already been implicitly considered in the description of equilibrium solutions for the two regions by denoting the expansion ratio and the traction at $R = A$ by the same symbols Λ and T, respectively.

If the applied expansion ratio $\bar{\Lambda}$ is sufficiently small, the traction transferred to the particle also remains small so that the particle remains intact (noncavitating mode). If the expansion ratio increases to a certain extent, two modes of the particle deformation become possible, i.e., cavitating and noncavitating modes.

For the noncavitating mode, the set of equations to be solved is (9) and (23)–(26) for the unknowns $\tilde{\tau}_A$, $\tilde{\tau}_B$, Λ, T, and $\bar{T}$. Likewise, for the cavitating mode (16) and (23)–(26) are solved. Once these parameters are determined, the stress and the deformation fields in the matrix can be calculated by the integrals (18), (19), and (22). The two modes of deformation are obtained below by solving the two corresponding sets of equations numerically by the Newton-Raphson method.

The hardening characteristics of the matrix is now expressed by the following equation of Ramberg-Osgood type:

$$\epsilon_e^P = \alpha\left(\frac{\tau_e}{\tau_Y}\right)^m, \tag{27}$$

where τ_Y and α are in principle determined from uniaxial experiments. Although this form does not define an unambiguous yield point, the slope of the stress-strain curve becomes very small as the stress approaches τ_Y by choosing a high value of m. Also, τ_Y can be characterized as the flow stress corresponding to the plastic strain of magnitude α. In the numerical analysis below, $\alpha = 0.1$ is used and τ_Y is the ten percent strain flow stress, hereafter referred to as the reference flow stress.

Table 1 shows the values of the material parameters used for the numerical simulation. Three cases were examined to study the influence of the matrix flow stress τ_Y and the ratio between the particle radius and the matrix shell thickness B/A. The first case, Case I, serves as the reference. In Case II, the matrix has comparatively low flow stress while keeping other parameters unchanged. In Case III, the matrix volume surrounding the particle is smaller than Case I with other factors retained. The numerical values were all chosen to reasonably represent practical material systems, except that intrinsic strain softening common to polymers is not accounted for presently. It should be noted that since the bulk modulus of the particle is of comparative order as, even smaller than, the bulk modulus of the matrix, the ordinary approximation of incompressible hyperelastic particle (with infinite bulk modu-

Downloaded 04 May 2010 to 171.66.16.27. Redistribution subject to ASME license or copyright; see http://www.asme.org/terms/Terms_Use.cfm

Table 1 Material parameters used for numerical simulation

	Case I (Reference)	Case II (Low τ_Y)	Case III (Low B/A)
Matrix/particle ratio of radii, B/A	2.0	2.0	1.3
Matrix reference flow stress, τ_Y [MPa]	70	20	70
Matrix Young's modulus, E [MPa]	3000	3000	3000
Matrix Poisson's ratio, ν	0.39	0.39	0.39
Matrix reference plastic strain, α	0.1	0.1	0.1
Matrix hardening exponent, m	20	20	20
Particle shear modulus, μ [MPa]	1.0	1.0	1.0
Particle bulk modulus, K_p [MPa]	2000	2000	2000

lus) might lead to inaccurate predictions. In the present analysis, the finite bulk modulus of the particle is accounted for even though its Poisson's ratio is quite close to the incompressibility limit 0.5, i.e., $\nu_p \cong 0.49975$ (the corresponding value of the parameter ϵ is quite small and approximately 5.0×10^{-4}).

Results and Discussion

Cavitation Behavior of the Particle. Before proceeding to the discussion of the response of the particle-matrix system, the cavitation behavior of the particle is summarized briefly. Although the issue has been revisited repeatedly (Horgan and Polignone, 1995), the results obtained for the slightly compressible neo-Hookean solid (6) appear new. When the expansion ratio Λ applied to the particle is small, the particle remains intact. In this situation the traction acting on the particle surface is governed by (9) which is the response of the hyperelastic solid (6) at pure volume expansion. When Λ is sufficiently large, this solution is still possible but another competing solution having a cavity at the center can exist. Letting $\Delta \to \Lambda \to \Lambda_{CR}$ in (15), the critical value of the expansion ratio Λ_{CR} can be solved implicitly from

$$(\Lambda_{CR}^3 - 1)/(1 + 2\Lambda_{CR}^{-1} - \Lambda_{CR}^{-4}/2) = \epsilon. \tag{28}$$

As Λ exceeds Λ_{CR} determined above, the function $F(\Lambda)$ in (17) changes its sign. Since $F'(\Lambda) > 0$ for $\Lambda > 1$, this means that $F(\Lambda) < 0$ for $\Lambda < \Lambda_{CR}$ and $F(\Lambda) > 0$ for $\Lambda > \Lambda_{CR}$. Therefore, the cavitating solution exists when $\Lambda > \Lambda_{CR}$ based on (17). Using Λ_{CR}, the corresponding critical value of the surface radial stress T_{CR} reads

$$T_{CR} = \mu(3\Lambda_{CR}^{-1} - \Lambda_{CR}^{-4}/2). \tag{29}$$

The dependence of Λ_{CR} and T_{CR} on the compressibility parameter ϵ is shown in Fig. 2. It is observed that due to the slight bulk compliance the critical expansion ratio increases to a certain extent while the critical Cauchy radial stress decreases.

The response of the particle before and after cavitation is shown in Fig. 3. It is important for later discussion to recognize that the radial stress increases rather proportionally as the particle expansion ratio when cavitation does not occur, while after the occurrence of cavitation it tends to only sustain a stress level slightly below the cavitation stress. To plot this figure, the parameter ϵ is chosen as 0.012 as this value may illustrate the slope of the stress-expansion relation more visibly. For the situations selected in Table 1, it is remarked that ϵ becomes much smaller and the slope for the noncavitating solution is actually much greater. For the incompressibility limit with $\epsilon \to 0$, one immediately recovers the well-known results for the incompressible neo-Hookean material.

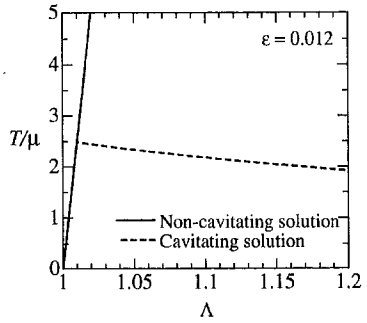


Fig. 3 Relation between particle expansion ratio and stress for noncavitating and cavitating solutions

Overall Response of the Composite Sphere. The variation of the stress $\bar{T}$, referred to as the composite radial stress, with $\bar{\Lambda}$, the composite expansion ratio, is shown in Fig. 4 for the three cases introduced above. This relation may be interpreted as the overall response of the composite sphere system, and it is the purpose here to examine how the behavior of the composite sphere depends on the occurrence of cavitation.

In the three cases in Fig. 4, noncavitating solutions show quite steep stress-expansion slopes, which indicates that unless cavitation occurs, the composite system has a large overall stiffness against volume change. This large overall bulk stiffness relates to the fact that the particle has a bulk modulus comparable to that of the matrix. This further implies that as the expansion ratio is increased a large amount of bulk strain energy is stored both in the particle and the matrix. On the other hand, the cavitating solutions involve much lower overall stiffness, and show a softening behavior once the stress reaches the corresponding maximum stress level. The cavitation stress of the particle, and the radial traction that the particle sustains thereafter, are relatively small for the stress range shown in Fig. 4. That is, cavitation occurs at quite an early stage of the straining (the stretches of the composite sphere at cavitation were roughly $\bar{\Lambda} \cong 1.0002$ in every case), and afterwards the cavitated composite sphere essentially behaves as a hollow elastoplastic matrix sphere loaded in the radial direction. This overall response is akin to what have been confirmed for elas-

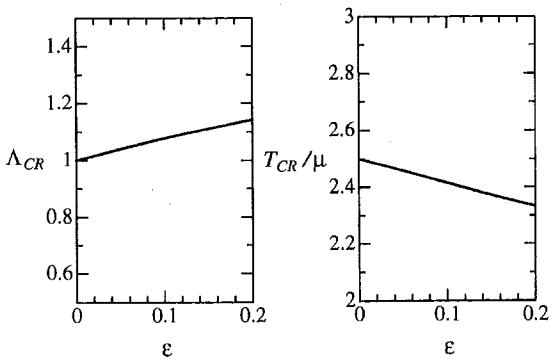


Fig. 2 Influence of particle bulk compliance on the critical expansion ratio and the critical stress

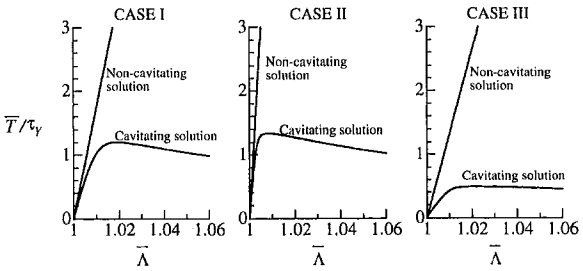


Fig. 4 Relation between composite expansion ratio and stress for noncavitating and cavitating solutions

Downloaded 04 May 2010 to 171.66.16.27. Redistribution subject to ASME license or copyright; see http://www.asme.org/terms/Terms_Use.cfm

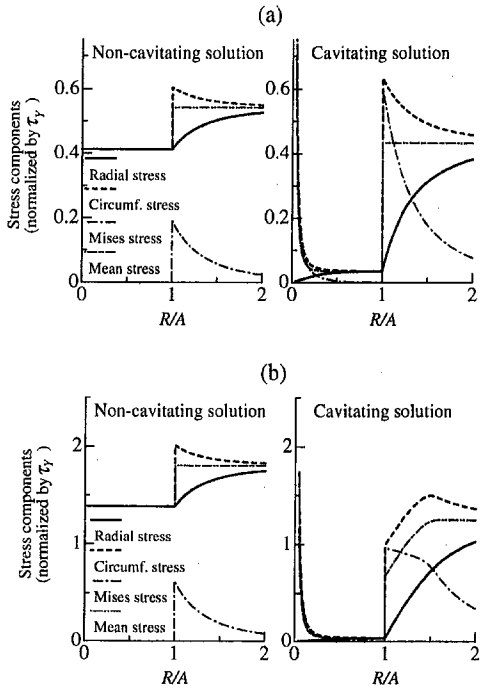


Fig. 5 Distribution of radial, circumferential, Mises, and mean stresses in the composite sphere. (*a*) $\bar{\Lambda} = 1.003$ and (*b*) $\bar{\Lambda} = 1.01$.

toplastic solids with an initial infinitesimal void in a series of detailed numerical studies by Huang et al. (1991), Tvergaard et al. (1992), and Tvergaard and Hutchinson (1993). Besides these studies on elastoplastic materials, expressions for the cavitation stress and description of related response have been given by Chung et al. (1986), Hou and Abeyaratne (1992), and Huang et al. (1996) for incompressible hardening elastoplastic solids, and by Huang et al. (1991) for nonhardening elastoplastic solids with elastic compressibility. In particular, based on the Durban-Baruch theory aforementioned, Biwa (1997) obtained the cavitation stress for hardening elastoplastic solids, which is expressed by aid of (21) as

$$\frac{\bar{T}_{CR}}{\tau_Y} = \int_0^\infty \xi(\bar{\tau}) d\bar{\tau}, \tag{30}$$

accounting for the elastic compressibility. When the ratio A/B becomes negligibly small, the maximum stress on the cavitating solution curves in Fig. 4 approaches the cavitation stress of the matrix material itself given by (30).

Cavitation-Induced Transition of Stress States in the Matrix. The stress distribution in the particle as well as the matrix is of definite interest regarding possible ensuing failure mechanisms. To this end, qualitative features of the stress distribution in the composite sphere for noncavitating and cavitating modes are shown in Fig. 5 as function of the undeformed radial coordinate, and compared at different loading stages, (a) and (b). Case I is chosen as the representative. The Mises and the mean stresses are defined as $\tau_e = \tau_\theta - \tau_r$ and $\tau_m = (\tau_r + 2\tau_\theta)/3$, respectively, for the particle and the matrix. For the matrix, the Mises stress controls the growth of plastic strains.

In Fig. 5(*a*), the prescribed composite expansion ratio is $\bar{\Lambda} = 1.003$. Already at this value of the expansion ratio, noncavitating and cavitating solutions coexist. For the noncavitating mode, the stress state in the particle is uniform and hydrostatic, i.e., $\tau_r = \tau_\theta = \tau_m$. The hydrostatic state in the particle makes the stress state in the matrix nearly hydrostatic, with high mean stress and less significant Mises stress. On the other hand, for the cavitating

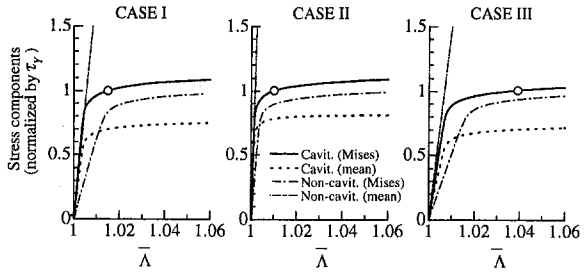


Fig. 6 Evolution of matrix Mises and mean stresses with increase of composite expansion ratio for noncavitating and cavitating solutions

solution, the particle only sustains small stress except the circumferential component that is singular as $R \to 0$. This makes the matrix stress near the particle close to biaxial tension, and a high Mises stress develops in the vicinity of the particle. At this stage, however, elastic deformation dominates in the matrix and no significant plastic strains are present.

When the expansion ratio is further increased to $\bar{\Lambda} = 1.01$ as in Fig. 5(*b*), the matrix experiences plastic deformation for the cavitating solution. It is observed that when a cavity is present in the particle, the matrix mean stress drops as the particle boundary is approached. In contrast, the noncavitating mode retains quite high stress levels, since without cavitation the particle can sustain the radial traction that is of comparable magnitude to the matrix stress. At this value of $\bar{\Lambda}$, there already exists significant gap between the stress levels of cavitating and noncavitating solutions. This gap continues to increase as $\bar{\Lambda}$ is further increased. Therefore, cavitation acts so as to suppress the stress state in the matrix, in particular the mean stress, and to put the matrix stress in the particle's neighborhood into a nearly biaxial state.

Figure 6 shows the evolution of the Mises and the mean stresses in the matrix as the expansion ratio of the composite sphere is increased. These values are plotted for a fixed location $R \to A^+$, i.e., as R approaches the particle-matrix boundary from inside of the matrix, as this is the location where the relevant stresses take on maximum values. It is observed that the particle cavitation drastically reduces the growth rate of the mean (triaxial) stress, which could otherwise escalate with rather steep slope as the composite sphere expands. Cavitation not only suppresses the triaxial stress in the matrix, but also tends to accelerate the development of the Mises stress. Circles on the curves indicate the point where the Mises stress passes by the reference flow stress τ_Y, which location would imply how easily the plastic deformation can build up in the matrix.

The enhancement of plastic yielding due to cavitation can be visualized in an alternative way in Fig. 7, where the evolution of the equivalent plastic strain ϵ_e^P with the expansion of the composite sphere is illustrated. In all the cases, the plastic strains tend to grow up as the expansion ratio with an almost

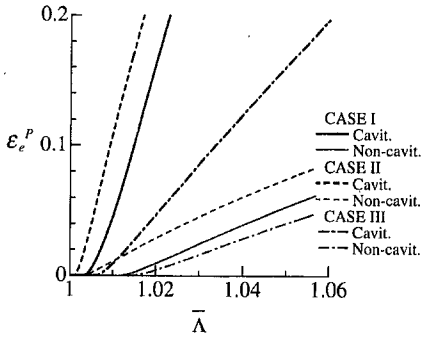


Fig. 7 Evolution of matrix plastic strain with increase of composite expansion ratio for noncavitating and cavitating solutions

Downloaded 04 May 2010 to 171.66.16.27. Redistribution subject to ASME license or copyright; see http://www.asme.org/terms/Terms_Use.cfm

constant slope. It is seen that the slopes for the cavitating solutions are much greater than those for the noncavitating ones. Among the three cases considered, Case II gives the highest slope, which may be understood as the consequence of the lower flow stress. On the other hand, Case III exhibits the lowest slope. The reason for this is thought to be that in Case III the matrix shell is thinner and is more capable of accommodating the given expansion ratio in an elastic manner.

Concluding Remarks

Cavitation of a spherical hyperelastic particle contained in an elastoplastic matrix was considered via equilibrium analysis for the pertinent finite radial deformation field. Based on the description of exact solutions for the radial deformation and the stress fields, two modes of composite sphere expansion were identified, namely the noncavitating mode with the pure expansion of the particle, and the cavitating mode with a cavity opening in the particle. Influence of the occurrence of cavitation on the magnitude and the distribution of the stress state in the composite sphere as well as the growth of plastic deformation in the matrix was analyzed in detail.

Summarizing the findings of the present analysis, it is noted that in equitriaxial stress conditions the particle can cavitate at a small strain level applied to the matrix, where the deformation in the matrix is still sustained elastically. The subsequent evolution of the stress state in the matrix depends critically on whether cavitation occurs or not. Particle cavitation suppresses the growth of triaxial stress and set up a relatively high Mises stress, thereby promoting shear yielding to develop. These findings appear consistent with the idea often reported from an experimental point of view as mentioned in Introduction. In real systems, however, it is not only the local plastic yielding in the particle's neighborhood but also the massive shear band formation on a greater spatial scale that dissipates the energy and makes the material tougher against failure. The analysis of this whole phenomenon would require the prediction of the macroscopic response involving a population of cavitating particles as well as the microscopic particle-particle interaction for shear band initiation. Such an analysis should be better carried out in a multiaxial and possibly three-dimensional framework, which is out of the scope of the present analysis: unit-cell finite element simulations recently made by Steenbrink and van der Giessen (1997) and Chen and Mai (1998) are worthy of attention towards this direction.

Acknowledgments

The author is grateful to the anonymous reviewers of this manuscript for very helpful suggestions. Discussions with Dr. J. G. Murphy, Institute of Technology Tallaght, Dublin, have partly led to this line of investigation and are highly appreciated. This work has been supported by the Ministry of Education, Science, Sports and Culture, Japan (Grant-in-Aid for Encouragement of Young Scientists).

References

Ball, J. M., 1982, "Discontinuous Equilibrium Solutions and Cavitation in Nonlinear Elasticity," *Philosophical Transactions of the Royal Society of London,* Vol. A306, pp. 557–611.

Beahan, P., Thomas, A., and Bevis, M., 1976, "Some Observations on the Micromorphology of Deformed ABS and HIPS Rubber-Modified Materials," *Journal of Materials Science,* Vol. 11, pp. 1207–1214.

Biwa, S., 1995, "Critical Stretch for Formation of a Cylindrical Void in a Compressible Hyperelastic Material," *International Journal of Non-Linear Mechanics,* Vol. 30, No. 6, pp. 899–914.

Biwa, S., 1997, "Finite Expansion of an Infinitesimal Void in Elastic-Plastic Materials Under Equitriaxial Stress," *JSME International Journal, Series A,* Vol. 40, No. 1, pp. 23–30.

Breuer, H., Haaf, F., and Stabenow, J., 1977, "Stress Whitening and Yielding Mechanism of Rubber-Modified PVC," *Journal of Macromolecular Science—Physics,* Vol. B14, No. 3, pp. 387–417.

Bucknall, C. B., Heather, P. S., and Lazzeri, A., 1989, "Rubber Toughening of Plastics, Part 12: Deformation Mechanisms in Toughened Nylon 6,6," *Journal of Materials Science,* Vol. 16, pp. 2255–2261.

Chen, X. H., and Mai, Y.-W., 1998, "The Effects of Triaxial Constraint on Toughening Mechanisms of Rubber-Modified Epoxy System," *Proceedings of the International Workshop on Polymer Blends and Polymer Composites* (L. Ye, and Y.-W. Mai, eds, Sydney, 1997); *Key Engineering Materials,* Vol. 137, pp. 115–122.

Chung, D.-T., Horgan, H. O., and Abeyaratne, R., 1986, "A Note on a Bifurcation Problem in Finite Plasticity Related to Void Nucleation," *International Journal of Solids and Structures,* Vol. 23, pp. 983–988.

Durban, D., and Baruch, M., 1977, "Analysis of an Elasto-Plastic Thick Walled Sphere Loaded by Internal and External Pressure," *International Journal of Non-Linear Mechanics,* Vol. 12, pp. 9–21.

Gent, A. N., and Lindley, P. B., 1958, "Internal Rupture of Bonded Rubber Cylinders in Tension," *Proceedings of the Royal Society of London,* Vol. A249, pp. 195–205.

Horgan, C. O., and Pence, T. J., 1989, "Cavity Formation at the Center of a Composite Incompressible Nonlinearly Elastic Sphere," ASME JOURNAL OF APPLIED MECHANICS, Vol. 56, pp. 302–308.

Horgan, C. O., and Polignone, D. A., 1995, "Cavitation in Nonlinearly Elastic Solids: A Review," ASME *Applied Mechanics Reviews,* Vol. 48, pp. 471–485.

Hou, H.-S., and Abeyaratne, R., 1992, "Cavitation in Elastic and Elastic-Plastic Solids," *Journal of the Mechanics and Physics of Solids,* Vol. 40, No. 3, pp. 571–592.

Huang, Y., Hutchinson, J. W., and Tvergaard, V., 1991, "Cavitation Instabilities in Elastic-Plastic Solids," *Journal of the Mechanics and Physics of Solids,* Vol. 39, No. 2, pp. 223–241.

Huang, Y., Hu, K. X., Yeh, C. P., Li, N.-Y., and Hwang, K. C., 1996, "A Model Study of Thermal Stress-Induced Voiding in Electronic Packages," ASME *Journal of Electronic Packaging,* Vol. 118, pp. 229–234.

Levinson, M., and Burgess, I. W., 1971, "A Comparison of Some Simple Constitutive Relations for Slightly Compressible Rubberlike Materials," *International Journal of Mechanical Sciences,* Vol. 13, pp. 563–572.

Steenbrink, A. C., and van der Giessen, E., 1997, "A Numerical Study of Cavitation and Yield in Amorphous Polymer-Rubber Blends," ASME *Journal of Engineering Materials and Technology,* Vol. 119, pp. 256–261.

Stringfellow, R., and Abeyaratne, R., 1989, "Cavitation in an Elastomer: Comparison of Theory with Experiment," *Materials Science and Engineering,* Vol. A112, pp. 127–131.

Tvergaard, V., Huang, Y., and Hutchinson, J. W., 1992, "Cavitation Instabilities in a Power Hardening Elastic-Plastic Solid," *European Journal of Mechanics, A/Solids,* Vol. 11, No. 2, pp. 215–231.

Tvergaard, V., and Hutchinson, J. W., 1993, "Effect of Initial Void Shape on the Occurrence of Cavitation Instabilities in Elastic-Plastic Solids," ASME JOURNAL OF APPLIED MECHANICS, Vol. 60, pp. 807–812.

van der Giessen, E., 1997, "Localized Plastic Deformations in Glassy Polymers," *European Journal of Mechanics, A/Solids,* Vol. 16, Special Issue, pp. 87–106.

Yee, A. F., and Pearson, R. A., 1986, "Toughening Mechanisms in Elastomer-Modified Epoxies, Part 1: Mechanical Studies," *Journal of Materials Science,* Vol. 21, pp. 2462–2474.

Downloaded 04 May 2010 to 171.66.16.27. Redistribution subject to ASME license or copyright; see http://www.asme.org/terms/Terms_Use.cfm

Dynamic Analysis of Systems With Varying Constraints

S. Djerassi
P.O. Box 2250
Haifa 32101, Israel

This paper deals with constrained dynamical systems which are subject, during motion, to the replacement of one set of constraints with another. The theory of imposition and removal of constraints is used to formulate equations governing motions of such systems. To this end, the terms minimally constrained state (MCS), phase of motion, transition, and transition conditions are introduced. These terms are used to denote, respectively, state of a system subject only to constraints which are not removed throughout the motion, period of time during which an MCS system is subject to one set of constraints, event characterized by the instantaneous removal of one set of constraints and the imposition of another, and conditions, satisfaction of which initiate a transition. The indicated formulation enables the simulation of motions of the systems in question, including the evaluation of changes in the motion variables associated with the transitions. The formulation is particularly efficient in that the impulses arising during the transitions are automatically eliminated. The formulation is used to simulate motions of a number of systems, including a legged machine.

1 Introduction

Figure 1(*a*) shows a simple pendulum consisting of a particle P and a massless cord C of length L, having one point O fixed in **N**, a Newtonian reference frame. The pendulum moves in a gravitational field parallel to a unit vector $\mathbf{n}_1$. Let q_1 be the angle between $\mathbf{a}_1$, a unit vector aligned with C, and $\mathbf{n}_1$. Let E be a fixed support, located so that when q_1 becomes zero, then point R of C coincides with point $\bar{R}$ of E. Thereafter, the portion OR of C, called A, remains fixed in **N** and the portion RP of C, called B, becomes a cord of a simple pendulum of length L_2, aligned with a unit vector $\mathbf{b}_1$. This system possesses one degree of freedom at all times. However, at certain instants either $\mathbf{a}_1$ or $\mathbf{b}_1$ become aligned with $\mathbf{n}_1$, and one set of constraints is replaced with another.

The pendulum described above represents a class of systems that are subject, while in motion, to varying constraints. The objective of this work is to set out an efficient formulation of equations governing motions of this class of systems. This task is carried out with the aid of the theory of imposition and removal of constraints introduced by Djerassi (1994, 1998). The main results of the theory are presented, modified and cast into a five-step procedure for the formulation of the desired equations. The procedure is applied to the pendulum shown in Fig. 1(*a*), to a bar in planar motion and, finally, to a six-legged walking machine.

2 The Theory of Imposition-Removal of Constraints: Main Results

Let S be a system of ν particles P_i $(i = 1, \ldots, \nu)$ of mass m_i possessing $\bar{n}$ generalized coordinates $q_1, \ldots, q_{\bar{n}}$ and n (where $n \leq \bar{n}$) generalized speeds $u_1, \ldots, u_n$ in **N**. Then the idea of imposition of constraints (Djerassi, 1994) comes to light in connection with the following three-phase motion of S. Phase A occurs in the time interval $0 \leq t \leq t_1$. The motion of S in **N** is *defined* as unconstrained, and governed by n dynamical equations, namely,

$$F_r + F_r^* = 0 \quad (r = 1, \ldots, n) \tag{1}$$

where F_r and F_r^* are the rth generalized active force and the rth generalized inertia force for S, respectively. Phase B, a transition phase, occurs in the time interval $t_1 \leq t \leq t_2$, where $t_2 - t_1$ is "infinitely small," e.g., compared to time constants relating to the motion of S. Then m constraints represented by the equations

$$u_k = \sum_{r=1}^{p} C_{kr} u_r + D_k \quad (k = p + 1, \ldots, n) \tag{2}$$

are imposed on the motion of S, where

$$p \triangleq n - m \tag{3}$$

and C_{kr} and D_k are functions of $q_1, \ldots, q_{\bar{n}}$ and time t. In this phase, the configuration of S in **N** remains unaltered, i.e.,

$$q_r(t_2) = q_r(t_1) \quad (r = 1, \ldots, \bar{n}), \tag{4}$$

and the number of independent, generalized speeds is reduced from n to p. Now, t_2 is the first instant at which the Eqs. (2) are valid, hence

$$u_k(t_2) = \sum_{r=1}^{p} C_{kr} u_r(t_2) + D_k \quad (k = p + 1, \ldots, n). \tag{5}$$

Additionally, if the magnitudes of the active forces contributing to Eqs. (1) are all bounded (i.e., nonimpulsive), and if particles of S exert contact forces on one another, and possibly on particles belonging to R_B, a set of rigid bodies with motion unaffected by the forces exerted on them by particles of S, then the relations between $u_s(t_2)$ $(s = 1, \ldots, n)$ and $u_s(t_1)$ $(s = 1, \ldots, n)$ are given by

$$\sum_{s=1}^{n} (m_{rs} + \sum_{k=p+1}^{n} C_{kr} m_{ks})[u_s(t_2) - u_s(t_1)] = 0 \quad (r = 1, \ldots, p). \tag{6}$$

Here, m_{rs}, the element in row r, column s of the mass matrix associated with Eqs. (1), is defined

$$m_{rs} \triangleq -\sum_{i=1}^{\nu} m_i \frac{\partial \mathbf{v}^{P_i}}{\partial u_r} \cdot \frac{\partial \mathbf{v}^{P_i}}{\partial u_s} \tag{7}$$

Contributed by the Applied Mechanics Division of THE AMERICAN SOCIETY OF MECHANICAL ENGINEERS for publication in the ASME JOURNAL OF APPLIED MECHANICS.
Discussion on the paper should be addressed to the Technical Editor, Professor Lewis T. Wheeler, Department of Mechanical Engineering, University of Houston, Houston, TX 77204-4792, and will be accepted until four months after final publication of the paper itself in the ASME JOURNAL OF APPLIED MECHANICS.
Manuscript received by the ASME Applied Mechanics Division, Sept. 15, 1998; final revision, Dec. 3, 1998. Associate Technical Editor: N. C. Perkins.

 Copyright © 1999 by ASME

Downloaded 04 May 2010 to 171.66.16.27. Redistribution subject to ASME license or copyright; see http://www.asme.org/terms/Terms_Use.cfm

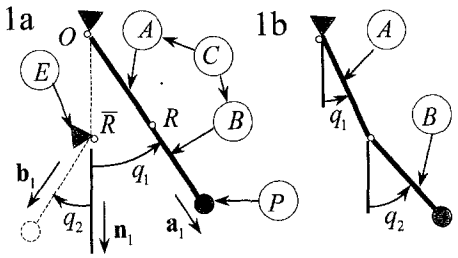


Fig. 1 Simple pendulum with varying constraints

where $\mathbf{v}^{P_i}$ is the velocity of P_i in $\mathbf{N}$. These $m + p$ relations between $u_s(t_2)$ and $u_s(t_1)$ $(s = 1, \ldots, n)$ enable the evaluation of the former, given the latter, with C_{kr}, D_k $(k = p + 1, \ldots, n; r = 1, \ldots, p)$ and m_{rs} $(r, s = 1, \ldots, n)$ calculated at $t = t_1$. Phase C occurs when $t \geq t_2$. Then the *state* of S is determined by Eqs. (2), the motion of S in $\mathbf{N}$ is defined as constrained, and governed by p dynamical equations, namely,

$$F_r + F_r^* + \sum_{k=p+1}^{n} C_{kr}(F_k + F_k^*) = 0 \quad (r = 1, \ldots, p). \quad (8)$$

Equations (8) are Kane's equations of motion for constrained systems (Kane and Levinson, 1985).

Removal of constraints occurs when the order of Phases A, B, and C is reversed. The constrained phase (now called Phase A), the transition, removal phase (Phase B), and the unconstrained phase (now called Phase C) occur when $0 \leq t \leq t_1$, $t_1 \leq t \leq t_2$ and $t \geq t_2$. The motion in these phases is governed by Eqs. (8) and (2), (4)–(6), and (1), respectively, with t_1 replacing t_2 in Eqs. (5). If Eqs. (2) are satisfied both at t_1 and at t_2, then

$$u_s(t_2) = u_s(t_1) \quad (s = 1, \ldots, n). \quad (9)$$

3 Application to Systems Subject to Varying Constraints

Equations of motion of systems with varying constraints involve different sets of constraint equations at different times. These can be cast in the form of Eqs. (2), and if N is the number of such sets, then

$$u_k = \sum_{r=1}^{p^{(j)}} C_{kr}^{(j)} u_r + D_k^{(j)}$$

$$(k = p^{(j)} + 1, \ldots, n; j = 1, \ldots, N), \quad (10)$$

where the superscript (j) indicates association with the jth set. It is thus implied that, occasionally, one set of constraints is replaced with another. This state of affairs can be dealth with analytically with the aid of the following definitions.

jth phase of motion (MP_j)—a period of time during which S is subject to the jth set of constraints. ${}^kMP_j$ denotes the kth repetition of MP_j.

K-L transition phase $(TP_{K\text{-}L})$—an infinitely small period of time during which the motion is characterized by the removal of the Kth set of constraints and the imposition of the Lth. ${}^kTP_{K\text{-}L}$ denotes the kth repetition of $TP_{K\text{-}L}$.

K-L transition conditions $(TC_{K\text{-}L})$—conditions, the satisfaction of which initiate the K-L transition phase. ${}^kTC_{K\text{-}L}$ denotes the kth occurrence of $TC_{K\text{-}L}$.

Minimally constrained state (MCS)—a state of a system subject to constraints none of which is removed throughout the motion.

Now, the definition of an MCS of a particular system is a matter of choice. However, this choice should be made so that when N sets of constraints are imposed, one at a time, then motions characterizing the respective phases emerge. With this in mind, suppose that expressions for $F_r + F_r^*$ $(r = 1, \ldots, n)$ have been generated for a system in a minimally constrained state, and that N sets of constraint equations have been formulated. Then equations governing the motion of the system in each of the phases can be obtained by substitutions in Eqs. (8). These are

$$F_r + F_r^* + \sum_{k=p^{(j)}+1}^{n} C_{kr}^{(j)}(F_k + F_k^*) = 0$$

$$(r = 1, \ldots, p^{(j)}; j = 1, \ldots, N). \quad (11)$$

Note that Eqs. (10) imply that $u_1, \ldots, u_{p^{(j)}}$ are independent. However, if any $p^{(j)}$ of $u_1, \ldots, u_n$ are independent, then Eqs. (11) are valid if interpreted accordingly.

Next, suppose that initial conditions place the system in the Kth phase, and that for $j = K$, Eqs. (11) are integrated in conjunction with the time derivatives of Eqs. (10). Furthermore, suppose that at time t_1 the K-L transition conditions are met. Then transition from the Kth phase to the Lth phase occurs between t_1 and t_2. The transition is accompanied by changes in the motion variables; and, if t_2-t_1 is assumed to be infinitely small, then these changes can be evaluated with the aid of t' and t'', points in time satisfying the relation

$$t_1 < t' < t'' < t_2. \quad (12)$$

It is assumed that the Kth set of constraints, represented by Eqs. (10), is removed between t_1 and t', so that, in accordance with Eqs. (9)

$$u_s(t') = u_s(t_1) \quad (s = 1, \ldots, n), \quad (13)$$

where t' plays the role of t_2. Equations (1) become valid between t' and t''; however,

$$u_s(t'') = u_s(t') \quad (s = 1, \ldots, n) \quad (14)$$

because $t'' - t'$ is infinitely small. Finally, the Lth set of constraints is imposed between t'' and t_2. The associated changes in the generalized speeds can be evaluated with the aid of Eqs. (6), with $C_{kr}^{(L)}$ and $p^{(L)}$ replacing C_{kr} and p, respectively, and t'' replacing t_1. In view of Eqs. (13) and (14), however, $u_s(t'') = u_s(t_1)$ $(s = 1, \ldots, n)$, so that $u_s(t_2)$ are related to $u_s(t_1)$ $(s = 1, \ldots, n)$ as follows:

$$\sum_{s=1}^{n} (m_{rs} + \sum_{k=p^{(L)}+1}^{n} C_{kr}^{(L)} m_{ks})[u_s(t_2) - u_s(t_1)] = 0$$

$$(r = 1, \ldots, p^{(L)}). \quad (15)$$

In addition, t_2 is the first instant at which the Lth set of Eqs. (10) is valid, hence

$$u_k(t_2) = \sum_{r=1}^{p^{(L)}} C_{kr}^{(L)} u_r(t_2) + D_k^{(L)} \quad (k = p^{(L)} + 1, \ldots, n). \quad (16)$$

Using Eqs. (15) and (16) one can evaluate $u_s(t_2)$ $(s = 1, \ldots, n)$ in terms of $u_s(t_1)$ $(s = 1, \ldots, n)$, which then serve as initial conditions for the integration of Eqs. (11) with $j = L$, equations governing the motion in the Lth phase. Note that the changes in u_s $(s = 1, \ldots, n)$ depend solely on the Lth set of constraint equations; and that the last instant at which Eqs. (10) with $j = K$ are valid is t_1, hence

$$u_k(t_1) = \sum_{r=1}^{p^{(K)}} C_{kr}^{(K)} u_r(t_1) + D_k^{(K)} \quad (k = p^{(K)} + 1, \ldots, n). \quad (17)$$

Equations (15)–(17) enable the evaluation of $u_s(t_2)$ $(s = 1, \ldots, n)$ in terms of $u_s(t_1)$ $(s = 1, \ldots, p)$.

In conclusion, the following steps can be taken in order to

Downloaded 04 May 2010 to 171.66.16.27. Redistribution subject to ASME license or copyright; see http://www.asme.org/terms/Terms_Use.cfm

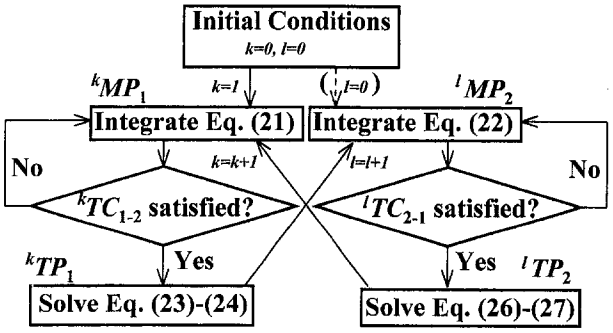


Fig. 2 Algorithm flowchart

generate equations governing motions of systems subject to varying constraints.

(a) Determine the MCS for the system in question, and generate the associated expressions for $F_r + F_r^*$ $(r = 1, \ldots, n)$.

(b) Identify N phases of motion $MP_1, \ldots, MP_N$ and generate N sets of constraint equations, namely Eqs. (10).

(c) Form N sets of dynamical equations for N phases of motion, namely Eqs. (11).

(d) Set N^2–N transition conditions from each phase to the remaining N-1 phases.

(e) Formulate N sets of algebraic equations relating $u_s(t_2)$ $(s = 1, \ldots, n)$ to $u_s(t_1)$ $(s = 1, \ldots, n)$ for N transitions to the Lth phase $(L = 1, \ldots, N)$ using Eqs. (15) and (16). Alternatively, formulate N^2–N sets of algebraic equations relating $u_s(t_2)$ $(s = 1, \ldots, n)$ to $u_s(t_1)$ $(s = 1, \ldots, p)$ for N^2–N transitions from the Kth phase to the Lth $(K, L = 1, \ldots, N, K \neq L)$, using Eqs. (15)–(17).

These steps will next be applied to three illustrative examples.

4 A Simple Pendulum With Varying Constraints

Step a. Figure 1(*b*) shows the MCS of the simple pendulum depicted in Fig. 1(*a*). Two angles q_1 and q_2 define the configuration of the pendulum. Moreover, two generalized speeds u_1 and u_2 are defined $u_1 \triangleq {}^N\omega^A \cdot \mathbf{n}_3$ and $u_2 \triangleq {}^N\omega^B \cdot \mathbf{n}_3$, where ${}^N\omega^A$ and ${}^N\omega^B$ are the angular velocities of A and B in $\mathbf{N}$, respectively, so that $\dot{q}_r = u_r$ $(r = 1, 2)$. Accordingly,

$$F_1 + F_1^* = m[-\dot{u}_1 L_1^2 - \dot{u}_2 L_1 L_2 \cos(q_2 - q_1) + u_2^2 L_1 L_2 \sin(q_2 - q_1) - gL_1 \sin(q_1)]$$

$$F_2 + F_2^* = m[-\dot{u}_1 L_1 L_2 \cos(q_2 - q_1) - \dot{u}_2 L_2^2 - u_1^2 L_1 L_2 \sin(q_2 - q_1) - gL_2 \sin(q_2)] \quad (18)$$

where g is the gravitational constant, and $L_1 = L - L_2$.

Step b. Two phases of motion can be identified. Phase 1 is associated with the constraint equation ${}^N\omega^A = {}^N\omega^B$, or

$$MP_1: u_2 = u_1; \quad (19)$$

and Phase 2 is associated with the constraint equation ${}^N\omega^A = 0$, or

$$MP_2: u_1 = 0 \quad (20)$$

(so that the independent generalized speed is u_2).

Step c. Substitutions from Eqs. (18) and (19) in Eqs. (11) for $n = 2$, $j = 1$, $p^{(1)} = 1$ and $q_2 = q_1$ lead to the equation

$$j = 1: -mL[L\dot{u}_1 + g \sin(q_1)] = 0 \quad (21)$$

whereas substitutions from Eqs. (18) and (20) in Eqs. (11) for $n = 2$, $j = 2$, $p^{(2)} = 1$ and $q_1 = 0$ lead to the equation

$$j = 2: -mL_2[L_2\dot{u}_2 + g \sin(q_2)] = 0. \quad (22)$$

Equations (21) and (22) govern the motion in Phases 1 and 2, respectively.

Step d. Transition from Phase 1 to Phase 2 involves the removal of the constraint represented by Eq. (19), and the imposition of the constraint represented by Eq. (20). The associated changes in the generalized speeds are obtained after m_{rs} $(r, s = 1, 2)$ and $C_{kr}^{(2)}$ $(k = 1, r = 2)$ are identified in Eqs. (18) and (20), and substituted in Eqs. (15). Then the following is obtained:

$$-L_1 L_2 \cos(q_2 - q_1)[u_1(t_2) - u_1(t_1)] - L_2^2[u_2(t_2) - u_2(t_1)] = 0. \quad (23)$$

At t_2, Eq. (20) plays the role of Eqs. (16), yielding

$$u_1(t_2) = 0. \quad (24)$$

Solving Eqs. (23) and (24) for $u_1(t_2)$ and $u_2(t_2)$, noting, in view of Eqs. (19) and (17), that $u_2(t_1) = u_1(t_1)$, one has

$$TP_{1\text{-}2}: u_1(t_2) = 0, \quad u_2(t_2) = (L/L_2)u_1(t_1). \quad (25)$$

Similarly, the transition from Phase 2 to Phase 1 involves the removal of the constraint represented by Eq. (20) and the imposition of the constraint represented by Eq. (19). Substitutions from Eqs. (18) and (19) in Eqs. (15) for $n = 2$ and $p^{(1)} = 1$ lead to

$$[-L_1^2 - L_1 L_2 \cos(q_2 - q_1)][u_1(t_2) - u_1(t_1)] + [-L_1 L_2 \cos(q_2 - q_1) - L_2^2][u_2(t_2) - u_2(t_1)] = 0. \quad (26)$$

In addition

$$u_2(t_2) = u_1(t_2), \quad (27)$$

and, since $u_1(t_1) = 0$, a result derived from Eqs. (20) and (17), then

$$MP_{2\text{-}1}: u_2(t_2) = u_1(t_2) = (L_2/L)u_2(t_1). \quad (28)$$

Step e. Transition conditions are determined by inspection:

$$TC_{1\text{-}2}: u_1 < 0, \quad q_1 = 0 \quad (29)$$

$$TC_{2\text{-}1}: u_2 > 0, \quad q_2 = 0. \quad (30)$$

Simulation of motion of the simple pendulum with variable constraints can now be constructed in accordance with the flowchart of Fig. 2. With $m = 1$ kg, $L = 0.4$, and $L_2 = 0.2$ m one obtains q_2 and u_2 as in Fig. 3 if initially $q_1 = q_2 = 30$ deg and $u_1 = 0$ (Phase 1).

Note that $|{}^N\mathbf{v}^P(t_2)| = |{}^N\mathbf{v}^P(t_1)|$ for each transition. This means that the mechanical energy of the system is conserved throughout the motion. In general, however, the mechanical energy of a system undergoing imposition of constraints decreases, as shown by Djerassi (1998). This is the case with the next example.

5 A Rigid Bar in Planar Motion With Varying Constraints

Figure 4 shows a rigid, uniform bar B of length L undergoing a planar motion which can be described as follows. Let P_1, P_2, ... be points of a line l fixed in $\mathbf{N}$, and let the distance between P_i and

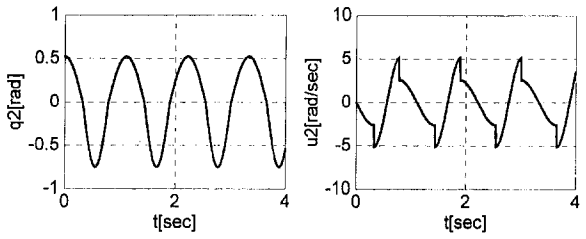


Fig. 3 q_2 and u_2 as functions of time

Downloaded 04 May 2010 to 171.66.16.27. Redistribution subject to ASME license or copyright; see http://www.asme.org/terms/Terms_Use.cfm

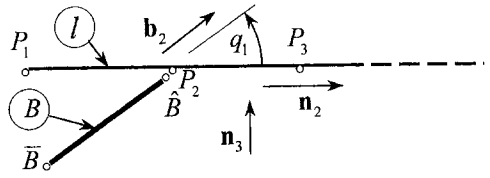


Fig. 4 Rigid bar with varying constraints

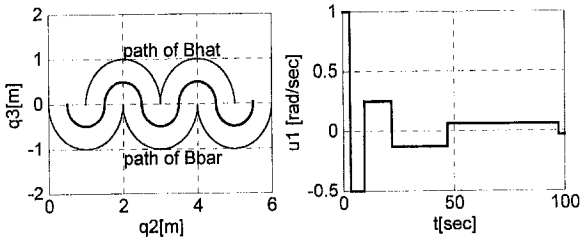


Fig. 5 Paths traversed by B^*, $\bar{B}$ and $\hat{B}$ (left) and the angular speed of B

P_{i+1} $(i = 1, 2, \ldots)$ be L. Let $\bar{B}$ and $\hat{B}$, the endpoints of B, coincide initially with P_1 and P_2, respectively. Let $\mathbf{n}_i$ and $\mathbf{b}_i$ be triads of dextral, mutually perpendicular unit vectors fixed in $\mathbf{N}$ and in B, respectively, and let $\mathbf{b}_2$ be aligned with B. Finally, let q_1 be the angle between $\mathbf{n}_2$ and $\mathbf{b}_2$, as shown in Fig. 4.

Next, assume that $\hat{B}$ is pivoted at P_2, and that B moves so as to increase q_1. Moreover, suppose that when $q_1 = 180$ deg—then $\bar{B}$ coincides with P_3—the pivot at $\hat{B}$ is removed and $\bar{B}$ is pivoted at P_3. Thereafter B rotates about $\bar{B}$ so as to decrease q_1. When $q_1 = 0$, the pivot at $\bar{B}$ is removed and $\hat{B}$ is pivoted at P_4, etc.

In connection with the motion of B in $\mathbf{N}$, the following steps lead to the governing equations.

Step a. The MCS of B is the state of a rigid body in planar motion. Accordingly, let u_1, u_2, and u_3 be defined such that ${}^{\mathbf{N}}\omega^B$ and ${}^{\mathbf{N}}\mathbf{v}^{B^*}$, the angular velocity of B in $\mathbf{N}$, and the velocity in $\mathbf{N}$ of B^*, the mass center of B, are given by ${}^{\mathbf{N}}\omega^B = u_1\mathbf{n}_1$ and ${}^{\mathbf{N}}\mathbf{v}^{B^*} = u_2\mathbf{n}_2 + u_3\mathbf{n}_3$. Then

$$F_1 + F_1^* = -J_B\dot{u}_1, \quad F_2 + F_2^* = -m_B\dot{u}_2,$$

$$F_3 + F_3^* = -m_B\dot{u}_3 \tag{31}$$

where m_B is the mass of B and J_B is the central moment of inertia of B for $\mathbf{n}_1$.

Step b. Two phases of motion can be identified. With ${}^{\mathbf{N}}\mathbf{v}^{\hat{B}}$ and ${}^{\mathbf{N}}\mathbf{v}^{\bar{B}}$ as the velocities in $\mathbf{N}$ of $\hat{B}$ and $\bar{B}$, respectively, the associated constraint equations are ${}^{\mathbf{N}}\mathbf{v}^{\hat{B}} = 0$ and ${}^{\mathbf{N}}\mathbf{v}^{\bar{B}} = 0$, or

$$MP_1\text{: } u_2 = L/2 \sin(q_1)u_1, \quad u_3 = -L/2 \cos(q_1)u_1 \tag{32}$$

$$MP_2\text{: } u_2 = -L/2 \sin(q_1)u_1, \quad u_3 = L/2 \cos(q_1)u_1. \tag{33}$$

Step c. The equations governing the motion of B in the two phases are identical, and read

$$j = 1, 2\text{: } -(J_B + m_BL^2/4)\dot{u}_1 = 0. \tag{34}$$

Step d. The transition from Phase 1 to Phase 2 occurs so that

$$-J_B[u_1(t_2) - u_1(t_1)] + m_BL/2[u_3(t_2) - u_3(t_1)] = 0 \tag{35}$$

$$u_2(t_2) = -L/2 \sin(q_1)u_1(t_2),$$

$$u_3(t_2) = L/2 \cos(q_1)u_1(t_2). \tag{36}$$

Substituting $q_1 = 180$ deg and using the fact that at t_1

$$u_2(t_1) = L/2 \sin(q_1)u_1(t_1),$$

$$u_3(t_1) = -L/2 \cos(q_1)u_1(t_1) \tag{37}$$

one has

$$TP_{1\text{-}2}\text{: } u_1(t_2) = (J_B - m_BL^2/4)/(J_B + m_BL^2/4)u_1(t_1); \tag{38}$$

or, if $J_B = m_BL^2/12$, then $u_1(t_2) = -u_1(t_1)/2$. This result is also obtained for a transition from Phase 2 to Phase 1. One may conclude that with each transition the direction of the angular velocity is reversed and its magnitude is halved.

Step e. Transition conditions are determined by inspection:

$$TC_{1\text{-}2}\text{: } u_1 > 0, \quad q_1 = 180 \text{ deg} \tag{39}$$

$$TC_{2\text{-}1}\text{: } u_1 < 0, \quad q_1 = 0 \text{ deg}. \tag{40}$$

Letting $L = 1$ m, $m = 1$ kg and $u_1(0) = 1$ rad/sec, one obtains Fig. 5, showing $q_3(q_2)$ and $u_1(t)$.

6 A Six-Legged Machine as a System With Varying Constraints

A vast amount of work regarding two, four and six-legged machines has been carried out in the last two decades. The underlying motivation is that two-legged machines are expected to undertake human tasks (Nechyba and Xu, 1995), whereas four and six-legged machines are believed to be potentially superior to wheeled machines as far as terrain crossing is concerned (Klein et al., 1983, Ozguner et al., 1984). It is widely recognized that gaits of multilegged machines comprise multiphase events (Tzafestas et al., 1996; Lee and Song, 1991; Orin, 1982). Nevertheless, none of the studies has presented a general approach for the generation of the associated dynamical equations. It is the purpose of this section to show, by reference to the six-legged machine depicted in Fig. 6, that the five steps of Section 3 form the basis to such an approach. The following brief review places the machine of Fig. 6—a reproduction of the hexapod presented by Eltze and Pfeiffer (1995)—in the proper context of legged machines.

Usually a walking machine is designed to be statically stable; i.e., the line parallel to the gravity field that passes through the mass center of the machine intersects the surface enclosed by the "supporting polygon." The supporting polygon is one whose sides connect the points of contact of the supporting legs with the ground. The formation of such a supporting polygon requires at least three supporting points. Accordingly, legs of four and six-legged machines are designed to touch the ground essentially at their endpoints (Hirose and Kuienda, 1991; Orin, 1982; Bares and Whittaker, 1993), whereas legs of two-legged machines are

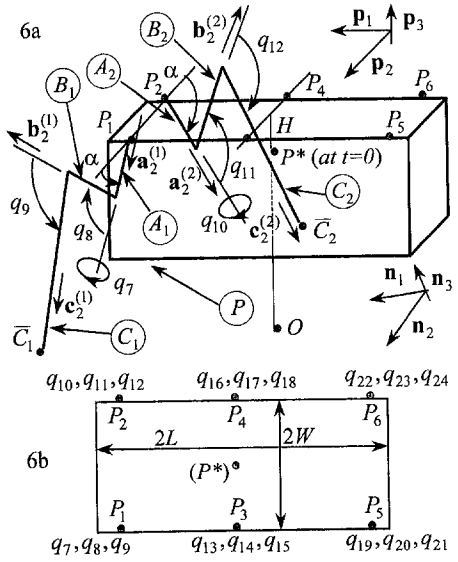


Fig. 6 Hexapod (Eltze and Pfeiffer, 1995): a system with varying constraints

Downloaded 04 May 2010 to 171.66.16.27. Redistribution subject to ASME license or copyright; see http://www.asme.org/terms/Terms_Use.cfm

equipped with a surface containing a number of supporting points (Shih et al., 1993).

Now, legs of four and six-legged machines usually comprise a number of links connected to one another and to the main body of the machine by revolute joints. Three-link structures (Hirose and Kuienda, 1991; Eltze and Pfeiffer, 1995) and pantograph structures (Lee and Song, 1990; Zhang and Song, 1992) are the most common. At times, one or two of the revolute joints are replaced with prismatic joints (Byrd and DeVries, 1990; Bares and Whittaker, 1993).

Different kinds of gaits are the subject of extensive studies. Continuous, periodic wave-crab gaits discussed, e.g., by Zhang and Song (1990) and Orin (1982), and turning gaits, discussed by, e.g., Lee and Song (1991), and Zhang and Song (1993), are designed for even terrain. Discontinuous nonperiodic wave-crab gaits discussed, e.g., by Hirose and Kunieda (1991), and Kumar and Waldorn (1989), and turning gaits, discussed in, e.g., by Santos and Jimenez (1995), are designed for uneven terrain. By looking at different variations of the indicated gaits, researchers try to optimize paths, stability, speed, and energy consumption.

The machine in Fig. 6 has six legs, each with three links interconnected by revolute joints. Here, a rectilinear, statically stable motion on a planar, horizontal surface will be considered.

Some of many works deal with the general structure of walking machines (Eltze and Pfeiffer, 1995; Byrd and DeVries, 1990) and with path planning and control (Kumar and Waldorn, 1989; Lee and Song, 1991). Others deal with direct and inverse kinematic analysis (Lee and Song, 1990; Zhang and Song, 1990), direct and inverse dynamic analysis (Eltze and Pfeiffer, 1995; Shih et al., 1993) and stability analysis (Zhang and Song, 1990; Santos and Jimenez, 1995) of various types of machines. Considering dynamic analyses, one cannot proceed before modeling the leg-earth contact (Lee and Song, 1991; Kumar and Waldorn, 1989). Some researchers assume that the contact is noncompliant (Shih et al., 1993; Eltze and Pfeiffer, 1995), and hence involve the imposition and removal of constraints. These are associated with changes in the kinematical loops formed between the legs, the body of the machine and the ground, occurring as the gait proceeds. Some researchers avoid the problem, assuming leg-end compliance (Freeman and Orin, 1991). As indicated, no work considering the various phases of motion as a whole can be found, although a number of attempts to do so have been made. For example, Tzafestas et al. (1996) generate equations governing two phases of motion of a biped robot, and then deal with the transition; however, they do so as if these events are isolated. Blajer and Schiehlen (1992) deal with the single support phase and the double support phase of a planar, seven-link biped robot. However, they introduce a "zero impact" PD-control, hence do not deal with the effect of the impact which in general may occur during transitions.

Here it is suggested to regard the gait of a multilegged machine as a motion of a system subject to varying constraints. Accordingly, the five steps of Section 3 will next be used to generate equations governing motions of the six-legged machine S shown in Fig. 6. The machine comprises a main body P and six legs $L_1, \ldots, L_6$ each consisting of three uniform bars A_k, B_k, and C_k ($k = 1, \ldots, 6$) of length L_A, L_B, and L_C, respectively. $\mathbf{n}_i$, $\mathbf{p}_i$, $\mathbf{a}_i^{(k)}$, $\mathbf{b}_i^{(k)}$, and $\mathbf{c}_i^{(k)}$ ($i = 1, 2, 3$) are sets of three dextral, mutually perpendicular unit vectors fixed in $\mathbf{N}$, P, A_k, B_k and C_k ($k = 1, \ldots, 6$), respectively. $P_1, \ldots, P_6$ are six points of P arranged as shown in Fig. 6(b), so that, for example, the position vector from P^*, the mass center of P, to P_1, is given by $\mathbf{p}^{P^*/P_1} = L\mathbf{p}_1 + W\mathbf{p}_2 + H\mathbf{p}_3$, etc., where L, W, and H are as shown in Fig. 6. The endpoints of $A_1, \ldots, A_6$, coincide, respectively, with $P_1, \ldots, P_6$, and $\mathbf{a}_2^{(k)}$, $\mathbf{b}_2^{(k)}$ and $\mathbf{c}_2^{(k)}$ are aligned with A_k, B_k and C_k ($k = 1, \ldots, 6$), respectively. Finally, $\mathbf{n}_3$ is aligned with the local vertical. Now, one possible motion of S is considered here, whereby P^* moves along a straight line parallel to $\mathbf{n}_1$, whereas the orientation of P in $\mathbf{N}$ remains unaltered. This motion can be produced if legs $L_1 - L_4 - L_5$ and legs $L_2 - L_3 - L_6$ are used to support and propel P, alternately, so that the roles of the legs are interchanged during the transitions phases (tripod gait). One can generate equations underlying this motion, invoking the five-step procedure as follows.

Step a. Let $q_1, \ldots, q_{24}$ be generalized coordinates and, considering $q_1, \ldots, q_9$ first, let q_1, q_2 and q_3 be angles defining the orientation of P in $\mathbf{N}$; and let q_4, q_5, and q_6 be defined as $q_{3+r} \triangleq \mathbf{p}^{O/P^*} \cdot \mathbf{n}_r$ ($r = 1, 2, 3$), where O is a point fixed in $\mathbf{N}$. Focusing attention on L_1, let A_1 (or $\mathbf{a}_2^{(1)}$) be temporarily aligned with $\mathbf{p}_2$ and subject A_1 to a $-\alpha\mathbf{p}_1$ rotation, so that $\alpha = \cos^{-1}(\mathbf{p}_2 \cdot \mathbf{a}_2^{(1)}) =$ constant. Furthermore, A_1, B_1 and C_1 lie in a plane p_1 at all times, and this plane undergoes a $q_7\mathbf{a}_2^{(1)}$ rotation in P. Thus, $\mathbf{a}_1^{(1)}$, $\mathbf{b}_1^{(1)}$ and $\mathbf{c}_1^{(1)}$ are all perpendicular to p_1. Accordingly, q_8 and q_9, describing the rotations of B_1 in A_1 and of C_1 in B_1, respectively, can be defined as $q_8 \triangleq \cos^{-1}(\mathbf{b}_2^{(1)} \cdot \mathbf{a}_2^{(1)})$ and $q_9 \triangleq \cos^{-1}(\mathbf{c}_2^{(1)} \cdot \mathbf{b}_2^{(1)})$.

Next, let $u_1, \ldots, u_{24}$ be generalized speeds, and define $u_1, \ldots, u_9$ such that $u_r \triangleq {}^N\omega^P \cdot \mathbf{p}_r$ ($r = 1, 2, 3$), $u_{r+3} \triangleq {}^N\mathbf{v}^{P^*} \cdot \mathbf{n}_r$ ($r = 1, 2, 3$), $u_7 \triangleq {}^P\omega^{A_1} \cdot \mathbf{a}_2^{(1)}$, $u_8 \triangleq {}^{A_1}\omega^{B_1} \cdot \mathbf{a}_1^{(1)}$ $u_9 \triangleq -{}^{B_1}\omega^{C_1} \cdot \mathbf{a}_1^{(1)}$, where ${}^N\omega^P$, ${}^P\omega^{A_1}$, ${}^{A_1}\omega^{B_1}$, and ${}^{B_1}\omega^{C_1}$ are the angular velocities of P in $\mathbf{N}$, of A_1 in P, of B_1 in A_1, and of C_1 in B_1; and ${}^N\mathbf{v}^{P^*}$ is the velocity of P^* in $\mathbf{N}$. Then the angular velocities of P, A_1, B_1, and C_1 in $\mathbf{N}$ can be expressed by ${}^N\omega^P = u_1\mathbf{p}_1 + u_2\mathbf{p}_2 + u_3\mathbf{p}_3$, ${}^N\omega^{A_1} = {}^N\omega^P + u_7\mathbf{a}_2^{(1)}$, ${}^N\omega^{B_1} = {}^N\omega^{A_1} + u_8\mathbf{a}_1^{(1)}$ and ${}^N\omega^{C_1} = {}^N\omega^{B_1} - u_9\mathbf{a}_1^{(1)}$. Noting that ${}^N\mathbf{v}^{P^*} = u_4\mathbf{n}_1 + u_5\mathbf{n}_2 + u_6\mathbf{n}_3$, one can express the velocities in $\mathbf{N}$ of A_1^*, B_1^*, and C_1^*, the mass centers of A_1, B_1, and C_1, respectively, and of $\bar{C}_1$, the endpoint of C_1, in terms of $u_1, \ldots, u_9$. Similar expressions for angular velocities of bodies and for velocities of points associated with L_2 can be written if A_2 (or $\mathbf{a}_2^{(2)}$) is temporarily aligned with $\mathbf{p}_2$ and is then subject to a $(\pi + \alpha)\mathbf{p}_1$ rotation; and if q_{10}, q_{11}, q_{12}, u_{10}, u_{11}, and u_{12} play, in connection with L_2, the role played by q_7, q_8, q_9, u_7, u_8, and u_9 in connection with L_1. Then ${}^N\omega^{A_2} = {}^N\omega^P + u_{10}\mathbf{a}_2^{(2)}$, ${}^N\omega^{B_2} = {}^N\omega^{A_2} - u_{11}\mathbf{a}_1^{(2)}$, and ${}^N\omega^{C_2} = {}^N\omega^{B_2} + u_{12}\mathbf{a}_1^{(2)}$. Finally, angular velocities of bodies and velocities of points of legs L_3 and L_5 and of legs L_4 and L_6 can be expressed similarly to angular velocities of bodies and velocities of points of legs L_1 and L_2, respectively. The respective generalized coordinates are numbered in Fig. 6(b). The kinematical equations are $\dot{q}_1 = (u_1\cos q_3 - u_2\sin q_3)/\cos q_2$, etc. (for a body-three 1-2-3 rotation sequence of P in $\mathbf{N}$), and $\dot{q}_r = u_r$ ($r = 4, \ldots, 24$).

The MCS for this system is defined as one in which none of $\bar{C}_k$, the endpoints of C_k ($k = 1, \ldots, 6$), touch the ground. One can then formulate $F_r + F_r^*$ ($r = 1, \ldots, 24$) with $-m_P g\mathbf{n}_3$, $-m_{A1}g\mathbf{n}_3, \ldots$, etc., as the gravitational forces acting on P, A_1, etc.; and with

$$\mathbf{T}_{PA}^{(k)} = \mathbf{T}_{PA}^{(k)}\mathbf{a}_2^{(k)}, \quad \mathbf{T}_{AB}^{(k)} = T_{AB}^{(k)}\mathbf{a}_1^{(k)},$$
$$\mathbf{T}_{BC}^{(k)} = \mathbf{T}_{BC}^{(k)}\mathbf{a}_1^{(k)} \quad (k = 1, \ldots, 6) \tag{41}$$

as the control torques exerted by P on A_k, by A_k on B_k and by B_k on C_k ($k = 1, \ldots, 6$), respectively. Expressions for $F_r + F_r^*$ ($r = 1, \ldots, 24$) were generated, in connection with the present analysis, with the aid of AUTOLEV 3 (Kane and Levinson, 1996), a symbol manipulation program, which enables the generation of motion equations of multibody mechanical systems. The indicated expressions are lengthy and will not be reported here in full.

Step b. Two phases will be considered: Phase 1, in which L_1, L_4, and L_5 are the supporting legs, and Phase 2, in which L_2, L_3, and L_6 are the supporting legs. The associated constraint equations can be written as follows:

$$MP_1\text{: } {}^N\mathbf{v}^{\bar{C}_k} \cdot \mathbf{n}_i = 0 \quad (i = 1, 2, 3;\ k = 1, 4, 5) \tag{42}$$

$$MP_2\text{: } {}^N\mathbf{v}^{\bar{C}_k} \cdot \mathbf{n}_i = 0 \quad (i = 1, 2, 3;\ k = 2, 3, 6), \tag{43}$$

where ${}^N\mathbf{v}^{\bar{C}_k}$ is the velocity of $\bar{C}_k$ ($k = 1, \ldots, 6$) in $\mathbf{N}$. Thus, each phase involves nine constraint equations. Casting these in the form of Eqs. (10), one obtains

Downloaded 04 May 2010 to 171.66.16.27. Redistribution subject to ASME license or copyright; see http://www.asme.org/terms/Terms_Use.cfm

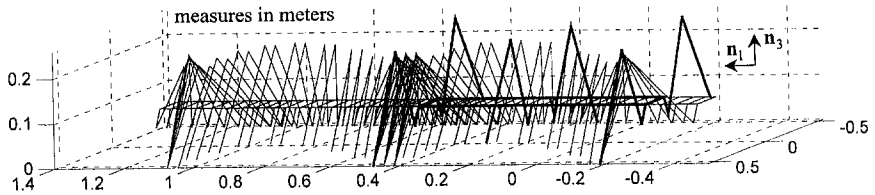


Fig. 7 Snapshots of the three first paces ($^1MP_1$, $^1MP_2$, and $^2MP_1$) with PD-control

$$MP_1\colon\ u_k = \sum_{r=1}^{6} C_{kr}^{(1)} u_r + D_k^{(1)} \qquad (k = 7, 8, 9, 16, \ldots, 21) \quad (44)$$

$$MP_2\colon\ u_k = \sum_{r=1}^{6} C_{kr}^{(2)} u_r + D_k^{(2)} \qquad (k = 10, \ldots, 15, 22, 23, 24). \quad (45)$$

Equations (44) and (45) were also generated with the aid of AUTOLEV 3.

Step c. Motion equations of the two phases are obtained by substitutions in Eqs. (11) for $j = 1$ and $j = 2$ from Eqs. (44) and (45), respectively, as follows:

$$j = 1:\quad F_r + F_r^* + \sum_{k=7,8,9,16,\ldots,21} C_{kr}^{(1)}(F_k + F_k^*) = 0 \qquad (r = 1, \ldots, 6, 10, \ldots, 15, 22, 23, 24) \quad (46)$$

$$j = 2:\quad F_r + F_r^* + \sum_{k=10,\ldots,15,22,23,24} C_{kr}^{(2)}(F_k + F_k^*) = 0 \qquad (r = 1, \ldots, 6, 7, 8, 9, 16, \ldots, 21). \quad (47)$$

Note that $C_{kr}^{(1)} = 0$ for $r = 10, \ldots, 15, 22, 23, 24$, whereas $C_{kr}^{(2)} = 0$ for $r = 7, 8, 9, 16, \ldots, 21$. Integration of Eqs. (46) and (47) and of the time derivatives of both side of Eqs. (44) and (45) produces results characterizing the desired motion (whereby ${}^N\mathbf{v}^{P*}|_d = f(t)\mathbf{n}_1$ and ${}^N\boldsymbol{\omega}^P|_d = 0$) if adequate torques are applied at the various joints; i.e., if $T_{PA}^{(k)}$, $T_{AB}^{(k)}$ and $T_{BC}^{(k)}$ ($k = 1, \ldots, 6$) in Eqs. (41) are determined for each phase. This, in turn, can be done if the desired motion is specified. For Phase 1, the desired motion of P is characterized here by $q_1|_d = q_2|_d = q_3|_d = q_5|_d = 0$, $q_4|_d = 0.5L'[1 - \cos(\pi t/T')]$ and $q_6|_d = \mathbf{p}^{O/P*} \cdot \mathbf{n}_3 = (L_A + L_C)\sin\alpha - L_B\cos\alpha - H$, $u_1|_d = u_2|_d = u_3|_d = u_5|_d = u_6|_d = 0$ and $u_4|_d = f(t) = 0.5\pi L'/T' \sin(\pi t/T')$. L' is the pace (i.e., the distance traversed by P^* in each phase), T' is the pace duration, and L'/T' is the average speed of P^* in the $\mathbf{n}_1$-direction. Thus the (static) stability margin of this gait is $(L - L')/2L$ (Kumar and Waldorn, 1989).

Whereas these definitions determine u_7, u_8, u_9, $u_{16}, \ldots, u_{21}$, which are variables associated with L_1, L_4, and L_5 via Eqs. (44), more should be said about the motion of L_2, L_3, and L_6. This motion must be designed so as to bring L_2, L_3, and L_6 to a configuration where they are prepared to undertake the role of the supporting legs at the end of Phase 1 ($t = T'$). Accordingly, three conditions must be specified in connection with the motion of each of the legs L_2, L_3, and L_6. For L_2 the selected conditions were $u_{10}|_d = -0.5404195\pi/T' \sin(\pi t/T')$, ${}^N\mathbf{v}^{C_2} \cdot \mathbf{n}_3|_d = \pi/T'A \sin(2\pi t/T')$ where A is a constant; and ${}^N\mathbf{v}^{C_2} \cdot \mathbf{p}_2|_d = 0$. These conditions, when written explicitly, specify $u_{10}|_d$, $u_{11}|_d$, and $u_{12}|_d$ as functions of $u_1|_d, \ldots, u_6|_d$, themselves known functions of time; and time. Similar conditions are associated with the motions of L_3 and L_6. Thus, the desired motion of S is specified. Note that $u_r|_d(0) = u_r|_d(T') = 0$ ($r = 1, \ldots, 24$), so that at $t = 0$ and at $t = T'$ S is expected to be momentarily motionless.

One way to determine the torques producing this desired motion is to solve the associated inverse dynamic problem. Choosing $T_{BC}^{(k)}$ ($k = 1, 4, 5$) to be known functions of time (then the solution to the inverse problem is unique) one can show, using curve-fitting procedures, that the required torques can be approximated by the following polynomials:

$$T_{PA}^{(k)} = p_{PA1}^{(k)} h_1 + p_{PA2}^{(k)} h_2, \quad T_{AB}^{(k)} = p_{AB1}^{(k)} h_1 + p_{AB2}^{(k)} h_2,$$
$$T_{BC}^{(k)} = p_{BC1}^{(k)} h_1 + p_{BC2}^{(k)} h_2 \quad (k = 1, \ldots, 6) \qquad (48)$$

where

$$h_1 = [1 - (t - T'/2)/|t - T'/2|]$$
$$h_2 = [1 + (t - T'/2)/|t - T'/2|],$$
$$p_{PAi}^{(k)} = a_{PAi}^{(k)} + b_{PAi}^{(k)} t + c_{PAi}^{(k)} t^2 + d_{PAi}^{(k)} t^3 + e_{PAi}^{(k)} t^4 + f_{PAi}^{(k)} t^5 \qquad (i = 1, 2;\ k = 1, \ldots, 6), \quad (49)$$

etc. For $T_{BC}^{(k)} = 0$ ($k = 1, 4, 5$), the values of $a_{PAi}^{(k)}, \ldots, f_{BCi}^{(k)}$ ($i = 1, 2$; $k = 1, \ldots, 6$) depend on the initial values of q_r ($r = 1, \ldots, 24$), which, for $\alpha = \pi/4$, $A = 0.05$, $L' = 0.3$, $L = 0.33$, $W = 0.0875$, $H = 0$, $L_A = 0.055$, $L_B = 0.25$ and $L_C = 0.325$ m are chosen to be as follows: $q_1 = q_2 = q_3 = 0$ rad, $q_4 = q_5 = 0$, $q_6 = 0.09192388$ m, $q_7 = q_{10} = -q_{13} = -q_{16} = q_{19} = q_{22} = 0.5404195$ rad, $q_8 = q_{11} = q_{14} = q_{17} = q_{20} = q_{23} = 1.560122$ rad, $q_9 = q_{12} = q_{15} = q_{18} = q_{21} = q_{24} = 1.431889$ rad. This choice places P^* initially at a distance $L'/2$ from its location at the "midpace" configuration of $^1MP_1$ (Phase 1, first repetition), in which $q_{4+3r} = 0$, $q_{5+3r} = q_{6+3r} = \pi/2$ ($r = 1, \ldots, 6$) as indicated in Fig. 7 by heavy lines. The initial configuration of S is denoted in Fig. 8 by heavy lines. Using self-explanatory notations for inertial properties, one obtains, for $M_P = 120$, $M_A^{(k)} = 0.6$, $M_B^{(k)} = M_C^{(k)} = 1.2$ kg ($k = 1, \ldots, 6$), $I_{P1} = 0.6$, $I_{P2} = I_{P3} = 4.66$, $I_{A2}^{(k)} = 0.00015$, $I_{B1}^{(k)} = I_{B3}^{(k)} = 0.0062$, and $I_{C1}^{(k)} = I_{C3}^{(k)} = 0.0105$ kg-m^2 ($k = 1, \ldots, 6$), the approximate expressions for $T_{PA}^{(k)}$, $T_{AB}^{(k)}$, and $T_{BC}^{(k)}$ ($k = 1, \ldots, 6$) reported in the Appendix.

Furthermore, to compensate for deviations from the desired motion associated with the approximate expressions given by Eqs. (48) and (49), one can apply, in addition, PD-control torques, so that, for example, $T_{PA}^{(k)}$ is expressed as follows:

$$T_{PA}^{(k)} = p_{PA1}^{(k)} h_1 + p_{PA2}^{(k)} h_2 + \sum_{i=1}^{6} [K_{PAi}^{(k)}(q_i - q_1|_d) + B_{PAi}^{(k)}(u_i - u_i|_d)] \qquad (k = 1, \ldots, 6), \quad (50)$$

etc. Numerical integration of Eqs. (46) shows that, for PD-control constants having values as in the Appendix, the deviations of q_1, q_2, and q_3 and of q_4, q_5, and q_6 from their desired values is 10^{-5} rad/sec and 10^{-4} m, respectively, throughout Phase 1.

Phase 2 can be treated similarly if note is taken of the fact that

$$p_{PAj}^{(i)}|_{MP_2} = -p_{PAj}^{(i+1)}|_{MP_1}, \quad i = 1, 3, 5;\ j = 1, 2$$
$$p_{PAj}^{(i)}|_{MP_2} = -p_{PAj}^{(i-1)}|_{MP_1}, \quad i = 2, 4, 6;\ j = 1, 2,$$

Downloaded 04 May 2010 to 171.66.16.27. Redistribution subject to ASME license or copyright; see http://www.asme.org/terms/Terms_Use.cfm

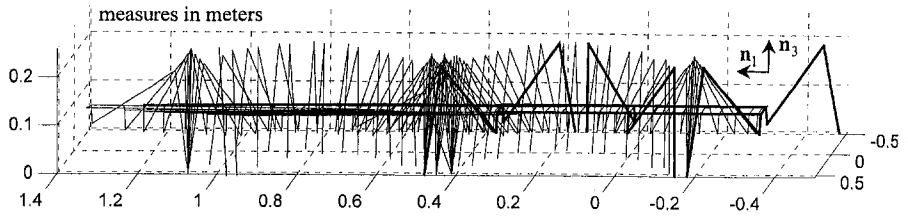


Fig. 8 Snapshots of the three first paces ($^1MP_1$, $^1MP_2$, and $^2MP_1$) without PD-control

etc., and if the various PD-control constants are as in the Appendix.

Step d. Changes in u_r ($r = 1, \ldots, 24$) associated with the transition from Phase 1 to Phase 2 are obtained by substitutions in Eqs. (15) for $L = 2$. This requires knowledge of m_{rs} ($r, s = 1, \ldots, 24$) and $C_{kr}^{(2)}$ ($k = 10, \ldots, 15, 22, 23, 24$, $r = 1, \ldots, 6$), which can be identified as coefficients appearing in the expressions for $F_r + F_r^*$ ($r = 1, \ldots, 24$) and in Eqs. (45), respectively. Changes in u_r ($r = 1, \ldots, 24$) associated with the transition from Phase 2 to Phase 1 are obtained similarly.

Step e. The transition conditions are approximated here as follows:

$$^1TC_{1\text{-}2}\text{: } t = 0.3; \quad ^1TC_{2\text{-}1}\text{: } t = 0.6; \quad ^2TC_{1\text{-}2}\text{: } t = 0.9; \quad \text{etc.} \quad (51)$$

The approximation lies in the assumption that at the indicated instants the endpoints of the supporting legs are all in contact with the ground.

A simulation code based on these steps was built and was used to show that if one applies $T_{PA}^{(k)}$, $T_{AB}^{(k)}$, and $T_{BC}^{(k)}$ ($k = 1, \ldots, 6$) without PD-control, then one obtains, for the first three paces, the snapshots of L_1, L_3, and L_5 shown in Fig. 8 (only odd-numbered legs are shown for clarity). The addition of PD-control leads to the snapshots shown in Fig. 7. The changes in u_r ($r = 1, \ldots, 24$) during the third transition (from the third pace $-{}^2MP_1-$ to the fourth pace $-{}^2MP_2-$) are $\Delta u_1 = -0.000203$, $\Delta u_2 = -0.0023$, $\Delta u_3 = -0.00198$ rad/sec, $\Delta u_4 = 0.00274$, $\Delta u_5 = 0.00127$, $\Delta u_6 = -0.000384$ m/sec etc., with PD-control, and $\Delta u_1 = -0.0183$, $\Delta u_2 = -0.147$, $\Delta u_3 = 0.047$ rad/sec $\Delta u_4 = 0.0509$, $\Delta u_5 = -0.0106$, $\Delta u_6 = -0.108$ m/sec etc., without.

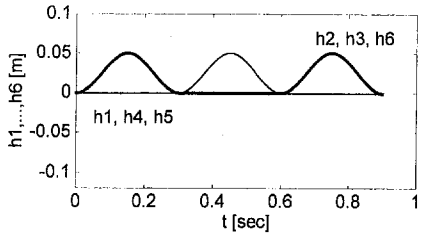


Fig. 9 Heights of $\bar{C}_k$ ($k = 1, \ldots, 6$) during the three first paces with PD-control

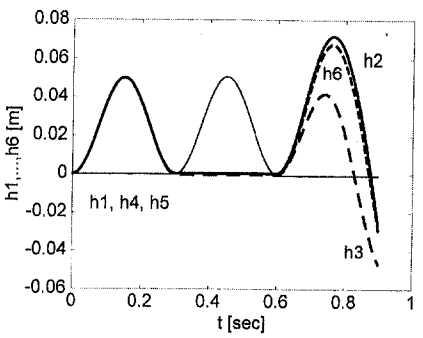


Fig. 10 Heights of $\bar{C}_k$ ($k = 1, \ldots, 6$) during the three first paces without PD-control

Finally, Figs. 9 and 10 show the heights $h_1, \ldots, h_6$ of $\bar{C}_k$ ($k = 1, \ldots, 6$) during the three first paces with and without PD-control, respectively. These results indicate the rapid departure from the desired motion occurring without PD-control.

It is worth noting that the motion equations governing the various phases were validated with the aid of energy-associated integrals, automatically generated by AUTOLEV 3 (Kane and Levinson, 1996); and by inspection of the animations underlying Figs. 7 and 8. In addition, the following relation was used to test the validity of the computation of Δu_s ($s = 1, \ldots, n$) associated with each transition, namely, $E(t_2) - E(t_1) = \sum_{r=1}^{n} \sum_{s=1}^{n} m_{rs} \Delta u_r \Delta u_s$ (Djerassi, 1998, Eq. (39)). Here $E(t_2)$ and $E(t_1)$ are the numerical values of the mechanical energy of the system at t_2 and t_1, respectively, instants defined in Section 2.

7 Summary

A methodology was presented for the construction of sets of equations governing motions of mechanical systems with varying constraints. Accordingly, the motion is decomposed into phases, separated by transitions. One set of motion constraints governs the motion at any given phase. The removal of one set of constraints and the imposition of another set takes place during the transition from one phase of motion to another; and the associated changes in the motion variables are evaluated and taken into account.

The methodology was applied to simple and complex examples, and, in connection with the latter, led to a simulation of motion of a six-legged machine performing a few paces. With this tool in hand, structural optimizations and control strategies can be tested with reference to different kinds of gaits on even and on uneven terrain.

References

Bares, J. E., and Whittaker, W. L., 1993, "Configurations of Autonomous Walkers for Extreme Terrain," *The International Journal of Robotics Research,* Vol. 2, No. 6, pp. 535–559.

Blajer, W., and Schiehlen, W., 1992, "Walking without Impacts as Motion/Force Control Problem," ASME *Journal of Dynamic Systems, Measurements and Control,* Vol. 114, pp. 660–665.

Byrd, J. S., and DeVries, K. R., 1990, "A Six-Legged Telerobot for Nuclear Applications Development," *The International Journal of Robotics Research,* Vol. 9, No. 2, pp. 43–52.

Djerassi, S., 1994, "Imposition of Constraints," ASME JOURNAL OF APPLIED MECHANICS, Vol. 61, pp. 434–439.

Djerassi, S., 1998, "Conservation Principles for Systems with a Varying Number of Degrees of Freedom," ASME JOURNAL OF APPLIED MECHANICS, Vol. 65, pp. 719–726.

Eltze, J., and Pfeiffer, F., 1995, "Optimization of a Leg Design," *Journal of Robotic System,* Vol. 12, No. 11, pp. 757–765.

Freeman, P. S., and Orin, D. E., 1991, "Efficient Dynamic Simulation of a Quaruped Using Decoupled Tree-Structure Approach," *The International Journal of Robotics Research,* Vol. 10, No. 6, pp. 619–627.

Hirose, S., and Kunieda, O., 1991, "Generalized Standard Foot Trajectory for a Quadruped Walking Vehicle," *The International Journal of Robotics Research,* Vol. 10, No. 1, pp. 3–12.

Kane, T. R., and Levinson, D. A., 1996, "Dynamics Online: Theory and Implementation with AUTOLEV," *Online Dynamics,* Sunnyvale, CA.

Kane, T. R., and Levinson, D. A., 1985, *Dynamics: Theory and Applications,* McGraw-Hill, New York.

Klein, C. A., Olson, K. W., and Pugh, D. R., 1983, "Use of Force and Altitude Sensors for Locomotion of a Legged Vehicle over Irregular Terrain," *The International Journal of Robotics Research,* Vol. 2, No. 2, pp. 3–17.

Kumar, V. R., and Waldorn, K. J., 1989, "Adaptive Gait Control for a Walking Robot," *Journal of Robotic Systems,* Vol. 6, No. 1, pp. 4–76.

Lee, J. K., and Song, S. M., 1991, "Path Planning and Gait of Walking Machine in an Obstacle-Strewn Environment," *Journal of Robotic Systems,* Vol. 8, No. 6, pp. 801–827.

Downloaded 04 May 2010 to 171.66.16.27. Redistribution subject to ASME license or copyright; see http://www.asme.org/terms/Terms_Use.cfm

Lee, J. K., and Song, S. M., 1990, "A Study of Instantaneous Kinematics of Walking Machines," *International Journal of Robots and Automation,* Vol. 5, No. 3, pp. 131–138.

Nechyba, M. C., and Xu, Y., 1995, "Human-Robot Cooperation in Space: SM^2 for New Space Station Structure," *IEEE Robotics and Automation Magazine,* Vol. 2, No. 4, pp. 4–11.

Orin, D. E., 1982, "Supervisory Control of a Multilegged Robot," *The International Journal of Robotics Research,* Vol. 1, No. 1, pp. 79–91.

Ozguner, F., Tsai, S. J., and McGee, R. B., 1984, "An Approach to the Use of Terrain Preview Information on Rough Terrain Locomotion by Hexapod Walking Machines," *The International Journal of Robotics Research,* Vol. 3, No. 2, pp. 134–146.

Santos, P. G., and Jimenez, M. A., 1995, "Generation of Discontinuous Gaits for Quaduped Walking Machines," *Journal of Robotic Systems,* Vol. 12, No. 9, pp. 599–611.

Shih, C. L., Gruver, W. A., and Lee, T. T., 1993, "Inverse Kinematics and Inverse Dynamics for Control of a Biped Walking Machine," *Journal of Robotic Systems,* Vol. 10, No. 4, pp. 531–555.

Tzafestas, S., Raibert, M., and Tzafestas, C., 1996, "Robust Sliding-Mode Control Applied to a Five-Link Biped Robot," *Journal of Intelligent and Robotic Systems,* Vol. 15, No. 1, pp. 67–133.

Zhang, C. D., and Song, S. M., 1990, "Stability Analysis of Wave-Crab Gaits of a Quadruped," *Journal of Robotic Systems,* Vol. 7, No. 2, pp. 243–276.

Zhang, C. D., and Song, S. M., 1992, "Forward Kinematics of Walking Machines with Pantograph Legs Based on Selection of Independent Joints," *Journal of Robotic Systems,* Vol. 9, No. 7, pp. 955–972.

Zhang, C. D., and Song, S. M., 1993, "Turning Gaits of a Quadrupedal Walking Machine," *Advanced Robotics,* Vol. 7, No. 2, pp. 121–157.

APPENDIX

Control Torques

Inverse dynamics control torques (approximated): Phase 1

$$T_{PA}^{(1)} = (-109.2656 + 7.06862t + 8969.122t^2 + 19199.79t^3 - 832425.6t^4 + 3415330t^5)h1 + (1603.454 - 33211.63t + 270881.4t^2 - 1098554t^3 + 2218550t^4 - 1785899t^5)h2$$

$$T_{PA}^{(2)} = (-15.10625 + 0.769967t + 675.7512t^2 + 1868.804t^3 - 13901.3t^4 + 6803.911t^5)h1 + (-0.3330375 - 314.9841t + 3311.97t^2 - 8689.234t^3 + 3695.432t^4 + 6803.911t^5)h2$$

$$T_{PA}^{(3)} = -T_{PA}^{(2)}$$

$$T_{PA}^{(4)} = (91.66794 + 9.584533t - 9932.824t^2 + 21842.19t^3 + 333849.6t^4 - 1523968t^5)h1 + (1208.73 - 25717.6t + 221466.8t^2 - 949106.2t^3 + 1952094t^4 - 1523960t^5)h2$$

$$T_{PA}^{(5)} = (11.15966 - 18.01579t + 1993.436t^2 - 43604.45t^3 + 460307.2t^4 - 1785933t^5)h1 + (-2775.139 + 58992.87t - 498891.8t^2 + 2094147t^3 - 4290705t^4 + 3415450t^5)h2$$

$$T_{PA}^{(6)} = T_{PA}^{(2)}$$

$$T_{AB}^{(1)} = (-17.77296 - 4.795363t + 2506.51t^2 - 11000.65t^3 - 103920.5t^4 + 511415.5t^5)h1 + (454.2548 - 12351.18t + 127150.2t^2 - 623564.1t^3 + 1411015t^4 - 1184290t^5)h2$$

$$T_{AB}^{(2)} = (-5.96627 - 0.653332t + 774.3019tt^2 - 1393.264t^3 - 23585.76t^4 + 71532.59t^5)h1 + (8.686276 - 437.5539t + 6097.851t^2 - 34683.15t^3 + 83713.12t^4 - 71532.59t^5)h2$$

$$T_{AB}^{(3)} = -T_{AB}^{(2)}$$

$$T_{AB}^{(4)} = (116.3199 + 16.83693t - 11966.14t^2 + 34230.6t^3 + 287522.1t^4 - 1039893t^5)h1 + (-229.3797 + 8984.201t - 106671.1t^2 + 556662.5t^3 - 1272355t^4 + 1039927t^5)h2$$

$$T_{AB}^{(5)} = (-92.42256 - 2.42412t + 8131.888t^2 - 3791.2t^3 - 365427.2t^4 + 1184307t^5)h1 + (310.3913 - 8018.96t + 74580.64t^2 - 324609.7t^3 + 663289.4t^4 - 511488t^5)h2$$

$$T_{AB}^{(6)} = T_{AB}^{(2)}$$

$$T_{BC}^{(1)} = 0$$

$$T_{BC}^{(2)} = (0.2848357 - 0.548376t + 84.82526t^2 - 1255.28t^3 + 4183.204t^4 + 1718.244t^5)h1 + (11.92133 - 232.7961t + 1677.929t^2 - 5310.984t^3 + 6760.569t^4 - 1718.244t^5)h2$$

$$T_{BC}^{(3)} = -T_{BC}^{(2)}, \quad T_{BC}^{(4)} = 0, \quad T_{BC}^{(5)} = 0, \quad T_{BC}^{(6)} = T_{BC}^{(2)}$$

Nonzero PD-Control constants: Phase 1

$$B_{AB1}^{(1)} = 100, \quad B_{AB2}^{(1)} = -100, \quad B_{AB3}^{(1)} = -100, \quad B_{AB1}^{(4)} = 200,$$

$$B_{AB1}^{(5)} = 100, \quad B_{AB2}^{(5)} = 100, \quad B_{AB3}^{(5)} = 100$$

$$B_{BC6}^{(1)} = -10000, \quad B_{BC6}^{(4)} = 20000, \quad B_{BC6}^{(5)} = -10000,$$

$$B_{PA4}^{(1)} = 200, \quad B_{PA4}^{(4)} = -400, \quad B_{PA4}^{(5)} = 200$$

$$K_{AB1}^{(1)} = 200, \quad K_{AB2}^{(1)} = -200, \quad K_{AB3}^{(1)} = -200, \quad K_{AB1}^{(4)} = 400,$$

$$K_{AB1}^{(5)} = 200, \quad K_{AB2}^{(5)} = 200, \quad K_{AB3}^{(5)} = 200$$

$$K_{PA4}^{(1)} = 1600, \quad K_{PA4}^{(4)} = -3200, \quad K_{PA4}^{(5)} = 1600$$

Nonzero PD-Control constants: Phase 2

$$B_{AB1}^{(2)} = 100, \quad B_{AB2}^{(2)} = 100, \quad B_{AB3}^{(2)} = -100, \quad B_{AB1}^{(3)} = 200,$$

$$B_{AB1}^{(6)} = 100, \quad B_{AB2}^{(6)} = -100, \quad B_{AB3}^{(6)} = 100$$

$$B_{BC6}^{(2)} = 10000, \quad B_{BC6}^{(3)} = -20000, \quad B_{BC6}^{(6)} = 10000,$$

$$B_{PA4}^{(2)} = -200, \quad B_{PA4}^{(3)} = 400, \quad B_{PA4}^{(6)} = -200$$

$$K_{AB1}^{(2)} = 200, \quad K_{AB2}^{(2)} = 200, \quad K_{AB3}^{(2)} = -200, \quad K_{AB1}^{(3)} = 400,$$

$$K_{AB1}^{(6)} = 200, \quad K_{AB2}^{(6)} = -200, \quad K_{AB3}^{(6)} = 200$$

$$K_{PA4}^{(2)} = -1600, \quad K_{PA4}^{(3)} = 3200, \quad K_{PA4}^{(6)} = -1600$$

Downloaded 04 May 2010 to 171.66.16.27. Redistribution subject to ASME license or copyright; see http://www.asme.org/terms/Terms_Use.cfm

A. C. Palmer
Engineering Department,
Cambridge University,
Cambridge CB2 1PZ, UK

L. Tebboth
BP Amoco,
Sunbury-on-Thames,
Middlesex TW16 7LN, UK

D. Miles
Engineering Department,
Cambridge University,
Cambridge, CB2 1PZ, UK
and
Andrew Palmer and Associates SAIC Ltd.,
40 Carden Place,
Aberdeen AB10 1UP, UK

C. R. Calladine
Engineering Department,
Cambridge University,
Cambridge CB2 1PZ, UK

Instability of Pipelines on Slopes

A serious incident occurred during construction of a 36-inch pipeline in Colombia. A 500 m length of pipe on a hillside slipped on its supports, buckled, and slid down the hill, causing deaths and serious material damage. On a steep slope friction is not large enough to carry the downslope component of the weight. The frictional force from the supports then acts upslope. If the temperature subsequently increases, the frictional force partially reverses. The longitudinal force becomes more compressive and the pipeline can lift off the supports in overbends. A graphical construction gives a simple method of assessing the stability of the pipe in an arbitrary profile. The incident has important lessons for the construction of pipelines in steep terrain.

Introduction

A serious incident occurred during construction of a 36-inch pipeline in Colombia. Construction had moved up a hill with an average slope of about 20 degrees, starting at an anchor at the foot of the hill, and parallel to a previously excavated trench. The sequence of construction was to align each length of pipe and complete the root pass of the girth weld while the pipe was supported on timber supports or on earth mounds. Other teams followed some 20 joints behind the lineup and root pass team, but not all the welds had been completed in the upper half of the hill.

The brow of the hill had been reached during the evening before the incident. A small-magnitude Richter 2.27 earthquake had occurred during the night, and it had rained lightly. There is no information about temperature changes.

Work had restarted at 07:00, an hour before the incident. Witnesses close to the brow of the hill saw the leading length of pipe suddenly drop and then move downhill, dragging round the sideboom that supported it. The pipe dropped into the trench. A witness further down the hill saw the pipe move, looked up the hill and saw the pipe moving towards him, and then looked down the hill and saw the pipe arching upward off its supports. As the pipe moved down the hill, it broke up into several segments. Some 500 m of pipe slipped, covering the whole distance from the top of the pipe to the anchor. Some sections slid down the trench, and others were bent and lay across the trench. Four people were killed, and six others were severely injured.

Figure 1 is a photograph of part of the site after the accident. Figure 2 is an elevation showing the profile of the topmost section of the pipeline before the accident.

Following the incident, an accident investigation inquiry was initiated. An aim of the inquiry was to establish the cause of the incident, and to understand what measures could be implemented to prevent a reoccurrence. Cambridge University Engineering Department was asked to investigate the behavior of pipelines on slopes, as part of ongoing research on pipeline buckling.

Mechanics of Instability on a Slope

When a length of pipeline rests on a slope, whether directly on the ground or on supports, the weight of the pipeline generates a reaction between the supports and the pipe. The component of the reaction at right angles to the slope is the component of the weight acting in that direction, and is carried by normal reactions, through the supports, the interface between the supports and the anticorrosion coating, the coating itself, the interface between the coating and the pipe, and the pipe. Internal stresses equilibrate the reaction and the self-weight. If the supports are properly designed to carry the weight and to spread the load on the coating, if the soil is strong enough to bear the reactions, and if the pipe is not so thin that it cannot carry its own weight, these loads can be carried without difficulty.

The weight also requires a tangential reaction, parallel to the slope, which balances the downhill component of the weight. That reaction has to be carried tangentially, by shear in the coating and its interface with the pipe, by forces parallel to the slope between the pipe and the supports, and by tangential forces through the supports and into the soil. The system is not statically determinate: if the weight of each length of pipe can be carried locally, the pipe can be in equilibrium without any longitudinal force, but longitudinal force may still be present, if, for example, temperature changes lead to thermal expansion which is resisted by support reactions. On the other hand, if the weight of some section of the pipe cannot be carried locally, then equilibrium requires the presence of longitudinal force.

If the pipe is to remain in equilibrium, each segment of the load path must be able to carry these forces. Failure could occur:

1 by shear in the pipe material;
2 by shear at the interface between the pipe and the anticorrosion coating;
3 by shear within the coating;

Contributed by the Applied Mechanics Division of THE AMERICAN SOCIETY OF MECHANICAL ENGINEERS for publication in the ASME JOURNAL OF APPLIED MECHANICS.
Discussion on the paper should be addressed to the Technical Editor, Professor Lewis T. Wheeler, Department of Mechanical Engineering, University of Houston, Houston, TX 77204-4792, and will be accepted until four months after final publication of the paper itself in the ASME JOURNAL OF APPLIED MECHANICS.
Manuscript received by the ASME Applied Mechanics Division, Aug. 17, 1998; final revision, Dec. 18, 1998. Associate Technical Editor: S. Kyriakides.

 Copyright © 1999 by ASME

Downloaded 04 May 2010 to 171.66.16.27. Redistribution subject to ASME license or copyright; see http://www.asme.org/terms/Terms_Use.cfm

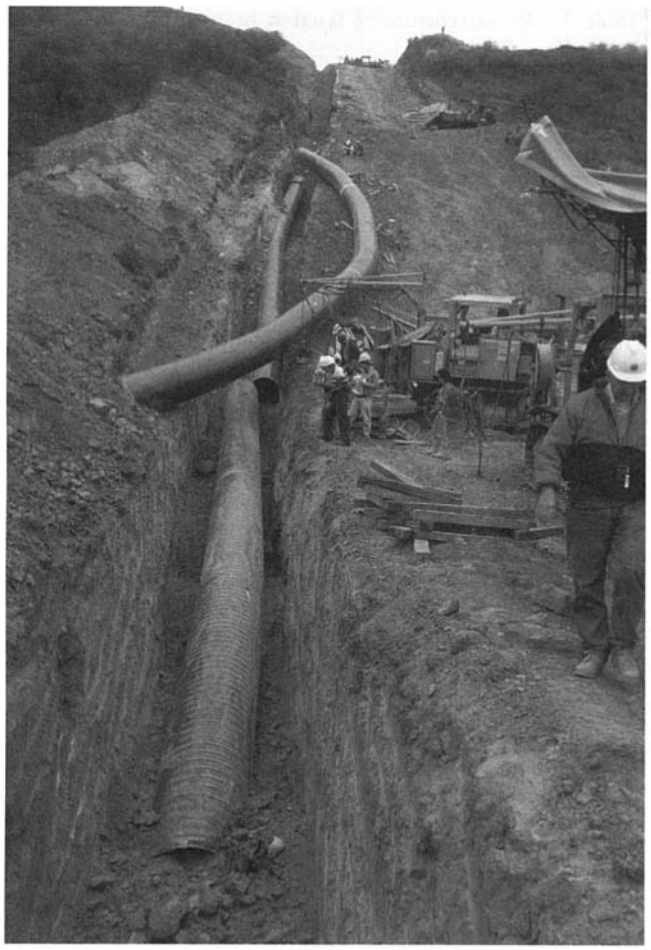


Fig. 1 Site after the incident

4 by shear at the interface between the pipe and the supports;
5 by collapse of the supports under a combination of tangential and normal loads;
6 by sliding of the supports;
7 by shear failure within the ground.

In this instance, 1, 2, 3, and 7 can be discounted immediately. The pipe was 914.4-mm (36-inch) outside diameter, 15.88-mm (0.625-inch) wall, and grade API ×70, which corresponds to a specified minimum yield stress of 482.6 MPa (70,000 psi). The strength of the pipe is far higher than necessary to carry this kind of load. The interface between the coating and the pipe can fail when it is very heavily loaded, in laybarge pipelaying for example, or under severe soil loading, but measurements of the strength of that interface (Palmer, 1982) suggest that there is a wide margin of safety against both 2 and 3. Though no measurements of ground strength are available, site photographs suggest that it is a strong and competent soil.

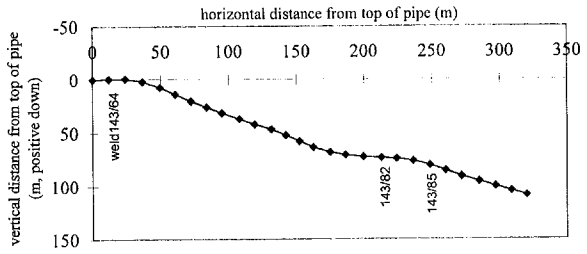


Fig. 2 Profile before the incident

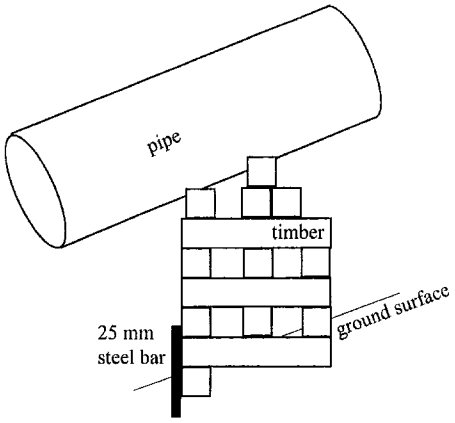


Fig. 3 Sketch of one support

Less is known about the transverse strength of the wooden supports, which were constructed from roughly hewn 1200 × 150 × 100 mm balks of eucalyptus wood, arranged criss-cross in layers but not bolted or spiked together and held by friction. Figure 3 is a sketch of one of the supports. It would be possible for the supports to fail by internal sliding. Steel rods driven into the ground on the downslope side of the supports provided additional strength against sliding, but they would impose relatively high localized loading on the soil and might have slipped or torn out. The scheme would not have distributed the horizontal loads evenly between the rods.

The weakest link in the load path is 4, the interface between the pipeline external polyethylene coating and the wooden supports. Tangential load can be carried through that interface by "friction," but friction between polymers and other materials is notoriously uncertain and variable (Bartenev, 1981). Friction of polymers is not consistent with conventional ideas about friction embodied in the Coulomb-Amonton "laws." In particular, the tangential load that can be carried is not proportional to the normal load, so that there is no constant "coefficient of friction," the maximum ratio of the tangential load to the normal load that can be reached before sliding begins. The ratio decreases with increasing load, and can reach very low values. The ratio is extremely sensitive to surface condition, and to the presence of water or oil.

On a gentle slope, say five degrees, the downhill component of the weight of each joint can be transmitted to the support beneath it. In this instance, each joint weighs about 4200 kg, and so the tangential component on a 5-deg slope is 4200 sin (5 deg), which is 360 kg (3.6 kN), a load which can probably be safely transmitted through the load path. On a gentle slope each pipe supports itself, and does not rely on any support from other joints downhill or uphill.

On a much steeper slope, say 45 degrees, the tangential force is much larger: 4200 sin (45 deg) is 2970 kg (29.1 kN), which probably cannot be safely transmitted through the load path through the support to the ground. The pipeline can therefore only remain in equilibrium with the help of longitudinal forces transmitted along the slope, either upslope or downslope.

If the pipeline were anchored at the top of the slope, equilibrium would be maintained by a longitudinal tensile force. The pipe would have no tendency to buckle.

If, as in this instance, the pipe were free at the top of the slope and anchored at the bottom, equilibrium could be maintained by a longitudinal compressive force which would steadily increase downslope from zero at the top. The longitudinal compressive force would increase to balance the share of the downslope component of the weight of each pipe which could not be carried by local frictional transmission downward through the coating and supports and into the ground. In some sections with gentler slopes, the longitudinal force might become less compressive, because in those sections the local downslope component of the weight would

Downloaded 04 May 2010 to 171.66.16.27. Redistribution subject to ASME license or copyright; see http://www.asme.org/terms/Terms_Use.cfm

be smaller, and the supports would be able to carry by friction more than that local downslope component.

The longitudinal compressive force in a pipeline has potential harmful effects. At overbends, the interaction between the longitudinal compressive force and the overbend curvature reduces the local reaction between the pipe and its supports, normal to the ground. If the combination of longitudinal compressive force and overbend curvature is sufficiently severe, the reaction reduces to zero and the pipe lifts off its support, like an arch. Once it has lifted off, the local curvature increases further, and the upward force on the section of pipe at the liftoff point increases with it. The system then becomes unstable, and runs away, forming a raised upheaval loop. The behavior parallels upheaval buckling in buried pipelines (Palmer et al., 1990). However, a raised loop in an unburied pipeline is generally itself unstable and temporary. The pipe has the same flexural stiffness laterally as vertically, so once it has freed itself from its supports by buckling upwards, the supports no longer exert any restraint on sideways movement, and the pipe then buckles sideways. That may well be what happened in the present incident, but this was not completely clarified by the witness statements.

Even if the reaction between the pipeline and its supports does not fall to zero, the interaction between the longitudinal compressive force at an overbend and the local overbend curvature tends to reduce lateral stability. The resistance to lateral movement is provided by "friction" between the pipe and the supports, and that friction depends on normal reaction at right angles to the slope, though not in a simple way. The interaction reduces the normal reaction, and therefore reduces the resistance to sideways movement.

This effect is enhanced if the overbend in the vertical profile coincides with a sideways bend. The same interaction between longitudinal compressive force and curvature occurs on horizontal bends as well as overbends. If there is a horizontal curvature, the supports have to carry a transverse horizontal force per unit length of pipe, equal to the local curvature multiplied by the longitudinal compressive force.

This suggests that the analysis should look particularly at overbends in the pipeline profile. In this instance, the profile (Fig. 2) includes a definite "bench" near weld 143/82, with an overbend between the bench and the steeper slope below it. Below weld 143/85, the slope is about 21 degrees. Going uphill, the profile slope falls to about six degrees at weld 143/82. The overbend curvature is then approximately 0.0073 rad/m, corresponding to a radius of 137 m, a rather severe overbend. The slope then steepens again, to 32 degrees at 143/70. There is a more severe second overbend between 143/68 (where the slope is about 32 degrees) and the end of the pipe at 143/64 (where the slope is close to zero), corresponding to a curvature of 0.0116 rad/m. However, that is only just below the free end of the pipe, and so there the longitudinal compressive force is quite low and the product of overbend curvature and longitudinal compressive force correspondingly small.

The situation is made worse by the mechanics of friction. Friction opposes motion, so that if slip occurs on a frictional interface the tangential force aligns itself with the direction in which slip occurs. This effect can readily be observed experimentally. If the pipe is on the point of slipping downhill, the direction of the frictional force is aligned uphill, parallel to the pipe, and there is then no frictional resistance at all to lateral motion, in the horizontal direction perpendicular to the pipe.

Horizontal bends tends to reduce stability (and this is implicitly recognized by pipeline constructors, who endeavor to construct upslope with the pipeline in a vertical plane). In this instance, there was a small horizontal bend coincident with the overbend, and some lateral resistance may have been provided by a V-shaped arrangement of timbers on either side of the pipe.

Analysis is complicated by the fact that the friction is not necessarily limiting everywhere along the pipe. If the pipe is on the point of moving downhill, the normal reaction can be determined, and a limiting friction relationship can be assumed, then the local tangential force per unit length acts uphill and its magnitude can be determined. If the pipe is on the point of moving uphill, the local tangential force per unit length acts downhill and its magnitude can again be determined. If the pipe is not on the point of moving, however, the direction and magnitude of the frictional force are not known (except that they lie within the limits corresponding to uphill and downhill movement).

Table 1 Measurements of friction between pipe and wood supports

Conditions	Angle at which sliding does not occur	Angle at which sliding does occur
Timbers able to rotate, coating and timbers dry	10	11.5
Timbers able to rotate, coating and timbers wet	6	10
Timbers fixed, coating and timbers dry	11.5	12.5
Timbers fixed, coating and timbers wet	7.5	11.5

The effects of thermal expansion are significant. In a tropical high-altitude location like Colombia, it is reasonable to assume that the pipe cooled during the night, when it also rained, and warmed up in the morning, between sunrise at about 06:00 and the accident at 08:10. The free expansion of 500 m of pipe subjected to a temperature rise of 10°C is 59 mm. The pipe would not have expanded as much as that, because of frictional restraint by the supports, but that constraint would only be present if the forces exerted by the supports on the pipe were to act in the downslope direction, and thereby generating an additional compressive force. Some movement on the supports is necessary to mobilise the friction. If the pipe were fully restrained longitudinally, the increase of axial force generated by a 10°C temperature rise would be 112 tonnes (1.10 MN), which is comparable with the longitudinal forces generated by the weight.

The actual longitudinal forces induced by temperature change are somewhat less than this. A detailed analysis of temperature effects is complicated, because it depends on the temperature history as the pipe is constructed.

"Friction" Between the Pipe and the Wooden Supports

The sliding resistance between the pipe and the supports was measured in the field. Two lengths of pipe were welded together to make a 23.82-m string which weighed 8331 kg. The string was supported on two wooden supports, built in the same way as the original supports. One end was then lifted vertically by a pipe sling attached to an excavator, and one of the supports was built up to increase the inclination of the pipe axis. The angle at which the pipe slid on the supports was measured. This is in some ways a crude test, but it has the great advantage that the force between the pipe and the support is the same as in the prototype system. In particular, the misleading Coulomb-Amonton "law" is not relied on.

Four cases were investigated, with dry and wet wood, and with support components fixed or free to rotate. The results are listed in Table 1.

The prototype case corresponds to wet wood and the possibility of some movement within the support. In those conditions, the pipe did not move when the inclination was six degrees but did move when the angle was ten degrees. Taking the mean of these two values, the coefficient of friction is tan (8 deg) which is 0.14. Many pipeline engineers would be surprised by this low value.

Measurements after the incident on small blocks of wood sliding on polyethylene gave much higher coefficients of the order of 0.40 (arctan (22 deg)), which confirms that the coefficient depends on load.

Downloaded 04 May 2010 to 171.66.16.27. Redistribution subject to ASME license or copyright; see http://www.asme.org/terms/Terms_Use.cfm

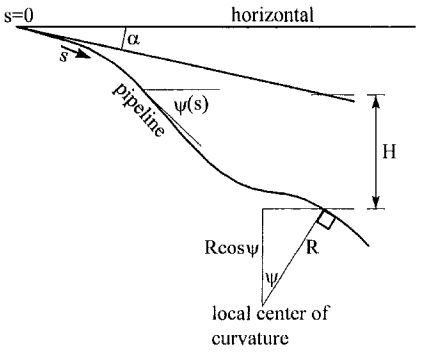


Fig. 4 Notation and pipe profile

Two-Dimensional Analysis of a Pipeline on an Irregular Slope

Consider the pipeline profile depicted in Fig. 4. The pipeline lies in a vertical plane, so that in plan it appears as a straight line. The upper end, on the left, is free; the lower end, on the right, is anchored. Distance along the pipeline is denoted s, measured from the top. The inclination of the pipeline to the horizontal is denoted ψ, and is in general a function $\psi(s)$ of s. That function completely defines the profile. Curvature is $d\psi/ds$, positive in overbends and negative in sagbends; radius of curvature R is $1/(d\psi/ds)$.

The pipeline weight per unit length is w. The normal force per unit length between the pipeline and the ground is N. The tangential force per unit length between the pipeline and the ground is T, positive upslope. The axial force in the pipeline is P, compressive positive. The pipeline is idealized as a string in which shear force and bending moment can be neglected: This idealization is examined below.

From the equilibrium of an element ds,

$$dP/ds = w \sin \psi - T \tag{1}$$

$$N = w \cos \psi - Pd\psi/ds. \tag{2}$$

If the pipeline is on the point of sliding downhill,

$$T = +N\mu = +N \tan \alpha, \tag{3}$$

where μ is a coefficient of friction, equal to tan α where α is an angle of friction. If the pipeline is on the point of sliding uphill, the plus sign in (3) is replaced by a minus sign.

Substituting from (3) into (2) and (1),

$$dP/ds - P\mu d\psi/ds = w(\sin \psi - \mu \cos \psi). \tag{4}$$

We first consider a special case. If there is no friction, the second and fourth terms in (4) vanish, and the axial force at a point where s takes the value S is given by

$$P(S) = \int_0^S w \sin \psi(s) ds \tag{5}$$

so that if w is constant the axial force at any point is simply the weight per unit length multiplied by the vertical height to the upper end of the pipeline.

Reverting to the complete form, (4) is a first-order differential equation in P, and $\exp(-\mu\psi(s))$ is an integrating factor if μ is independent of P and s. Multiplying by the factor and integrating with respect to s from the top end of the pipe $s = 0$ to a point where $s = S$,

$$P(S) \exp(-\mu\psi(S)) = w \int_0^S (\sin \psi(s) - \mu \cos \psi(s)) \exp(-\mu\psi(s)) ds. \tag{6}$$

If the exponentials in (6) are both expanded as power series, the first term in the expansion for $P(S)$ is

$$w \int_0^S (\sin \psi(s) - \mu \cos \psi(s)) ds \tag{7}$$

and this component of P is weight per unit length w multiplied by the vertical distance H from the pipeline to a line drawn from the top of the pipe downwards at an angle α to the horizontal. The same result can be obtained by neglecting the final term in (4). The second term in the expansion is

$$\mu w \int_0^S (\psi(S) - \psi(s))(\sin \psi(s) - \mu \cos \psi(s)) ds. \tag{8}$$

This term generally makes a positive contribution to $P(S)$ if the slope has significant convex sections where $d\psi/ds$ is positive. Expression (7) is therefore not a reliable approximation to $P(S)$, or a lower bound.

The reaction between the pipe and the ground falls to zero when

$$R = \frac{1}{d\psi/ds} = \frac{P}{w \cos \psi} \tag{9}$$

from (2).

If there is no friction, so that the axial force is given by (5), this leads to a very simple interpretation. At any arbitrary point on the pipe, the reaction falls to zero if the vertical distance from the point to the local center of curvature is equal to the vertical distance from the point to the top end of the pipe.

The idealization as a string with no shear force or bending moment is of course imperfect. It was adopted for two related reasons. The first relates to the initial unloaded configuration of the pipe and the limitations of the available data. The pipeline is not straight in the unloaded configuration, but is composed of straight and uniformly curved 12-m sections, prebent before welding to fit the profile of the slope (although the fit is not perfect, and does not need to be). The analysis is based on the initial configuration defined by the known length and curvature of each section. If a shear force term is added to Eq. (2), and if the bending moment is taken as proportional to the change of curvature, then the shear force is proportional to the change of $d^2\psi/ds^2$, the first derivative of the change of curvature. There was no possibility of obtaining that derivative from the data.

The second reason is that it is known from analogous pipeline problems such as lateral and upheaval buckling (Palmer et al., 1990, 1997) and deepwater pipelay (Palmer et al., 1974) that the large-scale behavior is primarily governed by the interaction between axial force and curvature, and that flexural rigidity plays only a secondary part, though it may be significant locally (as in the boundary layer at the touchdown point in pipelaying).

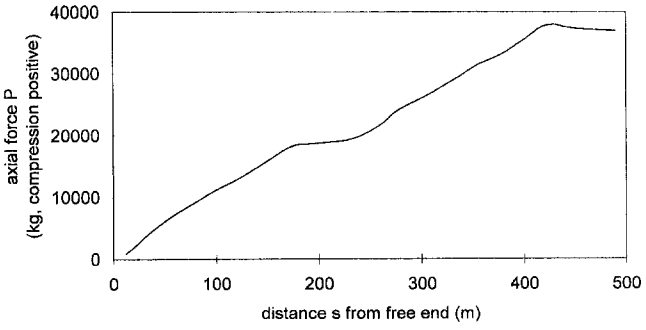


Fig. 5 Axial force as a function of distance from free end

Downloaded 04 May 2010 to 171.66.16.27. Redistribution subject to ASME license or copyright; see http://www.asme.org/terms/Terms_Use.cfm

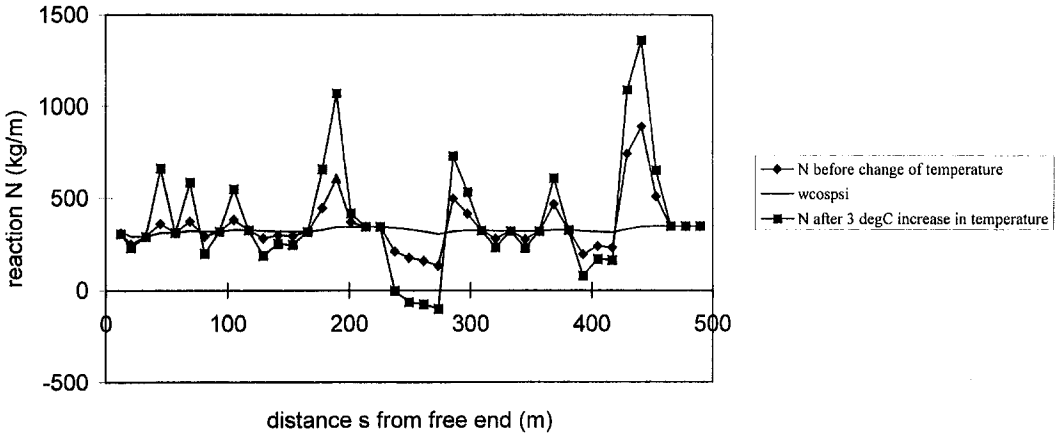


Fig. 6 Normal reaction *N* between pipeline and supports

Application to Incident

An accurate profile of the pipe configuration immediately before the incident is not available. The profile had to be reconstructed from the general geometry of the slope, and from records of the length and bend angle of each section of pipe. The geometry had therefore to be idealised as a series of circular arcs, each corresponding to one section of pipe.

The axial force can be calculated from the analysis in the previous section. Figure 5 plots the calculated axial force P as a function of distance s from the top of the pipe at weld 143/64. It assumes that the coefficient of friction μ is uniformly the measured value 0.14, and that friction acts uphill.

Figure 6 plots N against s, and compares it with the local weight term $w \cos \psi$ in (2). As expected, N is high at sagbends and low at overbends. N falls to its lowest value at the overbend, which confirms that this is the critical segment. However, even if the coefficient is zero, N remains positive, and so the pipe does not lift off. Figure 6 is plainly somewhat jagged: this is an inevitable consequence of the discontinuous changes of curvature from one section of pipe to the next.

This is the condition reached on the evening before the accident. The pipe had been constructed up the hill during the day, and increasing compressive force transmitted downhill would have compressed the lower sections of the pipe. The pipe would have moved slightly downhill, and the frictional force would have acted uphill, against the movement. In addition, the temperature would have fallen during the late afternoon, and after nightfall, so that the pipe would have contracted downhill, again mobilizing a frictional force acting uphill.

It can be surmised that the lowest temperature in the pipe would have occurred at dawn, and that the pipe warmed up as the sun rose. A modest increase of temperature leads to a substantial increase in compressive axial force. At the top end of the pipe, the pipe expands against the frictional resistance, which now acts downhill, opposing motion. This effect only extends a small distance below the top, and in the lower section the incremental response to the temperature increase is the same as in a fully constrained pipeline.

In summary, then, the compressive force at the overbend is the sum of two components:

1 the first component is the axial force present because the weight of the pipeline is greater than the uphill component of the mobilized friction;
2 the second component is an additional increase of compressive force, resulting from a temperature increase from the minimum reached when the pipeline is coldest, and equal to the increase in compressive axial force in a fully constrained pipe subject to the same temperature increase.

If the reaction N becomes equal to zero, the pipe lifts off its support. Once that has happened, the curvature increases further. Unstable buckling is the most likely outcome, (though the response is complicated by concurrent lateral instability and by the effect of stress concentrations at incomplete welds).

As the axial force becomes more compressive, the reaction N decreases in overbends. The resistance to *lateral* motion then decreases. If the horizontal curvature is $d\varphi/ds$, the required lateral resistance is $P\ d\varphi/ds$ per unit length. The lateral resistance is not necessarily the same as the longitudinal resistance, particularly as there are potential failure planes between the timbers in the support structures.

These numbers are consistent with the incident in the field, though it is unfortunate that the temperature history is unknown. On the basis of the data described earlier in this section, and on the assumption that friction acts uphill throughout, the minimum value of N before any temperature increase is reached at joint 34, where N is 131 kg/m, P is 23,700 kg and $d\psi/ds$ is 0.00725/m. Figure 6 also includes the distribution of N after a temperature increase of 3°C. N has become negative over a length of about 35 m, so that an additional downward force would be required to hold the pipe in contact with the supports. In the absence of an additional downward force, the pipe lifts off its supports, and then becomes vertically and laterally unstable.

The increment of axial force required to reduce the minimum value of N to zero corresponds to a temperature increase of only 1.8°C. It seems entirely reasonable that a temperature increase at least as great as this occurred in the two hours between sunrise and the accident.

This suggests that the accident resulted from a combination of two factors, the low coefficient of friction between the pipe and the supports and the increase of temperature in the morning. The lateral bend in the overbend region would have further increased the likelihood of buckling.

Conclusions

Pipelines on slopes steeper than the angle of friction develop large compressive forces, which can be increased by thermal cycling induced by ambient temperature changes. These compressive forces can cause the pipe string to be both vertically and laterally unstable, particularly if there are concurrent overbends and sidebends, even quite small ones.

This analysis supports the view that the incident could have been initiated by an inherent instability of the pipe on a slope. The analysis of this particular incident is complicated by the incomplete welding of the pipeline, which provided fracture initiation

Downloaded 04 May 2010 to 171.66.16.27. Redistribution subject to ASME license or copyright; see http://www.asme.org/terms/Terms_Use.cfm

points and conceivably allowed a local instability to develop into a full-scale incident.

The coefficient of friction is critical. It must be determined by tests, carried out with the actual surface coating of the pipe, the actual material of the supports, the surface conditions that will be present during construction, and approximately the same level of load between the pipe and the supports as will occur during construction. It must not be assumed that the coefficient of friction is independent of load. "Handbook" values of friction coefficients are essentially worthless.

Acknowledgments

The authors thank BP and OCENSA for permission to publish this paper, and thank two reviewers for helpful suggestions. Andrew Palmer is supported by the Jafar Foundation, and David Miles was supported by the Engineering and Physical Sciences Research Council and by BP.

References

Bartenev, G. M., 1981, *Friction and wear of polymers,* Elsevier, New York.

Palmer, A. C., Hutchinson, G., and Ells, J. E., 1974, "Configuration of submarine pipelines during laying operations," ASME *Journal of Engineering for Industry,* Vol. 96, pp. 1112–1118.

Palmer, A. C., 1982, "Concrete coating for submarine pipelines," *Magazine of Concrete Research,* Vol. 34, No. 120, pp. 119–129.

Palmer, A. C., Calladine, C. R., Miles, D., and Kaye, D., 1997, "Lateral buckling of submarine pipelines," *Proceedings, Offshore Oil and Gas Pipeline Technology Conference,* Amsterdam.

Palmer, A. C., Ellinas, C. P., Richards, D. M., and Guijt, J., 1990, "Design of submarine pipelines against upheaval buckling," *Proceedings, Twenty-second Offshore Technology Conference,* Houston, TX, Vol. 2, ASME, New York, pp. 551–560.

Downloaded 04 May 2010 to 171.66.16.27. Redistribution subject to ASME license or copyright; see http://www.asme.org/terms/Terms_Use.cfm

Self-Excited Vibration in Flexible Rotating Disks Subjected to Various Transverse Interactive Forces: A General Approach

J. Tian
Graduate Student

S. G. Hutton
Professor,
Mem. ASME

Department of Mechanical Engineering,
The University of British Columbia,
Vancouver, BC V6T 1Z4, Canada

A generalized approach to predict the physical instability mechanisms that are involved in the interaction between a rotating flexible disk and a stationary constraining system is developed. Based upon equations derived for an energy flux analysis, unified instability conditions for various lateral interactive forces are presented. These developments lead to a clear understanding of the physical mechanisms involved in the development of vibrational instabilities. New developments also involve the stability analysis of a rotating disk subjected to multiple moving concentrated regenerative and follower interactive forces that act over a space-fixed sector. The lateral regenerative interactive forces that are responsible for self-excited vibrations in saw-blade cutting are identified and modeled. The generalized Fourier series method is proposed to develop a characteristic equation for time-varying dynamic systems with or without time lag. The resulting equation can be solved efficiently by using Müller's algorithm with deflation.

Introduction

Computer floppy disk drives, circular sawing systems, turbine engines, and other machines contain rotating disks which interact with other components of the system or with a work-piece. In such systems, the driving energy for the steady rotation can, under certain circumstances, be channeled into lateral vibration and lead to unstable behavior. In order to prevent such energy transmission, an understanding of the instability mechanisms is essential.

In the past three decades, numerous papers have been published on disk dynamics. Most of them have focused on mathematical modeling and the development of solutions to a specific interactive force. The physical mechanisms involved in such rotating systems have not been adequately explained by previous researchers, especially for the instability mechanisms caused by an arbitrary interactive force.

Mote et al. (1970, 1977) and Iwan and Stahl (1973) studied the instability of a stationary disk with a moving load system. Iwan and Moeller (1976), Hutton et al. (1987) and many other researchers mathematically investigated the onset of instability for a rotating disk-stationary load system. Ono et al. (1991) and Chen and Bogy (1992) also looked into the instabilities of a rotating disk system subjected to a mass-spring-dashpot constraint with a friction effect. Shen and Mote (1991) presented an explanation of the instability mechanisms for a stationary circular plate subjected to a rotating damped spring-mass system.

In previous research, the self-excited instability in saw-blade cutting has been assumed to be produced by a stationary constant or harmonic in-plane edge load. The self-excited vibration due to multiple moving interactive forces under cutting conditions has not been previously solved. Carlin et al. (1975) first studied the effects of a concentrated radial edge load on the natural frequencies of a spinning disk. Chen (1994) reformulated the problem of a rotating disk subjected to a stationary concentrated in-plane radial load with the effects of gyroscopic terms included. Shen and Song (1996) treated a cutting saw blade as a rotating disk subjected to stationary follower edge loads with both radial and tangential components. Chen (1997) modeled a saw-blade system as a spinning disk under a space-fixed periodically varying edge load.

An important force: a lateral regenerative cutting force, which may play a very important role in self-excited vibration of a saw blade during cutting, has not been investigated in previous studies.

This paper aims to establish a generalized approach, based on energy flux analysis, to investigate the instability mechanisms that are involved in the interaction between a rotating disk and an interactive stationary system. Rotating disk models with different types of interactive forces, including multiple moving lateral regenerative cutting forces, are used to develop an unified understanding of the physical mechanisms of the instabilities involved in such systems. Through this effort, the possible instabilities due to various interactive forces can be identified based on the energy flux analysis derived.

A further aim of this paper is to develop a stability analysis for a rotating disk subjected to multiple moving concentrated regenerative and follower cutting forces applied over a given space-fixed sector. The basic Fourier series method is extended to solve the time-varying equations with or without time lag.

Energy Flux Equation for a Rotating Disk Subjected to Interactive Forces

Figure 1 shows a centrally clamped circular plate of inner radius a, outer radius b, and thickness h, rotating at a constant angular velocity Ω, in contact with a constraint that applies a lateral force to the disk. The governing equation for transverse vibration in terms of the lateral displacement $w(r, \theta, t)$ with respect to space-fixed coordinates can be written as (Hutton et al., 1987; Chen, 1994):

Contributed by the Applied Mechanics Division of THE AMERICAN SOCIETY OF MECHANICAL ENGINEERS for publication in the ASME JOURNAL OF APPLIED MECHANICS.
Discussion on the paper should be addressed to the Technical Editor, Professor Lewis T. Wheeler, Department of Mechanical Engineering, University of Houston, Houston, TX 77204-4792, and will be accepted until four months after final publication of the paper itself in the ASME JOURNAL OF APPLIED MECHANICS.
Manuscript received by the ASME Applied Mechanics Division, Oct. 9, 1998; final revision, Apr. 29, 1999. Associate Technical Editor: A. A. Ferri.

 Copyright © 1999 by ASME

Downloaded 04 May 2010 to 171.66.16.27. Redistribution subject to ASME license or copyright; see http://www.asme.org/terms/Terms_Use.cfm

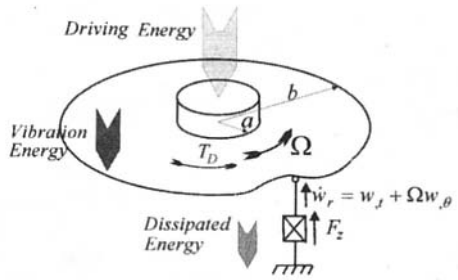


Fig. 1 Schematic of a rotating disk interacting with a stationary constraint or workpiece

$$D\nabla^4 w + \rho h(w_{,tt} + 2\Omega w_{,t\theta} + \Omega^2 w_{,\theta\theta}) + L_s(w) = L_n(w) + f_g(t) + f_c(t) \quad (1)$$

where D and ρ are the flexural rigidity and mass density of the plate, respectively. L_s is the membrane operator associated with the axisymmetrical stress fields due to the centrifugal force and/or residual stresses. L_n is the membrane operator associated with the asymmetric stress fields generated by in-plane edge loads, such as in-plane cutting forces, which, under certain circumstances, may cause instability. $f_g(t)$ represents the transverse forces generated by the interaction between the plate and the constraint. In the case where the constraints can be modeled as stationary mass-spring-dashpot systems with friction effects, the transverse force becomes

$$f_g(t) = -\sum_j (1/r)\delta(r - r_j)\delta(\theta - \theta_j)[m_j w_{,tt} + c_j w_{,t} + k_j w + (1/r)\mu_j w_{,\theta}] \quad (2)$$

where, m_j, k_j, c_j, and μ_j represent the mass, stiffness, damping, and friction of the jth constraint, respectively. $\delta(\ )$ is the Dirac delta function. (r_j, θ_j) defines the location of the jth constraint observed from space-fixed coordinates. $f_c(t)$ represents the transverse forces generated by the interaction between the disk and a work-piece. The multiple moving lateral regenerative cutting forces, which are involved in sawing, are an example of such forces.

The energy variation ΔE of the disk over a period $[0, \tau]$ for a constant rotating speed can be derived through a lengthy mathematical procedure (Tian, 1998) and the resulting equation for energy flux analysis can be expressed as

$$\Delta E = \int_0^\tau \left\{ \iint_A [q(w, r, \theta, \tau)\dot{w}_r] r dr d\theta \right\} dt \quad (3)$$

where $q(w, r, \theta, t) = L_n(w) + f_g(t) + f_c(t)$ represents a generalized transverse force, and $\dot{w}_r = w_{,t} + \Omega w_{,\theta}$ represents the transverse velocity observed in disk-fixed coordinates. This expression can be viewed from a fundamental viewpoint in terms of the change in energy equaling the work done, which is equal to the time integral of the applied force and the velocity of the particle on which the force acts.

From Eq. (3) it is apparent that the change of total energy ΔE of this system will increase when $q(w, r, \theta, t)$ is in phase with $\dot{w}_r$. In this case driving energy required to maintain constant speed will be transferred into transverse vibration and instability will occur. Thus, Eq. (3) is the basic relationship that provides physical insight into the stability characteristics of the system. Under stable conditions ΔE will be a nonzero periodic function of time, but over a complete cycle the change of total energy will be zero.

Instabilities Due to Moving Forces and Stationary Constraints

In the following section, the possibility of instability occurring for a rotating disk subjected to different types of interactive forces will be studied based upon Eq. (3).

1 Stationary Mass-Spring Constraint With Conservative Forces. For a single constraint, substituting Eq. (2) into Eq. (3) yields

$$\Delta E = \int_0^\tau F_z(t)[w_{,t}(r_0, \theta_0, t) + \Omega w_{,\theta}(r_0, \theta_0, t)]dt \quad (4)$$

where

$$F_z(t) = -[kw(r_0, \theta_0, t) + mw_{,tt}(r_0, \theta_0, t) + cw_{,t}(r_0, \theta_0, t) + (1/r_0)\mu w_{,\theta}(r_0, \theta_0, t)] \quad (5)$$

$F_z(t)$ is the total lateral force caused by the interaction between the disk and the constraint at (r_0, θ_0). When $F_z(t)$ is in phase with the velocity $w_{,t}(r_0, \theta_0, t) + \Omega w_{,\theta}(r_0, \theta_0, t)$, driving energy is switched into vibration energy of the disc through the constraint.

For those cases when the interactive force is a conservative elastic or inertial force, $F_z(t)$ is always perpendicular to the velocity $w_{,t}(r_0, \theta_0, t)$ measured in space-fixed coordinates. Thus, Eq. (4) can be written as

$$\Delta E = \int_0^\tau [F_k(t) + F_m(t)][\Omega w_{,\theta}(r_0, \theta_0, t)]dt = \int_0^\tau \Omega r_0[F_{\theta k}(t) + F_{\theta m}(t)]dt = \int_0^\tau \Omega(T_k + T_m)dt \quad (6)$$

where $F_k(t) = -kw(r_0, \theta_0, t)$ and $F_m(t) = -m\ddot{w}(r_0, \theta_0, t)$. $F_{\theta k} = F_k[w_{,\theta}(r_0, \theta_0, t)/r_0]$ and $F_{\theta m} = F_m[w_{,\theta}(r_0, \theta_0, t)/r_0]$ are the circumferential components of the interactive elastic and inertial forces, respectively. The torques generated by these circumferential forces are $T_k = F_{\theta k} r_0$ and $T_m = F_{\theta m} r_0$. If the work done by the sum of the individual torques ($T_D = T_k + T_m$ in this case) is greater than zero unstable behavior will result.

Figure 2 shows the Campbell diagram (i.e., the eigenvalue variation with respect to rotating speed) of a rotating disk ($a = 0.076m$, $b = 0.28m$, $h = 1.12e - 3m$, $E = 2.08e + 11$ N/m^2,

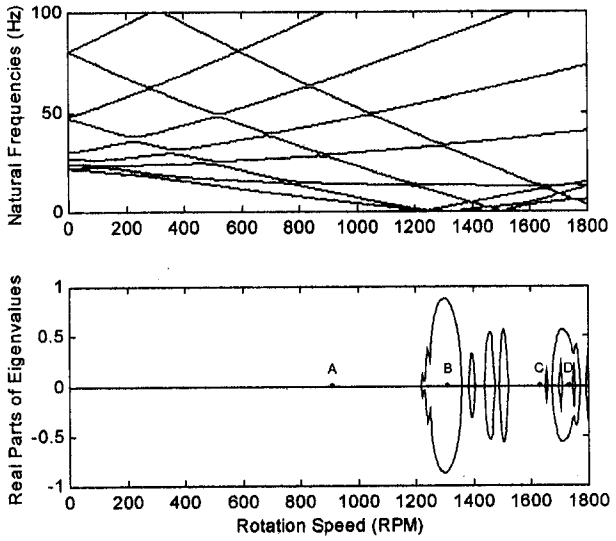


Fig. 2 Instability regions of a rotating disk subjected to a stationary spring (k = 2000 N/m)

Downloaded 04 May 2010 to 171.66.16.27. Redistribution subject to ASME license or copyright; see http://www.asme.org/terms/Terms_Use.cfm

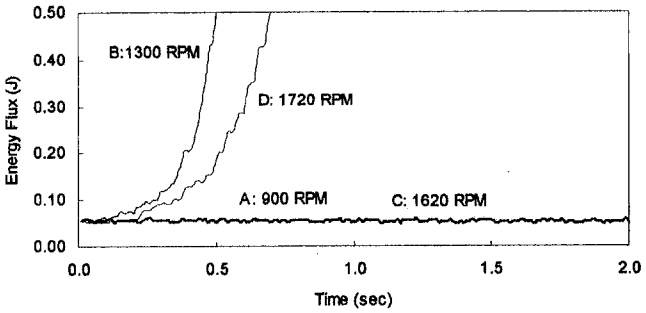


Fig. 3 Energy flux at different rotating speeds due to a stationary stiffness constraint

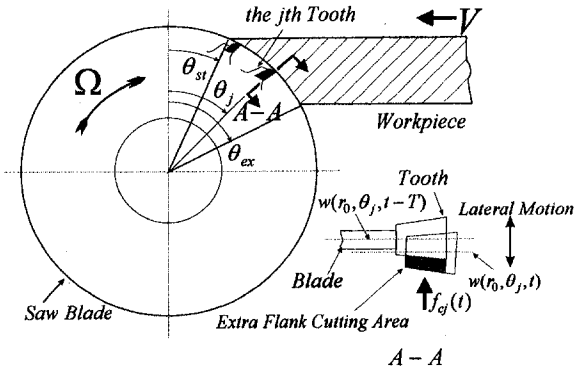


Fig. 5 Lateral regenerative cutting force for a rotating circular saw cutting wood over a space-fixed sector of the saw

$\rho = 7850$ kg/m^3, $v = 0.3$) constrained by a stationary spring ($k = 2000$ N/m). As shown in Fig. 2, divergence and coupling flutter instabilities occur in several supercritical-speed regions. In such regions the interactive elastic force is in phase with $w_{,t}(r_0, \theta_0, t) + \Omega w_{,\theta}(r_0, \theta_0, t)$. The coupling flutter instability will occur when the interactive elastic force caused by one of the two coupled modes is in phase with the velocity $w_{,t}(r_0, \theta_0, t) + \Omega w_{,\theta}(r_0, \theta_0, t)$ of the other mode.

Figure 3 shows the energy flux ΔE at different frequencies A, B, C, and D as illustrated in Fig. 2. ΔE is computed by using the Galerkin discretization and using an integration procedure in which the interactive forces are included in the generalized force vector. From these figures it can be seen that the energy flux analyses agree very well with the Campbell diagrams. The energy flux analysis was also conducted for the case where the constraint was a stationary mass and the results also correspond to those of the Campbell diagram.

2 Stationary Constraint With Damping and Friction Forces. For the case when the interactive force is a nonconservative force, such as a viscous damping force or a friction force, Eq. (4) can be written in the following forms.

For the case of stationary viscous damping:

$$\Delta E = \int_0^\tau [\Omega r_0 F_{\theta c}(t) - c w_{,t}^2(r_0, \theta_0, t)]dt$$

$$= \int_0^\tau F_c(t)[w_{,t}(r_0, \theta_0, t) + \Omega w_{,\theta}(r_0, \theta_0, t)]dt. \quad (7)$$

For the case of a stationary frictional force:

$$\Delta E = \int_0^\tau F_\mu(t)[w_{,t}(r_0, \theta_0, t) + \Omega w_{,\theta}(r_0, \theta_0, t)]dt \quad (8)$$

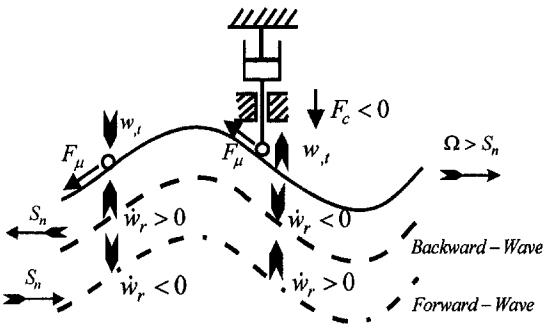


Fig. 4 Physical explanations for instabilities due to a viscous damper and friction constraint

where $F_c(t) = -cw_{,t}(r_0, \theta_0, t)$ and $F_\mu(t) = -\mu w_{,\theta}(r_0, \theta_0, t)/r_0$.

From Eq. (7) and (8) it is noted that there are two energy flows associated with these nonconservative interactive forces: one is the energy required to overcome the damping or friction force and the other is that dissipated by the same element.

Figure 4 schematically illustrates the effects of viscous damping and friction upon the instability of the travelling-wave modes. The solid curve represents the forward wave or the backward wave at supercritical speeds (where Ω is greater than the wave speed S_n of a given mode) observed in space-fixed coordinates, and the dashed curves represent the backward and forward waves observed in disk-fixed coordinates. From the interaction shown in this figure it can be seen that the lateral damping force (F_c) caused by the backward wave at supercritical speeds is always in phase with the backward wave velocity $\dot{w}_r(r_0, \theta_0, t)$ but the damping force (F_c) due to the backward wave at subcritical speeds is always out of phase with the velocity $\dot{w}_r(r_0, \theta_0, t)$ whose direction is independent of the rotating speed. It may also be noted that the damping force induced by the forward wave mode is out of phase with the forward wave velocity $\dot{w}_r(r_0, \theta_0, t)$ measured in disk-fixed coordinates. Therefore, instability can only occur when the backward wave mode is subjected to the stationary damping force at supercritical speeds.

From Fig. 4 it may also be noted that, in the case of friction, F_μ is always out of phase with $\dot{w}_r(r_0, \theta_0, t)$ for the backward wave mode and is always in phase with $\dot{w}_r(r_0, \theta_0, t)$ for the forward wave mode, regardless of rotating speed. This result agrees with the theoretical eigenvalue analysis (Ono et al., 1991).

Instabilities Due to Multiple Moving Interactive Forces

In the dynamics of saw-blade cutting the cutting forces have traditionally been modeled as constant or pulsating in-plane edge loads (Song and Shen, 1996; Chen, 1997). A further important cutting force is that produced by flank cutting, which gives rise to multiple moving regenerative cutting forces acting over a given space-fixed sector. Such forces are modeled and solved, it appears, for the first time in this paper. In addition, the lateral components of multiple moving follower tangential cutting forces are also considered. The Fourier series method is generalized to conduct the stability analysis of the resulting time-varying equations with time delay.

1 Instability Due to Multiple Moving Regenerative Forces

Figure 5 shows a rotating circular saw blade which cuts a work piece over a specified space-fixed sector. It can be seen from the sectional plot A-A that, if the blade oscillates laterally, there is an extra lateral cutting area between two successive teeth associated with both the transverse response $w(r_0, \theta_j, t)$ of the current tooth

Downloaded 04 May 2010 to 171.66.16.27. Redistribution subject to ASME license or copyright; see http://www.asme.org/terms/Terms_Use.cfm

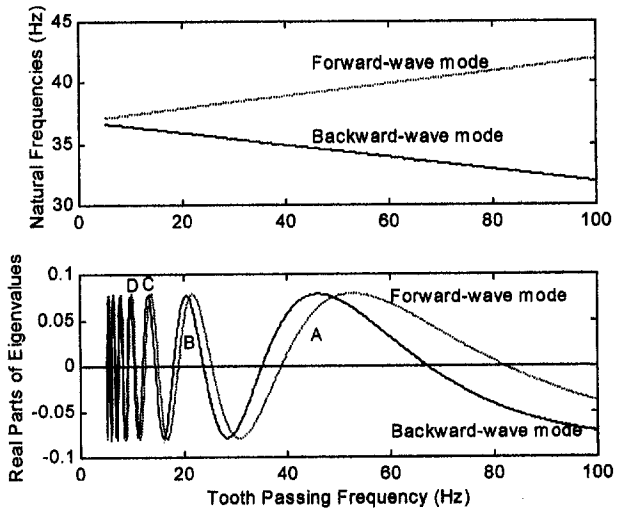


Fig. 6 Instability regions of a rotating disk due to moving regenerative cutting forces (Mode = (0, 2), K_r = 10 N/m; zero-order approximation)

(the jth tooth) and the transverse response $w(r_0, \theta_j, t - T)$ of the previous tooth (the $(j\text{-}1)$th tooth) at a given location (r_0, θ_j) on the work-piece. $T = 2\pi/(\Omega N_t)$ is the tooth passing period (i.e., the period between successive tooth engagements). N_t is the total number of saw teeth. Lateral compression between the work-piece and the teeth of the blade in this extra cutting area causes the lateral cutting force $f_{cj}(t)$. This type of cutting force is called regenerative.

The lateral regenerative cutting forces are assumed to be

$$f_c(t) = \sum_{j=1}^{N_t} f_{cj}(t) = -\sum_{j=1}^{N_t} (1/r)K_r[w(r, \theta, t) - w(r, \theta, t - T)]\delta(r - r_0)\delta(\theta - \theta_j)g(\theta_j) \quad (9)$$

where K_r is a cutting force coefficient which is determined by the geometry, properties, and speeds of the blade and by the characteristics of the work-piece. For an anisotropic material work-piece, K_r is a function of the position θ_j in the space-fixed coordinates.

$$\theta_j = \theta_{st} + \Omega t + (j - 1)\theta_p$$

($\theta_1 = \theta_{st}$ when $t = 0$; θ_p is the angular tooth pitch)

$$g_j(\theta_j) = 1 \text{ when } \theta_{st} < \theta_j < \theta_{ex} \text{ and } g_j(\theta_j) = 0 \text{ otherwise}$$

where θ_{st}, θ_{ex} are the start and exit immersion angles of the cutting teeth, respectively.

Applying the Galerkin procedure to Eq. (1) leads to an equation of motion in the form

$$[M]\{\ddot{x}\} + [G]\{\dot{x}\} + [K]\{x\} + (1 - e^{-TD})[A(t)]\{x\} = \{0\} \quad (10)$$

where $[M]$, $[G]$, and $[K]$ represent the mass, gyroscopic, and stiffness matrices, respectively, which may contain centrifugal stiffening and/or stress tensioning effects. e^{-TD} is a time-delay operator (i.e., $e^{-TD}w(t) = w(t - T)$). $[A(t)]$ is a time-varying matrix associated with the cutting forces. It can be easily proven that each term in $[A(t)]$ is periodic with period T (i.e., $[A(t + T)] = [A(t)]$).

The solution of Eq. (10) with periodic coefficient terms may be assumed in the form of a Fourier series with frequency components $\lambda \pm ik\omega$ $(k = 0, 1, 2, \ldots)$ $(i = \sqrt{-1}, \omega = 2\pi/T)$ (Bolotin, V. V., 1964; Lengoc, 1995):

$$\{x(t)\} = [\{b_0\}/2 + \sum_{k=1}^{\infty} (\{a_k\}\sin k\omega t + \{b_k\}\cos k\omega t)]e^{\lambda t} \quad (11)$$

where $\{b_0\}$, $\{b_k\}$, and $\{a_k\}$ are time-invariant complex coefficient vectors. λ is the characteristic variable of the system.

Since $[A(t)]$ is periodic, it can also be expressed as a Fourier series:

$$[A(t)] = \frac{1}{2}[B_0] + \sum_{k=1}^{\infty} ([A_k]\sin k\omega t + [B_k]\cos k\omega t) \quad (12)$$

where

$$[B_0] = \frac{2}{T}\int_0^T [A(t)]dt, \quad [B_k] = \frac{2}{T}\int_0^T [A(t)]\cos(k\omega t)dt,$$

$$[A_k] = \frac{2}{T}\int_0^T [A(t)]\sin(k\omega t)dt.$$

Substituting Eqs. (11) and (12) into Eq. (10) and equating the coefficients of $e^{\lambda t}$, $e^{\lambda t}\sin k\omega t$, and $e^{\lambda t}\cos k\omega t$ to zero lead to the following form of the characteristic equation of the system

$$(\lambda^2[H_2] + \lambda[H_1] + [H_0](1 - e^{-T\lambda})[L]]\{s\} = \{0\} \quad (13)$$

where $\{s\} = (\{b_0\}\{a_1\}\{b_1\} \ldots \{a_{N_s}\}\{b_{N_s}\})^T$. N_s is the number of components included in the Fourier series. The coefficient matrices $[H_2]$, $[H_1]$, $[H_0]$, and $[L]$ consist of $[K]$, $[G]$, $[M]$, $[B_0]$, $[B_k]$, $[A_k]$, and ω. The Müller's algorithm with deflation is used to find the roots of Eq. (13) (Mathews, 1992).

Figure 6 shows the Campbell diagram for a rotating circular disk clamped at its inner radius ($a = 0.08m$, $b = 0.28m$, $h = 0.0015m$, $E = 2.08e + 11$ N/m^2, $\rho = 7850$ kg/m^3, $v = 0.3$, $\theta_{st} = 20$ deg, $\theta_{ex} = 50$ deg, $N_t = 40$). From this figure it is found that the primary instability (i.e., the widest unstable region A) occurs when the tooth passing frequency f_t $(=(\Omega/2\pi)N_t)$ is in the region $[f_n(\Omega), 2f_n(\Omega)]$, where $f_n(\Omega)$ is the natural frequency of the nth mode. A general expression for the unstable ranges (A, B, C, $D \cdots$) of tooth passing frequencies is given by

$$f_t = \left[\frac{1}{k}f_n(\Omega), \frac{1}{k - 0.5}f_n(\Omega)\right] \quad (k = 1, 2, \ldots). \quad (14)$$

It was found that this expression is true for all modes for all simulations conducted in this study.

The equation for energy flux analysis can be expressed from Eq. (3) as

$$\Delta E = \sum_i \int_0^\tau \dot{w}_{ri}(t)f_{ci}(t)dt = \sum_i \int_0^\tau (\dot{w}_i + \Omega w_{,\theta i})f_{ci}(t)dt \quad (15)$$

where $f_{ci}(t)$ is the regenerative cutting force produced by the ith active cutting tooth. $\dot{w}_{ri}(t)$ represents the velocity at the ith cutting tooth observed in the blade-fixed coordinates. If the regenerative cutting forces are in phase with the velocities at the cutting points measured in the blade-fixed coordinates the driving energy of this system will be switched into the vibrational energy of the blade, which implies instability in the system.

Figures 7 illustrate the real parts of the eigenvalues of the disk when $K_r = 100(N/m)$ and Fig. 8 shows the energy flux calculated at the frequencies (A–G) shown in Fig. 7. It is clear that the energy flux analysis matches the eigenvalue analysis very well.

From numerous simulations it was found the zero-order approximation of Eq. (12) gives very accurate predictions for the eigenvalues of the system even when K_r and the time-varying compo-

Downloaded 04 May 2010 to 171.66.16.27. Redistribution subject to ASME license or copyright; see http://www.asme.org/terms/Terms_Use.cfm

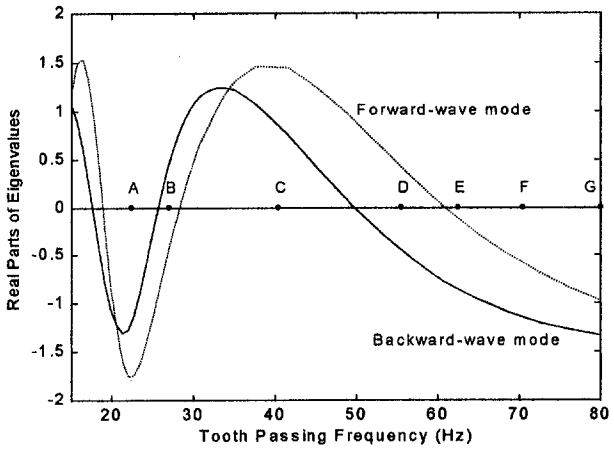


Fig. 7 Instability regions caused by moving regenerative cutting forces (Mode = (0, 1), K_r = 100 N/m; zero-order approximation)

nents in $[A(t)]$ are very large compared to $[K]$. The reason for this fact is that the high-order response in Eq. (13) is much smaller than that of the zero-order approximation.

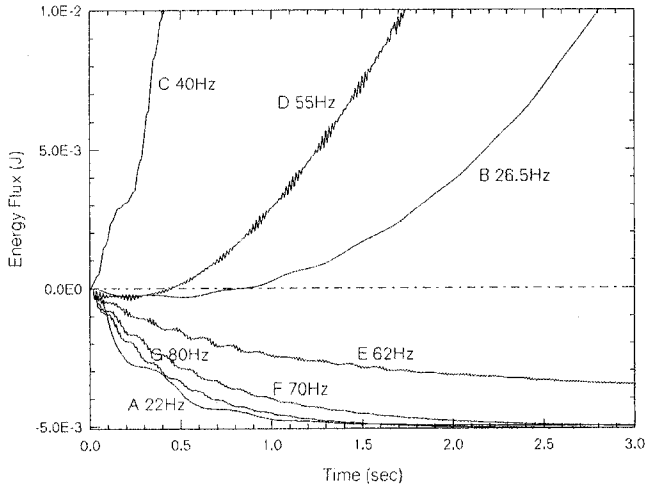


Fig. 8 Energy flux at the different tooth passing frequencies defined in Fig. 7 (K_r = 100 N/m)

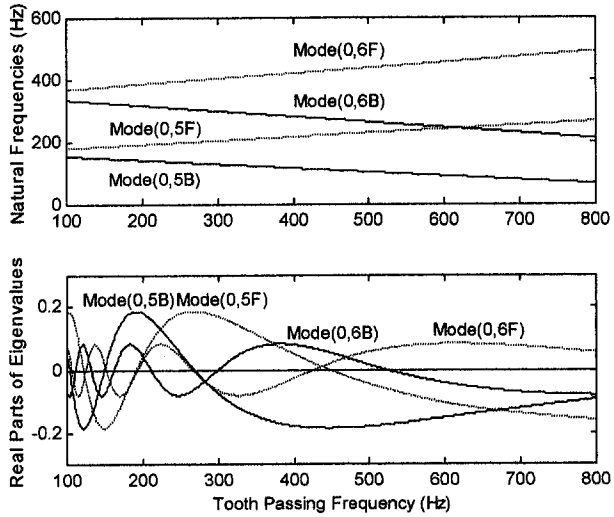


Fig. 9 Instability regions caused by moving regenerative cutting forces (Two modes (0, 5) and (0, 6), K_r = 100 N/m; zero-order approximation)

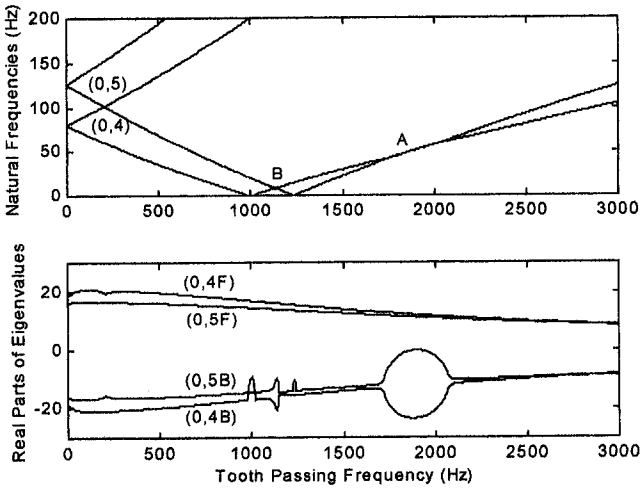


Fig. 10 Instability characteristics (follower tangential cutting force) (Two-mode solution, C_{ft} = 500 N; zero-order approximation)

Figure 9 shows a two-mode solution for the same rotating circular saw blade. As may be noted, the results related to each mode in the two-mode solution are very similar to the one from the single-mode solution and no coupling instability regions are found at subcritical speeds. This figure also reveals that the real parts of the eigenvalues in mode (0, 5) are greater than those in mode (0, 6).

2 Instability Due to Multiple Moving Tangential Cutting Forces

Celep (1979) examined a free circular plate subjected to a nonconservative radial force and only a divergence instability was found. Ono et al. (1991) studied the stability characteristics of a computer disk which interacts with the recording head. Mottershead and Chan (1995) also employed the finite element method and a multiple-scale algorithm to study the parametric instability for an annular braking disk loaded by rotating concentrated and distributed follower forces. It was observed that the circumferential friction tends to destabilize certain vibration modes over the entire rotating speed range.

In the present paper, follower tangential cutting forces are modeled as multiple moving concentrated forces which is somewhat more realistic than the models used in previous research. The multiple moving circumferential cutting forces are assumed to be tangential to the blade. The transverse components of such forces can be modeled as follows:

$$f_c(t) = \sum_{j=1}^{N_t} f_{cj}(t)$$

$$= -\sum_{j=1}^{N_t} (1/r)\delta(r - r_0)\delta(\theta - \theta_j)g(\theta_j)[F_{tj}(t)w_{,\theta}(t)/r] \quad (16)$$

where $F_{tj}(t)$ is assumed to have the linear form: $F_{tj}(t) = K_t h H_j(t)$. $H_j(t) = F \sin \theta_j$ is the cutting depth, which is a function of the position θ_j for a circular saw blade. F is the feed per tooth of the work-piece; h is the thickness of the blade; and K_t is the cutting force coefficient determined by the cutting tool geometry and the work-piece.

Application of the Galerkin procedure results in equations of motion in the following matrix form:

$$[M]\{\ddot{x}\} + [G]\{\dot{x}\} + [K]\{x\} + [D_t(t)]\{x\} = \{0\} \quad (17)$$

where $[D_t(t)]$ is a time-varying matrix associated with the tangential cutting forces, which is also periodic with the tooth passing period T. Following a procedure similar to that in the derivation of

Downloaded 04 May 2010 to 171.66.16.27. Redistribution subject to ASME license or copyright; see http://www.asme.org/terms/Terms_Use.cfm

Eq. (13) will result in a characteristic equation of this system without time delay, which can easily be solved using a traditional eigenvalue solver.

Figures 10 show a two-mode solution of the same disk used in the previous section. It is clear from Fig. 10 that all the forward-wave modes are destabilized and all the backward-wave modes are stabilized by the follower tangential cutting forces. It may also be noted from this figure that the modal interaction of two reflected-wave modes (such as region *A*) or the modal interaction between one nonreflected wave mode and one reflected wave mode (such as region *B*) is of the coupling type. From this figure it can also be seen that the real parts of the eigenvalues in the low-order modes are greater than those in the high-order modes due to the relatively high stiffness of the high-order modes compared to the time-varying matrix $[D_t(t)]$ in Eq. (17). Energy flux analysis using Eq. (15) verifies that instability occurs in the entire rotating speed range.

Conclusions

This paper has presented a general approach, based upon an energy flux analysis, to study the physical instability mechanisms involved in the interaction between a rotating flexible disk and arbitrary interactive forces. The formulation and solution of dynamic models of a rotating disk subjected to multiple moving concentrated regenerative and follower interactive forces applied over a space-fixed sector have also been presented.

Specific conclusions are:

(1) instability occurs when a nonconservative interactive force applied to a rotating disk is in phase with the velocity at the interactive point observed in rotating coordinates;
(2) when a conservative lateral force, acting on a rotating disk, is in phase with the circumferential slope at the interactive point, a coupling type of instability will occur;
(3) the occurrence of instability due to an arbitrary interactive force may be identified based on energy flux analysis, in some cases even without solving equations;
(4) instability cannot occur when a rotating disc is subjected to a stationary constant load, but a stationary harmonic lateral force, a moving constant lateral force, or a moving harmonic lateral force may cause instability;
(5) the primary instability due to regenerative cutting forces in circular saw blades occurs when the tooth passing frequency f_t is greater than a given resonant frequency f_n of the blade, but less than $2f_n$;
(6) all the forward-wave modes are destabilized but all the backward-wave modes are stabilized by multiple moving tangential follower cutting forces in the entire speed range;
(7) the zero-order approximation of the generalized Fourier series method can usually give satisfactory results for circular sawing systems even when interactive cutting forces are fairly large compared to the elastic forces of the disk.

Acknowledgment

This work was supported by a grant from the National Science and Enginering Research Council of Canada.

References

Botltin, V. V., 1964, *The Dynamic Stability of Elastic Systems,* Holden-Day, San Francisco.

Carlin, J. F., Appl, F. C., Bridwell, H. C., and Dubios, R. P., 1975, "Effects of Tension on Buckling and Vibration of Circular Saw Blades," ASME *Journal of Engineering for Industry,* Vol. 97, pp. 37–48.

Celep, Z., 1979, "Axially Symmetric Stability of a Completely Free Circular Plate Subjected to a Non-conservative Edge Load," *Journal of Sound and Vibration,* Vol. 65, pp. 549–556.

Chen, J. S., 1997, "Parametric Response of a Spinning Disk Under Space-Fixed Pulsating Edge Loads," ASME JOURNAL OF APPLIED MECHANICS, Vol. 64, pp. 139–143.

Chen, J. S., 1994, "Stability Analysis of a Spinning Elastic Disk Under a Stationary Concentrated Edge Load," ASME JOURNAL OF APPLIED MECHANICS, Vol. 61, pp. 788–792.

Chen, J. S., and Bogy, D. B., 1992, "Effects of Load Parameters on the Natural Frequencies and Stability of a Flexible Spinning Disk With a Stationary Load System," ASME JOURNAL OF APPLIED MECHANICS, Vol. 59, pp. 230–235.

Hutton, S. G., Chonan, S., and Lehman, B. G., 1987, "Dynamic Response of a Guided Circular Saw," *Journal of Sound and Vibration,* Vol. 112, pp. 527–539.

Iwan, W. D., and Stahl, K. J., 1973, "The Response of an Elastic Disc With a Moving Mass System," ASME JOURNAL OF APPLIED MECHANICS, Vol. 40, pp. 445–451.

Iwan, W. D., and Moeller, T. L., 1976, "The Stability of a Spinning Elastic Disk With a Transverse Load System," ASME JOURNAL OF APPLIED MECHANICS, Vol. 43, pp. 485–490.

Lengoc, L., 1995, "Wide Bandsaw Blade Under Cutting Condition, Part II: Stability of a Plate Moving in its Plane While Subjected to Parametric Excitation," *Journal of Sound and Vibration,* Vol. 186, pp. 143–162.

Mathews, J. H., 1992, *Numerical Methods for Mathematics, Science and Engineering,* 2nd Ed., Prentice-Hall, Englewood Cliffs, NJ.

Mote, C. D., 1970, "Stability of Circular Plates Subjected to Moving Loads," *Journal of Franklin Institute,* Vol. 290, pp. 329–344.

Mote, C. D., 1977, "Moving-Load Stability of a Circular Plate on a Floating Central Collar," *Journal of the Acoustical Society of America,* Vol. 61, pp. 439–447.

Mottershead, J. E., and Chan, S. N., 1995, "Flutter Instability of Circular Discs with Frictional Follower Loads," ASME *Journal of Vibration and Acoustics,* Vol. 117, pp. 161–163.

Ono, K., Chen, J. S., and Bogy, D. B., 1991, "Stability Analysis for the Head-Disk Interface in a Flexible Disk Drive," ASME JOURNAL OF APPLIED MECHANICS, Vol. 58, pp. 1005–1014.

Shen, I. Y., and Song, Y., 1996, "Stability and Vibration of a Rotating Circular Plate Subjected to Stationary In-Plane Edge Loads," ASME JOURNAL OF APPLIED MECHANICS, Vol. 63, pp. 121–127.

Shen, I. Y., and Mote, C. D., Jr., 1991, "On the Mechanism of Instability of a Circular Plate Under a Rotating Spring-Mass-Dashpot," *Journal of Sound and Vibration,* Vol. 148, pp. 307–318.

Tian, J. F., 1998, "Self-Excited Vibrations of Rotating discs and Shafts with Applications to Sawing and Milling," Ph.D. dissertation, Department of Mechanical Engineering, University of British Columbia, Vancouver, B.C., Canada.

Downloaded 04 May 2010 to 171.66.16.27. Redistribution subject to ASME license or copyright; see http://www.asme.org/terms/Terms_Use.cfm

Journal of Applied Mechanics

Brief Notes

A Brief Note is a short paper that presents a specific solution of technical interest in mechanics but which does not necessarily contain new general methods or results. A Brief Note should not exceed 1500 words *or equivalent* (a typical one-column figure or table is equivalent to 250 words; a one line equation to 30 words). Brief Notes will be subject to the usual review procedures prior to publication. After approval such Notes will be published as soon as possible. The Notes should be submitted to the Technical Editor of the JOURNAL OF APPLIED MECHANICS. Discussions on the Brief Notes should be addressed to the Editorial Department, ASME, United Engineering Center, 345 East 47th Street, New York, N. Y. 10017, or to the Technical Editor of the JOURNAL OF APPLIED MECHANICS. Discussions on Brief Notes appearing in this issue will be accepted until two months after publication. Readers who need more time to prepare a Discussion should request an extension of the deadline from the Editorial Department.

Thermoelastic Contact Problems for the Layer

J. L. Barber[1] and L. G. Hector[2]

Introduction

Thermoelastic contact problems involving layers arise in a variety of engineering applications, including disk brakes and clutches (Lee and Barber, 1993) and unidirectional solidification of castings (Richmond et al., 1990). A typical problem might involve the (frictionless) unilateral contact relations

$$g(x) = 0;\ p(x) > 0 \quad \text{in contact regions,} \tag{1}$$

$$p(x) = 0;\ g(x) > 0 \quad \text{in separation regions,} \tag{2}$$

where $p(x)$ is the contact pressure, $g(x)$ is the gap between the surfaces, and the inequalities serve to determine the extent of the contact region. Notice that $g(x)$ is determined by the displacement component $u_y(x)$ at the contact surface and a function describing the shape and rigid-body displacement of the other contacting body.

In order to enforce these conditions, we need to know the relations between $p(x)$, $u_y(x)$ and the (presumably known) temperature profile $T(x, y)$ in the layer. In some special cases, these results can be obtained without determining the entire thermoelastic stress and displacement fields. For example, if the temperature field is in the steady state and the boundaries are traction-free ($p(x) = 0$), Dundurs (1974) has shown that

$$\frac{\partial^2 u_y}{\partial x^2} = -\beta \frac{\partial T}{\partial y} = \frac{\beta}{K} q_y, \tag{3}$$

where q_y is the local heat flux in the y-direction,

$$\beta = \alpha \quad \text{in plane stress,} \tag{4}$$

$$= \alpha(1 + \nu) \quad \text{in plane strain} \tag{5}$$

and α, ν, K are, respectively, the coefficient of thermal expansion, Poisson's ratio, and thermal conductivity for the material. Imposition of this condition at the contact surface provides a relation between the heat input (or temperature gradient) at the boundary and the corresponding distorted shape of the surface. Applications to contact problems are discussed by Barber (1980).

The Half-Plane

Results not restricted to steady-state temperature fields have been obtained for the case of the half-plane $y > 0$, which can be regarded as the limit of a thick layer. Ruiz Ayala et al. (1996) showed that if the half-plane is pressed against a frictionless rigid plane with a sufficient mean pressure to maintain full contact (and hence $u_y(x) = 0$) and if the temperature in the half-plane has the form

$$T(x, y) = T_m(y) \cos(mx), \tag{6}$$

the corresponding perturbation in contact pressure due to the temperature field will be

$$p(x) = p_m \cos(mx), \tag{7}$$

where

$$p_m = \frac{8\beta\mu m}{(\kappa + 1)} \int_0^\infty e^{-ms} T_m(s) ds, \tag{8}$$

μ is the modulus of rigidity, and

$$\kappa = \left(\frac{3 - \nu}{1 + \nu}\right) \quad \text{in plane stress,} \tag{9}$$

$$= (3 - 4\nu) \quad \text{in plane strain.} \tag{10}$$

The isothermal half-plane subjected to a contact pressure of the form (7) develops a surface waviness described by

$$u_y(x) = u_m \cos(mx), \tag{11}$$

where

$$u_m = \frac{(\kappa + 1)p_m}{4\mu m} \tag{12}$$

(see, for example, Johnson, 1985, Section 13.2).

[1] Department of Mechanical Engineering and Applied Mechanics, University of Michigan, Ann Arbor, MI 48109-2125.

[2] Surface Technology Center, Alcoa Technical Center, Alcoa Center, PA 15069.

Contributed by the Applied Mechanics Division of THE AMERICAN SOCIETY OF MECHANICAL ENGINEERS for publication in the ASME JOURNAL OF APPLIED MECHANICS. Manuscript received by the ASME Applied Mechanics Division, Feb. 17, 1997; final revision, Apr. 4, 1999. Associate Technical Editor: J. L. Bassani.

 Copyright © 1999 by ASME

Downloaded 04 May 2010 to 171.66.16.27. Redistribution subject to ASME license or copyright; see http://www.asme.org/terms/Terms_Use.cfm

Superposing these results, we find the following general relation between p_m, u_m, $T_m(y)$ for the half-plane:

$$p_m = \frac{8\beta\mu m}{(\kappa+1)}\int_0^\infty e^{-ms}T_m(s)ds + \frac{4\mu m u_m}{(\kappa+1)}. \quad (13)$$

Generalization to an arbitrary x-variation of these quantities is achieved by writing them as Fourier transforms, i.e.,

$$p(x) = \int_{-\infty}^{\infty} e^{imx}p(m)dm;\ u_y(x) = \int_{-\infty}^{\infty} e^{imx}u(m)dm;$$

$$T(x, y) = \int_{-\infty}^{\infty} e^{imx}T(m, y)dm, \quad (14)$$

where

$$p(m) = \frac{8\beta\mu m}{(\kappa+1)}\int_0^\infty e^{-ms}T(m, s)ds + \frac{4\mu m u(m)}{(\kappa+1)}. \quad (15)$$

The purpose of the present note is to establish a similar result for the case of the layer of finite thickness $2h$.

The Thermoelastic Solution

Following Ruiz Ayala et al. (1996), we first consider the layer $-h < y < h$ with the temperature field of Eq. (6) and confined between frictionless rigid planes, so that

$$u_y = 0;\ \sigma_{yx} = 0;\ y = \pm h. \quad (16)$$

A particular solution to the thermoelastic equations can be constructed in the form

$$2\mu\mathbf{u} = \nabla\phi \quad (17)$$

(Westergaard, 1964), where the scalar potention function ϕ satisfies the equation

$$\nabla^2\phi = \frac{8\beta\mu T}{(\kappa+1)}. \quad (18)$$

In view of the form of the temperature distribution (6), it is appropriate to consider functions of the form

$$\phi(x, y) = \frac{8\beta\mu}{(\kappa+1)}f(y)\cos(mx), \quad (19)$$

in which case the governing Eq. (18) reduces to the ordinary differential equation

$$\frac{d^2f}{dy^2} - m^2f = T_m(y). \quad (20)$$

The left-hand side of this equation can be factorized into two linear operators. Appropriate integrating factors then permit the equation to be written

$$e^{my}\frac{d}{dy}\left\{e^{-2my}\frac{d}{dy}(e^{my}f)\right\} = T_m(y), \quad (21)$$

the solution of which is

$$f(y) = e^{-my}\int_{-h}^{y}\int_{-h}^{z} e^{(2mz-ms)}T_m(s)dsdz + A\cosh(my) + B\sinh(my), \quad (22)$$

where A, B are arbitrary constants of integration.

The integral term in (22) can be simplified by changing the order of integration and performing the inner integral, with the result

$$f(y) = \frac{1}{m}\int_{-h}^{y}\sinh(m(y-s))T_m(s)ds + A\cosh(my) + B\sinh(my). \quad (23)$$

The stress components associated with the solution of Eqs. (17), (18) are

$$\sigma_{xx} = -\frac{\partial^2\phi}{\partial y^2};\ \sigma_{xy} = \frac{\partial^2\phi}{\partial x\partial y};\ \sigma_{yy} = -\frac{\partial^2\phi}{\partial x^2}. \quad (24)$$

It follows that all the four boundary conditions (16) can be satisfied by imposing the two conditions

$$f'(-h) = 0;\ f'(h) = 0, \quad (25)$$

which in turn can be satisfied with an appropriate choice of the constants A, B. Thus, with these particular boundary conditions, it is not necessary to supplement the particular solution with a homogeneous solution.

We are interested only in the contact pressures

$$p(\pm h) = -\sigma_{yy}(x, \pm h) = -\frac{8\beta\mu m^2}{(\kappa+1)}f(\pm h)\cos(mx). \quad (26)$$

Using (25) to find A, B and substituting into (23), we obtain, after some routine manipulations,

$$f(\pm h) = -\frac{1}{m\sinh(2mh)}\int_{-h}^{h}\cosh(m(s \pm h))T_m(s)ds \quad (27)$$

and hence

$$p_m(\pm h) = \frac{8\beta\mu m}{(\kappa+1)\sinh(2mh)}\times\int_{-h}^{h}\cosh(m(s \pm h))T_m(s)ds. \quad (28)$$

In the limit $mh \gg 1$ it can be shown that these results tend to Eq. (8), with an appropriate change of coordinate system.

The Isothermal Solution

To introduce the effect of a nonzero gap function $g(x)$, we need the layer equivalent of the isothermal solution of Eqs. (11), (12)—i.e., the contact pressure distribution needed to satisfy the boundary conditions

$$\sigma_{yx}|_{y=h} = \sigma_{yx}|_{y=-h} = 0;\ u_y|_{y=h} = u_{1m}\cos(mx);\ u_y|_{y=-h} = u_{2m}\cos(mx). \quad (29)$$

This is a routine boundary value problem in elasticity and the details of the solution will be omitted here for brevity. A convenient solution method is to use solutions A and D of Green and Zerna (1954), with harmonic potential functions of the form (sinh (my), cosh (my)) cos (mx).

We find that

$$p(h) \equiv -\sigma_{yy}(h) = p_{1m}\cos(mx);\ p(-h) \equiv -\sigma_{yy}(-h) = p_{2m}\cos(mx), \quad (30)$$

where

$$p_{1m} = \frac{2\mu m}{(\kappa+1)}(u_{2m}f_2(mh) - u_{1m}f_1(mh)), \quad (31)$$

Downloaded 04 May 2010 to 171.66.16.27. Redistribution subject to ASME license or copyright; see http://www.asme.org/terms/Terms_Use.cfm

$$p_{2m} = \frac{2\mu m}{(\kappa + 1)} (u_{2m} f_1(mh) - u_{1m} f_2(mh)) \quad (32)$$

and

$$f_1(s) = \frac{2 \cosh^3(s) \sinh(s) - \cosh(s) \sinh(s) + s}{\sinh^2(s) \cosh^2(s)}, \quad (33)$$

$$f_2(s) = \frac{\cosh(s) \sinh(s) + 2s \cosh^2(s) - s}{\sinh^2(s) \cosh^2(s)}. \quad (34)$$

Complete Solution

Superposing the isothermal and thermoelastic solutions, we obtain the following relations between the contact pressure and displacement amplitudes p_{1m}, p_{2m}, u_{1m}, u_{2m} and the temperature function $T_m(y)$:

$$p_{1m} = \frac{2\mu m}{(\kappa + 1)} \left(\frac{4\beta}{\sinh(2mh)} \int_{-h}^{h} \cosh(m(s + h)) T_m(s) ds + u_{2m} f_2(mh) - u_{1m} f_1(mh) \right), \quad (35)$$

$$p_{2m} = \frac{2\mu m}{(\kappa + 1)} \left(\frac{4\beta}{\sinh(2mh)} \int_{-h}^{h} \cosh(m(s - h)) T_m(s) ds + u_{2m} f_1(mh) - u_{1m} f_2(mh) \right). \quad (36)$$

When using these results in connection with conditions (1), (2), note that a positive displacement $u_y(x, -h)$ increases the gap $g_2(x)$ at $y = -h$, but a positive value of $u_y(x, h)$ *reduces* $g_1(x)$ at $y = h$. Extension to more general distributions by Fourier transformation is routine, as in Eqs. (14), (15) above.

Alternatively, Eqs. (35), (36) can be inverted to express the displacements in terms of the pressures, i.e.,

$$u_{1m} = \frac{(\kappa + 1)(p_{2m} f_4(mh) - p_{1m} f_3(mh))}{8\mu m} + \frac{\beta}{\sinh(2mh)} \int_{-h}^{h} [f_3(mh) \cosh(m(s + h)) - f_4(mh) \cosh(m(s - h))] T_m(s) ds, \quad (37)$$

$$u_{2m} = \frac{(\kappa + 1)(p_{2m} f_3(mh) - p_{1m} f_4(mh))}{8\mu m} + \frac{\beta}{\sinh(2mh)} \int_{-h}^{h} [f_4(mh) \cosh(m(s + h)) - f_3(mh) \cosh(m(s - h))] T_m(s) ds, \quad (38)$$

where

$$f_3(s) = \frac{2 \sinh(s) \cosh^3(s) - \sinh(s) \cosh(s) + s}{\sinh^2(s) \cosh^2(s) - s^2}, \quad (39)$$

$$f_4(s) = \frac{2s \cosh^2(s) + \sinh(s) \cosh(s) - s}{\sinh^2(s) \cosh^2(s) - s^2}. \quad (40)$$

Conclusions

Equations (35), (36) or (37), (38) enable us to formulate the general thermoelastic contact problem for the layer in terms of boundary values only. By setting $p_{1m} = p_{2m} = 0$ in Eqs. (37), (38), we can also determine the distorted shape of the traction-free layer due to an arbitrary sinusoidal temperature distribution.

References

Barber, J. R., 1980, "Some Implications of Dundurs' Theorem for Thermoelastic Contact and Crack Problems," *Journal of Mechanical Engineering Science,* Vol. 22, pp. 229–232.

Dundurs, J., 1974, "Distortion of a Body Caused by Free Thermal Expansion," *Mechanics Research Communications,* Vol. 1, pp. 121–124.

Green, A. E., and Zerna, W., 1954, *Theoretical Elasticity,* Clarendon Press, Oxford, UK, Section 5.6.

Johnson, K. L., 1985, *Contact Mechanics,* Cambridge University Press, Cambridge, UK, Section 13.2.

Lee, K., and Barber, J. R., 1993, "Frictionally Excited Thermoelastic Instability in Automotive Disk Brakes," ASME *Journal of Tribology,* Vol. 115, pp. 607–614.

Richmond, O., Hector, L. G., and Fridy, J. M., 1990, "Growth Instability During Nonuniform Directional Solidification of Pure Metals," ASME JOURNAL OF APPLIED MECHANICS, Vol. 57, pp. 529–536.

Ruiz Ayala, J. R., Lee, K., Rahman, M., and Barber, J. R., 1996, "Effect of Intermittent Contact on the Stability of Thermoelastic Sliding Contact," ASME *Journal of Tribology,* Vol. 118, pp. 102–108.

Westergaard, H. M., 1964, *Theory of Elasticity and Plasticity,* Dover, New York, Section 64.

On the Application of Potential Theory in Piezoelasticity

W.-Q. Chen[1]

Introduction

A recent state-of-the-art survey by Rao and Sunar (1994) has revealed the wide and important applications of piezoelectric materials (PZMs) in many branches of science and technology. A great number of theoretical works thus have appeared, concerned with various aspects of piezoelectric problems, such as vibrations of plates and shells (Tiersten, 1969; Ding et al., 1997b), inhomogeneities and cracks (Deeg, 1980; Pak, 1990), and general solutions and Green's functions (Ding et al., 1996, 1997a, c), among others.

Though the potential theory has been shown to be very useful in analyzing mixed and mixed-mixed boundary value problems in elasticity (Fabrikant, 1989, 1991), it seems no one has noticed its application in piezoelasticity to date. In this note, we therefore intend to show how to generalize the potential theory to analyze mixed boundary value problems in piezoelasticity. To this end, the problem of a piezoelectric half-space subjected to mixed boundary conditions on its surface is analyzed. Further developments can be expected based on the generalized potential theory method proposed here as well as the elegant results of Fabrikant (1989, 1991).

Basic Formulations

In Cartesian coordinates (with the z-axis being normal to the plane of isotropy), the linear constitutive relations of a transversely isotropic piezoelectric medium (class 6 mm) are (Tiersten, 1969)

$$\sigma_x = c_{11} \frac{\partial u}{\partial x} + c_{12} \frac{\partial v}{\partial y} + c_{13} \frac{\partial w}{\partial z} + e_{31} \frac{\partial \Phi}{\partial z},$$

$$\sigma_y = c_{12} \frac{\partial u}{\partial x} + c_{11} \frac{\partial v}{\partial y} + c_{13} \frac{\partial w}{\partial z} + e_{31} \frac{\partial \Phi}{\partial z},$$

[1] Department of Civil Engineering, Zhejiang University, Hangzhou 310027, P. R. China.

Contributed by the Applied Mechanics Division of THE AMERICAN SOCIETY OF MECHANICAL ENGINEERS for publication in the ASME JOURNAL OF APPLIED MECHANICS. Manuscript received by the ASME Applied Mechanics Division, June 22, 1998; final revision, Dec. 2, 1998. Associate Technical Editor: M.-J. Pindera.

Downloaded 04 May 2010 to 171.66.16.27. Redistribution subject to ASME license or copyright; see http://www.asme.org/terms/Terms_Use.cfm

$$p_{2m} = \frac{2\mu m}{(\kappa + 1)} (u_{2m} f_1(mh) - u_{1m} f_2(mh)) \quad (32)$$

and

$$f_1(s) = \frac{2 \cosh^3(s) \sinh(s) - \cosh(s) \sinh(s) + s}{\sinh^2(s) \cosh^2(s)}, \quad (33)$$

$$f_2(s) = \frac{\cosh(s) \sinh(s) + 2s \cosh^2(s) - s}{\sinh^2(s) \cosh^2(s)}. \quad (34)$$

Complete Solution

Superposing the isothermal and thermoelastic solutions, we obtain the following relations between the contact pressure and displacement amplitudes p_{1m}, p_{2m}, u_{1m}, u_{2m} and the temperature function $T_m(y)$:

$$p_{1m} = \frac{2\mu m}{(\kappa + 1)} \left(\frac{4\beta}{\sinh(2mh)} \int_{-h}^{h} \cosh(m(s + h)) T_m(s) ds + u_{2m} f_2(mh) - u_{1m} f_1(mh) \right), \quad (35)$$

$$p_{2m} = \frac{2\mu m}{(\kappa + 1)} \left(\frac{4\beta}{\sinh(2mh)} \int_{-h}^{h} \cosh(m(s - h)) T_m(s) ds + u_{2m} f_1(mh) - u_{1m} f_2(mh) \right). \quad (36)$$

When using these results in connection with conditions (1), (2), note that a positive displacement $u_y(x, -h)$ increases the gap $g_2(x)$ at $y = -h$, but a positive value of $u_y(x, h)$ *reduces* $g_1(x)$ at $y = h$. Extension to more general distributions by Fourier transformation is routine, as in Eqs. (14), (15) above.

Alternatively, Eqs. (35), (36) can be inverted to express the displacements in terms of the pressures, i.e.,

$$u_{1m} = \frac{(\kappa + 1)(p_{2m} f_4(mh) - p_{1m} f_3(mh))}{8\mu m} + \frac{\beta}{\sinh(2mh)} \int_{-h}^{h} [f_3(mh) \cosh(m(s + h)) - f_4(mh) \cosh(m(s - h))] T_m(s) ds, \quad (37)$$

$$u_{2m} = \frac{(\kappa + 1)(p_{2m} f_3(mh) - p_{1m} f_4(mh))}{8\mu m} + \frac{\beta}{\sinh(2mh)} \int_{-h}^{h} [f_4(mh) \cosh(m(s + h)) - f_3(mh) \cosh(m(s - h))] T_m(s) ds, \quad (38)$$

where

$$f_3(s) = \frac{2 \sinh(s) \cosh^3(s) - \sinh(s) \cosh(s) + s}{\sinh^2(s) \cosh^2(s) - s^2}, \quad (39)$$

$$f_4(s) = \frac{2s \cosh^2(s) + \sinh(s) \cosh(s) - s}{\sinh^2(s) \cosh^2(s) - s^2}. \quad (40)$$

Conclusions

Equations (35), (36) or (37), (38) enable us to formulate the general thermoelastic contact problem for the layer in terms of boundary values only. By setting $p_{1m} = p_{2m} = 0$ in Eqs. (37), (38), we can also determine the distorted shape of the traction-free layer due to an arbitrary sinusoidal temperature distribution.

References

Barber, J. R., 1980, "Some Implications of Dundurs' Theorem for Thermoelastic Contact and Crack Problems," *Journal of Mechanical Engineering Science,* Vol. 22, pp. 229–232.

Dundurs, J., 1974, "Distortion of a Body Caused by Free Thermal Expansion," *Mechanics Research Communications,* Vol. 1, pp. 121–124.

Green, A. E., and Zerna, W., 1954, *Theoretical Elasticity,* Clarendon Press, Oxford, UK, Section 5.6.

Johnson, K. L., 1985, *Contact Mechanics,* Cambridge University Press, Cambridge, UK, Section 13.2.

Lee, K., and Barber, J. R., 1993, "Frictionally Excited Thermoelastic Instability in Automotive Disk Brakes," ASME *Journal of Tribology,* Vol. 115, pp. 607–614.

Richmond, O., Hector, L. G., and Fridy, J. M., 1990, "Growth Instability During Nonuniform Directional Solidification of Pure Metals," ASME JOURNAL OF APPLIED MECHANICS, Vol. 57, pp. 529–536.

Ruiz Ayala, J. R., Lee, K., Rahman, M., and Barber, J. R., 1996, "Effect of Intermittent Contact on the Stability of Thermoelastic Sliding Contact," ASME *Journal of Tribology,* Vol. 118, pp. 102–108.

Westergaard, H. M., 1964, *Theory of Elasticity and Plasticity,* Dover, New York, Section 64.

On the Application of Potential Theory in Piezoelasticity

W.-Q. Chen[1]

Introduction

A recent state-of-the-art survey by Rao and Sunar (1994) has revealed the wide and important applications of piezoelectric materials (PZMs) in many branches of science and technology. A great number of theoretical works thus have appeared, concerned with various aspects of piezoelectric problems, such as vibrations of plates and shells (Tiersten, 1969; Ding et al., 1997b), inhomogeneities and cracks (Deeg, 1980; Pak, 1990), and general solutions and Green's functions (Ding et al., 1996, 1997a, c), among others.

Though the potential theory has been shown to be very useful in analyzing mixed and mixed-mixed boundary value problems in elasticity (Fabrikant, 1989, 1991), it seems no one has noticed its application in piezoelasticity to date. In this note, we therefore intend to show how to generalize the potential theory to analyze mixed boundary value problems in piezoelasticity. To this end, the problem of a piezoelectric half-space subjected to mixed boundary conditions on its surface is analyzed. Further developments can be expected based on the generalized potential theory method proposed here as well as the elegant results of Fabrikant (1989, 1991).

Basic Formulations

In Cartesian coordinates (with the z-axis being normal to the plane of isotropy), the linear constitutive relations of a transversely isotropic piezoelectric medium (class 6 mm) are (Tiersten, 1969)

$$\sigma_x = c_{11} \frac{\partial u}{\partial x} + c_{12} \frac{\partial v}{\partial y} + c_{13} \frac{\partial w}{\partial z} + e_{31} \frac{\partial \Phi}{\partial z},$$

$$\sigma_y = c_{12} \frac{\partial u}{\partial x} + c_{11} \frac{\partial v}{\partial y} + c_{13} \frac{\partial w}{\partial z} + e_{31} \frac{\partial \Phi}{\partial z},$$

[1] Department of Civil Engineering, Zhejiang University, Hangzhou 310027, P. R. China.

Contributed by the Applied Mechanics Division of THE AMERICAN SOCIETY OF MECHANICAL ENGINEERS for publication in the ASME JOURNAL OF APPLIED MECHANICS. Manuscript received by the ASME Applied Mechanics Division, June 22, 1998; final revision, Dec. 2, 1998. Associate Technical Editor: M.-J. Pindera.

Downloaded 04 May 2010 to 171.66.16.27. Redistribution subject to ASME license or copyright; see http://www.asme.org/terms/Terms_Use.cfm

$$\sigma_z = c_{13}\frac{\partial u}{\partial x} + c_{13}\frac{\partial v}{\partial y} + c_{33}\frac{\partial w}{\partial z} + e_{33}\frac{\partial \Phi}{\partial z},$$

$$\tau_{xz} = c_{44}\left(\frac{\partial u}{\partial z} + \frac{\partial w}{\partial x}\right) + e_{15}\frac{\partial \Phi}{\partial x},$$

$$\tau_{yz} = c_{44}\left(\frac{\partial v}{\partial z} + \frac{\partial w}{\partial y}\right) + e_{15}\frac{\partial \Phi}{\partial y},$$

$$\tau_{xy} = c_{66}\left(\frac{\partial u}{\partial y} + \frac{\partial v}{\partial x}\right),$$

$$D_x = e_{15}\left(\frac{\partial u}{\partial z} + \frac{\partial w}{\partial x}\right) - \epsilon_{11}\frac{\partial \Phi}{\partial x},$$

$$D_y = e_{15}\left(\frac{\partial v}{\partial z} + \frac{\partial w}{\partial y}\right) - \epsilon_{11}\frac{\partial \Phi}{\partial y},$$

$$D_z = e_{31}\frac{\partial u}{\partial x} + e_{31}\frac{\partial v}{\partial y} + e_{33}\frac{\partial w}{\partial z} - \epsilon_{33}\frac{\partial \Phi}{\partial z}, \quad (1)$$

where Φ and D_i are the electric potential and electric displacement vector, respectively; c_{ij}, ϵ_{ij}, and e_{ij} are the elastic, dielectric, and piezoelectric constants, respectively. In addition, the conventional notation for stresses and displacements has been employed. Note that there are only five independent elastic constants for materials with transverse isotropy, since $c_{11} = c_{12} + 2c_{66}$. While the equilibrium equations are the same as those of linear elasticity, the Gauss' law of electrostatics is (in the absence of free charge density in the body)

$$\frac{\partial D_x}{\partial x} + \frac{\partial D_y}{\partial y} + \frac{\partial D_z}{\partial z} = 0. \quad (2)$$

The general solution to the basic equations has been obtained by Ding et al. (1997a) and can be rewritten in the following compact form:

$$U = \Lambda\left(\sum_{i=1}^{3} F_i + iF_4\right), \quad w = \sum_{i=1}^{3} \alpha_{i1}\frac{\partial F_i}{\partial z_i},$$

$$\Phi = \sum_{i=1}^{3} \alpha_{i2}\frac{\partial F_i}{\partial z_i}, \quad (3)$$

where $U = u + iv$, $\Lambda = \partial/\partial x + i\partial/\partial y$, α_{i1} and α_{i2} can be found in Ding et al. (1997a). In addition, $z_i = s_i z$, $s_4^2 = c_{66}/c_{44}$, and s_i^2 $(i = 1, 2, 3)$ are roots of the following algebraic equation

$$as^6 - bs^4 + cs^2 - d = 0, \quad (4)$$

where expressions for a, b, c, and d were given in Ding et al. (1996). It is noted here that the general solution given in Eq. (3) is only valid for distinct s_i^2, while for other cases, different forms should be adopted (Ding et al., 1997a).

Moreover, $F_i(z)$ satisfy the following quasi-harmonic equations, respectively,

$$\left(\Delta + \frac{\partial^2}{\partial z_i^2}\right) F_i = 0, \ (i = 1, 2, 3, 4) \quad (5)$$

where, $\Delta = \partial^2/\partial x^2 + \partial^2/\partial y^2$. From Eqs. (1) and (3), one can get the following expressions for stresses and electric displacements:

$$\sigma_1 = 2\sum_{i=1}^{3}\frac{\partial^2}{\partial z_i^2}[(c_{66} - c_{11}) + c_{13}s_i\alpha_{i1} + e_{31}s_i\alpha_{i2}]F_i$$

$$= 2\Delta\sum_{i=1}^{3}[(c_{11} - c_{66}) - c_{13}s_i\alpha_{i1} - e_{31}s_i\alpha_{i2}]F_i,$$

$$\sigma_2 = 2c_{66}\Lambda^2(F_1 + F_2 + F_3 + iF_4),$$

$$\sigma_z = \sum_{i=1}^{3}\frac{\partial^2}{\partial z_i^2}\gamma_{1i}F_i = -\Delta\sum_{i=1}^{3}\gamma_{1i}F_i,$$

$$\tau_z = \Lambda\left(\sum_{i=1}^{3}[c_{44}(s_i + \alpha_{i1}) + e_{15}\alpha_{i2}]\frac{\partial}{\partial z_i}F_i + is_4c_{44}\frac{\partial}{\partial z_4}F_4\right),$$

$$D = \Lambda\left(\sum_{i=1}^{3}[e_{15}(s_i + \alpha_{i1}) - \epsilon_{11}\alpha_{i2}]\frac{\partial}{\partial z_i}F_i + is_4e_{15}\frac{\partial}{\partial z_4}F_4\right),$$

$$D_z = \sum_{i=1}^{3}\frac{\partial^2}{\partial z_i^2}\gamma_{2i}F_i = -\Delta\sum_{i=1}^{3}\gamma_{2i}F_i, \quad (6)$$

where, $\sigma_1 = \sigma_x + \sigma_y$, $\sigma_2 = \sigma_x - \sigma_y + 2i\tau_{xy}$, $\tau_z = \tau_{xz} + i\tau_{yz}$ and $D = D_x + iD_y$, and,

$$\gamma_{1i} = -c_{13} + c_{33}s_i\alpha_{i1} + e_{33}s_i\alpha_{i2},$$

$$\gamma_{2i} = -e_{31} + e_{33}s_i\alpha_{i1} - \epsilon_{33}s_i\alpha_{i2}.$$

The Generalized Potential Theory Method

Consider a transversely isotropic piezoelectric half-space subject to the following mixed boundary conditions on the surface $z = 0$:

$$\sigma_z = -p(x, y), \ D_z = q(x, y), \text{ for } (x, y) \in S;$$

$$w = \Phi = 0, \text{ for } (x, y) \notin S;$$

$$\tau_z = 0, \text{ for } -\infty < (x, y) < \infty. \quad (7)$$

Such a problem can arise in the symmetric crack problem of an infinite piezoelectric medium. It can be shown that these conditions can be satisfied by a representation in terms of two harmonic functions G and H. In fact, by extending the potential theory for elasticity (Fabrikant, 1989), assume

$$F_i(z) = c_iG(z_i) + d_iH(z_i), \ (i = 1, 2, 3); \ F_4(z) = 0 \quad (8)$$

where c_i and d_i are constants to be determined. To satisfy the third condition in (7), one can set

$$\sum_{i=1}^{3} c_i[c_{44}(s_i + \alpha_{i1}) + e_{15}\alpha_{i2}] = 0,$$

$$\sum_{i=1}^{3} d_i[c_{44}(s_i + \alpha_{i1}) + e_{15}\alpha_{i2}] = 0. \quad (9)$$

The two functions G and H are now given as two potentials of a simple layer, respectively,

$$G(\rho, \phi, z) = \int\int_S \frac{\omega(N)}{R(M, N)}\,dS,$$

$$H(\rho, \phi, z) = \int\int_S \frac{\varphi(N)}{R(M, N)}\,dS, \quad (10)$$

where ω and φ stand for the surface displacement $w(x, y, 0)$ and electric potential $\Phi(x, y, 0)$, respectively. $R(M, N)$ is the distance between the points $M(\rho, \phi, z)$, and $N(r, \psi, 0)$ (hereafter, the cylindrical coordinates (ρ, ϕ, z) are alternatively used for the sake of convenience), and the integration is taken over the domain S.

Downloaded 04 May 2010 to 171.66.16.27. Redistribution subject to ASME license or copyright; see http://www.asme.org/terms/Terms_Use.cfm

Here the new potential of a simple layer H is introduced to include the effect of electric field in PZMs. Making use of the property of the potential of a simple layer, the second condition in Eq. (7) is already identically satisfied, while inside the domain S one has,

$$\left.\frac{\partial G}{\partial z}\right|_{z=0} = -2\pi\omega = -2\pi w(x, y, 0),$$

$$\left.\frac{\partial H}{\partial z}\right|_{z=0} = -2\pi\varphi = -2\pi\Phi(x, y, 0). \tag{11}$$

The following relations then can be obtained from Eqs. (3), (8), and (11):

$$\sum_{i=1}^{3} c_i\alpha_{i1} = -\frac{1}{2\pi}, \sum_{i=1}^{3} d_i\alpha_{i1} = 0,$$

$$\sum_{i=1}^{3} c_i\alpha_{i2} = 0, \sum_{i=1}^{3} d_i\alpha_{i2} = -\frac{1}{2\pi}. \tag{12}$$

One can thus find c_i and d_i from Eqs. (9) and (12). Now consideration of the first condition in Eq. (7) leads to the following integro-differential equations:

$$p(N_0) = -g_1\Delta\int\int_S \frac{\omega(N)}{R(N_0, N)}\,dS - g_2\Delta\int\int_S \frac{\varphi(N)}{R(N_0, N)}\,dS,$$

$$q(N_0) = -g_3\Delta\int\int_S \frac{\omega(N)}{R(N_0, N)}\,dS - g_4\Delta\int\int_S \frac{\varphi(N)}{R(N_0, N)}\,dS, \tag{13}$$

where, as above, $R(N_0, N)$ represents the distance between two points N_0 and N, and both N_0, $N \in S$. The constants g_i, $(i = 1, 2, 3, 4)$ are defined as follows:

$$g_1 = -\sum_{i=1}^{3} c_i\gamma_{1i}, \quad g_2 = -\sum_{i=1}^{3} d_i\gamma_{1i},$$

$$g_3 = \sum_{i=1}^{3} c_i\gamma_{2i}, \quad g_4 = \sum_{i=1}^{3} d_i\gamma_{2i}, \tag{14}$$

From Eq. (13), one obtains

$$g_4p(N_0) - g_2q(N_0) = -\frac{1}{4\pi^2A}\Delta\int\int_S \frac{\omega(N)}{R(N_0, N)}\,dS, \tag{15}$$

$$g_1q(N_0) - g_3p(N_0) = -\frac{1}{4\pi^2A}\Delta\int\int_S \frac{\varphi(N)}{R(N_0, N)}\,dS, \tag{16}$$

where $A = 1/4\pi^2(g_1g_4 - g_2g_3)$. Generally speaking, Eqs. (15) and (16) can be solved using numerical methods. For the particular case that S occupies a circular domain, explicit solutions can be derived; this will be shown in the next section.

Circular Domain Case

Suppose the center of the circular domain S is located at the origin of the coordinates and a is the radius. By virtue of the results of Fabrikant (1989), the following exact solutions to Eqs. (15) and (16) are obtained:

$$\omega = \frac{2A}{\pi}\int_0^{2\pi}\int_0^{a}\frac{1}{R}\tan^{-1}\left(\frac{\eta}{R}\right)[g_4p(\rho_0, \phi_0) - g_2q(\rho_0, \phi_0)]\rho_0 d\rho_0 d\phi_0,$$

$$\varphi = \frac{2A}{\pi}\int_0^{2\pi}\int_0^{a}\frac{1}{R}\tan^{-1}\left(\frac{\eta}{R}\right)[g_1q(\rho_0, \phi_0) - g_3p(\rho_0, \phi_0)]\rho_0 d\rho_0 d\phi_0, \tag{17}$$

where

$$R = [\rho^2 + \rho_0^2 - 2\rho\rho_0\cos(\phi - \phi_0)]^{1/2},$$

$$\eta = (a^2 - \rho^2)^{1/2}(a^2 - \rho_0^2)^{1/2}/a. \tag{18}$$

To obtain the whole elastoelectric field, substitution of Eq. (18) into Eq. (10) gives

$$G(\rho, \phi, z) = \frac{2A}{\pi}\int_0^{2\pi}\int_0^{a}K(\rho, \phi, z; \rho_0, \phi_0)[g_4p(\rho_0, \phi_0) - g_2q(\rho_0, \phi_0)]\rho_0 d\rho_0 d\phi_0,$$

$$H(\rho, \phi, z) = \frac{2A}{\pi}\int_0^{2\pi}\int_0^{a}K(\rho, \phi, z; \rho_0, \phi_0)[g_1q(\rho_0, \phi_0) - g_3p(\rho_0, \phi_0)]\rho_0 d\rho_0 d\phi_0, \tag{19}$$

where the so-called Green's function K reads (Fabrikant, 1989)

$$K(M; N_0) = K(\rho, \phi, z; \rho_0, \phi_0) = \int_0^{2\pi}\int_0^{a}\frac{1}{R(N, N_0)} \times \tan^{-1}\left[\frac{(a^2 - r^2)^{1/2}(a^2 - \rho_0^2)^{1/2}}{aR(N, N_0)}\right]\frac{rdrd\psi}{R(M, N)}. \tag{20}$$

Here $R(\cdot, \cdot)$ denotes the distance between respective points: $M(\rho, \phi, z)$, $N(r, \psi, 0)$, and $N_0(\rho_0, \phi_0, 0)$. It becomes obvious now that the main conclusion reached by Fabrikant (1989) for elasticity can be generalized here for piezoelasticity as follows: For any polynomial form distributions of p and q, all elastoelectric field variables can be finally expressed in terms of elementary functions. In particular, when both p and q are uniformly distributed, the following results can be derived:

$$\omega = 4A(g_4p - g_2q)(a^2 - \rho^2)^{1/2},$$

$$\varphi = 4A(g_1q - g_3p)(a^2 - \rho^2)^{1/2} \tag{21}$$

$$G = 2\pi A(g_4p - g_2q)\left[(2a^2 + 2z^2 - \rho^2)\sin^{-1}\left(\frac{a}{l_2}\right) - \frac{2a^3 - 3l_1^2}{a}(l_2^2 - a^2)^{1/2}\right]$$

$$H = 2\pi A(g_1q - g_3p)\left[(2a^2 + 2z^2 - \rho^2)\sin^{-1}\left(\frac{a}{l_2}\right) - \frac{2a^3 - 3l_1^2}{a}(l_2^2 - a^2)^{1/2}\right] \tag{22}$$

where $l_{1,2} = \frac{1}{2}\{[(\rho + a)^2 + z^2]^{1/2} \mp [(\rho - a)^2 + z^2]^{1/2}\}$. One can then derive the corresponding elastoelectric field variables from Eq. (22). To show the piezoelectric effect on the elastic field, the distributions of w and σ_z on the axis of symmetry (z-axis) are shown in Figs. 1 and 2, respectively, in nondimensional manner. For comparison, it is assumed that only uniform normal stress ρ_0 is applied over the circular domain $r \le a$. Calculation is made for three different piezoelectric materials as shown in both figures, and for the corresponding elastic materials (followed by (E)) in which the piezoelectric effect is neglected. All material constants are the same as those given in Dunn and Taya (1994). It can be shown that

Downloaded 04 May 2010 to 171.66.16.27. Redistribution subject to ASME license or copyright; see http://www.asme.org/terms/Terms_Use.cfm

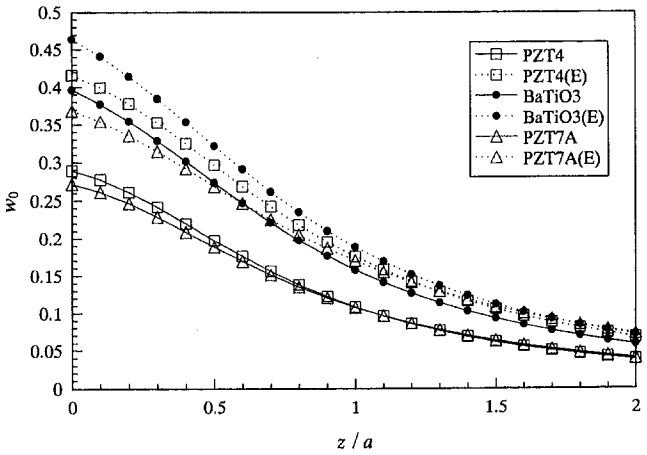


Fig. 1 Comparison between curves of the nondimensional displacement $w_0 = c_{44}w(0, \phi, z)/(a\rho_0)$ versus the nondimensional coordinate z/a for piezoelectric materials (solid lines) and those for corresponding elastic materials (dotted lines)

the piezoelectric characteristic has an important effect on the distribution of displacement w.

Closure

The potential theory method has been generalized here to analyze the mixed boundary value problem of a piezoelectric half-space. A new potential of a simple layer is therefore introduced to consider the effect of electric field. As an example, a circular domain problem is considered and explicit solutions are obtained by using Fabrikant's results.

As mentioned earlier in this paper, the general solution should take other forms for equal eigenvalue cases. The corresponding derivations are similar to those that have been described above. However, as pointed out by Fabrikant (1989), one can also derive the corresponding results for equal eigenvalues directly from the ones for distinct eigenvalues, by utilizing the well-known L'Hospital rule.

Although the present analysis is limited to boundary conditions (7), it is not difficult to investigate analytically other boundary value problems such as the tangential loading case and the indentation of a piezoelectric half-space by circular indentors of different shapes. In fact, using the idea suggested here, any solution for elasticity presented in Fabrikant (1989, 1991) can be generalized to the one for piezoelectricity without any extra mathematical difficulty. For other cases, however, details are omitted for simplicity and the reader is referred to Fabrikant (1989, 1991).

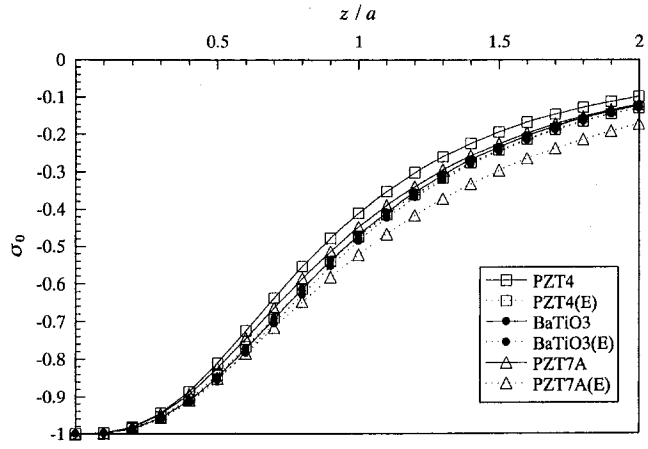


Fig. 2 Comparison between curves of the nondimensional stress $\sigma_0 = \sigma_z(0, \phi, z)/\rho_0$ versus the nondimensional coordinate z/a for piezoelectric materials (solid lines) and those for corresponding elastic materials (dotted lines)

Acknowledgment

The work was supported by the National Natural Science Foundation of China (No. 19872060). The financial support from the Japanese Ministry of Education, Science, Sports and Culture is also acknowledged. The author would like to express sincere thanks to the editor and the reviewers for their kind help in improving the presentation of this note.

References

Deeg, W. F., 1980, "The analysis of dislocation, crack, and inclusion problems in piezoelectric solids," Ph.D. dissertation, Stanford University, Stanford, CA.

Ding, H. J., Chen, B., and Liang, J., 1996, "General solutions for coupled equations for piezoelectric media," *International Journal of Solids and Structures,* Vol. 33, pp. 2283–2298.

Ding, H. J., Chen, B., and Liang, J., 1997a, "On the Green's functions for two-phase transversely isotropic piezoelectric media," *International Journal of Solids and Structures,* Vol. 34, pp. 3041–3057.

Ding, H. J., Chen, W. Q., Guo, Y. M., and Yang, Q. D., 1997b, "Free vibrations of piezoelectric cylindrical shells filled with compressible fluid," *International Journal of Solids and Structures,* Vol. 34, pp. 2025–2034.

Ding, H. J., Wang, G. Q., and Chen, W. Q., 1997c, "Green's functions for a two-phase infinite piezoelectric plane," *Proceedings of the Royal Society of London,* Vol. A453, pp. 2241–2257.

Dunn, M. L., and Taya, M., 1994, "Electroelastic Field Concentrations in and Around Inhomogeneities in Piezoelectric Solids," ASME JOURNAL OF APPLIED MECHANICS, Vol. 61, pp. 474–475.

Fabrikant, V. I., 1989, *Applications of potential theory in mechanics: A selection of new results,* Kluwer Academic Publishers, Dordrecht, The Netherlands.

Fabrikant, V. I., 1991, *Mixed boundary value problems of potential theory and their applications in engineering,* Kluwer Academic Publishers, Dordrecht, The Netherlands.

Pak, Y. E., 1990, "Crack Extension Force in a Piezoelectric Material," ASME JOURNAL OF APPLIED MECHANICS, Vol. 57, pp. 647–653.

Rao, S. S., and Sunar, M., 1994, "Piezoelectricity and its use in disturbance sensing and control of flexible structures: a survey," ASME *Applied Mechanics Reviews,* Vol. 47, pp. 113–123.

Tiersten, H. F., 1969, *Linear piezoelectric plate vibrations,* Plenum Press, New York.

Application of the Cosserat Spectrum Theory to Stokes Flow

W. Liu[1,3] and A. Plotkin[2,3]

This paper presents an application of the Cosserat spectrum theory in elasticity to the solution of low Reynolds number (Stokes flow) problems. The velocity field is divided into two components: a solution to the vector Laplace equation and a solution associated with the discrete Cosserat eigenvectors. Analytical solutions are presented for the Stokes flow past a sphere with uniform, extensional, and linear shear freestream profiles.

1 Introduction

E. Cosserat and F. Cosserat (1898) discovered that the homogeneous Navier equations in elasticity

[1] Graduate Student.

[2] Professor. Fellow ASME.

[3] Department of Aerospace Engineering and Engineering Mechanics, San Diego State University, San Diego, CA 92182.

Contributed by the Applied Mechanics Division of THE AMERICAN SOCIETY OF MECHANICAL ENGINEERS for publication in the ASME JOURNAL OF APPLIED MECHANICS. Manuscript received by the ASME Applied Mechanics Division, Aug. 15, 1997; final revision, July 8, 1998. Associate Technical Editor: D. A. Siginer.

Downloaded 04 May 2010 to 171.66.16.27. Redistribution subject to ASME license or copyright; see http://www.asme.org/terms/Terms_Use.cfm

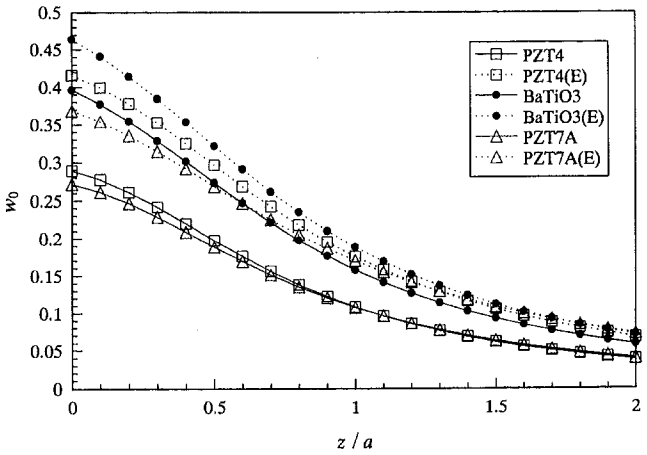


Fig. 1 Comparison between curves of the nondimensional displacement $w_0 = c_{44}w(0, \phi, z)/(a\rho_0)$ versus the nondimensional coordinate z/a for piezoelectric materials (solid lines) and those for corresponding elastic materials (dotted lines)

the piezoelectric characteristic has an important effect on the distribution of displacement w.

Closure

The potential theory method has been generalized here to analyze the mixed boundary value problem of a piezoelectric half-space. A new potential of a simple layer is therefore introduced to consider the effect of electric field. As an example, a circular domain problem is considered and explicit solutions are obtained by using Fabrikant's results.

As mentioned earlier in this paper, the general solution should take other forms for equal eigenvalue cases. The corresponding derivations are similar to those that have been described above. However, as pointed out by Fabrikant (1989), one can also derive the corresponding results for equal eigenvalues directly from the ones for distinct eigenvalues, by utilizing the well-known L'Hospital rule.

Although the present analysis is limited to boundary conditions (7), it is not difficult to investigate analytically other boundary value problems such as the tangential loading case and the indentation of a piezoelectric half-space by circular indentors of different shapes. In fact, using the idea suggested here, any solution for elasticity presented in Fabrikant (1989, 1991) can be generalized to the one for piezoelectricity without any extra mathematical difficulty. For other cases, however, details are omitted for simplicity and the reader is referred to Fabrikant (1989, 1991).

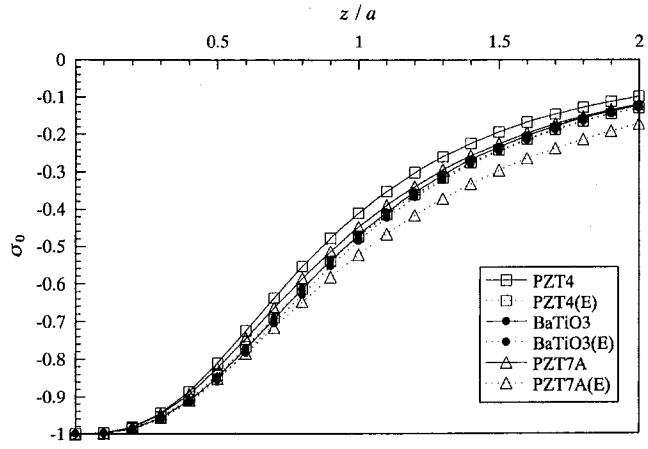


Fig. 2 Comparison between curves of the nondimensional stress $\sigma_0 = \sigma_z(0, \phi, z)/\rho_0$ versus the nondimensional coordinate z/a for piezoelectric materials (solid lines) and those for corresponding elastic materials (dotted lines)

Acknowledgment

The work was supported by the National Natural Science Foundation of China (No. 19872060). The financial support from the Japanese Ministry of Education, Science, Sports and Culture is also acknowledged. The author would like to express sincere thanks to the editor and the reviewers for their kind help in improving the presentation of this note.

References

Deeg, W. F., 1980, "The analysis of dislocation, crack, and inclusion problems in piezoelectric solids," Ph.D. dissertation, Stanford University, Stanford, CA.

Ding, H. J., Chen, B., and Liang, J., 1996, "General solutions for coupled equations for piezoelectric media," *International Journal of Solids and Structures,* Vol. 33, pp. 2283–2298.

Ding, H. J., Chen, B., and Liang, J., 1997a, "On the Green's functions for two-phase transversely isotropic piezoelectric media," *International Journal of Solids and Structures,* Vol. 34, pp. 3041–3057.

Ding, H. J., Chen, W. Q., Guo, Y. M., and Yang, Q. D., 1997b, "Free vibrations of piezoelectric cylindrical shells filled with compressible fluid," *International Journal of Solids and Structures,* Vol. 34, pp. 2025–2034.

Ding, H. J., Wang, G. Q., and Chen, W. Q., 1997c, "Green's functions for a two-phase infinite piezoelectric plane," *Proceedings of the Royal Society of London,* Vol. A453, pp. 2241–2257.

Dunn, M. L., and Taya, M., 1994, "Electroelastic Field Concentrations in and Around Inhomogeneities in Piezoelectric Solids," ASME JOURNAL OF APPLIED MECHANICS, Vol. 61, pp. 474–475.

Fabrikant, V. I., 1989, *Applications of potential theory in mechanics: A selection of new results,* Kluwer Academic Publishers, Dordrecht, The Netherlands.

Fabrikant, V. I., 1991, *Mixed boundary value problems of potential theory and their applications in engineering,* Kluwer Academic Publishers, Dordrecht, The Netherlands.

Pak, Y. E., 1990, "Crack Extension Force in a Piezoelectric Material," ASME JOURNAL OF APPLIED MECHANICS, Vol. 57, pp. 647–653.

Rao, S. S., and Sunar, M., 1994, "Piezoelectricity and its use in disturbance sensing and control of flexible structures: a survey," ASME *Applied Mechanics Reviews,* Vol. 47, pp. 113–123.

Tiersten, H. F., 1969, *Linear piezoelectric plate vibrations,* Plenum Press, New York.

Application of the Cosserat Spectrum Theory to Stokes Flow

W. Liu[1,3] and A. Plotkin[2,3]

This paper presents an application of the Cosserat spectrum theory in elasticity to the solution of low Reynolds number (Stokes flow) problems. The velocity field is divided into two components: a solution to the vector Laplace equation and a solution associated with the discrete Cosserat eigenvectors. Analytical solutions are presented for the Stokes flow past a sphere with uniform, extensional, and linear shear freestream profiles.

1 Introduction

E. Cosserat and F. Cosserat (1898) discovered that the homogeneous Navier equations in elasticity

[1] Graduate Student.

[2] Professor. Fellow ASME.

[3] Department of Aerospace Engineering and Engineering Mechanics, San Diego State University, San Diego, CA 92182.

Contributed by the Applied Mechanics Division of THE AMERICAN SOCIETY OF MECHANICAL ENGINEERS for publication in the ASME JOURNAL OF APPLIED MECHANICS. Manuscript received by the ASME Applied Mechanics Division, Aug. 15, 1997; final revision, July 8, 1998. Associate Technical Editor: D. A. Siginer.

Downloaded 04 May 2010 to 171.66.16.27. Redistribution subject to ASME license or copyright; see http://www.asme.org/terms/Terms_Use.cfm

$$\Delta \mathbf{u} + \omega \nabla \nabla \cdot \mathbf{u} = 0 \tag{1}$$

with homogeneous boundary conditions of displacement or traction admit nontrivial solutions when ω takes some special value lying outside the physical range of Poisson's ratio called the Cosserat spectrum (eigenvalue) $\tilde{\omega}$. The corresponding nonzero solution $\tilde{\mathbf{u}}$ is accordingly called the Cosserat eigenfunction (eigenvector). In Eq. (1), $\omega = (\lambda + \mu)/\mu = 1/(1 - 2\nu)$, λ and μ being the Lame's constants, ν the Poisson's ratio, $\mathbf{u}$ the displacement.

The Cosserat spectrum theory was fully developed by Mikhlin (1973) who proved the completeness and orthogonality of the Cosserat eigenfunctions and represented the displacement field $\mathbf{u}$ as a summation of the Cosserat eigenfunctions for the boundary value problems of displacement or traction. Markenscoff and Paukshto (1998) have applied the Cosserat spectrum theory to problems in elasticity and thermoelasticity.

In this paper we apply the Cosserat spectrum theory to the solution of Stokes flow problems in fluid mechanics. Analytical solutions are presented for the Stokes flow past a sphere with uniform, extensional, and shear freestream profiles.

2 Application of the Cosserat Spectrum Theory to Stokes Flow

The Navier-Stokes equations for Stokes flow in a domain Ω have the form

$$\Delta \mathbf{u} = \frac{\nabla p}{\mu} \quad \text{in} \quad \Omega \tag{2a}$$

$$\nabla \cdot \mathbf{u} = 0 \quad \text{in} \quad \Omega \tag{2b}$$

$$\rho = \rho_0 \quad \text{in} \quad \Omega \tag{2c}$$

where $\mathbf{u}$, p, and ρ are the velocity, pressure, and density, respectively, and ρ_0 is the constant density, μ the dynamic viscosity. The velocity on the boundary $\partial\Omega$ is written as

$$\mathbf{u} = \mathbf{u}_b \quad \text{on} \quad \partial\Omega. \tag{3}$$

This system of nonhomogeneous equations with nonhomogeneous boundary conditions is now divided into two subsystems as follows:

$$\mathbf{u} = \mathbf{u}_0 + \mathbf{u}_c. \tag{4}$$

The system associated with $\mathbf{u}_0$ is one with homogeneous equations and nonhomogeneous boundary conditions:

$$\Delta \mathbf{u}_0 = 0 \quad \text{in} \quad \Omega \tag{5a}$$

$$\mathbf{u}_0 = \mathbf{u}_b \quad \text{on} \quad \partial\Omega. \tag{5b}$$

Equation (5) can be solved without involving the unknown pressure p. Solutions to the vector Laplace equation may be found in Hill (1954). The second system associated with $\mathbf{u}_c$ is one with nonhomogeneous equations and homogeneous boundary conditions:

$$\Delta \mathbf{u}_c + \omega \nabla(\nabla \cdot \mathbf{u}_c) = \frac{\nabla p}{\mu} \quad \text{in} \quad \Omega \tag{6a}$$

$$\mathbf{u}_c = 0 \quad \text{on} \quad \partial\Omega \tag{6b}$$

where $\omega = 0$ for incompressible flow. In the Cosserat spectrum theory, Eq. (6) admits a simplified representation (Liu, 1998)

$$\mathbf{u}_c = \sum_n f_n \tilde{\mathbf{u}}_n \tag{7a}$$

where

$$f_n = \frac{\tilde{\omega}_n}{\mu(\omega - \tilde{\omega}_n)} \int_\Omega \nabla p \cdot \tilde{\mathbf{u}}_n dV \tag{7b}$$

and $\tilde{\omega}_n$ and $\tilde{\mathbf{u}}_n$ are the discrete Cosserat eigenvalues and eigenfunctions, respectively, and dV is the integration element in Ω.

Substituting Eq. (7*a*) into Eq. (6*a*), using the homogeneous Navier equations for the discrete eigenvalues $\tilde{\omega}_n$ and eigenvectors $\tilde{\mathbf{u}}_n$, and integrating will give

$$p = p_0 + \mu \sum_n f_n(\omega - \tilde{\omega}_n) \nabla \cdot \tilde{\mathbf{u}}_n \tag{8}$$

where p_0 is an integration constant.

The coefficients f_n can be evaluated by use of the continuity equation Eq. (2*b*) which now takes the form

$$\nabla \cdot \mathbf{u}_0 + \sum_n f_n \nabla \cdot \tilde{\mathbf{u}}_n = 0. \tag{9}$$

Each term in Eq. (9) is multiplied by $\nabla \cdot \tilde{\mathbf{u}}_m$, then integrated over the domain Ω, and using the orthogonality conditions of the Cosserat eigenfunctions for the first boundary value problem, we have

$$f_n = \tilde{\omega}_n \int \nabla \cdot \tilde{\mathbf{u}}_n \nabla \cdot \mathbf{u}_0 dV. \tag{10}$$

Once the discrete Cosserat eigenvalues and eigenvectors with respect to the specific domain Ω are given, the problem may be considered solved: One only needs to add the Cosserat solution $\mathbf{u}_c$ to $\mathbf{u}_0$; the pressure p is given by Eq. (8).

3 Examples

Let (r, θ, φ) represent a spherical coordinate system. For a general first boundary value problem in the domain outside a rigid solid sphere of radius r_0, the discrete Cosserat eigenvalue $\tilde{\omega}_n$, the discrete Cosserat eigenvector $\tilde{\mathbf{u}}_{n,m}$ are (Liu, 1998)

$$\tilde{\omega}_n = -\frac{2n + 1}{n + 1} \tag{11a}$$

$$\tilde{\mathbf{u}}_{n,m} = C_{n,m}(r^2 - r_0^2) \nabla F_{-(n+1),m} \tag{11b}$$

where $n = 1, 2, \ldots, m = 0, 1, \ldots, n$, and

$$(C_{n,m})^2 = \frac{2n - 1}{8(n + 1)\pi r_0^3} \frac{(n - m)!}{(n + m)! \delta_m} \tag{11c}$$

$$F_{-(n+1),m} = \left(\frac{r_0}{r}\right)^{n+1} Y_n^m(\theta, \varphi) \tag{11d}$$

$$\delta_m = \begin{cases} 2 & m = 0 \\ 1 & m \neq 0 \end{cases} \tag{11e}$$

In Eq. (11*d*), $Y_n^m(\theta, \varphi) = P_n^m(\cos\theta)\{\begin{smallmatrix}\cos m\varphi \\ \sin m\varphi\end{smallmatrix}\}$ and $P_n^m(\cos\theta)$ is the associated Legendre polynomial of the first kind. If a boundary value problem is axisymmetric, then $m = 0$ and Eqs. (11*b*–11*d*) can be simplified as follows:

$$\tilde{\mathbf{u}}_n = C_n(r^2 - r_0^2) \nabla F_{-(n+1)} \tag{12a}$$

$$(C_n)^2 = \frac{2n - 1}{16(n + 1)\pi r_0^3} \tag{12b}$$

$$F_{-(n+1)} = \left(\frac{r_0}{r}\right)^{n+1} P_n(\cos\theta) \tag{12c}$$

Downloaded 04 May 2010 to 171.66.16.27. Redistribution subject to ASME license or copyright; see http://www.asme.org/terms/Terms_Use.cfm

where $n = 1, 2, \ldots$ and $P_n(\cos\theta)$ is the Legendre polynomial of degree n.

To illustrate the solution technique described above, we consider the Stokes flow past a sphere with three different freestream profiles. The freestream is in the x-direction and θ increases clockwise from the negative x-direction.

3.1 Uniform Flow Past a Sphere. The velocity boundary conditions for a uniform freestream are

$$\mathbf{u}_b = \begin{cases} 0 & r = r_0 \\ U_0\mathbf{e}_x = -U_0\cos\theta\ \mathbf{e}_r + U_0\sin\theta\ \mathbf{e}_\theta & r = \infty. \end{cases} \quad (13)$$

This problem is axisymmetric. As described above, it is now divided into two subproblems. The first part associated with homogeneous equations and nonhomogeneous boundary conditions is solved as

$$\mathbf{u}_0 = -U_0\left(1 - \frac{r_0}{r}\right)\cos\theta\mathbf{e}_r + U_0\left(1 - \frac{r_0}{r}\right)\sin\theta\mathbf{e}_\theta. \quad (14)$$

The second part of the problem is the Cosserat eigenvalue problem of the first kind, which is solved as

$$\mathbf{u}_c = \sum_n f_n\tilde{\mathbf{u}}_n \quad (15a)$$

$$f_1 = -8\pi C_1 r_0^2 U_0 \quad \text{and} \quad C_1 = \pm\sqrt{\frac{1}{32\pi r_0^3}} \quad (15b)$$

$$f_n = 0 \quad n \geq 2. \quad (15c)$$

The solutions to the Stokes flow over a sphere with uniform freestream are

$$\mathbf{u} = \mathbf{u}_0 + f_1\tilde{\mathbf{u}}_1 = U_0\left(-1 + \frac{3r_0}{2r} - \frac{r_0^3}{2r^3}\right)\cos\theta\mathbf{e}_r + U_0\left(1 - \frac{3r_0}{4r} - \frac{r_0^3}{4r^3}\right)\sin\theta\mathbf{e}_\theta \quad (16)$$

$$p = p_0 + \mu f_1(\omega - \tilde{\omega}_1)\nabla\cdot\tilde{\mathbf{u}}_1 = p_0 + \frac{3\mu r_0 U_0}{2r^2}\cos\theta. \quad (17)$$

3.2 Extensional Flow Past a Sphere. The velocity boundary conditions for an extensional freestream are

$$\mathbf{u}_b = \begin{cases} 0 & r = r_0 \\ \dfrac{U_0}{r_0}(2x\mathbf{e}_x - y\mathbf{e}_y - z\mathbf{e}_z) = U_0\left[\dfrac{2r}{r_0}P_2\mathbf{e}_r + \dfrac{r}{r_0}\dfrac{dP_2}{d\theta}\mathbf{e}_\theta\right] & r = \infty. \end{cases} \quad (18)$$

Repeating the procedures outlined above, we obtain the first and second parts of the solution as

$$\mathbf{u}_0 = 2U_0\left(\frac{r}{r_0} - \frac{r_0^2}{r^2}\right)P_2\mathbf{e}_r + U_0\left(\frac{r}{r_0} - \frac{r_0^2}{r^2}\right)\frac{dP_2}{d\theta}\mathbf{e}_\theta \quad (19)$$

$$\mathbf{u}_c = \sum_n f_n\tilde{\mathbf{u}}_n \quad (20a)$$

$$f_2 = 16\pi C_2 r_0^2 U_0 \quad \text{and} \quad C_2 = \pm\sqrt{\frac{1}{16\pi r_0^3}} \quad (20b)$$

$$f_n = 0 \quad n \neq 2. \quad (20c)$$

The solutions to the Stokes flow over a sphere with extensional freestream are

$$\mathbf{u} = \mathbf{u}_0 + f_2\tilde{\mathbf{u}}_2 = U_0\left(\frac{2r}{r_0} - \frac{5r_0^2}{r^2} + \frac{3r_0^4}{r^4}\right)P_2\mathbf{e}_r + U_0\left(\frac{r}{r_0} - \frac{r_0^4}{r^4}\right)\frac{dP_2}{d\theta}\mathbf{e}_\theta \quad (21)$$

$$p = p_0 + \mu f_2(\omega - \tilde{\omega}_2)\nabla\cdot\tilde{\mathbf{u}}_2 = p_0 - \frac{10\mu r_0^2 U_0}{r^3}P_2. \quad (22)$$

3.3 Shear Flow Past a Sphere. The velocity boundary conditions for a shear freestream are

$$\mathbf{u}_b = \begin{cases} 0 & r = r_0 \\ \dfrac{U_0}{r_0}y\mathbf{e}_x = \dfrac{U_0 r\sin\theta\cos\varphi}{r_0}(-\cos\theta\mathbf{e}_r + \sin\theta\mathbf{e}_\theta) & r = \infty. \end{cases} \quad (23)$$

This problem is not axisymmetric. The first and second parts of the solution are

$$\mathbf{u}_0 = U_0\left(\frac{r}{r_0} - \frac{r_0^2}{r^2}\right) \times (-\sin\theta\cos\theta\cos\varphi\mathbf{e}_r + \sin^2\theta\cos\varphi\mathbf{e}_\theta) \quad (24)$$

$$\mathbf{u}_c = \sum_{n,m} f_{n,m}\tilde{\mathbf{u}}_{n,m} \quad (25a)$$

$$f_{2,1} = -8\pi C_{2,1} r_0^2 U_0 \quad \text{and} \quad C_{2,1} = \pm\sqrt{\frac{1}{48\pi r_0^3}} \quad (25b)$$

$$f_{n,m} = 0 \quad n \neq 2, \quad m \neq 1. \quad (25c)$$

The solutions to the Stokes flow over a sphere with a shear freestream are

$$\mathbf{u} = \mathbf{u}_0 + f_{2,1}\tilde{\mathbf{u}}_{2,1} = U_0\left(-\frac{r}{r_0} + \frac{5r_0^2}{2r^2} - \frac{3r_0^4}{2r^4}\right)\sin\theta\cos\theta\cos\varphi\,\mathbf{e}_r + U_0\left(\frac{r}{r_0}\sin^2\theta - \frac{r_0^2}{2r^2} + \frac{r_0^4}{2r^4}(\cos^2\theta - \sin^2\theta)\right)\cos\varphi\mathbf{e}_\theta + \frac{U_0}{2}\left(\frac{r_0^2}{r^2} - \frac{r_0^4}{r^4}\right)\cos\theta\sin\varphi\mathbf{e}_\varphi \quad (26)$$

$$p = p_0 + \mu f_{2,1}(\omega - \tilde{\omega}_2)\nabla\cdot\tilde{\mathbf{u}}_{2,1} = p_0 + \frac{5\mu r_0^2 U_0}{r^3}\sin\theta\cos\theta\cos\varphi. \quad (27)$$

4 Summary

We have applied the Cosserat spectrum theory to the solution of Stokes flow problems. The velocity field is divided into two components: a solution of the vector Laplace equation and a solution associated with the discrete Cosserat eigenvectors $\tilde{\mathbf{u}}_n$. Once the discrete Cosserat eigenvalues and eigenvectors relating to the specific domain Ω are available, the solutions can be found by evaluating the coefficients f_n of the corresponding Cosserat eigenvectors $\tilde{\mathbf{u}}_n$. The pressure is closely related to the divergence of the Cosserat eigenvectors div $\tilde{\mathbf{u}}_n$.

By applying the Cosserat spectrum theory, we present the analytical solutions of the Stokes flows over a sphere with three different free stream profiles. The second parts $\mathbf{u}_c$ of the Stokes flows with the uniform, extensional, and shear freestreams are contributed from the discrete Cosserat eigenfunctions $\tilde{\mathbf{u}}_1$, $\tilde{\mathbf{u}}_2$, and $\tilde{\mathbf{u}}_{2,1}$, respectively. These Stokes flow solutions are in agreement with those presented by Chwang and Wu (1975) who used the method of surface singularities.

Acknowledgment

The authors would like to thank Prof. X. Markenscoff of UCSD for introducing them to the Cosserat spectrum theory.

Downloaded 04 May 2010 to 171.66.16.27. Redistribution subject to ASME license or copyright; see http://www.asme.org/terms/Terms_Use.cfm

References

Chwang, A. T., and Wu, T. Y., 1975, "Hydromechanics of Low-Reynolds-Number Flow. Part 2. Singularity Method for Stokes Flows," *Journal of Fluid Mechanics,* Vol. 67, No. 4, pp. 787–815.

Cosserat, E., and Cosserat, F., 1898, "Sur les equations de la theorie de l'elasticite," *C. R. Acad. Sci. Paris,* Vol. 126, pp. 1089–1091.

Hill, E. L., 1954, "The Theory of Vector Spherical Harmonics," *American Journal of Physics,* Vol. 22, pp. 211–214.

Liu, W., 1998, "The Cosserat Spectrum Theory and its Applications," Ph.D. dissertation, Joint Doctoral Program in Engineering Sciences/Applied Mechanics, University of California, San Diego and San Diego State University.

Markenscoff, X., and Paukshto, M. V., 1998, "The Cosserat Spectrum in the Theory of Elasticity and Applications," *Proc. R. Soc. Lond.,* Vol. A454, pp. 631–643.

Mikhlin, S. G., 1973, "The Spectrum of a Family of Operators in the Theory of Elasticity," *Uspekhi Mat. Nauk* (in Russian), Vol. 28, No. 3, pp. 43–82; English translation in *Russian Math Surveys,* Vol. 28, No. 3, pp. 45–88.

Nonlinear Thermal Vibrations on Elastic Shallow Spherical Shell Under Linear and Parabolic Temperature Distributions

U. K. Mandal[1] and P. Biswas[2]

Introduction

Nonlinear dynamic behavior of shell structures under thermal loading is of some technical importance to designers. Compared to linear analysis, very few problems have been dealt with for nonlinear vibrations of thermally stressed thin shallow shells.

In this brief note, basic governing equations in the von Karman sense have been derived in terms of displacement components with the inclusion of thermal loading. These equations are solved by Galerkin's method considering linear and parabolic temperature fields. Tangential clamped movable and immovable edge conditions are considered. A parametric study of such structures is presented.

Governing Differential Equations and Solution

A thin shallow axisymmetric spherical shell, made of elastic, homogeneous, and isotropic material of uniform thickness is considered. Figure 1 shows the shell geometry, coordinate system, and displacement components. The function $z(r)$ is represented by

$$z(r) = \frac{R^2}{2R_0}\left[1 - \frac{r^2}{R^2}\right]. \tag{1}$$

The temperature field, independent of θ and z coordinates, is assumed as follows:

$$T(r) = T_0\left[1 - \left[\frac{r}{R}\right]^i\right] \tag{2}$$

where $i = 1$ and 2 for linear and parabolic variations of temperature, respectively, and T_0 = temperature at the center of the shell.

The governing equations of nonlinear thermal vibrations, for such structures in the von Karman sense with usual notations, are derived in the forms

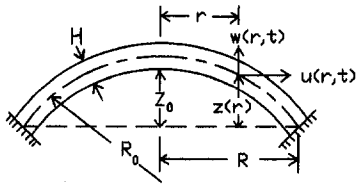


Fig. 1 Shell geometry and the coordinate systems

$$r^2u_{,rr} + ru_{,r} - u = \frac{(\nu - 1)}{2} rw_{,r}^2 + (\nu - 1)rw_{,r}z_{,r}$$

$$- r^2w_{,r}w_{,rr} - r^2(w_{,r}z_{,rr} + w_{,rr}z_{,r}) + \frac{r^2(1 - \nu^2)}{EH}(N_T)_{,r} \tag{3}$$

$$D\nabla^4 w + \rho H w_{,tt} + \nabla^2 M_T = \frac{1}{r}(rN_{rr}w_{,r})_{,r}. \tag{4}$$

The deflection $w(r, t)$ is assumed as

$$w(r, t) = A\left[1 - \frac{r^2}{R^2}\right]^2 F(t). \tag{5}$$

Using Eqs. (3) and (4) and applying Galerkin's method yields a cubic time-differential equation whose solution, with initial conditions $F(0) = 1$ and $F_{,t}(0) = 1$, after Bhattacharya (1976), is given by

$$\frac{{}^{\omega}NL}{\omega_L} = \left[1 + \frac{A^2}{H^2}\left[\frac{3}{4}\frac{\lambda_3}{\lambda_1} - \frac{5}{6}\left[\frac{\lambda_2}{\lambda_1}\right]^2\right]\right]^{1/2} \tag{6}$$

where ${}^{\omega}NL$ is the nonlinear frequency and ω_L is the linear frequency of the structure. The parameters λ's are known.

Numerical Results, Observations, and Discussions

Numerical results are presented in this section to understand the effects of different parameters viz. (i) nondimensional curvature $\xi = (R^2/R_0H)$ (Fig. 2), (ii) nondimensional amplitude A/H (Fig. 3), (iii) R/H ratio (Fig. 4), and (iv) temperature fields and its magnitude T_0 (Fig. 5), etc., on dynamic behavior of such structures. For illustrative examples material properties are considered as follows: $\nu = 0.3$; $\rho = 7.833 \times 10^{-6}$ kg/mm^3; $E = 2.0 \times 10^5$ N/mm^2; $\alpha_t = 12 \times 10^{-6}$/°C.

Both hardening and softening types of behavior are observed for both edge conditions. The behavior changes from hardening to softening type when ξ becomes greater than the transition value. Similar behaviors are also observed by Sinharay and Banerjee (1985) with some numerical deviations due to different ap-

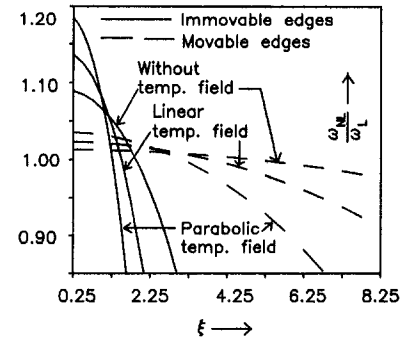


Fig. 2 Variation of ${}^{\omega}NL/\omega_L$ with ξ when A/H = 1.0 and R/H = 50.0 (for movable edges T_0 = 500.0°C and immovable edges T_0 = 50.0°C)

[1] Lecturer in Civil Engineering, Jalpaiguri Government Engineering College, Jalpaiguri 735102, West Bengal, India.

[2] Reader in Mathematics, P. D. Women's College, Jalpaiguri 725101, West Bengal, India. Presently, Principal, A. C. College of Commerce, Jalpaiguri 735101, West Bengal, India.

Contributed by the Applied Mechanics Division of THE AMERICAN SOCIETY OF MECHANICAL ENGINEERS for publication in the ASME JOURNAL OF APPLIED MECHANICS. Manuscript received by the ASME Applied Mechanics Division, June 8, 1998; final

Downloaded 04 May 2010 to 171.66.16.27. Redistribution subject to ASME license or copyright; see http://www.asme.org/terms/Terms_Use.cfm

References

Chwang, A. T., and Wu, T. Y., 1975, "Hydromechanics of Low-Reynolds-Number Flow. Part 2. Singularity Method for Stokes Flows," *Journal of Fluid Mechanics,* Vol. 67, No. 4, pp. 787–815.

Cosserat, E., and Cosserat, F., 1898, "Sur les equations de la theorie de l'elasticite," *C. R. Acad. Sci. Paris,* Vol. 126, pp. 1089–1091.

Hill, E. L., 1954, "The Theory of Vector Spherical Harmonics," *American Journal of Physics,* Vol. 22, pp. 211–214.

Liu, W., 1998, "The Cosserat Spectrum Theory and its Applications," Ph.D. dissertation, Joint Doctoral Program in Engineering Sciences/Applied Mechanics, University of California, San Diego and San Diego State University.

Markenscoff, X., and Paukshto, M. V., 1998, "The Cosserat Spectrum in the Theory of Elasticity and Applications," *Proc. R. Soc. Lond.,* Vol. A454, pp. 631–643.

Mikhlin, S. G., 1973, "The Spectrum of a Family of Operators in the Theory of Elasticity," *Uspekhi Mat. Nauk* (in Russian), Vol. 28, No. 3, pp. 43–82; English translation in *Russian Math Surveys,* Vol. 28, No. 3, pp. 45–88.

Nonlinear Thermal Vibrations on Elastic Shallow Spherical Shell Under Linear and Parabolic Temperature Distributions

U. K. Mandal[1] and P. Biswas[2]

Introduction

Nonlinear dynamic behavior of shell structures under thermal loading is of some technical importance to designers. Compared to linear analysis, very few problems have been dealt with for nonlinear vibrations of thermally stressed thin shallow shells.

In this brief note, basic governing equations in the von Karman sense have been derived in terms of displacement components with the inclusion of thermal loading. These equations are solved by Galerkin's method considering linear and parabolic temperature fields. Tangential clamped movable and immovable edge conditions are considered. A parametric study of such structures is presented.

Governing Differential Equations and Solution

A thin shallow axisymmetric spherical shell, made of elastic, homogeneous, and isotropic material of uniform thickness is considered. Figure 1 shows the shell geometry, coordinate system, and displacement components. The function $z(r)$ is represented by

$$z(r) = \frac{R^2}{2R_0}\left[1 - \frac{r^2}{R^2}\right]. \tag{1}$$

The temperature field, independent of θ and z coordinates, is assumed as follows:

$$T(r) = T_0\left[1 - \left[\frac{r}{R}\right]^i\right] \tag{2}$$

where $i = 1$ and 2 for linear and parabolic variations of temperature, respectively, and T_0 = temperature at the center of the shell.

The governing equations of nonlinear thermal vibrations, for such structures in the von Karman sense with usual notations, are derived in the forms

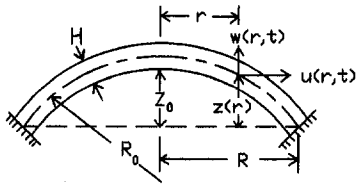


Fig. 1 Shell geometry and the coordinate systems

$$r^2u_{,rr} + ru_{,r} - u = \frac{(\nu - 1)}{2} rw_{,r}^2 + (\nu - 1)rw_{,r}z_{,r}$$

$$- r^2w_{,r}w_{,rr} - r^2(w_{,r}z_{,rr} + w_{,rr}z_{,r}) + \frac{r^2(1 - \nu^2)}{EH}(N_T)_{,r} \tag{3}$$

$$D\nabla^4 w + \rho H w_{,tt} + \nabla^2 M_T = \frac{1}{r}(rN_{rr}w_{,r})_{,r}. \tag{4}$$

The deflection $w(r, t)$ is assumed as

$$w(r, t) = A\left[1 - \frac{r^2}{R^2}\right]^2 F(t). \tag{5}$$

Using Eqs. (3) and (4) and applying Galerkin's method yields a cubic time-differential equation whose solution, with initial conditions $F(0) = 1$ and $F_{,t}(0) = 1$, after Bhattacharya (1976), is given by

$$\frac{{}^{\omega}NL}{\omega_L} = \left[1 + \frac{A^2}{H^2}\left[\frac{3}{4}\frac{\lambda_3}{\lambda_1} - \frac{5}{6}\left[\frac{\lambda_2}{\lambda_1}\right]^2\right]\right]^{1/2} \tag{6}$$

where ${}^{\omega}NL$ is the nonlinear frequency and ω_L is the linear frequency of the structure. The parameters λ's are known.

Numerical Results, Observations, and Discussions

Numerical results are presented in this section to understand the effects of different parameters viz. (i) nondimensional curvature $\xi = (R^2/R_0H)$ (Fig. 2), (ii) nondimensional amplitude A/H (Fig. 3), (iii) R/H ratio (Fig. 4), and (iv) temperature fields and its magnitude T_0 (Fig. 5), etc., on dynamic behavior of such structures. For illustrative examples material properties are considered as follows: $\nu = 0.3$; $\rho = 7.833 \times 10^{-6}$ kg/mm^3; $E = 2.0 \times 10^5$ N/mm^2; $\alpha_t = 12 \times 10^{-6}$/°C.

Both hardening and softening types of behavior are observed for both edge conditions. The behavior changes from hardening to softening type when ξ becomes greater than the transition value. Similar behaviors are also observed by Sinharay and Banerjee (1985) with some numerical deviations due to different ap-

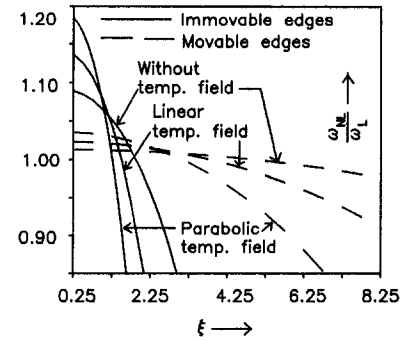


Fig. 2 Variation of ${}^{\omega}NL/\omega_L$ with ξ when A/H = 1.0 and R/H = 50.0 (for movable edges T_0 = 500.0°C and immovable edges T_0 = 50.0°C)

[1] Lecturer in Civil Engineering, Jalpaiguri Government Engineering College, Jalpaiguri 735102, West Bengal, India.

[2] Reader in Mathematics, P. D. Women's College, Jalpaiguri 725101, West Bengal, India. Presently, Principal, A. C. College of Commerce, Jalpaiguri 735101, West Bengal, India.

Contributed by the Applied Mechanics Division of THE AMERICAN SOCIETY OF MECHANICAL ENGINEERS for publication in the ASME JOURNAL OF APPLIED MECHANICS. Manuscript received by the ASME Applied Mechanics Division, June 8, 1998; final

Downloaded 04 May 2010 to 171.66.16.27. Redistribution subject to ASME license or copyright; see http://www.asme.org/terms/Terms_Use.cfm

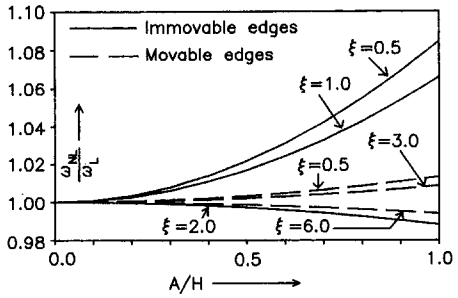


Fig. 3 Variation of $^{\omega}NL/\omega_L$ with A/H

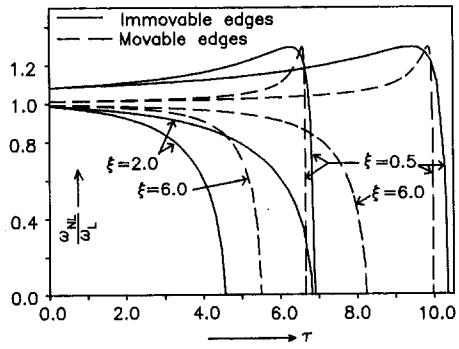


Fig. 4 Variation of $^{\omega}NL/\omega_L$ with T_0 (°C) when A/H = 1.0 and R/H = 50.0 (for movable edges $T_0 = 12.5\tau$ and immovable edges $T_0 = 120\tau$)

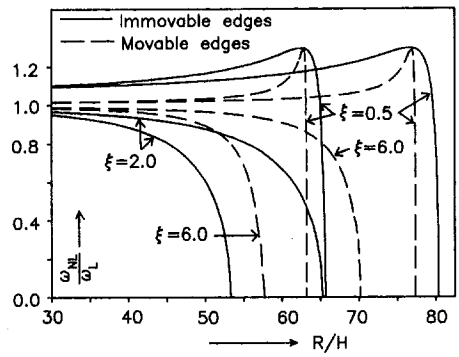


Fig. 5 Variation of $^{\omega NL/\omega L}$ with R/H when A/H = 1.0 (for movable edges T_0 = 500.0°C and immovable edges T_0 = 50.0°C)

proaches. For a particular value of A/H and for ξ, which is less than the transition value, it is observed that with increase of T_0 and R/H, the relative nonlinear frequency increases up to a maximum value at a certain point and then decreases abruptly to zero. Again, for a particular value A/H and for ξ, greater than the transition value, the relative nonlinear frequency decreases with increase of T_0 and R/H at a slower rate and after a certain point it decreases abruptly to zero.

Acknowledgment

The second author (P. Biswas) acknowledges receipt of financial support from the University Grant Commission, New Delhi-11002 in partial fulfillment of a Major Research Project.

References

Bhattacharya, A. P., 1976, "Nonlinear Flexural Vibrations of Thin Shallow Translational Shells," ASME JOURNAL OF APPLIED MECHANICS, Vol. 43, pp. 180–182.

Sinharay, G. C., and Banerjee, B., 1985, "Large Amplitude Free Vibration of Shallow Spherical Shell and Cylindrical Shell—A New Approach," *Int. Journal of Non-linear Mechanics,* Vol. 20, No. 2, pp. 69–78.

Moment Value at the Center of Circular Plates Under Central Point Load

C. M. Wang[1] and C. H. Ang[1]

It is a well-known fact that the bending moment at the center of a circular plate under a central point load becomes infinite. So, "what is a sensible finite moment value, that one may adopt, at the center of a circular plate under a central point load?" This study addresses this interesting and fundamental question. In order to obtain a finite value to the bending moment, we draw upon the exact deflection expressions from the classical and higher-order plate theories of Mindlin and of Reddy, and make some reasonable assumptions such as the maximum deflection of Mindlin plate being equal to the maximum deflection of the corresponding Reddy plate and the constancy of the Mindlin shear correction factor.

Introduction

It is well known that the bending moment at the center of a circular plate under a point load is unbounded (see standard texts on plates, for example, Timoshenko and Woinowsky-Krieger, 1959). This moment singularity occurs whether one adopts the Kirchhoff (or classical thin) plate theory, or the first-order shear deformation plate theory of Mindlin (1951), or the third-order shear deformation plate theory of Reddy (1984, 1997). Also, the central deflection value is unbounded for the aforementioned loaded plate when using the Mindlin plate theory because (a) the deflection component due to the transverse shear deformation is a function of the bending moment of the Kirchhoff plate and (b) the fact that the Mindlin shear correction factor is assumed to take on a constant value.

This gives rise to the often-asked question, "What is a sensible moment value that one may adopt at the center of a circular plate undergoing axisymmetric bending due to a central point load?" To provide an answer to this question, we shall draw on the interesting features found in the exact deflection expressions obtained from the classical and the higher-order plate theories such as the Mindlin and Reddy plate theories. We propose that the infinite central deflection value of a circular Mindlin plate be made finite by equating it with the finite central deflection value of the corresponding circular Reddy plate. This assumption is reasonable as it is known among researchers, working in higher-order plate theories, that the maximum deflection values of a transversely loaded, isotropic Mindlin plate and its corresponding Reddy plate are somewhat close to each other. The foregoing assumption leads to an expression for the bending moment value that is finite provided the Mindlin shear correction factor is approximated by a constant value. We obtain this constant value by studying the case of circular plates under a partial uniform load about the plate center and calibrating the Mindlin correction factor using the Reddy plate solutions.

Deflection and Moment Expressions From Various Plate Theories

Kirchhoff Plate Theory. Based on the Kirchhoff plate theory, the axisymmetric transverse deflection function $w(r)$ of the middle

[1] Department of Civil Engineering, The National University of Singapore, Kent Ridge, Singapore 119260.

Contributed by the Applied Mechanics Division of THE AMERICAN SOCIETY OF MECHANICAL ENGINEERS for publication in the ASME JOURNAL OF APPLIED MECHANICS. Manuscript received by the ASME Applied Mechanics Division, July 24, 1997; final revision, Nov. 26, 1997. Associate Technical Editor: J. N. Reddy.

Downloaded 04 May 2010 to 171.66.16.27. Redistribution subject to ASME license or copyright; see http://www.asme.org/terms/Terms_Use.cfm

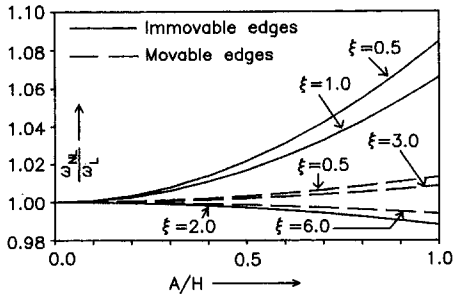


Fig. 3 Variation of $^{\omega}NL/\omega_L$ with A/H

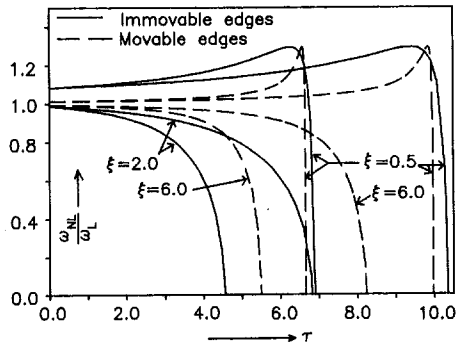


Fig. 4 Variation of $^{\omega}NL/\omega_L$ with T_0 (°C) when A/H = 1.0 and R/H = 50.0 (for movable edges $T_0 = 12.5\tau$ and immovable edges $T_0 = 120\tau$)

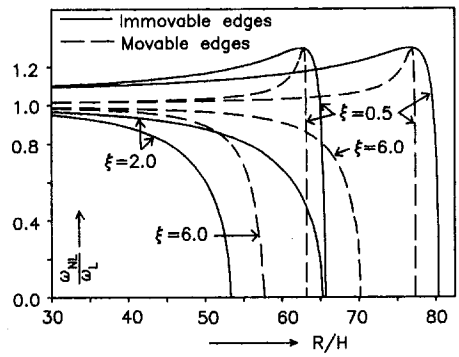


Fig. 5 Variation of $^{\omega NL/\omega L}$ with R/H when A/H = 1.0 (for movable edges T_0 = 500.0°C and immovable edges T_0 = 50.0°C)

proaches. For a particular value of A/H and for ξ, which is less than the transition value, it is observed that with increase of T_0 and R/H, the relative nonlinear frequency increases up to a maximum value at a certain point and then decreases abruptly to zero. Again, for a particular value A/H and for ξ, greater than the transition value, the relative nonlinear frequency decreases with increase of T_0 and R/H at a slower rate and after a certain point it decreases abruptly to zero.

Acknowledgment

The second author (P. Biswas) acknowledges receipt of financial support from the University Grant Commission, New Delhi-11002 in partial fulfillment of a Major Research Project.

References

Bhattacharya, A. P., 1976, "Nonlinear Flexural Vibrations of Thin Shallow Translational Shells," ASME JOURNAL OF APPLIED MECHANICS, Vol. 43, pp. 180–182.

Sinharay, G. C., and Banerjee, B., 1985, "Large Amplitude Free Vibration of Shallow Spherical Shell and Cylindrical Shell—A New Approach," *Int. Journal of Non-linear Mechanics,* Vol. 20, No. 2, pp. 69–78.

Moment Value at the Center of Circular Plates Under Central Point Load

C. M. Wang[1] and C. H. Ang[1]

It is a well-known fact that the bending moment at the center of a circular plate under a central point load becomes infinite. So, "what is a sensible finite moment value, that one may adopt, at the center of a circular plate under a central point load?" This study addresses this interesting and fundamental question. In order to obtain a finite value to the bending moment, we draw upon the exact deflection expressions from the classical and higher-order plate theories of Mindlin and of Reddy, and make some reasonable assumptions such as the maximum deflection of Mindlin plate being equal to the maximum deflection of the corresponding Reddy plate and the constancy of the Mindlin shear correction factor.

Introduction

It is well known that the bending moment at the center of a circular plate under a point load is unbounded (see standard texts on plates, for example, Timoshenko and Woinowsky-Krieger, 1959). This moment singularity occurs whether one adopts the Kirchhoff (or classical thin) plate theory, or the first-order shear deformation plate theory of Mindlin (1951), or the third-order shear deformation plate theory of Reddy (1984, 1997). Also, the central deflection value is unbounded for the aforementioned loaded plate when using the Mindlin plate theory because (a) the deflection component due to the transverse shear deformation is a function of the bending moment of the Kirchhoff plate and (b) the fact that the Mindlin shear correction factor is assumed to take on a constant value.

This gives rise to the often-asked question, "What is a sensible moment value that one may adopt at the center of a circular plate undergoing axisymmetric bending due to a central point load?" To provide an answer to this question, we shall draw on the interesting features found in the exact deflection expressions obtained from the classical and the higher-order plate theories such as the Mindlin and Reddy plate theories. We propose that the infinite central deflection value of a circular Mindlin plate be made finite by equating it with the finite central deflection value of the corresponding circular Reddy plate. This assumption is reasonable as it is known among researchers, working in higher-order plate theories, that the maximum deflection values of a transversely loaded, isotropic Mindlin plate and its corresponding Reddy plate are somewhat close to each other. The foregoing assumption leads to an expression for the bending moment value that is finite provided the Mindlin shear correction factor is approximated by a constant value. We obtain this constant value by studying the case of circular plates under a partial uniform load about the plate center and calibrating the Mindlin correction factor using the Reddy plate solutions.

Deflection and Moment Expressions From Various Plate Theories

Kirchhoff Plate Theory. Based on the Kirchhoff plate theory, the axisymmetric transverse deflection function $w(r)$ of the middle

[1] Department of Civil Engineering, The National University of Singapore, Kent Ridge, Singapore 119260.

Contributed by the Applied Mechanics Division of THE AMERICAN SOCIETY OF MECHANICAL ENGINEERS for publication in the ASME JOURNAL OF APPLIED MECHANICS. Manuscript received by the ASME Applied Mechanics Division, July 24, 1997; final revision, Nov. 26, 1997. Associate Technical Editor: J. N. Reddy.

Downloaded 04 May 2010 to 171.66.16.27. Redistribution subject to ASME license or copyright; see http://www.asme.org/terms/Terms_Use.cfm

surface of a circular plate a central point load P is given by (Szilard, 1974)

$$w^K(r) = \begin{cases} \dfrac{Pa^2}{16\pi D}\left[\left(1-\dfrac{r^2}{a^2}\right)+2\dfrac{r^2}{a^2}\ln\dfrac{r}{a}\right], \\ \quad \text{for clamped plate} \\ \dfrac{Pa^2}{16\pi D}\left[\left(\dfrac{3+\nu}{1+\nu}\right)\left(1-\dfrac{r^2}{a^2}\right)+2\dfrac{r^2}{a^2}\ln\dfrac{r}{a}\right], \\ \quad \text{for simply supported plate} \end{cases} \tag{1}$$

where a is the radius of the circular plate, $D = Eh^3/[12(1-\nu^2)]$ the flexural rigidity of the plate, E the modulus of elasticity, h the plate thickness, ν the Poisson's ratio, r the radial coordinate measured from the plate center, and the superscript K denotes the quantity in the Kirchhoff plate theory.

The radial and circumferential bending moments are, respectively, given by

$$M_{rr}^K(r) = \begin{cases} -\dfrac{P}{4\pi}\left[1+(1+\nu)\ln\dfrac{r}{a}\right], \\ \quad \text{for clamped plate} \\ -\dfrac{P}{4\pi}(1+\nu)\ln\dfrac{r}{a}, \\ \quad \text{for simply supported plate} \end{cases} \tag{2a}$$

$$M_{\theta\theta}^K(r) = \begin{cases} -\dfrac{P}{4\pi}\left[\nu+(1+\nu)\ln\dfrac{r}{a}\right], \\ \quad \text{for clamped plate} \\ \dfrac{P}{4\pi}\left[(1-\nu)-(1+\nu)\ln\dfrac{r}{a}\right], \\ \quad \text{for simply supported plate} \end{cases} \tag{2b}$$

Mindlin Plate Theory. Recently, Wang and Lee (1996) showed that the relationships between the bending solutions of Mindlin circular plates and the corresponding Kirchhoff circular plates are given by

$$w^M(r) = w^K(r) + \frac{\mathcal{M}^K(r) - \mathcal{M}^K(a)}{\kappa^2 Gh} = w^K(r) - \frac{P}{2\pi\kappa^2 Gh}\ln\left(\frac{r}{a}\right) \tag{3}$$

$$M_{rr}^M = M_{rr}^K \quad \text{and} \quad M_{\theta\theta}^M = M_{\theta\theta}^K \tag{4a, b}$$

where $\mathcal{M} = (M_{rr} + M_{\theta\theta})/(1+\nu)$ is the moment sum, G the shear modulus, κ^2 the shear correction factor, and the superscript M denotes the quantities in the Mindlin plate theory. The shear correction factor is introduced to compensate for the error of assuming a constant transverse shear stress distribution through the plate thickness in the Mindlin plate theory which violates the zero-stress requirement at the free plate surfaces. Note that (3) and (4a, b) are valid for both clamped plates and simply supported plates.

Reddy Plate Theory. More recently, Reddy and Wang (1998) derived the relationships for axisymmetric bending solutions of Reddy and Kirchhoff circular plates. The deflection relationships are given below:

$$w^R = w^K + \frac{3P}{5\pi Gh}\left\{\frac{1-\Omega K_1(\Omega)}{\Omega I_1(\Omega)}\left[I_0\left(\frac{\Omega r}{a}\right)-I_0(\Omega)\right] - \left[K_0\left(\frac{\Omega r}{a}\right)-K_0(\Omega)\right] - \ln\left(\frac{r}{a}\right)\right\}, \quad \text{for clamped plate} \tag{5a}$$

$$w^R = w^K + \frac{3P}{5\pi Gh}\left\{\frac{\Omega(1-\nu)K_1(\Omega)+\Omega^2K_0(\Omega)+\nu-1}{\Omega(\nu-1)I_1(\Omega)+\Omega^2I_0(\Omega)} \times\left[I_0\left(\frac{\Omega r}{a}\right)-I_0(\Omega)\right] - \left[K_0\left(\frac{\Omega r}{a}\right)-K_0(\Omega)\right] - \ln\left(\frac{r}{a}\right)\right\}, \quad \text{for simply supported plate} \tag{5b}$$

where $\Omega = (a/h)\sqrt{420(1-\nu)}$; $K_0(\cdot)$, $I_0(\cdot)$ are the modified Bessel functions of the first and second kind of the zeroth order; $K_1(\cdot)$, $I_1(\cdot)$ the modified Bessel functions of the first and second kind of the first order; and the superscript R denotes quantities in the Reddy plate theory. Note that in the Reddy plate theory, there is no need for a shear correction factor because the theory accounts for a quadratic distribution of the transverse shear stresses with zero values at the free surfaces.

Similar to the Mindlin plate case, Reddy and Wang (1998) have shown that the bending moments for Reddy plates are the same as those for Kirchhoff plates, i.e.

$$M_{rr}^R = M_{rr}^K \quad \text{and} \quad M_{\theta\theta}^R = M_{\theta\theta}^K. \tag{6a, b}$$

Proposed Finite Moment Values

In view of Eq. (1), the central deflection of the Kirchhoff plate is given by

$$w^K(0) = \begin{cases} \dfrac{Pa^2}{16\pi D}, & \text{for clamped plate} \\ \dfrac{Pa^2}{16\pi D}\left(\dfrac{3+\nu}{1+\nu}\right), & \text{for simply supported plate} \end{cases} \tag{7}$$

These deflection values are finite but the bending moments given by Eqs. (2a) and (2b) are infinite at the plate center (i.e., $= 0$) due to the presence of the logarithmic term $\ln(r/a)$.

From Eqs. (3) and (4), it is clear that both the Mindlin deflection and bending moments at the center of the circular plate under a point load are infinite! Note that the Mindlin deflection for this plate problem becomes infinite because the deflection component due to the transverse shear deformation is a function of the bending moments of the corresponding Kirchhoff plate and the assumption that the shear correction factor κ^2 is a constant value.

Although the Reddy plate bending moments at the plate center are infinite from Eqs. (6a, b) and (2a, b), the deflection at the plate center is, however, interestingly finite. In view of Eqs. (5a, b), the finite central deflection values for Reddy plates are given by

$$w^R(0) = \frac{Pa^2}{16\pi D} + \frac{3P}{5\pi Gh}\left\{\frac{1-\Omega K_1(\Omega)}{\Omega I_1(\Omega)}[1-I_0(\Omega)] + K_0(\Omega) + \gamma + \ln\left(\frac{\Omega}{2}\right)\right\}, \quad \text{for clamped plate} \tag{8a}$$

$$w^R(0) = \frac{Pa^2}{16\pi D}\left(\frac{3+\nu}{1+\nu}\right) + \frac{3P}{5\pi Gh}\left\{\frac{\Omega(1-\nu)K_1(\Omega)+\Omega^2K_0(\Omega)+\nu-1}{\Omega(\nu-1)I_1(\Omega)+\Omega^2I_0(\Omega)} \times[1-I_0(\Omega)] + K_0(\Omega) + \gamma + \ln\left(\frac{\Omega}{2}\right)\right\}, \quad \text{for simply supported plate} \tag{8b}$$

where γ is the Euler's constant, 0.5772157 . . . . Note that comparable deflection result for the case of the clamped plate was obtained by Lee et al. (1990) who used a higher-order plate theory which assumes that the in-plane rotation tensor does not vary across the plate thickness.

Based on the foregoing observations of the deflection values of

Downloaded 04 May 2010 to 171.66.16.27. Redistribution subject to ASME license or copyright; see http://www.asme.org/terms/Terms_Use.cfm

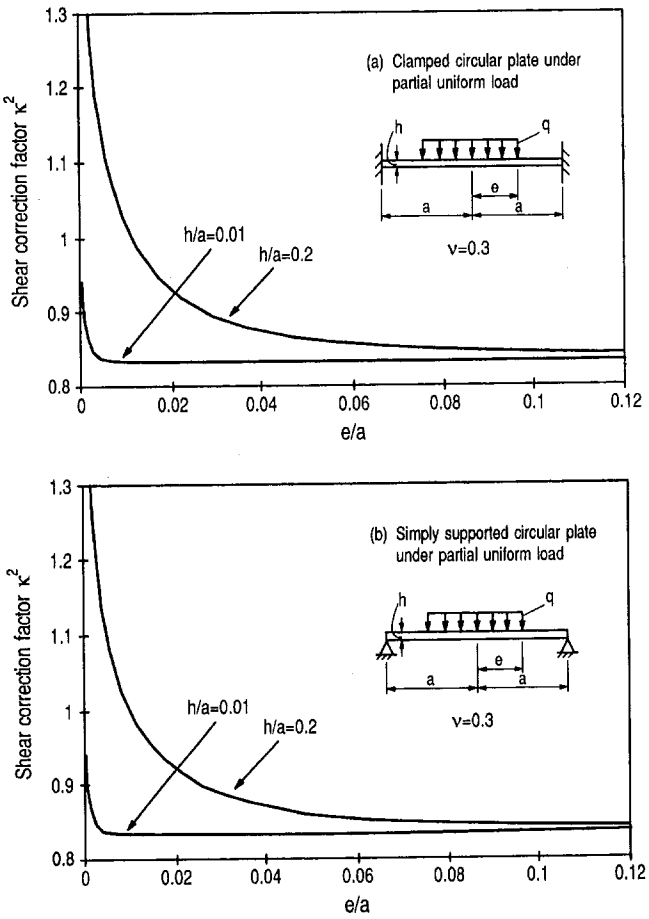


Fig. 1 Calibrated Mindlin shear correction factors using Reddy solutions for circular plates under partial uniform loading about plate center

the considered circular plate problem, finite values for the central bending moments will be proposed. From earlier studies (e.g., Lee et al., 1990; Reddy and Wang, 1998) it has been generally found that the maximum deflections for Mindlin and Reddy plates are more or less equal in the case of transversely loaded, isotropic plates. Consequently, a very reasonable approximation would be to let the central deflection values of the Mindlin and Reddy circular plates be equal. Thus, by setting

$$w^M(0) = w^R(0) \tag{9}$$

we obtain a finite central deflection value for the Mindlin plate. The substitution of Eqs. (3) and (8) into Eq. (9) yields

$$\mathcal{M}^K(0) = \kappa^2 Gh[w^R(0) - w^K(0)] + \mathcal{M}^K(a). \tag{10}$$

It can be seen that the assumption as stated in Eq. (9) leads to the above finite value of bending moment sum provided that the shear correction factor κ^2 is assumed to be finite. To obtain a reasonable approximation of this shear correction factor, we analyze a circular plate under a partial uniformly distributed load covering a radius e by using both the Mindlin and Reddy plate theories. By equating the maximum deflection values of the Mindlin and Reddy plates we may calibrate the Mindlin shear correction factors. The variations of the shear correction factor with respect to the load span e are shown in Figs. 1(a) and 1(b) for clamped plates and simply supported plates, respectively. As expected, the shear correction factor increases rapidly when $e \to 0$, since the correction factor becomes proportional to $-\ln(r/a)$ in the limit. In order to obtain a finite moment value we propose that the shear correction factor be taken as a constant value of $\kappa^2 = \frac{5}{6}$, which is approximately the value associated with the flat portion of the curves in Fig. 1. It must be emphasized that this assumption, although inconsistent with the actual variation of the shear correction factor shown in Fig. 1, is necessary if a finite central moment solution is to be obtained.

Using the proposed value of $\frac{5}{6}$ for the shear correction factor and Eq. (10), one then obtains a sensible finite value for the central moment sum given by

$$\mathcal{M}^K(0) = \frac{P}{2\pi}\left\{\frac{1-\Omega K_1(\Omega)}{\Omega I_1(\Omega)}[1 - I_0(\Omega)] + K_0(\Omega) + \gamma + \ln\left(\frac{\Omega}{2}\right) - \frac{1}{2}\right\}, \quad \text{for clamped plate} \tag{11a}$$

$$\mathcal{M}^K(0) = \frac{P}{2\pi}\left\{\frac{\Omega(1-\nu)K_1(\Omega) + \Omega^2 K_0(\Omega) + \nu - 1}{\Omega(\nu-1)I_1(\Omega) + \Omega^2 I_0(\Omega)} \times [1 - I_0(\Omega)] + K_0(\Omega) + \gamma + \ln\left(\frac{\Omega}{2}\right) + \frac{1-\nu}{2(1+\nu)}\right\},$$

for simply supported plate. (11b)

In view of Eqs. (2a) and (2b), the radial and circumferential bending moments at the plate center for both clamped and simply supported plates are thus given by

$$M_{rr}(0) = -\frac{P}{8\pi}(1-\nu) + \frac{1+\nu}{2}\mathcal{M}^K(0) \tag{12a}$$

$$M_{\theta\theta}(0) = \frac{P}{8\pi}(1-\nu) + \frac{1+\nu}{2}\mathcal{M}^K(0) \tag{12b}$$

where the central Marcus moment $\mathcal{M}^K(0)$ is given by Eq. (11). Note that Eq. (12) furnishes a finite bending moment value for a given load magnitude P, Poisson's ratio ν, and thickness-to-radius ratio h/a.

It is interesting to compare the proposed finite moment values given by Eqs. (11) and (12) with those usually taken by practicing engineers where the central moments are computed at the vicinity of the plate center. Table 1 shows a comparison example for $\nu = 0.3$, $h/a = 0.01$, and various values of r/a. The results show that the proposed finite moment values are somewhat close to those evaluated at $r/a = 10^{-3}$ for the considered plate thickness value and Poisson's ratio.

Concluding Remarks

This study presents a sensible moment value to an otherwise infinite moment value for a circular plate under a point load. The approximate central moment value is obtained from equating the central deflection values of circular plates analyzed according to the Mindlin plate theory and the Reddy plate theory and then making the assumption that the shear correction factor is a constant value. It is hoped that the solution obtained herein will be useful to

Table 1 Comparison of Moment Values ($\nu = 0.3$, $h/a = 0.01$)

Clamped circular plate	Eq. (2) with $r/a = 10^{-2}$	Eq. (2) with $r/a = 10^{-3}$	Eq. (2) with $r/a = 10^{-4}$	Eq. (11) and Eq. (12)
$\mathcal{M}^K(0)/P$	0.8494	1.3258	1.8022	1.0871
$M^K_{rr}(0)/P$	0.3968	0.6350	0.8732	0.6788
$M^K_{\theta\theta}(0)/P$	0.4525	0.6907	0.9289	0.7345
Simply supported circular plate	**Eq. (2) with $r/a = 10^{-2}$**	**Eq. (2) with $r/a = 10^{-3}$**	**Eq. (2) with $r/a = 10^{-4}$**	**Eq. (11) and Eq. (12)**
$\mathcal{M}^K(0)/P$	1.0085	1.4849	1.9613	1.2097
$M^K_{rr}(0)/P$	0.4764	0.7146	0.9528	0.7584
$M^K_{\theta\theta}(0)/P$	0.5321	0.7703	1.0085	0.8141

Downloaded 04 May 2010 to 171.66.16.27. Redistribution subject to ASME license or copyright; see http://www.asme.org/terms/Terms_Use.cfm

both academicians and practicing engineers who have been puzzled as to what value one may assign to the infinite moment value at the plate center.

Interestingly, this study also reveals a deficiency of the Mindlin plate theory in that the shear correction factor κ^2 is not uniform over the plate based on the calibration study using Reddy plate solutions.

Acknowledgment

The project is funded by Research Grant RP 950684 made available by The National University of Singapore. The first author is grateful to Assoc. Prof. K. H. Lee, Department of Mechanical and Production Engineering, The National University of Singapore, for his constructive comments on this study.

References

Lee, K. H., Senthilnathan, N. R., and Lim, S. P., 1990, "Axisymmetric bending of thick circular plates," *Mechanics Research Communications,* Vol. 17, No. 2, pp. 111–116.

Mindlin, R. D., 1951, "Influence of Rotary Inertia and Shear in Flexural Motion of Isotropic, Elastic Plates," ASME JOURNAL OF APPLIED MECHANICS, Vol. 18, pp. 1031–1036.

Reddy, J. N., 1984, "A Simple Higher-Order Theory for Laminated Composite Plates," ASME JOURNAL OF APPLIED MECHANICS, Vol. 51, pp. 745–752.

Reddy, J. N., 1997, *Mechanics of Laminated Composite Plates: Theory and Analysis,* CRC Press, Boca Raton, FL.

Reddy, J. N., and Wang, C. M., 1998, "Relationships between solutions of classical and shear deformation theories of axisymmetric bending of circular plates," *AIAA Journal,* Vol. 35, No. 12, pp. 1862–1868.

Szilard, R., 1974, *Theory and Analysis of Plates,* Prentice-Hall, Englewood Cliffs, NJ.

Timoshenko, S. P., and Woinowsky-Krieger, S., 1959, *Theory of Plates and Shells,* McGraw-Hill, New York.

Wang, C. M., and Lee, K. H., 1996, "Deflection and stress-resultants of axisymmetric Mindlin plates in terms of corresponding Kirchhoff solutions," *Int. J. Mech. Sci.,* Vol. 38, No. 11, pp. 1179–1185.

The Effect of Strain Rate on the Dynamic Expansion of Cylindrical Cavities

T. L. Warren[1]

Introduction

In a previous paper by Warren and Forrestal (1998) the authors developed models for the dynamic expansion of spherical cavities from zero initial radii in an infinite medium for elastic-plastic rate-dependent materials with power-law strain hardening. These models considered the material as incompressible and compressible. A closed-form solution was obtained for the incompressible material, whereas the compressible solution required the numerical solution of a set of coupled nonlinear ordinary differential equations.

In this brief note we develop a closed-form solution for the dynamic expansion of long cylindrical cavities (plane strain) from zero initial radii in an infinite medium for elastic-plastic rate-dependent materials with power-law strain hardening. With this model we require the plastic region to be incompressible and the elastic region to be compressible as done by Forrestal et al. (1990) for power-law strain-hardening materials. A physically realistic solution is not possible if both the plastic and elastic regions are considered to be incompressible due to the fact that the radial stress becomes infinite at an infinite radial distance as discussed by Crozier and Hunter (1970). Furthermore, the stress state associated with the cylindrical cavity expansion problem is not a hydrostatic tension superposed on a uniaxial compressive stress as with the spherical cavity expansion problem (Hill, 1950); therefore, a compressible solution can not be obtained using the method described by Warren and Forrestal (1998).

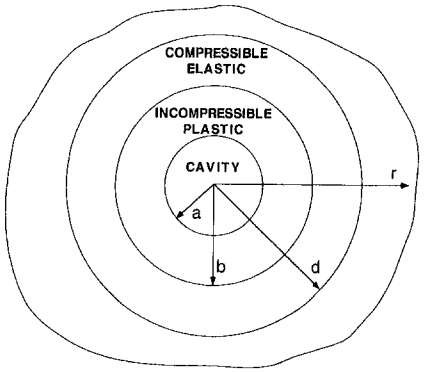


Fig. 1 Response regions for the cavity-expansion problem

Recent high strain-rate Hopkinson bar data (Mosher, 1996) and pressure-shear data (Yadav et al., 1995) have shown that 6061-T6511 aluminum is quite sensitive to strain rate as discussed by Warren and Forrestal (1998). In this note results are presented which illustrate the effect of strain rate on the expansion of cylindrical cavities in 6061-T6511 aluminum.

Analysis

For this problem a cylindrically symmetric cavity is expanded from zero initial radius to radius a as shown in Fig. 1. This expansion produces plastic and elastic response regions. The plastic region is bounded by the radii $r = a$ and $r = b$, where r is the radial Eulerian coordinate, $b = ct$ is the interface position between the plastic and elastic response regions, t is time, and c is the elastic-plastic interface velocity. Similarly, the elastic region is bounded by $r = b$ and $r = d$, where $d = c_d t$ and c_d is the elastic dilatational wave speed.

The material in the plastic region is assumed to be incompressible. The equations of momentum and mass conservation in Eulerian coordinates with cylindrical symmetry are

$$\frac{\partial \sigma_r}{\partial r} + \frac{(\sigma_r - \sigma_\theta)}{r} = -\rho\left(\frac{\partial v}{\partial t} + v\frac{\partial v}{\partial r}\right) \tag{1a}$$

$$\frac{\partial}{\partial r}[(r-u)^2] = 2r, \tag{1b}$$

where σ_r and σ_θ are the radial and hoop components of the Cauchy stress, measured positive in compression, and ρ is the material density. Particle displacement u and particle velocity v in the radial direction (outward motion taken positive) are related by

$$\frac{\partial u}{\partial t} = v\left(1 - \frac{\partial u}{\partial r}\right). \tag{2}$$

True strain rates and the logarithmic (true) strain-displacement relations are, respectively,

$$\dot{\epsilon}_r = -\frac{\partial v}{\partial r}, \quad \dot{\epsilon}_\theta = -\frac{v}{r}, \tag{3a,b}$$

and

[1] Sandia National Laboratories, P. O. Box 5800, Albuquerque, NM 87185-0315. Assoc. Mem. ASME.

Contributed by the Applied Mechanics Division of THE AMERICAN SOCIETY OF MECHANICAL ENGINEERS for publication in the ASME JOURNAL OF APPLIED MECHANICS. Manuscript received by the ASME Applied Mechanics Division, Aug. 26, 1998; final revision, Mar. 3, 1999. Associate Technical Editor: K. T. Ramesh.

Downloaded 04 May 2010 to 171.66.16.27. Redistribution subject to ASME license or copyright; see http://www.asme.org/terms/Terms_Use.cfm

both academicians and practicing engineers who have been puzzled as to what value one may assign to the infinite moment value at the plate center.

Interestingly, this study also reveals a deficiency of the Mindlin plate theory in that the shear correction factor κ^2 is not uniform over the plate based on the calibration study using Reddy plate solutions.

Acknowledgment

The project is funded by Research Grant RP 950684 made available by The National University of Singapore. The first author is grateful to Assoc. Prof. K. H. Lee, Department of Mechanical and Production Engineering, The National University of Singapore, for his constructive comments on this study.

References

Lee, K. H., Senthilnathan, N. R., and Lim, S. P., 1990, "Axisymmetric bending of thick circular plates," *Mechanics Research Communications,* Vol. 17, No. 2, pp. 111–116.

Mindlin, R. D., 1951, "Influence of Rotary Inertia and Shear in Flexural Motion of Isotropic, Elastic Plates," ASME JOURNAL OF APPLIED MECHANICS, Vol. 18, pp. 1031–1036.

Reddy, J. N., 1984, "A Simple Higher-Order Theory for Laminated Composite Plates," ASME JOURNAL OF APPLIED MECHANICS, Vol. 51, pp. 745–752.

Reddy, J. N., 1997, *Mechanics of Laminated Composite Plates: Theory and Analysis,* CRC Press, Boca Raton, FL.

Reddy, J. N., and Wang, C. M., 1998, "Relationships between solutions of classical and shear deformation theories of axisymmetric bending of circular plates," *AIAA Journal,* Vol. 35, No. 12, pp. 1862–1868.

Szilard, R., 1974, *Theory and Analysis of Plates,* Prentice-Hall, Englewood Cliffs, NJ.

Timoshenko, S. P., and Woinowsky-Krieger, S., 1959, *Theory of Plates and Shells,* McGraw-Hill, New York.

Wang, C. M., and Lee, K. H., 1996, "Deflection and stress-resultants of axisymmetric Mindlin plates in terms of corresponding Kirchhoff solutions," *Int. J. Mech. Sci.,* Vol. 38, No. 11, pp. 1179–1185.

The Effect of Strain Rate on the Dynamic Expansion of Cylindrical Cavities

T. L. Warren[1]

Introduction

In a previous paper by Warren and Forrestal (1998) the authors developed models for the dynamic expansion of spherical cavities from zero initial radii in an infinite medium for elastic-plastic rate-dependent materials with power-law strain hardening. These models considered the material as incompressible and compressible. A closed-form solution was obtained for the incompressible material, whereas the compressible solution required the numerical solution of a set of coupled nonlinear ordinary differential equations.

In this brief note we develop a closed-form solution for the dynamic expansion of long cylindrical cavities (plane strain) from zero initial radii in an infinite medium for elastic-plastic rate-dependent materials with power-law strain hardening. With this model we require the plastic region to be incompressible and the elastic region to be compressible as done by Forrestal et al. (1990) for power-law strain-hardening materials. A physically realistic solution is not possible if both the plastic and elastic regions are considered to be incompressible due to the fact that the radial stress becomes infinite at an infinite radial distance as discussed by Crozier and Hunter (1970). Furthermore, the stress state associated with the cylindrical cavity expansion problem is not a hydrostatic tension superposed on a uniaxial compressive stress as with the spherical cavity expansion problem (Hill, 1950); therefore, a compressible solution can not be obtained using the method described by Warren and Forrestal (1998).

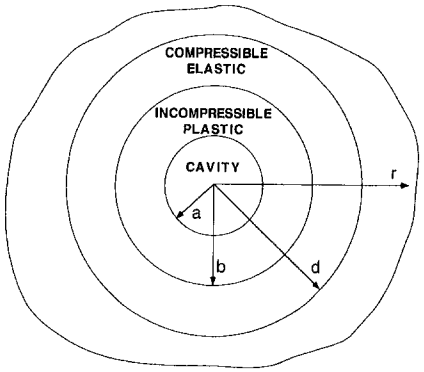


Fig. 1 Response regions for the cavity-expansion problem

Recent high strain-rate Hopkinson bar data (Mosher, 1996) and pressure-shear data (Yadav et al., 1995) have shown that 6061-T6511 aluminum is quite sensitive to strain rate as discussed by Warren and Forrestal (1998). In this note results are presented which illustrate the effect of strain rate on the expansion of cylindrical cavities in 6061-T6511 aluminum.

Analysis

For this problem a cylindrically symmetric cavity is expanded from zero initial radius to radius a as shown in Fig. 1. This expansion produces plastic and elastic response regions. The plastic region is bounded by the radii $r = a$ and $r = b$, where r is the radial Eulerian coordinate, $b = ct$ is the interface position between the plastic and elastic response regions, t is time, and c is the elastic-plastic interface velocity. Similarly, the elastic region is bounded by $r = b$ and $r = d$, where $d = c_d t$ and c_d is the elastic dilatational wave speed.

The material in the plastic region is assumed to be incompressible. The equations of momentum and mass conservation in Eulerian coordinates with cylindrical symmetry are

$$\frac{\partial \sigma_r}{\partial r} + \frac{(\sigma_r - \sigma_\theta)}{r} = -\rho\left(\frac{\partial v}{\partial t} + v\frac{\partial v}{\partial r}\right) \tag{1a}$$

$$\frac{\partial}{\partial r}[(r-u)^2] = 2r, \tag{1b}$$

where σ_r and σ_θ are the radial and hoop components of the Cauchy stress, measured positive in compression, and ρ is the material density. Particle displacement u and particle velocity v in the radial direction (outward motion taken positive) are related by

$$\frac{\partial u}{\partial t} = v\left(1 - \frac{\partial u}{\partial r}\right). \tag{2}$$

True strain rates and the logarithmic (true) strain-displacement relations are, respectively,

$$\dot{\epsilon}_r = -\frac{\partial v}{\partial r}, \quad \dot{\epsilon}_\theta = -\frac{v}{r}, \tag{3a,b}$$

and

[1] Sandia National Laboratories, P. O. Box 5800, Albuquerque, NM 87185-0315. Assoc. Mem. ASME.

Contributed by the Applied Mechanics Division of THE AMERICAN SOCIETY OF MECHANICAL ENGINEERS for publication in the ASME JOURNAL OF APPLIED MECHANICS. Manuscript received by the ASME Applied Mechanics Division, Aug. 26, 1998; final revision, Mar. 3, 1999. Associate Technical Editor: K. T. Ramesh.

Downloaded 04 May 2010 to 171.66.16.27. Redistribution subject to ASME license or copyright; see http://www.asme.org/terms/Terms_Use.cfm

$$\epsilon_r = \ln\left(1 - \frac{\partial u}{\partial r}\right), \quad \epsilon_\theta = \ln\left(1 - \frac{u}{r}\right), \qquad (4a,b)$$

where $(\dot{\ldots}) \equiv d(\ldots)/dt$ (i.e., material derivative operator), and for an incompressible material under plane-strain conditions $\epsilon_r = -\epsilon_\theta$ and $\epsilon_z = 0$.

The constitutive equation used for our analysis is the same as that used by Warren and Forrestal (1998) for the spherical cavity expansion problem. For a state of uniaxial stress, the stress-strain relation is given by

$$\sigma = \begin{cases} E\epsilon, & \sigma \le Y_d \\ Y\left(\frac{E\epsilon}{Y_d}\right)^n + \alpha\left(\frac{\dot{\epsilon}}{\dot{\epsilon}_o}\right)^m, & \sigma > Y_d \end{cases}, \qquad (5a,b)$$

where σ is the Cauchy stress (true stress), ϵ is the logarithmic strain (true strain), $\dot{\epsilon}$ is the strain rate, E is Young's modulus, Y is the quasi-static yield strength, n is the strain-hardening exponent, m is the strain-rate sensitivity exponent, $\dot{\epsilon}_o$ is a reference strain rate, α is a curve fitting parameter with units of stress, and Y_d is the dynamic yield stress given by

$$Y_d = Y + \alpha\left(\frac{\dot{\epsilon}}{\dot{\epsilon}_o}\right)^m. \qquad (5c)$$

The first term in (5*b*) is similar to the modified Ludwik equation (Chakrabarty, 1987) that describes strain hardening and the second term describes the increase in yield stress due to the strain-rate effects (Yadav et al., 1995).

Plastic flow is introduced by the method presented by Forrestal (1990). We assume that the octahedral shear stress τ_n is a definite function of the octahedral shear strain γ_n and strain rate $\dot{\gamma}_n$ for all strain configurations. For a uniaxial compression test

$$\tau_n = \sqrt{2}\sigma/3, \quad \gamma_n = \sqrt{2}\epsilon, \quad \dot{\gamma}_n = \sqrt{2}\dot{\epsilon}. \qquad (6a\text{–}c)$$

Substitution of (6) into (5*b*) gives the relation

$$\frac{3\tau_n}{\sqrt{2}} = Y\left[\frac{E\gamma_n}{\sqrt{2}Y_d}\right]^n + \alpha\left[\frac{\dot{\gamma}_n}{\sqrt{2}\dot{\epsilon}_o}\right]^m. \qquad (7)$$

For the cylindrical cavity-expansion problem with incompressibility and plane-strain conditions $\sigma_z = (\sigma_r + \sigma_\theta)/2$, and

$$\tau_n = \tfrac{1}{3}\sqrt{\tfrac{3}{2}}(\sigma_r - \sigma_\theta), \quad \gamma_n = 2\sqrt{\tfrac{2}{3}}\epsilon_r, \quad \dot{\gamma}_n = 2\sqrt{\tfrac{2}{3}}\dot{\epsilon}_r. \qquad (8a\text{–}c)$$

Plastic flow for the cylindrical cavity-expansion problem is obtained by substituting (8) into (7). Thus,

$$\sigma_r - \sigma_\theta = \left(\frac{2}{\sqrt{3}}\right)^{1+n} Y\left[\frac{E\epsilon_r}{Y_d}\right]^n + \left(\frac{2}{\sqrt{3}}\right)^{1+m} \alpha\left(\frac{\dot{\epsilon}_r}{\dot{\epsilon}_o}\right)^m, \qquad (9a)$$

$$Y_d = Y + \left(\frac{2}{\sqrt{3}}\right)^m \alpha\left(\frac{\dot{\epsilon}_r}{\dot{\epsilon}_o}\right)^m. \qquad (9b)$$

The boundary condition at the cavity surface $r = a$ is $u = a(t)$. Integrating (1*b*) subject to this condition gives the radial particle displacement as

$$u = r\left[1 - \left(1 - \frac{a^2}{r^2}\right)^{1/2}\right]. \qquad (10)$$

Particle velocity in the radial direction is obtained by differentiating (10) and substituting into (2) giving

$$v = \frac{a\dot{a}}{r}, \qquad (11)$$

where the cavity radius a is only a function of time. From (3) and (11) the strain rates are

$$\dot{\epsilon}_r = \frac{a\dot{a}}{r^2}, \quad \dot{\epsilon}_\theta = -\frac{a\dot{a}}{r^2}, \qquad (12)$$

and from the plane-strain condition $\dot{\epsilon}_z = 0$. Substituting (4), (9*b*), (10), and (12) into (9*a*) allows the yield criterion to be expressed in terms of the radial distance r and cavity radius a. Thus,

$$\sigma_r - \sigma_\theta = \left(\frac{2}{\sqrt{3}}\right)^{1+n} Y^{1-n}E^n\left[\frac{-\frac{1}{2}\ln\left(1 - (a/r)^2\right)}{1 + \psi\dot{a}^m(a/r)^{2m}}\right]^n + \left(\frac{2}{\sqrt{3}}\right)^{1+m}\alpha\left(\frac{a\dot{a}}{r^2\dot{\epsilon}_o}\right)^m, \qquad (13a)$$

where

$$\psi = \frac{\alpha}{Y}\left(\frac{2}{\sqrt{3}a\dot{\epsilon}_o}\right)^m. \qquad (13b)$$

Conservation of momentum (1*a*) in the plastic region $a \le r \le b$ can be expressed in terms of r and a using (11) and (13). Then integrating with respect to r throughout the plastic region gives

$$\sigma_r(a) = \sigma_r(b) + \left(\frac{2}{\sqrt{3}}\right)^{1+n} Y\left(\frac{E}{Y}\right)^n \int_a^b \left[\frac{-\frac{1}{2}\ln\left(1 - (a/r)^2\right)}{1 + \psi\dot{a}^m(a/r)^{2m}}\right]^n \frac{dr}{r} - \frac{\alpha}{2m}\left(\frac{2}{\sqrt{3}}\right)^{1+m}\left(\frac{a\dot{a}}{\dot{\epsilon}_o}\right)^m\left(\frac{1}{b^{2m}} - \frac{1}{a^{2m}}\right) + \rho\left[(\ddot{a}a + \dot{a}^2)\ln\left(\frac{b}{a}\right) + \frac{a^2\dot{a}^2}{2}\left(\frac{1}{b^2} - \frac{1}{a^2}\right)\right]. \qquad (14)$$

In the elastic region $b \le r \le d$ we assume the material to be compressible elastic and employ the similarity solution given by Forrestal et al. (1990). The similarity solution requires the cavity to expand from a zero initial radius at a constant velocity $\dot{a}$ (i.e., $\ddot{a} \equiv 0$). It is assumed that displacements are small in the elastic region; therefore, the convective term in (1*a*) can be neglected and the density can be assumed to be constant. Thus, (1*a*) can be expressed as

$$\frac{\partial^2 u}{\partial r^2} + \frac{1}{r}\frac{\partial u}{\partial r} - \frac{u}{r^2} = \frac{1}{c_d^2}\frac{\partial^2 u}{\partial t^2}, \qquad (15a)$$

where elastic stress-displacement relations have been employed and the elastic dilatational wave speed is given by

$$c_d^2 = \frac{E(1 - \nu)}{\rho(1 + \nu)(1 - 2\nu)}, \qquad (15b)$$

where ν is Poisson's ratio.

At the elastic-plastic interface we neglect strain-rate effects and take $Y_d = Y$ which was shown by Warren and Forrestal (1998) to have a negligible effect on the radial stress at the cavity surface for the spherical cavity expansion problem. Thus, the boundary conditions for the elastic region are $\sigma_r(b) - \sigma_\theta(b) = 2Y/\sqrt{3}$ at the elastic-plastic interface and zero displacement at the elastic wave front. Solving (15*a*) using a similarity solution (Forrestal et al., 1990) subject to the above boundary conditions gives the velocity and radial stress at the elastic plastic interface as

$$v(b) = \frac{2(1 + \nu)Y}{\sqrt{3E}}c \qquad (16a)$$

Downloaded 04 May 2010 to 171.66.16.27. Redistribution subject to ASME license or copyright; see http://www.asme.org/terms/Terms_Use.cfm

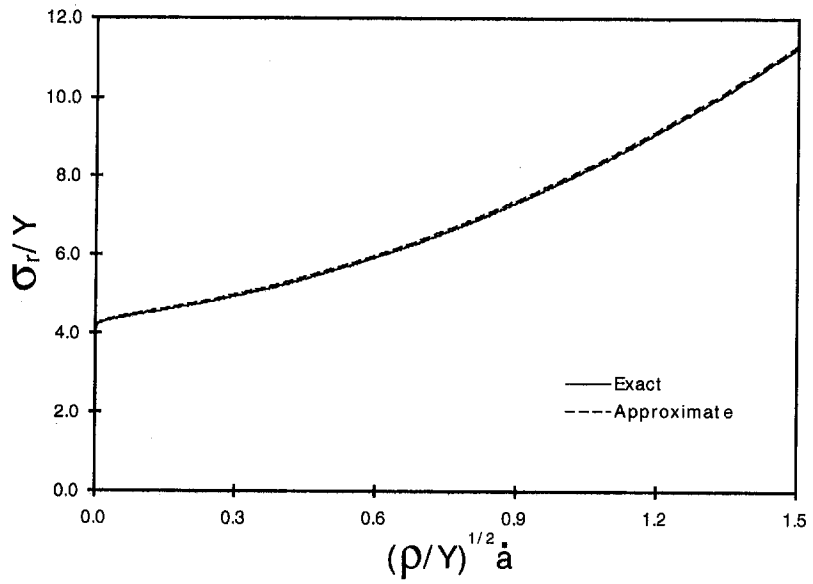


Fig. 2 Radial stress at the cavity surface versus cavity-expansion velocity obtained from the solutions given by Eqs. (18*a*) and (19)

$$\sigma_r(b) = \frac{Y}{\sqrt{3}}\left[1 + \frac{\lambda^2}{(1-2\nu)\sqrt{1-\lambda^2}}\ln\left(\frac{1+\sqrt{1-\lambda^2}}{\lambda}\right)\right], \tag{16b}$$

where $\lambda = c/c_d$. From the assumption of constant density, the stress and particle velocity are continuous across the elastic-plastic interface (Forrestal et al., 1990). Thus, using $a = \dot{a}t$, $b = ct$ and equating (16*a*) with (11) at $r = b$ gives the ratio

$$\frac{a}{b} = \left(\frac{2(1+\nu)Y}{\sqrt{3}E}\right)^{1/2}. \tag{17}$$

Using (16*b*) and (17) in (14) gives

$$\sigma_r(a) = \frac{Y}{\sqrt{3}}\left[1 + \left(\frac{E}{\sqrt{3}Y}\right)^n \times \int_0^{1-[2(1+\nu)Y/\sqrt{3}E]} \frac{[-\ln x]^n}{(1-x)[1+\psi\dot{a}^m(1-x)^m]^n}\,dx\right]$$

$$+ \frac{\rho\dot{a}^2}{2}\left[\frac{1}{(1-\nu)\sqrt{1-\lambda^2}}\ln\left(\frac{1+\sqrt{1-\lambda^2}}{\lambda}\right) - \ln\left(\frac{2(1+\nu)Y}{\sqrt{3}E}\right) + \left(\frac{2(1+\nu)Y}{\sqrt{3}E}\right) - 1\right] + \frac{\alpha}{\sqrt{3}m}\left(\frac{2\dot{a}}{\sqrt{3}a\dot{\epsilon}_o}\right)^m\left[1 - \left(\frac{2(1+\nu)Y}{\sqrt{3}E}\right)^m\right], \tag{18a}$$

where

$$\lambda = \left(\frac{\sqrt{3}(1-2\nu)\rho}{2(1-\nu)Y}\right)^{1/2}\dot{a}. \tag{18b}$$

The first term in (18*a*) corresponds to the strain hardening component of the solution, and in general the integral requires numerical integration using an open integration formula (Press et al., 1989). The second term in (18*a*) corresponds to the inertial part of the solution, and the last term accounts for the

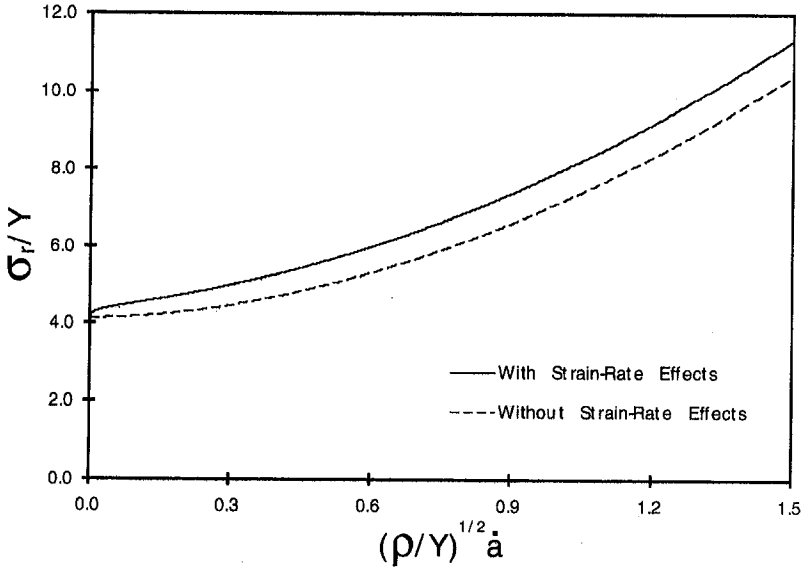


Fig. 3 Radial stress at the cavity surface versus cavity-expansion velocity obtained from Eq. (19) with and without strain-rate effects

Downloaded 04 May 2010 to 171.66.16.27. Redistribution subject to ASME license or copyright; see http://www.asme.org/terms/Terms_Use.cfm

strain-rate effects. The term $2(1 + \nu)Y/\sqrt{3}E$ in the inertial part of the solution accounts for the error in neglecting the convective term in the elastic solution and is generally negligible. It was shown by Warren and Forrestal (1998) that neglecting the dynamic effects in the integral of the first term in (18*a*) has a negligible effect on the radial stress at the cavity surface for the spherical cavity expansion problem. Thus, with the above simplifications (18*a*) reduces to

$$\sigma_r(a) = \frac{Y}{\sqrt{3}}\left[1 + \left(\frac{E}{\sqrt{3}Y}\right)^n \int_0^{1-[2(1+\nu)Y/\sqrt{3}E]} \frac{[-\ln x]^n}{(1-x)}\,dx\right] + \frac{\rho\dot{a}^2}{2}\left[\frac{1}{(1-\nu)\sqrt{1-\lambda^2}}\ln\left(\frac{1+\sqrt{1-\lambda^2}}{\lambda}\right) - \ln\left(\frac{2(1+\nu)Y}{\sqrt{3}E}\right) - 1\right] + \frac{\alpha}{\sqrt{3}m}\left(\frac{2\dot{a}}{\sqrt{3}a\dot{\epsilon}_o}\right)^m\left[1 - \left(\frac{2(1+\nu)Y}{\sqrt{3}E}\right)^m\right], \quad (19)$$

where now the rate dependence is confined entirely to the last term; therefore, the solution in (19) consists of three uncoupled effects: (*a*) a quasi-static strain-hardening term, (*b*) inertial terms, and (*c*) a strain-rate term.

In this solution the strain-rate term introduces a length scale which is the cavity radius. Thus, a similarity transformation is not possible in the plastic region as done by Forrestal et al. (1990).

Numerical Results and Conclusions

Numerical results are presented for 6061-T6511 aluminum. The constitutive equation constants in (5) for this material are given by Warren and Forrestal (1998) as $E = 68.9$ GPa, $Y = 276$ MPa, $n = 0.072$, $\alpha = 32.0$ MPa, $\dot{\epsilon}_o = 1000\ s^{-1}$, and $m = 0.348$. The density and Poisson's ratio of the aluminum are taken as $\rho = 2710$ kg/m^3, and $\nu = \frac{1}{3}$, respectively, and the cavity radius is taken to be $a = 3.55$ mm which corresponds to the projectile shank radius in Warren and Forrestal (1998).

Figure 2 compares the radial stresses at the cavity surface as a function of cavity-expansion velocity which are obtained from (18*a*) and (19). This result illustrates that (19) provides an excellent approximation, and indicates that strain rate does not have a significant effect on the strain-hardening term in the solution.

Figure 3 compares the radial stresses at the cavity surface as a function of cavity-expansion velocity obtained from (19) with and without strain-rate effects. This result indicates that the strain rate effect increases the radial stress for a given velocity by around ten percent for this particular cylindrical cavity-expansion problem.

Acknowledgments

This work was supported by the United States Department of Energy and the Joint DoD/DOE Munitions Technology Development Program. Sandia is a multiprogram laboratory operated by Sandia Corporation, a Lockheed Martin Company, for the United States Department of Energy under Contract DE-AC04-94AL85000. The author also gratefully acknowledges numerous discussions with M. J. Forrestal and D. A. Mosher.

References

Chakrabarty, J., 1987, *Theory of Plasticity*, McGraw-Hill, New York.

Crozier, R. J. M., and Hunter, S. C., 1970, "Similarity solution for the rapid uniform expansion of a cylindrical cavity in a compressible elastic-plastic solid," *Quarterly J. Mech. Appl. Math.*, Vol. 23, No. 3, pp. 349–363.

Forrestal, M. J., Luk, V. K., and Brar, N. S., 1990, "Perforation of aluminum plates with conical-nose projectiles," *Mech. Mater.*, Vol. 10, pp. 97–105.

Hill, R., 1950, *The Mathematical Theory of Plasticity*, Oxford University Press, London.

Mosher, D. A., 1996, "Results from 6061-T6511 aluminum and 4340 steel testing," private communication, Sandia National Laboratories, Livermore, CA.

Press, W. H., Flannery, B. P., Teukolsky, S. A., and Vetterling, W. T., 1989, *Numerical Recipes, The Art of Scientific Computing*, Cambridge University Press, Cambridge, UK.

Warren, T. L., and Forrestal, M. J., 1998, "Effects of strain hardening and strain-rate sensitivity on the penetration of aluminum targets with spherical-nosed rods," *Int. J. Solids Structures*, Vol. 35, Nos. 28–29, pp. 3737–3753.

Yadav, S., Chichili, D. R., and Ramesh, K. T., 1995, "The mechanical response of a 6061-T6 Al/Al_2O_3 metal matrix composite at high rates of deformation," *Acta Metall. Mater.*, Vol. 43, No. 12, pp. 4453–4464.

An Axisymmetric Interface Edge of Bonded Transversely Isotropic Piezoelectric Materials Under Torsion

Y.-H. Liu,[1] J.-Q. Xu,[2] and H.-J. Ding[3]

1 Introduction

During the past decades, axisymmetric interface edges of bonded dissimilar isotropic materials with particular geometrical shapes under torsion have been examined by many researchers (such as Westmann, 1968; Keer and Freeman, 1970; Prasad and Chatterjee, 1973; Erdogan and Ozbek, 1970; Erdogan and Gupta, 1973; Tsuji et al., 1991) due to their wide applications in engineering. However, there is no study on a general axisymmetric interface edge under torsion. Furthermore, piezoelectric materials have found wide technological applications as transducers, sensors, and actuators. The electric and mechanical properties of piezoelectric materials may be affected by defects such as cracks. Some studies on bonded dissimilar piezoelectric materials in the context of plane elasticity have been reported (such as Beom and Atluri, 1996). In this brief note, a general axisymmetric interface edge of bonded transversely isotropic piezoelectric materials under torsion, shown in Fig. 1, is analyzed. This model may have a wide range of applications for composite materials provided that the interface angle and joining angles, as well as materials, are selected appropriately (see Liu et al., 1999).

2 Basic Equations

Let the axisymmetric axis, z-axis, be perpendicular to the transversely isotropic plane in the cylindrical coordinate system (ρ, ψ, z), as shown in Fig. 1. Based on the general solution to the axisymmetric torsion problem of a transversely isotropic piezoelectric material (Ding et al., 1996), and using a method similar to the method described in our previous paper (Liu et al., 1999), we obtain the following nontrivial displacement $u_{\psi m}$, stresses $\tau_{r\psi m}$ and $\tau_{\psi\theta m}$ as well as electric displacement $D_{\psi m}$ near the interface edge O' inside the material $m (m = 1, 2)$, expressed in the coordinate system (r, ψ, θ)

$$u_{\psi m} = r^{\lambda} R_m^{\lambda-1}[A_m(f_{1m}\sin\theta_{sm} + f_{2m}\cos\theta_{sm}) + B_m(f_{1m}\cos\theta_{sm} - f_{2m}\sin\theta_{sm})],$$

[1] Associate Professor, Department of Applied Mathematics and Mechanics, Hefei University of Polytechnic, Hefei 230009, P. R. China.

[2] Professor, Department of Mechanics, Zhejiang University, Hangzhou 310027, P. R. China.

[3] Professor, Department of Civil Engineering, Zhejiang University, Hangzhou 310027, P. R. China.

Contributed by the Applied Mechanics Division of THE AMERICAN SOCIETY OF MECHANICAL ENGINEERS for publication in the ASME JOURNAL OF APPLIED MECHANICS. Manuscript received by the ASME Applied Mechanics Division, July 28, 1998; final revision, Mar. 16, 1999. Associate Technical Editor: M.-J. Pindera.

Downloaded 04 May 2010 to 171.66.16.27. Redistribution subject to ASME license or copyright; see http://www.asme.org/terms/Terms_Use.cfm

strain-rate effects. The term $2(1 + \nu)Y/\sqrt{3}E$ in the inertial part of the solution accounts for the error in neglecting the convective term in the elastic solution and is generally negligible. It was shown by Warren and Forrestal (1998) that neglecting the dynamic effects in the integral of the first term in (18*a*) has a negligible effect on the radial stress at the cavity surface for the spherical cavity expansion problem. Thus, with the above simplifications (18*a*) reduces to

$$\sigma_r(a) = \frac{Y}{\sqrt{3}}\left[1 + \left(\frac{E}{\sqrt{3}Y}\right)^n \int_0^{1-[2(1+\nu)Y/\sqrt{3}E]} \frac{[-\ln x]^n}{(1-x)}\,dx\right] + \frac{\rho\dot{a}^2}{2}\left[\frac{1}{(1-\nu)\sqrt{1-\lambda^2}}\ln\left(\frac{1+\sqrt{1-\lambda^2}}{\lambda}\right) - \ln\left(\frac{2(1+\nu)Y}{\sqrt{3}E}\right) - 1\right] + \frac{\alpha}{\sqrt{3}m}\left(\frac{2\dot{a}}{\sqrt{3}a\dot{\epsilon}_o}\right)^m\left[1 - \left(\frac{2(1+\nu)Y}{\sqrt{3}E}\right)^m\right], \quad (19)$$

where now the rate dependence is confined entirely to the last term; therefore, the solution in (19) consists of three uncoupled effects: (*a*) a quasi-static strain-hardening term, (*b*) inertial terms, and (*c*) a strain-rate term.

In this solution the strain-rate term introduces a length scale which is the cavity radius. Thus, a similarity transformation is not possible in the plastic region as done by Forrestal et al. (1990).

Numerical Results and Conclusions

Numerical results are presented for 6061-T6511 aluminum. The constitutive equation constants in (5) for this material are given by Warren and Forrestal (1998) as $E = 68.9$ GPa, $Y = 276$ MPa, $n = 0.072$, $\alpha = 32.0$ MPa, $\dot{\epsilon}_o = 1000\ s^{-1}$, and $m = 0.348$. The density and Poisson's ratio of the aluminum are taken as $\rho = 2710$ kg/m^3, and $\nu = \frac{1}{3}$, respectively, and the cavity radius is taken to be $a = 3.55$ mm which corresponds to the projectile shank radius in Warren and Forrestal (1998).

Figure 2 compares the radial stresses at the cavity surface as a function of cavity-expansion velocity which are obtained from (18*a*) and (19). This result illustrates that (19) provides an excellent approximation, and indicates that strain rate does not have a significant effect on the strain-hardening term in the solution.

Figure 3 compares the radial stresses at the cavity surface as a function of cavity-expansion velocity obtained from (19) with and without strain-rate effects. This result indicates that the strain rate effect increases the radial stress for a given velocity by around ten percent for this particular cylindrical cavity-expansion problem.

Acknowledgments

This work was supported by the United States Department of Energy and the Joint DoD/DOE Munitions Technology Development Program. Sandia is a multiprogram laboratory operated by Sandia Corporation, a Lockheed Martin Company, for the United States Department of Energy under Contract DE-AC04-94AL85000. The author also gratefully acknowledges numerous discussions with M. J. Forrestal and D. A. Mosher.

References

Chakrabarty, J., 1987, *Theory of Plasticity*, McGraw-Hill, New York.

Crozier, R. J. M., and Hunter, S. C., 1970, "Similarity solution for the rapid uniform expansion of a cylindrical cavity in a compressible elastic-plastic solid," *Quarterly J. Mech. Appl. Math.*, Vol. 23, No. 3, pp. 349–363.

Forrestal, M. J., Luk, V. K., and Brar, N. S., 1990, "Perforation of aluminum plates with conical-nose projectiles," *Mech. Mater.*, Vol. 10, pp. 97–105.

Hill, R., 1950, *The Mathematical Theory of Plasticity*, Oxford University Press, London.

Mosher, D. A., 1996, "Results from 6061-T6511 aluminum and 4340 steel testing," private communication, Sandia National Laboratories, Livermore, CA.

Press, W. H., Flannery, B. P., Teukolsky, S. A., and Vetterling, W. T., 1989, *Numerical Recipes, The Art of Scientific Computing*, Cambridge University Press, Cambridge, UK.

Warren, T. L., and Forrestal, M. J., 1998, "Effects of strain hardening and strain-rate sensitivity on the penetration of aluminum targets with spherical-nosed rods," *Int. J. Solids Structures*, Vol. 35, Nos. 28–29, pp. 3737–3753.

Yadav, S., Chichili, D. R., and Ramesh, K. T., 1995, "The mechanical response of a 6061-T6 Al/Al_2O_3 metal matrix composite at high rates of deformation," *Acta Metall. Mater.*, Vol. 43, No. 12, pp. 4453–4464.

An Axisymmetric Interface Edge of Bonded Transversely Isotropic Piezoelectric Materials Under Torsion

Y.-H. Liu,[1] J.-Q. Xu,[2] and H.-J. Ding[3]

1 Introduction

During the past decades, axisymmetric interface edges of bonded dissimilar isotropic materials with particular geometrical shapes under torsion have been examined by many researchers (such as Westmann, 1968; Keer and Freeman, 1970; Prasad and Chatterjee, 1973; Erdogan and Ozbek, 1970; Erdogan and Gupta, 1973; Tsuji et al., 1991) due to their wide applications in engineering. However, there is no study on a general axisymmetric interface edge under torsion. Furthermore, piezoelectric materials have found wide technological applications as transducers, sensors, and actuators. The electric and mechanical properties of piezoelectric materials may be affected by defects such as cracks. Some studies on bonded dissimilar piezoelectric materials in the context of plane elasticity have been reported (such as Beom and Atluri, 1996). In this brief note, a general axisymmetric interface edge of bonded transversely isotropic piezoelectric materials under torsion, shown in Fig. 1, is analyzed. This model may have a wide range of applications for composite materials provided that the interface angle and joining angles, as well as materials, are selected appropriately (see Liu et al., 1999).

2 Basic Equations

Let the axisymmetric axis, z-axis, be perpendicular to the transversely isotropic plane in the cylindrical coordinate system (ρ, ψ, z), as shown in Fig. 1. Based on the general solution to the axisymmetric torsion problem of a transversely isotropic piezoelectric material (Ding et al., 1996), and using a method similar to the method described in our previous paper (Liu et al., 1999), we obtain the following nontrivial displacement $u_{\psi m}$, stresses $\tau_{r\psi m}$ and $\tau_{\psi\theta m}$ as well as electric displacement $D_{\psi m}$ near the interface edge O' inside the material $m (m = 1, 2)$, expressed in the coordinate system (r, ψ, θ)

$$u_{\psi m} = r^{\lambda} R_m^{\lambda-1}[A_m(f_{1m}\sin\theta_{sm} + f_{2m}\cos\theta_{sm}) + B_m(f_{1m}\cos\theta_{sm} - f_{2m}\sin\theta_{sm})],$$

[1] Associate Professor, Department of Applied Mathematics and Mechanics, Hefei University of Polytechnic, Hefei 230009, P. R. China.

[2] Professor, Department of Mechanics, Zhejiang University, Hangzhou 310027, P. R. China.

[3] Professor, Department of Civil Engineering, Zhejiang University, Hangzhou 310027, P. R. China.

Contributed by the Applied Mechanics Division of THE AMERICAN SOCIETY OF MECHANICAL ENGINEERS for publication in the ASME JOURNAL OF APPLIED MECHANICS. Manuscript received by the ASME Applied Mechanics Division, July 28, 1998; final revision, Mar. 16, 1999. Associate Technical Editor: M.-J. Pindera.

Downloaded 04 May 2010 to 171.66.16.27. Redistribution subject to ASME license or copyright; see http://www.asme.org/terms/Terms_Use.cfm

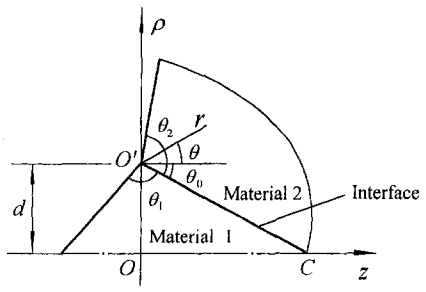


Fig. 1 General model of the axisymmetric interface edge

$$\tau_{r\psi m} = r^{\lambda-1}c_{66m}\lambda R_m^{\lambda-3}[A_m(f_{3m}\sin\theta_{sm} + f_{4m}\cos\theta_{sm}) + B_m(f_{3m}\cos\theta_{sm} - f_{4m}\sin\theta_{sm})]/4,$$

$$\tau_{\psi\theta m} = -r^{\lambda-1}c_{66m}\lambda R_m^{\lambda-3}[A_m(f_{5m}\sin\theta_{sm} - f_{6m}\cos\theta_{sm}) + B_m(f_{5m}\cos\theta_{sm} + f_{6m}\sin\theta_{sm})]/4,$$

$$D_{\psi m} = r^{\lambda-1}e_{15m}\lambda R_m^{\lambda-3}[A_m(f_{7m}\sin\theta_{sm} + f_{8m}\cos\theta_{sm}) + B_m(f_{7m}\cos\theta_{sm} - f_{8m}\sin\theta_{sm})]/2, \quad (1)$$

where $\lambda(0 < \lambda < 1)$ is an eigenvalue to be determined, A_m and B_m are coefficients to be determined, $\theta_{sm} = (\lambda + 1)\tan^{-1}(s_m^{-1}\tan\theta)$, $s_m = (c_{66m}/c_{44m})^{1/2}$,

$$R_m = [1 + (s_m^2 - 1)\cos^2\theta]^{1/2}, \quad f_{1+km} = s_m^k \sin(\theta + k\pi/2),$$

$$f_{3+2km} = 4\sin(\theta + k\pi/2)[1 - (-1)^k(s_m^2 - 1)\cos^2\theta],$$

$$f_{4+2km} = 4s_m\cos(\theta - k\pi/2)[1 - (-1)^k(s_m^{-2} - 1)\sin^2\theta],$$

$$f_{7m} = 2s_m^2\sin 2\theta, \quad f_{8m} = 2s_m[(s_m^2 + 1)\cos^2\theta - 1], \quad (k = 0, 1), \quad (2)$$

e_{15m} is the piezoelectric constant, c_{44m} and c_{66m} are the elastic stiffness constants.

3 Singularity at the Interface Edge

In the coordinate system (r, ψ, θ), the continuity conditions on the interface $O'C$ and the free boundary conditions can be represented as

$$u_{\psi 1}(r, -\theta_0) = u_{\psi 2}(r, -\theta_0),$$

$$\tau_{\psi\theta 1}(r, -\theta_0) = \tau_{\psi\theta 2}(r, -\theta_0), \quad (3)$$

$$\tau_{\psi\theta 1}[r, -(\theta_1 + \theta_0)] = \tau_{\psi\theta 2}(r, \theta_2 - \theta_0) = 0. \quad (4)$$

Since $D_{\theta 1} = D_{\theta 2} = 0$, the continuity and boundary conditions of the electric displacements are satisfied automatically.

Substituting (1) into (3) and (4), a system of four homogeneous linear algebraic equations can be obtained for the four unknown coefficients A_m and B_m $(m = 1, 2)$. The nontrivial solution condition leads to the following characteristic equation for λ:

$$(\Gamma s_1 p_1 q_2 + s_2 p_2 q_1)\sin\tilde{\theta}_1\sin\tilde{\theta}_2 - (\Gamma s_1 p_2 q_1 + s_2 p_1 q_2)\cos\tilde{\theta}_1\cos\tilde{\theta}_2 - (\Gamma s_1 p_1 p_2 - s_2 q_1 q_2)\sin\tilde{\theta}_1\cos\tilde{\theta}_2 + (\Gamma s_1 q_1 q_2 - s_2 p_1 p_2)\cos\tilde{\theta}_1\sin\tilde{\theta}_2 = 0, \quad (5)$$

where $\Gamma = c_{662}/c_{661}$, $\tilde{\theta}_1 = \theta_{s11} - \theta_{s10}$, $\tilde{\theta}_2 = \theta_{s22} + \theta_{s20}$, $\theta_{s11} = \theta_{s1|\theta=\theta_1+\theta_0}$, $\theta_{s22} = \theta_{s2|\theta=\theta_2-\theta_0}$, $\theta_{sm0} = \theta_{sm|\theta=\theta_0}$,

$$p_m = s_m\sin\theta_m,$$

$$q_m = \{(s_m^2 + 1)\cos\theta_m + (s_m^2 - 1)\cos[\theta_m - (-1)^m 2\theta_0]\}/2. \quad (6)$$

It should be pointed out that the eigenvalue λ is related to the interface angle θ_0, the joining angles θ_1 and θ_2 as well as the composite elastic constants Γ and s_m. It can be noted that the piezoelectric constant e_{15m} and the distance between the interface edge O' and the z-axis (i.e., d) have no effect on the eigenvalue.

4 Fields Near the Interface Edge

The nonzero solutions of the aforementioned system of four homogeneous linear algebraic equations for λ can be obtained as follows:

$$A_1 = (F_{21}F_{42} - F_{11}F_{41})A, \quad A_2 = F_3F_{41}A,$$

$$B_1 = (F_{22}F_{41} + F_{12}F_{42})A, \quad B_2 = F_3F_{42}A, \quad (7)$$

where A is the only coefficient to be determined, and

$$F_{kn} = (\Gamma s_1 + s_2)[1 + (s_2^2 - 1)\cos^2\theta_0]^{(\lambda-1)/2} \times \sum_{i=1}^{2}\sum_{j=1}^{2}(-1)^{(i+n)(j-1)}T_{ij}\sin\{(\lambda + 1) \times [\theta_{s10} - (-1)^j\theta_{s20}] - (-1)^j(k - i)\pi/2\},$$

$$F_3 = 2s_2[1 + (s_1^2 - 1)\cos^2\theta_0]^{(\lambda+1)/2},$$

$$F_{4k} = \sin(\theta_2 - \theta_0)\sin[(\lambda + 1)\theta_{s22} + (k - 1)\pi/2] + s_2\cos(\theta_2 - \theta_0)\cos[(\lambda + 1)\theta_{s22} + (k - 1)\pi/2],$$

$$T_{1k} = \gamma^{2-k}\sin\theta_0[s_1 - (-1)^k s_2]\cos\theta_0,$$

$$T_{2k} = \gamma^{2-k}[\sin^2\theta_0 + (-1)^k s_1 s_2\cos^2\theta_0], (k, n = 1, 2), \quad (8)$$

in which γ is defined below,

$$\gamma = (\Gamma s_1 - s_2)/(\Gamma s_1 + s_2). \quad (9)$$

Here, $\gamma(-1 \le \gamma \le 1)$ is a composite parameter of bonded transversely isotropic bimaterials, which has similar meaning as the Dundurs' parameters α and β for the anisotropic bimaterials in plane elasticity problems (Beom and Atluri, 1995); hence it can be also called Dundurs' parameter of transversely isotropic bimaterials. It should be pointed out that the electric displacement has the same order of singularity as stresses in (1) although the singularity does not depend on the piezoelectric constant. Moreover, the electric displacement and stress fields can be described by the same intensity coefficient which is related to the coefficient A.

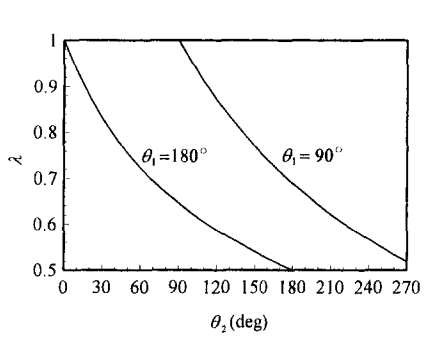


Fig. 2 Variation of eigenvalue λ with the joining angle θ_2 when the interface angle $\theta_0 = 0$

5 Results and Discussion

As an application of Eq. (5), some eigenvalues are given for the bonded piezoelectric ceramics PZT-4 ($c_{441} = 25.6$ GPa, $c_{661} = 30.6$ GPa, $e_{151} = 12.7$ C/m^2) and PZT-5 ($c_{442} = 35.3$ GPa, $c_{662} = 35.5$ GPa, $e_{152} = 17.0$ C/m^2), as shown in Figs. 2 and 3.

Downloaded 04 May 2010 to 171.66.16.27. Redistribution subject to ASME license or copyright; see http://www.asme.org/terms/Terms_Use.cfm

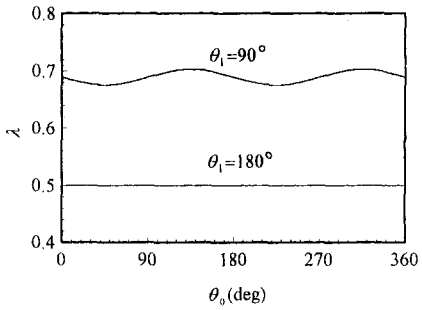


Fig. 3 Variation of eigenvalue λ with the joining angle θ_0 when the interface angle θ_2 = 180 deg

It is observed in Fig. 2 that there is no singularity in the region $0 < \theta_2 \leq 90$ deg when $\theta_0 = 0$ and $\theta_1 = 90$ deg. For interface cracks (i.e., $\theta_1 = \theta_2 = 180$ deg), the singularity is independent of the interface angle θ_0, as shown in Fig. 3.

For some particular geometries of interface edges defined by $\theta_0 = k\pi/2$ ($k = 0, 1, 2, 3$), the solution of Eq. (5) can be easily obtained as follows:

(1) $\theta_1 = \theta_2 = \pi/2$, there is no solution for λ in the open interval (0, 1);
(2) $\theta_1 = \pi/2$ and $\theta_2 = \pi$, $\lambda = 1 - \pi^{-1} \cos^{-1}[(1 + \gamma)/2]$;
(3) $\theta_1 = \pi/2$ and $\theta_2 = 3\pi/2$, $\lambda = 1 - \pi^{-1} \cos^{-1}(\gamma/2)$;
(4) $\theta_1 = \pi$ and $\theta_2 = \pi/2$, $\lambda = 1 - \pi^{-1} \cos^{-1}[(1 - \gamma)/2]$;
(5) $\theta_1 = \theta_2 = \pi$, $\lambda = \frac{1}{2}$;
(6) $\theta_1 = 3\pi/2$ and $\theta_2 = \pi/2$, $\lambda = \pi^{-1} \cos^{-1}(\gamma/2)$.

It is found that, with the exception of the first case, there is just one real eigenvalue for these particular geometries.

For the case of bonded isotropic bimaterials, taking $e_{15m} = 0$ and $c_{44m} = c_{66m} = \mu_m$ (μ is the shear modulus), Eq. (5) can be simplified to

$$\sin \lambda(\theta_1 + \theta_2) - \gamma \sin \lambda(\theta_1 - \theta_2) = 0, \qquad (10)$$

where $\gamma = (\mu_2 - \mu_1)/(\mu_2 + \mu_1)$. In this case, the singularity generally depends on the joining angles θ_1 and θ_2 as well as the Dundurs' parameter γ. However, it is independent of the material properties when $\theta_1 = \theta_2$ and it disappears when $\theta_1 = \theta_2 \leq \pi/2$. It can be easily proved that the eigenvalue λ of Eq. (10) is always real for all cases. Equation (10) coincides with the known results for some particular geometries (Westmann, 1968; Keer et al., 1970; Erdogan et al., 1970, 1973; Prasad et al., 1973; Tsuji et al., 1991).

Acknowledgments

This work was supported by the National Natural Science Foundation of China under Grant No. 19502011.

References

Beom, H. G., and Atluri, S. N., 1995, "Dependence of Stress on Elastic Constants in an Anisotropic Bimaterial Under Plane Deformation; and the Interfacial Crack," *Comp. Mech.* Vol. 16, pp. 106–113.

Beom, H. G., and Atluri, S. N., 1996, "Near-Tip Fields and Intensity Factors for Interfacial Cracks in Dissimilar Anisotropic Piezoelectric Media," *Int. J. Fract.,* Vol. 75, pp. 163–183.

Ding, H. J., Chen, B., and Liang, J., 1996, "General Solutions for Coupled Equations for Piezoelectric Media," *Int. J. Solids Struct.,* Vol. 33, pp. 2283–2298.

Erdogan, F., and Ozbek, T., 1970, "Shrink-Fit Cylinders Under Torsion," ASME JOURNAL OF APPLIED MECHANICS, Vol. 37, pp. 232–234.

Erdogan, F., and Gupta, G. D., 1973, "The Load Transfer Problem in Shafts Coupled Through a Sleeve," ASME JOURNAL OF APPLIED MECHANICS, Vol. 40, pp. 997–1003.

Keer, L. M., and Freeman, N. J., 1970, "Load Transfer Problem for an Embedded Shaft in Torsion," ASME JOURNAL OF APPLIED MECHANICS, Vol. 37, pp. 959–964.

Liu, Y. H., Xu, J. Q., and Ding, H. J., 1999, "Singular Stress Field Near Axisymmetric Interface Edge of Bonded Dissimilar Materials," ASME JOURNAL OF APPLIED MECHANICS, in press.

Prasad, S. N., and Chatterjee, S. N., 1973, "Load Transfer in Torsion of Compound Cylinders With a Cylindrical Crack," ASME JOURNAL OF APPLIED MECHANICS, Vol. 40, pp. 773–779.

Tsuji, T., Noda, N., Shibuya, T., and Koizumi, T., 1991, "Stress Singularity in Torsion Problem for Bonded Bars," *Int. J. Solids Struct.,* Vol. 27, pp. 1059–1071.

Westmann, R. A., 1968, discussion. ASME JOURNAL OF APPLIED MECHANICS, Vol. 35, pp. 197–198.

Downloaded 04 May 2010 to 171.66.16.27. Redistribution subject to ASME license or copyright; see http://www.asme.org/terms/Terms_Use.cfm

Journal of Applied Mechanics

Discussion

Hybrid Stochastic Finite Elements and Generalized Monte Carlo Simulation[1]

M. Ostoja-Starzewski.[2] This paper outlines a procedure for solution of stochastic partial differential equations that are the reason for generalizations of deterministic finite element methods into stochastic finite element methods (SFE). Such equations arise in continuum mechanics principally due to the randomness of the microstructure, which renders the constitutive coefficients (such as the Hooke's law) random fields. These random fields need to be set up on the basis of micromechanics analyses, whereby the most important facts to note are (Ostoja-Starzewski, 1993, 1994, 1998a, 1999):

(i) Except for the fundamental random field description of the (usually) highly fluctuating material microstructure, the random field (continuum) approximation, as dictated by the choice of a given finite element mesh, is necessarily dependent on the size of the finite element (FE) relative to the microscale of the given microstructure: the larger the FE size, the weaker the noise.

(ii) This random field approximation is *nonunique,* and strongly depends on the type of boundary conditions: The effective elastic response of an FE is bounded by the equivalent energy estimates of the Dirichlet and Neumann boundary value problems. These bounds are consistent with classical results of micromechanics, such as the Hashin-Shtrikman bounds (Ostoja-Starzewski and Schulte, 1996).

(iii) These two estimates, separately, provide inputs to two finite element schemes—based on minimum potential and complementary energy principles, respectively—for bounding the global response. While in the classical case of a homogeneous material, these bounds are convergent with the finite elements becoming infinitesimal, the finite size of an FE relative to the microscale prevents such a convergence in a random medium setting.

(iv) The actual response of any given realization of the material must fall between these two bounds (Ostoja-Starzewski and Wang, 1999).

(v) The approximating random fields have almost surely (i.e., with probability one) realizations that are locally anisotropic tensor fields.

The paper under discussion (just like the majority of other works in SFE) overlooks these facts and postulates the random fields—and hence, the governing stochastic partial differential equations—on intuitive grounds, rather than from a mechanics standpoint. As a result, the method presented in this paper cannot claim to offer an actual solution to a random medium problem, because it is not clear how far (or how close) from (to) an actual response of the microstructure the obtained solution is. It is not even certain whether the computed response falls between the bounds mentioned in (iv). In a large measure, this is due to the assumption of the Karhunen-Loéve expansions for the random fields—a model whose connection to any type of material heterogeneity has not been clarified.

Finally, the author proposes a refinement of the mesh—this, in view of (i) and (ii) above, is correct only if the random field of material coefficients is changed according to the scale-dependence of constitutive laws pertinent to a given material (polycrystalline, granular, fiber-composite, cellular, etc.).

References

Ostoja-Starzewski, M., 1993, "Micromechanics as a Basis of Stochastic Finite Elements and Differences—An Overview," *Appl. Mech. Rev.,* Vol. 46 (11, Part 2), pp. S136–S147.

Ostoja-Starzewski, M., 1994, "Micromechanics as a Basis of Continuum Random Fields," *Appl. Mech. Rev.,* Vol. 47 (1, Part 2), pp. S221–S230.

Ostoja-Starzewski, M., 1998, "Random Field Models of Heterogeneous Materials," *Int. J. Solids Struct.,* Vol. 35, pp. 2429–2455.

Ostoja-Starzewski, M., 1999, "Microstructural Disorder, Mesoscale Finite Elements, and Macroscopic Response," *Proc. Roy. Soc. Lond. A,* Vol. 455, pp. 3189–3199.

Ostoja-Starzewski, M., and Schulte, J., 1996, "Bounding of Effective Thermal Conductivities of Multiscale Materials by Essential and Natural Boundary Conditions," *Phys. Rev. B.,* Vol. 54, pp. 278–285.

Ostoja-Starzewski, M., and Wang, X., 1999, "Stochastic Finite Elements as a Bridge Between Random Material Microstructure and Global Response," *Comp. Meth. Appl. Mech. Eng.,* Vol. 168, pp. 35–49.

Author's Closure[3]

I would first like to take this opportunity to thank Professor Ostoja-Starzewski for his careful comments on my paper. I will present this note in two parts. In the first part, I will try to address a misunderstanding that I believe Dr. Ostoja-Starzewski has with this particular paper, this will be followed in the second part by an evaluation of his comments in the more general context of finite element analysis of media whose properties have modeled as stochastic processes.

In a number of his publications, Dr. Ostoja-Starzewski has presented the Karhunen-Loeve expansion as an alternative to perturbation approaches, or approaches based on the Neumann expansion, or Monte Carlo simulation approaches. This is incorrect. Indeed, the Karhunen-Loeve expansion is simply an expansion of a stochastic process in terms of the eigenfunctions of its covariance function. This expansion can be used in conjunction with perturbation, Neumann expansions, or Monte Carlo simulations. It can also be used in conjunction with a weighted residual optimization as done in this paper. As far as the Karhunen-Loeve expansion is concerned, it is immaterial how the covariance function is ob-

[1] by R. Ghanem and published in the Dec. 1998 issue of the ASME Journal of Applied Mechanics, Vol. 65, pp. 1004–1009.

[2] Institute of Paper Science and Technology, and Georgia Institute of Technology, 500 10th Street, N.W., Atlanta, GA 30318-5794.

[3] Professor R. G. Ghanem, The Johns Hopkins University, 201 Latrobe Hall, Baltimore, MD 21218. e-mail: ghanem@jhu.edu.

 Copyright © 1999 by ASME

Downloaded 04 May 2010 to 171.66.16.27. Redistribution subject to ASME license or copyright; see http://www.asme.org/terms/Terms_Use.cfm

AS I REMEMBER[1]

by

O. C. Zienkiewicz

1 Introduction

It is a great pleasure and honor to be included in the distinguished list of recipients of the Stephen Timoshenko Medal. I would like to take this opportunity to thank the American Society of Mechanical Engineers and the various friends I have in it who must have been responsible for my selection.

Because of my age and my long involvement in the field I know personally, or have known, more than half of the previous recipients of this award. Indeed, the very first recipient and namesake of the award, Stephen Timoshenko, was one of these. We met in 1960 at Northwestern University when he visited one of his early doctoral students, much distinguished in the field, Prof. Nick Hetenyi. Both of these acquaintances are now gone, having worked long and contributed much to the subject of applied mechanics. In the long list of recipients, now departed, I find my own Ph.D. supervisor, Sir Richard Southwell, and an old adviser and friend, Prof. William Prager. Among those no longer here is another friend, James Lighthill. Though he received his medal as early as 1963, he was still healthy and fit this year. But many may not know that it is only a few months ago that he met his end—trying to swim round the Island of Sark in the Channel Islands, a feat much younger men would not attempt and which he, using his knowledge of the tides, previously accomplished more than once. I salute his courage and achievements.

2 Timoshenko: Teaching and Research

Though my first personal encounter with Stephen Timoshenko was in 1960, he was well known to me by that time. In my Ph.D. studies which started in 1943, his book, *Theory of Elasticity,* became by bible. At the outset of my study with Professors Pippard and Southwell I had to acquaint myself with the earlier numerical solutions produced in 1910 by J. F. Richardson. As that work used the Airy stress function to formulate the solution, some introduction to elasticity was clearly necessary. I had many gaps in my knowledge having just completed the very brief, two-year wartime degree at Imperial College. Therefore, after some unsuccessful encounters with various texts I followed the recommendation of a senior colleague and invested in Timoshenko's famous book which today still holds a privileged place in my library. That text solved my problem completely. In the first two chapters I found all that was needed and it was only his excellent presentation which made me read further.

This episode—and indeed later contact with the works of Timoshenko—made two important impressions on me. *First,* I realised that even quite complex ideas could be presented in a lucid form. This was most helpful to me later when I was compiling my own first book on the finite element method. Of course this was some 20 years later but I have always tried to follow the master by avoiding the alternative process, very popular among some scientific writers. They follow the maxim quite probably coined by a German philosopher, which simply said: *"Warum einfach machen wenn man auch kompliziert sein kann."*

Second, which perhaps took me longer to realize, was the fact that good teaching cannot be practised properly without underlying research. Certainly the example of Timoshenko provided an example for me when I became a young teacher.

The conflict between the two directions of teaching and research, still much discussed in academia, was originally the subject which I wanted to discuss in this talk—but, enough has been said on this matter. It was after reading Timoshenko's autobiography that I changed my mind and in true "plagiaristic" spirit I adopted his title for the present talk—*"As I Remember."* This will allow me (1) to reminisce a little on my own origins and (2) to discuss the development of my own research and how this led to my present involvement with the finite element method.

3 As I Remember—The Linking of Life's Strands

Timoshenko's autobiography was written in Paris in 1963 and was translated into English with his help five years later when he reached the ripe old age of 90. Reading this book was a most interesting experience, especially when I realized that our own life's strands were interlinked and even intersected on many occasions.

Timoshenko was born in the Ukraine in 1878, five years after the birth of my father. The places of their birth, as far as I can trace from the available atlases, were about 100 miles apart and each, a similar distance from Kiev. Both of them were citizens of Imperial Russia at the time of their birth but their nationalities were different. Timoshenko was basically Ukrainian and my father was Polish—both facts quite well recognised at that time when nationalities and citizenships were separate entities.

Though my father was a lawyer and Timoshenko and engineer, it is interesting to speculate whether their paths at one time or another crossed. Certainly, for a limited period, both of them lived in Kiev and it is also certain that during later years both were much involved with St. Petersburg where, after the Revolution, the first liberal, provisional, government in Russia was formed under the premiership of Kerenski.

It was during that provisional government time that the divergence of their paths occurred. My father, perhaps because of his English wife and knowledge of the English language, was chosen to be the Consul in England of Kerenski's provisional Russian government. However, my father was stranded and started a new life when the Bolshevik revolution erupted in Russia. It was in England that both my sister and I were born. Timoshenko, on the other hand, left Russia by a completely different route. This led him later, via Turkey and Serbia, to Zagreb in Croatia, where he became a professor at the Technical University for some time, before moving finally to the U.S.A. in 1922.

Those who read his autobiography will find full details of the adventures of his life at that time, and the story of his rise to fame in the American continent and indeed in Europe. He first established his position firmly as an engineer and teacher at Westinghouse, then became a professor at the University of Michigan in Ann Arbor in 1927. Finally, in 1936 he reached Stanford University. The Chair he held there became his last permanent employment although he finished his life in Switzerland—a country he had much loved in his younger days.

So how did our life strands interlink again? Well, I have already mentioned the importance of his text in producing my doctoral work under Professors Pippard and Southwell. It is through the work of the latter that the connection will arise again.

Professor (later Sir) Richard Southwell was, at the time of my doctorate studies, leading a research team concerned with the solution of finite difference equations in elasticity for various problems of realistic application. Indeed many of these problems were concerned with the war effort and therefore confidential. Others were not—like my own analysis of a dam—though the methodology was not publishable during the war. Even the proceedings of the Royal Society were at that time "confidential." It

[1] Acceptance speech given on November 19, 1998 on receipt of the S. Timoshenko Medal

 Copyright © 1999 by ASME

Downloaded 04 May 2010 to 171.66.16.27. Redistribution subject to ASME license or copyright; see http://www.asme.org/terms/Terms_Use.cfm

was then that I acquired a general interest, not only in elasticity, but also in fluid mechanics which to Sir Richard presented just one more problem to be dealt with by a general numerical procedure.

It happened that Southwell was one of Timoshenko's guests at the University of Michigan as early as 1935. This in turn led to a later encounter after the war in 1949 and again at Ann Arbor. At Timoshenko's invitation both were involved in a summer course and this meeting was to be more important. Certainly Timoshenko was always the engineer, and being at that stage engaged in the quantitative solution of problems, he was much impressed by the generality which was established by using numerical, finite difference solutions. I believe this caused him to write an extensive appendix when the second edition of his book, *Theory of Elasticity,* now co-authored by J. N. Goodier, appeared in 1951. This appendix included a full description of Southwell's procedures and solutions. He remained at all times a protagonist of numerical solutions and it was here that our interests began to overlap.

4 The Engineering Beginnings of Numerical Analysis

The first finite difference solutions of equations of elasticity dated back to the work of Runge in 1908 and Richardson in 1910. The latter indeed solved the problem of stress distribution in a gravity dam, a subject of much interest at the time in view of the construction of the Aswan Dam in Egypt. Indeed, during the same period, inconsistencies and difficulties of using standard "cantilever" approximations were realized and a true elastic solution was obviously needed to settle the controversy.

As Southwell's relaxation methods were available, Professor Pippard—my doctoral supervisor—set me the goal of providing a very accurate answer to the above question. I was eventually successful and in 1945 I duly handed in my thesis solving that problem, as well as others on meshes very much finer than those initially used by Richardson. The success was due to the use of relaxation methods but why were they so successful and wherein lay their magic?

It is my belief that the ideas introduced by Southwell which were of considerable importance could be summarized as

(i) the recognition that the finite difference equations could be made equivalent to an analogous discrete structural system, and
(ii) the solution of the structural discrete system could be performed most efficiently by an iterative process.

As is well known, discrete structural systems, which provide the basic work for all civil, aeronautical, and structural engineers, can be formulated using either the so-called "displacement" method or the "force" method. The first of these methods is obvious and direct, though it is well known that the second, the force method, is also useful in many simple cases of redundant structures for which it provides an economical and elegant solution. It is difficult to say who first formulated the direct displacement (or direct stiffness) approach. Certainly the method was well known at the beginning of this century and certainly it was included in the education of engineers in the 1930s. In this approach stiffness coefficients were obtained for each element of the structure and the system equation was obtained by a simple addition of such coefficients. Matrix ideas were useful in this process and certainly provided a shorthand. They were not, however, essential to the understanding or indeed to the solution of the equations. Fraser, Duncan, and Collar in the 1930s appeared to be the first to use matrices for such problems in structural engineering in the aeronautical industry.

The procedures used in the direct stiffness approach were precisely the same for many other engineering systems, typically those that occurred in the solution of pipe network systems or electric networks. In each of these exactly the same formulation applied and in all cases the procedures were the same. It is therefore worthwhile to talk about a *standard discrete system* in this context and we observe in the literature a rapid diffusion of ideas from one area of application to another.

Southwell's method of relaxation used for iterative solution of structures, or similar problems formulated in a discrete system, was a procedure he named "systematic relaxation of constraints" in 1934. In this process, each "nodal" displacement or similar system quantity was first assumed to be fixed in an arbitrary position by imaginary constraints (which he often described as "jacks"). On "relaxing" of such a constraint by removing the "jack," the load was transferred to adjacent nodes and the node in question then was displaced by an amount which was easily calculable. Obviously, in the continuing process of constraint relaxation the load transfer in the structure would ultimately lead to correct solutions when all the load was thus transferred to the supports.

Mathematically, of course, the procedure was carried out in a sequence similar to that of the Gauss-Seidel iteration, but in a manner guided by the user. However, the physical interpretation of the process made it very understandable and such methods as moving a whole group of nodes simultaneously, etc., could be used effectually by an intelligent operator to accelerate convergence.

The "structural" relaxation procedure of the Southwell type was apparently used as early as 1922 in Zagreb by a man called Calisev, (viz. Timoshenko). However, much more important was the development of the so-called "method of moment distribution" by Hardy Cross in the U.S.A. in 1932. This preceded the Southwell process by only two years but *the Hardy Cross Method* gained fame internationally and became the standard process for solution of framed buildings, etc., in the 1930s and 1940s.

It is of interest to make a marginal remark that there is a good reason for the success of the Hardy Cross moment distribution method vis-à-vis the Southwell relaxation method then applied to tension bar structures. The "carry over" factor in bending computations was one half rather than unity in bar structures and this of course led to a very much more rapid convergence.

When Southwell entered the area of finite difference computations he generally endowed the discrete equations with a structural interpretation. Thus the Poisson equation, which was well known could represent the deformation of stretched membrane, became in the finite difference net the deformation of a string net with given tensions. The string net being a simple structure could of course be solved by precisely the same procedures as Southwell applied earlier to actual discrete structures and thus the *Systematic Relaxation Constraints* of 1934 could be used again.

It is of interest to note that such a physical interpretation of finite difference equations, when used for elasticity, was simultaneously and independently derived in the U.S.A. The conditions of wartime secrecy and the resulting restrictions on exchange of documents prevented Southwell's work with this being widely known there. However, two important developments were derived in the U.S.A. The first one was arrived at by Hrenikoff who in 1941 established a so-called *framework analogy* to the finite difference equations of elasticity, and the second was arrived at by McHenry who in 1943 presented the *lattice analogy.* Clearly engineers liked this physical manner of interpreting equations which also simplified boundary conditions which were now purely physical. These analogue procedures were the precursors of the concept of *finite elements.*

In the classic paper of 1956, Turner, Clough, Martin, and Topp presented the idea of dividing the real continuum directly into *elements* of arbitrary shape and directly establishing their stiffness. This became known as the method of finite elements only in 1960, following a paper presented by Ray Clough. In the original work very explicit physical models were used, thus completely avoiding the writing down of either finite difference or differential equations.

Much later the finite element method was to become based on the use of variational or weighted residual procedures of Galerkin type applied directly to the differential equations used to model rationally the elements of a continuum. Though most engineers applied this initially to the elasticity equations, it must be remarked that Courant did this much earlier in 1943—i.e., precisely when Southwell, Hrenikoff, and McHenry were active. In his work he showed that such direct procedures could be used for the Poisson

Downloaded 04 May 2010 to 171.66.16.27. Redistribution subject to ASME license or copyright; see http://www.asme.org/terms/Terms_Use.cfm

equation. Courant introduced what is essentially the same linear triangle as that derived in 1956. Being, however, a mathematician he did not see the need nor did he have the desire to seek a physical interpretation. This perhaps accounts for the fact that his work was only unearthed several years after the mainstream engineers had been happily using the finite element procedure for solving their structural problems.

5 Is the Finite Element Method's Success due to its Intuitive Appeal or its Generality?

There is no doubt that it is the intuitive appeal of the finite element process which makes it so popular today. When in the late 1950s I met Ray Clough and for the first time encountered his idea of splitting a continuum into "physical lumps," the procedure did not appeal to me. Surely it all could be done more precisely and conveniently with finite processes I learned from Southwell and used successfully over many years? We did, however, agree that one problem remained which needed solution. That problem was *the analysis of shells of arbitrary shape* as these were much encountered at the time in the design of arch dams and in architectural flights of fancy.

The twin difficulties of the finite difference approach that I had been using were: (a) deciding which set of governing equations to use. Here the choice was wide with many authors contributing different approximations, and (b) establishing analytically the coordinates of an arbitrary shell in which the governing equations were to be approximated.

Both Ray and I agreed that here the finite element approach could well be used, employing as elements flat facets of a triangular or rectangular shape with the former of course being needed for arbitrary shells. In such a manner both difficulties could be simultaneously avoided.

For such a finite element formulation the "in-plane" stiffnesses were already well established and surely the corresponding bending stiffnesses based on the Kirchhoff thin plate theory could easily be added.

It was on these problems that Ray's and my own research students spent much time during the early 1960s. By 1965 both of the groups were successful and found suitable formulations for triangular plates. Two years later they established the possibility, and indeed were successful in solving arbitrarily shaped shells.

The thin shell modeling by flat facets proved convergent despite a few variational crimes committed on the way, but both the problem and its solution were overtaken by events which occurred in parallel.

My colleague, Bruce Irons, and myself also developed in 1965 the first three-dimensional solution using higher-order elements which could be curved by an isoparametric mapping to fit almost any shape. Clearly, by making such elements thin, any curved shell or plate could be modeled without introducing the superhuman efforts needed to establish C1 continuity or the necessity of introducing thin plate and shell theory assumptions.

This development resulted in the fact that by the end of the decade the thin plate and shell problem disappeared, being today largely of historical interest. But many difficulties still were encountered in establishing a robust formulation. I shall not dwell on them except to say that by the mid-1980s all of these were overcome.

Did intuition or mathematics drive the second development to success? Who knows? But without the proper and precise use of mathematics the present ease of dealing with thin wall structures would not exist.

Further, the developments of rational approaches to such new fields as those of fluid mechanics, electromagnetism, etc., would not be possible.

Which way should we direct our research now?

6 Which Way Now?

It is recognized by many that the finite element process of today is but a particular form of the weighted residual approach. The latter was classified well by Stephen Crandall in his excellent book of 1955, though the fundamentals were established by Galerkin somewhat earlier in 1915. (This occurred, I believe, in St. Petersburg and must have coincided with the time Stephen Timoshenko was there!)

The difference between the various approximation procedures which are today still used is that of the specific trial or weighting functions that are employed. Much of the research done today centers on finding better, newer, and more efficient designs.

Von Karman said:

"The scientist studies what is, the engineer creates what has never been."

Surely this requires more efficient analysis procedures to design what "never has been."

Charles H. Duell, commissioner of U.S. Office of Patents in 1899 mentioned at the time that

"Everything that can be invented has been invented."

I do not share this pessimistic view and I think we shall see many exciting developments in the coming years. It is evident that both applied mechanicians and mathematicians will continue to contribute to the numerical analysis field.

However, I have reservations about making predictions for the future, especially since in public speeches these may lead to such mistakes as the famous one of Thomas Watson, Chairman of IBM in 1943. His prediction was that

"I think there is a world market for maybe five computers."

. . . probably more than a trivial miscalculation.

This can only be rivalled, however, by a statement by the famous British scientist, Lord Kelvin, who was the President of the Royal Society in 1895 and apparently said:

"Heavier-than-air flying machines are impossible."

Perhaps silence on matters of predicting the future is golden—and here I shall rest.

Downloaded 04 May 2010 to 171.66.16.27. Redistribution subject to ASME license or copyright; see http://www.asme.org/terms/Terms_Use.cfm